

EDITOR IN CHIEF

Rudy J. M. Konings

*European Commission, Joint Research Centre,
Institute for Transuranium Elements, Karlsruhe, Germany*

SECTION EDITORS

Todd R. Allen

Department of Engineering Physics, University of Wisconsin, Madison, WI, USA

Roger E. Stoller

Materials Science and Technology Division, Oak Ridge National Laboratory, Oak Ridge, TN, USA

Shinsuke Yamanaka

Division of Sustainable Energy and Environmental Engineering, Graduate School of Engineering, Osaka University, Osaka, Japan

Elsevier
Radarweg 29, PO Box 211, 1000 AE Amsterdam, The Netherlands
The Boulevard, Langford Lane, Kidlington, Oxford OX5 1GB, UK
225 Wyman Street, Waltham, MA 02451, USA

Copyright © 2012 Elsevier Ltd. All rights reserved

The following articles are US Government works in the public domain and not subject to copyright:

Radiation Effects in UO₂

TRISO-Coated Particle Fuel Performance

Composite Fuel (cermet, cercler)

Metal Fuel-Cladding Interaction

No part of this publication may be reproduced, stored in a retrieval system or transmitted in any form or by any means electronic, mechanical, photocopying, recording or otherwise without the prior written permission of the publisher

Permissions may be sought directly from Elsevier's Science & Technology Rights Department in Oxford, UK: phone (+44) (0) 1865 843830; fax (+44) (0) 1865 853333; email: permissions@elsevier.com. Alternatively you can submit your request online by visiting the Elsevier web site at <http://elsevier.com/locate/permissions>, and selecting *Obtaining permission to use Elsevier material*

Notice

No responsibility is assumed by the publisher for any injury and/or damage to persons or property as a matter of products liability, negligence or otherwise, or from any use or operation of any methods, products, instructions or ideas contained in the material herein. Because of rapid advances in the medical sciences, in particular, independent verification of diagnoses and drug dosages should be made

British Library Cataloguing in Publication Data

A catalogue record for this book is available from the British Library

Library of Congress Catalog Number: 2011929343

ISBN (print): 978-0-08-056027-4

For information on all Elsevier publications
visit our website at books.elsevier.com

Cover image courtesy of Professor David Sedmidubský, The Institute of Chemical Technology, Prague

Printed and bound in Spain

12 13 14 15 16 10 9 8 7 6 5 4 3 2 1

Working together to grow
libraries in developing countries

www.elsevier.com | www.bookaid.org | www.sabre.org

ELSEVIER

BOOK AID
International

Sabre Foundation

Editorial: Gemma Mattingley

Production: Nicky Carter

EDITORS BIOGRAPHIES



Rudy Konings is currently head of the Materials Research Unit in the Institute for Transuranium Elements (ITU) of the Joint Research Centre of the European Commission. His research interests are nuclear reactor fuels and actinide materials, with particular emphasis on high temperature chemistry and thermodynamics. Before joining ITU, he worked on nuclear fuel-related issues at ECN (the Energy Research Centre of the Netherlands) and NRG (Nuclear Research and Consultancy Group) in the Netherlands. Rudy is editor of *Journal of Nuclear Materials* and is professor at the Delft University of Technology (Netherlands), where he holds the chair of 'Chemistry of the nuclear fuel cycle.'



Roger Stoller is currently a Distinguished Research Staff Member in the Materials Science and Technology Division of the Oak Ridge National Laboratory and serves as the ORNL Program Manager for Fusion Reactor Materials for ORNL. He joined ORNL in 1984 and is actively involved in research on the effects of radiation on structural materials and fuels for nuclear energy systems. His primary expertise is in the area of computational modeling and simulation. He has authored or coauthored more than 100 publications and reports on the effects of radiation on materials, as well as edited the proceedings of several international conferences.



Todd Allen is an Associate Professor in the Department of Engineering Physics at the University of Wisconsin – Madison since 2003. Todd's research expertise is in the area of materials-related issues in nuclear reactors, specifically radiation damage and corrosion. He is also the Scientific Director for the Advanced Test Reactor National Scientific User Facility as well as the Director for the Center for Material Science of Nuclear Fuel at the Idaho National Laboratory, positions he holds in conjunction with his faculty position at the University of Wisconsin.



Shinsuke Yamanaka is a professor in Division of Sustainable Energy and Environmental Engineering, Graduate School of Engineering, Osaka University since 1998. He has studied the thermophysics and thermochemistry of nuclear fuel and materials. His research for the hydrogen behavior in LWR fuel cladding is notable among his achievements and he received the Young Scientist Awards (1980) and the Best Paper Awards (2004) from Japan Atomic Energy Society. Shinsuke is the program officer of Japan Science and Technology Agency since 2005 and the visiting professor of Fukui University since 2009, and he is also the associate dean of Graduate School of Engineering, Osaka University since 2011.

PREFACE

There are essentially three primary energy sources for the billions of people living on the earth's surface: the sun, radioactivity, and gravitation. The sun, an enormous nuclear fusion reactor, has transmitted energy to the earth for billions of years, sustaining photosynthesis, which in turn produces wood and other combustible resources (biomass), and the fossil fuels like coal, oil, and natural gas. The sun also provides the energy that steers the climate, the atmospheric circulations, and thus 'fuelling' wind mills, and it is at the origin of photovoltaic processes used to produce electricity. Radioactive decay of primarily uranium and thorium heats the earth underneath us and is the origin of geothermal energy. Hot springs have been used as a source of energy from the early days of humanity, although it took until the twentieth century for the potential of radioactivity by fission to be discovered. Gravitation, a non-nuclear source, has been long used to generate energy, primarily in hydropower and tidal power applications.

Although nuclear processes are thus omnipresent, nuclear technology is relatively young. But from the moment scientists unraveled the secrets of the atom and its nucleus during the twentieth century, aided by developments in quantum mechanics, and obtained a fundamental understanding of nuclear fission and fusion, humanity has considered these nuclear processes as sources of almost unlimited (peaceful) energy. The first fission reactor was designed and constructed by Enrico Fermi in 1942 in Chicago, the CP1, based on the fission of uranium by neutron capture. After World War II, a rapid exploration of fission technology took place in the United States and the Union of Soviet Socialist Republics, and after the Atoms for Peace speech by Eisenhower at the United Nations Congress in 1954, also in Europe and Japan. A variety of nuclear fission reactors were explored for electricity generation and with them the fuel cycle. Moreover, the possibility of controlled fusion reactions has gained interest as a technology for producing energy from one of the most abundant elements on earth, hydrogen.

The environment to which materials in nuclear reactors are exposed is one of extremes with respect to temperature and radiation. Fuel pins for nuclear reactors operate at temperatures above 1000 °C in the center of the pellets, in fast reactor oxide fuels even above 2000 °C, whereas the effects of the radiation (neutrons, alpha particles, recoil atoms, fission fragments) continuously damage the material. The cladding of the fuel and the structural and functional materials in the fission reactor core also operate in a strong radiation field, often in a dynamic corrosive environment of the coolant at elevated temperatures. Materials in fusion reactors are exposed to the fusion plasma and the highly energetic particles escaping from it. Furthermore, in this technology, the reactor core structures operate at high temperatures. Materials science for nuclear systems has, therefore, been strongly focussed on the development of radiation tolerant materials that can operate in a wide range of temperatures and in different chemical environments such as aqueous solutions, liquid metals, molten salts, or gases.

The lifetime of the plant components is critical in many respects and thus strongly affects the safety as well as the economics of the technologies. With the need for efficiency and competitiveness in modern society, there is a strong incentive to improve reactor components or to deploy advanced materials that are continuously developed for improved performance. There are many examples of excellent achievements in this respect. For example, with the increase of the burnup of the fuel for fission reactors, motivated by improved economics and a more efficient use of resources, the Zircaloy cladding (a Zr–Sn alloy) of the fuel pins showed increased susceptibility to coolant corrosion, but within a relatively short period, a different zirconium-based alloy was developed, tested, qualified, and employed, which allowed reliable operation in the high burnup range.

Nuclear technologies also produce waste. It is the moral obligation of the generations consuming the energy to implement an acceptable waste treatment and disposal strategy. The inherent complication of radioactivity, the decay that can span hundreds of thousands of years, amplifies the importance of extreme time periods in the issue of corrosion and radiation stability. The search for storage concepts that can guarantee the safe storage and isolation of radioactive waste is, therefore, another challenging task for materials science, requiring a close examination of natural (geological) materials and processes.

The more than 50 years of research and development of fission and fusion reactors have undoubtedly demonstrated that the statement ‘technologies are enabled by materials’ is particularly true for nuclear technology. Although the nuclear field is typically known for its incremental progress, the challenges posed by the next generation of fission reactors (Generation IV) as well as the demonstration of fusion reactors will need breakthroughs to achieve their ambitious goals. This is being accompanied by an important change in materials science, with a shift of discovery through experiments to discovery through simulation. The progress in numerical simulation of the material evolution on a scientific and engineering scale is growing rapidly. Simulation techniques at the atomistic or meso scale (e.g., electronic structure calculations, molecular dynamics, kinetic Monte Carlo) are increasingly helping to unravel the complex processes occurring in materials under extreme conditions and to provide an insight into the causes and thus helping to design remedies.

In this context, *Comprehensive Nuclear Materials* aims to provide fundamental information on the vast variety of materials employed in the broad field of nuclear technology. But to do justice to the comprehensiveness of the work, fundamental issues are also addressed in detail, as well as the basics of the emerging numerical simulation techniques.

R. J. M. Konings

*European Commission, Joint Research Centre,
Institute for Transuranium Elements, Karlsruhe, Germany*

T. R. Allen

*Department of Engineering Physics,
Wisconsin University, Madison, WI, USA*

R. Stoller

*Materials Science and Technology Division,
Oak Ridge National Laboratory, Oak Ridge, TN, USA*

S. Yamanaka

*Division of Sustainable Energy and Environmental Engineering,
Graduate School of Engineering, Osaka University, Osaka, Japan*

FOREWORD

‘Nuclear materials’ denotes a field of great breadth and depth, whose topics address applications and facilities that depend upon nuclear reactions. The major topics within the field are devoted to the materials science and engineering surrounding fission and fusion reactions in energy conversion reactors. Most of the rest of the field is formed of the closely related materials science needed for the effects of energetic particles on the targets and other radiation areas of charged particle accelerators and plasma devices. A more complete but also more cumbersome descriptor thus would be ‘the science and engineering of materials for fission reactors, fusion reactors, and closely related topics.’ In these areas, the very existence of such technologies turns upon our capabilities to understand the physical behavior of materials. Performance of facilities and components to the demanding limits required is dictated by the capabilities of materials to withstand unique and aggressive environments. The unifying concept that runs through all aspects is the effect of radiation on materials. In this way, the main feature is somewhat analogous to the unifying concept of elevated temperature in that part of materials science and engineering termed ‘high-temperature materials.’

Nuclear materials came into existence in the 1950s and began to grow as an internationally recognized field of endeavor late in that decade. The beginning in this field has been attributed to presentations and discussions that occurred at the First and Second International Conferences on the Peaceful Uses of Atomic Energy, held in Geneva in 1955 and 1958. *Journal of Nuclear Materials*, which is the home journal for this area of materials science, was founded in 1959. The development of nuclear materials science and engineering took place in the same rapid growth time period as the parent field of materials science and engineering. And similarly to the parent field, nuclear materials draws together the formerly separate disciplines of metallurgy, solid-state physics, ceramics, and materials chemistry that were early devoted to nuclear applications. The small priesthood of first researchers in half a dozen countries has now grown to a cohort of thousands, whose home institutions are anchored in more than 40 nations.

The prodigious work, ‘*Comprehensive Nuclear Materials*,’ captures the essence and the extensive scope of the field. It provides authoritative chapters that review the full range of endeavor. In the present day of glance and click ‘reading’ of short snippets from the internet, this is an old-fashioned book in the best sense of the word, which will be available in both electronic and printed form. All of the main segments of the field are covered, as well as most of the specialized areas and subtopics. With well over 100 chapters, the reader finds thorough coverage on topics ranging from fundamentals of atom movements after displacement by energetic particles to testing and engineering analysis methods of large components. All the materials classes that have main application in nuclear technologies are visited, and the most important of them are covered in exhaustive fashion. Authors of the chapters are practitioners who are at the highest level of achievement and knowledge in their respective areas. Many of these authors not only have lived through a substantial part of the history sketched above, but they themselves are the architects. Without those represented here in the author list, the field would certainly be a weaker reflection of itself. It is no small feat that so many of my distinguished colleagues could have been persuaded to join this collective endeavor and to make the real sacrifices entailed in such time-consuming work. I congratulate the Editor, Rudy Konings, and

the Associate Editors, Roger Stoller, Todd Allen, and Shinsuke Yamanaka. This book will be an important asset to young researchers entering the field as well as a valuable resource to workers engaged in the enterprise at present.

Dr. Louis K. Mansur
Oak Ridge, Tennessee, USA

Permission Acknowledgments

The following material is reproduced with kind permission of Cambridge University Press

Figure 15 of Oxide Dispersion Strengthened Steels

Figure 15 of Minerals and Natural Analogues

Table 10 of Spent Fuel as Waste Material

Figure 21b of Radiation-Induced Effects on Microstructure

www.cambridge.org

The following material is reproduced with kind permission of American Chemical Society

Figure 2 of Molten Salt Reactor Fuel and Coolant

Figure 22 of Molten Salt Reactor Fuel and Coolant

Table 9 of Molten Salt Reactor Fuel and Coolant

Figure 6 of Thermodynamic and Thermophysical Properties of the Actinide Nitrides

www.acs.org

The following material is reproduced with kind permission of Wiley

Table 3 of Properties and Characteristics of SiC and SiC/SiC Composites

Table 4 of Properties and Characteristics of SiC and SiC/SiC Composites

Table 5 of Properties and Characteristics of SiC and SiC/SiC Composites

Figure 5 of Advanced Concepts in TRISO Fuel

Figure 6 of Advanced Concepts in TRISO Fuel

Figure 30 of Material Performance in Supercritical Water

Figure 32 of Material Performance in Supercritical Water

Figure 19 of Tritium Barriers and Tritium Diffusion in Fusion Reactors

Figure 9 of Waste Containers

Figure 13 of Waste Containers

Figure 21 of Waste Containers

Figure 11 of Carbide Fuel

Figure 12 of Carbide Fuel

Figure 13 of Carbide Fuel

Figure 4 of Thermodynamic and Thermophysical Properties of the Actinide Nitrides

Figure 2 of The U–F system

Figure 18 of Fundamental Point Defect Properties in Ceramics

Table 1 of Fundamental Point Defect Properties in Ceramics

Figure 17 of Radiation Effects in SiC and SiC–SiC

Figure 21 of Radiation Effects in SiC and SiC–SiC

Figure 6 of Radiation Damage in Austenitic Steels

Figure 7 of Radiation Damage in Austenitic Steels

Figure 17 of Ceramic Breeder Materials

Figure 33a of Carbon as a Fusion Plasma-Facing Material

Figure 34 of Carbon as a Fusion Plasma-Facing Material

Figure 39 of Carbon as a Fusion Plasma-Facing Material

Figure 40 of Carbon as a Fusion Plasma-Facing Material

Table 5 of Carbon as a Fusion Plasma-Facing Material

www.wiley.com

The following material is reproduced with kind permission of Springer

Figure 4 of Neutron Reflector Materials (Be, Hydrides)

Figure 6 of Neutron Reflector Materials (Be, Hydrides)

Figure 1 of Properties and Characteristics of SiC and SiC/SiC Composites

Figure 3 of Properties and Characteristics of SiC and SiC/SiC Composites

Figure 4 of Properties and Characteristics of SiC and SiC/SiC Composites

Figure 5 of Properties and Characteristics of SiC and SiC/SiC Composites

Figure 6 of Properties and Characteristics of SiC and SiC/SiC Composites

Figure 7 of Properties and Characteristics of SiC and SiC/SiC Composites

Figure 8 of Properties and Characteristics of SiC and SiC/SiC Composites

Figure 9 of Properties and Characteristics of SiC and SiC/SiC Composites

Figure 10 of Properties and Characteristics of SiC and SiC/SiC Composites

Figure 11 of Properties and Characteristics of SiC and SiC/SiC Composites

Figure 12 of Properties and Characteristics of SiC and SiC/SiC Composites

Figure 22d of Fission Product Chemistry in Oxide Fuels

Figure 3 of Behavior of LWR Fuel During Loss-of-Coolant Accidents

Figure 14a of Irradiation Assisted Stress Corrosion Cracking

Figure 14b of Irradiation Assisted Stress Corrosion Cracking

Figure 14c of Irradiation Assisted Stress Corrosion Cracking

Figure 25a of Irradiation Assisted Stress Corrosion Cracking

Figure 25b of Irradiation Assisted Stress Corrosion Cracking

Figure 1 of Properties of Liquid Metal Coolants

Figure 5b of Fast Spectrum Control Rod Materials

Figure 3 of Oxide Fuel Performance Modeling and Simulations

Figure 8 of Oxide Fuel Performance Modeling and Simulations

Figure 10 of Oxide Fuel Performance Modeling and Simulations

Figure 11 of Oxide Fuel Performance Modeling and Simulations

Figure 14 of Oxide Fuel Performance Modeling and Simulations

Figure 5 of Thermodynamic and Thermophysical Properties of the Actinide Nitrides

Figure 51 of Phase Diagrams of Actinide Alloys

Figure 6 of Thermodynamic and Thermophysical Properties of the Actinide Oxides

Figure 7b of Thermodynamic and Thermophysical Properties of the Actinide Oxides

Figure 9b of Thermodynamic and Thermophysical Properties of the Actinide Oxides

Figure 35 of Thermodynamic and Thermophysical Properties of the Actinide Oxides

Table 11 of Thermodynamic and Thermophysical Properties of the Actinide Oxides

Table 13 of Thermodynamic and Thermophysical Properties of the Actinide Oxides

Table 17 of Thermodynamic and Thermophysical Properties of the Actinide Oxides

Figure 18 of Radiation Damage of Reactor Pressure Vessel Steels

Figure 7 of Radiation Damage Using Ion Beams

Figure 9b of Radiation Damage Using Ion Beams

Figure 28 of Radiation Damage Using Ion Beams

Figure 34 of Radiation Damage Using Ion Beams

Figure 35 of Radiation Damage Using Ion Beams

Figure 36d of Radiation Damage Using Ion Beams

Figure 37 of Radiation Damage Using Ion Beams

Table 3 of Radiation Damage Using Ion Beams

Figure 5 of Radiation Effects in UO_2
Figure 9a of *Ab Initio* Electronic Structure Calculations for Nuclear Materials
Figure 9b of *Ab Initio* Electronic Structure Calculations for Nuclear Materials
Figure 9c of *Ab Initio* Electronic Structure Calculations for Nuclear Materials
Figure 10a of *Ab Initio* Electronic Structure Calculations for Nuclear Materials
Figure 23 of Thermodynamic and Thermophysical Properties of the Actinide Carbides
Figure 25 of Thermodynamic and Thermophysical Properties of the Actinide Carbides
Figure 26 of Thermodynamic and Thermophysical Properties of the Actinide Carbides
Figure 27 of Thermodynamic and Thermophysical Properties of the Actinide Carbides
Figure 28a of Thermodynamic and Thermophysical Properties of the Actinide Carbides
Figure 28b of Thermodynamic and Thermophysical Properties of the Actinide Carbides
Figure 2 of Physical and Mechanical Properties of Copper and Copper Alloys
Figure 5 of Physical and Mechanical Properties of Copper and Copper Alloys
Figure 6 of The Actinides Elements: Properties and Characteristics
Figure 10 of The Actinides Elements: Properties and Characteristics
Figure 11 of The Actinides Elements: Properties and Characteristics
Figure 12 of The Actinides Elements: Properties and Characteristics
Figure 15 of The Actinides Elements: Properties and Characteristics
Table 1 of The Actinides Elements: Properties and Characteristics
Table 6 of The Actinides Elements: Properties and Characteristics
Figure 25 of Fundamental Properties of Defects in Metals
Table 1 of Fundamental Properties of Defects in Metals
Table 7 of Fundamental Properties of Defects in Metals
Table 8 of Fundamental Properties of Defects in Metals
www.springer.com

The following material is reproduced with kind permission of Taylor & Francis

Figure 9 of Radiation-Induced Segregation
Figure 6 of Radiation Effects in Zirconium Alloys
Figure 1 of Dislocation Dynamics
Figure 25 of Radiation Damage Using Ion Beams
Figure 26 of Radiation Damage Using Ion Beams
Figure 27 of Radiation Damage Using Ion Beams
Figure 4 of Radiation-Induced Effects on Material Properties of Ceramics (Mechanical and Dimensional)
Figure 7 of The Actinides Elements: Properties and Characteristics
Figure 20 of The Actinides Elements: Properties and Characteristics
Figure 18a of Primary Radiation Damage Formation
Figure 18b of Primary Radiation Damage Formation
Figure 18c of Primary Radiation Damage Formation
Figure 18d of Primary Radiation Damage Formation
Figure 18e of Primary Radiation Damage Formation
Figure 18f of Primary Radiation Damage Formation
Figure 1 of Radiation-Induced Effects on Microstructure
Figure 27 of Radiation-Induced Effects on Microstructure
Figure 5 of Performance of Aluminum in Research Reactors
Figure 2 of Atomic-Level Dislocation Dynamics in Irradiated Metals
Figure 3 of Atomic-Level Dislocation Dynamics in Irradiated Metals
Figure 5 of Atomic-Level Dislocation Dynamics in Irradiated Metals
Figure 10a of Atomic-Level Dislocation Dynamics in Irradiated Metals
Figure 10b of Atomic-Level Dislocation Dynamics in Irradiated Metals
Figure 10c of Atomic-Level Dislocation Dynamics in Irradiated Metals

Figure 10d of Atomic-Level Dislocation Dynamics in Irradiated Metals
Figure 12a of Atomic-Level Dislocation Dynamics in Irradiated Metals
Figure 12b of Atomic-Level Dislocation Dynamics in Irradiated Metals
Figure 12c of Atomic-Level Dislocation Dynamics in Irradiated Metals
Figure 12d of Atomic-Level Dislocation Dynamics in Irradiated Metals
Figure 16a of Atomic-Level Dislocation Dynamics in Irradiated Metals
Figure 16b of Atomic-Level Dislocation Dynamics in Irradiated Metals
Figure 16c of Atomic-Level Dislocation Dynamics in Irradiated Metals
Figure 16d of Atomic-Level Dislocation Dynamics in Irradiated Metals
Figure 16e of Atomic-Level Dislocation Dynamics in Irradiated Metals
Figure 17a of Atomic-Level Dislocation Dynamics in Irradiated Metals
Figure 17b of Atomic-Level Dislocation Dynamics in Irradiated Metals
Figure 17c of Atomic-Level Dislocation Dynamics in Irradiated Metals
Figure 17d of Atomic-Level Dislocation Dynamics in Irradiated Metals
www.taylorandfrancisgroup.com

2.01 The Actinides Elements: Properties and Characteristics

R. J. M. Konings, O. Beneš, and J.-C. Griveau

European Commission, Joint Research Centre, Institute for Transuranium Elements, Karlsruhe, Germany

© 2012 Elsevier Ltd. All rights reserved.

2.01.1	Introduction	1
2.01.2	Crystallographic Properties	2
2.01.2.1	Crystal Structure	2
2.01.2.2	Effects of Pressure	3
2.01.2.3	Effects of Temperature	4
2.01.2.4	Effects of Radiation	5
2.01.3	Thermodynamic Properties	7
2.01.3.1	Heat Capacity and Entropy of the Crystalline State	7
2.01.3.2	Heat Capacity of the Liquid State	10
2.01.3.3	Heat Capacity and Entropy of the Gaseous State	11
2.01.4	Thermophysical and Electronic Properties	12
2.01.4.1	Thermal Expansion and Density of the Crystalline State	12
2.01.4.2	Electrical Resistivity of the Crystalline State	12
2.01.4.3	Thermopower of the Crystalline State	14
2.01.4.4	Thermal Conductivity of the Crystalline State	15
2.01.4.5	Thermal Conductivity of the Liquid State	17
2.01.4.6	Density of the Liquid State	18
2.01.4.7	Viscosity	18
2.01.4.8	Surface Tension	18
2.01.5	Summary and Outlook	18
References		19

Abbreviations

dhcp	Double hexagonal close-packed
fcc	Face-centered cubic
IUPAC	International Union of Pure and Applied Chemistry
OECD/NEA	Organisation for Economic Cooperation and Development/ Nuclear Energy Agency

2.01.1 Introduction

The actinides are the 15 elements with atomic numbers 89–103 in the periodic system. The International Union of Pure and Applied Chemistry (IUPAC) has recommended that these elements are named actinoids (meaning ‘like actinium’), but this has never found general acceptance. In these elements, the 5f electron sub-shell is progressively filled, leading to the generalized

[Rn 7s²5f^{*n*}] configuration. Unlike the lanthanides, in which the 4f electrons lie in the interior of the xenon core region and thus hardly contribute to the chemical bonds (called ‘localized’), the 5f electrons show a much more diverse character, particularly in the metallic state.¹ The 5f electrons in the elements thorium to neptunium are placed in the valence shell (often called ‘itinerant’ or ‘delocalized’) and show substantial covalent bonding, whereas the 5f electrons in the elements americium to lawrencium are localized. Plutonium and americium have a transition position, showing both localized and delocalized behavior depending on temperature, pressure, and magnetic field.²

The actinides are radioactive elements, their isotopes having strongly variable half-lives. Owing to the short half-life, compared with the age of the earth, majority of the actinides have decayed and cannot be found in nature. Only the long-lived isotopes ²³²Th, ²³⁵U, and ²³⁸U are of primordial origin, and possibly ²⁴⁴Pu. Also, ²³¹Pa is found in very low concentrations in natural minerals (e.g., pitchblende ores), but it is a

product of the ^{235}U ($4n + 3$) decay chain.³ Most other actinides are man-made elements. They were synthesized by nuclear reactions using reactors and accelerators in the period 1940 (Np) to 1961 (Lr). The metals from Th to Cm are available in gram quantities that have allowed experimental determination of (some of) their physicochemical properties; Bk and Cf metals have been prepared in milligram quantities and Es in microgram quantities and therefore only limited investigations have been possible. The metals Fm and beyond have not been prepared in pure form.

The main technological relevance of the actinides is their use as fuel for nuclear fission reactors, particularly the nuclides ^{233}U , ^{235}U , and ^{239}Pu , which fission with thermal neutrons. ^{235}U and ^{239}Pu occur in the so-called U/Pu fuel cycle. ^{235}U is present in 0.7% in natural uranium; ^{239}Pu is formed when uranium is irradiated in a reactor as a result of neutron capture by ^{238}U . ^{233}U is formed by neutron capture of ^{232}Th in the Th/U fuel cycle. The vast majority of nuclear power reactors use oxide fuel, but carbide and nitride as well metallic alloys fuels have been studied since the early days of reactor development.⁴

In this chapter, we discuss the physicochemical properties of the actinide metals, with emphasis on the elements Th to Cm for which experimental data on bulk samples generally exist. The trends and systematics in the properties of the actinide series will be emphasized and compared with those of the 4f series. These physicochemical data are essential for understanding and describing the properties of multielement alloys (see **Chapter 2.05, Phase Diagrams of Actinide Alloys**) and actinide containing compounds (**Chapter 2.02, Thermodynamic and Thermophysical Properties of the Actinide Oxides**).

2.01.2 Crystallographic Properties

2.01.2.1 Crystal Structure

The stable crystallographic modifications of the actinides at atmospheric pressure are listed in **Table 1**. Compared to the lanthanide series in which the hexagonal close-packed (hcp) and the face-centered cubic (fcc) structures dominate, the actinide metals show a remarkable variation in the structural

Table 1 The crystal structure of the actinide metals

		Structure	Space group	a (pm)	b (pm)	c (pm)	Angle(s)	V_m (cm ³ mol ⁻¹)	ρ (g cm ⁻³)
Ac	α	Cubic	$Fm\bar{3}m$	531.5				22.59	10.05
Th	α	Cubic	$Fm\bar{3}m$	508.42				19.79	11.73
	β	Cubic	$Im\bar{3}m$	411				20.90	11.10
Pa	α	Tetragonal	$I4/mmm$	392.1		323.5		14.98	15.43
	β	Cubic	$Fm\bar{3}m$	501.8				19.02	12.15
U	α	Orthorhombic	$Cmcm$	285.4	587.0	495.5		12.50	19.05
	β	Tetragonal	^a	565.6		1075.9		12.95	18.37
	γ	Cubic	$Im\bar{3}m$	352.4				13.18	18.06
Np	α	Orthorhombic	$Pnma$	666.3	472.3	488.7		11.58	20.48
	β	Tetragonal	$P4_2$	489.7		338.8		11.79	20.11
	γ	Cubic	$Im\bar{3}m$	351.8				13.11	18.08
Pu	α	Monoclinic	$P2_1/n$	618.3	482.2	1096.3	$\beta = 101.79^\circ$	12.04	19.85
	β	Monoclinic	$I2/m$	928.4	1046.3	785.9	$\beta = 93.13^\circ$	13.50	17.71
	γ	Orthorhombic	$Fddd$	315.9	576.8	1016.2		13.94	17.15
	δ	Cubic	$Fm\bar{3}m$	463.71				15.01	15.92
	δ'	Tetragonal	$I4/mmm$	334		444		14.91	16.03
	ϵ	Cubic	$Im\bar{3}m$	363.61				14.48	16.51
Am	α	Hexagonal	$P6_3/mmc$	346.81		1124.1	$\gamma = 120^\circ$	17.63	13.67
	β	Cubic	$Fm\bar{3}m$	489.4				17.65	13.66
	γ	Cubic							
Cm	α	Hexagonal	$P6_3/mmc$	349.6		1113.3	$\gamma = 120^\circ$	17.74	13.76
	β	Cubic	$Fm\bar{3}m$	503.9				19.26	12.67
Bk	α	Hexagonal	$P6_3/mmc$	341.6		1106.9	$\gamma = 120^\circ$	16.84	14.79
Cf	α	Hexagonal	$P6_3/mmc$	338.4		1104.0	$\gamma = 120^\circ$	16.48	15.23
Es	α	Cubic	$Fm\bar{3}m$	575				28.62	8.88

^a $P4_2/mnm$, $P4_2/nm$ or $P4n2$.

Source: Edelstein, N. M.; Fuger, J.; Katz, J. J.; Morss, L. R. In *The Chemistry of the Actinide and Transactinide Elements*; Morss, L. R., Edelstein, N., Fuger, J., Katz, J. J., Eds.; Springer Verlag, 2006; Chapter 15, pp 1753–1835.

properties at room temperature, as shown in **Figure 1**. Particularly, the elements Pa–Pu have unusual low symmetry (distorted) crystal structures. α -Pa is body-centered tetragonal, and α -U and α -Np are orthorhombic but with slightly different space groups. α -Pu has a monoclinic crystal structure with 16 atoms in the unit cell at room temperature. Plutonium is unique in the periodic table of the elements with six allotropes at atmospheric pressure and one more at elevated pressure.

This complexity of the structural properties of the actinides is also evident from **Figure 2**, which shows the variation of the molar volume of the α -phases of the actinides at room temperature and atmospheric pressure, indicating that the actinides Pa to Pu follow the trend in the (itinerant) d -transition

metals, whereas the actinides Am to Bk follow that of the (localized) $4f$ metals. It is generally accepted that this complex behavior is due to the active role of the f -electron in the metallic bond and the changes in temperature and pressure by which the f -electron bonding character is affected. Experimental observations and electronic structure calculations have indeed shown that the bonding in the transition metals is dominated by d -electron contributions, that in the lanthanides there is a lack of f -electron contribution, and that the actinides fall in between.⁵

2.01.2.2 Effects of Pressure

Pressure is expected to drive the atoms in the crystal lattice closer to each other, forcing the electrons to

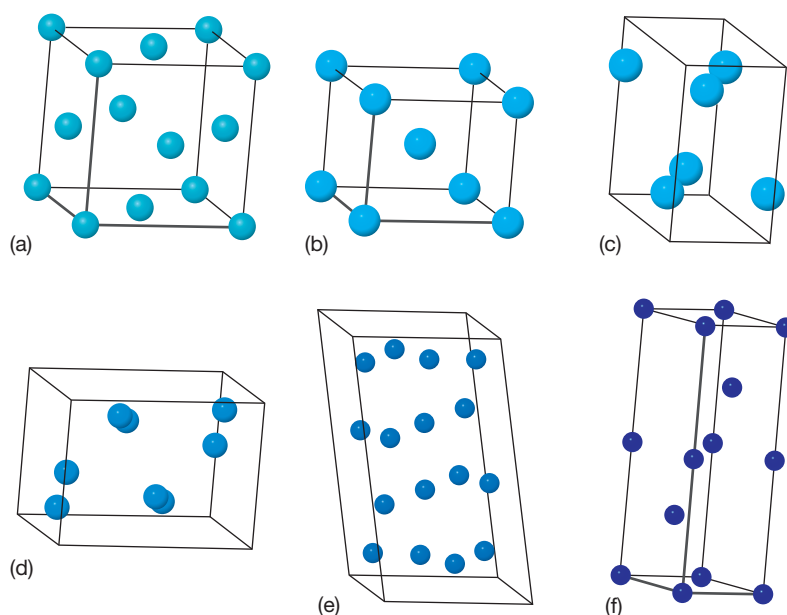


Figure 1 The crystal structures of the actinides at room temperatures: (a) α -Th, (b) α -Pa, (c) α -U, (d) α -Np, (e) α -Pu, (f) α -Am.

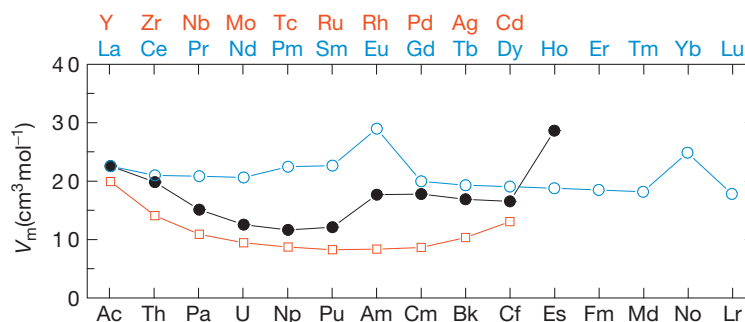


Figure 2 The molar volume of the actinide elements (●) compared with that of the lanthanides (○) and the 4d transition metals (□).

participate in the binding (delocalization),⁶ which particularly affects the heavy actinides with localized f-electron behavior at ambient pressure. Recent studies using diamond anvil cells coupled to synchrotron radiation have provided strong evidence for that. As discussed by Heathman *et al.*,⁷ americium shows a remarkable decrease in volume with increasing pressure (at ambient temperature) with three transitions up to 100 GPa (Figure 3). Its structure changes from hcp (Am-I) through fcc (Am-II) to orthorhombic (Am-III and Am-IV), indicating the appearance of the itinerant character 5f electrons. This behavior is also observed in curium, with a puzzling supplementary magnetically stabilized Cm-III structure at 40–60 GPa.⁸ Uranium shows a comparatively straightforward behavior and the α -structure is stable up to 100 GPa, with a much smaller volume decrease.⁶ A similar behavior has been found for protactinium, its α -form being stable up to

80 GPa. This is clearly reflected in the isothermal bulk modulus (Table 2), which is around 100 GPa for the elements Pa to Np but around 30–40 GPa for Am and Cm. The Am-IV phase shows a large bulk modulus (more similar to that of uranium), as expected for a metal with appreciable 5f-electron character in its bonding. This is also evident from the comparison of the actinide and lanthanide metals (Figure 4).

Uncertainty still exists about the bulk modulus of α -plutonium. As discussed by Ledbetter *et al.*,¹² the published B_0 values at ambient range show a large variation, as do the theoretical calculations. The most accurate results for the isothermal bulk modulus vary between 51(2) GPa¹³ and 43(2) GPa.¹⁴

2.01.2.3 Effects of Temperature

Detailed studies show that the crystal lattice of most actinide metals expands with increasing temperature

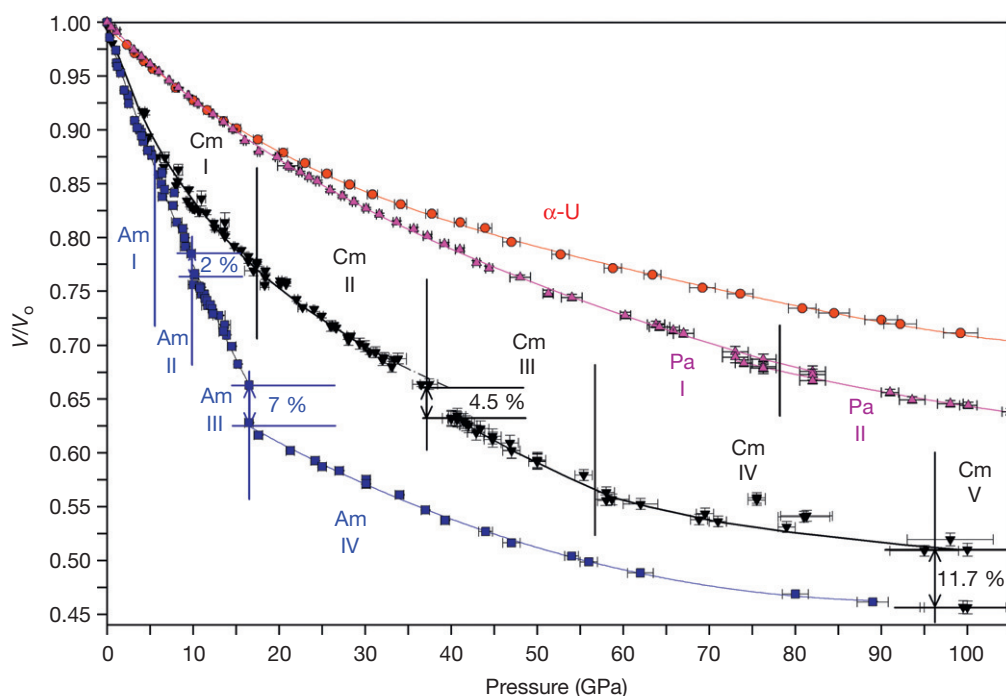


Figure 3 The relative volumes as a function of pressure of several actinide metals.

Table 2 The isothermal bulk modulus (B_0) and its pressure derivative (B'_0) of the actinide elements at ambient temperature

	α -Th	α -Pa	α -U	α -Np	α -Pu	α -Am	α -Cm
B_0 (GPa)	58(1)	118(2)	104(2)	118(2)	49	29.8(2)	36.5(3)
B'_0	4.2(3)	3.3(2)	6.2(2)	6.6(6)	12.4	3.6(2)	4.6(2)
References	9	6	6	10	11	6	8

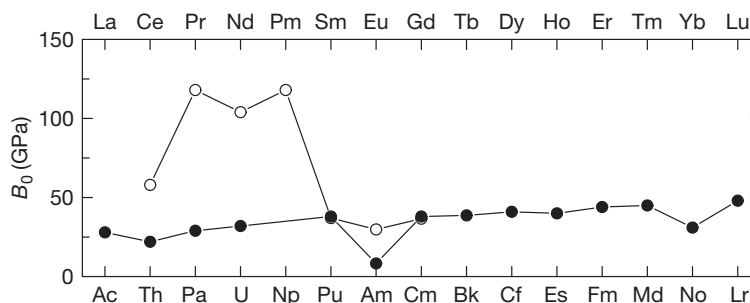


Figure 4 The isothermal bulk modulus (B_0) of the actinide elements (○) compared with that of the lanthanides (●).

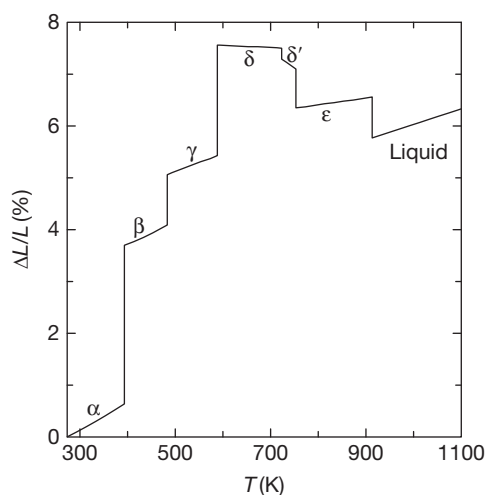


Figure 5 The thermal expansion of Pu. Made after Schonfeld, F. W.; Tate, R. E. Los Alamos National Laboratory, Technical Report LA-13034-MS; 1996.

and evolves to a simple cubic arrangement close to their melting temperature, similar to the lanthanide elements. (For numerical data on the thermal expansion, see [Section 2.01.4.1](#)) As the atoms move away from each other, the electrons in the 5f metals tend to favor a localized state. As discussed by Vohra and Holzapfel,¹⁵ this is particularly important for Np and Pu, which are on the threshold of localization/itinerancy. The case for plutonium is much more complex, as shown in [Figure 5](#). The crystal lattice of plutonium expands for the α -, β -, γ -, and ε -phases, and the γ - to δ -transition has a positive expansion. The δ - and δ' -phases have negative thermal expansion and the δ - to δ' - and δ' - to ε -transitions show a negative volume change, as is the case upon melting. Dynamic mean field calculations show that the monoclinic α -phase of Pu is metallic, whereas fcc δ is slightly on the localized side of the localization–delocalization transition.¹⁶

Moreover, the stability of the crystalline state of the actinide metals varies significantly. The melting temperature is high for thorium, similar to that of the transition metals in group IVB, and low for Np and Pu ([Figure 6](#)).

When applying high temperature as well as high pressure to the actinides, phase changes can be suppressed, as is shown in [Figure 7](#). For example, the triple point for the α – β – γ equilibrium in uranium is found at about 1076 K and 31.5 kbar; above this pressure, orthorhombic α -U directly transforms in fcc γ -U.¹⁷ In plutonium, the γ -, δ -, and δ' -phases disappear at relatively low pressure and are replaced by a new phase designated ζ . In contrast to the other actinides, plutonium shows a negative slope for the liquidus down to the β – ζ –liquid triple point (773 K, 27 kbar) reflecting the increase in density upon melting.¹⁷

2.01.2.4 Effects of Radiation

The α -decay of the actinides taking place in the crystal lattice creates an alpha particle and a recoil atom. The recoil atom produced has a range of about 12 nm and causes a dense collision cascade with typically about 2300 displacements (Frenkel pairs) within a short distance, around 7.5 nm in size. The α -particle has a path of about 10 μ m, with a cascade of about 265 displacements at the end of its range.¹⁸ Although recombination will take place, point defects and eventually extended defects (dislocations, dislocation loops) will survive in the crystal lattice, resulting in changes in the properties of the materials. Computer simulations of the radiation effects in fcc plutonium have shown that the defect recombination stage is much longer than that in other metals and that the vacancies do not seem to form clusters.¹⁹ In addition to the radiation damage, helium ingrowth takes place.

As discussed by Hecker and Martz,²⁰ the expansion of the lattice of α -Pu is significant due to

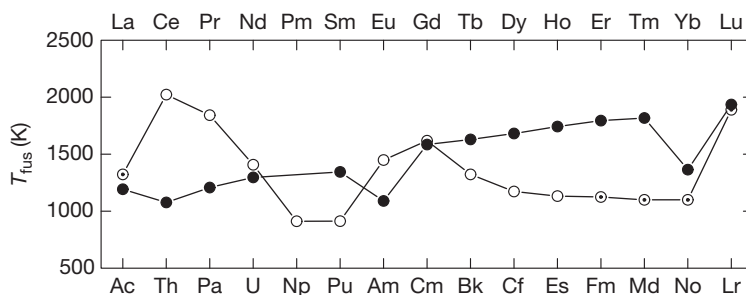


Figure 6 The melting point of the lanthanide (●) and actinide (○) metals. The estimated values are indicated by ⊙.

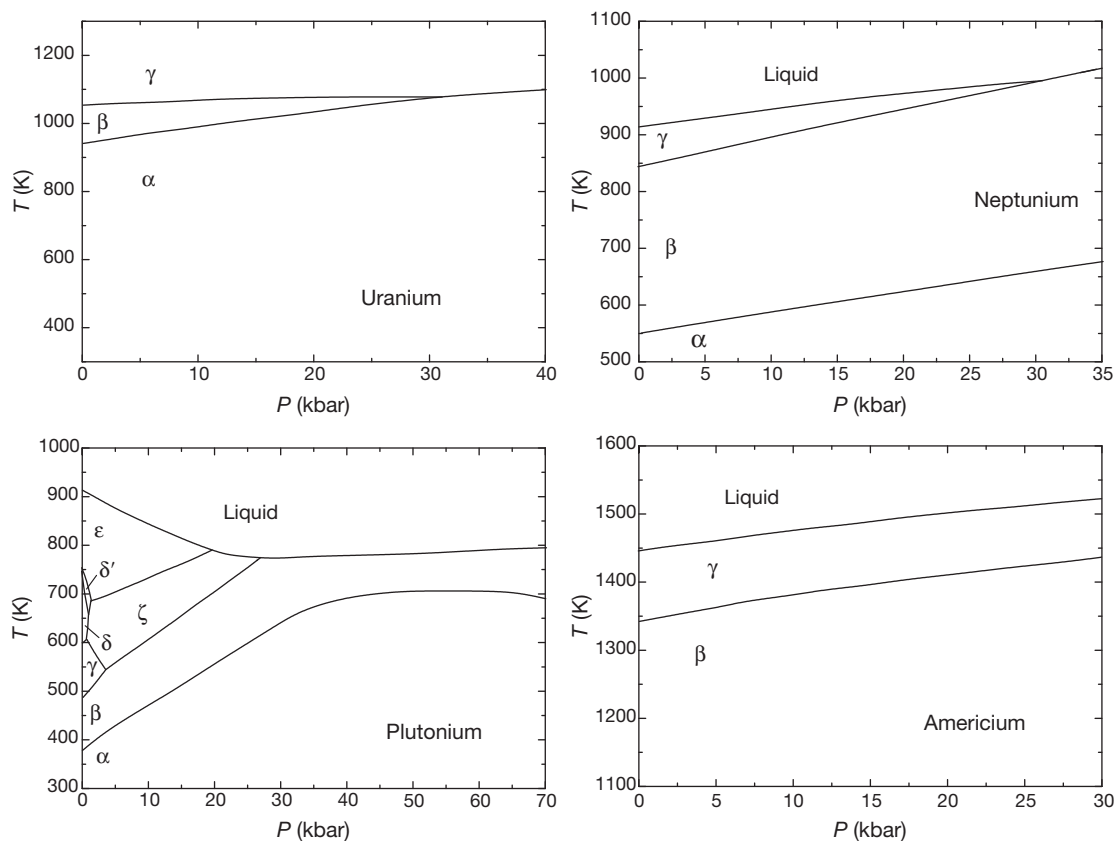


Figure 7 The pressure–temperature phase diagrams for U, Pu, Np, and Am. Reproduced from Lee, J. A.; Waldron, M. B. *Contemp. Phys.* **1972**, 13, 113–133.

self-irradiation, when held at cryogenic temperatures, saturating at about 10 vol.%. In contrast, the (Ti-stabilized) β -phase shows a slight contraction and the (Al-stabilized) δ -phase a substantial contraction, the latter saturating at 15 vol.%. Of course this is also reflected in other properties such as electrical resistivity.^{21,22} The radiation effects recover upon annealing to room temperature, a few percent of the damage remaining. Gorbunov and Seleznev²³ observed that α -Pu containing predominantly ^{239}Pu

retains its crystal structure after prolonged storage at room temperature. A sample of predominantly shorter lived ^{238}Pu ($t_{1/2} = 87.74$ years) contains both the α - and β -forms at immediate examination and additionally the γ -, η -, and ϵ -phases after a similar storage period. Chung *et al.*²⁴ showed by X-ray diffraction and dilatometry measurements on ^{238}Pu -doped δ -phase plutonium samples that the lattice expansion by self-irradiation appears to be the primary cause for dimensional changes during

the initial 23 years of aging. Following the initial transient, the density change is primarily caused by a constant helium ingrowth rate as a result of particle decay. The two effects were combined in an equation for the expansion $\Delta L/L$ with an exponential (radiation damage) and a linear (helium ingrowth) part:

$$\Delta L/L \cong A[1 - \exp(-Bt)] + Ct \quad [1]$$

where A , B , and C are constants and t is time.

The self-irradiation is one of the main causes that complicates the study of the heavy actinide metals. For example, berkelium metal ($t_{1/2} = 314$ days; $\sim 0.2\%$ ^{249}Cf growth per day) shows signs of amorphization (weak and diffuse X-ray spectra) at room temperature, which improved after annealing and thermal cycling, and the samples were found to contain two crystallographic structures at room temperature, double hexagonal close-packed (dhcp) and fcc, of which the former is the stable form.²⁵ An extreme case is Es; its crystal structure has been resolved only by rapid electron diffraction of thin film material due to the very short half-life of the isotope used.²⁶

2.01.3 Thermodynamic Properties

Many critical reviews of the thermodynamic properties of the actinide metals have been made since the 1960s. The first milestone was the review by Oetting and coworkers,²⁷ which gave recommended values for Th to Cm. Ward *et al.*²⁸ treated the same elements but also gave recommendations for Cf and Es. In addition, the room temperature thermodynamic properties for the major actinides Th and U have been reviewed by the CODATA team for key values for Thermodynamics,²⁹ while Th, U, Np, Pu, and Am have been reviewed by the OECD/NEA team.^{30–33} The most recent evaluation was made by Konings and Beneš,³⁴ with emphasis on the high-temperature properties. There are no large differences between these studies for the major actinides and it is thus clear that the recommendations given in this chapter rely heavily on these studies (Tables 3 and 4).

2.01.3.1 Heat Capacity and Entropy of the Crystalline State

The low-temperature heat capacity has been measured for the actinides Th through Am, in most cases showing anomalies. The origin of these anomalies has generally not been explained adequately³⁵ but is likely related to ordering phenomena and

f-electron promotion. The measurements for the major actinides Th, U, and Pu in the α -structure were made on gram-scale quantities, and the results should thus be of an acceptable accuracy.

However, although the low-temperature heat capacity of plutonium was measured by a remarkably large number of authors,^{36–42} there is considerable scatter among the results above 100 K (see Figure 8), probably due to self-heating and radiation damage. But even the results for ^{242}Pu samples from the same batch,^{40,41} which are affected less due to its much longer half-life, differ considerably. The differences in the heat capacity have a pronounced effect on the standard entropy at $T = 298.15$ K: $56.03 \text{ J K}^{-1} \text{ mol}^{-1}$,³⁹ $56.32 \text{ J K}^{-1} \text{ mol}^{-1}$,⁴⁰ $54.46 \text{ J K}^{-1} \text{ mol}^{-1}$,⁴¹ and $57.1 \text{ J K}^{-1} \text{ mol}^{-1}$.⁴² Especially, the results of Lashley *et al.*⁴² indicate a very different shape of the heat capacity curve of α -Pu, rising much steeper up to $T = 100$ K and saturating at a lower value near room temperature. Although the relaxation method used in that study is less accurate ($\pm 1.5\%$ as claimed by the authors) than the traditional adiabatic technique used in the other studies, the difference is significant. Lashley *et al.*⁴² attributed this to the buildup of radiation damage at the lowest temperatures, which they tried to avoid by measuring upon cooling, and below $T = 30$ K by intermediate annealing at room temperature. However, other authors also addressed this issue. For example, Gordon *et al.*⁴¹ performed a heating run from room temperature to $T = 373$ K before each low-temperature run. Moreover, no substantial difference between the results for ^{239}Pu and ^{242}Pu was observed in that study.

The electronic Sommerfeld heat capacity coefficient (γ_e), a property proportional to the density of states at the Fermi level, varies strongly in the actinide series (Table 5). It increases steadily up to Pu but is very low for Am. For δ -Pu the electronic heat capacity coefficient γ_e is even three times higher than that of α -Pu. This corresponds well with the results of photoemission spectra⁴⁸ that show α -Th has a small density of states at the Fermi level compared with that of α -U, α -Np, and α -Pu (Figure 9). In α -Am, the valence band is well removed from the Fermi level. The low-temperature heat capacity of other modifications of plutonium has been measured recently. Specifically, the δ -structure stabilized by Am or Ce doping shows clearly enhanced values of the electronic heat capacity coefficient γ_e at very low temperature.^{50,51}

The standard entropies derived from the low-temperature heat capacity data are given in Table 3,

Table 3 Recommended entropy ($\text{J K}^{-1} \text{mol}^{-1}$) and the heat capacity ($\text{J K}^{-1} \text{mol}^{-1}$) of actinide elements in the solid and liquid phase

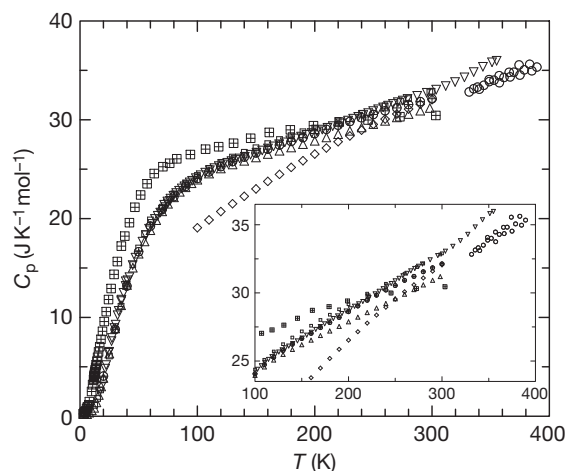
	Phase	$S^0 (298.15)$	$C_p = A + B \times T \text{ (K)} + C \times T^2 \text{ (K)} + D \times T^3 \text{ (K)} + E \times T^{-2} \text{ (K)}$				Temperature range (K)
			A	B	C	D or E	
Th	α	51.8 ± 0.50	23.435	8.945×10^{-3}		$E = -1.140 \times 10^4$	298–1650
	β	–	15.702	11.950×10^{-3}			1650–2020
	Liquid	–	46				2020–2500
Pa	α	51.6 ± 0.80	21.6522	12.426×10^{-3}			298–1443
	β	–	39.7				1443–1843
	Liquid	–	47.3				1843–2500
U	α	50.20 ± 0.20	28.4264	-6.9587×10^{-3}	29.8744×10^{-6}	$E = -1.1888 \times 10^5$	298–941
	β	–	47.12				941–1049
	γ	–	61.6420			$E = -33.1644 \times 10^6$	1049–1407
	Liquid	–	46.45				1407–2500
Np	α	50.45 ± 0.40	30.132	-36.2372×10^{-3}	1.1589×10^{-4}		298–553
	β	–	40				553–850
	γ	–	36				850–913
	Liquid	–	46				913–2500
Pu	α	54.46 ± 0.80	17.6186	45.5523×10^{-3}			298–399
	β	–	27.4160	13.060×10^{-3}			399–488
	γ	–	22.0233	22.959×10^{-3}			488–596
	δ	–	28.4781	10.807×10^{-3}			596–741
	δ'	–	35.56				741–759
	ε	–	33.72				759–913
	Liquid	–	42.80				913–2500
Am	α	55.4 ± 2.0	30.0399	-29.053×10^{-3}	5.2026×10^{-5}	$D = -1.8961 \times 10^{-8}$	298–1042
	β	–	8.4572	33.167×10^{-3}	-7.587×10^{-6}		1042–1350
	γ	–	43				1350–1449
	Liquid	–	52				1449–2500
Cm	α	70.8 ± 3.0	28.409	-4.142×10^{-4}	3.280×10^{-6}		298–1569
	β	–	28.2				1569–1619
	Liquid	–	37.2				1619–2500

Source: Konings, R. J. M.; Beneš, O. *J. Phys. Chem. Ref. Data* **2010**, 39, 043102.

Table 4 Recommended transition temperatures (K), enthalpies (kJ mol⁻¹), and entropies (J K⁻¹ mol⁻¹) of the actinide metals

	Transition	T _{trs} (K)	Δ _{trs} H	Δ _{trs} S
Th	α→β	1650 ± 15	3.5 ± 0.1	2.12
	β→liq.	2020 ± 10	13.8 ± 1.3	6.83
Pa	α→β	1443 ± 50	6.6 ± 2.0	4.57
	β→liq.	1843 ± 50	12.3 ± 2.0	6.67
U	α→β	941 ± 2	2.85 ± 0.15	3.03
	β→γ	1049 ± 2	4.62 ± 0.50	4.40
	γ→liq.	1407 ± 2	8.47 ± 1.00	6.02
Np	α→β	553 ± 5	4.7 ± 0.5	8.50
	β→γ	850 ± 3	3.0 ± 0.5	3.53
	γ→liq.	913 ± 3	3.2 ± 0.5	3.50
Pu	α→β	399 ± 1	3.706 ± 0.030	9.29
	β→γ	488 ± 1	0.478 ± 0.020	0.98
	γ→δ	596 ± 2	0.713 ± 0.050	1.20
	δ→δ'	741 ± 4	0.065 ± 0.020	0.09
	δ'→ε	759 ± 4	1.711 ± 0.050	2.25
	ε→liq.	913 ± 2	2.766 ± 0.1	3.03
Am	α→β	1042 ± 10	0.34 ± 0.10	0.33
	β→γ	1350 ± 5	3.8 ± 0.4	2.81
	γ→liq.	1449 ± 5	8.0 ± 2.0	5.52
Cm	α→β	1569 ± 50	4.5 ± 0.5	0.29
	β→liq.	1619 ± 50	11.7 ± 1.0	7.23

Source: Konings, R. J. M.; Beneš, O. *J. Phys. Chem. Ref. Data* **2010**, 39, 043102.

**Figure 8** The low-temperature heat capacity of plutonium; ◇, ³⁷; ⊕, ³⁸; ⊕, ³⁹; ▽, ⁴⁰; Δ, ⁴¹; ⊕, ⁴²; ○, ⁴³.

and the variation along the actinide metal series is shown in **Figure 10**. The entropies of the elements Th to Am are close to the lattice entropies of the corresponding lanthanides, showing the absence of magnetic contributions. The entropies of the other actinide elements must be derived from estimations, as experimental studies do not exist. To this purpose Ward *et al.*²⁸ suggested a general formula by correlating the entropy with metallic radius (r), atomic weight (M), and magnetic entropy (S_μ):

$$S_u(298.15\text{K}) = S_k(298.15\text{K})\frac{r_u}{r_k} + \frac{3}{2}R\ln\frac{M_u}{M_k} + S_\mu \quad [2]$$

where u refers to the unknown (lanthanide or actinide) element and k refers to the known element. S_μ is taken equal to $S_{\text{spin}} = (2\mathcal{J} + 1)$, where \mathcal{J} is the total angular momentum quantum number. The entropy of Cm thus obtained is significantly higher than that of the preceding elements, showing its magnetic character.

The heat capacity of the actinide metals from room temperature up to the melting temperature has been reported for Th, U, and Pu with reasonable accuracy and for Np for the α -phase only. The values for the other metals are based on estimations. For example, Konings⁵² estimated the heat capacity of americium metal from the harmonic, dilatation, electronic, and magnetic contributions, $C_p = C_{\text{har}} + C_{\text{dil}} + C_{\text{ele}} + C_{\text{mag}}$, whereas the heat capacity of γ -americium was obtained from the trends in the 4f and 5f series. The high-temperature heat capacity data for the actinide metals was analyzed in detail by Konings and Beneš,³⁴ who gave recommendations for the elements Ac to Fm. The results for the elements Th to Cm are summarized in **Table 3**.

Figure 11 shows the variation of the sum of the transition entropies from the crystalline room temperature phase to the liquid phase for the lanthanide and actinide series. This value is about constant in the lanthanide series but shows large variation in the actinide series, particularly for the elements U–Np–Pu. The deviation from the baseline

Table 5 The electronic heat capacity coefficient (γ_e) and Debye temperature (Θ_D) of the actinide elements

	Th	Pa	U	Np	Pu	Am
γ_e (mJ K ⁻² mol ⁻¹)	4.3(0.05)	5.0(0.5)	9.1 ^a	13.7(0.7)	17(1)	1(1)
Θ_D (K)	163.3(0.7)	185(5)	256 ^a	240(4)	153(2)	120(20)
References	44	45	46	41	42	47

^aThese values are for single crystal material, $\gamma_e = 9.9 \text{ mJ K}^{-2} \text{ mol}^{-1}$ and $\Theta_D = 184 \text{ K}$ for polycrystalline material.

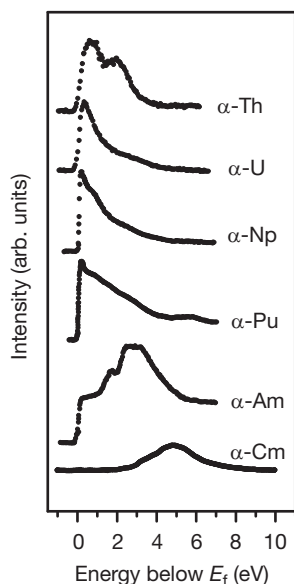


Figure 9 Valence-band photoemission spectra of the actinide metals. Modified from Moore, K. T.; van der Laan, G. *Rev. Mod. Phys.* **2009**, *81*, 235–298 by adding the results for α -Cm by Gouder *et al.*⁴⁹ Note that the spectrum for α -Th is scaled up compared to the other spectra so that it is easily visualized. In reality, it is much lower in intensity due to a small f density of states at the Fermi level.

correlates well with the atomic volume of the metals that is also anomalous for these elements, indicating that the itinerant behavior of the $5f$ electrons and the resulting lowering of the room temperature crystal symmetry require additional entropy to reach a similar disordered liquid state.

2.01.3.2 Heat Capacity of the Liquid State

The heat capacity of the actinide elements in the liquid state is relatively poorly known. Experimental data exist for Th, U, and Pu, and only the values for Th and U are known with an acceptable accuracy. They were measured by drop calorimetric techniques in a reasonable wide temperature range. Semi-empirical models for liquid uranium suggest a large electronic contribution to the heat capacity of this element.⁵³ The data for Pu, also obtained by calorimetry, are scattered and measured in a limited temperature range and the heat capacity value for the liquid of this element is thus uncertain. **Figure 12** also shows the estimated values for Am and Cm, based on assumptions considering the electron configurations.^{52,54}

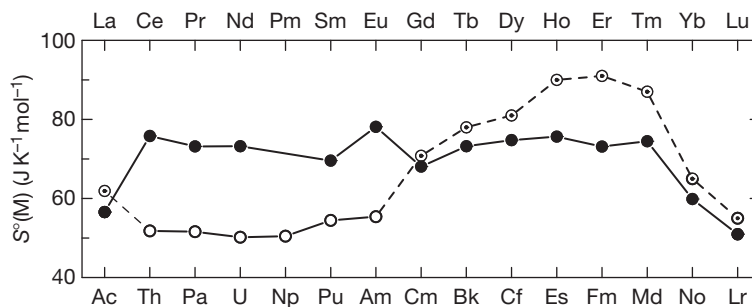


Figure 10 The standard entropies of lanthanide (●) and actinide (○) metals at $T = 298.15$ K; estimated values are indicated by (◐).

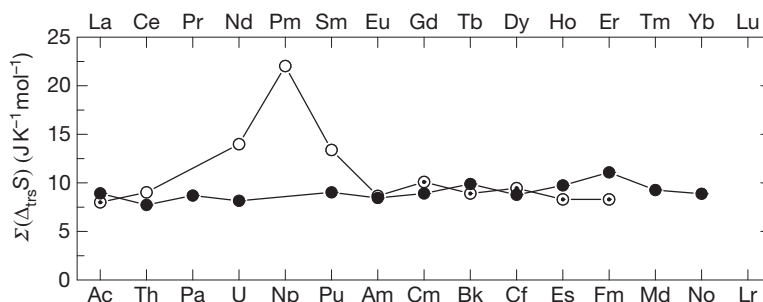


Figure 11 The sum of the transition entropies of the lanthanide (●) and actinide (○) metals. The estimated values are indicated by (◐).

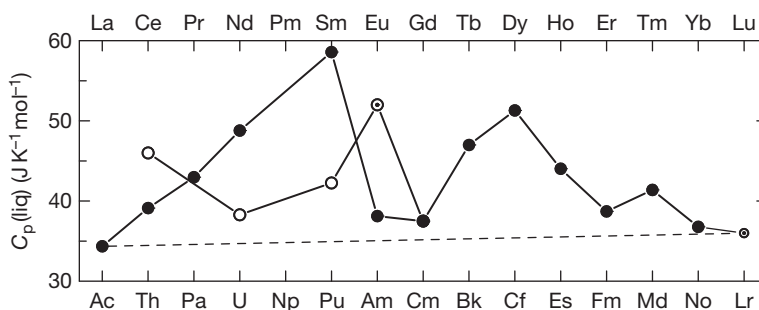


Figure 12 The heat capacity of the lanthanide (●) and actinide (○) metals in the liquid phase. Estimated values are indicated by (◐).

2.01.3.3 Heat Capacity and Entropy of the Gaseous State

The heat capacity and standard entropy for the ideal gas can be calculated from the atomic energy levels up to about 2000 K with reasonable accuracy using statistical thermodynamic methods³⁴ from the atomic energy levels. As discussed in detail by Brewer,⁵⁵ the electronic states of the gaseous actinide elements are complete (through experiments and estimations) to about 15000 cm⁻¹. The energies of the lowest electronic states for the elements Th to Cm are listed in **Table 6**. **Figure 13** shows a schematic representation of the atomic spectra of the actinide elements, based on the most recent assessments.^{56,57}

The derived room temperature values for the entropy and the high-temperature heat capacity equations are shown in **Table 7** and are taken from the assessment by Konings and Beneš.³⁴

The vapor pressure has been measured for all actinide metals except Md, No, and Lr. The majority of the results deal with the elements Th–Am. Measurements have also been made for Ac⁵⁸ but they are of a very approximate nature. The vapor pressure measurements for Es⁵⁹ and Fm⁶⁰ have been made on samples containing 10⁻⁵–10⁻⁷ at.% of the actinides in rare earth alloys in combination with Henry's law for dilute solutions. These measurements have been carefully reviewed by Konings and Beneš³⁴ and the recommended enthalpies of sublimation derived from these studies are listed in **Table 7**. The assessed vapor pressure curves (ln(*p*) vs. 1/*T*) are shown in **Figure 14**, indicating that the vapor pressure of the actinide metals varies strongly within the series. It roughly increases with the atomic number but with prominent exceptions. For example, americium is much more volatile than the neighboring Pu and Cm.

The enthalpies of sublimation of the actinides are plotted in **Figure 15** together with the values

Table 6 Spectroscopic characteristics of the ground state and the lowest lying electronic states of the actinide elements

	State	Spectroscopic term	Energy level (cm ⁻¹)
Th	6d ² 7s ²	³ F ₂	0
	6d ² 7s ²	³ P ₀	2558.06
	6d ² 7s ²	³ F ₃	2869.26
	6d ² 7s ²	³ P ₂	3687.99
	6d ² 7s ²	³ P ₁	3865.48
Pa	5f ² 6d7s ²	⁴ K _{11/2}	0
	5f ² 6d7s ²	⁴ I _{9/2}	825.42
	5f ² 6d7s ²	⁴ G _{5/2}	1618.325
	5f6d ² 7s ²	⁴ I _{9/2}	2659.405
	5f ² 6d7s ²	⁴ H _{7/2}	2966.53
U	5f ³ 6d7s ²	⁵ L ₆ ^o	0
	5f ³ 6d7s ²	⁵ K ₅ ^o	620.323
	5f ³ 6d7s ²	⁵ L ₇ ^o	3800.830
	5f ³ 6d7s ²	⁵ H ₃ ^o	3868.486
	5f ³ 6d7s ²	⁵ I ₄ ^o	4453.419
Np	5f ⁴ 6d7s ²	⁶ L _{11/2}	0
	5f ⁴ 6d7s ²	⁶ L _{9/2}	2033.94
	5f ⁴ 6d7s ²	⁶ I _{7/2}	3450.995
	5f ⁴ 6d7s ²	⁶ L _{13/2}	3502.855
	5f ⁴ 6d7s ²	⁶ I _{9/2}	6643.51
Pu	5f ⁶ 7s ²	⁷ F ₀	0
	5f ⁶ 7s ²	⁷ F ₁	2203.61
	5f ⁶ 7s ²	⁷ F ₂	4299.659
	5f ⁶ 7s ²	⁷ F ₃	6144.515
	5f ⁶ 6d7s ²	⁷ K ₄	6313.866
Am	5f ⁷ 7s ²	⁸ S _{7/2}	0
	5f ⁶ 6d7s ²	⁸ H _{3/2}	10684
	5f ⁶ 6d7s ²	⁸ H _{5/2}	12974
	5f ⁷ 6d7s	¹⁰ D _{5/2}	14000
	5f ⁷ 7s ²	⁶ P _{7/2}	14258
Cm	5f ⁷ 6d7s ²	⁹ D ₂ ^o	0
	5f ⁷ 6d7s ²	⁹ D ₃ ^o	302.15
	5f ⁷ 6d7s ²	⁹ D ₄ ^o	815.655
	5f ⁷ 6d7s ²	⁹ D ₅ ^o	1764.268
	5f ⁷ 6d7s ²	⁹ D ₆ ^o	3809.358

Source: Blaise, J.; Wyart, J. F. <http://www.lac.u-psud.fr/Database/Contents.html>, 2009; Worden, E. F.; Blaise, J.; Fred, M.; Trautmann, N.; Wyart, J. F. In *The Chemistry of the Actinide and Transactinide Elements*; Morss, L. R.; Edelstein, N.; Fuger, J.; Katz, J. J., Eds.; Springer Verlag, 2006; Chapter 16, pp 1836–1892.

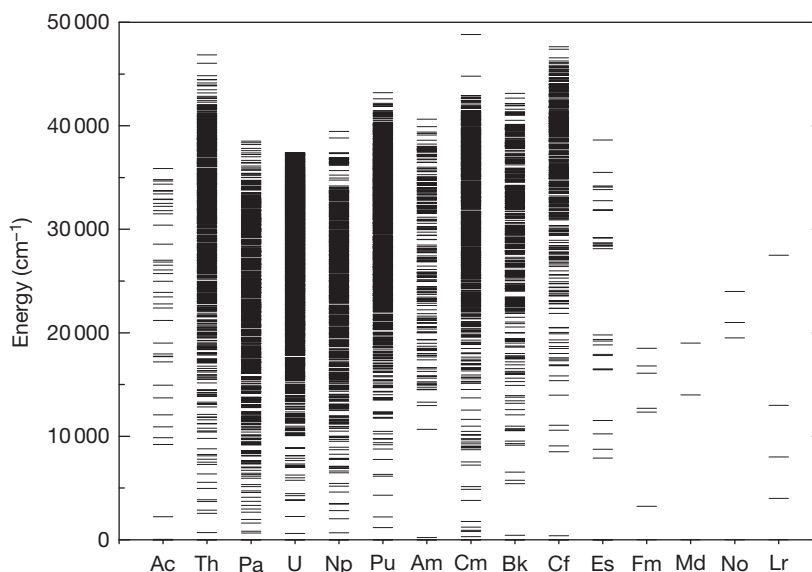


Figure 13 Schematic representation of the atomic spectra of the actinide elements.

for lanthanide metals. The trend in the latter series shows a typical pattern, with La, Gd, and Lu forming an approximate linear baseline from which the others systematically deviate. This trend can be understood from the electronic states of the condensed and gaseous atoms, as discussed by Nugent *et al.*⁶¹ These authors argued that the values for La, Gd, and Lu are almost identical, due the fact that they have the same number of valence electrons in the ground states of the gaseous metal atom and the crystal. In between, the enthalpy of sublimation decreases regularly because of a corresponding increase in stability of the divalent ground states in the gaseous metal atoms. A similar explanation can be applied to the actinide series, although Th, Pa, U, Np, and Pu deviate from this trend due to unusually large cohesive energies of the crystalline metals, resulting from the large number of valence electrons in the metal.

2.01.4 Thermophysical and Electronic Properties

2.01.4.1 Thermal Expansion and Density of the Crystalline State

The thermal expansion of a number of actinide metals has been studied, particularly for uranium and plutonium. The 1975 review by Touloukian *et al.*⁶² lists 48 studies for uranium, including single crystal and polycrystalline materials. The data show that α -uranium has a different expansion along the three crystallographic axes; the a - and c -axis expand whereas the b -axis shrinks with increasing temperature (Figure 16).

Also, α -Pa shows distinct different expansion along the crystallographic axes (Figure 16). α -Np, in contrast, expands along the three axes of the crystal.

The complex thermal expansion behavior of plutonium has already been discussed in Section 2.01.2.4 and is shown in Figure 5. Schofield and Tate⁶³ reviewed the wealth of data for the various plutonium modifications and the recommended values from their work are listed in Table 9. α -Pu expands along all three axes of the crystal, and the lattice expansion continues for the β - and γ -phases, but the cell parameter of the cubic δ and δ' modifications decreases. Americium, the last actinide for which thermal expansion data exist, shows a regular thermal expansion in both crystallographic directions.⁶⁸

Table 8 summarizes the linear thermal expansion ($\Delta L/L_0$) for the actinide metals. The density can be calculated from these data using the formula:

$$\rho(T) = \frac{M}{V_0(1 + 3\Delta L/L_0(T))} \quad [3]$$

where M is the atomic mass, and V_0 is the molar volume at the reference temperature (see Table 1). Note that the linear thermal expansion corresponds to the average of the thermal expansion along the three crystallographic axes.

2.01.4.2 Electrical Resistivity of the Crystalline State

The electrical resistivity (ρ) of the elements Th to Cm has been measured in the cryogenic temperature range and the values up to 300 K are shown in

Table 7 The enthalpy of formation (kJ mol^{-1}), the absolute entropy ($\text{J K}^{-1} \text{mol}^{-1}$), and the heat capacity ($\text{J K}^{-1} \text{mol}^{-1}$) of lanthanide and actinide gas phases

	$\Delta_f H^\circ(298.15)$	$S^\circ(298.15)$	$C_p = A + B \times T \text{ (K)} + C \times T^2 \text{ (K)} + D \times T^3 \text{ (K)} + E \times T^4 \text{ (K)} + F \times T^{-2} \text{ (K)}$						Temperature range (K)
			A	B	C	D	E	F	
Th	602 ± 6	190.171 ± 0.050	28.7108	-33.4618×10^{-3}	45.7409×10^{-6}	-14.1005×10^{-9}	–	-1.4548×10^5	298–1400
	–	–	29.8483	9.3756×10^{-3}	-2.1081×10^{-6}	0.2225×10^{-9}	–	-1.3137×10^7	1400–4000
Pa	548 ± 26	198.11 ± 0.10	21.3965	8.1883×10^{-3}	1.8634×10^{-6}	-1.0847×10^{-9}	–	-9.4644×10^4	298–1800
	–	–	25.7107	15.7656×10^{-3}	-5.6052×10^{-6}	0.5709×10^{-9}	–	-1.1144×10^7	1800–4000
U	533 ± 8	199.79 ± 0.10	35.1688	-32.2466×10^{-3}	27.0474×10^{-6}	-5.3433×10^{-9}	–	-3.6652×10^5	298–1800
	–	–	4.9298	10.4892×10^{-3}	3.7043×10^{-6}	-0.7598×10^{-9}	–	6.8108×10^6	1800–4000
Np	470 ± 5	197.72 ± 0.10	28.7334	-41.2476×10^{-3}	76.2347×10^{-6}	-45.8415×10^{-9}	9.9079×10^{-12}	-1.1134×10^5	298–1400
	–	–	68.4689	-48.7544×10^{-3}	28.4161×10^{-6}	-6.1153×10^{-9}	4.4618×10^{-13}	-1.6109×10^7	1400–4000
Pu	348.9 ± 3.0	177.19 ± 0.10	24.2954	-37.0413×10^{-3}	95.1224×10^{-6}	-65.8404×10^{-9}	16.2344×10^{-12}	6.7865×10^4	298–1400
	–	–	–112.0172	187.5714×10^{-3}	-86.6780×10^{-6}	18.8245×10^{-9}	-1.5431×10^{-12}	2.7817×10^7	1400–4000
Am	285.5 ± 3.0	194.66 ± 0.20	20.786	–	–	–	–	–	298–900
	–	–	19.9856	0.0434×10^{-3}	1.6974×10^{-6}	-1.5984×10^{-9}	4.4407×10^{-13}	2.1403×10^5	900–2400
	–	–	268.8101	-179.4359×10^{-3}	45.9178×10^{-6}	-3.5637×10^{-9}	–	-1.7767×10^8	2400–4000
Cm	389 ± 10	197.58 ± 0.20	26.1234	24.8448×10^{-3}	-45.9572×10^{-6}	21.6951×10^{-9}	–	-1.7020×10^4	298–1000
	–	–	22.3529	1.7417×10^{-3}	-0.4385×10^{-6}	0.2286×10^{-9}	–	2.6514×10^6	1000–4000

Source: Konings, R. J. M.; Beneš, O. *J. Phys. Chem. Ref. Data* **2010**, 39, 043102.

Figure 17, which reveals a strong variation. Th, Pa, U, Np, and Am show a regular increase from 0 K to room temperature, typical for nonmagnetic metals in which transport carriers (electrons) are scattered by phonons (lattice vibrations). Pu and Cm show, however, a different behavior. The electrical resistivity of α -Pu has a maximum of about $150 \mu\Omega \text{ cm}$ at about 100 K. Boring and Smith⁷¹ argue that this high value is an indication of enhanced scattering of conduction electrons caused by electron correlations involving spin and charge interactions. Curium is the first actinide metal that is magnetic. α -Cm orders antiferromagnetically below 65 K,⁷² while its high-temperature phase, β -Cm with fcc structure, presents ferromagnetic order above 200 K similarly to Gd, its 4f counterpart. The change in the resistivity curve occurs around the ordering temperature, which is similar to that in magnetic rare earth metals and especially Gd.

The electrical resistivity of the actinide metals above ambient temperature is well known for the major actinides. Chioti and coworkers⁷³ showed that this property is very sensitive to impurities in the samples,

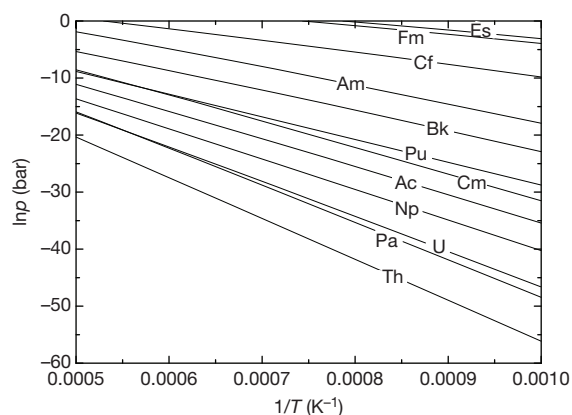


Figure 14 The vapor pressure of the actinide elements, calculated from assessed thermochemical data.

particularly carbon. Sahu *et al.*⁶⁴ reported measurements for high purity α -Th in a wide temperature range, and Aaraj *et al.*⁶⁵ for uranium up to 1000 K, covering the α -, β -, and γ -phases. Sandenaw and Gibby⁶⁷ reported measurements for plutonium from 27 to 800 K, covering all allotropes. A large decrease was observed for the α - to β -transition, as shown in **Figure 18**. Neptunium shows a similar behavior as Pu. The recommended values are summarized in **Table 9**.

2.01.4.3 Thermopower of the Crystalline State

The thermopower (S) has been reported for the elements Th to Pu in the cryogenic range and up to 300 K.⁷⁴ **Figure 19** shows the values and the sign of S for the α -phase of these actinide elements. It can be observed that it varies from Th to Pu and depends strongly on temperature range. As no carrier is available at 0 K, S is reduced when approaching very low temperatures. The thermopower of U and Np at high temperature shows discontinuities at the structural phase transition (α - β and consecutive).⁶⁵ The high-temperature thermopower of Pu is not well known and is very sensitive to impurities. Experimental

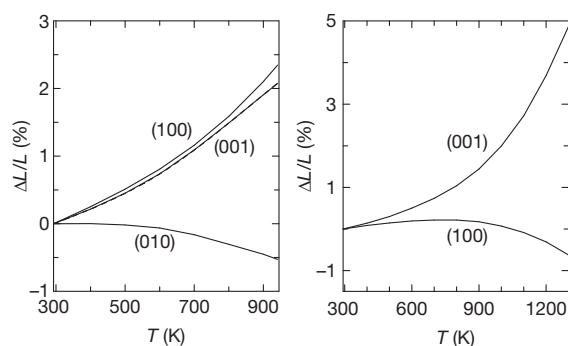


Figure 16 The thermal expansion of U (left) and Pa (right) along the different crystallographic axes.

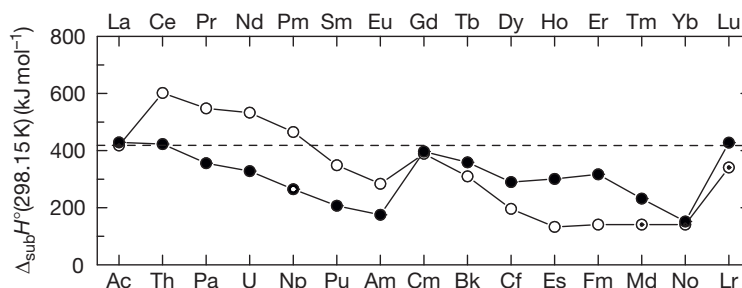


Figure 15 The sublimation enthalpy at $T = 298.15 \text{ K}$ of the lanthanide (●) and actinide (○) metals. The estimated values are indicated by ⊙.

Table 8 Linear thermal expansion ($\Delta L/L_0$) of the actinide metals; L_0 refers to 293 K

		$\Delta L/L_0(T) = a + b \times T(K) + c \times T^2(K) + d \times T^3(K)$				References
		a	b	c	d	
Th	α	-2.80×10^{-3}	8.190×10^{-6}	5.286×10^{-9}	-1.432×10^{-12}	61
Pa	α	-3.745×10^{-3}	1.555×10^{-5}	-1.144×10^{-8}	6.794×10^{-12}	61
U	α	-3.79×10^{-3}	1.264×10^{-5}	-8.982×10^{-10}	6.844×10^{-12}	61
	β	8.04×10^{-5}	1.729×10^{-5}			61
	γ	-1.49×10^{-3}	1.775×10^{-5}	4.382×10^{-11}	-1.239×10^{-12}	61
Np	α	-8.381×10^{-3}	2.848×10^{-5}			68
	β	-1.258×10^{-2}	5.282×10^{-5}			68
Pu	α	-9.291×10^{-3}	1.266×10^{-5}	7.498×10^{-8}	-2.952×10^{-11}	62
	β	2.561×10^{-3}	4.249×10^{-5}	-1.048×10^{-7}	1.608×10^{-8}	62
	γ	3.279×10^{-2}	3.469×10^{-3}			62
	δ	7.437×10^{-2}	1.208×10^{-6}	1.782×10^{-9}	5.926×10^{-12}	62
	δ'	0.1189	-6.510×10^{-3}			62
	ε	5.241×10^{-2}	1.325×10^{-3}			62
	liquid	2.912×10^{-2}	3.010×10^{-3}			62
Am	α	-2.315×10^{-3}	6.965×10^{-6}	3.176×10^{-9}		69
Cm	α	-3.262×10^{-3}	1.094×10^{-5}			53

Table 9 Electrical resistivity of the actinide metals

		$\rho(\mu\Omega\text{ cm}) = a + b \times T(K) + c \times T^2(K) + d \times T^3(K) + e \times T^4(K)$					Temperature range (K)	References
		a	b	c	d	e		
Th	α	-1.8305	0.0593				300–800	63
	α	-18.312	0.1064	-3.3116×10^{-3}			800–1300	63
U	α	22.455	-4.5806×10^{-2}	3.2797×10^{-4}	-3.8929×10^{-9}	1.4372×10^{-10}	300–941	64
	β	16.971	8.6655×10^{-2}	-4.6720×10^{-5}			941–1049	64
	γ	67.819	-3.1502×10^{-2}	1.8947×10^{-5}			1049–1400	64
Np	α	86	0.415	-1.5×10^{-4}			300–553	65
	β	-94	0.7217	-8.5×10^{-4}	3.333×10^{-7}		553–850	65
	γ	110					850–900	65
Pu	α	158.09	-0.0411				300–399	66
	β	117.18	-0.0245				399–488	66
	γ	108.87	-0.0089				488–596	66
	δ	90.22	0.0072				596–741	66
	δ'	-75.08	0.2315				741–759	66
	ε	106.4					759–913	66

results indicate that the actinide metals have thermo-power values close to those of the lanthanides⁷⁵ but larger than the transition metals. This essentially can be related to large band structures and a huge density of states at the Fermi level.

2.01.4.4 Thermal Conductivity of the Crystalline State

The thermal conductivity of the actinide metals varies strongly within the series. This is particularly true at low temperatures for which the data for α -Th and α -Pu differ by two orders of magnitude,

as shown in Figure 20. This trend is opposite to that for the electrical conductivity and is in line with the Wiedemann–Franz law that states that the ratio between thermal conductivity and electrical conductivity ($\sigma = 1/\rho$) is a constant for any temperature ($\lambda/\sigma = LT$, where L is the Lorenz number, $2.44 \times 10^{-8} \text{ W } \Omega \text{ K}^{-2}$). One can notice that thermal conductivity of Pu at 100 K is the lowest reported for any pure metal ($3.5 \text{ W m}^{-1} \text{ K}^{-1}$).

Experimental data for high temperatures are known only for the major actinides Th, U, and Pu in a reasonable temperature range, whereas the measurement for Np is made close to room temperature

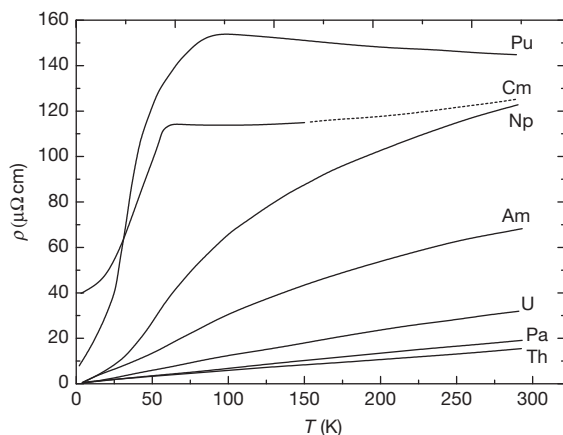


Figure 17 The low-temperature electrical resistivity of the actinide elements. Reproduced from Schenkel, R. *Solid State Comm.* **1977**, 23, 389–392.

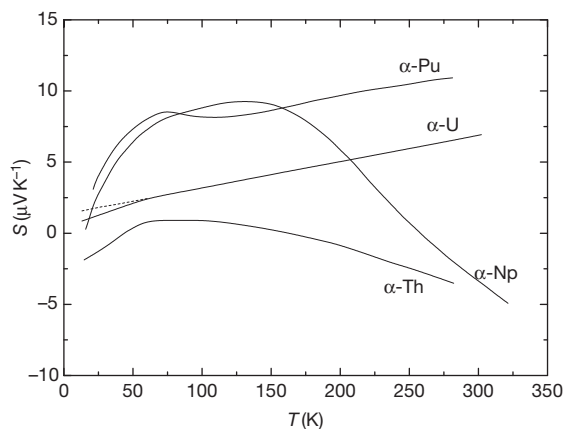
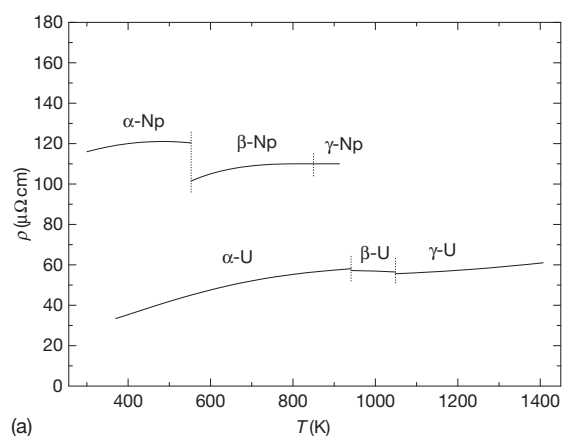
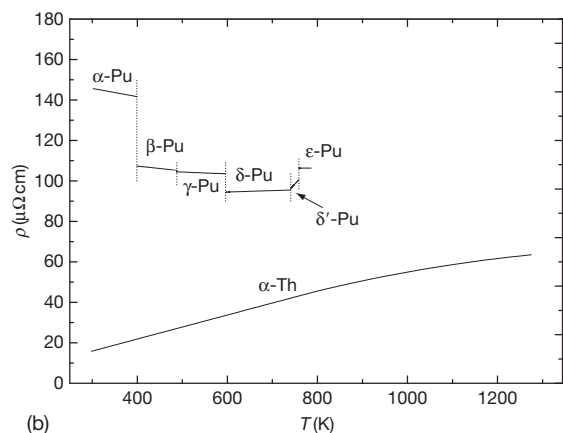


Figure 19 The thermopower below 300 K of the actinide elements. Reproduced from Meaden, G. T. *Proc. Roy. Soc. Lond.* **1963**, 276A, 553–570.



(a)



(b)

Figure 18 The high-temperature electrical resistivity of the actinide elements.

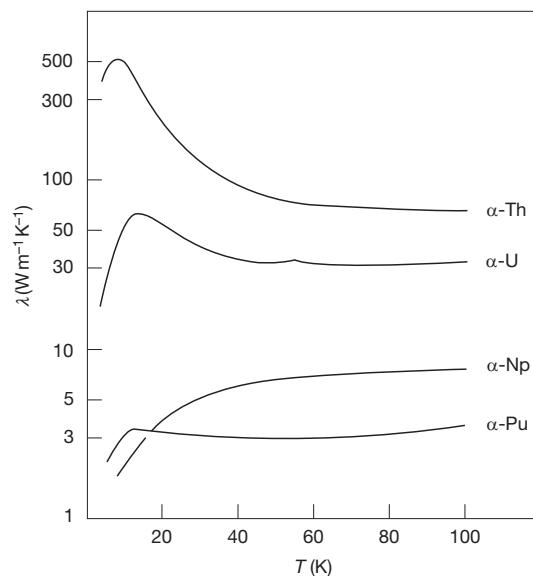


Figure 20 The low-temperature thermal conductivity of the actinide elements. Reproduced from Lee, J. A.; Waldron, M. B. *Contemp. Phys.* **1972**, 13, 113–133.

(Figure 21). The recommended equations are given in Table 10. The values for Th, taken from the assessment by Touloukian and coworkers,⁷⁶ show a slight increase with temperature. It should be noted that our graphs show a discrepancy between the low- and high-temperature data near $T = 300$ K, which is probably related to the purity of the samples, as it is known that the properties of thorium metal are highly sensitive to carbon impurities.⁷³ The values for U, also from the assessment by Touloukian and coworkers,⁷⁶ are based on a set of several concordant

measurements and cover the temperature range for the α -, β -, and γ -phases but do not show distinct differences.

Thermal conductivity data above ambient temperature exist for all crystal phases of plutonium. The data for α -Pu from 100 to about 400 K were reported by Sandenaw and Gibney.⁴⁰ However, the agreement with other values at ambient temperature is poor, which might be due to the differences in purity and to the accumulated radiation damage. Wittenberg and coworkers^{77,78} measured the thermal diffusivity (D) of the δ , δ' , and ϵ phases from which they derived the thermal conductivity, which was found to be constant in all three cases. However, the numbers in the early publication⁷⁸ for the thermal diffusivity are different from those in the later publication.⁷⁷ The values in Table 10 are taken from the latter work, which we consider to be the final results. Note that only the early values are cited in the

Gmelin review from 1976.⁶⁶ As discussed by Wittenberg, the data indicate that the thermal conductivity of the γ - and δ -phases are nearly the same (13 ± 1) $\text{W m}^{-1} \text{K}^{-1}$. These trends are in qualitative agreement with the electrical resistivity measurements, as discussed in Section 2.01.4.2. Wittenberg also noted that the large decrease in the thermal conductivity of the ϵ -phase is not expected to be comparable with the electrical resistivity measurements, and he suggested that this value may be too low as a result of the difficulty in maintaining good thermal contact after the volume contraction during the δ - to ϵ -phase transformation.

Although the Wiedemann–Franz law states that the ratio between thermal conductivity and electrical conductivity is almost constant for metals, it was shown that the value for $\lambda/\sigma T$ at $T = 298 \text{ K}$ varies regularly in the lanthanide series, as shown in Figure 22. The values for Th, U, and Np are close to the Lorenz value, and that of Pu is slightly higher. The values for Am and Cm in this figure are suggestions,⁷⁹ assuming that the thermal conductivity of Cm is close to that of Gd.

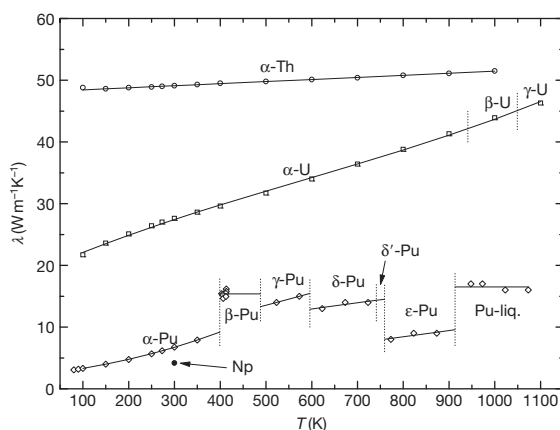


Figure 21 The thermal conductivity of the actinide elements.

2.01.4.5 Thermal Conductivity of the Liquid State

Only data available for the thermal diffusivity and conductivity of the liquid state of plutonium have been reported. Wittenberg and coworkers^{77,78} measured the thermal diffusivity (D) from which they derived the thermal conductivity, which is constant in the measured range (973 to 1073 K). As discussed above, the two publications by these authors are not consistent. In the early one,⁷⁸ Wittenberg gave 0.017–0.021 and 0.022–0.023 $\text{cm}^2 \text{s}^{-1}$ for the thermal diffusivity in two experiments with different heating

Table 10 Thermal conductivity ($\text{W m}^{-1} \text{K}^{-1}$) of the actinide metals above room temperature

Phase	$\lambda = a + b \times T \text{ (K)} + c \times T^2 \text{ (K)} + d \times T^3 \text{ (K)}$				T (K)	References
	a	b	c	d		
Th	48.101	0.00336			100–1000	75
U	19.019	0.03256	-1.8235×10^{-5}	1.0343×10^{-5}	100–100	75
Np	4.18				300	75
Pu	α	2.264	0.00696	2.5332×10^{-5}	100–399	75
	β	15.4			399–488	66
	γ	3.54	0.02		488–596	76
	δ, δ'	6.94	0.01		596–759	76
	ϵ	0.44	0.01		759–913	76
	Liquid	16.5			913–1073	76

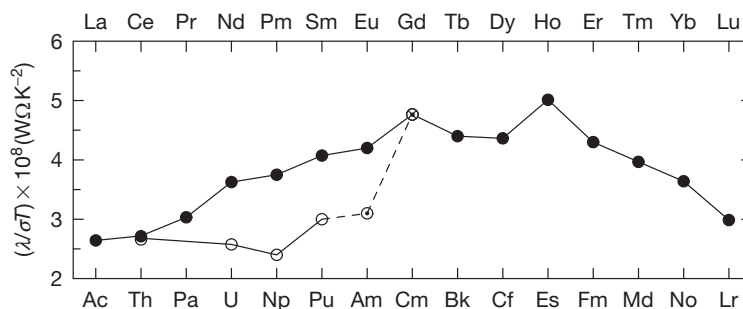


Figure 22 The variation of $\lambda/\sigma T$ of the actinide (○) and lanthanide (●) metals. The estimated values are indicated by ○.

rates, yielding to $\lambda = 5.4 \text{ W m}^{-1} \text{ K}^{-1}$ and $6.3 \text{ W m}^{-1} \text{ K}^{-1}$, respectively. In the later publication,⁷⁷ Wittenberg reports $D = 0.057\text{--}0.056 \text{ cm}^2 \text{ s}^{-1}$ for the temperature range 948 to 1073 K, yielding $\lambda = (17 \pm 1) \text{ W m}^{-1} \text{ K}^{-1}$. This latter value is recommended here.

2.01.4.6 Density of the Liquid State

The density of liquid uranium was measured by Grosse *et al.*,⁸⁰ Rohr and Wittenberg,⁸¹ and Shpil'rain *et al.*⁸² The results of the latter two studies are in very good agreement but deviate significantly from the results of Grosse *et al.*, which has been explained by errors caused by surface tension forces in the hydrostatic weighing method used in that work.⁸³ We have therefore selected the combined results from Rohr and Wittenberg⁸¹ and Shpil'rain *et al.*,⁸² as recommended by the latter authors:

$$\rho(\text{kg m}^{-3}) = 20332 - 2.146T(\text{K}) \quad [4]$$

The density of liquid plutonium was measured by Olsen *et al.*⁸⁴ and Serpan and Wittenberg.⁸⁵ The results are very close and the average of the two equations is recommended:

$$\rho(\text{kg m}^{-3}) = 18004 - 1.486T(\text{K}) \quad [5]$$

2.01.4.7 Viscosity

The viscosity of liquid uranium and plutonium has been measured using a direct oscillating method by researchers at the Mound Laboratory in the 1960s. These data are still the only available to date. For liquid uranium, Ofte⁸⁶ reported:

$$\log_{10}\eta(\text{cP}) = 1587.7/T(\text{K}^{-1}) - 0.3243 \quad [6]$$

The viscosity of liquid plutonium was reported in several studies, and the following equation is the recommended representation of the results⁸⁷:

$$\log_{10}\eta(\text{cP}) = 672/T(\text{K}) + 0.037 \quad [7]$$

These equations give for the viscosity at the melting point 6.5 cP for uranium and 6.0 cP for plutonium. These values are somewhat higher than the values predicted by Grosse,⁸⁸ who used an empirical relationship between the activation energy for viscosity for liquid metals and their melting points, to obtain 5.9 cP for U, 4.5 cP for Pu, and 5.0 cP for Th at the melting point.

2.01.4.8 Surface Tension

The surface tension of liquid uranium was measured by Cahill and Kirshenbaum⁸⁹ from 1406 to 1850 K. The results can be represented by the equation:

$$\sigma(\text{N m}^{-1}) = 1.747 - 0.1410^{-3}T(\text{K}) \quad [8]$$

This equation yields 1.55 N m^{-1} at the melting point. The surface tension of plutonium was reported by Olsen *et al.*⁸⁴ These authors obtained $\sigma(\text{N m}^{-1}) = 1.29 - 0.967 \times 10^{-3}T(\text{K})$, yielding 0.40 N m^{-1} at the melting point. It has been suggested that this value is too low because of dissolved tantalum. Spriet⁴⁹ reported the surface tension of liquid plutonium to be 0.55 N m^{-1} , which is generally accepted.

2.01.5 Summary and Outlook

The actinide elements pose a very interesting paradox. Uranium and especially plutonium are materials that are very difficult to handle because of their radioactive nature, but they are among the most

extensively studied elements in the periodic table. This is of course due to the importance of these two elements in nuclear technology. The properties of the other actinides are relatively poorly known and are generally obtained from estimations. However, due to the changes in the electronic properties of the 5f electrons, varying from delocalized to localized, going from Th to Am, the systematics in the properties of the actinides are difficult to predict, and analogies with the 4f lanthanides are not (always) obvious. Theoretical predictions based on atomistic calculations could help to solve this, but the predictive potential of such calculations is still being explored. Clearly, more experimental studies are needed, particularly on the minor actinides.

References

- Johansson, B.; Rosengren, A. *Phys. Rev. B* **1975**, *11*, 1367–1373.
- Edelstein, N. M.; Fuger, J.; Katz, J. J.; Morss, L. R. In *The Chemistry of the Actinide and Transactinide Elements*; Morss, L. R., Edelstein, N., Fuger, J., Katz, J. J., Eds.; Springer Verlag, 2006; Chapter 15, pp 1753–1835.
- Myasoedov, B. F.; Kirby, H. W.; Tananaev, I. G. In *The Chemistry of the Actinide and Transactinide Elements*; Morss, L. R., Edelstein, N., Fuger, J., Katz, J. J., Eds.; Springer Verlag, 2006; Chapter 4, pp 161–252.
- Konings, R. J. M.; Wiss, T.; Gueneau, C. In *The Chemistry of the Actinide and Transactinide Elements*; Morss, L. R., Edelstein, N., Fuger, J., Katz, J. J., Eds.; Springer Verlag, 2010; Chapter 34.
- Brooks, M. S.; Eriksson, O.; Johansson, B. *J. Alloys Comp.* **1995**, *223*, 204–210.
- Lindbaum, A.; Heathman, S.; Le Bihan, T.; Haire, R. G.; Idiri, M.; Lander, G. H. *J. Phys. Condens. Matter* **2003**, *15*, S2297–S2303.
- Heathman, S.; Haire, R. G.; Le Bilan, T.; *et al.* *Phys. Rev. Lett.* **2000**, *85*, 2961–2964.
- Heathman, S.; Haire, R. G.; Le Bihan, T.; *et al.* *Science* **2005**, *309*(5731), 110–113.
- Bellussi, G.; Benedict, U.; Holzapfel, W. B. *J. Less Common Met.* **1981**, *78*, 147–153.
- Dabos, S.; Dufour, C.; Benedict, U.; Pagès, M. *J. Magn. Mater.* **1987**, *63/64*, 661–663.
- Bridgman, P. W. *J. Appl. Phys.* **1959**, *30*, 214.
- Ledbetter, H.; Migliori, A.; Betts, J.; Harrington, S.; El-Khatib, S. *Phys. Rev. B* **2005**, *71*, 172101.
- Bridgman, P. W. *J. Appl. Phys.* **1959**, *30*, 214–220.
- Dabos-Seignon, S.; Dancausse, J. P.; Gering, E.; Heathman, S.; Benedict, U. *J. Alloy. Comp.* **1993**, *190*, 237–242.
- Vohra, Y. K.; Holzapfel, W. B. *Phys. Lett.* **1982**, *89A*, 149–150.
- Savrasov, S. Y.; Kotliar, G.; Abrahams, E. *Nature* **2001**, *410*, 793–795.
- Lee, J. A.; Waldron, M. B. *Contemp. Phys.* **1972**, *13*, 113–133.
- Wolfer, W. G. *Los Alamos Sci.* **2000**, *26*, 274–285.
- Jomard, G.; Berlu, L.; Rosa, G.; Faure, P.; Nadal, J.; Baclet, N. *J. Alloys Comp.* **2007**, *360*, 242–254.
- Hecker, S.; Martz, J. C. *Los Alamos Sci.* **2000**, *26*, 238–243.
- King, E.; Lee, J. A.; Mendelssohn, K.; Wigley, D. A. *Proc. Roy. Soc. Lond. A* **1965**, *284*, 325–343.
- Wigley, D. A. *Proc. Roy. Soc. Lond. Ser. A* **1965**, *284*, 344–354.
- Gorbunov, S. I.; Seleznev, A. G. *Radiochemistry* **2001**, *43*, 111–117.
- Chung, B. W.; Saw, C. K.; Thompson, S. R.; *et al.* *J. Alloys Comp.* **2007**, *444–445*, 329–332.
- Peterson, D. T.; Fahey, J. A.; Baybarz, R. D. *J. Inorg. Nucl. Chem.* **1971**, *33*, 3345–3351.
- Haire, R. G.; Baybarz, R. D. *J. Inorg. Nucl. Chem.* **1973**, *35*, 489496.
- Oetting, F. L.; Rand, M. H.; Ackermann, R. J. *The Chemical Thermodynamics of Actinide Elements and Compounds. Part 1. The actinide Elements*. IAEA: Vienna, 1976.
- Ward, J. W.; Kleinschmidt, P. D.; Peterson, D. E. *Handbook on the Physics and Chemistry of the Actinides*; Freeman, A. J., Keller, C., Eds.; North Holland: Amsterdam, 1986; Vol 4, Chapter 7, pp 309–412.
- Cox, J. D.; Wagman, D. D.; Medvedev, V. A. *CODATA Key Values for Thermodynamics*; Hemisphere: New York, 1989.
- Grenthe, I.; Fuger, J.; Konings, R. J. M.; *et al.* *Chemical Thermodynamics of Uranium*; Elsevier: Amsterdam, 1992.
- Silva, R. J.; Bidoglio, G.; Rand, M. H.; Robouch, P. B.; Wanner, H.; Puigdomenech, I. *Chemical Thermodynamics of Americium*; Elsevier: Amsterdam, 1995.
- Lemire, R. J.; Fuger, J.; Nitsche, H.; *et al.* *Chemical Thermodynamics of Neptunium and Plutonium*; Elsevier: Amsterdam, 2001.
- Rand, M.; Fuger, J.; Grenthe, I.; Neck, V.; Rai, D. *Chemical Thermodynamics of Thorium*; OECD: Paris, 2009.
- Konings, R. J. M.; Beneš, O. *J. Phys. Chem. Ref. Data* **2010**, *39*, 043102.
- Müller, W.; Schenkel, R.; Schmidt, H. E.; *et al.* *J. Low Temp. Phys.* **1980**, *30*, 561–578.
- Sandenaw, T. A.; Olsen, C. E.; Gibney, R. B. In *Plutonium 1960*; Cleaver-Hume Press: London, 1961; pp 66–79.
- Sandenaw, T. A. *Phys. J. Chem. Solids* **1962**, *23*, 1241.
- Taylor, J. C.; Loasby, R. G.; Dean, D. J.; Linford, P. F. *J. Inst. Met.* **1968**, *96*, 178–186.
- Lee, J. A.; Mendelssohn, K.; Sutcliffe, P. W. *Proc. Roy. Soc. Lond. A* **1970**, *317*, 303–317.
- Sandenaw, T. A.; Gibby, R. B. *J. Chem. Thermodyn.* **1971**, *3*, 85–95.
- Gordon, J. E.; Hall, R. O. A.; Lee, J. A.; Mortimer, M. J. *Proc. Roy. Soc. Lond.* **1976**, *351A*, 179–196.
- Lashley, J. C.; Singleton, J.; Migliori, A.; *et al.* *Phys. Rev. Lett.* **2003**, *91*, 205901.
- Oetting, F. L.; Adams, R. O. *J. Chem. Thermodyn.* **1983**, *15*, 537.
- Gordon anmd, J. E.; Montgomery, H.; Noer, R. J.; Pickett, G. R.; Tobón, R. *Phys. Rev.* **1966**, *152*, 432–437.
- Stewart, G. R.; Smith, J. L.; Spirelet, J. C.; Müller, W. In *Proceedings of 3rd Conference on Superconductivity in 5f and 6d metals*, La Jolla, CA; Subl, H., Maple, M. B., Eds.; Academic Press: New York, 1979, pp 65–70.
- Mihaila, B.; Opeil, C. P.; Drymiotis, F. R.; *et al.* *Phys. Rev. Lett.* **2006**, *96*, 076401.
- Hall, R. O. A.; Lee, J. A.; Mortimer, M. J.; McElroy, D. L.; Müller, W.; Spirelet, J. C. *J. Low Temp. Phys.* **1980**, *41*, 397.
- Moore, K. T.; van der Laan, G. *Rev. Mod. Phys.* **2009**, *81*, 235–298.
- Gouder, T.; van der Laan, G.; Shick, A. B.; Haire, R. G.; Caciuffo, R. *Phys. Rev. B* **2011**, *83*, 125111.
- Javorský, P.; Havela, L.; Wastin, F.; Colineau, E.; Bouëxière, D. *Phys. Rev. Lett.* **2006**, *96*, 156404.

51. Havela, L.; Javorsky, P.; Shick, A. B.; *et al.* *Phys. Rev. B* **2010**, 82, 155140.
52. Konings, R. J. M. *J. Alloys Comp.* **2003**, 348, 38–42.
53. Young, D. A. Lawrence Livermore Laboratory, Technical Report UCRL-52352; 1977.
54. Konings, R. J. M. *J. Nucl. Mater.* **2001**, 295, 57–63.
55. Brewer, L. *High Temp. Sci.* **1984**, 17, 1.
56. Blaise, J.; Wyart, J. F. <http://www.lac.u-psud.fr/Database/Contents.html>, 2009.
57. Worden, E. F.; Blaise, J.; Fred, M.; Trautmann, N.; Wyart, J. F. In *The Chemistry of the Actinide and Transactinide Elements*; Morss, L. R., Edelstein, N., Fuger, J., Katz, J. J., Eds.; Springer Verlag, 2006; Chapter 16, pp 1836–1892.
58. Foster, K. W. Technical Report MLM-901; 1953.
59. Kleinschmidt, P. D.; Ward, J. W.; Matlack, G. M.; Haire, R. G. *J. Chem. Phys.* **1984**, 81, 473–477.
60. Haire, R. G.; Gibson, J. K. *J. Chem. Phys.* **1989**, 91, 7085–7096.
61. Nugent, L. J.; Burnett, J. L.; Morss, L. R. *J. Chem. Thermodyn.* **1973**, 5, 665–678.
62. Touloukian, Y. S.; Kirby, R. K.; Taylor, R. E.; Desai, P. D. *Thermophysical Properties of Matter, Vol. 12: Thermal Expansion*; IFI/Plenum: New York-Washington, 1975.
63. Schonfeld, F. W.; Tate, R. E. Los Alamos National Laboratory, Technical Report LA-13034-MS; 1996.
64. Sahu, P. C.; Yousuf, M.; Rajan, K. G. *Physica B* **1989**, 160, 177–182.
65. Arais, S.; Flora, R. H.; Anderson, E. E. *J. Nucl. Mater.* **1970**, 37, 89–95.
66. Koch, G. *Gmelin Handbuch der Anorganische Chemie. Band B1 Transurane*. (Ed.), Springer Verlag: Berlin, 1976.
67. Sandenaw, T. A.; Gibby, R. B. *J. Phys. Chem. Solids* **1958**, 6, 81–87.
68. McWhan, D. B.; Wallmann, J. C.; Cunningham, B. B.; Asprey, L. B.; Ellinger, F. H.; Zachariasen, W. H. *J. Inorg. Nucl. Chem.* **1960**, 15, 185–192.
69. Zachariasen, W. H. *Acta Cryst.* **1952**, 5, 664–666.
70. McWhan, D. B.; Cunningham, B. B.; Wallmann, J. C. *J. Inorg. Nucl. Chem.* **1962**, 24, 1025–1038.
71. Boring, A. M.; Smith, J. L. *Los Alamos Sci.* **2000**, 26, 91–127.
72. Huray, P. G.; Nave, S. E.; Peterson, J. R.; Haire, R. G. *Physica* **1980**, 102B, 217–220.
73. Chiotti, P.; Gartner, G. J.; Stevens, E. R.; Saito, Y. *J. Chem. Eng. Data* **1966**, 11, 571.
74. Meaden, G. T. *Proc. Roy. Soc. Lond.* **1963**, 276A, 553–570.
75. Still, L. R.; Legvold, S. *Phys. Rev.* **1965**, 137, A1139.
76. Touloukian, Y. S.; Powell, R. W.; Ho, C. Y.; Klemens, P. G. *Thermophysical Properties of Matter, Vol. 1: Thermal Conductivity*; IFI/Plenum: New York-Washington, 1975.
77. Wittenberg, L. J. *Thermochim. Acta* **1973**, 7, 13–23.
78. Wittenberg, J. L.; Engel, K.; Vaughn, A. In *Plutonium 1970*, Proceedings of 4th International Conference on Plutonium and Other Actinides; 1970; p 46.
79. Konings, R. J. M. *J. Nucl. Mater.* **2001**, 298, 255–268.
80. Grosse, A. V.; Cahill, J. A.; Kishenbaum, A. D. *J. Am. Chem. Soc.* **1961**, 83, 4665–4666.
81. Rohr, W. G.; Wittenberg, L. J. *J. Phys. Chem.* **1970**, 74, 1151–1152.
82. Shpil'rain, É. É.; Fomin, V. A.; Kachalov, V. V. *High. Temp.* **1989**, 26, 690–697.
83. Fischer, E. A. Technical Report FZKA 6387; 2000.
84. Olsen, C. E.; Sandenaw, T. A.; Herrick, C. C. Los Alamos Scientific Laboratory, Los Alamos, NM, Technical Report LA-2358; 1955.
85. Serpan, C. Z.; Wittenberg, L. J. *Trans. Metall. Soc. AIME* **1961**, 221, 1017–1020.
86. Ofte, D. *J. Nucl. Mater.* **1967**, 22, 28–32.
87. Jones, L. V.; Ofte, D.; Rohr, L. J.; Wittenberg, L. J. *Am. Soc. Met. Trans. Quart.* **1962**, 55, 819–825.
88. Grosse, A. V. *Inorg. J. Nucl. Chem.* **1961**, 23, 333–339.
89. Cahill, J. A.; Kirshenbaum, A. D. *J. Inorg. Nucl. Chem.* **1965**, 27, 73–76.
90. Spriet, B. *Mem. Etud. Sci. Rev. Met.* **1963**, 60, 531.

2.02 Thermodynamic and Thermophysical Properties of the Actinide Oxides

C. Guéneau, A. Chartier, and L. Van Brutzel

Commissariat à l'Energie Atomique, Gif-sur-Yvette, France

© 2012 Elsevier Ltd. All rights reserved.

2.02.1	Introduction	22
2.02.2	Phase Diagrams of Actinide–Oxygen Systems	23
2.02.2.1	U–O System	23
2.02.2.2	Pu–O System	23
2.02.2.3	Th–O and Np–O Systems	25
2.02.2.4	Am–O System	26
2.02.2.5	Cm–O System	26
2.02.2.6	Bk–O System	27
2.02.2.7	U–Pu–O System	27
2.02.2.7.1	UO ₂ –PuO ₂	27
2.02.2.7.2	U ₃ O ₈ –UO ₂ –PuO ₂ –Pu ₂ O ₃	27
2.02.2.8	UO ₂ –ThO ₂ and PuO ₂ –ThO ₂ Systems	29
2.02.3	Crystal Structure Data and Thermal Expansion	30
2.02.3.1	Actinide Dioxides	30
2.02.3.1.1	Stoichiometric dioxides	30
2.02.3.1.2	Stoichiometric mixed dioxides	31
2.02.3.1.3	Nonstoichiometric actinide dioxides	33
2.02.3.2	Actinide Sesquioxides	34
2.02.3.3	Other Actinide Oxides	35
2.02.4	Thermodynamic Data	36
2.02.4.1	Binary Stoichiometric Compounds	36
2.02.4.1.1	Actinide dioxides	36
2.02.4.1.2	Actinide sesquioxides	38
2.02.4.1.3	Other actinide oxides with O/metal > 2	39
2.02.4.2	Mixed Oxides	39
2.02.4.3	Nonstoichiometric Dioxides	40
2.02.4.3.1	Defects	40
2.02.4.3.2	Oxygen potential data	42
2.02.5	Vaporization	46
2.02.5.1	Pu–O and U–O	47
2.02.5.2	U–Pu–O	48
2.02.5.3	U–Pu–Am–O	48
2.02.6	Transport Properties	48
2.02.6.1	Self-Diffusion	48
2.02.6.1.1	Oxygen diffusion	49
2.02.6.1.2	Cation diffusion	51
2.02.6.2	Thermal Conductivity	51
2.02.6.2.1	Actinide dioxides	51
2.02.6.2.2	Actinide sesquioxides	54
2.02.7	Thermal Creep	54
2.02.8	Conclusion	55
References		55

Abbreviations

CALPHAD	Computer coupling of phase diagrams and thermochemistry
CODATA	The Committee on Data for Science and Technology
DFT	Density functional theory
EMF	Electromotive force
EXAFS	Extended X-ray absorption fine structure
fcc	Face-centered cubic
IAEA	International atomic energy agency
MD	Molecular dynamics
MOX	Mixed dioxide of uranium and plutonium
NEA	The Nuclear Energy Agency of the OECD
OECD	The Organisation for Economic Co-operation and Development
XAS	X-ray absorption spectroscopy
XPS	X-ray photoelectron spectroscopy

2.02.1 Introduction

Owing to the wide range of oxidation states +2, +3, +4, +5, and +6 that can exist for the actinides, the chemistry of the actinide oxides is complex. The main known solid phases with different stoichiometries are shown in Table 1.

Actinide oxides mainly form sesquioxides and dioxides. The +3 oxides of actinides have the general formula M_2O_3 , in which 'M' (for metal) is any of the actinide elements except thorium, protactinium, uranium, and neptunium; they form hexagonal, cubic, and/or monoclinic crystals.

Crystalline compounds with the +4 oxidation state exist for thorium, protactinium, uranium, neptunium, plutonium, americium, curium, berkelium, and californium. The dioxides MO_2 are all isostructural with the fluorite face-centered cubic (fcc)

structure. Most of these actinide compounds can be prepared in a dry state by igniting the metal itself, or one of its other compounds, in an atmosphere of oxygen. The stability of the dioxides decreases with the atomic number Z . All dioxides are hypostoichiometric (MO_{2-x}). Only uranium dioxide can become hyperstoichiometric (MO_{2+x}). The thermodynamic properties of the dioxides vary with both temperature and departure from the stoichiometry $O/M = 2$.

Only uranium, neptunium, and protactinium form oxide phases with oxygen/metal ratio >2 . An oxidation state greater than +4 can exist in these phases. The +6 state exists for uranium and neptunium in UO_3 and NpO_3 . Intermediate states are found in U_4O_9 and U_3O_8 arising from a mix of several oxidation states (+4, +5, +6).

Detailed information on the preparation of the binary oxides of the actinide elements can be found in the review by Haire and Eyring.¹

The absence of features at the Fermi level in the observed XPS spectra indicates that all the dioxides are semiconductors or insulators.²

Systematic investigations of the actinide oxides using first-principles calculations were very useful to explain the existing oxidation states of the different oxides in relation with their electronic structure. For example, Petit and coworkers^{3,4} clearly showed that the degree of oxidation of the actinide oxides is linked to the degree of f -electron localization. In the series from U to Cf, the nature of the f -electrons changes from delocalized in the early actinides to localized in the later actinides. Therefore, in the early actinides, the f -electrons are less bound to the actinide ions which can exist with valencies as high as +5 and +6 for uranium oxides, for example. In the series, the f -electrons become increasingly bound to the actinide ion, and for Cf only the +3 valency occurs. With the same method, Andersson *et al.*⁵ studied the oxidation thermodynamics of UO_2 , NpO_2 , and PuO_2 within fluorite structures. The results show that UO_2 exhibits strong negative energy of oxidation, while NpO_2 is harder to oxidize and

Table 1 Known stable phases of actinide oxides. The phases marked with * are considered as metastable phases

	<i>Ac</i>	<i>Th</i>	<i>Pa</i>	<i>U</i>	<i>Np</i>	<i>Pu</i>	<i>Am</i>	<i>Cm</i>	<i>Bk</i>	<i>Cf</i>	<i>Es</i>
+2		ThO*		UO*		PuO*					EsO
+3	Ac ₂ O ₃					Pu ₂ O ₃	Am ₂ O ₃	Cm ₂ O ₃	Bk ₂ O ₃	Cf ₂ O ₃	Es ₂ O ₃
+4		ThO ₂	PaO ₂	UO ₂	NpO ₂	PuO ₂	AmO ₂	CmO ₂	BkO ₂	CfO ₂	
+5			Pa ₂ O ₅	U ₄ O ₉ U ₃ O ₈	Np ₂ O ₅						
+6				UO ₃	NpO ₃						

PuO_2 has a positive or slightly negative oxidation energy. As in Petit and coworkers,^{3,4} the authors showed that the degree of oxidation is related to the position of the 5f electrons relative to the 2p band. For PuO_2 , the overlap of 5f and 2p states suppresses oxidation. The presence of H_2O can turn oxidation of PuO_2 into an exothermic process. This explains clearly why hyperstoichiometric PuO_{2+x} phase is observed only in the presence of H_2O or hydrolysis products.⁶

Solid actinide monoxides 'MO' were reported to exist for Th, Pu, and U. According to the experimental characterization of plutonium oxide phases by Larson and Haschke,⁷ these phases are generally considered as metastable phases or as ternary phases easily stabilized by carbon or/and nitrogen. From first-principles calculations, Petit *et al.*³ confirmed that the divalent configuration M^{2+} is never favored for the actinides except maybe for EsO . On the contrary, the monoxides of actinide $\text{MO}(\text{g})$ are stable as vapor species that are found together with other gas species $\text{M}(\text{g})$, $\text{MO}_2(\text{g})$, $\text{MO}_3(\text{g})$ which fraction depends on oxygen composition and temperature when heating actinide oxides.

In Sections 2.02.2 and 2.02.3, the phase diagrams of the actinide–oxygen systems, the crystal structure data, and the thermal expansion of the different oxide phases will be described. The related thermodynamic data on the compounds and the vaporization behavior of the actinide oxides will be presented in Sections 2.02.4 and 2.02.5. Finally, the transport properties (diffusion and thermal conductivity) and the thermal creep of the actinide oxides will be reviewed in Sections 2.02.6 and 2.02.7.

2.02.2 Phase Diagrams of Actinide–Oxygen Systems

There is no available phase diagram for the Ac–O, Pa–O, Cf–O, and Es–O systems. For the other systems, the phase diagrams remain very uncertain. In most of the cases, only the regions of the diagrams relevant to the binary oxides have been investigated because of the great interest in actinide oxides as nuclear fuels. As a consequence, the metal–oxide part of the actinide–oxygen systems is generally not well known except for the U–O system, which is the most extensively investigated system. For the actinide–oxygen systems, a miscibility gap in the liquid state is generally expected at high temperature like in many metal–oxygen systems; it leads to the

simultaneous formation of a metal-rich liquid in equilibrium with an oxide-rich liquid. But the extent of the miscibility gap and the solubility limit of oxygen in the liquid metals are generally not known. The existing phase diagram data on the binary U–O, Pu–O, Th–O, Np–O, Am–O, Cm–O, Bk–O, and ternary U–Pu–O, UO_2 –Th O_2 , and PuO_2 –Th O_2 are presented.

2.02.2.1 U–O System

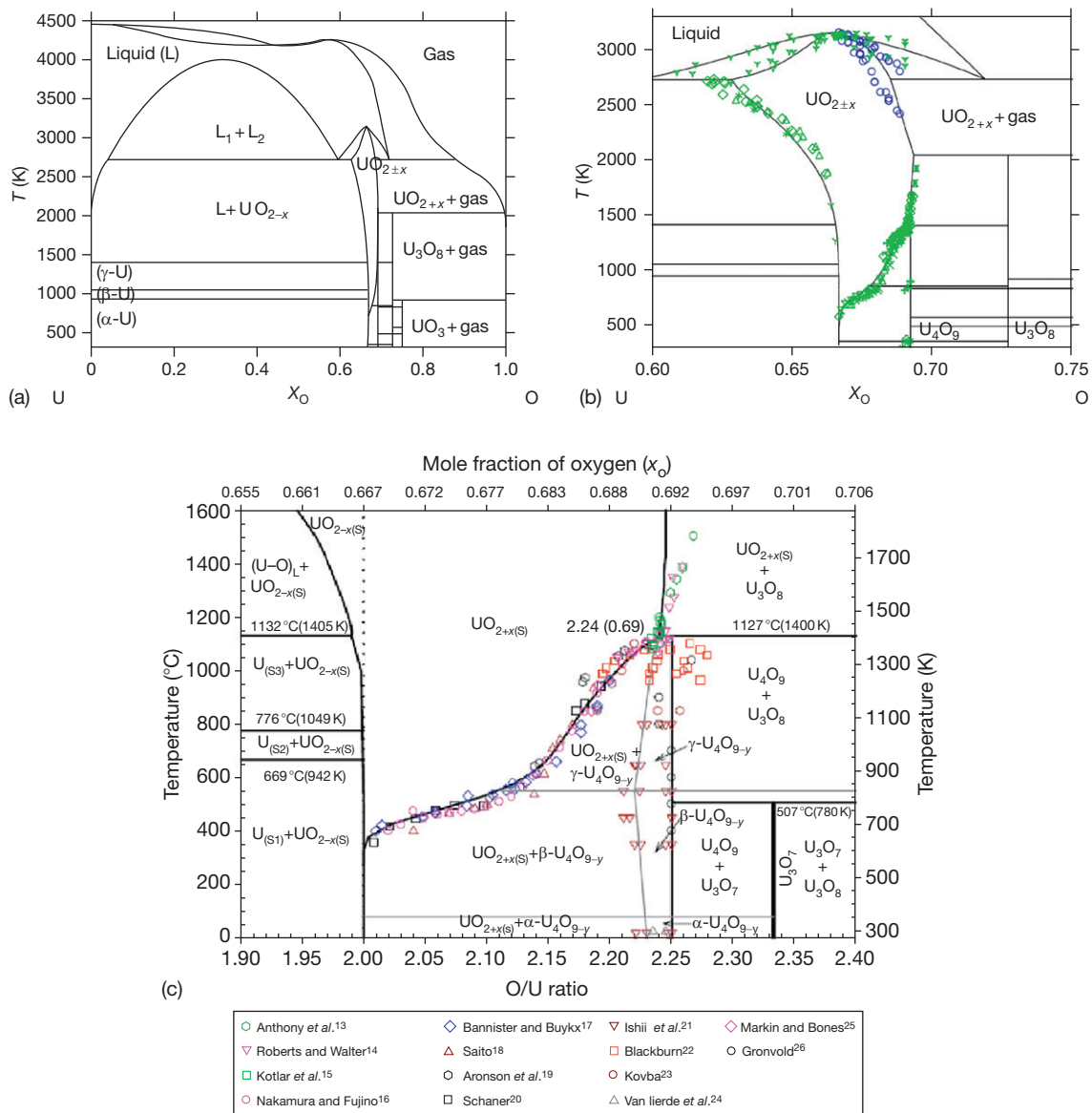
The phase diagram of the uranium–oxygen system, calculated by Guéneau *et al.*⁸ using a CALPHAD thermochemical modeling, is given in Figure 1(a) and 1(b) from 60 to 75 at.% O. In the U– UO_2 region, a large miscibility gap exists in the liquid state above 2720 K. The homogeneity range of uranium dioxide extends to both hypo- and hyperstoichiometric compositions in oxygen. The minimum and maximum oxygen contents in the dioxide correspond to the compounds with the formula of respectively $\text{UO}_{1.67}$ at 2720 K and $\text{UO}_{2.25}$ at approximately 2030 K. The phase becomes hypostoichiometric above approximately 1200 K while the dioxide incorporates additional oxygen atoms at low temperature, above 600 K. The dioxide melts congruently at 3120 ± 20 K. The melting temperature decreases with departure from the stoichiometry. The experimental data on solidus/liquidus temperature for UO_{2+x} from Manara *et al.*,¹¹ reported in Figure 1(b), are significantly lower than those reported in Baichi *et al.*⁹ and will have to be taken into account in new thermodynamic assessments.

In the UO_2 – UO_3 region (Figure 1(b) and 1(c)), the oxides U_4O_9 , U_3O_8 , and UO_3 are formed with different crystal forms. U_4O_9 and U_3O_8 are slightly hypostoichiometric in oxygen as shown in Figure 1(c). The U_3O_7 compound is often found as an intermediate phase formed during oxidation of UO_2 . This compound is reported in the phase diagram proposed by Higgs *et al.*¹² and considered as a metastable phase by Guéneau *et al.*⁸

2.02.2.2 Pu–O System

A thermodynamic model of the Pu–O system was proposed by Kinoshita *et al.*²⁷ and Guéneau *et al.*²⁸ The calculated phase diagram by Guéneau *et al.*²⁸ reproduces the main features of the phase diagram proposed by Wriedt²⁹ in his critical review (Figure 2).

In the Pu– Pu_2O_3 region of the phase diagram, the experimental data are rare. The existence of



*The horizontal line constructions (gray) at 80 and 550 °C reflect the inability to distinguish the transformation temperatures in the adjacent two-phase fields.

Figure 1 U–O phase diagram (a) calculated using the model derived by Guéneau *et al.*⁸; (b) calculated from 60 to 75 at.% O₂; the green points come from the critical review by Baichi *et al.*⁹ and Labroche *et al.*¹⁰ and the blue points show the results of Manara *et al.*¹¹; (c) calculated from O/U = 1.9 to 2.4 after Higgs *et al.*¹² The references of the experimental data are given in Higgs *et al.*¹² © Elsevier, reprinted with permission.

a miscibility gap in the liquid state was shown by Martin and Mrazek.³⁰ The monotectic reaction was measured at 2098 K.³⁰ There are no data on the oxygen solubility limit in liquid plutonium.

More data are available in the region between Pu₂O₃ and PuO₂. The phase relations are complex below 1400 K. PuO_{2-x} starts to lose oxygen above

approximately 900 K. A narrow miscibility gap was found to exist in the fluorite phase below approximately 900 K leading to the simultaneous presence of two fcc phases with different stoichiometries in oxygen. Two intermediate oxide phases were found to exist with the formula PuO_{1.61} and PuO_{1.52}. The PuO_{1.61} phase exhibits a composition range and is

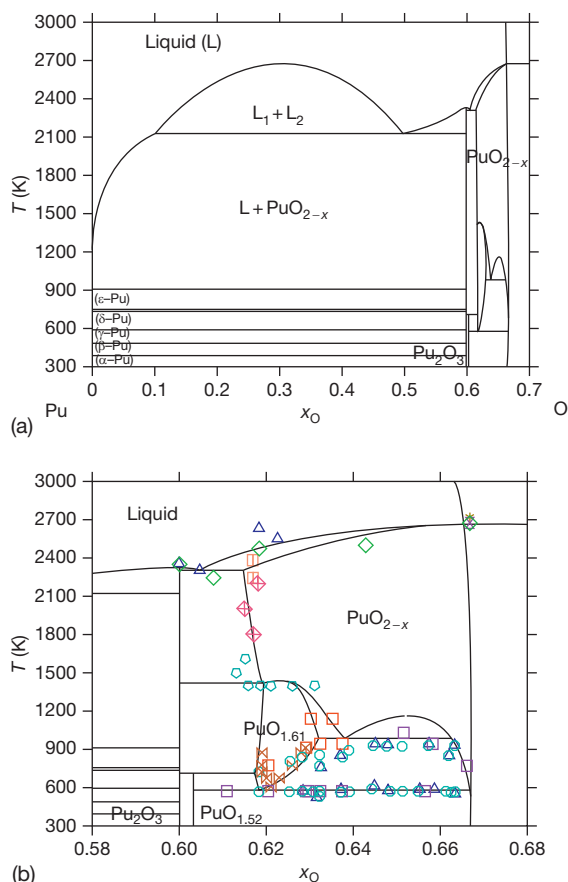


Figure 2 (a) Calculated Pu–O phase diagram after Guéneau *et al.*²⁸ on the basis of the critical analysis by Wriedt²⁹; (b) calculated phase diagram with experimental data from 58 to 68 at. % O as reported in Guéneau *et al.*²⁸

stable between 600 and 1400 K. The $\text{PuO}_{1.52}$ compound only exists at low temperature ($T < \sim 700$ K).

Above ~ 1400 K, the dioxide PuO_{2-x} exhibits a large homogeneity range with a minimum O/Pu ratio equal to approximately 1.6 and is in equilibrium with the sesquioxide Pu_2O_3 . The liquidus temperatures between Pu_2O_3 and PuO_2 remain uncertain and would need future determinations.

The melting temperature of PuO_2 is still a subject of controversy. The recommended value for the melting of PuO_2 was for a long time $T_m = 2674 \pm 20$ K, based on measurements from Riley.³¹ Recent measurements are available that suggest higher values. In 2008, Kato *et al.*³² measured the melting point of PuO_2 at 2843 K that is higher by 200 K than the previous measurements. The authors used the same thermal arrest method as in previously published works but paid more attention to the sample/crucible

chemical interaction by using rhenium instead of tungsten for the container. Very recently, a reassessment of the melting temperature of PuO_2 was performed by De Bruycker *et al.*³³ using a novel experimental approach used in Manara *et al.*¹¹ for UO_2 . The new value of 3017 ± 28 K exceeds the measurement by Kato *et al.* by 174 K. The noncontact method and the short duration of the experiments undertaken by De Bruycker *et al.*³³ give confidence to their new value which has been very recently taken into account in the thermodynamic modeling of the Pu–O system.⁴² Both studies agree on the fact that the values measured in the past were underestimated.

2.02.2.3 Th–O and Np–O Systems

The Th–O and Np–O phase diagrams, according to the experimental studies by Benz³⁴ and Richter and Sari³⁵ are given, respectively, in Figure 3(a) and 3(b).

In the Th–O phase diagram (Figure 3(a)), only the dioxide ThO_2 exists. At low temperature, according to Benz,³⁴ the oxygen solubility limit in solid Th is low ($\text{O}/\text{Th} < 0.003$). A eutectic reaction occurs at 2008 ± 20 K with a liquid composition very close to pure thorium. The existence of a miscibility gap has been found to occur above 3013 ± 100 K that leads to the formation of two liquid phases with O/Th ratios equal to 0.4 and 1.5 ± 0.2 , respectively. The phase boundary of ThO_{2-x} in equilibrium with liquid thorium was measured. The lower oxygen composition for ThO_{2-x} at the monotectic reaction corresponds to $\text{O}/\text{Th} = 1.87 \pm 0.04$. The melting point of ThO_2 recommended by Konings *et al.*³⁶ is $T_m = 3651 \pm 17$ K. This value corresponds to the measurement by Ronchi and Hiernaut,³⁷ which is in good agreement with the one reported on the phase diagram proposed by Benz³⁴ in Figure 3(a).

The Np–O phase diagram looks very similar to the Th–O system but the experimental information is very limited. In the Np– NpO_2 region, a miscibility gap in the liquid system is expected but no experimental data exist on the oxygen solubility limit in liquid neptunium and on the extent of this miscibility gap. The dioxide exhibits a narrow hypostoichiometric homogeneity range (NpO_{2-x}) for temperatures above 1300 K. The phase boundary of NpO_{2-x} in equilibrium with the liquid metal is not well known. The minimum O/Np ratio is estimated to be about 1.9 at approximately 2300 K according to Figure 3(b). The recommended melting point for NpO_2 is $T_m = 2836 \pm 50$ K.^{36,38} Only the part richer in oxygen differs from Th–O with the presence of the

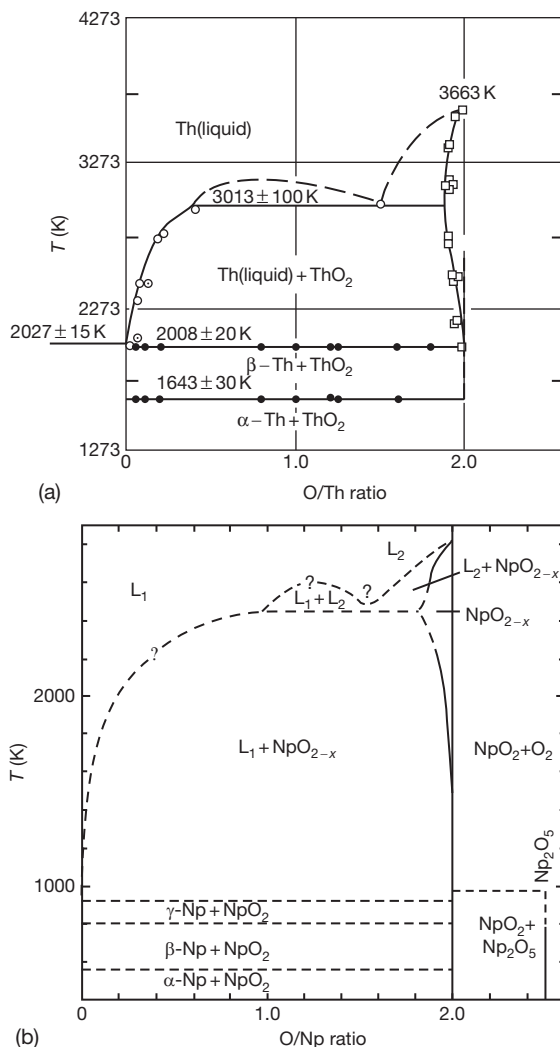


Figure 3 Th–O (a) and Np–O (b) phase diagrams after respectively Benz³⁴ and Richter and Sari.³⁵ © Elsevier, reproduced with permission.

Np_2O_5 oxide which decomposes at 700 K to form NpO_2 and gaseous oxygen. The thermodynamic properties of the Np–O system were modeled by Kinoshita *et al.*³⁹ using the CALPHAD method, but the calculated phase diagram does not reproduce correctly the available experimental data for the oxygen solubility limit in NpO_{2-x} in equilibrium with liquid neptunium.

2.02.2.4 Am–O System

The tentative Am–O phase diagram between Am_2O_3 and AmO_2 shown in Figure 4 has been proposed by Thiriet and Konings,⁴⁰ based on an analysis of the experimental data available in the literature.

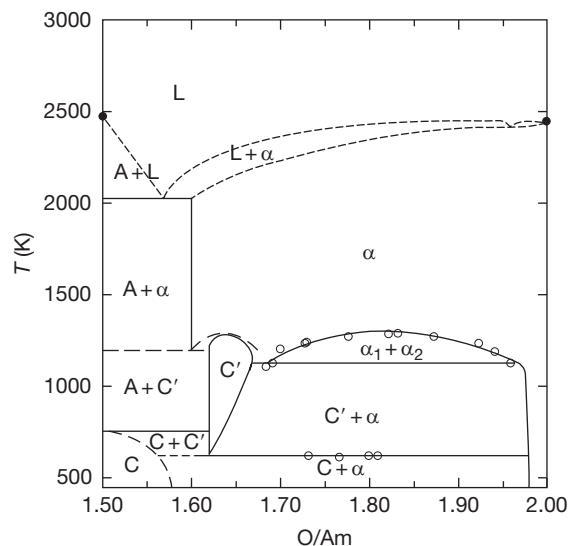


Figure 4 Am_2O_3 – AmO_2 phase diagram from Thiriet and Konings.⁴⁰ © Elsevier, reproduced with permission.

No data are available in the Am– Am_2O_3 region. The Am_2O_3 – AmO_2 region looks very similar to the Pu_2O_3 – PuO_2 phase diagram (Figure 2(b)). The sesquioxide Am_2O_3 exists with hexagonal (A) and cubic (C) forms. The dioxide AmO_2 (α) starts to lose oxygen above approximately 1200 K. AmO_{2-x} has a wide composition range at high temperature with a minimum O/Am ratio equal to approximately 1.6. As in the Pu–O system, the existence of a narrow miscibility gap in the fcc phase and an intermediate oxide phase with the formula $\text{AmO}_{1.62}$ (C') were found by Sari and Zamorani.⁴¹ A thermodynamic model of the Am–O system has been very recently derived by Gotcu-Freis *et al.*⁴² using the CALPHAD method. The calculated phase diagram is quite consistent with the proposed one by Thiriet and Konings.⁴⁰

2.02.2.5 Cm–O System

A complete review of the Cm_2O_3 – CmO_2 region of the Cm–O phase diagram was performed by Konings⁴³ who proposed the revised tentative Cm_2O_3 – CmO_2 phase diagram in Figure 5, on the basis of the suggestion by Smith and Peterson.⁴⁴

The sesquioxide exists in several forms: cubic (C-type), monoclinic (B-type), and hexagonal (A-type) and X. Intermediate phases were observed: a bcc phase σ , with a variable composition (O/Cm between 1.52 and 1.64), a rhombohedral phase with the formula $\text{CmO}_{1.71}$ (I), and a fluorite phase $\text{CmO}_{1.83}$ (δ). CmO_2 (α) is stable up to 653 K at which temperature it

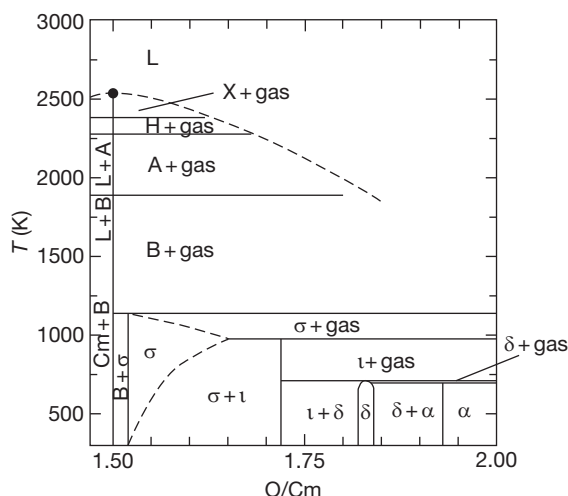


Figure 5 The tentative Cm_2O_3 – CmO_2 phase diagram ($p_{\text{O}_2} = 0.2$ bar) according to the critical review by Konings.⁴³ © Elsevier, reprinted with permission.

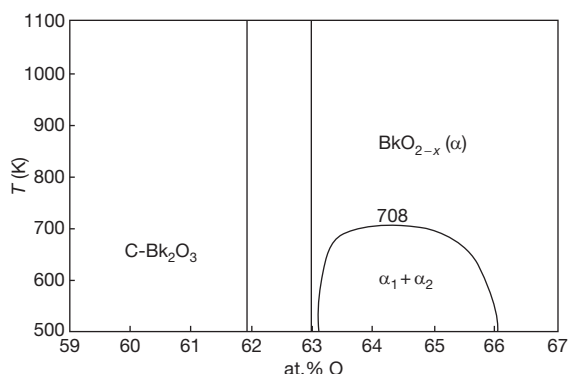


Figure 6 Partial Bk–O phase diagram according to Okamoto.⁴⁵

decomposes into gas and intermediate oxides ($\text{CmO}_{1.83}$ and $\text{CmO}_{1.71}$). CmO_{2-x} exhibits a small range of composition with a minimum O/Cm ratio of 1.97.

2.02.2.6 Bk–O System

A partial phase diagram of the Bk–O system is shown in Figure 6 as proposed in the review by Okamoto.⁴⁵ A high-temperature X-ray diffraction study by Turcotte *et al.*⁴⁶ showed the existence of C- Bk_2O_3 (bcc) and α - BkO_2 (fcc) oxides. A miscibility gap in the α - BkO_2 fcc phase was found to exist below 708 K. The sesquioxide exists with several forms: C- Bk_2O_3 (bcc) transforms to B- Bk_2O_3 (monoclinic) at 1473 ± 50 K according to Baybarz.⁴⁷ The monoclinic

phase B- Bk_2O_3 transforms to the hexagonal form A- Bk_2O_3 (hexagonal) at approximately 2023 K, which melts at 2193 K.

2.02.2.7 U–Pu–O System

It is important to mention that the phase diagram of the U–Pu–O system is still not well known. There are no data on the metal-oxide region U–Pu– Pu_2O_3 – UO_2 of the U–Pu–O phase diagram. The solubility of the oxide phases in the metallic liquid (U,Pu) is not known. Only few experimental data exist in the region of stability of the oxide phases delimited by the compounds U_3O_8 – UO_2 – Pu_2O_3 – PuO_2 .

2.02.2.7.1 UO_2 – PuO_2

UO_2 and PuO_2 form a continuous solid solution and the solidus and liquidus temperatures show a nearly ideal behavior, as shown in the UO_2 – PuO_2 pseudo-binary phase diagram in Figure 7(a). As expected, the melting point of the mixed oxide decreases with the plutonium content in the solid solution. The recommended equations for the solidus and liquidus curves from Adamson *et al.*⁵¹ are

$$T_{\text{solidus}}(\text{K}) = 3120 - 355.3x + 336.4x^2 - 99.9x^3 \quad [1]$$

$$T_{\text{liquidus}}(\text{K}) = 3120 - 388.1x - 30.4x^2 \quad [2]$$

It must be mentioned that recent measurements were performed by Kato *et al.*³² on UO_2 – PuO_2 solid solutions. The resulting solidus and liquidus temperatures are higher than those from the previous studies (eqns [1] and [2]). As reported in Section 2.02.2.2, the melting point of pure oxide PuO_2 measured by Kato *et al.* and later by De Bruycker *et al.*³³ was higher than the recommended value. New determinations are necessary to confirm the validity of these new data.

Recent measurements on hypostoichiometric solid solutions $(\text{U,Pu})\text{O}_{2-x}$ were also performed by Kato *et al.*⁵⁰ The solidus temperatures decrease with increasing Pu content and with decreasing O to metal ratio. A congruent melting line was found to exist that connects the hypostoichiometric $\text{PuO}_{1.7}$ to stoichiometric UO_2 .

2.02.2.7.2 U_3O_8 – UO_2 – PuO_2 – Pu_2O_3

Isothermal sections of the U–Pu–O phase diagram in the oxide-rich region are available only at 300, 673, 873, and 1073 K according to the review by Rand and Markin⁵² which is mainly on the basis of the

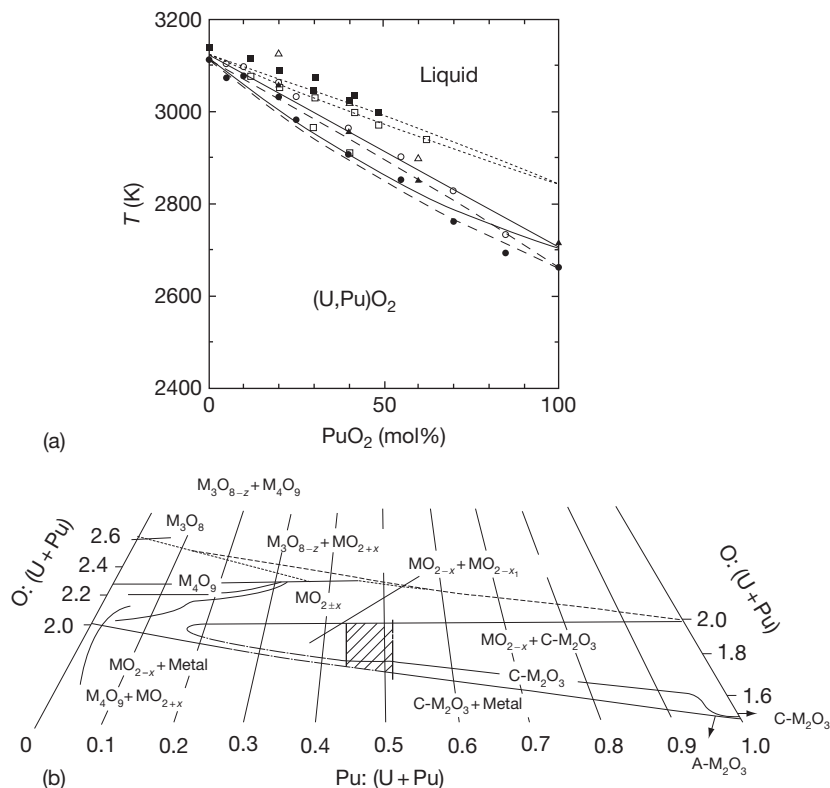


Figure 7 U–Pu–O phase diagram at room temperature (a) UO_2 – PuO_2 region; the circles correspond to the experimental data by Lyon and Bailey,⁴⁸ the triangles by Aitken and Evans,⁴⁹ and the squares by Kato *et al.*⁵⁰; the solid lines represent the recommended liquidus and solidus by Adamson *et al.*,⁵¹ the broken line represents the ideal liquidus and solidus based on Lyon and Bailey,⁴⁸ and the dotted line the liquidus and solidus suggested by Kato *et al.*⁵⁰ (b) U_3O_8 – UO_2 – PuO_2 – Pu_2O_3 region at room temperature. Reproduced from Konings, R. J. M.; Wiss, T.; Guéneau, C. In *The Chemistry of the Actinide and Transactinide Elements* 4th ed.; Morss, L. R., Fuger, J., Edelstein, N. M., Eds.; Nuclear Fuels; Springer: Netherlands, 2010; Vol. 6, Chapter 34, pp 3665–3812. © Springer, reprinted with permission.

experimental investigation by Markin and Street.⁵³ The isothermal section at room temperature was later slightly modified by Sari *et al.*⁵⁴ The fluorite-type structure of the mixed oxide $(\text{U,Pu})\text{O}_2$ has the ability to tolerate both addition of oxygen (by oxidation of the uranium) and its removal (by reduction of the plutonium only), leading to the formation of a wide homogeneity range of formula $\text{MO}_{2\pm x}$. Thus, at high temperature, the solid solution is a single phase that extends toward hypo- and hyperstoichiometry. But the extent of the single-phase domain is not well known at high temperature.

At low temperature, as shown in Figure 7(b) (redrawn in Konings *et al.*⁵⁵ from Rand and Markin,⁵² Markin and Street,⁵³ and Sari *et al.*⁵⁴), the oxide-rich part of the U–Pu–O phase diagram is complex:

- Region with O/metal ratio < 2

The mixed oxide $(\text{U}_{100-y}\text{Pu}_y)\text{O}_{2-x}$ with $y \leq 20$ at. % of Pu is a single phase. The hypostoichiometric

oxide is in equilibrium with (U,Pu) alloy. At $T < 900$ K, the mixed oxides $(\text{U}_{100-y}\text{Pu}_y)\text{O}_{2-x}$ with a plutonium content $y > 20$ at. % enter a two-phase region that leads to the decomposition into two fcc oxide phases with two different stoichiometries x and x_1 in oxygen, MO_{2-x} and MO_{2-x_1} . This is consistent with the existence of a miscibility gap in the fcc phase in the Pu–O system. This phase separation was recently observed in mixed oxides $(\text{U,Pu})\text{O}_2$ with small addition of Am and Np by Kato and Konashi.⁵⁶ For higher Pu contents ($y > 50$ at. %), the mixed oxide can enter other two-phase regions [$\text{MO}_{2-x} + \text{M}_2\text{O}_3$ (C)] and [$\text{MO}_{2-x} + \text{PuO}_{1.62}$]. The existence of these two-phase regions comes from the complex phase relations encountered in the Pu_2O_3 – PuO_2 phase diagram at $T < 1400$ K (Figure 2(b)). The isothermal sections at 673, 873, and 1073 K in Rand and Markin⁵² show that the extent of the two-phase regions decreases with temperature. The existence

of a single phase region M_2O_3 (C) was reported along the Pu_2O_3 – UO_2 composition line.

- Region with O/metal ratio > 2

At room temperature, the oxidation of mixed oxides with a Pu content lower than 50% results in either a single fcc phase, MO_{2+x} with a maximum O/M ratio of 2.27, or in two-phase regions $[\text{MO}_{2+x} + \text{M}_4\text{O}_9]$, $[\text{M}_4\text{O}_9 + \text{M}_3\text{O}_8]$ and $[\text{MO}_{2+x} + \text{M}_3\text{O}_8]$. The M_4O_9 and M_3O_8 phases are reported to incorporate a significant amount of plutonium. However, the exact amount is not known.

Yamanaka *et al.*⁵⁷ developed a CALPHAD model on the U–Pu–O system that reproduces some oxygen potential data in the mixed oxide $(\text{U,Pu})\text{O}_{2\pm x}$ and allows calculating the phase diagram. This model predicts the two-phase region $[\text{MO}_{2-x} + \text{PuO}_{1.62}]$ but does not reproduce the existence of the miscibility gap in the fcc phase. This region was recently reinvestigated by Agarwal *et al.*⁵⁸ using a thermochemical model. The resulting UO_2 – PuO_2 – Pu_2O_3 phase diagram is presented in Figure 8. The extent of the miscibility gap in the fcc phase is described as a function of temperature, Pu content, and O/metal ratio. This description of the phase diagram is not complete as it does not take into account the existence of the $\text{PuO}_{1.52}$ and $\text{PuO}_{1.61}$ phases that may lead to the formation of other two-phase regions involving the fcc phase.

In conclusion, no satisfactory description of the U–Pu–O system exists. Both new developments of models and experimental data are required.

2.02.2.8 UO_2 – ThO_2 and PuO_2 – ThO_2 Systems

Bakker *et al.*⁵⁹ performed a critical review of the phase diagram and of the thermodynamic properties of the UO_2 – ThO_2 system. Solid UO_2 and ThO_2 form an ideal continuous solid solution. The phase diagram proposed by Bakker *et al.*⁵⁹ on the basis of the available experimental data is presented in Figure 9(a). The authors report the large uncertainties on the phase diagram because of the experimental difficulties. The thermodynamic properties of $(\text{Th}_{1-y}\text{U}_y)\text{O}_2$ solid solutions have been recently investigated by Dash *et al.*⁶⁰ using a differential scanning calorimeter and a high-temperature drop calorimeter. The ternary compound ThUO_5 was synthesized and characterized by X-ray diffraction. The thermodynamic data on this compound were estimated.

Like UO_2 , PuO_2 forms a continuous solid solution with ThO_2 in the whole composition range. Limited melting point data were measured by Freshley and Mattys.⁶¹ The results indicate a nearly constant melting point up to 25 wt.% ThO_2 . In view of the

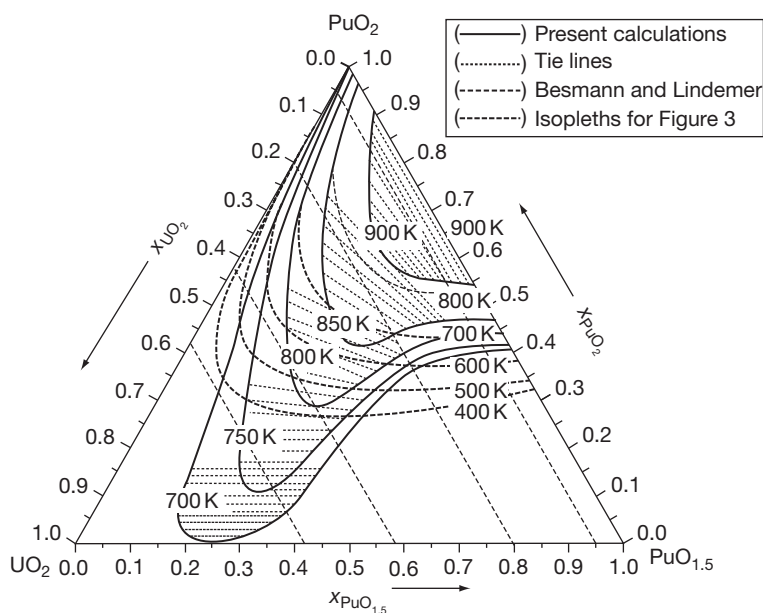


Figure 8 Miscibility gap in the fcc phase of the UO_2 – PuO_2 – Pu_2O_3 region according to Agarwal *et al.*⁵⁸ © Elsevier, reprinted with permission.

instability of PuO_2 at high temperature (high $p\text{O}_2$ over PuO_2), this behavior could be due to a change of the stoichiometry of the samples. The available liquidus temperature measurements do not reproduce the recommended value for the melting point of PuO_2 . The full lines in **Figure 9** give the solidus and liquidus curves considering an ideal behavior of the PuO_2 – ThO_2 system.

2.02.3 Crystal Structure Data and Thermal Expansion

The lattice parameters of actinide oxides are usually measured in glove boxes because of radioactivity and chemical hazards. In fact, the radioactive decay may drastically modify the cell parameters with

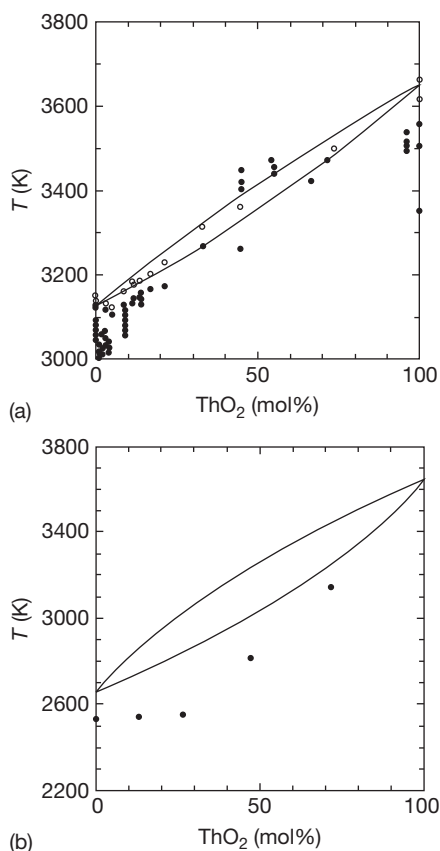


Figure 9 Pseudobinary (a) UO_2 – ThO_2 and (b) PuO_2 – ThO_2 phase diagrams. The solid lines represent the liquidus and solidus assuming an ideal solid solution. Details on the experimental data are given in Bakker *et al.*⁵⁹ Reprinted with permission from Konings, R. J. M.; Wiss, T.; Guéneau, C. *Chemistry of the Actinide and Transactinide Elements*, 4th edn.; Springer, 2010; Vol. 6, Chapter 24 (in press). © Springer.

characteristic time of months (see measurements on $(\text{Pu},\text{Am})\text{O}_2$ by Jankowiak *et al.*,⁶² on CmO_2 in the review by Konings,⁴³ and on sesquioxides by Baybarz *et al.*⁶³). Indeed, point defects (caused by irradiation or simply because of off-stoichiometry) may also induce expansion or contraction of the lattices.

The thermal expansion of the cell usually occurs when increasing the temperature, and it is usually measured starting at room temperature. Because of experimental difficulties – already mentioned – for measuring properties (and thus thermal expansion coefficients) in actinides, some *ab initio* and/or *molecular dynamics* (MD) calculations are nowadays done. In the framework of MD calculations, the evolution of the cell parameter can easily be followed as a function of temperature (see the calculations by Arima *et al.*⁶⁴ on UO_2 and PuO_2 , and by Uchida *et al.*⁶⁵ on AmO_2). The method is slightly different when *ab initio* calculations are performed (see, e.g., the work of Minamoto *et al.*⁶⁶ on PuO_2). One currently calculates the phonon spectra, estimates the free energy as a function of temperature by means of quasiharmonic approximation, and then extracts the linear thermal expansion. Such procedure may also be based on experimental data assuming some hypothesis and simplifications on the phonon spectra (see, e.g., Sobolev and coworkers^{67–69}).

2.02.3.1 Actinide Dioxides

2.02.3.1.1 Stoichiometric dioxides

The actinide dioxides exhibit a fluorite or CaF_2 structure (**Figure 10**). Each metal atom is surrounded by eight nearest neighbor O atoms. Each O atom is surrounded by a tetrahedron of four equivalent M atoms. The cell parameters are reported in **Table 2**. They are

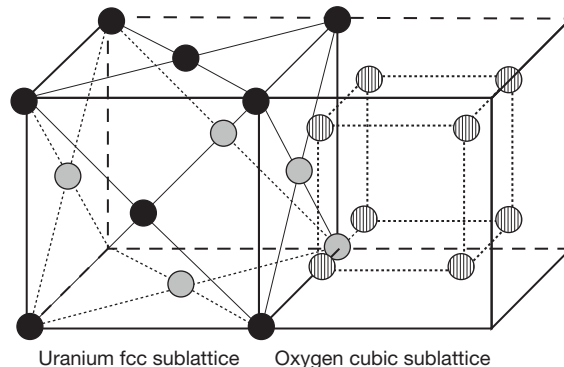
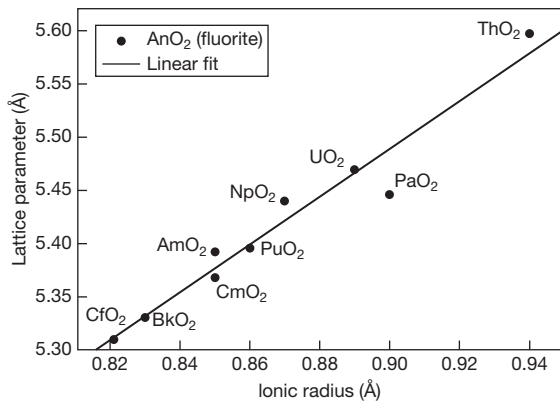


Figure 10 UO_2 fluorite (CaF_2) structure; the actinide (left) sublattice is fcc while the oxygen (right) sublattice is primitive cubic.

Table 2 Cell parameters and thermal expansion coefficients (eqn [3]) of actinides dioxides

	b_0 (pm)	$b_1 \times 10^3$ (pm K ⁻¹)	$b_2 \times 10^7$ (pm K ⁻²)	$b_3 \times 10^{10}$ (pm K ⁻³)	a_{298} (pm)	References
ThO ₂	558.348	4.628	0.04708	2.512	559.74	Yamashita <i>et al.</i> ⁷¹
PaO ₂					544.6	Stchouzkoy <i>et al.</i> ⁷²
UO ₂	545.567	4.581	0.10355	-2.736	547.02	Yamashita <i>et al.</i> ⁷¹
NpO ₂	542.032	4.276	9.075	-1.362	543.38	Yamashita <i>et al.</i> ⁷¹
PuO ₂	538.147	4.452	7.184	0.1995	539.54	Yamashita <i>et al.</i> ⁷¹
AmO ₂	537.330	4.340	0.143	-	537.43	Shannon ⁷⁷
CmO ₂	537.873	1.016	-	-	536.8	Konings ^{43,74}
BkO ₂	533.040	4.320	0.16	-	533.15	Shannon ⁷³
CfO ₂					531.00	Baybarz <i>et al.</i> ⁶³

No thermal expansion data are available for PaO₂ and CfO₂.

**Figure 11** Evolution of the lattice parameters at room temperature as a function of the ionic radii⁷³ plotted using the data from Table 2.

indeed (almost) linearly dependent upon the ionic radius of the actinide cations (see Figure 11). It is noteworthy that the cell parameters reported may be significantly affected by self-irradiation, as mentioned, for example, in CmO₂ by Konings⁴³ based on measurements by Mosley.⁷⁰

A first review of the linear thermal expansion of stoichiometric actinide dioxides has been done by Fahey *et al.*⁷⁵ in the 1970s. This has been updated by Taylor⁷⁶ in the 1980s and later by Yamashita *et al.*⁷¹ and Konings⁴³ in the 1990s. In the simple case of cubic crystals (such as actinide dioxides; see below), the evolution of the cell parameter as a function of temperature is fitted using a polynomial expression up to the third (sometimes fourth) degree as follows:

$$a(T) = b_0 + b_1 T + b_2 T^2 + b_3 T^3 \quad [3]$$

Selected values of the parameters obtained are shown in Table 2. Overall, the values reported for the b_1 parameters are of the same order of magnitude.

In fact, the recommended values⁷⁷ for UO₂ are as follows:

$$\begin{aligned} \text{For } 273\text{K} < T < 923\text{K: } a(T) = & a_{273}(9.973 \times 10^{-1} \\ & + 9.082 \times 10^{-6} T - 2.705 \times 10^{-10} T^2 \\ & + 4.391 \times 10^{-13} T^3) \end{aligned} \quad [4]$$

$$\begin{aligned} \text{For } 923\text{K} < T < 3120\text{K: } a(T) = & a_{273}(9.9672 \times 10^{-1} + 1.179 \times 10^{-5} T \\ & - 2.429 \times 10^{-9} T^2 + 1.219 \times 10^{-12} T^3) \end{aligned} \quad [5]$$

Sobolev and coworkers^{67–69} recently proposed an alternative approach for determining the thermal expansion of actinide dioxides from experimental data. It is based on the evaluation (from experiments) of the specific heat C_V from the phonon spectra at the expense of some approximations. The thermal expansion α_p is then deduced using the following relation:

$$\alpha_p(V, T) = \frac{\gamma_G C_V(V, T)}{B_T(V, T)V} \quad [6]$$

The thermal expansion coefficient α_p depends upon the bulk modulus B_T , the heat capacity C_V , and the Grüneisen parameter γ_G . The results obtained by Sobolev (see figures in Sobolev and coworkers^{67–69}) reproduce quite well the available experimental data and allow the extrapolation to temperatures higher than the measurements.

2.02.3.1.2 Stoichiometric mixed dioxides

Few binary, ternary, and quaternary mixed actinide dioxides have been investigated experimentally. The cell parameters at room temperature along the mixed oxides solid solutions usually follow the Vegard's law quite well – that is, a linear evolution between the end members of the solid solution.

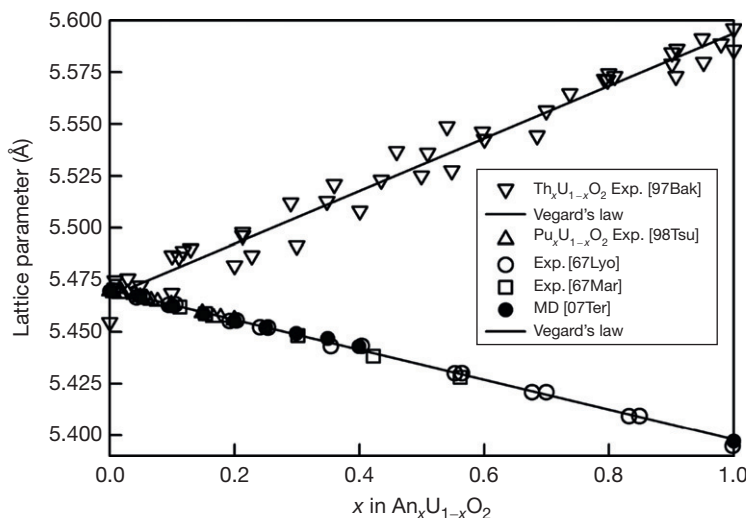


Figure 12 Evolution of the lattice parameters of the $\text{Th}_x\text{U}_{1-x}\text{O}_2$ solid solution measured at room temperature (triangles) reported by Bakker *et al.*⁵⁹ and of the $\text{Pu}_x\text{U}_{1-x}\text{O}_2$ solid solution obtained at room temperature by means of molecular dynamics (MD) calculations (filled circles) by Terentyev *et al.*⁸⁰ (and shifted for the cell parameter of UO_2) and measured by Tsuji *et al.*⁷⁹ (triangles), Lyon and Bailey⁴⁸ (open circles), and Markin and Street⁵³ (squares). The lines represent the Vegard's law.

This has been evidenced for $\text{Th}_{1-x}\text{U}_x\text{O}_2$ by Bakker *et al.*⁵⁹ on the basis of collected experimental data (see Figure 12) and observed later by Yang *et al.*⁷⁸

According to experimental work by Tsuji *et al.*,⁷⁹ Lyon and Bailey,⁴⁸ and Markin and Street,⁵³ Vegard's law applies for $\text{U}_{1-x}\text{Pu}_x\text{O}_2$ too (see Figure 12), and this trend is nicely reproduced by MD calculations by Terentyev⁸⁰ and Arima *et al.*⁸¹ (see Figure 13). MD calculations are consequently currently used for more complex mixed dioxides, for example, by Kurosaki *et al.*⁸² on the ternary mixed dioxides $\text{U}_{0.7-x}\text{Pu}_{0.3}\text{Am}_x\text{O}_2$.

Recently, experimental measurements done by Kato *et al.*⁵⁶ showed that the Vegard's law is valid for ternary and quaternary mixed dioxides. The evolution of the lattice parameter a in $\text{U}_{1-z-y'-y''}\text{Pu}_z\text{Am}_y\text{Np}_{y''}\text{O}_{2.00}$ for low contents of Am, Pu, and Np obeys quite well the following linear relation with the ionic radii r_{U} , r_{Pu} , r_{Am} , r_{Np} and r_{O} and the composition:

$$a = \frac{4}{\sqrt{3}}[r_{\text{U}}(1 - z - y' - y'') + r_{\text{Pu}}z + r_{\text{Am}}y' + r_{\text{Np}}y'' + r_{\text{O}}] \quad [7]$$

Kato *et al.*⁵⁶ tried to extract the valence of americium in $\text{U}_{1-z-y'-y''}\text{Pu}_z\text{Am}_y\text{Np}_{y''}\text{O}_{2.00}$, from the evolution of the cell parameter as a function of the americium

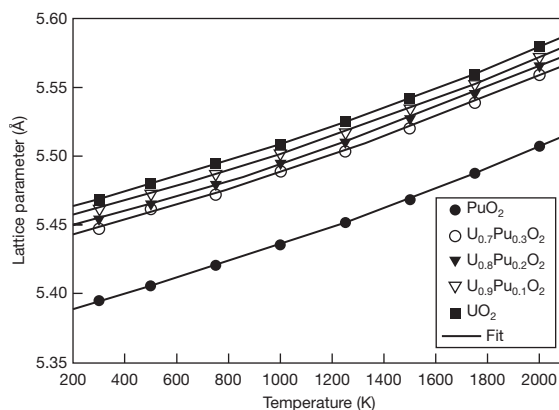


Figure 13 Evolution of the lattice parameter as a function of temperature of ternary mixed $(\text{U,Pu})\text{O}_2$ obtained by molecular dynamics calculations. From Arima, T.; Yamasaki, S.; Inagaki, Y.; Idemitsu, K. *J. Alloys Comp.* **2006**, *415*, 43–50.

content. They deduced that americium is +4 rather than +3 for the $\text{U}_{1-z-y'-y''}\text{Pu}_z\text{Am}_y\text{Np}_{y''}\text{O}_{2.00}$ solid solution, owing to the fact that the ionic radii depend on both the nature and the valence of the element.

The thermal expansion of mixed actinide dioxides $\text{Np}_x\text{Pu}_{1-x}\text{O}_2$ has been measured by Yamashita *et al.*⁷¹ The thermal expansion coefficients are so similar to each other along the mixed oxide solid solution (see Table 3) that Carbajo *et al.*⁸⁴ recommended in

Table 3 Thermal expansion coefficients of the $\text{Np}_x\text{Pu}_{1-x}\text{O}_2$ obtained by Yamashita *et al.*⁷¹

x	b_0 (pm)	$b_1 \times 10^3$ (pm K ⁻¹)	$b_2 \times 10^7$ (pm K ⁻¹)	$b_3 \times 10^{10}$ (pm K ⁻³)	a_{298} (pm)
0.0	538.397	3.169	0.2359	-6.262	539.53
0.05	538.534	3.395	0.2067	-5.137	539.72
0.1	538.793	3.178	0.2395	-6.639	539.94
0.2	539.163	3.202	0.2420	-6.993	540.31
0.5	540.328	3.551	0.1854	-4.373	541.54

Table 4 Thermal expansion coefficients of the $\text{Np}_x\text{U}_{1-x}\text{O}_2$ obtained by Yamashita *et al.*⁸³

X	b_0 (pm)	$b_1 \times 10^3$ (pm K ⁻¹)	$b_2 \times 10^7$ (pm K ⁻²)	$b_3 \times 10^{10}$ (pm K ⁻³)	a_{298} (pm)
0.0	545.567	4.581	0.1036	-2.736	547.02
0.1	545.203	4.193	0.1382	-3.872	546.67
0.3	544.396	6.878	0.1615	-4.365	545.68
0.5	543.903	3.468	0.2111	-6.028	545.11
0.7	543.245	3.462	0.2063	-5.925	544.45
1.0	542.032	4.276	0.09075	-1.362	543.38

Table 5 Thermal expansion coefficients of the $\text{U}_x\text{Th}_{1-x}\text{O}_2$ solid solution obtained by Anthonysamy *et al.*⁸⁵

	b_0 (pm)	$b_1 \times 10^3$ (pm K ⁻¹)	$b_2 \times 10^7$ (pm K ⁻²)	$b_3 \times 10^{10}$ (pm K ⁻³)	a_{298} (pm)
0.13	556.90	3.93301	8.0665		
0.55	552.01	3.36692	11.5537		
0.91	547.27	3.00954	14.387		

their review a single equation for the whole solid solution. The thermal expansion coefficients as a function of neptunium and thorium composition in UO_2 have been measured by Yamashita *et al.*,⁸³ and by Anthonysamy *et al.*⁸⁵ The data are reported in **Tables 4** and **5**. In the $\text{U}_x\text{Th}_{1-x}\text{O}_2$ solid solution, the evolution of those coefficients b_i ($0 \leq i \leq 3$, eqn [3]) follows a quadratic relation with the composition, as shown by Anthonysamy *et al.*⁸⁵ or Bakker *et al.*⁵⁹ But in many cases, the simple Vegard's law is applied to the evolution of lattice parameters as a function of composition and temperature. Results obtained by MD calculations show that such a simplification works well in the MOX (see Arima *et al.*⁸¹ in **Figure 13** or Kurosaki *et al.*⁸² for ternary mixed (U,Pu,Am) O_2).

2.02.3.1.3 Nonstoichiometric actinide dioxides

Interestingly, the lattice parameters also depend linearly on the stoichiometry in hypo- and hyperstoichiometric actinide (mixed or not) dioxides. The variation of the volume $\Delta\Omega/\Omega$ induced by single

isolated defects may be related to the variation of the macroscopic volume $\Delta V/V$, as follows:

$$\frac{\Delta V}{V} \propto \frac{\Delta\Omega}{\Omega} \quad [8]$$

Depending on the sign of $\Delta\Omega$, there will be a swelling or a contraction of the volume. The evolution of the cell parameter is linear as function of stoichiometry x in UO_{2+x} and $(\text{U,Pu})\text{O}_{2\pm x}$ (see **Figure 14**), with different slopes for hypo- and hyperstoichiometric dioxides from Javed,⁸⁶ Grønvold²⁶ in UO_{2+x} , and Markin *et al.*⁵³ in $(\text{U,Pu})\text{O}_{2\pm x}$. This is because the formation volumes $\Delta\Omega$ of oxygen defects are different. Concerning the thermal expansion, the coefficients are roughly similar to each other, whatever be the stoichiometry considered, as can be seen in **Figure 15**. Such a behavior is well reproduced by MD calculations (see Watanabe *et al.*⁸⁷ and Yamasaki *et al.*⁸⁸).

The evolution of the lattice parameters as a function of stoichiometry has been summarized by Kato *et al.*⁵⁶ in minor actinides containing MOX (see **Figure 16(b)**). The hypostoichiometry induces a swelling of the lattice as in UO_{2+x} . Such behavior has been seen in americium containing PuO_2 by

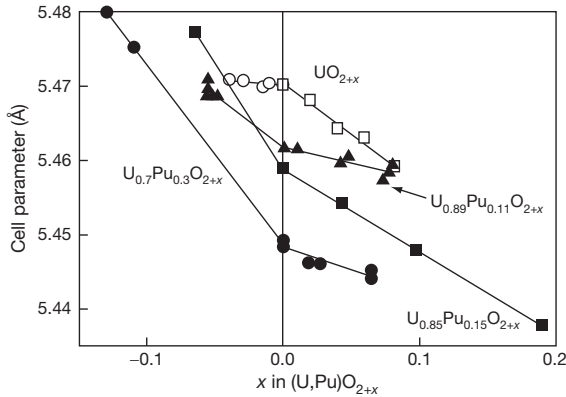


Figure 14 Evolution of the lattice parameters of UO_{2+x} and $(\text{U,Pu})\text{O}_{2+x}$ as a function of stoichiometry. Circles are extracted from Javed⁸⁶ and squares are extracted from Grönvold.²⁶ The filled symbols are reported from Markin and Street.⁵³ The lines are linear fits.

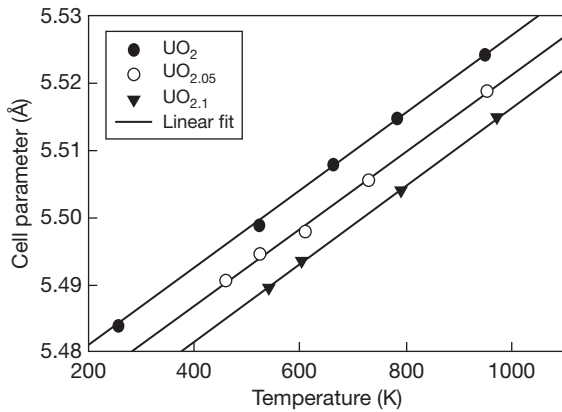


Figure 15 Thermal expansion of UO_{2+x} as a function of stoichiometry x . The data are extracted from Grönvold.²⁶ The lines are linear fits.

Miwa *et al.*⁹⁰ and in pure MOX (see Arima *et al.*,⁸¹ and references therein), and this is qualitatively reproduced by MD calculations (see Figure 16(a)). The thermal expansion coefficients of hypostoichiometric dioxides (not reproduced here) simply follow the Vegard's law (see Arima *et al.*⁸¹), as evidenced in urania in the previous section.

2.02.3.2 Actinide Sesquioxides

The actinide sesquioxides can crystallize with three different forms: a hexagonal close-packed (a), a monoclinic (b), or a cubic (c) structure. The hexagonal form is in most of the cases the stable phase at room

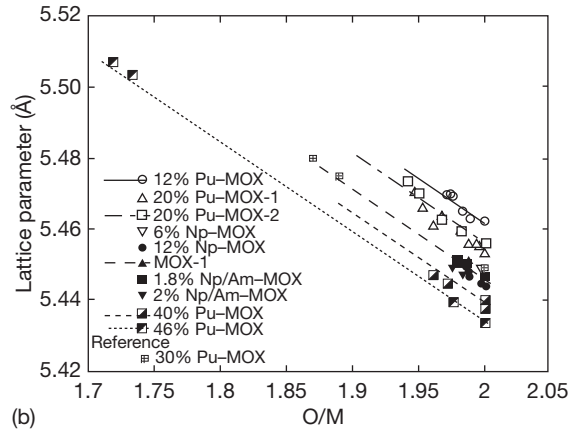
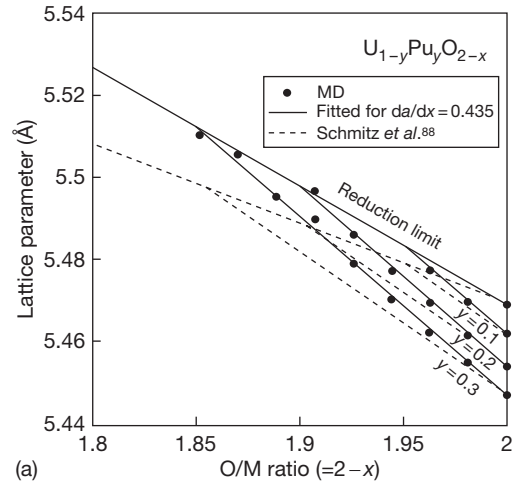


Figure 16 Evolution of the lattice parameters of (a) MOX from Arima *et al.*⁸¹ and (b) minor actinides containing MOX from Kato and Konashi.⁵⁶ © Elsevier, reprinted with permission.

temperature. The cubic phase may be considered as a fluorite structure from which 1/4 of the oxygen ions have been removed. The crystal data on the actinide sesquioxides are listed in Table 6.

Few experimental data are available concerning the thermal expansion coefficients of actinide sesquioxides. The thermal expansion can be fitted with the following equation (in percentage):

$$\frac{\Delta L}{L_0} = a_0 + a_1 \times T + a_2 \times T^2 \quad [9]$$

Konings⁴³ has extracted from experiments the thermal expansion of monoclinic $\text{B-Cm}_2\text{O}_3$. We have done the same for Pu_2O_3 (from Taylor⁷⁶). In the case of Am_2O_3 , we have used the data obtained by Uchida *et al.*⁶⁵ by MD calculations. A summary is available in Table 7.

Table 6 Crystalline structure data of the actinide sesquioxides

Phase	Cell parameters (nm)	Symmetry	Space group	References
Ac ₂ O ₃	$a = 0.408(1)$ $c = 0.630(2)$	Hexagonal	$P\bar{3}m1$	Zachariasen ⁹¹
A-Pu ₂ O ₃	$a = 0.3838(1)$ $c = 0.5918(1)$	Hexagonal	$P\bar{3}m1$	Wulff and Lander ⁹²
C-Pu ₂ O ₃	$a = 1.1$	Cubic	$la\bar{3}$	Chikalla <i>et al.</i> ⁹³
A-Am ₂ O ₃	$a = 0.3817$ $c = 0.5971$	Hexagonal	$P\bar{3}m1$	Haire and Eyring ¹
C-Am ₂ O ₃	$a = 1.1$	Cubic	$la\bar{3}$	Chikalla and Eyring ⁹⁴
A-Cm ₂ O ₃	$a = 0.3792(9)$ $c = 0.5985(12)$	Hexagonal	$P\bar{3}m1$	Noé <i>et al.</i> ⁹⁵
B-Cm ₂ O ₃	$a = 1.422(4)$ $b = 0.364(1)$ $c = 0.884(3)$	Monoclinic $\beta = 100.5(1)^\circ$	C2/m	Nave <i>et al.</i> ⁹⁶
C-Cm ₂ O ₃	$a = 1.0996$	Cubic	$la\bar{3}$	Mosley ⁹⁷
A-Bk ₂ O ₃	$a = 0.3754(2)$ $c = 0.5958(2)$	Hexagonal	$P\bar{3}m1$	Baybarz ⁴⁷
B-Bk ₂ O ₃	$a = 1.4197(7)$ $b = 0.3606(3)$ $c = 0.8846(5)$	Monoclinic $\beta = 100.23(9)^\circ$	C2/m	Baybarz ⁴⁷
C-Bk ₂ O ₃	$a = 1.0880(5)$	Cubic	$la\bar{3}$	Baybarz ⁹⁸
A-Cf ₂ O ₃	$a = 0.372(1)$ $c = 0.596(1)$	Hexagonal	$P\bar{3}m1$	Baybarz ⁴⁷
B-Cf ₂ O ₃	$a = 1.4121(15)$ $b = 0.3592(4)$ $c = 0.8809(7)$	Monoclinic $\beta = 100.34(8)^\circ$	C2/m	Baybarz <i>et al.</i> ⁶³
C-Cf ₂ O ₃	$a = 1.078(1)$	Cubic	$la\bar{3}$	Baybarz <i>et al.</i> ⁶³
A-Es ₂ O ₃	$a = 0.37$ $c = 0.60$	Hexagonal	hexagonal	Haire and Baybarz ⁹⁹
B-Es ₂ O ₃	$a = 1.41$ $b = 0.359$ $c = 0.880$	Monoclinic $\beta = 100^\circ$	monoclinic	Haire and Baybarz ⁹⁹
C-Es ₂ O ₃	$a = 1.0766(6)$	Cubic	$la\bar{3}$	Haire and Baybarz ⁹⁹

Table 7 Thermal expansion of some actinide sesquioxides

		a_0	$a_1 \times 10^4 (K^{-1})$	$a_2 \times 10^7 (K^{-2})$	References	Data
B-Cm ₂ O ₃	$\Delta L/L_0$	−0.1646	4.4449	3.6066	Konings ⁴³	Exp.
C-Am ₂ O ₃	$\Delta a/a_0$	−0.1621	5.8186	2.3691	Uchida <i>et al.</i> ⁶⁵	MD
A-Am ₂ O ₃	$\Delta a/a_0$	−0.2644	7.9393	1.6171	Uchida <i>et al.</i> ⁶⁵	MD
	$\Delta c/c_0$	−0.4150	1.3981	1.8806	Uchida <i>et al.</i> ⁶⁵	MD
A-Pu ₂ O ₃	$\Delta a/a_0$	−0.1082	3.6895	2.2062	Taylor ⁷⁶	Exp.
	$\Delta c/c_0$	−0.5534	1.6857	1.0462	Taylor ⁷⁶	Exp.

2.02.3.3 Other Actinide Oxides

As mentioned in Section 2.02.3.1, the fluorite structure of UO₂ has empty octahedral sites that can be occupied by O^{2−} ions to form UO_{2+x}. The phase diagram data show that the maximum oxygen content corresponds to $x = 0.25$ (or U₄O₉) (Figure 1). From his interpretation of neutron diffraction data on UO_{2.13}, Willis¹⁰⁰ found that the interstitials tend to

aggregate to form clusters made of oxygen interstitials interacting with normal oxygen anions.^{101,102} The so-called cluster 2:2:2 is composed of two oxygen vacancies and four interstitials. Below 1400 K, these clustered excess oxygens tend to form an ordered phase with the composition U₂O_{9−y}.

U₄O₉ is a narrowly hypostoichiometric phase (U₄O_{9−y}) and exists with three different forms:

α - U_4O_{9-y} (at $T < 353$ K), β - U_4O_{9-y} (at $353 \text{ K} < T < 823$ K), and γ - U_4O_{9-y} (at $823 \text{ K} < T < 1400$ K). The structure of the β - U_4O_9 phase was studied by Bevan *et al.*¹⁰³ who showed that this phase is a superlattice structure based on the fluorite structure of UO_2 with a unit cell 64 times the volume of the UO_2 cell. The additional O atoms are arranged in cuboctahedral clusters. According to the later analysis by Cooper and Willis,¹⁰⁴ the centers of the clusters are unoccupied, whereas they are occupied by single O-ions according to Bevan *et al.*¹⁰³ U_4O_9 decomposes at 1400 K into UO_{2+x} (disordered with $x \sim 0.25$) and U_3O_8 (see **Figure 1**).

U_3O_8 is a mixed valence compound with U(V) and U(VI) cations. U_3O_8 exists in several forms as a function of temperature. At room temperature, α - U_3O_8 is orthorhombic and transforms to a pseudo-hexagonal structure β - U_3O_8 at 483 K. Heat capacity measurements by Inaba *et al.*¹⁰⁵ showed other phase transitions at 568 and 850 K.

UO_3 can crystallize in six forms. The stable form at room temperature α - UO_3 is orthorhombic.

Partial information on crystal data of plutonium and curium intermediate oxides with O/metal ratio below 2 is given in **Table 8**.

2.02.4 Thermodynamic Data

2.02.4.1 Binary Stoichiometric Compounds

The thermodynamic data on the actinide oxides are based on the critical reviews by Konings *et al.*^{36,38} and are generally in good agreement with the CODATA Key values¹²¹ and with the NEA reviews.¹²² The thermodynamic properties of the binary thorium, uranium, neptunium, and plutonium oxides are well established from experimental data. For the other actinide oxides, some experimental data are missing, and some values were estimated using the analogy with the lanthanide oxides by Konings *et al.*^{36,38}

2.02.4.1.1 Actinide dioxides

2.02.4.1.1.1 Standard enthalpy of formation and entropy

For the actinide dioxides, the enthalpy data in **Table 9** are well established for ThO_2 , UO_2 , NpO_2 , PuO_2 , AmO_2 , and CmO_2 from measurements. On the contrary, the enthalpy of formation of PaO_2 , BkO_2 , and CfO_2 was never measured. For these compounds, the values were estimated from the reaction enthalpy of the idealized dissolution reaction $[\text{AnO}_2(\text{c}) + 4\text{H}^+(\text{aq}) \rightarrow \text{An}^{4+}(\text{aq}) + 2\text{H}_2\text{O}(\text{l})]$ that is assumed to

vary regularly in the actinide series as the enthalpy of dissolution of the dioxides $[\Delta_f H(\text{AnO}_2) - \Delta_f H(\text{An}^{4+})]$ is a function of ionic size.

The standard entropies in **Table 9** were deduced from heat capacity measurements for the solid dioxides from ThO_2 to PuO_2 . For the other oxides, the data were estimated by Konings.^{43,123} For AmO_2 and CmO_2 , the entropy was modeled as the sum of a lattice term due to the lattice vibrations and an excess component arising from f-electron excitation: $S = S_{\text{lat}} + S_{\text{exc}}$. S_{lat} term was assumed to be the value for ThO_2 , and S_{exc} was calculated from the crystal field energies of the compounds by Krupa and coworkers.^{124,125} A similar method was applied to estimate the entropies of PaO_2 , BkO_2 , CfO_2 , and EsO_2 . In absence of crystal field data, the excess term was calculated from the degeneracy of the unsplit ground state, which probably overestimates the entropy.

As shown in **Table 9**, the stability of the dioxides decreases with the atomic number Z . This is consistent with the fact that the melting points of the dioxides decrease from ThO_2 to CmO_2 . This can explain that the heavier tetravalent dioxides are difficult to prepare. Another difficulty comes from the production of daughter products leading to an increasing contamination of the oxides with time. Finally, the dioxides lose oxygen leading to the decrease of their oxygen stoichiometry with temperature. The least stable dioxides CmO_2 and CfO_2 can evolve to form Cm_2O_3 and Cf_2O_3 .

2.02.4.1.1.2 Heat capacity

For UO_2 and PuO_2 , high-temperature measurements of both heat capacity and enthalpy increment are available. For ThO_2 , NpO_2 , and AmO_2 , the high-temperature heat capacities were deduced from measurements of high-temperature enthalpy increment.

The recommended equations for UO_2 , PuO_2 , ThO_2 , AmO_2 , and NpO_2 from Konings *et al.*^{36,38} are given in **Table 10** and in **Figure 11**.

For ThO_2 , UO_2 , and PuO_2 , the data are close to the Dulong–Petit value between 500 and 1500 K. The lattice contribution is the major one with a small contribution of 5f electron excitations, which can be calculated from electronic energy levels.

For UO_2 , above 1500 K, a rapid increase of the heat capacity was observed with a peak measured at 2670 K by Hiernaut *et al.*¹³³ This unusual behavior has been subject of numerous studies that are reported by Ruello *et al.*¹²⁶ Several contributions can be taken into account: the harmonic phonons, the thermal expansion, the U^{4+} crystal field, the electronic

Table 8 Crystalline data of other actinide oxides

Phase	Cell parameters (nm)	Symmetry	Space group	References
α -U ₄ O ₉ ($T < 348$ K)	$a = 2.1764\text{--}2.1776$	Rhombohedral $\alpha = 90.078^\circ$		Vanlierde ¹⁰⁶
β -U ₄ O ₉ ($348\text{ K} < T < 893\text{ K}$)	$a = 2.187$	Cubic	$I\bar{4}3d$	Cooper ¹⁰⁴
γ -U ₄ O ₉ ($893\text{ K} < T < 1400\text{ K}$)	$a = 2.176$	Cubic	$I4_132$	Masaki ¹⁰⁷
α -U ₃ O ₇	$a = 0.5472$ $c = 0.5397$	Tetragonal		Westrum ¹⁰⁸
β -U ₃ O ₇	$a = 0.5363$ $c = 0.5531$	Tetragonal		Westrum ¹⁰⁸
γ -U ₃ O ₇	$a = 0.5407$ $c = 0.5497$	Tetragonal		Hoekstra ¹⁰⁹
α -U ₃ O ₈ ($T < 483$ K)	$a = 0.6715$ $b = 1.196$ $c = 0.4146$	Orthorhombic	C2mm	Ball ¹¹⁰
β -U ₃ O ₈ ($483\text{ K} < T < 568\text{ K}$)	$a = 0.707$ $b = 1.145$ $c = 0.830$	Orthorhombic	$P\bar{6}2m$	Loopstra ¹¹¹
α -UO ₃	$a = 0.684$ $b = 4.345$ $c = 0.4157$	Orthorhombic		Greaves ¹¹²
β -UO ₃	$a = 1.034(1)$ $b = 1.433(1)$ $c = 0.3910(4)$	Monoclinic $\beta = 99.03^\circ$	P2 ₁	Debets ¹¹³
γ -UO ₃	$a = 0.69013(5)$ $c = 1.99754(18)$	Tetragonal	$I4_1/amd$	Loopstra ¹¹⁴
δ -UO ₃	$a = 0.4165(8)$	Cubic	$Pm\bar{3}m$	Weller ¹¹⁵
ϵ -UO ₃	$a = 0.4002$ $b = 0.3841$ $c = 0.4165$	Triclinic $\alpha = 98.10^\circ$ $\beta = 90.20^\circ$ $\gamma = 120.17^\circ$		Kovba ¹¹⁶
ν -UO ₃	$a = 0.7511(9)$ $b = 0.5466(8)$ $c = 0.5224(8)$	Orthorhombic	P2 ₁ 2 ₁ 2 ₁	Siegel ¹¹⁷
Np ₂ O ₅	$a = 0.8168(2)$ $b = 0.6584(1)$ $c = 0.9313(1)$	Monoclinic $\beta = 116.09(1)^\circ$	P2/c	Forbes ¹¹⁸
CmO _{1.72}	$a = 6.677(4)$	Rhombohedral $\alpha = 99.52(7)^\circ$		Mosley ⁹⁷
CmO _{1.81}	$a = 5.435(1)$	Cubic		Mosley ⁹⁷
PuO _{1.52}	$a = 1.1045$	Cubic	$Ia\bar{3}$	Boivineau ¹¹⁹
PuO _{1.62}	$a = 1.0991$	Cubic	$Ia\bar{3}$	Sari ¹²⁰

Table 9 Thermodynamic data on the actinide dioxides after Konings *et al.*^{36,38}

	Melting T (K)	$\Delta_f H^0$ (298.15 K) (kJ mol ⁻¹)	S^0 (298.15 K) (JK ⁻¹ mol ⁻¹)	$\Delta_f G^0$ (298.15 K) (kJ mol ⁻¹)
ThO ₂	3651 ± 17	-1226.4 ± 3.5	65.23 ± 0.2	-1169.2 ± 3.5
PaO ₂		-1107 ± 15	80 ± 5	-1054 ± 15
UO ₂	3120 ± 20	-1085.0 ± 1.0	77.03 ± 0.2	-1031.8 ± 1.0
NpO ₂	2836 ± 50	-1074.0 ± 2.5	80.3 ± 0.4	-1021.7 ± 2.5
PuO ₂	2674 ± 20	-1055.8 ± 1.0	66.13 ± 0.30	-998.1 ± 1.0
AmO ₂	2386	-932.2 ± 3.0	75.5 ± 5	-877.0 ± 3.0
CmO ₂	Unstable at $T > 653$ K	-912.1 ± 6.8	65 ± 5 [4]	-849 ± 6.8
BkO ₂		-1023 ± 9	83 ± 5	-963 ± 9
CfO ₂		-857 ± 14	87 ± 5	-798 ± 14

Estimated values in italics.³⁸

Table 10 Heat capacity functions for the actinide dioxides according to Konings *et al.*^{36,38}

Oxide	Heat capacity equation for the solid oxides ($\text{JK}^{-1}\text{mol}^{-1}$)
ThO ₂	$C_p = 55.9620 + 51.2579 \times 10^{-3}T - 36.8022 \times 10^{-6}T^2 + 9.2245 \times 10^{-9}T^3 - 574031T^{-2}$
UO ₂	$C_p = 66.7437 + 43.1393 \times 10^{-3}T - 35.640 \times 10^{-6}T^2 + 11.655 \times 10^{-9}T^3 - 1168630T^{-2}$
NpO ₂	$C_p = 72.767 + 14.781 \times 10^{-3}T - 975530T^{-2}$
PuO ₂	$C_p = 36.2952 + 0.15225T - 127.255 \times 10^{-6}T^2 + 36.289 \times 10^{-9}T^3 - 347593T^{-2}$
AmO ₂	$C_p = 66.8904 + 19.1123 \times 10^{-3}T - 4.6356 \times 10^{-6}T^2 - 548830T^{-2}$

These equations do not reproduce the heat capacity around the λ -transition.

disorder, and the oxygen anti-Frenkel disorder. According to the analysis by Ronchi and Hyland,¹³² the lambda transition observed at $T \sim 0.8 T_m$ is governed by the formation of anion Frenkel defects. From X-ray and neutron diffraction experiments, Ruello *et al.*¹²⁶ measured thermal expansion data that give evidence of an anomaly near 1300 K, suggesting a new model for the heat capacity in which an electronic disorder contribution is considered. Yakub *et al.* investigated this premelting λ -transition in UO₂ using a thermodynamic model¹²⁷ and MD.¹²⁸ The authors interpreted this transition by the increasing instability in the oxygen sublattice with temperature. According to Ruello *et al.*,¹²⁶ a coupling of the lattice and electrical defects is possible. Further investigations are still required to clarify the interpretation of the heat capacity of UO₂.

For ThO₂, an excess enthalpy was measured above $T = 2500$ K. Ronchi and Hiernaut³⁷ using a thermal arrest technique concluded that a λ -type premelting transition occurs at 3090 K, which was attributed to order-disorder anion displacements in the oxygen sublattice (Frenkel oxygen defects). The recommended equation in Table 10 comes from the fit of the enthalpy measurements by Southard,¹²⁹ Hoch and Johnson,¹³⁰ and Fischer *et al.*¹³¹

The same type of effect was observed for the C_p of PuO₂ from the enthalpy measurements by Ogard¹³⁴ for PuO₂, with a rapid increase of the heat capacity above 2370 K. This effect was later attributed to an interaction between the sample and the W crucible by Fink¹³⁵ and Oetting and Bixby.¹³⁶ New measurements will be helpful.

The thermophysical properties of NpO₂, AmO₂, and CmO₂ were recently calculated by Sobolev.⁶⁹

The heat capacity of NpO₂ calculated by Sobolev⁶⁹ (see Section 2.02.3) is in good agreement with the recently measured data from 334 to 1071 K by Nishi *et al.*¹³⁷ using a drop calorimetry method and with the estimated data by Serizawa,¹³⁸ recommended by Konings *et al.*³⁸ Very recent measurements of enthalpy increments of NpO₂ were undertaken by Benes *et al.*¹³⁹ using drop calorimetry from 376 to 1770 K. The heat capacity of NpO₂ derived from these enthalpy measurements is in very good agreement with the data of Nishi *et al.*¹³⁷ A new heat capacity function was proposed by Benes *et al.*¹³⁹ that take into account a value of $66.2 \text{ JK}^{-1} \text{ mol}^{-1}$ at 298.15 K.

No measurement exists on AmO₂ and CmO₂. The heat capacity for AmO₂ calculated by Sobolev⁶⁹ is in very good agreement with the data estimated by Thiriet and Konings⁴⁰ from the heat capacity of ThO₂ and the crystal field energies for the ground state and the excited states. For CmO₂, the heat capacity data calculated by Sobolev⁶⁹ are lower than the data of Konings⁴³ estimated by the same method applied for AmO₂ (Figure 17).

2.02.4.1.2 Actinide sesquioxides

2.02.4.1.2.1 Standard enthalpy of formation and entropy

The recommended data for the standard enthalpy of formation and entropy are listed in Table 11.

The enthalpies of formation of Am₂O₃, Cm₂O₃, and Cf₂O₃ are well established from experimental data measured using solution calorimetry. The same systematic approach as the one used for the dioxides using the reaction enthalpy of the idealized dissolution reaction $[\text{An}_2\text{O}_3(\text{cr}) + 6\text{H}^+(\text{aq}) \rightarrow 2\text{An}^{3+}(\text{aq}) + 3\text{H}_2\text{O}(\text{l})]$ was applied by Konings *et al.*³⁸ to estimate the enthalpy of formation for Ac₂O₃, Bk₂O₃, and Es₂O₃ taking into account their different crystalline structures.

No low-temperature heat capacity measurements exist except for Pu₂O₃, the only phase for which the entropy was derived. For the other sesquioxides, the entropy values were estimated by Konings⁴³ from the entropy of Pu₂O₃ by calculating the excess entropy term from the crystal field energies. The lattice term was obtained by scaling the values from the lanthanide series.

As shown in Table 11, the evolution of the stability of the actinide sesquioxides with the atomic number Z is less pronounced than for the dioxides. The measured melting points of actinide

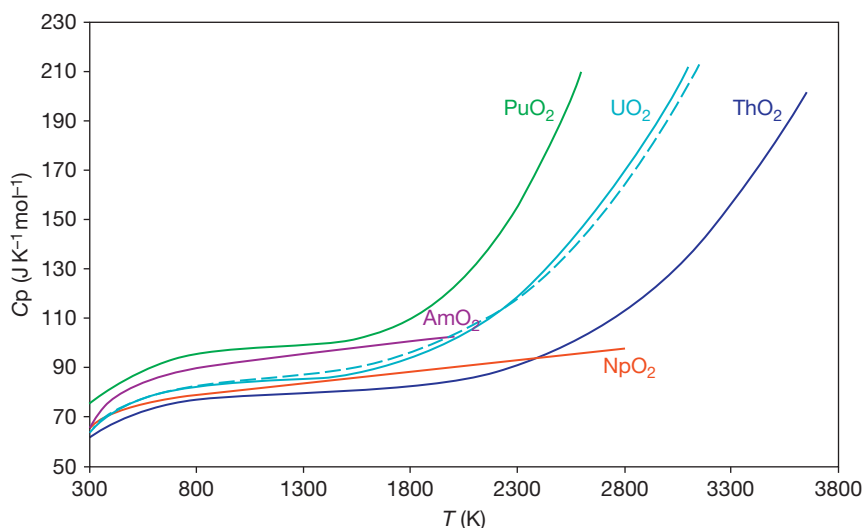


Figure 17 The high-temperature heat capacity of ThO₂, UO₂, PuO₂, NpO₂, and AmO₂ recommended by Konings *et al.*³⁸ – the dashed lines correspond to the recent recommendation by Konings *et al.*³⁶ for UO₂ and are from the recent enthalpy measurement by Benes *et al.*¹³⁹ for NpO₂.

Table 11 Thermodynamic data on the actinide sesquioxides after Konings *et al.*²

	Melting T (K)	$\Delta_f H^0$ (298.15 K) (kJ mol ⁻¹)	S^0 (298.15 K) (JK ⁻¹ mol ⁻¹)	$\Delta_f G^0$ (298.15 K) (kJ mol ⁻¹)
Ac ₂ O ₃	2250	-1756	141.1 ± 5.0	-1681
Pu ₂ O ₃	2352 ± 10	-1656 ± 10	163.02 ± 0.65	-1595 ± 10
Am ₂ O ₃	2481 ± 15	-1690.4 ± 8.0	133.6 ± 5.0	-1619.5 ± 8.0
Cm ₂ O ₃	2543 ± 25	-1684 ± 14	167.0 ± 5.0	-1609 ± 14
Bk ₂ O ₃	2193 ± 25	-1694	173.8 ± 5.0	-1615
Cf ₂ O ₃	2023	-1653 ± 10	176.0 ± 5.0	-1572 ± 10
Es ₂ O ₃		-1696	180.0 ± 5.0	-1609

Estimated values are in italics.

sesquioxides slightly increase from Ac₂O₃ to Cm₂O₃ for which a maximum is observed and then decrease from Cm₂O₃ to Cf₂O₃.

2.02.4.1.2.2 Heat capacity

There are no measurements of the heat capacity or enthalpy at high temperature for Pu₂O₃, Am₂O₃, and Cm₂O₃. The equations given in Table 12 are based on comparison between actinide and lanthanide oxides by Konings *et al.*³⁶

2.02.4.1.3 Other actinide oxides with O/metal > 2

The thermodynamic data for uranium and neptunium oxides with oxygen/metal ratios > 2 are reported in Tables 13 and 14 based on the review by Konings *et al.*³⁸

For UO₃, the recommended heat capacity function is based on the fit of the experimental heat

Table 12 Heat capacity function for actinide sesquioxides according to Konings *et al.*³⁶

Oxide	Heat capacity equation for solid oxides (JK ⁻¹ mol ⁻¹)
Pu ₂ O ₃	$C_p = 130.6670 + 18.4357 \times 10^{-3}T - 1705300T^{-2}$
Am ₂ O ₃	$C_p = 115.580 + 22.976 \times 10^{-3}T - 1087100T^{-2}$
Cm ₂ O ₃	$C_p = 123.532 + 14.550 \times 10^{-3}T - 1348900T^{-2}$

capacity data from Popov *et al.*¹⁴⁰ and enthalpy increment by Moore and Kelley.¹⁴¹ For U₃O₈ and U₄O₉, the equation for the heat capacity is taken from Cordfunke and Konings.¹⁴²

2.02.4.2 Mixed Oxides

Carbajo *et al.*⁸⁴ did a review of the thermophysical properties of MOX and UO₂ fuels. All the available

Table 13 Thermodynamic data on the actinide dioxides with O/metal ratio >2 after Konings *et al.*³⁸

	C_p (298.15 K)	$\Delta_f H^0$ (298.15 K) (kJ mol ⁻¹)	S^0 (298.15 K) (JK ⁻¹ mol ⁻¹)	$\Delta_f G^0$ (298.15 K) (kJ mol ⁻¹)
γ -UO ₃	81.67 ± 0.16	-1223.8 ± 2.0	96.11 ± 0.40	-1145.7 ± 2.0
β -UO ₃	81.34 ± 0.16	-1220.3 ± 1.3	96.32 ± 0.40	-1142.3 ± 1.3
α -UO ₃	81.84 ± 0.30	-1212.41 ± 1.45	99.4 ± 1.0	-1134.4 ± 1.5
δ -UO ₃		-1213.73 ± 1.44		
ε -UO ₃		-1217.2 ± 1.3		
Am-UO ₃		-1207.9 ± 1.4		
U ₃ O ₈	237.94 ± 0.48	-3574.8 ± 2.5	282.55 ± 0.50	-3369.5 ± 2.5
α -U ₃ O ₇	214.26 ± 0.90		246.51 ± 1.50	
β -U ₃ O ₇	215.52 ± 0.42	-3423.0 ± 6.0	250.53 ± 0.60	-3238.7 ± 6.0
U ₄ O ₉	293.36 ± 0.45	-4512 ± 7	334.1 ± 0.7	-4276 ± 7
NpO ₃		-1070 ± 6	100 ± 10	-993 ± 6
Np ₂ O ₅		-2162.7 ± 9.3	186 ± 15	-2035.2 ± 9.3

Estimated values are in italics.

Table 14 Heat capacity functions for uranium oxides with O/U ratio >2 according to Konings *et al.*³⁶

Oxide	Heat capacity equation for solid oxides (JK ⁻¹ mol ⁻¹)
UO ₃	$C_p = 90.2284 + 13.85332 \times 10^{-3}T - 1127950T^{-2}$
U ₃ O ₈	$C_p = 279.267 + 27.480 \times 10^{-3}T - 4311600T^{-2}$
U ₄ O ₉	$C_p = 319.163 + 49.691 \times 10^{-3}T - 3960200T^{-2}$

experimental data and equations for heat capacity and enthalpy data are given in that paper.

Recent measurements were performed by Duriez *et al.*¹⁴³ and by Kandan *et al.*¹⁴⁴ Duriez *et al.*¹⁴³ measured the heat capacity of stoichiometric (U,Pu)O₂ samples with up to 15% Pu in the temperature range 473–1573 K using differential scanning calorimetry. Kandan *et al.*¹⁴⁴ measured enthalpy increment for MOX with 21%, 28%, and 40% Pu using a high-temperature differential calorimeter in the temperature range 1000–1780 K. The agreement between all the experimental data is good.

As reported in all these studies, the experimental results are in good agreement (within 2–3%) with the Neumann–Kopp rule:

$$C_p(T, U_{1-y}Pu_yO_2) = (1-y)C_p(T, UO_2) + yC_p(T, PuO_2) \quad [10]$$

2.02.4.3 Nonstoichiometric Dioxides

As mentioned above, the actinide dioxides always exhibit a composition range with a deficit and an excess in oxygen where the thermodynamic properties vary with both deviation from stoichiometry and temperature.

2.02.4.3.1 Defects

Owing to the large range of nonstoichiometry with temperature in UO_{2±x}, different types of defects (metal and oxygen vacancies and interstitials) and clusters are expected to form. In slightly hypostoichiometric UO_{2-x} for example, oxygen vacancies are expected to be the dominant defects. In that simple case, one knows from point defect model (see See-Bauer and Kratzer¹⁴⁵) that the concentration of oxygen vacancies $[V_O^{\bullet\bullet}]$ is a function of the oxygen pressure pO_2 (see also Figure 18):

$$[V_O^{\bullet\bullet}] \propto pO_2^{-1/6} \quad [11]$$

Such a simple description can be applied to slightly hyperstoichiometric dioxides too (see Figure 18). This means that – in principle – one can extract the nature of defects and the concentration of, for example, oxygen vacancies $[V_O^{\bullet\bullet}]$ (or oxygen interstitials $[V_O^{\prime\prime}]$), which depends upon the slope of the curve, here 1/6, from SeeBauer and Kratzer¹⁴⁵ and Ling,¹⁴⁶ and the formation energy of those defects in hypostoichiometric urania, from the measurements of oxygen potential (eqn [12]) as a function of temperature and stoichiometry. This simple model was developed in the 1980s by Matzke¹⁴⁷ on the basis of the experimental oxygen potential data.

Unfortunately, nonstoichiometric urania cannot be rationalized using simple point defects – such as oxygen interstitials or vacancies – within the large nonstoichiometric composition range (see phase diagrams in Figure 1). For large deviations from stoichiometry, the defects become nonisolated and start to interact with each other. The oxygen ions are known to aggregate and form Willis clusters according to Willis¹⁰² and cuboctahedral clusters. According to electrical

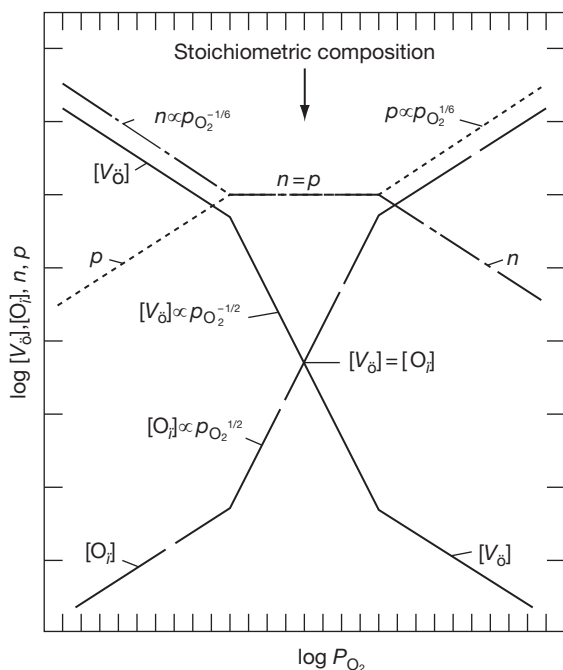


Figure 18 Brouwer diagram for dioxide at equilibrium, showing the concentration of defects as a function of partial pressure of oxygen.

conductivity measurements by Ruello *et al.*,¹⁴⁸ these clusters have a net charge of -1. Park and Olander¹⁴⁹ derived in the 1990s a point defect model that takes into account the Willis defect (2:2:2)'. Their model also included the oxygen interstitials (I_o''), oxygen vacancies [$V_o^{\bullet\bullet}$], polarons (U^{3+}), holes (U^{5+}), and vacancy dimers ($(V_o:V_o)^{\bullet\bullet}$). In this model, the structural defect in UO_2 is the oxygen Frenkel pair. The cation Frenkel defect and the anion and cation Schottky defects can be neglected (unless cation diffusion is considered). In hyperstoichiometric urania ($x > 0.01$), the oxygen interstitials form Willis clusters. No clusters were found experimentally in UO_{2-x} . However, vacancy dimers were assumed to form.

For highly concentrated point defects in oxides (such as ceria), Ling¹⁴⁶ added Coulombic interactions as well as generalized exclusion effects to improve the description depicted by simple point defect models. Stan and Cristea implemented such defect model in plutonia and urania.^{150–154} Stan and Cristea¹⁵⁰ considered in PuO_{2-x} small polarons (Pu^{3+}), singly charged vacancies (V_o^{\bullet}), doubly charged vacancies ($V_o^{\bullet\bullet}$), neutral pairs ($(PuV_o)^x$), and singly charged pairs ($(PuV_o)^x$) as defect species. The model predicts that the small polarons and doubly charged oxygen vacancies are the dominant defects in the very low nonstoichiometric region. The intermediate region is

controlled by singly charged vacancies and the deep nonstoichiometric region by neutral pairs. For UO_{2+x} , Stan *et al.*¹⁵³ developed a simple model with four major defects: oxygen Frenkel pairs, doubly negatively charged oxygen interstitials (I_o''), positively charged (U_U or U^{5+}) uranium ions, and positively doubly charged oxygen vacancies [$V_o^{\bullet\bullet}$].

Recently, Kato *et al.*¹⁵⁵ analyzed oxygen potential data for $(U_{0.7}Pu_{0.3})O_{2 \pm x}$ and $(U_{0.8}Pu_{0.2})O_{2 \pm x}$ versus oxygen stoichiometry and temperature using a point defect model. It showed that intrinsic ionization is the dominant defect in stoichiometric mixed oxide. The defect model reproduces quite well the experimental oxygen potential data as a function of stoichiometry.

The reverse approach consists in calculating the formation energy of well-chosen defects using atomistic simulations (*ab initio* and/or MD). One can then estimate the oxygen pressure as a function of stoichiometry. This was done in the 1980s by means of empirical potentials MD by Catlow and Tasker,¹⁵⁶ and later by Jackson *et al.*¹⁵⁷ More recently Yakub¹⁵⁸ used the same method to investigate the formation of different types of clusters (Willis's 2:2:2 interstitial dimers, and cuboctahedral tetra- and pentamers) in UO_{2+x} .

Numerous studies were performed using the density functional theory (DFT) by Petit *et al.*,¹⁵⁹ Crocombette *et al.*,¹⁶⁰ Freyss *et al.*,¹⁶¹ Gupta *et al.*,¹⁶² Nerikar *et al.*,¹⁶³ and Yu *et al.*¹⁶⁴ The energy of formation of clusters were determined by Geng *et al.*,^{165–167} and by Andersson *et al.*^{5,168} Recently a Brouwer diagram of urania was drawn by Crocombette *et al.*¹⁶⁹ based on charged point defect formation energies. The hypostoichiometric part is in agreement with the oxygen potential data from Baichi *et al.*⁹ and evidenced the existence of both $(V_o)^{\bullet}$ and $(V_o)^{\bullet\bullet}$. All these works using DFT are subjects of controversy in relation to the problems to be encountered when using *ab initio* for actinides (see **Chapter 1.08, *Ab Initio* Electronic Structure Calculations for Nuclear Materials**).

Konashi *et al.*¹⁷⁰ used first principle MD simulation to investigate the point defects in PuO_2 . They show that in PuO_{2-x} , the oxygen vacancy is bound by two neighboring Pu ions which lead to the change of plutonium valency from 4 to 3. The most favorable position of the two Pu^{3+} cations is nearby the oxygen vacancy.

Martin *et al.*¹⁷¹ characterized $(U_{1-x}Pu_x)O_2$ solid solutions using X-ray powder diffraction, X-ray absorption spectroscopy (XAS), and extended X-ray

absorption fine structure measurements (EXAFS). The EXAFS results suggested that for Pu content lower than 30 at.%, the mixed oxide has a disordered hyperstoichiometric structure $(U_{1-x}Pu_x)O_{2+x}$ with cuboctahedral defects that are located around uranium atoms and not in the Pu environment.

2.02.4.3.2 Oxygen potential data

The oxygen potential in oxides reflects the equilibrium between oxygen in the crystal lattice and oxygen in the gas phase and is defined as

$$\mu(O_2) = RT \ln(pO_2/p^0) \quad [12]$$

where R is the gas constant, T is the temperature, pO_2 is the partial pressure of oxygen, and p^0 is the standard pressure.

As the actinide dioxides are nonstoichiometric phases, the oxygen potential data strongly vary with the O/metal ratio and with temperature.

2.02.4.3.2.1 Binary solid solutions

Numerous experimental data exist on the variation of the oxygen potential for both uranium and plutonium oxides as a function of the oxygen to metal ratio and temperature. A critical review of these experimental data was performed by Baichi *et al.*⁹ in the U–UO₂ region and by Labroche *et al.*¹⁰ from UO₂ to U₃O₈.

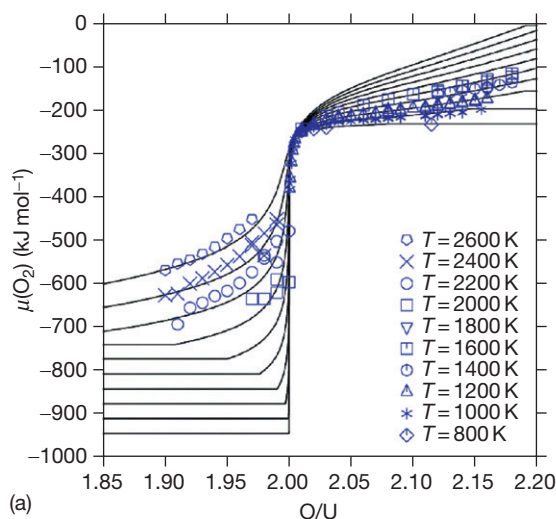
Thermochemical models were derived to describe the thermodynamic properties of uranium oxide by Blackburn,¹⁷² Besmann and Lindemer,^{173–175} Park and Olander,¹⁴⁹ Guéneau *et al.*,⁸ Chevalier *et al.*,^{176,177} Yakub *et al.*¹²⁷ and plutonium oxide by Kinoshita *et al.*,²⁷ Guéneau *et al.*,²⁸ Stan and Cristea,¹⁵⁰ and Besmann and Lindemer¹⁷³ that allow describing the oxygen potential data.

The most extensively used is the associate model developed by Besmann and Lindemer^{173–175} that describes the oxide solution as a mixture of associates $U_{1/3}$, UO₂, U₂O_{4.5} (or U₃O₇ for oxygen potential higher than $-266\,700 + 16.5(T \text{ (K)})$ (J mol⁻¹)) for UO_{2±x} and Pu_{4/3}O₂ and PuO₂ for PuO_{2–x}. This model reproduces very well the available experimental data on UO_{2±x}, PuO_{2–x} and (U,Pu)O_{2±x} from the extrapolation of the binary oxides. However, this approach does not allow calculating the phase diagrams. More recently, thermochemical models were developed using the CALPHAD method in order to describe both the phase diagram and all the thermodynamic properties of the phases by Chevalier *et al.*^{176,177} and Guéneau *et al.*⁸ for U–O, and by Kinoshita *et al.*²⁷ and Guéneau *et al.*²⁸ for Pu–O. In

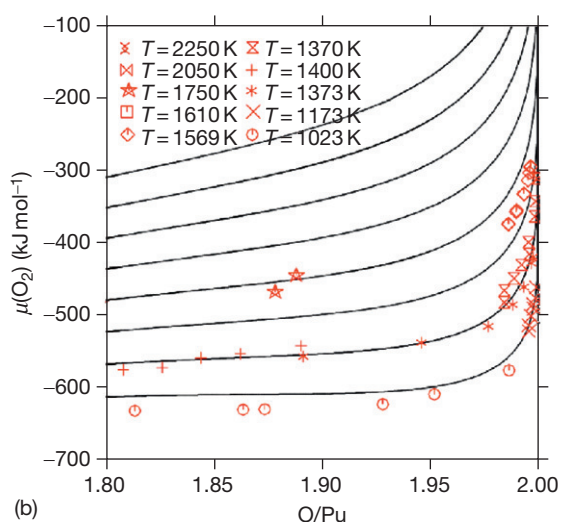
the model proposed by Chevalier *et al.*¹⁷⁷ for U–O, the solid solution is described with a three sublattice model $(U)_1(O,V)_2(O,V)_1$ where ‘V’ designates oxygen vacancies. The hypostoichiometric region is taken into account by introducing oxygen vacancies, and the oxygen-rich part with O/metal ratio >2 is described by considering interstitial oxygen atoms in the third sublattice. In the model developed by Guéneau *et al.*,⁸ the uranium dioxide is represented using a three sublattice model with ionic species $(U^{3+}, U^{4+}, U^{6+})_1(O^{2-}, V)_2(O^{2-}, V)_1$. The third sublattice is the site for interstitial oxygen anions to describe the excess of oxygen in urania. The electroneutrality of the phase is maintained by introducing U³⁺ or U⁶⁺ cations on the first sublattice for, respectively, hypo- or hyperstoichiometric compositions of urania. The oxygen potential data, as derived by Guéneau *et al.* for UO_{2±x}⁸ and PuO_{2–x},²⁸ are presented in **Figure 19(a)** and **19(b)**, showing that the oxygen potential is lower in UO_{2–x} than in PuO_{2–x}.

Few measurements exist for the other actinide oxides: Ackermann and Tetenbaum¹⁷⁸ reported data for ThO_{2–x}, Bartscher and Sari¹⁷⁹ for NpO_{2–x}, and Chikalla and Eyring,^{94,180} Casalta,¹⁸¹ and Otobe *et al.*¹⁸² for AmO_{2–x} solid solutions. A thermochemical model using the CALPHAD method was derived by Konishita *et al.*³⁹ to reproduce the experimental data on ThO_{2–x} and NpO_{2–x} (**Figure 20(a)** and **20(b)**). For the Np–O system, the oxygen potential data are well reproduced, but the phase diagram assessed by Kinoshita³⁹ is not in good agreement with the experimental data on the solubility limit of NpO_{2–x} in equilibrium with the liquid metal.

An associate model was derived by Thiriet and Konings⁴⁰ to reproduce the oxygen potential data of Chikalla and Eyring⁹⁴ on the AmO_{2–x} solid solution (**Figure 21(a)**). Very recently, Besmann¹⁸³ has derived a thermochemical model on AmO_{2–x} using the Compound Energy Formalism as in Guéneau *et al.*²⁸ for Pu–O. It is worth mentioning that for the Am–O system, the experimental data of Chikalla and Eyring⁹⁴ and the recent measurements by Otobe *et al.*¹⁸² are in disagreement with the phase diagram determined experimentally by Sari and Zamorani⁴¹ that shows the presence of a miscibility gap in the fluorite phase like in the Pu–O and Ce–O systems (see **Figure 21(b)**). The data of Casalta¹⁸¹ are consistent with the existence of the miscibility gap but are in poor agreement with the values of Chikalla and Eyring⁹⁴ and Otobe *et al.*¹⁸² for the oxygen potential near AmO₂. Otobe *et al.*¹⁸² proposed a new tentative phase diagram based on their



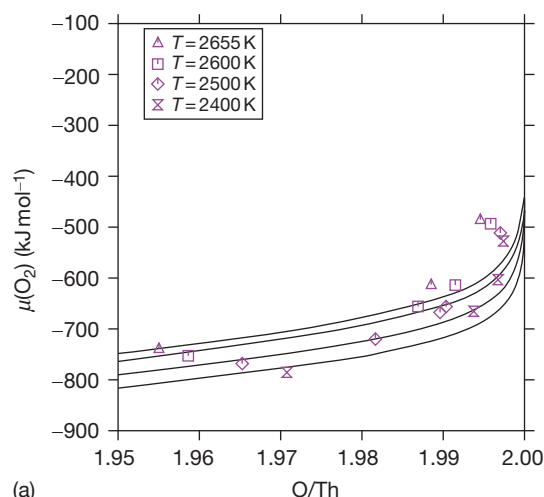
(a)



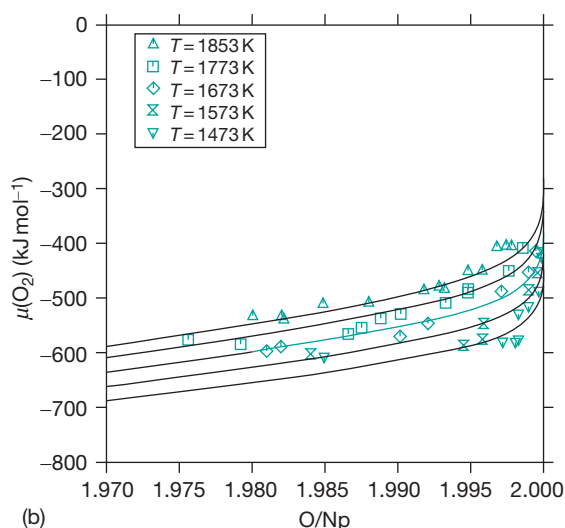
(b)

Figure 19 Oxygen potential data versus O/metal ratio in (a) UO_{2-x} ; the lines correspond to the calculations between 800 and 2600 K with 200 K intervals using the model derived by Guéneau *et al.*⁸ and (b) PuO_{2-x} according to the model derived by Guéneau *et al.*²⁸; the calculations were performed from 1000 to 2600 K with 200 K intervals; see Guéneau *et al.*^{8,28} for the references of the experimental data.

oxygen potential measurements and an analogy with the Ce–O system. The phase diagram is in disagreement with the one determined by Sari and Zamorani.⁴¹ Very recently, a CALPHAD model derived by Gotcu-Freis *et al.*⁴² allows to account consistently both oxygen potential data for O/Am ratios above 1.9 from Chikalla and Eyring⁹⁴ and Sari and Zamorani phase diagram data. New experimental determinations on the phase diagram will be helpful to interpret these discrepancies and to fix the thermodynamic properties of this system.



(a)



(b)

Figure 20 Oxygen potential data versus O/metal ratio in (a) ThO_{2-x} at 2400, 2500, 2600, and 2655 K; the experimental data come from Ackermann and Tetenbaum¹⁷⁸ and (b) NpO_{2-x} at 1473, 1573, 1673, 1773, and 1853 K according to the model derived by Kinoshita *et al.*³⁹; the experimental data come from Bartscher and Sari.¹⁷⁹

The oxygen potential was measured in Cm–O by Chikalla and Eyring¹⁸⁴ and by Turcotte *et al.*,¹⁸⁵ in Bk–O by Turcotte *et al.*,^{186,46} and in Cf–O systems.¹⁸⁷

A comparison of the oxygen potential data calculated at 1600 K using the thermochemical models derived by Kinoshita *et al.*³⁹ for ThO_{2-x} and NpO_{2-x} , Thiriet and Konings⁴⁰ for AmO_{2-x} , Guéneau *et al.* for UO_{2-x} ⁸ and PuO_{2-x} ²⁸ is presented in Figure 22. The oxygen potential data are the lowest for ThO_{2-x} , then UO_{2-x} , NpO_{2-x} , PuO_{2-x} , and finally AmO_{2-x} for which the highest values were measured. This trend corresponds

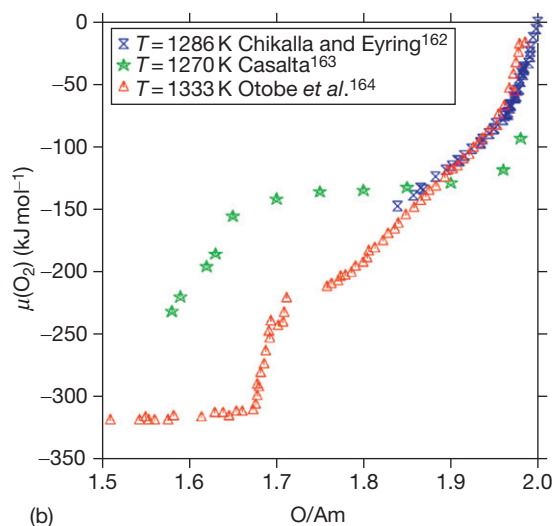
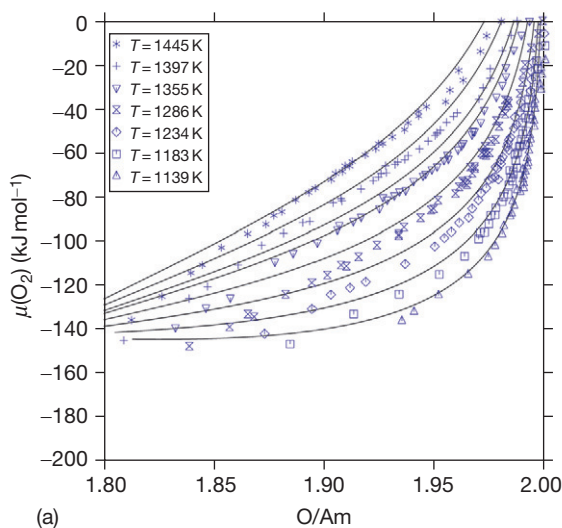


Figure 21 Oxygen potential data in AmO_{2-x} (a) at 1139, 1183, 1234, 1286, 1355, 1397, and 1445 K as derived by the model developed by Thiriet and Konings⁴⁰ compared to the experimental data of Chikalla and Eyring⁹⁴ (in blue); (b) measured at 1286 K by Chikalla and Eyring⁹⁴ (in blue), at 1270 K by Casalita¹⁸¹ (in green), and at 1333 K by Otobe *et al.*¹⁸² (in red).

to the order of the elements in the actinide series and to a decreasing stability of the actinide dioxides from ThO_2 to AmO_2 as reported in Section 2.02.4.1.1. It can also be concluded that the oxygen ions are the most strongly bonded in the ThO_{2-x} lattice.

2.02.4.3.2.2 Higher-order solid solutions

2.02.4.3.2.2.1 $(\text{U,Pu})\text{O}_{2\pm x}$ The available oxygen potential data on $(\text{U,Pu})\text{O}_{2\pm x}$ were compiled by Besmann and Lindemer^{173,175} when they presented their thermochemical model on $(\text{U,Pu})\text{O}_{2\pm x}$ solid

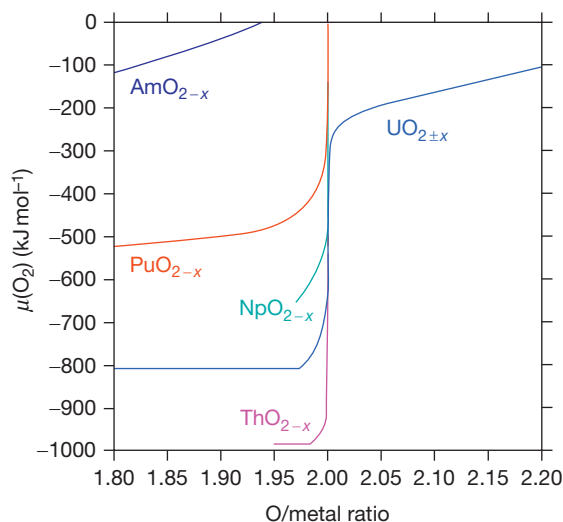


Figure 22 Comparison of the oxygen chemical potential data at 1600 K for the binary actinide oxides using the thermochemical modeling by Kinoshita *et al.*³⁹ for ThO_{2-x} and NpO_{2-x} , Thiriet and Konings⁴⁰ for AmO_{2-x} , and Guéneau *et al.*^{8,28} for $\text{UO}_{2\pm x}$ and PuO_{2-x} .

solution based on the description of the two subsystems U–O and Pu–O. Because of the increasing interest for mixed oxide fuels for fast breeder reactors, more recent measurements are available. Oxygen potentials were measured for $(\text{Pu}_{0.3}\text{U}_{0.7})\text{O}_{2-x}$ by Kato *et al.*¹⁸⁸ using thermogravimetry, for $(\text{Pu}_{0.2}\text{U}_{0.8})\text{O}_{2-x}$ by Kato *et al.*¹⁸⁹ by a gas equilibration method, for $(\text{Pu}_{0.79}\text{U}_{0.21})\text{O}_{2-x}$ and $(\text{Pu}_{0.72}\text{U}_{0.28})\text{O}_{2-x}$ by Vasudeva Rao *et al.*¹⁹⁰ using a gas equilibration technique, followed by solid-state EMF measurements.

The thermochemical model of the U–Pu–O system proposed by Yamanaka *et al.*⁵⁷ using the CALPHAD method allows calculating the oxygen potential in the MOX fuel, and the calculated data are compared to a limited number of experimental data. As reported in Section 2.02.4.3.1, a point defect model was recently proposed by Kato *et al.*¹⁵⁵ to represent the experimental oxygen potential data in $(\text{U}_{0.7}\text{Pu}_{0.3})\text{O}_{2\pm x}$ and $(\text{U}_{0.8}\text{Pu}_{0.2})\text{O}_{2\pm x}$. Recently, a thermochemical analysis was proposed by Vana Varamban *et al.*¹⁹¹ to estimate the oxygen potential for mixed oxides. The fuel is treated as a pseudoquaternary solution of $\text{UO}_2\text{--U}_c\text{O}_d\text{--PuO}_2\text{--Pu}_d\text{O}_b$ with $b=1.5a$ and $d=2.25c$. The values $a=2$ and $c=8$ were derived to represent the oxygen potential in mixed oxides with 21, 28, and 44% of plutonium.

The oxygen potential data of $(\text{U}_{0.9}\text{Pu}_{0.1})\text{O}_{2\pm x}$ and $(\text{U}_{0.7}\text{Pu}_{0.3})\text{O}_{2\pm x}$, as derived from the model developed by Besmann and Lindemer,¹⁷⁵ are presented in Figure 23. As expected from the above reported

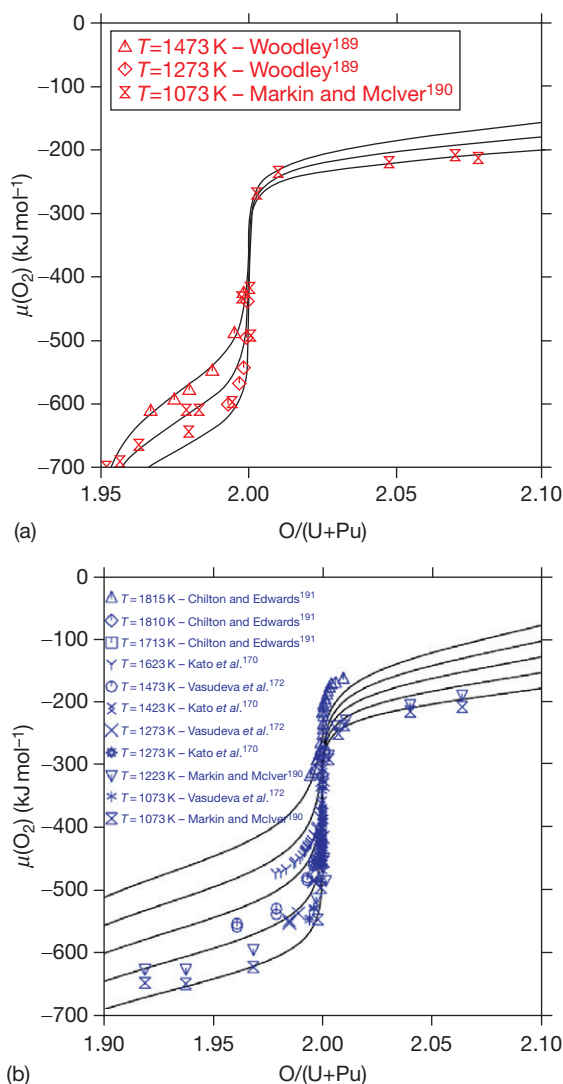


Figure 23 The oxygen potential of (a) $(U_{0.9}Pu_{0.1})O_{2\pm x}$ at 1073, 1273, and 1473 K and (b) $(U_{0.7}Pu_{0.3})O_{2\pm x}$ at 1073, 1273, 1473, 1673, and 1873 K as derived from the model proposed by Besmann and Lindemer.^{173,175}

data on the pure oxides, the oxygen potential of $(U,Pu)O_{2\pm x}$ increases with the plutonium content and temperature. In the hypostoichiometric region, the oxygen potentials were analyzed considering the change of the oxidation state of Pu from 4+ to 3+ by Rand and Markin.⁵²

2.02.4.3.2.2.2 $UO_{2\pm x}$, PuO_{2-x} , and $(U,Pu)O_{2\pm x}$ containing minor actinides The effect of the minor actinides Am, Np, and Cm on the oxygen potential of uranium and plutonium oxides and mixed oxides was investigated for different compositions as presented in Table 15.

As expected from the data for the binary oxides UO_{2-x} , PuO_{2-x} , and AmO_{2-x} (see Figure 22), the presence of americium leads to an increase of the oxygen potential in the ternary oxides $(U,Am)O_{2-x}$ and $(Pu,Am)O_{2-x}$ (Figure 24).

According to the comparison performed by Osaka *et al.*,¹⁹⁶ for a O/metal ratio above 1.96, the oxygen potential is the highest for AmO_{2-x} , then $(Pu_{0.91}Am_{0.09})O_{2-x}$ followed by $(U_{0.5}Am_{0.5})O_{2-x}$, $(U_{0.685}Pu_{0.270}Am_{0.045})O_{2-x}$, PuO_{2-x} , and finally $(U_{0.6}Pu_{0.4})O_{2-x}$. The experimental data are analyzed by considering the change of the oxidation states of the actinides Am and Pu. When the O/metal ratio decreases with stoichiometry, Am is first reduced from Am^{4+} to Am^{3+} , then after all Am is reduced, Pu is similarly reduced. The recent Calphad model on the Am-Pu-O system derived by Gotcu-Freis *et al.*⁴² allows the description of the oxygen potential in the whole composition range of the $(Am,Pu)O_{2\pm x}$ solid solution.

Hirota *et al.*²⁰¹ derived a thermochemical model for the $(U,Pu,Np)O_{2\pm x}$ oxide using the CALPHAD method. According to these calculations and to the experimental data of Morimoto *et al.*¹⁹⁹ on $(U_{0.58}Pu_{0.3}Np_{0.12})O_2$, it was found that Np has a small influence on the oxygen chemical potential of $(U,Pu)O_{2-x}$.

Table 15 Oxygen potential measurements in mixed oxides with minor actinides

Oxide	Method	References
$(U_{0.5}Am_{0.5})O_{2-x}$	Gas equilibration	Bartscher and Sari ¹⁹⁵
$(Pu_{0.91}Am_{0.09})O_{2-x}$	Thermogravimetry	Osaka <i>et al.</i> ¹⁹⁶
$(Am_{0.5}Pu_{0.5})O_{2-x}$	Electromotive force method	Otobe <i>et al.</i> ¹⁹⁷
$(Am_{0.5}Np_{0.5})O_{2-x}$	Electromotive force method	Otobe <i>et al.</i> ¹⁹⁸
$(U_{0.65}Pu_{0.3}Np_{0.05})O_2$ $(U_{0.58}Pu_{0.3}Np_{0.12})O_2$		Morimoto <i>et al.</i> ¹⁹⁹
$(U_{0.685}Pu_{0.270}Am_{0.045})O_{2-x}$	Thermogravimetry	Osaka <i>et al.</i> ²⁰⁰
$(U_{0.66}Pu_{0.30}Am_{0.02}Np_{0.02})O_{2-x}$	Gas equilibration method	Kato <i>et al.</i> ¹⁸⁹

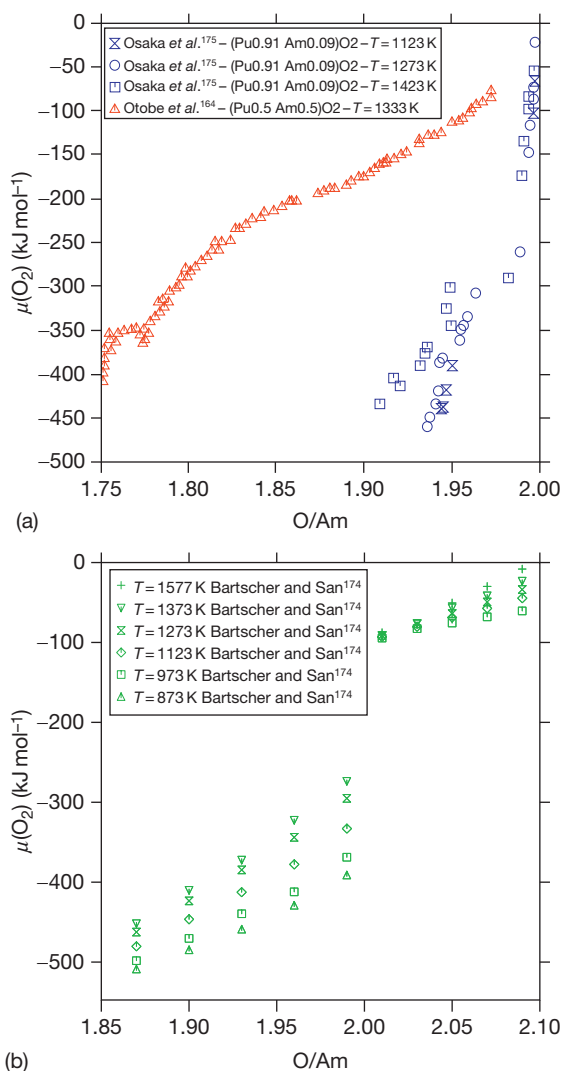


Figure 24 Oxygen potential data (a) in (Am_{0.5}Pu_{0.5})O_{2-x} at 1333 K according to Otohe *et al.*¹⁹⁷ and in (Am_{0.09}Pu_{0.91})O_{2-x} at 1273 and 1423 K by Osaka *et al.*¹⁹⁶, (b) in (Am_{0.5}U_{0.5})O₂ at 873–1577 K by Bartscher and Sari.¹⁹⁵

The oxygen potentials were measured for (U_{0.66}Pu_{0.30}Am_{0.02}Np_{0.02})O_{2-x} at 1473–1623 K by a gas equilibration method using (Ar, H₂, H₂O) mixture by Kato *et al.*¹⁸⁹ The values were compared to the oxygen potential data in (U_{0.7}Pu_{0.3})O_{2-x}¹⁸⁸ without minor actinides. The $\mu(\text{O}_2)$ data are 10 kJ mol⁻¹ higher in the mixed oxide containing Am and Np. The increase might be due to Am content.

2.02.4.3.2.2.3 (U,Th)O₂ and (Th,Pu)O₂ solid solutions Oxygen potential of (U_yTh_{1-y})O_{2+x} solid solutions was measured by Anderson *et al.*²⁰² using thermogravimetry for $y=0.03$, 0.063, and

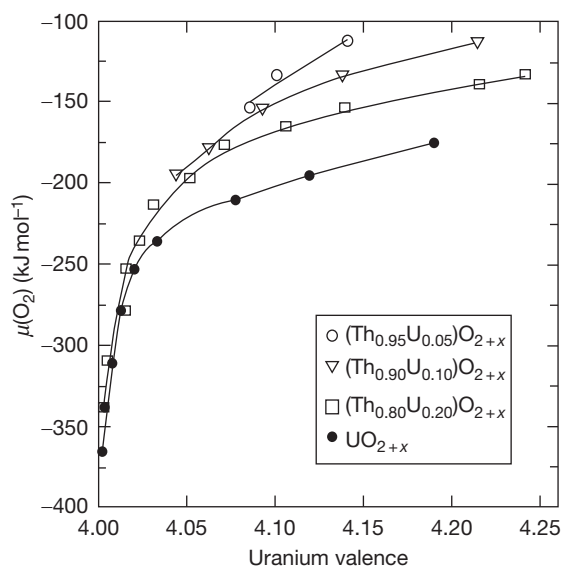


Figure 25 Oxygen potential data of (Th_{1-y}U_y)O_{2+x} solid solutions at 1473 K for various values of y after Ugajin.²⁰⁶

0.244, by Roberts *et al.*²⁰³ using pressure measurements for $y=0.05$ –0.06, by Aronson and Clayton²⁰⁴ using electromotive force method for $y=0.3$ –0.9, by Tanaka *et al.*²⁰⁵ using electromotive force method for $y=0.05$ –0.3, by Ugajin²⁰⁶ using thermogravimetry for $y=0.05$ –0.2, by Matsui *et al.*²⁰⁷ using thermogravimetry for $y=0.2$ –0.4, and by Anthonysamy *et al.*²⁰⁸ for $y=0.54$ –0.9 using a gas equilibration method. The analysis by Ugajin²⁰⁶ suggests that the oxygen potential is controlled by the change of uranium oxidation state as shown in Figure 25.

The results show that there is a systematic increase of the oxygen potential values with increasing thorium content. The oxygen potential data were retrieved and analyzed by Schram²⁰⁹ using the thermochemical model of Lindemer and Besmann with a mixture of the species ThO₂, UO₂, and U_aO_b for UO_{2+x}.

Recent experimental data on enthalpy increments and heat capacities of (U_{0.1}Th_{0.9})O₂, (U_{0.5}Th_{0.5})O₂, and (U_{0.9}Th_{0.1})O₂ solid solutions were measured by Kandan *et al.*²¹⁰ using, respectively, drop calorimetry at 479–1805 K and differential scanning calorimetry at 298–800 K. The results show that the solid solutions obey the Neumann–Kopp's rule.

2.02.5 Vaporization

The known gaseous actinide oxide molecules are listed in Table 15. Experimental data exist only from Th to Cm oxides. The thermochemical properties of these

Table 16 Known gaseous actinide oxides

	Th	Pa	U	Np	Pu	Am	Cm
+2	ThO	PaO	UO	NpO	PuO	AmO	CmO
+4	ThO ₂	PaO ₂	UO ₂	NpO ₂	PuO ₂	AmO ₂	CmO ₂
+6			UO ₃	NpO ₃	PuO ₃		

Table 17 Thermodynamic data on gaseous actinide oxides molecules according to Konings *et al.*³⁸

	$\Delta_f H^\circ (298.15\text{ K})$ (kJ mol ⁻¹)	$S^\circ (298.15\text{ K})$ (JK ⁻¹ mol ⁻¹)
ThO	-21.5 ± 10.0	240.1 ± 2.0
ThO ₂	-435.6 ± 12.6	285.2 ± 2.0
PaO	4 ± 30	250.8 ± 6
PaO ₂	-514 ± 30	276.7 ± 6
UO	21.4 ± 10.0	252.14 ± 2
UO ₂	-462.1 ± 12	277.0 ± 2.5
UO ₃	-795.0 ± 10.0	310.6 ± 3.0
NpO	-16.6 ± 10	253.0 ± 5
NpO ₂	-444 ± 20	277.2 ± 6.0
PuO	-51.7 ± 15	252.2 ± 3.0
PuO ₂	-411.9 ± 15	278.7 ± 5
PuO ₃	-567.6 ± 15	319.4 ± 4
AmO	-15 ± 50	259.1 ± 10
CmO	-75.4 ± 20	259.1 ± 10.0

gaseous species reviewed and compiled by Konings *et al.*³⁸ are listed in **Tables 16** and **17**.

The recommended vapor pressures over solid UO₂, ThO₂, PuO₂, and liquid UO₂ are given in the review by IAEA.²¹² The equation of state of uranium dioxide was investigated by Ronchi *et al.*²¹¹

2.02.5.1 Pu–O and U–O

In the system Pu–O, the partial pressures of the gaseous species Pu(g), PuO(g), and PuO₂(g) vary with the O/Pu ratio and temperature as a large composition range exists for PuO_{2-x}. The variation of the gaseous species calculated at 1970 K is shown in **Figure 26(a)** as a function of the O/Pu ratio using the CALPHAD model developed by Guéneau *et al.*²⁸ In the two-phase region [Pu₂O₃ + PuO_{2-x}], the major species are PuO(g), Pu(g), and PuO₂(g). With increasing O/Pu ratio in PuO_{2-x} phase, the partial pressures of PuO(g) and Pu(g) decrease whereas PuO₂(g) partial pressure slightly increases. Close to the stoichiometry, O(g) and O₂(g) become the major gaseous species. The curve giving the total pressure of the gas as a function of the O/Pu ratio shows a minimum that corresponds to the congruent vaporization of plutonia occurring for a slightly hypostoichiometric oxygen composition.

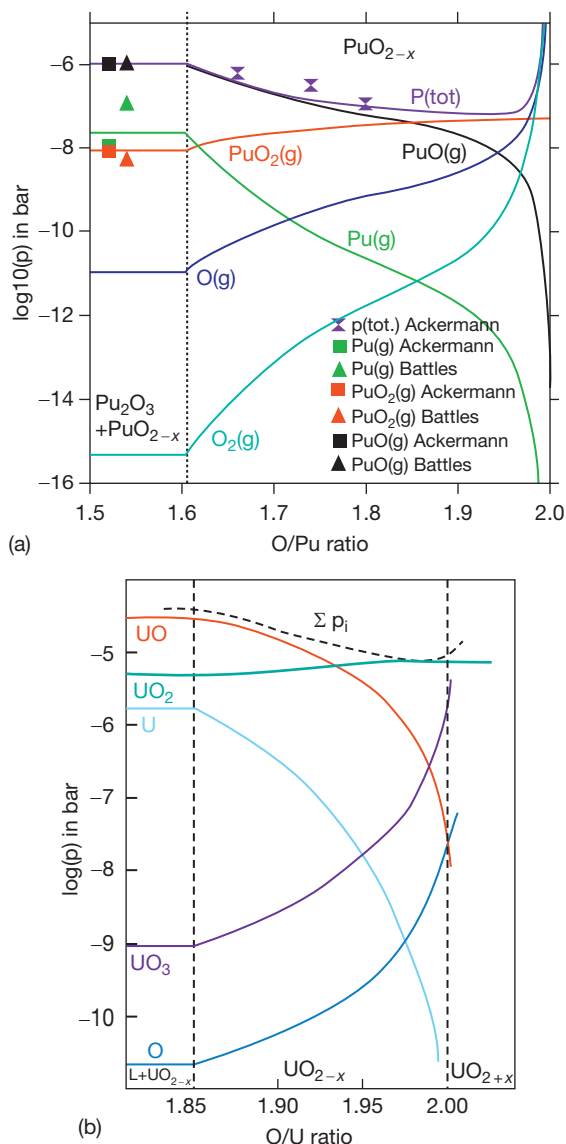


Figure 26 Calculated partial pressures of (a) Pu(g), PuO(g), PuO₂(g), O(g), and O₂(g) in the Pu–O system at 1970 K as a function of the O/Pu ratio derived from the thermochemical model developed by Guéneau *et al.*²⁸; see Guéneau *et al.*²⁸ for information on experimental data; (b) of UO(g), UO₂(g), U(g), UO₃(g), and O(g) at 2250 K in the U–O system according to the measurements using mass spectrometry by Pattoret.²¹³

In the U–O system, the vaporization is more complex due to the existence of both the hypo- and hyperstoichiometric composition ranges of uranium dioxide. According to the measurements by Pattoret²¹³ using mass spectrometry, reported in **Figure 26(b)**, a sample with a composition UO_{2-x} heated at 2250 K will tend to lose preferentially U via UO(g) to reach the

congruent composition UO_{2-x} with a O/U ratio equal to 1.987 ± 0.01 corresponding to the minimum in total pressure, that is, the congruency. A sample with a composition UO_2 or UO_{2+x} will lose oxygen via $\text{UO}_3(\text{g})$ to reach the same congruent composition. Above solid UO_2 , the largest contribution is from $\text{UO}_2(\text{g})$.

2.02.5.2 U–Pu–O

The partial pressures of the different gaseous actinide oxide molecules were calculated by Rand and Markin⁵² over $\text{U}_{0.85}\text{Pu}_{0.15}\text{O}_{2 \pm x}$ at 2000 K using the thermodynamic data on the solid and gas phases (Figure 27). $\text{UO}_3(\text{g})$ is the predominant gas species in the hyperstoichiometric region. This is due to the fact that in the MOX, the oxygen potentials are higher than in UO_2 (see Section 2.02.4.2.2). The composition of the vapor is enriched in uranium and oxygen in comparison to the solid. It means that the solid will lose uranium and oxygen. In the hypostoichiometric region, the uranium species are less in the vapor than in the solid for O/metal ratio below 1.96. It means that the solid will preferentially lose plutonium. A review of the previous experimental studies on vaporization of (U,Pu) O_2 oxides was reported by Viswanathan and Krishnaiah.²¹⁴ The authors derived a thermochemical model to calculate the partial and total pressures

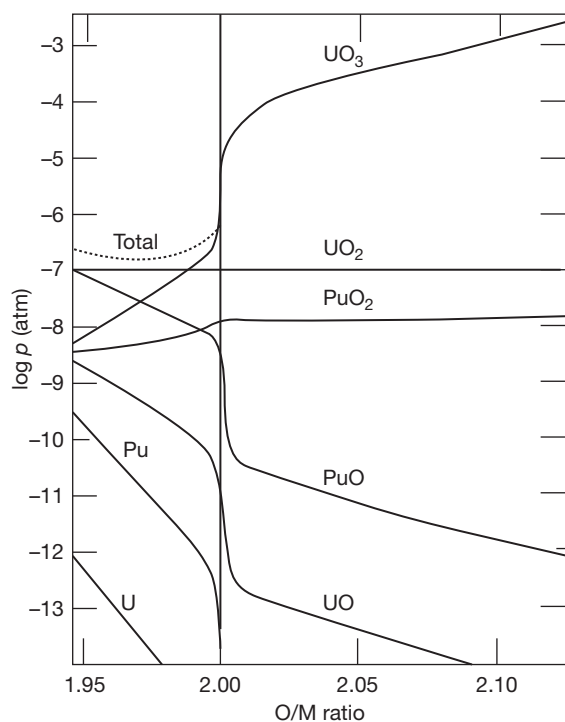


Figure 27 Calculated partial pressures over $\text{U}_{0.85}\text{Pu}_{0.15}\text{O}_{2 \pm x}$ at 2000 K according to Rand and Markin.⁵²

above MOX with up to 40% mol. PuO_2 . The different studies show that a quasi-congruent vaporization is reached where $(\text{O}/\text{Metal})_{\text{vapor}} = (\text{O}/\text{Metal})_{\text{solid}}$ which corresponds to a slightly hypostoichiometric mixed oxide in oxygen like in the binary oxides UO_2 and PuO_2 .

2.02.5.3 U–Pu–Am–O

Calculations of the same type were recently performed by Maeda *et al.*²¹⁵ above a mixed oxide with the composition $(\text{U}_{0.69}\text{Pu}_{0.29}\text{Am}_{0.02})\text{O}_{2 \pm x}$ at 2073 and 2273 K (see Figure 28). The results show that in the hyperstoichiometric region, $\text{UO}_3(\text{g})$ remains the predominant gas species. But for O/metal ratio below 1.96 corresponding to the congruent composition, the $\text{AmO}(\text{g})$ species becomes the major molecule in the vapor. Very recently, an experimental study on vaporization of AmO_2 and (Pu,Am) O_2 oxides was performed by Gotcu-Freis *et al.*^{216,42} using mass spectrometry.

2.02.6 Transport Properties

2.02.6.1 Self-Diffusion

The diffusion of oxygen or cations has been mainly investigated in the actinide dioxides MO_2 with the fluorite structure. Usually, the diffusion coefficient D is expressed using an Arrhenius law-type equation

$$D = D_0 \exp\left(-\frac{E_{\text{mig.}}}{k_B T}\right) \quad [13]$$

where D_0 is the prefactor, $E_{\text{mig.}}$ is an effective migration energy, k_B is the Boltzmann constant, and T is the temperature. While very commonly used, the details of the diffusion are unfortunately hidden behind this equation. The prefactor depends upon hopping frequency and geometrical factors while the effective migration energy should be expressed as a free energy (see, e.g., Ando and Oishi²¹⁷ or Howard and Lidiard²¹⁸) and should include the formation energy of the migrating defect. In pure dioxides, for example, the oxygen diffusion occurs via vacancy/interstitial migration, depending on the stoichiometry – that is, on the oxygen partial pressure (see Section 2.02.4.3.1 on defects).

In general, the diffusion depends strongly on any type of defects present in the crystal lattice. Also the grain boundaries play a major role, as they act as shortcuts for the diffusion (see Vincent-Aublant *et al.*²¹⁹ and Sabioni *et al.*²²⁰). Thus, the reliability of the diffusion measurements is related to the control/measurement of the stoichiometry and microstructure.

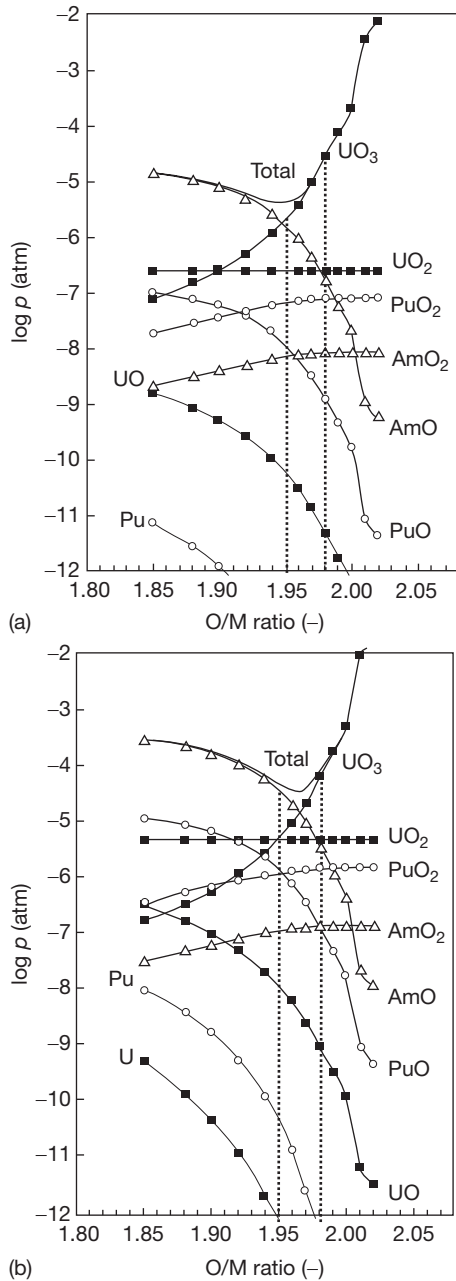


Figure 28 Calculated partial pressures of the actinide oxide gaseous species over $(\text{U}_{0.69}\text{Pu}_{0.29}\text{Am}_{0.02})\text{O}_{2 \pm x}$ at 2073 K (a) and 2273 K (b) according to Maeda *et al.*²¹⁵ © Elsevier, reprinted with permission.

Those experimental issues lead to a very large scatter of data (see, e.g., Sabioni *et al.*,²²⁰ Belle and Berman,²²¹ Sabioni *et al.*²²²), and hence complementary *ab initio* and MD calculations by Terentyev,⁸⁰ Stan and Cristea,¹⁵⁰ Stan,¹⁵⁴ Andersson *et al.*,¹⁶⁸ Vincent-Aublant *et al.*,²¹⁹ and Kupryazhkin *et al.*²²³ are performed to bring microscopic insights to the experiments, but with various degrees of success. The proposed models cannot generally overcome the identification of the defects responsible for the diffusion. This is because the types of the stable defects themselves (vacancies, interstitials, and also complex defects such as clusters; see Section 2.02.4.3.1) are far from being resolved. Hence, the diffusion coefficients as a function of stoichiometry are fitted on semi-empirical equations. Another way to circumvent this issue is to follow Siethoff.²²⁴ He has recently reexhibited a relation between the effective migration energies and the elastic properties in many crystallographic families, including the fluorite structures.

As many reviews have been written on the self-diffusion in actinide dioxides in the past, and as the data collected are so inconsistent to each other, we refer the reader to the review done by Belle and Berman²²¹ for UO_2 , PuO_2 , and ThO_2 for the studies done before 1984 to get the experimental data. Recently, new data have been reported, and we refer the reader to the studies by Sabioni *et al.*,^{220,222} Mendez *et al.*,²²⁵ Korte *et al.*,²²⁶ Sali *et al.*,²²⁷ Arima *et al.*,²²⁸ Ruello *et al.*,²²⁹ Kato *et al.*,²³⁰ and Garcia *et al.*²³¹ and references therein. In the following, we will limit ourselves to report some semiempirical equations in known cases.

2.02.6.1.1 Oxygen diffusion

As mentioned above, the microscopic mechanisms of oxygen diffusion vary as a function of stoichiometry in the actinide dioxides. A schematic view of the (simplified) possible mechanisms has been reported in Table 18. Dorado *et al.*²³² combining both experimental and theoretical approaches identified the oxygen migration as an interstitialcy mechanism.

For $x < 0$ in MO_{2-x} (hypostoichiometric dioxides), the dominant defects in urania and plutonia are the oxygen vacancies. Hence, the migration energy could

Table 18 Simplified view of the migration energies of oxygen as a function of stoichiometry in $\text{MO}_{2 \pm x}$

Mechanism	$x < 0$	$x = 0$	$x > 0$
Vacancy	$E_{\text{act.}}(V_{\text{O}}^{\bullet\bullet})$	$E_{\text{f}}(\text{O}_{\text{FP}})/2 + E_{\text{act.}}(V_{\text{O}}^{\bullet\bullet})$	$E_{\text{f}}(\text{O}_{\text{FP}}) + E_{\text{act.}}(V_{\text{O}}^{\bullet\bullet})$
Interstitial	$E_{\text{f}}(\text{O}_{\text{FP}}) + E_{\text{act.}}(I_{\text{O}}'')$	$E_{\text{f}}(\text{O}_{\text{FP}})/2 + E_{\text{act.}}(I_{\text{O}}'')$	$E_{\text{act.}}(I_{\text{O}}')$

$E_{\text{act.}}$ and E_{f} set for activation and formation energies, respectively. FP, V, and I set for Frenkel pair, vacancy, and interstitial, respectively.

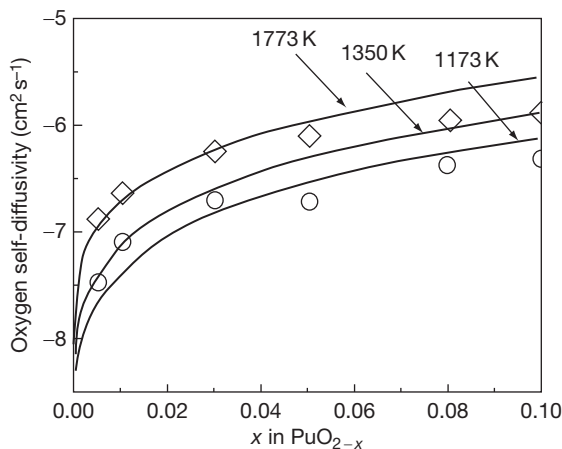


Figure 29 Oxygen self-diffusion coefficient in PuO_{2-x} as a function of stoichiometry from Stan *et al.*¹⁵³ Symbols are experimental data. © Elsevier, reprinted with permission.

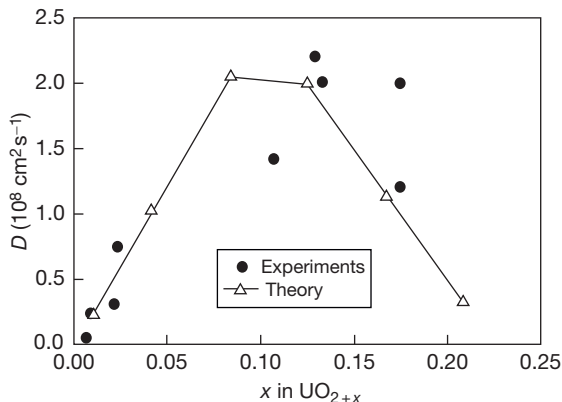


Figure 30 Comparison between the experimental self-diffusion coefficients of oxygen in hyperstoichiometric UO_{2+x} and the calculated ones at 1073 K. From Andersson, D. A.; Watanabe, T.; Deo, C.; Uberuaga, B. P. *Phys. Rev.* **2009**, 80B, 060101.

be reduced to the activation energy for oxygen vacancy migration $E_{\text{act.}}(V_{\text{O}}^{\bullet\bullet})$ as reported in the Table 18.

In fact, Stan *et al.*^{150,152} have shown that the point defects in hypostoichiometric plutonia PuO_{2-x} do not reduce to oxygen vacancy. They determined (from a point defect model) that five different defects are at work in PuO_{2-x} and hence contribute to the formation of oxygen vacancies. According to them, the prefactor D_0 (eqn [13]) can then be written as a function of (i) a stoichiometry-dependent correlation factor from Tahir-Kheli²³³ and (ii) the formation energy of oxygen vacancy (determined using the point defect model). The results of such a model are reported in Figure 29.

Recently Kato *et al.*²³⁰ have studied the oxygen diffusion in hypostoichiometric MOX, and they

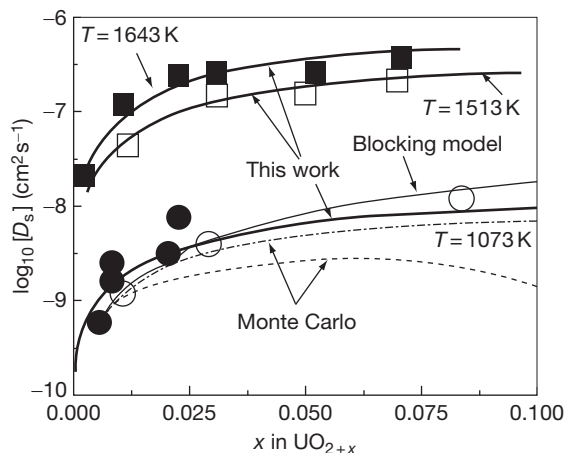


Figure 31 Self-diffusion coefficient of oxygen in hyperstoichiometric UO_{2+x} . Symbols are experimental data. From Stan, M. *Nucl. Eng. Tech.* **2009**, 41, 39–52, reprinted with permission.

concluded that the diffusion coefficient of oxygen linearly depends upon the concentration of Pu in MOX.

For $x > 0$ in MO_{2+x} (hyperstoichiometric dioxides), two recent studies evidenced that the oxygen interstitials are not the only contribution to oxygen diffusion. Experimental data obtained by Ruello *et al.*²²⁹ in UO_{2+x} show the important role of the Willis clusters. Theoretical calculations based on coupled *ab initio*/kinetic Monte Carlo done by Andersson *et al.*¹⁶⁸ have shown also that the diinterstitial cluster of oxygen may contribute to the oxygen diffusion for highly hyperstoichiometric UO_{2+x} . In fact, the diffusion of oxygen in hyperstoichiometric dioxides is due to the diffusion of interstitial oxygen and to the (counteracting) contribution of more complex oxygen clusters. Hence, the diffusion coefficient increases with stoichiometry, reaches a maximum, and decreases as may be seen in Figure 30.

Recently, Stan *et al.*¹⁵³ proposed a semiempirical relation between the diffusion coefficient D and the stoichiometry for UO_{2+x} that includes a maximum:

$$D(T, x) = xD_0 \exp\left(-\frac{E_0}{k_B T}\right) \exp(-\theta x) \quad [14]$$

In this expression, $D_0 = 1.3 \times 10^{-2} \text{ cm}^2 \text{ s}^{-1}$, $E_0 = 1.039 \text{ eV}$, and $\theta = 6.1$. The last term of the product corresponds to the blocking effect of the complex oxygen clusters. Such a semiempirical model reproduces the experimental data fairly well (see Figure 31), up to $x < 0.1$. For higher values of x ($0.0 < x < 0.2$ from 300 up to 1800 K), Ramirez *et al.*¹⁵¹ established a somewhat different semiempirical relation.

2.02.6.1.2 Cation diffusion

The cation diffusion occurs in actinide dioxides via cation vacancies in the vicinity of oxygen vacancy according to Jackson *et al.*²³⁴ As a consequence, cation diffusion may occur in hyperstoichiometric dioxides MO_{2+x} (with $x > 0$). The diffusion coefficient increases drastically with departure from stoichiometry as x^2 in MO_{2+x} as follows:

$$D(x, T) = D_0 x^2 \exp\left(-\frac{E_0}{k_B T}\right) \quad [15]$$

Recently, Gao *et al.*²³⁵ obtained the prefactor $D_0 = 2.341 \times 10^{-2} \text{ m}^2 \text{ s}^{-1}$ and migration energy $E_0 = 2.5 \text{ eV}$ for UO_{2+x} .

Knorr *et al.*²³⁶ mentioned that the effect of the intergranular grain boundary is to change the prefactor to a linear dependence upon stoichiometry. The diffusion coefficient is expressed as follows:

$$D = D_0 x \exp\left(-\frac{E_0}{k_B T}\right) \quad [16]$$

They found for UO_{2+x} , $D_0 = 7.5 \times 10^{-4} \text{ m}^2 \text{ s}^{-1}$ and $E_0 = 2.47 \text{ eV}$.²³⁶

This apparent activation energy is very close to the one obtained by Gao *et al.*²³⁵ A systematic study of the difference between monocrystals and polycrystals done by Sabioni *et al.*²²⁰ led the authors to the conclusion that most of the activation energies reported by previous authors probably refer to polycrystals.

2.02.6.2 Thermal Conductivity

The thermal conductivity of the actinide dioxides is known to be mainly described by phonon mechanism, and more specifically by longitudinal acoustic modes (Yin and Savrasov²³⁷). Other terms (e.g., electronic conductivity) remain at few percent of the total conductivity, except for UO_2 (see, e.g., Carbajo *et al.*⁸⁴ and Inoue²³⁸) where the electronic conductivity increases at high temperatures. Any defect (point defect, grain boundary, void, porosity, impurity, etc.; see, e.g., Buyx²³⁹), as referred to the ideal perfect lattice, may contribute to decrease the thermal conductivity by phonon scattering (see, e.g., Millet *et al.*²⁴⁰). The thermal conductivity λ may consequently be expressed as

$$\lambda = \frac{1}{A + B \times T} + \frac{C}{T^2} \exp\left(-\frac{D}{T}\right) \quad [17]$$

The last term, that is dependent upon C and D parameters, is related to the electronic conductivity

(see Buyx²³⁸). A is related to the phonon defect scattering and B to the phonon–phonon scattering. The value of A is affected by the concentration of defects (interstitials, vacancies, grain boundaries, dislocations, etc.), and thus does change with stoichiometry (see, e.g., Buyx²³⁸). The value of B is less affected by defects, as long as the symmetry of the crystal is preserved. Hence, the evolution of the thermal conductivity as a function of composition relies on the variation of the parameter A . This parameter has been shown to change linearly with composition according to Murti and Matthews²⁴¹ and Morimoto *et al.*²⁴² Indeed, as irradiations produce significant amounts of defects and impurities, they will contribute to the modification of A (see, Ronchi *et al.*²⁴³ for example).

The characterization of the microstructure, the stoichiometry, the purity, etc., of each sample is also of utmost importance for the quality of the experimental data collected. From this characterization, *ad hoc* equations are used in order to infer the thermal conductivity.

Among the above-mentioned parameters, porosity is one of the most important. Usually, the analytical equation of Schulz²⁴⁴ is used to infer the thermal conductivity λ_{TD} of the fully dense material:

$$\lambda = \lambda_{\text{TD}}(1 - P)^x \quad [18]$$

P is the porosity and x is related to the shape of the closed pores; in the spherical case, $x = 1.5$. Bakker *et al.*²⁴⁵ proposed a value around 1.7 for nuclear fuel with complex pore shapes and distributions. As already mentioned, chemical and radioactive hazards have limited the number of experimental data. MD and *ab initio* calculations are nowadays used to investigate the thermal conductivities of actinides. The thermal conductivity is calculated either by a direct method (using the Fick's law) or equivalently by the Green–Kubo relationship (Schelling *et al.*²⁴⁶) at different temperatures in the MD framework.

2.02.6.2.1 Actinide dioxides

2.02.6.2.1.1 Stoichiometric dioxides

The parameters (of eqn [17]) of the thermal conductivities of actinide dioxides have been reported in Table 19. Among the dioxides, UO_2 has indeed been subject to many experiments. It is the only one to exhibit a nonnegligible electronic conductivity contribution. Complementary theoretical calculations (see MD calculations by Arima *et al.*,⁶⁴ Uchida *et al.*,⁶⁵ Kurosaki *et al.*,²⁴⁷ or models based on approximated phonon spectra by Sobolev^{67–69} and Lemehov

*et al.*²⁴⁸) have been performed recently to extend (in temperature and composition) the available experimental data. The results obtained recently by Sobolev^{67–69} reproduce quite well the experimental data available. Lemehov *et al.*²⁴⁸ have shown that such a model works for irradiated dioxides too.

2.02.6.2.1.2 Stoichiometric mixed dioxides

The thermal conductivity of few mixed dioxides has been investigated experimentally. Among the most well known are indeed the uranium–plutonium and the uranium–thorium mixed dioxides. Some data are available for (Np,U)O₂ (see Lemehov *et al.*²⁴⁸) and for the rest of mixed dioxides, one can refer to MD calculations (see Arima *et al.*,⁶⁴ Terentyev,⁸⁰ Arima *et al.*,⁸¹ and Kurosaki *et al.*⁸²). We have gathered the most recently obtained parameters (eqn [17]) of the thermal conductivity (see Yang *et al.*,⁷⁸ Duriez *et al.*,¹⁴³ Vasudeva Rao *et al.*,¹⁹⁰ Kutty

et al.,²⁴⁹ and Pillai and Raj²⁵²) in Tables 20 and 21, respectively, for U_{1–x}Pu_xO₂ and for U_xTh_{1–x}O₂.

Some attempts have been made with various degrees of success to relate the solid solution ratio (x in U_{1–x}Pu_xO₂ (see Duriez *et al.*¹⁴³) or y in Th_{1–y}U_yO₂ (see Bakker *et al.*⁵⁹)) and the parameters A and B (eqn [17]) of the thermal conductivity. For example, for Th_{1–y}U_yO₂ with $y < 0.1$, in the temperature range 300–1173 K and a density of 95%, both A and B parameters are related to the stoichiometry by a quadratic dependence by Bakker *et al.*⁵⁹:

$$A = 4.195 \times 10^{-4} + 1.112y - 4.499y^2 \text{ and}$$

$$B = 2.248 \times 10^{-4} - 9.170 \times 10^{-4}y + 4.164 \times 10^{-3}y^2$$

The thermal conductivity of the more complex americium and neptunium containing MOX dioxides has been recently investigated by Morimoto *et al.*^{242,253} In this case, the parameter A of eqn [17]

Table 19 Parameters (of eqn [17]) of the thermal conductivities in stoichiometric dioxides

	$A \times 10^2 \text{ (mK W}^{-1}\text{)}$	$B \times 10^4 \text{ (m W}^{-1}\text{)}$	$C \times 10^{-11}$	$D \times 10^{-4} \text{ (K)}$	T (K)	References
ThO ₂	0.042	2.25	–	–	300–1800	Bakker <i>et al.</i> ⁵⁹
UO ₂	6.548	2.3533	2.024	1.635	298–3120	IAEA ²¹²
NpO ₂	9.447	1.797	–	–	573–1473	Nishi <i>et al.</i> ¹³⁷
PuO ₂	1.22	2.75	–	–		Bielenberg <i>et al.</i> ²⁵⁰
	0.46	1.282	–	–	373–1474	Gibby ²⁵¹
AmO ₂	2.1	3.19	–	–	298–1573	Bakker <i>et al.</i> ⁵⁹

Table 20 Parameters (of eqn [17]) of the thermal conductivity of U_{1–x}Pu_xO₂ fitted from the data of Vasudeva Rao *et al.*¹⁹⁰ and Duriez *et al.*¹⁴³

U _{1–x} Pu _x O ₂	$A \times 10^2 \text{ (mK W}^{-1}\text{)}$	$B \times 10^4 \text{ (m W}^{-1}\text{)}$	T (K)	%TD	References
0.03	3.96	2.875	300–1300	95	Duriez <i>et al.</i> ¹⁴³
0.06	3.27	2.96	300–1300	95	Duriez <i>et al.</i> ¹⁴³
0.10	3.96	2.894	300–1300	95	Duriez <i>et al.</i> ¹⁴³
0.15	2.17	3.039	300–1300	95	Duriez <i>et al.</i> ¹⁴³
0.21	5.74	1.734	700–1500	96	Vasudeva Rao <i>et al.</i> ¹⁹⁰
0.28	17.08	1.157	700–1500	96	Vasudeva Rao <i>et al.</i> ¹⁹⁰
0.40	15.81	2.301	700–1500	96	Vasudeva Rao <i>et al.</i> ¹⁹⁰

Table 21 Parameters (of eqn [17]) of the thermal conductivity in U_xTh_{1–x}O₂ solid solution, obtained by Kutty *et al.*,²⁴⁹ Pillai and Raj,²⁵² and Yang *et al.*⁷⁸

U _x Th _{1–x} O ₂	$A \times 10^2 \text{ (mK W}^{-1}\text{)}$	$B \times 10^4 \text{ (m W}^{-1}\text{)}$	T (K)	%TD	References
0.00	3.34	1.374	400–1800	92	Kutty <i>et al.</i> ²⁴⁹
0.00	2.16	2.12	300–1250	94	Pillai and Raj ²⁵²
0.02	4.694	2.13	300–1250	94	Pillai and Raj ²⁵²
0.04	4.97	1.475	400–1800	94	Kutty <i>et al.</i> ²⁴⁹
0.20	25.16	2.359	400–1800	90	Kutty <i>et al.</i> ²⁴⁹
0.355	14.7	2.13	300–1500	96–98	Yang <i>et al.</i> ⁷⁸
0.655	13.3	2.11	300–1500	96–98	Yang <i>et al.</i> ⁷⁸

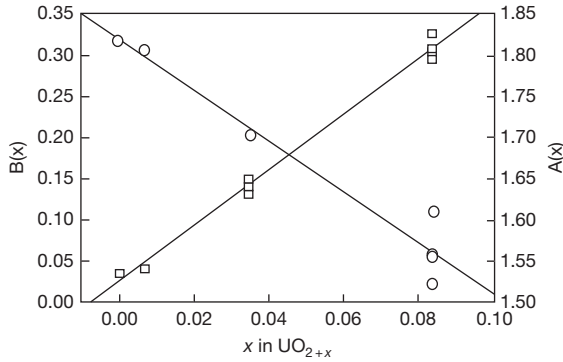


Figure 32 Evolution of $A(x)$ and $B(x)$ as a function of stoichiometry x in UO_{2+x} from Lucata *et al.*²⁵⁵

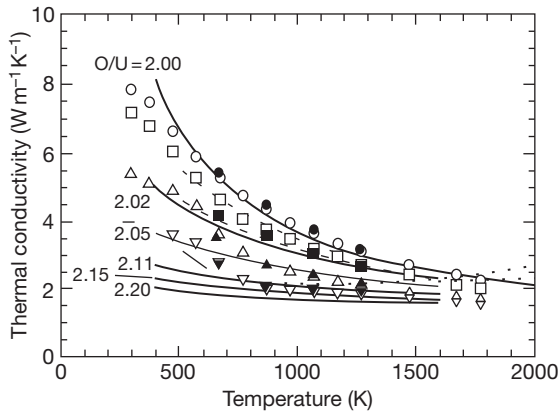


Figure 33 Thermal conductivity of in UO_{2+x} as a function of stoichiometry x from Amaya *et al.*²⁵⁶ © Reprinted with permission.

(B being fixed) is linearly related to the stoichiometry of $\text{Am}_{z1}\text{Np}_{z2}\text{Pu}_{0.3}\text{U}_{0.7-z1-z2}\text{O}_2$ as follows: $A = 0.3583z_1 + 0.06317z_2 + 0.01595$ (mK W^{-1}) with $B = 2.493 \times 10^{-4}$ (m W^{-1}).

2.02.6.2.1.3 Nonstoichiometric dioxides

In general, the thermal conductivity decreases with departure from stoichiometry. This has been seen in AmO_{2-x} by Nishi *et al.*²⁵⁴ and in $\text{UO}_{2\pm x}$ by Watanabe *et al.*⁸⁷ and also by Yamashita *et al.*⁸⁸

Lucata *et al.*²⁵⁵ found a linear relation between the thermal conductivity and the stoichiometry x in UO_{2+x} for $0 < x < 0.10$ (see Figure 32): $A(x) = 0.0257 + 3.34x$ and $B(x) = (2.206 - 6.86x)$.

Amaya *et al.*²⁵⁶ proposed a somewhat different and more complicated expression, but valid for $0.0 < x < 0.20$:

$$\lambda = \lambda_0 \{ \arctan(\theta) / \theta \} + CT^3 \quad [19]$$

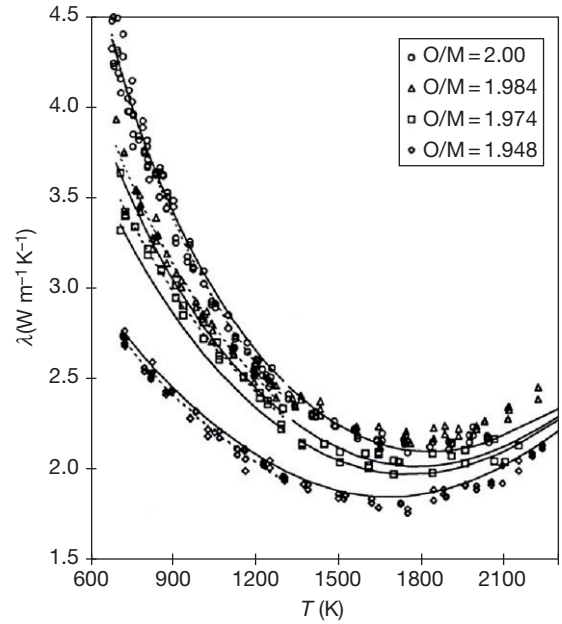


Figure 34 Thermal conductivity of 15% plutonium containing UO_2 as a function of temperature and stoichiometry from Duriez *et al.*¹⁴³ © Elsevier, reprinted with permission.

where $\lambda_0 = 1/(A + BT)$, $\theta = D\sqrt{2x\lambda_0}$, and $D = D_0 \exp(DT)$.

The fit performed by Amaya *et al.*²⁵⁶ leads to $A = 3.24 \times 10^{-2} \text{ K m W}^{-1}$, $B = 2.51 \times 10^{-4} \text{ m W}^{-1}$, $C = 5.95 \times 10^{-11} \text{ W m}^{-1} \text{ K}^{-4}$, $D_0 = 3.67 \text{ m}^{1/2} \text{ K}^{1/2} \text{ W}^{-1/2}$, and $D_1 = -4.73 \times 10^{-4} \text{ K}^{-1}$. It allows a good description of hyperstoichiometric urania (see Figure 33).

For even higher-order oxides, in the case of U_3O_8 , the thermal conductivity coefficients are from Pillai *et al.*²⁵⁷: $A = 29.3 \times 10^{-2} \text{ mK W}^{-1}$ and $B = 5.39 \times 10^{-4} \text{ m W}^{-1}$.

For $\text{U}_{1-y}\text{Pu}_y\text{O}_{2-x}$ with a low amount of Pu, Duriez *et al.*¹⁴³ obtained almost no dependence on the plutonium content in the range of $0.03 < y < 0.15$ (see Table 19). The extrapolation to pure UO_2 indicates that a small amount of Pu is sufficient for altering the thermal conductivity of UO_2 . Because of the proximity to the pure UO_2 end member, Duriez *et al.*¹⁴³ found an electronic contribution to the thermal conductivity at high temperature. The parameters (of eqn [17]) are $A(x) = 2.85x + 3.5 \times 10^{-2} \text{ K m W}^{-1}$, $B(x) = (-7.15x + 2.86)10^{-4} \text{ m W}^{-1}$, $C = 1.689 \times 10^9 \text{ W K}^{-1} \text{ m}$, and $D = 1.3520 \times 10^4 \text{ K}$.

As an example for the evolution of the thermal conductivity as a function of temperature and stoichiometry, we show the figure from Duriez *et al.*¹⁴³ for a sample containing 15% urania (Figure 34).

For higher amount of plutonium ($0.15 < y < 0.30$), Inoue²³⁸ obtained a somewhat different dependence (qualitatively reproduced by MD calculations by Arima *et al.*⁸¹): $A(x) = 0.06059 + 0.2754\sqrt{x} \text{ K m W}^{-1}$, $B = 2.011 \times 10^{-4} \text{ m W}^{-1}$, $C = 4.715 \times 10^9 \text{ W K}^{-1} \text{ m}$, and $D = 1.6361 \times 10^4 \text{ K}$.

Finally, the thermal conductivity continues to decrease as a function of plutonium content, as shown by Sengupta *et al.*²⁵⁹ in $\text{Pu}_{0.44}\text{U}_{0.66}\text{O}_2$.

Morimoto *et al.*²⁵⁸ have investigated the effect of hypostoichiometry on the thermal conductivity of $\text{U}_{0.68}\text{Pu}_{0.30}\text{Am}_{0.02}\text{O}_{2.00-x}$ ($0.00 < x < 0.08$). Both parameters $A(x)$ and $B(x)$ (of eqn [17], $C = D = 0$) depend on the stoichiometry x as follows: $A(x) = 3.31x + 9.92 \times 10^{-3} \text{ K m W}^{-1}$ and $B(x) = (-6.68x + 2.46)10^{-4} \text{ m W}^{-1}$.

Lemehov *et al.*²⁴⁸ brought a physical model for the thermal conductivity of actinide dioxides. They were able to fit the few experimental data available and to analyze the effect of hypostoichiometry (and irradiation) in $(\text{Am,U})\text{O}_{2-x}$ and $(\text{Am,Np,U})\text{O}_{2-x}$ solid solutions.

2.02.6.2.2 Actinide sesquioxides

The parameters of the thermal conductivity as a function of temperature are available only for curium sesquioxide Cm_2O_3 . The values recommended by Konings *et al.*⁴³ are $A = 36.29 \times 10^{-2} \text{ mK W}^{-1}$ and $B = 1.78 \times 10^{-4} \text{ m W}^{-1}$.

Lemehov²⁴⁸ and Uchida⁶⁵ have investigated the behavior of Am_2O_3 . But their theoretical results are not consistent to each other and hardly consistent with the few experimental data available.

2.02.7 Thermal Creep

Creep relates to the slow plastic deformation of the material under the influence of stress and temperature. It is a long-term process with different mechanisms. Actinide oxides mainly have a brittle behavior. Therefore, plastic deformation due to dislocation motion requires high energy to form and move. Hence, at low temperature, plasticity occurs at very high stress or operates at very low rates, which are not measurable before the point of catastrophic failure.²⁶⁰ The only measurable plasticity is then because of thermal creep.

Classically, thermal creep rate is modeled in actinide oxides by the sum of two mechanisms if the fission process is not taken into account. The first mechanism is the viscous creep with some grain boundary sliding

occurring at low stresses. The second mechanism is the dislocation-climb process, which operates at stresses greater than a transition stress that is governed by the grain size.^{261,262} Over the past few years, several more or less successful models have been proposed to express these two mechanisms. Recently, Malygin *et al.*²⁶⁴ have proposed a model that seems to best fit the experimental data.^{263–267} This model is described by a sum of two terms, related to the two mechanisms reported above:

$$\frac{d\varepsilon}{dt} = \frac{\alpha\Omega\sigma D_V}{k_B T G^2} + \frac{\beta\sigma^{4.5} D_V}{k_B T \sqrt{bN}\mu^{3.5}} \quad [20]$$

where α and β are constants that depend on the degree of relaxation of the tangential stresses at the boundary of a grain, Ω is the atomic volume, σ is the stress, D_V is the volume diffusion coefficient, k is Boltzmann's constant, T is the absolute temperature, G is the grain size, b is the Burgers vector, N is the density of mobile dislocations, and μ is the shear modulus.

For low stress ($\sigma \leq 30\text{--}40 \text{ MPa}$), the experimental data show that the thermal creep of UO_2 under compression is a linear function of the stress and is inversely proportional to the squared grain size. Malygin *et al.*²⁶⁸ report that at low stress, the creep is controlled by uranium diffusion by a vacancy mechanism. At higher stress ($\sigma > 40 \text{ MPa}$), a power law dependence with an exponent of 4.5 is observed that is controlled by a dislocation climbing process.

To model the dependence of the creep rate for a nonstoichiometric UO_2 , Malygin *et al.*²⁶⁸ developed a point defect model and a relation giving the diffusion coefficient of uranium vacancies as a function of temperature and composition. A final relation is given in Malygin *et al.*²⁶⁸ to calculate the dependence of the creep rate as a function of temperature, stress, density, grain size, and oxygen stoichiometry. The results show that the creep rate increases with the departure from the oxygen stoichiometry (see Figure 35).

The same authors have recently performed the same analysis in Malygin *et al.*²⁶⁹ using the experimental data published in Routbort,^{270–272} Javed,²⁶⁶ Perrin,²⁷³ Caillot²⁷⁴ for mixed uranium–plutonium oxides. As shown in eqn [21], the mixed oxides have the same behavior as UO_2 :

$$\frac{d\varepsilon}{dt} = \frac{A\sigma D_V}{G^2} + B\sigma^{4.5} D_V \quad [21]$$

A and B are coefficients that depend on the oxide density and on the plutonium content.

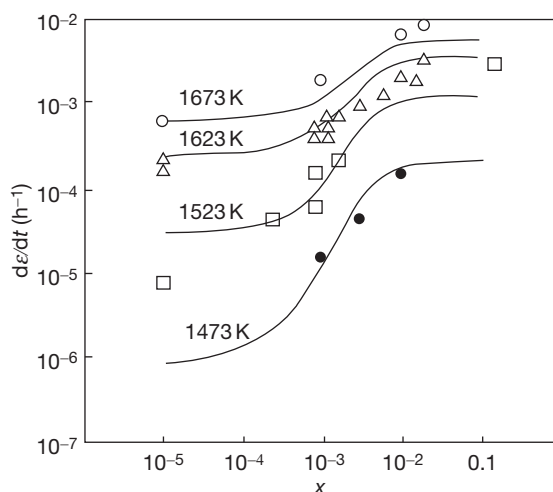


Figure 35 Comparison between the calculated (lines) and experimental data (symbols) on creep rate of uranium dioxide with grain size of 7 μm on departure from stoichiometry with $\sigma = 20\text{ MPa}$ according to Malýgin *et al.*²⁷⁴

2.02.8 Conclusion

The most relevant physicochemical properties of actinide oxides were reviewed. Numerous studies were done in the past on these materials that are crucial for nuclear applications. The current increased interest in oxide fuels for Generation IV systems, and particularly the incentive to partition and transmute the minor actinides, has led to a renewed interest in the studies on the actinide oxides using both theoretical methods such as atomistic simulation and (new) experimental approaches. Our review has shown that in spite of the large amount of information available, basic data are still missing. This is especially true for the minor actinide oxides, for which experiments are more difficult because of their high radioactivity and/or limited availability. But, even for the ‘major actinides’ such as uranium and plutonium, uncertainties remain as, for example, the recent work on the melting point of PuO_2 has shown.

References

1. Haire, R. G.; Eyring, L. In *Handbook on the Physics and Chemistry of Rare Earths*, Vol. 18: *Lanthanides/Actinides: Chemistry*; Gschneidner, K. A., Eyring, L., Choppin, G. R., Lander, G. R., Eds.; Elsevier: Amsterdam, 1994; pp 449–478.

2. Jollet, F.; Petit, T.; Gota, S.; Thromat, N.; Gautier-Soyer, M.; Pasturel, A. *J. Phys. Condens. Matter* **1997**, *9*, 9393–9401.
3. Petit, L.; Svane, A.; Szotek, Z.; Temmerman, W. M.; Stocks, G. M. *Phys. Rev.*; 2010, 81B, 045108–1–12.
4. Petit, L.; Svane, A.; Szotek, Z.; Temmerman, W. M.; Stocks, G. M. *Mater. Sci.* 2009, arXiv:0908.1806v1 (cond-mat.str-el).
5. Andersson, D. A.; Lezama, J.; Uberuaga, B. P.; Deo, C.; Conradson, S. D. *Phys. Rev.* **2009**, *79B*, 024110.
6. Korzhavyi, P. A.; Vitos, L.; Andersson, D. A.; Johansson, B. *Nat. Mater.* **2004**, *3*, 225–228.
7. Larson, D. T.; Haschke, J. M. *Inorg. Chem.* **1981**, *20*(7), 1945–1950.
8. Guéneau, C.; Baichi, M.; Labroche, D.; Chatillon, C.; Sundman, B. *J. Nucl. Mater.* **2002**, *304*, 2–3, 161–175.
9. Baichi, M.; Chatillon, C.; Ducros, G.; Froment, K. *J. Nucl. Mater.* **2006**, *304*, 2–3, 161–175.
10. Labroche, D.; Dugne, O.; Chatillon, C. *J. Nucl. Mater.* **2003**, *312*, 21–49.
11. Manara, D.; Ronchi, C.; Sheindlin, M.; Lewis, M.; Brykin, M. *J. Nucl. Mater.* **2005**, *342*, 1–3, 148–163.
12. Higgs, J. D.; Lewis, B. J.; Thompson, W. T.; He, Z. *J. Nucl. Mater.* **2007**, *366*, 99–128.
13. Anthony, A. M.; Kiyoura, R.; Sata, T. *J. Nucl. Mater.* **1963**, *10*(1), 8.
14. Roberts, L. E. J.; Walter, A. J. *J. Inorg. Nucl. Chem.* **1961**, *22*, 213.
15. Kotlar, A.; Gerdanian, P.; Dode, M. *J. Chim. Phys.* **1968**, *65*, 687.
16. Nakamura, A.; Fujino, T. *J. Nucl. Mater.* **1987**, *149*, 80.
17. Bannister, M. J.; Buykx, W. J. *J. Nucl. Mater.* **1974**, *55*, 345.
18. Saito, Y. *J. Nucl. Mater.* **1974**, *51*, 112.
19. Aronson, S.; Rulli, J. E.; Schaner, B. E. *J. Phys. Chem.* **1961**, *35*(4), 1382.
20. Schaner, B. E. *J. Nucl. Mater.* **1960**, *2*, 110.
21. Ishii, T.; Naito, K.; Oshima, K. *Solid State Commun.* **1970**, *8*, 677.
22. Blackburn, P. E. *J. Phys. Chem.* **1958**, *62*(8), 897.
23. Kovba, L. M. (Presented by Academician V. I. Spitsyn, January 26, 1970) Translated from *Doklady Akademii Nauk SSSR*, **1970**, *194*(1), 98.
24. Van Lierde, W.; Pelsmaekers, J.; Lecocq-Robert, A. *J. Nucl. Mater.* **1970**, *37*, 276.
25. Markin, T. L.; Bones, R. J. Determination of changes in free energy for uranium oxides using a high temperature galvanic cell, part 1, UKAEA, Report AERE-R 4042, 1962.
26. Grønvold, F. *J. Inorg. Nucl. Chem.* **1955**, *1*, 357–370.
27. Kinoshita, H.; Uno, M.; Yamanaka, S. *J. Alloys Comp.* **2003**, *354*, 129–137.
28. Guéneau, C.; Chatillon, C.; Sundman, B. *J. Nucl. Mater.* **2008**, *378*(3), 257–272.
29. Wriedt, H. A. *Bull. Alloy Phase Diagrams* **1990**, *11*(2), 184–202.
30. Martin, A. E.; Mrazek, F. C. *Phase Diagram Studies of Plutonium Compounds*, USAEC, ANL-7575; Argonne National Laboratory Report, 1969.
31. Riley, B. *Sci. Ceram.* **1970**, *5*, 83–109.
32. Kato, M.; Morimoto, K.; Sugata, H.; Konashi, K.; Kashimura, M.; Abe, T. *J. Nucl. Mater.* **2008**, *373*, 237–245.
33. De Bruycker, F.; Boboridis, K.; Manara, D.; Pöml, P.; Rini, M.; Konings, R. J. M. *Materials Today* **2010**, *13*, 52–55.
34. Benz, R. *J. Nucl. Mater.* **1969**, *29*, 43–49.
35. Richter, K.; Sari, C. *J. Nucl. Mater.* **1987**, *148*, 266–271.

36. Konings, R. J. M.; Benes, O.; Manara, D.; Sedmindubsky, D.; Gorokhov, L.; Iorish, V. S. *J. Phys. Chem.* **2011**.
37. Ronchi, C.; Hiernaut, J. P. *J. Alloys Comp.* **1996**, 240, 179.
38. Konings, R. J. M.; Morss, L. R.; Fuger, J. *The Chemistry of the Actinides and Transactinide Elements*; Springer: The Netherlands, **2006**; pp 2113–2224.
39. Kinoshita, H.; Setoyama, D.; Saito, Y.; *et al.* *J. Chem. Thermodyn.* **2003**, 35, 719–731.
40. Thiriet, C.; Konings, R. J. M. *J. Nucl. Mater.* **2003**, 320(3), 292–298.
41. Sari, C.; Zamorani, E. *J. Nucl. Mater.* **1970**, 37, 324–330.
42. Gotcu-Freis, P.; Colle, J.-Y.; Guéneau, C.; Dupin, N.; Sundman, B.; Konings, R. J. M. *J. Nucl. Mater.* **2011**, 414, 408–421.
43. Konings, R. J. M. *J. Nucl. Mater.* **2001**, 298(3), 255–268.
44. Smith, P. K.; Peterson, D. E. *J. Chem. Phys.* **1970**, 52, 4963.
45. Okamoto, H. *J. Phase. Equilibria* **1999**, 20(3), 351.
46. Turcotte, R. P.; Chikalla, T. D.; Haire, R. G.; Fahey, J. A. *J. Inorg. Anal. Chem.* **1980**, 42, 1729–1733.
47. Baybarz, R. D. *J. Inorg. Nucl. Chem.* **1973**, 35, 4149–4158.
48. Lyon, W. L.; Bailey, W. E. *J. Nucl. Mater.* **1967**, 22, 332–339.
49. Aitken, E. A.; Evans, S. K. Technical Report, USAEC GEAP-5672, General Electric, 1968.
50. Kato, M.; Morimoto, K.; Sugata, H.; Konashi, K.; Kashimura, M.; Abe, T. *J. Alloys Comp.* **2008**, 452, 48–53.
51. Adamson, M. G.; Aitken, E. A.; Caputi, R. W. *J. Nucl. Mater.* **1985**, 130, 349–365.
52. Rand, M. H.; Markin, T. L. In *Thermodynamics of Nuclear Materials* 1967, Proceedings of the AIEA Symposium, Vienna, 1967; p 637.
53. Markin, T. L.; Street, R. S. *J. Inorg. Nucl. Chem.* **1967**, 29, 2265–2280.
54. Sari, C.; Benedict, U.; Blank, H. *J. Nucl. Mater.* **1970**, 35, 267–277.
55. Konings, R. J. M.; Wiss, T.; Guéneau, C. In *The Chemistry of the Actinide and Transactinide Elements* 4th ed.; Morss, L. R., Fuger, J., Edelstein, N. M., Eds.; *Nuclear Fuels*; Springer: Netherlands, 2010; Vol. 6, Chapter 34, pp 3665–3812.
56. Kato, M.; Konashi, K. *J. Nucl. Mater.* **2009**, 385, 117–121.
57. Yamanaka, S.; Kinoshita, H.; Kurosaki, K. *J. Nucl. Mater.* **2004**, 326, 185–194.
58. Agarwal, R.; Sen, B. K.; Venugopal, V. *J. Nucl. Mater.* **2009**, 385(1), 112–116.
59. Bakker, K.; Cordfunke, E. H. P.; Konings, R. J. M.; Schram, R. P. C. *J. Nucl. Mater.* **1997**, 250, 1–12.
60. Dash, S.; Parida, S. C.; Singh, Z.; Sen, B. K.; Venugopal, V. *J. Nucl. Mater.* **2009**, 393, 267–281.
61. Freshley, M. D.; Mattys, H. M. *General Electric Report HW-76559*, 1962; p 116.
62. Jankowiak, A.; Maillard, C.; Donnet, L. *J. Nucl. Mater.* **2009**, 393, 87–91.
63. Baybarz, R. D.; Haire, R. G.; Fahey, J. A. *J. Inorg. Nucl. Chem.* **1972**, 34, 557–565.
64. Arima, T.; Yamasaki, S.; Inagaki, Y.; Idemitsu, K. *J. Alloys Comp.* **2005**, 400, 43–50.
65. Uchida, T.; Arima, T.; Idemitsu, K.; Inagaki, Y. *Comput. Mater. Sci.* **2009**, 45, 229–234.
66. Minamoto, S.; Kato, M.; Konashi, K.; Kawazoe, Y. *J. Nucl. Mater.* **2009**, 385, 18–20.
67. Sobolev, V. *J. Nucl. Mater.* **2005**, 344, 198–205.
68. Sobolev, V.; Lemehov, S. *J. Nucl. Mater.* **2006**, 352, 300–308.
69. Sobolev, V. *J. Nucl. Mater.* **2009**, 389, 45–51.
70. Mosley, W. C. *J. Am. Ceram. Soc.* **1971**, 54, 475–479.
71. Yamashita, T.; Nitani, N.; Tsuji, T.; Inagaki, H. *J. Nucl. Mater.* **1997**, 245, 72–78.
72. Stchouzkoy, T.; Pézerat, H.; Bouissières, G.; Muxart, R. *Comptes Rendus Hebdomadaires des Séances de l'Académie des Sciences* **1964**, 259, 3016–3018.
73. Shannon, R. D. *Acta Crystallogr.* **1976**, 32A, 751.
74. Morss, L. R.; Richardson, J. W.; Williams, C. W.; *et al.* *J. Less Common Met.* **1989**, 156, 273–289.
75. Fahey, J. A.; Turcotte, R. P.; Chikalla, T. D. *Inorg. Nucl. Chem. Lett.* **1974**, 80, 459–465.
76. Taylor, D. *Trans. J. Br. Ceram. Soc.* **1984**, 83, 32–37.
77. Fink, J. K. *J. Nucl. Mater.* **2000**, 279, 1–18.
78. Yang, J. H.; Kang, K. W.; Song, K. W.; Lee, C. B. *Nucl. Tech.* **2004**, 147, 113–119.
79. Tsuji, T.; Iwashita, M.; Yamashita, T.; Ohuchi, K. *J. Alloy Comp.* **1998**, 271–273, 391–394.
80. Terentyev, D. *Comput. Mater. Sci.* **2007**, 40, 319–326.
81. Arima, T.; Yamasaki, S.; Inagaki, Y.; Idemitsu, K. *J. Alloys Comp.* **2006**, 415, 43–50.
82. Kurosaki, K.; Adachi, J.; Katayama, M.; *et al.* *J. Nucl. Sci. Tech.* **2006**, 43, 1224–1227.
83. Yamashita, T.; Nitani, N.; Tsuji, T.; Kato, T. *J. Nucl. Mater.* **1997**, 247, 90–93.
84. Carbajo, J. J.; Yoder, G. L.; Popov, S. G.; Ivanov, V. K. *J. Nucl. Mater.* **2001**, 299, 181–198.
85. Anthonysamy, S.; Panneerselvam, G.; Bera, S.; Narasimham, S. V.; Vasudeva Rao, P. R. *J. Nucl. Mater.* **2000**, 281, 15–21.
86. Javed, N. A. *J. Nucl. Mater.* **1972**, 43, 219–224.
87. Watanabe, T.; Srivilliputhur, S. G.; Schelling, P. K.; Tulenko, J. S.; Sinnott, S. B.; Phillpot, S. *J. Am. Ceram. Soc.* **2009**, 92, 850–856.
88. Yamasaki, S.; Arima, T.; Idemitsu, K.; Inagaki, Y. *Int. J. Therm.* **2007**, 28, 661–673.
89. Schmitz, F.; Dean, G.; Halachmy, M. *J. Nucl. Mater.* **1971**, 40, 325.
90. Miwa, S.; Osaka, M.; Yoshimochi, H.; *et al.* *J. Alloys Comp.* **2007**, 444–445, 610–613.
91. Zachariasen, W. H. *Acta Crystallogr.* **1949**, 2, 388–390.
92. Wulff, M.; Lander, G. H. *J. Chem. Phys.* **1988**, 89, 3295–3299.
93. Chikalla, T. D.; McNeilly, C. E.; Skavdahl, R. E. *J. Nucl. Mater.* **1964**, 12, 131–141.
94. Chikalla, T. D.; Eyring, L. *J. Inorg. Nucl. Chem.* **1968**, 30, 133–145.
95. Noé, M.; Fuger, J.; Duyckaerts, G. *Inorg. Nucl. Chem. Lett.* **1970**, 6, 111–119.
96. Nave, S. E.; Haire, R. G.; Huray, P. G. *Phys. Rev. B* **1983**, 28(5), 2317–2327.
97. Mosley, W. C. *J. Inorg. Nucl. Chem.* **1972**, 34, 539–555.
98. Baybarz, R. D. *J. Inorg. Nucl. Chem.* **1968**, 30, 1769–1773.
99. Haire, R. G.; Baybarz, R. D. *J. Inorg. Nucl. Chem.* **1973**, 35, 489–496.
100. Willis, B. T. M. *Nature* **1963**, 197, 755–756.
101. Willis, B. T. M. *Proc. Br. Ceram. Soc.* **1974**, 1, 9.
102. Willis, B. T. M. *Acta Crystallogr.* **1978**, A34, 38.
103. Bevan, D. J. M.; Grey, I. E.; Willis, B. T. M. *J. Solid State Chem.* **1986**, 61, 1.
104. Cooper, R. I.; Willis, B. T. M. *Acta Crystallogr.* **2004**, A60, 322–325.
105. Inaba, H.; Shimizu, H.; Keiji, N. *J. Nucl. Mater.* **1977**, 64, 66–70.
106. Vanlierde, W.; Pelsmaekers, J.; Lecocq-Robert, A. *J. Nucl. Mater.* **1970**, 37, 276–285.
107. Masaki, N. *J. Appl. Crystallogr.* **1974**, 7, 247–250.

108. Westrum, E. F.; Gronvold, F. *J. Phys. Chem. Solids* **1962**, 23, 39.
109. Hoekstra, H. R.; Siegel, S.; Gallagher, F. X. *J. Inorg. Nucl. Chem.* **1970**, 32, 3237.
110. Ball, R. G. J.; Dickens, P. G. *J. Mater. Chem.* **1991**, 1, 105–112.
111. Loopstra, B. O. *Acta Crystallogr.* **1970**, 26B, 656–657.
112. Greaves, C.; Fender, B. E. F. *Acta Crystallogr.* **1972**, 28B, 3609–3614.
113. Debets, P. C. *Acta Crystallogr.* **1966**, 21A, 589–593.
114. Loopstra, B. O.; Taylor, J. C.; Waugh, A. B. *J. Solid State Chem.* **1977**, 20, 9–19.
115. Weller, M. T.; Dickens, P. G.; Penny, D. J. *Int. J. Inorg. Organometal. Chem.* **1988**, 7(3), 243–244.
116. Kovba, L. M.; Vidavskii, L. M.; Labut, E. L. *Zhur Struct. Khim* **1963**, 4, 627.
117. Siegel, S.; Hoekstra, H.; Sherry, E. *Acta Crystallogr.* **1966**, 20A, 292–295.
118. Forbes, T. Z.; Burns, P. C.; Skanthakumar, S.; Soderholm, L. *J. Am. Chem. Soc.* **2007**, 129, 2760–2761.
119. Boivineau, J. C. *J. Nucl. Mater.* **1976**, 60, 31.
120. Sari, C.; Benedict, U.; Blank, H. *Thermodynamics of Nuclear Materials*, 1967; IAEA: Vienna, 1968; pp 587–611.
121. Cox, J. D.; Wagman, D. D.; Medvedev, V. A. *CODATA Key Values for Thermodynamics*; Hemisphere: New York, 1989.
122. Guillaumont, R.; Fanghanel, T.; Neck, V.; et al. *Update on the Chemical Thermodynamics of Uranium, Neptunium, Plutonium, Americium and Technetium*; OECD, NEA, Databank: France, 2003; Vol. 5.
123. Konings, R. J. M. *J. Chem. Thermodyn.* **2004**, 36, 121–126.
124. Krupa, J. C.; Gajek, Z. *Eur. J. Solid State Chem.* **1991**, 28, 143–146.
125. Krupa, J. C. Personal Communication, 2001.
126. Ruello, P.; Desgranges, L.; Baldinozzi, G.; et al. *J. Phys. Chem. Solids* **2005**, 66, 823–831.
127. Yakub, E.; Ronchi, C.; Iosilevski, I. *J. Phys. Condens. Matter* **2006**, 18, 1227–1248.
128. Yakub, E.; Ronchi, C.; Staicu, D. *J. Chem. Phys.* **2007**, 127, 094508.
129. Southard, J. C. *J. Am. Chem. Soc.* **1941**, 63, 3142.
130. Hoch, M.; Johnson, H. *J. Phys. Chem.* **1961**, 65, 1184.
131. Fischer, D. F.; Fink, J. K.; Leibowitz, L. *J. Nucl. Mater.* **1981**, 102, 220–222.
132. Ronchi, C.; Hyland, H. *J. Alloys Comp.* **1994**, 213(214), 159–168.
133. Hiernaut, J. P.; Hyland, G. J.; Ronchi, C. *Int. J. Thermophys.* **1993**, 14, 259–283.
134. Ogard, A. E. In *Plutonium 1970 and Other Actinides*; Miner, W. N., Ed.; Nuclear Metallurgy Series; Metall. Soc. AIME: Warrendale, PA, 1970; Vol. 17, pp 78–83.
135. Fink, J. K. *Int. J. Thermophys.* **1982**, 3, 165–200.
136. Oetting, F. L.; Bixby, G. E. *J. Nucl. Mater.* **1982**, 105, 257–261.
137. Nishi, T.; Itoh, A.; Takano, M.; et al. *J. Nucl. Mater.* **2008**, 376, 78–82.
138. Serizawa, H.; Arai, Y.; Nakajima, K. *J. Chem. Thermodyn.* **2001**, 33, 615–628.
139. Benes, O.; Gotcu-Freis, O.; Schwörer, F.; Konings, R. J. M.; Fanghanel, Th. *J. Chem. Thermodyn.* 2010.
140. Popov, M. M.; Galchenko, G. L.; Senin, M. D. *Zh. Neorg. Khim.* **1958**, 3, 1734–1737.
141. Moore, G. E.; Kelley, K. K. *J. Am. Chem. Soc.* **1947**, 69, 2105–2107.
142. Cordfunke, E. H. P.; Konings, R. J. M. *Thermochemical Data for Reactor Materials and Fission Products*; North-Holland: Amsterdam, 1990.
143. Duriez, C.; Alessandri, J. P.; Gervais, T.; Philipponneau, Y. *J. Nucl. Mater.* **2000**, 277, 143–158.
144. Kandan, R.; Babu, R.; Nagarajan, K.; Vasudeva Rao, P. R. *J. Nucl. Mater.* **2004**, 324, 215–219.
145. SeeBauer, E. G.; Kratzer, M. *Mater. Sci. Eng. R Rep.* **2006**, 55, 57–149.
146. Ling, S. *Phys. Rev.* **1994**, 49B, 864–880.
147. Matzke, H. *J. Chem. Soc. Faraday Trans.* **1987**, 2(83), 1121–1142.
148. Ruello, P.; Petit-Ervas, G.; Petot, C.; Desgranges, L. *J. Am. Ceram. Soc.* **2005**, 88, 604–611.
149. Park, K.; Olander, D. R. *High Temp. Sci.* **1990**, 29, 203–222.
150. Stan, M.; Cristea, P. *J. Nucl. Mater.* **2005**, 344, 213–218.
151. Ramirez, J. C.; Stan, M.; Cristea, P. *J. Nucl. Mater.* **2006**, 359, 174–184.
152. Cristea, P.; Stan, M.; Ramirez, J. C. *J. Opt. Adv. Mater.* **2007**, 9, 1750–1756.
153. Stan, M.; Ramirez, J. C.; Cristea, P.; et al. *J. Alloys Comp.* **2007**, 444–445, 415–423.
154. Stan, M. *Nucl. Eng. Tech.* **2009**, 41, 39–52.
155. Kato, M.; Konashi, K.; Nakae, N. *J. Nucl. Mater.* **2009**, 389, 164–169.
156. Catlow, C. R.; Tasker, P. W. *Phil. Mag.* **1984**, 48, 649–659.
157. Jackson, R. A.; Catlow, C. R.; Murray, A. D. *J. Chem. Soc. Faraday Trans.* **1987**, 2(83), 1171–1176.
158. Yakub, E.; Ronchi, C.; Staicu, D. *J. Nucl. Mater.* **2009**, 389, 119–126.
159. Petit, T.; Lemaignan, C.; Jollet, F.; Bigot, B.; Pasturel, A. *Phil. Mag.* **1998**, 77B, 779–786.
160. Crocombette, J. P.; Jollet, F.; Nga, L. T.; Petit, T. *Phys. Rev.* **2001**, 64B, 104107.
161. Freyss, M.; Petit, T.; Crocombette, J. P. *J. Nucl. Mater.* **2005**, 347, 44–51.
162. Gupta, F.; Brillant, G.; Pasturel, A. *Phil. Mag.* **2007**, 87, 2561–2569.
163. Nerikar, P.; Watanabe, T.; Tulenko, J. S.; Phillpot; Sinnott, S. B. *J. Nucl. Mater.* **2009**, 384, 61–69.
164. Yu, J.; Devanathan, R.; Weber, W. J.; Phys, J. *Cond. Matt.* **2009**, 21, 435401.
165. Geng, H. Y.; Chen, T.; Kaneta, Y.; Iwasawa, M.; Ohnuma, T.; Kinoshita, M. *Phys. Rev.* **2008**, 77B, 104120.
166. Geng, H. Y.; Chen, Y.; Kaneta, Y.; Kinoshita, M. *Phys. Rev.* **2008**, 77B, 180101.
167. Geng, H. Y.; Chen, Y.; Kaneta, Y.; Kinoshita, M. *Appl. Phys. Lett.* **2009**, 93, 201903.
168. Andersson, D. A.; Watanabe, T.; Deo, C.; Ueberuaga, B. P. *Phys. Rev.* **2009**, 80B, 060101.
169. Crocombette, J.-P.; Torumba, D.; Chartier, A. *Phys. Rev. B* **2011**, 83, 184107.
170. Konashi, K.; Matsui, H.; Kawazoe, Y.; Kato, M.; Minamoto, S. *Phys. J. Soc. Jpn.* **2006**, 75, 143–145.
171. Martin, P.; Grandjean, S.; Valot, C.; et al. *J. Alloys Comp.* **2007**, 444–445, 410–414.
172. Blackburn, P. E. *J. Nucl. Mater.* **1973**, 46, 244–252.
173. Besmann, T. M.; Lindemer, T. B. *J. Nucl. Mater.* **1985**, 130, 489–504.
174. Lindemer, T. B.; Besmann, T. M. *J. Nucl. Mater.* **1985**, 130, 473–488.
175. Besmann, T. M.; Lindemer, T. B. *J. Nucl. Mater.* **1986**, 137, 292–293.
176. Chevalier, P. Y.; Fischer, E. *J. Nucl. Mater.* **1998**, 257, 213–255.
177. Chevalier, P. Y.; Fischer, E.; Cheynet, B. *J. Nucl. Mater.* **2002**, 303, 1–28.
178. Ackermann, R. J.; Tetenbaum, M. *High Temp. Sci.* **1980**, 13, 91–105.

179. Bartscher, W.; Sari, C. *J. Nucl. Mater.* **1986**, *140*, 473–488.
180. Chikalla, T. D.; Eyring, L. *J. Inorg. Nucl. Chem.* **1967**, *2281*, 29.
181. Casalta, S. Ph.D. thesis, University Aix-Marseille I, 1996.
182. Otobe, H.; Akabori, M.; Minato, K. *J. Am. Ceram. Soc.* **2008**, *91*(6), 1981–1985.
183. Besmann, T. *J. Nucl. Mater.* **2010**, *402*, 25–29.
184. Chikalla, T. D.; Eyring, L. *J. Inorg. Nucl. Chem.* **1969**, *31*, 85.
185. Turcotte, R. P.; Chikalla, T. D. *J. Inorg. Nucl. Chem.* **1973**, *35*, 809–816.
186. Turcotte, R. P.; Chikalla, T. D. *J. Inorg. Nucl. Chem.* **1971**, *33*, 3749–3763.
187. Turcotte, R. P.; Haire, R. G. In *Transplutonium 1975*; Muller, W., Lindner, R., Eds.; North-Holland: Amsterdam, 1976; p 267.
188. Kato, M.; Tamura, T.; Konashi, K.; Aono, S. *J. Nucl. Mater.* **2005**, *344*, 235–239.
189. Kato, M.; Tamura, T.; Konashi, K. *J. Nucl. Mater.* **2009**, *385*, 419–423.
190. Vasudeva Rao, P. R.; Anthonysamy, S.; Krishnaiah, M. V.; Chandramouli, V. *J. Nucl. Mater.* **2006**, *348*, 329–334.
191. Vana Varamban, S.; Ganesan, V.; Vasudeva Rao, P. R. *J. Nucl. Mater.* **2009**, *389*, 72–77.
192. Woodley, R. E. *J. Nucl. Mater.* **1981**, *96*, 5–14.
193. Markin, T. L.; McIver, E. J. Thermodynamics and Phase studies for Plutonium and Uranium-Plutonium oxides with Application to Compatibility calculations, in “Plutonium 1965”, (Chapman and Hall, London) p. 845.
194. Chilton, G. R.; Edwards, J. United Kingdom Atomic Energy Authority Northern Division Report, ND-R-276(W), March 1980.
195. Bartscher, W.; Sari, C. *J. Nucl. Mater.* **1983**, *118*, 220–223.
196. Osaka, M.; Kurosaki, K.; Yamanaka, S. *J. Nucl. Mater.* **2006**, *357*, 69–76.
197. Otobe, H.; Akabori, M.; Arai, Y. *J. Nucl. Mater.* **2009**, *389*, 68–71.
198. Otobe, H.; Akabori, M.; Arai, Y.; Minato, K. *J. Am. Ceram. Soc.*, **2009**, *92*, 174–178.
199. Morimoto, K.; Nishiyama, M.; Kato, M.; Endo, H.; Kono, S. *Proceedings of the Global 2001 Conference*, Paris, 2001; Vol. 1(38), p 1.
200. Osaka, M.; Sato, I.; Namekawa, T.; Kurosaki, K.; Yamanaka, S. *J. Alloys Comp.* **2005**, *397*, 110–114.
201. Hirota, M.; Kurosaki, K.; Setoyama, D.; et al. *J. Nucl. Mater.* **2005**, *344*, 84–88.
202. Anderson, J. S.; Edgington, D. N.; Roberts, L. E. J.; Wait, E. *J. Chem. Soc.* **1954**, 3324–3331.
203. Roberts, L. E. J.; Russel, L. E.; Adwick, A. G.; Walter, A. J.; Rand, M. H. *P/26 UK Geneva Conference of Peaceful Uses of Atomic Energy 1958*; Vol. 28, p 215.
204. Aronson, S.; Clayton, J. C. *J. Chem. Phys.* **1960**, *32*, 749–754.
205. Tanaka, S.; Kimura, E.; Yamaguchi, A.; Moriyama, J. *J. Jpn. Inst. Met.* **1972**, *36*, 633.
206. Ugajin, M. *J. Nucl. Mater.* **1982**, *110*, 140–146.
207. Matsui, T.; Naito, K. *J. Nucl. Mater.* **1985**, *132*, 212–221.
208. Anthonysamy, S.; Nagarajan, K.; Vasudeva Rao, P. R. *J. Nucl. Mater.* **1997**, *247*, 273–276.
209. Schram, R. P. C. *J. Nucl. Mater.* **2005**, *344*, 223–229.
210. Kandam, R.; Babu, B.; Manikandan, P.; Venkata Krishnan, R.; Nagajaran, K. *J. Nucl. Mater.* **2009**, *384*, 231–235.
211. Ronchi, C.; Iosilevski, I. L.; Yakub, E. *Equation of State of Uranium Dioxide, Data Collection*; Springer: Berlin, 2004.
212. Thermophysical Properties Database of Materials for Light Water Reactors and Heavy Water Reactors, IAEA-TECDOC-1496, IAEA, June 2006.
213. Pattoret, A. Ph.D. thesis, Université Libre de Bruxelles, May 1969.
214. Viswanathan, R.; Krishnaiah, M. V. *J. Nucl. Mater.* **2001**, *294*, 69–76.
215. Maeda, K.; Sasaki, S.; Kato, M.; Kihara, Y. *J. Nucl. Mater.* **2009**, *389*, 78–84.
216. Gotcu-Freis, P.; Colle, J.-Y.; Hiernaut, J.-P.; Konings, R. J. M. *J. Nucl. Mater.* **2011**, *409*, 194–198.
217. Ando, K.; Oishi, Y. *J. Nucl. Sci. Tech.* **1983**, *20*, 973–982.
218. Howard, R. E.; Lidiard, A. B. *Rep. Prog. Phys.* **1964**, *27*, 161–240.
219. Vincent-Aublant, E.; Delaye, J. M.; Van Brutzel, L. *J. Nucl. Mater.* **2009**, *392*, 114–120.
220. Sabioni, A. C. S.; Ferraz, W. B.; Millot, F. *J. Nucl. Mater.* **2000**, *278*, 364–369.
221. Belle, J.; Berman, R. M. Thorium Dioxide: Properties and Nuclear Applications, Report DOE/NE-0060, 1984.
222. Sabioni, A. C. S.; Ferraz, W. B.; Millot, F. *J. Nucl. Mater.* **1998**, *257*, 180–184.
223. Kupryazhkin, A. Ya.; Zhiganov, A. N.; Risovany, D. V.; Nekrassov, K. A.; Risovany, V. D.; Golosanov, V. N. *J. Nucl. Mater.* **2008**, *372*, 233–238.
224. Siethoff, H. *Basic Solid State Phys.* **2007**, *244B*, 1296–1303.
225. Mendez, S.; Pillon, S.; Warin, D.; Lorenzelli, R. *J. Phys. IV* **1995**, *5*(C3), 297–303.
226. Korte, C.; Janek, J.; Timm, H. *Solid State Ionics* **1997**, *101–103*, 465–470.
227. Sali, S. K.; Sampath, S.; Venugopal, V. *J. Nucl. Mater.* **1998**, *252*, 131–134.
228. Arima, T.; Kitano, K.; Takamura, K.; Funuya, H. *Thermochem. Acta* **2000**, *344*, 37–45.
229. Ruella, P.; Chirlesan, G.; Petot-Ervas, G.; Petot, C.; Desgranges, L. *J. Nucl. Mater.* **2004**, *325*, 202–209.
230. Kato, M.; Morimoto, K.; Tamura, T.; et al. *J. Nucl. Mater.* **2009**, *389*, 416–419.
231. Garcia, P.; Fracziewicz, M.; Davoisne, C.; et al. *J. Nucl. Mater.* **2010**, *400*(2), 112–118.
232. Dorado, B.; Garcia, P.; Carlot, G.; et al. *Phys. Rev. B* **2011**, *83*, 035126.
233. Tahir-Kheli, R. A. *Phys. Rev.* **1987**, *35B*, 5503–5508.
234. Jackson, R. A.; Murray, A. D.; Harding, J. H.; Catlow, C. R. A. *Phil. Mag.* **1986**, *53A*, 27–50.
235. Gao, J.; Yang, X.; Li, R.; Wang, Y.; Zhong, F. *J. Mater. Sci.* **2007**, *42*, 5936–5940.
236. Knorr, D. B.; Cannon, R. M.; Coble, R. L. *Acta Metall.* **1989**, *37*, 210.
237. Yin, Q.; Savrasov, S. *Phys. Rev. Lett.* **2008**, *100*, 225504–225508.
238. Inoue, M. *J. Nucl. Mater.* **2000**, *282*, 186–195.
239. Buyx, W. J.; Amer, J. *Ceram. Soc.* **1979**, *62*, 326–332.
240. Millet, P. C.; Wolf, D.; Desai, T.; Rokkam, S.; El-Azab, A. *J. Appl. Phys.* **2008**, *104*, 033512–033518.
241. Srirama Murti, P.; Mathews, C. K. *J. Phys. D Appl. Phys.* **1991**, *24*, 2202.
242. Morimoto, K.; Kato, M.; Ogasawara, M.; Kashimura, M. *J. Nucl. Mater.* **2009**, *389*, 179–185.
243. Ronchi, C.; Ottaviani, J. P.; Degueldre, C.; Calabresse, R. *J. Nucl. Mater.* **2003**, *320*, 54–65.
244. Schulz, B. *High Temp. High Pressure* **1981**, *13*, 649.
245. Bakker, K.; Kwast, H.; Cordfunke, E. H. P. *J. Nucl. Mater.* **1995**, *226*, 128–143.
246. Schelling, P. K.; Phillpot, S. R.; Keblinski, P. *Phys. Rev.* **2002**, *65B*, 144306–144318.

247. Kurosaki, K.; Imamura, M.; Sato, I.; Namekawa, T.; Uno, M.; Yamanaka, S. *J. Nucl. Sci. Tech.* **2004**, *41*, 827–831.
248. Lemehov, S. E.; Sobolev, V.; Van Uffelen, P. *J. Nucl. Mater.* **2003**, *320*, 66–76.
249. Kutty, T. R. G.; Kulkarni, R. V.; Sengupta, P.; *et al.* *J. Nucl. Mater.* **2008**, *373*, 309–318.
250. Bielenberg, P. A.; Prenger, F. C.; Veirs, D. K.; Jones, G. F. *Int. J. Heat Mass Transf.* **2006**, *49*, 3229–3239.
251. Gibby, R. L. *J. Nucl. Mater.* **1971**, *38*, 163–177.
252. Pillai, C. G. S.; Raj, P. *J. Nucl. Mater.* **2000**, *277*, 116–119.
253. Morimoto, K.; Kato, M.; Ogasawara, M.; Kashimura, M.; Abe, T. *J. Alloys Comp.* **2008**, *452*, 54–60.
254. Nishi, T.; Takano, M.; Itoh, A.; *et al.* *J. Nucl. Mater.* **2008**, *373*, 295–298.
255. Lucuta, P. G.; Matzke, H. j.; Hastings, I. J. *J. Nucl. Mater.* **1996**, *232*, 166–180.
256. Amaya, M.; Kubo, T.; Korei, Y. *J. Nucl. Sci. Tech.* **1996**, *33*, 636–640.
257. Pillai, C. G. S.; Dua, A. K.; Raj, P. *J. Nucl. Mater.* **2001**, *288*, 87–91.
258. Morimoto, K.; Kato, M.; Ogasawara, M.; Kashimura, M. *J. Nucl. Mater.* **2008**, *374*, 378–385.
259. Sengupta, A. K.; Khan, K. B.; Panakkal, J.; Kamath, H. S.; Banerjee, S. *J. Nucl. Mater.* **2009**, *385*, 173–177.
260. Poteat, L. E.; Yust, C. S. *J. Am. Ceram. Soc.* **1966**, *49*, 410.
261. Wolfe, R. A.; Kaufmann, S. F. WAPD-TM-587, Bettis Atomic Power Laboratory, 1967.
262. Seltzer, M. S.; Clauer, A. H.; Wilcox, B. A. *J. Nucl. Mater.* **1970**, *34*, 351–353.
263. Bozhko, Yu. V.; Malygin, V. B.; Miloserdin, Yu. V.; Naboichenko, K. V. *Energet. Tekhnol.* **1982**, *1*(11), 75–78.
264. Barton, B.; Reynolds, G. *Acta Met.* **1973**, *23*, 1641–1647.
265. Seltzer, M.; Perrin, J.; Clauer, A.; Wilcox, B. USAEC Report BMI-1906, July 1971.
266. Javed, N. *Proceedings of International Conference on IAEA Thermodynamics of Nuclear Materials* 1974; Vol. 1, pp 435–446.
267. Perrin, J. *J. Nucl. Mater.* **1971**, *39*, 175–179.
268. Malygin, V. B.; Naboichenko, K. V.; Shapovalov, A. S.; Bibilashvili, Yu. K. *Atomic Energy* **2009**, *107*(6), 381–386.
269. Malygin, V. B.; Naboichenko, K. V.; Shapovalov, A. S.; Bibilashvili, Yu. K. *Atomic Energy* **2010**, *108*(6), 15–20.
270. Routbort, J. *J. Am. Ceram. Soc.* **1973**, *56*(6), 330–338.
271. Routbort, J. *J. Nucl. Mater.* **1972**, *44*, 247–253.
272. Bohaboy, P.; Evans, S. *Proceedings of 4th International Conference on Plutonium 1970 and Other Actinides*, 1970; Vol. 17, pp 478–487.
273. Perrin, J. *J. Nucl. Mater.* **1972**, *42*, 101–104.
274. Caillot, L.; Ninon, C.; Basini, V. *Proceedings of International Seminar on Pellet–Clad Interaction in Water Reactor Fuels*, Cadarache, France, Mar 9–11, 2004; pp 205–212.

2.03 Thermodynamic and Thermophysical Properties of the Actinide Nitrides

M. Uno

University of Fukui, Fukui, Japan

T. Nishi and M. Takano

Japan Atomic Energy Agency, Tokai-mura, Ibaraki, Japan

© 2012 Elsevier Ltd. All rights reserved.

2.03.1	Introduction	61
2.03.2	Phase Diagrams and Crystal Structure	62
2.03.2.1	Uranium Nitrides	62
2.03.2.2	Plutonium Nitride	63
2.03.2.3	Thorium Nitride	63
2.03.2.4	Neptunium, Americium, and Curium Nitrides	64
2.03.2.5	Nitride Solid Solutions and Mixtures	65
2.03.3	Thermal Properties	67
2.03.3.1	Melting or Decomposition	67
2.03.3.2	Vaporization Behavior	68
2.03.3.3	Heat Capacity	71
2.03.3.4	Gibbs Free Energy of Formation	72
2.03.3.4.1	Uranium mononitride	73
2.03.3.4.2	Plutonium mononitride	74
2.03.3.4.3	Uranium and plutonium mononitride	75
2.03.3.4.4	Neptunium mononitride and americium mononitride	75
2.03.3.5	Thermal Conductivity	76
2.03.4	Mechanical Properties	79
2.03.4.1	Mechanical Properties of UN	79
2.03.4.2	Thermal Expansion of UN	81
2.03.4.3	Mechanical Properties of PuN	81
2.03.4.4	Mechanical Properties of Other MA or MA-Containing Fuels	82
2.03.5	Summary	83
References		83

Abbreviations

ADS	Accelerator-driven system
An	Actinide
CTE	Coefficients of linear thermal expansion
fcc	Face-centered cubic
HD	(diamond point) Hardness
LTE	Linear thermal expansion
TD	Theoretical density
MA	Minor actinide
MD	Molecular dynamics
XRD	X-ray diffraction

2.03.1 Introduction

Uranium nitride UN not only has the same isotropic crystal structure as uranium dioxide UO_2 but also has a higher melting point, higher metal atom density, and higher thermal conductivity, compared to UO_2 . UN thus has advantages as a nuclear fuel compared to UO_2 , is well studied, and many of its material properties have been known for a long time. However, UN has some disadvantages as a nuclear fuel because of its low chemical stability and the problem of ^{14}C .

Plutonium nitride and thorium nitride have been also well studied, mainly with regard to their suitability as nuclear fuels. Other actinide nitrides with higher atomic number are also important as potential nuclear fuels but the data on these fuels are insufficient because they are difficult to obtain and handle.

In this section, the physicochemical properties of the actinide nitrides, mainly uranium nitrides and plutonium nitride, are discussed. First of all, phase stability and crystal structures of the nitrides are described. Then, their thermal, thermodynamic, and mechanical properties which are relevant to their suitability as nuclear fuels, are discussed. Characteristics of their preparation and irradiation as nuclear fuels are described in Chapter 3.02, **Nitride Fuel**.

2.03.2 Phase Diagrams and Crystal Structure

2.03.2.1 Uranium Nitrides

References for specific data are given separately for each section below, but readers are also referred to a classic, outstanding book¹ which summarizes, from the viewpoint of suitability as nuclear fuels, the various properties of not only the nitrides but also the other compounds. The binary phase diagram shown in Figure 1² is taken from data published in 1960,³⁻⁷ and is still valid. The phase stability of U–N systems

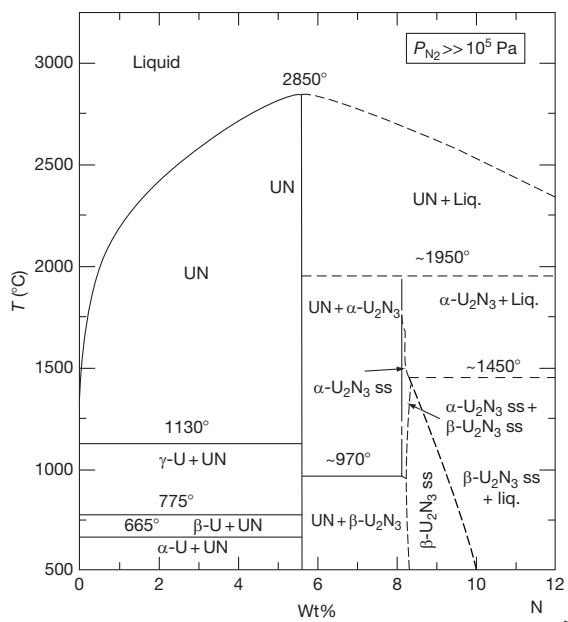


Figure 1 U–N phase diagram at nitrogen pressure larger than 105 Pa. Data from Levinskii, Yu. V. *Atom. Energ.* **1974**, 37(1), 216–219; *Sov. Atom. Energ. (Engl. Transl.)* **1974**, 37(1), 929–932.

has been summarized by Chevalier *et al.*⁸ There are two uranium nitrides, UN and U₂N₃; the former has an NaCl-type cubic structure, and the latter has an M₂O₃-type cubic structure at low temperature (α-U₂N₃) and hexagonal structure at higher temperature (β-U₂N₃), as shown in Figure 2. The lattice parameter of UN is reported to be about 4.890 Å at room temperature⁹⁻¹¹; this, however, can vary, depending on the presence of carbon impurities.¹⁰ The lattice parameter of α-U₂N₃ is 10.688–10.70 Å,^{9,11} but U₂N₃ becomes a solid solution, with N₂, at a higher nitrogen pressure (126 atm); and its lattice parameter decreases with an increase in nitrogen content. The lattice parameters of β-U₂N₃ are reported to be $a = 3.69$ and $c = 5.83$ Å⁹ or $a = 3.70$ and $c = 5.80$ Å.¹⁰

Although the phase diagram, where nitrogen pressure is greater than 10⁵ Pa (Figure 1), shows that UN melts at 3123 K and that UN and U₂N₃ have a wide range of nonstoichiometry, at lower nitrogen pressure; UN decomposes such that UN and U₂N₃ have little nonstoichiometry, as shown in Figure 3^{12,13}; here the β-U₂N₃ in the previous graph is denoted as UN₂. The N/U ratio of UN below a nitrogen pressure of 2 atm is reported to be nearly 1.00 at temperatures between 1773 and 2373 K.¹⁴

U₂N₃ actually decomposes to UN and UN decomposes to U and nitrogen at nitrogen pressure below 2.5 atm. As the decomposition of UN must influence the properties of the fuel pellets, and the decomposition of U₂N₃ is the last stage in the formation of UN through carbothermic reduction, the equilibrium nitrogen pressure of UN and U₂N₃ is very important from the viewpoint of their use as nuclear

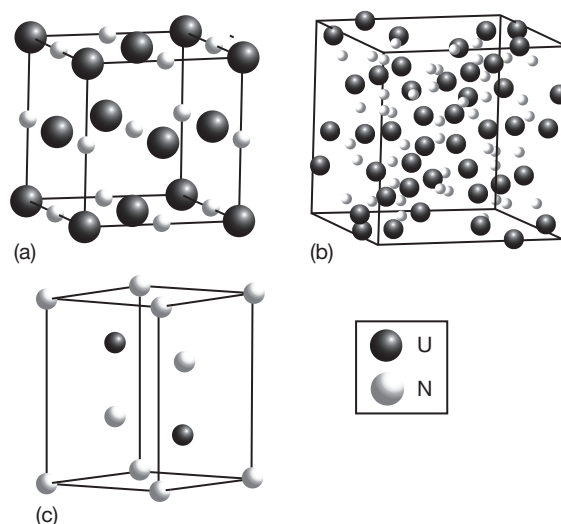


Figure 2 Crystal structures of (a) UN, (b) α-U₂N₃, and (c) β-U₂N₃.

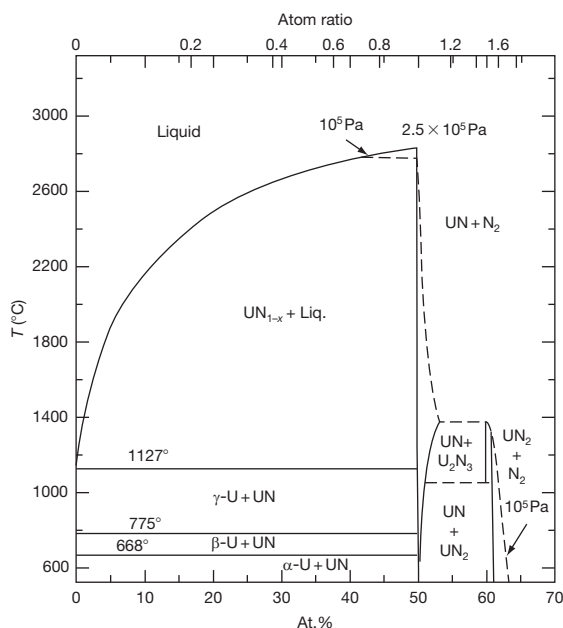


Figure 3 U–N phase diagram at nitrogen pressure smaller than 2 atm. Data from Storms, E. K. *Special Report to the Phase Equilibria Program*; American Ceramic Society: Westerville, OH, 1989; Muromura, T.; Tagawa, H. J. *Nucl. Mater.* **1979**, 79, 264.

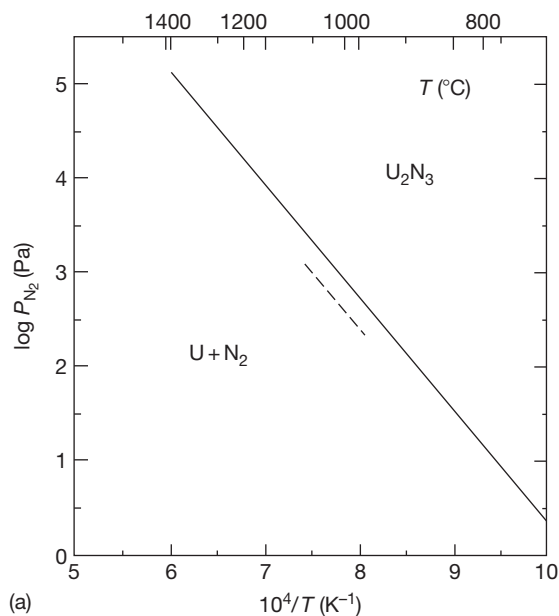
fuel. The reported decomposition curves are shown in [Figure 4](#).³ It is seen from these graphs, for example, that UN decomposes at 3073 K and U_2N_3 decomposes 1620 K at nitrogen pressure of 1 atm. More detailed decomposition behavior of UN as well as other actinide nitrides will be discussed in [Section 2.03.3.1](#).

2.03.2.2 Plutonium Nitride

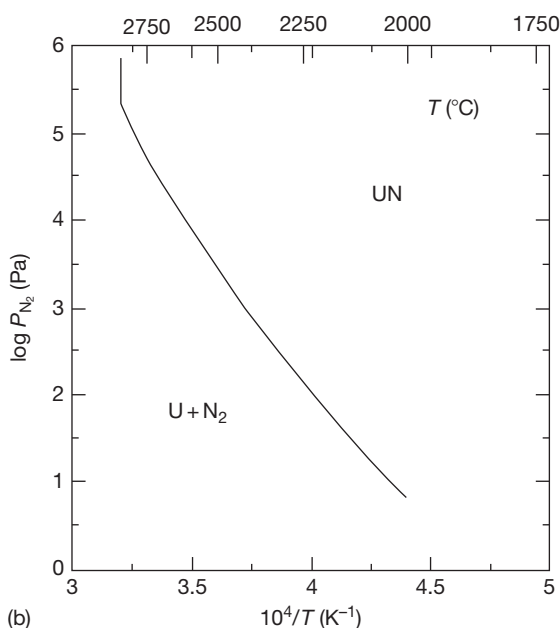
In the Pu–N system, as shown in [Figure 5](#),¹⁵ there is only one structure for the mononitride, PuN: an NaCl-type face-centered cubic (fcc) structure with $a = 4.904 \text{ \AA}$. PuN is a line compound with little non-stoichiometry, and is reported not to congruently melt up to 25 bar nitrogen pressure.¹⁶ However, there is a study on the safety assessment of fuels on the basis of vaporization behavior in which the melting temperature of Pu–N is given as 2993 K under a nitrogen pressure of $1.7 \times 10^4 \text{ Pa}$.¹⁷

2.03.2.3 Thorium Nitride

Though thorium is a fertile material, recent research on thorium and its compounds as nuclear fuel is scanty. The Th– Th_3N_4 phase diagram, reported in 1966¹⁸, is shown in [Figure 6](#). There are two solid compounds in this system, ThN and Th_3N_4 ; the former is an NaCl-type cubic structure with



(a)



(b)

Figure 4 (a) Decomposition curve of U_2N_3 . (b) Decomposition curve of UN. Reproduced from Bugli, J.; Bauer, A. A. J. *Am. Ceram. Soc.* **1964**, 47(9), 425–429, with permission from Springer. The dotted line is referred from P. Gross, C. Hayman and H. Clayton, “Heats of Formation of Uranium Silicides and Nitrides”; In *Thermodynamics of Nuclear Materials- Proceedings of Symposium on Thermodynamics of Nuclear Materials*, Vienna, May 1962, International Atomic Energy Agency.

$a = 5.169 \text{ \AA}$,¹⁸ and the latter is a rhombohedron with $a = 9.398 \text{ \AA}$ and $\alpha = 23.78^\circ$.¹⁹ The congruent melting point is 2820°C at nitrogen pressure of

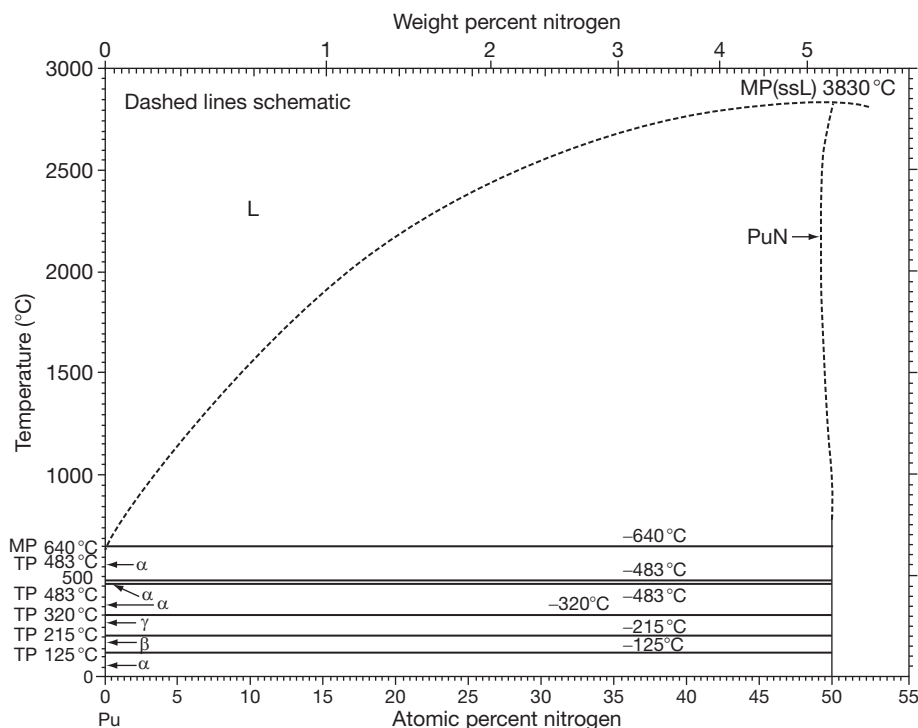


Figure 5 Phase diagram of Pu–N. Reproduced from Wriedt, H. A. *Bull. Alloys Phase Diagrams* **1989**, 10, 593, with permission from American Chemical Society.

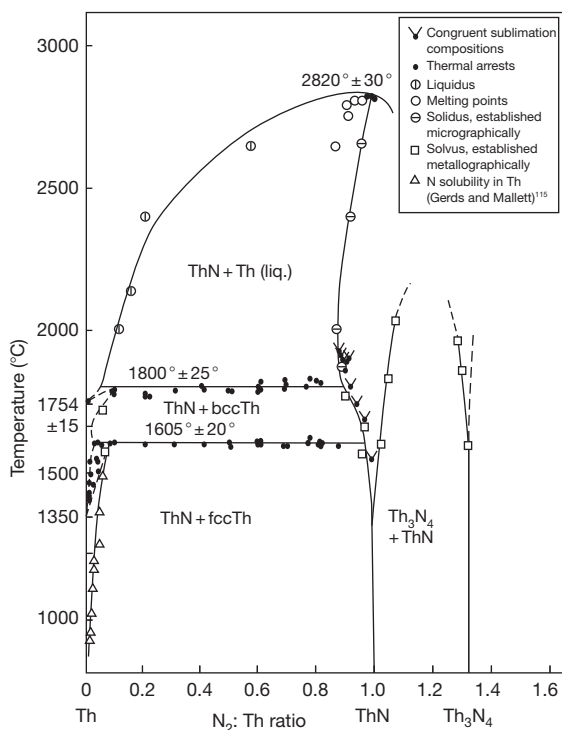


Figure 6 Phase diagram of Th–N. Reproduced from Benz, R.; Hoffman, C. G.; Rupert, G. N. *J. Am. Chem. Soc.* **1967**, 89, 191–197, with permission from Elsevier.

2 atm. Hypo- and hyper-ThN appear above 1350 °C. Th₃N₄ decomposes to ThN in vacuum above 1400 °C with the formation of a small amount of oxide.²⁰ As ThN oxidizes more easily than UN it is important to consider the temperature and nitrogen and oxygen pressures during the preparation of ThN by thermal decomposition of Th₃N₄.²¹

2.03.2.4 Neptunium, Americium, and Curium Nitrides

These nitrides are also usually prepared by carbothermic reduction of the oxides.^{22–24} As it is very difficult to prepare bulk samples due to their high radioactivity, there have been no systematic studies on their phase stability. However, it has been established that there is only mono nitride in these systems from the fact that no nitrogen absorption occurred upon cooling in nitrogen atmospheres during carbothermic reduction. These mono nitrides have an NaCl-type face-centered cubic structure, and their lattice parameter ranges from 0.4899 to 0.5041 Å, as shown in Table 1.²⁴ The similarity in the crystal structure of these three nitrides, as well as uranium and plutonium nitrides, is advantageous as nuclear

Table 1 Lattice parameter of some actinide nitrides

Mononitride	Lattice parameter a (nm)	Lattice parameter difference	
		$ a_{\text{PuN}} - a $ (nm)	$ a_{\text{AmN}} - a $ (nm)
UN	0.4888	0.0017	0.0103
NpN	0.4899	0.0006	0.0092
PuN	0.4905	–	0.0086
AmN	0.4991	0.0086	–
CmN	0.5041	0.0136	0.0050
YN	0.4891	0.0014	0.0100
ZrN	0.4576	0.0329	0.0415
TiN	0.4242	0.0663	0.0749

Source: Minato, K.; *et al. J. Nucl. Mater.* **2003**, 320, 18–24, with permission from Elsevier.

fuels, especially as accelerator-driven system (ADS) targets of nitride solid solutions that contain a large amount of minor actinides (MAs). Experimental research on their vaporization behavior has revealed that the congruent melting temperature of NpN was 2830 °C.²⁵ There are scarcely any data on the phase stability and other properties of pure CmN. Some data on Cm and U or Pu solid solutions have been reported, and these will be discussed in the next section.

2.03.2.5 Nitride Solid Solutions and Mixtures

As (U,Pu)N were some of the most promising candidates for the first breeder reactors, they are the best studied nitride solid solution fuels. UN and PuN form a continuous solid solution, and the lattice parameter increases with an increase in the plutonium content, and is accompanied by a large deviation from Vegard's law, as shown in Figure 7,²⁶ suggesting the nonideality of the solution. A diagram of the calculated U–Pu–N ternary phase at 1000 °C, shown in Figure 8,¹ suggests that there is a relatively narrow range of possible (U,Pu)N compositions, as is the case with U–N and Pu–N binary systems. It is suggested that the sesquinitride solid solution (U,Pu)N_{1.5} exists in a system in which PuN may constitute up to 15 mol%²⁷, although this is not depicted in Figure 8.

As uranium monocarbide and plutonium monocarbide, as well as other actinide carbides, have an NaCl-type fcc structure, actinide nitrides and actinide carbides form solid solutions. Some research performed on actinide nitride carbides, for example, U–N–C, Pu–N–C,^{28–30} have investigated the suitability of these carbonitride fuels and the impurities in nitride fuels after carbothermic reduction. Phase

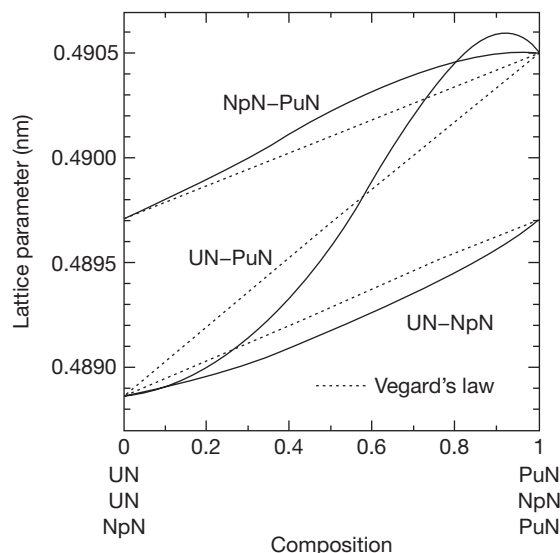


Figure 7 Lattice parameter of some actinide nitride solid solution. Reproduced from Minato, K.; *et al. J. Nucl. Mater.* **2003**, 320, 18–24.

stability graphs of U and/or Pu–N–C, both with and without oxygen, also have been constructed in order to make pure nitride fuels.^{31,32} The irradiation behavior of (U and/or Pu)–N–C fuels also has been reported,³³ but the details of this data are out of the scope of this chapter.

As MAs are usually burnt with uranium and plutonium for transmutation, and as Am originally exists in Pu, (MA,U)N or (MA,Pu)N have also been well studied. As mentioned above, the vaporization behavior of (Pu,Am)N has been studied³⁴, and abnormal vaporization of Pu and Am was observed. The lattice parameters of (U,Np)N and (Np,Pu)N increase with increase in Np and Pu content, and with a small deviation from ideality, as shown in Figure 7.²⁴ Although scarcely any data for pure CmN has been obtained, X-ray diffraction data for (Cm_{0.4}Pu_{0.6})N has been reported, as shown in Figure 9.²⁴

Inert matrix fuels, where MA as well as uranium and plutonium are embedded in a matrix, are also being considered for use in ADS for transmutation. Recent research in MAs has focused on using various nitride solid solutions and nitride mixtures as inert matrix fuels. For ADS targets, matrices have been designed and selected so as to avoid the formation of hot spots and to increase the thermal stability, especially in the case of Americium nitride. Considering their chemical stability and thermal conductivity, ZrN, YN, TiN, and AlN were chosen as candidates for the matrix.^{16,35} ZrN has an NaCl-type

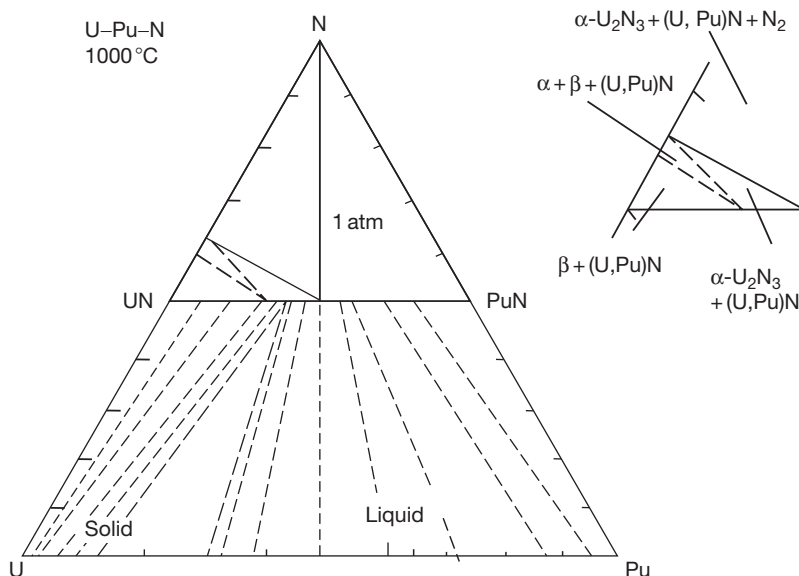


Figure 8 U–Pu–N ternary phase diagram at 1000 °C. Reproduced from Matzke, H. J. *Science of Advanced LMFBR Fuels*; North Holland: Amsterdam, 1986, with permission from Elsevier.

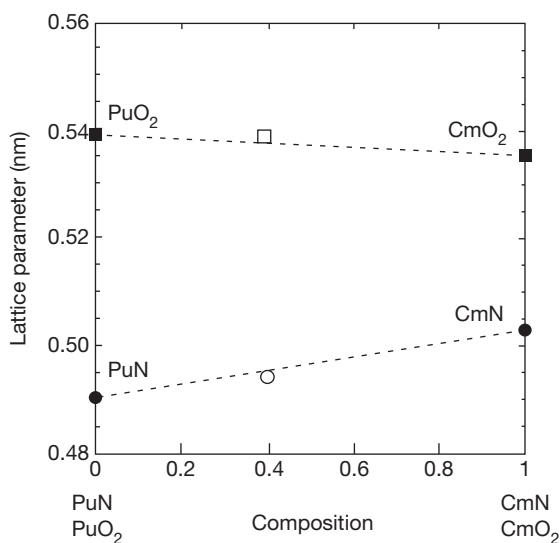


Figure 9 Lattice parameter of (Pu,Cm)N and (Pu,Cm)O₂. Reproduced from Minato, K.; *et al. J. Nucl. Mater.* **2003**, 320, 18–24, with permission from Elsevier.

fcc structure with $a = 4.580 \text{ \AA}$ and has nearly the same thermal conductivity as UN, has a high melting point, good chemical stability in air, and a tolerable dissolution rate in nitric acid. Recently, abundant data have been made available for ZrN-based inert matrix fuels. It is planned that (Pu,Zr)N, with about 20–25% Pu, will be used to burn Pu in a closed fuel cycle.³⁶ The lattice parameter of (Pu,Zr)N decreases with an

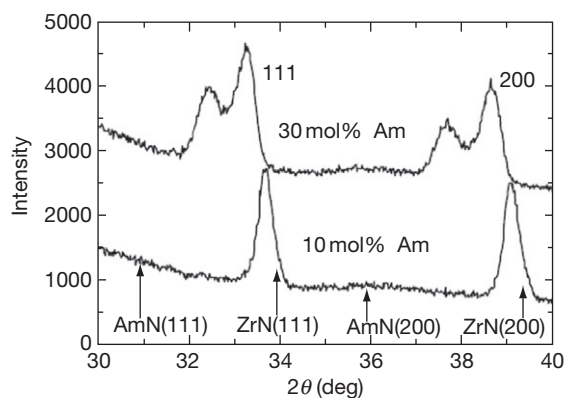


Figure 10 X-ray diffraction patterns for Am–ZrN. Reproduced from Minato, K.; *et al. J. Nucl. Mater.* **2003**, 320, 18–24.

increase in the Zr content, and is between that of PuN and ZrN, in accordance with Vegard's law.²⁴ It has also been estimated, using a model, that (Pu,Zr)N with 20–40 mol% PuN, does not melt till up to 2773 K; this is based on experimental thermodynamic data which show that U_{0.9}Zr_{0.8}N does not melt till up to 3073 K.³⁷ In the case of (Am,Zr)N, it is reported that two solid solutions are obtained when Am content is over 30%²⁴, as shown in Figure 10. The Am content of the two phases have been estimated, from the lattice parameter, to be 14.5 and 43.1 mol%. A thermodynamic modeling of a uranium-free inert

matrix fuel, for example, $(\text{Am}_{0.20}\text{Np}_{0.04}\text{Pu}_{0.26}\text{Zr}_{0.60})$, has also been accomplished.³⁸

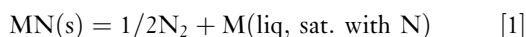
In contrast to ZrN, TiN does not dissolve MA nitrides even though TiN also has an NaCl-type fcc structure. This is explained by the differences in lattice parameter, which was estimated by Benedict.³⁹ A mixture of PuN and TiN was obtained by several heat treatments above 1673 K, and the product, in which one phase was formed, did not contain the other phase.⁴⁰ TiN, as well as ZrN, have nonstoichiometry. It is also reported that a TiN + PuN mixture may be hypostoichiometric although $(\text{Pu,Zr})\text{N}$ is hyperstoichiometric.

2.03.3 Thermal Properties

2.03.3.1 Melting or Decomposition

In this section, the melting points and decomposition temperatures of actinide mononitrides are discussed in conjunction with the nitrogen pressures because this behavior depends on the nitrogen partial pressure of the system. The vapor pressure of a metal gas over the solid nitride is discussed in the next section as ‘vaporization behavior.’

The liquid mononitride MN (liq.) can be observed when congruent melting occurs under a pressurized nitrogen atmosphere; otherwise the solid mononitride MN (s) decomposes into nitrogen gas and liquid metal that is saturated with nitrogen, according to the following reaction,



Olson and Mulford have determined the decomposition temperatures of ThN,⁴¹ UN,⁶ NpN,²⁵ and PuN⁴² by the optical observation of the nitride granules when they were heated under controlled nitrogen pressures. Figure 11 shows the relationship between the nitrogen pressure p (atm) in logarithmic scale and the reciprocal decomposition temperature $1/T$ (K^{-1}). The solid curves show the following equations:

$$\begin{aligned} \text{ThN: } \log p(\text{atm}) &= 8.086 - 33224/T + 0.958 \times 10^{-17} T^5 \\ (2689 \leq T(\text{K}) \leq 3063) \end{aligned} \quad [2]$$

$$\begin{aligned} \text{UN: } \log p(\text{atm}) &= 8.193 - 29540/T + 5.57 \times 10^{-18} T^5 \\ (2773 \leq T(\text{K}) \leq 3123) \end{aligned} \quad [3]$$

$$\begin{aligned} \text{NpN: } \log p(\text{atm}) &= 8.193 - 29540/T + 7.87 \times 10^{-18} T^5 \\ (2483 \leq T(\text{K}) \leq 3103) \end{aligned} \quad [4]$$

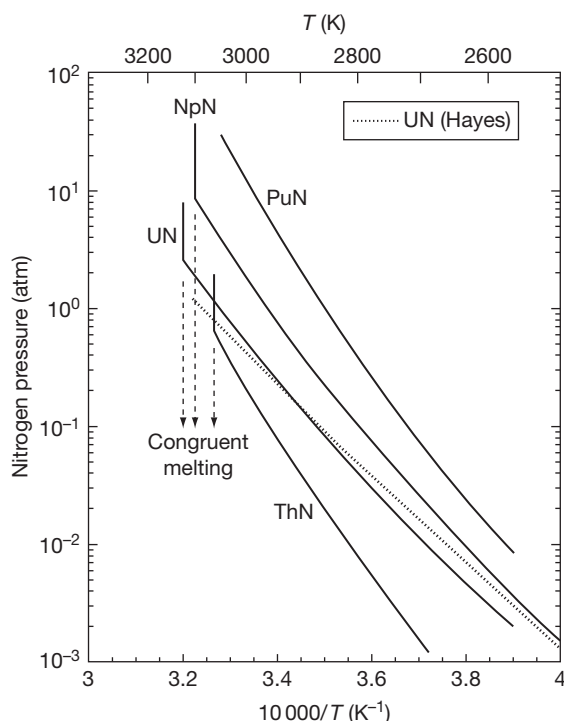


Figure 11 Decomposition pressures of ThN, UN, NpN, and PuN as a function of reciprocal temperature above 2500 K reported by Olson and Mulford.^{6,25,41,42}

$$\begin{aligned} \text{PuN: } \log p(\text{atm}) &= 8.193 - 29540/T + 11.28 \times 10^{-18} T^5 \\ (2563 \leq T(\text{K}) \leq 3043) \end{aligned} \quad [5]$$

The temperature at which the vertical rise in nitrogen pressure is observed for ThN, UN, and NpN corresponds to the congruent melting point, and is 3063 ± 30 K for ThN ($p \geq 0.7$ atm), 3123 ± 30 K for UN ($p \geq 2.5$ atm), and 3103 ± 30 K for NpN ($p \geq 10$ atm). The congruent melting for PuN was not achieved in the nitrogen pressure range up to 24.5 atm.

The presence of an oxide phase, as an impurity, seems to lower the melting point and decomposition temperature. In the case of ThN mentioned above, the melting point and decomposition temperature of a specimen containing 0.6 wt% oxygen fell by ~ 130 K from those of the oxygen-free specimens (~ 0.04 wt% oxygen). A similar experiment conducted by Eron'yan *et al.*⁴³ with ZrN, a transition metal nitride that has the same crystal structure, has revealed a decrease in the melting point by 200–300 K when the oxygen content increased from 0.15 to 0.5–1.0 wt%.

Some data sets on the equilibrium nitrogen pressure, in eqn [1] for UN and uranium carbonitride

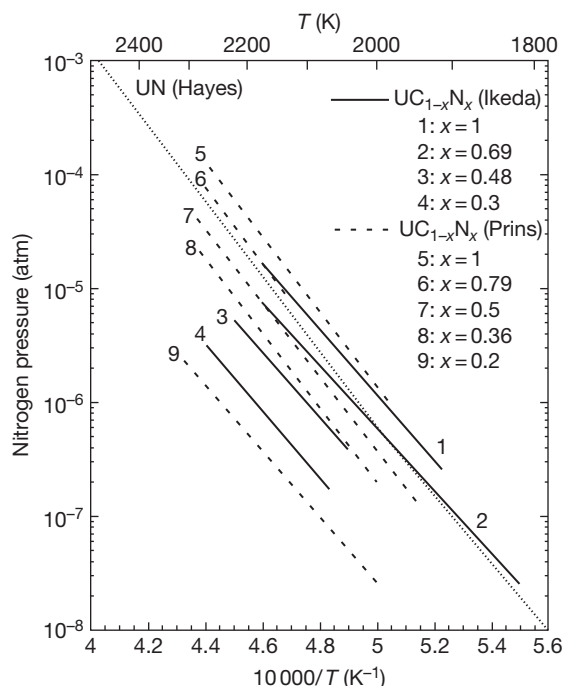


Figure 12 Decomposition pressures of $U(C,N)$ as a function of reciprocal temperature below 2400 K. Solid lines by Ikeda *et al.*⁴⁴ and broken lines by Prins *et al.*⁴⁵. Dotted line for UN reviewed by Hayes *et al.*⁴⁶

$U(C,N)$, as measured by the Knudsen-cell and mass-spectroscopic technique at lower temperatures, are available and are shown in Figure 12. The dotted curve represents the correlation for UN developed by Hayes *et al.*⁴⁶ using eight data sets available in literature.^{4-6,44,45,47-49} The nitrogen pressure is given as:

$$\log p(\text{atm}) = 1.8216 + 1.882 \times 10^{-3} T - 23543.4/T \quad (1400 \leq T(\text{K}) \leq 3170) \quad [6]$$

The N_2 pressure for decomposition of $UC_{1-x}N_x$, as measured by Ikeda *et al.*⁴⁴ and Prins *et al.*⁴⁵, decreases with a decrease in x , together with a lowering in the activity of UN in $UC_{1-x}N_x$. The nitrogen pressure over $UC_{0.5}N_{0.5}$, at a certain temperature in the graph, is approximately one-fifth of that of UN. When considering a nitride or carbide as nuclear fuel for fast reactors, it should be noted that the decomposition pressure of nitrogen can be lowered and that the reactivity of carbide with moisture can be moderated by employing the carbonitride instead of the nitride or carbide.

No experimental data on the melting behavior of transplutonium nitrides such as AmN and CmN have

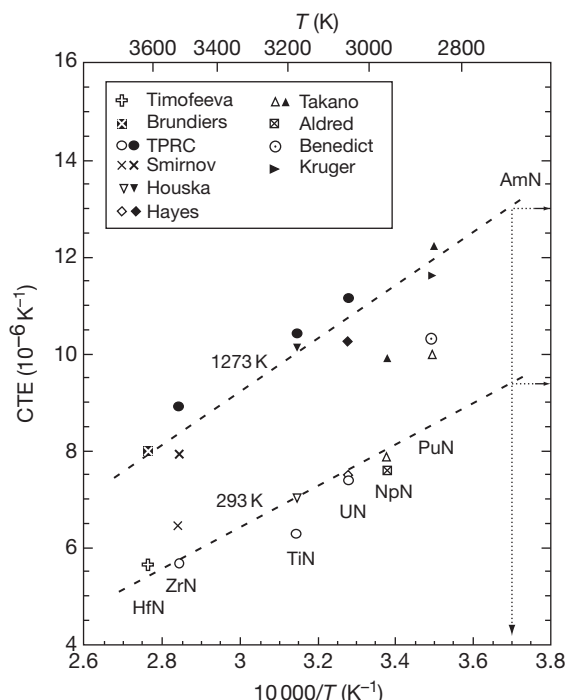


Figure 13 Coefficients of linear thermal expansion at 293 (open symbols) and 1273 K (closed symbols) for some transition metal nitrides and actinide nitrides plotted against reciprocal decomposition temperature under 1 atm of nitrogen. For references see Table 2.

been reported. Takano *et al.*²² have examined the relationship between the decomposition temperature and the instantaneous coefficients of linear thermal expansion (CTE) and used it to predict the decomposition temperature of AmN. Figure 13 shows the CTE at 293 and 1273 K plotted against reciprocal decomposition temperature under 1 atm of nitrogen for some transition metal nitrides (TiN, ZrN, HfN) and actinide nitrides (UN, NpN, PuN). The data used for this is summarized in Table 2^{6,22,25,41-43,50-59} with references. Except for the large CTE value for PuN at 293 K, a reasonable linear relationship is shown by the agreement of the broken lines. From the CTE values for AmN, determined by the high-temperature X-ray diffraction technique, the decomposition temperature of AmN under 1 atm of nitrogen was roughly predicted to be 2700 K, which is much lower than that of PuN.

2.03.3.2 Vaporization Behavior

In this section, the vapor pressure of a metal gas over a solid actinide nitride is summarized.

Table 2 Summary of melting point, decomposition temperature and linear thermal expansion coefficient (CTE) for some transition metal nitrides and actinide nitrides

Nitride	Congruent melting point (m.p.) (K)	Decomposition temperature ^a (K)	References	CTE (10^{-6} K^{-1})		References	Method or comment
				293 K	1273 K		
TiN	3550	3180	50	7.0	10.1	52	XRD, TiN _{0.95}
ZrN	3970	3520	43	6.3	10.4	51	TPRC
				6.5	7.9	53	XRD, ZrN _{0.99}
HfN	NA ^b	3620	50	5.7	8.9	51	TPRC
				5.7	–	54	XRD
ThN	3063	(3063) ^c	41	–	8.0	55	XRD
UN	3123	3050	6	–	–	–	–
				7.5	10.3	56	XRD
NpN	3103	2960	25	7.4	11.1	51	TPRC
				7.9	9.9	22	XRD
PuN	NA	2860	42	7.6	–	57	XRD
				10.0	12.2	22	XRD
AmN	NA	(–2700?)	22	10.3	–	58	XRD
				–	11.6	59	Dilatometer
				9.4	13.0	22	XRD

^aUnder 1 atm of nitrogen.^bNot available.^cCongruent melting under 1 atm of nitrogen.

The major vapor species observed over UN are nitrogen gas, N₂(g), and mono-atomic uranium gas, U(g). UN(g) can also be detected in addition to U(g) and N₂(g),⁶⁰ but its pressure is three orders of magnitude lower than that of U(g); therefore, the contribution of UN(g) can be ignored in practice. Some data on the pressures of N₂(g) and U(g) over solid UN(s) are shown in Figure 14.

Hayes *et al.*⁴⁶ have derived equations for the pressures of N₂(g) and U(g), which were developed by fitting the data from eight experimental investigations. According to that paper, the reported data on N₂(g) agree with each other, but that of U(g) over UN(s) vary somewhat. The U(g) pressure obtained by Suzuki *et al.*⁶¹ is a little higher than that predicted from the equation developed by Hayes *et al.*, but is in agreement with values given by Alexander *et al.*⁶² It is well known that the evaporation of UN is accompanied by the precipitation of a liquid phase, where UN(s) = U(l) + 1/2N₂(g) and U(l) = U(g). The reported vapor pressure of U(g) over UN(s) is close to or a little lower than that over metal U.⁶³ It is suggested that the dissolution of nitrogen and/or impurity metal from crucibles into the liquid phase could affect the observed partial pressure. Some scattering of the previously reported data on U(g) over UN(s) may be also caused by a reaction of the liquid phase in UN with the crucible material. From this viewpoint, it appears that the partial pressure of U(g)

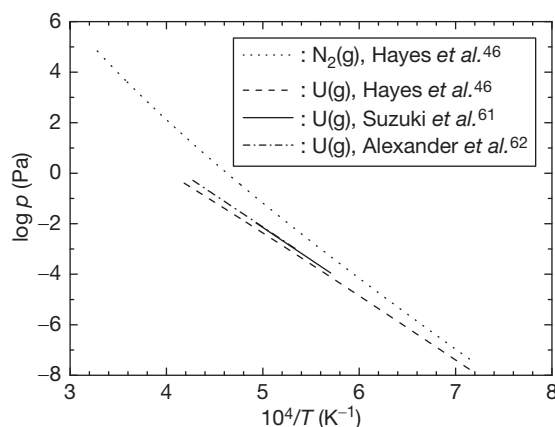


Figure 14 Partial pressure of N₂(g) and U(g) over UN(s) as a function of temperature. Adapted from Hayes, S. L.; Thomas, J. K.; Peddicord, K. L. *J. Nucl. Mater.* **1990**, 171, 300–318; Suzuki, Y.; Maeda, A.; Arai, Y.; Ohmichi, T. *J. Nucl. Mater.* **1992**, 188, 239–243; Alexander, C. A.; Ogden, J. S.; Pardue, W. H. *J. Nucl. Mater.* **1969**, 31, 13–24.

over UN(s) should be a little higher than that proposed by Hayes *et al.*

The vapor species over PuN are nitrogen gas N₂(g) and mono-atomic plutonium gas Pu(g). PuN(g) is not detected because PuN is more unstable than UN.⁶⁴ The N₂ pressure over PuN has been reported by Alexander *et al.*,⁶⁵ Olson and Mulford,⁴²

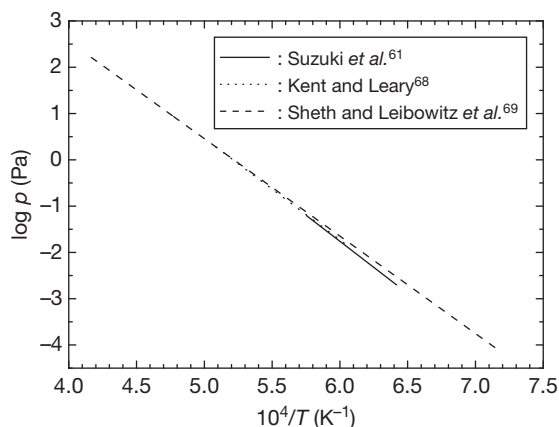


Figure 15 Partial pressure of Pu(g) over PuN(s) as a function of temperature. Data from Suzuki, Y.; Maeda, A.; Arai, Y.; Ohmichi, T. *J. Nucl. Mater.* **1992**, 188, 239–243; Kent, R. A.; Leary, J. A. *High Temp. Sci.* **1966**, 1, 176–183; Sheth, A.; Leibowitz, L. ANL-AFP-2, Argonne National Laboratory; Chemical Engineering Division: Argonne, WI, 1975.

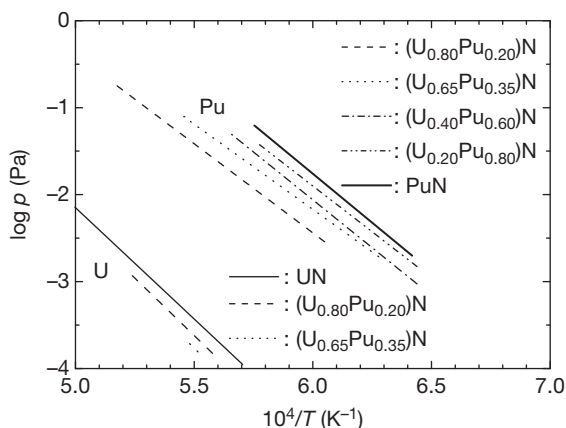


Figure 16 Partial pressure of U(g) and Pu(g) over UN(s), PuN(s) and mixed nitride as function of temperature. Reproduced from Suzuki, Y.; Maeda, A.; Arai, Y.; Ohmichi, T. *J. Nucl. Mater.* **1992**, 188, 239–243.

Pardue *et al.*,⁶⁶ and Campbell and Leary.⁶⁷ These data seem to agree with each other.

The vapor pressure of Pu(g) over PuN(s), as a function of temperature, is shown in **Figure 15**. The values reported in the different studies almost completely agree with each other.^{61,68,69}

According to Alexander *et al.*,⁶⁵ the ratio Pu(g)/N₂(g) is 5.8 throughout the investigated temperature range of 1400–2400 K, which suggests that PuN evaporates congruently; that is, PuN(s) = Pu(g) + 1/2N₂(g). However, Suzuki *et al.* have reported that Pu(g) over PuN(s), at temperatures lower than 1600 K, is a little higher than the values extrapolated from the high-temperature data, and that it approaches that over Pu metal with further decrease in temperature. There is some possibility that a liquid phase forms at the surface of the sample during the cooling stages of the mass-spectrometric measurements, because PuN has a nonstoichiometric composition range at elevated temperatures, while it is a line compound at low temperatures.

The vapor pressure of U(g) and Pu(g) over UN(s), (U,Pu)N(s), and PuN(s) are shown in **Figure 16**. **Table 3** gives the vapor pressures of U(g) and Pu(g) which are represented in **Figure 16** in the form of logarithmic temperature coefficients. It is noteworthy that the vapor pressure of Pu(g) over mixed nitride was observed to increase with an increase in the PuN content.

Nakajima *et al.*⁷⁰ have measured the vapor pressure of Np(g) over NpN(s) in the temperature range of 1690–2030 K by using the Knudsen-cell effusion mass spectrometry. This data is plotted in **Figure 17** as a function of temperature. The partial pressure of Np(g) can be expressed using the following equation:

$$\log p \text{ Np(g)}(\text{Pa}) = 10.26 - 22\,200/T \quad [7]$$

The vapor pressures of Np(g) over NpN(s) obtained by Nakajima *et al.* are similar to those of Np(g) over

Table 3 Partial pressure of U and Pu over UN, PuN, and (U,Pu)N

Compound	Vapor species	Vapor pressure $\log p$ (Pa)	Temperature range (K)
UN	U	$10.65-25\,600T^{-1}$ (T,K)	1753–2028
(U _{0.80} Pu _{0.20})N	U	$10.90-26\,400T^{-1}$ (T,K)	1793–1913
	Pu	$9.86-20\,500T^{-1}$ (T,K)	1653–1933
(U _{0.65} Pu _{0.35})N	U	$11.03-26\,900T^{-1}$ (T,K)	1813–1833
	Pu	$9.59-19\,600T^{-1}$ (T,K)	1593–1833
(U _{0.40} Pu _{0.60})N	Pu	$11.14-22\,000T^{-1}$ (T,K)	1553–1773
(U _{0.20} Pu _{0.80})N	Pu	$10.76-21\,100T^{-1}$ (T,K)	1553–1733
PuN	Pu	$11.74-22\,500T^{-1}$ (T,K)	1558–1738

Source: Suzuki, Y.; Maeda, A.; Arai, Y.; Ohmichi, T. *J. Nucl. Mater.* **1992**, 188, 239–243.

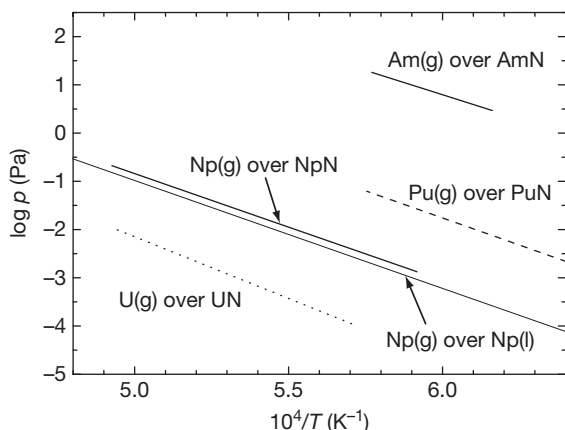


Figure 17 Temperature dependence of partial pressure of Np(g) over Np(l), Np(g) over NpN(s) and Am(g) over AmN(s) together with those of U(g) and Pu(g) over UN(s) and PuN(s) as a function of temperature. Adapted from Suzuki, Y.; Maeda, A.; Arai, Y.; Ohmichi, T. *J. Nucl. Mater.* **1992**, *188*, 239–243; Nakajima, K.; Arai, Y.; Suzuki, Y. *J. Nucl. Mater.* **1997**, *247*, 33–36; Ackermann, R. J.; Rauh, E. G. *J. Chem. Thermodyn.* **1975**, *7*, 211–218; Takano, M.; Itoh, A.; Akabori, M.; Minato, K.; Numata, M. In *Proceedings of GLOBAL 2003, Study on the Stability of AmN and (Am,Zr)N*, New Orleans, LA, Nov 16–20, 2003; p 2285, CD-ROM.

liquid Np metal found by Ackermann and Rauh⁷¹; these all are shown in **Figure 17**. Therefore, the decomposition mechanism is considered to be the following reaction: $\text{NpN(s)} = \text{Np(l)} + 1/2\text{N}_2\text{(g)}$, $\text{Np(l)} = \text{Np(g)}$.

Takano *et al.*⁷² have estimated the vapor pressure of Am(g) over AmN by using values of the Gibbs free energy of formation available in literature.³⁴ The evaporation of AmN obeys the following reaction: $\text{AmN(s)} = \text{Am(g)} + 1/2\text{N}_2\text{(g)}$. The estimated vapor pressure of Am over AmN, expressed as a function of temperature, is

$$\log p \text{ Am(g)}(\text{Pa}) = 12.913 - 20197/T$$

$$(1623 < T(\text{K}) < 1733) \quad [8]$$

The calculated vapor pressures of Am over AmN are plotted in **Figure 17** as a function of temperature. The vapor pressure of Am over AmN is higher than those of other actinide vapor species over their respective nitrides.

2.03.3.3 Heat Capacity

Data on the heat capacities of actinide nitrides are very limited due to the experimental difficulties. In this section, the heat capacities of uranium nitride

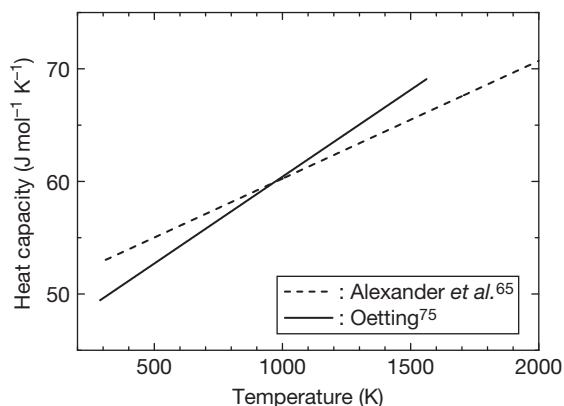


Figure 18 Heat capacities of PuN. Data from Alexander, C. A.; Clark, R. B.; Kruger, O. L.; Robins, J. L. *Plutonium and Other Actinides* 1975; North-Holland: Amsterdam, 1976; pp 277; Oetting, F. L. *J. Chem. Thermodyn.* **1978**, *10*, 941–948.

UN, plutonium nitride PuN, neptunium nitride NpN, and americium nitride AmN are summarized.

Hayes *et al.*⁴⁶ recommended an equation for the heat capacity of UN based on a comparison of nine data sets; these seem to agree with each other at low temperatures but their data are limited, and to some extent scattered, at elevated temperatures. The previously reported values for the heat capacity of UN exhibit an almost linear increase with temperature, except those reported by Conway and Flagella.⁷³ They report that C_p - T curves exhibit a strong upward trend at temperatures over 1500 K. This behavior is analogous to that of the actinide carbides, as pointed out by Blank.⁷⁴ The assessment by Hayes *et al.* uses the results of Conway and Flagella. Thus, the heat capacity data reported by Hayes *et al.* can be considered reliable. The heat capacity of UN, expressed by Hayes *et al.*, is as follows:

$$C_p(\text{J mol}^{-1} \text{K}^{-1}) =$$

$$51.14 \left(\frac{\theta}{T} \right)^2 \frac{\exp(\frac{\theta}{T})}{[\exp(\frac{\theta}{T}) - 1]^2} + 9.491 \times 10^{-3} T$$

$$+ \frac{2.642 \times 10^{11}}{T^2} \exp\left(-\frac{18081}{T}\right)$$

$$(298 < T(\text{K}) < 2628) \quad [9]$$

where θ is the empirically determined Einstein temperature of UN, 365.7 K.

The heat capacities of PuN are shown in **Figure 18**.

Information on the heat capacity of PuN is very scarce and is limited to the low temperatures. Moreover, the two data sets on PuN given by Alexander

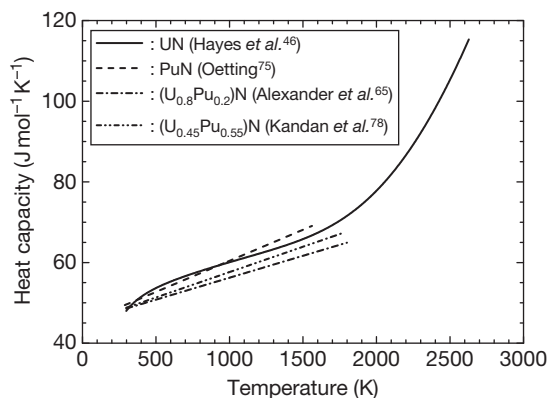


Figure 19 Heat capacities of UN, PuN, and (U,Pu)N. Data from Hayes, S. L.; Thomas, J. K.; Peddicord, K. L. *J. Nucl. Mater.* **1990**, 171, 300–318; Oetting, F. L. *J. Chem. Thermodyn.* **1978**, 10, 941–948; Alexander, C. A.; Ogden, J. S.; Pardue, W. M. Thermophysical properties of (UPu)N. In *Plutonium 1970 and Other Actinides PT.1*; 1970, 17, 95–103; Kandan, R.; Babu, R.; Nagarajan, K.; Vasudeva Rao, P. R. *Thermochim. Acta* **2007**, 460, 41–43.

*et al.*⁶⁵ and Oetting⁷⁵ are not consistent. Matsui and Ohse⁷⁶ have critically reviewed the heat capacity data of PuN and have argued that the Oetting correlation is more reliable. Therefore, the heat capacity data, as reported by Oetting, is given here. The heat capacity function of PuN given by Oetting is

$$C_p(\text{J mol}^{-1}\text{K}^{-1}) = 1.542 \times 10^{-2} T + 45.00 \quad (298 < T(\text{K}) < 1562) \quad [10]$$

The heat capacities of UN, PuN, and (U,Pu)N are shown in **Figure 19**. If the heat capacities of solid solutions can be estimated from those of its raw materials with the same structure on the basis of the additive law, it can be expected that the values for the (U,Pu)N solid solutions are an intermediate between those of UN and PuN. However, the heat capacities of (U,Pu)N, as reported by Alexander *et al.*⁷⁷ and Kandan *et al.*,⁷⁸ are smaller than those of UN, by Hayes *et al.*, and PuN, by Oetting. In addition, the temperature dependencies of the heat capacities of PuN and its solid solutions are almost linear, although it has been suggested that they can shift toward larger values at elevated temperatures, as does UN. It is considered that these discrepancies are probably due to the lack of experimental data. Thus, it is necessary to obtain the accurate heat capacity of PuN and (U,Pu)N.

Recently, the heat capacities of NpN and AmN were determined by drop calorimetry.⁷⁹ The samples

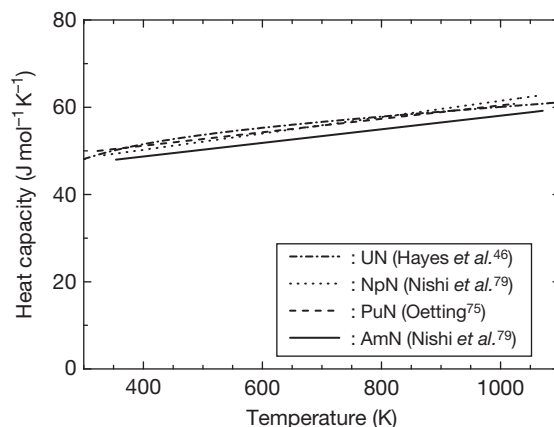


Figure 20 Heat capacities of UN, NpN, PuN, and AmN. Adapted from Hayes, S. L.; Thomas, J. K.; Peddicord, K. L. *J. Nucl. Mater.* **1990**, 171, 300–318; Oetting, F. L. *J. Chem. Thermodyn.* **1978**, 10, 941–948; Nishi, T.; Itoh, A.; Takano, M.; *et al. J. Nucl. Mater.* **2008**, 377, 467–469.

of NpN and AmN were prepared by the carbothermic reduction of their respective oxides. The enthalpy increments were measured using a twin-type drop calorimeter in a glove box. The heat capacities were determined by derivatives of the enthalpy increments. The measured heat capacity of NpN is expressed by

$$C_p(\text{J mol}^{-1}\text{K}^{-1}) = 1.872 \times 10^{-2} T + 42.75 \quad (334 < T(\text{K}) < 1562) \quad [11]$$

The measured heat capacity of AmN is expressed by

$$C_p(\text{J mol}^{-1}\text{K}^{-1}) = 1.563 \times 10^{-2} T + 42.44 \quad (354 < T(\text{K}) < 1071) \quad [12]$$

These are shown in **Figure 20**, together with those of UN,⁴⁶ NpN,⁷⁹ and PuN.⁷⁵ Although there are no distinct differences, the heat capacity of AmN was slightly lower than those of UN, NpN, and PuN.

The heat capacities of (Np,Am)N and (Pu,Am)N solid solutions were also obtained. The heat capacities decreased slightly with an increase in Am content. This tendency was attributed to the heat capacity of AmN being slightly smaller than those of NpN and PuN.⁸⁰

2.03.3.4 Gibbs Free Energy of Formation

Some data on the Gibbs free energy of formation for actinide nitrides exist. In this section, the Gibbs free energy of formation of uranium nitride, UN, plutonium nitride, PuN, uranium and plutonium mixed nitride, (U,Pu)N, neptunium nitride, NpN, and americium nitride, AmN are summarized.

Table 4 The standard thermodynamic functions of UN

T (K)	C_p ($\text{J mol}^{-1} \text{K}^{-1}$)	$H-H_{298}$ (J mol^{-1})	S ($\text{J mol}^{-1} \text{K}^{-1}$)	$-(G-H_{298})/T$ ($\text{J mol}^{-1} \text{K}^{-1}$)	$\Delta_f G$ (J mol^{-1})
298	47.95	0	62.68	62.68	-270 978
300	48.04	96	63.00	62.68	-270 812
400	51.49	5089	77.34	64.62	-262 582
500	53.64	10 352	89.08	68.37	-254 530
600	55.27	15 801	99.01	72.67	-246 614
700	56.63	21 397	107.63	77.06	-238 788
800	57.84	27 121	115.27	81.37	-231 011
900	58.98	32 963	122.15	85.53	-223 235
1000	60.06	38 915	128.42	89.51	-215 267
1100	61.12	44 975	134.19	93.31	-206 948
1200	62.18	51 140	139.56	96.94	-198 457
1300	63.28	57 413	144.57	100.41	-190 019
1400	64.47	63 799	149.28	103.71	-181 626
1500	65.81	70 312	153.74	106.87	-172 640
1600	67.38	76 969	157.98	109.87	-163 550
1700	69.27	83 798	162.01	112.72	-154 384
1800	71.59	90 837	165.87	115.41	-145 111
1900	74.40	98 132	169.58	117.93	-135 687
2000	77.81	105 738	173.14	120.28	-126 062
2100	81.86	113 716	176.58	122.43	-116 178
2200	86.62	122 133	179.90	124.39	-105 969
2300	92.11	131 063	183.12	126.14	-95 367
2400	98.35	140 580	186.24	127.67	-84 302
2500	105.33	150 757	189.28	128.98	-72 701
2600	113.04	161 669	192.23	130.05	-60 489
2628	115.32	164 866	193.04	130.31	-56 954

The values of $\Delta_f G$ for UN were calculated from the values of ΔH_{298} and thermal functions for uranium and nitrogen.

Source: Hayes, S. L.; Thomas, J. K.; Peddicord, K. L. *J. Nucl. Mater.* **1990**, 171, 300–318; Matsui, T.; Ohse, R. W. *High Temp. High Press.* **1987**, 19, 1–17; Cordfunke, E. H. P.; Konings, R. J. M.; Potter, P. E.; Prins, G.; Rand, M. H. *Thermochemical Data for Reactor Materials and Fission Products*; Elsevier: Amsterdam, 1990; p 667; Chase, M. W.; Curnutt, J. L.; Prophet, H. *JANAF Thermochemical Tables*; Dow Chemical Co.: Midland, MA, 1965.

2.03.3.4.1 Uranium mononitride

The Gibbs free energy (G) for UN has been reported by Hayes *et al.*⁴⁶ On the basis of the equations for C_p and $H-H_{298}$, they have determined other thermal functions of UN(s) in the temperature range of 298–2628 K. They have then calculated the values of the thermal functions from their equations for heat capacity, setting S_{298} to be $62.68 \text{ J mol}^{-1} \text{K}^{-1}$; these are given in Table 4. The values of Gibbs free energy of formation $\Delta_f G$ for UN were thus calculated from the values of ΔH_{298} ⁷⁶ and thermal functions of uranium⁸¹ and nitrogen.⁸² The values of entropy S , free energy function $-(G-H_{298})/T$, and Gibbs free energy of formation $\Delta_f G$ of UN(s) are also given in Table 4.

The values of $\Delta_f G$ at various temperatures were fitted to a polynomial function of temperature using the least-squares method. The $\Delta_f G$ of UN was thus expressed as the following equation:

$$\begin{aligned} \Delta_f G(\text{Jmol}^{-1}) = & -2.941 \times 10^5 + 80.98 T - 0.04640 T^2 \\ & + 3.085 \times 10^{-6} T^3 - 1.710 \times 10^6 / T \\ & (298 < T(\text{K}) < 2628) \end{aligned} \quad [13]$$

Matsui and Ohse⁷⁶ have also reported $\Delta_f G$ values for UN. The temperature dependences of $\Delta_f G$ for UN are shown in Figure 21. The UN $\Delta_f G$ values of these two studies agree well with each other below 1800 K, but there seems to be some discrepancy between them at higher temperatures. It should be noted that the values of $\Delta_f G$ for UN contain some uncertainty due to the inaccuracy of the data on the $H-H_{298}$ values. The values of $\Delta_f G$, as estimated by Matsui and Ohse have a large range of error because the calculation was performed by extrapolating the values of $H-H_{298}$. Thus, the data for the $\Delta_f G$ of UN, as reported by Hayes *et al.*, are considered to be the reference standard at the present.

2.03.3.4.2 Plutonium mononitride

The most reliable standard thermodynamic function data for PuN are those reported by Matsui and Ohse.⁷⁶ Matsui *et al.* have calculated the thermal functions of PuN(s) using the recommended

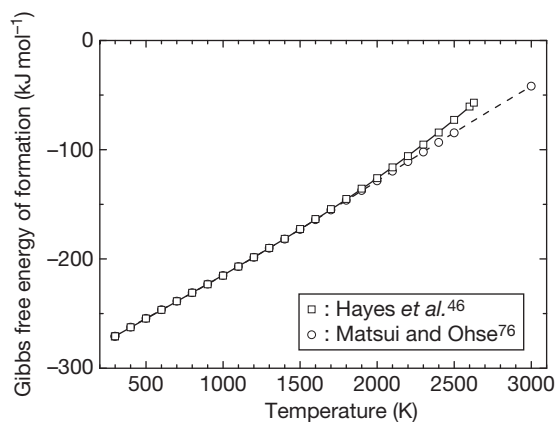


Figure 21 Temperature dependences of the Gibbs free energy of formation, $\Delta_f G$ for UN(s). Data from Hayes, S. L.; Thomas, J. K.; Peddicord, K. L. *J. Nucl. Mater.* **1990**, 171, 300–318; Matsui, T.; Ohse, R. W. *High Temp. High Press.* **1987**, 19, 1–17.

equations for C_p and the $H-H_{298}$ values of Oetting⁷⁵, and setting S_{298} to be $64.81 \text{ J mol}^{-1} \text{ K}^{-1}$; these are summarized in **Table 5**. The values of C_p and $H-H_{298}$ higher than 1600 K are extrapolations of the data reported by Oetting.⁷⁵

The values of $\Delta_f G$ for PuN were calculated with ΔH_{298} set at $-299.200 \text{ J mol}^{-1}$ ⁽⁸³⁾ and the thermal functions for plutonium⁸⁴ and nitrogen.⁸² The values of entropy S , the free energy function $-(G-H_{298})/T$, and Gibbs free energy of formation $\Delta_f G$ of PuN(s) are also given in **Table 5**.

The $\Delta_f G$ of PuN is expressed with the following equation:

$$\begin{aligned} \Delta_f G (\text{J mol}^{-1}) = & -3.384 \times 10^5 + 152.0T - 0.03146T^2 \\ & - 5.998 \times 10^{-6}T^3 + 6.844 \times 10^6/T \\ (298 < T(\text{K}) < 3000) \end{aligned} \quad [14]$$

The temperature dependencies of the $\Delta_f G$ for PuN are shown in **Figure 22**. The values of $\Delta_f G$ are close to those derived from the precise vapor pressure measurements by Kent and Leary,⁶⁸ with a difference of around 1 kJ mol^{-1} at 1000 K and 6 kJ mol^{-1} at 2000 K.

Table 5 The standard thermodynamic functions of PuN

$T (\text{K})$	$C_p (\text{J mol}^{-1} \text{ K}^{-1})$	$H-H_{298} (\text{J mol}^{-1})$	$S (\text{J mol}^{-1} \text{ K}^{-1})$	$-(G-H_{298})/T (\text{J mol}^{-1} \text{ K}^{-1})$	$\Delta_f G (\text{J mol}^{-1})$
298	49.60	0	64.81	64.81	-273 247
300	49.63	92	65.12	64.81	-273 073
400	51.17	5132	79.61	66.78	-264 338
500	52.71	10 326	91.19	70.54	-254 777
600	54.26	15 674	100.94	74.81	-245 152
700	55.80	21 177	109.42	79.16	-235 469
800	57.34	26 834	116.97	83.43	-225 714
900	58.88	32 645	123.81	87.54	-215 918
1000	60.42	38 610	130.09	91.48	-205 913
1100	61.97	44 729	135.92	95.26	-195 883
1200	63.51	51 003	141.38	98.88	-185 888
1300	65.05	57 430	146.53	102.35	-175 923
1400	66.59	64 012	151.40	105.68	-166 005
1500	68.13	70 749	156.05	108.88	-156 135
1600	69.68	77 639	160.50	111.97	-146 323
1700	71.22	84 685	164.76	114.95	-136 571
1800	72.76	91 884	168.88	117.83	-126 892
1900	74.30	99 237	172.85	120.63	-117 270
2000	75.84	106 744	176.70	123.33	-107 730
2100	77.38	114 405	180.44	125.96	-98 274
2200	78.93	122 221	184.08	128.52	-88 895
2300	80.47	130 191	187.62	131.02	-79 594
2400	82.01	138 314	191.08	133.45	-70 388
2500	83.55	146 593	194.46	135.82	-61 269
3000	91.26	190 296	210.37	146.94	-17

Source: Matsui, T.; Ohse, R. W. *High Temp. High Press.* **1987**, 19, 1–17.

2.03.3.4.3 Uranium and plutonium mononitride

The standard thermodynamic function data for $(\text{U}_{0.8}\text{Pu}_{0.2})\text{N}$ were determined using an ideal-solution model. Matsui *et al.* have estimated the entropy at 298 K (S_{298}) for $(\text{U}_{0.8}\text{Pu}_{0.2})\text{N}$ to be $67.07 \text{ J mol}^{-1} \text{ K}^{-1}$

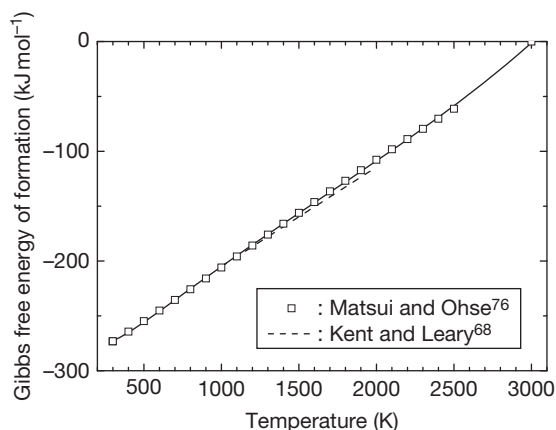


Figure 22 Temperature dependences of the Gibbs free energy of formation, $\Delta_f G$ for PuN(s) . Data from Matsui, T.; Ohse, R. W. *High Temp. High Press.* **1987**, 19, 1–17; Kent, R. A.; Leary, J. A. *High Temp. Sci.* **1969**, 1, 176–183.

from S_{298} values for UN ($62.43 \text{ J mol}^{-1} \text{ K}^{-1}$) and PuN ($64.81 \text{ J mol}^{-1} \text{ K}^{-1}$) coupled with an entropy of mixing term, assuming an ideal solution. The values of the thermal functions for $(\text{U}_{0.8}\text{Pu}_{0.2})\text{N}$ have been calculated by Matsui *et al.* and are summarized in **Table 6**. The enthalpy of formation for $(\text{U}_{0.8}\text{Pu}_{0.2})\text{N}$ was estimated to be $-296.5 \text{ kJ mol}^{-1}$, on the basis of an ideal-solution model with $\Delta H_{298}(\text{UN}) = -295.8 \text{ kJ mol}^{-1}$ and $\Delta H_{298}(\text{PuN}) = -299.2 \text{ kJ mol}^{-1}$. The values of entropy S , free energy function $-(G-H_{298})/T$, and Gibbs free energy of formation $\Delta_f G$ of $(\text{U}_{0.8}\text{Pu}_{0.2})\text{N(s)}$ are also given in **Table 6**. The equation of ΔG for $(\text{U}_{0.8}\text{Pu}_{0.2})\text{N}$ is given as

$$\begin{aligned} \Delta_f G(\text{J mol}^{-1}) = & -2.909 \times 10^5 + 67.56T + 0.007980T^2 \\ & - 1.098 \times 10^{-6}T^3 - 7.455 \times 10^5/T \\ & (298 < T(\text{K}) < 3000) \end{aligned} \quad [15]$$

2.03.3.4.4 Neptunium mononitride and americium mononitride

Nakajima *et al.*⁷⁰ have estimated the values of $\Delta_f G$ for NpN(s) . **Figure 23** shows the temperature dependence of $\Delta_f G$, together with $\Delta_f G$ for UN(s), as given

Table 6 The standard thermodynamic functions of $(\text{U}_{0.8}\text{Pu}_{0.2})\text{N}$

$T(\text{K})$	$C_p(\text{J mol}^{-1} \text{ K}^{-1})$	$H-H_{298}(\text{J mol}^{-1})$	$S(\text{J mol}^{-1} \text{ K}^{-1})$	$-(G-H_{298})/T$ ($\text{J mol}^{-1} \text{ K}^{-1}$)	$\Delta_f G(\text{J mol}^{-1})$
298	48.18	0	67.07	67.07	-272 623
300	48.26	96	67.39	67.07	-272 463
400	51.46	5172	83.85	70.92	-264 527
500	53.57	10 354	93.47	72.77	-256 576
600	55.24	15 796	103.39	77.07	-248 723
700	56.71	21 395	112.02	81.45	-240 926
800	58.07	27 134	119.68	85.76	-233 156
900	59.37	33 007	126.60	89.92	-225 395
1000	60.63	39 007	132.92	93.91	-217 422
1100	61.87	45 184	138.91	97.83	-209 381
1200	63.12	51 433	144.35	101.49	-201 030
1300	64.35	57 806	149.45	104.98	-192 746
1400	65.57	64 302	154.26	108.33	-184 520
1500	66.79	70 921	158.83	111.55	-175 853
1600	68.01	77 661	163.18	114.64	-167 164
1700	69.22	84 522	167.34	117.62	-158 499
1800	70.43	91 505	171.33	120.49	-149 859
1900	71.64	98 608	175.17	123.27	-141 237
2000	72.85	105 832	178.87	125.96	-132 654
2100	74.05	113 177	182.45	128.56	-124 114
2200	75.26	120 643	185.93	131.09	-115 614
2300	76.46	128 228	189.30	133.55	-107 156
2400	77.66	135 935	192.58	135.94	-98 723
2500	78.87	143 761	195.77	138.27	-90 365
3000	84.87	184 696	210.68	149.12	-45 975

Source: Matsui, T.; Ohse, R. W. *High Temp. High Press.* **1987**, 19, 1–17.

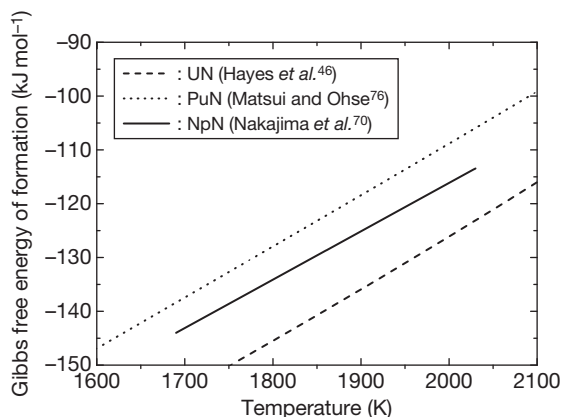


Figure 23 Temperature dependences of the Gibbs free energy of formation, $\Delta_f G$ for NpN(s) compared with those for UN(s) and PuN(s). Data from Hayes, S. L.; Thomas, J. K.; Peddicord, K. L. *J. Nucl. Mater.* **1990**, 171, 300–318; Matsui, T.; Ohse, R. W. *High Temp. High Press.* **1987**, 19, 1–17; Nakajima, K.; Arai, Y.; Suzuki, Y. *J. Nucl. Mater.* **1997**, 247, 33–36.

by Hayes *et al.*⁴⁶ and the $\Delta_f G$ for PuN(s), as given by Matsui and Ohse.⁷⁶ The line for NpN(s) is that of the following equation and was determined by a least-squares treatment of the data:

$$\Delta_f G(\text{J mol}^{-1}) = -295\,900 + 89.88T \quad (1690 < T(\text{K}) < 2030) \quad [16]$$

Nakajima *et al.* have evaluated these results in the temperature range of 1690–2030 K using the data of $\text{N}_2(\text{g})$ pressure over NpN(s) + Np(l) derived upon extrapolation of the experimental data given by Olson *et al.* Then, Nakajima *et al.*⁸⁵ have also carried out a mass-spectrometric study on NpN(s) co-loaded with PuN(s) in order to control the $\text{N}_2(\text{g})$ pressure by the congruent vaporization of PuN(s). The $\Delta_f G$ value calculated for NpN(s) almost completely agrees with that obtained from eqn [16].

Ogawa *et al.*³⁴ have estimated the Gibbs free energy of formation for AmN from the partial pressure of Am(g) over (Pu,Am)N. Their values of ΔG for AmN(s) are given by the following equation:

$$\Delta G(\text{J mol}^{-1}) = -297\,659 + 92.054T \quad (298 < T(\text{K}) < 1600) \quad [17]$$

2.03.3.5 Thermal Conductivity

In order to determine the thermal conductivity, it is necessary to obtain the thermal diffusivity. Thermal diffusivity is determined by the laser flash method.

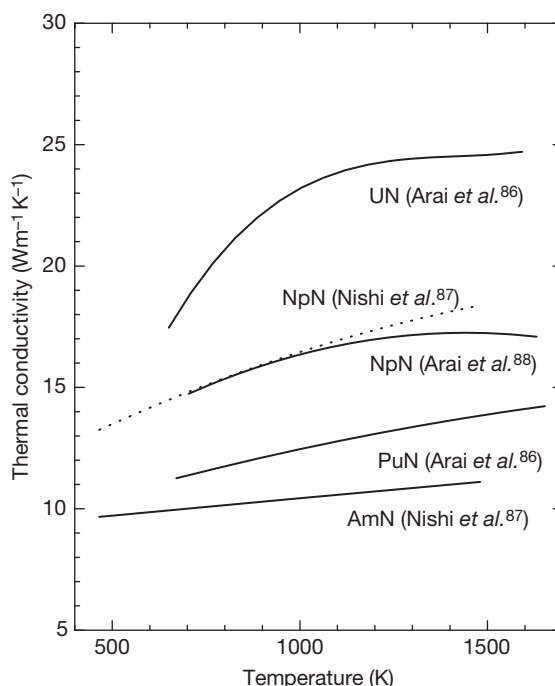


Figure 24 Thermal conductivities of actinide mononitrides. Data from Arai, Y.; Suzuki, Y.; Iwai, T.; Ohmichi, T. *J. Nucl. Mater.* **1992**, 195, 37–43; Nishi, T.; Takano, M.; Itoh, A.; Akabori, M.; Arai, Y.; Minato, K. In *Proceedings of the Tenth OECD/NEA International Information Exchange Meeting on Actinide and Fission Product Partitioning and Transmutation, Thermal Conductivities of Neptunium and Americium Mononitrides*, Mito, Japan, Oct 6–10, 2008; 2010, CD-ROM; Arai, Y.; Okamoto, Y.; Suzuki, Y. *J. Nucl. Mater.* **1994**, 211, 248–250.

The temperature dependence of the thermal conductivities of actinide mononitrides is shown in Figure 24. The thermal conductivity of UN was assessed by Arai *et al.*,⁸⁶ that of NpN was assessed by Nishi *et al.*⁸⁷ and Arai *et al.*,⁸⁸ that of PuN was assessed by Arai *et al.*⁸⁶ and that of AmN was assessed by Nishi *et al.*⁸⁷ These are plotted here. The thermal conductivities of the actinide mononitrides increased with an increase in temperature over the temperature range investigated. The increase in thermal conductivities of the actinide mononitrides is probably due to the increase in the electronic component.

Figure 24 clearly shows that the thermal conductivity of the actinide mononitrides decreases with increase in the atomic number of actinide elements. Although phonons and electrons both may contribute to the thermal conductivity of actinide mononitrides, the electronic contribution is probably predominant at higher temperatures. The electrical resistivity of actinide mononitrides increases with an increase in the

atomic number, so the tendency of the thermal conductivity to decrease with an increase in the atomic number would indicate a reduction in electronic contribution.⁸⁹

The thermal conductivity values of NpN, as reported by Nishi and by Arai, agree well with each other below 1100 K, but there is some discrepancy between the two data sets at higher temperatures. It should be noted that the thermal conductivity values of NpN have some uncertainty due to the inaccuracy of the heat capacity data. Nishi has determined thermal conductivity values using experimental heat capacity values. However, the thermal conductivity of NpN has a large range of error because the heat capacity of NpN at temperatures higher than 1067 K were calculated by simply extrapolating eqn [11]. As a result, the data sets of Arai *et al.* are taken here as the reference standard for the thermal conductivities of UN, NpN, and PuN. The thermal conductivities of UN, NpN, and PuN corrected to 100% TD (theoretical density) are given by

$$\begin{aligned} \text{UN: } \lambda = & -17.75 + 0.08808T - 6.161 \times 10^{-5}T^2 \\ & + 1.447 \times 10^{-8}T^3 \\ & (680 < T(\text{K}) < 1600) \end{aligned} \quad [18]$$

$$\begin{aligned} \text{NpN: } \lambda = & 7.89 + 0.0127T - 4.32 \times 10^{-6}T^2 \\ & (740 < T(\text{K}) < 1600) \end{aligned} \quad [19]$$

$$\begin{aligned} \text{PuN: } \lambda = & 8.18 + 0.0522T - 9.44 \times 10^{-7}T^2 \\ & (680 < T(\text{K}) < 1600) \end{aligned} \quad [20]$$

The thermal conductivity of AmN, corrected to 100% TD, has been reported only by Nishi *et al.*⁸⁷

The thermal conductivities of Am, corrected to 100% TD, in the temperature range from 473 to 1473 K. can be expressed by

$$\lambda = 8.99 + 0.00147T - 2.54 \times 10^{-8}T^2 \quad [21]$$

The thermal conductivities of (U,Pu)N solid solutions have been reported by Arai *et al.*,⁸⁶ Ganguly *et al.*,⁹⁰ Alexander *et al.*,⁷⁷ and Keller.⁹¹ The data of Arai *et al.* for the (U,Pu)N solid solutions agrees with the data of the other investigations. The data reported by Arai *et al.* are plotted in Figure 25.

The temperature dependence of thermal conductivity for (U,Pu)N solid solutions is similar to the other mononitrides; but thermal conductivity decreases rapidly with the addition of PuN. This means that a simple averaging method cannot be applied for the evaluation of the thermal conductivity of the solid solutions of actinide mononitrides.

The thermal conductivities of (U,Np)N and (Np,Pu)N solid solutions have been reported by Arai *et al.*⁸⁹ and those of (Np,Am)N and (Pu,Am)N solid solutions have been reported by Nishi *et al.*⁸⁰ Data on (U,Np)N and (Np,Pu)N solid solutions are plotted in Figure 26 and the data on (Np,Am)N and (Pu,Am)N solid solutions are plotted in Figure 27. The behavior of (U,Np)N, (Np,Pu)N, (Np,Am)N, and (Pu,Am)N solid solutions was found to be similar to that of (U,Pu)N.

The composition dependence of the thermal conductivities for (U,Pu)N, (U,Np)N, (Np,Pu)N, (Np,Am)N, and (Pu,Am)N solid solutions at 773 and 1073 K are shown in Figure 28. It can be seen from these graphs that the thermal conductivities of (U,Pu)N and

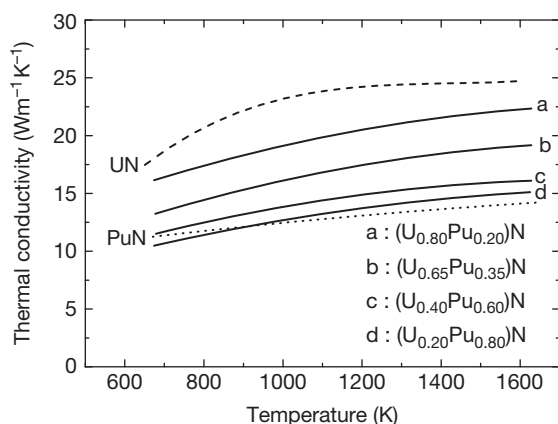


Figure 25 Thermal conductivity of (U,Pu)N solid solutions. Reproduced from Arai, Y.; Suzuki, Y.; Iwai, T.; Ohmichi, T. *J. Nucl. Mater.* **1992**, 195, 37–43.

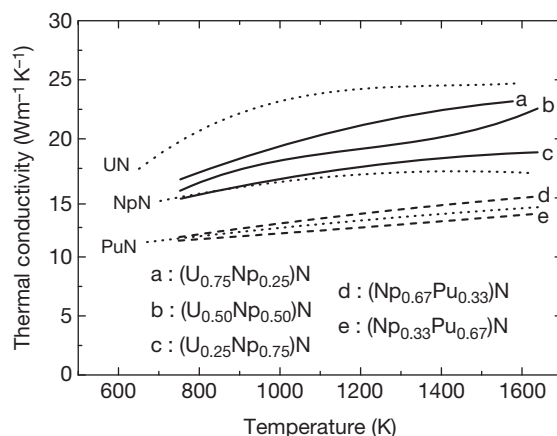


Figure 26 Thermal conductivity of (U,Np)N and (Np,Pu)N solid solutions. Reproduced from Arai, Y.; Nakajima, K.; Suzuki, Y. *J. Alloys Compd.* **1998**, 271–273, 602–605.

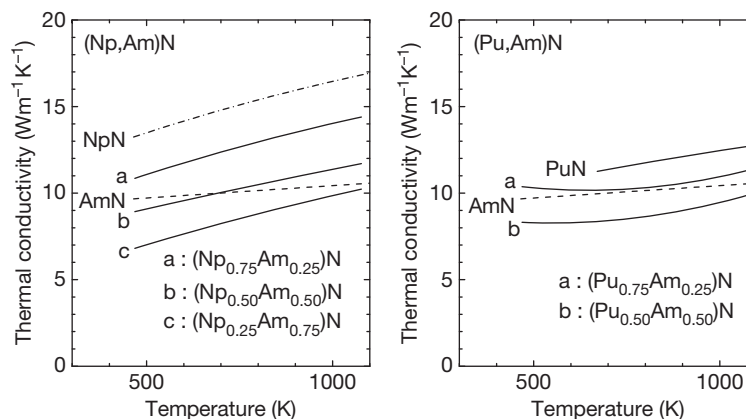


Figure 27 Thermal conductivities of (Np,Am)N and (Pu,Am)N solid solutions. Reproduced from Nishi, T.; Takano, M.; Itoh, A.; *et al. IOP Conf. Ser. Mater. Sci. Eng.* **2010**, 9, 012017.

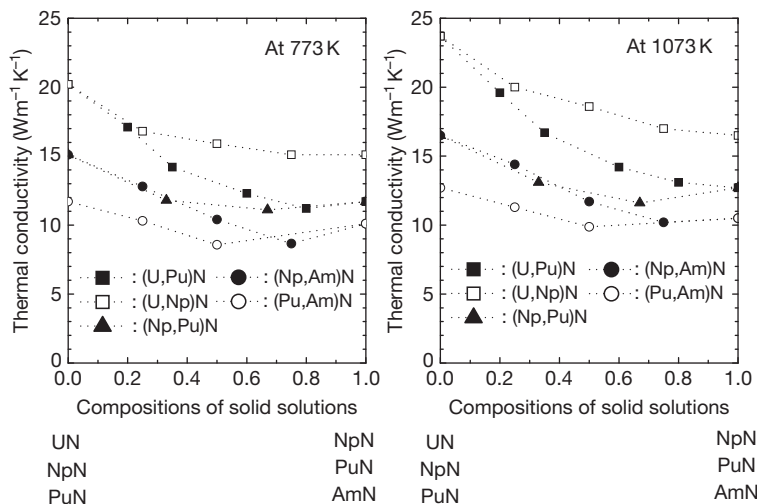


Figure 28 Composition dependence of the thermal conductivities of (U,Pu)N, (U,Np)N, (Np,Pu)N, (Np,Am)N, and (Pu,Am)N solid solutions at 773 and 1073 K. Reproduced from Nishi, T.; Takano, M.; Itoh, A.; *et al. IOP Conf. Ser. Mater. Sci. Eng.* **2010**, 9, 012017.

(Np,Pu)N decrease with an increase in the Pu content; that of (U,Np)N decreases with an increase in Np content, and those of (Np,Am)N and (Pu,Am)N decrease with an increase in Am content.

It has been proposed that the thermal conductivities of the actinide mononitrides decrease with an increase in the atomic number of the actinide element because the electrical resistivities of the actinide mononitrides have a tendency to increase with an increase in the atomic number.⁸⁹ Thus, the decrease in thermal conductivity with an increase in Pu or Np or Am content may correspond to the lowering of the electronic contribution. These data suggest that the thermal conductivities of the binary actinide nitride solid solutions are lower than those

derived from the arithmetic mean of their constituent nitrides. In addition, the thermal conductivities of (Np_{0.33}Pu_{0.67})N, (Np_{0.25}Am_{0.75})N, and (Pu_{0.50}Am_{0.50})N, at 773 and 1073 K, were smaller than those of PuN or AmN, especially at lower temperature. Although the mechanism for this degradation in the thermal conductivity of the solid solutions has not yet been clarified, it might be caused by phonon scattering between Np and Pu, and Np or Pu and Am atoms, as this tendency was prominent at the lower temperature.

Porosity correction is necessary to estimate the thermal conductivity with 100% TD (λ_{TD}) for the present handbook from the measured values (λ), with λ_{TD} being needed to compare the thermal conductivity of the actinide mononitrides. Arai *et al.* have

made this correction using the Maxwell–Eucken equation:

$$\lambda_{TD} = \frac{(1 + \beta P)\lambda}{(1 - P)} \quad [22]$$

where P is porosity and the constant β is related to the characteristics of pores in the matrix. Unity is a popular value of β , and is used in the case where samples are fabricated by a conventional powder-metallurgical route. However, it should be noted that β might be about 3 when samples have large and closed pores, especially when they are prepared by using pore formers, as pointed out by Arai *et al.*⁸⁶ On the other hand, Nishi *et al.*^{80,87,92} have made a porosity correction using the Schulz equation:

$$\lambda = \lambda_{TD}(1 - P)^X \quad [23]$$

They have proposed a parameter $X=1.5$ for closed pores that are spherical in shape. Among a variety of porosity correction formulas, eqn [23] was in the best agreement with the results of finite element computations in a wide range of porosities up to 0.3, as reported by Bakker *et al.*⁹³

2.03.4 Mechanical Properties

During irradiation in reactors, the fuel pellets are deformed by various processes, including densification, thermal expansion, swelling by fission products, and creep. This deformation may eventually lead to an interaction with the cladding, which has resulted in reactor failure. The elastic and plastic properties of fuel pellets, as well as creep rate, are very important,

given the above interaction. The swelling behavior is also important and is described in another chapter. Thermal expansion is discussed in this chapter.

2.03.4.1 Mechanical Properties of UN

The mechanical properties of UN have been summarized by Hayes *et al.*⁹⁴ A summary of the different measurements of creep rate is plotted in Figure 29. As the creep rate depends on many parameters such as stress level, stoichiometry, density, and impurity, as well as temperature, there is no systematic trend at each specific temperature. High temperature, steady state creep is generally expressed by the following equation,⁹⁴

$$\dot{\epsilon} = Ad^{-m}\sigma^n \exp\{-Q/RT\} \quad [24]$$

where $\dot{\epsilon}$ is creep rate, A is a constant, d is grain size, σ is stress, m is the grain size exponent, n is the stress exponent, Q is the activation energy, R is the gas constant, and T is the temperature. n and m are involved in the creep mechanism, and the value of n is especially important in determining the mechanism that controls the creep. Hayes *et al.* have tried to estimate the n values using several creep data sets reported in individual studies, and they have found that almost all n values were in the range of 4.0–5.9, suggesting a dislocation climb mechanism in UN. Assuming a dislocation climb mechanism, where creep rate does not depend on grain size, with an average n value of 4.5, and an m value of zero, the following correlation⁹⁴ is suggested;

$$\dot{\epsilon} = 2.054 \times 10^{-3} \sigma^{4.5} \exp\{-39369.5/T\} \quad [25]$$

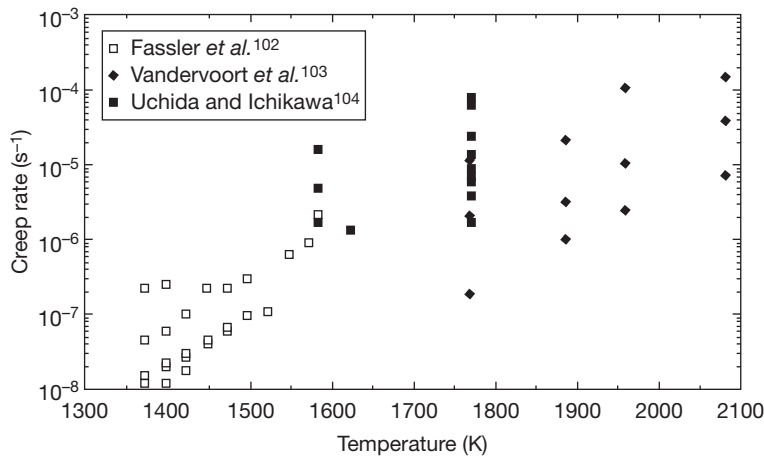


Figure 29 Experimental data for steady state creep rate of UN. Reproduced from Hayes, S. L.; Thomas, J. K.; Peddicord, K. L. *J. Nucl. Mater.* **1990**, 171, 271–288, with permission from Elsevier.

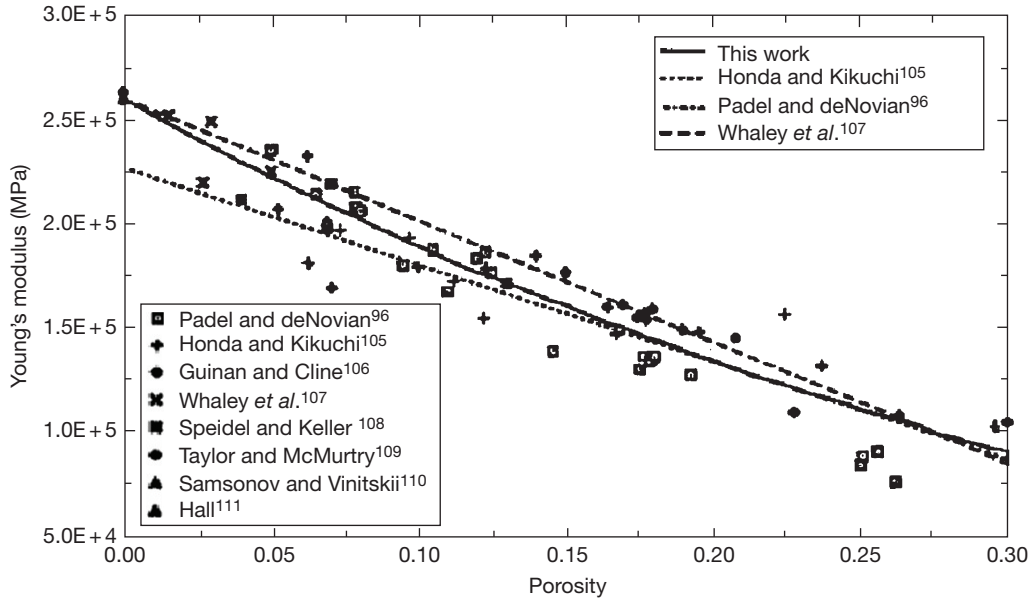


Figure 30 Measured Young's modulus and fitting curves for UN. Reproduced from Hayes, S. L.; Thomas, J. K.; Peddicord, K. L. *J. Nucl. Mater.* **1990**, 171, 271–288, with permission from Elsevier.

This equation is valid only for the creep of theoretically dense UN in the temperature range of 1770–2083 K and under stress ranging from 20 to 34 MPa. It has been reported that if the density of UN is below the TD, the creep rate can be obtained by multiplying it with the following factor,⁹⁵

$$f(p) = \frac{0.987}{(1-p)^{27.6}} \exp\{-8.65p\} \quad [26]$$

where p is the porosity.

Various measurements of Young's modulus at room temperature are summarized in Figure 30. Young's modulus depends not only on temperature but also on porosity. The variation in Young's modulus, as a function of porosity, has been measured by two different methods, velocity measurement and frequency measurement; but no clear difference between the results of these two methods has been found. A power law relation was fitted to these experimental data at room temperature and was combined with the linear temperature dependence data reported by Padel and deNovion⁹⁶ and the following correlation was obtained⁹⁴:

$$E = 0.258D^{3.002}[1 - 2.375 \times 10^{-5}T] \quad [27]$$

where E is the Young's modulus and D is the ratio of density with TD in percent. This equation is valid where the ratio of TD is from 75% to 100% and the temperature ranges from 298 to 1473 K. As this equation fits well with all the experimental data obtained

from samples with uncontrolled pore shape and orientation, porosity distribution, average grain size, grain shape, orientation, and impurities, as shown in Figure 30, the dependence of Young's modulus on these parameters is small.

The following correlation⁹⁴ of the shear modulus with density and temperature was obtained by a method similar to that used for determining the Young's modulus:

$$G = 1.44 \times 10^{-2}D^{3.446}[1 - 2.375 \times 10^{-5}T] \quad [28]$$

where G is the shear modulus. This relation is valid under the same density and temperature conditions as the Young's modulus.

As the data for the bulk modulus could not be measured directly and was calculated from measurements of Young's and shear modulus in the various studies, the degree of data scatter is larger here, compared to the other properties. The following correlation⁹⁴ with density and temperature was obtained in a method similar to that used for Young's modulus and shear modulus:

$$K = 1.33 \times 10^{-3}D^{4.074}[1 - 2.375 \times 10^{-5}T] \quad [29]$$

where K is the bulk modulus.

Poisson's ratio for UN was assumed to be independent of temperature. Similar to the bulk modulus, Poisson's ratio can be estimated from measurements of Young's modulus and shear modulus, and small errors in measurements of Young's and shear

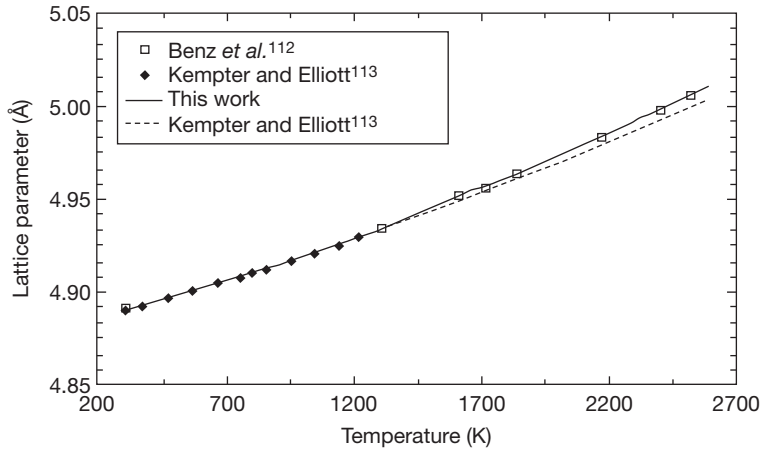


Figure 31 Variation of lattice parameter of UN with temperature. Reproduced from Hayes, S. L.; Thomas, J. K.; Peddicord, K. L. *J. Nucl. Mater.* **1990**, 171, 262–270, with permission from Elsevier.

modulus have resulted in the large scatter of these calculations. Under the assumption that Poisson's ratio is independent of temperature, the following correlation⁹⁴ with porosity is obtained:

$$\nu = 1.26 \times 10^{-3} D^{1.174} \quad [30]$$

where ν is Poisson's ratio and D is the density ranging 70–100%.

The hardness values, which are easily obtained experimentally, decreased with porosity and temperature. The hardness decrease with porosity linearly and decrease with temperature exponentially. In the porosity range of 0–0.26 and the temperature range of 298–1673 K, the following correlation⁹⁴ is valid:

$$\text{HD} = 951.8 \{1 - 2.1p\} \exp\{-1.882 \times 10^{-3} T\} \quad [31]$$

where HD is the diamond point hardness.

2.03.4.2 Thermal Expansion of UN

The thermal expansion of UN has also been estimated by Hayes *et al.*⁵⁶, as shown in **Figure 31**. As thermal expansion, measured by the dilatometer method, is affected by sample density and has a large degree of uncertainty, thermal expansion was calculated from the temperature dependence of the lattice parameter. The lattice parameter also is influenced by impurities, but the variation due to impurities is much less than the variation with temperature.

The temperature dependence of lattice parameter⁵⁶ is given by:

$$a = 4.879 + 3.254 \times 10^{-5} T + 6.889 \times 10^{-9} T^2 \quad [32]$$

where a is the lattice parameter in Angstroms. The linear thermal expansion coefficient⁵⁶ is given by:

$$\alpha = 7.096 \times 10^{-6} + 1.409 \times 10^{-9} T \quad [33]$$

where α is the mean linear thermal expansion coefficient and T is temperature.

2.03.4.3 Mechanical Properties of PuN

There are very few studies on the mechanical properties of pure PuN. Matzke¹ has reported the elastic moduli of $(\text{U}_{0.8}\text{Pu}_{0.2})\text{N}$ at room temperature, the porosity dependence of its Young's modulus, its Poisson ratio, and the temperature dependence of its elastic moduli. The Young's modulus of $(\text{U}_{0.8}\text{Pu}_{0.2})\text{N}$ is about 5% higher than that of pure UN. According to Matzke, the room temperature hardness of pure PuN is 3.3 GPa, about half that of UN.

Thermal expansion of PuN has been recently reexamined by Takano *et al.*²² The temperature dependence of the lattice parameter of PuN a_T (nm) can be expressed as

$$a_T = 0.48913 + 4.501 \times 10^{-6} T + 6.817 \times 10^{-10} T^2 - 4.939 \times 10^{-14} \quad [34]$$

The linear thermal expansion of PuN is higher than that of UN, as shown in **Figure 32**.²²

The recent progress in material chemistry calculation techniques has enabled the prediction of those properties of the actinide compounds which have not been experimentally measured. **Figure 33** shows the temperature dependence of the linear

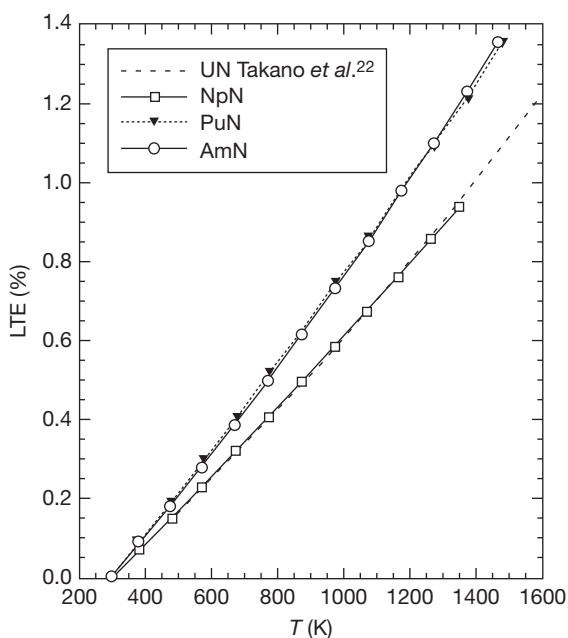


Figure 32 Temperature dependence of linear thermal expansion of PuN. Reproduced from Takano, M.; Akabori, M.; Arai, Y.; Minato, K. *J. Nucl. Mater.* **2008**, 376, 114–118, with permission from Elsevier.

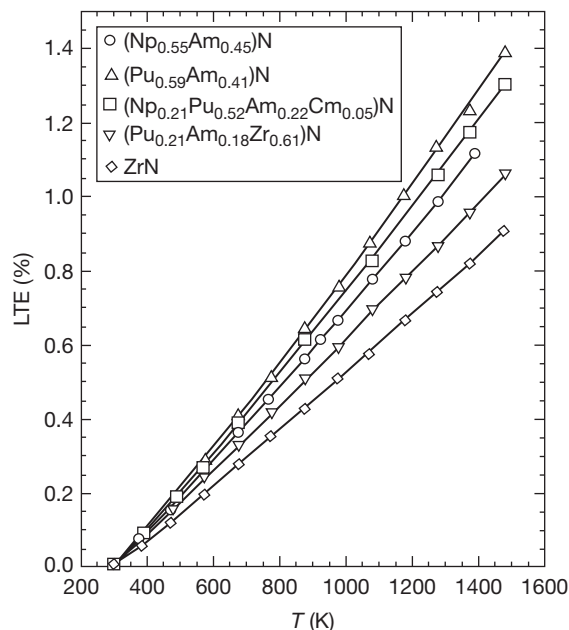


Figure 34 Temperature dependence of linear thermal expansion of minor actinide containing nitride fuels. Reproduced from Takano, M.; Akabori, M.; Arai, Y.; Minato, K. *J. Nucl. Mater.* **2009**, 389, 89–92, with permission from Elsevier.

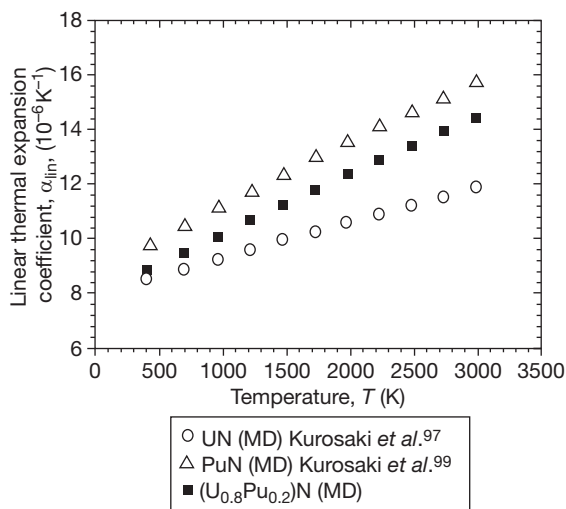


Figure 33 Temperature dependence of calculated linear thermal expansion of PuN. Reproduced from Kurosaki, K.; Yano, K.; Yamada, K.; Uno, M.; Yamanaka, S. *J. Alloys Compd.* **2001**, 319, 253–257, with permission from Elsevier.

thermal expansion of PuN which was calculated by a molecular dynamic method.⁹⁷ It is seen that the calculation predicts a high thermal expansion of PuN and an increase in the thermal expansion of (U,Pu)N

by doping with Pu. This calculation study also reported the compressibility and other thermal and thermodynamic properties of PuN.

2.03.4.4 Mechanical Properties of Other MA or MA-Containing Fuels

Recent studies on MA-containing fuels have measured the thermal expansion of various Np–Pu–Am–Cm–N compounds (shown in Figure 34⁹⁸), as well as those of NpN and AmN (Figure 32). As shown in Figure 32, the thermal expansion of AmN is the same as that of PuN; however, the thermal expansion of NpN is smaller than PuN and AmN, but is the same as that of UN. The thermal expansion of Np–Pu–Am–Cm–N fuels decreases with a decrease in Np content, as shown in Figure 34. The thermal expansion of ZrN inert matrix fuels also decreases due to the low thermal expansion of ZrN. Molecular dynamics (MD) calculations have also predicted the thermal expansion of some MA nitrides; these are shown in Figure 35.⁹⁹

The lack of data on MA nitrides, especially the nitrides of pure transuranium elements, is due to the difficulty in obtaining and treating bulk samples. There have been some attempts to calculate the

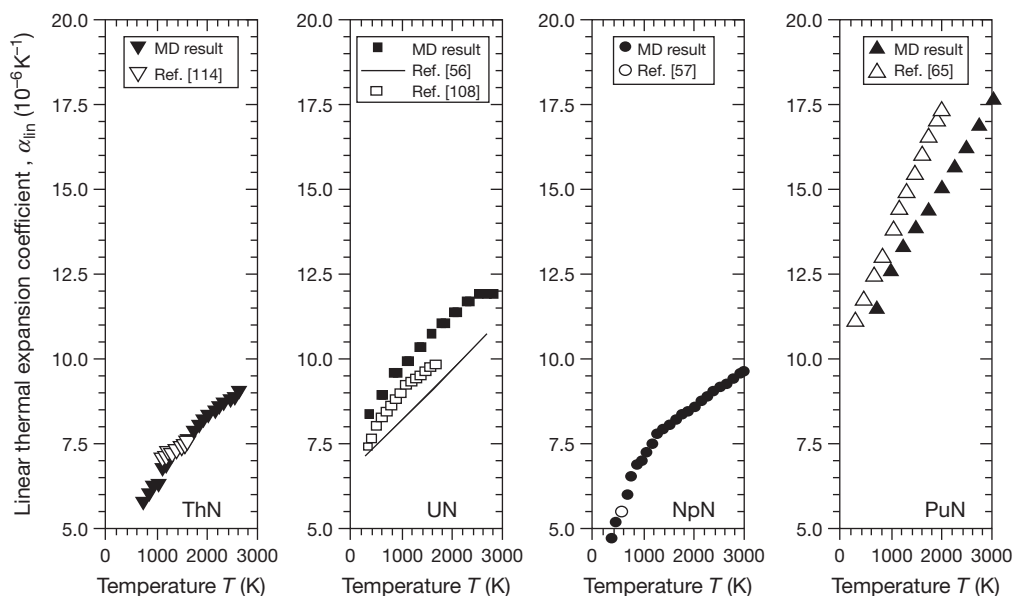


Figure 35 Temperature dependence of calculated linear thermal expansion of minor actinide nitrides. Reproduced from Kurosaki, K.; Adachi, J.; Uno, M.; Yamanaka, S. *J. Nucl. Mater.* **2005**, *344*, 45–49, with permission from Elsevier.

mechanical properties of these actinide nitride samples. One such attempt combined the calculations for longitudinal velocity and porosity.¹⁰⁰ In the method employed, a newly proposed correlation between Poisson's ratio and the ultrasonic longitudinal velocity was utilized, and the elastic properties of uranium nitride as well as uranium dioxide were estimated from the porosity and longitudinal velocity derived from ultrasonic sound velocity measurements; these had been previously used to determine mechanical properties of actinide materials. Another method estimated fracture toughness from the Young's modulus, hardness, the diagonal length and the length of micro cracks. Except for Young's modulus, all the other properties were obtained by an indentation method.¹⁰¹ In this study, not only was the fracture toughness reported, but its load dependence, in the case of UN, was also reported.

2.03.5 Summary

In this chapter, various properties of actinide nitrides have been discussed. As nitride fuels have some advantages over the oxide fuels, thermal and thermodynamic properties of UN, PuN and their solid solutions have been thoroughly studied. On the other hand, some properties (especially physical) need bulk samples for measurements, especially the trans-uranium elements such as NpN, AmN, and CmN;

these are difficult to obtain and handle and are scarce. Some properties of the inert matrix fuels such as (An,Zr)N solid solution and AnN and TiN mixture have been obtained through recent studies on the targets for transmutation in an ADS. Recent progress in experimental procedures and estimation methods, which are supported by developments in model calculation, have also been discussed.

The progress made in experimental techniques and calculation science has brought about growth in the understanding of the behavior of these nitrides. However, we need to accumulate more data, especially in the thermal and mechanical properties around 1673 K, in-reactor temperature, and the variation of those with burnup, in order to accurately predict the in-reactor behavior of these fuels (see [Chapter 3.02, Nitride Fuel](#)).

References

1. Matzke, H. J. *Science of Advanced LMFBR Fuels*; North Holland: Amsterdam, 1986.
2. Levinskii, Yu. V. *Atom. Energ.* **1974**, *37*(1), 216–219; *Sov. Atom. Energ. (Engl. Transl.)* **1974**, *37*(1), 929–932.
3. Bugl, J.; Bauer, A. A. *J. Am. Ceram. Soc.* **1964**, *47*(9), 425–429.
4. Inouye, H.; Leitnaker, J. M. *J. Am. Ceram. Soc.* **1968**, *51*(1), 6–9.
5. Gingerich, K. A. *J. Chem. Phys.* **1969**, *51*(10), 4433–4439.

6. Olson, W. M.; Mulford, R. N. R. *J. Phys. Chem.* **1963**, 67(4), 952–954.
7. Tagawa, H. *J. Nucl. Mater.* **1971**, 41(3), 313–319.
8. Chevalier, P. Y.; Fischer, E.; Cheynet, B. *J. Nucl. Mater.* **2000**, 280, 136–150.
9. Hansen, M.; Anderko, K. *Constitution of Binary Alloys*; McGraw-Hill: New York, 1958.
10. Elliott, R. P. *Constitution of Binary Alloys, First Supplement*; McGraw-Hill: New York, 1965.
11. Shunk, F. A. *Constitution of Binary Alloys, Second Supplement*; McGraw-Hill: New York, 1969.
12. Storms, E. K. *Special Report to the Phase Equilibria Program*; American Ceramic Society: Westerville, OH, 1989.
13. Muromura, T.; Tagawa, H. *J. Nucl. Mater.* **1979**, 79, 264.
14. Benz, R.; Bowman, M. G. *J. Am. Chem. Soc.* **1966**, 88(2), 264.
15. Wriedt, H. A. *Bull. Alloys Phase Diagrams* **1989**, 10, 593.
16. Kleykamp, H. *J. Nucl. Mater.* **1999**, 275, 1–11.
17. Joseph, M.; Sivakumar, N.; Manoravi, P. *Annu. Nucl. Energ.* **2004**, 31, 1163–1175.
18. Benz, R.; Hoffman, C. G.; Rupert, G. N. *J. Am. Chem. Soc.* **1967**, 89, 191–197.
19. Benz, R.; Zachariasen, W. H. *Acta Crystallogr.* **1969**, 21, 838.
20. Uno, M.; Katsura, M.; Miyake, M. *J. Alloys Compd.* **1986**, 121, 615–619.
21. Uno, M.; Katsura, M.; Miyake, M. *Inorg. Chim. Acta* **1987**, 140, 123–126.
22. Takano, M.; Akabori, M.; Arai, Y.; Minato, K. *J. Nucl. Mater.* **2008**, 376, 114–118.
23. Takano, M.; *et al.* Synthesis of americium mononitride by carbothermic reduction method. In: *Proceedings Global '99*, Jackson Hole, WY, Aug 29–Sept 3, 1999; CD-ROM, 1999.
24. Minato, K.; *et al.* *J. Nucl. Mater.* **2003**, 320, 18–24.
25. Olson, W. M.; Mulford, R. N. R. *J. Phys. Chem.* **1966**, 70, 2932–2934.
26. Suzuki, Y.; Arai, Y. *J. Alloys Compd.* **1998**, 271–273, 577–582.
27. Potter, P. E. *J. Nucl. Mater.* **1973**, 47, 7.
28. Williams, J.; Sambell, R. A. *J. Less Common Met.* **1959**, 1, 217–226.
29. Katsura, M.; Naoumidis, A.; Nickel, H. *J. Nucl. Mater.* **1970**, 36, 169–179.
30. Bradbury, M. H.; Matzke, H. *J. Nucl. Mater.* **1980**, 91, 13–22.
31. Ogawa, T.; Shirasu, Y.; Minato, K.; Serizawa, H. *J. Nucl. Mater.* **1997**, 247, 151–157.
32. Sood, D.; Argarwal, R.; Venugopal, V. *J. Nucl. Mater.* **1997**, 247, 293–300.
33. Walker, C. T. *Nucl. Technol.* **1978**, 39, 289–296.
34. Ogawa, T.; Ohmichi, T.; Maeda, A.; Arai, Y.; Suzuki, Y. *J. Alloys Compd.* **1995**, 224, 55–59.
35. Itoh, A.; Akaboti, M.; Takano, M.; Ogawa, T.; Numata, M.; Itonaga, F. *J. Nucl. Sci. Technol.* **2002**, (Suppl. 3), 737–740.
36. Ciriello, A.; *et al.* *J. Alloys Compd.* **2009**, 473, 265–271.
37. Thetford, R.; Mignaneli, M. *J. Nucl. Mater.* **2003**, 320, 44–53.
38. Jolkonen, M.; Streit, M.; Wallenius, J. *J. Nucl. Sci. Technol.* **2004**, 41, 457–465.
39. Benedict, U. The solubility of solid fission products in carbides and nitrides of uranium and plutonium, part II: Solubility rules based on lattice parameter differences, EUR 5766EN; 1977.
40. Arai, Y.; Nakajima, K. *J. Nucl. Mater.* **2000**, 281, 244–247.
41. Olson, W. M.; Mulford, R. N. R. *J. Phys. Chem.* **1965**, 69, 1223–1226.
42. Olson, W. M.; Mulford, R. N. R. *J. Phys. Chem.* **1964**, 68, 1048–1051.
43. Eron'yan, M. A.; Avarbe, R. G.; *et al.* *Izv. Akad. Nauk Sssr Neorg. Mater.* **1976**, 12, 247–249.
44. Ikeda, Y.; Tamaki, M.; Matsumoto, G. *J. Nucl. Mater.* **1976**, 59, 103–111.
45. Prins, G.; Cordfunke, E. H. P.; Depaus, R. *J. Nucl. Mater.* **1980**, 89, 221–228.
46. Hayes, S. L.; Thomas, J. K.; Peddicor, K. L. *J. Nucl. Mater.* **1990**, 171, 300–318.
47. Alexander, C. A.; Ogden, J. S.; *et al.* *Trans. Am. Nucl. Soc.* **1969**, 12, 581.
48. Vozzella, P. A.; DeCrescente, M. A. Thermodynamic Properties of Uranium Mononitride, Pratt and Whitney Aircraft Co., PWAC-479; 1965.
49. Bugle, J.; Bauer, A. A. *J. Am. Ceram. Soc.* **1964**, 47, 425–429.
50. Eron'yan, M. A.; Avarbe, R. G.; *et al.* *Teplofizika Vysokikh Temp.* **1976**, 14, 398–399.
51. Touloukian, Y. S. *et al.*, Eds. *Thermophysical Properties of Matter*; IFI/Plenum: New York, 1977; Vol. 13.
52. Houska, C. R. *J. Phys. Chem. Solids* **1964**, 25, 359–366.
53. Smirnov, V. S.; Kosukhin, V. V.; *et al.* *Izv. Akad. Nauk Sssr Neorg. Mater.* **1991**, 27, 2565–2569.
54. Timofeeva, I. I.; Shvedova, L. K.; *et al.* *Izv. Akad. Nauk Sssr Neorg. Mater.* **1972**, 8, 1169–1170.
55. Brundiers, G. D. Herstellung, Aufbau und Eigenschaften von Hafnium-verbindungen im System Hf-C-N-O, KFK 2161; 1975.
56. Hayes, S. L.; Thomas, J. K.; Peddicord, K. L. *J. Nucl. Mater.* **1990**, 171, 262–270.
57. Aldred, A. T.; Dunlap, B. D.; Harvey, A. R.; Lander, D. J. G. H.; Muller, M. H. *Phys. Rev. B* **1974**, 9, 3766–3779.
58. Benedict, U.; Dufour, C.; *et al.* *J. Nucl. Mater.* **1978**, 73, 208–212.
59. Kruger, O. L.; Moser, S. B. USAEC Report ANL-7155: 105; 1965.
60. Venugopal, V.; Kulkarni, S. G.; Subbanna, C. S.; Sood, D. D. *J. Nucl. Mater.* **1992**, 186, 259–268.
61. Suzuki, Y.; Maeda, A.; Arai, Y.; Ohmichi, T. *J. Nucl. Mater.* **1992**, 188, 239–243.
62. Alexander, C. A.; Ogden, J. S.; Pardue, W. H. *J. Nucl. Mater.* **1969**, 31, 13–24.
63. Ackermann, R. J.; Rauh, E. G. *J. Phys. Chem.* **1969**, 73, 769–778.
64. Green, D. W.; Reedy, G. T. *J. Chem. Phys.* **1978**, 69, 552–555.
65. Alexander, C. A.; Clark, R. B.; Kruger, O. L.; Robins, J. L. *Plutonium and Other Actinide* 1975; North-Holland: Amsterdam, 1976; p 277.
66. Pardue, W. M.; Storhok, V. W.; Smith, R. A. *Plutonium* 1965; Chapman and Hall: London, 1967; p 721.
67. Campbell, G. M.; Leary, J. A. *J. Phys. Chem.* **1966**, 70, 2703–2707.
68. Kent, R. A.; Leary, J. A. *High Temp. Sci.* **1969**, 1, 176–183.
69. Sheth, A.; Leibowitz, L. ANL-AFP-2, Argonne National Laboratory; Chemical Engineering Division: Argonne, WI, 1975.
70. Nakajima, K.; Arai, Y.; Suzuki, Y. *J. Nucl. Mater.* **1997**, 247, 33–36.
71. Ackermann, R. J.; Rauh, E. G. *J. Chem. Thermodyn.* **1975**, 7, 211–218.
72. Takano, M.; Itoh, A.; Akabori, M.; Minato, K.; Numata, M. In *Proceedings of GLOBAL 2003, Study on the Stability of AmN and (Am,Zr)N*, New Orleans, LA, Nov 16–20, 2003; p 2285, CD-ROM.

73. Conway, J. B.; Flagella, P. N. GEMP-1012; 1969.
74. Blank, H. In *Materials Science and Technology*; Nuclear Materials; VCH: Weinheim, 1994; Vol. 10A, p 203.
75. Oetting, F. L. *J. Chem. Thermodyn.* **1978**, *10*, 941–948.
76. Matsui, T.; Ohse, R. W. *High Temp. High Press.* **1987**, *19*, 1–17.
77. Alexander, C. A.; Ogden, J. S.; Pardue, W. M. Thermophysical properties of (UPu)N. In *Plutonium 1970 and Other Actinides PT.1*; 1970, 17, 95–103.
78. Kandan, R.; Babu, R.; Nagarajan, K.; Vasudeva Rao, P. R. *Thermochim. Acta* **2007**, *460*, 41–43.
79. Nishi, T.; Itoh, A.; Takano, M.; *et al.* *J. Nucl. Mater.* **2008**, *377*, 467–469.
80. Nishi, T.; Takano, M.; Itoh, A.; *et al.* *IOP Conf. Ser. Mater. Sci. Eng.* **2010**, *9*, 012017.
81. Cordfunke, E. H. P.; Konings, R. J. M.; Potter, P. E.; Prins, G.; Rand, M. H. *Thermochemical Data for Reactor Materials and Fission Products*; Elsevier: Amsterdam, 1990; p 667.
82. Chase, M. W.; Curnutt, J. L.; Prophet, H. *JANAF Thermochemical Tables*; Dow Chemical Co.: Midland, MA, 1965.
83. Johnson, G. K.; VanDeventer, E. H.; Kruger, O. L.; Hubbard, W. H. *J. Chem. Thermodyn.* **1969**, *1*, 89–98.
84. Oetting, F. L.; Rand, M. H.; Ackermann, R. J. *The Chemical Thermodynamics of Actinide Elements and Compounds, Part 1: The Actinide Elements*; IAEA: Vienna, 1976; p 87.
85. Nakajima, K.; Arai, Y.; Suzuki, Y. *J. Nucl. Mater.* **1999**, *275*, 332–335.
86. Arai, Y.; Suzuki, Y.; Iwai, T.; Ohmichi, T. *J. Nucl. Mater.* **1992**, *195*, 37–43.
87. Nishi, T.; Takano, M.; Itoh, A.; Akabori, M.; Arai, Y.; Minato, K. In *Proceedings of the Tenth OECD/NEA International Information Exchange Meeting on Actinide and Fission Product Partitioning and Transmutation, Thermal Conductivities of Neptunium and Americium Mononitrides*, Mito, Japan, Oct 6–10, 2008; 2010, CD-ROM.
88. Arai, Y.; Okamoto, Y.; Suzuki, Y. *J. Nucl. Mater.* **1994**, *211*, 248–250.
89. Arai, Y.; Nakajima, K.; Suzuki, Y. *J. Alloys Compd.* **1998**, *271–273*, 602–605.
90. Ganguly, C.; Hegde, P. V.; Sengupta, A. K. *J. Nucl. Mater.* **1991**, *178*, 234–241.
91. Keller, D. L. BMI-1845; 1968.
92. Nishi, T.; Takano, M.; Itoh, A.; Akabori, M.; Minato, K.; Kizaki, M. *J. Nucl. Mater.* **2006**, *355*, 114–118.
93. Bakker, K.; Kwast, H.; Cordfunke, E. H. P. *J. Nucl. Mater.* **1995**, *223*, 135–142.
94. Hayes, S. L.; Thomas, J. K.; Peddicord, K. L. *J. Nucl. Mater.* **1990**, *171*, 271–288.
95. Hayes, S. L.; Thomas, J. K.; Peddicord, K. L. Development of creep rate porosity correction factor; Advanced Nuclear Fuel Laboratory; Department of Nuclear Engineering, Texas A&M University, ANFL-10-O; 1989.
96. Padel, A.; deNovion, Ch. *J. Nucl. Mater.* **1969**, *33*, 40–51.
97. Kurosaki, K.; Yano, K.; Yamada, K.; Uno, M.; Yamanaka, S. *J. Alloys Compd.* **2001**, *319*, 253–257.
98. Takano, M.; Akabori, M.; Arai, Y.; Minato, K. *J. Nucl. Mater.* **2009**, *389*, 89–92.
99. Kurosaki, K.; Adachi, J.; Uno, M.; Yamanaka, S. *J. Nucl. Mater.* **2005**, *344*, 45–49.
100. Phani, K. K.; Sanyal, D.; Sengupta, A. K. *J. Nucl. Mater.* **2007**, *366*, 129–136.
101. Adachi, J.; *et al.* *J. Nucl. Mater.* **2009**, *384*, 6–11.
102. Fassler, M. H.; Hugel, F. J.; Decrescente, M. A. Compressive Creep of UC and UN, PWAC-482, Pratt and Whitney Aircraft Co., 1965.
103. Vandervoort, R. R.; Barmore, W. L.; Cline, C. F. *Trans. Met. Soc. AIME* **1968**, *242*, 1466.
104. Uchida, M.; Ichikawa, M. *J. Nucl. Mater.* **1973**, *49*, 91.
105. Honda, T.; Kikuchi, T. *J. Nucl. Sci. Technol.* **1968**, *6*, 59.
106. Guinan, M.; Cline, C. F. *J. Nucl. Mater.* **1971**, *43*, 205.
107. Whaley, H. L.; Potter, R. A.; Fulkerson, W. Ultrasonic Velocity Measurements in UN, ORNL-4370, Oak Ridge National Laboratory, 1968.
108. Speidel, E. O.; Keller, D. L. Fabrication and Properties of Hot-Pressed Uranium Mononitride, BMI-1633, Battelle Memorial Institute, 1963.
109. Taylor, K. M.; McMurtry, C. H. Synthesis and Fabrication of Refractory Uranium Compounds, ORO-400, Carborundum Co., 1961.
110. Samsnov, G. V.; Vinitskii, I. M. *Handbook of Refractory Compounds*; IFI/Plenum DATA Co.: New York, 1980; p 303.
111. Hall, A. R. *J. Nucl. Mater.* **1970**, *37*.
112. Benz, R.; Balog, G.; Baca, B. H. *High Temp. Sci.* **1970**, *15*, 221.
113. Kempter, C. P.; Elliot, R. O. *J. Chem. Phys.* **1959**, *30*, 1524.
114. Aronson, S.; Cisney, E.; Guingerich, K. A. *J. Am. Ceram. Soc.* **1967**, *50*(5), 248.
115. Gerds, A. F.; Mallet, M. W. *J. Electrochem. Soc.* **1954**, *101*, 175.

2.04 Thermodynamic and Thermophysical Properties of the Actinide Carbides

D. Manara and F. De Bruycker

European Commission, Joint Research Centre, Institute for Transuranium Elements, Karlsruhe, Germany

A. K. Sengupta, R. Agarwal, and H. S. Kamath

Bhabha Atomic Research Centre, Mumbai, India

© 2012 Elsevier Ltd. All rights reserved.

2.04.1	Introduction	89
2.04.1.1	Carbides	89
2.04.1.2	General Properties of Actinide Carbides	89
2.04.1.2.1	Structure of the matter	90
2.04.1.2.2	Phase stability	93
2.04.1.2.3	Preparation	93
2.04.1.2.4	Applications	95
2.04.2	Thorium Carbides	96
2.04.2.1	Phase Relationships	96
2.04.2.2	Physicochemical Properties	97
2.04.2.2.1	Crystallography	97
2.04.2.2.2	Thermodynamic properties	99
2.04.2.2.3	Transport properties	102
2.04.2.2.4	Mechanical properties	103
2.04.2.2.5	Optical properties	103
2.04.2.2.6	Multielement thorium carbides	104
2.04.3	Protactinium Carbides	104
2.04.3.1	Properties	105
2.04.4	Uranium Carbides	105
2.04.4.1	Phase Relationships	105
2.04.4.2	Physicochemical Properties	107
2.04.4.2.1	Crystallography	107
2.04.4.2.2	Thermodynamic properties	109
2.04.4.2.3	Transport properties	113
2.04.4.2.4	Mechanical properties	115
2.04.4.2.5	Optical properties	117
2.04.4.2.6	Multielement uranium carbides	118
2.04.5	Neptunium Carbides	121
2.04.5.1	Preparation	121
2.04.5.2	Properties	122
2.04.6	Plutonium Carbides	122
2.04.6.1	Phase Relationships	122
2.04.6.2	Physicochemical Properties	123
2.04.6.2.1	Triplutonium dicarbide Pu_3C_2	123
2.04.6.2.2	Plutonium monocarbide PuC	124
2.04.6.2.3	Plutonium sesquicarbide Pu_2C_3	125
2.04.6.2.4	Plutonium dicarbide	125
2.04.6.2.5	Vapor pressures	126
2.04.6.2.6	Transport properties	126
2.04.6.2.7	Mechanical properties	127
2.04.6.2.8	Optical properties	127
2.04.6.2.9	Plutonium carbide oxides and nitrides	127

2.04.7	Minor Actinide Carbides	128
2.04.7.1	Americium Carbides	128
2.04.7.2	Curium Carbides	128
2.04.8	Mixed Carbides	128
2.04.8.1	Thorium–Uranium Carbides	129
2.04.8.2	Plutonium–Uranium Carbides	130
2.04.9	Summary	133
References		133

Abbreviations

ADS	Accelerator-driven system
bcc	Body-centered cubic crystal structure
CALPHAD	CALculation of PHase Diagrams (Thermodynamic optimization of phase diagrams)
CIM	Conductivity integral margin to melting
DFT	Density functional theory
DOS	Density of states (density of quantum electronic states per energy unit per atom)
EAM	Embedded atom method
EMF	Electromotive force
EOS	Equation of state (equation relating the parameters of a thermodynamic system to its state functions)
fcc	Face-centered cubic crystal structure
GFR	Gas fast reactor
HTR	High-temperature reactor
HV	Vickers Hardness
LWR	Light water reactor
PCS	Principle of the corresponding states
SEM	Scanning electron microscope
SI	International System of units (Meter Kelvin Second Ampère)
SIMS	Secondary ion mass spectrometry
TB LMTO	Tight-binding linear muffin tin orbital
TOF	Time of Flight
Va	Vacancy
VHTR	Very high-temperature reactor
XRD	X-ray diffraction

Symbols

a	Lattice parameter
α_T	Linear thermal expansion coefficient; $\alpha_T = l_0^{-1}(dl/dT)$
$\bar{\alpha}_T$	Average linear thermal expansion coefficient

α_Y	Vaporization coefficient of species Y
B	Bulk modulus; $B = V^{-1}(\partial^2 E / \partial V^2)$
c	Lattice parameter (cell height in noncubic lattices)
c	Velocity of light in vacuum
c_{ij}	Adiabatic elastic constants (<i>ij</i> component of the elastic tensor)
C_p	Heat capacity at constant pressure
C_v	Heat capacity at constant volume
d	Crystal grain size
D_0	Diffusion coefficient
D_x^Y	Self-diffusion coefficient of species x in the compound Y
\bar{D}_x^Y	Chemical diffusion coefficient of species x in the compound Y
E	Young elastic modulus
E_F	Fermi Energy (Fermi level)
$G_{(x)}$	Gibbs free energy (of component x)
$H_{(x)}$	Enthalpy (of component x)
k_B	Boltzmann's constant
m	Mass
n	Refractive index (real part)
n	Neutron absorption (in nuclear reactions)
N	Number of electrons in a given state (e.g., $N(E_F)$ = number of electrons at the Fermi energy)
P	Porosity fraction
P	Total pressure
p_i	Partial pressure of the component <i>i</i>
q	Heat flux
Q_s	Activation energy for Soret's diffusion
Q_X	Activation energy for the diffusion of species X
R	Ideal gas constant
S	Entropy
t	Time
T	Absolute temperature
T_c	Critical temperature
T_m	Melting point (melting temperature)
T_N	Néel temperature

V	Volume
V_{FY}	Energy of formation of a vacancy for the species Y
V_{MY}	Energy of migration of a vacancy for the species Y
x	Stoichiometry parameter in carbides
x_Y	Molar fraction of species Y
y	Stoichiometry parameter in carbides
β	Beta decay (in nuclear reactions)
$\Delta_f A_Y$	Variation of the thermodynamic function A upon formation of compound Y
$\Delta_m A_Y$	Variation of the thermodynamic function A upon melting of compound Y
$\Delta_{mix} A$	Variation of the thermodynamic function A upon mixing
$\Delta_{sub} A_Y$	Variation of the thermodynamic function A upon sublimation of compound Y
$\Delta_{vap} A_Y$	Variation of the thermodynamic function A upon vaporization of compound Y
$\Delta_f G$	Gibbs free energy of formation
$\Delta_{vap} G$	Gibbs free energy of vaporization
$\Delta_f H$	Enthalpy of formation
$\Delta_m H$	Enthalpy of melting
$\Delta_{vap} H$	Enthalpy of vaporization
ϵ	Elastic deformation, elongation
$\dot{\epsilon}$	Deformation rate (creep)
$\epsilon, \epsilon_\lambda$	Spectral emissivity
ϵ_τ	Total emissivity
γ	Temperature coefficient of the electronic heat capacity
γ	Gamma decay (in nuclear reactions)
$\bar{\gamma}$	Average volumetric thermal expansion coefficient
κ	Optical absorption constant
λ	Wavelength of the electromagnetic radiation
λ	Thermal conductivity
λ_{PH}	Phonon contribution to the thermal conductivity
λ_E	Electron contribution to the thermal conductivity
ν	Poisson's ratio
θ_D	Debye's temperature
θ_E	Einstein's temperature
ρ	Density
ρ	Optical reflectivity
ρ_c	Critical density
σ	Axial stress
σ_c	Compressive rupture axial stress (compressive strength)

2.04.1 Introduction

Research on actinide carbides as nuclear fuel began in the 1950s. Then, uranium dioxide and mixed uranium–plutonium oxides began to be preferred as nuclear fuel in most of the Generation II and III power plants, due to the fact that the option of fast reactors for civil purposes had mostly been abandoned. This led to an abrupt interruption in actinide carbide research between the first half of the 1970s and the second half of the 1990s. In the last decade, there has been renewed interest in actinide carbides in view of a nuclear fuel more suitable for high burnup and high-temperature operation with a reduced ‘margin to melting,’ in the framework of the ‘Generation IV’ nuclear systems development.¹ Consequently, actinide carbides are now being studied with more and more advanced methods, both experimental and computational.

The goal of the present monograph is to summarize the state-of-the-art knowledge of the most relevant physical and chemical properties of actinide carbides. This work is largely based on a few earlier reviews on the same subject: Storms,² Rand,³ Holley *et al.*,⁴ Matzke,⁵ the Gmelin Handbooks,^{6–9} and the OECD-NEA reviews.^{10–13} More detailed and/or more recent data are taken from single references.

2.04.1.1 Carbides

Carbides are chemical compounds in which carbon bonds with less electronegative elements. Depending on the difference in electronegativity and the valence state of the constituting elements, they exist as different bonding types. Accordingly, they are classified as salt-like compounds (in which carbon is present as a pure anion and the other elements are sufficiently electropositive), covalent compounds (SiC and B₄C), interstitial compounds (with transition metals of the groups 4, 5, and 6 except chromium), and ‘intermediate’ transition metal carbides.¹⁴

In general, carbides display metallic properties, and they are mostly refractory (high melting). Their more specific properties depend on the constituting elements.

2.04.1.2 General Properties of Actinide Carbides

Actinides are known to form three main types of stoichiometric carbides (Table 1): monocarbides of the type AnC, sesquicarbides of the type An₂C₃,

and dicarbides of the type AnC_2 (sometimes called 'acetylides'). Mono- and dicarbides have been observed for protactinium, thorium, uranium, neptunium, and plutonium. Sesquicarbides have been identified for thorium, uranium, neptunium, plutonium, americium, and, recently, curium.

Other types of actinide carbides such as CmC_3 and Pu_3C_2 have been observed.

Data for mixed U–Th and U–Pu carbides, briefly summarized and discussed in the last section of this chapter, have mostly been indigenously collected from the few nuclear plants using this kind of fuel.¹⁵

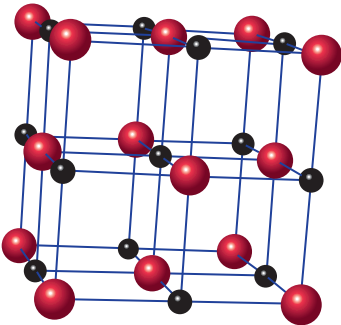
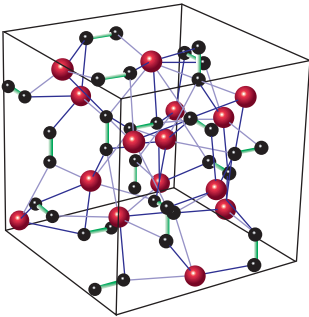
2.04.1.2.1 Structure of the matter

In general, actinide carbides are of the 'salt-like' type. In these compounds, carbon is present as single anions, ' C^{4-} ' in the monocarbides; as two atom

units, ' C_2^{2-} ' in the acetylides; and as three atom units, ' C_3^{2-} ' in the sesquicarbides. This model, useful for a first visual description of these materials, is physically inconsistent with their essentially metallic properties. The An–C bonds are certainly more covalent than ionic, as recently confirmed.¹⁶ Actinide compounds are characterized by a peculiar electronic structure, where the extended nature of the 5f electron wave functions yields a unique interplay between localized and band electrons. This feature leads, in particular, to properties associated with covalent bonding in these compounds, which show crystal structures normally associated with ionic bonding.⁵

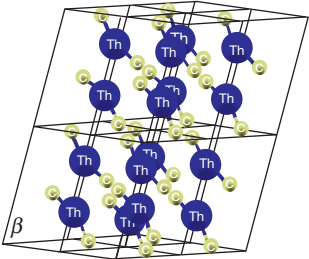
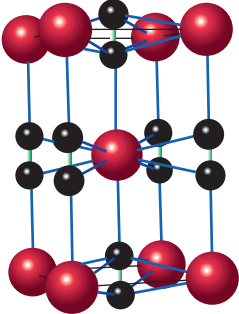
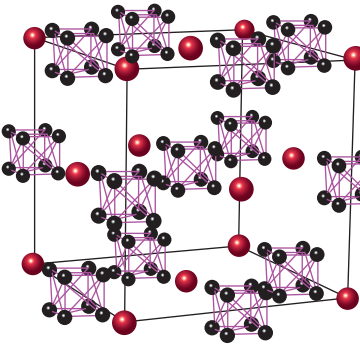
Monocarbides $\text{AnC}_{1\pm x}$ (An = Th, Pa, U, Np, Pu, Am) crystallize in the NaCl-type space group $Fm\bar{3}m$ – No. 225 (Table 1). The elementary cell is

Table 1 Synopsis of the known actinide carbides

Compound and lattice parameters	Composition and temperature range	Space group	Structure ● - Actinide; ● - C
$\text{ThC}_{1\pm x}$ 508.8 pm (Th) to 534.4 pm ($\text{ThC}_{0.98}$ in equilibrium with ThC_2)	C/Th = 0–1.96 Eutectic $\text{ThC}_{1\pm x} = 1980 \text{ K}$ Congruent $T_m = 2780 \text{ K}$ for C/Th = 0.975	NaCl-fcc $O_h^5 - Fm\bar{3}m$ (Nr.225)	
PaC 506.08 pm	–		
$\text{UC}_{1\pm x}$ 4.9605 Å ($\text{UC}_{1.0}$) 4.9563 Å ($\text{UC}_{0.93}$)	C/U = 0.82–1.86 $T_m = 2780 \text{ K}$ for C/U = 1		
$\text{NpC}_{1\pm x}$ 499.1 pm for $\text{NpC}_{0.82}$ to 501.0 pm for $\text{NpC}_{1.0}$	$0.82 \leq \text{C/Np} \leq 1.0$		
PuC_{1-x} $a = 498.13 - 1.50$ $(1 - \text{C/Pu})\text{pm}$	C/Pu = 0.74–0.94 $T_{\text{peritectic}} =$ $1910 \pm 20 \text{ K}$		
AmC_{1+x} 502 pm	$\text{AmC}_{1.04}$, $\text{AmC}_{1.25}$		
Th_2C_3 $855.13 \leq a \leq 856.09 \text{ pm}$ in a narrow homogeneity range	$\text{Th}_2\text{C}_{3-y}$ ($0 \leq y \leq 0.05$) Under high $p > 2.8 \text{ GPa}$	bcc – eight molecules per unit cell $T_d^6 - I\bar{4}3d$ (Nr.220)	
U_2C_3 808.99 pm	$\text{U}_2\text{C}_3 \rightarrow \text{UC} + \text{UC}_2$ (>2093 K)		
Np_2C_3 810.3 pm	–		
Pu_2C_3 $812.1 \leq a \leq 813.4$	C/Pu = 1.45–1.5 Stable under 2300 K		
Am_2C_3 827.57 pm	–		
Cm_2C_3 839.4 pm	–		

Continued

Table 1 Continued

Compound and lattice parameters	Composition and temperature range	Space group	Structure ● - Actinide; ● - C
α -ThC ₂ $a = 668.4 \pm 0.02$ pm; $b = 422.0 \pm 0.1$ pm; $c = 673.5 \pm 0.2$ pm; $\beta = 103.91 \pm 0.01^\circ$	ThC _{1.94} Stable up to 1713 K	Monoclinic C2/c (No. 15)	
β -ThC ₂ $a = 422.1$ pm; $c = 539.4$ pm (in equilibrium with graphite)	Stable for 1713 K $\leq T \leq 1768$ K	CaC ₂ -tetragonal $D_{4h}^{17} - I4/mmm$ (Nr. 139)	
α -PaC ₂ $a = 361$ pm; $c = 611$ pm	Observed around 2500 K		
α -UC ₂ $a = 352.45 + 0.75$ (C/U-1.80) pm; $c = 1.702a$	C/U = 1.75–1.9 UC ₂ \rightarrow U ₂ C ₃ + C (< 1790 K)		
Stable in range 1790–2050 K $T^m = 2720$ K	α UC ₂ \rightarrow UC + β UC ₂ (> 2050 K)		
α -PuC ₂ $a = 363$ pm; $c = 6.094$ Å	Stable for 1933 K $\leq T \leq 1983$ K		
γ -ThC ₂ $a = 581.3$ – 584.1 pm	Stable above 1768 K $T_m \cong 2883$ K	KCN-fcc $O_h^5 - Fm3m$ (Nr. 225)	
β -UC ₂ $a = 548.8$ pm	Stable above 2050 K $T_m \cong 2750$ K		
β -PuC ₂ $a = 572$ pm	Stable above 1983 K $T_m \cong 2520$ K		

Other actinide carbides with little information: PaC₂, NpC₂, probably isostructural to CaC₂, Pu₃C₂, stable between 300 and 800 K, but unknown structure; Cm₃C with fcc Fe₄N-like lattice with $a = 517.2 \pm 0.2$ pm.

represented by four formula units. The lattice parameter is dependent on the C/An ratio, and the oxygen and nitrogen impurities. The lattice parameter of pure monocarbides increases with the dissolution of carbon in the ideal face-centered cubic (fcc) lattice in an essentially linear manner.

The sesquicarbides of Th, U, Np, Pu, Am, and Cm have been identified to be body-centered cubic (bcc) of the $I\bar{4}3d$ type, with eight molecules per unit cell

(Table 1). This structure is more complex than that of the mono- and dicarbides, and is often difficult to form. Thus, Th₂C₃ was observed only under high pressure (2.8–3.5 GPa), and U₂C₃ is produced by a complex preparation procedure. Both decompose into a mixture of mono- and dicarbides at high temperatures. The situation is different in the case of Pu₂C₃, which is the most stable among the Pu carbides and forms easily at temperatures ranging from

room temperature to the melting point. Unlike the fcc modifications of mono- and dicarbides, sesquicarbides can hardly accommodate lattice defects; therefore, they essentially exist as line compounds.

Actinide dicarbides AnC_{2-x} have been observed in a larger variety of allotropes (Table 1). At intermediate temperatures, generally between 1700 and 2050 K, Th, U, Pu, and probably, Pa and Np, form tetragonal dicarbides of the type CaC_2 ($I4mmm$ – Group 139). Th also forms a monoclinic $C2/c$ (No. 15) substoichiometric dicarbide that is stable from room temperature to 1713 K. The high-temperature form of actinide dicarbides has been observed to be fcc of the type KCN, which belongs to the same symmetry group as NaCl, $Fm\bar{3}m$. Such structure, clearly established for γ - ThC_2 , was observed with more difficulty by high-temperature X-ray diffraction (XRD) for β - UC_2 and β - PuC_2 . The lattice transition between tetragonal and cubic fcc dicarbide ($\alpha \rightarrow \beta$ for U and Pu, $\beta \rightarrow \gamma$ for Th) is diffusionless of the martensitic type. It occurs very rapidly despite its important enthalpy change, mostly due to the lattice strain contribution. For this reason, the high-temperature cubic modification is impossible to quench to room temperature, hence the difficulty in investigating its properties. fcc allotropies of mono- and dicarbides are mostly miscible at high temperature, and for uranium and thorium, they can be considered as a single high-temperature cubic phase with a wide nonstoichiometry range. In fact, this solid solution can easily accommodate interstitial excess carbon atoms and lattice vacancies. The first ensure the existence of a broad hypostoichiometry range of the dicarbides, where most of the excess carbons form C_2 dumbbells in the $(\frac{1}{2}, 0, 0)$, $(0, \frac{1}{2}, 0)$, and $(0, 0, \frac{1}{2})$ positions as in the KCN lattice (see Table 1). The second are responsible for the existence of hypostoichiometric monocarbides An_{1-x} extending to the pure metal for thorium but only to a narrow UC_{1-x} domain for uranium. The situation is different for Pu carbides due to the high stability of Pu_2C_3 up to its melting point and to the fact that fcc plutonium monocarbide exists only in a vacancy-rich hypostoichiometric form, with $0.74 \leq C/Pu \leq 0.94$. This originality, common to other Pu compounds, is certainly related to the peculiar behavior of the six 5f electrons of plutonium, which exhibit behavior on the limit between valence and conduction, and can follow one or the other (or both) in different compounds.

The electronic (band) structure of actinide carbides has been studied rather extensively, both experimentally (by low-temperature calorimetry and X-ray

photoelectron spectroscopy, XPS) and theoretically (by tight-binding methods and, more recently, by density functional theory techniques). These compounds are, in general, good electronic and thermal conductors, with a nonzero density of electronic states at the Fermi level (Figure 1).

However, the actual filling of the levels largely depends on the peculiar behavior of the 5f electrons,

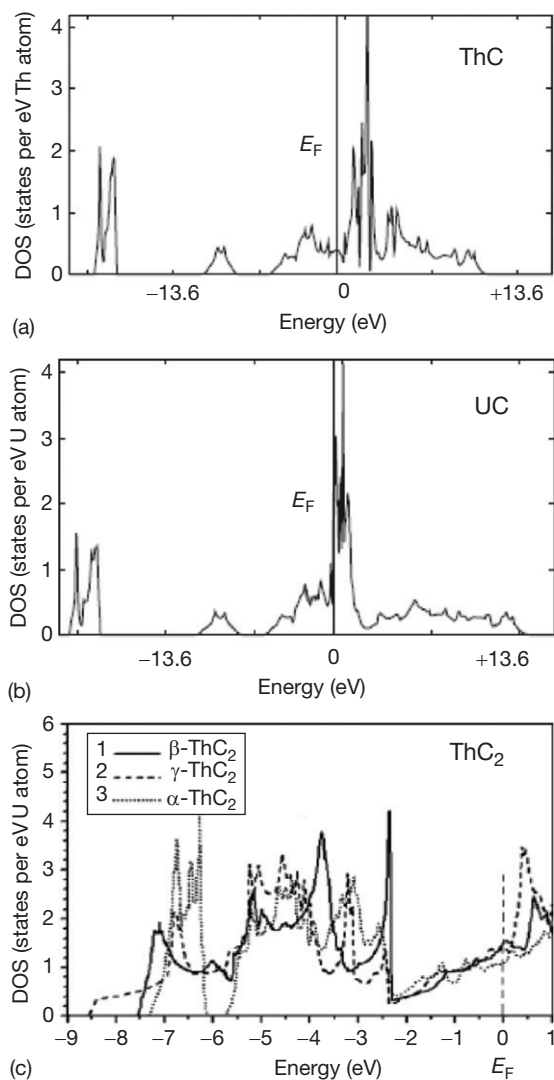


Figure 1 (a, b) The theoretical density of electronic states in thorium and uranium monocarbides. Reproduced from Das, T.; Deb, S.; Mookerjee, A. *Phys. B* **2005**, 367, 6–18. The original calculation was performed using Rydberg energy units. The agreement with low-temperature calorimetric measurements is only qualitative. (c) The theoretical density of electronic states in thorium dicarbides. Reproduced from Shein, I. R.; Ivanovskii, A. L. *J. Nucl. Mater.* **2009**, 393, 192–196.

which tend to be more localized or more itinerant according to the actinide and the compound involved. Thus, Pu carbides have much higher electrical resistivity than Th and U carbides. Similarly, mono- and dicarbides are better electronic conductors than sesquicarbides are. Magnetic transitions have been observed at low temperatures in sesquicarbides, and Np and Pu monocarbides.

The electronic structure dependence on defect and impurity concentrations has been studied in a number of cases. For example, in ThC_{1-x} , the density of states (DOS) increases with increasing carbon vacancy concentration. Auskern and Aronson¹⁷ showed by thermoelectric power and Hall coefficient measurements that a two-band conductivity model can be applied for ThC_{1-x} : the bands overlap more and the number of carriers increases with decreasing C/Th ratio. The valence bands have mainly a carbon 2p and a thorium 6d_γ character, while the Th-6d_ε character dominates the conduction bands. Also, the increase of the DOS at the Fermi level with vacancy concentration is due to the 6d thorium electronic states. In stoichiometric ThC, the 6d E_g states are hybridized with the 2p states of carbon and are split between low-energy bonding and high-energy antibonding states. In hypostoichiometric ThC_{1-x} , the 6d E_g dangling bonds contribute to an increase of the DOS in the vicinity of the Fermi level.¹⁸

For uranium carbides, it was shown that, following the general rules of Hill¹⁹ that imply that U–U distance is $< 3.54 \text{ \AA}$, these compounds exhibit a metallic electronic structure due to the overlaps of f-orbitals. This rule applies to uranium monocarbide for which the U–U distance is 3.50 \AA , as shown by experimental measurements as well as by *ab initio* calculations.^{20,21} For hyperstoichiometric uranium carbides, the metallic character persists and the C–C bonds are covalent as in graphite. In an X-ray and ultraviolet photoelectron spectroscopy (XPS and UPS) study of sputtered UC_x thin films ($0 < x < 12$), Eckle *et al.*²² showed that the U-4f core levels do not change strongly with increasing carbon content, and demonstrated the predominantly itinerant character of U-5f electrons. Similarly, valence region spectra show three types of carbon species for different UC_x films, which are differentiated by their C-2p signals. A strong hybridization between C-2p and U-5f states is detected in UC, while the C-2p signal in UC_2 appears only weakly hybridized, and for higher carbon contents, a π -band characteristic of graphite appears.

Calculated charge distribution maps for stoichiometric fcc ThC and tetragonal β - ThC_2 ²³ are shown

in Figure 2, giving an idea of the covalent or ionic nature of the different bonds in these structures.

The analysis by Shein *et al.*²³ revealed that bonding in ThC_2 polymorphs is of a mixed covalent–ionic–metallic character. That is, the covalent bonding is formed due to the hybridization effects of C–C states (for C_2 dumbbells) and C_2 –Th states. In addition, ionic bonds emerge between the thorium atoms and C_2 dumbbells owing to the charge transfer $\text{Th} \rightarrow \text{C}_2$, with about 1.95 electrons redistributed between the Th atoms and C_2 dumbbells. The metallic Th–Th bonds are formed by near-Fermi delocalized d and f states. Similar charge distributions have been calculated for uranium carbides.²⁴

2.04.1.2.2 Phase stability

The composition versus temperature phase diagram constitutes the most basic information for each carbide system, fundamental to correlate thermophysical, thermodynamic, and chemical data of compounds in a consistent way. Thus, phase stability data are first given for each actinide carbide system, followed by a review of the available information on physicochemical data.

Although the general properties have been assessed, especially for the most studied systems, Th–C, U–C, and Pu–C, doubts still remain about the effective stability or ‘meta’-stability of certain crucial phases (e.g., UC_2 at room temperature). The current phase diagrams, often completed with newer data and assessed by more recently developed thermodynamic optimization methods (CALPHAD), seem to generally, but not always, confirm the data obtained in the 1950s–1960s with traditional thermal analysis techniques. The discrepancies are sometimes linked to the deviation of the samples investigated from an ideal behavior, mostly due to oxygen and nitrogen contamination, a well-known and common issue related to carbides.

A short discussion of the most common actinide carbide oxides and carbide nitrides is, therefore, presented, with the goal of providing a hint of the main effects of oxygen and nitrogen additions on the physicochemical properties of pure carbides.

2.04.1.2.3 Preparation

Actinide mono- and dicarbides for research purposes are preferentially prepared by arc-melting a mixture of metal and graphite in the right proportions. This process is normally performed under ~ 1 bar of helium or argon. Special care is needed to avoid oxygen, nitrogen, and water impurities in the furnace.

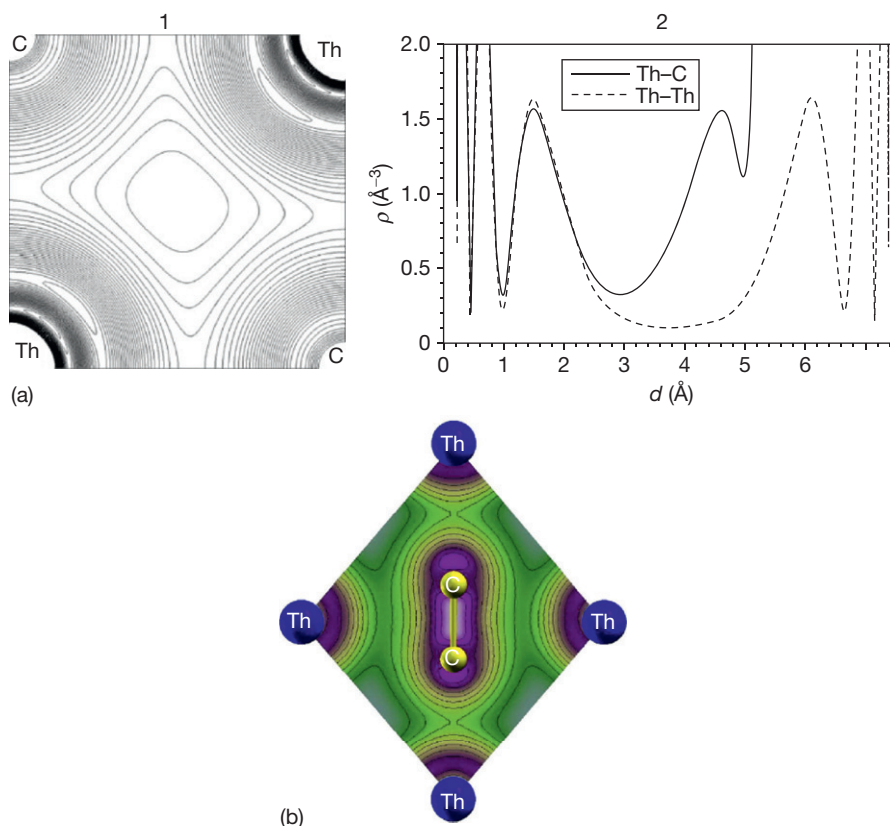
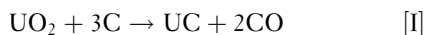


Figure 2 DFT calculations of (a) 1 – charge density map and 2 – charge density profiles along the Th–C and Th–Th bonding lines in the (100) plane of face-centered cubic ThC (reproduced from Shein, I. R.; Shein, K. I.; Ivanovskii, A. L. *J. Nucl. Mater.* **2006**, 353, 19–26). (b) Charge density map in the (110) plane of tetragonal β -ThC₂ (reproduced from Shein, I. R.; Ivanovskii, A. L. *J. Nucl. Mater.* **2009**, 393, 192–196).

The preparation of oxygen and nitrogen-free carbides is hardly possible.

Probably the most used method for industrial applications is the carbothermic reaction of AnO₂, based on a reaction of the type:

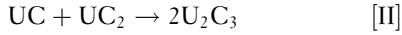


normally performed under vacuum (1.25×10^{-5} bar) at 1700–1850 K for 4 h.

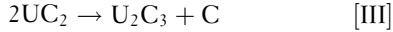
Other possible preparation methods are reaction of An hydrides with carbon, aluminothermic reaction of AnF₄, pyrolytic reaction of AnCl₄ with CH₄, and An–Hg amalgam distillation in a hydrocarbon atmosphere. Single crystals have been obtained by electron-beam melting, quenching, and annealing of polycrystalline samples. Potter²⁵ showed that carbothermic reduction of PuO₂ cannot yield oxygen-free Pu monocarbide, because the very high Pu pressures corresponding to the Pu₂C₃–PuC_{1–x}O_x equilibrium would lead to the formation of Pu₂O₃ or Pu₂C₃ in equilibrium with PuC_{1–x}.

The preparation of sesquicarbides is more complicated. Th₂C₃ and U₂C₃ have been obtained with complex experimental procedures, whereas the preparation of Pu₂C₃ is rather straightforward, thanks to the high thermodynamic stability of this phase. Th₂C₃ was successfully synthesized by Krupka and coworkers^{26,27} starting from arc-melted 57–67 at.% C alloys then sintered in a belt-type high pressure die under a pressure of 2.8–3.5 GPa between 1323 and 1623 K for 1 h.

The preparation of U₂C₃ is extremely difficult and it commonly requires a long (~ 1 day) annealing of a two-phase UC + UC₂ metastable starting material in a narrow temperature range, between approximately 1720 and 1900 K. The annealing time can be reduced to a few minutes under particular conditions, for example, under high pressure or in a suitable atmosphere. Several ways of preparing U₂C₃ have been successfully explored. They can be regrouped in two main categories: those employing the ‘synthetic reaction’



and those based on the ‘decomposition reaction’



Several methods based on the synthetic reaction are available in the literature. For example, Matzke and Politis⁵ obtained U_2C_3 by annealing cast $\text{UC}_{1.5}$ two-phase samples at 1720 K for 20 h under high vacuum. U_2C_3 was also obtained by Krupka²⁸ at 1220 K under a pressure of 15 kbar for 2.75 min. In the light of this latter work, it seems difficult to believe that the application of mechanical strain has no influence on the synthesis of U_2C_3 , as proposed by a few researchers.^{29,30} The work of Henney *et al.*³¹ showed that even a high content of oxygen impurities can have an important influence on the U_2C_3 synthesis rate. Starting from a $\text{UC}_{1.58}$ sample with 2900 ppm of oxygen, these authors obtained almost pure U_2C_3 after annealing for 74 h at 1773 K under vacuum. The extra carbon reacted with oxygen to form CO and CO_2 , fostering the formation of the sesquicarbide.

Producing or quenching cubic fcc-KCN-like actinide dicarbides to room temperature is virtually impossible due to the martensitic nature of the cubic→tetragonal transformation and its extremely fast kinetics. Tetragonal dicarbides, on the other hand, are easily quenched even when they are not in a thermodynamically stable phase at room temperature (as in the case of $\alpha\text{-UC}_2$).

The rate of oxidation of PuC and ThC in air is much higher than that of UC and (Th,U)C and (U,Pu)C solid solutions, whereas it is much lower in sesquicarbides.

The oxidation of actinide carbides occurs sometimes with the formation of flames (pyrophoricity), especially in samples with large specific surface (fine powders).

Actinide carbides tend to hydrolyze in water and even on exposure to laboratory air, where they exfoliate, increase in weight, and produce final hydrolysis products.

2.04.1.2.4 Applications

If uncertainties regarding the behavior of An carbides, mostly linked to metastability and uncontrollable oxygen and nitrogen impurities, still represent an obstacle to the fabrication and employment of these materials as an alternative nuclear fuel to oxides, their higher fissile density constitutes a big advantage. Moreover, the metallic thermal conductivity (Figure 3) and high melting temperature of An carbides ensure a higher conductivity integral margin to melting (CIM), defined by eqn [1], for these materials with respect to the traditional UO_2 , $\text{UO}_2\text{-PuO}_2$, and ThO_2 fuels:

$$\text{CIM} = \int_{T_{\text{op}}}^{T_{\text{m}}} \lambda(T) dT \quad [1]$$

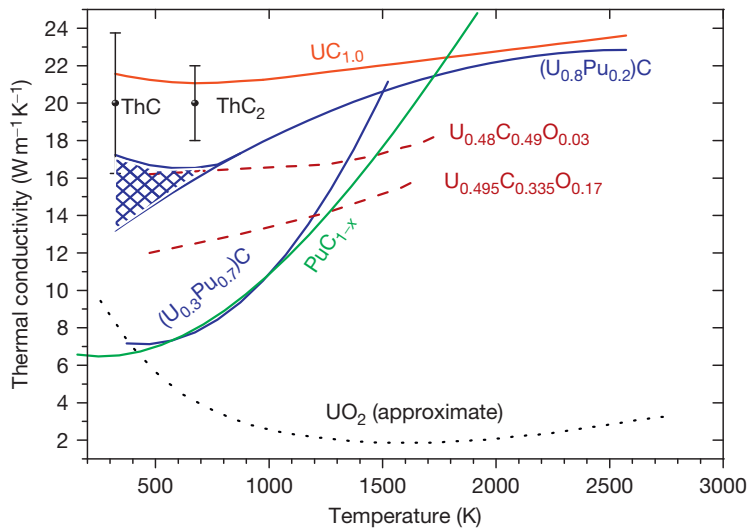
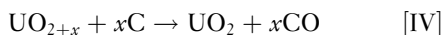


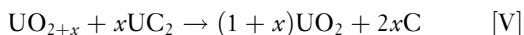
Figure 3 The thermal conductivity of some actinide carbides and carbide oxides compared to uranium dioxide. Each curve has $\pm 10\%$ uncertainty bands. The shaded area in the low-temperature part of the $\text{U}_{0.8}\text{Pu}_{0.2}\text{C}$ curve indicates larger uncertainty in the low-temperature values for this compound. Single data points are very dispersed depending on the material microstructure, porosity, and impurity content.

Here, T_{op} is the reactor operational temperature at the fuel-cladding interface (around 500 K for light water reactor (LWR), and up to 1500 K for the Generation IV very high-temperature reactors, VHTRs) and T_{m} is the fuel melting temperature. The better compatibility of carbides with liquid metal coolants compared to oxides is a further reason for making them good alternative candidates for high burnup and/or high temperature nuclear fuel.

Uranium carbide was traditionally used as fuel kernel for the US version of pebble bed reactors as opposed to the German version based on uranium dioxide.⁸ Among the Generation IV nuclear systems, mixed uranium-plutonium carbides (U, Pu)C constitute the primary option for the gas fast reactors (GFRs) and UCO is the first candidate for the VHTR.¹ In the former case, the fuel high actinide density and thermal conductivity are exploited in view of high burnup performance. In the latter, UCO is a good compromise between oxides and carbides both in terms of thermal conductivity and fissile density. However, in the American VHTR design, the fuel is a 3:1 ratio of $\text{UO}_2\text{:UC}_2$ for one essential reason, explained by Olander.³² During burnup, pure UO_2 fuel tends to oxidize to UO_{2+x} . UO_{2+x} reacts with the pyrocarbon coating layer according to the equilibrium:



The production of CO constitutes an issue in the VHTR because the carbon monoxide accumulates in the porosity of the buffer layer. The CO pressure in this volume can attain large values and, along with the released fission gas pressure, it can compromise the integrity of the coating layers and contribute to the kernel migration in the fuel particle ('amoeba effect'). In the presence of UC_2 , the following reaction occurs rather than reaction [IV] in the hyperstoichiometric oxide fuel:



Because no CO is produced in reaction [V], the latter is more desirable than [IV] in view of the fuel integrity.

Thanks to its fast neutron spectrum, the GFR can suit a ^{232}Th – ^{233}U fuel concept, in the chemical form of (Th,U) C_2 mixed carbides.^{33,34} However, the thorium cycle is at the moment not envisaged in Generation IV systems.

The use of Pu-rich mixed carbide fuel has recently been proposed for the Indian Fast Breeder Test Reactor.³⁵ However, pure plutonium carbides present

a low solidus temperature and low thermal conductivity, which are important drawbacks, with respect to pure U- or mixed carbides, for a nuclear fuel.

More details about the use and behavior of uranium carbides as nuclear fuel can be found in [Chapter 3.03, Carbide Fuel](#).

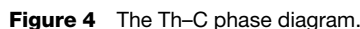
2.04.2 Thorium Carbides

^{232}Th , the only natural Th isotope, can absorb thermal neutrons to produce fissile ^{233}U and is therefore used as fertile material in breeder reactors. Nowadays, the thorium fuel cycle is mostly envisaged in India, which has about one-fourth of the total world thorium resources, but this option is kept open in other countries such as Norway and Australia, which also have abundant Th ores.³³ Thorium dicarbide is a candidate fertile material for the Generation IV high-temperature reactor (HTR) and VHTR systems, and it is also exploitable for accelerator-driven system (ADS) burners. Solid solutions of UC_2 – ThC_2 were candidate fuels for the Dragon High Temperature Reactor-coated particle fuels.³⁶ However, thorium-based fuel is difficult to recycle because of the radioprotection issues generated by the hard γ -emission of ^{208}Tl (2.6 MeV), formed in the ^{232}Th – ^{233}U spent fuel.

2.04.2.1 Phase Relationships

Atmospheric pressure phase equilibria in the Th–C system are reported in [Figure 4](#).

Thorium metal has an fcc (α) structure below 1633 K and a bcc structure (β) at higher temperatures. The first can accommodate carbon atoms as interstitials, resulting in the formation of thorium monocarbide without any lattice change.⁵ The $\text{ThC}_{1\pm x}$ fcc solid solution range, extending from pure Th to $\text{ThC}_{1.96}$ at high temperatures, is stable between $\text{ThC}_{0.67}$ and $\text{ThC}_{0.97}$ below ~ 1300 K. The exact high carbon limit is still under debate.³⁷ A miscibility gap seems to exist in the ThC_{1-x} phase field, between $\text{ThC}_{0.06}$ around 1000 K,³⁸ $\text{ThC}_{0.30}$ at 1413 (± 40) K,³⁹ and $\text{ThC}_{0.67}$ at 1150 K,² probably extending to room temperature with approximately the same composition boundaries. At higher temperatures, single carbon interstitials can be replaced by C_2 groups up to $\text{ThC}_{1.96}$. Thus, only two compounds have been observed in the Th–C system at atmospheric pressure: the fcc monocarbide with its broad nonstoichiometry range and the dicarbide, more often observed



The commonly accepted melting point of pure Th is 2020 ± 10 K.⁶ In the low-carbon domain, a eutectic

The boiling point of ThC₂ was extrapolated to be 5400 K at 1 atm.⁴³

2.04.2.2.1.1 Thorium monocarbide ThC

In the solid solution between $\text{ThC}_{0.67}$ and $\text{ThC}_{0.98}$, the value of α_{Ti} lower than the thermal expansion

coefficient of pure Th ($\alpha_{\text{Th}} \cong 11.6 \times 10^{-6} \text{ K}^{-1}$ at room temperature⁴⁷), increases slightly with carbon content and seems to have little dependence on oxygen and nitrogen impurities.

2.04.2.2.1.2 Thorium sesquicarbide Th_2C_3

The lattice parameter of Th_2C_3 varies between 855.13 and 856.09 pm in a narrow homogeneity range $\text{Th}_2\text{C}_{3-y}$ ($0 \leq y \leq 0.05$). The compound synthesized and analyzed by Krupka²⁷ had a composition of $\text{Th}_2\text{C}_{2.96}$ with a lattice parameter of 855.13 pm, corresponding to a theoretical density $\rho = 10.609 \text{ g cm}^{-3}$.

2.04.2.2.1.3 Thorium dicarbide ThC_2

Gantzel and Baldwin⁴⁸ published an XRD pattern for monoclinic ThC_{2-x} completed by Jones *et al.*⁴⁹ by neutron diffraction analysis. The assessed values

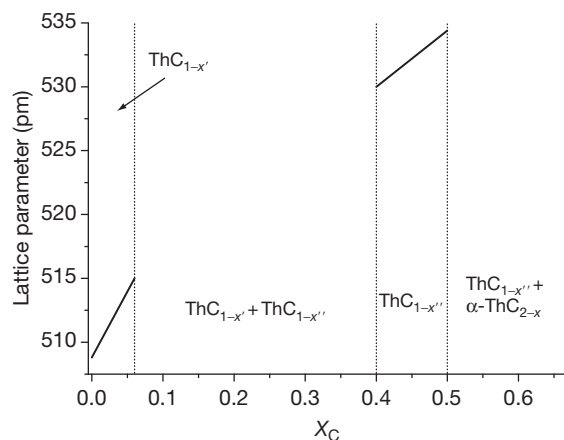


Figure 5 The room-temperature lattice parameter of thorium monocarbide.

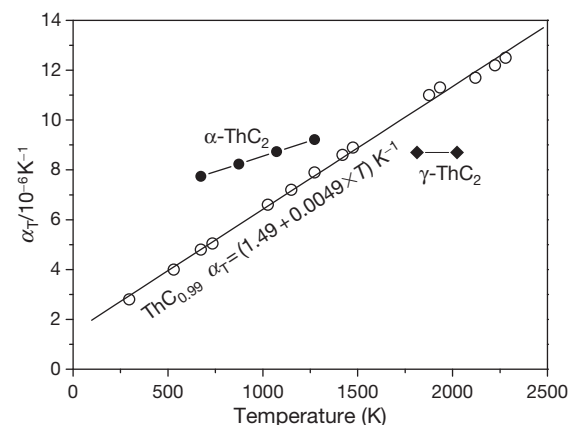


Figure 6 Thermal expansion coefficient of thorium carbides.

for the room-temperature lattice parameters are reported in [Table 1](#). Shein and Ivanovskii⁵⁰ performed *ab initio* density functional theory (DFT) calculations on α -, β -, and γ - ThC_2 , obtaining good agreement with the experimental results, and also suggesting a C–C distance of 132.8 pm. Pialoux and Zaug⁴² measured the lattice parameters a , b , c , and β of α - ThC_2 by XRD as a function of temperature up to 1673 K. The results are plotted in [Figure 7](#).

Bowman *et al.*⁴⁰ provided the most recent experimental data for the lattice parameters of β - ThC_2 in equilibrium with graphite and 550 ppm O_2 at 1723 K: $a = 422.1 \pm 0.3 \text{ pm}$ and $c = 539.4 \pm 0.3 \text{ pm}$. Pialoux and Zaug⁴² studied the dependence of a and c on the temperature, composition, and purity of β - ThC_2 . While the parameter a of β - ThC_2 in equilibrium with C at 1740 K seems in good agreement with the values of Bowman *et al.*,⁴⁰ the lattice parameter a for single-phase β - ThC_2 was observed to increase from around 420 pm at 1640 K to 422 pm at 1740 K. β - ThC_2 in equilibrium with ThC shows a lattice parameter a of the order of 417 pm at 1640 K, decreasing to about 414.5 pm at 1768 K. The parameter c was observed to increase with temperature for β - ThC_2 in equilibrium with ThC, varying from 540 pm at 1613 K to 545 pm at 1768 K, while the value $c = 541 \pm 1 \text{ pm}$ is acceptable at all temperatures at which β - ThC_2 is the equilibrium as a pure phase or with graphite. 0 K DFT calculations of structural parameters by Shein and Ivanovskii⁵⁰ are not in agreement with the experimental results for β - ThC_2 . Obviously, ideal ordering of C_2 dumbbells along the c axis and exact 2.00 stoichiometry, both postulated in Shein and Ivanovskii's model, constitute too rough hypotheses for this phase. This complex part of the phase diagram needs further assessment.

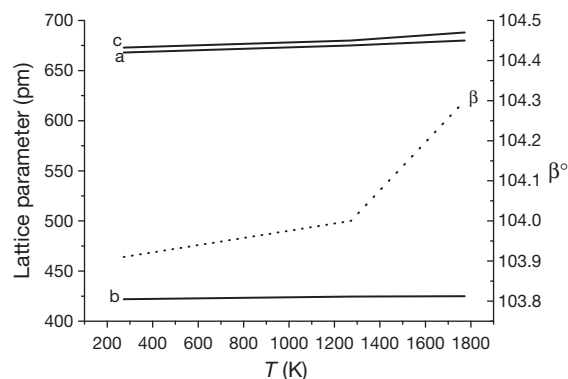


Figure 7 The temperature dependence of the lattice parameters in monoclinic α - ThC_2 . Reproduced from Pialoux, A.; Zaug, J. J. *Nucl. Mater.* **1976**, 61, 131–148.

The high-temperature γ -modification of ThC_2 has an fcc KCN-like structure. The C_2 dumbbells, centered in the $(1/2, 1/2, 1/2)$ position, rotate freely.^{6,40} The lattice parameter of $\gamma\text{-ThC}_2$ was measured by Pialoux and Zaug⁴² between 1858 and 2283 K, and observed to vary between 581.3 and 584.1 pm, respectively. The same authors observed that the lattice parameter of $\gamma\text{-ThC}_2$ in equilibrium with ThO_2 depends on the CO partial pressure. Its value is constant and close to 570 pm between 2173 and 2228 K for $p_{\text{CO}} < 10^{-3}$ bar, but increases to 584 pm for higher p_{CO} . The nearest C–C distance was estimated by Bowman *et al.*⁴⁰ to be 124 ± 4 pm. The $\beta \rightarrow \gamma\text{-ThC}_2$ transformation is diffusionless,⁵¹ which explains why all attempts to quench $\gamma\text{-ThC}_2$ to room temperature failed.⁵²

The linear thermal expansion $(l_T - l_0)/l_0$ and the linear thermal expansion coefficient α_T were measured by dilatometry up to 1323 K⁵³ and by XRD⁵⁴ up to 1608 K for $\alpha\text{-ThC}_{2-x}$ and up to 2028 K for $\gamma\text{-ThC}_{2-x}$. Values are reported in Figure 6 for samples with ~ 510 ppm O_2 .

Ganzel *et al.*⁵⁴ reported $\alpha_T = 8.7 \times 10^{-6} \text{ K}^{-1}$ for $\gamma\text{-ThC}_{2-x}$ between 1813 and 2028 K.

The average volumetric thermal expansion coefficient $\bar{\gamma}$ was estimated to be $78 \times 10^{-6} \text{ K}^{-1}$ between 298 and 2883 K.⁶

Ganzel *et al.*⁵⁴ estimated that the volume increase on the $\alpha \rightarrow \beta\text{-ThC}_{2-x}$ transformation was 0.8% and 0.7% for the $\beta \rightarrow \gamma\text{-ThC}_{2-x}$ transformation. Dalton *et al.*⁵⁵ estimated the overall volume expansion for both transformations to be 1.3%.

2.04.2.2.2 Thermodynamic properties

Heat capacity and Gibbs energy of formation data for thorium carbides are summarized in Tables 2 and 3 and Figures 8 and 9.

2.04.2.2.2.1 Thorium monocarbide ThC

The heat capacity of $\text{ThC}_{0.965}$ was measured by Harness *et al.*⁵⁶ between 1.8 and 4.2 K and by Danan⁵⁷ up to 300 K. No superconductive transition was observed around 9 K, unlike the measurements of Costa and Lallement.⁵⁸ The room-temperature value is $C_p(298) = 45.1 \pm 0.5 \text{ J K}^{-1} \text{ mol}^{-1}$. The resulting entropy difference $S(298) - S(0) \cong 58 \text{ J K}^{-1} \text{ mol}^{-1}$ would give, with a randomization entropy $S(0) = -R(0.97 \ln 0.97 + 0.03 \ln 0.03) = 1.12 \text{ J K}^{-1} \text{ mol}^{-1}$, $S(298) = 59.12 \text{ J K}^{-1} \text{ mol}^{-1}$, although there is a possibility that the ThC phase contains some C_2 groups compensated by some carbon vacancies.⁴ The Debye temperature of ThC is a function of composition and varies from ~ 170 K for $\text{ThC}_{0.063}$ to 308 K for $\text{ThC}_{1.00}$, calculated by Lindemann's formula.⁶

The high-temperature heat capacity of ThC, reported in Table 2, has been obtained by comparison with UC and from the low-temperature data reported above.

Formation enthalpies, corrected for impurities, were measured by Huber *et al.*⁵⁹ and Lorenzelli *et al.*⁶⁰

The Gibbs energy of formation of $\text{ThC}_{0.97}$ at its homogeneity range upper boundary was reviewed by Holley *et al.*⁴ according to the reported heat capacity as in Table 3 and Figure 8.

Vaporization studies performed on $\text{ThC}_{0.891}$, $\text{ThC}_{0.975}$, $\text{ThC}_{1.007}$, and $\text{ThC}_{1.074}$ between 2060 and 2330 K by Knudsen effusion and mass spectrometry⁶¹ yielded $\Delta_f G^\circ(\text{ThC}, s)$ values in fair agreement with the earlier ones. According to this study, atomic Th is the predominant species in the gaseous phase, and partial molar sublimation enthalpies are 522 kJ mol^{-1} for $\text{ThC}_{0.891}$, 553 kJ mol^{-1} for $\text{ThC}_{0.975}$, 660 kJ mol^{-1} for $\text{ThC}_{1.007}$, and 578 kJ mol^{-1} for $\text{ThC}_{1.074}$.

The equation of state (EOS) of solid ThC was studied by Das *et al.* by density functional and

Table 2 The heat capacity C_p of thorium carbides at atmospheric pressure (in $\text{J K}^{-1} \text{ mol}^{-1}$)

Compound	$T < 10 \text{ K}$	$10 \text{ K} \leq T \leq 300 \text{ K}$	$T > 300 \text{ K}$	Total T range
ThC	$2.12 \times 10^{-3}T$ + $108 \times 10^{-6}T^3$	$5 + 6R \left(\frac{467}{T} \right)^2 \frac{\exp\left(\frac{467}{T}\right)}{\left(\exp\left(\frac{467}{T}\right) - 1\right)^2}$	$46.046 + 2.553 \times 10^{-2}T$ – $1.883 \times 10^{-5}T^2$ + $5.442 \times 10^{-9}T^3$ – $6.279 \times 10^5 T^{-2}$ (liquid ThC) 89	$2 \text{ K} \leq T \leq 2270 \text{ K}$
Th_2C_3	–	–	–	–
$\alpha\text{-ThC}_2$	$3.13 \times 10^{-3}T$ + $1 \times 10^{-6}T^3$	$63.5 + 1.209 \times 10^{-2}T$ – $9.25 \times 10^5 T^{-2}$ ($200 \text{ K} \leq T \leq 350 \text{ K}$)	$44.8 + 8.4 \times 10^{-2}T$ – $8 \times 10^{-5}T^2$ + $3.0 \times 10^{-8}T^3$ – $5.9 \times 10^5 T^{-2}$	$5 \text{ K} \leq T \leq 2500 \text{ K}$
$\beta, \gamma\text{-ThC}_2$ ($T > 1700 \text{ K}$)	–	–	84	

Table 3 Thermodynamic functions of thorium carbides (in SI units)

Compound	$\Delta_f H^\circ$ (kJ mol ⁻¹)	$\Delta_f G^\circ$ (J mol ⁻¹)	$S^\circ(298)$ (J K ⁻¹ mol ⁻¹)	Transition ΔH° (J mol ⁻¹)	Bulk modulus $B = V^{-1}$ ($\partial^2 E / \partial V^2$) (GPa)	Critical parameters
ThC	69 ± 7 for ThC _{0.75} 126 ± 6 for ThC _{0.97}	-128 000 - 10 · T for 298 K ≤ T < 2023 K -133 400 - 2.9 · T for 2023 K ≤ T ≤ 2773 K	59.12	$\Delta_m H^\circ = 46\,000^{(R)}$	120 ^{est} dB/dT ≅ 3	$T_c = 9600$ K; $p_c = 152$ MPa; $\rho_c = 1.1458$ g cm ⁻³ ; $V_c = 0.000213$ m ³ mol
Th ₂ C ₃ ^a	-	-226 000 ± 21 000 at 298 K ^a ; -471 400 + 137 · T for 1573 K ≤ T < 1873 K	-	-	-	-
α-ThC ₂	-124.8 ± 6.7 for ThC _{1.91}	-127 900 + 7.7 T ^{est}	70.37	$\Delta_{\alpha \rightarrow \beta} H^\circ = 2100^{est}$	129.1 dB/dT ≅ 3.84	-
β-, γ-ThC ₂ (T > 1700 K)	-		-	$\Delta_{\beta \rightarrow \gamma} H^\circ = 10\,500^{est}$ $\Delta_m H^\circ = 72\,000^{(R)}$	β-ThC _{2-x} : 149.2 dB/ dT ≅ 4.13 γ-ThC _{2-x} : 0.6 dB/dT ≅ =3.71	-

For ΔH_f data, see Holley *et al.*⁴^(R) = Richard's rule and ^{est} = estimated.^aTh₂C₃ is only stable at high pressure. $\Delta_f G^\circ(\text{Th}_2\text{C}_3) = (\Delta_f G^\circ - 2.32 \text{ p kbar}^{-1})$.

tight-binding linear muffin tin orbital method (TB LMTO) calculations,¹⁶ obtaining a bulk modulus $B = V^{-1}(\partial^2 E / \partial V^2) = 43$ GPa. This differs by almost exactly a factor 3 from the value, 125 MPa, recommended by Gomošov *et al.*⁶² In this case, the discrepancy might be attributed to some factor (probably dimensional) missing in the calculations. A reasonable value for B is actually around 120 MPa, also directly deduced from the elastic constants reported in **Section 2.04.2.2.4**.

The EOS of liquid ThC was studied starting from the significant structure theory, which takes into account the complex vaporization behavior of ThCx.⁶³ The resulting enthalpy of melting is 35.2 kJ mol⁻¹. This value is considerably lower than that estimated by applying Richard's law to the accepted melting temperature.^{64,65} A direct measurement of $\Delta_m H(\text{ThC})$ is still required to solve this discrepancy. Gigli *et al.*⁶³ obtained the following values from their EOS for liquid ThC: $S^\circ = 207.6$ J K⁻¹ mol⁻¹; $C_p = 89$ J K⁻¹ mol⁻¹; $C_v = 50$ J K⁻¹ mol⁻¹; cubic thermal expansion coefficient $\alpha = 1.4 \times 10^{-4}$ K⁻¹; isothermal compressibility $k = V^{-1}(\partial V / \partial p) = 3.7 \times 10^{-11}$ m² N⁻¹, plus the critical constants reported in **Table 3**. Liquid ThC total pressure was calculated up the critical temperature as

$$\log p = 22.210 - 39282 T^{-1} - 4.2380 \log T + 2.0313 \times 10^{-4} T \quad [2]$$

with p in bar and T in K.

2.04.2.2.2 Thorium sesquicarbide Th₂C₃

The Gibbs energy of formation of Th₂C₃ at 1 atm estimated by Potter⁶⁶ from the phase field distribution of isothermal sections of the Th–Pu–C system between 1573 and 1873 K is reported in **Table 3** and **Figure 9**.

The reported values are consistent with the inequality

$$\Delta_f G^\circ(\text{Th}_2\text{C}_3, s) > \Delta_f G^\circ(\text{ThC}, s) + \Delta_f G^\circ(\text{ThC}_2, s)_2 \quad [3]$$

$$\forall T \leq T_{\text{melting}}$$

which justifies the thermodynamic instability of Th₂C₃ at atmospheric pressure and all temperatures.

The volume change for the reaction ThC + ThC₂ = Th₂C₃ is $\Delta V = -2.32 \times 10^{-6}$ m³ mol⁻¹. Krupka²⁷ having estimated that $\Delta_f G^\circ = (\Delta_f G^\circ - 2.32p)$ J mol⁻¹ and that the $p \cdot \Delta V$ term (in SI units) provides an excess $\Delta_f G$ term $\Delta_f G^{\text{ex}} \cong -7$ kJ mol⁻¹, the room-temperature standard Gibbs energy of formation for Th₂C₃ can be extrapolated as

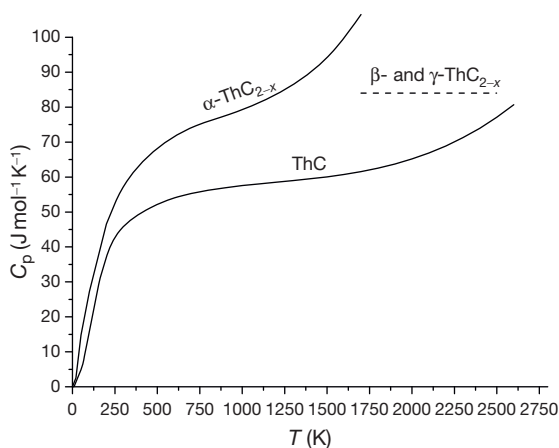


Figure 8 The heat capacity of thorium carbides.

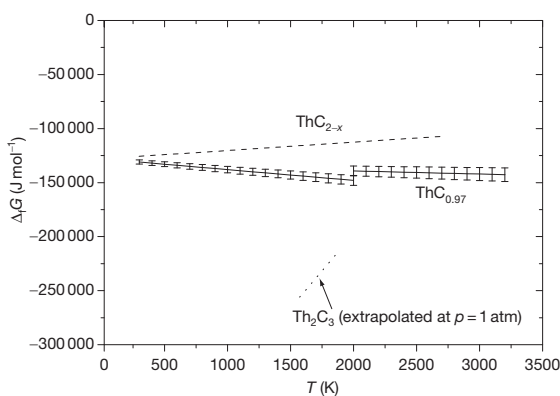


Figure 9 The Gibbs free energies of formation for thorium carbides.

$$\Delta_f G_{298}^\circ(\text{Th}_2\text{C}_3, \text{s}) = -226 \pm 21 \text{ kJ mol}^{-1}$$

Giorgi *et al.*^{67–69} studied the electronic and magnetic properties of thorium sesquicarbide. The valence electron concentration of Th_2C_3 is exactly 4.0. Magnetic susceptibility measurements show a superconductive transition in $\text{ThC}_{1.45}$ treated under high pressure. The transition temperature is 4.1 ± 0.2 K, with a pressure dependence $dT_c/dp = -0.040$ K kbar^{-1} between 0 and 10 kbar.

2.04.2.2.2.3 Thorium dicarbide ThC_2

Bates and Unstead⁷⁰ suggested the value $3.13 \text{ mJ K}^{-2} \text{ mol}^{-1}$ for the temperature coefficient γ of the electronic heat capacity. The heat capacity C_p of $\alpha\text{-ThC}_{2-x}$ was measured by low-temperature adiabatic calorimetry between 5 and 350 K, for $\text{ThC}_{1.93}$ by Westrum *et al.*⁷¹ and for nominal $\text{ThC}_{1.98}$ by

Takahashi *et al.*⁷² (Table 2 and Figure 8). The values measured in the two cases were consistent. The resulting standard entropy was $S^\circ(298) - S^\circ(0) = 68.49 \pm 0.07 \text{ J K}^{-1} \text{ mol}^{-1}$, which would give $S(298) = 70.37 \text{ J K}^{-1} \text{ mol}^{-1}$ if one assumes a randomization entropy $S(0) = 1.88 \text{ J K}^{-1} \text{ mol}^{-1}$, corresponding to a random mixing of C and C_2 groups. The other recommended values at 298 K are $C_p(298) = 56.69 \pm 0.06 \text{ J K}^{-1} \text{ mol}^{-1}$, $H^\circ(298) - H^\circ(0) = 10\,238 \pm 10 \text{ J mol}^{-1}$, and $(G^\circ(298) - H^\circ(0))/298 = 34.175 \pm 0.034 \text{ J K}^{-1} \text{ mol}^{-1}$.

Holley *et al.*⁴ estimated the thermodynamic functions of $\alpha\text{-ThC}_2$ at high temperature by extrapolating the data of Westrum up to 1400 K. The expression recommended by these authors up to 1700 K exhibits a positive curvature of C_p in the high-temperature region (298–1700 K), similar to the behavior of $\text{UC}_{1.9}$ (Table 2 and Figure 8). The heat capacities of β - and $\gamma\text{-ThC}_2$ between 1700 and 2500 K were estimated by the same authors to be around $84 \text{ J K}^{-1} \text{ mol}^{-1}$.

Holley *et al.*⁴ also estimated the enthalpies for $\alpha \rightarrow \beta$ - and $\beta \rightarrow \gamma\text{-ThC}_2$ transformations. The $\alpha \rightarrow \beta$ transformation implies minor crystallographic changes and is thus associated with a small ΔH° , $\sim 2.1 \text{ kJ mol}^{-1}$. ΔH° for the $\beta \rightarrow \gamma\text{-ThC}_2$ transformation was estimated to be 10.5 kJ mol^{-1} from the similar transition occurring in UC_{2-x} .

The $\gamma\text{-ThC}_2$ melting enthalpy is estimated to be $\Delta_m H = 72 \text{ kJ mol}^{-1}$, from Richard's law. The third-law enthalpy of sublimation of $\alpha\text{-ThC}_2$ at 298 K is of the order of $\Delta_{\text{sb}} H \approx 800 \text{ kJ mol}^{-1}$.⁷³

Many authors have studied the enthalpy and Gibbs free energy of formation of ThC_2 .⁴ Huber *et al.*⁵⁹ measured the enthalpy of formation of $\alpha\text{-ThC}_{1.91}$ at 298 K by oxygen combustion calorimetry in the presence of 410 ppm O_2 , obtaining $\Delta_f H_{298}^\circ(\text{ThC}_{1.91}, \text{s}) = -125 \pm 5 \text{ kJ mol}^{-1}$. This value is recommended as the most reliable.

The Gibbs free energy of formation for ThC_{2-x} is recommended to be $-125 \pm 6.7 \text{ kJ mol}^{-1}$ at room temperature,⁴ being the entropy contribution comparable to the uncertainty. EMF and combustion have probably yielded the most reliable $\Delta_f G^\circ$ data. The graph of Figure 9 is essentially based on these data. However, this trend, recommended between 298 and 2718 K, is subject to a large unquantifiable uncertainty due to the unknown oxygen content in the investigated samples and to the fact that high-temperature C_p and entropy values are mostly estimated.

ThC_{2-x} in equilibrium with carbon preferentially loses gaseous carbon,⁴ causing the congruently vaporizing composition in the Th–C system at

2000–2800 K to lie well within the ThC_{1+x} domain. Gaseous species over the ThC_2 – ThC system were generated by thermal ion emission (Langmuir vaporization) and Knudsen effusion, and analyzed by mass spectrometry.^{74–76} These studies revealed the presence of ThC_n species up to $n=4$. Gupta and Gingerich⁷⁷ also detected ThC_5 and ThC_6 in the vapor. Sasaki *et al.*⁷⁵ determined the vaporization coefficient ratio $\alpha_{\text{ThC}_2}/\alpha_{\text{Th}}$ to be close to one within the experimental error. The partial pressures of the species in the vapor differ strongly and only the ThC_2 and ThC_4 species seem to have significant contributions to the total vapor pressure.

All these data have been obtained by assuming, in the entropy calculations, that ThC_2 and ThC_4 molecules have linear structure. This point has been more recently discussed by Kovács and Konings⁷⁸ who suggest, based on quantum chemical calculations, that the ThC_2 and ThC_4 molecules are more likely to have cyclic structures. This result leads to new entropy values of the gas molecules, higher than the (deduced) previous ones by $\sim 5\%$ on average.

2.04.2.2.3 Transport properties

2.04.2.2.3.1 Thorium monocarbide

ThC room-temperature thermal conductivity (see Figure 1) was estimated in an arc-melted specimen (100% theoretical density assumed) from electrical resistivity measurements and the Wiedemann–Franz relationship: $\lambda = 29 \text{ W K}^{-1} \text{ m}^{-1}$ at 298 K.⁴¹ However, a more recent estimate based on an extrapolation from the thermal conductivity of $(\text{Th}, \text{U})\text{C}$ gave $\lambda = 12 \text{ W K}^{-1} \text{ m}^{-1}$ at 298 K.⁶ A more systematic study of ThC_x as a function of both temperature and composition is needed.

The self-diffusion of carbon in fcc α - $\text{Th}(\text{C})$ was measured by Peterson⁷⁹ in a ThC -coated Th cylinder between 1273 and 1473 K for C concentrations up to 1.1 wt%. The best fit over three experimental data points obtained at 1273, 1373, and 1473 K leads to the values $D_0 = 2.7 \times 10^{-6} \text{ m}^2 \text{ s}^{-1}$ and $Q = 159 \text{ kJ mol}^{-1}$, to be substituted in

$$D_c = D_0 \exp(-Q/RT) \quad [4]$$

At higher temperatures, between 1713 and 1988 K, and up to 0.4 wt% of C, Peterson *et al.*⁸⁰ found $D_0 = 2.2 \times 10^{-6} \text{ m}^2 \text{ s}^{-1}$ and $Q = 113 \text{ kJ mol}^{-1}$. In the same work, the electro transport of carbon in β - $\text{Th}(\text{C})$ was measured between 1713 and 1948 K. Carbon migrated in the same direction as the electron flow, with carbon mobility μ_C between 1.2×10^{-8} and $7.8 \times 10^{-8} \text{ m}^2 \text{ V}^{-1} \text{ s}^{-1}$; D_C varied between 8×10^{-10}

and $3.2 \times 10^{-9} \text{ m}^2 \text{ s}^{-1}$, and the effective valence of carbon between -2.1 and -3.8 .

The electrical resistivity ρ of Th – C alloys has been measured in samples with different compositions and oxygen contents. The extrapolated ρ for pure Th at room temperature is $\rho_{298}^{\text{Th}} = 0.162 \mu\Omega \text{ m}$.⁸¹ The electrical resistivity of low-carbon ThC_{1-x} increases linearly with the carbon content up to $\sim 0.32 \mu\Omega \text{ m}$ in $\text{ThC}_{0.041}$ samples with 100 ppm O_2 , but ρ_{ThC} certainly increases more steeply in samples with a higher oxygen content. Kleykamp *et al.*⁸ have compiled a review of $\text{ThC}_{1\pm x}$ electrical resistivity (Figure 10). The resistivity of Th monocarbide appears to be higher than that of the dicarbides at all temperatures.

Further results on Th carbide samples between $\text{ThC}_{0.25}$ and ThC_2 (+C) were obtained up to 2673 K.⁸² ρ was observed to reach its highest value ($\cong 3 \mu\Omega \text{ m}$) for compositions near ThC and temperature around 2000 K.

2.04.2.2.3.2 Thorium dicarbide

The thermal conductivity λ of α - ThC_2 was estimated⁴¹ from electrical resistivity measurements and the Wiedemann–Franz relationship, giving $\lambda = 24 \text{ W K}^{-1} \text{ m}^{-1}$ at 298 K, for a sample with assumed 100% th.d. Marchal and Trouvé⁸³ measured λ by a comparative flux method obtaining, for α - ThC_2 with 72% th.d., $24.1 \text{ W K}^{-1} \text{ m}^{-1}$ at 443 K and $20.5 \text{ W K}^{-1} \text{ m}^{-1}$ at 627 K. Grossman⁸⁴ obtained $\lambda = 13 \text{ W K}^{-1} \text{ m}^{-1}$ by a radial heat flow method for β - and γ - ThC_2 and $1713 \text{ K} < T < 2333 \text{ K}$.

All the ThC_2 modifications have metallic electrical conductivity, as confirmed both experimentally

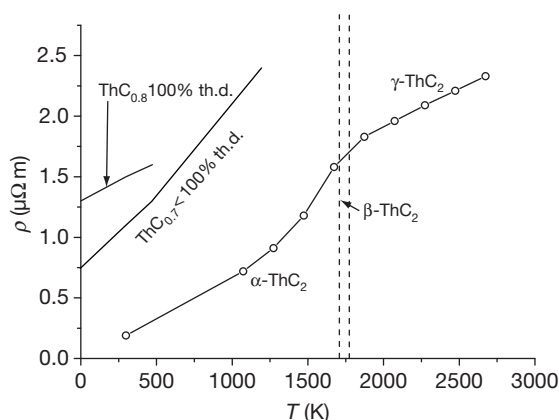


Figure 10 The electrical resistivity of some thorium carbides. Data taken from Holleck, H.; Kleykamp, H. In *Gmelin Handbook of Inorganic Chemistry U Supplement Volume C12*; Springer-Verlag: Berlin, 1987.

and theoretically. A review of available electrical resistivity (ρ) data for high-density $\text{ThC}_{1.93}$ between 298 and 2673 K is provided in Figure 10.⁸²

2.04.2.2.4 Mechanical properties

2.04.2.2.4.1 Thorium monocarbide

The theoretical density of a given crystal structure can be obtained from the lattice parameters if also the molecular weight is known. Using $a = 534.60$ pm for $\text{ThC}_{0.98}$ at room temperature yields $\rho = 10.60$ g cm⁻³. Considering the thermal expansion, the th.d. of solid ThC at the melting point is $\rho = 10.2$ g cm⁻³.

The adiabatic elastic constants c_{ij} were measured only on a $\text{ThC}_{0.063}$ sample by the pulse echo overlap method between 4.2 and 300 K along the [110] crystallographic directions.⁸⁵ The resulting adiabatic bulk modulus $B = 1/2(c_{11} + 2c_{12}) = 60.49$ GPa at 300 K. The adiabatic shear modulus was obtained in the Voigt approximation to be $G = 31.87$ GPa. Geward *et al.*^{86,87} evaluated the isothermal bulk modulus of $\text{ThC}_{0.8}$ from high-pressure XRD measurements up to 50 GPa, yielding $B_{\text{ThC}_{0.8}} = 109 \pm 4$ GPa at 300 K, with $dB/dT \cong +3$. As the direct Th–C bonding formation leads to a pronounced increase of structural rigidity from metal to carbide, the Th carbide bulk modulus increases with C content starting from metallic α -Th, and a value of around 120 GPa for B seems reasonable for stoichiometric ThC.

$\text{ThC}_{1 \pm x}$ Vickers hardness increases from 50 HV for 0.02 wt% C to 850 HV (with a load of 2 N) for $\text{ThC}_{0.98}$ (with 1 at.% of oxygen).⁶

According to these results, the addition of carbon to thorium drastically reduces its cold workability. Untempered samples with C contents >6 at.% are stiff and brittle with room elongations at fracture $\varepsilon_F = 0$. Thus, tensile properties could be studied for low C content only. The 0.2% offset yield stress $\sigma_{0.2}$ varies from 165 MPa for 0.10 wt% C to 250 MPa for 0.20 wt% C. The yield stress, σ_y , varies from 166 MPa for 0.04 wt% C to ~ 370 MPa for 0.22 wt% C ($\text{ThC}_{0.05}$ in equilibrium with $\text{ThC}_{0.67}$ at room temperature). The elongation at fracture ε_F goes from 35% for 0.04 wt% C to 11% in $\text{ThC}_{0.05}$ in equilibrium with $\text{ThC}_{0.67}$, to nearly zero for higher C contents. In the same composition range, the ultimate tensile strength σ_U ranges between 250 and 400 MPa at room temperature and rapidly decreases with temperature (around 50 MPa at 1000 K).⁶

The creep and flow stress behavior in ThC alloys up to 2.83 wt% C ($\text{ThC}_{0.54}$) between 4.2 and 573 K was reviewed by Kleykamp *et al.*⁶ It was found to be composed of a thermally activated and an

athermal component. The first increases with carbon content and the strain rate. The 2% offset yield stress at a strain rate $d\varepsilon/dt = 3.3 \times 10^{-5}$ s⁻¹ was obtained as a function of temperature. At room temperature, it ranges from 50 MPa for 0.077 wt% C to 250 MPa for 2.83 wt% C. This value increases considerably at 4.2 K, where it is measured around 1.3 GPa.

2.04.2.2.4.2 Thorium dicarbide

The theoretical XRD density of monoclinic α - ThC_2 is 9.14 g cm⁻³ and 8.80 g cm⁻³ for tetragonal β - ThC_2 with C/Th = 1.94 at 1768 K. Fink *et al.*⁴³ estimated the density of γ - ThC_2 to be around 9.0 g cm⁻³ at the melting point.

Oikawa and Hanaoka⁸⁸ give a value of Young's modulus $E = 1$ –2 GPa and a compressive strength $\sigma_{uc} = 20$ MPa for low-density ThC_{2-x} in equilibrium with C at room temperature. Room temperature Vickers hardness of arc-melted, two-phase α - ThC_2 in equilibrium with C under a load of 2 N is 600 HV. This value is increased up to 650 HV after heat treatment to 1873 K, and it obviously depends on the oxygen-impurity content, which can make it increase up to 970 HV.^{6,89}

Values of the bulk modulus $B = V^{-1}(\partial^2 E / \partial V^2) = V^{-1}(\partial P / \partial V)$ and its pressure derivative $B' = \partial B / \partial P$ reported in Table 3 were calculated at 0 K for the three ThC_{2-x} allotropies by Shein and Ivanovskii.⁵⁰

2.04.2.2.5 Optical properties

2.04.2.2.5.1 Thorium monocarbide

Freshly broken surfaces of ThC have a shiny metallic gray color which darkens in the presence of oxygen. Optical constants of nearly stoichiometric ThC have been measured in liquid samples by Bober *et al.*⁹⁰ by a laser integrating sphere reflectometer between 2900 and 3900 K and $\lambda = 458, 514, 647$, and 752 nm. For unpolarized light, ρ at the melting point (2773 K) was measured to be close to 0.45 at $\lambda = 647$ nm and $\theta = 45^\circ$, this value not being very much dependent on the angle. Optical constants are deduced from these results: the real refractive index n (between 1.6 and 2.0) and the absorption constant k (between 1.7 and 2.5). Both n and k slightly increase with wavelength and decrease with temperature.

2.04.2.2.5.2 Thorium dicarbide

α - ThC_{2-x} crystals are transparent and look yellowish under the optical microscope. Freshly broken surfaces of ThC_{2-x} crystals display a very pale metallic yellowish appearance which darkens with time in the presence of oxygen.⁶

Grossman⁸⁴ reported measurements of spectral normal emissivity ε_λ of ThC_{2-x} (9.24 wt% C, <0.5% O_2) for 1500 K < T < 2100 K, yielding an average value $\varepsilon_\lambda = 0.58 \pm 0.03$. The same author also reported an average value of the total spherical emissivity between 1800 and 2150 K, $\varepsilon_\tau = 0.475 \pm 0.025$.

2.04.2.2.6 Multielement thorium carbides

A number of multielement thorium carbides have been studied. They occur as mixed phases of binary thorium carbides with other elements by the formation of either continuous solid solutions, like ternary carbides, or immiscible compounds. The most interesting are certainly the carbide-oxides and-nitrides. They form relatively easily during the ThC_x preparation and on exposure to air. It is therefore useful to explore some of their properties, at least for the Th-rich compositions.

2.04.2.2.6.1 Thorium carbide oxides

The Th–C–O ternary system⁶ was extensively studied by Potter.⁶⁶ It is characterized by a hypostoichiometric Th monocarbide oxide fcc solid solution $\text{Th}(\text{C},\text{O})_{1-x}$ with $x > 0$, stable around 1800 K. It was experimentally observed that the maximum solubility of oxygen in ThC in equilibrium with ThC_2 and ThO_2 corresponds to the composition $\text{ThC}_{0.8}\text{O}_{0.2}$ (1.3 wt% oxygen). Heiss and Djemal⁹¹ observed that the maximum solubility of oxygen in $\text{ThC}_{1.94}$ corresponds to the composition $\text{ThC}_{1.94}\text{O}_{0.04}$ (0.25 wt% oxygen), at 2273 K. The room-temperature lattice parameter of oxygen-saturated $\text{ThC}_{0.8}\text{O}_{0.2}$ is estimated to be between 532.6 and 532.9 pm.

2.04.2.2.6.2 Thorium carbide nitrides

The Th–C–N system has been investigated more than the Th–C–O system, thanks in particular to Benz *et al.*,⁹² Pialoux,⁹³ and Benz and Troxel.⁹⁴

For low nitrogen contents, the addition of nitrogen has been observed to raise the $\alpha \rightarrow \beta$ transition temperature of Th-rich ThC_{2-x} . The effect on the same transition in C-saturated ThC_{2-x} and on the $\beta \rightarrow \gamma$ transition temperature seems negligible, indicating that N is probably more soluble in α - ThC_{2-x} than it is in γ - ThC_{2-x} . Similar to oxygen, the addition of nitrogen to the fcc ThC_{1-x} phase reduces its lattice parameter.

For N contents >0.05 at.%, literature data are few and scattered. The Th–Th(C,N) region is characterized by a continuous fcc NaCl-type solid solution between ThN, stoichiometric ThC, and slightly hypostoichiometric ThC_{1-x} . Hyperstoichiometric

$\text{Th}(\text{C},\text{N})_{1+x}$ exists as a solid solution on the ThC side above 2073 K. ThN and very hypostoichiometric ThC_{1-x} are separated by a two-phase field. No eutectic has been observed in the Th–ThC–ThN region, but a peritectic four-phase equilibrium between α -Th, β -Th, Th(C,N), and liquid is postulated at 1993 ± 30 K. Alloys with C/Th ≈ 1 were observed to melt at 2473 K under 2 bar of N_2 , and a ternary eutectic exists just below 2500 K with composition $\text{Th}_{0.38}\text{C}_{0.35}\text{N}_{0.27}$. The lattice parameter of the Th(C,N) solid solution between ThC and ThN follows Vegard's law almost exactly, from approximately 534 pm for ThC to 516 pm for ThN. The lattice parameter of Th(C,N) in equilibrium with Th_3N_4 and ThCN, $a = 522.4 \pm 0.6$ pm, corresponds to the composition $\text{ThC}_{0.35}\text{N}_{0.65}$ and is almost independent of temperature. $\text{ThC}_{0.35}\text{N}_{0.65}$ is also the congruently melting composition of the Th(C,N) solid solution, with $T_m = 3183 \pm 35$ K. The solidus temperature was observed to increase with nitrogen pressure.

The lattice parameter of Th(C,N) in equilibrium with ThC_2 and ThCN, $a = 519.7 \pm 0.5$ pm, corresponds to the composition $\text{ThC}_{0.20}\text{N}_{0.80}$. The Th(C,N)–C region is characterized by the ternary compound ThCN, which exists in two modifications. α -ThCN crystallizes in the prototype C-centered monoclinic structure, with space group $C2/m$ (No. 12) and lattice parameters $a = 702.5 \pm 0.5$ pm, $b = 394.6 \pm 0.1$ pm, $c = 727.7 \pm 0.2$ pm, and $\beta = 95.60 \pm 0.1^\circ$. At 1398 K, this phase transforms into β -ThCN, having a hexagonal structure with the space group $P\bar{3}1m$ (No. 162) and lattice parameters $a = 703.5$ pm and $c = 732.4$ pm. β -ThCN decomposes into Th_3N_4 and C at sufficiently high nitrogen pressure.

The metallic electrical resistivity of the Th(C,N) solid solution decreases from 1.8 to <0.05 $\mu\Omega\text{m}$ with increasing nitrogen content and decreasing temperature. The electrical properties of this phase depend primarily on the conduction electrons and the vacancy concentration in the fcc lattice.⁹⁵ Th(C,N) becomes superconducting at low temperature, with a maximum transition temperature of 5.8 K for the composition $\text{ThC}_{0.78}\text{N}_{0.22}$, sharply decreasing with increasing carbon content. The decrease is more gradual at higher nitrogen content, up to 3.2 K for pure ThN.

2.04.3 Protactinium Carbides

Protactinium (^{91}Pa) is one of the rarest of the natural elements. Its most important isotope is ^{231}Pa (half-life = 3.276×10^4 years), but the most interesting

from an industrial viewpoint is the artificial isotope ^{233}Pa (half-life = 27.0 days). This is an intermediate isotope in the production of fissile ^{233}U in thorium breeder reactors.

Some studies on PaC and PaC₂ can be found in the literature.^{96–99} Lonsdale and Graves⁹⁸ prepared a dilute solution of Pa in ThC₂ by neutron irradiation of ThO₂, followed by carbothermic reduction. The monocarbide was prepared by carbothermic reduction of Pa₂O₅ by Lorentz *et al.*⁹⁹ Products of reaction at 2473 K contained a second phase, possibly PaC₂.

Pa metal has been prepared from PaC in the presence of iodine using the Van Arkel method.¹⁰⁰

2.04.3.1 Properties

Lorentz *et al.*⁹⁹ found by room- and high-temperature XRD that PaC is isostructural with other actinide monocarbides, displaying fcc symmetry with $a = 506.08 \pm 0.02$ pm, corresponding to a theoretical density of 12.95 g cm^{-3} . At the highest temperatures (~ 2500 K), extra lines were observed, corresponding to a tetragonal body-centered structure (CaC₂ type) with $a = 361 \pm 1$ pm and $c = 611 \pm 1$ pm, attributed to PaC₂.

Lonsdale and Graves studied, by Knudsen effusion, the vapor pressure of Pa from a dilute solution of Pa in ThC₂, showing that PaC₂ has stability similar to ThC₂.

The formation of Gibbs energy for PaC was estimated to be

$$\Delta_f G(\text{PaC}) \cong 182.5 - 0.0841 T (\text{kJ mol}^{-1}) \quad [5]$$

Enthalpy, entropy, and Gibbs energy of formation of PaC and PaC₂ are reported in Table 4 as estimated by assuming that the thermodynamic functions for Pa carbides lie between those of Th and U carbides.⁴ The considerable uncertainties stem from the large lack of data.

2.04.4 Uranium Carbides

The main application of uranium carbides is as a fuel for nuclear reactors, usually in the form of pellets or

tablets, but also in nuclear thermal rockets, where their high thermal conductivity and fissile atom density could be entirely exploited.

2.04.4.1 Phase Relationships

The most recent thermodynamic optimization of the U–C phase diagram is due to Chevalier and Fischer.¹⁰¹ An assessment of the uranium–carbon phase diagram is reported in Figure 11.

Blumenthal¹⁰² studied the constitution of low-carbon alloys in the uranium–carbon system and proposed three different structures for the pure metal. The observed transition temperatures are 940 ± 1.3 , 1047.8 ± 1.6 , and 1405.3 ± 0.8 K for the α – β , β – γ transitions and melting point, respectively. The low-temperature solubility of carbon in uranium is low: < 3 ppm in α -uranium, < 10 ppm in the β -U, and between 0.07 and 0.09 at.% in γ -U. In the presence of carbon, the system has a eutectic point at 1390 K and two eutectoid reactions at temperatures slightly lower than the pure crystal structure transition. The solubility of carbon in uranium increases with temperature. A few studies on the solubility of carbon in liquid uranium between 1500 and 2800 K have been assessed in the following equation¹⁰³:

$$\ln\left(\frac{C}{U}\right) = 68.129 - 5.2922 \frac{10^5}{T} + 1.5347 \frac{10^9}{T^2} - 1.9721 \frac{10^{12}}{T^3} + 9.2191 \frac{10^{14}}{T^4} \quad [6]$$

Stoichiometric uranium monocarbide is stable from room temperature to its melting point (2780 K). However, at high temperature (> 1400 K), UC can exist in both hypostoichiometric and hyperstoichiometric forms.¹⁰⁴ It can accommodate both carbon vacancies and excess atoms by substituting a single carbon with two carbons. This behavior implies some variations in its lattice parameter.

At a higher carbon content, two more compounds are known to exist in the U–C system: U₂C₃ and UC_{2–x}.

If U₂C₃ is the thermodynamically stable phase until its peritectoid decomposition temperature (2106 K), it is normally not found in samples quenched from above this temperature, where UC and UC₂ are identified instead. On the other hand, as explained in Section 2.04.1.2.3, U₂C₃, once produced, can be easily quenched to room temperature. However, its thermodynamic stability below 1250 K is still controversial as some authors reported

Table 4 Thermodynamic functions of protactinium carbides

Thermodynamic function (298 K)	PaC (kJ mol ^{–1})	PaC ₂ (kJ mol ^{–1})
$\Delta_f H^\circ$	-113 ± 16	-100 ± 16
$\Delta_f S^\circ$	4 ± 12	8 ± 12
$\Delta_f G^\circ$	-113 ± 16	-120 ± 16

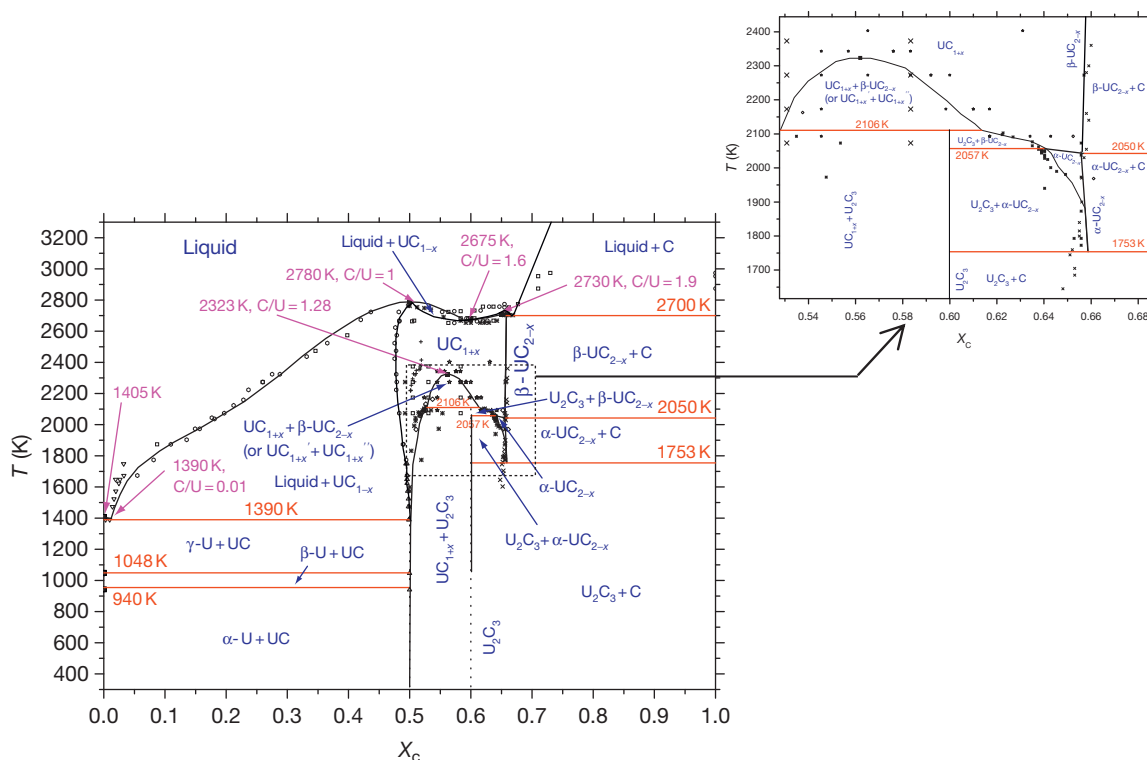


Figure 11 The equilibrium U–C Phase diagram based on calculated and experimental data. β - UC_{2-x} and UC_{1+x} have the same face-centered cubic $Fm\bar{3}m$ structure, and are completely miscible at high temperature, but display a miscibility gap up to 2323 K. Some authors identify these modifications as UC_{1+x}' and UC_{1+x}'' to distinguish the high and low – carbon boundaries of the miscibility gap.

the decomposition of $\text{UC} + \text{C}$ at lower temperature.¹⁰⁵ This sesquicarbide has a body-centered (bcc) cubic structure of the Pu_2C_3 type (Table 1). The study of U_2C_3 presents important experimental issues, and results are often controversial and affected by low accuracy. Above the peritectoid temperature, U_2C_3 decomposes into UC_{1+x} and $\beta\text{-UC}_{2-y}$. A miscibility gap between these two phases has been determined by Sears¹⁰⁶ by microstructure analysis on quenched samples. Its low-temperature boundary corresponds to the peritectoid (2106 K) delimited by $\text{UC}_{1.1}$ and $\text{UC}_{1.7}$ and its maximum temperature is 2323 K at a composition close to $\text{UC}_{1.3}$. The complex mechanisms of these transformations were described by Ashbee *et al.*¹⁰⁷ At higher temperature, UC_{1+x} and $\beta\text{-UC}_{2-y}$ are fully miscible, so that some authors¹⁰⁸ identify them rather as UC_{1+x}' and UC_{1+x}'' . Uranium dicarbide exists in two different structures, a α tetragonal form between 1753 and 2050 K, and a β cubic form at higher temperatures. UC_2 decomposes so slowly upon cooling that it is normally observed as the stable phase in equilibrium with pure carbon at room temperature. It was

therefore decided to establish a ‘metastable’ uranium–carbon phase diagram, where U_2C_3 is left out and $\alpha\text{-UC}_2$ is the stable phase in equilibrium with UC and C at room temperature¹⁰⁸ (Figure 12).

UC_2 is hypostoichiometric. Its phase boundary in equilibrium with C varies from $\text{UC}_{1.89}$ at the lowest temperatures to $\text{UC}_{1.92}$ at the highest.⁸ Laugier¹⁰⁸ based on some high-temperature XRD studies, proposed the decomposition of tetragonal UC_2 into U_2C_3 below 1753 K and redefined the transition domain between UC_2 and U_2C_3 . The hypostoichiometry domain of $\alpha\text{-UC}_2$ extends from the carbon-rich boundary to a phase limit in equilibrium with U_2C_3 , which reaches $\text{UC}_{1.77}$ at its maximum temperature (2057 K – Figure 11). At higher temperature, U_2C_3 is in equilibrium with $\beta\text{-UC}_{2-x}$. The martensitic transformation from α - to $\beta\text{-UC}_2$ occurs at 2050 ± 20 K. Bowman *et al.*¹⁰⁹ investigated the dicarbide behavior by high-temperature neutron diffraction. They showed that $\beta\text{-UC}_2$ is of the type B1 KCN. This result rules out the CaF_2 structure previously proposed by Wilson (based on high-temperature XRD analysis)¹¹⁰ and agree with the complete

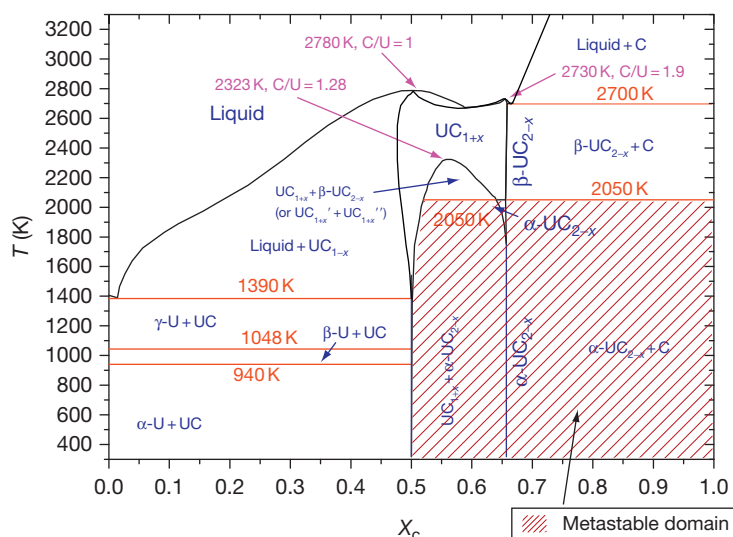


Figure 12 The metastable U–C phase diagram.

miscibility of UC and UC₂ at high temperature, already proven by many authors.^{4,111,112}

The liquidus line presents two maxima between UC and UC₂ at 2780 ± 20 K and 2730 ± 20 K corresponding to the melting point of UC and UC_{1.9}, respectively. A minimum temperature around 2675 K is observed between UC_{1.5} and UC_{1.6}. Although the literature melting temperature data show some dispersion, probably due to the sample impurities and alteration during the heat treatment, the points assessed by Chevalier and Fischer¹⁰¹ and confirmed by Utton *et al.*¹¹³ seem reliable within the reported uncertainties. The liquidus and solidus lines are very close together at all compositions and can hardly be distinguished experimentally.

2.04.4.2 Physicochemical Properties

2.04.4.2.1 Crystallography

2.04.4.2.1.1 Uranium monocarbide UC

The UC lattice parameter was studied by many authors⁸ as a function of the C/U ratio, temperature, and O and N impurity level (Figure 13 and Table 1).¹¹⁴ The recommended value is $a = 496.05 \pm 0.02$ pm for pure UC in equilibrium with higher carbides, and can be retained as a room-temperature reference. The lattice parameter is slightly smaller for UC in equilibrium with uranium, strongly dependent on the sample thermal history. For hyperstoichiometric UC_{1+x}, the excess carbon is stabilized by substituting a single carbon with two carbons, leading to a homogeneous transformation from the NaCl structure of stoichiometric UC to

the isomorphous KCN high-temperature structure of β -UC₂.¹¹⁵ For this reason, many of the uranium monocarbide high-temperature properties, including the lattice parameter, extend homogeneously up to the β -UC₂ composition.

N and O impurities have opposite effects on the UC lattice parameter. The substitution of carbon by nitrogen results in an approximately linear decrease of α -UC in equilibrium with higher carbides. The substitution of carbon by oxygen, instead, gives a lattice dilatation with a maximum between 1000 and 2000 ppm of oxygen.

The electronic structure of uranium carbides is rather complex. The density of state at the Fermi level $N(E_F)$ can be calculated from the temperature coefficient γ of the electronic heat capacity, and an average value can be estimated to be 18.9 ± 1 mJ K⁻² mol⁻¹, to yield $N(E_F) = 3\gamma/2\pi^2 k_B^2 \approx 4.0$ eV⁻¹ atom⁻¹. This value, which explains the metallic electrical conductivity of UC, agrees only qualitatively with the tight-binding calculations by Adachi and Imoto¹¹⁶ and Das *et al.*¹⁶ (Figure 1), but the agreement with the self-consistent linearized ‘muffin tin orbital’ band structure calculations (LMTO) by Brooks is good.¹¹⁷ According to these calculations, a strong f–p bond exists. Wedgwood¹¹⁸ studied the phonon spectra of UC_{0.95} by time-of-flight (TOF) neutron scattering, obtaining rather flat optical branches, resulting from the large mass difference and the weak interaction between U and C atoms, with a frequency maximum of 11.7 THz at $q=0$. The U–C bond force constant

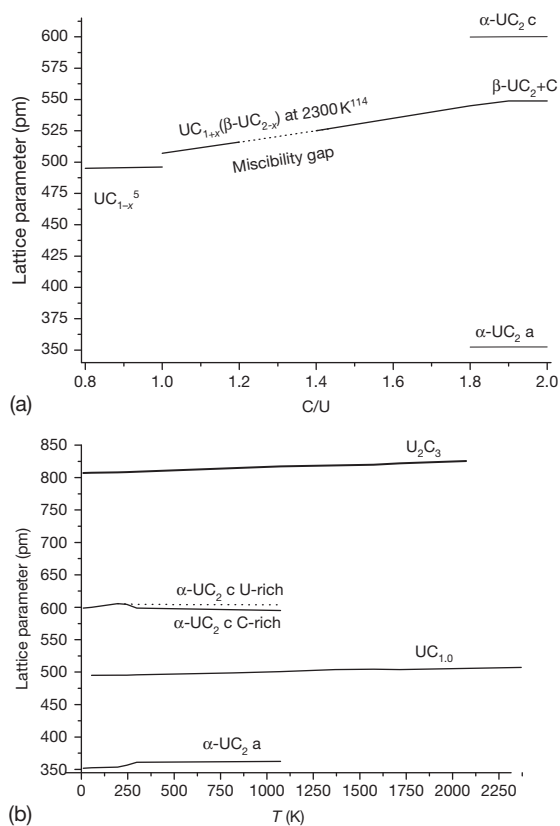


Figure 13 (a) The uranium carbide lattice parameter as a function of the C/U ratio and (b) the uranium carbide lattice parameter as a function of temperature.

was calculated to be $4.55 \times 10^{-8} \text{ N m}^{-1}$. According to these data, it seems reasonable to hypothesize a UC bulk modulus higher than that calculated by Das *et al.* (65 GPa). By comparison with the values recently calculated by Shi *et al.*,¹¹⁹ a value close to $B_{\text{UC}} = 180 \text{ GPa}$ seems realistic.

Point defect behavior in UC was extensively studied in the 1970s, and Matzke has highlighted the complexity of the microscopic mechanisms in his review.⁵ The energies of formation (V_F) and migration (V_M) of uranium and carbon vacancies were determined from electrical resistivity measurements of quenched samples. Matsui and Matzke¹²⁰ recommended the following values: $V_{\text{FU}} = 1.55 \text{ eV}$, $V_{\text{FC}} = 0.8 \text{ eV}$, $V_{\text{MU}} = 2.4 \text{ eV}$, and $V_{\text{MC}} = 0.9 \text{ eV}$. For V_{MC} , the value 1.0 eV should probably be retained, as it is in better agreement with the sharp rise in the heat capacity of UC above 1500 K,⁸ and with earlier measurements by Schüle and Spindler.¹²¹ In stoichiometric UC, the carbon octahedral sites are partly doubly occupied, the resulting carbon excess being balanced by vacancies. At the melting

point (2780 K), the vacancy concentration was estimated to amount to about 8% for both C and U sublattices.⁸ The formation of dislocations in unirradiated and irradiated UC is discussed by Matzke.⁵ Dislocations with a Burgers vector $b = a [100]$ exist in the (100) plane of a UC–UC₂ phase boundary (in the Widmanstätten structure).¹²² Dislocation loops formed by precipitation of fission-induced point defects and stringers of loops were found adjacent to UC₂ platelets.

2.04.4.2.1.2 Uranium sesquicarbide U_2C_3

The lattice parameter of cubic U_2C_3 was studied up to 2073 K by XRD, and no anomalies were detected either at low or high temperature. Its values vary from 807.3 pm at 10 K¹²³ to 825.6 pm at 2073 K.¹¹⁴

Oetting *et al.*¹²⁴ determined the energy of formation for vacancies in the U_2C_3 lattice to be $\sim 0.8 \text{ eV}$, from the heat capacity increase above 1000 K.

The temperature coefficient of the electronic heat capacity was estimated to be $\gamma \approx 84 \text{ mJ K}^{-2} \text{ mol}^{-1}$ from low T heat capacity measurements, in agreement with the metallic character of uranium sesquicarbide. U_2C_3 is antiferromagnetic below the Néel temperature $T_N \approx 55 \pm 4 \text{ K}$.⁸

2.04.4.2.1.3 Uranium dicarbide UC_2

Tagawa *et al.*¹²⁵ showed that the lattice parameter of $\alpha\text{-UC}_2$ increases linearly between $\text{UC}_{1.80}$ and $\text{UC}_{1.96}$ according to the following relation:

$$a = 352.45 + 0.75 \times (\text{C/U} - 1.80) \quad [7]$$

An uncertainty of $\pm 0.01 \text{ pm}$ stems from the different sample preparation methods. Tagawa *et al.*¹²⁶ also showed that the c/a ratio is 1.702 at room temperature, and does not detectably vary as a function of the C/U ratio between $\text{UC}_{1.80}$ and $\text{UC}_{1.96}$, where c stays approximately constant and close to 600 pm. Atoji¹²⁷ measured the lattice parameters of $\text{UC}_{1.86}$ at 5 K by neutron diffraction, finding $a = 351.7 \pm 0.1 \text{ pm}$ and $c = 598.9 \pm 0.1 \text{ pm}$. No phase transitions were detected between 5 and 300 K. The c/a ratio decreases with increasing temperature above 1473 K. Whereas a increases from 353.6 pm at 1073 K to 362.5 pm at 1973 K, there is no complete agreement about the behavior of c . Laugier and Blum¹⁰⁸ suggested that c decreases from 605.6 pm at 1073 K to 594.9 pm at 1700 K on the U-rich side of the tetragonal UO_{2-x} phase field, whereas it varies from 605.6 to 603.9 pm on the C-rich side.

The transformation $\alpha \rightarrow \beta$ is diffusionless of the martensitic type. It occurs without movement of

the U atoms, and with a slight deformation of the C sublattice. The transformation shear angle is between 4° and 6° . β -UC_{2-x} crystallizes in a fcc structure of the KCN-type with $a_0 = 548.8$ pm.¹⁰⁹

UC_{2-x} is a metal. The UC₂ electronic state density at the Fermi level was recently calculated by Shi *et al.*,¹¹⁹ in reasonable agreement with the temperature coefficient γ of the electronic heat capacity. This was estimated to be $16.3 \text{ mJ K}^{-2} \text{ mol}^{-1}$, to yield $N(E_F) \approx 3.45 \text{ eV}^{-1} \text{ atom}^{-1}$ for UC_{1.90} and $16.7 \text{ mJ K}^{-2} \text{ mol}^{-1}$, to yield $N(E_F) \approx 3.53 \text{ eV}^{-1} \text{ atom}^{-1}$ for UC_{1.94}.

Atoji¹²⁷ showed that α -UC_{2-x} is paramagnetic down to 5 K, without superconductivity.

2.04.4.2.2 Thermodynamic properties

2.04.4.2.2.1 Uranium monocarbide UC

Thermodynamic functions of uranium carbides have been extensively reviewed by Holley *et al.*⁴ and, more recently, by Chevalier and Fisher.¹⁰¹ Numerical data are reported in Tables 5 and 6 and plotted in Figures 14 and 15.

A few authors measured the heat capacity of UC from low to high temperature. Holley *et al.*⁴ assessed

the temperature coefficient γ of the electronic heat capacity ($18.9 \pm 1 \text{ mJ K}^{-2} \text{ mol}^{-1}$), the Debye temperature $\theta_D = 328 \text{ K}$, and the high-temperature behavior for $298 \text{ K} \leq T \leq 2780 \text{ K}$.

Most of the U and Pu carbides show steep increase in heat capacities at temperatures above $0.6 T^m$, attributed to the formation of defects.⁴

The 0 K randomization entropy is zero for stoichiometric UC, but an additional term $S(0) = R \ln x$ should be added for nonstoichiometric UC_{1+x} compositions. The formation enthalpy of stoichiometric UC was also assessed by Holley *et al.*⁴ Its value is composition-dependent and slightly decreasing in the hypostoichiometric carbide, as suggested by the uranium vaporization study by Storms¹²⁸ and the carbon activity measurements of Tetenbaum and Hunt.¹²⁹ The UC room-temperature Gibbs energy of formation was calculated from the enthalpy and the standard entropy, and the value $\Delta_f G(\text{UC}, s, 298) = -98.89 \text{ kJ mol}^{-1}$ was proposed by Holley *et al.* for the reaction $\text{U} + \text{C} = \text{UC}$. The error affecting this value was estimated to be around 2.1 kJ mol^{-1} from the uncertainty in the U and C activities, strongly

Table 5 The heat capacity C_p of uranium carbides at atmospheric pressure (in $\text{J K}^{-1} \text{ mol}^{-1}$)

Compound	$T < 10 \text{ K}$	$10 \text{ K} \leq T \leq 300 \text{ K}$	$T > 300 \text{ K}$	Total T range
UC		$9R \left(\frac{328}{T} \right)^3 \int_0^{328/T} \frac{x^4 e^x}{(e^x - 1)^2} dx$	$50.124 + 2.571 \times 10^{-2} T - 1.868 \times 10^{-5} T^2 + 5.716 \times 10^{-9} T^3 - 6.187 \times 10^5 T^{-2}$ (solid UC) $49.887 + 7.794 \times 10^{-3} T$ (liquid UC)	$1.5 \text{ K} \leq T \leq 4800 \text{ K}$
U ₂ C ₃	Figure 14 ^a		$150.71 - 47.89 \times 10^{-3} T + 41.37 \times 10^{-6} T^2 - 29.06 \times 10^6 T - 2$ ($50 \text{ K} \leq T \leq 2000 \text{ K}$)	$5 \text{ K} \leq T \leq 2000 \text{ K}$
α -UC ₂		$9R \left(\frac{304}{T} \right)^3 \int_0^{304/T} \frac{x^4 e^x}{(e^x - 1)^2} dx$	$48.97 + 8.2487 \times 10^{-2} T - 7.8109 \times 10^{-5} T^2 + 3.0267 \times 10^{-8} T^3 - 5.9258 \times 10^5 T^{-2}$	$5 \text{ K} \leq T \leq 2073 \text{ K}$
β -UC ₂ ($T > 2070 \text{ K}$)	–	–	122.9	$2073 \text{ K} \leq T \leq 2700 \text{ K}$

^aNo satisfactory fit for these points, probably due to marked change in slope around 10 K.

Table 6 Thermodynamic functions of uranium carbides (in SI units).

Compound	$\Delta_f H^\circ (298)$ (kJ mol^{-1})	$\Delta_f G^\circ$ (J mol^{-1})	$S^\circ (298)$ ($\text{J K}^{-1} \text{ mol}^{-1}$)	Transition ΔH° (J mol^{-1})	Bulk modulus $B = V^{-1} (\partial^2 E / \partial V^2)$ (GPa)	Critical parameters
UC	-97.95^3	$-31465.6 - 499.228T + 64.7501T \ln(T) - 7984166/T - 0.01447^2$ for $298 \text{ K} \leq T \leq 2780 \text{ K}$	59.12^3	$\Delta_m H^\circ = 48900$	180^{est}	$T_c = 8990 \text{ K};$ $p_c = 1580 \text{ bar};$ $\rho_c = 1.3159 \text{ g cm}^{-3}$ [Gigli]
U ₂ C ₃	182.5	$-732.422 - 806.686T + 107.049T \ln(T) - 11285627/T - 0.030297^2$ for $298 \text{ K} \leq T < 2000 \text{ K}$	137.8	–	208	–
α -UC ₂	85.4 ± 4.2 for UC _{1.94}	$21591.6 - 930.689T + 123.806T \ln(T) - 13384440/T - 0.037087^2$	68.3	$\Delta_{\alpha \rightarrow \beta} H^\circ = 10100^{\text{est}}$	216	–
β -UC ₂	–	–	–	$\Delta_m H^\circ = 67000^{(\text{R})}$	–	–

^(R)=Richard's rule and ^{est}=estimated.

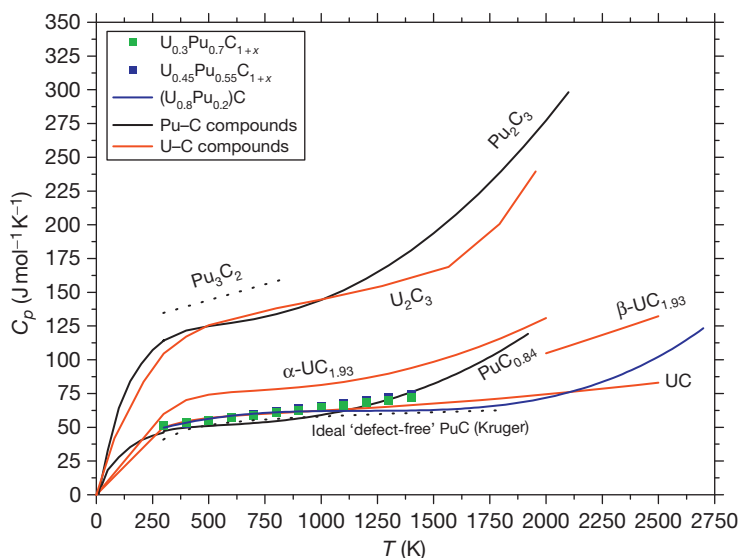


Figure 14 Comparison of the heat capacities of uranium and plutonium carbides and mixed carbides. Note: The values correspond to the reported chemical formulae. For example, $C_p(\text{UC}_{1.5}) = 1/2 C_p(\text{U}_2\text{C}_3)$, $C_p(\text{PuC}_{0.67}) = 1/2 C_p(\text{Pu}_3\text{C}_2)$, and so on.

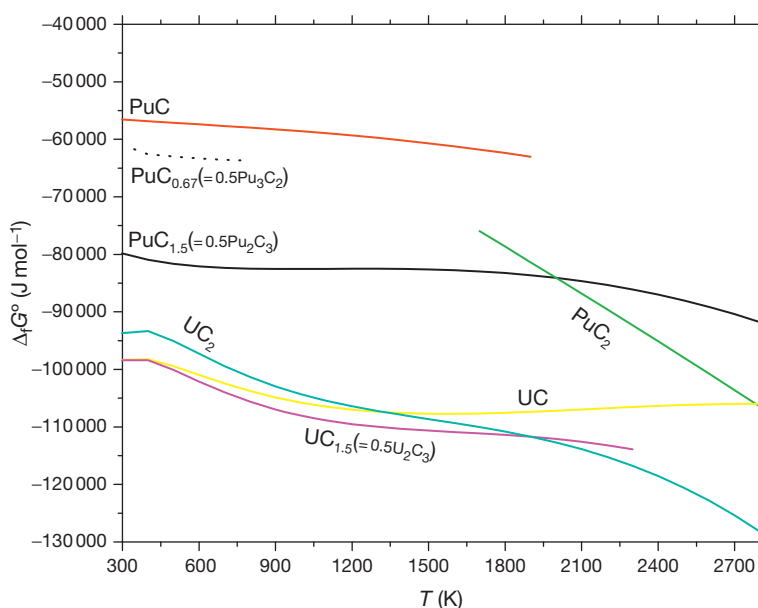


Figure 15 Comparison of Gibbs energies of formation of plutonium and uranium carbides. The values correspond to the reported chemical formulae.

dependent on composition and oxygen impurities. Sheth *et al.*¹³⁰ proposed $\Delta_m H^\circ = 48.9 \text{ kJ mol}^{-1}$ for the enthalpy of fusion and the following data for liquid UC up to 4800 K:

$$C_p(\text{UC, liquid}) = 49.887 + 7.794 \times 10^{-3} T (\text{J K}^{-1} \text{mol}^{-1}) \quad [8]$$

$$H^\circ(T) - H^\circ(298)(\text{UC, liquid}) = 51362 + 49887T + 3.987 \times 10^{-3} T^2 (\text{J mol}^{-1}) \quad [9]$$

The recently assessed and optimized Gibbs energy data gave excellent fit with both thermodynamic properties and phase diagram data. Therefore, Gibbs energies of formation of binary compounds of both

U–C and Pu–C systems can be calculated using Gibbs energy functions given by Chevalier and Fischer¹⁰¹ and Fischer,¹³¹ respectively. To recalculate the Gibbs energy of formation of the compounds here, the free energy of the pure elements, in their stable reference state at a given temperature, is subtracted from that of the compounds. The following expression can be retained for UC from 298.15 K to the melting point:

$$\Delta_f G^\circ(\text{UC})(\text{J mol}^{-1}) = -31465.6 - 499.228T + 64.7501T \ln(T) - 7984166/T - 0.0144T^2 \quad [10]$$

This temperature dependence of $\Delta_f G(\text{UC})$ is shown in **Figure 15** and compared with the ones of other uranium and plutonium binary carbides.

The partial pressures of the actinide species play an important role in the redistribution of actinides and the restructuring of fuel elements during burnup (**Figure 16**).

In the case of U–C system, gaseous UC_n molecules with $n = 1$ –6 have been detected by mass spectrometry.⁸ The partial pressure equations of $\text{UC}_2(\text{g})$, $\text{C}_1(\text{g})$, $\text{C}_2(\text{g})$, and $\text{C}_3(\text{g})$ are derived from the Gibbs energies

of formation and the activities of uranium and carbon.^{4,132–134} In the composition range, $\text{C}/\text{U} = 0.92$ –1.10, the partial pressure of $\text{U}(\text{g})$ is almost equal to the total pressure, the next predominant species being $\text{C}_1(\text{g})$. The following equations⁴ can be used to calculate the U sublimation enthalpy in single-phase regions on the complete U–C system at 2100 K:

$$\log p(2100\text{ K})(\text{bar}) = \frac{2.56}{\exp(29x) + 1} - \frac{2.34}{\exp(-10(x-1)) + 1} - 9.27 + 0.56x + \frac{\Delta_{\text{sub}}H}{9.455} - 1000 \frac{\Delta_{\text{sub}}H}{4.503T} \quad [11]$$

$$\Delta_{\text{sub}}H(\text{kJ mol}^{-1}) = 724 - \frac{305.58}{\exp(40x) + 1} - 192.56x + 58.6 \exp(-100(x-0.86)^2) \quad [12]$$

$x = \text{C}/\text{U} - 1$. The partial pressure of uranium decreases with increasing C/U, showing a steep change in the UC_{1+x} phase field. Correspondingly, the U enthalpy of vaporization increases with C/U up to $711.62 \text{ kJ mol}^{-1}$ at $\text{C}/\text{U} \sim 1.08$. The congruent vaporizing composition was recommended as $\text{UC}_{1.11}$ at 2300 K and $\text{UC}_{1.84}$ at 2100 K.¹⁰¹ At the melting point,

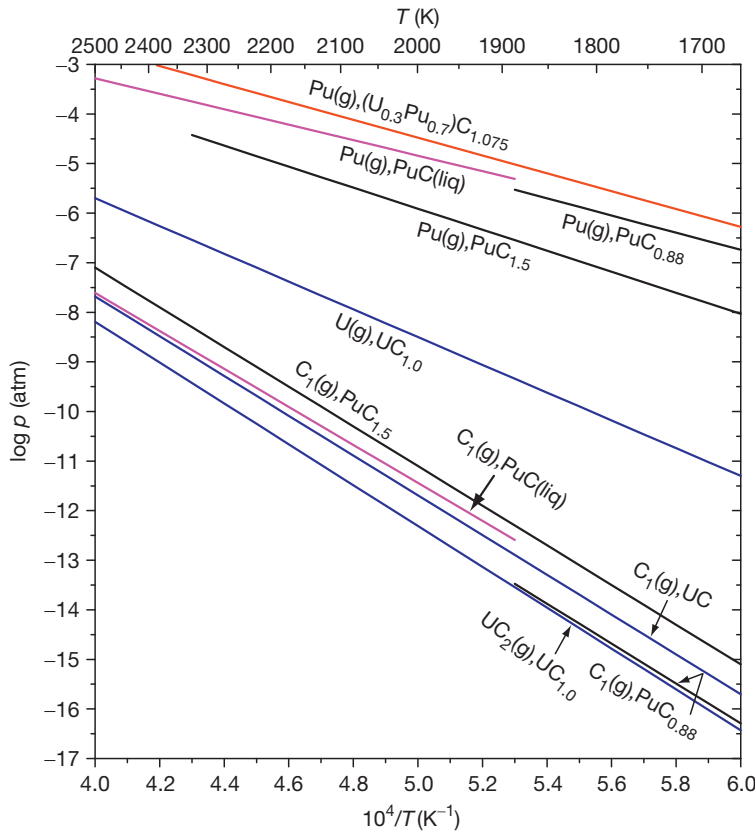


Figure 16 Partial pressures of different species in equilibrium with uranium, plutonium, and mixed carbides.

the sublimation enthalpy is $\Delta_{\text{sub}}H(\text{UC}, 2780) = 661 \text{ kJ mol}^{-1}$, and the vaporization enthalpy $\Delta_{\text{vap}}H(\text{UC}, 2780) = 611 \text{ kJ mol}^{-1}$. The UC total pressure at the melting point is $2.8 \times 10^{-5} \text{ bar}$.⁸ Sheth and Leibowitz¹³³ and Joseph *et al.*¹³⁵ calculated the high-temperature vapor pressures of different species over liquid regions of UC_{1+x} and $\text{MC} + \text{M}_2\text{C}_3$ systems. Sheth and Leibowitz calculated their values from fusion enthalpies and Gibbs energies of formation for condensed and vapor species, whereas Joseph *et al.* used a semi-empirical method based on the Principles of Corresponding States (PCS).¹³⁵ They calculated the critical parameters of the compounds and the total vapor pressure over the liquid up to $\sim 9000 \text{ K}$. Interestingly, the partial pressures of metal species dominate the vapor phase at low temperatures, but at very high temperatures, $T > 4000 \text{ K}$, the partial pressures of carbon-bearing species prevail. Finn *et al.*¹³⁶ provided the following expression to estimate the total pressure (in bar) above liquid UC between 2800 and 10 000 K:

$$\log p = 6.110 - \frac{31704}{T} + 0.197 \log T \quad [13]$$

Ohse *et al.*¹³⁷ obtained the boiling point of UC by extrapolation of the vapor pressure curve to 4700 K. Gigli *et al.*¹³⁸ calculated the isotherms and isochores in the pressure–internal energy coordinates between 5200 and 13 600 K, proposing the following critical quantities: $T_c = 8990 \text{ K}$; $p_c = 1580 \text{ bar}$; $\rho_c = 1.3159 \text{ g cm}^{-3}$. Thermal expansion of crystalline UC results from the lattice expansion and, at very high temperatures, the generation of Schottky defects.⁸ The following expression for the linear thermal expansion coefficient $\alpha_T = l_0^{-1}(dl/dT)$ (l_0 = sample length at 298 K) is a slight modification of an earlier one,¹³⁹ which underestimated the values measured by Richards at 2773 K¹⁴⁰:

$$\alpha_T = 10.08 \times 10^{-6} + 5.802 \times 10^{-9} (T - 273.16)(T \text{ in K}) \quad [14]$$

It can be useful to note that, as UC displays a higher thermal conductivity than does U_2C_3 , there can be internal stresses for a two-phase mixture of UC + U_2C_3 . This factor should be taken into account in multiphased samples.

2.04.4.2.2.2 Uranium sesquicarbide U_2C_3

The low-temperature heat capacity of U_2C_3 was determined by adiabatic calorimetry between 5 and 375 K.^{141,142} The Debye temperature could not be determined because of a reproducible inflection at

10 K. Oetting *et al.*¹²⁴ measured C_p of U_2C_3 by drop calorimetry up to 2000 K. The heat capacity of uranium sesquicarbide is higher than that of all other uranium carbides at all temperatures, as reported in Figure 14.

The room-temperature thermodynamic functions reported in Table 6 were recommended by Holleck and Kleykamp⁸ and by Holley *et al.*⁴

The Gibbs energies of formation of U_2C_3 between 298 K and the decomposition temperature (Table 6 and Figure 15) have been obtained by the same procedure used for UC (Section 2.04.4.2.2.1).

The bulk modulus of U_2C_3 was calculated by Shi *et al.*²⁴ to be 208 GPa, in agreement with the early EOS by Munaghan.¹⁴³

2.04.4.2.2.3 Uranium dicarbide UC_2

Low-temperature heat capacity of $\alpha\text{-UC}_{2-x}$ was studied by adiabatic calorimetry between 5 and 350 K,⁸ yielding the already reported temperature coefficient of the electronic heat capacity, and values of the Debye temperature θ_D of 302 for $\text{UC}_{1.90}$ and 304 K for $\text{UC}_{1.94}$.

Assessed thermodynamic functions for $\alpha\text{-UC}_{1.94}$ are reported in Table 6. The randomization entropy of $\text{UC}_{1.90}$ was calculated by Storms² taking into account the disordered and incomplete sublattice: $S^\circ = 2.7 \text{ J K}^{-1} \text{ mol}^{-1}$.

Heat capacity measurements at higher temperatures could be affected by partial decomposition of $\alpha\text{-UC}_2$ into UC and C below 1790 K. Results were critically assessed by Holley *et al.*⁴ (Table 6 and Figure 15), as well as the latent enthalpy and entropy of the $\text{UC}_{2-x} \alpha \rightarrow \beta$ transition.

Fink *et al.*⁴³ proposed a value for the enthalpy of solid $\beta\text{-UC}_{2-x}$ at the melting point, $H^f(2720) - H^\circ(298) \approx 256 \text{ kJ mol}^{-1}$.

The Gibbs energy of formation values given by Holley *et al.* for UC_{2-x} are higher than those of Chevalier and Fischer.¹⁰¹ The expression in Table 6 is recommended here.

A complete treatment of the vapor pressures over the $\text{UC}_{1+x}\text{--UC}_{2-x}$ phase field is reported by Holley.⁴ Norman and Winchell¹⁴⁴ proposed the following values for the enthalpy and entropy of sublimation of $\beta\text{-UC}_{2-x}$ at the average $T = 2500 \text{ K}$: $\Delta_{\text{sub}}H^\circ(2500) \approx 774 \text{ kJ mol}^{-1}$ and $\Delta_{\text{sub}}S^\circ(2500) \approx 160 \text{ kJ mol}^{-1} \text{ K}^{-1}$.

The $\alpha\text{-UC}_{2-x}$ low-temperature values for the average linear thermal expansion coefficients yielded by neutron diffraction spectra at temperatures between 5 and 298 K¹²⁷ were $\alpha_{T_a} = (9 \pm 1) \times 10^{-6} \text{ K}^{-1}$ and $\alpha_{T_c} = (6 \pm 1) \times 10^{-6} \text{ K}^{-1}$. These values for $\alpha\text{-UC}_{2-x}$

were observed to increase at higher temperature, $\alpha_{Ta} = (16.6 \pm 0.2) \times 10^{-6} \text{ K}^{-1}$ and $\alpha_{Tc} = (10.4 \pm 0.2) \times 10^{-6} \text{ K}^{-1}$ between 298 and 1208 K. Neutron scattering studies between 1273 and 2573 K yielded the following average coefficient of thermal expansion for quasi-isotropic $\alpha\text{-UC}_2$: $\alpha_{Ta} = 18 \times 10^{-6} \text{ K}^{-1}$ (up to 2050 K) and $\alpha_{Ta} = 25 \times 10^{-6} \text{ K}^{-1}$ for $\beta\text{-UC}_2$ at higher temperature. The coefficient of average cubic thermal expansion for $\beta\text{-UC}_{2-x}$ between 298 K and the melting point was suggested by Storms² as $\bar{\gamma} = 4 \times 10^{-5} \text{ K}^{-1}$.

The bulk modulus of $\alpha\text{-UC}_{2-x}$ was measured to be $B = 216 \text{ GPa}$.¹⁴⁵

2.04.4.2.3 Transport properties

2.04.4.2.3.1 Uranium monocarbide UC

The thermal conductivity of UC is plotted in **Figure 1** as a function of temperature.^{5,8} Data are scattered due to the sample impurities, thermal history, experimental conditions, etc. The only obvious conclusion is that between room temperature and about 600 K, the expected hyperbolic decrease of the lattice conductivity occurs from about $22 \text{ W K}^{-1} \text{ m}^{-1}$ to about $20 \text{ W K}^{-1} \text{ m}^{-1}$, with a scatter of about $\pm 10\%$. This behavior follows the trend of phonon contribution to heat conduction, optimized by Storms,¹⁴⁶ between room temperature and 1100 K:

$$\lambda_{PH} = \frac{8 \times 10^{-4}}{T \left[1.154 \times 10^3 \exp\left(\frac{-18356}{T}\right) + (1 - C/U) + 6 \times 10^{-4} \right]^2} \quad (\text{WK}^{-1} \text{ m}^{-1}) \quad [15]$$

Here, the term in square brackets accounts for vacancies: the exponential term describes the thermal formation of vacancies, the term $(1 - C/U)$ represents chemical vacancies, and 6×10^{-4} represents a small room temperature vacancy concentration to prevent λ from approaching infinity. This λ dependence was postulated by analogy with zirconium carbide. For $T > 1500 \text{ K}$, λ increases very slowly with temperature as expected for the electron contribution to heat conduction. It can then be represented by the electrical resistivity ρ_E combined with Lorenz equation:

$$\lambda_E = \frac{2.4T}{\rho_E} (\text{WK}^{-1} \text{ m}^{-1}) \quad [16]$$

Involved uncertainties are obviously manifold: the measured λ may reflect the presence of nonequilibrium quenched-in C atoms (interstitials or C_2 pairs), the effect of O and N impurities is neglected, etc. Thus, it seems difficult to assess, based on the available literature, the heat conductivity behavior as a

function of the C/U ratio, whereas oxygen impurities clearly lead to a decrease of λ , which can reach up to a factor 2 for 15 at.% O, as shown in **Figure 3**.⁸ The thermal conductivity of UC was reported to increase with the grain size at equal porosity.⁸ For modeling purposes, this rather complex behavior of λ is usually simplified by employing handier analytical relations, as for example⁵:

$$\lambda_{UC} = 20 \quad (\text{WK}^{-1} \text{ m}^{-1} \text{ for } T < 773 \text{ K}) \quad [17]$$

$$\lambda_{UC} = 20 + 1.3 \times 10^{-3} (T - 773) \quad (\text{WK}^{-1} \text{ m}^{-1} \text{ for } T \geq 773 \text{ K}) \quad [18]$$

Diffusion in uranium carbides is strongly related to the formation and migration of point defects, namely, vacancies, interstitials, and Frenkel pairs.¹¹⁵ Results are once more affected by the phase separation, impurity content, the C/U ratio, the presence of metastable tetragonal UC_2 impurities at low temperature, grain size, and other preparation-, storage-, and thermal-history-dependent properties of the samples.

Available data assessed and compared with embedded atom method (EAM) potential calculations¹¹⁵ are summarized in **Figure 17**.

The uranium self-diffusion coefficient proposed by Holleck and Kleykamp⁸ can be retained as the most reliable:

$$D_U^{UC} \approx 1 \times 10^{-3} \exp(-Q_U/RT) (\text{m}^2 \text{ s}^{-1}) \quad [19]$$

$Q_U = 594 \text{ kJ mol}^{-1}$ for uranium in stoichiometric UC with $< 30 \text{ ppm}$ impurities between 1770 and 2400 K, and

$$D_C^{UC} \approx 2 \times 10^{-3} \exp(-Q_C/RT) (\text{m}^2 \text{ s}^{-1}) \quad [20]$$

$Q_C = 350 \text{ kJ mol}^{-1}$ as an average value for carbon self-diffusion between 1570 and 2350 K.

The following expression is recommended⁸ for polycrystalline, cast, stoichiometric UC with 130 ppm metallic impurities between 1750 and 2780 K:

$$D_U^{UC} \approx 6.9 \times 10^{-4} \exp(-590/RT) + 3.6 \times 10^{-9} \exp(-354/RT) (\text{m}^2 \text{ s}^{-1}) \quad [21]$$

The diffusion of uranium in UC can be explained by a single-vacancy mechanism in the single-phase region. Its activation energy increases with the C content from $\sim 370 \text{ kJ mol}^{-1}$ for $C/U = 0.92$ to $\sim 750 \text{ kJ mol}^{-1}$ for $C/U = 1.07$. Below 1700 K, U diffusion seems to be possible only if metallic impurities lower its activation energy.

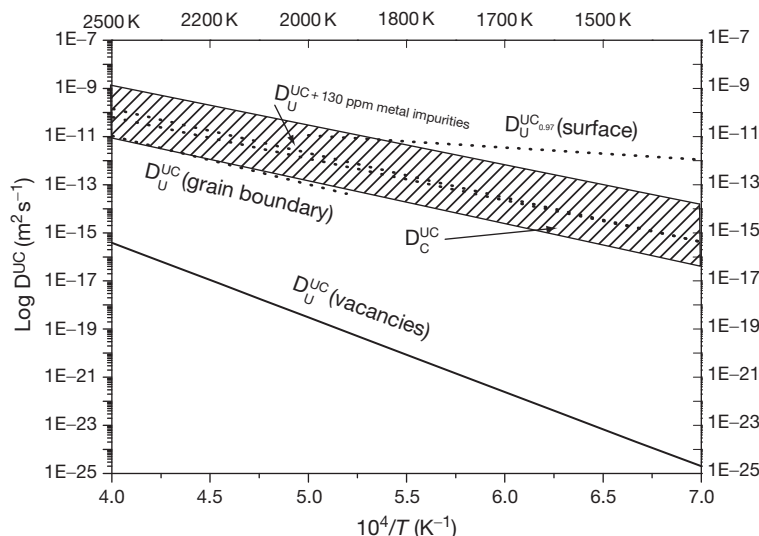


Figure 17 The behavior of self-diffusion coefficients for U in stoichiometric monocrystalline UC, U in polycrystalline UC with 130 ppm of metal impurities, and C (shaded area) in nearly stoichiometric UC. Impurities considerably affect the self-diffusion coefficient of uranium and so do grain boundaries and surfaces. The shaded area shows an uncertainty limit estimate for C diffusivity, taking into account deviations from stoichiometry ($0.92 \leq C/U \leq 1.5$) and impurity content. Adapted from Atkinson, A. *Solid State Ionics* **1984**, 12, 309–320; Matzke, H.j. *Science of Advanced LMFBR Fuels*; North Holland: Amsterdam, 1986.

The diffusion coefficient of carbon, D_C^{UC} , and the activation energy of carbon diffusion, Q_C , are independent of the C/U ratio in hypostoichiometric UC, where $D_{0C}^{UC_{1-x}} \approx 1 \times 10^{-22} \text{ m}^2 \text{ s}^{-1}$ and $Q_C^{UC_{1-x}} \approx 380 \text{ kJ mol}^{-1}$. In the hyperstoichiometric range, $Q_C^{UC_{1+x}}$ decreases to $\sim 230 \text{ kJ mol}^{-1}$ and D_C^{UC} rises by about one order of magnitude up to C/U = 1.07, where the two-phase region begins.

The diffusion of carbon in hypostoichiometric UC is explained by a vacancy mechanism. For C/U ≥ 1.00 up to the phase boundary, the diffusion of C_2 pairs becomes increasingly significant by the interstitial mechanism.⁸

Assessment of a few experimental studies on the chemical diffusion of C in stoichiometric UC yielded, between 1458 and 2620 K⁸:

$$\overline{D}_C^{UC} \approx 3 \times 10^{-5} \exp(-266/RT) (\text{m}^2 \text{ s}^{-1}) \quad [22]$$

Grain boundary and surface U and C diffusion can also play a relevant role in UC as fast diffusion or short-circuit paths, as described by Atkinson.¹⁴⁷ Wallace *et al.*¹⁴⁸ showed that in a UC_{1+x} sample under temperature gradient, C is transported to the cold end. The Soret diffusion coefficient is characterized, for $UC_{1.06}$, by a transport enthalpy $Q_S = 22 \text{ kJ mol}^{-1}$. This value, probably underestimated, was

observed to decrease with the C/U ratio up to C/U = 1.84.

UC has metallic electrical conductivity, and at high temperature ($T > 1000 \text{ K}$ approximately), it follows Lorenz equation [16] which relates thermal and electrical conductivity. Measurements of electrical resistivity are therefore important for understanding the technologically more interesting thermal conductivity plus other basic properties such as phase boundaries and point defects. The recommended room temperature for quasipure UC is^{5,8}

$$\rho_{UC} = 0.34 \pm 0.02 \text{ } \mu\Omega \text{ m} \quad [23]$$

This value can be considered as a minimum, as ρ has been observed to increase with both vacancies (in UC_{1-x}) and interstitials (in UC_{1+x}), with the formation of higher carbides (U_2C_3 , UC_{2-x}) in equilibrium with UC and with increasing temperature. The recommended ρ curves for UC, α - UC_2 , U_2C_3 , and an example of oxycarbide are summarized in Figure 18. Linear and parabolic dependencies of ρ on temperature have been proposed, but they do not seem to describe data very convincingly. The UC electrical conductivity decreases continuously with increasing pressure, approximately by a factor 10 at 50 kbar and 298 K.¹⁴⁹ No superconductivity has been observed in UC at $T \geq 1.20 \text{ K}$.

2.04.4.2.3.2 Uranium sesquicarbide U_2C_3

U_2C_3 thermal conductivity is lower than UC and UC_2 . From the study reported by De Coninck *et al.*,¹⁵⁰ the following equation can be used between 298 and 2073 K:

$$\lambda_{U_2C_3} = 6.58 + 0.00563(T - 273.16)(Wm^{-1}K^{-1}) \quad [24]$$

The electrical resistivity of U_2C_3 has been observed to be much larger than for any other U–C composition, with a room-temperature value $\rho_{U_2C_3} = 2.20 \pm 0.05 \mu\Omega m$ ¹⁵¹ (Figure 18). It shows an interesting temperature dependence, with a kink around 54 K and $1.6 \mu\Omega m$, probably corresponding to a ferromagnetic–paramagnetic transition.

Carbon chemical diffusion in U_2C_3 was studied by Wallace *et al.*,¹⁴⁸ who obtained

$$\bar{D}_C^{U_2C_3} \approx 2.3 \times 10^{-2} \exp(-411/RT)(m^2s^{-1}) \quad [25]$$

The diffusion of uranium in U_2C_3 is slower and occurs via two independent diffusion mechanisms not yet fully understood.⁵ The self-diffusion coefficient values proposed for the two diffusion rates are

$$D_{U1}^{U_2C_3} \approx 3.4 \times 10^{-4} \exp(-450/RT)(m^2s^{-1}) \quad [26]$$

$$D_{U2}^{U_2C_3} \approx 5.9 \times 10^{-8} \exp(-400/RT)(m^2s^{-1}) \quad [27]$$

2.04.4.2.3.3 Uranium dicarbide UC_2

Trends for the thermal conductivity λ of α - UC_2 were reported by De Coninck *et al.*,¹⁵² based on thermal diffusivity measurements between 873 and 2333 K:

$$\begin{aligned} \lambda_{\alpha-UC_2} = & 11.5 + 2.7 \times 10^{-3}(T - 273.15) \\ & + 2.8 \times 10^{-8}(T - 273.15)^2 + 3.035 \times 10^{-10} \\ & (T - 273.15)^3 (Wm^{-1}K^{-1}) \quad 873K \leq T \leq 2013K \end{aligned} \quad [28]$$

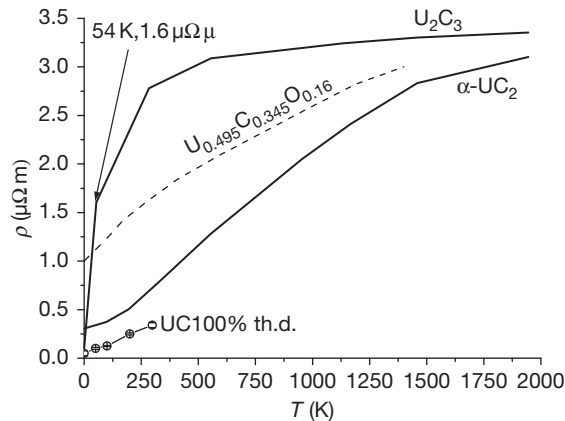


Figure 18 The electrical resistivity of uranium carbides. Dotted line: example relative to one uranium oxycarbide.

$$\lambda_{\beta-UC_2} = 8.2 + 5.64 \times 10^{-3}(T - 273.16)(Wm^{-1}K^{-1})$$

$$\text{for } 2103K \leq T \leq 2333K \quad [29]$$

Matsui *et al.*¹⁵¹ observed that the electrical resistivity of UC_2 at room temperature is $\rho_{UC_2} = 0.70 \pm 0.03 \mu\Omega m$, that is, about twice that of UC (Figure 18). At high temperature, ρ_{UC_2} is about 40% larger than ρ_{UC} . Biphased samples of UC_{1+x} containing Widmanstätten structure of UC_2 needles in a UC matrix show ρ values approaching those of pure UC_2 .

Matzke and Politis¹⁵³ and Routbort and Matzke¹⁵⁴ studied the uranium self-diffusion in UC_2 between 1670 and 2500 K by the α -energy degradation method with a ^{233}U tracer. The U diffusion coefficient in α - UC_{2-x} and β - UC_{2-x} resulted to be

$$D_U(UC_{2-x}) = 0.07 \exp(-550/RT)(m^2s^{-1}) \quad [30]$$

with a small discontinuity observed at the $\alpha \rightarrow \beta$ transition temperature, where D_U jumps from 2×10^{-16} to $6 \times 10^{-16} m^2s^{-1}$. It was also observed that the grain boundary diffusion coefficient is higher by a factor around 10^3 than the bulk diffusion coefficient for both α - and β - UC_{2-x} . Holleck and Kleykamp⁸ report also values for the chemical diffusion coefficient of carbon in both α - and β - UC_{2-x} :

$$\begin{aligned} \bar{D}_C(\alpha - UC_{2-x}) = & 1.56 \times 10^{-2} \exp(-377/RT) \\ & (m^2s^{-1} \text{ for } 1798K \leq T \leq 2050K) \end{aligned} \quad [31]$$

$$\begin{aligned} \bar{D}_C(\beta - UC_{2-x}) = & 9.5 \times 10^{-4} \exp(-323/RT) \\ & (m^2s^{-1} \text{ for } 2103K \leq T \leq 2620K) \end{aligned} \quad [32]$$

2.04.4.2.4 Mechanical properties

2.04.4.2.4.1 Uranium monocarbide UC

The XRD theoretical density of UC (natural U) at 298 K is $\rho_0 = 13.60 g cm^{-3}$. The following temperature dependence for ρ , based on the dilatometrically determined thermal expansion of UC,¹⁵⁵ is recommended:

$$\rho = \rho_0 \left[1 + 3 \left(\frac{\Delta l}{l_0} \right) + 3 \left(\frac{\Delta l}{l_0} \right)^2 + \left(\frac{\Delta l}{l_0} \right)^3 \right]^{-1} \quad [33]$$

Estimated values at the melting point are $\rho_{SOLID} \approx 12.3 g cm^{-3}$; $\rho_{LIQUID} \approx 9.84 g cm^{-3}$.

For liquid UC, the following expression can be retained:

$$\rho_{LIQ} = \frac{12.57}{1 + 9.98 \times 10^{-5} T} \quad [34]$$

leading to a boiling point density $\rho = 8.5 \text{ g cm}^{-3}$ for a boiling temperature of 4797 K. Sheth *et al.*¹⁵⁶ gave an analytical expression for the UC density between the melting point and the critical temperature, yielding $\rho_c = 2.3 \text{ g cm}^{-3}$.

The Young, torsion, and bulk moduli (E , T , and ν , respectively) of UC were determined from the velocity of sound in polycrystalline UC of various porosities 157. Results are summarized in Table 8. Padel and de Novion¹⁵⁷ gave expressions for the fractional porosity P dependency of E and ν :

$$E = E_0(1 - 2.31P) \text{ GPa} \quad [35]$$

$$\nu = \nu_0(1 - 0.986P) \quad [36]$$

$0 \leq P < 1$.

The temperature dependence of E follows approximately the equation⁵:

$$E(T) = E_0[1 - 0.92 \times 10^{-4}(T - 298)] \text{ GPa} \quad [37]$$

In the last three formulas, E_0 and ν_0 represent the room-temperature values of the moduli, for a 100% th.d. The temperature effect on 100% th.d. UC is very small (ν was observed to decrease from 0.288 to 0.278 between 298 and 1850 K¹⁵⁸), but it is more important in samples with higher porosity.¹⁵⁹ The fission products effect is very small, at least up to a burnup of 8%.⁵

UC is known to have good plasticity under load and at high temperature, which allows its fabrication by extrusion. The brittle–ductile transition occurs between 1273 and 1473 K, depending on deformation and grain size.

The room temperature Vickers hardness (HV) of UC_{1.00} was reported by Matzke⁵ to be 6.7 GPa for a load of 4.9 N. This value increases slightly for the hypostoichiometric carbides (7.3 GPa for UC_{0.91}) and decreases in the hyperstoichiometric ones (6.5 GPa in UC_{1.05}), at least in the vicinity of C/U = 1.00⁸.

HV data for UC exist between room temperature and 1800 K.⁸ A precise trend of HV versus T is difficult to define, as experimental data are often dependent on the sample thermal history, grain size, impurity content, C/U ratio, and porosity. As a fair approximation, HV decreases with increasing temperature by a factor 4 between 300 and 1100 K, and by another factor 4 between 1100 and 1800 K.

Creep behavior in uranium monocarbide was reviewed by Holleck and Kleykamp in 1987⁸ and will be presented more extensively in Chapter 3.03, Carbide Fuel of this Comprehensive. Primary creep

was investigated both in single crystals and polycrystalline samples. A general time dependence

$$\dot{\epsilon} = t^n \quad [38]$$

can be assumed for $t < 3 \text{ h}$ at $1273 \text{ K} \leq T \leq 2128 \text{ K}$, with $n = -0.66$ at 1543 K and $n = -0.4$ at 2128 K. For $t > 3 \text{ h}$, a trend of the type

$$\log \dot{\epsilon} = -kt \quad [39]$$

was observed at 1543 K, with $k = 0.084 \text{ h}^{-1}$. Secondary creep in UC has been more extensively studied, and the creep rate can be quantitatively described by the empirical relationship

$$\dot{\epsilon} = Ad^{-m}\sigma^n \exp\left(-\frac{Q}{RT}\right) \quad [40]$$

where A , m , and n are constant for a particular composition and structure, d is the grain size, σ is the stress, and Q is the apparent activation energy. For hyperstoichiometric fuel, the constants A , n , and Q were estimated by Hall¹⁵⁹ to be $1.57 \times 10^{11} (\text{h}^{-1})$, 2.4 and 506 kJ mol^{-1} , respectively. These values seem too uncertain to be used as input data for fuel performance models. In fact, the C/U ratio, porosity, grain size, and impurities can independently change the creep rate by several orders of magnitude. Stoichiometric and hypostoichiometric carbides ($\text{C/U} < 1.01$) creep faster than hyperstoichiometric carbides, due to UC_{2- x} precipitation. The stress exponent for single crystals is much higher ($n > 5$) than it is in polycrystalline UC.

2.04.4.2.4.2 Uranium sesquicarbide U₂C₃

The U₂C₃ XRD density is 12.85 g cm^{-3} .

Holleck and Kleykamp⁸ assessed the Vickers hardness of U₂C₃. Under a load of 0.5 N, HV 1500 is recommended at 298 K. High-temperature hardness varies from HV 500 at 1273 K to HV 12 at 1573 K, under a load of 10 N.

Nelson and Foster¹⁶⁰ reported the 0.2% compressive yield stress $\sigma_{0.2}$ annealed U₂C₃ to be $\sigma_{0.2} = 620 \text{ MN m}^{-2}$ at 1473 K and $\sigma_{0.2} = 350 \text{ MN m}^{-2}$ at 1873 K, close to the brittle–ductile transition temperature.

Creep tests were carried out on uranium sesquicarbide and reviewed by Holleck and Kleykamp.⁸ The stress exponent n lies between 1.2 and 2.8 in the creep law formulation $\dot{\epsilon} = \sigma^n$ and rises with temperature between 1473 and 1673 K.¹⁶¹ These results show that the bcc U₂C₃ creep rate at 1473 K under a compressive stress σ_C of about 40 MN m^{-2} is of the order of 100 times lower than the one of slightly hypostoichiometric fcc UC_{1- x} under the same conditions.

2.04.4.2.4.3 Uranium dicarbide UC₂

The XRD density of metastable α -UC₂ at room temperature is 11.69 g cm⁻³ for C/U = 1.94. The theoretical density of β -UC₂ can be estimated to be 10.81 g cm⁻³ for C/U = 1.94 with $a = 548.8$ pm (value at 2173 K). Holleck and Kleykamp⁸ report an estimated value $\rho_{\beta\text{-UC}_{2-x}} = 10.6$ g cm⁻³ at the melting point.

Clarck and Mountford¹⁶² reported a Vickers hardness value HV 790 under a load of 1 N at room temperature for cast α -UC_{1.96}. This result shows that the hardness of α -UC₂ at room temperature is similar to the hardness of UC. The Vickers hardness of melted α -UC₂ rich in carbon was observed to vary from HV 350 to HV 780 when the applied load varies from 0.1 to 0.6 N at room temperature and depending on the crystal orientation.¹⁶³

The compressive rupture strength σ_c of α -UC_{1.94} is reported in Holleck and Kleykamp⁸ to be 910 MN m⁻², higher than the one of UC (around 300 MN m⁻²) and slightly lower than the one of U₂C₃ (around 1150 MN m⁻²). This trend seems to continue up to high temperature, where σ_c of α -UC_{1.94} was observed to decrease from 750 MN m⁻² at 1573 K to 450 MN m⁻² at 1873 K. The transverse rupture strength of cast α -UC_{1.94} was reported by Chubb and Dickerson¹⁶⁴ to be 55 MN m⁻² at room temperature.

Kurasawa and Kiruchi¹⁶⁵ studied the creep behavior in α -UC_{2-x} with $1.90 \leq \text{C/U} \leq 1.94$, 90% th.d., between 14 and 103 MN m⁻² and between 1473 and 1673 K, showing that the secondary creep rate is slightly slower in α -UC_{2-x} than in UC.

2.04.4.2.5 Optical properties

2.04.4.2.5.1 Uranium monocarbide UC

Freshly cleaved UC is bright gray with a metallic shine. It promptly darkens in contact with oxygen, due to the formation of a thin oxide layer on the surface.

Bober *et al.*¹⁶⁶ studied the spectral reflectivity ρ of liquid UC, using a laser sphere reflectometer with a polarized laser beam at different angles and wavelengths (458, 514, 647, and 752 nm). The refractive index n and absorption constant κ were obtained. n resulted to be around 2 at 458 and 514 nm, and 2.5 at 647 nm, slightly decreasing with temperature in both cases, up to 1.7 at 4100 K and 458 nm and 2.1 at 647 nm. The value of n at 752 nm is 1.7, independent of temperature. The same trend was observed for κ , which takes the value 2.5 at 458 and 514 nm and 3.1 at 647 nm, decreasing with T , whereas $\kappa = 2.5$ at 752 nm is independent of T .

The normal spectral emissivity ε_λ of UC has been investigated at 650 nm in polycrystalline samples. Results are certainly affected by oxidation of the sample surface. The most complete trend is the one proposed by Bober *et al.*,^{167,168} based on reflectivity measurements on 96.5% th.d. UC (with 0.36 wt% O and 0.02 wt% N) between 300 and 2780 K and in liquid UC between 2780 and 4200 K:

$$\varepsilon_{650} = 0.566 - 2.7209 \times 10^{-6} T + 2.7697 \times 10^{-9} T^2 - 2.7102 \times 10^{-12} T^3 + 2.8618 \times 10^{-16} T^4 \quad [41]$$

for $300 \text{ K} \leq T \leq 2780 \text{ K}$, and

$$\begin{aligned} \varepsilon_{650} = & 0.452 - 4.3247 \times 10^{-6} (T - 2780) \\ & + 3.1967 \times 10^{-9} (T - 2780)^2 \\ & - 1.6784 \times 10^{-12} (T - 2780)^3 \\ & - 4.6641 \times 10^{-16} (T - 2780)^4 \end{aligned} \quad [42]$$

for $2780 \text{ K} \leq T \leq 4200 \text{ K}$. An experimental error of $\pm 5\%$ should be taken into account, leading to uncertainty bands larger than the proposed emissivity variation as a function of temperature. Even considering those uncertainty bands, a marked discontinuity of about 0.1 in ε_λ upon melting remains clear. Such a gap is probably dependent on the oxygen-impurity content.¹⁶⁹ For practical purposes, it is reasonable to assume for solid UC $\varepsilon_{650} = 0.55 \pm 0.02$ and for liquid UC $\varepsilon_{650} = 0.45 \pm 0.02$. De Bruycker¹⁶⁹ provided the following wavelength dependence of solid and liquid UC spectral emissivity for $488 \text{ nm} \leq \lambda \leq 900 \text{ nm}$:

$$\text{Solid UC: } \varepsilon_\lambda = 0.75746 - 0.46791\lambda + 0.1849\lambda^2 \quad [43]$$

$$\text{Liquid UC: } \varepsilon_\lambda = 0.79998 - 0.75545\lambda + 0.39036\lambda^2 \quad [44]$$

De Coninck *et al.*¹⁷⁰ measured the total hemispherical emissivity ε_T of nearly stoichiometric UC, obtaining $\varepsilon_T = 0.45$ between 1400 and 2100 K.

2.04.4.2.5.2 Uranium sesquicarbide U₂C₃

Freshly cleaved uranium sesquicarbide is bright gray with a metallic luster. U₂C₃ optical functions have never been studied so far.

2.04.4.2.5.3 Uranium dicarbide UC₂

α -UC_{2-x} is bright gray with a metallic shine and darkens upon oxidation. The normal spectral emissivity of α - and β -UC_{2-x} at 650 and 2300 nm was

studied by Grossman¹⁷¹ and by De Croninck *et al.*¹⁵² The results of this latter work, in agreement with Grossman's, are shown in Figure 19. The total hemispherical emissivity was estimated to be around 0.55 between 1300 and 2350 K. These results suggest that the emissivity of UC_{2-x} does not detectably vary in the visible range upon the $\alpha \rightarrow \beta$ transformation, whereas it varies very little in the infrared range.

2.04.4.2.6 Multielement uranium carbides

An overview of the ternary uranium–plutonium and uranium–thorium carbides is given later in this chapter. Here, a short introduction to uranium carbide oxides and carbide nitrides is presented. Ternary species of this kind form relatively easily in UC_x in contact with air.

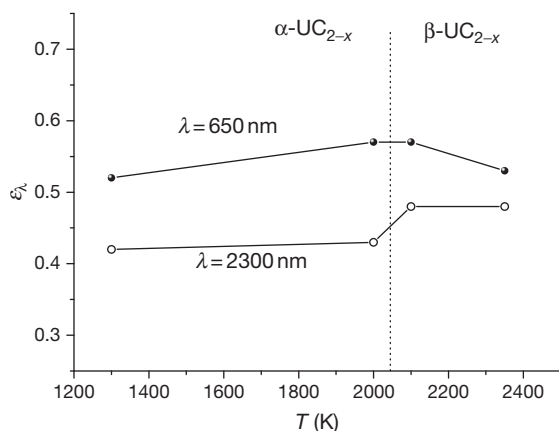


Figure 19 The spectral emissivity of UC_2 at two different wavelengths. Reproduced from De Coninck, R.; De Batist, R.; Gijs, A. *High Temp. High Press.* **1976**, 8, 167–176.

2.04.4.2.6.1 Uranium carbide oxides

The oxidation of uranium carbide is a complex process dependent on temperature, the O_2 partial pressure, the separation of the reaction products, and the process state. A comprehensive review on the oxidation of uranium carbides can be found in Le Guyadec.¹⁷² In this paper, two mechanisms for UC ignition between 413 and 473 K are proposed, shown in Figure 20, based on the nature of the oxide layers or bilayers formed (UCO solid solution and UO_2 oxide) and on the sudden or progressive fracture of these layers. The formation of U_3O_8 was instead observed above 573 K.

Earlier, Camagni *et al.*¹⁷³ had shown that the oxide layer formed on UC in air can have a passivating effect, hindering further bulk oxidation.

Many studies have been carried out in the U–C–O system, not only motivated by the usual presence of oxygen impurities in uranium carbides, but also because the oxycarbide themselves can be suitable for nuclear applications.³² In the technological context of the TRISO fuel development, the system U–C–O has been recently reviewed both from the viewpoint of the oxygen-impurity contamination of uranium carbide fuel¹⁷⁴ and the interaction of UO_2 fuel with the pyrolytic graphite buffer layer.^{175,176} The only real ternary compound is the solid solution $UC_{1\pm x}O_y$ (or $U(C,O)$), besides the slight solubility of oxygen in UC_2 with the resulting dicarbide stabilization. Henry¹⁷⁷ measured the composition of $UC_{1\pm x}O_y$ in equilibrium with UO_2 and metal as $UC_{0.66}O_{0.34}$ at 1973 K, with a fcc NaCl lattice parameter $a = 494.8 \pm 0.1$ pm. These measurements are in fair agreement with more experimental data assessed by

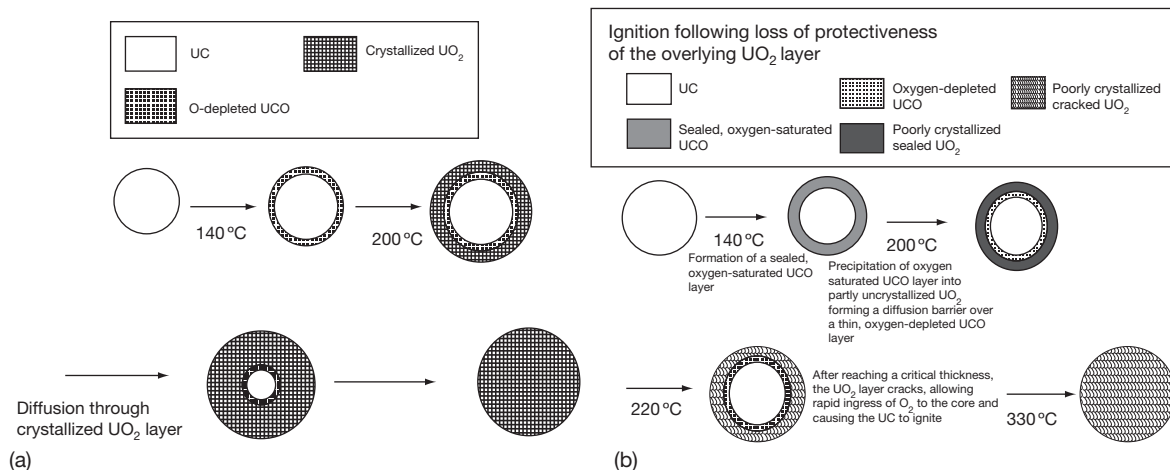


Figure 20 (a and b) The two mechanisms proposed by Le Guyadec *et al.*¹⁷² for the ignition of uranium carbide.

Holleck and Kleykamp,⁸ and were essentially used by Guéneau *et al.*¹⁷⁴ in their thermodynamic study. Up to 5% vacancies can be formed in the nonmetal sublattice of U(C, O). The phase diagram U–C–O is illustrated through the isothermal sections given in Figure 21.¹⁷⁴

These isothermal sections of the ternary system U–C–O were constituted from thermodynamic functions of the U–O, U–C, and C–O binary systems.^{101,178} The thermodynamic functions of both $\text{UC}_{1\pm x}\text{O}_y$ and $\text{UC}_{2-x}\text{O}_x$ were evaluated from Henry's data¹⁷⁷ and the free energy of formation estimated by Potter.¹⁷⁹ For $\text{UC}_{1\pm x}\text{O}_y$, a (C1,C2,O, Va)1(U)1 sublattice model was used, allowing to take into account a U/(C + O) ratio different than 1. For the dioxycarbide, a similar model (C1,C2,O, Va)1(U)1 was chosen, assuming an ideal solution between UC_2 and UO_2 . A solubility of several percents of oxygen in UC_2 was obtained. It was reported by Heiss¹⁸⁰ that up to 6% of carbon atoms can be replaced by oxygen in the anion sublattice of $\alpha\text{-UC}_2$. However, the temperature of formation of the ternary phase $\text{UC}_{2-x}\text{O}_x$ in U–O–C is not known. Only uncertain experimental data exist for $T < 1573$ K, where more calculations have recently

been compared with some mass spectroscopy data.¹⁷⁵ Blum *et al.*^{181,182} observed at 1390 K the ternary eutectic of the U–C–O system. The eutectic of the pseudo-binary UC– UO_2 system was reported at 2523 K.¹⁸³

The enthalpy of formation of $\text{UC}_{1-x}\text{O}_x$ was measured¹⁸⁴ by combustion calorimetry:

$\Delta H^\circ_f(298 \text{ K}) = -90.8 - 454x \text{ kJ mol}^{-1}$ up to $x = 0.84$ (well beyond the oxygen solubility limit). In the same work, the heat capacity of $\text{UC}_{1-x}\text{O}_x$ between 313 and 643 K was also measured by adiabatic calorimetry, obtaining

$$C_p = 58.4 + 0.00134T - 799\,000T^{-2} (\text{J K}^{-1} \text{mol}^{-1}) \quad [45]$$

The standard entropy of $\text{UC}_{1-x}\text{O}_x$ at 298 K was estimated to be $S^\circ(298 \text{ K}) = 47.3 + 2.97 \cdot x \text{ J K}^{-1} \text{mol}^{-1}$. More thermodynamic data can be found elsewhere.^{174–176}

The equilibrium CO partial pressures in the $\text{UO}_2\text{--UC}_2\text{--C}$ section of the U–C–O system were critically assessed by Gossé *et al.*¹⁷⁶ Figure 22(a) shows the CO pressure values for the monovariant equilibrium $\text{UO}_{2-x} + \text{UC}_2 + \text{C}$ in the temperature range 1473–2140 K and Figure 22(b) reports the

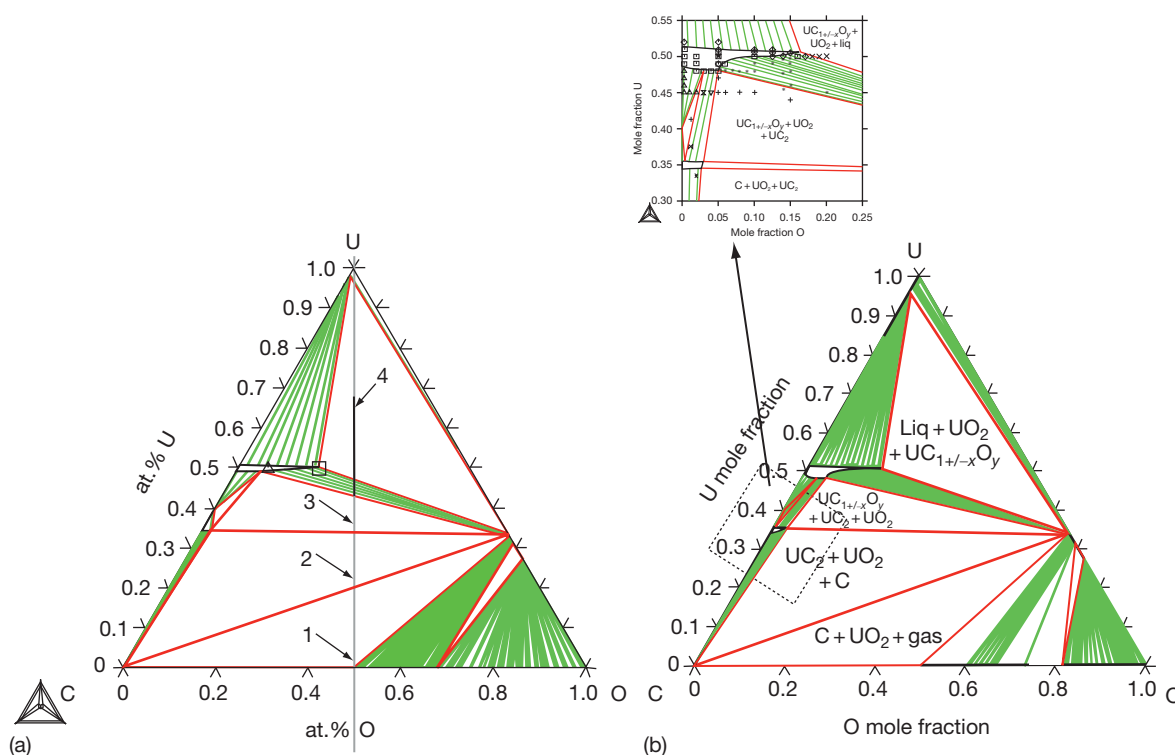


Figure 21 The U–C–O ternary phase diagram: isothermal sections at 1773 K (a) and 1973 K (b) (reproduced from Guéneau, C.; Chatain, S.; Gossé, S.; *et al.* *J. Nucl. Mater.* **2005**, 344, 191–197). Numbers on the U–CO line in (a) correspond to the plateaus of (b).

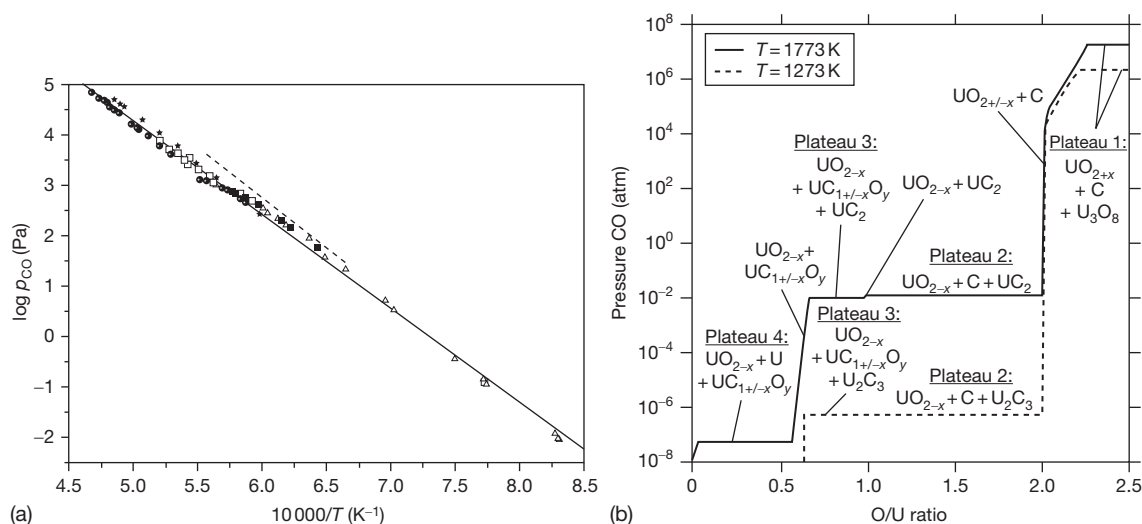


Figure 22 (a) Corrected CO pressure values for the monovariant equilibrium $\text{UO}_{2-x} + \text{UC}_2 + \text{C}$ between 1473 and 2140 K (reproduced from Gosse, S.; Gueneau, C.; Chatillon, C.; Chatain, S. *J. Nucl. Mater.* **2006**, 352, 13–21). (b) CO partial pressure variation along the U–CO composition line at 1273 and 1773 K. Numbers correspond to the U–CO line in graph (a) of [Figure 20](#) (reproduced from Gueneau, C.; Chatain, S.; Gossé, S.; *et al.* *J. Nucl. Mater.* **2005**, 344, 191–197).

equilibrium CO partial pressure on a line U–CO in the ternary phase diagram at increasing oxygen content.¹⁷⁴

The thermal conductivity of ternary $\text{UC}_{1-x}\text{O}_x$ samples decreases with x , this effect being well visible even for $x=0.02$. This phenomenon is mitigated at high temperature because of the thermal expansion ([Figure 1](#)).¹⁸⁵

The electrical resistivity of $\text{UC}_{1-x}\text{O}_x$ samples decreases with x as measured between 80 and 1200 K by Larin and Vlasov¹⁸⁶ and reported in [Figure 18](#).

All these data indicate how the metallic character of uranium carbides is gradually lost with the addition of oxygen, already starting at some atomic percent of oxygen. This trend has been observed also on the spectral emissivity.¹⁸⁷

2.04.4.2.6.2 Uranium carbide nitrides

Many studies have been performed on the system U–O–N in the 1960s–1970s.⁸ We summarize here some essential results limited to low N contents.

The U–C–N ternary system is characterized by the complete miscibility between UC and UN in the solid state ([Figure 23](#)).

Three invariant points limit the three-phase equilibrium domains: $\text{UC}_{1-x}\text{N}_x + \text{U}_2\text{N}_3 + \text{C}$ (point 1), $\text{UC}_{1-x}\text{N}_x + \text{UC}_2 + \text{C}$ (point 2), and $\text{UC}_{1-x}\text{N}_x + \text{U}_2\text{C}_3 + \text{UC}_2$ (point 3). Their composition depends mostly on temperature and nitrogen partial pressure.⁸

$\text{UC}_{1-x}\text{N}_x$ is the only ternary compound known in this system. It crystallizes as NaCl-like fcc (group $Fm\bar{3}m$). Its lattice parameter varies continuously from $a = 496$ pm for UC to $a = 488$ pm for UN. A slight deviation from Vegard's law in the positive direction was observed by Cordfunke,¹⁸⁸ who studied the complex behavior of the lattice parameters of α - and β - UC_2 in equilibrium with $\text{UC}_{1-x}\text{N}_x$ between 1773 and 2273 K by high-temperature XRD. Increasing nitrogen content and temperature were observed to lead to shrinkage of the lattice, attributed to the formation of nonstoichiometric carbide nitrides where nitrogen atoms substitute either CN groups or C_2 pairs.

Benz¹⁸⁹ obtained maxima in the solidus temperature for (C + N)/U ratios close to one in the UC–UN pseudobinary plane. $\text{UC}_{0.25}\text{N}_{0.75}$ was observed to melt at 3183 K, higher of both UC (2780 K) and UN (3103 K). This result is consistent with a slightly negative deviation of $\text{UC}_{1-x}\text{N}_x$ from the ideal solution behavior for intermediate values of x , confirmed by activity calculations performed at various N_2 partial pressures¹⁹⁰ and similar anomalies in other physical properties such as Young's modulus¹⁹¹ and the creep behavior.¹⁹² Young's modulus extrapolated at zero porosity was observed to be highest at approximately $\text{UC}_{0.2}\text{N}_{0.8}$ (280 GN m⁻²), whereas the compressive creep rate was reported to have a maximum near the composition $\text{UC}_{0.75}\text{N}_{0.25}$ (2×10^{-1} h⁻¹ with a load of 4 kg mm⁻² at 1773 K) and a minimum near the

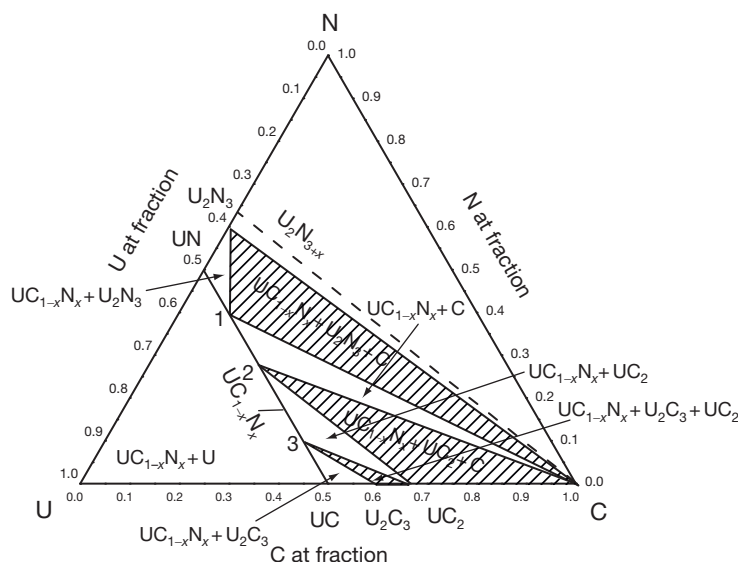


Figure 23 Qualitative structure of the U–C–N ternary phase diagram at $T < T_{\text{solidus}}$. Reproduced from Holleck, H.; Kleykamp, H. In *Gmelin Handbook of Inorganic Chemistry U Supplement Volume C12*; Springer-Verlag: Berlin, 1987.

composition $\text{UC}_{0.75}\text{N}_{0.25}$ ($2 \times 10^{-2} \text{ h}^{-1}$ with a load of 4 kg mm^{-2} at 1773 K). Padel *et al.*¹⁹¹ observed a maximum even in the Debye temperature (around 300 K) near $\text{UC}_{0.20}\text{N}_{0.80}$, corresponding to an optimal filling of the binding molecular orbital $6d-2p$.

The thermal conductivity of $\text{UC}_{1-x}\text{N}_x$ was observed to decrease upon addition of nitrogen to pure UC for $300 \text{ K} \leq T \leq 900 \text{ K}$,¹⁹³ this trend being less and less marked at increasing temperature and even inverted for $T > 1000 \text{ K}$ approximately.

The electrical resistivity of $\text{UC}_{1-x}\text{N}_x$ with $x \geq 0.5$ increases with decreasing temperature, and particularly below room temperature, due to localized magnetic moments.⁸

The electronic coefficient of the low-temperature heat capacity slightly increases with nitrogen content, and has a maximum for $\text{UC}_{0.13}\text{N}_{0.87}$.⁸

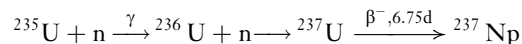
The coefficient of linear thermal expansion of $\text{UC}_{0.78}\text{N}_{0.21}\text{O}_{0.01}$ was measured between 298 and 2400 K , obtaining values ($9.5 \times 10^{-6} \text{ K}^{-1}$ at 298 K and $13.8 \times 10^{-6} \text{ K}^{-1}$ at 2400 K) lower than those of pure UC.⁸

The carbon self-diffusion coefficient changes little for small additions of nitrogen to UC, but can decrease by several orders of magnitude for $\text{N}/(\text{N} + \text{C}) > 0.5$.

The total hemispherical emissivity ε_{τ} of $\text{UC}_{0.55}\text{N}_{0.45}$ was reported to be 0.21 ± 0.03 between 1300 and 1700 K .⁸ This value, indicating a strongly metallic behavior, should be confirmed by further investigation.

2.04.5 Neptunium Carbides

Neptunium is the first transuranic element. Its most stable isotope, ^{237}Np (half-life = 2.144×10^6 years), is a by-product of nuclear reactors and plutonium production, formed either by α -decay of ^{241}Am or from ^{235}U by neutron capture:



It is also found in trace amounts in uranium ores due to transmutation reactions.

^{237}Np is the most mobile actinide in the deep geological repository environment.¹⁹⁴ Moreover, because of its long half-life, it becomes the major contributor of the total radiation in $10\,000$ years. This makes it and its predecessors such as ^{241}Am candidates of interest for destruction by nuclear transmutation. Knowledge of Np carbide properties is therefore important for the management of carbide fuel waste, as well as for transmutation concepts, such as the ‘deep-burn,’ involving the production of fuel in contact with carbon.¹⁹⁵

2.04.5.1 Preparation

Single-phase $\text{NpC}_{0.94}$ was prepared by Lorenzelli¹⁹⁶ by reacting Np hydride (obtained by reacting Np metal and water at 423 K) with carbon at 1673 K for 4 h under vacuum. The final material had oxygen impurities of about 0.3 wt\% . Lorenzelli

also observed that the solid state equilibrium between Np monocarbide and carbon at 1673 K under vacuum evolved after powdering and sintering with the formation of Np_2C_3 . Sandenaw *et al.*¹⁹⁷ obtained purer $\text{NpC}_{0.91}$ samples by arc-melting Np metal and carbon (0.024 wt% O_2).

Neptunium dicarbide was prepared by heating NpO_2 with graphite under H_2 between 2930 and 3070 K.¹⁹⁸ However, the preparation of neptunium dicarbide could not be repeated, not even by melting Np_2C_3 in a graphite crucible,¹⁹⁶ and the identification of this compound therefore remains controversial.

2.04.5.2 Properties

No systematic study of the Np–C phase diagram has yet been performed. Neptunium monocarbide NpC_{1-x} and neptunium sesquicarbide Np_2C_3 are the only two phases definitely observed. The structure of Np monocarbide was extensively investigated in the early studies performed at ANL.^{4,9} Compositions between $\text{NpC}_{0.82}$ and $\text{NpC}_{1.0}$ were identified to have fcc rock-salt structure ($Fm\bar{3}m$), with the lattice parameter increasing slightly with the carbon content, from 499.1 ± 0.1 pm for $\text{NpC}_{0.82}$ to 501.0 ± 0.1 pm for $\text{NpC}_{1.0}$. Some data dispersion was attributed to oxygen impurities.

Np_2C_3 crystallizes in a bcc Pu_2C_3 -like lattice ($I\bar{4}3d$). The lattice parameter was measured with precision by Mitchell and Lam,¹⁹⁹ who found $a = 810.30 \pm 0.01$ pm. The stoichiometry range of this compound is believed to be narrow because Lorenzelli found nearly the same lattice parameter for the phase in equilibrium with the monocarbide and with pure carbon.

The structure of NpC_2 was reported to be isostructural with tetragonal CaC_2 (same as $\alpha\text{-UC}_2$), but data are uncertain.

The heat capacity of $\text{NpC}_{0.91}$ determined by Sandenaw *et al.*¹⁹⁷ showed a λ -type anomaly with a peak at 228.4 ± 0.2 K. This feature was attributed to ferromagnetic ordering, in agreement with the ferromagnetic Curie temperature reported by Lam *et al.*²⁰⁰ and by Lander and Mueller.²⁰¹ The latter authors also report that NpC orders antiferromagnetically around 300 K, and attribute the difficulties in having reproducible results for $T > T_{\text{Curie}}$ to the strong dependence of magnetic properties on the carbon content. This lack of reproducibility introduces some uncertainty into the room-temperature thermodynamic parameters (Table 7). Only the enthalpy of formation of $\text{NpC}_{0.91 \pm 0.02}$ and $\text{NpC}_{1.5}$ was directly

Table 7 Estimated values of the thermodynamic functions for $\text{NpC}_{0.91}$ and $\text{NpC}_{1.5}$

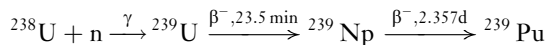
	$\text{NpC}_{0.91}$	$\text{NpC}_{1.5}$
$\Delta_f H^\circ$ (298) $\text{kJ}^{-1} \text{mol}^{-1}$	-71.5 ± 5.9	-93.7 ± 9.6
$\Delta_f S^\circ$ (298) $\text{kJ}^{-1} \text{K}^{-1} \text{mol}^{-1}$	13.4 ± 2.1	8 ± 4
$\Delta_f G^\circ$ (298) $\text{kJ}^{-1} \text{mol}^{-1}$	-71.5 ± 6.3	-96 ± 12

measured by oxygen bomb combustion. The other values and the temperature dependence were estimated by assuming neptunium carbides to have intermediate behavior between uranium and plutonium carbides.⁴

2.04.6 Plutonium Carbides

Pu carbides and nitrides were produced and investigated soon after the detection and synthesis of plutonium by Seaborg in 1941, as researchers were seeking the best chemical form under which this fissile element could be used as nuclear fuel or as an explosive, or as a target for the production of other nuclides.

Pu can be produced by neutron capture in any reactor using ^{238}U , according to the chain:



Currently, the use of plutonium carbides as nuclear fuel is only envisaged in the context of the mixed U–Pu carbide fuel.

The study of pure plutonium carbides is a starting point for the investigation of the more complex multicomponent carbide and carbide oxide systems. This binary system presents a great scientific interest, as it features very specific and original properties with respect to other actinide carbides.

2.04.6.1 Phase Relationships

The Pu–C system has been recently critically reviewed by Fischer, who proposed a phase diagram based on Gibbs energy CALPHAD optimization.¹³¹

Four stable Pu–C compounds have been identified: Pu_3C_2 , PuC_{1-x} , Pu_2C_3 , and PuC_2 .

The Pu-rich solid region (T less than melting point of Pu = 910 ± 5 K) is characterized by the six allotropies of Pu: α -Pu (simple monoclinic, stable up to 390 K), β -Pu (body-centered monoclinic, stable up to 473 K), γ -Pu (face-centered orthorhombic, stable up to 573 K), δ -Pu (fcc), δ' -Pu (body-centered

tetragonal, stable up to 748 K), and ϵ -Pu (bcc, stable up to 910 K).²⁰² The allotropic temperatures of pure Pu are not influenced by C additions, consistently with the negligible solubility of C in all the different Pu forms. The melting temperature of ϵ -Pu is reported to decrease by 8 K upon addition of C traces. The Pu–C miscibility gap extends to 40 at.% C, corresponding to the composition Pu_3C_2 . This compound (also called ζ -phase) was already observed by researchers in the 1960s, but its structure has not been determined yet. Pu_3C_2 decomposes into Pu + PuC_{1-x} at 848 K.

Despite similarities in the crystal structures of uranium and plutonium carbides, the phase diagrams of these two systems are very different, as reflected by the poorer stability of plutonium monocarbide with respect to UC. UC is almost a line compound up to ~ 1400 K and has a very wide nonstoichiometry at higher temperatures. PuC_{1-x} exists only as a hypostoichiometric compound, possibly because of the smaller size of Pu atoms compared to U, resulting in larger vacant sites of carbon interstitials. Its narrow homogeneity range extends to $0.74 \leq \text{C}/\text{Pu} \leq 0.94$. PuC_{1-x} decomposes peritectically into Pu_2C_3 + liquid at 1900 ± 30 K.^{131,203}

Pu_2C_3 is probably the most stable compound in the Pu–C system. It also decomposes peritectically into PuC_2 + liquid at 2300 ± 25 K.^{203,204} Its small nonstoichiometry region has not been well established yet.

Like UC_2 , tetragonal α - PuC_2 is stable in a narrow temperature range. This phase can be metastably quenched to room temperature and has been observed to transform into fcc KCN-like (β - PuC_2 , same as β - UC_2) by Harper *et al.*²⁰⁵ around 1983 K.

Fischer's phase diagram¹³¹ has been slightly corrected in Figure 24 to take into account more experimental values, including the α - $\text{PuC}_2 \rightarrow \beta$ - PuC_2 transition.

It is still unclear whether cubic PuC_2 melts peritectically (into liquid + graphite) or congruently. The first possibility was suggested in all the early investigations.²⁰⁶ The second was proposed by Marcon²⁰⁷ with congruent melting at 2520 ± 30 K: it implies the existence of a PuC_2 –C eutectic which would better explain the experimental Pu–partial pressure curves in this phase domain, and would agree with Fischer's Gibbs energy calculations.¹³¹

2.04.6.2 Physicochemical Properties

2.04.6.2.1 Triplutonium dicarbide Pu_3C_2

Not much is known on the $\text{PuC}_{0.67}$ line compound, detected since the beginning of the 1960s.²⁰⁴ Its structure, probably related to defective PuC, is still unknown. Rosen *et al.*²⁰⁸ found that Pu_3C_2 forms very slowly with the peritectoidal reaction ϵ -Pu + $2\text{PuC} = \text{Pu}_3\text{C}_2$. Samples containing 40 at.% of C (exact Pu_3C_2 stoichiometry) were annealed at 831 K for 17 days. Pu_3C_2 was observed to crystallize

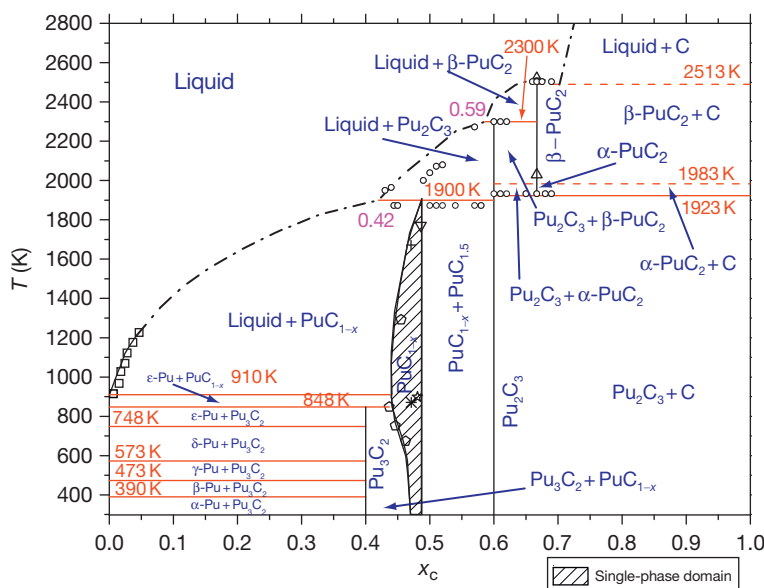


Figure 24 The Pu–C phase diagram with some selected experimental points.

as platelets in the Pu matrix, where also PuC_{1-x} dendrites were visible. The Pu_3C_2 phase was analyzed by XRD, but results could not be associated with any known crystal lattice.

Kruger²⁰⁹ found that arc-melted $\text{PuC}_{0.74}$ was a mixture of PuC and Pu_3C_2 . A rock-salt fcc structure was identified for this mixture, probably corresponding to PuC, whereas the real structure of triplutonium dicarbide remained obscure.

Pu_3C_2 is stable with respect to Pu and $\text{PuC}_{0.88}$ between 300 and 800 K, and decomposes peritectically into ϵ -Pu and PuC at 848 K.^{208–210} No high-temperature data exist for this compound. Holley *et al.*⁴ obtained thermal functions, by interpolating the low-temperature values by Haines *et al.* for $\text{PuC}_{0.64}$ and $\text{PuC}_{0.68}^{212}$ (Table 8). Holley *et al.* also estimated values for the Gibbs energy of formation of Pu_3C_2 from obvious Gibbs energy constraints at several temperatures. These calculations corrected with the full randomization entropy of $15.82 \text{ J K}^{-1} \text{ mol}^{-1}$ (corresponding to random vacancies in the carbon sublattice of fcc $\text{PuC}_{0.67}$) give the free energy of formation curve shown in Figure 15.

Pu_3C_2 displays a peculiar irreversible behavior of the thermal expansion coefficient between 373 and 673 K,⁹ estimated to be $40 \times 10^{-6} \text{ K}^{-1}$.

2.04.6.2.2 Plutonium monocarbide PuC

Hypostoichiometric plutonium monocarbide crystallizes in the rock-salt fcc ($Fm\bar{3}m$) structure like the other known actinide monocarbides. The lattice constant of PuC_{1-x} was studied by Rosen *et al.*²⁰⁸ Its value for $\text{PuC}_{0.74}$ was measured to be $a = 495.4 \pm 0.2 \text{ pm}$ for samples quenched to room temperature from $673 \text{ K} \leq T \leq 908 \text{ K}$. This value was observed to remain constant for compositions richer in Pu, whereas it increases up to $497.3 \pm 0.1 \text{ pm}$ at the C-rich boundary in equilibrium with bcc Pu_2C_3 . Based on those data, Rosen *et al.* proposed the following formula to interpolate lattice constant data in the homogeneity domain of PuC_{1-x} (Figure 25):

$$a(\text{PuC}_{1-x}) = 498.13 - 11.50(1 - \text{C/Pu}) \text{ pm} \quad [46]$$

Of course, these data are affected by oxygen and nitrogen impurities.

The number of valence electrons per Pu atom in PuC is between 4 and 4.5,^{211,212} with a complex Fermi level occupancy of 5f electrons.²¹¹ C/Pu variations in PuC_{1-x} are also reflected in the magnetic ordering temperature. It was observed that PuC_{1-x} at the C-rich limit undergoes a magnetic phase transition at $\approx 100 \text{ K}$, leading to a simple antiferromagnetic structure with Pu moments along the (0, 0, 1) direction.²¹³

Haines *et al.*²¹⁴ provided the most recent set of low-temperature ($10 \text{ K} \leq T \leq 300 \text{ K}$) heat capacity experimental data for $\text{PuC}_{0.865}$, $\text{PuC}_{0.89}$, and $\text{PuC}_{0.9}$. The three samples showed a broad peak in the heat capacity curve between 75 and 95 K, certainly confirming the antiferromagnetic transition observed by Green *et al.*²¹³ with neutron diffraction. The resulting room-temperature thermal functions suggested by Holley *et al.*⁴ for $\text{PuC}_{0.84}$ are reported in Table 8.

The heat capacities of plutonium carbides increase very sharply with carbon content in the nonstoichiometric composition range of plutonium monocarbide, where available data are not always consistent. Oetting²¹⁵ measured enthalpy increments of $\text{PuC}_{0.82}$ and reported a sharp increase in heat capacity at $\sim 950 \text{ K}$, not observed by Kruger and Savage²¹⁶ in $\text{PuC}_{0.87}$. The heat capacity of plutonium monocarbide is slightly lower than that of UC, probably due to hypostoichiometry and higher O and N impurities, resulting in a nearly stoichiometric Pu–C–O–N lattice.

Holley *et al.*⁴ interpolated the low-temperature data with the high-temperature data of Kruger and Savage and Oetting. The resulting equation is given in Table 9 and plotted in Figure 14. This trend differs slightly from the data of Kruger and Savage, which are, however, recommended for the calculation of the heat capacity of mixed monocarbides (U,Pu)C

Table 8 Thermodynamic functions of plutonium carbides (in SI units)

Compound	$\Delta_f H^\circ (298)/H(298)$ (kJ mol^{-1})	$\Delta_f G^\circ$ (J mol^{-1})	$S^\circ (298)$ ($\text{J K}^{-1} \text{ mol}^{-1}$) ^a
Pu_3C_2	$\Delta_f H^\circ (298) = -112.968$ $H(298) - H(0) = 26.602 \pm 0.523$	–	194.23 ± 3.8
PuC	$H(298) - H(0) = 9.8371 \pm 0.4186$	$-54\,882.2 - 23.57T + 3.37 \ln(T) - 0.0063057^2$	74.768 ± 0.628
Pu_2C_3	$H(298) - H(0) = 21.850 \pm 0.5023$	$-69\,601.7 - 167.97T + 24.027T \ln(T) - 0.010967^2$	150.06 ± 2.9302
α -PuC ₂	$H(298) - H(0) = -28.46 \pm 10.465$	$-20\,078.2 - 117.86T + 12.279T \ln(T) - 0.003747^2$	100.88 ± 4.186

^aRandomization entropy neglected.

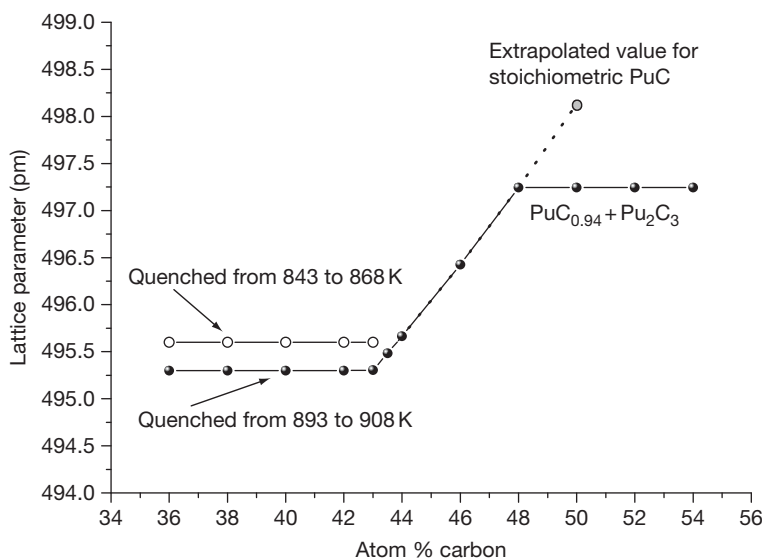


Figure 25 The lattice constant of plutonium monocarbide as a function of carbon content. Reproduced from Holleck, H.; Kleykamp, H. In *Gmelin Handbook of Inorganic Chemistry Transurane Teil C: Verbindungen*; Springer-Verlag: Berlin, 1972.

by the Newman–Kopps’ rule. In fact, the data of Kruger and Savage are closer to the values of hypothetical, vacancy free, PuC. They are well interpolated between 425 and 1295 K by

$$C_p(\text{PuC}_{\text{KS}}) = 54.76 - 4.79 \times 10^{-4}T - 1.353 \times 10^6 T^{-2} \quad (\text{Jmol}^{-1}\text{K}^{-1}) \quad [47]$$

The Gibbs free energy of formation of Pu monocarbide reported in Table 8 from 298 K to the peritectic temperature (Figure 15) is based on the reviews of Holley *et al.*⁴ and Fischer.¹³¹

2.04.6.2.3 Plutonium sesquicarbide Pu_2C_3

bcc Pu_2C_3 is probably the most stable phase in the Pu–C system. Its lattice parameter was already measured to be $a = 812.9 \pm 0.1$ pm by Zachariasen in 1952.²¹⁷ However, a certain scatter of data between samples in equilibrium with PuC_{1-x} (minimum $a = 812.10 \pm 0.1$ pm²¹⁸) and samples in equilibrium with graphite (maximum $a = 813.4 \pm 0.1$ pm²¹⁹) suggest the existence of a narrow nonstoichiometric homogeneity range, estimated as about 1 at.%.²²⁰ The high-temperature lattice constant was reported to be 834.0 pm at 1773 K.⁹ C_2 pairs distance was established to be 139.5 ± 0.5 pm.²¹³

Unlike PuC_{1-x} , $\text{PuC}_{1.5}$ is paramagnetic.²¹¹ Photoelectron spectroscopy showed that the main difference between the electronic structures of the

two carbides essentially consists of the partial occupancy of the $5f^6$ states in Pu_2C_3 .²¹¹

The heat capacity of Pu_2C_3 was measured by Danan²²¹ and Haines *et al.*²¹⁴ at low temperatures, starting from 10 K. Lower temperature measurements were hindered by the self-irradiation heating of Pu. For this reason, Einstein or Debye temperatures could not be obtained. Holley *et al.*⁴ assessed low- and high-temperature values based on these experimental data, plus the enthalpy data of Oetting²¹⁵ (Figure 14 and Table 9).

Johnson *et al.*²²² measured the formation enthalpies. Other thermodynamic parameters based on these and Fischer’s¹³¹ reviews are reported in Table 8.

2.04.6.2.4 Plutonium dicarbide

Plutonium dicarbide exists only at high temperature, between 1923 and 2513 K. It is difficult to quench the dicarbide to room temperature because the transformation of PuC_2 to $\text{Pu}_2\text{C}_3 + \text{C}$ is extremely rapid. Nonetheless, its structure was identified to be tetragonal of the CaC_2 type ($I4/mmm$), with $a = 363$ pm and $c = 609.4$ pm.²⁰⁶ Harper *et al.*²⁰⁵ observed by high-temperature XRD that PuC_2 undergoes a martensitic phase transition similar to $\alpha\text{-UC}_2 \rightarrow \beta\text{-UC}_2$ around 1983 K. The high-temperature structure was fcc $Fm\bar{3}m$ (KCN) with a lattice parameter $a = 570 \pm 1$ pm. Previous investigation performed on quenched samples could only identify the tetragonal phase.

Table 9 The heat capacity C_p of plutonium carbides at atmospheric pressure (in $\text{J K}^{-1} \text{mol}^{-1}$)

Compound	$T \leq 298 \text{ K}$	$T > 298 \text{ K}$	Total T range
Pu_3C_2	–	$C_p(298) = 136.88 \pm 2$; $C_p = 120.72 + 46.88 \times 10^{-3} \cdot T + 19.46 \times 10^{-4} \cdot T^{-2}$	$298 \text{ K} \leq T \leq 848 \text{ K}$
PuC_{1-x}	$C_p = 8.040 + 2.34 \times 10^{-1}T$ $- 3.6 \times 10^{-4}T^2 - 9.35 \times 10^2 T^{-2a}$	$C_p(298) = 47.070$; $dC_p/dT = 0.0418 \text{ J K}^{-2} \text{mol}^{-1}$; $C_p = 57.887 - 1.45 \times 10^{-2}T + 7.71 \times 10^{-6}T^2 +$ $8.618 \times 10^{-9}T^3 - 6.556 \times 10^5 T^{-2}$	$50 \text{ K} \leq T \leq 1875 \text{ K}$
Pu_2C_3	$C_p = 2.569 + 7.02 \times 10^{-1}T$ $- 1.11 \times 10^{-3}T^2 - 8.41 \times 10^2 T^{-2a}$	$C_p(298) = 114$; $dC_p/dT = 0.100 \text{ J K}^{-2} \text{mol}^{-1}$; $C_p = 156.075 - 7.991 \times 10^{-2}T + 7.045 \times 10^{-5}T^2$ $- 5.2 \times 10^5 T^{-2}$	$50 \text{ K} \leq T \leq 2285 \text{ K}$
PuC_2 ($T > 1923 \text{ K}$)	–		

^aTrend estimated on few experimental points.

Standard enthalpy and entropy of $\alpha\text{-PuC}_2$ at 298 K reported in Table 8 are extrapolated.⁹ $\Delta_f G^\circ$ for $\alpha\text{-PuC}_2$ (Figure 15) is calculated using the data recommended by Fischer and Holley *et al.* No data are available for $\beta\text{-PuC}_2$.

2.04.6.2.5 Vapor pressures

Vapor pressures of species in the Pu–C system were reviewed by Marcon,²⁰⁷ Holley *et al.*,⁴ and Matzke.⁵ The vapor phase in equilibrium with Pu carbides is always richer in plutonium than the condensed phase is. The partial pressure of Pu(g) dominates over other gaseous species, to the point that those are almost negligible in comparison. Therefore, any vaporization study on this system should take into account segregation effects in the condensed phase, and it is impossible to treat the different Pu–C compounds separately. Marcon's results,²⁰⁷ summarized in the following equations, were obtained with longer measurement times in order to vent out oxygen impurities, leading to vapor pressures in equilibrium with pure carbides.

$$\log p_{\text{Pu}} = -\frac{18\,800}{T} + 4.3 \quad [48]$$

in the Pu–PuC and PuC–Pu₂C₃ domain, from room temperature to the melting point

$$\log p_{\text{Pu}} = -\frac{20\,200}{T} + 4.23 \quad [49]$$

in the Pu₂C₃–C domain, between 1500 and 2000 K;

$$\log p_{\text{Pu}} = -\frac{25\,200}{T} + 6.8 \quad [50]$$

in the Pu₂C₃–PuC₂ domain, between 2000 and 2300 K;

$$\log p_{\text{Pu}} = -\frac{18\,150}{T} + 3.15 \quad [51]$$

in the PuC₂–C domain, between 2000 and 2500 K.

Pu(g) partial pressure over Pu–C system is higher than U(g) pressure over U–C system in the same

temperature and composition ranges (Figure 16). The partial pressure p_{C1} of C(g) is much higher than the partial pressures of other carbon-bearing species, which can be neglected in comparison to it. In Figure 16, the partial pressure values in equilibrium with PuC(liq) were extrapolated from those in equilibrium with PuC(s) including a correction for the enthalpy of melting.

2.04.6.2.6 Transport properties

Plutonium carbides have peculiar transport properties with respect to uranium and thorium carbides. Although the metallic nature of Pu carbides is confirmed by nonzero DOS at the Fermi level,²¹¹ the conduction properties are mostly due to 5f electrons in these compounds, resulting in poorer thermal and electrical conductivities. The electrical resistivity of PuC_{0.90} and Pu₂C₃, for example, was measured to be about two orders of magnitude higher than in U and Th carbides.⁹ Matzke⁵ suggested the following equations:

$$\rho_{\text{el}} = 258 - 0.029T + 3.2 \times 10^{-5}T^2 \mu\Omega\text{cm} \quad [52]$$

for single-phased PuC_{0.85}

$$\rho_{\text{el}} = 278.5 - 0.017T + 3.9 \times 10^{-5}T^2 \mu\Omega\text{cm} \quad [53]$$

for single-phased PuC_{1.0} (PuC_{1-x} + Pu₂C₃).

The thermal diffusivity and conductivity of sintered PuC was also assessed by Matzke⁵ and measured by Sengupta *et al.* by laser flash.²²³ The earlier results reported by Matzke are probably correct for almost pure PuC_{1-x}, because Sengupta's samples contained a 20 wt% of Pu₂C₃. Matzke recommends the following equation:

$$\lambda_{\text{PuC}} = 7.45 - 4.04 \times 10^{-3}T + 1.20 \times 10^{-5}T^2 \quad [54]$$

($\text{WK}^{-1} \text{m}^{-1}$)

$373 \text{ K} \leq T \leq 1573 \text{ K}$

Sengupta's values are lower, showing that the sesquicarbide has an even lower thermal conductivity than the monocarbide:

$$\lambda_{\text{PuC}+20\text{wt}\%\text{Pu}_2\text{C}_3} = 7.50 \times 10^{-1} - 5.79 \times 10^{-3} T \\ + 1.25 \times 10^{-5} T^2 - 1.03 \times 10^{-9} T^3 (\text{WK}^{-1}\text{m}^{-1}) \quad [55]$$

$$373 \text{ K} \leq T \leq 1573 \text{ K}$$

More details about these last data are reported in **Chapter 3.03, Carbide Fuel** of this Comprehensive.

2.04.6.2.7 Mechanical properties

Pu_3C_2 density was measured to be 15.3 g cm^{-3} .²⁰⁸ The density of the other Pu carbides can be calculated knowing the C/Pu ratio, the lattice structure, and the Pu-isotopic composition: $\rho = 13.51 \text{ g cm}^{-3}$ for fcc $^{239}\text{PuC}_{0.88}$ and $\rho = 12.69 \text{ g cm}^{-3}$ for bcc $^{239}\text{Pu}_2\text{C}_3$.

Hardness of Pu carbides was observed to decrease with increasing carbon content, from $0.8 \pm 0.1 \text{ GPa}$ for Pu_3C_2 to $9 \pm 0.5 \text{ GPa}$ for Pu_2C_3 . PuC_{1-x} compositions take intermediate values between 0.345 and 0.85 GPa at increasing C content.⁹

Values of the linear thermal expansion coefficients of PuC_{1-x} are reported⁹ between 298 and 1000 K. The average thermal expansion coefficient between 298 and 873 K is $\bar{\alpha}_T = (10.8 \pm 0.2) \cdot 10^{-6} \text{ K}^{-1}$ for $\text{PuC}_{0.85}$. The value recommended for Pu_2C_3 between 298 and 973 K is $\bar{\alpha}_T = 14.8 \times 10^{-6} \text{ K}^{-1}$.

2.04.6.2.8 Optical properties

Pu carbides have a metallic gray shine. A recent multiwavelength pyrometry study¹⁶⁹ has shown that the spectral optical emissivity of PuC_{1-x} is similar to that of UC (close to 0.5) in the spectral range $500 \text{ nm} \leq \lambda \leq 900 \text{ nm}$.

2.04.6.2.9 Plutonium carbide oxides and nitrides

O and N dissolve in monocarbide by substituting carbon or by occupying vacant C-sites in the lattice. For example, in PuC_{1-x} , the small oxygen atoms can easily fill the vacant carbon sites, leading to a compound close to stoichiometric. PuC can accommodate more oxygen (up to 78 mol% PuO) than UC ($\leq 35 \text{ mol}\%$ UO), probably because of the smaller size of the Pu atoms.⁹

Solid compact plutonium carbide has been observed to react slowly with air between room temperature and 573 K. However, it can burn in pure oxygen at 673 K.^{9,224} Pu_2C_3 was observed to be somewhat more stable than the other Pu carbides with respect to oxidation.

The pseudobinary PuC–PuO system follows a nearly ideal solution behavior. Anselin *et al.*²²⁵ measured the evolution of the PuC_{1-x} lattice parameter (in the presence of metallic Pu) with the addition of oxygen. They noticed a first rapid increase (from 496.1 to 497.3 pm) between 0 and 20 mol% PuO. This behavior was explained as resulting from a change in the actual C/Pu ratio and from lattice expansion following the occupation of vacant sites. Vegard's law was then followed for composition richer in oxygen. The lattice parameter varied from 497.3 pm at 20 mol% PuO to 495.6 pm at 78 mol% PuO, where the solubility limit was reached (**Figure 26**). Extrapolated values agree with literature data on the pure compounds.

The same investigation carried out on the pseudobinary PuC– PuO_2 showed very limited variation of the lattice parameter upon oxygen addition.²²⁵

XRD and chemical analyses of the Pu–C–O system have shown that both monocarbide and sesquicarbide of plutonium are hypostoichiometric at low oxygen content and become stoichiometric at high oxygen content ($\geq 6000 \text{ ppm}$ oxygen). In the biphasic mixed carbide system, $\text{MCO} + \text{MC}_{1.5}$, calculations indicate that carbon activity increases with 'O' substitution in the monocarbide. This carbon activity increase is, however, less pronounced than it is in U-rich fuel, due to the higher tolerance of 'O' substitution in PuC_{1-x} , which also implies a lower p_{CO} in Pu-rich fuels.

PuC and PuN form solid solutions. As in the case of the Pu–C–O system, the high vacancy concentration of PuC and the preferential formation of Pu_2C_3

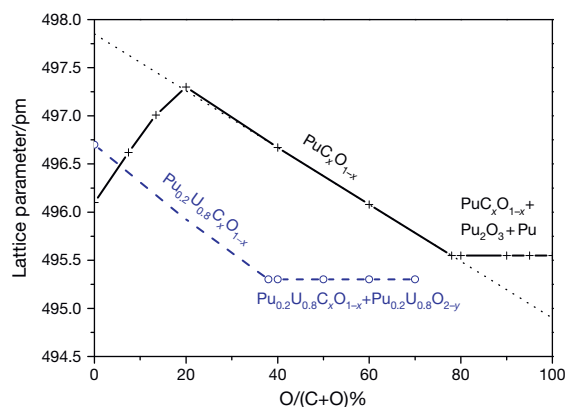


Figure 26 Lattice parameter of plutonium monocarbide oxides and mixed plutonium–uranium carbide-oxides. Reproduced from Holleck, H.; Kleykamp, H. In *Gmelin Handbook of Inorganic Transurane Teil C: Verbindungen*; Springer-Verlag: Berlin, 1972.

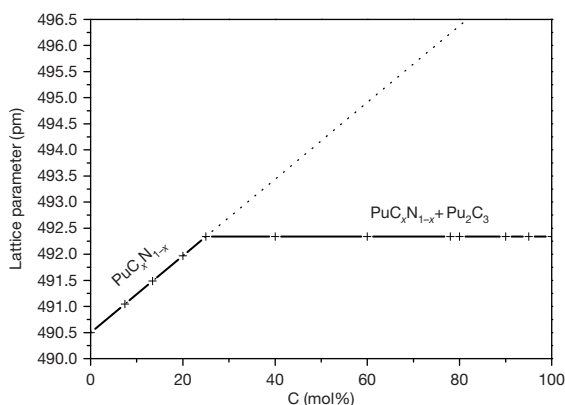


Figure 27 Lattice parameter of plutonium monocarbide nitride. Reproduced from Holleck, H.; Kleykamp, H. In *Gmelin Handbook of Inorganic Chemistry Transurane Teil C: Verbindungen*; Springer-Verlag: Berlin, 1972.

lead to important deviations from Vegard's law in the C-rich part of the PuC–PN pseudobinary system (Figure 27).⁹ The PuC hypostoichiometry is curtailed at high temperature by the addition of nitrogen, especially near the PuN side. N addition increases the carbon activity and reduces the actinide activity in monocarbides. Moreover, nitrogen was observed to stabilize PuC₂ below its decomposition temperature.⁹

2.04.7 Minor Actinide Carbides

Among the minor actinides, only carbides of americium and curium have been identified and investigated so far.

2.04.7.1 Americium Carbides

The two most stable isotopes of americium, ²⁴¹Am (432.2 years) and ²⁴³Am (7370 years), are formed by β -decay of ²⁴¹Pu and ²⁴³Pu, respectively. Therefore, a certain percentage (order of 10^{−1} at.%) of americium is commonly present in plutonium. As a consequence, traces of americium carbides can be formed in plutonium or mixed carbide matrices.²²⁶

Although the Am–C phase diagram has not been investigated in any detail, the monocarbide and the sesquicarbide have been identified, prepared by carbothermic reduction and arc-melting.²²⁷ Samples of nominal composition Am_{1.04} and Am_{1.25} were thus obtained and annealed at 1273 K for 24 h, and then characterized by XRD at room temperature. The main phase displayed a fcc NaCl *Fm* $\bar{3}m$ lattice, with lattice parameter $a = 502$ pm. Although the precise

composition and the oxygen and nitrogen contents were not determined, this phase corresponded most probably to the monocarbide. Traces of a bcc phase (most likely the sesquicarbide) were also detected. Mitchell and Lam¹⁹⁹ prepared americium sesquicarbide Am₂C₃ and analyzed it by XRD at room temperature. The material was found to be isostructural with Pu₂C₃, bcc, *I* $\bar{4}3d$, with eight formula units per unit cell. After annealing, the lattice parameter was found to be $a = 827.57 \pm 0.2$ pm. Holley *et al.*⁴ estimated the thermodynamic functions for the formation of americium sesquicarbide: $\Delta_f H^\circ(298) = -75 \pm 20$ kJ mol^{−1}, $\Delta_f S^\circ(298) = 8 \pm 8$ kJ K^{−1} mol^{−1}, and $\Delta_f G^\circ(298) = -77 \pm 20$ kJ mol^{−1}. These values were estimated by assuming that Am₂C₃ is similar to Pu₂C₃ and that the trend toward lower values of $\Delta_f H$ and $\Delta_f G$ with increasing atomic number continues beyond Pu₂C₃.

2.04.7.2 Curium Carbides

Curium has a few long-lived isotopes, some of which are strong α -emitters (particularly ²⁴²Cm and ²⁴⁴Cm). Their formation in U–Pu nuclear fuel, therefore, increases the radiotoxicity of the waste. However, even after a few years of irradiation at burnups >100 GWd ton^{−1}, the total Cm concentration in MOX was observed to be very low, $\sim 10^{-3}$ at.%.²²⁸ In this scenario, the rare literature studies on Cm carbides have an essentially academic profile.

The substantially covalent (σ) Cm–C bonding in gaseous curium–carbon complexes obtained by laser metal–polymer coablation was studied in the late 1990s.²²⁹

More recently, Radchenko *et al.*²³⁰ prepared the first samples of curium carbides by high-vacuum high-temperature condensation of metallic ²⁴⁴Cm onto an iridium support coated with amorphous carbon. Cm₂C₃ and Cm₃C, isostructural to Am₂C₃ and Sm₃C, respectively, were identified by XRD. Cm₂C₃ has a bcc crystal lattice of the *I* $\bar{4}3d$ space group with $a = 839.04 \pm 0.05$ pm. Cm₃C has fcc Fe₄N-like lattice (already observed for some lanthanides) with $a = 517.2 \pm 0.2$ pm.

Since no other carbides were detected at any carbon concentration, these authors concluded that Cm₂C₃ and Cm₃C are the only existing Cm carbides.

2.04.8 Mixed Carbides

Holleck and Kleykamp⁸ assessed the solubility of actinide mono- and dicarbides (Figure 28).

	ThC	PaC	UC	NpC	PuC
ThC		(+)	+	+	+
PaC	(+)		(+)	(+)	(+)
UC	+	(+)		(+)	+
NpC	+	(+)	(+)		(+)
PuC	+	(+)	+	(+)	

(a)

	ThC ₂	UC ₂	PuC ₂
ThC ₂		+	+
UC ₂	+		+
PuC ₂	+	+	

(b)

Figure 28 The solubility of pseudobinary actinide monocarbides (a) and dicarbides (b). +, complete solubility demonstrated and (+), complete solubility supposed. Reproduced from Holleck, H.; Kleykamp, H. In *Gmelin Handbook of Inorganic Chemistry U Supplement Volume C12*; Springer-Verlag: Berlin, 1987.

Complete solubility is likely to occur in all the actinide binary mono- and dicarbide systems, although probably not at all temperatures.

Mixed actinide carbides have technological importance in the nuclear industry. Among these systems, the ternary U–Pu–C has been broadly investigated in the last five decades in the framework of the U–Pu fuel cycle. Similarly, the system Th–U–C has been investigated in the framework of the Th–U fuel cycle, although the latter has been less frequently considered as a fuel option. Other mixed actinide carbide systems (Th–Pu–C, Th–U–Pu–C, etc.) have been occasionally studied; however, they are not addressed in this chapter. Some details about the physicochemical properties of the ternary Th–U–C and U–Pu–C systems are given in this section. More technical information related to the in-pile behavior of U–Pu carbides can be found in **Chapter 3.03, Carbide Fuel** of this Comprehensive.

2.04.8.1 Thorium–Uranium Carbides

The monocarbides UC and ThC are completely miscible,⁸ and the lattice parameter obeys Vegard's law, probably with a small negative deviation. Slightly hypostoichiometric Th-rich mixed (U,Th) carbides are miscible, but it seems that only small amounts of uranium are soluble in ThC_{1-x} with $x > 0.5$.

Most of the results available in carbon-rich samples were obtained on quenched specimens,²³¹ making them a relevant source of uncertainty, as most high-temperature phase transitions in this

system occur with fast kinetics. It is therefore impossible to recommend any sound ternary phase diagram. For example, the phase boundaries of the monoclinic to tetragonal transformation in (U,Th)C₂ is still unclear. The monoclinic form is probably stable at $T \leq 1500$ K and for Th contents > 45 at.%, the tetragonal phase more likely below 1500 K both in the U-rich and in the Th-rich domain, but a miscibility gap between (U,Th)C_{2-x} and (Th,U)C_{2-x} is believed to exist.

The high-temperature fcc form of the mixed dicarbide is stable and completely miscible above approximately 2100 K. For $1500 \text{ K} \leq T \leq 2100 \text{ K}$, this homogeneity range shrinks, and around 1500 K and 40 at.% Th, the cubic dicarbide is believed to decompose eutectoidally into the U-rich tetragonal and the Th-rich monoclinic (or tetragonal) forms.

The solidus temperatures for the (U, Th)C₂ system are reported to increase from 2750 ± 25 K for pure UC₂ to 2883 ± 50 K for pure ThC₂, but the observed solidus seems to stay almost constant within the experimental uncertainty up to 67 at.% UC₂.

The heat capacity of (U,Th)C containing up to 15 at.% Th was measured between 1.5 and 4.2 K.⁵⁶ The resulting temperature coefficient of the electronic heat capacity was observed to decrease from ~ 19.4 to $16.7 \text{ mJ K}^{-2} \text{ mol}^{-1}$ with increasing UC content, corresponding to 3.97–3.11 states per eV per molecule at the Fermi level. Theoretical values of the magnetic susceptibility determined from these data were lower than the experimental values by a factor 3–4.⁷⁰

Data exist on the linear thermal expansion coefficient α and average linear thermal expansion coefficient α_T of mixed (U, Th) dicarbides.⁸ α_T was observed to monotonically increase from $8.7 \times 10^{-6} \text{ K}^{-1}$ for pure ThC_2 to $13.5 \times 10^{-6} \text{ K}^{-1}$ for pure UC_2 , but α shows a less regular behavior probably reaching a maximum of around $17 \times 10^{-6} \text{ K}^{-1}$ at $\sim 65 \text{ at.}\% \text{ UC}_2$.

Data on the relative partial molar Gibbs energy of UC, ThC, and Th, plus the free energy of mixing of the (U,Th)C solid solution as a function of the UC mole fraction at 1173 K were measured.²³² The free energy of mixing for $\text{U}_x\text{Th}_{1-x}\text{C}$ follows approximately the equation:

$$\Delta_{\text{mix}}G = -200x(1-x) (\text{kJ mol}^{-1}) \quad [56]$$

Thermal conductivity measurements were performed on arc-melted $\text{U}_{0.1}\text{Th}_{0.9}\text{C}$ and $\text{U}_{0.1}\text{Th}_{0.9}\text{C}_2$ samples between 473 and 1273 K. The results are summarized in the following equations⁸:

$$\lambda = 9.8182 + 0.0066T \text{ (W m}^{-1}\text{K}^{-1}) \quad [57]$$

for $\text{U}_{0.1}\text{Th}_{0.9}\text{C}$ and

$$\lambda = 16.236 + 0.0080T \text{ (W m}^{-1}\text{K}^{-1}) \quad [58]$$

for $\text{U}_{0.1}\text{Th}_{0.9}\text{C}_2$.

Electrical and magnetic properties of the (U,Th)C solid solution up to 0.15 at.% UC were studied elsewhere.²³³ The electrical resistivity was observed to increase up to $1.81 \mu\Omega \text{ m}$ for 0.05 at.% UC and then decrease for higher uranium contents.

The hemispherical spectral emissivity of $\text{U}_{0.8}\text{Th}_{0.2}\text{C}$ is reported to be $\varepsilon_\lambda = 0.6$ at 650 nm and 1900 K.⁸

2.04.8.2 Plutonium–Uranium Carbides

Phase relationships in the U–Pu–C system have been studied extensively in Los Alamos Scientific Lab of the University of California and Argonne National Laboratory.^{234–237} The most recent review of the U–Pu–C system is due to Fischer.²³⁸

A few general results are commonly accepted:

1. with increasing ‘Pu’ content, the sesquicarbide becomes more stable
2. segregation occurs, resulting in a sesquicarbide phase richer in plutonium²³⁸
3. the lattice defect concentration typical of Pu–C compounds decreases with the addition of uranium
4. the melting point decreases with increasing Pu content.^{239,240}

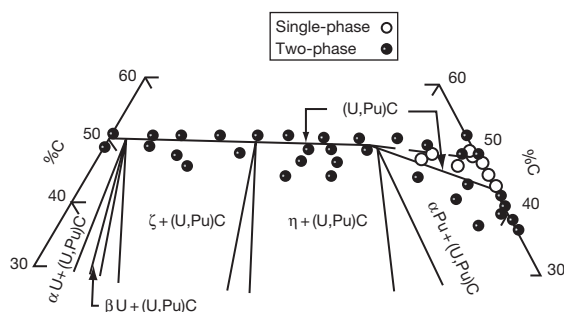


Figure 29 Phases present in the ternary U–Pu–C phase diagram around the MC composition at 843 K according to Rosen *et al.*²³⁴

Many properties of (U,Pu) mixed carbides can be deduced from these points.

Uranium monocarbide forms a complete solid solution with plutonium monocarbide. An isothermal section at 843 K of the ternary U–Pu–C diagram is shown in **Figure 29**. The (U,Pu)C phase is stoichiometric in regard to its carbon content in a composition range from 0 to 35 at.% Pu. With a further increase in Pu content, it tends to become hypostoichiometric.

The biphasic field, MC+MC_{1.5}, exists between 50 and 60 at.% C, depending upon the Pu/U ratio. Mardon and Potter²⁴¹ calculated segregation in the MC+M₂C₃ region at 1200 and 1800 K. Holleck²⁴² reports segregation at 1773 K at two defined conodes: [$x_{\text{Pu}}^{\text{MC}} = 0.095, x_{\text{Pu}}^{\text{M}_2\text{C}_3} = 0.172$] and [$x_{\text{Pu}}^{\text{MC}} = 0.17, x_{\text{Pu}}^{\text{M}_2\text{C}_3} = 0.264$], indicating that the higher the plutonium content, the more pronounced is the plutonium segregation into two phases. This effect is reduced at higher temperature. Accordingly, the lattice parameter trend in the pseudobinary UC–PuC_{1-x} and U₂C₃–Pu₂C₃ systems often deviates from Vegard’s law (**Figure 30**). This behavior has been explained as due to the abundant lattice vacancies and the phase segregation toward the formation of the sesquicarbide in the Pu-rich composition range ($\geq 65 \text{ at.}\% \text{ PuC}_{1-x}$). Interestingly, a clear negative deviation from Vegard’s law and from the ideal solution behavior was observed in the U-rich carbides too.²³⁵ A slightly negative deviation from Vegard’s law was also reported for the solid solution U₂C₃–Pu₂C₃.⁹

Ohse and Capone²⁴⁰ studied (U_{0.8}Pu_{0.2})–C in the temperature range 1773–2731 K, and the composition range, C/M = 0.95–1.4, and reported (i) MC/(MC+M₂C₃) phase boundaries: 2000 K for $x_c = 0.517$, 2100 K for $x_c = 0.524$ and 2200 K for $x_c = 0.532$; (ii) MC/(MC+M₂C₃+MC₂) phase boundary: 2300 K, $x_c = 0.539$; and (iii) MC/(MC+MC₂)

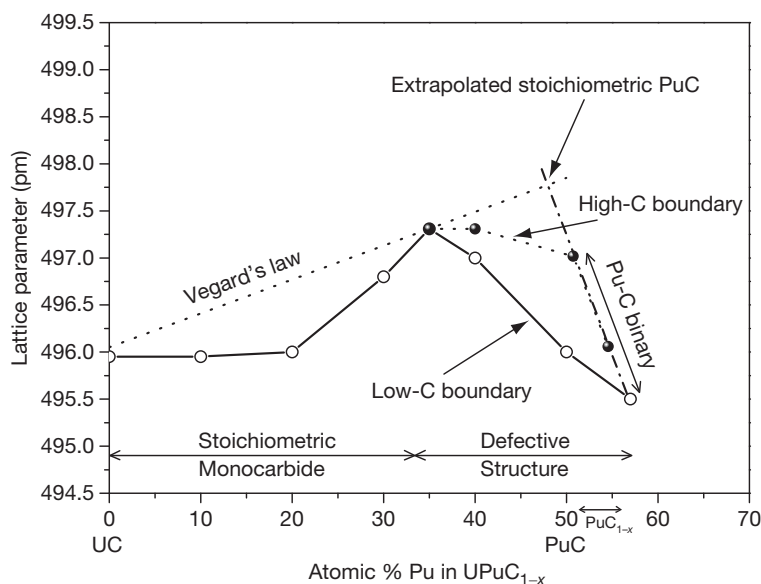


Figure 30 Lattice parameter as a function of plutonium content in $(\text{U}, \text{Pu})\text{C}_{1-x}$. Reproduced from Rosen, S.; Nevitt, M. V.; Barker, J. J. J. *Nucl. Mater.* **1963**, *9*, 128–136.

phase boundaries: 2400 K for $x_c = 0.547$ and 2500 K for $x_c = 0.551$.

The $(\text{U}, \text{Pu})\text{C}_{1.0}$ solidus–liquidus curves are plotted together with experimental data in **Figure 31**. The higher solidus line was calculated by assuming an ideal solution behavior of both solid and liquid $(\text{U}, \text{Pu})\text{C}$. However, solidus data reported by Dalton by high-temperature XRD²⁴³ are lower, and in better agreement with the phase boundary calculated by Fischer²³⁸ using a substitutional solution model.

This confirms the nonideal behavior of the $(\text{U}, \text{Pu})\text{C}$ solution. The formation of a M_2C_3 phase in the Pu-rich part of the UC–PuC diagram explains the partial disagreement between the observed melting temperature of high-Pu mixed carbides and the peritectic of pure PuC_{1-x} ^{131,238} (cf. **Figure 32(b)** below).

Complete solubility of plutonium sesquicarbide in uranium sesquicarbide has been observed below 2033 K. The equilibrium temperature of the transformation $\text{MC}_{1.5} \rightarrow \text{MC} + \text{MC}_2$ increases with increasing plutonium content from 2106 K for $\text{UC}_{1.5}$ to 2273 K for $(\text{U}_{0.9}\text{Pu}_{0.1})_{0.45}\text{C}_{0.55}$ and 2445 K for $(\text{U}_{0.9}\text{Pu}_{0.2})\text{C}_{1.5}$. However, this decomposition reaction is not observed for $(\text{U}_{0.9}\text{Pu}_{0.1})_{0.48}\text{C}_{0.52}$ ²³⁹ as uranium-rich monocarbide can accommodate extra carbon at high temperatures.

By mass spectrometry and electron microprobe analyses, Browning *et al.*²⁴⁴ established the reaction $\text{MC}_2 \rightarrow \text{M}_2\text{C}_3 + \text{C}$ for $\text{Pu}/(\text{U} + \text{Pu}) = 0.575$ at 2128 ± 10 K, 100 K higher than Dalton²⁴³ and Reavis

*et al.*¹³² At high temperatures, U-rich MC_{2-x} forms a continuous solid solution with MC, as observed for the binary U–C system. However, small amounts of plutonium get segregated as sesquicarbides phase because $\text{PuC}_{1.5}$ is more stable than PuC_2 .

The compositions $\text{U}_{0.5}\text{Pu}_{0.5}\text{C}_2$ and $\text{U}_{0.5}\text{Pu}_{0.5}\text{C}_{1.5}$ undergo peritectoid decomposition and melting transitions at 2018 and 2598 K, and 2018 and 2613 K, respectively. Data are not always consistent due to inaccurate determination of the C content and the presence of N and O impurities.

Udovskii and Alekseeva²⁴⁵ used the experimental data from the literature to construct the phase diagram of the U–Pu–C system. They also presented a schematic projection of the liquidus surface. Similarly, Mardon and Potter²⁴¹ calculated phase equilibria for isothermal sections at 2573, 2473, 2373, and 2273 K. No ternary compounds have been observed in the U–Pu–C system.²⁴²

The pseudobinary UC_2 – PuC_2 system is little known and still controversial.⁹ The solidus–liquidus lines appear rather close to each other and regular between the melting points of the two end members. The cubic dicarbide phase appears to be more stable in the mixed dicarbide than it is in the pure Pu dicarbide, and the tetragonal dicarbide seems to exist for U-rich compositions only ($\text{PuC}_2 < 20$ at.%).

As a summary of the discussed results, **Figure 32 (a)–32(d)** show the $x_c = 0.60$ isopleth section of the U–Pu–C ternary phase diagram proposed by

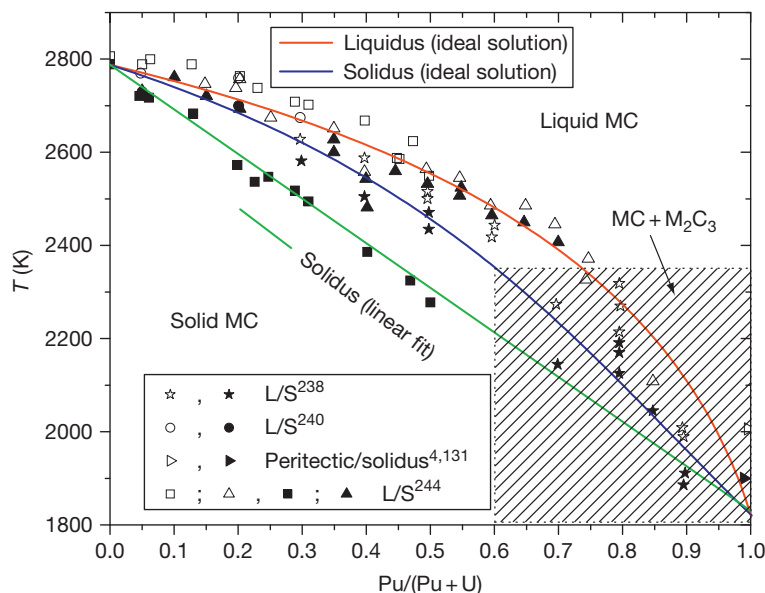


Figure 31 Solidus-liquidus temperature of uranium-plutonium mixed carbide fuels as a function of $\text{Pu}/(\text{Pu} + \text{U})$ ratio.

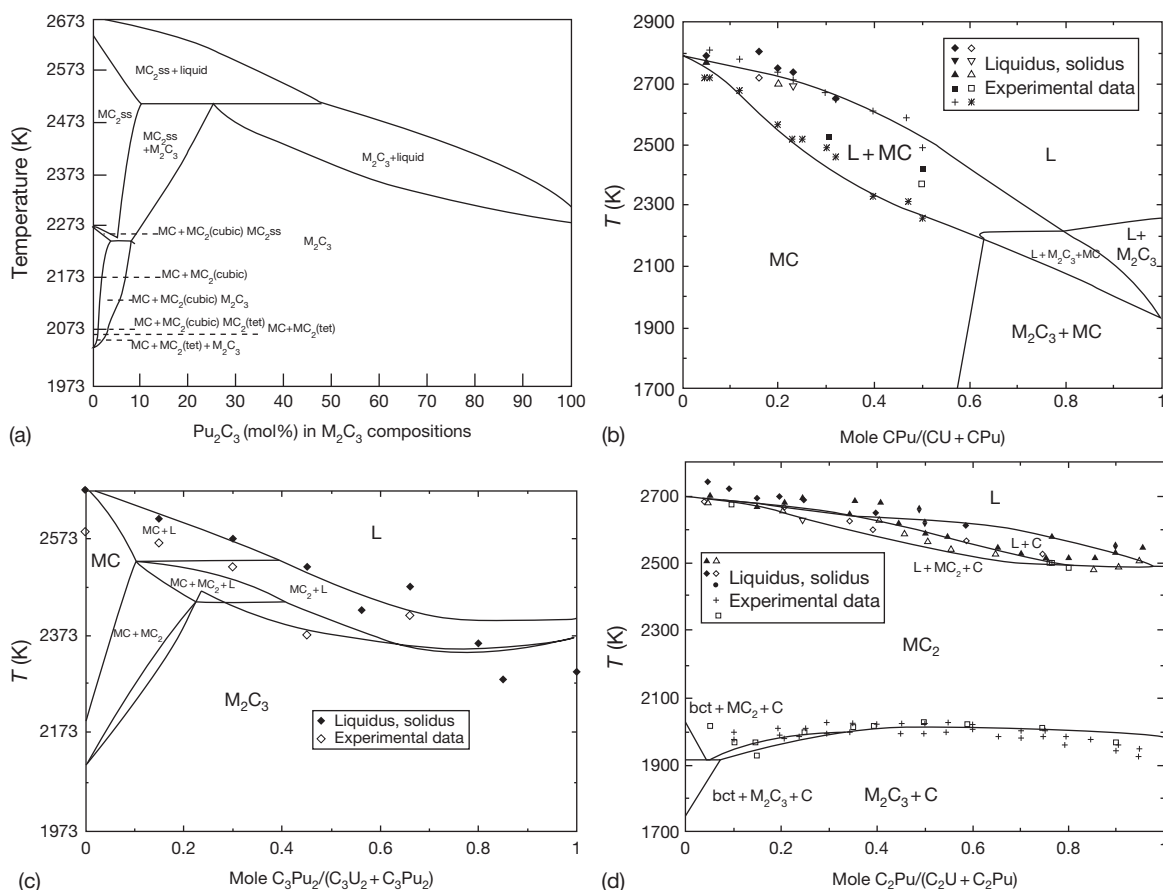


Figure 32 (a) Isopleth section of the U-Pu-C phase diagram at constant $X_c = 0.6$, as proposed by Dalton²⁴³ (reproduced from Fischer, E. *Calphad* **2009**, 33, 487–494). (b) MC isopleth section of the U-Pu-C phase diagram optimized by Fischer.²³⁸ (c) The M_2C_3 isopleth section of the U-Pu-C phase diagram optimized by Fischer.²³⁸ (d) The MC_2 isopleth section of the U-Pu-C phase diagram optimized by Fischer.²³⁸ Courtesy of Dr. E. Fischer.

Dalton²⁴³ and the MC, M₂C₃, and MC₂ isoplethal sections optimized by Fischer,²³⁸ respectively.

The thermal conductivity of (U,Pu)C decreases with increasing Pu content (up to 1273 K), as reported in Figure 1. The electrical resistivity increases with increasing Pu content by a factor 3 between 10 at.% PuC and pure PuC.

Sengupta *et al.*^{246,247} observed that the thermal expansion coefficient of (U,Pu) carbides increases with Pu content. Although no creep data are available for pure plutonium carbides, Sengupta *et al.* observed that Pu-rich carbide fuel is harder than U-rich fuel up to 1553 K (average volumetric temperature of the fuel pin).²⁴⁸

2.04.9 Summary

Research on actinide carbides is seeing a renaissance after the 'Generation IV' International Forum relaunched the design of nuclear plants with fast neutron spectra.¹ In the last decade, early experimental results have been assessed and reinterpreted in the light of recent theoretical calculations. In parallel, a few new experimental results are being produced with novel techniques. More complex geometries and interactions are also being studied, as for example, the behavior of coated carbides in fuel particles.

It appears that the properties of actinide carbides are strongly dependent on the experimentally unavoidable oxygen and nitrogen impurities. For this reason, a deeper understanding of the behavior of these materials as a function of oxygen and nitrogen contents will be of fundamental importance. This is true for both fundamental physicochemical properties and technologically important ones, such as the mechanical parameters and the behavior under irradiation.

References

- US DOE Nuclear Energy Research Advisory Committee and the Generation IV International Forum, A Technology Roadmap for Generation IV Nuclear Energy Systems, Dec 2002.
- Storms, E. K. *The Refractory Carbides*; Academic Press: New York, 1967.
- Rand, M. H. *Thorium: Physico-Chemical Properties of Its Compounds and Alloys. Part 1: Atomic Energy Review*; Special Issue No. 5; IAEA: Vienna, 1975.
- Holley, C. E., Jr; Rand, M. H.; Storms, E. K. *The Chemical Thermodynamics of Actinide Elements and Compounds. Part 6: The Actinide Carbides*; IAEA: Vienna, 1984.
- Matzke, H. j. *Science of Advanced LMFBR Fuels*; North Holland: Amsterdam, 1986.
- Kleykamp, H.; Keim, R.; Keller, C. In *Gmelin Handbook of Inorganic Chemistry Th Supplement Volume C6*; Springer-Verlag: Berlin, 1992.
- Keller, C. In *Gmelin Handbook of Inorganic Chemistry Pa System-Nummer 51*; Springer-Verlag: Berlin, 1977.
- Holleck, H.; Kleykamp, H. In *Gmelin Handbook of Inorganic Chemistry U Supplement Volume C12*; Springer-Verlag: Berlin, 1987.
- Holleck, H.; Kleykamp, H. In *Gmelin Handbook of Inorganic Chemistry Transurane Teil C: Verbindungen*; Springer-Verlag: Berlin, 1972.
- Rand, M. H.; Fuger, J.; Grenthe, I.; Neck, V.; Rai, D. *Chemical Thermodynamics of Thorium*; OECD Nuclear Energy Agency; Chemical Thermodynamics Series; Elsevier, North-Holland: Paris, 2008; Vol. 11.
- Grenthe, I.; Fuger, J.; Konings, R. J. M.; *et al.* *Chemical Thermodynamics of Uranium*; OECD Nuclear Energy Agency; Chemical Thermodynamics Series; Elsevier, North-Holland: Paris, 2004; Vol. 1.
- Lemire, R. J.; Fuger, J.; Nitsche, H.; *et al.* *Chemical Thermodynamics of Neptunium and Plutonium*; OECD-NEA; Chemical Thermodynamics Series; Elsevier, North-Holland: Paris, 2001; Vol. 4.
- Silva, R. J.; Bidoglio, G.; Rand, M. H.; Robouch, P. B.; Wanner, H.; Puigdomenech, I. *Chemical Thermodynamics of Americium*; OECD-NEA; Chemical Thermodynamics Series; Elsevier, North-Holland: Paris, 1995; Vol. 2.
- Greenwood, N. N.; Earnshaw, A. *Chemistry of Elements*; Pergamon: Cambridge, 1984.
- Majumdar, S.; Sengupta, A. K.; Kamath, H. S. *J. Nucl. Mater.* **2006**, 352, 165–173.
- Das, T.; Deb, S.; Mookerjee, A. *Phys. B* **2005**, 367, 6–18.
- Auskern, A. B.; Aronson, S. *J. Appl. Phys.* **1967**, 38, 3508–3514.
- de Novion, C. H. In *Actinides in Perspective*; Edelstein, N. M., Ed.; Pergamon: Oxford, 1982; pp 175–201.
- Hill, H. H. In *Plutonium and Other Actinides*; American Institute of Mining, Metallurgical and Petroleum Engineers: New York, 1970; Vol. 17, p 2.
- Kurihara, M.; Hirata, M.; Sekine, R.; *et al.* *J. Alloys Compd.* **1999**, 283, 128.
- Yamamoto, E.; Haga, Y.; Inada, Y.; *et al.* *J. Phys. Soc. Jpn.* **1999**, 68, 3953.
- Eckle, M.; Eloiardi, R.; Gouder, T.; Colarieti Tosti, M.; Wastin, F.; Rebizant, J. *J. Nucl. Mater.* **2004**, 334, 1.
- Shein, I. R.; Shein, K. I.; Ivanovskii, A. L. *J. Nucl. Mater.* **2006**, 353, 19–26.
- Shi, H.; Zhang, P.; Li, S. S.; Wang, B.; Sun, B. *J. Nucl. Mater.* **2010**, 396, 218–222.
- Potter, P. E. *J. Nucl. Mater.* **1972**, 42, 1–22.
- Krupka, M. C.; Giorgi, A. L.; Krikorian, N. H.; Szkwarz, E. G. *J. Less Common Met.* **1969**, 19, 113–119.
- Krupka, M. C. *J. Less Common Met.* **1970**, 20, 135–140.
- Krupka, M. C. *Am. Ceram. Soc. Bull.* **1969**, 48, 1133–1136.
- Chubb, W.; Phillips, W. M. *Trans. Am. Soc. Met.* **1961**, 53, 465–476.
- Chubb, W.; Dickerson, R. F. *Am. Ceram. Soc. Bull.* **1962**, 41, 564–570.
- Henney, J.; Livey, D. T.; Hill, N. A. AERE-R-4176; 1963.
- Olander, D. *J. Nucl. Mater.* **2009**, 389, 1–22.
- Thorium as an Energy Source*; Published by the Thorium Report Committee appointed by the Research Council of Norway, Feb 2008.
- Dekoussar, V.; Dyck, G. R.; Galperin, A.; Ganguly, C.; Todosow, M.; Yamawaki, M. *Thorium Fuel Cycle – Potential Benefits and Challenges*, IAEA-TECDOC 1450; IAEA: Vienna, 2005.

35. Sengupta, A. K.; Basak, U.; Kumar, A.; Kamath, H. S.; Banerjee, S. J. *Nucl. Mater.* **2009**, 385, 161–164.
36. Potter, P. E. *J. Nucl. Mater.* **2009**, 389, 29–44.
37. de Novion, C. H.; Fender, B. E. F.; Just, W. Plutonium 1975 and other actinides. In *Proceedings of the 5th International Conference*, Baden Baden, West Germany, 1975; pp 893–902.
38. Benesovsky, F.; Rudy, E. *Chem. Mon.* **1961**, 92, 1176–1183.
39. Von Goldbeck, O. *Thorium: Physico-Chemical Properties of Its Compounds and Alloys, Part II*; Atomic Energy Review, Special Issue 5; IAEA: Vienna, 1975.
40. Bowman, A. L.; Krikorian, N. H.; Arnold, G. P.; Wallace, T. C.; Nereson, N. G. *Acta Crystallogr. B* **1968**, 24, 1121–1123.
41. Kempter, P.; Krikorian, N. H. *J. Less Common Met.* **1962**, 4, 244–251.
42. Pialoux, A.; Zaug, J. *J. Nucl. Mater.* **1976**, 61, 131–148.
43. Fink, J. K.; Chasanov, M. G.; Leibowitz, L. ANL-CCEN-RSD-1-77; 1977.
44. Henney, J.; Jones, J. W. S.; Hill, N. A. Carbides in nuclear energy. In *Proceedings of the Symposium*, Harwell; 1963; pp 69–76.
45. Benz, R.; Balog, G. *High Temp. Sci.* **1971**, 3, 511–522.
46. Politis, C. Zur thermische Gitterdilatation einiger Übergangs metallverbindungen, Report KFK 2168; Kernforschungszentrum, Karlsruhe, 1975.
47. James, W. J.; Straumanis, M. E. *Acta Crystallogr.* **1956**, 9, 376–379.
48. Gantzel, P. K.; Baldwin, N. L. *Acta Crystallogr.* **1964**, 17, 772–773.
49. Jones, D. W.; Mc Colm, I. J.; Steadman, R.; Yerkess, J. *J. Solid State Chem.* **1987**, 68, 219–226.
50. Shein, I. R.; Ivanovskii, A. L. *J. Nucl. Mater.* **2009**, 393, 192–196.
51. Langer, S.; Gantzel, P. K.; Baldwin, N. L. *Inorg. Chem.* **1966**, 5, 2031–2040.
52. Langer, S.; Baldwin, N. L.; Gantzel, P. K.; Kester, F.; Hancock, C. *Nucl. Metall.* **1964**, 10, 359–386.
53. Cook, J. L. ORNL-TM-1188; 1965.
54. Ganzel, P. K.; Langer, S.; Baldwin, N. C.; Kester, F. L. *Adv. X Ray Anal.* **1965**, 8, 78–85.
55. Dalton, J. T.; Potter, P. E.; Shaw, J. L. In *Plutonium 1965, Proceedings of the Third International Conference on Plutonium*, London, Nov 22–26, 1965; Kay, A. E., Waldron, M. B., Eds.; Chapman and Hall: London, 1967; pp 775–805.
56. Harness, H. R.; Matthews, J. C.; Morton, N. *Br. J. Appl. Phys.* **1964**, 15, 963.
57. Danan, J. *J. Nucl. Mater.* **1975**, 57, 280–282.
58. Costa, P.; Lallement, R. *J. Phys. Chem. Solids* **1964**, 25, 559–565.
59. Huber, E. J.; Holley, C. E.; Krikorian, N. H. *J. Chem. Eng. Data* **1968**, 13, 253–256.
60. Lorenzelli, R.; De Dieuleveult, I.; Melamed, J. *J. Inorg. Nucl. Chem.* **1971**, 33, 3297–3304.
61. Yamawaki, M.; Koyama, T.; Takahashi, Y. *J. Nucl. Mater.* **1989**, 167, 113–121.
62. Gomozev, L. I.; Dedjurin, A. I.; Titov, S. G.; Ivanov, O. S. Plutonium 1975 and other actinides. In *Proceedings of the 5th International Conference*, Baden Baden, Germany; 1975; pp 915–934.
63. Gigli, G.; Guido, M.; De Maria, G. *High Temp. High Press.* **1982**, 14, 465–475.
64. Papon, P.; Leblond, J.; Meijer, P. H. E. *Physique des Transitions de Phases*; Dunod: Paris, 1999; p 116.
65. Epstein, L. F. *J. Nucl. Mater.* **1967**, 22, 340–349.
66. Potter, P. E. *J. Inorg. Nucl. Chem.* **1969**, 31, 1821–1829.
67. Giorgi, A. L.; Szklarz, E. G.; Krikorian, N. H.; Krupka, M. C. *J. Less Common Met.* **1970**, 22, 131–135.
68. Giorgi, A. L.; Hill, H. H.; Szklarz, E. G.; White, R. W. LA-UR-76-1535; 1976.
69. Giorgi, A. L.; Szklarz, E. G.; Krupka, M. C. In *Superconductivity in d- and f-Band Metals*; Douglass, D. H., Ed.; *Am. Inst. Phys.*; Plenum: New York, 1972; pp 147–153, LA-DC-13 299 (1970).
70. Bates, L. F.; Unstead, P. B. *Br. J. Appl. Phys.* **1964**, 15, 543–549.
71. Westrum, E. F.; Takahashi, Y.; Stout, N. D. *J. Phys. Chem.* **1965**, 69, 1520–1524.
72. Takahashi, Y.; Westrum, E. F.; Kent, R. A. *J. Chem. Eng. Data* **1965**, 10, 128–129.
73. Lonsdale, H. K.; Graves, J. N. In *Proceedings of Symposium on Thermodynamics of Nuclear Materials*; IAEA: Vienna, 1962; pp 601–623.
74. Jackson, D. D.; Barton, G. W.; Krikorian, O. H.; Newbury, R. S. *J. Phys. Chem.* **1964**, 68, 1516–1523.
75. Sasaki, N.; Kubo, K.; Asano, M. *J. Nucl. Sci. Technol.* **1971**, 8, 614–621.
76. Gingerich, K. *Chem. Phys. Lett.* **1978**, 59, 136–139.
77. Gupta, S. K.; Gingerich, K. A. *J. Chem. Phys.* **1980**, 72, 2795–2801.
78. Kovács, A.; Konings, R. J. M. *J. Nucl. Mater.* **2008**, 372, 391–393.
79. Peterson, D. T. *Trans. Am. Soc. Met.* **1961**, 53, 765–773.
80. Peterson, D. T.; Schmidt, F. A.; Verhoeven, J. D. *Trans. Metall. Soc. AIME* **1966**, 236, 1311–1315.
81. Chiotti, P.; Dooley, G. J. *J. Nucl. Mater.* **1967**, 23, 45–54.
82. Chiotti, P.; Korbitz, F. W.; Dooley, G. J. *J. Nucl. Mater.* **1967**, 23, 55–67.
83. Marchal, M.; Trouvé, J. CEA-R-3677; 1962.
84. Grossman, L. N. GEST-2015; 1963.
85. Greiner, J. D.; Peterson, D. T.; Smith, J. F. *J. Appl. Phys.* **1977**, 48, 3357–3361.
86. Geward, L.; Olsen, J. S.; Benedict, U.; Itié, J. P.; Spirlet, J. P. *J. Appl. Crystallogr.* **1986**, 19, 308–310.
87. Geward, L.; Olsen, J. S.; Benedict, U.; Luo, H. J. *Less Common Met.* **1990**, 161, L11–L14.
88. Oikawa, T.; Hanaoka, T. *J. Nucl. Sci. Technol.* **1969**, 6, 120–127.
89. Dalton, J. T.; Griffin, R. M. AERE-R-4742; 1964.
90. Bober, M.; Singer, J.; Wagner, K. *J. Nucl. Mater.* **1984**, 124, 120–128.
91. Heiss, A.; Djemal, M. *Rev. Int. Hautes Temp. Refract.* **1971**, 8, 287–290.
92. Benz, R.; Arnold, G. P.; Zachariasen, W. H. *Acta Crystallogr. B* **1972**, 28, 1724–1727.
93. Pialoux, A. *J. Nucl. Mater.* **1980**, 91, 127–148.
94. Benz, R.; Troxel, J. E. *High Temp. Sci.* **1971**, 3, 422–432.
95. Auskern, A. B.; Aronson, S. *J. Appl. Phys.* **1970**, 41, 227–232.
96. Sellers, P. A.; Fried, S.; Elson, R. E.; Zachariasen, W. H. *J. Am. Chem. Soc.* **1954**, 76, 5935–5938.
97. Lindner, R. Tech. Hochsch. Brunswick Report BMWF-FBK-68–56; 1968.
98. Lonsdale, H. K.; Graves, J. N. In *Proceedings of Symposium on Thermodynamics of Nuclear Materials*; IAEA: Vienna, 1962; p 601.
99. Lorentz, R.; Scherff, H. L.; Toussaint, N. *J. Inorg. Nucl. Chem.* **1969**, 31, 2381–2390.
100. Keller, C. In *Gmelin Handbuch der Anorganischen Chemie, Ergänzungsband 2*; Springer-Verlag: Berlin, 1977.
101. Chevalier, P. Y.; Fischer, E. *J. Nucl. Mater.* **2001**, 288, 100–129.
102. Blumenthal, B. *J. Nucl. Mater.* **1960**, 2, 197–208.

103. Storms, E. K. *A Report to the Vienna Panel (1968) – The Uranium–Carbon and Plutonium–Carbon Systems*; Los Alamos Scientific Laboratory Report, 1968.
104. Guinet, P.; Vaugoyeau, H.; Blum, P. L. *Métallographie – Sur le système binaire uranium-monocarbure d'uranium*; C. R. Acad. Sc. Paris, t. 261 Groupe 7; 1965; pp 1312–1314.
105. Benz, R.; Stone, P. L. *High Temp. Sci.* **1969**, *1*, 342–359.
106. Sears, M. B.; Ferris, L. M. *J. Nucl. Mater.* **1969**, *32*, 101–112.
107. Asbhee, K. H. G.; Franck, F. C.; Du Bose, F. K. H. *J. Nucl. Mater.* **1973**, *47*, 323–335.
108. Laugier, J.; Blum, P. L. *J. Nucl. Mater.* **1971**, *39*, 245–252.
109. Bowman, A. L.; Arnold, G. P.; Witterman, W. G.; Wallace, T. C.; Nereson, N. G. *Acta Crystallogr.* **1966**, *21*, 670–671.
110. Wilson, W. B. *J. Am. Ceram. Soc.* **1960**, *43*, 77–81.
111. Benedict, U. *J. Less Common Met.* **1987**, *128*, 7–45.
112. Storms, E. K. *The Refractory Carbides*; Academic Press: New York, 1967.
113. Utton, C. A.; De Bruycker, F.; Boboridis, K.; et al. *J. Nucl. Mater.* **2009**, *385*, 443–448.
114. Benz, R.; Farr, J. D. *J. Nucl. Mater.* **1972**, *42*, 217–222.
115. Chartier, A.; Van Brutzel, L. *Nucl. Instrum. Meth. Phys. Res.* **2007**, *255*, 46–50.
116. Adachi, H.; Imoto, S. *J. Nucl. Sci. Technol.* **1969**, *6*, 371–379.
117. Brooks, M. S. S. *J. Phys. F Met. Phys.* **1984**, *14*, 639–652.
118. Wedgwood, F. A. *J. Phys. C* **1974**, *7*, 3203–3218.
119. Shi, H.; Zhang, P.; Li, S. S.; Wang, B.; Sun, B. *J. Nucl. Mater.* **2010**, *396*, 218–222.
120. Matsui, H.; Matzke, H. J. *J. Nucl. Mater.* **1980**, *89*, 41–52.
121. Schüle, W.; Spindler, P. *J. Nucl. Mater.* **1969**, *32*, 20–29.
122. Whitton, J. L. *J. Nucl. Mater.* **1964**, *12*, 115–119.
123. Boutard, J. L.; de Novion, C. H. *Solid State Commun.* **1974**, *14*, 181–185.
124. Oetting, L.; Navratil, J. D.; Storms, E. K. *J. Nucl. Mater.* **1973**, *45*, 271–283.
125. Tagawa, H. *J. Nucl. Mater.* **1970**, *34*, 116–118.
126. Tagawa, H.; Fujii, K.; Sasaki, Y. *J. Nucl. Sci. Technol. (Tokyo)* **1971**, *8*, 244–249.
127. Atoji, M. *J. Chem. Phys.* **1967**, *47*, 1188–1189.
128. Storms, E. K. In *Proceedings of Symposium on Thermodynamics*; IAEA: Vienna, 1965; Vol. 1, p 309.
129. Tetenbaum, M.; Hunt, P. D. *J. Nucl. Mater.* **1971**, *40*, 104.
130. Sheth, A.; Tetenbaum, M.; Leibowitz, L. *Trans. Am. Nucl. Soc.* **1975**, *22*, 233–234.
131. Fischer, E. *Calphad* **2008**, *32*, 371–377.
132. Reavis, J. G.; Shupe, M. W.; Bjorklund, C. W.; Leary, J. A. *Trans. Am. Nucl. Soc.* **1967**, *10*, 111–112.
133. Sheth, A.; Leibowitz, L. ANL-AFP-11; 1975.
134. Tetenbaum, M.; Sheth, A.; Olson, W. ANL-AFP-8; 1975.
135. Joseph, M.; Mathews, C. K.; Bhaskar Rao, P. *J. Nucl. Mater.* **1989**, *168*, 220–227.
136. Finn, P. A.; Sheth, A.; Winslow, G.; Leibowitz, L. In *Advanced LMFBR Fuels Topical Meeting Proceedings*, Tucson, AZ, 1977; pp 189–204, ERDA-4455.
137. Ohse, R. W.; Babelot, J. F.; Frezzotti, A.; et al. *High Temp. Sci.* **1980**, *13*, 35–78.
138. Gigli, G.; Guido, M.; de Maria, G. *J. Nucl. Mater.* **1981**, *98*, 35–46.
139. Momin, A. C.; Karkhanavala, M. D. *High Temp. Sci.* **1979**, *11*, 179–185.
140. Richards, H. K. *Nucl. Technol.* **1971**, *10*, 54–61.
141. Farr, J. D.; Wittermann, W. G.; Stone, P. L.; Westrum, E. F. Advanced thermophysical properties extreme temperature pressures. In *Papers 3rd Symposium Thermophysical Properties*, Lafayette, IN, 1965; pp 162–166.
142. Andon, R. J.; Counsell, J. F.; Martin, J. F.; Hedger, H. J. *Trans. Faraday Soc.* **1964**, *60*, 1030–1037.
143. Murnaghan, F. D. *Proc. Natl. Acad. Sci. USA* **1944**, *30*, 244.
144. Norman, J. H.; Winchell, P. *J. Phys. Chem.* **1964**, *68*, 3802–3805.
145. Dancausse, J. P.; Heathman, S.; Benedict, U.; Gerward, L.; Staun Olsen, J.; Hulliger, F. *J. Alloys Compd.* **1993**, *191*, 309–312.
146. Storms, E. K. Los Alamos Report 95241; 1982.
147. Atkinson, A. *Solid State Ionics* **1984**, *12*, 309–320.
148. Wallace, T. C.; Witterman, W. G.; Radosevich, C. L.; Bowman, M. G. LA-DC-8840; 1968; pp 1–45.
149. Govinda Rajan, K.; Khanna, R.; Sankara Sastry, V.; Sundarajan, A. R.; Rafi Ahmed, A. G. *J. Nucl. Mater.* **1981**, *102*, 313–318.
150. De Coninck, R.; Van Lierde, W.; Gijs, A. *J. Nucl. Mater.* **1973**, *46*, 213–216.
151. Matsui, H.; Tamaki, M.; Nasu, S.; Kurasawa, T. *J. Phys. Chem. Solids* **1980**, *41*, 351–355.
152. De Coninck, R.; De Batist, R.; Gijs, A. *High Temp. High Press.* **1976**, *8*, 167–176.
153. Matzke, H. J.; Politis, C. *Solid State Commun.* **1973**, *12*, 401–404.
154. Routbort, J. L.; Matzke, H. J. *J. Am. Ceram. Soc.* **1972**, *55*, 14–18.
155. Andrew, J. F.; Latimer, T. W. LA-6037-MS; 1975.
156. Sheth, A.; Leibowitz, L.; Winslow, G. *Trans. Am. Nucl. Soc.* **1976**, *23*, 130–131.
157. Padel, A.; de Novion, C. H. *J. Nucl. Mater.* **1969**, *33*, 40–51.
158. Balakin, S. A.; Belevantsev, V. S.; Bubnov, A. S.; Zelyanin, V. A.; Kotelnikov, R. B.; Sokorov, D. M. *At. Energ. (USSR)* **1980**, *48*, 49–50.
159. Hall, A. R. *J. Nucl. Mater.* **1970**, *37*, 314–323.
160. Nelson, S. G.; Foster, E. L. *Trans. Am. Nucl. Soc.* **1965**, *8*, 38–39.
161. Kurasawa, T. *J. Nucl. Mater.* **1978**, *71*, 327–332.
162. Clark, N. J.; Mountford, R. *J. Inorg. Nucl. Chem.* **1972**, *34*, 2729–2738.
163. Fenish, R. G. ORO-501; 1960; pp 34–51.
164. Chubb, W.; Dickerson, R. F. *Am. Ceram. Soc. Bull.* **1962**, *41*, 564–569.
165. Kurasawa, T.; Kikuchi, T. *J. Nucl. Mater.* **1976**, *60*, 330–338.
166. Bober, M.; Singer, J.; Wagner, K. *J. Nucl. Mater.* **1984**, *124*, 120–128.
167. Bober, M.; Karow, H. U.; Müller, K. *High Temp. High Press.* **1980**, *12*, 161–168.
168. Karow, H. U.; Bober, M. In *Proceedings of the International Symposium on Thermodynamics of Nuclear Materials*, Jülich (Germany), 1979; IAEA: Vienna, 1980; Vol. 1, pp 155–169.
169. De Bruycker, F. E. Ph.D. Thesis, Politech'Orléans, 2010.
170. De Coninck, R.; Van Lierde, W.; Gijs, A. *J. Nucl. Mater.* **1975**, *57*, 69–76.
171. Grossman, L. N. GEST-2015; 1963; pp 1–31.
172. Le Guyadec, F.; Rado, C.; Joffre, S.; Coullomb, S.; Chatillon, C.; Blanquet, E. *J. Nucl. Mater.* **2009**, *393*, 333–342.
173. Camagni, P.; Manara, A.; Landais, E. *Surf. Sci.* **1968**, *10*, 332–348.
174. Gueneau, C.; Chatain, S.; Gossé, S.; et al. *J. Nucl. Mater.* **2005**, *344*, 191–197.
175. Gossé, S.; Gueneau, C.; Alpettaz, T.; Chatain, S.; Chatillon, C.; Le Guyadec, F. *Nucl. Eng. Des.* **2008**, *238*, 2866–2876.

176. Gosse, S.; Gueneau, C.; Chatillon, C.; Chatain, S. *J. Nucl. Mater.* **2006**, *352*, 13–21.
177. Henry, J. L.; Paulson, D. L.; Blickensderfer, R.; Kelly, H. J. US Bureau of Mines Report 6968; 1967.
178. Guéneau, C.; Baichi, M.; Labroche, D.; Chatillon, C.; Sundman, B. *J. Nucl. Mater.* **2002**, *304*, 161–175.
179. Potter, P. E. *J. Nucl. Mater.* **1972**, *42*(1), 1–22.
180. Heiss, A. *J. Nucl. Mater.* **1975**, *55*, 207–223.
181. Blum, O. L.; Morlevat, J. P. *Compt. Rendus* **1964**, *258*, 6151–6153.
182. Besson, J.; Blum, P. L.; Morlevat, J. P. *Compt. Rendus* **1964**, *260*, 3390–3392.
183. Blum, P. L.; Morlevat, J. P. *Rev. Int. Hautes Temp. Réfract.* **1966**, *3*, 253–254.
184. Namba, S.; Imoto, S.; Sano, T. *Technol. Rep. Osaka Univ.* **1968**, *18*, 91–104.
185. Henry, J. L.; Blickensderfer, R.; Paulson, D.; Bates, J. L. *J. Am. Ceram. Soc.* **1970**, *53*, 335–339.
186. Larin, A. A.; Vlasov, V. G. *Russ. J. Inorg. Chem.* **1972**, *17*, 153–155.
187. Biasetto, L.; Zanonato, P.; Carturan, S.; et al. *J. Nucl. Mater.* **2010**, *404*, 68–76.
188. Cordfunke, E. H. P. *J. Nucl. Mater.* **1975**, *56*, 319–326.
189. Benz, R. *J. Nucl. Mater.* **1969**, *31*, 93–98.
190. Cordfunke, E. H. P.; Ouweltjes, W. *J. Nucl. Mater.* **1979**, *79*, 271–276.
191. Padel, A.; Groff, A.; De Novion, C. H. *J. Nucl. Mater.* **1970**, *36*, 297–303.
192. Uchida, M.; Ichikawa, M. *J. Nucl. Mater.* **1973/74**, *49*, 91–97.
193. Kamimoto, M.; Takahashi, Y.; Mukaibo, T. *J. Phys. Chem. Solids* **1974**, *35*, 393–399.
194. Eckhardt, R. C. *Los Alamos Sci.* **2000**, *26*, 464–489.
195. Rodriguez, C. *Nucl. Eng. Des.* **2003**, *222*, 299–317.
196. Lorenzelli, R. *Compt. Rendus* **1968**, *C266*, 900.
197. Sandenaw, T. A.; Gibney, R. B.; Holley, C. E., Jr. *J. Chem. Thermodyn.* **1973**, *5*, 41–47.
198. Sheft, I.; Fried, S. *J. Am. Chem. Soc.* **1953**, *75*, 1236–1237.
199. Mitchell, A. W.; Lam, D. J. *J. Nucl. Mater.* **1970**, *36*, 110–112.
200. Lam, D. J.; Mueller, M. H.; Paulikas, A. P.; Lander, G. H. *J. Phys. (Paris)* **1971**, *C1*, 917.
201. Lander, G. H.; Mueller, M. H. *Phys. Rev. B* **1974**, *10*, 1994–2003.
202. Baker, R. D.; Hecker, S. S.; Harbur, D. R. *Los Alamos Sci.* **1983**, *148*, 150–151.
203. Reavis, J. G.; Reese, L. *Differential Thermal Analyses; Quarterly Status Report-Advanced Plutonium Fuels Program*, Apr 1 to Jun 30, Los Alamos Scientific Laboratory of the University of California, LA-4494-MS, Project 463; 1970.
204. Mulford, R. N. R.; Ellinger, F. H.; Hendrix, G. S.; Albrecht, E. D. In *Plutonium 1960*; Grison, E., Ed.; Cleaver-Hume: London, 1961; pp 301–311.
205. Harper, E. A.; Hedger, H. J.; Dalton, J. T. *Nature* **1968**, *219*, 151.
206. Ogard, A. E.; Leary, J. A. *Plutonium Carbides*; LA-4415, UC-4, Chemistry, TID-4500; 1970.
207. Marcon, J. P. *J. Inorg. Nucl. Chem.* **1970**, *32*, 2581–2590.
208. Rosen, S.; Nevitt, M. V.; Mitchell, A. W. *J. Nucl. Mater.* **1963**, *10*, 90–98.
209. Kruger, O. L. *J. Nucl. Mater.* **1962**, *7*, 142–150.
210. Burnham, J. B.; Skavdahl, R. E.; Chikalla, T. D. In *Carbides for Nuclear Energy, Proceedings*, Harwell, Nov 1963; Russel, L. E., Bradbury, B. T., Harrison, J. D. L., Hedger, H. J., Mardon, P. G., Eds.; Macmillan & Co.: London, 1963; pp 51–68.
211. Gouder, T.; Havela, L.; Shick, A. B.; Huber, F.; Wastin, F.; Rebizant, J. *J. Phys. Condens. Matter* **2007**, *19*, 476201–476212.
212. Nevitt, M. V.; Rosen, S. *Acta Crystallogr. Suppl. A* **1963**, *16*, 18–23.
213. Green, J. L.; Arnold, G. P.; Leary, J. A.; Nereson, N. G. *J. Nucl. Mater.* **1970**, *34*, 281–289.
214. Haines, H. R.; Hall, R. O. A.; Lee, J. A.; Mortimer, M. J.; McElroy, D. *J. Nucl. Mater.* **1980**, *88*, 261–264.
215. Oetting, F. L. *J. Nucl. Mater.* **1980**, *88*, 265–272.
216. Kruger, O. L.; Savage, H. *J. Chem. Phys.* **1964**, *40*, 3324–3328.
217. Zachariasen, W. H. *Acta Crystallogr.* **1952**, *5*, 17–22.
218. Kruger, O. L. *J. Am. Ceram. Soc.* **1963**, *46*, 80–85.
219. Skavdahl, R. E. *Trans. Am. Nucl. Soc.* **1963**, *6*, 393–397.
220. Johnson, K. A. *Metallographic Preparation and Observations of Some Plutonium–Carbon Alloys*; LA-3191-MS; 1965.
221. Danan, J. *J. Nucl. Mater.* **1973**, *45*, 339–340.
222. Johnson, K. A.; Van Deventer, E. H.; Kruger, O. L.; Hubbard, W. N. *J. Chem. Thermodyn.* **1974**, *6*, 219–225.
223. Sengupta, A. K.; Aurora, K. B.; Majumdar, S.; Ganguly, C.; Roy, P. R. *J. Nucl. Mater.* **1986**, *139*, 282–283.
224. Mazaudier, F.; Tamani, C.; Galerie, A.; Marc, Y. *J. Nucl. Mater.* **2010**, *406*, 277–284.
225. Anselin, F.; Dean, G.; Lorenzelli, L.; Pascard, R. In *Carbides for Nuclear Energy, Proceedings*, Harwell, Nov 1963; Russel, L. E., Bradbury, B. T., Harrison, J. D. L., Hedger, H. J., Mardon, P. G., Eds.; Macmillan & Co.: London, 1963; pp 113–161.
226. Silva, R. J.; Bodoglio, G.; Rand, M. H.; Robouch, P. B.; Wanner, H.; Puigdomenech, I. In *Chemical Thermodynamics of Americium*; OECD; Chemical Thermodynamics Series Chemical; Elsevier, North-Holland: Paris, 1995; Vol. 2.
227. Benedict, U. Euratom Progress Report No. 15, Jan – Jun 1973, Communication 350 TUSR 15; European Institute for Transuranium Elements: Karlsruhe, 1973; pp 106–114.
228. Osaka, M.; Koyama, S.; Morozumi, K.; Namekawa, T.; Mitsugashira, T. *J. Nucl. Sci. Technol.* **2001**, *38*, 912–914.
229. Gibson, J. K.; Haire, R. G. *Organometallics* **1999**, *18*, 4471–4477.
230. Radchenko, V. M.; Seleznev, A. G.; Chernakova, T. A.; Ryabinin, M. A.; Gorbunov, S. I.; Nagaitsev, V. G. *Radiochemistry* **2004**, *46*, 6–11.
231. Rand, M. H. In *Thorium: Physico-Chemical Properties of Its Compounds and Alloys*, Atomic Energy Review Special Issue No.5; Kubaschewski, O., Ed.; IAEA: Vienna, 1975; pp 7–85.
232. Osaki, M.; Obata, T.; Kirihaara, T. *Jpn. Inst. Met.* **1973**, *37*, 100–103.
233. Auskern, A. B.; Aronson, S. *J. Nucl. Mater.* **1969**, *29*, 345–348.
234. Rosen, S.; Nevitt, M. V.; Barker, J. J. *J. Nucl. Mater.* **1963**, *9*, 128–136.
235. Rosen, S.; Nevitt, M. V.; Mitchell, A. W. *J. Nucl. Mater.* **1963**, *9*, 137–142.
236. Reavis, J. G. *Quarterly Status Report on the Advanced Plutonium Fuels Program*; Los Alamos Scientific Laboratory of the University of California, LA-3607-MS, Project 807; July 1966.
237. Reavis, J. G.; Reese, L. *Quarterly Status Report on the Advanced Plutonium Fuels Program*; Los Alamos Scientific Laboratory of the University of California, Project 463 LA-4073-MS (1969); LA-4193-MS (1969);

- LA-4284-MS (1969); LA-4307-MS (1969); LA-4494-MS (1970).
238. Fischer, E. *Calphad* **2009**, 33, 487–494.
239. Stahl, D.; Strasser, A. In *Carbides in Nuclear Energy*, Proceedings of a Symposium, Harwell, London, Nov 1963; Russell, L. E., Bradbury, B. T., Harrison, J. D. L., Hedger, H. J., Mardon, P. G., Eds.; Macmillan and Co.: London, 1964; Vol. 1, pp 373–391.
240. Ohse, R. W.; Capone, F. In *Plutonium and Other Actinides*; Blank, H., Lindner, R., Eds.; North-Holland: Amsterdam, 1976; pp 245–256.
241. Mardon, P. G.; Potter, P. E. *On the U–Pu–C Phase Diagram, Part II, The Freezing of the Alloys and Calculation of Some Equilibria*; AERE-R; 1970.
242. Holleck, H. In *Thermodynamics of Nuclear Materials*; IAEA: Vienna, 1975; Vol. 2, pp 213–264.
243. Dalton, J. T. In *Carbides in Nuclear Energy*, Proceedings of a Symposium, Harwell, London, Nov 1963; Russell, L. E., Bradbury, B. T., Harrison, J. D. L., Hedger, H. J., Mardon, P. G., Eds.; Macmillan and Co.: London, 1964; Vol. 1, pp 77–94.
244. Browning, P.; Phillips, B. A.; Potter, P. E.; Rand, M. H. *Plutonium and Other Actinides*; North-Holland: Amsterdam, 1976; pp 257–265.
245. Udovskii, A. L.; Alekseeva, Z. M. *Dokl. Phys. Chem. (Engl. Transl.)* **1982**, 262, 42–45.
246. Sengupta, A. K.; Banerjee, J.; Jarvis, T.; Kutty, T. R. G.; Ravi, K.; Majumdar, S. *Nucl. Technol.* **2003**, 142, 205–320.
247. Sengupta, A. K.; Majumdar, S.; Ganguly, C.; Purushothaman, D. S. C.; Roy, P. R. *Am. Ceram. Soc. Bull.* **1986**, 65, 1057–1060.
248. Sengupta, A. K.; Basak, U.; Ganguly, C. *J. Mater. Sci.* **1987**, 6, 20.

2.05 Phase Diagrams of Actinide Alloys

M. Kurata

Central Research Institute of Electric Power Industry, Komae, Tokyo, Japan

© 2012 Elsevier Ltd. All rights reserved.

2.05.1	Introduction	139
2.05.2	Comprehensive Features of Actinide Phase Diagrams	141
2.05.3	Various Types of Actinide Phase Diagrams	141
2.05.3.1	Actinide–Alkali Metals	141
2.05.3.2	Actinide–Alkaline-Earth Metals	145
2.05.3.3	Actinide: Sc, Y, Lanthanides	147
2.05.3.4	Actinide–Actinide	155
2.05.3.5	Actinide: Group IVa, Va, VIa, and VIIa Metals	160
2.05.3.6	Actinide: Group VIII Metals	172
2.05.3.7	Actinide: Group Ib and IIb Metals	179
2.05.3.8	Actinide: Group IIIb Metals	183
2.05.3.9	Actinide: Other Group b Metals or Semimetals	185
2.05.4	Summary	187
References		190

Abbreviations

APD	Alloy phase diagram
bcc	Body-centered cubic structure
CALPHAD	Calculation of phase diagram
CO	Phase diagram type introduced in the present article for convenience. CO means several compounds appear in the phase diagram.
DHCP	Double hexagonal close-packed structure
EDX	Energy disperse X-ray spectrometry
EMF	Electro-motive force
EP	Phase diagram type introduced in the present article for convenience. EP means eutectic or peritectic type phase diagram.
fcc	Close-packed face-centered cubic structure
FCCI	Fuel cladding chemical interaction
HCP	Hexagonal close-packed structure
IM	Phase diagram type introduced in the present article for convenience. IM means all phases are immiscible in the phase diagram.
LS	Phase diagram type introduced in the present article for convenience. LS means liquid and solid are miscible in the wide composition region of the phase diagram.

MG	Phase diagram type introduced in the present article for convenience. MG means several there is a limited miscibility gap in the phase diagram.
SEM	Scanning electron microscope
WDX	Wave length dispersive X-ray spectrometry

Symbols

f_i	Activity coefficient of i -component
R	Gas constant
T	Temperature (K)
G_{mix}^{φ}	Gibbs energy of mixing for φ -phase
${}^{\circ}G_i^{\varphi}$	Standard Gibbs energy for pure substance, i , for φ -phase
x_i	Mole fraction of i -component
μ_i^{φ}	Chemical potential of i -component for φ -phase
Ω^{φ}	Interaction parameter for φ -phase

2.05.1 Introduction

In this chapter, comprehensive features of and recent progress on the phase diagrams of actinide alloys are introduced. *Phase Diagrams of Binary Actinide Alloys* edited by Kassner and Peterson in 1995¹ summarized

384 binary phase diagrams involving actinide elements from Ac to Lr. Some phase diagrams were evaluated through the effort of the Alloy Phase Diagram (APD) program initiated by ASM International and the National Institute of Standards and Technology, while the remainder largely taken from *Binary Alloy Phase Diagrams*² and *Molybdenum*.³ The assessment by the APD program has been continued, and a handbook was published in 2000.⁴ The main part of the present compilation is based on these data books.

Regarding the phase relation among actinide elements, a composite phase diagram from Ac to Cm was suggested originally by Smith and Kmetko,⁵ and then a color version was given by Moore and van der Laan,⁶ as shown in Figure 1. The body-centered cubic (bcc) phase is formed prior to melting for the actinides below Cm, and the bcc phase is completely soluble between neighboring actinides as well as the liquid phase. The increase in complexity of the crystal structure of the low-temperature allotropes and the reduction in melting point are observed from Ac toward Pu. Many low-symmetry allotropes as well as the lowest melting temperatures are seen in the region between Np and Pu. In the early part between Ac and Th, the structure of the low-temperature allotropes is close-packed face-centered cubic (fcc) and somewhat similar to the transition metals, while beyond Am the typical structure seen for light lanthanides is observed, that is, double hexagonal close-packed (DHCP). These suggest that the alloying behavior of those actinide metals, such as Ac and Th, and beyond Am, with other series metals becomes similar to that of transition metals and light lanthanides, respectively. A wide

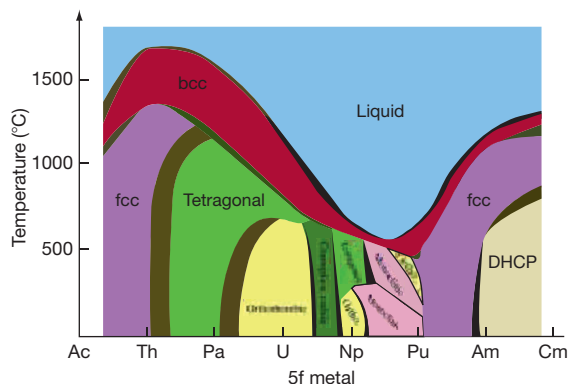


Figure 1 A 'pseudo-binary' phase diagram of the light to middle 5f actinide metals quoted from Moore and van der Laan,⁶ which was originally compiled by Smith and Kmetko.⁵

monophase region is seen even for the low-temperature allotropes in the case of neighboring actinides. However, several additional features can be pointed out. The solubilities of Pa and U into Th and Pa, respectively, are very limited in the low-temperature region, although those of Th and Pa in Pa and U, respectively, are very good. The mutual solubilities of Pu and Am for the low-temperature allotropes are very limited, with the only exception of the fcc phase. When observing the phase relation between actinides alternately in the periodic table, the miscibility becomes poorer. For instance, a miscibility gap appears for the liquid phase in the Th–U and Np–Am binary systems. Those features originate from the difference in the 5f electron characteristics. The details are discussed in other chapters. Simply put, the features on alloying of U, Np, and Pu with other elements are different from the other actinides. In general, the degree of the decrease in the Gibbs energy of mixing between U or Np and the other elements is smaller than that related to Ac through Th or beyond Am with several exceptions. Plutonium has intermediate characteristics.

As for the comprehensive observation of APD between actinides and other metals, it is still convenient and useful to take a semiempirical thermodynamic model into account for a brief understanding to the phase relations between various metals. The details of the semiempirical method, the so-called CALPHAD approach, are given in another chapter. In the present review, some phase diagrams are assessed in a semiempirical manner. The equation treated in the CALPHAD approach is given for the solution phases as follows:

$$G_{\text{mix}}^{\varphi}(T, x_B) = (1 - x_B) {}^0G_A^{\varphi} + x_B {}^0G_B^{\varphi} + RT[(1 - x_B)\ln(1 - x_B) + x_B\ln x_B] + \Omega^{\varphi}x_B(1 - x_B) \quad [1]$$

Here, is the Gibbs energy of mixing for the φ -phase; ${}^0G_A^{\varphi}$, ${}^0G_B^{\varphi}$ are the standard Gibbs energy of A and B for the φ -phase, Ω^{φ} is the interaction parameter of regular solution model for the φ -phase; x_B is the mole fraction of B; R is the gas constant; and T is the temperature (K) which indicates the Gibbs energy of mixing between the A and B components in the A–B binary system. It is useful to introduce the interaction parameter, Ω^{φ} , as an index to show the tendency of mixing between A and B. When the $\Omega^{\varphi} = 0$, A and B can form an ideal solution. When $\Omega^{\varphi} > 0$ or $\Omega^{\varphi} < 0$, G_{mix}^{φ} shifts to the positive and negative directions, respectively, and the degree of Ω^{φ} shows how large

the tendency of ‘mixing’ or ‘demixing’ is in the A–B alloy system. Usually, Ω^ϕ is indicated as a simple function of temperature and composition.

The partial molar Gibbs energies of the components A or B, that is, the chemical potentials of A or B, corresponding to the Gibbs energy expression given above, are obtained with eqns [2] and [3].

$$\mu_A^\phi(T, x_B) = {}^0G_A^\phi + RT \ln(1 - x_B) + \Omega^\phi x_B^2 \quad [2]$$

$$\mu_B^\phi(T, x_B) = {}^0G_B^\phi + RT \ln x_B + \Omega^\phi(1 - x_B)^2 \quad [3]$$

By introducing an activity coefficient, these equations are given alternatively by

$$\mu_A^\phi(T, x_B) = {}^0G_A^\phi + RT \ln f_A(1 - x_B) \quad [4]$$

$$\mu_B^\phi(T, x_B) = {}^0G_B^\phi + RT \ln f_B x_B \quad [5]$$

The Gibbs energy of formation of intermetallic compounds can be defined in a similar manner. A rough estimation of the order of the various Gibbs energies can be attempted by observing the feature of the actinide phase diagrams. The precision of parameters treated in the CALPHAD approach, that is, the interaction parameters in the regular solution model, is lower than those in the nonempirical approach such as an *ab initio* method. Sometimes, the interaction parameters must be treated as just simple fitting parameters. However, the Gibbs energies themselves estimated from the CALPHAD approach have quite good accuracy and are sufficient to reconstruct the actinide phase diagrams or to estimate the thermodynamic functions. Due to the lack of experimental data, this method may be often practically useful when taking actinide-containing systems into considerations.

2.05.2 Comprehensive Features of Actinide Phase Diagrams

Figure 2 categorizes the phase diagrams of Th–X, U–X, Np–X, Pu–X, and Am–X systems into six types, where X refers to various metallic elements. In the present chapter, the types of mixing are named for convenience as CO ($N:N > 3$), CO ($N:N = 1, 2, 3$), LS, EP, MG, and IM. Here, the CO represents a phase diagram type in which some kinds of intermetallic compounds exist, and N means the number of intermetallic compounds in the corresponding system. LS indicates a phase diagram in which wide ranges of liquid and solid solubility are observed, and the EP indicates the eutectic- or peritectic-type

phase diagrams. MG indicates a phase diagram in which a limited miscibility gap exists for the liquid phase. IM represents a phase diagram in which the solubility is extremely limited even in the liquid phase. The tendency of the decrease in miscibility obeys this order. By observing these figures carefully, several comprehensive features can be noticed. When comparing the Th–X and U–X systems, the miscibility in the Th–X system is generally better than that in the U–X system, with the exception of the relations against IVa, Va, VIa, and VIIa transition metals and Np. The miscibility of the Np–X system further becomes poorer than that of the U–X system, with the exception of the heavy actinides. Regarding the Np–Am system, for instance, several percent of the solid solubility and a limited miscibility of the liquid phase have been reported recently.⁷ A similar tendency is speculated to exist in the relation between Np and heavy actinides beyond Am. The Am–X system is estimated from the limited available experimental information and the expected similarity to the Ce–X system, as given in **Figure 2(f)**. The comprehensive tendency of the Am–X system is more similar to that of the Th–X system than that of the U–X, Np–X, and Pu–X systems with the exception of the relations against IVa, Va, VIa, and VIIa transition metals. The miscibility between Am and these Group a transition metals is poorer than that in the Th–X system in general. The Pu–X system has features that are intermediate between those of the U–X and Am–X systems. Plutonium is highly miscible with many types of elements with the exception of alkali and alkaline-earth metals. These comprehensive tendencies originate from the difference in the characteristics of the 5f electrons belonging to actinide elements. Detailed discussions are carried out in other chapters. In the next section, typical phase diagrams and the related thermodynamic characteristics are introduced based on the classical empirical points of view. When discussing actinide alloy systems, the classical method is still very suggestive.

2.05.3 Various Types of Actinide Phase Diagrams

2.05.3.1 Actinide–Alkali Metals

There is very limited experimental information on the relation between actinides and alkali metals. The solubility of U in liquid Li is 0.0015, 0.00087, 0.00018, and 0.000058 at.% at 1273, 1173, 1073, and 973 K, respectively⁸; that in liquid Na is <0.005 at.% at

Np-X																		0
I																		He
H																		IM
CO(2)																		IM
Li	II																IM	Ne
[IM]	Be																IM	Ar
Na	Mg	IIIa	IVa	Va	Vla	VIIa	VIII		lb	IIlb	IIIb	IVb	Vb	Vlb	VIIb	IM	Kr	
[IM]	[CO?]										Al	C	N	O	F	IM	IM	
	[MG]										CO(3)	CO(3)	CO(3)	CO(4)	[CO]			
K	Ca	Sc	Ti	V	Cr	Mn	Fe	Co	Ni	Cu	Zn	Ga	Ge	As	Se	Br	IM	
[IM]	[IM]	[MG]	[LS]	[EP]	EP	CO(1)	CO(2)	CO(>1)	CO(>1)	[LS?]	[CO?]	CO(2)	[CO?]	CO(3)	CO(4)	[CO]	IM	
Rb	Sr	Y	Zr	Nb	Mo	Tc	Ru	Rh	Pd	Ag	Cd	In	Sn	Sb	Te	I	IM	
[IM]	[IM]	IM	LS ³	[EP]	EP	[CO]	CO(>1)	CO(>1)	CO(2)	[IM]	CO(2)	[CO?]	CO(2)	CO(2)	CO(4)	CO(3)	IM	
Cs	Ba	Ln	Hf	Ta	W	Re	Os	Ir	Pt	Au	Hg	Tl	Pb	Bi	Po	At	IM	
[IM]	[IM]		[LS]	[EP]	EP	CO(1)	CO(>1)	CO(>1)	CO(3)	[LS?]	[CO]	[CO?]	[CO?]	CO(1)	[CO]	[CO]		
Fr	Ra	An																IM
[IM]	[IM]																	

CO(*N*) = compounds existing in the phase diagram, where *N* is the number of the compounds

LS = wide range of liquid and solid solutions

EP = eutectic or peritectic type

MG = liquid phase miscible but miscibility gap exists

IM = immiscible, where very limited mutual solubility even in liquid

[] = estimated

*1: close to the eutectic type

*2: miscibility gap observed in the liquid

*3: miscibility gap observed in the solid

*4: close to the solution type

*5: several percent of solid solubility

(c)

Pu-X																		0
I																		He
H																		IM
MG																		IM
Li	II																IM	Ne
IM	Be																IM	Ar
Na	CO(1)* ¹																IM	IM
IM	Mg																IM	IM
[IM]	CO(3)* ²																IM	IM
K	Ca	IIIa	IVa	Va	VIa	VIIa	VIII	IX	X	XI	XII	XIII	XIV	XV	XVI	XVII	XVIII	IM
[IM]	[IM]	[CO(1)* ⁴	EP	EP	EP	CO(1)	CO(2)	CO(6)	CO(6)	CO(4)	CO(7)	CO(11)	CO(3)	CO(1)	CO(4)	CO(2)	[CO]	IM
Rb	Sr	Y	Zr	Nb	Mo	Tc	Ru	Rh	Pd	Ag	Cd	In	Sn	Sb	Te	I	IM	IM
[IM]	[IM]	EP	CO(1)* ⁴	EP	EP	[CO]	CO(5)	CO(8)	CO(4)	CO(2)	CO(4)* ²	CO(5)	CO(7)	CO(2)	CO(5)	[CO]	IM	IM
Cs	Ba	Ln	Hf	Ta	W	Re	Os	Ir	Pt	Au	Hg	Tl	Pb	Bi	Po	At	IM	IM
[IM]	[IM]	An	CO(2)* ⁴	EP	EP	CO(1)	CO(4)	CO(4)	CO(8)	CO(8)	CO(2)	CO(2)	CO(6)	CO(3)	[CO]	[CO]	IM	IM
Fr	Ra																IM	IM
[IM]	[IM]																IM	IM
Ln	La	Ce	Pr	Nd	Pm	Sm	Eu	Gd	Tb	Dy	Ho	Er	Tm	Yb	Lu			
	MG* ⁵	MG* ⁵	MG* ⁵	MG* ⁵	[MG]* ⁵	MG* ⁵	MG	MG* ⁵	MG* ⁵	MG* ⁵	MG* ⁵	EP	EP	MG	EP			
An	Ac	Th	Pa	U	Np	Pu	Am	Cm	Bk	Cf	Es	Fm	Md	No	Lr			
	[MG]	CO(1)	[MG]	LS	LS	-	LS	LS	[LS]	[LS]	[MG]	[LS]	[LS]	[MG]	[LS]			

CO(*N*) = compounds existing in the phase diagram, where *N* is the number of the compounds

LS = wide range of liquid and solid solutions

EP = eutectic or peritectic type

MG = liquid phase miscible but miscibility gap exists

IM = immiscible, where very limited mutual solubility even in liquid

[] = estimated

*1: close to the eutectic type

*2: miscibility gap observed in the liquid

*3: miscibility gap observed in the solid

*4: close to the solution type

*5: several percent of solid solubility

(d)

Figure 2 (Continued)

Am-X

I																	0	
H CO(1)	II																He IM	
Li IM	Be CO(1)* [†]											IIIb		IVb	Vb	Vlb	Vllb	Ne IM
Na [IM]	Mg [MG]											B [CO]		C [CO]	N [CO]	O CO(3)	F [CO]	Ar IM
K [IM]	Ca [IM]	IIla	IVa	Va	Vla	Vlla	VIII		Ib		IIb	Al [CO]	Si [CO]	P [CO]	S [CO]	Cl [CO]	Kr IM	
Rb [IM]	Sr [IM]	Sc [LS]	Ti [MG]	V IM	Cr EP	Mn [MG]	Fe [CO]	Co [CO]	Ni [CO]	Cu [CO]	Zn [CO]	Ga [CO]	Ge [CO]	As [CO]	Se [CO]	Br [CO]	IM	
Cs [IM]	Ba [IM]	Y [LS]	Zr [MG]	Nb [MG]	Mo IM	Tc [MG]	Ru [CO]	Rh [CO]	Pd [CO]	Ag [CO]	Cd [CO]	In [CO]	Sn [CO]	Sb [CO]	Te [CO]	I [CO]	Xe IM	
Fr [IM]	Ra [IM]	Ln	Hf [MG]	Ta [MG]	W IM	Re [MG]	Os [CO]	Ir [CO]	Pt [CO]	Au [CO]	Hg [CO]	Tl [CO]	Pb [CO]	Bi [CO]	Po [CO]	At [CO]	Rn IM	
		An																
Ln		La [LS]	Ce [LS]	Pr [LS]	Nd [LS]	Pm [LS]	Sm [LS]	Eu [MG]	Gd [LS]	Tb [LS]	Dy [LS]	Ho [LS]	Er [LS]	Tm [LS]	Yb [MG]	Lu [LS]		
An		Ac [MG]	Th [LS]	Pa [LS]	U IM	Np MG	Pu LS	Am –	Cm [LS]	Bk [LS]	Cf [LS]	Es [MG]	Fm [LS]	Md [LS]	No [MG]	Lr [LS]		

CO(N) = compounds existing in the phase diagram, where N is the number of the compounds

LS = wide range of liquid and solid solutions

EP = eutectic or peritectic type

MG = liquid phase miscible but miscibility gap exists

IM = immiscible, where very limited mutual solubility even in liquid

[] = estimated

*1: close to the eutectic type

*2: miscibility gap observed in the liquid

*3: miscibility gap observed in the solid

*4: close to the solution type

*5: several percent of solid solubility

(e)

Ce-X

I																	0	
H CO(1)																	He IM	
Li MG	II															Ne IM		
Na [IM]	Be CO(1) ⁺¹															Ar IM		
K [IM]	Mg CO(5)	IIIa	IVa	Va	Vla	VIIa	VIII		Ib	IIb		IIIb	IVb	Vb	Vlb	VIIb	Kr IM	
Rb [IM]	Ca [IM]	Sc LS	Ti MG	V IM	Cr MG	Mn MG	Fe CO(2)	Co CO(6)	Ni CO(6)	Cu CO(5)	Zn CO(9)	Al CO(5)	Si CO(6)	P CO(3)	S CO(5)	Cl CO(1)	Br CO(1)	
Cs [IM]	Sr [IM]	Y LS	Zr MG	Nb MG	Mo MG	Tc [MG]	Ru CO(5)	Rh CO(7)	Pd CE(8)	Ag CO(4)	Cd CO(7)	Ga CO(5)	Ge CO(6)	As CO(3)	Se CO(4)	Te CO(6)	I CO(4)	
Fr [IM]	Ba IM	Ln	Hf MG	Ta IM	W IM	Re [MG]	Os CO(2)	Ir CO(9)	Pt CO(6)	Au CO(5)	Hg CO(5)	Tl CO(6)	Pb CO(2)	Bi CO(5)	Po [CO]	At [CO]	Xe IM	
	Ra [IM]	An																Rn IM
		Ln	La LS	Ce –	Pr LS	Nd LS	Pm [LS]	Sm LS	Eu MG	Gd LS	Tb LS	Dy LS	Ho LS	Er LS	Tm LS	Yb [MG]	Lu LS	
		An	Ac [MG]	Th LS	Pa [LS]	U IM	Np [MG]	Pu LS	Am LS	Cm [LS]	Bk [LS]	Cf [LS]	Es [MG]	Fm [LS]	Md [LS]	No [MG]	Lr [LS]	

$CO(N)$ = compounds existing in the phase diagram, where N is the number of the compounds

LS = wide range of liquid and solid solutions

EP = eutectic or peritectic type

MG = liquid phase miscible but miscibility gap exists

IM = immiscible, where very limited mutual solubility even in liquid

[] = estimated

*1: close to the eutectic type

*2: miscibility gap observed in the liquid

*3: miscibility gap observed in the solid

*4: close to the solution type

*5: several percent of solid solubility

(f)

Figure 2 (a) Phase diagram type of Th–X system. (b) Phase diagram type of U–X system. (c) Phase diagram type of Np–X system. (d) Phase diagram type of Pu–X system. (e) Phase diagram type of Am–X system. (f) Phase diagram type of Ce–X system.

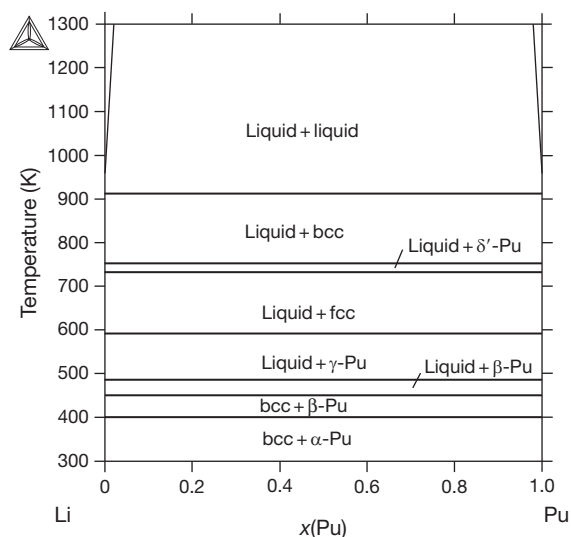


Figure 3 Calculated Pu–Li phase diagram by assuming large positive values ($\sim 50 \text{ kJ mol}^{-1}$) for the interaction parameters of each phase.

371 K.⁹ Na does not react with U at 973 K.¹⁰ According to Schonfeld *et al.*,¹¹ the Pu–Li, Pu–Na, and Pu–K systems are completely immiscible and the mutual solubility is extremely low even in the liquid phase. These suggest that in the U–alkali and Pu–alkali metal systems, allotropic transformation temperatures of both actinides and alkali metals are observed only in the phase diagrams. Systematically, similar reactions are expected for the Np–alkali metal systems. Figure 3 indicates the Pu–Li phase diagram as a typical example, which was calculated using the regular solution model by taking very large positive values ($\sim 50 \text{ kJ mol}^{-1}$) for the interaction parameters of each phase. There is no available information on the relation between Am and alkali metals. The Nd–Li phase diagram is reported in Ganiev *et al.*,¹² in which there is a limited miscibility gap for the liquid phase and several percent of Nd solubility in liquid Li. This may suggest that the miscibility between Am and alkali metals becomes slightly better than the other light actinide series elements. Regarding the Th–Na, Th–K, and U–Na systems, the existence of several compounds is reported elsewhere.¹³ However, it is claimed that these data are unreliable.¹ Th–alkali metal systems are reasonably predicted to be immiscible.

2.05.3.2 Actinide–Alkaline-Earth Metals

The phase relation between actinides and alkaline-earth metals changes with the increase in the atomic number of the latter. Regarding the Be-related

systems, a NaZn_{13} -type intermetallic compound (D_{23} -structure) is observed in the Th–Be, U–Be, and Pu–Be phase diagrams.^{1,4} These intermetallic compounds melt congruently near the Be terminal and the decomposition temperatures are estimated to be 2203, 2273, and 2223 K for ThBe_{13} , UBe_{13} , and PuBe_{13} , respectively. Since these data have at least $\pm 50 \text{ K}$ error, the decomposition temperatures are reasonably comparable. Figure 4 indicates the U–Be phase diagram as a typical example quoted from Okamoto,⁴ which was mainly constructed from the observations of Buzzard.¹⁴ The eutectic point appears near the U terminal at 1363 K, and a narrow liquid miscibility gap appears near the Be terminal in the U concentration region between ~ 0.7 and $\sim 2.2 \text{ at.}\%$. Although the latter was questioned by Hansen and Anderko,¹⁵ there is no other available experimental data for this system. According to Wilhelm *et al.*,¹⁶ this miscibility gap is thermodynamically unlikely and its presence is possible only if there is a strong clustering in the liquid phase, and thus thermodynamic functions for the U–Be system are estimated by introducing a simple thermodynamic model. As for the solid phase, a few percent of solid solubility of Be in γ -U was observed.¹⁴ Also, a spinodal composition was given in the central region.¹⁴ There are two different sources for the Pu–Be system.^{11,17} The significant differences between them are the congruent melting temperature of the PuBe_{13} and the shape of the liquidus. The latter phase diagram given in Konobeevsky¹⁷ was then modified based on the several unpublished results obtained at the Los Alamos National Laboratory, as shown by Ellinger *et al.*¹⁸ The modified Pu–Be phase diagram by Ellinger *et al.*¹⁸ was recommended by Okamoto,¹⁹ who showed phase relations that are mostly similar to those in the U–Be system, although the eutectic temperature lowered to $\sim 903 \text{ K}$. There is also a small percent solubility of Be in ϵ -Pu (bcc structure). The Th–Be phase diagram was mainly constructed by Okamoto¹⁹ from the observations by Badaeva and Kuznetsova.²⁰ When neglecting the ThBe_{13} compound, the Th–Be phase diagram looks like that of a typical eutectic type, and the eutectic point was reported to be at 1503 K and at 65 at.% Th. However, according to Okamoto,¹⁹ due to the cursory nature of the work of Badaeva and Kuznetsova,²⁰ the eutectic point is still only a rough estimation. Table 1 summarizes the thermodynamic functions for the Th–Be, U–Be, and Pu–Be systems, which were estimated by Okamoto¹⁹ with respect to the liquid phases. The NaZn_{13} -type intermetallic compound was also

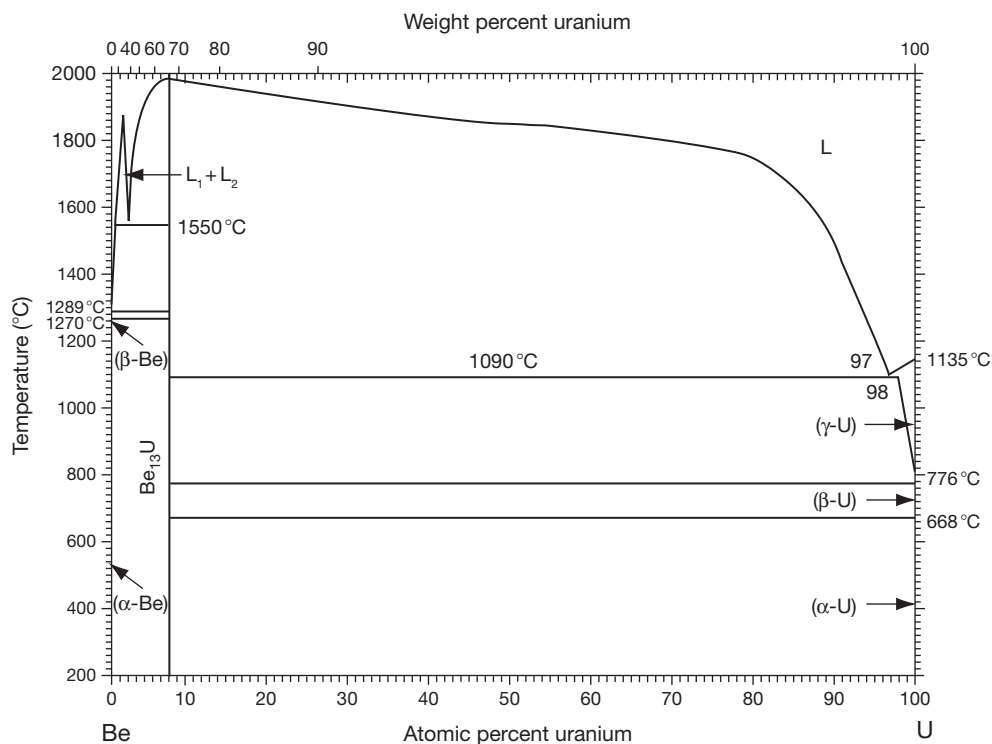


Figure 4 U-Be phase diagram taken from Okamoto.⁴

Table 1 Thermodynamic functions for actinide-Be systems

$G^\circ(\text{Be, liq}) = 0$
$G^\circ(\text{Th, liq}) = 0$
$G^\circ(\text{U, liq}) = 0$
$G^\circ(\text{Pu, liq}) = 0$
$G^\circ(\text{Be, bcc}) = -12\,600 + 8.067T$
$G^\circ(\text{Be, HCP}) = -14\,700 + 9.428T$
$G^\circ(\text{Th, bcc}) = -13\,807 + 6.808T$
$G^\circ(\text{Th, fcc}) = -17\,406 + 9.012T$
$G^\circ(\text{U, bcc}) = -9142 + 6.497T$
$G^\circ(\text{Be}_{13}\text{Th}) = -14\,630 + 4.902T$
$G^\circ(\text{Be}_{13}\text{U}) = -17\,100 + 6.470T$
$G^\circ(\text{Be}_{13}\text{Pu}) = -24\,980 + 9.400T$
$G^{\text{ex}}(\text{Th-Be, liq}) = x_{\text{Th}}(1 - x_{\text{Th}})(13\,520 - 830x_{\text{Th}})$
$G^{\text{ex}}(\text{U-Be, liq}) = x_{\text{U}}(1 - x_{\text{U}})(36\,100 - 5090x_{\text{U}} - 580x_{\text{U}}^2)$
$G^{\text{ex}}(\text{Pu-Be, liq}) = x_{\text{Pu}}(1 - x_{\text{Pu}})(10\,160)$

Source: Okamoto, H. In *Phase Diagrams of Binary Actinide Alloys*; Kassner, M. E., Peterson, D. E., Eds.; Monograph Series on Alloy Phase Diagrams No. 11; ASM International: Materials Park, OH, 1995; pp 22–24, 146–151, 164–168, 207–208, 218–219, 246–247, 297–300, 411–412, 423.

Note: values are in J mol^{-1} . T is in K. x is mole fraction.

observed in Pa-Be, Np-Be, Am-Be, and Cm-Be systems.^{21–23} The decomposition temperatures are predicted to be at least higher than 1673 K for the Np-Be system and 1773 K for the Am-Be and Cm-Be systems.

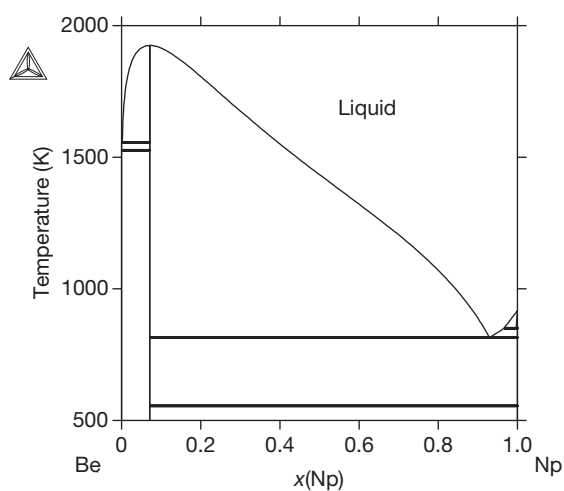


Figure 5 Hypothetically calculated Np-Be phase diagram.

Figure 5 shows the Np-Be phase diagram preliminarily estimated in the present study, assuming the interaction parameter for the liquid phase and the Gibbs energy of formation for NpBe_{13} are the same as those for the Pu-Be system. It is speculated that the phase relations in the Np-Be system will have a reasonably

similar shape with the Pu–Be system, with the exception of the Np terminal. By measuring the thermal arrests for several compositions, especially near the Be terminal, the speculated phase diagram will be modified efficiently.

Regarding the Th–Mg system, there are some conflicting issues among the available data.^{24–26} The tentatively assessed phase diagram was given in Nayeb-Hashemi and Clark.²⁷ However, the phase relations related to the gas phase were not given in the phase diagram, although the boiling point of Mg is 1380 K, which is lower than the transition temperature between α -Th and β -Th. Two intermetallic compounds, that is, Th₆Mg₂₃ and ThMg₂, exist near the Mg terminal in the low-temperature region. At the least, these decomposition temperatures are much lower than that for the ThBe₁₃, suggesting that the stability of the Th–Mg compounds is far lower than that of the Th–Be compounds. Thermodynamic functions for the ThMg₂ were determined by Novotny and Smith²⁸ between 692 and 812 K by means of vapor pressure measurement. The derived equation for the Gibbs energy of the formation is

$$\begin{aligned}\Delta_f G^0(\text{Mg}_2\text{Th}) = & -59.871 \pm 12.979 \\ & + (63.639 \pm 18.000) \\ & \times 10^{-3} T (\text{kJ mol}^{-1})\end{aligned}$$

Table 2 summarizes the thermodynamic values at 750 K. As for the enthalpy and entropy of formation, the higher values in the table were recommended by Nayeb-Hashemi and Clark.²⁷ A similar phase relation near the Mg terminal was reported for the Pu–Mg system,³⁰ although the phase relation at high temperature was different. There is a miscibility gap for the liquid phase in the high-temperature region of the Pu–Mg system. On the other hand, there are no intermetallic compounds in the U–Mg system, and the limited solubility even for the liquid phase was shown.³¹ These facts on the phase relation between actinides and Mg suggest that the miscibility between actinides and Mg becomes far poorer than that between actinides

and Be. By assuming the systematic variation in the actinide–Mg systems, partial phase diagrams for Pa–Mg, Np–Mg, and Am–Mg systems were proposed by Gulyaev and Dvorshkaya³² and there is limited solubility for the solid and liquid phases.

In the cases of the Ca-, Sr-, Ba-, and probably Ra-related systems, the miscibility between actinides and these heavy alkaline-earth metals is expected to be very poor even for the liquid phase, although the available information is very limited. Thorium metal was prepared by calciothermic reduction at around 1223 K, and the solubility of Ca in Th was found to be very low (<0.12 at.%).³³ No binary compounds between U and Ba were observed in the determination of the U–Ba–C ternary phase diagram.³⁴ The U–Ca, U–Sr, Pu–Ca, Pu–Sr, Pu–Ba, and Am–Ba systems were predicted to be immiscible, and the mutual solubility was extremely low even in the liquid phase.^{11,35–38} According to semi-empirical modeling,^{39,40} the limited mutual solubility and the absence of any intermetallic compounds were also predicted for the Th–Ba system, although there is no available experimental data. These suggest that, for the actinides–Ca, –Sr, –Ba, and possibly, –Ra systems, the allotropic transformation temperatures of both the actinides and alkaline-earth metals will only appear in the phase diagrams. **Figure 6** shows the Pu–Ca phase diagram as a typical example, which was calculated by taking very large positive values ($\sim 50 \text{ kJ mol}^{-1}$) for the interaction parameters of each phase. Other systems are considered to have a similar tendency.

2.05.3.3 Actinide: Sc, Y, Lanthanides

The phase relation between actinide and Group IIIA metals depends upon the characteristics of the actinide metals. **Table 3** summarizes the phase relations for the Th-related system, which can be divided into five groups. The first group consists of the Th–Sc, Th–Y, Th–Gd, Th–Tb, and Th–Dy systems. The mutual solubility of these systems is very

Table 2 Thermodynamic functions for Mg₂Th

Compound	Gibbs energy (kJ mol ^{−1})		Excess Gibbs energy (kJ mol ^{−1})	Enthalpy of formation (kJ mol ^{−1})	Entropy of formation (J mol ^{−1} K ^{−1})
Mg ₂ Th	−12.14	−14.72	−2.80	−46.89 to −72.85	−45.67 to −81.67
References	28	29	29	28	28

Source: Nayeb-Hashemi, A. A.; Clark, J. B. In *Phase Diagrams of Binary Actinide Alloys*; Kassner, M. E., Peterson, D. E., Eds.; Monograph Series on Alloy Phase Diagrams No. 11; ASM International: Materials Park, OH, 1995; pp 68–72.

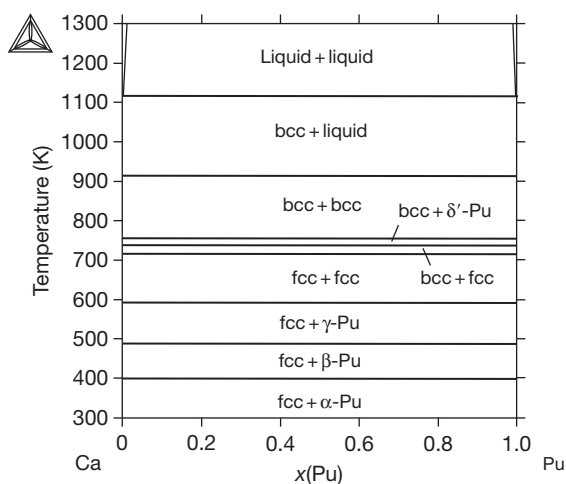


Figure 6 Calculated Pu–Ca phase diagram by assuming large positive values ($\sim 50 \text{ kJ mol}^{-1}$) for the interaction parameters of each phase.

good.^{41–43,47} These Group IIIa metals have two allotropes: the low-temperature α -phase (HCP structure) and the high-temperature β -phase (bcc structure). On the other hand, Th has the low-temperature α -phase (fcc structure) and the high-temperature β -phase (bcc structure). The β -phase in these systems is completely soluble as well as the liquid phase. The low-temperature α -phases have a large region of mutual solid solubility, although the crystal structure is different from each other. Regarding the solubility of Th in the α -phase of Sc, Y, Gd, Tb, and Dy, a systematic unlikely tendency is seen in Table 3, which possibly originates from the differences in the method of sample preparation. Figure 7 indicates the Th–Sc phase diagram as a typical example of this group quoted from Okamoto.⁴ The shape of the phase boundaries suggest that these systems can be modeled as a simple regular solution. The second group consists of the Th–La and Th–Ce systems, for which the experimental data were mainly given by Badayeva and Kuznetsova⁴³ and Moffatt.⁴⁴ Since the low-temperature phase (fcc structure) appears for La and Ce, a complete solubility even for the low-temperature fcc phase as well as the bcc and liquid phases was indicated in these previous studies. Figure 8 shows the Th–La phase diagram as a typical example shown in Kassner and Peterson.¹ As for the Th–Ce system, a similar phase diagram was originally proposed by Moffatt.⁴⁴ According to Okamoto and Massalski,⁴⁹ however, the shape of the phase boundaries in the Th–La system is thermodynamically

unlikely (abrupt change in phase boundary between the bcc and fcc phases shown in Figure 8). Also, the recent assessment for the Th–Ce system⁴ suggests that the separation of the high-temperature bcc-phase region is more likely. These conflicts are due to the difficulty in sample preparation for these systems, and further studies are necessary. The third group consists of the Th–Pr, Th–Nd, Th–Pm, and Th–Sm systems, for which the available data were reported by Moffatt,⁴⁴ Badayeva and Kuznetsova,⁴⁵ and Norman *et al.*⁴⁶ The low-temperature solid phase structure for these lanthanides is DHCP instead of HCP or fcc. The liquid and bcc phases are completely soluble. The solubility of Pr, Nd, Pm, and Sm in the α -Th phase (fcc) is very large and estimated to be higher than that of the other Group IIIa metals. Figure 9 shows the Th–Pr phase diagram as a typical example quoted from Okamoto.⁴ The shape of the phase boundaries suggests that these systems can also be explained by the simple regular solution model. The fourth group consists of the Th–Eu and Th–Yb systems. Since Eu and Yb behave as divalent metals, these systems are predicted to be fairly immiscible even for the liquid phase, as shown in Figure 10. The fifth group consists of the Th–Ho, Th–Er, Th–Tm, and Th–Lu systems. Although these lanthanides do not have the bcc allotrope in the unary system, the wide solid solubility for the bcc phase is seen in these systems. Figure 11 shows the Th–Er phase diagram as a typical example quoted from Okamoto.⁴ On observing carefully the shape of the liquidus and solidus for the Th–Group IIIa metal system, we can predict a slight positive interaction for the high-temperature solid phase (bcc) in the relation between Th and Sc, Y, or La to Sm; on the other hand, a slight negative interaction between Th and Gd to Ho, and mostly an ideal interaction between Th and Er, Tm, and Lu, can be predicted by assuming that the liquid phase behaves as an ideal solution.

Regarding the U–Group IIIa metal systems, the U–Sc phase diagram is the only exception in which several percent of mutual solid solubility and the complete liquid solubility were observed by Holcombe and Chapman⁵⁰ and Terekhov and Sinyakova.⁵¹ Figure 12 shows the U–Sc phase diagram quoted from Okamoto.⁴ The unique features of the U–Sc system are a miscibility gap for the liquid phase and a steep temperature variation on the phase boundary between the α -Sc and β -Sc phases near the Sc terminal. The latter feature needs further confirmation because it is thermodynamically

Table 3 Phase relation in Th-Group IIIA metals

Element	Th	Sc	Y	La	Ce	Pr	Nd	Pm ^a	Sm
Allotrope	α -Th (fcc) β -Th (bcc)	α -Sc (HCP) β -Sc (bcc)	α -Y (HCP) β -Y (bcc)	β -La (fcc) γ -La (bcc)	γ -Ce (fcc) δ -Ce (bcc)	α -Pr (DHCP) β -Pr (bcc)	α -Nd (DHCP) β -Nd (bcc)	α -Pm (DHCP) β -Pm (bcc)	β -Sm (DHCP) γ -Sm (bcc)
System	–	Th–Sc	Th–Y	Th–La	Th–Ce	Th–Pr	Th–Nd	Th–Pm	Th–Sm
Maximum solid solubility between low-temperature phases	–	~20 at.% Th in Sc ~60 at.% Sc in Th	~30 at.% Th in Y ~50 at.% Y in Th	Completely soluble	Completely soluble	~18 at.% Th in Pr ~80 at.% Pr in Th	~18 at.% Th in Nd ~80 at.% Nd in Th	~18 at.% Th in Pm ~80 at.% Pm in Th	~20 at.% Th in Sm ~60 at.% Sm in Th
Maximum solid solubility between bcc phases	–	Completely soluble	Completely soluble	Completely soluble	Completely soluble or miscibility gap	Completely soluble	Completely soluble	Completely soluble	Completely soluble
References		41	42	43	44 4	45	45	44	44 46
Element	Eu	Gd	Tb	Dy	Ho	Er	Tm	Yb	Lu
Allotrope	– α -Eu (bcc)	α -Gd (HCP) β -Gd (bcc)	α -Tb (HCP) β -Tb (bcc)	α -Dy (HCP) β -Dy (bcc)	α -Ho (HCP) –	α -Er (HCP) –	α -Tm (HCP) –	β -Yb (fcc) γ -Yb (bcc)	α -Lu (HCP) –
System	Th–Eu	Th–Gd	Th–Tb	Th–Dy	Th–Ho	Th–Er	Th–Tm	Th–Yb	Th–Lu
Maximum solid solubility between low-temperature phases	Immiscible	~13 at.% Th in Gd ~60 at.% Gd in Th	~24 at.% Th in Tb ~60 at.% Tb in Th	~10 at.% Th in Dy ~57 at.% Dy in Th	~20 at.% Th in Ho ~60 at.% Ho in Th	~8 at.% Th in Er ~55 at.% Er in Th	~10 at.% Th in Tm ~55 at.% Tm in Th	Immiscible	~25 at.% Th in Lu ~40 at.% Lu in Th
Maximum solid solubility between bcc phases	Immiscible	Completely soluble	Completely soluble	Completely soluble	~99 at.% Ho in Th	~99 at.% Er in Th	~20 at.% Th in Tm ~63 at.% Tm in Th	Immiscible	~6 at.% Th in Lu ~90 at.% Lu in Th
References	43	43	47	43	47	47	44 43	48	43

^aPhase relation for the Th–Pm system is estimated from the Th–Pr and Th–Nd systems.

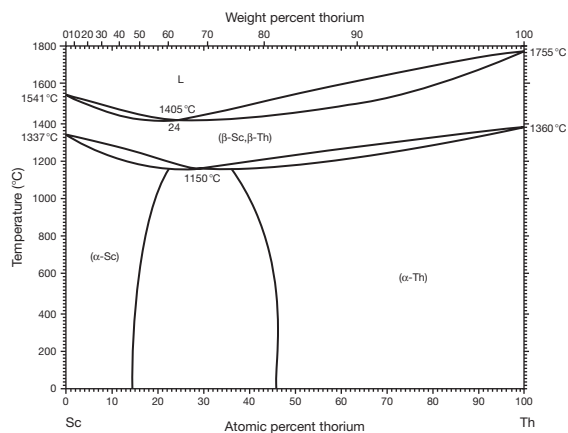


Figure 7 Th-Sc phase diagram taken from Okamoto.⁴

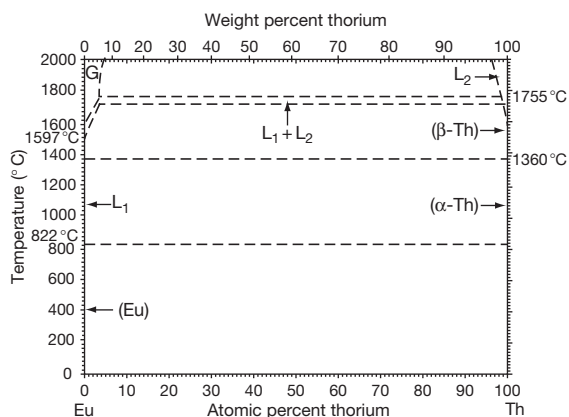


Figure 10 Th-Eu phase diagram taken from Okamoto.⁴

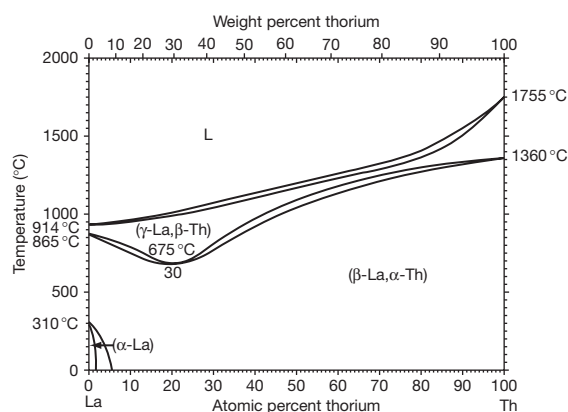


Figure 8 Th-La phase diagram taken from Okamoto.⁴

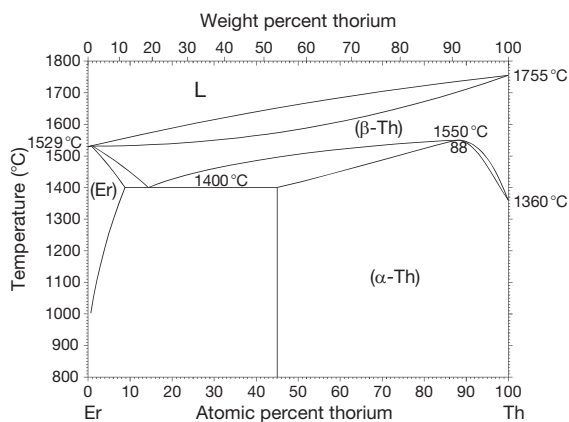


Figure 11 Th-Er phase diagram taken from Okamoto.⁴

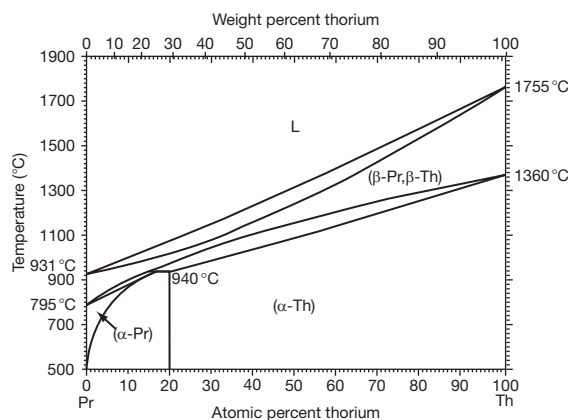


Figure 9 Th-Pr phase diagram taken from Okamoto.⁴

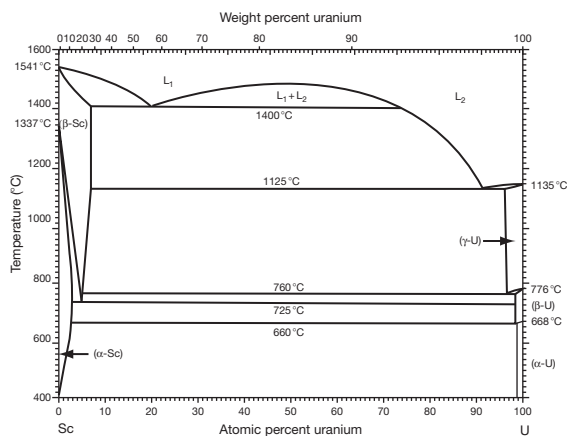


Figure 12 U-Sc phase diagram taken from Okamoto.⁴

unlikely.^{19,49} In the other U-Group IIIa metal systems, an extremely limited solubility was observed even for the liquid phase. Table 4 summarizes the solubility data for the liquid phase. Generally, it may

be said that the mutual solubility between U and light lanthanides is a little larger than that between U and heavy lanthanides. As for the solid solubility, the solubility of Gd and Ho in α -U was reported to

Table 4 Solubility of U in Group IIIa metals for the liquid phase and solubility of Group IIIa metals in U for the liquid phase

Temperature (K)	1273	1323	1373	1393	1423	1448	1473	1498	1523	References
<i>Solubility of U in Group IIIa metals</i>										
Sc				~9						51
La		0.25	0.34		0.34	0.40	0.48	0.46	0.60	52
Ce	0.76		1.43		1.48	1.72	2.16	1.79	2.15	52
Pr	0.63		0.71		0.93	0.90	1.19	1.04	1.21	52
Nd		0.79	0.60		1.02	0.95	1.22	1.01	1.07	52
Sm		0.48	0.48		0.48	0.63	0.86	0.86	0.70	52
Eu							0.72			52
Yb		0.13			~0.8 0.30		0.52		0.23	53 52
	1408	1423	1448	1473	1498	1523	1673	1751		References
<i>Solubility of Group IIIa metals in U</i>										
Sc							~20			51
Y			0.23	0.32	0.37	0.29				52
	0.17							1–2		54
La		1.31	1.30	1.38	1.43					52
Ce		1.95	2.11	1.94	1.69	2.52				52
Pr		0.37	0.46	0.51	0.54	0.66				52
Nd		0.23	0.26	0.30	0.20	0.31				52
Sm		0.32	0.33	0.40	0.40	0.33				52
Eu				0.33						52
Gd		0.11				0.23				55
			0.15							52
Tb		0.30				0.60				55
				0.48						52
Dy		0.22				0.29				55
				0.28						52
Ho		0.036				0.11				55
				0.072						52
Er		0.21				0.28				55
				0.26						52
Tm		0.035				0.098				55
					0.056					52
Yb		0.30		0.18		0.30				52
Lu		0.30								55
				0.54						52

be <0.08 and <0.2 at.%, respectively.⁵⁶ Figure 13 shows the U–Ce phase diagram calculated in the present work by assuming a regular solution model for each phase. The interaction parameter is estimated to be 53 kJ mol^{-1} by fitting the mutual solubility data.⁵² This preliminary estimation is practically useful not only to predict the phase diagrams but also to evaluate the safe performance of metallic nuclear fuels.

As for the Np–Group IIIa metal systems, the phase relation of the Np–La, Np–Nd, and Np–Lu systems was already studied by thermal analysis.⁵⁷ The melting points or the transformation temperatures are depressed by several degrees compared to those of the pure elements. This suggests that there is no intermetallic compound and only a small

percentage of mutual solubility in these systems. Figure 14 shows the Np–La phase diagram calculated in the present study by assuming a regular solution model for each phase. When the estimated interaction parameters for the liquid and bcc phases are ~ 42 and 52 kJ mol^{-1} , respectively, the depressions for the melting points of Np and La, which are of the order of 4 K, and those for the transformation temperature between β -La and γ -La, which are of the order of 13 K, are in good agreement with the experimental observations. Considering the systematic variation, the phase relation between Np and Y, Ce, Pr, Pm, Sm, Gd, Tb, Dy, Ho, Er, or Tm is expected to be similar to that of the Np–La system. Better miscibility is expected for the Np–Sc system from the comparison to the U–Sc system.

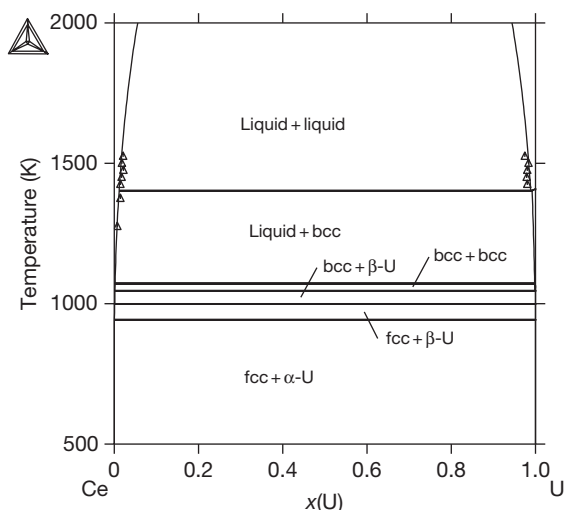


Figure 13 Calculated U-Ce phase diagram and experimental data taken from Haeffling and Daane.⁵²

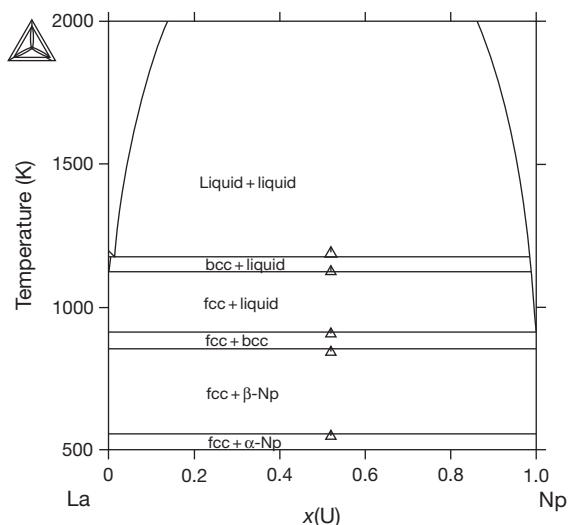


Figure 14 Calculated Np-La phase diagram, and experimental data taken from Gibson and Haire.⁵⁷

Table 5 summarizes the solubility data for the Pu-Group IIIa metal systems. The systematic variation in the Pu-related system is mostly similar to that in the Th-related system, with some exceptions. As for the first group, the shape of the previously reported Pu-Sc phase diagram⁴⁴ is different from that of the Pu-Y, Pu-Gd, Pu-Tb, and Pu-Dy phase diagrams.^{44,58,62,64} There are several similarities between the Pu-Sc and Th-Sc systems, such as the complete solubility for the liquid and bcc phases, several tens of percent of solubility even for

the low-temperature solid phase, etc. However, an intermediate ζ -phase appears in the Pu-Sc phase diagram, which suggests some degree of stabilization for the mixing between Pu and Sc in the low-temperature region. On observing the phase boundary between the liquid and bcc phases, on the other hand, we can conclude that these phases obey the simple regular solution model. Due to this conflict, the previously reported Pu-Sc phase diagram could not be modeled with a reasonable set of thermodynamic functions.⁶⁵ This indicated that some of the phase boundaries need substantial modifications.¹ Regarding the P-Y system, the shape of the phase boundary near the Y terminal is different from that for Gd, Tb, and Dy. A very thin monophasic region for β -Y appears and steeply depresses with increasing Pu concentration in the previously reported Pu-Y phase diagram.⁵⁸ This feature is thermodynamically unlikely. The phase relations for the Pu-La system are quite similar to those for the Pu-Gd, Pu-Tb, and Pu-Dy systems. **Figure 15** shows the Pu-La phase diagram as a typical example for this group, which is quoted from Okamoto.⁴ The phase diagram was originally reported in Ellinger *et al.*⁵⁹ It appears from the phase diagram that there are miscibility gaps for the liquid phase and large regions of solid solubility of Pu in the β -La (fcc) and γ -La (bcc) phases (~ 20 at.% at the maximum). The solid solubility of La in δ -Pu (fcc) is negligibly small, and that in ϵ -Pu (bcc) is estimated to be about 1 at.%. As for the third group, the Pu-Pr, Pu-Nd, Pu-Pm, and Pu-Sm systems have similar features,^{44,62,61} as well as the Th-related system. **Figure 16** shows the Pu-Nd phase diagram as a typical example, quoted from Okamoto.⁴ The phase relations shown in the Pu-Nd system are quite similar to those in the Pu-La system, with a few exceptions. Although the crystal structures for the low-temperature solid phase are different from each other, the shape of the phase boundaries around α -La and α -Nd are quite similar. A few percent of solid solubility in the δ -Pu phase (fcc) was observed not in the Pu-La system but in the Pu-Nd system, although pure La does take the fcc allotrope whereas Nd does not. Regarding the heavy lanthanides beyond Ho as well as Y, such as the Pu-Ho, Pu-Er, Pu-Tm, and Pu-Lu systems, the miscibility gap for the liquid phase is expected to disappear.^{44,64} **Figure 17** shows the Pu-Er phase diagram as a typical example quoted from Okamoto.⁴ However, the experimental information is limited and confirmation is necessary, for instance, by thermal arrest measurement for the high-temperature region.

Table 5 Phase relation in Pu–Group IIIa metals

Element	Pu	Sc ^a	Y ^b	La	Ce	Pr	Nd	Pm ^c	Sm
Allotrope	δ-Pu (fcc) ε-Pu (bcc)	α-Sc (HCP) β-Sc (bcc)	α-Y (HCP) β-Y (bcc)	β-La (fcc) γ-La (bcc)	γ-Ce (fcc) δ-Ce (bcc)	α-Pr (DHCP) β-Pr (bcc)	α-Nd (DHCP) β-Nd (bcc)	α-Pm (DHCP) β-Pm (bcc)	β-Sm (DHCP) γ-Sm (bcc)
System	–	Pu–Sc	Pu–Y	Pu–La	Pu–Ce	Pu–Pr	Pu–Nd	Pu–Pm	Pu–Sm
Maximum solid solubility between low-temperature phases	–	~48 at.% Pu in Sc ~22 at.% Sc in Th	~15 at.% Pu in Y ~0 at.% Y in Pu	~19 at.% Pu in La ~0 at.% La in Pu	~34 at.% Pu in Ce ~24 at.% Ce in Pu	~29 at.% Pu in Pr ~2 at.% Pr in Pu	~27 at.% Pu in Nd ~2 at.% Nd in Pu	~28 at.% Pu in Pm ~2 at.% Pm in Pu	~29 at.% Pu in Sm ~2 at.% Sm in Pu
Maximum solid solubility between bcc phases	–	Completely soluble	~17 at.% Pu in Y ~0 at.% Y in Pu	~20 at.% Pu in La ~1 at.% La in Pu	~18 at.% Pu in Ce ~15 at.% Ce in Pu	~30 at.% Pu in Pr ~2 at.% Pr in Pu	~33 at.% Pu in Nd ~2 at.% Nd in Pu	~35 at.% Pu in Pm ~2 at.% Pm in Pu	~33 at.% Pu in Sm ~2 at.% Sm in Pu
References		44	58	59	60	61	61	44 62	61
Element	Eu	Gd	Tb	Dy	Ho	Er	Tm	Yb	Lu
Allotrope	– α-Eu (bcc)	α-Gd (HCP) β-Gd (bcc)	α-Tb (HCP) β-Tb (bcc)	α-Dy (HCP) β-Dy (bcc)	α-Ho (HCP) –	α-Er (HCP) –	α-Tm (HCP) –	β-Yb (fcc) γ-Yb (bcc)	α-Lu (HCP) –
System	Pu–Eu	Th–Gd	Th–Tb	Th–Dy	Th–Ho	Th–Er	Th–Tm	Th–Yb	Th–Lu
Maximum solid solubility between low-temperature phases	Immiscible	~28 at.% Pu in Gd ~0 at.% Gd in Pu	~28 at.% Pu in Tb ~0 at.% Tb in Pu	~28 at.% Pu in Dy ~0 at.% Dy in Pu	~28 at.% Pu in Ho ~0 at.% Ho in Pu	~20 at.% Pu in Er ~0 at.% Er in Pu	~20 at.% Pu in Tm ~0 at.% Tm in Pu	Immiscible	~20 at.% Pu in Lu ~0 at.% Lu in Pu
Maximum solid solubility between bcc phases	Immiscible	~30 at.% Pu in Gd ~2 at.% Gd in Pu	~30 at.% Pu in Tb ~2 at.% Tb in Pu	~30 at.% Pu in Dy ~2 at.% Dy in Pu	~0 at.% Pu in Ho ~2 at.% Ho in Pu	~0 at.% Pu in Er ~2 at.% Er in Pu	~0 at.% Pu in Tm ~2 at.% Tm in Pu	Immiscible	~0 at.% Pu in Lu ~2 at.% Lu in Pu
References	63	44 64	44 64	44 62	44 64	44 64	44 64	44 64	44 64

^aPhase relation for the Pu–Sc system need substantial modification.⁶⁵^bPhase boundary of β-Y in the Pu–Y system shows thermodynamically unlikely feature.^cPhase relation for the Pu–Pm system is estimated from the Pu–Pr and Pu–Nd systems.

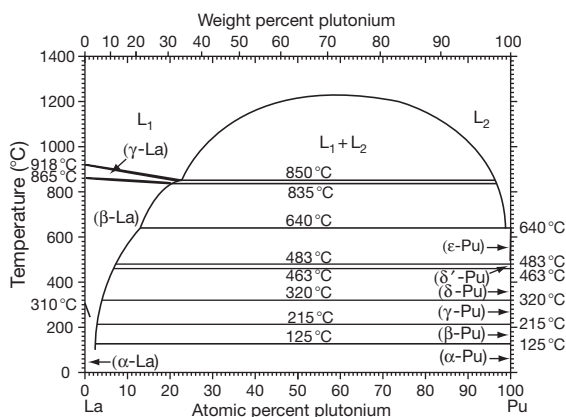


Figure 15 Pu-La phase diagram taken from Okamoto.⁴

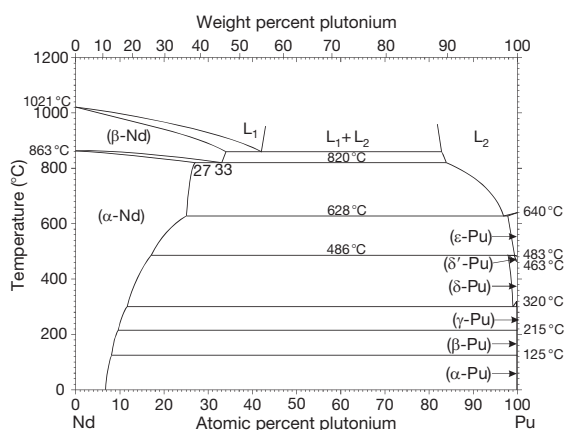


Figure 16 Pu-Nd phase diagram taken from Okamoto.⁴

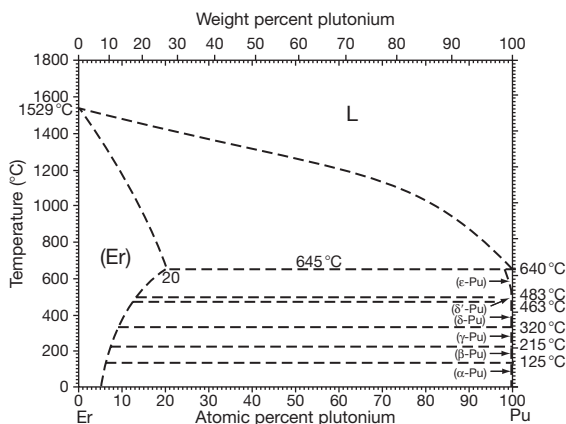


Figure 17 Pu-Er phase diagram taken from Okamoto.⁴

In the Pu-Eu and Pu-Yb systems, the mutual solubility is considered to be very low. The solid solubility of Pu in Eu was reported to be 0.74 at.%, and vice versa <0.02 at.%.⁶³ The phase relation in the Pu-Ce

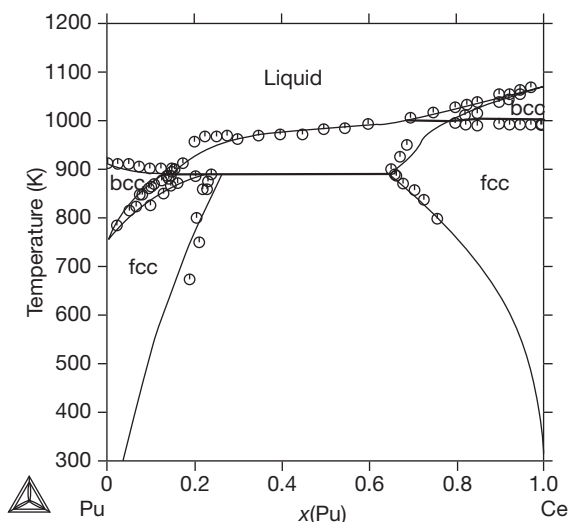


Figure 18 Calculated Pu-Ce phase diagram, and experimental data taken from Selle and Etter.⁶⁰ Data from Shirasu, N.; Kurata, M. Private communication.

Table 6 Calculated interaction parameters for the Pu-Ce system

$$\begin{aligned}
 G^{\circ}(\text{Pu, liq}), G^{\circ}(\text{Pu, bcc}), G^{\circ}(\text{Pu, fcc}): & \text{ given in Dinsdale}^{67} \\
 G^{\circ}(\text{Ce, liq}), G^{\circ}(\text{Ce, bcc}), G^{\circ}(\text{Ce, fcc}): & \text{ given in Dinsdale}^{67} \\
 G^{\circ}(\text{U, HCP}) = 5000 + G^{\circ}(\text{U, } \alpha\text{-U}) \\
 G^{\circ}(\text{Zr, } \beta\text{-U}), G^{\circ}(\text{Zr, } \alpha\text{-U}) = 5000 + G^{\circ}(\text{Zr, HCP}) \\
 G^{\circ}(\delta\text{-UZr}_2) = -13394 + 21.484T \\
 G^{\text{ex}}(\text{Ce-Pu, liq}) = x_{\text{Pu}}(1 - x_{\text{Pu}})(15080 + 0.2T - 1000 \\
 & (x_{\text{Ce}} - x_{\text{Pu}})) \\
 G^{\text{ex}}(\text{Ce-Pu, bcc}) = x_{\text{Pu}}(1 - x_{\text{Pu}})(16483 - 1595(x_{\text{Ce}} - x_{\text{Pu}})) \\
 G^{\text{ex}}(\text{Ce-Pu, fcc}) = x_{\text{Pu}}(1 - x_{\text{Pu}}) \\
 & (10076 + 6.0T + (5745 - 7.744T)(x_{\text{Ce}} - x_{\text{Pu}}))
 \end{aligned}$$

Source: Shirasu, N.; Kurata, M. Private communication.
Note: other allotropes for Pu are neglected.

system shows a unique feature near the Pu terminal.⁶⁰ The solid solubility of Ce in δ -Pu (fcc structure) is far larger compared to the other lanthanides and attains 24 at.% at the maximum. Also, the δ -Pu region is enlarged at lower temperature. This feature is observed in the Pu-Al or Pu-Ga system. Although La also has a β -La phase with fcc structure, this stabilization of δ -Pu phase was observed only in the Pu-Ce system among the Pu-lanthanide systems. Figure 18 indicates the Pu-Ce phase diagram calculated by the CALPHAD approach,⁶⁶ in which only the liquid, bcc, and fcc phases were modeled and other phases were omitted. Experimental data points, however, fit reasonably well with the calculated values when using the assessed interaction parameters indicated in Table 6.

Regarding the Am–Group IIIa metal systems, wide regions for the solid solubility were expected from the experimental observation by Kurata,⁶⁸ in which the phase relation of an annealed alloy containing U, Pu, Zr, Np, Am, Y, Ce, Nd, and Gd was studied by scanning electron microscopy/wavelength dispersive X-ray (SEM/WDX). Two and three phases were observed in the samples annealed at 973 and 773 K, respectively. These phases were identified: (1) A bcc phase rich in U, Pu, Zr, and Np and (2) a rare-earth phase rich in Pu, Am, Y, Ce, Nd, and Gd were detected in the samples annealed at 973 K; and (3) the ζ - and (4) δ -phases rich in U, Pu, Zr, and Np and (5) the rare-earth phase rich in Pu, Am, Y, Ce, Nd, and Gd were detected in the samples annealed at 773 K. The Pu and Am concentrations in those rare-earth phases were roughly 8 and 30 at.%, respectively, at both temperatures. The Pu concentration agrees reasonably well with the phase diagrams described earlier. Perhaps the Cm-related system systematically has features similar to those of Am.

2.05.3.4 Actinide–Actinide

Regarding the phase relation between Th and other actinides, the Ac–Th and Th–Pa systems were predicted to be soluble completely.⁵ Figure 19 shows the Th–U phase diagram quoted from Peterson.⁶⁹ The key literature sources for the assessment are Carlson,⁷⁰ Bentle,⁷¹ Murray,⁷² and Badayeva and Kuznetsova.⁷³ The general feature of the Th–U phase diagram looks similar to that for the Pu–light lanthanide phase diagrams. There is a miscibility gap for the liquid phase. The solid solubility of U in Th attains 12 at.% at the maximum, whereas that of Th in U is

extremely low. There is no intermetallic compound. Regarding the width of the miscibility gap for the liquid phase, there is conflict between two experimental data.^{70,72} Results given by Badayeva and Kuznetsova⁷³ agree well with the latter. The assessment for the Th–Pu system was also performed by Peterson⁶⁹ based on previous data.^{74–77} The assessed Th–Pu phase diagram is shown in Figure 20, which is quoted from Okamoto.⁴ The diagram is dominated by the high solid solubility of Pu in Th, whereas that of Th in Pu is relatively small. The system has a single intermetallic compound, named ζ , which is formed by a peritectic reaction with the liquid and ε -Pu phases. As for the composition of the ζ -phase, several values were reported previously.^{74,75,78,79} The composition of Th₃Pu₇ was determined by Portnoff and Calais⁷⁸ by microanalysis and by Marcon and Portnoff⁷⁹ by measuring the cell dimension and density, respectively, the latter value taken from Peterson.⁶⁹ As for the peritectic temperature, the value obtained by Poole *et al.*⁷⁴ of 888 K was selected by Peterson.⁶⁹ A partial phase relations near the Pu terminal was also assessed by Peterson⁶⁹ based on the work of Elliott and Larson.⁷⁶ Slight stabilization of δ -Pu (fcc structure) by mixing with Th is seen. Due to the difficulty of preparing the samples and measuring the transition temperatures for the Th-rich region, the phase boundaries for β -Th and liquid or α -Th still possibly could have large experimental errors. Nevertheless, it is predicted from the general feature of the Th–Pu phase diagram that the Gibbs energy of mixing for each phase slightly deviates to negative direction from the Raoult's law. There is no available data for the Th–Np and Th–Am systems. The partial solid solubility, possibly of the order of several percent, and the complete liquid solubility are predicted for the Th–Np system based on the

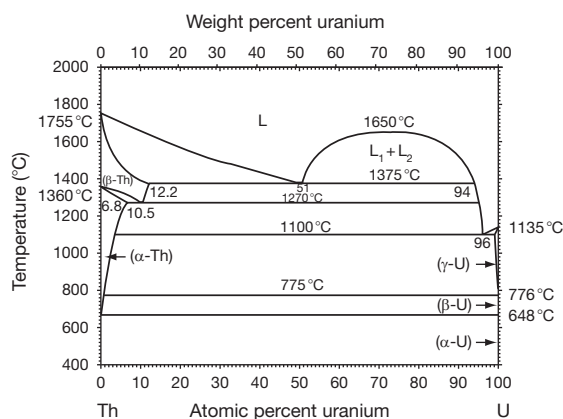


Figure 19 Th–U phase diagram taken from Peterson.⁶⁹

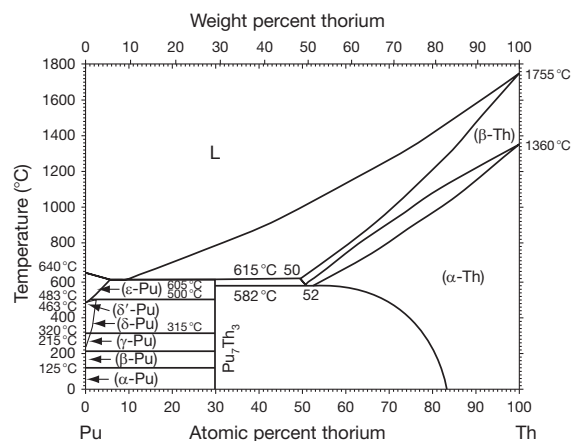


Figure 20 Th–Pu phase diagram taken from Okamoto.⁴

systematic similarity with the Th–U and Th–Pu systems. Better miscibility is also speculated for the Th–Am system based on the systematic similarity with the Th–lanthanide systems.

Regarding the phase relation between U and other actinides, the Pa–U system was predicted to be soluble completely.⁵ As for the phase relation among U–Np–Pu–Am, thermodynamic evaluation was performed by the CALPHAD approach.⁷ **Figure 21** indicates the U–Np phase diagram, which was calculated based on the work of Mardon and Pearce.⁸⁰ The calculated results agree well with the experimental data points, with the exception of the low-temperature region around α -Np. Kurata estimated,⁷ the Gibbs energy for the intermediate δ -phase from the hypothetical transformation temperatures obtained by enlarging the related phase boundaries to the Np or U terminal. The temperature dependence, therefore, has some degree of error. This might be a major reason for the inconsistency for the phase relations around α -Np. The shape of the liquidus and the solidus in the U–Np system suggests that U and Np can be mostly ideally soluble in both liquid and bcc phases. The δ -phase was proposed to be isomorphous with the ζ -phase appearing in the Pu–U system.⁸⁰ Regarding the U–Pu system, the phase diagram was previously assessed by Peterson and Foltyn,⁸¹ which was constructed mainly from the works of Calais *et al.*,⁷⁷ Ellinger *et al.*,⁸² and AEC Research and Development Report.⁸³ According to the criteria proposed by Okamoto,⁸⁴ several thermodynamically unlikely

features are present in the previous U–Pu phase diagrams. For example, when extrapolating some phase boundaries to the U or Pu terminal, a two-phase field does not close without introducing abrupt changes in the slope of its phase boundaries. A thermodynamically likely phase diagram was then proposed based on the CALPHAD method.⁸⁵ A modified U–Pu phase diagram was then proposed by Okamoto,¹⁹ in which, however, there are many differences between the assessed phase boundaries and the experimental data points given in the previous studies. A reassessed U–Pu phase diagram was proposed by Kurata,⁷ in which the other new data for the phase boundary⁸⁶ were also taken into consideration. The assessed phase boundaries give a better fit even for the previous experimental studies, with the exception of the low-temperature Pu-rich region. **Figure 22** shows the reassessed U–Pu phase diagram. In the previous model,⁸⁵ the liquid phase was assumed to be an ideal solution. Kurata,⁷ on the other hand, takes into consideration the Pu activity evaluated from vapor pressure measurements,^{87,89} in which a slight negative deviation was observed for the Gibbs energy of mixing for the liquid phase. **Figure 23** shows the calculated Pu activity in the U–Pu system at 1473 K along with the experimental data points. Although the data points are rather scattered, the negative variation from the Raoult's law is clearly observed. When evaluating a multielement phase diagram, for instance, the U–Pu–Zr ternary system

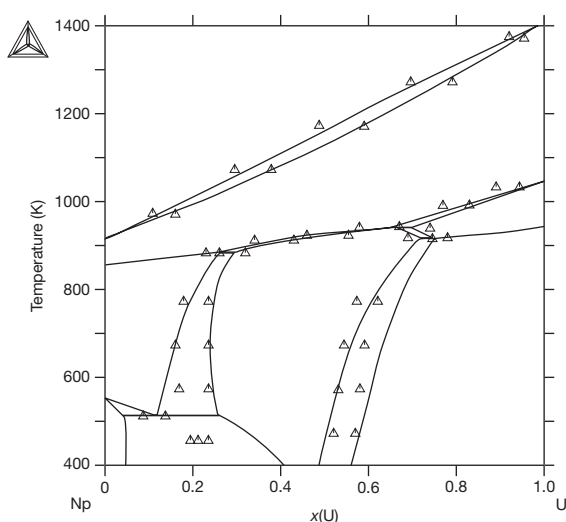


Figure 21 Calculated U–Np phase diagram taken from Kurata,⁷ and the experimental data taken from Mardon and Pearce.⁸⁰

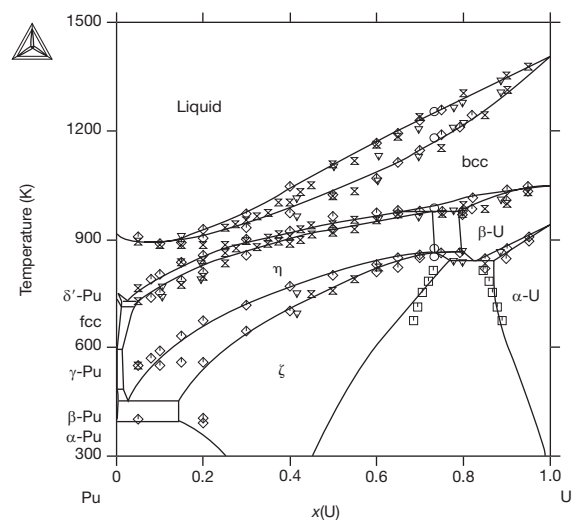


Figure 22 Calculated U–Pu phase diagram taken from Kurata,⁷ and experimental data taken from Ellinger *et al.*⁸² (x), Mound Laboratory Report⁸³ (◊), Okamoto *et al.*⁸⁶ (▽), Nakajima *et al.*⁸⁷ (◻), and Calais *et al.*⁸⁸ (◻).

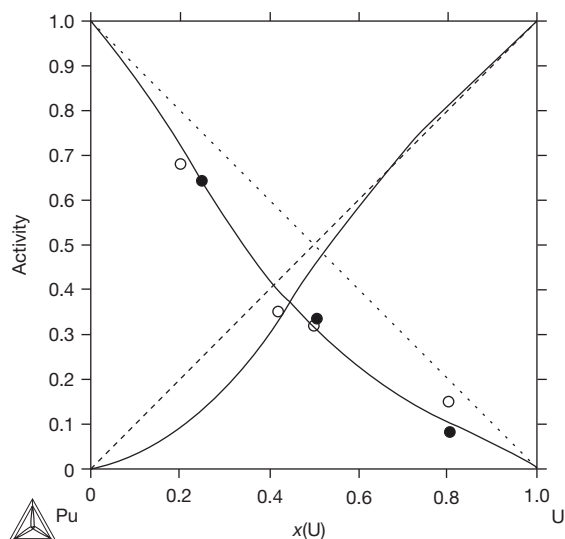


Figure 23 Calculated Pu activity at 1473 K in the U–Pu system taken from Kurata,⁷ and the experimental data taken from Kurata *et al.*⁸⁹ (○) and Nakajima *et al.*⁸⁷ (●).

discussed later in this chapter, the assessment for the binary subsystems using thermodynamic information, such as vapor pressure, electromotive force, etc., is extremely important to increase the accuracy not only for the assessment of the binary subsystems but also of the multielement system. The U–Am phase diagram was previously shown by Okamoto⁹⁰ based on the theoretical evaluation of Ogawa.⁹¹ A similar tendency with the Th–U phase diagram is observed: for instance, there are several percent of mutual solid solubility. According to the experimental observation,⁶⁸ however, the solubility between U and Am is extremely low. For instance, the solubility of Am in U is of the order of ~ 1 at.% even in the quenched sample from the liquid phase, which was prepared by the arc-melting method. The interaction parameter of the liquid phase in the newly assessed U–Am phase diagram is estimated to be 50 kJ mol^{-1} based on these experimental observations.⁷ Figure 24 shows the newly assessed U–Am phase diagram.

The Np–Pu phase diagram was previously redrawn by Okamoto⁴ based on the work of Mardon *et al.*⁹² and Poole *et al.*⁹³ Figure 25 shows the calculated Np–Pu phase diagram.⁷ The calculated phase boundaries are in reasonable agreement with the experimental data points, with some exceptions around the low-temperature Np-rich region. The Np–Pu phase diagram has a unique feature. Almost all parts in the phase diagram consist of the one-phase region and the width of the two-phase region is very narrow, with the exception of the β -Np and β -Pu phase

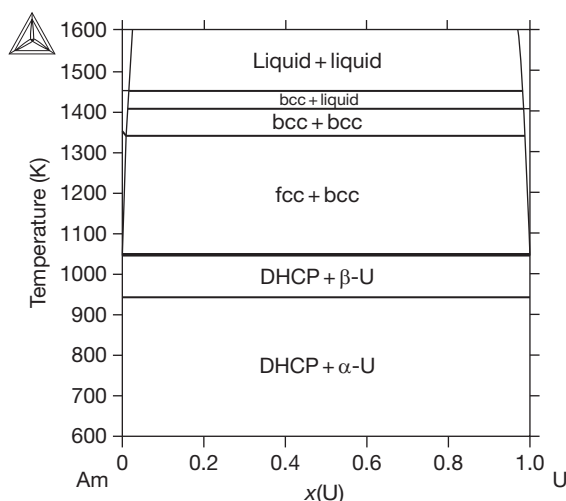


Figure 24 Calculated U–Am phase diagram taken from Kurata.⁷

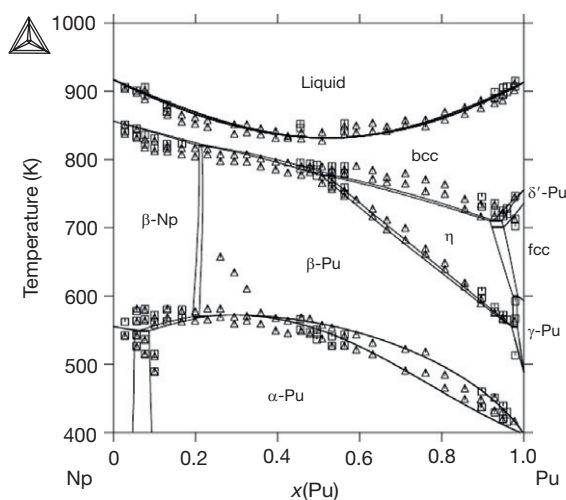


Figure 25 Calculated Np–Pu phase diagram taken from Kurata,⁷ and the experimental data taken from Mardon *et al.*⁹² (□) and Poole *et al.*⁹³ (Δ).

boundaries. Sheldon *et al.*⁹⁴ pointed out that the extremely high solubility of Np in the low-temperature Pu allotropes, such as the α -Pu and β -Pu phases, is an especially unique feature of this system, although the phase boundaries are quite uncertain. These suggest that the difference in the Gibbs energy of each phase for both Np and Pu, especially for the low-temperature allotropes, is rather small. Consequently, this small difference in the Gibbs energy makes it difficult to get an accurate assessment by the CALPHAD approach, because any small deviations on the interaction parameters may follow

the significant variations in the phase boundaries. Apparently, this difficulty appears clearly in the β -Np and β -Pu phase boundaries, as shown in **Figure 25**. Nevertheless, the assessed interaction parameters are practically very useful when evaluating the multielement systems, which are discussed later. The Np–Am phase diagram was given previously by Okamoto⁹⁰ based on the theoretical evaluation by Ogawa,⁹¹ in which the phase relation against α -Am was neglected. Thermal analysis was performed,⁵⁷ and six different thermal arrests were observed in the 54% Np–46% Am alloy samples, which indicated the depression of melting points and transformation temperatures. Furthermore, experimental observation indicates that the solubility of Np in Am is 2–3 at.% but of Am in Np it was 5–7 at.% for a 60% Np–40% Am sample that was quickly cooled from the arc-melted liquid phase.⁶⁸ The interaction parameters are assessed based on these experimental observations, which for the liquid phase, for instance, was estimated to be 20 kJ mol^{-1} .⁷ **Figure 26** shows the newly assessed Np–Am phase diagram, in which the depressions of melting point and transformation temperature agree reasonably well with calculations.

The Pu–Am phase diagram was previously introduced by Okamoto⁴ based on the work of Ellinger *et al.*⁹⁵ **Figure 27** shows the calculated Pu–Am phase diagram, in which the calculated phase boundaries more or less overlap with the experimental data points with the exception of the Am terminal. The Pu–Cm phase diagram was also introduced by Okamoto⁴

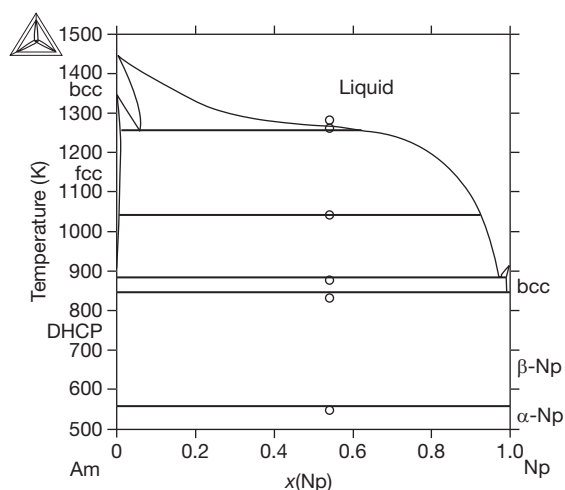


Figure 26 Calculated Np–Am phase diagram taken from Kurata,⁷ and the experimental data taken from Gibson and Haire.⁵⁷

based on the work of Shushanov and Chebotarev,⁹⁶ as indicated in **Figure 28**. The general feature looks similar to the phase diagram between Pu and heavy lanthanides. The α' -Cm is a faulted fcc structure, differing from the α -Cm (HCP) structure. However, the allotropy of Cm is still under discussion.

Table 7 summarizes the interaction parameters for the phase relation among the U–Np–Pu–Am system given by Kurata,⁷ in which some parameters are empirically estimated. Using the assessed interaction parameters, multielement phase diagrams can be reasonably predicted. A few examples are introduced here. The first example is a ternary relation of the U–Np–Pu system. According to Mardon and

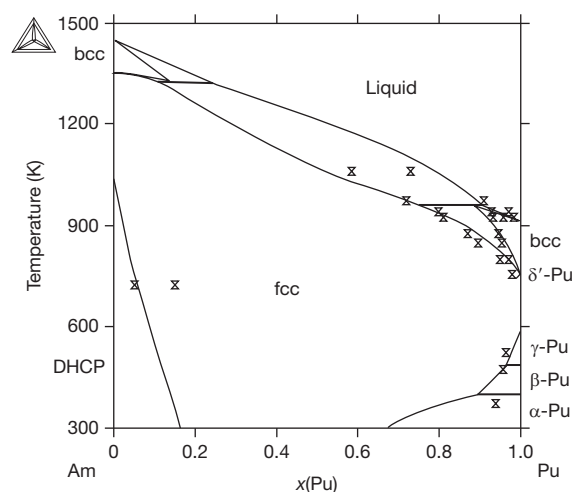


Figure 27 Calculated Pu–Am phase diagram taken from Kurata,⁷ and the experimental data taken from Ellinger *et al.*⁹⁵

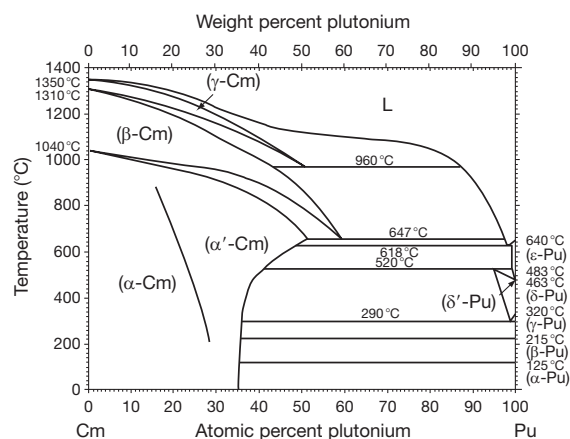


Figure 28 Pu–Cm phase diagram taken from Okamoto.⁴

Table 7 Calculated interaction parameters for the U–Np–Pu–Am system

$G^{\circ}(\text{U}, \text{liq}), G^{\circ}(\text{U}, \text{bcc}), G^{\circ}(\text{U}, \beta\text{-U}), G^{\circ}(\text{U}, \alpha\text{-U})$: given in Dinsdale⁶⁷
 $G^{\circ}(\text{Np}, \text{liq}), G^{\circ}(\text{Np}, \text{bcc}), G^{\circ}(\text{Np}, \beta\text{-Np}), G^{\circ}(\text{Np}, \alpha\text{-Np})$: given in Dinsdale⁶⁷
 $G^{\circ}(\text{Pu}, \text{liq}), G^{\circ}(\text{Pu}, \text{bcc}), G^{\circ}(\text{Pu}, \delta'\text{-Pu}), G^{\circ}(\text{Pu}, \text{fcc}), G^{\circ}(\text{Pu}, \gamma\text{-Pu}), G^{\circ}(\text{Pu}, \beta\text{-Pu}), G^{\circ}(\text{Pu}, \alpha\text{-Pu})$: given in Dinsdale⁶⁷
 $G^{\circ}(\text{Am}, \text{liq}), G^{\circ}(\text{Am}, \text{bcc}), G^{\circ}(\text{Am}, \text{fcc}), G^{\circ}(\text{Am}, \text{DHCP})$: given in Dinsdale⁶⁷
 $G^{\circ}(\text{U}, \beta\text{-Np}) = 260.4 + G^{\circ}(\text{U}, \beta\text{-U})$
 $G^{\circ}(\text{U}, \alpha\text{-Np}) = 2814.7 + G^{\circ}(\text{U}, \alpha\text{-U})$
 $G^{\circ}(\text{U}, \delta'\text{-Pu}), G^{\circ}(\text{U}, \text{fcc}), G^{\circ}(\text{U}, \text{DHCP}) = 5000 + G^{\circ}(\text{U}, \text{bcc})$
 $G^{\circ}(\text{U}, \gamma\text{-Pu}), G^{\circ}(\text{U}, \beta\text{-Pu}), G^{\circ}(\text{U}, \alpha\text{-Pu}) = 5000 + G^{\circ}(\text{U}, \alpha\text{-U})$
 $G^{\circ}(\text{U}, \eta) = 118.7 + G^{\circ}(\text{U}, \beta\text{-U})$
 $G^{\circ}(\text{U}, \zeta) = 337.8 + G^{\circ}(\text{U}, \text{bcc})$
 $G^{\circ}(\text{Np}, \beta\text{-U}), G^{\circ}(\text{Np}, \alpha\text{-U}) = 792 + G^{\circ}(\text{U}, \beta\text{-Np})$
 $G^{\circ}(\text{Np}, \delta'\text{-Pu}), G^{\circ}(\text{Np}, \text{fcc}), G^{\circ}(\text{Np}, \text{DHCP}) = 5000 + G^{\circ}(\text{Np}, \text{bcc})$
 $G^{\circ}(\text{Np}, \gamma\text{-Pu}) = 2000 + G^{\circ}(\text{Np}, \beta\text{-Np})$
 $G^{\circ}(\text{Np}, \beta\text{-Pu}) = 80.8 + G^{\circ}(\text{Np}, \beta\text{-Np})$
 $G^{\circ}(\text{Np}, \alpha\text{-Pu}) = 187.2 + G^{\circ}(\text{Np}, \alpha\text{-Np})$
 $G^{\circ}(\text{Np}, \eta) = 153.2 + G^{\circ}(\text{U}, \beta\text{-Np})$
 $G^{\circ}(\text{Np}, \zeta(\delta)) = 227.1 + G^{\circ}(\text{U}, \beta\text{-Np})$
 $G^{\circ}(\text{Pu}, \beta\text{-U}) = 209.6 + G^{\circ}(\text{Pu}, \delta'\text{-Pu})$
 $G^{\circ}(\text{Pu}, \alpha\text{-U}) = 652.7 + G^{\circ}(\text{Pu}, \beta\text{-Pu})$
 $G^{\circ}(\text{Pu}, \beta\text{-Np}) = 575.1 + G^{\circ}(\text{Pu}, \delta'\text{-Pu})$
 $G^{\circ}(\text{Pu}, \alpha\text{-Np}) = 1248.6 + G^{\circ}(\text{Pu}, \alpha\text{-Pu})$
 $G^{\circ}(\text{Pu}, \text{DHCP}) = 5000 + G^{\circ}(\text{Pu}, \text{fcc})$
 $G^{\circ}(\text{Pu}, \eta) = 51.1 + G^{\circ}(\text{U}, \text{fcc})$
 $G^{\circ}(\text{Pu}, \zeta) = 500 + G^{\circ}(\text{U}, \beta\text{-Pu})$
 $G^{\circ}(\text{Am}, \varphi) = 5000 + G^{\circ}(\text{Am}, \text{DHCP})$: φ means $\beta\text{-U}, \alpha\text{-U}, \beta\text{-Np}, \alpha\text{-Np}, \delta'\text{-Pu}, \gamma\text{-Pu}, \beta\text{-Pu}, \alpha\text{-Pu}, \eta$, and ζ .
 $G^{\text{ex}}(\text{Np}\text{--}\text{U}, \text{liq}) = x_{\text{U}}(1 - x_{\text{U}}) (0)$
 $G^{\text{ex}}(\text{Np}\text{--}\text{U}, \text{bcc}) = x_{\text{U}}(1 - x_{\text{U}}) (796.8)$
 $G^{\text{ex}}(\text{Np}\text{--}\text{U}, \beta\text{-U}) = x_{\text{U}}(1 - x_{\text{U}}) (753.3)$
 $G^{\text{ex}}(\text{Np}\text{--}\text{U}, \alpha\text{-U}) = x_{\text{U}}(1 - x_{\text{U}}) (-5310.1 + 6.92T)$
 $G^{\text{ex}}(\text{Np}\text{--}\text{U}, \beta\text{-Np}) = x_{\text{U}}(1 - x_{\text{U}}) (-1392.3 + 2.88T)$
 $G^{\text{ex}}(\text{Np}\text{--}\text{U}, \alpha\text{-Np}) = x_{\text{U}}(1 - x_{\text{U}}) (3652.9)$
 $G^{\text{ex}}(\text{Np}\text{--}\text{U}, \delta'\text{-Pu}), G^{\text{ex}}(\text{Np}\text{--}\text{U}, \text{fcc}), G^{\text{ex}}(\text{Np}\text{--}\text{U}, \gamma\text{-Pu}), G^{\text{ex}}(\text{Np}\text{--}\text{U}, \beta\text{-Pu}), G^{\text{ex}}(\text{Np}\text{--}\text{U}, \alpha\text{-Pu}), \eta = x_{\text{U}}(1 - x_{\text{U}}) (5000)$
 $G^{\text{ex}}(\text{Np}\text{--}\text{U}, \zeta) = x_{\text{U}}(1 - x_{\text{U}}) (-4268.5 + 5.14T + (-2467.7 + 2.80T) (x_{\text{Np}} - x_{\text{U}}) + (14741 - 15.48T) (x_{\text{Np}} - x_{\text{U}})^2)$
 $G^{\text{ex}}(\text{Pu}\text{--}\text{U}, \text{liq}) = x_{\text{U}}(1 - x_{\text{U}}) (32231 - 31.465T - 8980.2(x_{\text{Pu}} - x_{\text{U}}))$
 $G^{\text{ex}}(\text{Pu}\text{--}\text{U}, \text{bcc}) = x_{\text{U}}(1 - x_{\text{U}}) (19374 - 17.250T - 4939.5(x_{\text{Pu}} - x_{\text{U}}))$
 $G^{\text{ex}}(\text{Pu}\text{--}\text{U}, \beta\text{-U}) = x_{\text{U}}(1 - x_{\text{U}}) (5287.3)$
 $G^{\text{ex}}(\text{Pu}\text{--}\text{U}, \alpha\text{-U}) = x_{\text{U}}(1 - x_{\text{U}}) (6176.5)$
 $G^{\text{ex}}(\text{Pu}\text{--}\text{U}, \beta\text{-Np}), G^{\text{ex}}(\text{Pu}\text{--}\text{U}, \alpha\text{-Np}) = x_{\text{U}}(1 - x_{\text{U}}) (5000)$
 $G^{\text{ex}}(\text{Pu}\text{--}\text{U}, \delta'\text{-Pu}) = x_{\text{U}}(1 - x_{\text{U}}) (495.4)$
 $G^{\text{ex}}(\text{Pu}\text{--}\text{U}, \text{fcc}) = x_{\text{U}}(1 - x_{\text{U}}) (723.8)$
 $G^{\text{ex}}(\text{Pu}\text{--}\text{U}, \gamma\text{-Pu}) = x_{\text{U}}(1 - x_{\text{U}}) (4342.7)$
 $G^{\text{ex}}(\text{Pu}\text{--}\text{U}, \beta\text{-Pu}), G^{\text{ex}}(\text{Pu}\text{--}\text{U}, \alpha\text{-Pu}), G^{\text{ex}}(\text{Pu}\text{--}\text{U}, \text{DHCP}) = x_{\text{U}}(1 - x_{\text{U}}) (5000)$
 $G^{\text{ex}}(\text{Pu}\text{--}\text{U}, \eta) = x_{\text{U}}(1 - x_{\text{U}}) (4049.1 - 1.52T + (-617.4 - 3.41T) (x_{\text{Pu}} - x_{\text{U}}))$
 $G^{\text{ex}}(\text{Pu}\text{--}\text{U}, \zeta) = x_{\text{U}}(1 - x_{\text{U}}) (-6336.9 + 10.45T + (-19997 + 24.65T) (x_{\text{Pu}} - x_{\text{U}}) + (12364 - 7.84T) (x_{\text{Pu}} - x_{\text{U}})^2)$
 $G^{\text{ex}}(\text{Am}\text{--}\text{U}, \varphi) = x_{\text{U}}(1 - x_{\text{U}}) (50000)$: φ means all related phases.
 $G^{\text{ex}}(\text{Np}\text{--}\text{Pu}, \text{liq}) = x_{\text{Pu}}(1 - x_{\text{Pu}}) (0)$
 $G^{\text{ex}}(\text{Np}\text{--}\text{Pu}, \text{bcc}) = x_{\text{Pu}}(1 - x_{\text{Pu}}) (961.3)$
 $G^{\text{ex}}(\text{Np}\text{--}\text{Pu}, \beta\text{-U}), G^{\text{ex}}(\text{Np}\text{--}\text{Pu}, \alpha\text{-U}) = x_{\text{Pu}}(1 - x_{\text{Pu}}) (5000)$
 $G^{\text{ex}}(\text{Np}\text{--}\text{Pu}, \beta\text{-Np}) = x_{\text{Pu}}(1 - x_{\text{Pu}}) (-1617.8 + 2.73T)$
 $G^{\text{ex}}(\text{Np}\text{--}\text{Pu}, \alpha\text{-Np}) = x_{\text{Pu}}(1 - x_{\text{Pu}}) (-1307.6)$
 $G^{\text{ex}}(\text{Np}\text{--}\text{Pu}, \delta'\text{-Pu}) = x_{\text{Pu}}(1 - x_{\text{Pu}}) (-2569.8)$
 $G^{\text{ex}}(\text{Np}\text{--}\text{Pu}, \text{fcc}) = x_{\text{Pu}}(1 - x_{\text{Pu}}) (-2475.3)$
 $G^{\text{ex}}(\text{Np}\text{--}\text{Pu}, \gamma\text{-Pu}) = x_{\text{Pu}}(1 - x_{\text{Pu}}) (1108.5)$
 $G^{\text{ex}}(\text{Np}\text{--}\text{Pu}, \beta\text{-Pu}) = x_{\text{Pu}}(1 - x_{\text{Pu}}) (226.2)$
 $G^{\text{ex}}(\text{Np}\text{--}\text{Pu}, \alpha\text{-Pu}) = x_{\text{Pu}}(1 - x_{\text{Pu}}) (-2722.9)$
 $G^{\text{ex}}(\text{Np}\text{--}\text{Pu}, \eta) = x_{\text{Pu}}(1 - x_{\text{Pu}}) (596.9)$
 $G^{\text{ex}}(\text{Np}\text{--}\text{Pu}, \zeta) = x_{\text{Pu}}(1 - x_{\text{Pu}}) (5000)$
 $G^{\text{ex}}(\text{Am}\text{--}\text{Np}, \text{liq}) = x_{\text{Np}}(1 - x_{\text{Np}}) (20000)$

Continued

Table 7 Continued

$$G^{\text{ex}}(\text{Am-Np}, \text{bcc}) = x_{\text{Np}}(1 - x_{\text{Np}}) (38\,000 - 7T)$$

$$G^{\text{ex}}(\text{Am-Np}, \text{fcc}), G^{\text{ex}}(\text{Am-Np}, \beta\text{-Np}), G^{\text{ex}}(\text{Am-Np}, \alpha\text{-Np}), G^{\text{ex}}(\text{Am-Np}, \text{DHCP}) = x_{\text{Np}}(1 - x_{\text{Np}}) (38\,000)$$

$$G^{\text{ex}}(\text{Am-Np}, \varphi) = x_{\text{Np}}(1 - x_{\text{Np}}) (40\,000): \varphi \text{ means the other phases.}$$

$$G^{\text{ex}}(\text{Am-Pu}, \text{liq}) = x_{\text{Pu}}(1 - x_{\text{Pu}}) (5495.9 - 7.787T)$$

$$G^{\text{ex}}(\text{Am-Pu}, \text{bcc}) = x_{\text{Pu}}(1 - x_{\text{Pu}}) (7528.6)$$

$$G^{\text{ex}}(\text{Am-Pu}, \text{fcc}) = x_{\text{Pu}}(1 - x_{\text{Pu}}) (-22\,630 + 26.377T)$$

$$G^{\text{ex}}(\text{Am-Pu}, \varphi) = x_{\text{Pu}}(1 - x_{\text{Pu}}) (5000): \varphi \text{ means the other phases}$$

Source: Kurata, M. In *Proceedings of Actinides 2009*, San Francisco, CA, July 12–19, 2009.

Pearce,⁸⁰ the structure of the δ -phase is isomorphous with the ζ -phase appearing in the U–Pu system. Thus, these two phases are treated as the same as the one by Kurata.⁷ The ternary U–9 at.% Np–26 at.% Pu alloy was annealed at 923 K for a few days and then quickly cooled by Nakajima *et al.*⁸⁷ Energy disperse X-ray microscope (EDX) analysis detected three phases in the sample. Figure 29 indicates the calculated phase relation for the U–Np–Pu isotherm, with the average composition of each phase detected in the annealing test. The phase separation between the δ -(U, Np) and ζ -(U, Pu) phases is shown in the diagram. According to Nakajima *et al.*,⁸⁷ phase separation was also observed in the annealed U–Pu–Am and Np–Pu–Am samples annealed at 897 and 792 K, respectively. Figures 30 and 31 indicate the calculated U–Np–Am and U–Pu–Am ternary isotherms, respectively, as another example. The experimental data for the annealing test are also shown in the figures, such as the average composition of each phase detected in the annealing test. The results agree reasonably well with the experimental data points. A similar evaluation was performed by Dupin.⁹⁷ Reasonable phase diagrams among actinides were also shown, although the assessed phase boundaries in both estimations^{7,97} are slightly different from each other. This happens usually with the semiempirical methods used.

2.05.3.5 Actinide: Group IVa, Va, VIa, and VIIa Metals

Figures 32–34 show the Th–Ti, U–Ti, and Pu–Ti phase diagrams quoted from Okamoto,⁴ which were previously assessed by Murray.⁹⁸ A thermodynamic calculation using the CALPHAD approach was also attempted by Murray.⁹⁸ The results are summarized in Table 8. The Th–Ti phase diagram was assessed based mainly on the works of Carlson *et al.*⁹⁹ and Pedersen *et al.*,¹⁰⁰ and is categorized as a typical eutectic type. The liquid phase is completely miscible and the solid phases do not have any detectable

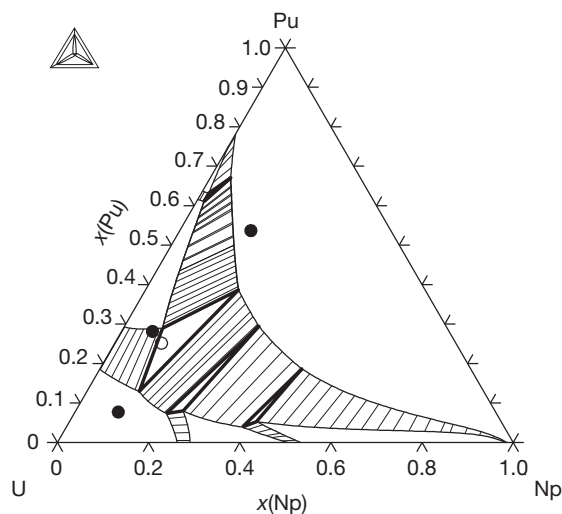


Figure 29 Calculated U–Np–Pu isotherm at 923 K with phase relation observed in Nakajima *et al.*⁸⁷: ○ initial composition of sample ● detected composition of each phase.

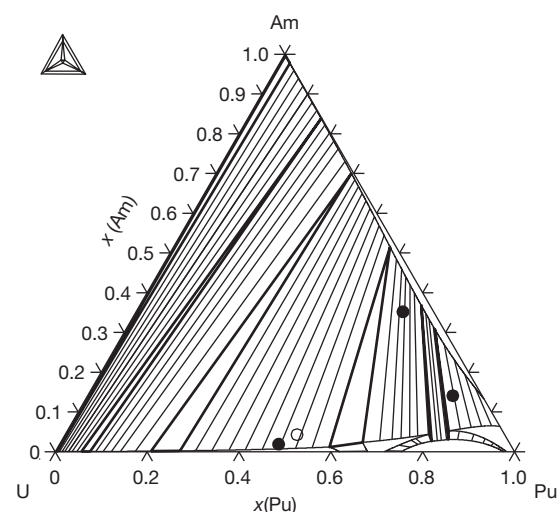


Figure 30 Calculated U–Pu–Am isotherm at 897 K taken from Kurata,⁷ with the phase relation observed in Nakajima *et al.*⁸⁷

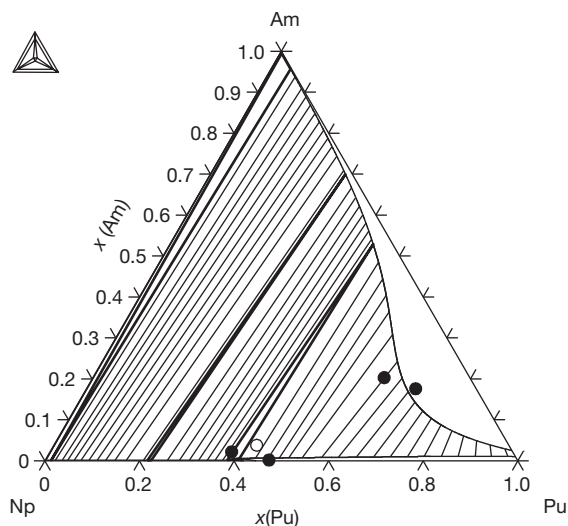


Figure 31 Calculated Np-Pu-Am isotherm at 792 K taken from Kurata,⁷ with phase relation observed in Nakajima *et al.*⁸⁷

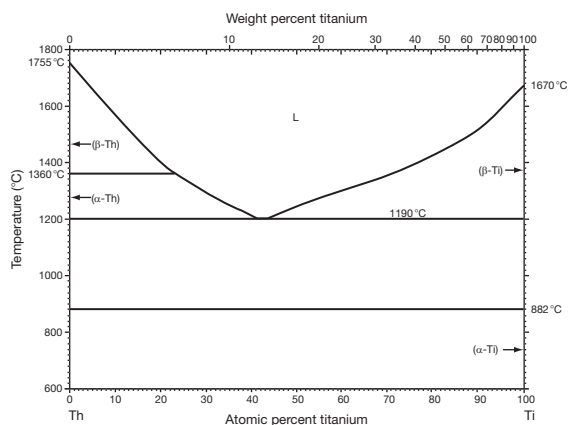


Figure 32 Th-Ti phase diagram taken from Okamoto.⁴

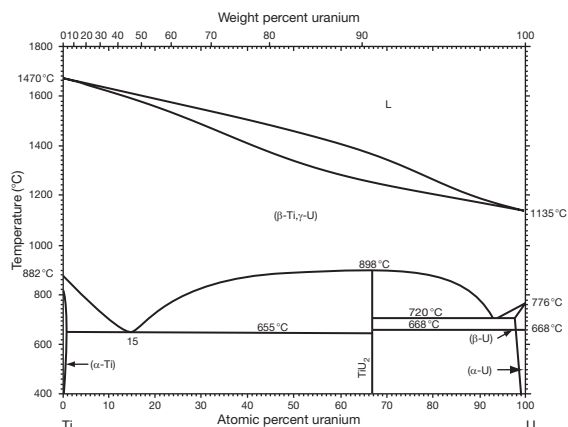


Figure 33 U-Ti phase diagram taken from Okamoto.⁴

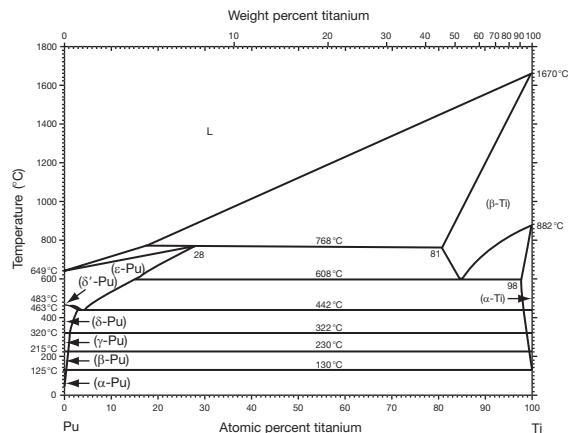


Figure 34 Pu-Ti phase diagram taken from Okamoto.⁴

Table 8 Calculated interaction parameters for actinides-Ti systems

$$\begin{aligned}
 G^{\circ}(\text{Ti, liq}) &= 0 \\
 G^{\circ}(\text{Th, liq}) &= 0 \\
 G^{\circ}(\text{U, liq}) &= 0 \\
 G^{\circ}(\text{Pu, liq}) &= 0 \\
 G^{\circ}(\text{Ti, bcc}) &= -16\,234 + 8.368T \\
 G^{\circ}(\text{Th, bcc}) &= -16\,121 + 7.937T \\
 G^{\circ}(\text{U, bcc}) &= -8519 + 6.0545T \\
 G^{\circ}(\text{Pu, bcc}) &= -3347 + 3.6659T \\
 G^{\circ}(\text{Ti, HCP}) &= -20\,585 + 12.134T \\
 G^{\circ}(\text{U, HCP}) &= -16\,103 + 13.594T \\
 G^{\circ}(\text{Pu, HCP}) &= -4477 + 8.14T \\
 G^{\circ}(\text{Ti, fcc}) &= -17\,238 + 12.134T \\
 G^{\circ}(\text{Th, fcc}) &= -18\,857 + 9.610T \\
 G^{\circ}(\text{Pu, fcc}) &= -4477 + 5.1944T \\
 G^{\circ}(\text{Ti, } \beta\text{-U}) &= -21\,000 + 15.0T \\
 G^{\circ}(\text{U, } \beta\text{-U}) &= -13\,311 + 10.627T \\
 G^{\circ}(\text{Ti, } \delta'\text{-Pu}) &= -12\,000 + 8.368T \\
 G^{\circ}(\text{Pu, } \delta'\text{-Pu}) &= -3933 + 4.4441T \\
 G^{\circ}(\text{Pu, } \gamma\text{-Pu}) &= -4561 + 5.3373T \\
 G^{\circ}(\text{Pu, } \beta\text{-Pu}) &= -6402 + 9.1568T \\
 G^{\circ}(\text{Pu, } \alpha\text{-Pu}) &= -9247 + 16.3960T \\
 G^{\circ}(\text{TiU}_2) &= -12\,313 + 6.162T \\
 G^{\text{ex}}(\text{Th-Ti, liq}) &= x_{\text{Th}}(1 - x_{\text{Th}})(16\,798 - 4853(x_{\text{Ti}} - x_{\text{Th}})) \\
 G^{\text{ex}}(\text{U-Ti, liq}) &= x_{\text{U}}(1 - x_{\text{U}})(17\,000 - 1458(x_{\text{Ti}} - x_{\text{U}})) \\
 G^{\text{ex}}(\text{U-Ti, bcc}) &= x_{\text{U}}(1 - x_{\text{U}})(18\,078 - 2425(x_{\text{Ti}} - x_{\text{U}})) \\
 G^{\text{ex}}(\text{U-Ti, HCP}) &= x_{\text{U}}(1 - x_{\text{U}})(31\,216 + 3257(x_{\text{Ti}} - x_{\text{U}})) \\
 G^{\text{ex}}(\text{U-Ti, } \beta\text{-U}) &= x_{\text{U}}(1 - x_{\text{U}})(25\,400) \\
 G^{\text{ex}}(\text{Pu-Ti, liq}) &= x_{\text{Pu}}(1 - x_{\text{Pu}})(10\,158) \\
 G^{\text{ex}}(\text{Pu-Ti, bcc}) &= x_{\text{Pu}}(1 - x_{\text{Pu}})(17\,559) \\
 G^{\text{ex}}(\text{Pu-Ti, HCP}) &= x_{\text{Pu}}(1 - x_{\text{Pu}})(31\,245) \\
 G^{\text{ex}}(\text{Pu-Ti, fcc}) &= x_{\text{Pu}}(1 - x_{\text{Pu}})(16\,677) \\
 G^{\text{ex}}(\text{Pu-Ti, } \delta'\text{-Pu}) &= x_{\text{Pu}}(1 - x_{\text{Pu}})(13\,730)
 \end{aligned}$$

Source: Murray, J. L. In *Phase Diagrams of Binary Actinide Alloys*; Kassner, M. E., Peterson, D. E., Eds.; Monograph Series on Alloy Phase Diagrams No. 11; ASM International: Materials Park, OH, 1995; pp 106–108, 233–238, 405–409.

mutual solubility. The eutectic point is at 1463 K with 57.5 at.% Th. Thermodynamic calculation for the Th–Ti system was attempted by assuming that the solid phases are completely immiscible, and then the calculated liquidus curve was found to fit reasonably well with the experimental data. Nevertheless, Murray⁹⁸ pointed out that the mutual solid solubilities should be reexamined using high-purity Ti. The Pu–Ti phase diagram was assessed based mainly on the works of Elliott and Larson,⁷⁶ Poole *et al.*,⁹³ Kutaitsev *et al.*,¹⁰¹ and Languille.¹⁰² The peritectic reaction among β -Ti, ϵ -Pu, and liquid phases dominates this system. The mutual solid solubilities in the Pu–Ti system are far larger than those in the Th–Ti system. The peritectic point is at 1041 K, and the composition for the β -Ti, ϵ -Pu, and liquid phases is 19, 72, and 82.5 at.% Pu, respectively. There is a miscibility gap for the bcc phase (β -Ti, ϵ -Pu), the critical point of which is thought to lie above the peritectic temperature. There are six other invariant reactions in the lower temperature region. The highest one is supposed to be the eutectoid reaction among the α -Ti, β -Ti, and ϵ -Pu phases, the eutectoid point of which is at 876 K, and the composition for the α -Ti, β -Ti, and ϵ -Pu phases is 2, 15, and 84 at.% Pu, respectively. Due to the lack of experimental data, the other five invariant reactions have large uncertainties. A detailed study around the δ' -Pu phase was carried out by Elliott and Larson.⁷⁶ A ‘self-plating’ effect was noted by these authors,⁷⁶ in which reaction with oxygen causes Ti to be depleted in the bulk of the sample and to form an oxide layer on the surface. This phenomenon makes it difficult to determine precisely the phase boundaries near the Pu terminal. Thermodynamic calculation of the Pu–Ti system was attempted only for the phase relation among the liquid, α -Ti, β -Ti, and ϵ -Pu phases in the temperature region above 773 K. The U–Ti phase diagram was assessed mainly based on the works of Udy and Boulger,¹⁰³ Knapton,¹⁰⁴ and Adda *et al.*¹⁰⁵ The general feature is different from the Th–Ti and Pu–Ti systems. The bcc phase (γ -U, β -Ti) is completely miscible as well as the liquid phase, and there is a U_2Ti intermetallic compound. The invariant temperatures and phase boundaries were determined by optimizing the Gibbs energy functions.⁹⁸ The U_2Ti phase transforms congruently to the bcc phase at 1171 K. Three eutectoid reactions appear in the system. The assessed eutectoid points are at 938 K, 15 at.% U; at 993 K, 93 at.% U; and at 941 K, 98 at.% U. Regarding the crystal structure for the U_2Ti phase, the AlB_2 -type, which is thought to be an

ordered hexagonal structure,⁹⁸ was recommended. The difference in the general features for the Th–Ti, U–Ti, and Pu–Ti phase diagrams suggests that the miscibility in the actinide–Ti system is qualitatively in the order U–Ti > Pu–Ti > Th–Ti. The interaction parameters for each system are slightly shifted to the negative direction. The previous thermodynamic assessments were carried out using only the phase boundary data of each system, and therefore, the assessed values possibly are relatively shifted depending upon the systems. Further studies might be required to evaluate the variation in the chemical potentials for these systems. According to systematic considerations, the Np–Ti is speculated to be ordered between the U–Ti and Pu–Ti and Am–Ti after Th–Ti. The shape of the phase relations for the Np–Ti and Am–Ti systems is speculated only preliminarily.

Figure 35 shows the Th–Zr phase diagrams quoted from Okamoto,⁴ which was constructed from the works of Gibson *et al.*¹⁰⁶ and Johnson and Honeycombe.¹⁰⁷ Complete miscibility for the bcc phase is observed as well as for the liquid phase. There is a miscibility gap for the bcc phase in the central region between 46 and 60 at.% Zr concentration, the critical temperature of which is 1228 K. The liquidus and the solidus shift to the lower temperatures, and the bcc phase (β -Th, β -Zr) congruently melts at 1623 K (\sim 46 at.% Zr). These facts suggest that the bcc phase is to be modeled as a simple regular solution and the interaction parameter slightly deviates to the positive direction from Raoult’s law. Although a large solid solubility of Zr in α -Th (fcc structure) is observed near the Th terminal, that of Th in α -Zr (HCP structure) is negligibly small. Regarding the U–Zr system,

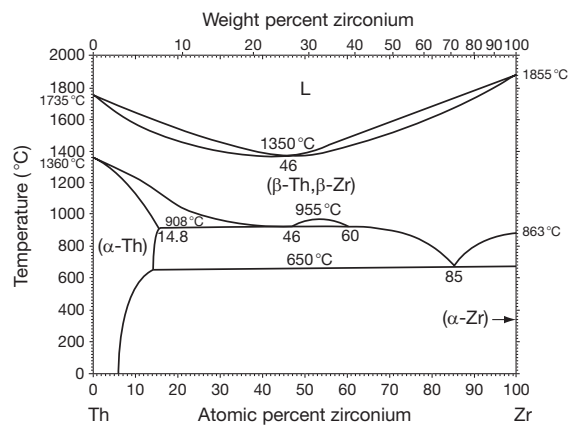


Figure 35 Th–Zr phase diagram taken from Okamoto.⁴

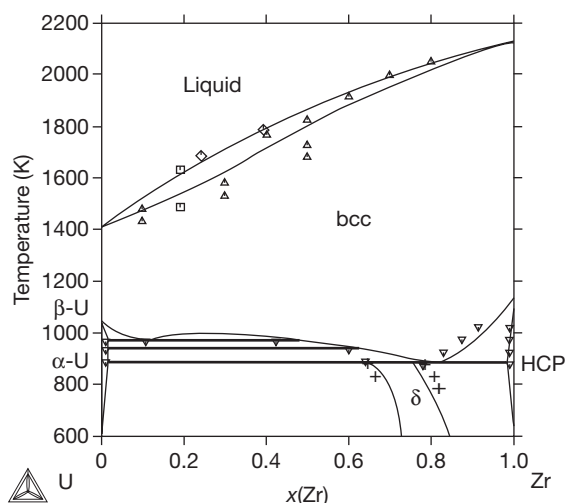
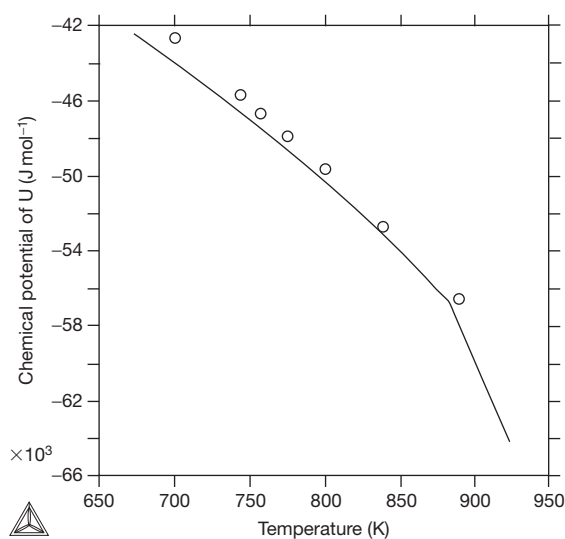
Table 9 Calculated interaction parameters for U–Zr systems

$G^{\circ}(\text{U,liq}), G^{\circ}(\text{U,bcc}), G^{\circ}(\text{U},\beta\text{-U}), G^{\circ}(\text{U},\alpha\text{-U})$: given in Dinsdale ⁶⁷
$G^{\circ}(\text{Zr,liq}), G^{\circ}(\text{Zr,bcc}), G^{\circ}(\text{Zr,HCP})$: given in Dinsdale ⁶⁷
$G^{\circ}(\text{U,HCP}) = 5000 + G^{\circ}(\text{U},\alpha\text{-U})$
$G^{\circ}(\text{Zr},\beta\text{-U}), G^{\circ}(\text{Zr},\alpha\text{-U}) = 5000 + G^{\circ}(\text{Zr,HCP})$
$G^{\circ}(\delta\text{-UZr}_2) = -13\,394 + 21.484T$
$G^{\text{ex}}(\text{U-Zr,liq}) = x_{\text{Zr}}(1 - x_{\text{Zr}}) (81\,206 - 57.494T)$
$G^{\text{ex}}(\text{U-Zr,bcc}) = x_{\text{Zr}}(1 - x_{\text{Zr}}) (57\,907 - 45.448T - 6004.2(x_{\text{U}} - x_{\text{Zr}}))$
$G^{\text{ex}}(\text{U-Zr,HCP}) = x_{\text{Zr}}(1 - x_{\text{Zr}}) (23\,559)$
$G^{\text{ex}}(\text{U-Zr},\beta\text{-U}) = x_{\text{Zr}}(1 - x_{\text{Zr}}) (24\,972)$
$G^{\text{ex}}(\text{U-Zr},\alpha\text{-U}) = x_{\text{Zr}}(1 - x_{\text{Zr}}) (25\,802)$

Source: Kurata, M. In *Proceedings of Actinides 2009*, San Francisco, CA, July 12–19, 2009.

various assessments have been performed previously.^{19,108–110} The unique features of this system are the existence of the miscibility gap for the bcc phase not in the central region but at the U-rich region and the intermediate δ -phase with a wide nonstoichiometric composition range. These suggest that the U–Zr system is slightly stabilized in the Zr-rich region compared to the U-rich region. The U activity in the δ -phase was recently evaluated by means of electromotive force (EMF) measurements.¹¹¹ Thermodynamic re-evaluation⁷ was then performed by the CALPHAD approach by taking into consideration the new data as well as the previous ones.^{108,112–115}

Table 9 summarizes the assessed results, in which the interaction parameters gradually decrease with increasing temperature, and this tendency agrees reasonably well with the features of the U–Zr phase relations, such as the complete solid solubility in the bcc phase, the very limited solid solubility in the low-temperature phases, etc. The calculated U–Zr phase diagram and the activity diagram are shown in **Figures 36** and **37**, respectively. By adapting the sublattice model for the δ -phase, the phase boundaries and the U activity for the δ -phase reasonably fit with the experimental data points,¹¹⁴ although the variation in the δ -phase boundary for the Zr-rich region looks thermodynamically unlikely.⁸⁴ Since the U activity in the δ -phase is almost unity (of the order of 0.8–0.99),¹¹¹ a slight variation in the experimental condition possibly changes the phase boundary. Regarding the Pu–Zr systems, two kinds of previously reported phase diagrams^{116,117} were introduced by Elliott.⁵³ Massalski *et al.*² recommended the former. The differences in the two diagrams are: (1) the reaction type between the fcc and bcc phases is congruent¹¹⁶ or eutectoid¹¹⁷;

**Figure 36** Calculated U–Zr phase diagram taken from Kurata,⁷ and the experimental data taken from Leibowitz *et al.*⁸⁵ (\square), Sheldon and Peterson¹⁰⁸ (∇), Summers-Smith¹¹² (Δ), Akabori *et al.*¹¹⁴ (+), and Maeda *et al.*¹¹⁵ (\diamond).**Figure 37** U activity in the δ -phase taken from Kurata⁷ and Murakami *et al.*¹¹¹

and (2) the low-temperature κ -phase (PuZr_2) transforms eutectoidally from the δ -Pu and α -Zr at ~ 74 at.% Zr¹¹⁶ or transforms congruently to the fcc phase near the stoichiometric composition.¹¹⁷ However, a later study indicated that the κ -phase is only found as an oxygen-stabilized phase.¹¹⁸ Annealing tests using the κ -phase composition sample were attempted at 625 K for 8 days, but the κ -phase was not found.¹¹⁹ The congruent transformation between the fcc and

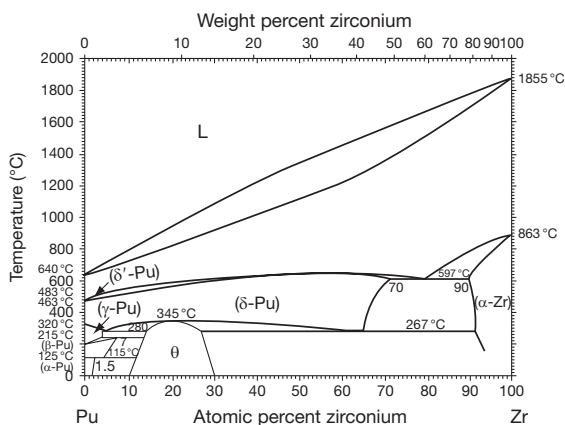


Figure 38 Pu–Zr phase diagram taken from Okamoto.⁴

Table 10 Calculated interaction parameters for Pu–Zr systems

$G^{\circ}(\text{Pu}, \text{liq})$, $G^{\circ}(\text{Pu}, \text{bcc})$, $G^{\circ}(\text{Pu}, \delta'\text{-Pu})$, $G^{\circ}(\text{Pu}, \delta\text{-Pu})$: given in Dinsdale⁶⁷

$G^{\circ}(\text{Zr}, \text{liq})$, $G^{\circ}(\text{Zr}, \text{bcc})$, $G^{\circ}(\text{Zr}, \text{HCP})$: given in Dinsdale⁶⁷

$G^{\circ}(\text{Pu}, \text{HCP}) = 5000 + G^{\circ}(\text{Pu}, \delta\text{-Pu})$

$G^{\circ}(\text{Zr}, \delta'\text{-Pu})$, $G^{\circ}(\text{Zr}, \delta\text{-Pu}) = 5000 + G^{\circ}(\text{Zr}, \text{HCP})$

$G^{\text{ex}}(\text{Pu-Zr}, \text{liq}) = x_{\text{Zr}}(1 - x_{\text{Zr}})(16156 - 12.622T)$

$G^{\text{ex}}(\text{Pu-Zr}, \text{bcc}) = x_{\text{Zr}}(1 - x_{\text{Zr}})(5730.0 - 3.4108T + 2759.7(x_{\text{Pu}} - x_{\text{Zr}}))$

$G^{\text{ex}}(\text{Pu-Zr}, \text{HCP}) = x_{\text{Zr}}(1 - x_{\text{Zr}})(1145.9)$

$G^{\text{ex}}(\text{Pu-Zr}, \delta'\text{-Pu}) = x_{\text{Zr}}(1 - x_{\text{Zr}})(3000)$

$G^{\text{ex}}(\text{Pu-Zr}, \delta\text{-Pu}) = x_{\text{Zr}}(1 - x_{\text{Zr}})(-7620.0 - 1.9961T + 15833(x_{\text{Pu}} - x_{\text{Zr}}) - 5974.7(x_{\text{Pu}} - x_{\text{Zr}})^2)$

Source: Kurata, M. In *Proceedings of Actinides 2009*, San Francisco, CA, July 12–19, 2009.

bcc phases was also confirmed by Suzuki *et al.*¹¹⁹ as observed by Bochvar *et al.*¹¹⁶ The liquidus and the solidus were calculated by Leibowitz *et al.*¹²⁰ based mainly on the experimental data of Marples¹¹⁷ by assuming that the liquid phase is an ideal solution. **Figure 38** shows the reassessed Pu–Zr phase diagram given by Okamoto^{4,19} based on the experimental data of Bochvar *et al.*,⁷⁵ Marples,¹¹⁷ Suzuki *et al.*,¹¹⁹ and Tayler¹²¹ and the calculations by Leibowitz *et al.*¹²⁰ Later, the vapor pressure of Pu in the Pu–Zr system was measured at 1473 and 1823 K as well as the liquidus and the solidus.¹²² Thermodynamic evaluation was performed again for the Pu–Zr system⁷ by additionally taking into consideration the data of Maeda *et al.*,¹²² in which a slight positive deviation from Raoult's law was shown for the liquid phase. **Table 10** summarizes the results. The newly calculated results reasonably overlap with the liquid, bcc,

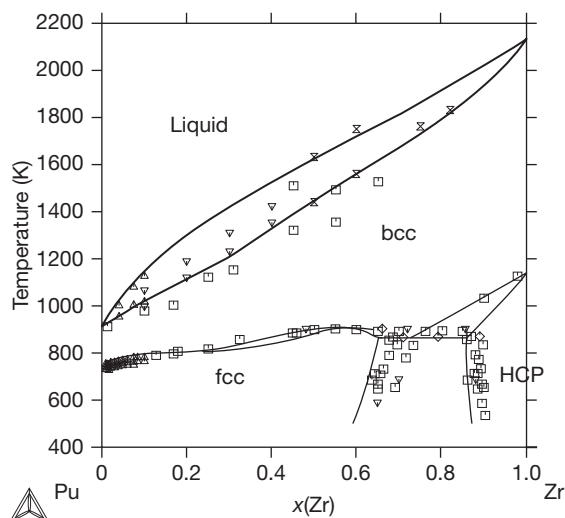


Figure 39 Pu–Zr phase diagram taken from Kurata,⁷ and experimental data taken from Bochvar *et al.*⁷⁵ (v), Marples¹¹⁷ (u), Suzuki *et al.*¹¹⁹ (◇), Tayler¹²¹ (Δ), and Maeda *et al.*¹²² (x).

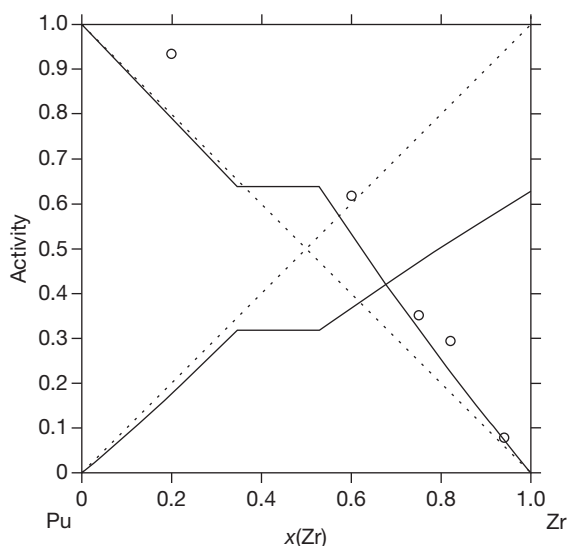


Figure 40 Pu activity in the Pu–Zr system at 1473 K, and experimental data taken from Maeda *et al.*¹²² Reproduced from Kurata, M. In *Proceedings of the MMSNF-6*, Tokyo University, Dec 13–14, 2007.

fcc, and HCP phase boundaries, as indicated in **Figure 39**, although the phase relations for the low-temperature phases were not assessed because of the lack of the thermodynamic data around the θ -phase. **Figure 40** shows the activity diagram with the experimental data of Maeda *et al.*¹²² The slightly positive deviation is clearly seen in the figure. As for the

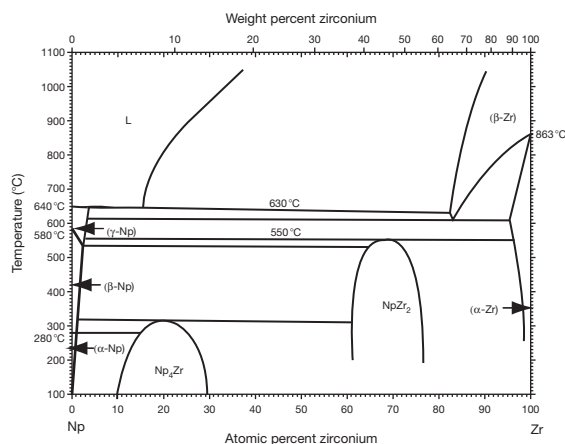


Figure 41 Np–Zr phase diagram taken from Okamoto.⁴

Table 11 Calculated interaction parameters for Np–Zr systems

$G^{\circ}(\text{Np}, \text{liq})$, $G^{\circ}(\text{Np}, \text{bcc})$, $G^{\circ}(\text{Np}, \beta\text{-Np})$, $G^{\circ}(\text{Np}, \alpha\text{-Np})$: given in Dinsdale ⁶⁷
$G^{\circ}(\text{Zr}, \text{liq})$, $G^{\circ}(\text{Zr}, \text{bcc})$, $G^{\circ}(\text{Zr}, \text{HCP})$: given in Dinsdale ⁶⁷
$G^{\circ}(\text{Np}, \text{HCP}) = 5000 + G^{\circ}(\text{Np}, \text{bcc})$
$G^{\circ}(\text{Zr}, \beta\text{-Np})$, $G^{\circ}(\text{Zr}, \alpha\text{-Np}) = 5000 + G^{\circ}(\text{Zr}, \text{HCP})$
$G^{\text{ex}}(\text{Np-Zr}, \text{liq}) = x_{\text{Zr}}(1 - x_{\text{Zr}})(16000 - 137T)$
$G^{\text{ex}}(\text{Np-Zr}, \text{bcc}) = x_{\text{Zr}}(1 - x_{\text{Zr}})(9000 - 37T)$
$G^{\text{ex}}(\text{Np-Zr}, \text{HCP}) = x_{\text{Zr}}(1 - x_{\text{Zr}})(15000)$
$G^{\text{ex}}(\text{Np-Zr}, \beta\text{-Np})$, $G^{\text{ex}}(\text{Np-Zr}, \alpha\text{-Np}) = x_{\text{Zr}}(1 - x_{\text{Zr}})(15000)$

Source: Kurata, M. In *Proceedings of Actinides 2009*, San Francisco, CA, July 12–19, 2009.

Np–Zr system, two kinds of inconsistent data were already reported.^{123,124} The former is preferred by Okamoto,¹²⁵ who observed the limited mutual solubility in the bcc phase (γ -Np, β -Zr), as given in **Figure 41**. According to the systematic similarity expected between the Np–Zr and Pu–Zr systems, the thermodynamic evaluation was performed by Kurata.⁷ **Table 11** summarizes the results. The calculated Np–Zr phase diagram using the assessed interaction parameters is in better agreement with the data of Rodriguez *et al.*,¹²⁴ as shown in **Figure 42**. Further study is required for the Np–Zr system, especially regarding the presence or absence of the miscibility gap for the bcc phase, although the significant difference in melting temperature between Np and Zr and the effect of oxygen impurity makes it difficult to obtain precise data points.

Since the U–Np–Zr ternary alloy is considered to be one of the promising candidate base alloys for metallic nuclear fuel, various studies on the U–Pu–Zr phase relation have been performed. Ternary

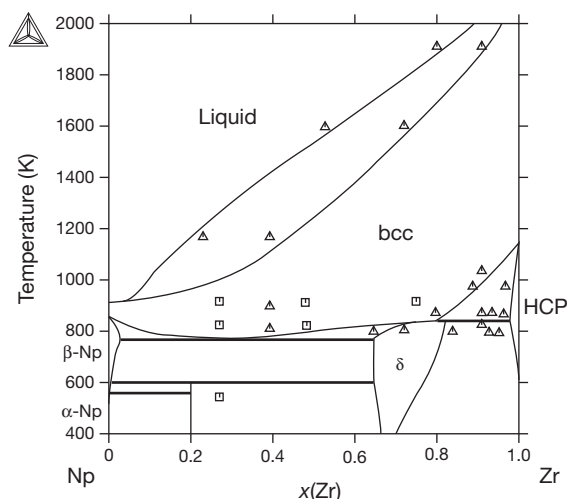


Figure 42 Calculated Np–Zr phase diagram based on the similarity to the Pu–Zr system taken from Kurata,⁷ and the experimental data taken from Gibson *et al.*¹²³ (□) and Rodriguez *et al.*¹²⁴ (Δ).

isotherms for the solid phase relation in the temperature region 773–973 K have been reported.¹²⁶ Calculated ternary isotherms were given by Kurata⁷ based on thermodynamic modeling for the U–Pu, U–Zr, and Pu–Zr binary subsystems described above. **Figures 43–45** compare both results at various temperatures. The experimental observations agree reasonably well with the calculation: for instance, the width of the miscibility gap for the bcc phase (γ -U, Pu, Zr) at 973 K, the decomposition of ζ -phase at around 943 K, the phase relation between the γ - and δ -phases at around 868 K, etc. **Figures 46** and **47** indicate the calculated liquidus and solidus of the U–Pu–Zr alloy along with the measured values shown in Leibowitz and Blomquist¹¹³ and Harbur *et al.*¹²⁷ The calculated values coincide with the measured one within ± 20 K variation. By introducing the thermodynamic data as well as the phase boundary data for the evaluation of the binary subsystems, reasonable accuracy of the calculated isotherms for the ternary is achieved. In order to solve the conflict for the Np–Zr system described above, the ternary information for the U–Np–Zr system may be useful. The similarity of the features between the U–Pu–Zr and the U–Np–Zr systems was shown by Rodriguez *et al.*¹²⁴

Regarding the actinide–Hf systems, the Th–Hf, U–Hf, and Pu–Hf phase diagrams were given by Okamoto.⁴ These phase diagrams have many similarities to those for the actinide–Ti and actinide–Zr

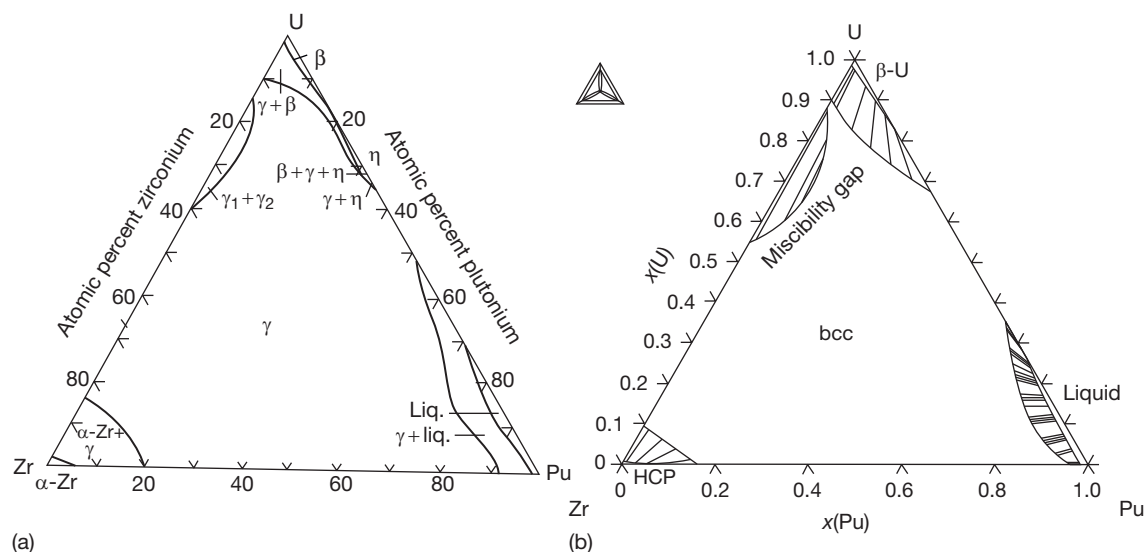


Figure 43 U–Pu–Zr ternary isotherms at 973 K (a) drawn from experimental information and (b) calculated from the thermodynamic assessment of three binary subsystems. Adapted from O’Boyle, D. R.; Dwight, A. E. In *Proceedings of the 4th International Conference on Plutonium and Other Actinides*, Santa Fe, New Mexico, 1970; Vol. 2, pp 720–732; Kurata, M. In *Proceedings of Actinides 2009*, San Francisco, CA, July 12–19, 2009.

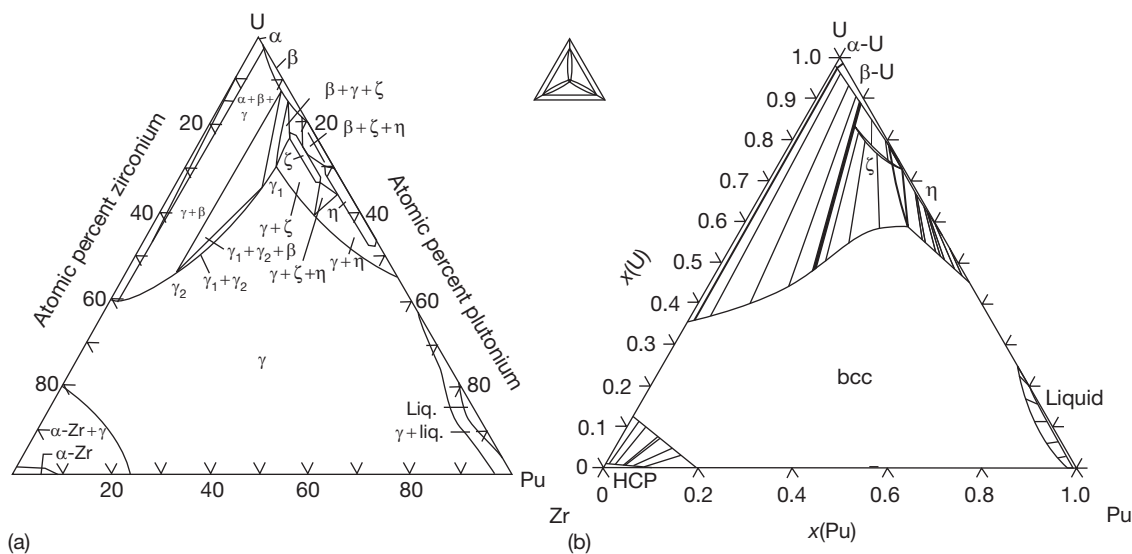


Figure 44 U–Pu–Zr ternary isotherms at 933 K (a) drawn from experimental information and (b) calculated from the thermodynamic assessment of three binary subsystems. Adapted from O’Boyle, D. R.; Dwight, A. E. In *Proceedings of the 4th International Conference on Plutonium and Other Actinides*, Santa Fe, New Mexico, 1970; Vol. 2, pp 720–732; Kurata, M. In *Proceedings of Actinides 2009*, San Francisco, CA, July 12–19, 2009.

systems, although the experimental data are still not sufficient. The Th–Hf phase diagram is categorized as eutectic type, although a larger mutual solid solubility is observed compared to the Th–Ti phase diagram.¹⁰⁶ The U–Hf phase diagram shows that the liquid and bcc phases are completely soluble and a miscibility gap exists in the central region of

the bcc phase.¹²⁸ The Pu–Hf phase diagram looks quite similar to that of Pu–Ti.⁵⁸

The very limited solid solubility and the miscibility gap even for the liquid phase are speculated on the Am or, possibly, Cm and Group IVa metal systems, which are concluded from the expected similarity with Ce and Ti, Zr, or Hf systems.^{2,129}

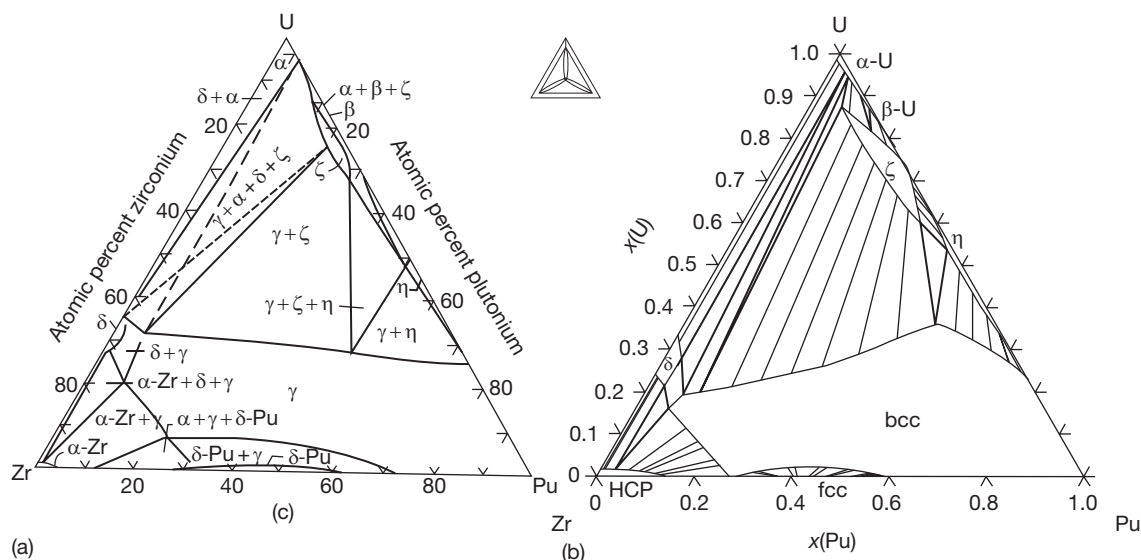


Figure 45 U–Pu–Zr ternary isotherms at 868 K (a) drawn from experimental information and (b) calculated from the thermodynamic assessment of three binary subsystems. Adapted from O’Boyle, D. R.; Dwight, A. E. In *Proceedings of the 4th International Conference on Plutonium and Other Actinides*, Santa Fe, New Mexico, 1970; Vol. 2, pp 720–732; Kurata, M. In *Proceedings of Actinides 2009*, San Francisco, CA, July 12–19, 2009.

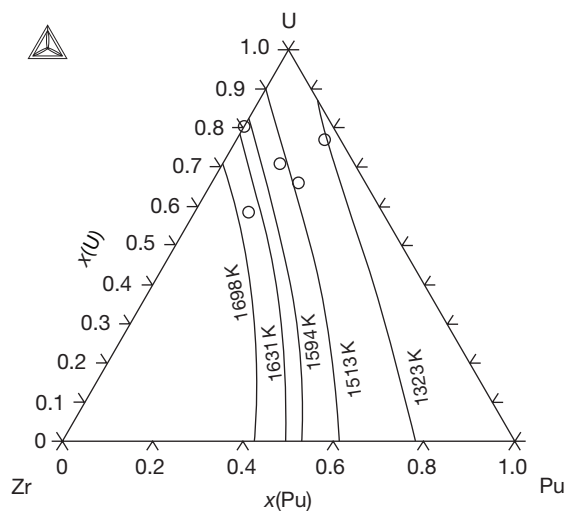


Figure 46 Calculated liquidus for U–Pu–Zr ternary system taken from Kurata,⁷ and the experimental data taken from Leibowitz and Blomquist¹¹³ and Harbur *et al.*¹²⁷

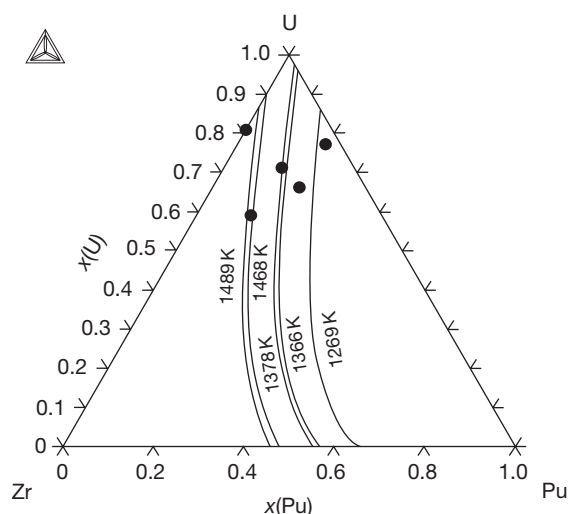


Figure 47 Calculated solidus for U–Pu–Zr ternary system quoted taken from Kurata,⁷ and the experimental data taken from Leibowitz and Blomquist¹¹³ and Harbur *et al.*¹²⁷

Due to the difficulty of the experimental study because of the high melting point of Group Va metals, such as V, Nb, and Ta, the experimental data points in these systems sometimes are rather scattered. Nine phase diagrams between Th, U, or Pu and V, Nb, or Ta were summarized by Okamoto.⁴ The Th–V, Th–Nb, and Th–Ta phase diagrams are categorized as eutectic type. The key references for these systems

are Carlson *et al.*,⁹⁹ Pedersen *et al.*,¹⁰⁰ Palmer *et al.*,¹³⁰ Bannister and Thomson,¹³¹ Smith *et al.*,¹³² McMasters and Larsen,¹³³ Ackermann and Rauh,^{134,135} and Saroja *et al.*¹³⁶ Their eutectic reactions appear to be more at high temperature and with high Th concentration, as given in Table 12. The thermodynamic functions were evaluated from the liquidus curve for the Th–V and Th–Ta systems by Smith *et al.*¹³²

Table 12 Phase relation in actinide–Group Va metal

<i>System</i>	<i>Th–V</i>	<i>Th–Nb</i>	<i>Th–Ta</i>	<i>U–V</i>	<i>U–Nb</i>	<i>U–Ta</i>	<i>Pu–V</i>	<i>Pu–Nb</i>	<i>Pu–Ta</i>
Phase diagram type	Eutectic	Eutectic	Eutectic	Eutectic	Solid solution monotectoid	Peritectic	Eutectic	Eutectic	Peritectic
Invariant temperature	1708 ± 10 K 79.7 at. % Th	1708 K 84 at. % Th	1953 ± 2 K 98 at. % Th	1313 ± 5 K 82 at. % U	920 K 30 ± 2 at. % U 86.7 at.% U	1433 K 97 at. % U	898 K 99.4 at. % Pu	903 K 99.5 at. % Pu	931 K 99.2 at. % Pu
References for phase relation	130	99 100 131 [75Smi]	133 134 135 136 149	137	138,139 141 142,143 147 150	135 136 144 148 149	17 145 151	140 145 –	11 140 146 151
Reference for thermodynamic modeling	132	–	–	–	–	–	–	–	–

and Krishnan *et al.*,¹⁴⁹ respectively. The Pu–V, Pu–Nb, and Pu–Ta phase diagrams are categorized as eutectic or peritectic type. However, the eutectic or peritectic point is very close to the Pu terminal like that in the Th–Ta system. The key references for the Pu–V system is Konobeevsky¹⁷ and Bowersox and Leary.¹⁴⁵ Thermodynamic modeling was performed by Baxi and Massalski¹⁵¹ based on both the experimental data and semiempirical estimation.⁴⁰ Since the shape of the Pu–V is quite simple, the thermodynamically calculated phase boundaries fit reasonably well with the experimental data points. However, the measurement of thermodynamic data is still necessary for more accurate evaluation. Also, in the Pu–V systems, a metastable amorphous phase possibly forms in spite of the high degree of immiscibility for the solid phases.¹⁵² The Pu–Nb system looks quite similar to the Pu–V system.^{140,145} The general shape of the Pu–Ta system is slightly different from the other systems. The invariant reaction is changed to peritectic from eutectic. However, the peritectic point is comparable to the eutectic points of the Pu–V and Pu–Nb systems. The thermodynamic modeling for the Pu–Ta system was performed in a similar manner to the Pu–V system.¹⁵¹ Regarding the U-related system, the U–V and U–Ta phase diagrams have mostly similar shapes. The eutectic point appears at 1313 ± 5 K with 82 at.% of U in the U–V system¹³⁷ as does the peritectic point at 1433 K with ~ 97 at.% of U in the U–Ta system.^{135,136,144,148} However, the solid solubilities in the U–V and U–Ta systems attain several percent at the maximum, which suggests that the miscibility in the U-related system is slightly better than that in the Th- and Pu-related systems. **Figure 48** shows the Pu–Nb phase diagram as a typical example

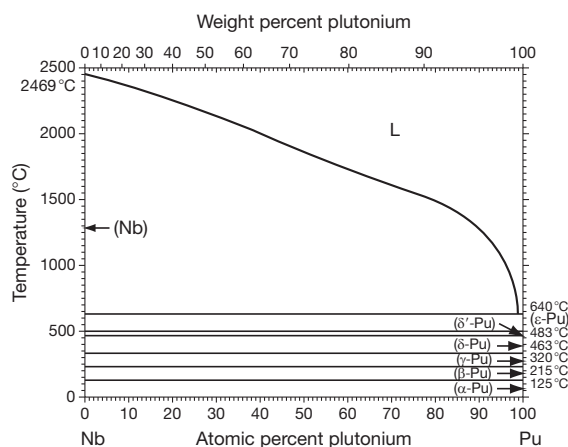


Figure 48 Pu–Nb phase diagram taken from Okamoto.⁴

for the relation between the actinide and Group Va metals. The only exception is the U–Nb system, in which γ -U and γ -Nb (bcc structure) are completely soluble and the general feature for the phase relations is rather similar to that in the U–Zr phase diagram. **Figure 49** shows the U–Nb phase diagram quoted from Okamoto.⁴ The key sources for the system are Pfeil *et al.*,¹³⁸ Rogers *et al.*,¹³⁹ Peterson and Ogilvie,¹⁴¹ Fizzotti and Maspereni,¹⁴² Terekhov,¹⁴³ and Romig.¹⁴⁷ There is a miscibility gap in the bcc phase and an invariant monotectoid reaction at 920 K.¹⁵⁰ The solid solubility of Nb in α -U and β -U attains a few percent at the maximum. A couple of reports indicated the formation of the δ -phase in the Nb-rich region during annealing of a diffusion couple between pure U and Nb.^{141,147} The δ -phase was observed only in the diffusion couples but not in the homogenized bulk specimen. This suggests that the δ -phase is metastable. Poor miscibility between Am, or possibly Cm, and Group Va metals is speculated from the phase relations between Ce and Group Va metals.⁴

The phase relation between actinides and Group VIa metals, such as Cr, Mo, and W, is mostly similar to that between actinides and Group Va metals. They are categorized in the simple eutectic- or peritectic-type phase diagram with the exception of the U–Mo system. **Figure 50** shows the Th–Cr phase diagram as a typical example for the actinide–Group VIa metal system, which is quoted from Okamoto.⁴ The phase diagram is redrawn from the assessment of Venkattraman *et al.*¹⁵³ The Th–Mo, Th–W, U–Cr, and Pu–Cr phase diagrams reveal a similar tendency on the phase relations, although the eutectic point is shifted toward the actinide terminal in the case of the W-related system due to the high melting point of

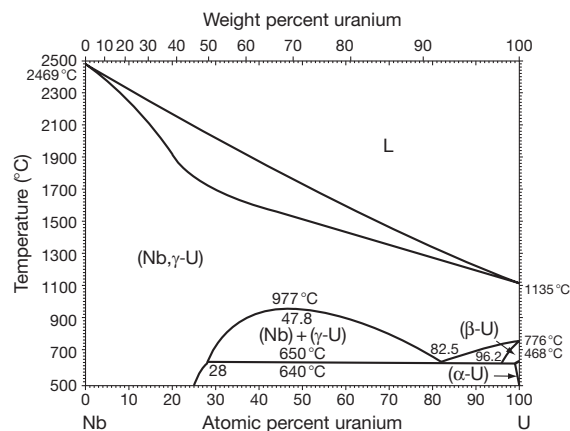


Figure 49 U–Nb phase diagram taken from Okamoto.⁴

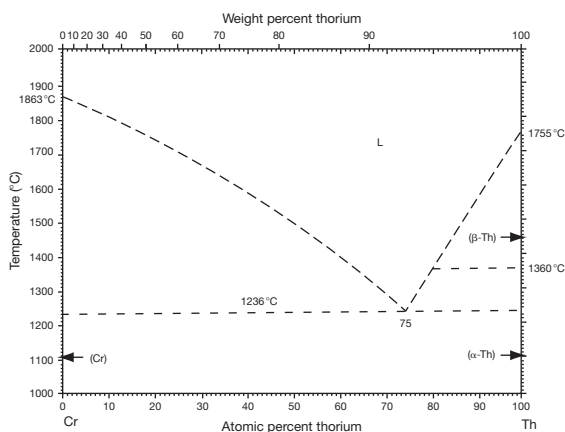


Figure 50 Th–Cr phase diagram taken from Okamoto.⁴

pure W. In the case of Pu–Mo and Pu–W systems, it is difficult to identify whether the invariant reaction is eutectic or peritectic, because the invariant points are very close to the Pu terminal. In the U–W system, the peritectic reaction appears instead of the eutectic reaction.¹⁵⁴ These phase relations are summarized in **Table 13**. A simple thermodynamic evaluation for the Cr-related system was carried out¹⁵³ by assuming that the liquid phase behaves as an ideal solution. Their estimated eutectic temperature for the Th–Cr and U–Cr systems is roughly a few hundred kelvin lower than the experimental observations. This might suggest the slightly positive deviation from Raoult's law for the liquid phase in these systems. The Ac–Cr, Np–Cr, Am–Cr, and Cm–Cr systems were also roughly evaluated by Venkatraman *et al.*¹⁵³ by assuming the liquid phase in the same manner. The U–Mo system shows some differences with respect to the other systems. The U–Mo phase diagram was proposed originally by Brewer,³ in which the solid solubility of Mo in U attains ~40 at.% at the maximum. However, a conflict was pointed out by Massalski *et al.*² as follows. According to Lundberg,¹⁶³ the MoU₂ compound exists up to at least 1525 K. The crystal structure for MoU₂ was reported to be MoSi₂-type tetragonal and different from that of TiU₂, which is AlB₂-type hexagonal,¹ although they have the same composition. Further study is needed to resolve the conflict. **Figure 51** shows a tentatively assessed U–Mo phase diagram.¹⁶⁴ Regarding the Mo-related systems, the eutectic type of the Np–Mo phase diagram was predicted from thermodynamic modeling.⁵ Probably, the features of the Np–W system are similar to those for the Np–Mo system. Poor miscibility between Am, or possibly Cm, and Group VIa metals is speculated from the phase relation between Ce and Group VIa metals.

After the Group VIIa of metals in the periodic table, it is observed that various types of intermetallic compounds are formed by reaction with actinides. This means that the interaction between the actinide and metals after the Group VIIa deviates to a large degree in the negative direction from the ideal solubility. The phase diagrams of actinide–Group VIIa metals, such as Mn, Tc, and Re, were summarized in Okamoto,⁴ in which the phase relations between actinide and Tc are speculated from that between the actinide and Re based on the similarity expected in the relations between Tc and Re.¹⁶⁵ **Figure 52** shows the U–Mn phase diagram as a typical example of the actinide–Group VIIa metal relation quoted from Okamoto.⁴ The phase diagram is constructed based mainly on the works of Wilhelm and Carlson.⁵⁴ There are two types of intermetallic compounds, U₆Mn and UMn₂, and two kinds of eutectic reaction in both the U-rich and Mn-rich regions. The phase relation in the U–Mn system looks similar to that in the U–Fe system to be shown later. This supposes that the order of the Gibbs energy of formation of these U–Mn compounds might be comparable to those in the U–Fe compounds, although the Gibbs energy of formation of U₆Mn and UMn₂ has not been reported yet. In the actinide–transition-metal relations, a MgCu₂-type compound with a cubic structure often appears. According to Lawson *et al.*,¹⁶⁶ β-UMn₂ of the MgCu₂-type transforms to γ-UMn₂ of the orthorhombic structure at about 230 K in the U–Mn relation. The crystal structure of U₆Mn is the same as that of U₆Fe. In the Th–Mn and Pu–Mn systems, the U₆Mn-type compound disappears and the decomposition temperature of the MgCu₂-type compound decreases.^{17,167} This suggests a decrease in the degree of the negative deviation on mixing in these systems with respect to the U–Mn system. **Figure 53** shows the U–Re phase diagram as a typical example of the phase relation between actinide and Re. The phase diagram was assessed from Jackson *et al.*,¹⁶⁸ Garg and Ackermann,¹⁵⁵ and Chandrasekharaish *et al.*¹⁶¹ The Re-rich side of the phase diagram shows similarity to that in the U–Mn system. However, the crystal structure of URe₂, that is, MnZn₂-type, is different from the other typical structure, that is, MgCu₂-type. The decomposition temperature of URe₂ decreases more than that of UMn₂ compared to that in the U–Fe system. On the U-rich side, U₂Re appears instead of the U₆Mn-type compound and the solid solubility of Re in U attains 8.8 at.%, which is significantly larger than that in the U–Mn system. In the U–Re system,

Table 13 Phase relation in actinide–Group VIa metal

<i>System</i>	<i>Th–Cr</i>	<i>Th–Mo</i>	<i>Th–W</i>	<i>U–Cr</i>	<i>U–Mo</i>	<i>U–W</i>	<i>Pu–Cr</i>	<i>Pu–Mo</i>	<i>Pu–W</i>
Phase diagram type	Eutectic	Eutectic	Eutectic	Eutectic	Peritectic	Peritectic	Eutectic	Eutectic? Peritectic?	Eutectic? Peritectic?
Invariant temperature	1509 K 75 at. % Th	1653 ± 12 K 86 ± 0.5 at. % Th	1968 K 98.8 at. % Th	1133 K 81 at. % U	1557 ± 2 K 60 at. % U	>1408 K 99 at. % U	893 K 99.16 at. % Pu	913 K ~100 at.% Pu	913 K ~100 at.% Pu
References for phase relation	16	155	134 135	137 156 157 159 162	155 29 158 160	135 136 144 161	76 116 145 140	145	11 37
Reference for thermodynamic modeling	153	3	154	153	–	154	153	3	154

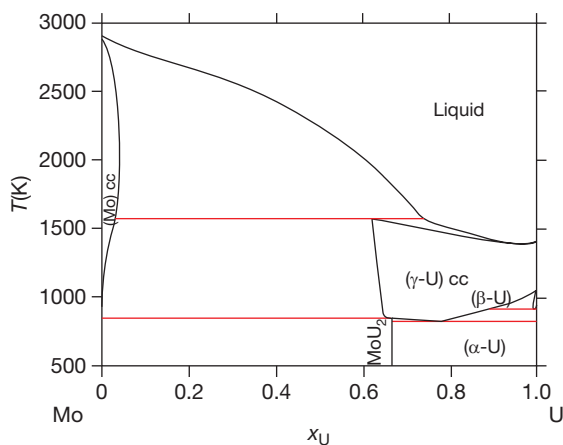


Figure 51 U-Mo phase diagram taken from Gueneau.¹⁶⁴

the negative deviation from the ideal solubility is speculated to be smaller than that in the U-Mn system based on these observations. In the Th-Re and Pu-Re systems,^{146,155} the MnZn₂-type compounds, such as ThRe₂ and PuRe₂, are the only compounds and the U₂Re-type does not appear. This suggests that the negative deviation from the ideal solution between Th-Re and Pu-Re becomes smaller than that in the U-Re as well as the tendency observed in the Mn-related system. Regarding the Np-related systems, the formation of NpMn₂ and NpRe₂, which have the MgCu₂-type and MgZn₂-type structures, respectively, was reported.¹⁶⁹ Poor miscibility between Am, or possibly Cm, and Group VIIa metals is speculated from the phase relation between Ce and Group VIIa metals.

2.05.3.6 Actinide: Group VIII Metals

Several intermetallic compounds ($N > 3$) appear in the phase diagrams between actinide and Group VIII metals, with the exception of Th-Os, U-Fe, Np-Fe, and Pu-Fe systems, in which $N = 2$ or 3. This suggests that the ordering between actinide and Group VIII metals is preferred to the random configuration, and the Gibbs energy of formation of these compounds is expected to be much larger than what appears in the actinide-Group IVa or VIIa metal systems. Table 14 summarizes the various intermetallic compounds reported for the actinide-Group VIII metal systems as well as the actinide-Mn system. A systematic variation is seen in the table with increasing atomic number of actinide or Group VIII metal. A unique feature is especially observed in the actinide-Fe systems. Five kinds of intermetallic compounds exist in the Th-Fe system (Th₂Fe₇ has two different allotropes)^{170,171,185} and these compositions are rather similar to those observed in the other Th-Group VIII metal systems. On the other hand, the U-Fe, Np-Fe, and Pu-Fe systems have only two kinds of intermetallic compounds (although PuFe₂ has three different allotropes) and are more similar to the Mn-related systems. This variation may correspond to the difference in the Gibbs energy of formation of these intermetallic compounds. Here, the existence of Np₆Fe has not been directly confirmed yet. A compatibility test between the U-Pu-Zr-Np-Am-Ce-Nd alloy and stainless steel was performed,¹⁸⁰ in which two or three kinds of phases were detected in the interaction layer, such as the MFe₂-type, M₆Fe-type, and RE-rich type (M: mixture of actinides). The existence of Np in the M₆Fe-type phase was detected,

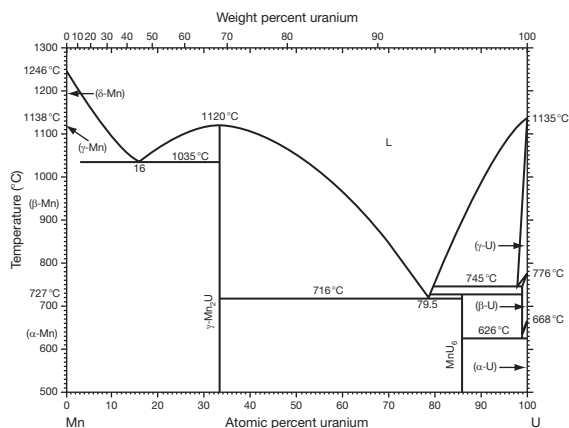


Figure 52 U-Mn phase diagram taken from Okamoto.⁴

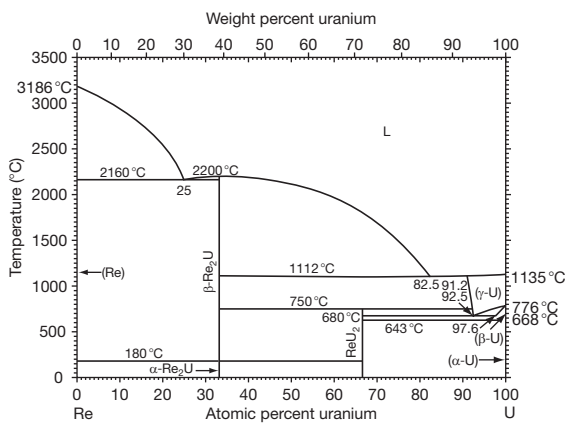


Figure 53 U-Re phase diagram quoted from Okamoto.⁴

Table 14 Intermetallic compounds between actinide and Mn, Fe, Co, or Ni

Group Element	VIIa	VIII		
	Mn	Fe	Co	Ni
Th	ThMn ₁₂ (ThMn ₁₂ -type) ThMn ₂ (MgZn ₂ -type) Th ₆ Mn ₂₃ (Th ₆ Mg ₂₃ -type) 167	Th ₇ Fe ₃ (Th ₇ Fe ₃ -type) ThFe ₃ (PuNi ₃ -type) α -Th ₂ Fe ₇ (Ce ₂ Ni ₇ -type) β -Th ₂ Fe ₇ (Gd ₂ Co ₇ -type) ThFe ₅ (CaCu ₅ -type) Th ₂ Fe ₁₇ (Th ₂ Zn ₁₇ -type) 170,171	Th ₇ Co ₃ (Th ₇ Fe ₃ -type) ThCo (CrB-type) α -Th ₂ Co ₇ (Ce ₂ Ni ₇ -type) β -Th ₂ Co ₇ (Er ₂ Co ₇ -type) ThCo ₅ (CaCu ₅ -type) Th ₂ Co ₁₇ (Th ₂ Zn ₁₇ -type) 172	Th ₇ Ni ₃ (Th ₇ Fe ₃ -type) ThNi (ND) Th ₄ Ni ₇ (ND) ThNi ₂ (AlB ₂ -type) α -Th ₂ Ni ₇ (ND) β -Th ₂ Ni ₇ (ND) ThNi ₅ (CaCu ₅ -type) Th ₂ Ni ₁₉ (ND) 173,174
U	U ₆ Mn (U ₆ Mn-type) α -UMn ₂ (ND) β -UMn ₂ (Cu ₂ Mg-type) γ -UMn ₂ (ND) 54	U ₆ Fe (U ₆ Mn-type) UFe ₂ (Cu ₂ Mg-type) 175,176	U ₆ Co (U ₆ Mn-type) UCo (Uco-type) UCo ₂ (Cu ₂ Mg-type) UCo ₃ (PuNi ₃ -type) UCo ₄ (ND) U ₂ Co ₁₁ (ND) 177	U ₆ Ni (U ₆ Mn-type) U ₇ Ni ₉ (ND) U ₅ Ni ₇ (ND) UNi ₂ (MgZn ₂ -type) δ (ND) ϵ (ND) UNi ₅ (AuBe ₅ -type) 178,179
Np ^a	NA	Np ₆ Fe? (U ₆ Mn-type) NpFe ₂ (Cu ₂ Mg-type) 169,180	NpCo ₂ (Cu ₂ Mg-type) 169	NpNi ₂ (Cu ₂ Mg-type) 169
Pu	PuMn ₂ (Cu ₂ Mg-type) 17	Pu ₆ Fe (U ₆ Mn-type) α -PuFe ₂ (Cu ₂ Mg-type) β -PuFe ₂ (MgNi ₂ -type) γ -PuFe ₂ (ND) 181,182	Pu ₆ Co (U ₆ Mn-type) Pu ₃ Co (BRe ₃ -type) Pu ₂ Co (Fe ₂ P-type) PuCo ₂ (Cu ₂ Mg-type) PuCo ₃ (NbBe ₃ -type) Pu ₂ Co ₁₇ (Th ₂ Ni ₁₇ -type) 93	PuNi (CrB-type) PuNi ₂ (Cu ₂ Mg-type) PuNi ₃ (NbBe ₃ -type) PuNi ₄ (PuNi ₄ -type) PuNi ₅ (CaCu ₅ -type) Pu ₂ Ni ₁₇ (Th ₂ Ni ₁₇ -type) 17,183
Am ^a	NA –	AmFe ₂ (Cu ₂ Mg-type) 184	AmCo ₂ 184	AmNi ₂ 169

^aAccording to systematic similarity, other intermetallic compounds are expected in the Np–Co, Np–Ni, Am–Co, and Am–Ni systems. According to the expected similarity of the Am–Mn system against the Ce–Mn system,⁴ there might be no intermetallic compounds in the Am–Mn system.

NA: there is no available information.

ND: the crystal structure is not determined yet.

and the composition of U and Np in M₆Fe was almost the same as that in the original alloy. This suggests that Np₆Fe might be formed in the equilibrium Np–Fe phase diagram.

Figures 54 and 55 show the U–Fe phase diagram and the variation in the U activity in the U–Fe system,⁸⁹ in which the assessment of the U–Fe system was performed by thermodynamic modeling (CALPHAD approach) based on the available data given in Leibowitz *et al.*,⁸⁵ Gordon and Kaufmann,¹⁸⁶ Grogan,¹⁸⁷ Michaud,¹⁸⁸ Chapman and Holcombe,¹⁷⁵ and Gardie *et al.*¹⁷⁶ The calculated results overlap well with the experimental data points in these diagrams. The U activity deviates slightly to the negative direction from Raoult's law, but not too significantly. **Figures 56 and 57** show the Np–Fe and Pu–Fe phase diagrams shown also in Kurata,⁷ in which thermodynamic modeling was performed for the Pu–Fe system using the works in Konobeevsky,¹⁷ Bochvar

et al.,¹¹⁶ Mardon *et al.*,¹⁸¹ Avivi,¹⁸² and Ofte and Wittenberg,¹⁸⁹ and then the Np–Fe system was estimated using the work of Gibson *et al.*¹⁹⁰ by assuming initially that the various interaction parameters in the Np–Fe system are almost the same as those in the Pu–Fe system. The calculated result for the Np–Fe system is similar to that for the Pu–Fe system, and the results reasonably overlap with the experimental data. Thermodynamic data were partially obtained for the Th–Fe, U–Fe, and U–Ni systems, as summarized in **Tables 15 and 16**. The partial Gibbs energy for the Pu₂Ni₁₇–Ni two-phase region and the Gibbs energy of formation of the Pu₂Ni₁₇ were estimated in Chiotti *et al.*¹⁹¹ from the EMF measurement¹⁹² as follows:

$$\Delta G_{\text{Pu}} = -83.76 + 12.34 \times 10^{-3} T (\text{kJ mol}^{-1}) (930 - 1113 \text{K})$$

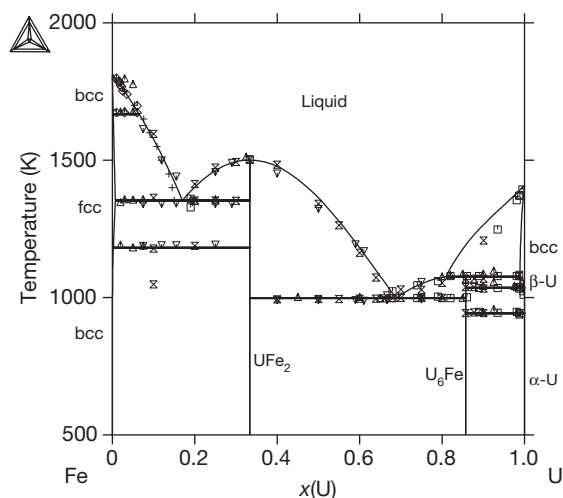


Figure 54 U-Fe phase diagram taken from Kurata *et al.*,⁸⁹ and the experimental data taken from Leibowitz *et al.*⁸⁵ (▽), Gordon and Kaufmann¹⁸⁶ (△), Grogan¹⁸⁷ (◻), Michaud¹⁸⁸ (◊), Chapman and Holcombe¹⁷⁵ (⊗), and Gardie *et al.*¹⁷⁶ (+).

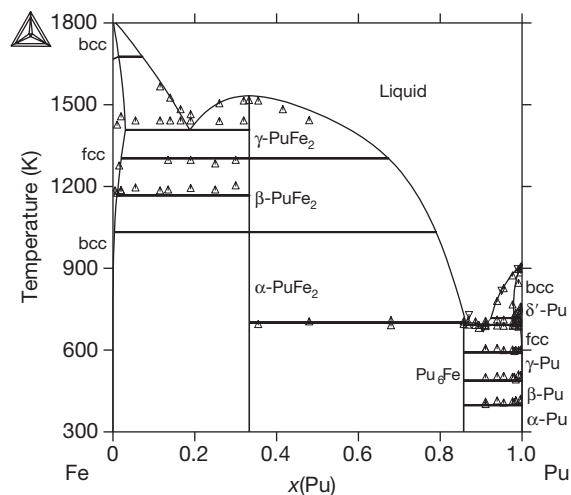


Figure 56 Calculated Pu-Fe phase diagram taken from Kurata,⁷ and the experimental data taken from Mardon *et al.*¹⁸¹ (△) and Ofte and Wittenberg¹⁸⁹ (▽).

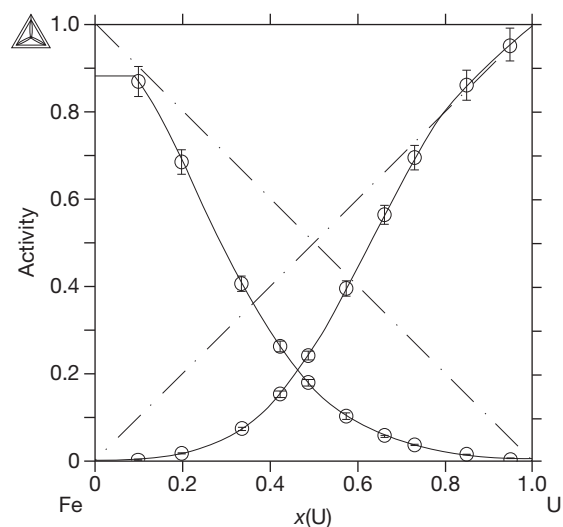


Figure 55 Activity in the U-Fe system at 1600 K taken from Kurata *et al.*⁸⁹ and Gardie *et al.*¹⁷⁶

$$\Delta_f G^0(\text{Pu}_2\text{Ni}_{17}) = -167.8 \\ + 24.69 \times 10^{-3} T(\text{kJ mol}^{-1})(913 - 1125\text{K})$$

Regarding the Fe-related system, the Gibbs energies were also estimated by Kurata,⁷ and are given in Table 17. The difference between the values shown in Tables 16 and 17 originates from the difference in the estimation of the Gibbs energy for the solution phases.

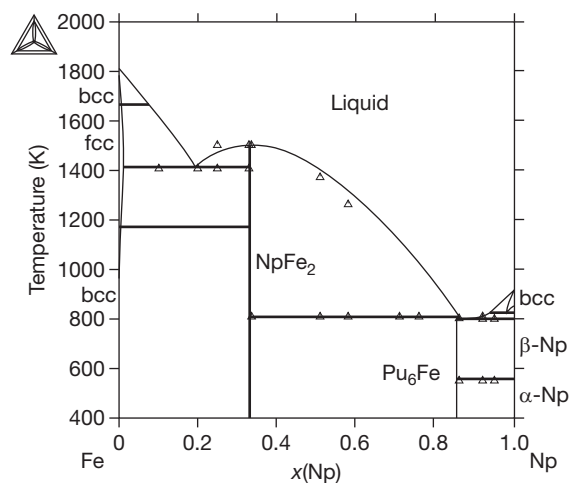


Figure 57 Calculated Np-Fe phase diagram taken from Kurata,⁷ and the experimental data taken from Gibson *et al.*¹⁹⁰

The ternary phase relation among actinide, Fe, and Zr is particularly important when considering the fuel-cladding chemical interaction (FCCI) between the metallic nuclear fuel and the stainless steel cladding (the details are discussed in another chapter). Regarding the U-Fe-Zr system, the phase relations were studied in the temperature region between 853 and 1073 K.¹⁹⁴ Three kinds of ternary intermetallic compounds, ε, λ, and χ, were found in the system. These compositions are U-(33–50) at.% Zr–33 at.% Fe; U-(21–25) at.% Zr–6 at.% Fe;

Table 15 Integral thermodynamic quantities for Th–Fe and U–Ni systems

System	Compound	$\Delta_f H$ (kJ mol ⁻¹)	$\Delta_f S$ (J mol ⁻¹ K ⁻¹)	$\Delta_f G$ (kJ mol ⁻¹)	Temperature (K)	Reference
Th–Fe	Th ₂ Fe ₁₇	–14.0	–5.92	–8.0	1000	191
	ThFe ₅	–20.6	–9.37	–11.2		
	Th ₂ Fe ₇	–24.5	–12.02	–12.4		
	ThFe ₃	–26.2	–113.3	–12.9		
	Th ₇ Fe ₃	–12.3	–5.34	–7.0		
System	Composition (at.% U)	H (kJ mol ⁻¹)	S (J mol ⁻¹ K ⁻¹)	G (kJ mol ⁻¹)	Temperature (K)	Reference
U–Ni	16.7	–44.4 ± 2.1	–15.9 ± 1.7	–28.7 ± 0.46	1000	191
	17.8	–46.4 ± 2.1	–16.3 ± 2.1	–30.0 ± 0.54		
	22.2	–53.1 ± 2.9	–19.2 ± 2.5	–34.4 ± 0.71		
	23.1	–53.6 ± 2.9	–18.8 ± 2.9	–34.8 ± 0.75		
	33.3	–54.0 ± 3.8	–19.2 ± 4.2	–34.6 ± 1.0		
	41.7	–54.8 ± 4.6	–23.0 ± 4.2	–31.8 ± 1.1		
	85.7	–21.3 ± 5.4	–10.0 ± 5.0	–11.3 ± 0.88		

Table 16 Thermodynamic functions for U–Fe systems taken from Okamoto¹⁹

$G^\circ(\text{Fe, liq}) = 0$
$G^\circ(\text{U, liq}) = 0$
$G^\circ(\text{Fe, bcc}) = -13\,800 + 7.169T$
$G^\circ(\text{Fe, fcc}) = -14\,640 + 8.123T$
$G^\circ(\text{U, bcc}) = -9142 + 6.492T$
$G^\circ(\text{Fe}_2\text{U}) = -25\,314 + 6.202T$
$G^\circ(\text{FeU}_6) = -26\,438 + 17.360T$
$G^{\text{ex}}(\text{U–Fe, liq}) = x_U(1 - x_U)(-38\,746 - 7\,736x_U)$

and U–32 at.% Zr–50 at.% Fe. The λ -phase decomposed at a temperature around 1000 K. The ε -phase was detected previously¹⁹⁵ and was confirmed later.¹⁹⁴ The thermodynamic assessment was performed by taking these data into consideration.¹⁹⁶ The assessed ternary isotherm at 988 K is shown in **Figure 58**, in which the three intermetallic compounds were modeled as stoichiometric compounds. The compositions were set to be U₃₀Zr₄₀Fe₃₀, U₃₀Zr₂₃Fe₆, and U₁₈Zr₃₂Fe₅₀ for the ε -, λ -, and χ -phases, respectively. The Gibbs energy of formation of these compounds was then estimated from the assessed phase relations to be $-1355 - 0.35T$, $-2380 + 0.225T$, and $+149 - 0.6T$ kJ mol⁻¹, for which the reference states are α -U, α -Zr, and α -Fe phases, respectively. The interaction between the U–Zr alloy and Fe was studied by Nakamura *et al.*¹⁹⁷ using diffusion couples. The diffusion path appeared to reasonably agree with the assessed U–Fe–Zr isotherms as shown in **Figure 59** but it changed in the temperature region between 923 and 973 K. In the low-temperature case, the two-phase region of UFe₂ and U₆Fe appear in the diffusion path, and in the high-temperature

region the two-phase region of UFe₂ and ZrFe₂ appear instead of UFe₂ and U₆Fe. The phase relation for the U–Pu–Fe system was also evaluated by experiments¹⁹⁸ and by thermodynamic modeling.⁸⁹ **Figure 60** summarizes the results. The phase relation between the M₆Fe and liquid phases is of particular importance for evaluating the FCCI to avoid liquefaction during the normal operation (details are discussed in another chapter). Thus, the interaction between U–Pu alloy and Fe was investigated by Nakamura *et al.*¹⁹⁹ The detected phases agree reasonably well with the above assessment. **Figure 61** shows the calculated phase relation for the U–Np–Fe system.⁷ A similar feature as that of the U–Pu–Fe system is speculated. The phase relations in the quaternary U–Pu–Zr–Fe system were evaluated by experiments²⁰⁰ and by thermodynamic modeling.⁸⁹ The mutual diffusion was studied using the diffusion couple of the U–Pu–Zr alloy and Fe.²⁰¹ The partial phase relation in the U–Pu–Fe–Zr quaternary system was constructed from these results, as shown in **Figure 62**. The observed diffusion path coincides well with the equilibrium phase relations even in the quaternary system.

In the actinide–Co or Ni system, the features of the phase diagrams vary from Th toward Pu due to the difference in the melting point of actinides. **Figures 63** and **64** compare the Th–Ni and Pu–Ni systems as an example. The Th–Ni phase diagram was assessed in Cirafici and Palenzona²⁰² based on the observations of Horn and Basserman¹⁷³ and Thomson,¹⁷⁴ in which seven kinds of the intermetallic compounds appear. The Pu–Ni phase diagram was assessed by Peterson⁶⁹ based on the observations of Konobeevsky¹⁷ and Wensch and Whyte,¹⁸³

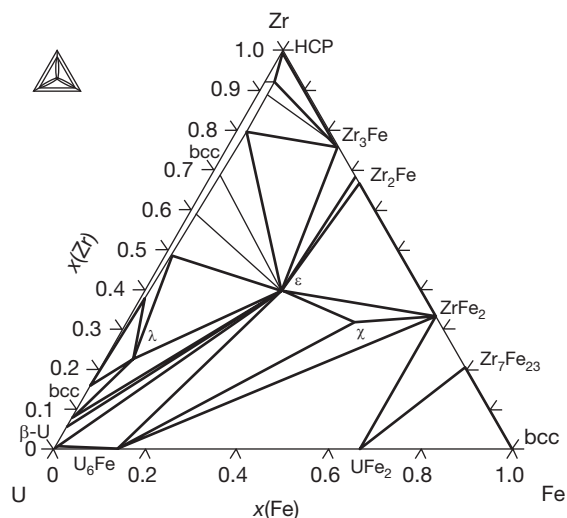
Table 17 Assessed interaction parameters for solution phases in Fe-containing system taken from Kurata⁷ (J mol⁻¹)

System phase	Fe-U ⁸⁹	Fe-Pu ⁸⁹	Fe-Zr ¹⁹³	Fe-Np	Fe-Am
Liquid	L ⁰ : -46 128 -0.13459T L ¹ : -11 776 L ² : 9258.5	L ⁰ : -35 332 +27.530T L ¹ : -8149.0 L ² : -4933.0	L ⁰ : -87 715 +18.690T L ¹ : -20 079 16.270T L ² : -13 743 L ⁰ : -42 807 +14.091T L ¹ : -8247.6	L ⁰ : -27 946 +16.436T L ¹ : -6112.2 L ² : 795.17	L ⁰ : -40 000 +30T L ¹ : -10 000 L ² : -5000
bcc	1204.5	L ⁰ : 13 000 L ¹ : 8500	L ⁰ : 15 300 L ¹ : 9000	15 000	
fcc	-3595.3	L ⁰ : 18 000 L ¹ : 3000	-48 766 +9.2932T	L ⁰ : 10 231 L ¹ : 9000	30 000
HCP	30 000	30 000	L ⁰ : -10 000 + 10T L ¹ : -25 298	30 000	30 000
α-U, β-U, α-Pu, β-Pu, γ-Pu, δ'-Pu, DHCP, η, ζ	30 000	30 000	30 000	30 000	30 000
α-Np, β-Np	30 000	30 000	30 000	10 000	30 000

L^v indicates the interaction parameter for Redlich–Kister polynomial.

System phase	Fe-U ^{89a}	Fe-Pu ^{89a}	Fe-Np ^a	Fe-Am ^a	Interaction parameter in actinide site
MFe ₂	-106 537 + 33.251T	-61 902 + 26.18T	-65 210 + 25.188T	-57 000 + 26T	20 000
β-PuFe ₂	-	-91 696 + 25.98T	-	-	-
γ-PuFe ₂	-	-61 435 + 25.78T	-	-	-
M ₆ Fe	-149 660 + 88.270T	-91 210 + 90.6T	-107 457 + 98.308T	-141 000 + 90T	30 000

^aReference state = liquid.

**Figure 58** U-Fe-Zr ternary isotherm at 988 K taken from Kurata *et al.*¹⁹⁶

in which six kinds of intermetallic compounds appear. The liquid phase exists in a rather low-temperature region in the Pu–Ni system and there are no Pu-rich intermetallic compounds, as compared to the Th–Ni system. This suggests an

asymmetric interaction for the Pu–Ni system. Possibly, far negative deviation from Raoult's law is speculated only for the Ni-rich region.

As for the actinide–Ru, Rh, or Pd phase relations, a systematic variation such as that seen in the actinide–Ni system is observed, with some exceptions. **Table 18** summarizes the intermetallic compounds in the actinide–Ru, Rh, or Pd systems as well as that in the actinide–Tc system. In case of Th, there are many similarities between the Th–Ru and Th–Rh systems. Relatively low eutectic points compared to the high melting points of Th (2028 K), Ru (2607 K), and Rh (2239 K) appear near the Th terminal, such as at 84 at.% Th (1535 K) and at 80 at.% Th (1510 K) for the Th–Ru and Th–Rh systems. Some intermetallic compounds have the same crystal structure, such as the Th₇Fe₃-type and the CrB-type. There is a stable Laves phase, such as the ThRu₂ and ThRh₂, and these melt congruently although the crystal structures of the Laves phase are different. These features are generally similar to those appearing in the Th–Ni system. The phase relations in the Pd-rich region of the Th–Pd system are, however, different from those in the Th–Ru and Th–Rh systems, although the Th-rich region shows some

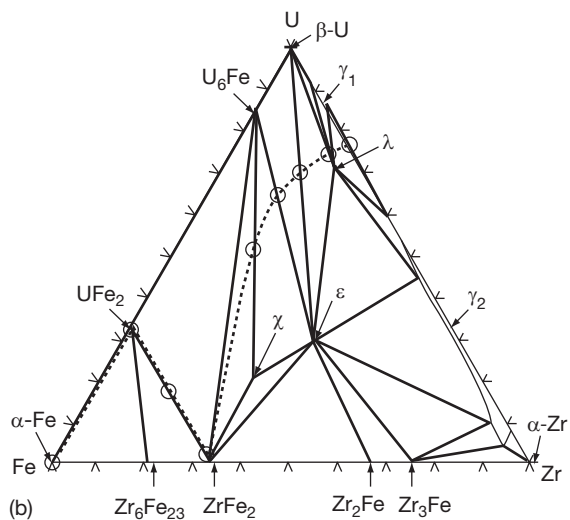
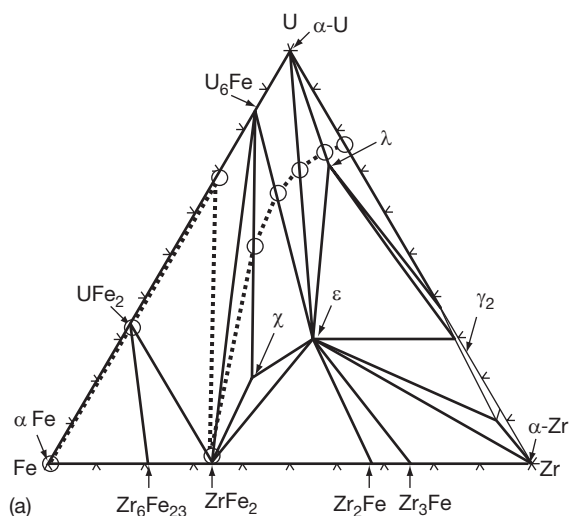


Figure 59 (a) U-Fe-Zr ternary isotherm at 923 K with the diffusion path observed in the U-Zr/Fe couple taken from Nakamura *et al.*¹⁹⁷ (b) U-Fe-Zr ternary isotherm at 973 K with the diffusion path observed in the U-Zr/Fe couple taken from Nakamura *et al.*¹⁹⁷

similarities. There is no Laves phase and significant solid solubility (14 at.% Th at the maximum) in the Pd-rich region of the Th-Pd system. In the case of U, some general similarities are still observed among the U-Ru, U-Rh, and U-Ni systems. There are several intermetallic compounds and relatively low eutectic points near the U terminal, such as 81.5 at.% U (1159 K), 75.5 at.% U (1128 K), and 67 at.% U (1013 K). There appears to be several percent of solid solubility of Ru or Rh in the γ -U (bcc structure). The phase relations in the U-Pd

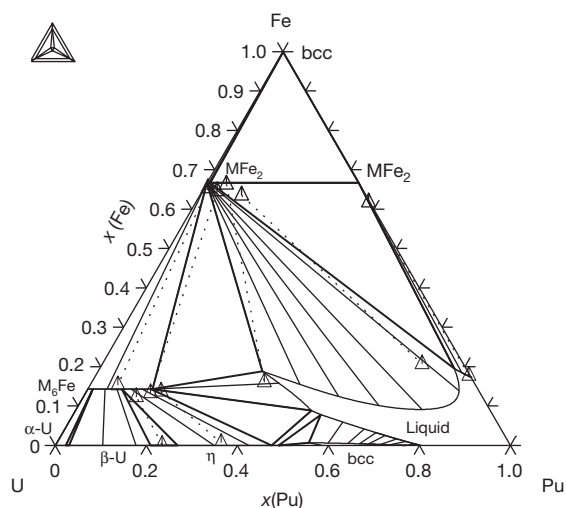


Figure 60 U-Pu-Fe ternary isotherm at 923 K taken from Kurata *et al.*,⁸⁹ and the experimental data taken from Nakamura *et al.*¹⁹⁸

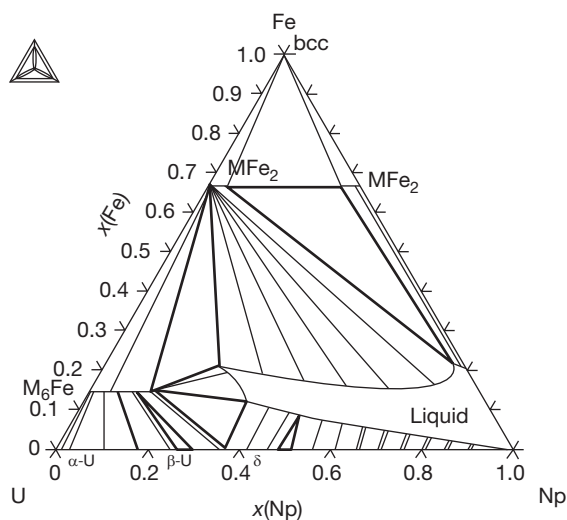


Figure 61 Expected U-Np-Fe ternary isotherm at 923 K taken from Kurata.⁷

system are rather different from those in the U-Ru and U-Rh systems, especially for the intermediate to the Pd-rich region. The solid solubility of U in Pd attains ~ 15 at.% U at the maximum. In the central region of the U-Pd phase diagram, two intermetallic compounds, that is, UPd and U_5Pd_6 , only exist in the very limited temperature region. According to Okamoto,¹⁹ however, there are still some unlikely situations in the presently suggested U-Pd phase diagram, such as the liquidus shape around UPd_3 , the relative relation between the liquidus and solidus

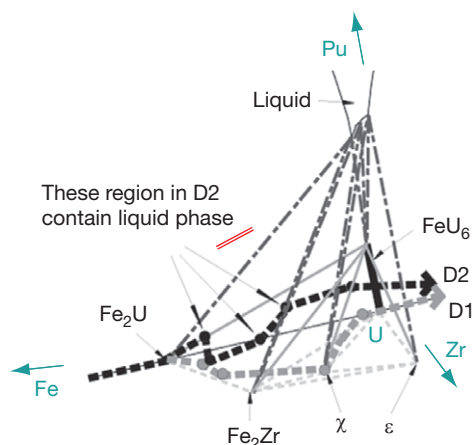


Figure 62 Relationship between diffusion path between U–Pu–Zr and Fe against U–Pu–Fe–Zr phase diagram at 923 K taken from Ogata *et al.*²⁰¹

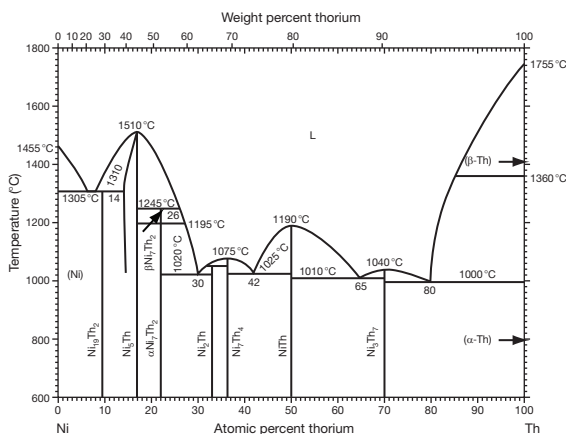


Figure 63 Th–Ni phase diagram taken from Okamoto.⁴

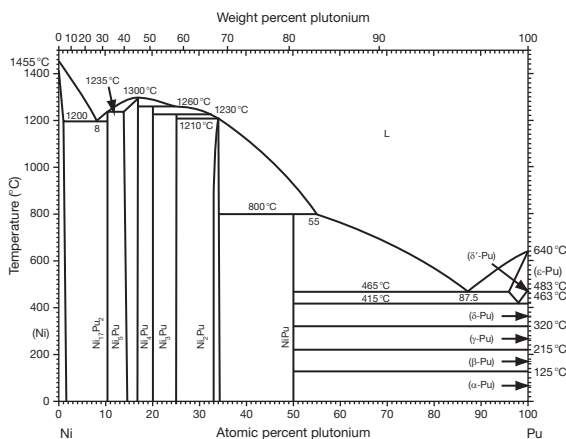


Figure 64 Pu–Ni phase diagram taken from Okamoto.⁴

near the Pd-terminal, and the crystal structure of UPd_8 . In case of Pu, the phase relations observed in the Pu–Ru and Pu–Rh systems are generally similar to those in the Pu–Ni system with some exceptions, such as the structure of the intermetallic compounds, the existence of the Pu_{19}Ru , etc. The general feature of the Pu–Pd system is similar to that of the U–Pd system. Figure 65 shows the Pu–Rh phase diagram as a typical example quoted from Okamoto,⁴ which was redrawn from the works of Land *et al.*²¹³ Significant degrees of the Gibbs energy of formation for the intermetallic compounds between actinide and these noble metals are expected from a general view of the phase diagrams. From the viewpoint of the phase stability in nuclear fuels under irradiation, the intermetallic compounds mostly rich in Ru, Rh, or Pd are of particular importance among these compounds (a detailed discussion is given in other chapters). These noble metals are observed to precipitate in the irradiated nuclear fuels and possibly contain a small amount of actinide from the fuel matrix. Unfortunately, the thermodynamic quantities of these compounds are not known.

The actinide–Os, Ir, or Pt phase relations are expected to be similar to those in the actinide–Ru, Rh, or Pd systems. Table 19 summarizes the intermetallic compounds in the actinide–Os, Ir, or Pt systems as well as those in the actinide–Re system. In case of Th, the general views of the phase relations of Th–Os, Th–Ir and Th–Pt are similar to those of Th–Ru, Th–Rh, and Th–Pd, respectively. Several intermetallic compounds have the same crystal structures. They are predicted to be thermodynamically stable and exist even at high temperatures. A similar tendency is also expected for the U- and Pu-related systems. In the actinide–Pt systems, the number of the intermetallic compounds generally is a maximum. The thermodynamic functions for the actinide–Pt systems were evaluated in Miedema,³⁹ Gingerich,²²⁶ Schmidt,²²⁷ Mobius,²²⁸ Peterson,²²⁵ and Mobius *et al.*,²²⁹ and given in Table 20, the values of which were determined mainly from EMF measurements. Although the values are scattered, the significant negative deviation is confirmed for the phase relation between actinides and Pt. Similar deviation is also expected for the relation between the actinides and the other noble metals, such as Ru, Rh, Pd, Os, and Ir.

Regarding Pa, Np, Am, and Cm, there are limited experimental observations. The high stabilization for the intermetallic compounds is speculated on in the phase relations between these actinides and Pt as well as Th, U, and Pu.

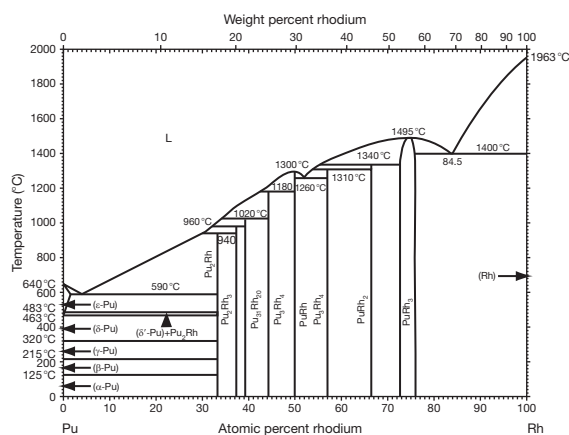
Table 18 Intermetallic compounds between actinide and Tc, Ru, Rh, or Pd

Group Element	VIIa	VIII		
	Tc	Ru	Rh	Pd
Th	ThTc ₂ (MgZn ₂ -type)	Th ₇ Ru ₃ (Th ₇ Fe ₃ -type) Th ₃ Ru ₂ (ND) ThRu (CrB-type) ThRu ₂ (Cu ₂ Mg-type)	Th ₇ Rh ₃ (Th ₇ Fe ₃ -type) ThRh (CrB-type) Th ₃ Rh ₄ (ND) Th ₃ Rh ₅ (ND) α-ThRu ₂ (ND) β-ThRu ₂ (Ni ₂ In-type) ThRu ₃ (AuCu ₃ -type) ThRu ₅ (ND)	Th ₂ Pd (Al ₂ Cu-type) ThPd (FeB-type) Th ₃ Pd ₄ (ND) Th ₃ Pd ₅ (Th ₃ Pd ₅ -type) ThPd ₃ (Ni ₃ Ti-type) ThPd ₄ (AuCu ₃ -type) Th ₃ Pd ₁₃ (ND)
Pa ^a	165 NA	203 NA	203 PaRh ₃ (AuCu ₃ -type)	204,205 NA
U	U ₂ Tc (ND.) UTc ₂ (ND)	U ₂ Ru (U ₂ Ru-type) URu (ND) U ₃ Ru ₄ (ND) U ₃ Ru ₅ (ND) URu ₃ (AuCu ₃ -type)	U ₄ Rh ₃ (ND) U ₃ Rh ₄ , (ND) U ₃ Rh ₅ (ND) URh ₃ (AuCu ₃ -type)	UPd (ND) U ₅ Pd ₆ (ND) UPd ₃ (Ni ₃ Ti-type) UPd ₄ (AuCu ₃ -type) UPd ₈ (ND)
Np ^a	165 NA	207 NpRu ₂ (MgZn ₂ -type)	208 NpRh ₃ (AuCu ₃ -type)	209,210 α-NpPd ₃ (Ni ₃ Ti-type) β-NpPd ₃ (AuCu ₃ -type)
Pu	— NA	169 Pu ₁₉ Ru, (ND) Pu ₃ Ru (ND) Pu ₅ Ru ₃ (W ₅ Si ₃ -type) PuRu (CsCl-type) PuRu ₂ (Cu ₂ Mg-type)	206 Pu ₂ Rh (ND) Pu ₅ Rh ₃ (ND) Pu ₃₁ Ru ₂₀ (Pu ₃₁ Ru ₂₀ -type) Pu ₅ Rh ₄ (Sm ₅ Ge ₄ -type) PuRh (ND) Pu ₃ Rh ₄ (ND) PuRh ₂ (ND) PuRh ₃ (ND)	206,211 Pu ₅ Pd ₄ (ND) PuPd (FeB-type) Pu ₄ Pd ₅ (ND) PuPd ₃ (AuCu ₃ -type)
Am ^a	— NA	212 AmRu ₂ (MgZn ₂ -type)	213 AmRh ₂ (Cu ₂ Mg-type) AmRh ₃ (AuCu ₃ -type)	212 AmPd ₃ (AuCu ₃ -type)
Cm ^a	— NA	184 NA	206 CmRh ₃ (AuCu ₃ -type)	206 CmPd ₃ (AuCu ₃ -type)
	—	—	206	206

^aAccording to systematic similarity, other intermetallic compounds are expected in the Pa-, Np-, Am-, and Cm-related systems.

NA: there is no available information.

ND: the crystal structure is not determined yet.

**Figure 65** Pu–Rh phase diagram taken from Okamoto.⁴

2.05.3.7 Actinide: Group Ib and IIb Metals

Various kinds of intermetallic compound appear in the phase diagrams between Th and Group Ib or IIb metals, like those existing in the phase diagrams

between Th and Group VIII metals. A gradual decrease in the decomposition temperature for these intermetallic compounds is observed from VIII toward Group IIb metals, in general. **Figures 66–68** indicate the typical examples, which compare among the Th–Pd, Th–Ag, and Th–Cd phase diagrams. These figures were given in Okamoto,⁴ in which they were redrawn mainly from Thomson,²⁰⁴ Terekhov *et al.*,²⁰⁵ Raub and Engel,²³⁰ Baren,²³¹ and Bates *et al.*,²³² Palenzona and Cirafici,²³³ and Dutkiewicz,²³⁴ respectively. A gradual decrease in the relative stability of these intermetallic compounds is speculated by observing the figures. Regarding the Th–Cd system, the enthalpy of solution of ThCd₁₁ in the liquid phase, $-90.5 \text{ kJ mol}^{-1}$, was derived from the slope of the solubility.²³⁵ A similar tendency is seen in the Pu-related systems and possibly the Np-related systems. In the case of the U-related systems, the decrease in stability appears more distinctly. **Figures 69** and **70** show the U–Pd and U–Ag phase diagrams given in Okamoto,⁴ which were redrawn

Table 19 Intermetallic compounds between actinide and Re, Os, Ir, or Pt

Group Element	VIIa	VIII		
	Re	Os	Ir	Pt
Th	ThRe ₂ (MgZn ₂ -type)	Th ₇ Os ₃ (Th ₇ Fe ₃ -type) ThOs _x , (ND) ThOs ₂ (Cu ₂ Mg-type)	Th ₇ Ir ₃ (Th ₇ Fe ₃ -type) Th _x Ir (ND) ThIr (CrB-type) ThIr ₂ (Cu ₂ Mg-type) ThIr ₃ (ND) ThIr ₅ (CaCu ₅ -type)	Th ₇ Pt ₃ (Th ₇ Fe ₃ -type) ThPt (CrB-type) Th ₃ Pt ₄ (ND) Th ₃ Pt ₅ (Th ₃ Pd ₅ -type) ThPt ₂ (ND) ThPt ₃ (ND) ThPt ₄ (ND) ThPt ₅ (SmPt ₅ -type)
Pa ^a	155 NA	214,215 NA	214,215 NA	214 PaPt ₃ (Ni ₃ Sn-type) PaPt ₅ (AuBe ₅ -type) 206,216
U	— U ₂ Re, (ND) α-URE ₂ (ND) β-URE ₂ (MgZn ₂ -type) 155,161	— U ₃ Os (ND) U ₂ Os (ND) U ₅ Os ₄ (ND) UOs ₂ (Cu ₂ Mg-type)	— U ₃ Ir (ND) U ₃ Ir ₂ (ND) UIr (ND) UIr ₂ (Cu ₂ Mg-type) UIr ₃ (AuCu ₃ -type)	UPT (CrB-type) UPT ₂ (Ni ₂ In-type) UPT ₃ (Ni ₃ Sn-type) UPT ₅ (Ni ₅ U-type)
Np ^a	NpRe ₂ (MgZn ₂ -type) 169	NpOs ₂ (MgZn ₂ -type) 217	NpIr ₂ (Cu ₂ Mg-type) 218–220	NpPt (CrB-type) NpPt ₃ (Ni ₃ Ti-type) NpPt ₅ (TmPt ₅ -type) 206,216,222
Pu	PuRe ₂ (MgZn ₂ -type)	α-Pu ₁₉ Os (ND) β-Pu ₁₉ Os (ND) α-Pu ₃ Os (ND) β- Pu ₃ Os (ND) Pu ₅ Os ₃ (W ₅ Si ₃ -type) PuOs ₂ (MgZn ₂ -type) 169	Pu ₃ Ir (ND) Pu ₅ Ir ₃ (W ₅ Si ₃ -type) Pu ₅ Ir ₄ (ND) PuIr ₂ (Cu ₂ Mg-type) 169	Pu ₂ Pt (Co ₂ Si-type) Pu ₅ Pt ₃ (Mn ₅ Si ₃ -type) Pu ₃₁ Pt ₂₀ (Pu ₃₁ Ru ₂₀ -type) PuPt (CrB-type) PuPt ₂ (Cu ₂ Mg-type) κ-PuPt ₃ (AuCu ₃ -type) κ'-PuPt ₃ (Ni ₃ P-type) κ''-PuPt ₃ (ND) PuPt ₄ (PuPt ₄ -type) PuPt ₅ (Pt ₅ Sm-type) 101,213,225
Am ^a	146 NA	17 AmOs ₂ (Cu ₂ Mg-type)	223,224 AmIr ₂ (Cu ₂ Mg-type)	Am ₇ Pt ₃ (ND) Am ₃ Pt ₂ (ND) AmPt (ND) Am ₃ Pt ₄ (ND) AmPt ₂ (Cu ₂ Mg-type) AmPt ₅ (CaCu ₅ -type) 69
Cm ^a	— NA	169 NA	206 NA	Cm ₃ Pt (ND) Cm ₇ Pt ₃ (ND) Cm ₂ Pt (ND) Cm ₅ Pt ₃ (ND) CmPt (ND) Cm ₃ Pt ₄ (ND) CmPt ₂ (Cu ₂ Mg-type) CmPt ₅ (SmPt ₅ -type) 69
	—	—	—	69

^aAccording to systematic similarity, other intermetallic compounds are expected in the Pa-, Np-, Am-, and Cm-related systems.

NA: There is no available information.

ND: The crystal structure is not determined yet.

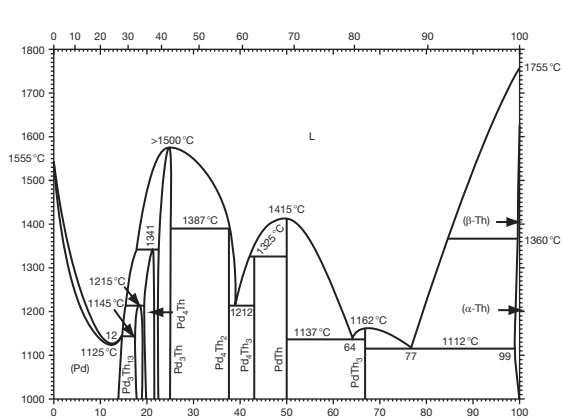
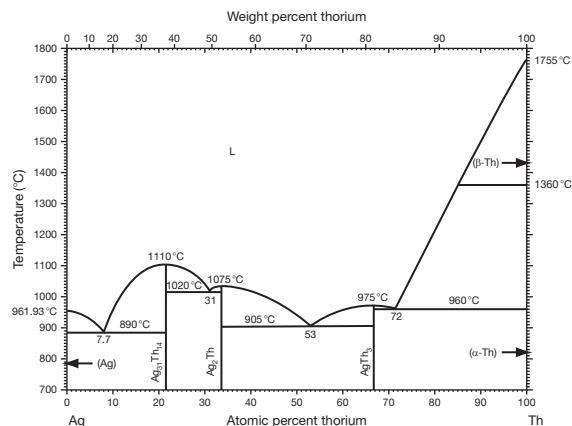
mainly from Catterall *et al.*,²⁰⁹ Pells,²¹⁰ Terekhov *et al.*,²³⁸ and Buzzard *et al.*,²³⁹ respectively. Figure 71 shows the assessed U–Cd phase diagram for the Cd-rich region given in Kurata and Sakamura,²³⁶ based on the work of Martin *et al.*²³⁷ Although there are several intermetallic compounds in the Pd-rich region of the U–Pd phase diagram, there is no compound in the U–Ag system, and only U₁₁Cd exists in the U–Cd system.

The actinide–Cd phase diagrams are particularly important when considering the pyrometallurgical reprocessing of the spent nuclear metal fuels. Thermodynamic evaluation on the actinide-rich region of the U–Cd, Np–Cd, and Pu–Cd systems was

performed in Kurata and Sakamura.^{236,240} Table 21 summarizes the assessed results, in which the Gibbs energy of formation of the intermetallic compounds is determined from the activity of actinide in the liquid Cd phase. The values were evaluated from the previous EMF measurements,^{242,243} with the exception of U₁₁Cd. The values for U₁₁Cd were given by Barin.²⁴¹ Figures 72 and 73 show the assessed Np–Cd and Pu–Cd phase diagrams of the actinide-rich region in which the solubility data of Krumpelt *et al.*²³⁵ and Johnson *et al.*²⁴³ are reasonably plotted on the calculated phase boundary. The data are in good agreement with each other. Using these evaluated data, the ternary isotherm of the U–Pu–Cd

Table 20 Thermodynamic functions for the actinide–Pt systems

Compound	Enthalpy of formation (kJ mol^{-1})	Entropy of formation ($\text{J mol}^{-1} \text{K}^{-1}$)	Gibbs energy of formation (kJ mol^{-1})	Temperature (K)	References
ThPt ₅	-560.5 ± 25	-67.5 ± 11		1323–1673	229
			–459	1500	229
			–419 to –481	1500	227
ThPt			–546.6	1773	226
UPt ₂	–380			1500	229
	–382	–46	–314	1500	227
UPt ₃	–440	–54	–359	1500	229
	–444	–54	–359	1500	227
UPt ₅	–485	–54	–408	1500	229
	–490	–55	–408	1500	227
NpPt ₃	–321	–35	–268	1500	229
			–272 to –314	1500	227
NpPt ₅	–310	–16	–287	1500	229
			–293 to –335	1500	227
PuPt ₂	-211.4 ± 18.5	-46.0 ± 11.1	-136 ± 20	1629	225
	–240			298	39
			–251 to –293	1200	227
PuPt ₃	–430			1400	229
	-246.9 ± 13.1	-61.0 ± 8.1	-167 ± 15	1579	225
	–252			298	39
			–293 to –335	1200	227
PuPt ₄	-272.8 ± 31.0	-70.8 ± 19.0	-162 ± 35	1596	225
	–260			298	39
PuPt ₅	–470			1400	229
	-299.9 ± 27.6	-85.7 ± 16.8	-162 ± 30	1614	225
			–314 to –377	1200	227
	–252			298	39
AmPt ₂	–413	–58	–326	1500	229
			–188 to –230	1500	227
AmPt ₅	–439	–48	–367	1500	229
			–251 to –293	1500	227

**Figure 66** Th–Pd phase diagram taken from Okamoto.⁴**Figure 67** Th–Ag phase diagram taken from Okamoto.⁴

system was predicted by Kurata *et al.*²⁴⁴ Figure 74 shows the calculated ternary isotherm of the U–Pu–Cd system at 773 K with the experimental observations given in Kato *et al.*²⁴⁵ and Uozumi

*et al.*²⁴⁶ in which the mixture of U and Pu was recovered in a liquid Cd cathode by electrolysis and then the cross section of the solidified Cd was analyzed by SEM-EDX after quick cooling. Two

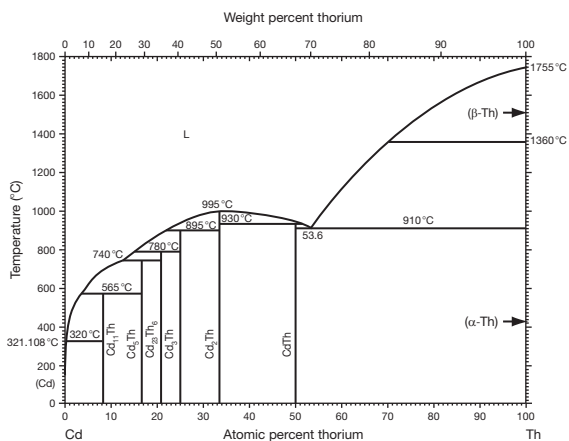


Figure 68 Th-Cd phase diagram taken from Okamoto.⁴

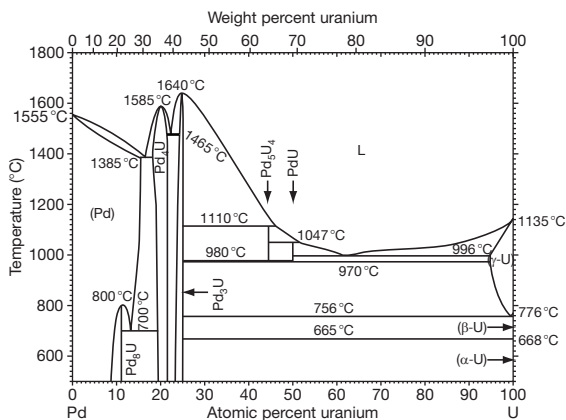


Figure 69 U-Pd phase diagram taken from Okamoto.⁴

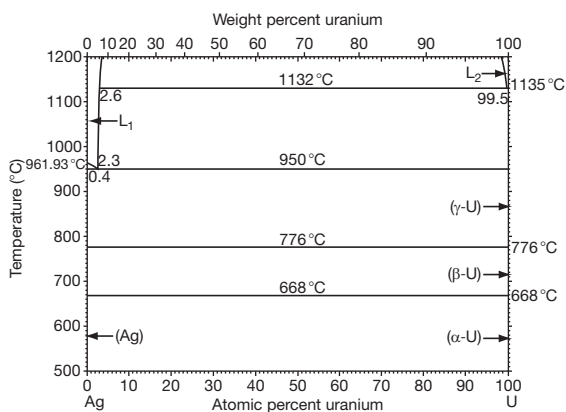


Figure 70 U-Ag phase diagram taken from Okamoto.⁴

or three different phases were detected in the samples. The open circle in the figure indicates the average composition of the liquid Cd cathode, and the black solid circle indicates the composition of

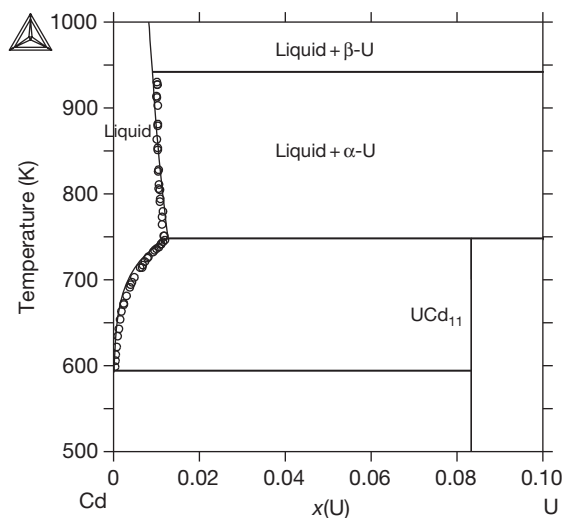


Figure 71 Calculated U-Cd phase diagram taken from Kurata and Sakamura,²³⁶ and the experimental data taken from Martin *et al.*²³⁷

Table 21 Assessed interaction parameters for U-Cd, Np-Cd, and Pu-Cd systems

$G^{\circ}(\text{U}, \text{liq})$, $G^{\circ}(\text{Np}, \text{liq})$, $G^{\circ}(\text{Pu}, \text{liq})$, $G^{\circ}(\text{Cd}, \text{liq})$: given in Dinsdale⁶⁷

$$G^{\text{ex}}(\text{Cd-U}, \text{liq}) = x_{\text{U}}(1 - x_{\text{U}}) (-22\,220 + 60.57T)$$

$$G^{\text{ex}}(\text{Cd-Np}, \text{liq}) = x_{\text{Np}}(1 - x_{\text{Np}}) (-84\,856 + 73.34T)$$

$$G^{\text{ex}}(\text{Cd-Pu}, \text{liq}) = x_{\text{Pu}}(1 - x_{\text{Pu}}) (-77\,167 + 63.38T - 30\,413(x_{\text{Cd}} - x_{\text{Pu}}))$$

$$G^{\text{form}}(\text{UCd}_{11}) = -154.6 + 1.643T - 0.3278T \ln T - 0.00002688T^2 + 1328/T: \text{ given in Barin}^{241}$$

$$G^{\text{form}}(\text{NpCd}_{11})^a = -175.9 + 0.162T$$

$$G^{\text{form}}(\text{PuCd}_{11})^a = -192.0 + 0.149T$$

$$G^{\text{form}}(\text{NpCd}_6)^a = -106.3 + 0.071T$$

$$G^{\text{form}}(\text{PuCd}_6)^a = -164.3 + 0.108T$$

Source: Kurata, M.; Sakamura, Y. *J. Phase Equil.* **2001**, 22(3), 232–240; Kurata, M.; Sakamura, Y. *J. Nucl. Sci. Technol.* **2002**, (Suppl. 3), 607–610.

^aThe reference state is a liquid phase.

the various phases detected. Some unique features appear in the isotherm. Although both the UCd_{11} and the PuCd_{11} decompose at 773 K in the U–Cd and Pu–Cd binary systems, respectively, they stabilize and exist in the intermediate region between these two compounds. Also, there is limited U solubility in PuCd_6 . By assuming a hypothetical Gibbs energy of formation for UCd_6 , the calculated results reasonably overlap with the experimental observations. The phase diagram of lanthanides–Cd system was evaluated from the available experimental information in Kurata and Sakamura.²³⁶ The activity coefficient for lanthanides in the liquid Cd was far

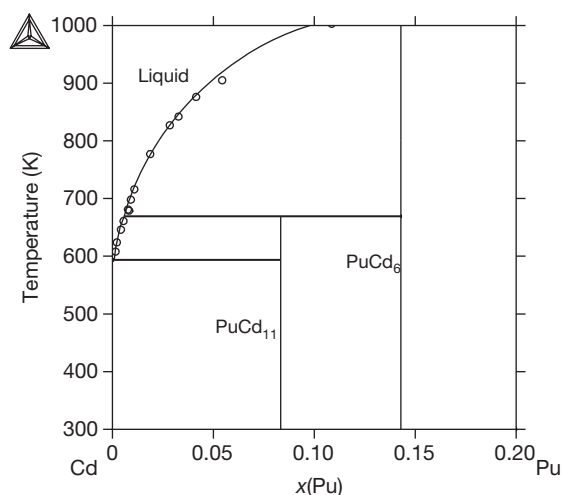


Figure 72 Calculated Pu–Cd phase diagram taken from Kurata and Sakamura,²³⁶ and the experimental data taken from Krumpelt *et al.*²³⁵

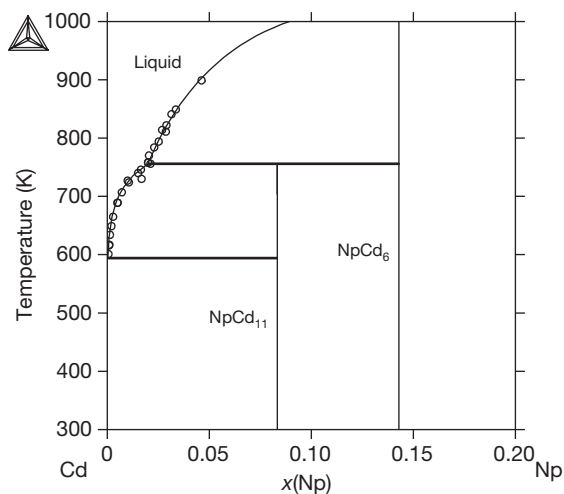


Figure 73 Calculated Pu–Cd phase diagram taken from Kurata and Sakamura,²⁴⁰ and the experimental data taken from Johnson *et al.*²⁴³

smaller than that for actinides, by a few orders. This may suggest that further stabilization appears in the Am–Cd or Cm–Cd systems compared to U–Cd, Np–Cd, and Pu–Cd systems. This stabilization for the Am, Cm, or lanthanides prevents not only the separation from U, Np, or Pu but also the separation among Am, Cm, and lanthanides.

The phase diagrams between actinides and Zn have features similar to those between actinide and Cd. However, the phase diagrams between actinides and Hg are completely different from those between actinides and Cd or Zn. The liquid phase is

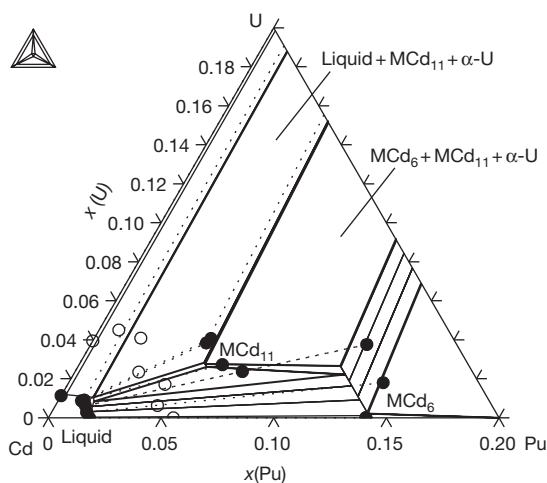


Figure 74 U–Pu–Cd ternary isotherm at 773 K taken from Kurata *et al.*,²⁴⁴ and the experimental data taken from Kato *et al.*²⁴⁵ and Uozumi *et al.*²⁴⁶ ○: average composition of liquid cadmium cathodes, ●: composition of each phase detected in liquid cadmium cathodes.

significantly stabilized in the Hg-related system, and various intermetallic compounds decompose at very low temperatures.

2.05.3.8 Actinide: Group IIIb Metals

As for the phase relations in the actinide–Group VIIIb metal systems, the phase diagrams between actinide and Al are of particular importance. The phase diagrams of Th–Al, U–Al, and Pu–Al were previously compiled in Kassner and Peterson¹ and Okamoto.⁴ The Al-rich sides of the actinide–Al system look similar to each other. An intermetallic compound AnAl_2 covers a large area and congruently melts at the highest temperature in both the systems. A peritectic phase relation is observed among AnAl_2 , AnAl_3 , and liquid and then among AnAl_3 , An_xAl_y , and liquid ($x=0.9$ and $y=4$ in the U–Al and Pu–Al systems and $x=2$ and $y=7$ in the Th–Al system). Concerning the crystal structure of these intermetallic compounds, there is similarity between the U–Al and Pu–Al systems (possibly the Np–Al system). UAl_2 and the PuAl_2 are Laves phases (the prototype is Cu_2Mg) and UAl_3 and PuAl_3 have a AuCu_3 -type structure. ThAl_2 and the ThAl_3 have different type structures, that is, the AlB_2 - and Ni_3Sn -types, respectively. The UAl_2 and the PuAl_2 phases dominate a large area in the phase diagrams and melt congruently at ~ 1893 and 1813 K, respectively. As for UAl_4 , there are some inconsistencies among the

previous experimental observations.^{186,247–249} According to Kassner and Peterson,¹ reasonable phase relations can be drawn by assuming unoccupied U sites and a variable stoichiometry. Kassner and Peterson¹ reassessed the phase relations around the previously named ‘PuAl₄’ compound by referring to previous studies in Bochvar *et al.*,¹¹⁶ Moeller and Schonfield,²⁵⁰ Grison,²⁵¹ Ellinger *et al.*,²⁵² Runnals and Boucher,²⁵³ and Runnals.²⁵⁴ They pointed out that the composition is near ‘Pu_{0.9}Al₄’ due to a large vacancy concentration in the Pu site. In the Al-rich region of the Th–Al phase diagram, Th₂Al₇ appears instead of U_{0.9}Al₄ or Pu_{0.9}Al₄.²⁵⁵ Regarding the actinide solubility in the solid Al phase, the values are 0.8 at.% Th,⁷² 0.007 at.% U,²⁵⁶ and 0.0056 at.% Pu²⁵⁶ at the maximum. On the other hand, the phase relations in the actinide-rich side vary largely with the difference in actinides. There are several intermetallic compounds in the Th–Al and Pu–Al systems, although no compound is observed in the U-rich side of the U–Al system. This might suggest that, in the U–Al system, an asymmetric variation in the Gibbs energy of mixing appears with the composition. The Al solubilities in the solid phase of each actinide allotrope are 0.85 at.% Al in α -Th,⁷² 0.54 at.% Al in β -U,²⁵⁷ 4.7 at.% Al in γ -U,²⁵⁷ 1 at.% Al in γ -Pu,¹¹⁶ 14.5 at.% Al in δ -Pu,¹¹⁶ 1 at.% Al in δ' -Pu,²⁵⁸ and 13 at.% Al in ϵ -Pu.¹¹⁶ Regarding the other U and Pu allotropes, the Al solubilities are negligibly small.

Figure 75 shows the U–Al phase diagram quoted from Okamoto,⁴ which was compiled mainly from Gordon and Kaufmann,¹⁸⁶ Runnals and Boucher,²⁴⁸ Chiotti and Kateley,²⁴⁹ and Storvok *et al.*²⁶⁰ Recently, the U–Al system was assessed using CALPHAD²⁶¹ and

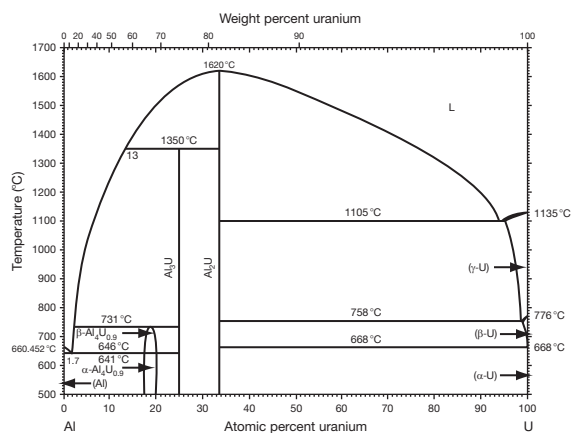


Figure 75 U–Al phase diagram taken from Sedmidubsky *et al.*²⁵⁹

using *ab initio* approaches.²⁵⁹ These calculations agree reasonably well with the experimental data points. A partial phase relation for the U–Al–Fe ternary system was also given by Russell.²⁶² Regarding the Np–Al system, partial experimental information on the intermetallic compounds was given by Runnals²⁶³ from their thermal analysis. The calculated Np–Al phase diagram was given by Sedmidubsky *et al.*²⁵⁹ using the *ab initio* approach. Figure 76 shows their results. The general shape of the Np–Al phase diagram is quite similar to that of the U–Al phase diagram.

The details for the Pu-rich region of the Pu–Al system were recently reviewed,²⁶⁴ in which the unique features of the δ -Pu phase were fully discussed. The previously compiled Pu–Al phase diagram was constructed mainly from the experimental observations,^{116,248,252,253,258} among which those of Bochvar *et al.*¹¹⁶ indicate that δ -Pu is stabilized by adding Al, which then undergoes eutectoid decomposition at about 448 K to form β -Pu and Pu₃Al. However, their results were not taken into consideration for the previous Pu–Al phase diagram due to conflicts against other experimental data, in which the eutectoid decomposition was not seen. The experimental data on the eutectoid decomposition for δ -Pu was shown in Hecker and Timofeeva²⁶⁴ and Timofeeva,²⁶⁵ and the value is about 363 K. The assessment for the Pu–Al system using the CALPHAD approach was then made.²⁶⁶ Figure 77 shows the newly constructed Pu–Al phase diagram, from which the eutectoid decomposition temperature of δ -Pu is estimated to be 368 K. The ternary phase relation of the Pu–Al–Fe system was also given by Turchi *et al.*²⁶⁶ The effect of pressure and temperature on the kinetics of the δ -Pu phase decomposition was fully discussed by Timofeeva.²⁶⁷

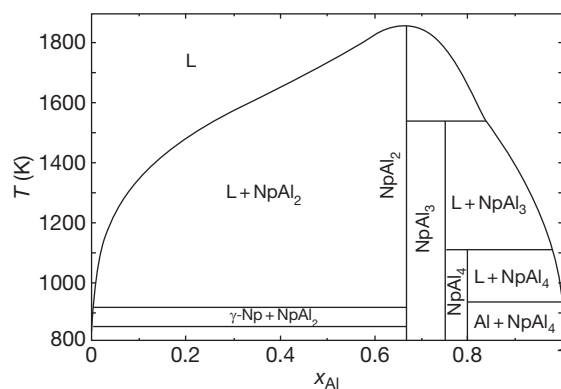


Figure 76 Np–Al phase diagram taken from Sedmidubsky *et al.*²⁵⁹

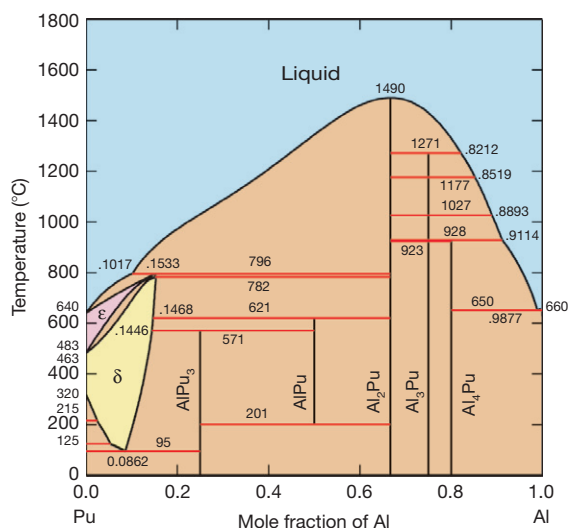


Figure 77 Newly assessed Pu–Al phase diagram taken from Turchi *et al.*²⁶⁶

Many attempts have been made to determine the thermodynamic parameters for the actinide–Al systems. [Table 22](#) summarizes the results.

Regarding the other IIIb metals, such as Ga, In, and Tl, the phase diagrams for the U–Ga, Pu–Ga, Th–In, Pu–In, and Th–Tl systems were compiled and partial information on the U–In system was given by Okamoto.⁴ Although there is no available data for the Th–Ga, U–Tl, and Pu–Tl systems, many similarities are seen between the actinides–Al and the actinides–Ga systems. On the other hand, the general views of the actinides–In and the actinides–Tl are different from those of actinides–Al and the actinides–Ga. The general view of the U–Ga phase relations is similar to that of the U–Al system but nevertheless, the crystal structures of some intermetallic compounds are different from each other. The most stable intermetallic compound, UGa_2 , melts congruently at around 1628 K. A eutectic reaction is seen in the U-rich region. There is solid solubility of several percent of Ga in the γ -U phase. However, there are conflicting reports on the composition of some intermetallic compounds. Makarov *et al.*²⁷⁶ and Dayan *et al.*²⁷⁷ reported the existence of UGa and U_5Ga_3 and, on the other hand, Buschow²⁷⁸ reported the existence of UGa_3 , UGa_2 , and U_2Ga_3 alternatively. The general view of the Pu–Ga phase relation is also similar to that of the Pu–Al system. There are many intermetallic compounds. The mostly stable Laves phase, PuGa_2 , melts congruently at around 1537 K. The previously assessed Pu–Ga phase diagram shown

in Kassner and Peterson¹ and Okamoto⁴ was compiled mainly from the experimental observations.^{279–281} The details for the Pu-rich region of the Pu–Ga system were reviewed in Hecker and Timofeeva,²⁶⁴ especially for the eutectoid decomposition of the δ -Pu phase as seen in the Pu–Al system. The eutectoid decomposition temperature was then estimated to be about 368 K by extrapolating the phase boundaries.^{264,265}

An assessment for the Pu–Ga system using the CALPHAD approach was performed.²⁶⁶ [Figure 78](#) shows the newly assessed Pu–Ga phase diagram, in which the eutectoid decomposition temperature of the δ -Pu is calculated to be 331 K. Turchi *et al.*²⁶⁶ also predicted the ternary phase relation among Pu, Ga, and Fe. The thermodynamic functions for the Pu–Ga alloy and for the Pu–Ga intermetallic compounds are given in [Table 23](#). A part of these previous data is inconsistent with the newly assessed phase diagram. The unique feature observed for the δ -Pu phase in the Pu–Al and Pu–Ga systems is not seen in the Pu–In and Pu–Tl systems.⁴ Also, the stable Laves phase does not appear in the actinide–In and actinide–Tl systems.

2.05.3.9 Actinide: Other Group b Metals or Semimetals

The general view on the phase diagram between actinides and Sn or Pb is slightly different from that between actinides and Al or Ga. Several intermetallic compounds with the same composition between actinide and the Group b metal appear in those phase diagrams, although some of the crystal structures are different from each other. The crystal structure of the Laves phase formed between actinides and Group b metals is summarized in [Table 24](#). In the actinide–Al or actinide–Ga systems, the typical Laves phases with the structure of AlB_2 or Cu_2Mg appear, with the exception of ThGa_2 . The Laves phase is the most stable compound in those systems and melts congruently. In the actinide–Sn systems, however, the Laves phase has different structures and decomposes with the peritectic reaction. In the Th–Pb and Pu–Pb systems, the phase relations are roughly similar to those in the actinide–Sn systems, although the crystal structure for the Laves phase is unknown. The general view of the U–Pb system is different from that of the Th–Pb and Pu–Pb systems, especially for the U-rich region. [Figure 79](#) shows the U–Pb phase diagram compiled by Okamoto,⁴ which was based mainly on Teitel,²⁸⁴ Frost and Maskrey,²⁸⁵ and Teitel.²⁸⁶ There are two intermetallic compounds

Table 22 Thermodynamic functions for actinide–Al systems

Compound	Enthalpy of formation (kJ mol^{-1})	Entropy of formation ($\text{J mol}^{-1} \text{K}^{-1}$)	Gibbs energy of formation (kJ mol^{-1})	Temperature (K)	References
Th_2Al_7			–142.8 –343.2 + 0.066T –418.8 + 0.148T	903 298–933 933–1149	268 191 191
ThAl_3			–108.5 –131.8 –132.6 + 0.005T –165.0 + 0.039T	1323 1323 298–933 933–1273	269 270 191 191
UAl_2	–92.5 ± 8.4 –99.6 ± 5.4 –93.3 ± 10.0 –86.1	–1.1	–86.6 + 0.00089T –113.0 + 0.0259T –123.9 + 0.026T ^b –142.2 + 0.0565T ^b	298 298 298 674–912 913–1003	249 271 272 259 ^a 249 1 273 1
UAl_3	–108.4 ± 8.4 –105.4 ± 0.2 –87.0	–13.1	–105.4 + 0.00204T –117.6 + 0.0223T –161.5 + 0.062T ^b –157.5 + 0.0645T ^b	298 298 674–912 913–1003	249 272 259 ^a 249 1 273 1
UAl_4	–124.7 ± 8.4 –130.5 ± 0.2 –91.4		–109.0 + 0.00469T –118.8 + 0.0223T –173.6 + 0.074T ^b –169.5 + 0.0760T ^b	298 298 674–912 913–1003	249 272 259 ^a 249 1 273 1
NpAl_2	–110.2	–2.3			259 ^a
NpAl_3	–122.9	–12.1			
NpAl_4	–105.6	–8.1			
Pu_3Al			–73.3 ± 10.5	843	191,274
PuAl			–64.9 ± 8.4	843	191,274
PuAl_2	–142 ± 3 –159.2	–1.4	–145.0 + 0.0285T ± 12.6	750–900 298	191,274 275 259 ^a
PuAl_3	–181 ± 3		–183.5 + 0.048T ± 8.4	750–900 298	191,274 275 259 ^a
$\text{PuAl}_3\text{–}3\text{H}$	–169.1	–10.4			
$\text{PuAl}_3\text{–}6\text{H}$	–172.4				
$\text{PuAl}_3\text{–}9\text{H}$	–174.3				
PuAl_4	–181 ± 3 –154.7		–183.6 + 0.0417T ± 4.2	750–900 298	191,274 275 259 ^a

^aAb initio calculation.^bReference states: γ -U and liq-Al.

UPb_3 and UPb , although there is a miscibility gap for the liquid phase even at high temperature. This might suggest that the variation in the Gibbs energy of mixing between U and Pb is asymmetric with variations in the composition. The Gibbs energy of formation for the UPb_3 and UPb was evaluated by vapor pressure²⁸⁷

and EMF measurements.^{270,288} Sheldon *et al.*⁹⁴ recommended the latter data and performed the assessment by the CALPHAD approach. Table 25 summarizes the thermodynamic properties for the U–Pb and the U–Sn systems evaluated in Sheldon *et al.*⁹⁴ and Chase.²⁸⁹ The excess term for the interaction

parameter for the U–Pb system is highly asymmetric with composition, although that for the U–Sn system is modeled as a simple regular solution (symmetric). Regarding the Pu–Pb intermetallic compounds, Foltyn and Peterson²⁹⁰ calculated the Gibbs energy of formation of PuPb₃ from the distribution of Pu between liquid Pb and Zn in the temperature region between 976 and 1038 K.²⁹¹ The value is $-94.1 \text{ kJ mol}^{-1}$.

The phase relations for the Th–Bi, U–Bi, and Pu–Bi systems have similar tendencies to the corresponding Pb-related system. The general view

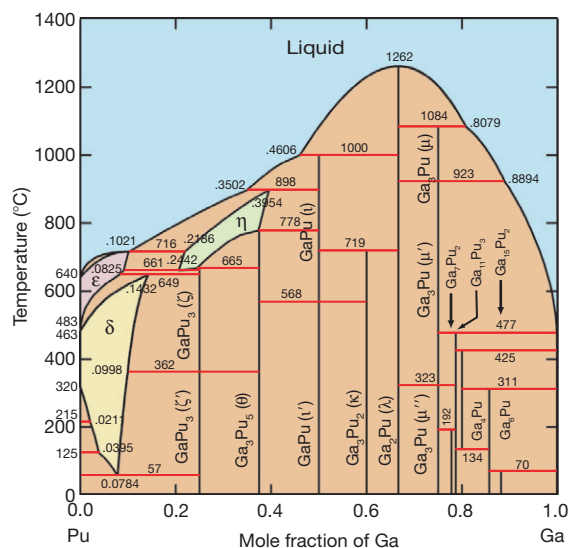


Figure 78 Newly assessed Pu–Ga phase diagram quoted from Turchi *et al.*²⁸⁶

of the U–Bi phase diagram is quite similar to that of the U–Pb system, although the number of intermetallic compounds is 3 in the U–Bi system instead of 2 in the U–Pb system. Thermodynamic evaluation for the U–Bi and Pu–Bi systems was performed²⁴⁰ using the CALPHAD approach. **Figures 80 and 81** show the calculated Pu–Bi phase diagram and the estimated variation in Pu activity with the experimental data points.^{292,293} The calculated phase boundaries and the Pu activity are in good accordance with the experimental data points. This suggests at least that the calculated Gibbs energy of formation of PuBi₂, which is the most Bi-rich compound, must give a reasonable value. The Pu activity in liquid Bi is extremely small, meaning that the actinide elements are stabilized by dissolving in liquid Bi. This phenomenon makes the separation ratio between actinide and lanthanide larger in the distribution using the molten salt/liquid Bi system. **Table 26** indicates the assessed parameters for the U–Bi and Pu–Bi systems.²⁴⁰

2.05.4 Summary

The salient features of the actinide phase diagrams containing actinide elements were summarized in this chapter. The phase diagrams largely differ from each other in accuracy due to differences in experimental information. Nevertheless, systematic observations with the periodic table and basic knowledge of the phase diagram type, as well as thermodynamic properties, still are practically useful at present.

Table 23 Thermodynamic functions for the Pu–Ga system

System or compound	Composition (at. % Ga)	Enthalpy (kJ mol^{-1})	Entropy ($\text{J mol}^{-1} \text{K}^{-1}$)	Heat capacity ($\text{J mol}^{-1} \text{K}^{-1}$)	Temperature (K)	References
Pu–Ga	2.6	–1.75	–34.6	27.0	100	282
		–4.62	–54.4	29.7	200	
		–7.64	–66.4	30.9	298.15	
	3.2	–1.79	–35.4	27.6	100	
		–4.70	–55.5	30.1	200	
		–7.73	–67.8	31.7	298.15	
	6.1	–1.82	–36.1	27.8	100	
		–4.78	–56.5	30.8	200	
		–7.86	–69.0	31.8	298.15	
Pu ₃ Ga		–158 ± 21				283
Pu ₅ Ga ₃		–420 ± 100				
PuGa		–120 ± 29				
PuGa ₂		–190 ± 31				
PuGa ₃		–230 ± 50				
PuGa ₄		–230 ± 33				
PuGa ₆		–238 ± 28				

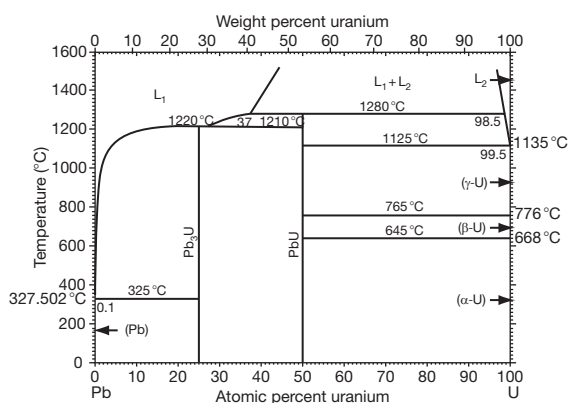
Table 24 Variation in crystal type and decomposition temperature for Laves phase

Transition metal group	Ib			IIb			IIIb			IVb			Vb	
Element	Cu	Ag	Au	Zn	Cd	Hg	Al	Ga	In	Tl	Sn	Pb	Bi	
m.p.	1358	1235	1678	693	594	234	934	303	430	577	505	601	545	
Th	AlB ₂	AlB ₂ ^a	AlB ₂ ^a	AlB ₂ ^a	AlB ₂	CaIn ₂	AlB ₂	ThSi ₂	–	–	ZrSi ₂	ND	Cu ₂ Sb	
m.p.=2028	1138	1308	1678	1328	1268	865 ^b	1793	–	–	–	1683 ^b	1503 ^b	1503 ^b	
U	–	–	CeCd ₂	–	–	AlB ₂	Cu ₂ Mg	AlB ₂	–	–	Ga ₂ Hf	–	Cu ₂ Sb	
m.p.=1408	–	–	1663	–	–	761 ^b	1893	1628	–	–	1633 ^b	–	1283 ^b	
Pu	CeCu ₂	ND	ND	Cu ₂ Mg	ND	–	Cu ₂ Mg	AlB ₂	–	–	Ga ₂ Hf	ND	ND	
m.p.=913	1288	1090 ^b	~1423	1208	1218	–	1813	1537	–	–	~1500 ^b	1402 ^b	1103 ^b	

^aThe composition does not melt congruently.^bDecomposition temperature is not the highest in the system.

ND not determined.

m.p. melting point.

**Figure 79** U–Pb phase diagram taken from Okamoto.⁴

In the present chapter, some phase diagrams were estimated hypothetically using the CALPHAD approach, and these are very helpful for starting new research activities efficiently. From the viewpoints of technological applications, further research is needed particularly for the following systems.

1. Minor actinide systems: When taking the transmutation of minor actinides into account using a metallic fuel fast reactor, which is believed to be one of the most promising transmutation systems, the experimental information on the phase diagram is insufficient for Np-, Am-, and Cm-related systems. Not only the phase diagrams between actinides, such as Pu–Am, Pu–Cm, and Np–Am, but also those between each minor actinide and Zr or Fe particularly are needed for the design of metallic fuels containing minor actinides. Zirconium is considered to be the best candidate for the metal fuel matrix constituent, and the most urgent and important study from this point

Table 25 Thermodynamic functions for U–Pb and U–Sn systems

$G^{\circ}(\text{Pb, liq}) = 4800 - 7.991T$
$G^{\circ}(\text{Sn, liq}) = 7195 - 14.244T$
$G^{\circ}(\text{U, liq}) = 16\,690 - 13.989T$
$G^{\circ}(\text{Pb, fcc}) = 0$
$G^{\circ}(\text{Sn, bcc}) = 0$
$G^{\circ}(\text{Sn, fcc}) = -1966 + 6.871T$
$G^{\circ}(\text{U, bcc}) = 7548 - 7.497T$
$G^{\circ}(\text{U, } \beta\text{-U}) = 2791 - 2.962T$
$G^{\circ}(\text{U, } \alpha\text{-U}) = 0$
$G^{\circ}(\text{Pb}_3\text{U}) = -72\,712 + 15.076T$
$G^{\circ}(\text{PbU}) = -64\,524 + 27.456T$
$G^{\circ}(\text{Sn}_2\text{U}_3) = -156\,530 + 27.725T$
$G^{\circ}(\text{Sn}_5\text{U}_3) = -233\,200 + 31.864T$
$G^{\circ}(\text{Sn}_3\text{U}) = -103\,864 + 10.008T$
$G^{\text{ex}}(\text{U–Pb, liq}) = x_{\text{U}}(1 - x_{\text{U}}) [49\,992 - 19.824T - 37\,151(1 - 2x_{\text{U}}) + 9\,068(1 - 2x_{\text{U}})^2 + 11\,778(1 - 2x_{\text{U}})^3]$
$G^{\text{ex}}(\text{U–Sn, liq}) = x_{\text{U}}(1 - x_{\text{U}}) (3287 - 8.686T)$

Source: Sheldon, R. I.; Foltyn, E. M.; Peterson, D. E. In *Phase Diagrams of Binary Actinide Alloys*; Kassner, M. E., Peterson, D. E., Eds.; Monograph Series on Alloy Phase Diagrams No. 11; ASM International: Materials Park, OH, 1995; pp 202–207, 223–227.

Regarding U–Sn system, the reference state for U is bcc instead of α -U.

of view is to solve the conflicts in the Np–Zr system. The certification of the phase relation for the Am–Fe and Cm–Fe systems is also valuable for evaluating the eutectic interaction between minor actinides and the stainless steel cladding. Since the eutectic interaction between Am and Fe was found in the irradiated U–Pu–Zr fuel, research on the Am–Fe system is helpful for designing not only the transmutation fuels but also the standard metallic fuels in which the minor actinides are not contained initially. From the viewpoint of modeling the eutectic

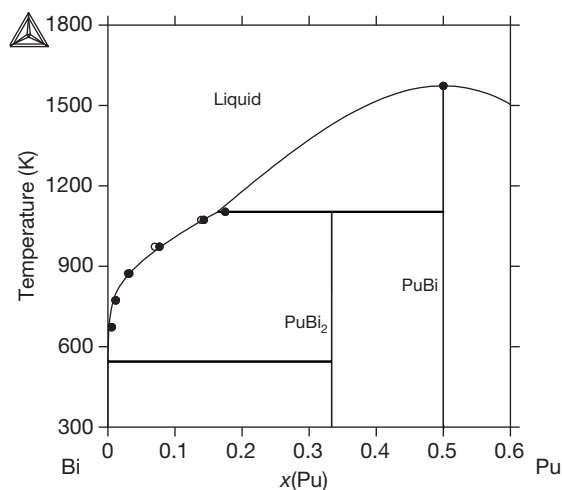


Figure 80 Calculated Pu-Bi phase diagram taken from Kurata and Sakamura,²⁴⁰ and the experimental data taken from Frost²⁹² (●) and Lebedev *et al.*²⁹³ (○).

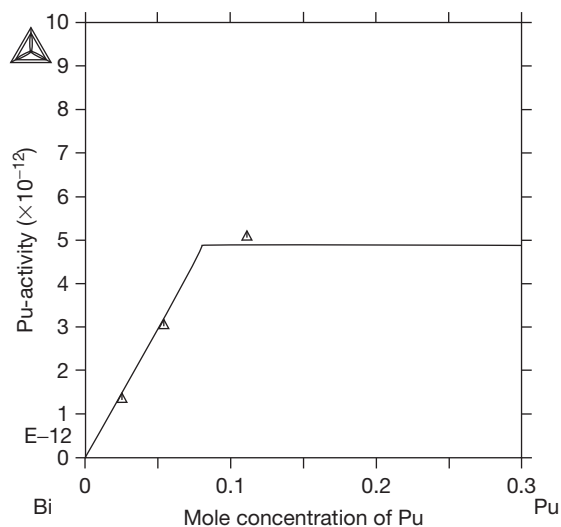


Figure 81 Pu activity in liquid Bi at 773 K taken from Kurata and Sakamura,²⁴⁰ and the experimental data taken from Lebedev *et al.*²⁹³

interaction, thermodynamic and phase relation data are very important. For instance, the temperature dependence on the Gibbs energy of formation of intermetallic compounds between Pu, Np, Am, or Cm and Fe is extremely valuable. The modeling of these actinide phase diagrams is practically helpful for the modeling of oxide, nitride, or carbide systems based on the CALPHAD approach.

2. Thorium systems: When taking the Th cycle into consideration, the metallic form would be a

Table 26 Thermodynamic functions for U-Bi and Pu-Bi systems

$G^{\circ}(\text{Bi, sol}), G^{\circ}(\text{Bi, liq}), G^{\circ}(\text{U, liq}), G^{\circ}(\text{Pu, liq})$: given in Dinsdale⁶⁷

$$G^{\circ}(\text{Bi}_2\text{U})^a = -186780 + 99.7857T$$

$$G^{\circ}(\text{Bi}_4\text{U}_3)^a = -482700 + 245.747T$$

$$G^{\circ}(\text{BiU})^a = -120710 + 55.667T$$

$$G^{\circ}(\text{Bi}_2\text{Pu})^a = -223750 + 72.7417T$$

$$G^{\circ}(\text{BiPu})^a = -204380 + 58.1817T$$

$$G^{\text{ex}}(\text{Bi-U, liq}) = x_{\text{U}}(1-x_{\text{U}})$$

$$[-5445.6 + 3.83777T + (-66562 + 5.01937)(1-2x_{\text{U}})]$$

$$G^{\text{ex}}(\text{Bi-Pu, liq}) = x_{\text{Pu}}(1-x_{\text{Pu}}) [-194370 + 3.12017T - 54753(1-2x_{\text{Pu}})]$$

^aReference state is liquid.

candidate for the fuel. In general, the experimental data for the Th-related systems are limited and scattered compared to the U- or Pu-related systems. Also, the phase diagram types between Th and other metals often are widely different from those between U or Pu and other metals. A systematic study for the Th-related systems is needed, especially for Th-lanthanides, Th-noble metals, Th-Zr, Th-Fe, etc. These data are also available for the basic modeling of oxide systems containing Th.

3. Noble metal systems: Under irradiation, the behavior of noble metal fission products in the metallic fuel is completely different from that of the oxide fuel due to the large differences in the oxygen potential. In the oxide fuel, noble metals condense as fine inclusions, which are the so-called nonsoluble residues. In a metallic fuel, on the other hand, the noble metals react with the actinide metals and form intermetallic compounds, such as UPdx, PuRh_x, PuRu_x, etc. Possibly, these intermetallic compounds are soluble in each other, or at least partially soluble, and form multielement compounds. These intermetallic compounds are considered to be thermodynamically very stable. As the burnup of the fuel becomes higher, the amount of these intermetallic compounds becomes larger, which changes the composition and morphology of the fuel matrix. Regarding the actinide-noble metal systems, not only the phase diagrams but also thermodynamic data for the intermetallic compounds are necessary to evaluate the fuel performance.
4. Multielement systems: In the metallic fuel, the behavior of each fission product is largely different from that in the oxide fuel. It is necessary for sufficient understanding to accumulate experimental

information regarding the multielement systems, including actinide metals. The thermodynamic database is practically useful from this point of view. In the Al-, Fe-, Ni-, Ti-, Zr-based alloy systems, the thermodynamic databases have already been prepared with sufficient accuracy. In the case of metallic fuels, the base alloy will be U–Zr or U–Pu–Zr. This database would be helpful when considering the behavior of the fission products in nitride or carbide fuels. Various approaches have been attempted for modeling the redistribution of fuel constituents or fission products under a temperature gradient. The thermodynamic database will be a practically useful tool for evaluating the driving force.

5. Liquid metal systems: In the various methods of pyrometallurgical processing of spent nuclear fuels, liquid metal is used as a solvent. The candidates are Al, Bi, Cd, Pb, Zn, etc. Phase diagrams between these liquid metals and actinides are needed for process design. Especially, the currently available solubility and thermodynamic data for Am and Cm are insufficient.

References

1. Kassner, M. E.; Peterson, D. E. *Phase Diagrams of Binary Actinide Alloys*; Monograph Series on Alloy Phase Diagrams No. 11; ASM International: Materials Park, OH, 1995.
2. Massalski, T. B.; Subramanian, P. R.; Okamoto, H.; Kacprzak, L. *Binary Alloy Phase Diagrams*, 2nd ed.; ASM International: Materials Park, OH, 1990; Vols. 1–3.
3. Brewer, L. In *Molybdenum: Physico-Chemical Properties of Its Compounds and Alloys*; Kubaschewski, O., Ed.; pp 170–173; International Atomic Energy Agency: Vienna, 1980; pp 170–173.
4. Okamoto, H. *Desk Handbook Phase Diagrams for Binary Alloys*; ASM International: Materials Park, OH, 2000.
5. Smith, J. L.; Kmetko, E. A. *J. Less Common Met.* **1983**, 90, 83.
6. Moore, K. T.; van der Laan, G. *Rev. Mod. Phys.* **2009**, 81, 235–298.
7. Kurata, M. In *Proceedings of Actinides 2009*, San Francisco, CA, July 12–19, 2009.
8. Bychkov, Y. F.; Rozanov, A. N.; Yakovleva, V. B. *Atom. Energy*. **1959**, 7, 531–536.
9. Douglass, T. B. *J. Res. NBS* **1954**, 52, 223–226.
10. Foote, F. C. USAEC Report, CT-2857; 1945.
11. Schonfeld, F. W.; Cramer, E. M.; Miner, W. M.; Ellinger, F. H.; Coffinberry, A. S. In *Plutonium Constitutional Diagrams*; Finniston, H. M., Howe, J. P., Eds.; Progress in Nuclear Energy, Series V; Pergamon Press: New York, 1959; Vol. 2, pp 579–599.
12. Ganiev, I. N.; Shamsiddinov, A. D.; Nazarov, Kh. M.; Badanov, M. D. *Russ. Metall.* **1996**, 4, 149–152.
13. Grube, G.; Botzenhardt, L. Z. *Electrochem.* **1942**, 48, 418–425.
14. Buzzard, R. W. *J. Res. Natl. Bur. Stand.* **1953**, 50(2), 63–67.
15. Hansen, M.; Anderko, K. *Constitution of Binary Alloys*; Genium: Schenectady, NY, 1958.
16. Wilhelm, H. A.; Newton, A. S.; Daane, A. H.; Neher, C. United States Atomic Energy Commission Report, CT-3714; 1946; 42–43.
17. Konobeevsky, S. T. In *Proceedings of the International Academy of Science of the USSR on the Peaceful Uses of Atomic Energy*, Chemical Science Volume, Geneva, 1955; pp 362–376, [in Russian].
18. Ellinger, F. H.; Land, C. C.; Gschneidner, K. A., Jr. In *Plutonium Handbook*; Wick, O. J., Ed.; Gordon and Breach: New York, 1967; Vol. 1, pp 191–247.
19. Okamoto, H. In *Phase Diagrams of Binary Actinide Alloys*; Kassner, M. E., Peterson, D. E., Eds.; Monograph Series on Alloy Phase Diagrams No. 11; ASM International: Materials Park, OH, 1995; pp 22–24, 146–151, 164–168, 207–208, 218–219, 246–247, 297–300, 411–412, 423.
20. Badaeva, T. A.; Kuznetsova, R. I. *Tr. Inst. Met. Baikova*; Gosatomizdat: Moscow, 1961; pp 358–368.
21. Benedict, U.; Buijs, K.; Dufour, C.; Toussaint, J. C. *J. Less Common Met.* **1975**, 42(3), 345–354.
22. Runnalls, O. J. C. *Acta Crystallogr.* **1954**, 7, 222–223.
23. Runnalls, O. J. C.; Boucher, R. R. *Nature* **1955**, 176, 1019–1020.
24. Jones, A.; Nash, R. R. WADCR Report, 53-113; 1953.
25. Yamamoto, A. S.; Rostoker, W. *Trans. ASM* **1958**, 50, 1090–1105.
26. Peterson, D. T.; Sundaram, C. V. Private communication quoted by Novotny and Smith in Ref. [28].
27. Nayeab-Hashemi, A. A.; Clark, J. B. In *Phase Diagrams of Binary Actinide Alloys*; Kassner, M. E., Peterson, D. E., Eds.; Monograph Series on Alloy Phase Diagrams No. 11; ASM International: Materials Park, OH, 1995; pp 68–72.
28. Novotny, D. B.; Smith, J. F. *J. Inst. Met.* **1963–1964**, 92, 122.
29. Hultgren, R.; Desai, P. D.; Hawkins, D. T.; Gleiser, M.; Kelley, K. K. *Selected Values of the Thermodynamic Properties of Binary Alloys*; American Society for Metals: Metals Park, OH, 1973.
30. Axler, K. M.; Foltyn, E. M.; Peterson, D. E.; Sheldon, R. I.; Hutchinson, X. W. B. *J. Nucl. Mater.* **1989**, 161, 132–139.
31. Chiotti, P.; Shoemaker, H. E. *Ind. Eng. Chem.* **1958**, 50(2), 137–140.
32. Gulyaev, B. B.; Dvorshkaya, G. F. In *Phase Diagrams of Metallic Systems*; Savitskii, E. M., Ed.; Nauka: Moscow, 1968; pp 267–273, [in Russian].
33. Fuhrman, N. F.; Holden, R. B.; Whitman, C. I. *J. Electrochem. Soc.* **1960**, 107, 127–131.
34. Peatfield, M.; Brett, N. H.; Potter, P. E. *J. Nucl. Mater.* **1980**, 89, 35–40.
35. Ahmann, D. H. Unpublished work (1945) quoted by Hansen and Anderko in Ref. [15].
36. Adda, Y.; Levy, V.; Hadari, Z.; Tournier, J. *Compt. Rend.* **1960**, 250, 536–538, [in French].
37. Schonfeld, F. W. In *The Metal Plutonium*; Coffinberry, A. S., Miner, W. N., Eds.; University of Chicago Press: Chicago, IL, 1961; pp 240–254.
38. McWhan, D. B.; Cunningham, B. B.; Wallman, J. C. *J. Inorg. Nucl. Chem.* **1962**, 24, 1025–1038.
39. Miedema, A. R. In *Proceedings of the 5th International Conference on Plutonium and Other Actinides*, Baden-Baden, Germany; Blank, H., Linder, R., Eds.; North-Holland: Amsterdam, 1975; Vol. 3.
40. Niessen, A. K.; de Boer, F. R.; Boom, R.; de Chatel, P. F.; Mattens, W. C. M.; Meidema, A. R. *Calphad* **1983**, 7, 51–70.

41. Terekhov, G. I.; Sinyakova, S. I. *Izv. Akad. Nauk SSSR Met.* **1990**, 3, 215–218, [in Russian].
42. Evans, D. S.; Raynor, G. V. *J. Nucl. Mater.* **1960**, 4, 66–69.
43. Badayeva, T. A.; Kuznetsova, P. I. *Russ. Metall.* **1969**, 5, 101–106.
44. Moffatt, W. G. *Handbook of Binary Phase Diagrams*, 8th ed.; American Society for Metals: Metals Park, OH, 1973; Vol. 8.
45. Badayava, T. A.; Kuznetsova, R. I. *Russ. Metall.* **1967**, 1, 89–92.
46. Norman, M.; Harris, J. R.; Raynor, G. V. *J. Less Common Met.* **1966**, 11, 395–402.
47. Badayava, T. A.; Kuznetsova, R. I. *Russ. Metall.* **1967**, 6, 99–100.
48. Evans, D. S.; Raynor, G. V. *J. Less Common Met.* **1961**, 3, 179–180.
49. Okamoto, H.; Massalski, T. B. *J. Phase Equil.* **1994**, 15(5), 500–521.
50. Holcombe, C. E., Jr.; Chapman, L. R. *J. Nucl. Mater.* **1986**, 139, 279–281; Sandia Report, SAND-86-0906C; Albuquerque, NM, 1986.
51. Terekhov, G. I.; Sinyakova, S. I. *Russ. Metall.* **1992**, 3, 187–190.
52. Haefling, J. F.; Daane, A. H. *Trans. AIME* **1959**, 215, 336–338.
53. Elliott, R. P. *Constitution of Binary Alloys*; Genium: Schenectady, NY, 1958; First supplement.
54. Wilhelm, H. A.; Carlson, O. N. *Trans. ASM* **1950**, 42, 1311–1325.
55. Wilhelm, H. A. *Nucl. Fuels Newsletter*. WASH-704; 1957, quoted by Elliott and Larson in Ref. [76].
56. Berndt, H. A. USAEC, ANL-6516; 1961 214–217.
57. Gibson, J. K.; Haire, R. G. *J. Nucl. Mater.* **1992**, 195, 156–165.
58. Kutaitsev, V. I.; Chebotarev, N. T.; Andrianov, M. A.; et al. *Atom. Energ.* **1967**, 23(6), 511–519, [in Russian].
59. Ellinger, F. H.; Land, C. C.; Johnson, K. A. *Trans. AIME* **1967**, 239(6), 895–898.
60. Selle, J. E.; Etter, D. E. *Trans. AIME* **1964**, 230, 1000–1005.
61. Ellinger, F. H.; Land, C. C.; Johnson, K. A. *J. Nucl. Mater.* **1969**, 29, 178–183.
62. Okamoto, H.; Massalski, T. B. *J. Phase Equil.* **1991**, 12(2), 148–168.
63. Wood, D. H.; Cramer, E. M. *J. Less Common Met.* **1969**, 19, 66–67.
64. Storhok, V. W. *Reactor Mater.* **1963**, 6(3), 14–15.
65. Baxi, H. C.; Massalski, T. B. Private communication (1989) quoted by Kassner and Peterson in Ref. [1].
66. Shirasu, N.; Kurata, M. Private communication.
67. Dinsdale, A. *Calphad* **1991**, 15, 317.
68. Kurata, M. In *Proceedings of the MMSNF-6*, Tokyo University, Dec 13–14, 2007.
69. Peterson, D. E. In *Phase Diagrams of Binary Actinide Alloys*; Kassner, M. E., Peterson, D. E., Eds.; Monograph Series on Alloy Phase Diagrams No. 11; ASM International: Materials Park, OH, 1995; pp 111–113, 351–354, 401–404, 444–446, 465–467.
70. Carlson, O. N. USAEC Report, AECU-3206; 1950.
71. Bentle, G. G. In *Proceedings of the United Nations International Conference on Peaceful Used of Atomic Energy*, Geneva, 1958; Vol. 6, pp 156–161.
72. Murray, J. R. *J. Inst. Met.* **1958**, 87, 349–352.
73. Badayeva, T. A.; Kuznetsova, R. I. *Izv. Akad. Nauk SSSR Met.* **1972**, 1, 196.
74. Poole, D. M.; Williamson, G. K.; Marples, J. A. C. *J. Inst. Met.* **1957–1958**, 86, 172.
75. Bocharov, A. A.; Konobeevskii, S. T.; Kutaitsev, V. I.; Men'shikova, T. S.; Chebotarev, N. T. *Sov. J. Atom. Energ.* **1958**, 5, 1177.
76. Elliott, R. O.; Larson, A. C. In *The Metal Plutonium*; Coffinbery, A. S., Miner, W. N., Eds.; University of Chicago Press: Chicago, IL, 1961; pp 265–280.
77. Calais, D.; Dupuy, M.; Mouchnino, M.; Portnoff, A. Y.; Van Craeynest, A. In *Plutonium 1965*; Kay, A. E., Waldron, M. B., Eds.; Chapman and Hall: London, 1967; p 387.
78. Portnoff, A. Y.; Calais, D. *J. Nucl. Mater.* **1967**, 24, 158.
79. Marcon, J. P.; Portnoff, A. Y. *J. Nucl. Mater.* **1968**, 28, 341.
80. Mardon, P. G.; Pearce, J. H. *J. Less Common Met.* **1959**, 1, 467–475.
81. Peterson, D. E.; Foltyn, E. M. *Bull. Alloy Phase Diagrams* **1989**, 10(2), 160–164.
82. Ellinger, F. H.; Elliott, R. O.; Cramer, E. M. *J. Nucl. Mater.* **1959**, 3, 233–243.
83. AEC Research and Development Report, MLM-1445, Mound Laboratory Report; 1967.
84. Okamoto, H. *J. Phase Equil.* **1991**, 12(6), 623–643.
85. Leibowitz, L.; Blomquis, R. A.; Pelton, A. D. *J. Nucl. Mater.* **1991**, 184, 59–64.
86. Okamoto, Y.; Maeda, A.; Suzuki, Y.; Ohmichi, T. *J. Alloys Compd.* **1994**, 213/214, 372–374.
87. Nakajima, K.; Iwai, T.; Arai, Y.; Kurata, M. Private communication.
88. Calais, D.; Dupuy, M.; Mouchnino, M.; Portnoff, A. Y.; Van Craeynest, A. In *Plutonium 1965*; Kay, A. E., Waldron, M. B., Eds.; Chapman and Hall: London, 1967; pp 358–391.
89. Kurata, M.; Nakamura, K.; Ogata, T. *J. Nucl. Mater.* **2001**, 294, 123–129.
90. Okamoto, H. *J. Phase Equil.* **1999**, 20(4), 450–452.
91. Ogawa, T. *J. Alloys Compd.* **1993**, 194, 1–7.
92. Mardon, P. G.; Pearce, J. H.; Marples, J. A. C. *J. Less Common Met.* **1961**, 3, 281–292.
93. Poole, D. M.; Bale, M. G.; Mardon, P. G.; Marples, J. A. C.; Nichols, J. L. In *Plutonium 1960*; Grison, E., Lord, W. B. H., Fowler, R. D., Eds.; Cleaver-Hume Press: London, 1961; pp 267–280.
94. Sheldon, R. I.; Foltyn, E. M.; Peterson, D. E. In *Phase Diagrams of Binary Actinide Alloys*; Kassner, M. E., Peterson, D. E., Eds.; Monograph Series on Alloy Phase Diagrams No. 11; ASM International: Materials Park, OH, 1995; pp 202–207, 223–227.
95. Ellinger, F. H.; Johnson, K. A.; Struebing, V. O. *J. Nucl. Mater.* **1966**, 20, 83–83.
96. Shushanov, V. D.; Chebotarev, N. T. *Radiokhimiya* **1995**, 37(6), 484–487, [in Russian].
97. Dupin, N. In *F-Bridge Meeting, PSI*, Switzerland, Apr 1–2, 2009.
98. Murray, J. L. In *Phase Diagrams of Binary Actinide Alloys*; Kassner, M. E., Peterson, D. E., Eds.; Monograph Series on Alloy Phase Diagrams No. 11; ASM International: Materials Park, OH, 1995; pp 106–108, 233–238, 405–409.
99. Carlson, O. N.; Dickenson, J. M.; Lung, H. E.; Wilhelm, H. A. *Trans. AIME* **1956**, 206, 132–136.
100. Pedersen, T. E.; Noack, M.; Verhoeven, J. D. *J. Mater. Sci.* **1980**, 15, 2115–2117.
101. Kutaitsev, V. I.; Chebotarev, N. T.; Lebedev, I. G.; Andrianov, M. A.; Konve, V. N.; Menshikova, T. S. In *Plutonium 1965*, Proceedings of the Third International Conference on Plutonium, London, 1965; pp 420–449.
102. Languille, A. *Mem. Sci. Rev. Met.* **1971**, 68(6), 435–441.
103. Udy, M. C.; Boulger, F. W. *Trans. AIME* **1954**, 200, 207–210.

104. Knapton, A. G. *J. Inst. Met.* **1954–1955**, 83, 497–504.
105. Adda, Y.; Beyeler, M.; Kirianenko, A.; Maurice, F. *Mem. Sci. Rev. Met.* **1961**, 58(9), 716–724, [in German].
106. Gibson, E. D.; Loomis, B. A.; Carlson, O. N. *Trans. AIME* **1958**, 50, 348–369.
107. Johnson, R. H.; Honeycombe, R. W. K. *J. Nucl. Mater.* **1961**, 4, 66–69.
108. Sheldon, R. I.; Peterson, D. E. *Bull. Alloy Phase Diagrams* **1989**, 10(2), 165–171.
109. Ogawa, T.; Iwai, T. *J. Less Common Met.* **1991**, 170, 101–108.
110. Okamoto, H. *J. Phase Equil.* **1992**, 13(1), 109–110.
111. Murakami, T.; Kato, T.; Kurata, M.; Yamana, H. *J. Nucl. Mater.* **2009**, 394, 131–135.
112. Summers-Smith, D. *J. Inst. Met.* **1954–1955**, 83, 277–282.
113. Leibowitz, L.; Blomquist, R. A. *J. Nucl. Mater.* **1991**, 184, 47–52.
114. Akabori, M.; Itoh, A.; Ogawa, T.; Kobayashi, F.; Suzuki, Y. *J. Nucl. Mater.* **1992**, 188, 249–254.
115. Maeda, A.; Suzuki, Y.; Ohmichi, T. *J. Alloys Compd. Lett.* **1992**, 179, L21–L24.
116. Bocharov, A. A.; Konobeevsky, S. T.; Kutaitsev, V. I.; Menshikova, T. S.; Chebotarev, N. T. In *Proceedings of the 2nd United Nations International Conference on the Peaceful Uses of Atomic Energy*, Geneva, 1958; Vol. 6, pp 184–193.
117. Marples, J. A. C. *J. Less Common Met.* **1960**, 2, 331–351.
118. Lauthier, J. C.; Housseau, N.; van Craeynest, V.; Calais, D. *J. Nucl. Mater.* **1967**, 23, 313–319, [in French].
119. Suzuki, Y.; Maeda, A.; Ohmichi, T. *J. Alloys Compd.* **1992**, 182(2), L9–L14.
120. Leibowitz, L.; Veleckis, E.; Blomquist, R. A.; Pelton, A. D. *J. Nucl. Mater.* **1988**, 154, 145–153.
121. Tayler, J. M. *J. Nucl. Mater.* **1969**, 30, 346–350.
122. Maeda, A.; Suzuki, Y.; Okamoto, Y.; Ohmichi, T. *J. Alloys Compd.* **1994**, 205, 35–38.
123. Gibson, J. K.; Haire, R. G.; Gensini, M. M.; Ogawa, T. *J. Alloys Compd.* **1994**, 213/214, 106–110.
124. Rodriguez, R. J.; Sari, C.; Portal, U. C. *J. Alloys Compd.* **1994**, 209, 263–268.
125. Okamoto, H. *J. Phase Equil.* **1996**, 17(2), 166–167.
126. O'Boyle, D.; Dwight, A. E. In *Proceedings of the 4th International Conference on Plutonium and Other Actinides*, Santa Fe, New Mexico, 1970; Vol. 2, pp 720–732.
127. Harbur, D. R.; Anderson, J. W.; Mariman, W. J. Los Alamos National Laboratory Report, LA-4512; 1970.
128. Peterson, D. T.; Beerntsen, D. J. *Trans. ASM* **1960**, 52, 763–777.
129. Murray, J. L. *Phase Diagrams of Binary Titanium Alloys*; ASM International: Metals Park, OH, 1987; pp 56–58.
130. Palmer, P. E.; McMasters, O. D.; Larsen, W. L. *Trans. ASM* **1962**, 55, 301–306.
131. Bannister, G. H.; Thomson, J. R. AERE-R4428; Atomic Energy Research Establishment: Harwell, 1963.
132. Smith, J. F.; Lee, K. J.; Peterson, D. E. In *Phase Diagrams of Binary Actinide Alloys*; Kassner, M. E., Peterson, D. E., Eds.; Monograph Series on Alloy Phase Diagrams No. 11; ASM International: Materials Park, OH, 1995; pp 113–116.
133. McMasters, O. D.; Larsen, W. L. *J. Less Common Met.* **1961**, 3, 312.
134. Ackermann, R. J.; Rauh, E. G. *High Temp. Sci.* **1972**, 4, 272–282.
135. Ackermann, R. J.; Rauh, E. G. *High Temp. Sci.* **1972**, 4, 496–505.
136. Saroja, A.; Bhatt, Y. J.; Garg, S. P. *J. Less Common Met.* **1985**, 114, 291–297.
137. Saller, H.; Rough, F. A. *Trans. AIME* **1953**, 197, 545–548.
138. Pfeil, P. C. L.; Browne, J. D.; Williamson, G. K. *J. Inst. Met.* **1958**, 87, 204–208.
139. Rogers, B. A.; Atkins, D. F.; Manthos, E. J.; Kirkpatrick, M. E. *Trans. Metall. Soc. AIME* **1958**, 212, 387–393.
140. Ellinger, F. H.; Miner, W. N.; O'Boyle, D. R.; Schonfeld, F. W. *Constitution of Plutonium Alloys*; LA-3870; Los Alamos, NM, 1968.
141. Peterson, N. L.; Ogilvie, R. E. *Trans. Metall. Soc. AIME* **1960**, 218, 439–444.
142. Fizzotti, C.; Maspereni, A. *Com. Naz. Energ. Nucl.* **1966**, 1–23; RTIMET(66)-1, [in Italian].
143. Terekhov, G. I. *Izv. Akad. Nauk SSSR Met.* **1982**, 4, 188–189, [in Russian].
144. Schramm, C. H.; Gordon, P.; Kaufman, A. R. *Trans. Metall. Soc. AIME J. Met.* **1950**, 188, 195–204.
145. Bowersox, D. F.; Leary, J. A. *J. Nucl. Mater.* **1968**, 27, 181–186.
146. Bowersox, D. F.; Leary, J. A. *J. Nucl. Mater.* **1967**, 21, 219–224.
147. Romig, A. D. *Metallurgical Technology of Uranium and Uranium Alloys*; American Society for Metals: Metals Park, OH, 1982; Vol. 1, pp 47–127.
148. Das, D. Ph.D. Thesis, Bombay University, Bombay, 1985.
149. Krishnan, R.; Garg, S. P.; Kirshnamurthy, N. In *Phase Diagrams of Binary Actinide Alloys*; Kassner, M. E., Peterson, D. E., Eds.; Monograph Series on Alloy Phase Diagrams No. 11; ASM International: Materials Park, OH, 1995; pp 101–104, 228–230.
150. Koike, J.; Kassner, M. E.; Tate, R. E. In *Phase Diagrams of Binary Actinide Alloys*; Kassner, M. E., Peterson, D. E., Eds.; Monograph Series on Alloy Phase Diagrams No. 11; ASM International: Materials Park, OH, 1995; pp 188–194.
151. Baxi, H. C.; Massalski, T. B. In *Phase Diagrams of Binary Actinide Alloys*; Kassner, M. E., Peterson, D. E., Eds.; Monograph Series on Alloy Phase Diagrams No. 11; ASM International: Materials Park, OH, 1995; pp 394–399, 412–416.
152. Rizzo, H. F.; Echeverria, A. W.; Wien, W. L.; Massalski, T. B. *Mater. Sci. Eng.* **1988**, 98, 57.
153. Venkatraman, M.; Neumann, J. P.; Peterson, D. E. In *Phase Diagrams of Binary Actinide Alloys*; Kassner, M. E., Peterson, D. E., Eds.; Monograph Series on Alloy Phase Diagrams No. 11; ASM International: Materials Park, OH, 1995; pp 34–35, 157–161, 308–310.
154. Pandian, S.; Nagender Naidu, S. V.; Rama Rao, P. In *Phase Diagrams of Binary Actinide Alloys*; Kassner, M. E., Peterson, D. E., Eds.; Monograph Series on Alloy Phase Diagrams No. 11; ASM International: Materials Park, OH, 1995; pp 116–119.
155. Garg, S. P.; Ackermann, R. J. *J. Nucl. Mater.* **1977**, 64, 265–274.
156. Daane, A. H.; Wilson, A. S. *Trans. AIME* **1955**, 203, 1219–1220.
157. Badaeva, T. A.; Kuznetsova, R. I. In *Phase Diagram of the Uranium–Chromium System*; Ivanov, O. S., Ed.; Gosatomizdat: Moscow, 1963; pp 87–91, [in Russian].
158. ASM Handbook Committee, Ed. *Metals Handbook, Metallography, Structures and Phase Diagrams*, 8th ed.; American Society for Metals: Metals Park, OH, 1973; Vol. 8.
159. Provov, D. M.; Fisher, R. W. *J. Less Common Met.* **1964**, 6, 313–321.

160. Gomozyov, L. I.; Lyutina, E. M.; Ivanov, O. S. *Izv. Akad. Nauk SSSR Met.* **1970**, 2, 210–215.
161. Chandrasekharish, M. S.; Dharwadkar, S. R.; Das, D. *Z. Metallkd.* **1986**, 77(8), 509–514.
162. Chapman, L. R. *J. Nucl. Mater.* **1983**, 116, 328–331.
163. Lundberg, L. B. *J. Nucl. Mater.* **1989**, 167, 64–75.
164. Gueneau, C. In *The Chemistry of the Actinide and Transactinide Elements*; Edelstein, N.M. Fuger, J., Morss, L. R., Eds.; Springer, 2010; Vol. 6.
165. Darby, J. B., Jr.; Berndt, A. F.; Downey, J. W. *J. Less Common Met.* **1965**, 9, 466–468.
166. Lawson, A. C.; Larson, A. C.; Von Dreele, R. B.; et al. *J. Less Common Met.* **1987**, 132, 229–235.
167. Aleksandrova, L. N.; Badaeva, T. *Storoenie Svoistva Splavordiya Atomic Energie*; Nauka: Moscow, 1973; 26.
168. Jackson, R. J.; Williams, D. E.; Larsen, W. L. *J. Less Common Met.* **1963**, 5, 443–461.
169. Lam, D. J.; Mitchell, A. W. *J. Nucl. Mater.* **1972**, 44(3), 279–284.
170. Flrio, J. V.; Baenziger, N. C.; Rundle, R. E. *Acta Crystallogr.* **1956**, 9, 367–372.
171. Buschow, K. H. J.; van der Goot, A. S. *J. Less Common Met.* **1971**, 23, 399–402.
172. Palenzona, A.; Cirafici, S. *J. Less Common Met.* **1989**, 154, 61–66.
173. Horn, L.; Basserman, C. *Z. Metallkd.* **1948**, 39, 272–275.
174. Thomson, J. R. *J. Less Common Met.* **1972**, 29, 183–188.
175. Chapman, L. R.; Holcombe, C. F., Jr. *J. Nucl. Mater.* **1984**, 126, 323–326.
176. Gardie, P.; Bordier, G.; Poupeau, J. J.; Le Ny, L. *J. Nucl. Mater.* **1992**, 189, 97–102.
177. Waldron, M. B.; Brown, J. D. Atomic Energy Research Establishment, 1956.
178. Foote, F. C.; Clark, J. R.; Cieslicki, M.; Nelson, B. J.; Lane, T. R. Manhattan Project Report, CT-3013; 1945.
179. Grogan, J. D.; Pleasance, R. J.; Williams, R. E. *J. Inst. Met.* **1953–1954**, 82, 141–147.
180. Sari, C.; Walker, C. T.; Kurata, M.; Inoue, T. *J. Nucl. Mater.* **1994**, 208, 201–210.
181. Mardon, P. G.; Haines, H. R.; Pearce, J. H.; Waldron, M. B. *J. Inst. Met.* **1957**, 86, 166–171.
182. Avivi, E. Comm. Energie At. Report, CEA-R-2444; 1964; 72.
183. Wensch, G. W.; Whyte, D. D. Los Alamos Scientific Laboratory Report, LA-1304; 1951.
184. Aldred, A. T.; Dunlap, B. D.; Lam, D. J.; Shenoy, G. K. In *4th International Transplutonium Element Symposium*, Baden-Baden, Germany, 1975; p 6.
185. Thomson, J. R. *J. Less Common Met.* **1966**, 10, 432–438.
186. Gordon, P.; Kaufmann, A. R. *Trans. AIME* **1950**, 188(1), 182–194.
187. Grogan, J. D. *J. Inst. Met.* **1950**, 77, 571–576.
188. Michaud, G. G. *Can. Metall. Q.* **1966**, 5(4), 355–365.
189. Ofte, D.; Wittenberg, L. J. *Trans. ASM* **1964**, 57, 916–924.
190. Gibson, J. K.; Haire, R. G.; Beahm, E. C.; Gensini, M. M.; Maeda, A.; Ogawa, T. *J. Nucl. Mater.* **1994**, 211, 215–222.
191. Chiotti, P.; Akhachinskij, V. V.; Ansara, I. In *The Chemical Thermodynamics of Actinide Elements and Compounds*; Medvedev, V., Rand, M. H., Westrum, E. F., Jr., Oetting, F. L., Eds.; Part 5: The Actinide Binary Alloys; International Atomic Energy Agency: Vienna, 1981.
192. Campbell, G. M. *J. Chem. Thermodyn.* **1974**, 6, 1110–1112.
193. Jiang, M.; Oikawa, K.; Ikeshoji, T.; Wulff, L.; Ishida, K. *J. Phase Equil.* **2001**, 22(4), 406–417.
194. Nakamura, K.; Kurata, M.; Ogata, T.; Itoh, A.; Akabori, M. *J. Nucl. Mater.* **1999**, 275, 151–157.
195. Annual Progress Report for 1965, Metallurgy Division, Argonne National Laboratory Report, ANL-7155; 1965.
196. Kurata, M.; Ogata, T.; Nakamura, K.; Ogawa, T. *J. Alloys Compd.* **1998**, 271–273, 636–640.
197. Nakamura, K.; Ogata, T.; Kurata, M.; Itoh, A.; Akabori, M. *J. Nucl. Mater.* **1999**, 275, 246–254.
198. Nakamura, K.; Kurata, M.; Ogata, T.; Yokoo, T.; Mignanelli, M. A. *J. Phase Equil.* **2000**, 22(3), 259–264.
199. Nakamura, K.; Ogata, T.; Kurata, M.; Yokoo, T.; Mignanelli, M. A. *J. Nucl. Sci. Technol.* **2001**, 38(2), 112–119.
200. Nakamura, K.; Ogata, T.; Kurata, M.; Yokoo, T.; Mignanelli, M. A. *J. Nucl. Mater.* **2002**, 304, 63–72.
201. Ogata, T.; Nakamura, K.; Kurata, M.; Yokoo, T.; Mignanelli, M. A. *J. Nucl. Sci. Technol.* **2000**, 37(3), 244–252.
202. Cirafici, S.; Palenzona, A. *Thermochim. Acta* **1990**, 162, 117–125.
203. Thomson, J. R. *J. Less Common Met.* **1963**, 5, 437–442.
204. Thomson, J. R. *J. Less Common Met.* **1964**, 6, 94–99.
205. Terekhov, G. I.; Aleksandrova, L. N.; Tagirova, R. Kh. *Izv. Akad. Nauk SSSR Met.* **1984**, 6, 189–193, [in Russian].
206. Erdmann, B.; Keller, C. *J. Solid State Chem.* **1973**, 7, 40–48.
207. Park, J. J. *J. Res. Natl. Bur. Stand.* **1968**, A72(1), 1.
208. Ivanov, O. S.; Badaeva, T. A.; Sofronova, R. M.; Kishenevskii, V. B.; Kushnir, N. P. *Phase Diagrams of Uranium Alloys*; Nauka: Moscow, 1972.
209. Catterall, J. A.; Grogan, J. D.; Pleasance, R. J. *J. Inst. Met.* **1956**, 85, 63–67.
210. Pells, G. P. *J. Inst. Met.* **1963–1964**, 92, 416–418.
211. Nellis, W. J.; Dweight, A. E.; Knott, H. W. *J. Appl. Phys.* **1972**, 5(4), 306–307.
212. Kutaitsev, V. I.; Chebotarev, N. T.; Andrianov, M. A.; et al. *Atom. Energ.* **1967**, 23, 511–519, [in Russian].
213. Land, C. C.; Peterson, D. E.; Root, R. B. *J. Nucl. Mater.* **1978**, 75, 262–273.
214. Thomson, J. R. *J. Less Common Met.* **1964**, 6, 3–10.
215. Kleykamp, H. *J. Less Common Met.* **1979**, 63, 25–33.
216. Erdmann, B.; Keller, C. *Inorg. Nucl. Chem. Lett.* **1971**, 7, 675–683.
217. Knapton, A. G. *J. Nucl. Mater.* **1963**, 9, 309–319.
218. Heal, T. J.; Williams, G. I. *Acta Crystallogr.* **1955**, 8, 494–498.
219. Dwight, A. E.; Downey, J. W.; Conner, R. A., Jr. *Acta Crystallogr.* **1961**, 14, 75–76.
220. Park, J. J.; Mullern, L. R. *J. Res. Natl. Bur. Stand. A* **1968**, 72(1), 19–25.
221. Park, J. J.; Fickle, D. P. *J. Res. Natl. Bur. Stand. A* **1960**, 64, 107–117.
222. Mitchell, A. W.; Lam, D. J. *J. Nucl. Mater.* **1974**, 52, 125–127.
223. Cope, R. G.; Lowe, J. N.; Miller, D. C. UK Atomic Energy Authority, AWRE-O-36/61; 1961; p 18.
224. Peterson, D. E.; Starzynski, J. S. *J. Less Common Met.* **1985**, 105, 273–281.
225. Peterson, D. E. *J. Nucl. Mater.* **1985**, 131, 44–52.
226. Gingerich, K. A. *Chem. Phys. Lett.* **1973**, 23(2), 270–274.
227. Schmidt, N. Kernforschungszentrum Karlsruhe Report, KFK-1987; 1974; pp 1–22, [in German].
228. Mobius, S. Kernforschungszentrum Karlsruhe Report, KFK-2634; 1978; [in German].
229. Mobius, S.; Hellwig, L.; Keller, C. *J. Less Common Met.* **1986**, 121, 43–48.

230. Raub, E.; Engel, M. Z. *Electrochem.* **1943**, 49, 487–493, [in German].
231. Baren, M. R. J. *Phase Equil.* **1991**, 12(3), 321–323.
232. Bates, J.; Adler, M.; Meisenhelder, J.; Shinn, W.; Tani, B. S.; Krumpelt, M. J. *Less Common Met.* **1981**, 77, 205–213.
233. Palenzona, A.; Cirafici, S. J. *Less Common Met.* **1981**, 77, 215–220.
234. Dutkiewicz, J. In *Phase Diagrams of Binary Actinide Alloys*; Kassner, M. E., Peterson, D. E., Eds.; Monograph Series on Alloy Phase Diagrams No. 11; ASM International: Materials Park, OH, 1995; pp 28–30.
235. Krumpelt, M.; Johnson, I.; Heiberger, J. J. *Less Common Met.* **1969**, 18, 35–40.
236. Kurata, M.; Sakamura, Y. J. *Phase Equil.* **2001**, 22(3), 232–240.
237. Martin, A. E.; Johnson, I.; Feder, H. M. *Trans. Met. Soc. AIME* **1961**, 221, 789–791.
238. Terekhov, G. I.; Sinyakova, S. I.; Vedernikov, M. V.; Ivanov, O. S. *Collection on the Physical Chemistry of Alloys and Refractory Compounds with Thorium and Uranium*, 1968; pp 103–107, Izd-vo Nauka, [in Russian].
239. Buzzard, R. W.; Fickle, D. P.; Park, J. J. *J. Res. Natl. Bur. Stand.* **1954**, 52(3), 149–152.
240. Kurata, M.; Sakamura, Y. J. *Nucl. Sci. Technol.* **2002**, (Suppl. 3), 607–610.
241. Barin, I. *Thermochemical Data of Pure Substances*, 3rd ed.; VCH Verlagsgesellschaft mbH: Weinheim, Germany, 1995.
242. Krumpelt, M.; Johnson, I.; Heiberger, J. J. *Metall. Trans.* **1974**, 5, 65.
243. Johnson, I.; Chasanov, M. G.; Yonco, R. M. *Trans. Met. Soc. AIME* **1965**, 233, 1408–1414.
244. Kurata, M.; Uozumi, K.; Kato, T.; Iizuka, M. J. *Nucl. Sci. Technol.* **2009**, 46, 1070–1075.
245. Kato, T.; Uozumi, K.; Inoue, T.; Shirai, O.; Iwai, T.; Arai, Y. In *Proceedings of the International Conference on Atoms for Prosperity: Updating Eisenhower's Global Vision for Nuclear Energy, Global 2003*, New Orleans, LA, Nov 16–20, 2003.
246. Uozumi, K.; Iizuka, M.; Kato, T.; et al. *J. Nucl. Mater.* **2004**, 325, 34–43.
247. Borie, B. S. *Trans. AIME* **1951**, 191, 800–802.
248. Runnalls, O. J. C.; Boucher, R. R. *Trans. Metall. Soc. AIME* **1965**, 233, 1726–1732.
249. Chiotti, P.; Kateley, J. A. J. *Nucl. Mater.* **1969**, 32, 132–145.
250. Moeller, R. D.; Schonfield, F. W. USAEC Report, LA-1000; Los Alamos, NM, 1950.
251. Grison, E. In *The Metal Plutonium*; Coffinberry, A. S., Miner, W. N., Eds.; University of Chicago Press: Chicago, IL, 1961; pp 265–280.
252. Ellinger, F. H.; Land, C. C.; Miner, W. N. *J. Nucl. Mater.* **1962**, 5, 165–172.
253. Runnalls, O. J. C.; Boucher, R. R. *J. Nucl. Mater.* **1965**, 15, 57–64.
254. Runnalls, O. J. C. In *Plutonium 1965*; Kay, A. E., Waldron, M. B., Eds.; Chapman and Hall: London, 1967; pp 341–357.
255. Frueh, A. J., Jr.; Sygusch, J. Z. *Kristallogr.* **1968**, 127, 139–144.
256. Roy, P. R. J. *Nucl. Mater.* **1964**, 11, 59–66.
257. Straatman, J. A.; Neuman, N. F. USAEC Report, MCW-1488; 1964.
258. Waldron, M. B.; Garstone, J.; Lee, J. A.; et al. In *Proceedings of the 2nd United Nations International Conference on Peaceful Uses of Atomic Energy*, Geneva, 1958; Vol. 6, pp 162–169.
259. Sedmidubsky, D.; Konings, R. J. M.; Soucek, P. J. *Nucl. Mater.* **2010**, 397, 1–7.
260. Storvick, V. W.; Bauer, A. A.; Dickerson, R. F. *Trans. ASM* **1961**, 53, 837–842.
261. Wang, J.; Liu, X.; Wang, C. J. *Nucl. Mater.* **2008**, 374, 79.
262. Russell, R. B. USAEC Report, NMI-2813; 1964; p 44.
263. Runnalls, O. *Trans. Am. Inst. Min. Metall. Petrol. Eng.* **1953**, 197, 1460.
264. Hecker, S. S.; Timofeeva, L. F. *Los Alamos Sci.* **2000**, 1(26), 196–203.
265. Timofeeva, L. F. In *Proceedings of the International Conference on Aging Studies and Lifetime Extension of Materials*; Kluwer, Plenum: New York, Dordrecht, 2001; pp 191–198.
266. Turchi, P. E. A.; Kaufman, L.; Zhou, S.; Liu, Z. J. *Alloys Compd.* **2007**, 444–445, 28–35.
267. Timofeeva, L. F. *J. Alloys Compd.* **2007**, 444–445, 124–128.
268. Poyarkov, A. M.; Lebedev, V. A.; Nichkov, I. F.; Raspopin, S. P. *Atom. Energ.* **1973**, 35, 434–435, [in Russian].
269. Raleigh, D. D. J. *Electrochem. Soc.* **1962**, 109, 521–525.
270. Johnson, I. *Nucl. Metall.* **1964**, 10, 171–182.
271. Dannohl, H. D.; Lukas, H. L. Z. *Metallkd.* **1974**, 65, 642–649.
272. Ivanov, M. I.; Tumbakov, V. A.; Podol'sskaya, N. S. *Atom. Energ.* **1958**, 5, 166–170, [in Russian].
273. Lebedev, V. A.; Sal'nikov, V. I.; Nichkov, I. F.; Raspopin, S. P. *Atom. Energ.* **1972**, 32(2), 115–118, [in Russian].
274. Lebedev, V. A.; Kober, V. I.; Sal'nikov, V. I.; et al. *Radiokhimiya* **1976**, 18, 123–127, [in Russian].
275. Akhachinsky, V. V.; Kopyten, L. M.; Ivanov, M. I.; Podol'skaya, N. S. In *Proceedings of the International Symposium on Thermodynamics of Nuclear Materials*; IAEA: Vienna, 1962; pp 309–317, [in Russian].
276. Makarov, E. S.; Levdiv, V. A. *Kristallografiya* **1956**, 1(6), 644–649, [in Russian].
277. Dayan, D.; Kimmel, G.; Dariel, M. P. J. *Nucl. Mater.* **1985**, 135, 40–45.
278. Buschow, K. H. J. *J. Less Common Met.* **1973**, 31, 165–168.
279. Ellinger, F. H.; Land, C. C.; Struebing, V. O. *J. Nucl. Mater.* **1964**, 12, 226–236.
280. Hocheid, B.; Tanon, A.; Bedere, S.; Despres, J.; Hay, S.; Miard, F. In *Plutonium 1965*, Proceedings of the 3rd International Conference on Plutonium, London, 1965; Kay, A. E., Waldron, M. B., Eds.; Chapman and Hall: London, 1967; pp 321–340.
281. Chebotarev, N. T.; Smotriskaya, E. S.; Andrianov, M. A.; Kostyuk, O. E. In *Plutonium 1975 and Other Actinides*; Blank, H., Lindner, R., Eds.; North-Holland: Amsterdam, 1976; pp 37–45.
282. Taylor, J. C.; Linford, P. F. T.; Dean, D. J. *J. Inst. Met.* **1968**, 96, 178–182.
283. Akhachinskij, V. V.; Kopytin, L. M. In *Thermodynamics of Nuclear Materials 1967*, Proceedings of the International Symposium; IAEA: Vienna, 1968; pp 789–792, [in Russian].
284. Teitel, R. J. *Trans. Am. Inst. Min. Metall. Eng.* **1952**, 194, 397–400.
285. Frost, B. R. T.; Maskrey, J. T. *J. Inst. Met.* **1953–1954**, 82, 171–180.
286. Teitel, R. J. *J. Inst. Met.* **1956–1957**, 85, 409–412.
287. Alcock, C. B.; Grieson, P. J. *Inst. Met.* **1961–1962**, 90, 304–310.

-
288. Johnson, I.; Feder, H. M. In *Proceedings of the International Symposium on Thermodynamics of Nuclear Materials*; IAEA: Vienna, 1962; pp 319–329.
289. Chase, M. W. *Bull. Alloy Phase Diagrams* **1983**, 4(1), 124.
290. Foltyn, E. M.; Peterson, D. E. In *Phase Diagrams of Binary Actinide Alloys*; Kassner, M. E., Peterson, D. E., Eds.; Monograph Series on Alloy Phase Diagrams No. 11; ASM International: Materials Park, OH, 1995; pp 372–375.
291. Cafasso, F. A.; Feder, H. M.; Johnson, I. *J. Phys. Chem.* **1964**, 66(7), 1944.
292. Frost, B. *Nucl. Eng.* **1956**, 1, 336.
293. Lebedev, V. A.; Babikov, L. G.; Vavilov, S. K.; Nichkov, I. F.; Raspopin, S. P.; Skiba, O. V. *Russ. J. Atom. Energ.* **1969**, 27, 748–750.

2.06 The U-F System

B. Morel

AREVA Comurhex, Pierrelatte, France

S. Chatain

Commissariat à l'Énergie Atomique et aux Énergies Alternatives, Gif-sur-Yvette, France

© 2012 Elsevier Ltd. All rights reserved.

2.06.1	Introduction	198
2.06.2	Phase Diagram	198
2.06.3	Condensed Phases	199
2.06.3.1	UF ₆ : Uranium Hexafluoride	199
2.06.3.1.1	Properties	199
2.06.3.1.2	Thermodynamic properties	200
2.06.3.1.3	Preparation	201
2.06.3.1.4	Uses	201
2.06.3.2	UF ₄ : Uranium Tetrafluoride	202
2.06.3.2.1	Properties	202
2.06.3.2.2	Thermodynamic properties	203
2.06.3.2.3	Preparation	204
2.06.3.2.4	Uses	204
2.06.3.3	UF _x (4 < X < 6) – Intermediate Fluorides	204
2.06.3.3.1	UF ₅ : Uranium pentafluoride	204
2.06.3.3.2	Intermediate fluorides U ₄ F ₁₇ (UF _{4.25}) and U ₂ F ₉ (UF _{4.5})	206
2.06.3.4	UF ₃ : Uranium Trifluoride	207
2.06.3.4.1	Preparation	207
2.06.3.4.2	Properties	207
2.06.4	Gaseous Compounds	209
2.06.4.1	Gaseous Uranium Hexafluoride	209
2.06.4.1.1	Molecular structure and physical properties	209
2.06.4.1.2	Thermodynamic properties	209
2.06.4.2	Gaseous Monomer and Dimer Uranium Pentafluoride	210
2.06.4.2.1	Molecular structure	210
2.06.4.2.2	Thermodynamic properties	210
2.06.4.3	Gaseous Uranium Tetrafluoride	211
2.06.4.3.1	Molecular structure	211
2.06.4.3.2	Thermodynamic properties	211
2.06.4.4	Gaseous Uranium Trifluoride	213
2.06.4.4.1	Vapor pressure	213
2.06.4.4.2	Enthalpy of formation	213
2.06.4.5	Gaseous Uranium Mono- and Difluoride	213
2.06.5	Outlook	214
References		214

Symbols

C_p^0	Standard heat capacity at constant pressure (J K ⁻¹ mol ⁻¹)
$H_T - H_{298}$	Enthalpy increment (kJ mol ⁻¹)
S^0	Standard entropy (J K ⁻¹ mol ⁻¹)
T_{fus}	Temperature of melting (K)

$\Delta_f H^0$	Standard enthalpy of formation (kJ mol ⁻¹)
$\Delta_{fus} H^0$	Standard enthalpy of fusion (kJ mol ⁻¹)
$\Delta_{fus} S^0$	Standard entropy of fusion (kJ mol ⁻¹)
$\Delta_{sub} H^0$	Standard enthalpy of sublimation (kJ mol ⁻¹)

ϵ	Dielectric constant (F m^{-1})
η	Viscosity (Pa s)
λ	Thermal conductivity ($\text{W m}^{-1} \text{ } ^\circ\text{C}^{-1}$)
ρ	Density (kg m^{-3} or g cm^{-3})

2.06.1 Introduction

Among the numerous compounds in the U–F system (UF_3 , UF_4 , U_4F_{17} , U_2F_9 , UF_5 , and UF_6 as condensed phases, and UF , UF_2 , UF_3 , UF_4 , UF_5 , U_2F_{10} , and UF_6 as gaseous species), UF_6 is certainly the most known because of the wide use of this gas to enrich the ^{235}U fraction in uranium. Indeed UF_6 has a vapor pressure of 1500 mbar ($1.5 \times 10^5 \text{ Pa}$) at 337 K that appears as a striking contrast with the refractory UO_2 , which melts at 3120 K.^{1,2} This difference is typical of fluoride/oxide difference, and also VI/IV oxidation state.

UF_6 was first prepared by Ruff in 1911³ through reaction of F_2 on U metal or carbide. The chemistry of UF_6 was then more completely investigated in the 1940s due to the development of nuclear technology. By the end of 1950, Agron had published a phase diagram including the intermediate fluorides U_4F_{17} , U_2F_9 , and UF_5 . Further research continued at a slower pace in the 1960s on these intermediate fluorides. The scientific interest later decreased with the rise of AVLIS laser-based enrichment technology of U metal that did not need UF_6 to enrich in ^{235}U . In this period, some R&D was also performed on UF_6 to define a dry reprocessing route using the fluoride volatility technique, such as the Fluorex process, to extract U from less-volatile fluorides such as fission products.

On the other end, UF_4 had been known for a long time as a green solid used for the preparation of UF_6 and uranium metal. It was first prepared by the reaction of aqueous HF on U_3O_8 by Hermann in 1861. More recently UF_4 is now considered for molten salt reactor technology.

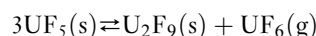
Finally, the UF_3 – UF_4 system was then studied more recently from an academic point of view, but UF_3 today does not present any industrial application.

Except for UF_4 that only yields a hydrate when exposed to air, all these compounds are unstable when exposed to the humidity of air yielding UO_2F_2 and/or UF_4 . UF_6 is also very corrosive and can act as a strong fluorinating reagent. Hence, the characterization of these intermediate fluorides has always been quite limited. For example, the description of the UF_5 liquid phase is not well known. UF_5

may melt congruently at 621 K or undergo decomposition. The eutectic compositions between UF_4 – UF_5 and UF_5 – UF_6 are unknown.

2.06.2 Phase Diagram

Agron has published a phase diagram (Figure 1) for the intermediate fluorides⁴ based on the three following reactions:



From the equilibrium constant of these reactions $K = K_0 e^{-\Delta G_0/RT} = P_{(\text{UF}_6)}$, the experimental results can be expressed as $\log P_{(\text{UF}_6)} = \log K_0 - (\Delta G_0/RT)$, where K_0 and $\Delta G_0/R$ are constants.

Plotting $\log P_{(\text{UF}_6)}$ versus $1/T$ gives the stability domain of these compounds.

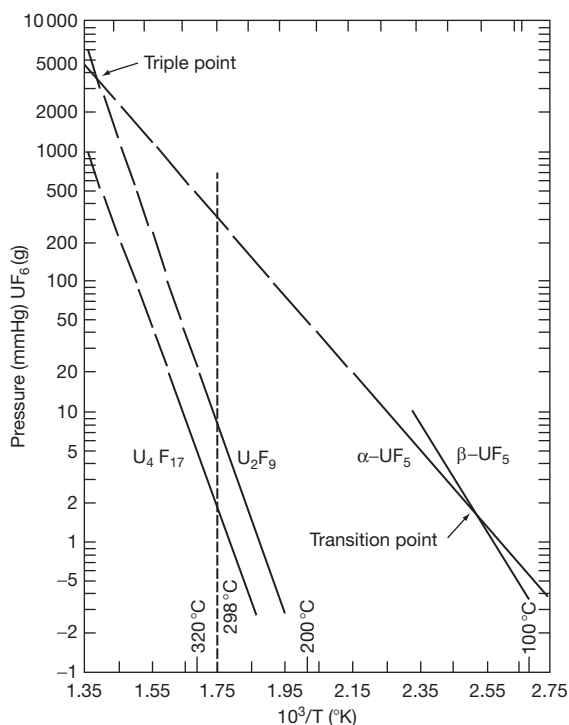


Figure 1 The equilibrium pressures of the various uranium fluorides in the composition range $4 < \text{F/U} < 5$ (Agron diagram). From Agron, P., 1948, AECD-1878, Courtesy of Oak Ridge National Laboratory, U.S. Department of Energy.

The UF_3 – UF_4 system has been studied by Khripin *et al.*⁵ and Slovianskikh *et al.*⁶ by differential thermal analysis; UF_3 being obtained through the reduction of UF_4 with H_2 . In the two cases, they found a eutectic transition at, respectively, (1152 ± 7) K and 1143 K, which is slightly lower than that at the temperature found by Thoma *et al.*⁷ and selected by Knacke *et al.*⁸ The eutectic composition is quite different between the two authors with 0.7835 at. F (atomic fraction of F) found by Khripin *et al.*⁵ (value extrapolated from

the liquidus and solidus data) and 0.788 at. F by Slovianskikh *et al.*⁶ In 1969 Knacke *et al.* published the most complete phase diagram (Figure 2) to date⁸ with three eutectics at 1165, 621, and 328 K and three congruently melting compounds UF_3 , UF_4 , and UF_6 at, respectively, 1700, 1309, and 337 K.

2.06.3 Condensed Phases

2.06.3.1 UF_6 : Uranium Hexafluoride

2.06.3.1.1 Properties

UF_6 is solid at room temperature with a significant vapor pressure ($P = 105$ mbar (1.05×10^4 Pa) at 298 K). The triple point is 337 K for $p = 1.5$ bar, as shown on the $P_{(\text{UF}_6)} = f(T)$ diagram (Figure 3).

The vapor pressure equations are detailed in Section 2.06.4.1.2.

The critical temperature was found between 513 and 518 K.⁹

Many other physical, thermodynamic, and crystallographic properties can be found, respectively, by Llewellyn,⁹ Settle *et al.*,¹⁰ and Hoard and Stroupe.¹¹

What can be noted about UF_6 is the large difference between the density of the liquid and that of the solid at the triple point (4830 kg m^{-3} vs. 3630 kg m^{-3}). If liquid UF_6 solidifies in a process pipe, care must be taken during heating because of the swelling. The recommended equations for the density of solid and liquid UF_6 are¹²

$$\rho_S = 5200 - 5.77(T - 273)$$

$$\rho_L = 3946 - 4.0628(T - 273) - 1.3610^2(T - 273)^2$$

where ρ is in kilogram per cubic meter.

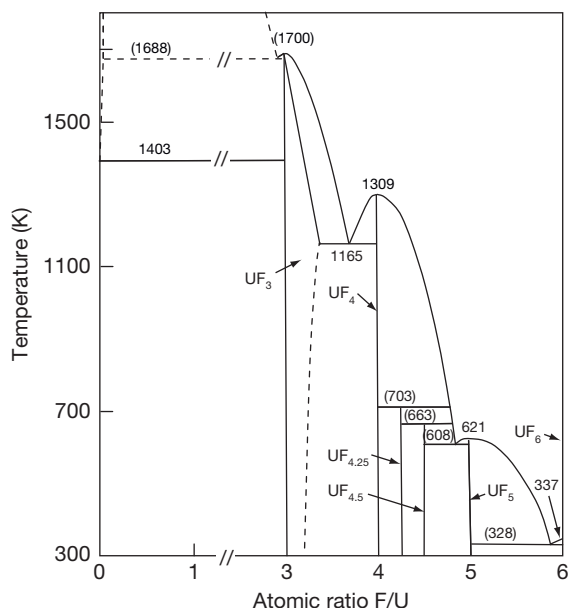


Figure 2 The U-F system. Reproduced from Knacke, V. O.; Lossmann, G.; Müller, F. *Z. Anorg. Allg. Chem.* **1969**, 370, 91-103.

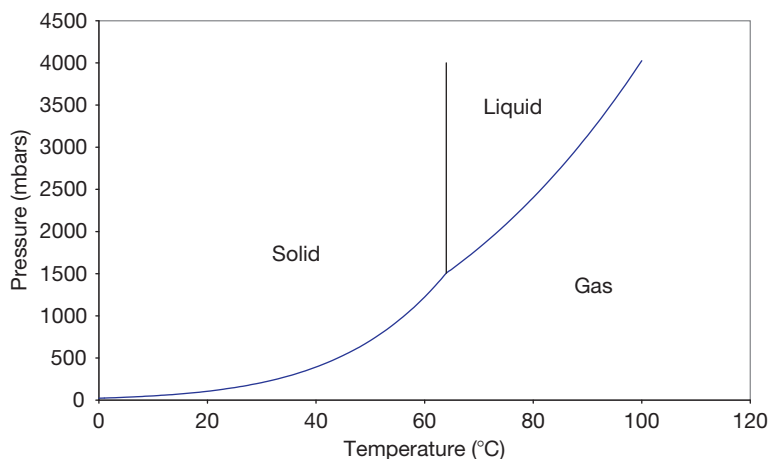


Figure 3 The UF_6 phase diagram.

The viscosity of liquid UF_6 is close to that of water (0.8 cps at 90°C): 0.91, 0.85, 0.80, and 0.75 cps at, respectively, 70, 80, 90, and 100°C .¹³ Liquid UF_6 usually flows by gravity to fill the 48Y containers. A 48Y is a container that contains approximately 12.5 tonnes UF_6 .

Liquid UF_6 has a dielectric constant $\epsilon = 2.18$ at 65°C typical of a nonpolar solvent. The solubility of ionic compounds is low.¹⁴

A review of thermal conductivity for UF_6 in the solid and liquid forms can be found in Lewis *et al.*¹⁵

Our recommended values are:

$$k = 1.1 \text{ W m}^{-1} \text{ }^\circ\text{C}^{-1} \text{ at } 55^\circ\text{C}$$

$$k = 0.16 \text{ W m}^{-1} \text{ }^\circ\text{C}^{-1} \text{ at } 90^\circ\text{C}$$

UF_6 is thermally stable up to 1000 K. However, it is very difficult to study the stability above 700 K due to rapid corrosion of the metal reactors. Also, UF_6 can be easily dissociated under UV source.¹⁶



The average U-F binding energy in UF_6 is 515 kJ mol^{-1} , lower than H-F or Si-F but higher than C-F or As-F.¹⁷

However, the first dissociation energy of UF_6 is as low as 286 kJ mol^{-1} , yielding UF_5 . When the polymerization energy of UF_5 (153 kJ mol^{-1}) is subtracted, one obtains an energy of 134 kJ mol^{-1} , close to the dissociation energy of fluorine (153 kJ mol^{-1}).

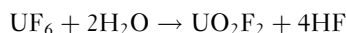
All these properties show that UF_6 will act as an oxidative/fluorinating agent. It will not act as a reducing agent due to its high ionization potential of 14 eV.

UF_6 is therefore a stronger oxidizing agent than MoF_6 or WF_6 . A lot of publications have been

devoted to various reactions of UF_6 in organic chemistry¹⁸ or mineral chemistry.¹⁹

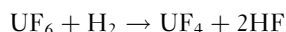
Two reactions are of industrial importance because of the need to convert the depleted UF_6 back into U_3O_8 .

- Hydrolysis of UF_6 with water:



In the presence of a large excess of UF_6 , other oxifluorides can be formed such as UOF_4 or $\text{U}_3\text{O}_5\text{F}_8$.²⁰

- Reduction with H_2 :



Apart from oxidative properties, UF_6 is also considered a Lewis acid and will react with Lewis bases such as KF, which is usually present in the F_2 used to produce UF_6 . NaF also forms Na_2UF_8 complexes that have been used to purify reprocessed UF_6 from fission products.

2.06.3.1.1 Crystal structure

The structure of solid UF_6 was determined by Hoard *et al.*²¹ from X-ray single-crystal data. UF_6 is orthorhombic, space group Pnma (D_{2h}^{16}) with $a = 9.00(2) \text{ \AA}$, $b = 8.962(2) \text{ \AA}$, and $c = 5.207(2) \text{ \AA}$ (Figure 4). This structure was confirmed by single-crystal neutron diffraction at 293 K by Taylor *et al.*²² with $a = 9.924(10) \text{ \AA}$, $b = 8.954(9) \text{ \AA}$, and $c = 5.198(5) \text{ \AA}$ and by Levy *et al.*²³ with $a = 9.92(5) \text{ \AA}$, $b = 8.97(5) \text{ \AA}$, and $c = 5.22 \text{ \AA}$.

2.06.3.1.2 Thermodynamic properties

The thermodynamic properties for the crystalline uranium hexafluoride are summarized in Table 1.

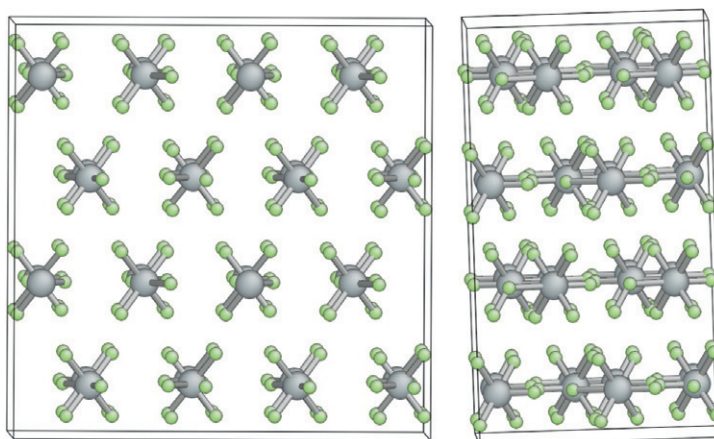
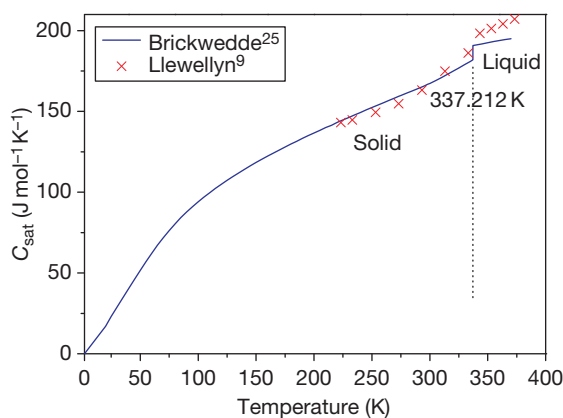


Figure 4 The crystal structure of UF_6 .

Table 1 Thermodynamic properties of the crystalline uranium hexafluoride

$\Delta_f H^\circ$ (UF ₆ , cr, 298.15 K) (kJ mol ⁻¹)	$-(2197.7 \pm 1.8)^{24}$
S° (UF ₆ , cr, 298.15 K) (J K ⁻¹ mol ⁻¹)	227.6 ± 1.3^{24}
C_p° (UF ₆ , cr, 298.15) (J K ⁻¹ mol ⁻¹)	166.8 ± 0.2^{24}
C_p° (UF ₆ , cr, T) (J K ⁻¹ mol ⁻¹)	$52.318 + 0.383798T$ (298–337) ²⁴
T_{fus} (K)	337.2^1
$\Delta H_{\text{fus}}^\circ$ (UF ₆ , cr, 337.2 K) (kJ mol ⁻¹)	19.196^1
C_p° (UF ₆ , l, T)	$215.338 -$ $2.876460 \times 10^{-6} T^{-2}$ $+ 1.9962 \times 10^{-3} T^1$

(298–337) is the temperature range for which the $C_p(T)$ function is valid.

**Figure 5** Experimental heat capacity measurements of the solid and liquid uranium hexafluoride.

2.06.3.1.2.1 Heat capacity

Heat capacity of solid and liquid uranium hexafluoride has been measured between 14 and 370 K by Brickwedde *et al.*²⁵ Some experimental difficulties were encountered due to calorimeter deformation, vapor presence, and lack of reproducibility. The heat capacity for the solid determined by Llewellyn⁹ is in good agreement with Brickwedde *et al.*²⁵ but the discrepancy increased near the fusion point (Figure 5). The heat capacity and entropy at room temperature have been derived from this work.

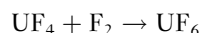
2.06.3.1.2.2 Enthalpy of formation

The enthalpy of formation of crystalline uranium hexafluoride is a key value for the U–F thermochemistry. The value was established by fluorine combustion calorimetry by Seattle *et al.* in 1963¹⁰ and then by Johnson *et al.*²⁶ with a difference of 11 kJ mol⁻¹

between the two results. The value selected by Grenthe *et al.*²⁴ is from Johnson *et al.*²⁶

2.06.3.1.3 Preparation

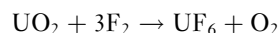
UF₆ is usually obtained through the direct fluorination of UF₄ above 600 K for kinetic reasons:



The reaction mechanism is usually considered as ‘shrinking core,’ the UF₄ particles reduce in size when burning in F₂ and gaseous UF₆ evolves.²⁷ The reaction rate is proportional to the square of the particles’ mean radius. In case of highly porous particles, a homogeneous reaction mechanism has also been proposed.²⁸

UF₆ will be industrially obtained in a flame reactor¹⁷ or in a fluidized bed reactor.²⁹ In the latter case, a fluidizing agent such as CaF₂ or Al₂O₃ is used. Construction materials will depend on the temperature of the wall. For high temperature, Monel or nickel are preferred, although there is corrosion occurring even on passivated NiF₂ surfaces.

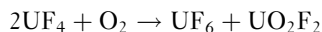
Alternatively, UF₆ can be obtained through direct fluorination of oxides, for example²⁰:



Such a process requires more F₂ and yields more energy to evacuate. Also other oxidants such as XeF₂ which will be reactive even at room temperature can be used, but the high cost of Xe limits their use for R&D purposes.

BrF₃ or ClF₃ can also be used but this is not economically attractive.

At high temperature $T > 873$ K, oxygen should be minimized because of potential reaction between UF₄ and O₂:



UO₂F₂ can also be converted by F₂ to UF₆ but the kinetics of the reaction are 100 times slower than that of UF₄. Activation can be provided by catalysts such as CaF₂.³⁰

2.06.3.1.4 Uses

Because of its high volatility, UF₆ is widely used in the ²³⁵U enrichment processes either the gas diffusion through ceramic membranes, centrifugation or SILEX process recently developed in Australia (Separation of Isotope by Laser EXcitation based on 16 μm laser exciting of gaseous ²³⁵UF₆). Moreover, F is the only halogen that presents only one isotope. This is needed for an enrichment process based on mass (gas

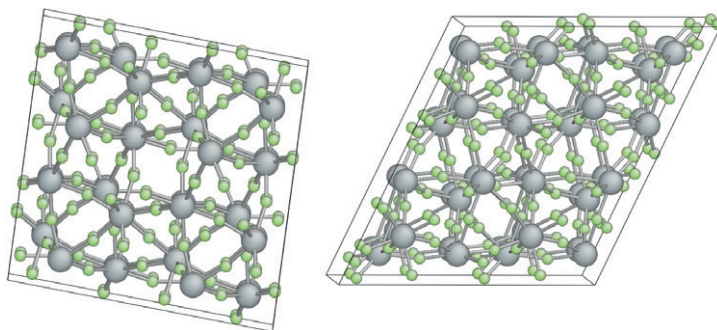


Figure 6 The crystal structure of UF_4 .

diffusion or centrifugation). The reconversion of UF_6 through the reductive pyrohydrolysis to UO_2 yields a sinterable powder that can be readily used to prepare fuel pellets.

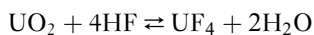
Reaction to form UF_6 is also a way to separate uranium from less-volatile compounds. It has been considered to separate reprocessed uranium from nonvolatile fission product and less-stable other hexafluorides such as PuF_6 and NpF_6 .³¹

2.06.3.2 UF_4 : Uranium Tetrafluoride

2.06.3.2.1 Properties

Although U^{IV} is not stable in aqueous solution, UF_4 is a very stable ionic solid that melts at 1309 K when many covalent tetrafluorides melt below 573 K and polymeric tetrafluorides (ZrF_4 , HfF_4 , SnF_4 , PbF_4 , ...) melt around 1100 K. This is due to its high lattice energy of $12\,970\text{ kJ mol}^{-1}$. UF_4 is a green solid with monoclinic C_{2h}^6 symmetry, $a = 12.73\text{ \AA}$, $b = 10.75\text{ \AA}$, $c = 8.43\text{ \AA}$, and $\beta = 126^\circ 20'$ ⁽³²⁾ (Figure 6) and a density of 6700 kg m^{-3} . UF_4 has a thermal conductivity of $1.96\text{ W m}^{-1}\text{ C}^{-1}$. In the granular form, the effective conductivity can be as low as $0.2\text{ W m}^{-1}\text{ C}^{-1}$. It has a small solubility in water (0.1 g l^{-1} at 298 K). When exposed to air, it will form an hydrate $\text{UF}_4 \cdot 2.5\text{H}_2\text{O}$ after several days.

UF_4 can be pyrohydrolyzed with water. The equilibrated reaction



has been studied³³ and is very significant above 673 K (Figure 7).

A compromise must be found for the synthesis of UF_4 from UO_2 with respect to the temperature. To obtain good kinetics, the temperature must be increased but to avoid pyrohydrolysis and UF_4 sintering, it must be lowered.

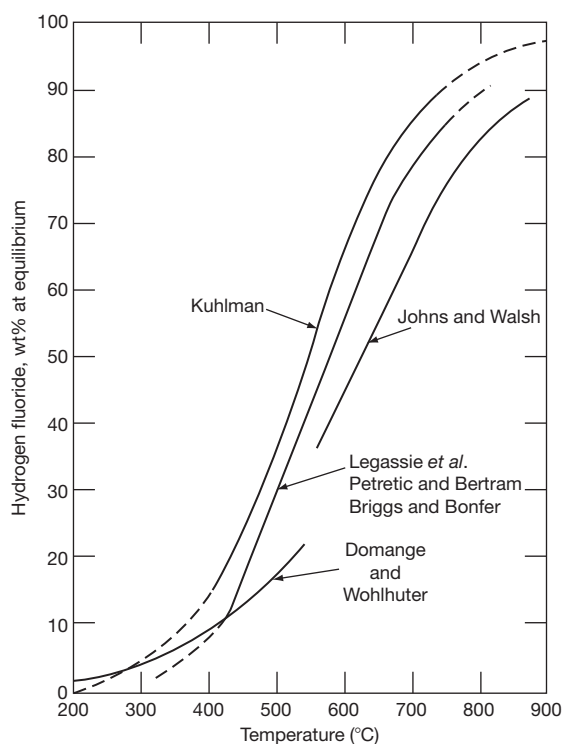


Figure 7 The UO_2 - UF_4 equilibrium. Reproduced from Harrington, C.; Ruenhle, A. *Uranium Production Technology*; Van Nostrand; p 69.

2.06.3.2.1.1 Density

The density of liquid UF_4 has been measured by Kirshenbaum and Cahill³⁴ from 1309 to 1445 K. The results can be represented by:

$$\rho(\text{kg m}^{-3}) = 7784 - 0.92 T \quad T(\text{K})$$

2.06.3.2.1.2 Viscosity

The viscosity of pure liquid UF_4 was measured from 1323 to 1428 K by Desyatnik *et al.*³⁵ and from 1138 to 1618 K by Kulifeyev and Panchishnyi.³⁶ The results are scattered.³⁵ They can be presented by the equation:

$$\eta(\text{mPas}) = 0.0159 \exp\left(\frac{8183}{T}\right) T(\text{K})$$

2.06.3.2.2 Thermodynamic properties

The thermodynamic properties of crystalline UF_4 have been analyzed in detail by Fuger *et al.*,³⁷ Grenthe *et al.*,²⁴ and updated by Guillaumont *et al.*³⁹ The recommended values are reported in Table 2.

2.06.3.2.2.1 Enthalpy of formation

UF_4 has been studied extensively. The heat of formation of UF_4 has been measured using fluorine bomb calorimetry by Hayman⁴⁰ at 315 K (without taking into account the impurities in the samples), by Wijbenga,⁴¹ and by Johnson.⁴² The value obtained by Hayman was recalculated by Wijbenga considering the impurities and the value of the heat of formation of $\text{UF}_6(\text{s})$ measured by Johnson.²⁶

Mal'tsev *et al.*⁴³ determined the heat of formation of the highest crystal hydrate of uranium tetrafluoride, $\text{UF}_4 \cdot 2.5\text{H}_2\text{O}$, as the sum of the heats of nine reactions. Using the heat of hydration of $\text{UF}_4 \cdot 2.5\text{H}_2\text{O}$ given by Popov *et al.*,⁴⁴ Mal'tsev *et al.* deduced the heat of formation of the anhydrous tetrafluoride. Several works reported the enthalpy of formation by solution calorimetry:

- At first, Khanaev *et al.*⁴⁵ used various ($\text{HCl} + \text{H}_3\text{BO}_3 + \text{FeCl}_3$) aqueous solutions at 323 K.
- A solution of hydrofluoric acid, hydrochloric acid, and aqueous aluminum chlorate $\text{AlCl}_3 \cdot 6\text{H}_2\text{O}$ was used by Hu *et al.*⁴⁶
- Finally, Cordfunke *et al.*⁴⁷ have chosen a mixed aqueous solvent containing sulfuric acid, boric acid, and ceric sulfate.

The results obtained are widely scattered from (-1884.9 ± 2.9) to $(-1921.3 \pm 4.2) \text{ kJ mol}^{-1}$.

The selected value came from the IAEA review,³⁷ which is a weighted average of the values published

Table 2 Thermodynamic properties of the crystalline uranium tetrafluoride

$\Delta_f H^0$ (UF_4 , cr, 298.15 K) (kJ mol^{-1})	$-(1914.2 \pm 4.2)^{24}$
S^0 (UF_4 , cr, 298.15 K) ($\text{J K}^{-1} \text{mol}^{-1}$)	151.7 ± 0.2^{24}
C_p^0 (UF_4 , cr, 298.15) ($\text{J K}^{-1} \text{mol}^{-1}$)	116.0 ± 0.1^{24}
C_p^0 (UF_4 , cr, T) ($\text{J K}^{-1} \text{mol}^{-1}$)	$114.5194 + 20.5549$ $\times 10^{-3}T - 4131597^{-2}$ (298–1309) ³⁸
T_{fus} (K)	1305 ± 30^{39}
ΔH_{fus}^0 (UF_4 , cr, 1305 K) (kJ mol^{-1})	47 ± 5^{39}
C_p^0 (UF_4 , l)	167 ± 15^{39}

(298–1309) is the temperature range for which the $C_p(T)$ function is valid.

by Johnson⁴² using fluorine combustion calorimetry (with the selected enthalpy of formation of $\text{UF}_6(\text{s})$) and Cordfunke *et al.*⁴⁷ using solution calorimetry (with the selected enthalpies of formation of $\text{HF}(\text{aq})$, $\text{U}_3\text{O}_8(\text{s})$, and $\gamma\text{-UO}_3$).²⁴ The values differ by 10.7 kJ mol^{-1} , therefore the NEA-TDB²⁴ recommended further measurements to resolve the discrepancies in the experimental values.

2.06.3.2.2.2 Heat capacity

The low-temperature heat capacity of crystalline uranium tetrafluoride was measured by:

- adiabatic calorimetry by Brickwedde *et al.*²⁵ from 20 to 350 K;
- adiabatic calorimetry by Osborne *et al.*⁴⁸ between 5 and 300 K;
- and isothermal calorimetry by Burns *et al.*⁴⁹ in the 1.3–20 K temperature range.

The values are very close except for the values of Brickwedde *et al.*²⁵ extrapolated at $T < 15 \text{ K}$ (Figure 8).

2.06.3.2.2.3 Other properties

Dworkin⁵⁰ measured the enthalpy increment of UF_4 from room temperature up into the liquid phase. These results are in very good agreement with unpublished results obtained by Cordfunke and reported by Fuger³⁷ (Figure 9).

Based on the results from both studies, the enthalpy is expressed as:

$$H_T - H_{298} (\text{kJ mol}^{-1}) = -35.058 + 0.1145 T \\ + 10.27745 \cdot 10^{-6} T^2 + 4.13159 \cdot 10^{-3} T^{-1} \\ (298 - 1309 \text{ K}) \text{ in solid state}$$

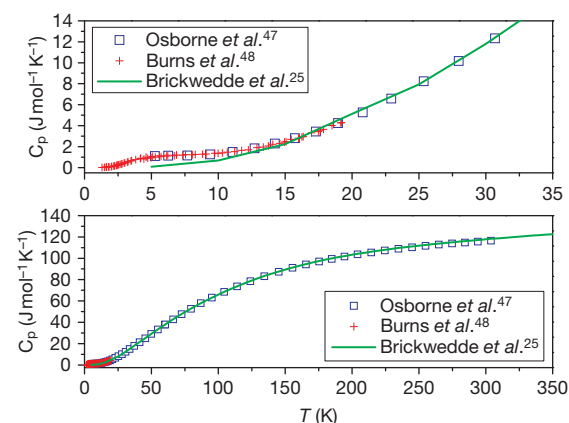


Figure 8 Comparison of the heat capacity measurements of the crystalline uranium tetrafluoride.

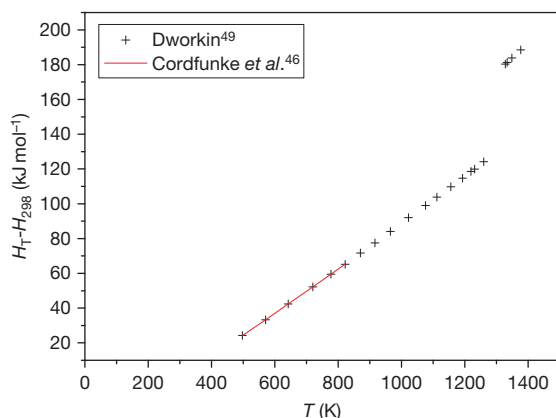


Figure 9 Comparison of the increment enthalpy of crystalline UF_4 experimental results.

$$H_T - H_{298}(\text{kJ mol}^{-1}) = -39.413 + 0.166T$$

(1309 – 1400 K) in liquid state with $T(\text{K})$

Dworkin deduced from his measurements the entropy and enthalpy of fusion at the fusion temperature

$$T_{\text{fus}} = 1309 \text{ K}$$

$$\Delta_{\text{fus}}H^\circ = 46986 \text{ J mol}^{-1}$$

$$\Delta S_{\text{fus}} = 35.98 \text{ JK}^{-1} \text{ mol}^{-1}$$

This enthalpy of fusion is higher than the approximate value calculated by Khripin⁵ from the differential thermal analysis in the UF_3 – UF_4 binary system ($\Delta_{\text{fus}}H^\circ(\text{UF}_4, \text{s}, 1309 \text{ K}) = 43\,514 \pm 2 \text{ kJ mol}^{-1}$).

The experimental data of Dworkin for the enthalpy of fusion has been recommended by Guillaumont *et al.*³⁹ in their review, although the vapor pressure data for $\text{UF}_4(\text{cr}, \text{l})$ are more consistent with a smaller value (36 kJ mol^{-1}).³⁹

2.06.3.2.3 Preparation

Two ways are industrially used to obtain UF_4 from UO_2 powder:

- the precipitation of UF_4 in HF aqueous solution,
- the reaction of UO_2 with gaseous HF at 573–773 K:
 $\text{UO}_2 + 4\text{HF} \rightarrow \text{UF}_4 + 2\text{H}_2\text{O}$.

As a consequence, the impurities in UF_4 are usually oxygen based, such as UO_2F_2 , UO_2 , or H_2O .

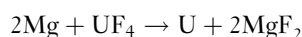
The large density variation between the fluoride and the oxide tends to hinder the reaction because swelling occurs and the porosity is easily blocked during the conversion. The kinetics of hydrofluorination will then depend much on the specific surface of the

UO_2 . A model has been developed that takes into account the grain and pellet sizes.⁵¹ Impurities such as sodium can also be detrimental because they may favor the sintering. The NaF – UF_4 eutectic melts close to 893 K.

UF_4 can be obtained in a rotating furnace, in a fluidized bed, or in a moving bed reactor where the UO_2 has been pelletized as described in Harrington and Ruenhle.³³ If the hydrofluorination temperature is maintained below 750 K, the effect of sodium is light.

2.06.3.2.4 Uses

UF_4 can be used to produce UF_6 (see previous section) or U metal using magnesium reduction in a bomb:



In all cases, the oxygen residual level in UF_4 will be very important. It will affect the conversion rate to U metal or UF_6 .

Mixtures of fluoride salts with UF_4 are candidates as fuel carrier of molten salt reactors⁵² (see [Chapter 3.13, Molten Salt Reactor Fuel and Coolant](#)).

2.06.3.3 UF_x ($4 < X < 6$) – Intermediate Fluorides

2.06.3.3.1 UF_5 : Uranium pentafluoride

2.06.3.3.1.1 Properties and preparation of UF_5

UF_5 was initially prepared by Ruff through the reaction of UCl_5 with anhydrous HF. More recent studies have been made on the reaction of gaseous UF_6 on UF_4 as a powder:



However, a low temperature ($T \leq 453 \text{ K}$ for $\text{pUF}_6 < 1 \text{ bar}$ (10^5 Pa)) is required to avoid the decomposition to U_2F_9 . This often means a very slow transformation (several days depending on the specific surface). UF_5 has a white color but with this technique a gray or black color powder is often obtained because of presence of U_2F_9 .

Asada has more recently prepared UF_5 at 643 K but under 3 bars ($3 \times 10^5 \text{ Pa}$) UF_6 .⁵³ However, corrosion problems have been experienced.

Probably the best way to obtain pure UF_5 from UF_4 and UF_6 is to allow evaporation of UF_5 at 573–673 K and condensation at ~ 346 –408 K. Blue UF_5 needles are then obtained.

UF_5 is often considered a key product because it may be involved in clogging reactors (flame reactor or fluidized bed) when no excess F_2 is maintained. UF_5 has a tendency to polymerize. This very important property tends to explain why the reactivity of

U(V) fluorides is lower than that of U(IV). Also UF_5 melts at a low temperature compared to UF_4 .

UF_5 has two crystalline forms that are both tetragonal (Figure 10):

- High-temperature $\alpha\text{-UF}_5$ that has an I41m symmetry with $a = 6.5259(3) \text{ \AA}$ and $c = 4.4717(2) \text{ \AA}$, which was confirmed by high-resolution neutron powder diffraction data of Howard *et al.*⁵⁴
- Low-temperature $\beta\text{-UF}_5$ that has an I42d symmetry with $a = 11.469(5) \text{ \AA}$ and $c = 5.215(2) \text{ \AA}$ ($a = 11.456(2) \text{ \AA}$, $c = 5.195(1) \text{ \AA}$, $Z = 8$).⁵⁵

The transition temperature is 398 K, independent of the UF_6 pressure. The α -phase is obtained from the β form when slowly raising the temperature (18 h at 458 K). The reverse transformation from α to β has not yet been achieved.

UF_5 can be separated from U(VI) compounds using anhydrous acetonitrile dissolution.⁵⁶ Again this property is linked to the polymerization trend of UF_5 .

2.06.3.3.1.2 Thermodynamic properties

The reviewed thermodynamic properties by Fuger *et al.*,³⁷ Grenthe *et al.*,²⁴ and Guillaumont *et al.*³⁹ of both α - and β -uranium pentafluoride are presented in Table 3.

Only a single reliable experimental study is reported for the uranium pentafluoride. The enthalpies of formation of both allotropic forms have been measured by solution calorimetric experiments in $\text{Ce}(\text{SO}_4)_2 + \text{H}_2\text{SO}_4$ by O'Hare *et al.*⁵⁷ They found:

$$\begin{aligned}\Delta_f H^0(\alpha\text{-UF}_5, \text{s}, 298.15 \text{ K}) &= -(2075.5 \pm 6.7) (\text{kJ mol}^{-1}) \\ \text{and } \Delta_f H^0(\beta\text{-UF}_5, \text{s}, 298.15 \text{ K}) \\ &= -(2083.0 \pm 6.3) (\text{kJ mol}^{-1}).\end{aligned}$$

This value is consistent with the earlier results of Agron when recalculated using the values of $\Delta_f H^0$ (UF_4 , s, 298.15 K) and $\Delta_f H^0$ (UF_6 , g, 298.15 K) recommended by Grenthe *et al.*²⁴

Katz and Rabinowitch⁵⁸ reported unpublished low-temperature heat capacity measurements on $\alpha\text{-UF}_5$ performed by Brickwedde *et al.* Because of the presence of 17 wt% UF_4 and UO_2F_2 in the $\alpha\text{-UF}_5$ samples, Fuger *et al.*³⁷ adjusted the result to be consistent with Agron's dissociation measurements.⁵⁹

The heat capacity variation with temperature is from Knacke *et al.*⁸ who did not distinguish between α - and β -phases. The value at 298.15 K is interpolated.

The UF_5 stability domain was revisited recently⁶⁰ at higher pressure than Agron's initial study. The results were found in good agreement (Figure 11).

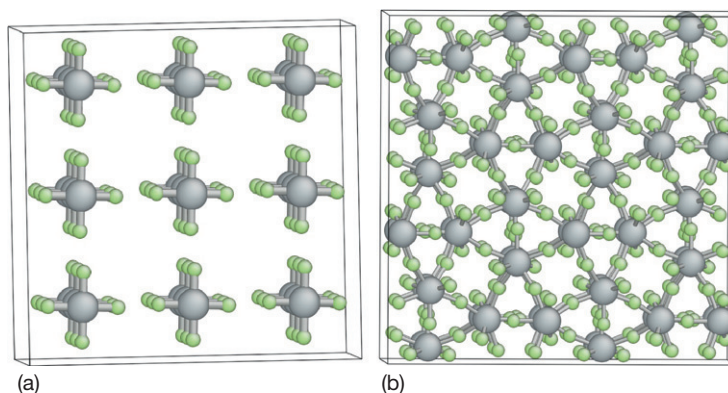


Figure 10 The crystal structure of (a) $\alpha\text{-UF}_5$ and (b) $\beta\text{-UF}_5$.

Table 3 Thermodynamic properties of the crystalline α and β -uranium pentafluoride

Properties	$\alpha\text{-UF}_5$	$\beta\text{-UF}_5$
$\Delta_f H^0$ (298.15 K) (kJ mol^{-1})	$-(2075.3 \pm 5.9)^{24}$	$-(2083.2 \pm 4.2)^{24}$
S^0 (298.15 K) ($\text{J K}^{-1} \text{mol}^{-1}$)	199.6 ± 12.6^{24}	179.5 ± 12.6^{24}
C_p^0 (298.15) ($\text{J K}^{-1} \text{mol}^{-1}$)	132.2 ± 4.2^{24}	132.2 ± 12.0^{24}
C_p^0 (T) ($\text{J K}^{-1} \text{mol}^{-1}$)	$125.159 + 3.0208 \times 10^{-2} T - 192\,500 T^{-2}$ (298–1000) ³⁹	$125.159 + 3.0208 \times 10^{-2} T - 192\,500 T^{-2}$ (298–1000) ³⁹
T_{fus} (K)	621 ¹	

(298–1000) is the temperature range for which the $C_p(T)$ function is valid.

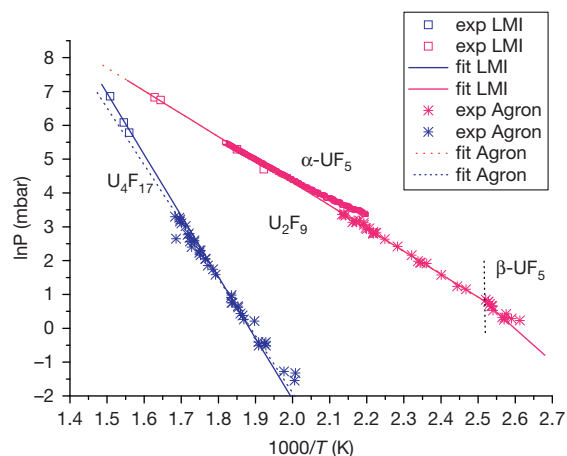


Figure 11 Phase stability domain for the intermediate fluorides after Agron⁵⁹ and Moch *et al.*⁶⁰

2.06.3.3.1.3 Properties of liquid uranium pentafluoride

Experimental studies on liquid UF_5 are difficult due to its volatility, corrosiveness, tendency to disproportionate, and sensitivity to moisture. Wolf *et al.*⁶¹ measured the melting point of $\alpha\text{-UF}_5$ under various UF_6 pressures in excess (from 7.1×10^4 Pa to 4.7×10^5 Pa) to avoid the disproportionation. They found $T_{\text{fus}}(\text{UF}_5, \text{cr}) = 621$ K. Asada *et al.*⁵³ have determined some physical properties over the temperature range 638–693 K under UF_6 pressure of 3×10^5 Pa:

$$\text{Density : } \rho_L = 4.5 \text{ g cm}^{-3}$$

$$\begin{aligned} \text{Electric conductivity : } (\Omega^{-1} \text{ cm}^{-1}) \\ = 2.63 \exp(-2.84/RT) \end{aligned}$$

$$\text{Viscosity } \eta(\text{cp}) = 1.6 \times 10^{-2} \exp(7.03/RT)$$

2.06.3.3.2 Intermediate fluorides U_4F_{17} ($\text{UF}_{4.25}$) and U_2F_9 ($\text{UF}_{4.5}$)

2.06.3.3.2.1 Preparation

U_2F_9 (which is called uranium ennefluoride) is prepared by treating UF_4 with UF_6 . The kinetics are faster (about 1 day) when the process is performed under higher pressure of UF_6 and high temperature. Another way is to start from the pentafluoride and decompose it into U_2F_9 . It is less convenient because it includes the synthesis of pure pentafluoride which is less stable. U_2F_9 is the more stable intermediate fluoride under argon atmosphere without moisture. It forms black needles.

U_4F_{17} was obtained by maintaining UF_4 at 593 K and introducing UF_6 at 2.3×10^3 Pa pressure

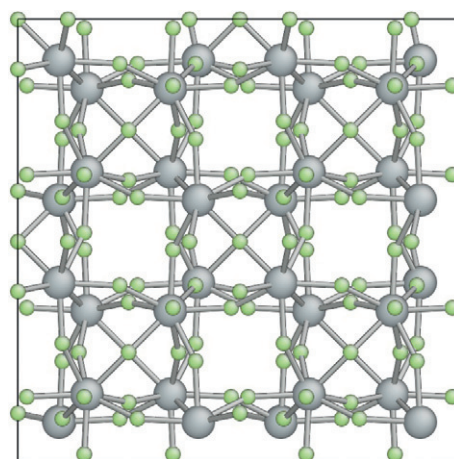


Figure 12 The crystal structure of U_2F_9 .

during 2 days.⁵⁹ The diffraction pattern of this material resembling that of UF_4 but containing uniquely different features is described as ‘distorted UF_4 .’ It is a black powder. This synthesis is to be avoided due to the corrosion problem at high temperature under UF_6 . It is easier to decompose higher intermediate fluorides such as UF_5 or U_2F_9 than synthesize directly.

We have found no physical properties for these compounds in the literature. Mixtures of $\text{UF}_5\text{--U}_2\text{F}_9$ have a tendency to melt at lower temperature than pure UF_5 .

2.06.3.3.2.2 Crystal structure

U_2F_9 as a body-centered cubic structure, space group $I\bar{4}3m - T_d^3$ with $a = 8.4716(5)$ Å (Figure 12) and a theoretical density $\rho_{\text{th}} = 7.06 \text{ g cm}^{-3}$.^{62,63} This symmetry was confirmed by high-resolution neutron powder diffraction data.⁵⁴

U_4F_{17} has a deformed UF_4 lattice. The symmetry is monoclinic, space group C_{2h}^6 , $C2/c$, with $a = 12.09$ (0.08) Å, $b = 10.81(2)$ Å, $c = 8.29(4)$ Å, and $\beta = 128.0(8)$.¹²

2.06.3.3.2.3 Thermodynamic properties

The thermodynamic data at room temperature on solid U_4F_{17} and U_2F_9 recommended by Grenthe *et al.*²⁴ are presented in Table 4.

With second-law analysis of disproportionation pressure measurements performed by Agron,⁵⁹ the enthalpy and entropy of each reaction at the mean temperature can be calculated. Assuming that $\Delta C_p \approx 0$, the thermodynamics properties of the U_4F_{17} and U_2F_9 can be calculated using the thermodynamic properties of $\text{UF}_4(\text{s})$ and $\text{UF}_6(\text{g})$ at 298.15 K.

Table 4 Thermodynamic properties of the crystalline U_4F_{17} and U_2F_9 compounds

Properties	U_4F_{17}	U_2F_9
$\Delta_f H^\circ$ (298.15 K) (kJ mol^{-1})	$-(7850 \pm 32)^{24}$	$-(4016 \pm 18)^{24}$
S° (298.15 K) ($\text{J K}^{-1} \text{mol}^{-1}$)	631 ± 40^{24}	329 ± 20^{24}
C_p° (298.15) ($\text{J K}^{-1} \text{mol}^{-1}$)	485.3 ± 33.0^{24}	251.0 ± 16.7^{24}
C_p° (T) ($\text{J K}^{-1} \text{mol}^{-1}$)	$453.546 + 1.18491 \times 10^{-1}T$ $- 26\,7776T^{-2}$ (298–600) ²⁴	$235.978 + 5.99149 \times 10^{-2}T$ $- 217568T^{-2}$ (298–600) ²⁴

(298–600) is the temperature range for which the $C_p(T)$ function is valid.

The different values found in the literature come from the selected data of the UF_6 and UF_4 and the analysis of Agron's measurements.⁶⁴

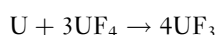
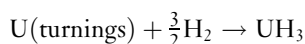
Rand and Kubaschewski⁶⁵ estimated the entropies of $\text{UF}_{4.5}(\text{cr})$ and $\text{UF}_{4.25}(\text{cr})$ in two ways: by Latimer's method⁶⁶ and by linear interpolation between the values for entropies of $\text{UF}_4(\text{s})$ and $\text{UF}_5(\text{s})$ obtained by Agron. They selected values intermediate between these two estimates.

Agron's diagram was revisited recently at higher pressure and temperature. The new values confirm the previous work of Agron. We note just a slight change of the $\text{U}_4\text{F}_{17}/\text{U}_2\text{F}_9$ domain (Figure 13).

2.06.3.4 UF_3 : Uranium Trifluoride

2.06.3.4.1 Preparation

Uranium trifluoride is most conveniently prepared by reduction of UF_4 with finely powdered uranium. Three methods of preparation of uranium fluoride have been investigated: (1) Palmer⁶⁷ reported the reduction of uranium tetrafluoride by hydrogen at 1000 °C in molybdenum boats using stainless-steel tubes ($\text{UF}_4(\text{s}) + 1/2\text{H}_2 \leftrightarrow \text{UF}_3(\text{s}) + \text{HF}$), (2) treatment of uranium trichloride with hydrogen fluoride,⁶⁸ and (3) reduction of uranium tetrafluoride with uranium. Uranium trifluoride was prepared by the reaction of uranium tetrafluoride with a stoichiometric amount of uranium hydride (obtained by a hydrogenation and dehydrogenation cycle of uranium metal repeated several times) in a slow stream of argon at temperatures that slowly increase from 700 to 900 K during 5 h. Tantalum carbide crucibles were used as containers. After cooling in argon, the sample was transferred to a glove box and homogenized.⁴⁷



Uranium trifluoride is a gray to black solid.

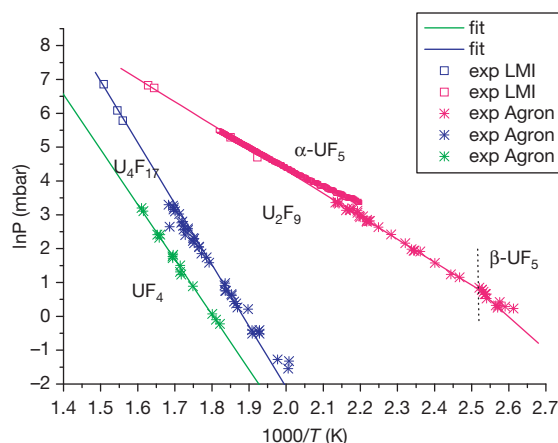


Figure 13 Measurements of the decomposition pressure over the intermediates fluorides obtained by Agron⁵⁹ and Moch et al.⁵⁹

2.06.3.4.2 Properties

As compared to other uranium(III) compounds, the trifluoride is remarkably stable on air at room temperature. At higher temperatures, UF_3 oxidizes and at 1173 K, it is quantitatively converted into U_3O_8 . Contrary to the other trivalent uranium halides, UF_3 is not hygroscopic.

The compound is thermally unstable even in an inert atmosphere and disproportionates to UF_4 and U at about 1273 K and to a smaller extent (0.1% per hour) also at 1073 K.⁶⁹

2.06.3.4.2.1 Crystal structure

UF_3 has a LaF_3 -type structure but the symmetry is reported to be either trigonal (space group $\text{P}\bar{3}\text{c}1$, D_{3d}^4) or hexagonal (space group $\text{P}6_3\text{cm}$, C_{6v}^3). The uranium atom in UF_3 is 11-coordinate^{68,70}

$$a_1 = (4.138 \pm 0.03) \text{ \AA} \text{ and } a_3 = 7.333 \pm 0.004 \text{ \AA}$$

for in agreement with

$$a_1 = (4.13 \pm 0.01) \text{ \AA} \text{ and } a_3 = (7.33 \pm 0.01) \text{ \AA}$$

Other crystallographic data can be found elsewhere.⁶⁹

Table 5 Thermodynamic properties of the crystalline uranium trifluoride compound

$\Delta_f H^0$ (UF ₃ , s, 298.15 K) (kJ mol ⁻¹)	$-(1501.4 \pm 4.7)^{24}$
S^0 (UF ₃ , s, 298.15 K) (J K ⁻¹ mol ⁻¹)	129.2 ± 0.5^1
C_p^0 (UF ₃ , s, 298.15) (J K ⁻¹ mol ⁻¹)	95.1 ± 0.4^{24}
C_p^0 (UF ₃ , s, T) (J K ⁻¹ mol ⁻¹)	$106.539 + 7.05 \times 10^{-4}T - 1035500 \times T^{-2}$ (298.15–1768 K) ³⁹
T_{fus} (K)	1768 ¹
$\Delta_{\text{fus}} H$ (UF ₃ , 298.15 K) (kJ mol ⁻¹)	36.8 ¹

(298.15–1768) is the temperature range for which the $C_p(T)$ function is valid.

The calculated density value with two molecules of UF₃ per unit cell varies between 8.99 and 8.95⁷¹ compared to the experimental one of 9.18.⁶⁸

2.06.3.4.2.2 Thermodynamic properties

The thermodynamic properties of crystalline uranium trifluoride recommended by NEA-TDB^{24,39} are presented in Table 5.

2.06.3.4.2.3 Enthalpy of formation

All the experimental results on the enthalpy of formation have been evaluated by Fuger *et al.*³⁷ and later by Grenthe *et al.*²⁴

The heat of formation of UF₃ has been measured using fluorine bomb calorimetry by Hayman⁴⁰ at 315 K and Wijbenga.⁴¹ The Hayman's value was recalculated by Wijbenga taking into account the impurities and the value of the heat of formation of UF₆(g) measured by Johnson.²⁶

Khanaev *et al.*⁷² and Cordfunke *et al.* reported the enthalpy of formation by solution calorimetry at 323 K, respectively, in:

- various (HCl + H₃BO₃ + FeCl₃) aqueous solutions;
- a mixed aqueous solvent containing sulfuric acid, boric acid, and ceric sulfate.

For UF₄, the samples' impurities complicate the fluorine combustion and the complex thermochemical cycles, involving up to 11 reactions, increase the uncertainties.

2.06.3.4.2.4 Other properties

The low-temperature heat capacity has been measured by adiabatic calorimetry from 5 to 350 K by Cordfunke *et al.*⁷³ (Figure 14). They derived, $C_p^0(298.15\text{K}) = 95.10 \text{ J mol}^{-1} \text{ K}^{-1}$ and $S^0(298.15\text{K}) = (123.46 \pm 0.5) \text{ J mol}^{-1} \text{ K}^{-1}$. The enthalpy increment measurements

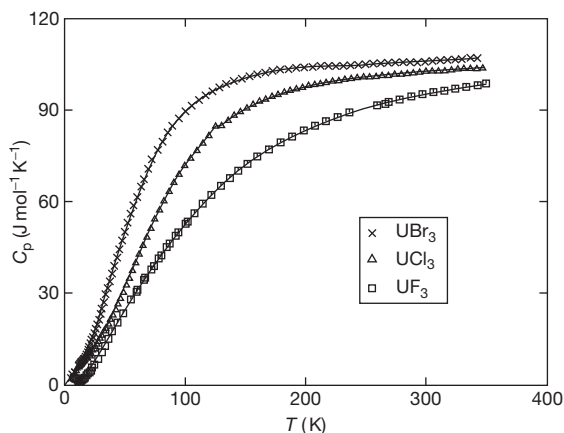


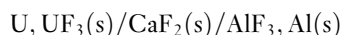
Figure 14 The low-temperature heat capacity of UF₃. Reproduced from Cordfunke, E. H. P.; Konings, R. J. M.; Westrum, E. F., Jr. *J. Nucl. Mater.* **1989**, 167, 205–212.

were done in an isothermal drop calorimeter from 398 to 866 K, relative to room temperature and is expressed as follows:

$$\{H^0(T) - H^0(298.15\text{K})\} = 106.541T + 35.271 \times 10^{-3}T^2 + 10.355 \times 10^5 T^{-1} - 35269.0$$

in J mol⁻¹ and T(K)

The free energy of formation of UF₃ was determined by EMF measurements with the following cells⁷⁴:



yielding for the free energy at 873 K $\Delta_f G^0(\text{UF}_3) = -1299.1 \text{ kJ mol}^{-1}$.

This value is compared at first with Wijbenga's data deduced from EMF measurements performed in the temperature range 950–1170 K using the cell Ni, W|Ni, NiF₂|CaF₂|UF₃, U|W, Ni⁴¹ and then with the values evaluated by Cordfunke *et al.*⁷³ from their heat capacity determinations and the enthalpy of formation assessed by Fuger *et al.*³⁷ It is in good agreement with the extrapolated results of Wijbenga and slightly higher than those of Cordfunke (Figure 15).

2.06.3.4.2.5 Enthalpy of melting

Khripin *et al.*⁵ obtained from their differential thermal analysis in the UF₃–UF₄ binary system the value of the heat of fusion of the $\Delta_{\text{fus}} H(\text{UF}_3, \text{s}, 1768\text{K}) = (36.8 \pm 0.8) \text{ kJ mol}^{-1}$ at the melting temperature measured by Tananev⁷⁵ and D'Eye and Martin at $T_{\text{fus}}(\text{UF}_3) = 1768 \text{ K}$.⁷⁶

2.06.4 Gaseous Compounds

2.06.4.1 Gaseous Uranium Hexafluoride

2.06.4.1.1 Molecular structure and physical properties

The gaseous UF_6 was studied extensively in the 1950s and 1960s. Gas-phase electron diffraction,⁷⁷ Raman, and infrared studies⁷⁸ have established the octahedral structure, O_h , of the gaseous UF_6 and the molecular and vibrational parameters (Table 6). The U–F distance is 2.00 Å. From the molecular and vibrational parameters, the entropy can be calculated accurately.

In the gas phase, the density of UF_6 can be described according to an equation which is similar in form to the ideal gas law.

$$\rho = 4291P / (T(1 - 1.3769 \cdot 10^6 P / T^3))$$

where ρ is in kg m^{-3} , P in atm, and $T(\text{K})$.¹⁵

The viscosity and thermal conductivity have been measured by Llewellyn.⁹

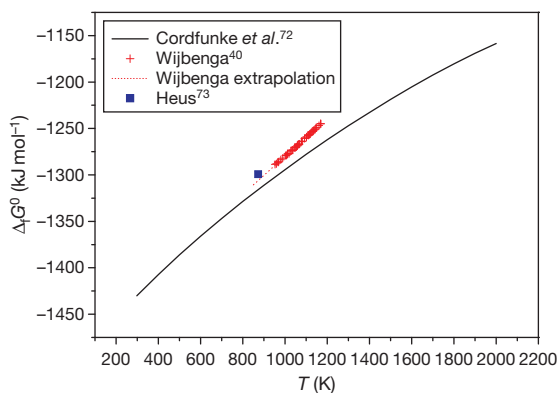


Figure 15 Comparison of the Gibbs energy of formation of UF_3 data.

Table 6 Molecular parameters of gaseous uranium hexafluoride

Point group (symmetry number)	Interatomic distance (Å)	Vibration frequencies (multiplicities) (cm^{-1})	Product of moments of inertia ($\text{g}^3 \text{cm}^{-6}$)
O_h (24)	1.9962	668.2 534.5(2) 627.7(3) 187.5(3) 201.0(3) 143.0(3)	1.27×10^{-112}

We report that:

$$\eta = 2.1 \cdot 10^{-4} \text{ P at } 100^\circ\text{C}$$

$$\lambda = 8 \cdot 10^{-3} \text{ W K}^{-1} \text{m}^{-1} \text{ at } 105^\circ\text{C}$$

2.06.4.1.2 Thermodynamic properties

The values recommended by Grenthe *et al.*²⁴ and updated by Guillaumont *et al.*³⁹ are presented in Table 7.

The enthalpy of sublimation was evaluated by third-law analysis of experimental vapor pressure data.

The thermal functions of $\text{UF}_6(\text{g})$ are calculated from the molecular parameters given in the comprehensive paper of Aldridge *et al.*⁷⁹

2.06.4.1.2.1 Enthalpy of formation

The enthalpy of formation of the gaseous uranium hexafluoride was investigated at the same time as for the crystalline UF_6 by fluorine bomb calorimetry by Seattle *et al.*¹⁰ and then by Johnson.⁸⁰ As for the crystal, a difference of 11 kJ mol^{-1} was found between the two authors. The enthalpies of formation can be obtained from the analyses of the vapor pressure measurements that have been performed and such data have been derived in the NEA-TDB series.

2.06.4.1.2.2 Vapor pressure

Several works were devoted to measure the vapor pressure above the solid and liquid uranium hexafluoride.²⁴ The agreement between the authors is excellent (Figure 16).

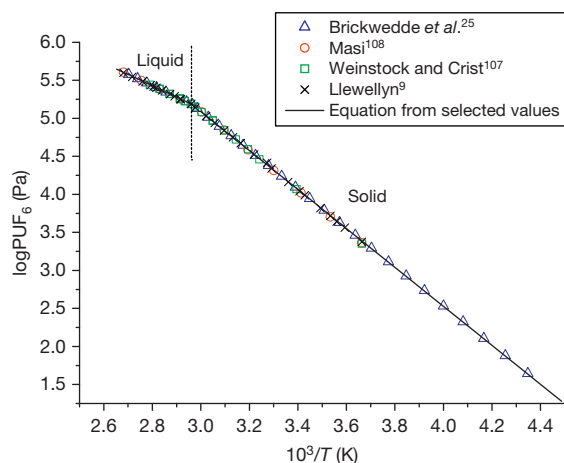
The vapor pressure equation based on the experimental data above the solid and liquid uranium hexafluoride is, respectively:

$$\log P(\text{Pa}) = -\frac{2562.46 \pm 3.64}{T} + (12.7767 \pm 0.01235) \\ [230 - 337 \text{ K}]$$

Table 7 Thermodynamic properties of the gaseous uranium hexafluoride

$\Delta_f H^0$ (UF ₆ , g, 298.15 K) (kJ mol ⁻¹)	$-(2148.6 \pm 1.9)^{24}$
S^0 (UF ₆ , g, 298.15 K) (J K ⁻¹ mol ⁻¹)	376.3 ± 1.0^{39}
C_p^0 (UF ₆ , g, 298.15) (J K ⁻¹ mol ⁻¹)	129.4 ± 0.5^{39}
C_p^0 (UF ₆ , g, T) (J K ⁻¹ mol ⁻¹)	$137.373 + 3.9605 \times 10^{-2}T$ $- 2.1788 \times 10^{-5}T^2$ $- 1.586870T^{-2}$ (298–700) ³⁹
$\Delta_{\text{sub}} H^0$ (UF ₆ , 298.15 K) (kJ mol ⁻¹)	49.1 ± 0.5^{24}

(298–700) is the temperature range for which the $C_p(T)$ function is valid.

**Figure 16** Vapor pressure experimental data above the solid and liquid UF₆.

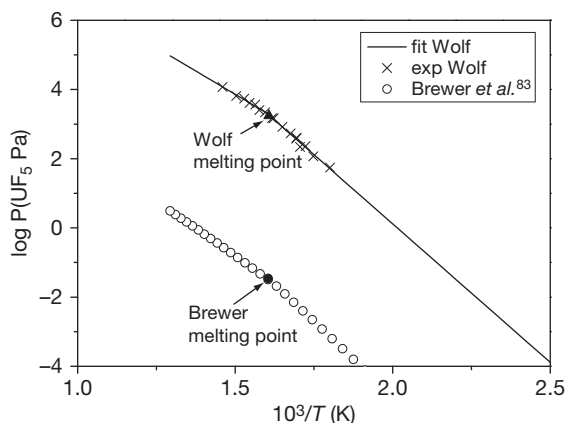
$$\log P(\text{Pa}) = -\frac{1490.27 \pm 6.56}{T} + (90.60167 \pm 0.01862) \quad [337 - 370 \text{ K}]$$

A comprehensive source of vapor pressure data has been published by Oliver *et al.*⁸¹

2.06.4.2 Gaseous Monomer and Dimer Uranium Pentafluoride

2.06.4.2.1 Molecular structure

The infrared data of UF₅ molecules isolated in Ar, Xe, and CO matrices obtained by Paine *et al.*⁸² were inconclusive about the structure of the pentafluoride gaseous molecule: two structures were possible, trigonal bipyramidal (D_{3h}) or square pyramidal (C_{4v}). The same year, Krohn *et al.*⁸³ calculated infrared absorption spectrum by fundamental modes for several assumed geometrical configurations of UF₅.

**Figure 17** Experimental vapor pressure equation above the solid and liquid UF₃ after Wolf *et al.*⁶⁰ and Brewer *et al.*⁸³

Comparing the predicted spectra with the observed spectrum of Paine *et al.*,⁸² they concluded that the structure is square pyramidal (C_{4v}) with the U atom above the F atom equatorial plane. This result was experimentally confirmed by infrared and Raman spectroscopies performed by Jones *et al.*⁸⁴ for UF₅ isolated in argon and neon matrices.

No experimental work was performed on the molecular structure of the dimer.

2.06.4.2.2 Thermodynamic properties

2.06.4.2.2.1 Vapor pressure

The first results published on vapor pressure above uranium pentafluoride are estimations from Brewer *et al.*⁸⁵ In 1960, Wolf *et al.*⁸⁶ measured the vapor pressure above the solid and liquid states, from 555 to 685 K, using the vapor transpiration method with UF₆ as carrier gas to avoid the disproportionation. In this study, they supposed that the gaseous UF₅ is a monomer in this temperature range. The results are shown in Figure 17.

The results are completely different. The melting point deduced from the vapor pressure measurements is estimated between 600⁸⁵ and 615 K.⁸⁶

The assumption of Wolf *et al.* was contradicted by Kleinschmidt *et al.*⁸⁷ who showed the existence of gaseous dimer, U₂F₁₀. The gaseous dimerization equilibrium 2UF₅(g) = U₂F₁₀(g) was then studied by high-temperature mass spectrometry over the range 600–870 K. Following Kleinschmidt *et al.*, saturated vapor obtained by Wolf *et al.* contained more than 90% of dimer U₂F₁₀. The experimental results of Wolf *et al.* were reanalyzed by Leitnaker⁸⁸ to take into account the dimerization of UF₅(g) and the

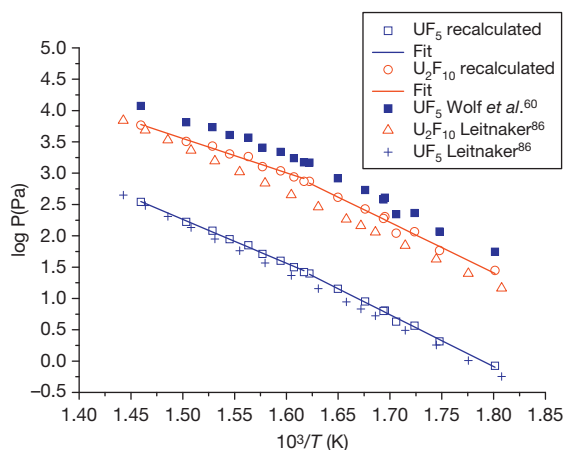


Figure 18 ■ Vapor pressures reported by Wolf⁶¹; + vapor pressures of UF₅ corrected by Leitnaker⁸⁸ Δ vapor pressures of U₂F₁₀ corrected by Leitnaker⁸⁸ (from Wolf *et al.* measurements taken into account the dimer in the vapor and U₂F₁₁ molecules); ○ vapor pressure of U₂F₁₀; □ vapor pressure of UF₅ calculated (from Wolf *et al.* measurements taken into account the equilibrium constant and effective pressure).

probable formation of U₂F₁₁(g) in the presence of UF₆ as transporting gas. New vapor pressure equations were proposed for gaseous UF₅ and U₂F₁₀.

$$\ln p_{\text{U}_2\text{F}_{10}} = \frac{-16900}{T(\text{K})} + 21704 \quad P \text{ in atm}$$

$$\ln p_{\text{UF}_5} = \frac{-18263}{T(\text{K})} + 20926 \quad P \text{ in atm}$$

Individual pressures of UF₅(g) and U₂F₁₀(g) can be calculated from the effective pressure given by Leitnaker,⁸⁸ $p_{\text{eff}} = p_{\text{UF}_5} + 2p_{\text{U}_2\text{F}_{10}}$ and the equilibrium constant given by Kleinschmidt *et al.*⁸⁷ $K_d = p_{\text{U}_2\text{F}_{10}}/p_{\text{UF}_5}^2$. These pressures are reported in Figure 18.

The values recommended by Grenthe *et al.*²⁴ and updated by Guillaumont *et al.*³⁹ for UF₅ and U₂F₁₀ are reported in Table 8.

2.06.4.2.2 Enthalpy of formation

There are numerous studies on gaseous equilibria by mass spectrometry from which the enthalpy of formation of UF₅(g) was deduced.

The critical analyses were performed by Fuger *et al.*³⁷ and updated by Grenthe *et al.*²⁴ and Guillaumont *et al.*³⁹ A considerable variation exists in the resulting data from −1894.5⁸⁹ to −1946.5.⁹⁰ This is mainly due to the many difficulties involved in the experiments and uncertainties in the auxiliary data. The thermal

Table 8 Thermodynamic properties of the gaseous uranium pentafluoride as monomer and dimer

$\Delta_f H^0$ (UF ₅ , g, 298.15 K) (kJ mol ^{−1})	−(1913 ± 15) ³⁹
$\Delta_f H^0$ (U ₂ F ₁₀ , g, 298.15 K) (kJ mol ^{−1})	−(3993 ± 30) ³⁹
S^0 (UF ₅ , g, 298.15 K) (J K ^{−1} mol ^{−1})	386.4 ± 10.0 ³⁹
S^0 (U ₂ F ₁₀ , g, 298.15 K) (J K ^{−1} mol ^{−1})	577.6 ± 10.0 ⁸⁷
C_p^0 (UF ₅ , g, 298.15) (J K ^{−1} mol ^{−1})	110.6 ± 5.0 ²⁴
C_p^0 (UF ₅ , g, 298.15) (J K ^{−1} mol ^{−1})	234.7 ± 5.0 ²⁴
C_p^0 (UF ₅ , g, T) (J K ^{−1} mol ^{−1})	116.738 + 3.13041 × 10 ^{−2} T − 1.2538 × 10 ^{−5} T ² − 1273000T ^{−2} (298–1100) ³⁸

functions of UF₅(g) are calculated from molecular parameters estimated by Glusko *et al.*⁹¹ Here the molecule is assumed to be a square pyramid with a slight distortion to reduce the symmetry to C_{2v}.³⁹

2.06.4.3 Gaseous Uranium Tetrafluoride

2.06.4.3.1 Molecular structure

The molecular structure was studied by electron diffraction by Girichev *et al.*⁹² to determine the U–F and F–F distances. The analysis of the results indicated that the structure was not tetrahedral but rather D_{2h} or C_{2v}. This was confirmed by the analysis of the thermodynamic (vapor pressure) studies.^{93–95} Konings *et al.*⁹⁶ have studied the infrared spectrum of UF₄ vapor between 1300 and 1370 K. Based on this, and a reanalysis of the previously determined gas electron diffraction data,⁹² they have demonstrated that the UF₄(g) molecule almost certainly has tetrahedral symmetry.

2.06.4.3.2 Thermodynamic properties

2.06.4.3.2.1 Vapor pressure

There are a lot of studies on uranium tetrafluoride in the gaseous phase. Except for Leitnaker,⁸⁸ all studies suggest that UF₄ vaporizes congruently to the UF₄ monomer.

The vapor pressure measurements above the solid and liquid UF₄ were performed by

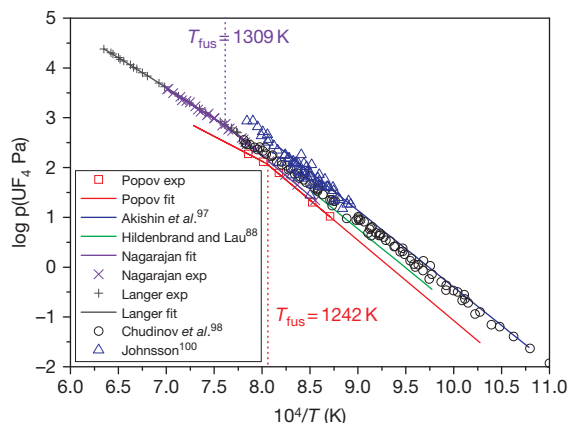
- transpiration method in the temperature range 1148–1273 K, using argon purified from oxygen and water vapor as carrier gas⁹⁷;
- combination of a quasistatic method and a boiling point technique from 1291 to 1575 K⁹⁸;

Table 9 Experimental vapor pressure equations above solid UF₄

References	Experimental method	Equation	T range (K)
Popov <i>et al.</i> ⁹⁷	Transpiration	$\log P(\text{Pa}) = 15.071 - \frac{16140}{T(\text{K})}$	1148–1223
Akishin <i>et al.</i> ⁹⁹	Mass spectrometry	$\log P(\text{Pa}) = 15.020 - \frac{70500}{4.576T(\text{K})}$	917–1041
Chudinov <i>et al.</i> ¹⁰⁰	Effusion	$\log P(\text{Pa}) = 30.663 - \frac{16504.9}{T(\text{K})} - 4.876 \log T(\text{K})$	823–1280
Hildenbrand ⁹³	Torsion-effusion	$\log P(\text{Pa}) = (14.91 \pm 0.5) - \frac{15691}{T(\text{K})}$	980–1130
Nagarajan <i>et al.</i> ¹⁰¹	Transpiration and evaporation	$\log P(\text{Pa}) = (15.03 \pm 0.14) - \frac{(15994 \pm 176)}{T(\text{K})}$	1169–1307

Table 10 Experimental vapor pressure equations above liquid UF₄

References	Experimental method	Equation	T range (K)
Popov <i>et al.</i> ⁹⁷	Transpiration	$\log P(\text{Pa}) = 10.127 - \frac{10000}{T(\text{K})}$	1248–1278
Langer <i>et al.</i> ⁹⁸	Quasistatic and boiling point	$\log P(\text{Pa}) = -\frac{16840 \pm 44}{T(\text{K})} - 7.549 \log T(\text{K}) + (39.086 \pm 0.03)$	1302–1575
Nagarajan <i>et al.</i> ¹⁰¹	Transpiration and evaporation	$\log P(\text{Pa}) = (11.99 \pm 0.24) - \frac{(12014 \pm 335)}{T(\text{K})}$	1312–1427

**Figure 19** Comparison of the experimental vapor pressure above solid and liquid UF₄.

- mass spectrometry between 917 and 1041 K⁹⁹;
- integral and differential effusion method¹⁰⁰ in 823–1280 K temperature range;
- torsion effusion method from 980 to 1130 K⁹³;
- both transpiration and evaporation temperature methods between 1169 and 1307 K and 1312 and 1427 K, respectively.¹⁰¹

The equations obtained above the solid and liquid are presented, respectively, in **Tables 9** and **10**.

The vapor pressure measurements above the solid UF₄ are scattered (**Figure 19**). The results of

Table 11 Thermodynamic properties of the gaseous uranium tetrafluoride

$\Delta_f H^0(\text{UF}_4, \text{g}, 298.15 \text{ K})$ (kJ mol ⁻¹)	$-(1605.2 \pm 6.5)^{39}$
$S^0(\text{UF}_4, \text{g}, 298.15 \text{ K})$ (J K ⁻¹ mol ⁻¹)	360.7 ± 5.0^{39}
$C_p^0(\text{UF}_4, \text{g}, 298.15)$ (J K ⁻¹ mol ⁻¹)	95.1 ± 3.0^{39}
$C_p^0(\text{UF}_4, \text{g}, T)$ (J K ⁻¹ mol ⁻¹)	$103.826 + 9.549 \times 10^{-3} T$ $- 1.451 \times 10^{-6} T^2$ $- 1.021 320 T^{-2}$ (298–3000) ³⁹
$\Delta_{\text{sub}} H^0(\text{UF}_4, 298.15)$ (kJ mol ⁻¹)	309.0 ± 5.0^{39}

(298–3000) is the temperature range for which the Cp(T) function is valid.

Nagarajan *et al.*¹⁰¹ and Popov *et al.*⁹⁷ are lower than those of Johnson,¹⁰² Akishin *et al.*,⁹⁹ and Chudinov *et al.*,¹⁰⁰ but the discrepancy is reduced at higher temperature and reaches 10% after the melting point.

For the pressure above the liquid, the data of Nagarajan *et al.*¹⁰¹ and Langer *et al.*⁹⁸ are very close. The values of Popov are excluded because the two points given in the liquid phase are in fact in solid phase.

Critical analysis of the vapor pressures measurements gives the selected enthalpy of sublimation (**Table 11**).

Table 12 Thermodynamic properties of the gaseous uranium trifluoride

$\Delta_f H^0$ (UF ₃ , g, 298.15 K) (kJ mol ⁻¹)	$-(1065 \pm 20)^1$
S^0 (UF ₃ , g, 298.15 K) (J K ⁻¹ mol ⁻¹)	347.5 ± 10^1
C_p^0 (UF ₃ , g, 298.15) (J K ⁻¹ mol ⁻¹)	76.2 ± 5.0^{24}
C_p^0 (UF ₃ , g, T) (J K ⁻¹ mol ⁻¹)	$81.327 - 4.3 \times 10^{-6}T$ $+ 2.427 \times 10^{-6}T^2$ $- 476300T^{-2}$ (298–1800) ³⁹
$\Delta_{\text{sub}} H^0$ (UF ₃ , 298.15) (kJ mol ⁻¹)	447.2 ± 15^{24}

(298–1800) is the temperature range for which the $C_p(T)$ function is valid.

The entropy and heat capacity at 298.15 K were calculated using molecular parameters for UF₄(g) reported by Konings and Hildenbrand¹⁰³ and electronic levels taken a part from Glushkov *et al.*⁹¹ and Konings and Hildenbrand.¹⁰³

2.06.4.4 Gaseous Uranium Trifluoride

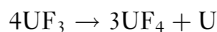
Molecular geometry has not been measured. Quantum chemical calculations for the uranium (III) fluoride indicate a pyramidal structure¹⁰⁴ but with a bond angle close to the planar 120°.

The thermodynamic data on solid uranium trifluoride recommended by Grenthe *et al.*²⁴ are presented in Table 12.

Values for the heat capacity and entropy of UF₃(g) are calculated from estimated molecular parameters given by Glushko *et al.*⁹¹

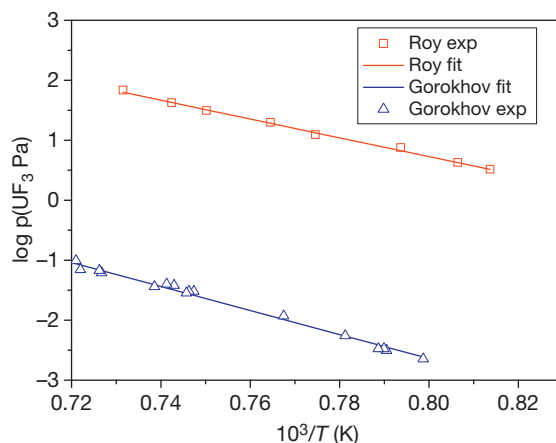
2.06.4.4.1 Vapor pressure

On heating, solid UF₃ does not vaporize congruently but disproportionately into solid UF₄ and uranium by the following reaction:



The vapor pressure measurements, which are difficult, can explain the scattered results (Figure 20). Roy *et al.*¹⁰⁵ determined the vapor pressure of UF₃(s) by the transpiration technique using hydrogen as the carrier gas in the 1229–1367 K temperature range, and Gorokhov *et al.*¹⁰⁶ deduced it from their mass spectrometry determinations. The temperature dependence of the vapor pressure is described, respectively, by the following equations^{105,106}

$$\log p_{\text{UF}_3} = (13.26 \pm 0.23) - (15666 \pm 302) \frac{1}{T(\text{K})} \quad (p \text{ in Pa})$$

**Figure 20** Comparison of the experimental vapor pressure of UF₃(s).

$$\log p_{\text{UF}_3} = (13.39 \pm 0.46) - (20040 \pm 0.62) \frac{1}{T(\text{K})} \quad (p \text{ in Pa})$$

The discrepancy is very large, about three orders magnitude.

2.06.4.4.2 Enthalpy of formation

Enthalpy of formation of gaseous UF₃ has been evaluated from experimental studies by Grenthe *et al.*²⁴ It has been deduced from

- the enthalpy of sublimation obtained by third-law analysis of the vapor pressure data measurements,¹⁰⁶
- mass spectrometric measurements.^{107,108}

2.06.4.5 Gaseous Uranium Mono- and Difluoride

There is no experimental data on the molecular structure for both species.

These molecules appear at high temperature. As for the uranium trifluoride, the mono- and difluoride of uranium have been identified in mass spectrometric measurements by different authors. Lau *et al.*¹⁰⁸ studied the exchange reactions of the lower uranium fluoride with BaF by mass spectrometry; Zmbov,¹⁰⁷ Gorokhov *et al.*,¹⁰⁶ and Hildenbrand *et al.*⁹⁰ studied the molecular equilibria between the uranium fluorides among themselves. The results for the uranium compounds have been analyzed in detail by Grenthe *et al.*²⁴ and updated by Guillaumont *et al.*³⁹ who demonstrated that the results are in reasonable agreement, considering the large number of approximations made in the analysis. Almost no experimental

Table 13 Thermodynamic properties of the gaseous uranium mono- and bifluoride

$\Delta_f H^0$ (UF ₂ , g, 298.15 K) (kJ mol ⁻¹)	-(540 ± 25) ¹
S^0 (UF ₂ , g, 298.15 K) (J K ⁻¹ mol ⁻¹)	315.7 ± 10 ³⁹
C_p^0 (UF ₂ , g, 298.15) (J K ⁻¹ mol ⁻¹)	56.2 ± 5.0 ²⁴
$\Delta_f H^0$ (UF, g, 298.15 K) (kJ mol ⁻¹)	-(47 ± 20) ³⁹
S^0 (UF, g, 298.15 K) (J K ⁻¹ mol ⁻¹)	251.8 ± 3.0 ³⁹
C_p^0 (UF, g, 298.15) (J K ⁻¹ mol ⁻¹)	37.9 ± 3.0 ²⁴

data on the molecular properties are available and thus the thermal functions are based rather on qualitative estimates, introducing large uncertainties.

Values for the heat capacity and entropy of UF(g) and UF₂(g) are calculated from estimated molecular parameters given by Glushko *et al.* (Table 13).

2.06.5 Outlook

Although UF₆ and UF₄ have been well characterized and used over the years, some work remains to be done on the intermediate fluorides and the phase diagram. In particular, the mechanisms leading to the formation of these undesirable compounds in industrial reactors are not very well known. This would help in improving yields in the UF₆ preparation process.

References

- Konings, R. J. M.; Morss, L. R.; Fuger, J. In *Thermodynamic Properties of Actinides and Actinide Compounds*; Springer: New York, 2006; Chapter 19, pp 2113–2224.
- Konings, R. J. M.; Benes, O.; Manara, D.; Sedmindubsky, D.; Gorokhov, L.; Iorish, V. S. The thermodynamic properties of f-elements. Part II. The lanthanide and actinide oxides; *J. Phys. Chem. Ref.*; Data Submitted.
- Ruff, O.; Heinzelmann, A. Z. *Anorg. Chem.* **1911**, 72, 63.
- Agron, P.; Grenall, A.; Kunin, R.; Weller, S. MDDC-1588; Oak Ridge, 1948.
- Khripin, L. A.; Poduzova, S. A.; Zadneprovskii, G. M. *Russ. J. Inorg. Chem.* **1968**, 13, 1439–1441.
- Slovianskikh, I. V. K.; Rozanov, A.; Gracheva, N. V. *Russ. J. Inorg. Chem.* **1978**, 11, 1720–1722.
- Thoma, R. E.; Brunton, G. D.; Burns, J. H.; *et al.* *Reactor Chemistry Division Annual Progress Report*; ORNL-3789; 1965.
- Knacke, V. O.; Lossmann, G.; Müller, F. Z. *Anorg. Allg. Chem.* **1969**, 370, 91–103.
- Llewellyn, D. R. *J. Chem. Soc.* **1953**, 28–36.
- Settle, J. L.; Feder, H. M.; Hubbard, W. N. *J. Phys. Chem.* **1963**, 67, 1892–1895.
- Hoard, J. L.; Stroupe, J. D. USAEC Report TID-5290 1958, Paper 45.
- Pascal, P. *Nouveau Traité de Chimie Minérale*. Masson et Cie ed. Tome XV Uranium et Transuraniens, Paris, 1961.
- Kigoshi, K. *Bull. Chem. Soc. Japan* **1950**, 23, 67.
- Saprygin, A. V.; Golile, V. M.; Izrailevich, I. S. *Radiochemistry* **1996**, 38, 468–471.
- Lewis, R. W.; Zheng, Y.; Gethin, D. T. *Nucl. Eng. Design* **1993**, 140, 229.
- Lewis, N. B.; Zeltmann, H. *J. Photochem.* **1980**, 12, 51–58.
- Bacher, V. W.; Jacob, E. *Chemiker Zeitung* **1982**, 106, 117–136.
- Orekho, V. T. *Russ. Chem. Rev.* **1977**, 46, 420–435.
- Wilson, P. W. *Rev. Pure Appl. Chem.* **1972**, 22, 1–12.
- Mandleberg, C.; Davies, D. J. *Inorg. Nucl. Chem.* **1960**, 20, 58–61.
- Hoard, J. L.; Stroupe, J. D. *The Chemistry of Uranium – Collected Papers*, TID-5290, Vol.1, 1959, pp 325–349.
- Taylor, J. C.; Wilson, P. W. *J. Solid State Chem.* **1975**, 14, 378–382.
- Levy, J. H.; Taylor, J. C.; Wilson, P. W. *J. C. S. Dalton* **1976**, 219–224.
- Grenthe, I.; Fuger, J.; Konings, R. J. M.; *et al.* *Chemical Thermodynamics*, Vol. 1 *Chemical Thermodynamics of Uranium*; OECD Nuclear Energy Agency, North-Holland: Amsterdam, 1992.
- Brickwedde, F. G.; Hoge, H. J.; Scott, R. B. *J. Chem. Phys.* **1948**, 16, 429–436.
- Johnson, G. K. *J. Chem. Thermodyn.* **1979**, 11, 483–490.
- Labaton, V.; Johnson, K. J. *Inorg. Nucl. Chem.* **1959**, 10, 74–85.
- Corella, J. *Chem. Eng. Sci.* **1980**, 35, 25–32.
- Janov, J.; Lepage, A. *Chemica 81*, 9th Australian Conference on Chemical Engineering, New Zealand, 1981.
- Birk, R. C. *J. Nucl. Mater.* **1986**, 140, 281–284.
- 70Sch.
- Larson, A. C.; Roof, R. B., Jr.; Cromer, D. T. *Acta Cryst.* **1964**, 17, 555–558.
- Harrington, C.; Ruenhle, A. *Uranium Production Technology*; Van Nostrand; p 69.
- Kirshenbaum, A. D.; Cahill, J. A. *J. Inorg. Nucl. Chem.* **1961**, 19, 65–68.
- Desyatnik, V. N.; Nechaev, A. I.; Chervinskii, Yu. F. *Russ. J. Phys. Chem.* **1979**, 53, 986–988.
- Kulifeev, V. K.; Panchishnyi, V. I. *Izv. Vyssh. Ucheb. Zaved. Tsvet. Met.* **1971**, 14, 92–94.
- Fuger, J. *The Actinide Halides, Chemical Thermodynamics of Actinide Elements and Compounds*; IAEA: Vienna, 1983; pp 47–78.
- Konings, R. J. M.; van der Meer, J. P. M.; Walle, E.; *Chemical Aspects of Molten Salt Reactor Fuel*, Tech. Rep. JRC-ITU-TN 2005/25, 2005.
- Guillaumont, R.; Fanghänel, T.; Fuger, J.; *et al.* In *Update on the Chemical Thermodynamics of Uranium, Neptunium, Plutonium, Americium and Technetium*; OECD Nuclear Energy Agency, Ed.; *Chemical Thermodynamics*; Elsevier: Amsterdam, 2003; Vol. 5.
- Hayman, C. In *Heats of Formation of Uranium Fluorides*, Proceedings of the Thermodynamik Symposium, Heidelberg, Germany, 1967; Schafer, K. L., Ed.; Paper no. 7.
- Wijbenga, G. Thermochemical investigations on intermetallic UMe₃ compounds (Me=Ru, Th, Pd), Thesis of Amsterdam University, ECN-102, 1981.
- Johnson, G. K. *J. Nucl. Mater.* **1985**, 130, 102–108.
- Mal'tsev, V. A.; Gagaranski, Y.; Popov, M. M. *Russ. J. Inorg. Chem.* **1960**, 5, 109–110.
- Popov, M. M.; Kostylev, F. A.; Karpova, T. F. *Zhur. Neorg. Khim.* **1957**, 2, 9–12.
- Khanaev, E. I.; Kripin, L. A. *Sov. Radiochem.* **1970**, 12, 158–160.
- Hu, R.; Ni, X.; Dai, M.; *et al.* *Sci. Sin.* **1980**, 23, 1386–1395.

47. Cordfunke, E. H. P.; Ouweltjes, W. *J. Chem. Thermodyn.* **1981**, *13*, 193–197.
48. Osborne, D. W.; Westrum, E. F., Jr.; Lohr, H. R. *J. Am. Chem. Soc.* **1955**, *77*, 2737–2739.
49. Burns, J. H.; Osborne, D. W.; Westrum, E. F., Jr. *J. Chem. Phys.* **1960**, *33*, 387–394.
50. Dworkin, A. S. *J. Inorg. Nucl. Chem.* **1972**, *34*, 135–138.
51. Nicole, C.; Patisson, F.; Ablitzer, D.; Houzelot, J. L. *Chem. Eng. Sci.* **1996**, *51*, 5213–5222.
52. Benes, O.; Konings, R. J. M. *J. Fluor. Chem.* **2009**, *130*, 22–29.
53. Asada, K.; Ema, K.; Tanaka, K.; Hayashi, K. *J. Inorg. Nucl. Chem.* **1981**, *43*, 2049–2051.
54. Howard, C. J.; Taylor, J. C.; Waugh, A. B. *J. Solid State Chem.* **1982**, *45*, 396–398.
55. Ryan, R. R.; Penneman, R. A.; Asprey, L. B. *Acta Cryst.* **1976**, *B32*, 3311–3313.
56. Halstead, G.; Eller, P.; Eastman, M. *Inorg. Chem.* **1979**, *18*, 2867–2872.
57. O'Hare, P. A. G.; Malm, J. G.; Eller, P. G. *J. Chem. Thermodyn.* **1982**, *14*, 323–330.
58. Katz, J. J.; Rabinowitch, E. *The Chemistry of Uranium*; Dover Publications: New-York, 1951.
59. Agron, P. A. In *Chemistry of Uranium – Collected Papers*; Katz, J. J., Rabinowitch, E., Eds.; US Atomic Energy Commission: Oak Ridge, TN, USA, 1958; pp 610–626.
60. Moch, L.; Morel, B.; Hamwi, A.; Chatain, S. Private communication, **2007**.
61. Wolf, A. S.; Posey, J. C.; Rapp, K. E. *Inorg. Chem.* **1965**, *4*, 751–754.
62. Zachariasen, W. H. *J. Chem. Phys.* **1948**, *16*, 425.
63. Zachariasen, W. H. *Acta Cryst.* **1949**, *2*, 390–393.
64. Leitnaker, J. M. *K/PS-352*, 1983.
65. Rand, M. H.; Kubascewski, O. *The Thermodynamical Properties of Uranium Compounds*; J. Wiley&Sons: New-York, 1963.
66. Latimer, W. M. *The Oxidation States of the Elements and Their Potentials in Aqueous Solutions*, 2nd ed.; Prentice-Hall, Inc.: New York, 1952.
67. Palmer, H. J. *Report B. R. 422*, 1944.
68. Warf, J. C. In *Chemistry of Uranium – Collected Papers*; Katz, J. J., Rabinowitch, E., eds.; US Atomic Energy Commission: Oak Ridge, TN, USA, 1958; pp 81–90.
69. Grenthe, I.; Drozdzyński, J.; Fujino, T.; Buck, E. C.; Albrecht-Schmitt, T. E.; Wolf, S. F. *Uranium in The Chemistry of the Actinide and Transactinide Elements*, 3rd ed.; Springer: New York, 2006; Vol. 1, Chapter 5; pp 253–698.
70. Taylor, J. C. *Coord. Chem. Rev.* **1976**, *20*, 197–273.
71. Zachariasen, W. H. Report LA-UR-75–1364, 1975.
72. Khanaev, E. I. *Izvest. Sib. Otd. Akad. Nauk. SSSR Ser. Khim Nauk.* **1968**, *9*, 123–125.
73. Cordfunke, E. H. P.; Konings, R. J. M.; Westrum, E. F., Jr. *J. Nucl. Mater.* **1989**, *167*, 205–212.
74. Heus, R. J.; Egan, J. J. *Z. Phys. Chem. Neue Folge.* **1966**, *49*, 38–43.
75. Tananaev, I. V.; et al. *Izv. Akad. Nauk. SSSR.* **1963**, 208–210.
76. D'Eye, R. W. M.; Martin, F. S. AERE CM 292, 1956.
77. Bauer, S. H. *J. Chem. Phys.* **1950**, *18*, 27–41.
78. Gaunt, J. J. *Trans. Faraday Soc.* **1953**, *49*, 1122–1131.
79. Aldridge, J. P.; Brock, E. G.; Filip, H.; et al. *J. Chem. Phys.* **1985**, *83*, 34–48.
80. Johnson, G. K. *J. Chem. Thermodyn.* **1979**, *11*, 483–490.
81. Oliver, G. D.; Milton, H. T.; Grisard, J. W. *J. Am. Chem. Soc.* **1953**, *75*, 2827–2829.
82. Paine, R. T.; McDowell, R. S.; Asprey, L. B.; Jones, L. H. *J. Chem. Phys.* **1976**, *64*, 3081–3083.
83. Krohn, B. J.; Person, W. B.; Overend, J. J. *J. Chem. Phys.* **1976**, *65*, 969–976.
84. Jones, L. H.; Ekberg, S. J. *J. Chem. Phys.* **1977**, *67*, 2591–2595.
85. Brewer, L.; Bromley, L. A.; Gilles, P. W.; Lofgren, N. L. MDDC-1543; United States Atomic Energy Commission: Oak Ridge, 1947.
86. Wolf, A. S.; Posey, J. C.; Rapp, K. E. K-1448, 1960.
87. Kleinschmidt, P. D.; Hildenbrand, D. L. *J. Chem. Phys.* **1979**, *71*, 196–201.
88. Leitnaker, J. M. *High Temp. Sci.* **1980**, *12*, 289–296.
89. Lau, K. H.; Britain, R. D.; Hildenbrand, D. L. *J. Phys. Chem.* **1985**, *89*, 4369–4373.
90. Hildenbrand, D. L.; Lau, K. H. *J. Chem. Phys.* **1991**, *94*, 1420–1425.
91. Glushko, V. P.; Gurvich, L. V.; Bergman, G. A.; et al. *Thermodynamic Properties of Individual Substances*; Moscow: Nauka, 1982; Vol. 4, in russian.
92. Girichev, G. V.; Petrov, V. M.; Giricheva, N. I.; Zazorin, E. Z.; Krasnov, K. S.; Kiselev, Y. M. *J. Struct. Chem.* **1983**, *24*, 61–65.
93. Hildenbrand, D. L. *J. Chem. Phys.* **1977**, *66*, 4788–4794.
94. Hildenbrand, D. L.; Lau, K. H.; Brittain, R. D. *J. Chem. Phys.* **1991**, *94*, 8270–8275.
95. Hildenbrand, D. L.; Lau, K. H. *Pure Appl. Chem.* **1992**, *64*, 87–92.
96. Konings, R. J. M.; Booiij, A. S.; Kovács, A.; Girichev, G. V.; Giricheva, N. I.; Krasnova, O. G. *J. Mol. Struct.* **1996**, *378*, 121–131.
97. Popov, M. M.; Kostylev, F. A.; Zubova, N. V. *Russ. J. Inorg. Chem.* **1959**, *4*, 770–771.
98. Langer, S.; Blankenship, F. F. *J. Inorg. Nucl. Chem.* **1960**, *4*, 26–31.
99. Akishin, P. A.; Khodeev, Y. S. *Russ. J. Phys. Chem.* **1961**, *35*, 574–575.
100. Chudinov, E. G.; Chaporov, D. Y. *Russ. J. Phys. Chem.* **1970**, *44*, 1106–1109.
101. Nagarajan, K.; Bhupathy, M.; Prasad, R.; Singh, Z.; Venugopal, V.; Sood, D. D. *J. Chem. Thermodyn.* **1980**, *12*, 329–333.
102. Johnsson, K. O. Y-42; Oak Ridge, 1947.
103. Konings, R. J. M.; Hildenbrand, D. L. *J. Alloys Compd.* **1998**, *271–273*, 583–586.
104. Joubert, L.; Maldivi, P. *J. Phys. Chem. A* **2001**, *105*, 9068–9076.
105. Roy, K. N.; Prasad, R.; Venugopal, V.; Singh, Z.; Sood, D. D. *J. Chem. Thermodyn.* **1982**, *14*, 389–394.
106. Gorokhov, L. N.; Smirnov, V. K.; Khodeev, Yu. S. *Russ. J. Phys. Chem.* **1984**, *58*, 980–983.
107. Zmbov, K. F. In *First International Conference on Calorimetry and Thermodynamics*, Warsaw, Poland, August 31 to Sept 4, 1969; pp 423–425.
108. Lau, K. H.; Hildenbrand, D. L. *J. Chem. Phys.* **1982**, *76*, 2646–2652.
109. Weinstock, B.; Crist, R. H. *J. Chem. Phys.* **1948**, *16*, 436–441.
110. Masi, J. F. *J. Chem. Phys.* **1949**, *17*, 755–758.

2.07 Zirconium Alloys: Properties and Characteristics

C. Lemaignan

Commissariat à l'Énergie Atomique, Grenoble, France

© 2012 Elsevier Ltd. All rights reserved.

2.07.1	Introduction	217
2.07.2	Physical Properties	218
2.07.3	Alloy Processing	219
2.07.3.1	Nuclear Grade Zr Base Metal	219
2.07.3.1.1	Ore decomposition	219
2.07.3.1.2	Hf purification and removal	219
2.07.3.1.3	Reduction to the metal	220
2.07.3.2	Alloy Melting	220
2.07.3.3	Forging	220
2.07.3.4	Tube Processing	221
2.07.3.4.1	Crystallographic texture development	221
2.07.4	Alloys	222
2.07.4.1	Alloying Elements and Phase Diagrams	222
2.07.4.2	Industrial Alloys	227
2.07.5	Mechanical Properties Before Irradiation	228
2.07.5.1	Strength and Ductility	228
2.07.5.2	Mechanical Properties in Temperature and Creep	229
2.07.5.3	Hydrogen Embrittlement and Other H Effects	229
2.07.5.4	Prospectives	230
References		231

Abbreviations

ASTM	American Society for Testing Materials
BWR	Boiling water reactor
CANDU	Canada Deuterium Uranium (heavy water pressurized reactor)
DHC	Delayed hydride cracking
DSA	Dynamic Strain Aging
hcp	Hexagonal closed packed
HPUF	Hydrogen pick-up fraction
LOCA	Loss of coolant accident
MIBK	Methyl-isobutyl-ketone
PWR	Pressurized water reactor
RBMK	Reaktor Bolshoy Moshchnosti Kanalniy (pressure tube power reactor)
RIA	Reactivity induced accident
SPP	Second phase particle
TEM	Transmission Electron Microscope
TM	Transition metal
VVER	Voda-Voda Energy Reactor (PWR of Russian design)

2.07.1 Introduction

Zirconium (Zr) exhibits a physical property of uppermost importance with respect to the design of in-core components of thermal neutron power reactors: it has a very low thermal neutron capture cross-section, and its alloys exhibit good engineering properties. For an improvement in neutron efficiency of the water-cooled reactors, the development of industrial-type Zr-based alloys started as early as the beginning of the nuclear reactor design, and is still continuing. The engineering properties of Zr and Zr alloys are therefore widely studied. Information exchanges and reviews are available in various sources; for example, the International Atomic Energy Agency issued reviews on Zr alloys for nuclear applications. For more detailed, up-to-date information, the reader is referred to a recent one,¹ or to the proceedings of the symposia on 'Zr in the nuclear industry,' organized at 2–3 year intervals by ASTM.²

It was found early that Zr is naturally mixed in its ore with its lower companion of the periodic table, hafnium, the latter being a strong neutron absorber. Purification of Zr from Hf contamination is therefore mandatory for nuclear applications. The development of the industrial alloys has been performed following the classical route: searching for elements of significant solubility that would improve the engineering properties, without too much impact on the nuclear ones. Tin, niobium, and oxygen are the main alloying elements, with minor additions of transition metals (TMs) (Fe, Cr, and Ni). Heat treatments aiming at homogeneous solid solutions, phase transformations, and precipitation control allow optimizing the structure of the alloys. In addition, the thermomechanical history of the components strongly impacts their behavior, via the formation of a crystallographic texture, because of the anisotropy linked to the hexagonal crystallography of Zr at low temperature.

A few Zr alloys are commonly used for structural components and fuel cladding in thermal neutron reactors. Zircaloy (Zry)-4 is used in pressurized water reactors (PWRs) and Zircaloy-2 in boiling water reactors (BWRs). The heavy water-moderated CANDU reactors, as well as the Russian VVER or RBMK reactors, use Zr–Nb alloys. New alloys are designed based on variants of the Zr–1% Nb, with small additions of Fe and sharp control of minor additions ($M5^{\text{®}}$), or variants of the quaternary alloys, such as Zirlo[®] and E635. More complex alloys with other types of alloying elements are also being tested in power plants, but the actual experience accumulated on these alloys is too low to consider them as commonly accepted, from an industrial point of view.

Fuel claddings are made out of Zry-2 or Zry-4. Those tubes have different geometries, depending on reactor design. In PWR's, the fuel cladding rods are 4–5 m long and have a diameter of 9–12 mm for a thickness of 0.6–0.8 mm. BWR fuel rods are usually slightly larger. The design is similar for the Russian VVER, with Zr–1%Nb. In CANDUs, the fuel bundles are shorter (0.5 m) and the cladding is thinner (0.4 mm) in order to collapse very fast on the UO_2 pellets.

Structural components of zirconium alloys are the guide tubes, the grids, and the end plates that maintain the components of the fuel assemblies. They have to maintain the structural integrity at the stress levels corresponding to normal or accidental operations. In addition, they should have very low corrosion rates in the hot, oxidizing coolant water. In BWRs, each assembly is surrounded by a Zircaloy-2 channel box that avoids cross-flow instabilities of

the two-phase coolant. Their geometrical stability is a mandatory requirement for the neutron physics design of the core.

In the case of CANDUs and RBMKs, the moderator is separated from the coolant water. The coolant water in contact with the fuel rods is contained in pressure tubes, usually made of Zr–Nb alloys. They are large components ($L \sim 10$ m, $\varnothing \sim 30$ cm, and $e \sim 5$ mm), with a design life expected to match the reactor life, that is, tens of years, with only minor corrosion and creep deformation.

2.07.2 Physical Properties

Natural zirconium has an atomic mass of 91.22 amu, with five stable isotopes (^{90}Zr : 51.46%, ^{91}Zr : 11.23%, ^{92}Zr : 17.11%, ^{94}Zr : 17.4%, and ^{96}Zr : 2.8%). The depletion of the most absorbing isotope (^{91}Zr , with $\sigma_a \sim 1.25 \times 10^{-28} \text{ m}^2$) would increase further the interest of using Zr alloys in reactors, but would clearly be economically inefficient. The cross-section for elastic interaction with neutrons is normal, with respect to its atomic number ($\sigma_{\text{diff}} \sim 6.5$ barn). Despite its high atomic mass, the large interatomic distance in the hcp crystals lead to a limited specific mass of 6.5 kg dm^{-3} .

The thermophysical properties correspond to standard metals: thermal conductivity $\sim 22 \text{ W m}^{-1} \text{ K}^{-1}$ and heat capacity $\sim 280 \text{ J kg}^{-1} \text{ K}^{-1}$, that is, close to $3R$ per mole.

Below 865°C , pure Zr has an hcp structure, with a c/a ratio of 1.593 (slightly lower than the ideal 1.633). The lattice parameters are $a = 0.323 \text{ nm}$ and $c = 0.515 \text{ nm}$.³ The thermal expansion coefficients show a strong anisotropy, with almost a twofold difference between the α_a and α_c coefficients (respectively 5.2 and $10.4 \times 10^{-6} \text{ K}^{-1}$).⁴ This anisotropic behavior of the thermal expansion induces internal stresses due to strain incompatibilities: After a standard heat treatment of 500°C , where the residual stresses will relax, cooling down to room temperature will result in internal stresses in the range of 100 MPa , depending on grain-to-grain orientations. The modulus of elasticity is also anisotropic, but with lower differences than for thermal expansion ($E_a = 99 \text{ GPa}$, and $E_c = 125 \text{ GPa}$).⁵ For industrial parts, the values recommended are close to $\alpha \sim 6.5 \times 10^{-6} \text{ K}^{-1}$ and $E \sim 96 \text{ GPa}$. The temperature evolution of the elasticity constants is unusual: the elasticity is strongly reduced as the temperature increases ($\sim 5\%$ per 100 K).^{6,7} This abnormal behavior is specific to the hcp metals of the IV-B row of the periodic table.⁸

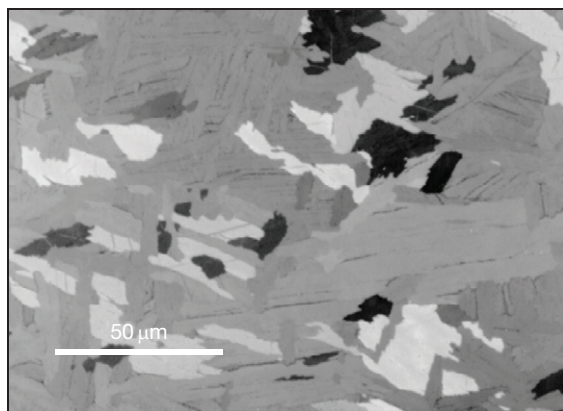


Figure 1 Microstructure of a β -quenched Zr alloys, with α -platelets of four different crystallographic orientations issued from the same former β -grain.

At 865 °C, Zr undergoes an allotropic transformation from the low temperature hcp α -phase to the bcc β -phase. On cooling, the transformation is usually bainitic, but martensitic transformation is obtained for very high cooling rates (above 500 K s⁻¹). The bainitic transformation occurs according to the epitaxy of the α -platelets on the old β -grains, as proposed by Burgers^{9,10}: $(0001)\alpha // \{110\}\beta$ and $\langle 11\bar{2}0 \rangle \alpha // \langle 111 \rangle \beta$. Among the 12 different possible variant orientations of the new α -grains, only a few are nucleated out of a given former β -grain during this transformation to minimize the internal elastic strain energy. This process leads to a typical ‘basket-weave’ microstructure (Figure 1). As a result, a β -quenching does not completely clear out the initial crystallographic texture that had been induced by the former thermomechanical processing.^{11,12} Although the alloying elements present in the Zr alloys change the transformation temperatures, with a 150 °C temperature domain in which the α - and β -phases coexist, the crystallographic nature of the α - β transformation is equivalent to that of pure Zr. Specific chemical considerations (segregations and precipitations) will be described later.

The melting of pure Zr occurs at 1860 °C, significantly above the melting temperature of other structural alloys, such as the structural or stainless steels. At high pressures, ($P > 2.2$ GPa) a low-density hexagonal structure is observed, known as the ω -phase.

2.07.3 Alloy Processing

2.07.3.1 Nuclear Grade Zr Base Metal

The most frequently used ore is zircon (ZrSiO₄), with a worldwide production of about 1 million metric

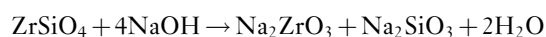
tons per year, out of which only 5% is processed into zirconium metal and alloys.

The processing of Zr alloy industrial components is rather difficult because of the high reactivity of the Zr metal with oxygen. It consists of several steps to obtain the Hf-free Zr base metal for alloy preparation: decomposition of the ore to separate Zr and Si, Hf purification, and Zr chloride or fluoride reduction.

2.07.3.1.1 Ore decomposition

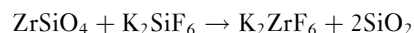
Three different processes are currently used for the Zr–Si separation:

- In alkali fusion, where the zircon is molten in a NaOH bath at 600 °C, the following reaction takes place:



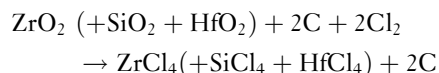
Water or acid leaching allows the precipitation of ZrO₂.

- The fluo-silicate fusion:



It produces a potassium hexafluorozirconate which, reacting with ammonia, leads to Zr hydroxide.

- The carbo-chlorination process is performed in a fluidized bed furnace at 1200 °C. The reaction scheme is the following:



The controlled condensation of the gaseous tetrachloride allows the separation of Zr and Si, but not of Hf from Zr.

2.07.3.1.2 Hf purification and removal

The processes described above separate Si from Zr, but the Zr compounds remain contaminated with the initial Hf concentration. The high neutron capture cross-section of Hf ($\sigma_a \sim 105$ barn, compared to 0.185 barn for Zr) requires its suppression in Zr alloys for nuclear application. Two major processes are used for this step: the MIBK-thiocyanate solvent extraction and the extractive distillation of tetrachlorides.

- In the first case, after reaction of zirconyl chloride (ZrOCl₂), obtained by hydrolysis of ZrCl₄, with ammonium thiocyanate (SCN-NH₄), a solution of hafnyl-zirconyl-thiocyanate (Zr/Hf)O(SCN)₂ is obtained. A liquid–liquid extraction is performed with methyl-isobutyl-ketone (MIBK,

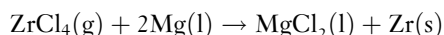
name of the process). Hf is extracted into the organic phase, while Zr remains in the aqueous one. Hf-free ZrO_2 is obtained after several other chemical steps: hydrochlorination, sulphation, neutralization with NH_3 , and calcination.

- In the dry route, after the transformation of zircon into its chloride ZrCl_4 , through the carbochlorination process, Zr and Hf are separated using a vapor phase distillation, at 350°C , within a mixture of KCl-AlCl_3 , where the liquid phase is enriched in Zr, and the vapor in Hf.

2.07.3.1.3 Reduction to the metal

The final step to obtain metallic Zr of nuclear grade is to reduce the Hf-free Zr compounds that have been obtained by the previous steps. Two processes are to be considered at an industrial scale: the Kroll process and the electrolysis.

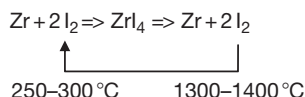
- In the Kroll process, the Zr metal is obtained by the reduction of ZrCl_4 in gaseous form by liquid magnesium, at about 850°C in an oxygen-free environment. The following reaction occurs:



After distillation of the remaining Mg and MgCl_2 , under vacuum at 950°C , sintering of the Zr agglomerate at 1150°C gives the metallic sponge cake.

- After wet chemical chemistry, the reduction of the ZrO_2 obtained by the MIBK process is often performed by electrolysis. It is realized with the mixed salt K_2ZrF_6 dissolved in NaCl or KCl at 850°C under inert gas, with stainless steel cathode on which Zr is deposited, and chlorine evolution at the graphite anode. This route is mainly used in the Russian Federation, the names of the Russian alloys starting with an 'E,' referring to electrolytic processing.

High purity Zr can be obtained by the Van Arkel process. It consists of reaction of Zr with iodine at moderate temperature, gaseous phase transport as ZrI_4 , and decomposition of the iodide at high temperature on an electrically heated filament. The iodine released at the high temperature side is used for the low temperature reaction in a closed loop transport process, according to the following scheme:



This source of metallic Zr (called 'iodide Zr') is used in Russia in addition to Zr obtained by the electrolytic

process for the melting of the alloys (typically 30% 'iodide Zr' in the first electrode to be melted).

2.07.3.2 Alloy Melting

Whatever the processing route followed for the production of Zr metal, the sponge or the chips obtained by scrapping out the electrodes are the base products for alloy ingot preparation. The melting of the alloys is performed using the vacuum arc remelting (VAR) process. This process is specific to highly reactive metals such as Zr, Ti, or advanced superalloys.

For industrial alloy preparation, an electrode is prepared by compaction of pieces of base metal fragments (sponge or scraps) with inclusion of the alloying elements. Typically, the elements to be added are the following: O (in the form of ZrO_2 powder), Sn, Nb, Fe, Cr, and Ni to the desired composition. In addition, a strict control of minor elements, such as C, N, S, and Si, is ensured by the producers, at concentrations in the range of 30–300 ppm, according to their requirements to fulfill the engineering properties.

A few specific impurities are strictly controlled for neutron physics reasons: Cd and Hf due to their impact on neutron capture cross-section, U for the contamination of the coolant by recoil fission fragments escaping from the free surface of the cladding, and Co for in-core activation, dissolution transport, contamination, and γ -irradiation.

The compact stack is melted in a consumable electrode electric vacuum furnace with water chilled Cu crucible. Electromagnetic fields are often used for efficient stirring of the liquid pool and reduced segregations. After three to four melts, the typical dimensions of the final ingots are 0.6–0.8 m diameter and 2–3 m length, that is, a mass of 4–8 tons.

2.07.3.3 Forging

Industrial use of Zr alloys requires either tube- or plate-shaped material. The first step in mechanical processing is forging or hot rolling in the β -phase, at a temperature near 1050°C , or at lower temperatures in the $\alpha + \beta$ range or even in the upper α range. The high oxidation kinetics of Zr alloys in air at high temperatures restricts the high temperature forging process to thick components, that is, with minimum dimensions larger than 10 cm, at least. Final dimensions after forging correspond to 10–25 cm diameter for billets and 10 cm for slabs.

A β -quenching is usually performed at the end of the forging step. This heat treatment allows complete

dissolution of the alloying elements in the β -phase and their homogenization above 1000 °C, followed by a water quench. During the corresponding bainitic β to α transformation, the alloying elements are redistributed, leading to local segregations: O and Sn preferring the middle of the α -platelets, while the TMs (Fe, Cr, and Ni) and Nb are being rejected to the interface between the platelets.¹³ These segregations lead to plastic deformation strains highly localized at the interplatelet zones for materials having a β -quenched structure (heat-affected zones, welds, or β -quenched without further thermomechanical processing). As described later, this β -quench controls the initial size distribution of the precipitates in Zircaloy, and further recovery heat treatments should be performed below the β - α transus only.

2.07.3.4 Tube Processing

For seamless tube production, first a hot extrusion is performed in the temperature range of 600–700 °C. For pressure tube fabrication, this step is followed by a single cold drawing step and a final stress relieving heat treatment. For cladding tubes, the extrusion produces a large extruded tube ('Trex' or 'shell'), of 50–80 mm in diameter and 15–20 mm in thickness, which is further reduced in size by cold rolling on pilger-rolling mills.

After each cold working step of plate or tube material, an annealing treatment is mandatory to restore ductility. It is usually performed in the range of 530–600 °C to obtain the fully recrystallized material (RX). The resultant microstructure is an equiaxed geometry of the Zr grains with the precipitates located at the α -grain boundaries or within the grains. The location of the precipitates at the grain boundaries is not due to intergranular precipitation but because they pin the grain boundaries during grain growth (Figure 9). These different heat treatments contribute to the control of the cumulative annealing parameter to be described below. For better mechanical properties of the final product, the temperature of the last annealing treatment can be reduced to avoid complete recrystallization. This is the stress-relieved (SR) state, obtained with final heat treatment temperature of 475 °C, which is characterized by elongated grains and a high density of dislocations, and by relief of the internal stresses, leading to a greater ductility than cold-worked materials. It is mostly applied to the PWR claddings, while for BWRs, a complete recrystallization is performed at 550–570 °C.

2.07.3.4.1 Crystallographic texture development

Two plastic deformation mechanisms are operating during low temperature deformation of the Zr alloys: dislocation slip and twinning. As reviewed by Tenckhoff,¹⁴ the most active deformation mechanism depends on the relative orientation of the grain in the stress field.

Dislocation slip occurs mostly on prism plane with an a Burgers vector. It is referred to as the $\{10\bar{1}0\}$ $\langle\bar{1}210\rangle$, or prismatic, system. The total strain imposed during mechanical processing of the Zr alloys cannot, however, be accounted for only with this single type of slip, as the different orientations of the crystal would only give two independent shear systems. At high deformations, and as the temperature is increased, $(c+a)$ type slip is activated on $\{11\bar{2}1\}$ or $\{10\bar{1}1\}$ planes. These are the pyramidal slip systems, having higher resolved shear stresses (Figure 2).

Different twinning systems may be activated depending on the stress state: for tensile stress in the c -direction, $\{10\bar{1}2\}$ $\langle\bar{1}011\rangle$ twins are the most frequent, while the $\{11\bar{2}2\}$ $\langle\bar{1}\bar{1}23\rangle$ system is observed when compression is applied in the c -direction. The resolved shear stresses of the twin systems have been shown to be higher than the one necessary for slip, but due to the dependence of the Schmid factor on orientation, twinning is activated before slip, for some well-oriented grains. Therefore, there are five independent deformation mechanisms operating in each grain, and thus the von Mises criterion for grain-to-grain strain compatibility is fulfilled.

At the large strains obtained during mechanical processing, steady-state interactions occur between the twin and slip systems that tend to align the basal planes parallel to the direction of the main deformation.^{15,16} For cold-rolled materials (sheets or tubes), the textures are such that the majority of the

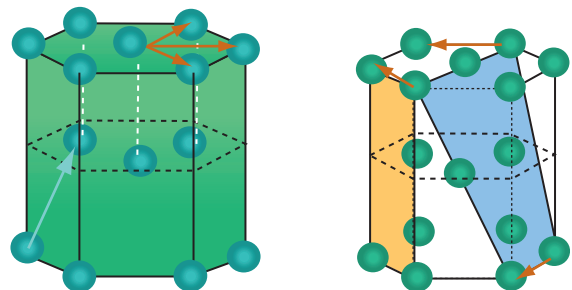


Figure 2 The two Burgers vectors (a and $c + a$) for strain dislocations in Zr alloys, and the two slip planes (prismatic and pyramidal) in hcp α -Zr.

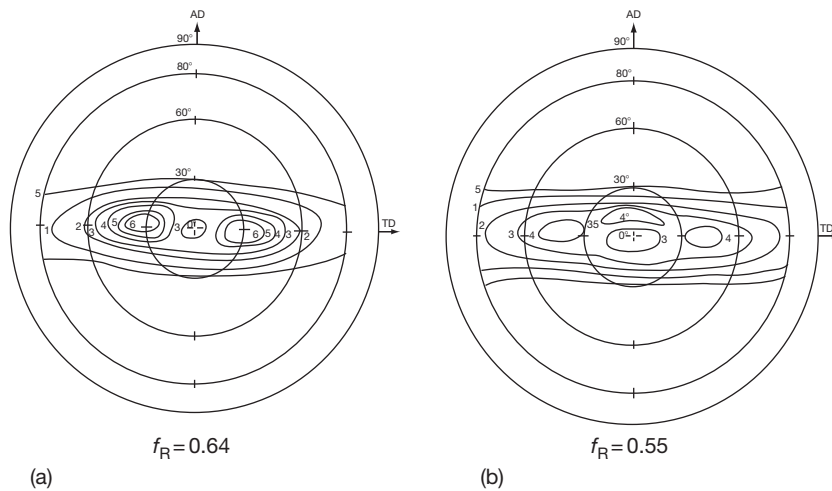


Figure 3 (0001) Pole figure of two cladding tubes with slightly different mechanical processing routes.

grains have their c -axis tilted $30\text{--}40^\circ$ away from the normal of the foil or of the tube surface toward the tangential direction, as can be seen in the (0001) pole figure of a cladding tube (Figure 3).

During tube rolling, the spread of the texture can be reduced by action on the ratio of the thickness to diameter reductions (Q factor): a reduction in thickness higher than the reduction in diameter gives a more radial texture, that is, a texture with the c poles closer to the radial direction.¹⁶

After cold processing, the $\langle 10\bar{1}0 \rangle$ direction is parallel to the rolling direction, and during a recrystallization heat treatment a 30° rotation occurs around the c -direction and the rolling direction is then aligned with the $\langle 11\bar{2}0 \rangle$ direction for most of the grains.

2.07.4 Alloys

2.07.4.1 Alloying Elements and Phase Diagrams

Like any metal, pure Zr exhibits rather poor engineering properties. To improve the properties of a given metal, the metallurgical engineering procedures are always the same: It consists in finding additions, any species of the periodic table could be considered, with significant solubility, or heat treatments producing new phases that could improve the properties. The relative solubility of the various alloying elements in the α - and β -phases is therefore one basis for the choice of additions, as well as for developing the heat treatments, for microstructure control.

For the nuclear applications, neutron physics requirements restrict the possibilities, by rejection

of the isotopes having high interaction cross-sections, or isotopes that would transmute to isotopes of high capture cross-section or having high irradiation impact (Co). Elements such as Hf, Cd, W, and Co have therefore not been considered for alloy developments. With low nuclear impact, O, Sn, and Nb have been selected (Al and Si having also low nuclear impacts were not retained because of degradation in corrosion resistance), while other TMs (Fe, Cr, Ni, etc.) can be accepted up to limited concentrations (below 0.5% total).

The additions have to improve the engineering properties. The main properties to be improved are the corrosion behavior in hot water and the mechanical strength (yield stress, ductility, and creep). As described below, Sn and Nb are added for corrosion resistance, and elements forming secondary phases (Nb and Fe, Cr, and Ni) or solid solutions are also used for increasing the mechanical properties.

Last, the microstructure obtained after the thermomechanical processing should not change without control under irradiation. Therefore, hardening obtained by precipitation or strain hardening can be considered only if the irradiation-induced evolution of the initial microstructure will be compensated by the development of irradiation-induced microstructural defects. In this respect, the evolution of precipitates in Zircalloys is of high importance for corrosion behavior and geometrical integrity. These points are discussed in **Chapter 5.03, Corrosion of Zirconium Alloys** and **Chapter 4.01, Radiation Effects in Zirconium Alloys**.

Most of the binary phase diagrams with Zr are already known and many ternary or higher-level

diagrams of industrial interest are now known.¹⁷ The need for a better control of the processing of the current alloys and the aim of finding new alloys and structures without too much experimental work have been a driving force for the modern trend in numerical simulation for material science. It is now also possible to extrapolate the binary data to multicomponent systems. In that respect, a thermodynamic database for Zr alloys, called ZIRCOBASE, has been developed under the Calphad methodology.¹⁸ This database contains 15 elements and is frequently updated. The most complex ternary or quaternary phase diagrams available are optimized or computed using this database, and, in the case of missing basic thermodynamic data, with the contribution of ‘*ab-initio*’ computations.¹⁹ The phase diagrams presented in this review were obtained according to this procedure.

Oxygen is highly soluble in the α -phase, and stabilizes at high temperature (Figure 4). Oxygen has to be considered as an alloying element. This use of oxygen for strengthening is rare in metallurgy, compared to the use of nitrogen. However, the use of nitrogen for strengthening would severely deteriorate the corrosion resistance, and nitrogen is removed as much as possible. The purpose of oxygen additions is to increase the yield strength by solution strengthening, without degradation of the corrosion resistance. The O content is not specified in the ASTM standards, but usually it is added to concentrations in the range of 600–1200 ppm, and this has to be agreed between producer and consumers. High O concentrations ($O > 2000$ ppm) reduce the ductility of the alloys; therefore, O additions above 1500 ppm are not recommended. In addition, O atoms interact with the dislocations at moderate temperatures,

leading to age-strengthening phenomena in temperature ranges depending on strain rate.²⁰ The oxygen in solid solution in α -zirconium is an interstitial in the octahedral sites. In the Zr–O system, the only available stable oxide is ZrO_2 . A monoclinic phase is stable at temperatures up to about 1200 °C, above which it transforms to a tetragonal structure. The impact on corrosion of the different phases of ZrO_2 , according to temperature and pressure is discussed in Chapter 5.03, **Corrosion of Zirconium Alloys**.

Tin tends to extend the α -domain, and has a maximal solubility in the hcp Zr of 9 wt% at 940 °C (Figure 5). It was originally added at concentrations of 1.2–1.7% to increase the corrosion resistance, especially by mitigating the deleterious effects of nitrogen. The amount of Sn needed to compensate the effect of 300 ppm of N is about 1% of Sn. However, in N-free Zr, Sn has been observed to deteriorate the corrosion resistance. Therefore, the modern trend is to reduce it, but only slightly, in order to maintain good creep properties.²¹

Iron, chromium, and nickel, at their usual concentrations, are fully soluble in the β -phase (Figure 6). However, in the α -phase, their solubilities are very low: in the region of 120 ppm for Fe and 200 ppm for Cr at the maximum solubility temperature.²² In the pure binary systems, various phases are obtained: $ZrFe_2$ and $ZrCr_2$ are Laves phases with cubic or hexagonal structure, while Zr_2Ni is a Zintl phase with a body-centered tetragonal C16 structure. These precipitates are called the Second Phase Particles (SPPs).

In the Zircalloys, the Fe substitutes for the corresponding TM and the intermetallic compounds found in Zircaloy are $Zr_2(Ni,Fe)$ and $Zr(Cr,Fe)_2$.

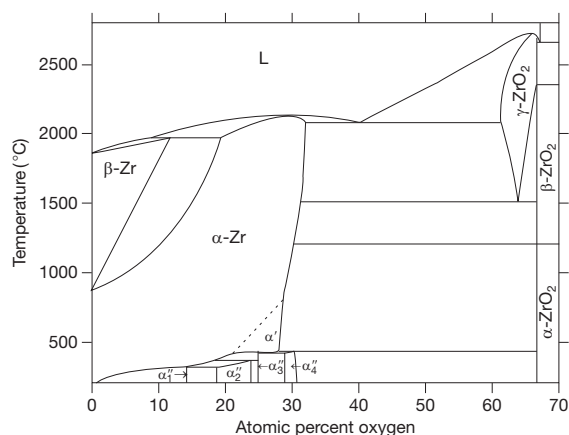


Figure 4 Zr–O binary phase diagram.

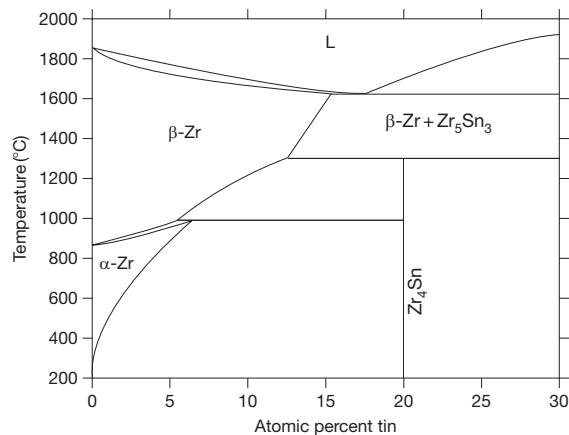


Figure 5 Zr–Sn binary phase diagram.

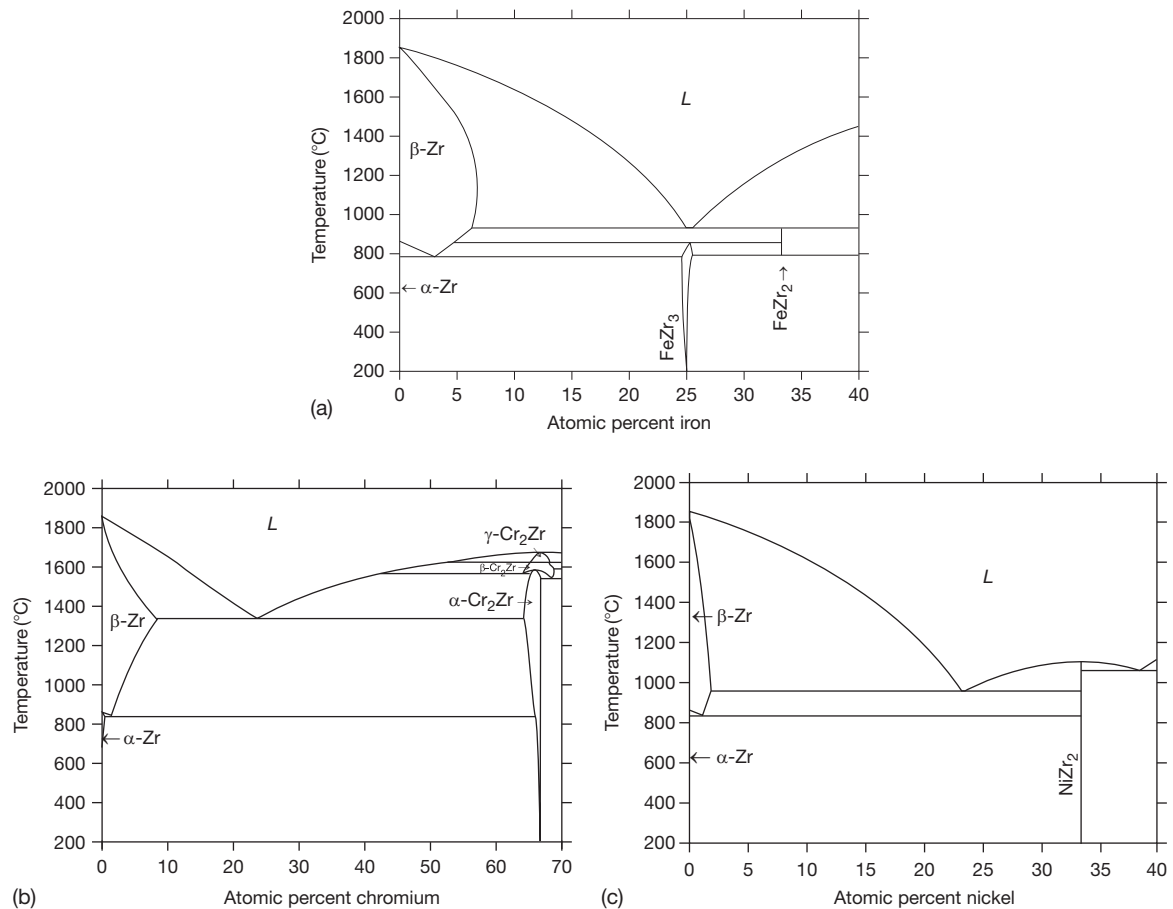


Figure 6 Zr-rich site of the Zr-transition metal binary phase diagram: (a) Zr-Fe, (b) Zr-Cr, (c) Zr-Ni.

The formation of these precipitates, and more complex ones in industrial alloys, is analyzed in detail for the control of the corrosion behavior of the Zircalloys. Indeed, a strong correlation has been observed between precipitate size distributions and corrosion kinetics, the behavior being opposite for BWRs and PWRs. A better uniform corrosion resistance is obtained for Zircalloys used in PWRs if they contain large precipitates, while better resistance to the localized forms of corrosion is seen in BWRs in materials that have finely distributed small precipitates.^{23,24} With an increase in the particle diameters from 0.05 to 0.1 μm or higher, the in-pile corrosion of Zircaloy cladding diminishes appreciably. However, nodular corrosion may occur in BWR cladding with a further increase in the particle diameters above about 0.15 μm ²⁵ (Figure 7).

Due to the low solubility of the transition metals (Fe, Cr and Ni) in the Zr matrix, coarsening of the precipitates, after the last β -quench, occurs at very

low rates, during the intermediate annealing heat treatments, following each step of the rolling process. Therefore, the precipitate growth integrates the thermal activation times of each recovery, and their temperatures and durations can be used to control the size of SPPs. This integrated coarsening activation time is referred as the '*A*' or ' ΣA ' parameter.

The *A*-parameter calculates the integral of the activation processes for the different anneal durations and temperatures. The annealing parameter is defined as $A = \sum_i (t_i \exp(-Q/RT_i))$, where t_i is the time (in hours) of the *i*th annealing step, at temperature T_i (in K); Q/T is the activation temperature of the process involved. The activation energy for the process should have been taken as the one controlling the coarsening, that is, the diffusion. However, as the early studies were undertaken with the aim of improving the corrosion resistance, an unfortunate practice has been induced to take 40 000 K as the value of Q/T . A more correct value would be

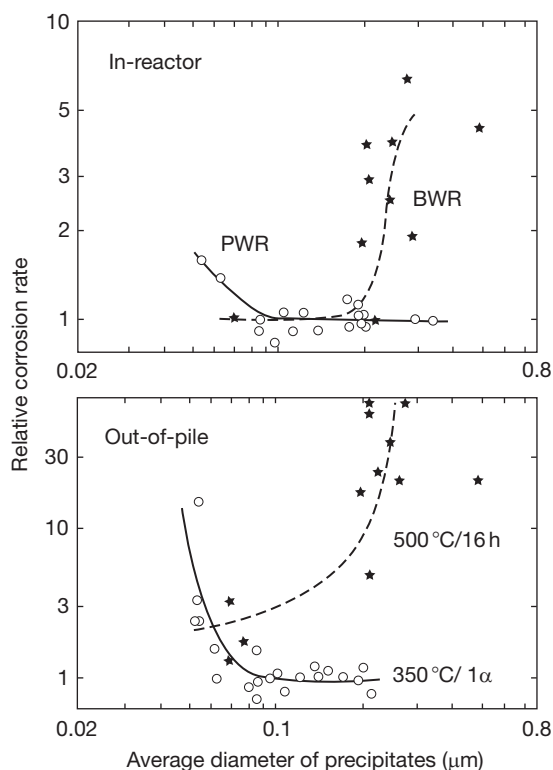


Figure 7 Effect of precipitate size on the corrosion kinetics of Zircalloys. Reproduced from Garzarolli, F.; Stehle, H. Behavior of structural materials for fuel and control elements in light water cooled power reactors, IAEA STI/PUB/721; International Atomic Energy Agency: Vienna, 1987; p 387.

32 000 K, which fits very well with the recrystallization kinetics. The influence of the A -parameter on the corrosion of Zircaloy is discussed in more detail in **Chapter 5.03, Corrosion of Zirconium Alloys**. High resistance to uniform corrosion in PWR is obtained for the A -parameter close to $(1.5\text{--}6.0) \times 10^{-19}$ h. In BWR, the A -parameter value for the Zircaloy-2 cladding in BWR has to be in the range $(0.5\text{--}1.5) \times 10^{-18}$ h (**Figure 7**).²⁵ This corresponds to precipitates larger than $0.18\text{ }\mu\text{m}$. The ΣA approach has been developed for the Zircalloys and is clearly not applicable for other alloys, such as the Zr–Nb alloys.

Niobium (columbium) is a β -stabilizer that can extend the bcc domain to a complete solid solution between pure Zr and pure Nb at high temperatures (**Figure 8**). A monotectoid transformation occurs at about $620\text{ }^\circ\text{C}$ and around 18.5 at.% Nb. The solubility of Nb in the α -phase is maximal at the monotectic temperature, and reaches 0.65%.

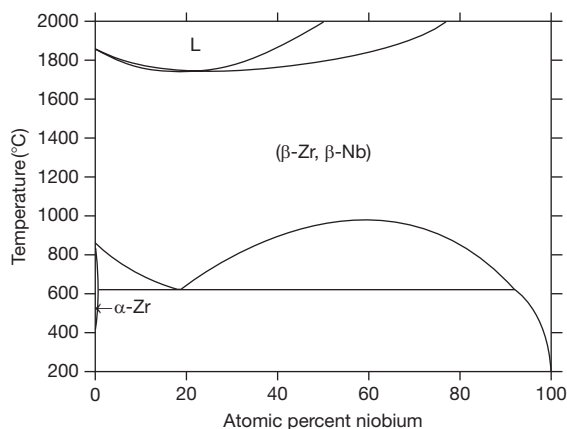


Figure 8 Zr–Nb binary phase diagram.

Water β -quenching of small pieces leads to the precipitation of α' martensite supersaturated in Nb. Tempering at intermediate temperature results in β -Nb precipitation within the α' needles and subsequent transformation of α' into α . When quenching is performed from an $\alpha + \beta$ region, a uniform distribution of α - and β -grains is obtained, and the Nb-rich β -phase does not transform. By aging at temperatures in the range of $500\text{ }^\circ\text{C}$, the metastable Nb-rich β -phase can be decomposed into an hcp ω -phase. This gives a sharp increase in mechanical strength because of the fine microstructure obtained by the β - ω transformation.²⁶ In the usual form of the Zr–2.5% Nb, the cold work condition after $\alpha + \beta$ extrusion and air-cooling, the microstructure consists of Zr grains with layers of β -Nb rich phase (close to eutectoid composition). Owing to the affinity of Fe for the β -phase, most of this element is found in the minor β -grains. These β -grains are metastable and decompose, upon aging, to a mixture of α -Zr and pure β -Nb. The Nb dissolved in the α -hcp Zr phase is itself metastable and the irradiation-induced precipitation of the supersaturated Nb solid solution is believed to be the origin of the improvement in corrosion resistance under irradiation of these alloys.²⁷

In the case of Zr–1% Nb used for VVER and RBMK, or M5[®] in PWRs, the concentration of Nb in the Zr matrix after processing corresponds to the maximum solubility near the monotectoid temperature, which is higher than the solubility at the service temperature. Owing to the slow diffusion of Nb, the equilibrium microstructure cannot be obtained thermally. However, the irradiation-enhanced diffusion allows precipitation of fine β -Nb needles in the grains after a few years in reactors.²⁸

Sulfur has recently been observed to be extremely efficient in improving the creep resistance, even at concentration as low as 30–50 ppm. This chemical species, formerly not considered as important, is now deliberately added during processing to reduce the scatter in behavior and to improve the high temperature mechanical properties.²⁹ The efficiency of such low concentrations on the creep properties has been explained by the segregation of the S atoms in the core of the dislocations, changing their core configurations. It does not affect the corrosion properties.³⁰

In the case of complex alloys, other thermodynamical interactions are expected and intermetallic compounds including three or four chemical elements are observed. The chemistry and the crystallography of these phases may be rather complex.

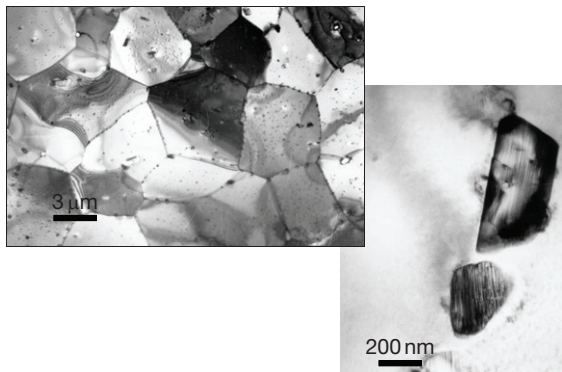


Figure 9 Microstructure of recrystallized Zry-4: $\text{Zr}(\text{Fe,Cr})_2$ precipitates in the $\text{Zr}(\text{Sn-O})$ matrix (TEM at two different scales).

Two examples will be given of the complex structure and behavior of these intermetallics.

- For the Zr–Cr and Zr–Ni binary alloys, the stable forms of the second phase are Zr_2Ni or ZrCr_2 . These phases are effectively the ones observed in the Zircalloys, with Fe substituting for the corresponding TM. Therefore, the general formulae of the intermetallic compounds in Zircalloys are $\text{Zr}_2(\text{Ni,Fe})$ and $\text{Zr}(\text{Cr,Fe})_2$. The crystal structure of the $\text{Zr}(\text{Cr,Fe})_2$ precipitates is either fcc (C15) or hcp (C14), depending on composition and heat treatment. Both structures are Laves phases, with characteristic stacking faults as seen in **Figure 9**. The equilibrium crystallographic structure is dependent upon the Fe/Cr ratio, cubic below 0.1 and above 0.9, and hexagonal in the middle. Under irradiation, these precipitates transform to amorphous state and release their Fe in the matrix, with strong impact on corrosion behavior under irradiation.³¹
- In the Zr–Nb–Fe ternary, other intermetallic compounds can be observed (**Figure 10**): the hexagonal $\text{Zr}(\text{Nb,Fe})_2$ phase and the cubic $(\text{Zr,Nb})_4\text{Fe}_2$.³² Although of apparent similar composition, the two phases are indeed different: Nb can substitute Fe in the hexagonal phase, while it will substitute Zr in the cubic phase. In these alloys, due to the slow diffusion of Nb, metastable phases are often present and the equilibrium microstructure after industrial heat treatments may be far from the stable one. Therefore, the final microstructure is strongly dependent on the exact thermomechanical history.

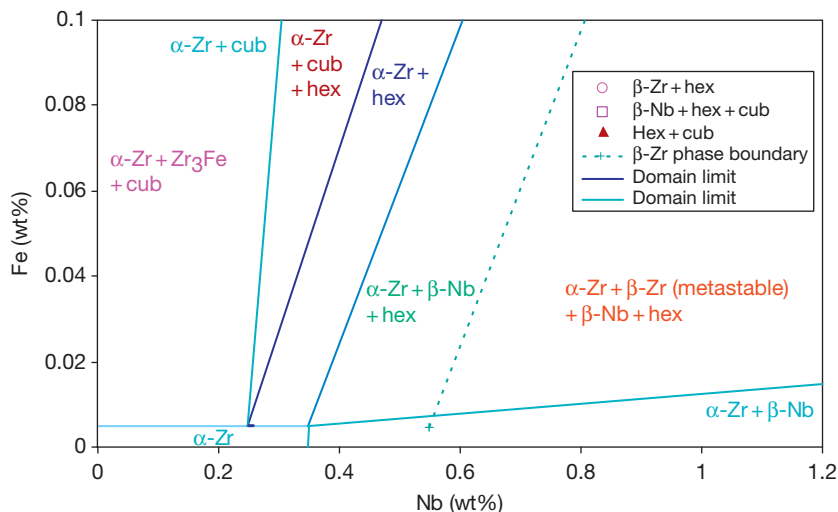


Figure 10 Zr-rich corner of the Zr–Nb–Fe ternary phase diagram at 580 °C.

In addition, the low solubility of these elements at operating temperatures drastically reduces the diffusion kinetics and requires more than a year to reach equilibrium at 450 °C, in the absence of irradiation.³³

Other minor constituents are often found in the form of precipitates. Among them are the carbide fcc-ZrC and silicides or phosphides of various stoichiometries (Zr_3Si , $ZrSi_2$, ZrP , and Zr_3P) that act as nucleation sites for the $\beta \rightarrow \alpha$ -phase transformation during quenching and, therefore contribute to control the α -platelets thickness and density.

2.07.4.2 Industrial Alloys

The zirconium alloys in use today for nuclear applications are limited in number: besides pure Zr, only four alloys are currently listed in the ASTM standards for Zr ingots for nuclear applications (ASTM-B350). Those are shown in Table 1. The first three are used for cladding and structural materials, such as guide tubes and channel boxes in PWRs and BWRs and structural materials in CANDU reactors, while grade R 60904 is used exclusively in pressure tubes for CANDU reactors. For cladding tubes, only Zircaloy-2 and -4 are listed in the applicable standard (ASTM B-811).

Alloys of more recent use such as ZIRLO[®], M5[®], E110, or E635 are now of common use in light water reactor cladding, but are not considered for ASTM designation in the near future. Due to the limited market of cladding tubes for nuclear reactors, and the small number of tube producers or fuel vendors, the exact chemistry, processing routes, or mechanical properties are usually agreed mutually between the contracting parties.

Historically, the first Zircaloy was conceived in the United States as a 2.5% Sn alloy. Owing to its poor long-term corrosion behavior, the tin content was reduced roughly by a factor of 2. A fortuitous

contamination of one melt by stainless scraps showed the drastic improvement induced by small additions of Fe, Cr, and Ni, the constituents of the austenitic stainless steels. Systematic composition variations to optimize the alloy introduced the Zircaloy-2. The capture of a significant amount of hydrogen by the alloy during corrosion was attributed to the presence of nickel. Its replacement by an equivalent amount of iron and chromium led to the Zircaloy-4.³⁴

Zr–Nb alloys were developed in Canada, Russia, and the United States, with initial high Nb concentrations (up to 4%). For the claddings of BWRs, they showed poor behavior and the Zr–Nb alloys development was stopped soon in the United States. Zr–2.5Nb was quite satisfactory for the pressure tubes, due to its low hydrogen pick-up during operation, and the engineering optimization of this alloy was continued in Canada and Russia. It remains the reference alloy for pressure tubes, in CANDUs. Zr–1% Nb has been developed for cladding in these countries and behaved very satisfactorily in VVER. A renewal of interest in such alloys in the western world in the 1990s led to the development of a Zr–1% Nb alloy, with controlled additions of Fe and S. The M5[®] alloy is now of regular use in PWRs, with excellent corrosion resistance, compared to the former Zry-4.³⁵

‘Quaternary’ alloys were conceived as a mixture of the Zircaloys and the Zr–Nb alloys, hoping to conserve the specificity of each of them in addition to the different alloying elements:

- Niobium for the resistance to hydrogenation during corrosion
- Tin for the corrosion resistance by reducing the dependence on deleterious impurities
- Iron also for corrosion resistance by mitigating the dependence on the coolant temperature.

The results appear to be in-line with the expectations for these alloys, which can be considered as variants

Table 1 Composition of the Zr alloys of industrial use (concentration in wt% or ppm)

	ASTM	Sn	Nb	Fe	Cr	Ni	O	S
Zircaloy-2	R 60802	1.2–1.5		0.07–0.2	0.1	0.05	0.12	
Zircaloy-4	R 60902	1.2–1.7		0.18–0.24	0.1		0.1–0.14	
M5			0.8–1.2	<500 ppm			0.11–0.16	10–35 ppm
E110			1	100 ppm			0.05–0.07	
Zr 2.5Nb	R 60904		2.5–2.7	<650 ppm			0.12–0.15	
E125			2.5–2.6				0.04–0.07	
Zirlo		1	1	0.1			0.09–0.12	
E635		1.2	1	0.35			0.05–0.07	

of the composition: Zr–1% Nb–1% Sn–TM alloys. The multicomponent alloys, namely, E635 and Zirlo[®] are, respectively, used in the cores of VVER and PWR.^{36,37} Both show low corrosion and very limited irradiation growth. Irradiation growth refers to the dimensional changes at constant volume of an unstressed material under irradiation.³⁸ The growth phenomenon is induced by the anisotropic clustering or disappearance of the point defects created by irradiation. The stability under irradiation of the precipitates present in these alloys appears to be the origin of such good dimensional stability (**Chapter 4.01, Radiation Effects in Zirconium Alloys**).³⁹

2.07.5 Mechanical Properties Before Irradiation

2.07.5.1 Strength and Ductility

The mechanical properties of the Zr alloys are strongly dependent on several parameters such as composition, texture, and metallurgical state. For practical purposes, the properties at 300–400 °C are most important and room temperature behavior is used mostly for comparison.

At room temperature, in the annealed state, pure, oxygen-free Zr has a low yield strength of about 150 MPa. However, the yield strength can be increased by solution strengthening, using oxygen, tin, or niobium. Tin causes only a small increase in tensile strength, but is efficient for creep improvement; Nb increases both yield and creep strength.⁴⁰

By contrast, the addition of 1000 ppm of oxygen increases the yield strength to 300 MPa. As a result of this, Zircalloys have minimal yield strengths in the range of 250–300 MPa and the Zr–2.5% Nb alloy, about 300 MPa. As in other metals, reduction in grain size is also used to obtain higher strength, leading to the request of a grain index of 7 or finer for standard products.

For all those materials, the ductility remains high, above 20%. Cleavage is never observed in Zr and Zr alloys, even at liquid nitrogen temperature. Additional strength is obtained by cold working, allowing the increase of the yield strength above 400–500 MPa. This is followed by a final stress-relief heat treatment to restore ductility without drastic reduction in strength, by relaxing the internal stresses.

Finally, the texture itself can increase alloy strength by changing the Schmid factor for slip or twinning. This can be observed by the differences in strength between the axial and transverse directions. In addition, due to the distorted shape of the yield locus, and consequently of the orientation of the strain vector, strain is also anisotropic.

Typical values of the strength of industrial alloys in various metallurgical states are given in **Table 2**.

Due to the absence of cleavage, the toughness properties of Zr alloys are not a matter of concern for unirradiated materials. Indeed, difficult measurements have obtained values of K_{IC} well above 50 MPa m^{1/2}. However, during irradiation, two processes deteriorate the ductility of the alloys:

Table 2 Typical values of the mechanical properties of industrial Zr alloys

Material	Heat treatment (°C)	Room temperature			350–375 °C		
		σ_Y (MPa)	UTS (MPa)	Ductility (%)	σ_Y (MPa)	UTS (MPa)	Ductility (%)
Zry-2 or-4 Stress relieved	480 °C 4 h	570	770	18	360	450	20
Zry-2 or-4 Recrystallized	500 °C 4 h	370	550	30	150	250	45
M5 Recrystallized	550 °C 2 h	320	480	35	130	250	40
E110 Recrystallized	570 °C 2.5 h	250	400	45	110	210	55
ZIRLO Recrystallized	580 °C 4 h	420	560	15	280	340	15
E635 Recrystallized	600 °C 4 h	300	480	30	150	270	35
E125 Annealed	550 °C 2 h	350	530	25	200	350	30
Zr 2.5Nb CANDU	Cold worked				350	510	15

UTS, Ultimate Tensile Strength.

- The first one is the formation of numerous fine dislocation loops that harden the materials and induce basal dislocation slip and localized strains. The macroscopic effect is a highly localized strain and highly reduced engineering ductility at fracture.^{41,42} The details of this ductility degradation induced by the irradiation are described in **Chapter 4.01, Radiation Effects in Zirconium Alloys**.
- The second mechanism of ductility degradation is linked to the impact of hydrogen trapped by the alloys during operation. The corresponding mechanisms are described in **Section 2.07.5.3**.

2.07.5.2 Mechanical Properties in Temperature and Creep

The thermal properties of Zr alloys are given in **Table 3**. The heat capacity increases with temperature, about 10% for 300 K. The anisotropy in any property is indeed decreasing with temperature, as the anisotropy in thermal expansion drives the hcp cell of Zr toward the ideal c/a ratio. In addition to the anisotropy of the thermal expansion coefficient, the elastic weakening in temperature has also to be considered.

As for any alloy, an increase in temperature results in a decrease in strength, but the evolution is not uniform, and a plateau in strength is observed near 200–400 °C. Known as the dynamic strain aging (DSA), it corresponds to the interaction of oxygen atoms with the dislocations. In this temperature range, oxygen atoms diffuse at rates commensurable with dislocation glide and hinder their motion. At higher temperatures, they are too mobile to affect the creep rates drastically.

Typical creep deformation rates are expressed by equations such as

$$\dot{\epsilon} = A\sigma^n \exp\left(\frac{-Q}{RT}\right)$$

Due to the transition induced by the oxygen in DSA, large discrepancies are observed in the creep

behavior of different alloys.⁴³ For conditions leading to strain rates below 10^{-9} s^{-1} (i.e., low temperatures and/or stresses), a low stress coefficient is observed: $n \sim 1-2$. Grain boundary sliding may be the mechanism involved in these conditions. For high creep rates, stress exponents larger than 4–6 have been reported. The mechanisms considered are complex, with predominance of dislocation glide controlled by local climb.⁴⁴ Similarly, the activation energy was measured to be as low as 40 kJ mol^{-1} for the low temperature regime, and 2 or 3 times larger for the high strain rates.

Most of the metallurgical parameters affect the creep rate. The effect of alloying elements on creep properties is different from their effect on tensile strength. Oxygen improves creep resistance, especially at low temperatures, but its effect is small compared to improvement in yield strength at room temperature. Despite its detrimental effect on corrosion, tin is maintained at significant levels in Zircalloys as an efficient alloying element to improve creep resistance.⁴⁵ For similar alloys with the same structure, creep behavior is similar; for example, Zircaloy-2 and Zircaloy-4 have similar creep strengths for the same thermomechanical processing. However, the metallurgical state of the material also influences the creep mechanisms; although SR material has higher tensile strength, its high dislocation density induces a two- to threefold increase in creep rate, compared to the RX state. Completely dissolved hydrogen increases the creep rate, while precipitated hydrides harden the alloys.⁴⁶ For additions as low as 50 ppm, sulfur drastically increases the creep strength, and is now an alloying element for specific alloys.⁴⁷

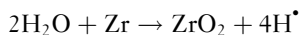
2.07.5.3 Hydrogen Embrittlement and Other H Effects

During oxidation of Zr alloy components in reactors or in autoclaves, the reduction of water by the Zr alloy follows the general reaction scheme:

Table 3 Thermal properties of Zr alloys

	Average	a-direction	c-direction
Heat capacity (RT)	$280 \text{ J kg}^{-1} \text{ K}^{-1}$		
Expansion coefficient	$8.5 \times 10^{-6} \text{ K}^{-1}$ (cladding tubes)	$5.2 \times 10^{-6} \text{ K}^{-1}$	$10.4 \times 10^{-6} \text{ K}^{-1}$
Modulus of elasticity			
Room temperature	90 GPa (cladding tubes)	99 GPa	125 GPa
400 °C		82 GPa	105 GPa

RT, Room temperature.



The reduction of the water molecules at the coolant-oxide interface releases four hydrogen atoms as radicals H^\bullet . They are chemically adsorbed at the tips of the oxide pores and their evolution controls the behavior of this chemical species. Most of the H atoms recombine, creating hydrogen molecules that escape and dissolve into the coolant. A limited amount can ingress in the oxide and migrate to the metallic matrix, where H is soluble, or interact with Zr to form hydrides (see **Chapter 5.03, Corrosion of Zirconium Alloys**). The fraction of the hydrogen that is trapped in the Zr alloy is called the hydrogen pick-up fraction (HPUF). For Zry-2, it is in the range of 30–60%, and for Zry-4 a lower HPUF is observed (15–25%), while the Zr–Nb alloys show the lowest one (4–10%). In order to reduce H pick-up, care should be taken to avoid the alloys catalyzers of the hydrogen molecule dissociation, such as Ni and Pt. This is the main reason for suppression of that element in Zircaloy-4: on removing Ni, HPUF is generally below 15% for standard PWR fuel cladding. Due to the strong variation of the solubility of H with temperature (~ 200 ppm at 350°C , but near 1 ppm at RT), hydrogen reacts with Zr to precipitate as hydrides as the alloy is cooled down.

One of the consequences of hydrogen ingress into Zr is the delayed hydride cracking (DHC).⁴⁸ This high temperature mechanism involves the ingress of hydrogen into a Zr-alloy component, its migration up the stress or thermal gradients, and its concentration in the regions of low temperature or higher tensile stress. When the local concentration exceeds the terminal solid solubility, the hydride phase precipitates.⁴⁹ At operation temperatures, a quasicontinuous crack growth is observed, whose rate depends on the hydrogen content, on the structure of the alloy, and on its crystallographic texture.⁵⁰ The failure of CANDU pressure tubes by this mechanism added pressure to the R&D in this field.⁵¹

At lower temperatures, corresponding to fuel handling and transport, the dissolved hydrogen precipitates as δ hydrides that have very brittle behavior. The hydrides are brittle below 200°C and crack when the stresses are high enough; failure of the components at low temperatures occurs because of percolation of the broken hydride platelets. Depending on the geometry and spatial distribution of the hydrides, very low ductilities can be observed. A slight increase in temperature would make the

hydrides ductile and the mechanical behavior of the claddings returns to normal above 200°C .^{52,53}

Hydrogen increases the creep strength of SR Zry, whatever be the H content. However, for RX alloys, H that gets completely dissolved enhances the creep rate, while precipitated hydrides harden the alloys.⁵⁴ This difference in behavior is connected to the effect of hydrides in inhibiting the thermal recovery. As described earlier, sulfur at very low concentrations drastically increases the creep strength, and even the yield strength.^{47,55}

Hydrogen in the cladding is also claimed to increase the corrosion rate due to the presence of an outer rim of hydrides,⁵⁶ and to deteriorate the behavior of the cladding during accident sequences, such as reactivity-induced accident (RIA), in which brittle hydrides drastically reduce the strain to failure,^{57–60} or loss of coolant accident (LOCA), where the cladding that is softened by hydrogen creeps faster and fails at lower temperatures than it would with lower hydrogen contents,⁶¹ or mixtures of these effects.

2.07.5.4 Prospectives

Although the use of Zr alloys has proven to be a good engineering solution, several properties are still subject to poor scientific understanding of their origins. Among them, deformation mechanisms (critical shear stresses on the different shear and twin systems), irradiation behavior (point defects interactions with alloying elements and mobilities), and corrosion mechanisms at atomic scales clearly need further basic scientific work.

For industrial purposes, the lot-to-lot variations in properties observed in many instances require larger margins in design and consequently reduce the efficiency of the power plants. Detailed analysis of the origins of these variations could be highly cost effective.

Last, the current development of computational materials science is a major opportunity for in-depth understanding and forecasting of the mechanisms of irradiation damage under irradiation. In that direction, multiscale modeling is particularly suited to nuclear materials. Zr alloys having no other sizable application than in the nuclear industry would strongly benefit from these new R&D techniques.

Acknowledgments

Special thanks are given to P. Barberis, A. Motta, and N. Dupin for their efficient support during the writing process of this chapter.

References

1. IAEA Monograph on Zirconium for Nuclear Applications; IAEA: Vienna, Austria, 2010.
2. *Zirconium in the Nuclear Industry*; ASTM International: West Conshohocken, PA, 2008; ASTM STP 1354, 1423, 1467.
3. Douglass, D. L. In *The Metallurgy of Zirconium*; Atomic Energy Review; IAEA: Vienna, Austria, 1971; Suppl. 1971.
4. Couterne, J. G.; Cizeron, G. *J. Nucl. Mater.* **1966**, 20(1), 75–82.
5. Northwood, D. O.; London, I. M.; Bahen, L. E. *J. Nucl. Mater.* **1975**, 55(3), 299–310.
6. Ashida, Y.; Yamamoto, M.; Naito, S.; Mabuchi, M.; Hashino, T. *J. Appl. Phys.* **1996**, 80(6), 3254–3258.
7. Cheong, Y. M.; Kim, S. S.; Kim, Y. S. *J. Nucl. Mater.* **2002**, 303(2–3), 83–91.
8. Fisher, E. S.; Renken, C. J. *Phys. Rev.* **1964**, 135(2A), A482.
9. Burgers, W. G. *Physica* **1934**, 1, 561–586.
10. Akhtar, A. *Meter. Trans. A* **1976**, 7A, 1735–1741.
11. Gey, N.; Humbert, M.; Gautier, E.; Béchade, J. L. *J. Nucl. Mater.* **2004**, 328(2–3), 137–145.
12. Romero, J.; Preuss, M.; Quinta da Fonseca, J. *Acta Mater.* **2009**, 57(18), 5501–5511.
13. Crepin, J.; Bertheau, T.; Caldemaison, D. *Acta Metall. Mater.* **1995**, 43, 3709–3719.
14. Tenckhoff, E. *Deformation Mechanisms, Texture and Anisotropy in Zirconium and Zircalloys*; ASTM International: West Conshohocken, PA, 1988; ASTM STP 966.
15. Tenckhoff, E. *Metall. Mater. Trans. A* **1978**, 9, 1401–1412.
16. Cook, C. S.; Sabol, G. P.; Sekera, K. R.; Randall, S. N. In *Zirconium in the Nuclear Industry*; ASTM International: West Conshohocken, PA, 1991; ASTM STP 1132, pp 80–95.
17. Massalski, T. B.; Okamoto, H. *Binary Alloy Phase Diagrams*; ASM International: Materials Park, OH, 1990; ISBN-13: 978-0871704030.
18. Dupin, N.; Ansara, I.; Servant, C.; Toffolon, C.; Lemaignan, C.; Brachet, J. C. *J. Nucl. Mater.* **1999**, 275(3), 287–295.
19. Barberis, P.; Dupin, N.; Lemaignan, C.; Pasturel, A.; Grange, J. J. *ASTM Int.* **2005**, 2, 129–156.
20. Kelly, P. M.; Smith, P. D. *J. Nucl. Mater.* **1973**, 46(1), 23–34.
21. Garzarolli, F.; Schumann, R.; Steinberg, E. In *Zirconium in the Nuclear Industry*; ASTM International: Conshohocken, PA, 1994; Vol. 10, ASTM STP 1245, pp 709–723.
22. Charquet, D.; Hahn, R.; Ortlieb, E.; Gros, J. P.; Wadier, J. F. In *Zirconium in the Nuclear Industry*, 8th Symposium; ASTM International: Conshohocken, PA, 1989; ASTM STP 1023, pp 405–422.
23. Kruger, R. M.; Adamson, R. B.; Brenner, S. S. *J. Nucl. Mater.* **1992**, 189(2), 193–200.
24. Beie, H. J.; Mitwalsky, A.; Garzarolli, F.; Ruhmann, H.; Sell, H. J. In *Zirconium in the Nuclear Industry*; ASTM International: Conshohocken, PA, 1994; Vol. 10, ASTM STP 1245, pp 615–643.
25. Garzarolli, F.; Goll, W.; Seibold, A.; Ray, I. In *Zirconium in the Nuclear Industry*, 11th International Symposium; ASTM International: Conshohocken, PA, 1996; ASTM STP 1295, pp 541–556.
26. Cheadle, B. A.; Aldridge, S. A. *J. Nucl. Mater.* **1973**, 47(2), 255–258.
27. IAEA. *Corrosion of Zirconium in Nuclear Power Plants*; TECDOC.684; 93.
28. Doriot, S.; Gilbon, D.; Bechade, J. L.; Mathon, M.; Legras, L.; Mardon, J. P. *J. ASTM Int. (JAI)* **2005**, 2(7), 175–201.
29. Ferrer, F.; Barbu, A.; Bertheau, T.; Crepin, J.; Willaime, F.; Charquet, D. In *Zirconium in the Nuclear Industry*, 13th International Symposium; ASTM International: Conshohocken, PA, 2002; ASTM STP 1423, pp 863–887.
30. Charquet, D. *J. Nucl. Mater.* **2002**, 304(2–3), 246–248.
31. Iltis, X.; Lefebvre, F. *J. Nucl. Mater.* **1995**, 224(2), 121–130.
32. Toffolon-Masclet, C.; Brachet, J. C.; Servant, C.; et al. In *Zirconium in the Nuclear Industry*, 13th International Symposium; ASTM International: Conshohocken, PA, 2002; ASTM STP 1423, pp 361–383.
33. Toffolon-Masclet, C.; Barberis, P.; Brachet, J. C.; Mardon, J. P.; Legras, L. *J. ASTM Int. (JAI)* **2005**, 2(5), 81–101.
34. Rickover, H. G. The Decision to Use Zirconium in Nuclear Reactors; TID-26740; 1975.
35. Mardon, J. P.; Charquet, D.; Senevat, J. In *Zirconium in the Nuclear Industry*, 12th International Symposium; ASTM International: Conshohocken, PA, 2000; ASTM STP 1354, pp 505–524.
36. Sabol, G. P. In *Zirconium in the Nuclear Industry*, 14th International Symposium; ASTM International: Conshohocken, PA, 2006; ASTM STP 1467, pp 3–24.
37. Shishov, V.; et al. In *Zirconium in the Nuclear Industry*, 14th International Symposium; ASTM International: Conshohocken, PA, 2005; ASTM STP 1467, pp 666–685.
38. Fidleris, V. *J. Nucl. Mater.* **1988**, 159, 22–42.
39. Nikulina, A. V.; Markelov, V. A.; Peregud, M. M.; Voevodin, V. N.; Panchenko, V. L.; Kobylansky, G. P. *J. Nucl. Mater.* **1996**, 238(2–3), 205–210.
40. Pahutova, M.; Cadec, J.; Cerny, V. *J. Nucl. Mater.* **1976**, 61(3), 285–296.
41. Onimus, F.; Bechade, J. L.; Prioul, C.; et al. In *Zirconium in the Nuclear Industry*, 14th International Symposium; ASTM International: Conshohocken, PA, 2005; ASTM STP 1467, pp 53–78.
42. Regnard, C.; Verhaerghe, B.; Lefebvre, F.; Lemaignan, C. In *Zirconium in the Nuclear Industry*, 13th International Symposium; ASTM International: Conshohocken, PA, 2002; ASTM STP 1423, pp 384–399.
43. Christodoulou, N.; Chow, C.; Turner, P.; Tome, C.; Klassen, R. *Metall. Mater. Trans. A* **2002**, 33(4), 1103–1115.
44. Murty, K. L.; Mahmood, S. In *Zirconium in the Nuclear Industry*; ASTM International: West Conshohocken, PA, 1991; ASTM STP 1132, pp 198–217.
45. McIntyre, N. S.; Baty, D. L.; Stein, K. O. In *Zirconium in the Nuclear Industry*, 8th Symposium; ASTM International: Conshohocken, PA, 1988; ASTM STP 1023, pp 621–640.
46. Bouffioux, P.; Rupa, N. In *Zirconium in the Nuclear Industry*, 12th International Symposium; ASTM International: Conshohocken, PA, 2000; ASTM STP 1354, pp 399–422.
47. Charquet, D.; Senevat, J.; Marcon, J. P. *J. Nucl. Mater.* **1998**, 255(1), 78–82.
48. Simpson, C. J.; Ellis, C. E. *J. Nucl. Mater.* **1974**, 52(2), 289–295.
49. Kammenzind, B. F.; Franklin, D.; Duffin, W. J.; Peters, H. R. In *Zirconium in the Nuclear Industry*, 11th International Symposium; ASTM International: Conshohocken, PA, 1995; ASTM STP 1295, pp 338–370.
50. Shi, S. Q.; Shek, G. K.; Puls, M. P. *J. Nucl. Mater.* **1995**, 218(2), 189–201.
51. Coleman, C. B.; Griffiths, M.; Grigoriev, V.; Kiseliiov, V.; Rodchenkov, B.; Markelov, V. *J. ASTM Int.* **2007**, 4, JAI101111.
52. Bertolino, G.; Meyer, G.; Perez Ipinia, J. *J. Nucl. Mater.* **2003**, 320(3), 272–279.

53. Shi, S. Q.; Puls, M. P. *J. Nucl. Mater.* **1999**, 275(3), 312–317.
54. Bouffieux, P.; Rupa, N. In *Zirconium in the Nuclear Industry*, 12th International Symposium; ASTM International: Conshohocken, PA, 2000; ASTM STP 1354, pp 399–424.
55. Chang, K. I.; Hong, S. I. *J. Nucl. Mater.* **2008**, 373(1–3), 16–21.
56. Blat, M.; Legras, L.; Noël, D.; Amanrich, H. In *Zirconium in the Nuclear Industry*, 12th International Symposium; ASTM International: West Conshohocken, PA, 2000; ASTM STP 1354, pp 563–591.
57. Schmitz, F.; Papin, J. *J. Nucl. Mater.* **1999**, 270(1–2), 55–64.
58. Vitanza, C. *J. Nucl. Sci. Technol.* **2006**, 43(9), 1074–1079.
59. Daum, R. S.; Majumdar, S.; Bates, D. W.; Motta, A.; Koss, D. A.; Billone, M. C. In *Zirconium in the Nuclear Industry*, 13th International Symposium; ASTM International: West Conshohocken, PA, 2002; ASTM STP 1423, pp 702–719.
60. Nakatsuka, M.; Une, K.; Tokunaga, K.; Ohta, T. Mechanical properties of high burnup BWR fuel cladding tubes under simulated RIA conditions. In *International Topical Meeting on Light Water Reactor Fuel Performance*, Orlando, FL, 2004; pp 526–535.
61. Portier, L.; Bredel, T.; Brachet, J. C.; Maillot, V.; Mardon, J. P.; Lesbros, A. In *Zirconium in the Nuclear Industry*, 14th International Symposium; ASTM International: West Conshohocken, PA, 2005; ASTM STP 1467, pp 896–920.

2.08 Nickel Alloys: Properties and Characteristics

T. Yonezawa

Tohoku University, Japan

© 2012 Elsevier Ltd. All rights reserved.

2.08.1	Introduction	234
2.08.2	Nickel and Nickel Alloy Systems	234
2.08.2.1	Ni and Ni–Cu Alloys	235
2.08.2.1.1	Chemical compositions, physical properties, and mechanical properties	235
2.08.2.1.2	Applications to nuclear power industrial fields	239
2.08.2.2	Ni–Cr–Fe and Ni–Cr–Fe–Mo Alloys	241
2.08.2.2.1	Chemical compositions, physical properties, and mechanical properties	241
2.08.2.2.2	Applications to nuclear power industrial fields	244
2.08.2.3	Ni–Mo–Fe, Ni–Mo–Cr–Fe, and Ni–Cr–Mo–Fe Alloys	250
2.08.2.3.1	Chemical compositions, physical properties, and mechanical properties	250
2.08.2.3.2	Applications to nuclear power industrial fields	253
2.08.2.4	Other Ni-Based Alloys	253
2.08.2.4.1	Chemical compositions, physical properties, and mechanical properties	253
2.08.2.4.2	Applications to nuclear power industrial fields	253
2.08.3	Fabrication of Ni-Based Alloys	254
2.08.3.1	Melting	254
2.08.3.2	Hot Forming	254
2.08.3.3	Cold Forming	255
2.08.3.4	Heat Treatment	256
2.08.3.5	Descaling and Pickling	257
2.08.3.6	Grinding and Machining	257
2.08.3.7	Welding	257
2.08.3.7.1	Weldability	257
2.08.3.7.2	Welding materials and example of welding condition	257
2.08.3.8	Applicable Specifications	258
2.08.4	Corrosion Resistance and Stress Corrosion Cracking Resistance	258
2.08.4.1	In Air and in Water	258
2.08.4.2	In Seawater and Chloride Solution	261
2.08.4.3	In Caustic Solutions	262
2.08.4.4	In Hydrochloride Gas, Chlorine, and Hydrofluoric Acid	262
2.08.4.5	In High-Temperature Water	262
2.08.4.6	In High-Temperature Gases	263
2.08.4.6.1	Oxidation	263
2.08.4.6.2	Nitriding	264
2.08.4.6.3	Sulfidation	264
2.08.5	Summary	265
References		265

Abbreviations

ASME	American Society of Mechanical Engineering
ASTM	American Society for Testing and Materials
BWR	Boiling water reactor

CRDM	Control rod drive mechanism
EBW	Electron beam welding
fcc	Face-centered cubic
FCAW	Flux cored arc welding
GTAW	Gas tungsten arc welding
HTGR	High-temperature gas-cooled reactor

HTH	Precipitation hardening at about 715°C after solution annealing at a high temperature near 1075°C
HTTR	High-temperature engineering HTGR test reactor
IGSCC	Intergranular stress corrosion cracking
LBW	Laser beam welding
MA	Mill-annealed
MAG	Metal active gas welding
MIG	Metal inert gas welding
PWR	Pressurized water reactor
PWSCC	Primary water stress corrosion cracking
SAW	Submerged arc welding
SCC	Stress corrosion cracking
SG	Steam generator
SMAW	Shielded metal arc welding
TT	Thermally treated or thermal treatment

2.08.1 Introduction

Nickel was first used as an alloying element for steels in the mid-eighteenth century. The development of corrosion-resistant steels was started in the nineteenth century.^{1,2} These studies led to the development of various kinds of stainless steels, particularly in the early 1900s. Particularly, the 300 series austenitic stainless steels were developed and became the ‘most widely used tonnage’ materials in the twentieth century.

The nickel–copper Alloy 400 (Monel 400, UNS N04400) was developed as the first nickel-based alloy at the beginning of the twentieth century.³ This alloy was developed as an alternative chloride-corrosion-resistant material to austenitic stainless steel.

Nickel is a less noble element than copper; however, it is more noble than iron and zinc. It exhibits higher corrosion resistance than iron in most environments due to the formation of denser and more protective corrosion films with superior passivation characteristics compared to iron.

Nickel has superior corrosion resistance in caustic or nonoxidizing acidic solutions, and in gaseous halogens. It can be relatively easily alloyed with various elements such as chromium, molybdenum, iron, and copper. Many nickel-based alloys have been developed and applied as corrosion-resistant alloys in various environments, as well as creep-resistant alloys in high-temperature applications.⁴

Based on their excellent properties, nickel-based alloys have been widely applied in a number of fields, for example, the aerospace industry, chemical industries, and electricity generation plants. In the nuclear

power industry, nickel-based alloys have been used in pressurized water reactors (PWRs) and boiling water reactors (BWRs) since their initial development in the early 1950s. In particular, Alloys X-750 (UNS N07750) and X-718 (UNS N07718) have been widely applied, for example, for jet-engine blades, due to their excellent creep strength. A high-creep-strength material is one that is highly resistant to stress relaxation at high temperatures. Alloys X-750 and 718 have therefore been applied as bolting and spring materials for PWRs and BWRs.

Alloy 600 (UNS N06600) has superior resistance to stress corrosion cracking (SCC) in boiling 42% MgCl₂ solution as high-chloride solutions.⁵ In the Shippingport and Yankee Rowe reactors, 347 stainless steel was used as a steam generator (SG) tube material. (The Shippingport reactor was the first full-scale nuclear powered electricity generation plant (prototype reactor), and the Yankee Rowe reactor was the first commercial PWR.) Beginning with the Connecticut Yankee PWR, the next electricity generation plant, Alloy 600 was used as the SG tube material, and then subsequently applied in PWRs worldwide, due to its superior SCC resistance in high-chloride solutions.

Among the other superior properties of Alloy 600, its thermal expansion coefficient is noted to be between that of ferritic steels and austenitic steels. Based on this, the residual stress and strain for dissimilar weld joints of ferritic steels and austenitic steels can be minimized by the use of Alloy 600 and its compatible weld metals. In nuclear power plants, ferritic steels and austenitic steels are widely used as the main component materials, especially for the pressure boundary. Numerous dissimilar metal weld joints are therefore found in nuclear power plants. Alloy 600 and its weld metals such as Alloys 82, 132, and 182 have also found widespread application in such plants.

Nickel-based alloys were developed not only as corrosion-resistant materials but also as heat-resistant materials. These alloys are suitable for various components and parts in light water reactors, heavy water reactors, gas reactors, etc.

The detailed features and various physical properties of these nickel-based alloys are described in the following sections.

2.08.2 Nickel and Nickel Alloy Systems

Nickel by itself is a very versatile corrosion-resistant metal and has a higher strength at elevated temperatures than steel. Nickel forms a complete solid solution

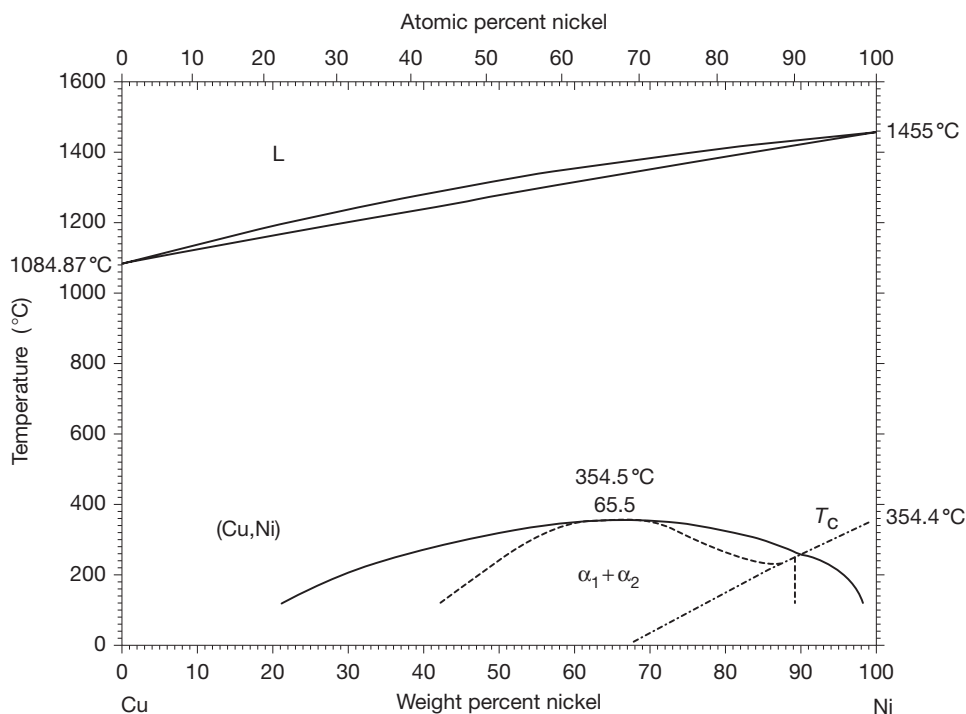


Figure 1 Copper–nickel binary phase diagram.

with copper (as shown in [Figure 1](#)), manganese, and gold.⁶ Nickel forms a peritectic with iron (as shown in [Figure 2](#)) and eutectics with many elements, such as chromium (as shown in [Figure 3](#)), molybdenum (as shown in [Figure 4](#)), silicon, titanium, aluminum, niobium.⁶ Nickel can form solid solutions with many elements and intermetallic compound with aluminum, titanium, niobium, and so on. The ternary constitutional diagram for the iron–nickel–chromium isothermal section at 650 °C shown in [Figure 5](#) indicates a wide region covered by the face-centered cubic (fcc) structure of nickel. But the fcc region is shrunk in the ternary constitutional diagram at 600 °C for nickel–chromium–molybdenum system, as shown in [Figure 6](#). In this alloy system, sigma phase and other intermetallic phases are found based on a composition range.⁶ The effects of alloying elements on the properties of nickel-based alloys are summarized in [Table 1](#).

Commercially pure nickel and various nickel-based alloys are representative of the newly developed materials during the twentieth century. These materials are typically encountered in various industrial systems, including chemical and petrochemical processing, aerospace engineering, fossil fuel and nuclear power generation, energy conversion, solar energy conversion, thermal processing and heat treatment, oil and gas production, pollution control and waste

processing, marine engineering, pulp and paper industry, agrichemicals, industrial and domestic heating, and electronics and telecommunication, among others.

Various nickel-based alloys, including binary, ternary, and other complex systems, were also developed in the twentieth century. The main features and applications of these commercially pure nickel and nickel-based alloys are summarized in [Figure 7](#).

Detailed properties and features of these nickel and nickel-based alloys are described in the following sections. The several of these nickel-based alloys have been applied or designed to various nuclear reactor materials as shown in [Table 2](#).

2.08.2.1 Ni and Ni–Cu Alloys

2.08.2.1.1 Chemical compositions, physical properties, and mechanical properties

The chemical compositions of nickel and typical nickel–copper alloys are shown in [Table 3](#), along with those of other nickel-based alloys.

Alloy 200 (UNS N02200) is a commercially pure (99.6%) wrought nickel. Alloy 201 (UNS N02201) is the low-carbon version of Alloy 200. These alloys have good mechanical properties and good resistance to corrosion at low to moderate temperatures in

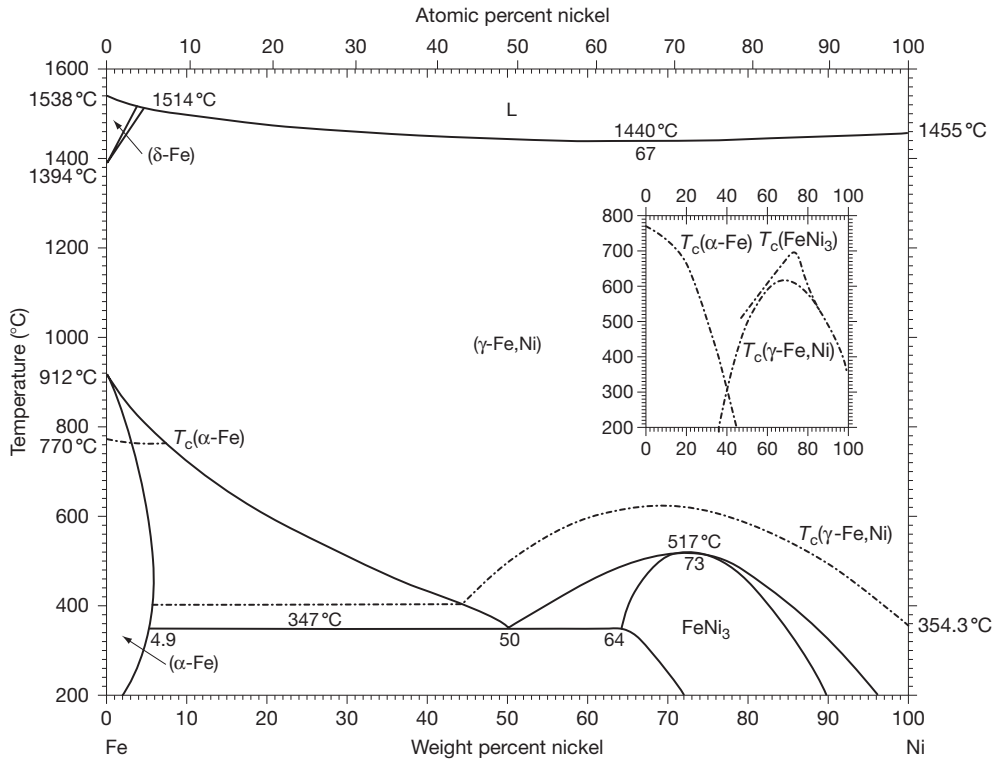


Figure 2 Iron–nickel binary phase diagram.

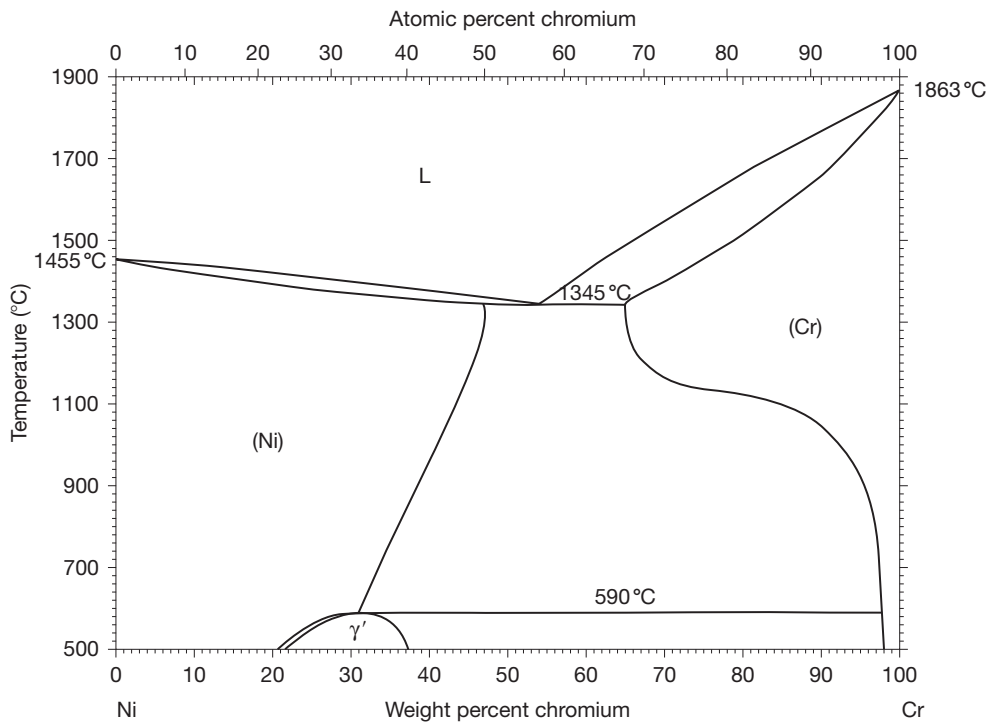


Figure 3 Nickel–chromium binary phase diagram.

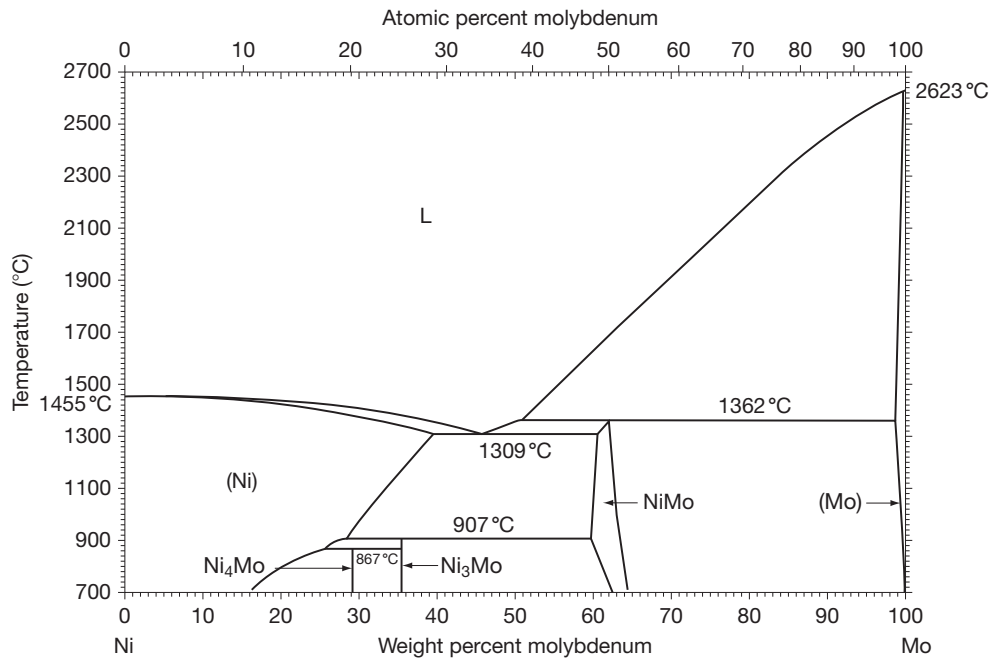


Figure 4 Nickel-molybdenum binary phase diagram.

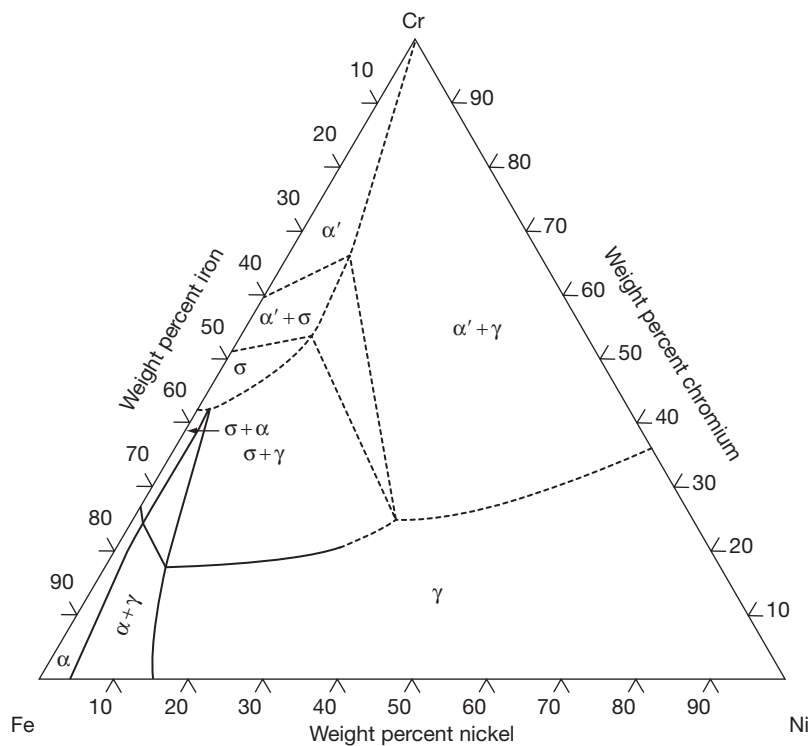


Figure 5 Iron-nickel-chromium ternary phase diagram (at 650 °C).

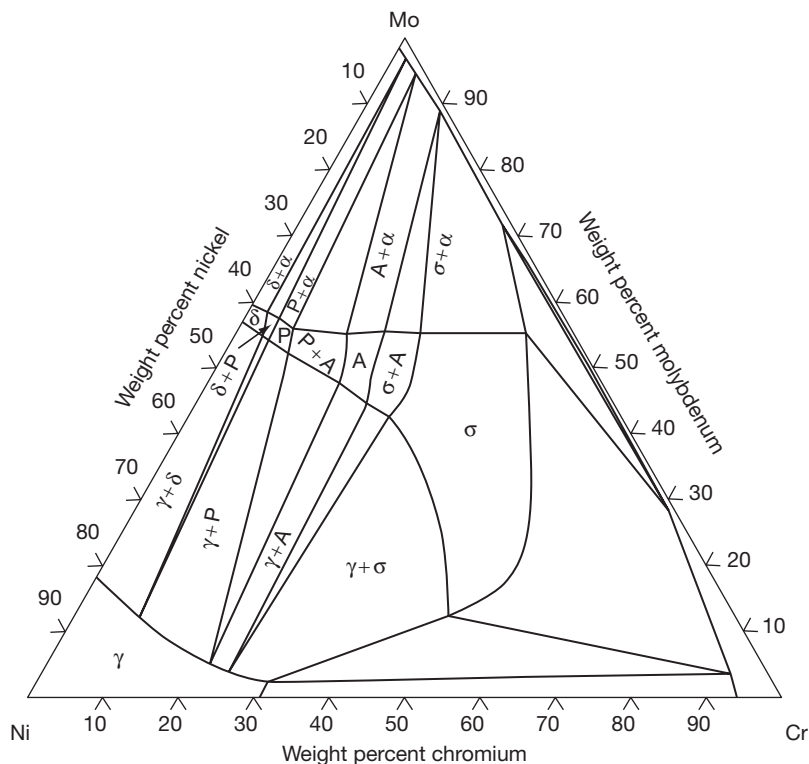


Figure 6 Nickel–chromium–molybdenum ternary phase diagram (at 600 °C).

caustic solutions such as NaOH or dilute deaerated solutions of common nonoxidizing mineral acids such as HCl, H₂SO₄, or H₃PO₄.⁷

The mechanical properties of Alloy 200 at elevated temperatures are shown in **Figures 8 and 9**.³ Alloy 200 is typically limited to use at temperatures below 315 °C. At higher temperatures, Alloy 200 products can suffer from graphitization, which can severely compromise the properties of the material. Alloy 200 is susceptible to embrittlement after long-term heating in the range of 425–760 °C, due to carbide precipitation along grain boundaries.⁴ For service above 315 °C, Alloy 201 is preferred.⁷

The reason for the good corrosion resistance of Alloys 200 and 201 is the fact that the standard oxidation–reduction potential of nickel is more noble than that of iron and less noble than that of copper. Due to nickel’s high overpotential for hydrogen evolution, hydrogen is not easily discharged from any of the common nonoxidizing acids, and a supply of oxygen is necessary for rapid corrosion to occur. Hence, in the presence of oxidizing species such as ferric ions, cupric ions, nitrates, peroxides, or oxygen, nickel can corrode rapidly. The outstanding corrosion-resistance characteristics of Alloy 200 to

caustic soda and other alkalis have led to its successful use in caustic evaporator tubes.⁷

The nickel–copper Alloy 400 is a complete solid-solution alloy that can be hardened only by cold-working. Alloy 400 contains about 30–33% copper in a nickel matrix and has similar characteristics as those of Alloy 200. It has high strength and toughness over a wide temperature range and good resistance to many corrosive environments. Alloy 400 exhibits excellent resistance to corrosion in many reducing media. It is also generally more resistant to attack by oxidizing environments compared to higher copper-content alloys. It is also widely used in marine applications. Alloy 400 products exhibit low corrosion rates in flowing seawater, whereas in stagnant conditions, crevice and pitting corrosion can be induced. It is also resistant to SCC and pitting in most fresh and industrial waters. Alloy 400 is highly resistant to hydrofluoric acid at all concentrations and at all temperatures up to their boiling points. It is therefore widely used in components for seawater applications, salt units, crude distillation, and as a structural material in chemical plants.⁸

Alloy K-500 (UNS N05500) is a precipitation-hardened version of Alloy 400. It contains aluminum

Table 1 The effects of alloying elements various properties of nickel-based alloys

<i>Alloying elements</i>	<i>Main feature for aqueous corrosion</i>	<i>Main feature for high-temperature applications</i>	<i>Other benefits</i>
Ni	Provides corrosion resistance to caustic solutions and dilute deaerated solutions of nonoxidizing mineral acids. Improves chloride SCC	Stabilization of austenitic phase. Provides precipitation of γ'	Thermal stability and fabricability
Cr	Provides resistance to oxidizing media Enhances localized corrosion resistance	Provides solid solution hardening Provides precipitation of $M_{23}C_6$, as benefit for notched rupture resistance	
Mo	Provides resistance to reducing media	Provides solid solution hardening; provides precipitation of M_6C	
W	Enhances localized corrosion resistance Behaves similar to Mo but less effective	Provides solid solution hardening	Detrimental to thermal stability
Al		Provides precipitation of M_6C Suppress precipitation of η phase (Ni_3Ti) Provides oxidation resistance	Deoxidizer in melting process
Ti Nb, Ta Si		Provides precipitation of γ' Provides precipitation of γ' and γ'' Provides oxidation resistance	Increases fluidity in casting process
C	Affects detrimental effect for sensitization	Provides solid solution hardening Provides precipitation of $M_{23}C_6$, M_6C , MC , etc., much precipitation of MC decreases precipitation of γ' and γ''	Mechanical properties
N		Austenitic stabilizer	Thermal stability and mechanical properties
Cu B, Zr	Improves resistance to seawater	Increases creep rupture strength Suppress precipitation of η phase	
La, Ce		Provides oxidation resistance	Deoxidizer in melting process

and titanium, and is hardened by the formation of submicroscopic particles of intermetallic compounds, $Ni_3(Ti, Al)$. The formation of intermetallic compounds occurs as a solid-state reaction during the thermal aging (precipitation hardening) treatment. Prior to the aging treatment, the alloy component needs to be solution-annealed to dissolve any phases that may have formed during previous processing. The solution annealing and aging are normally carried out in the temperature range 980–1040 °C and 540–590 °C, respectively. Alloy K-500 has the excellent corrosion-resistant features of Alloy 400 with the added benefits of increased strength up to 600 °C and hardness. The alloy has low magnetic permeability and is nonmagnetic up to 134 °C.

Some typical applications of Alloy K-500 include pump shafts, impellers, medical blades and scrapers, oil well drill collars and instruments, nonmagnetic

housings and other complementary tools, electronic components, springs, and valve trains.⁹

The mechanical and various physical properties of nickel and typical nickel–copper alloys are shown in **Tables 4** and **5**, respectively, along with those of other nickel-based alloys. Physical properties at elevated temperature are shown in **Tables 6–8**.

2.08.2.1.2 Applications to nuclear power industrial fields

Based on the high thermal conductivity (see **Table 6**) and high corrosion resistance of nickel–copper alloys in seawater, Alloy 400 has been widely applied in boiler feed water heat exchanger tubes and shells, and Alloy 500 has found wide use for pump shafts and impellers in seawater pumps. Based on such industrial applications, Alloy 400 was used for SG tubes in some CANDU reactors.

Alloy system	Alloy no.	Chemical compositions	Features
Ni	Alloy 200	Ni > 99.0	Commercial pure Ni. Applicable in caustic solution below 315°C
	Alloy 201	Ni > 99.0, C < 0.02	Low C commercial pure Ni. Applicable in caustic solution above 315°C
Ni-Cu alloy	Alloy 400	Ni-31Cu-2Fe (S ≤ 0.024)	Applicable to the components for sea water, salt unit, crude distillation, etc.
	Alloy R-405	Ni-31Cu-2Fe-0.04S	Free machining grade of Alloy 400
	Alloy K-500	Ni-30Cu-2Fe-0.6Ti-2.7Al	P.H. version of Alloy 400, up to 600°C. Applicable to pump-shaft, impellers, scrapers, etc.
Ni-Cr-Fe alloy	Alloy 600	Ni-15Cr-8Fe	Excellent resistant to in chloride SCC. Applicable to structural materials
	Alloy 601	Ni-23Cr-8Fe-1.4Al	Excellent resistant to high-temperature oxidation. Applicable to oxidation-resistant parts
	Alloy 690	Ni-29Cr-9Fe	Excellent resistant to many corrosive aqueous media, etc. Applicable to structural materials
	Alloy 800	Fe-33Ni-21Cr	Highly resistant to high-temperature oxidation. Applicable to components for high-temperature use
Ni-Cr-Fe/ Ni-Cr-Fe-Mo P.H. alloy	Alloy X-750	Ni-15Cr-7Fe-2.5Ti-1Nb-0.7Al	Typical P.H. Ni-based alloy. Applicable to parts which need high tensile, creep and creep rupture properties
	Alloy 718	Ni-19Cr-17Fe-3Mo-0.9Ti-0.5Al-5.1Nb	Higher strength level than Alloy X-750. Applicable to parts which need high tensile, creep and creep rupture, etc.
	Alloy A286	Fe-25Ni-15Cr-1.3Mo-2.1Ti-0.3Al	Age-hardenable alloy. Good strength and oxidation resistance up to 700°C
Ni-Mo-Fe alloy	Alloy B	Ni-28Mo-5Fe-2Co	Excellent resistant to hydrochloric acid. But, weak to solutions with mixing of oxidant
	Alloy B-2	Ni-28Mo-4Fe-2Co-Low Si, Low C	Improved on corrosion resistance in heat affected zone after welding of Alloy B
	Alloy B-3	Ni-30Mo-2Fe-2Co-2Cr-2W-2Mn	Minimized fabrication problems for Alloy B-2. Not applicable to the environment with ferric or cupric salt
Ni-Mo-Cr-Fe alloy	Alloy C	Ni-17Mo-16.5Cr-4.5W-5.3Fe-0.3V	Excellent high resistance to oxidation, corrosion in chlorine, compounds with chlorine, oxidizing acid, etc.
	Alloy C-276	Ni-16Mo-15.5Cr-5Fe-3.7W-2Co	Improved on fabricability and long range aging characteristics of Alloy C
	Alloy C-4	Ni-16Mo-16Cr-2Fe-1.5Co	Advanced Alloy B. Superior corrosion resistance to oxidizing environment compared to Alloy B
Ni-Cr-Mo-Fe alloy	Alloy C-22	Ni-21Cr-13.5Mo-4Fe-3W-2Co	Improved on corrosion resistance of Alloy C-276 in oxidizing environment
	Alloy 625	Ni-21.5Cr-9Mo-4Fe	High creep rupture strength and high resistance to corrosion and pitting in oxidizing environment
	Alloy 625LCF	Ni-21.5Cr-9Mo-4Fe	Improved on low cycle fatigue properties and cold formability of Alloy 625
	Alloy 686	Ni-21Cr-16Mo-4Fe-3.7W-1.2Al	High Cr content of Alloy C-276. Excellent resistance to SCC, pitting and crevice corrosion in aggressive media
	Alloy 59	Ni-23Cr-15.7Mo-1Fe-0.3Al	Pure Ni-Cr-Mo alloy. Excellent corrosion resistance and thermal stability
	Alloy 825	42Ni-21.5Cr-25Fe-3Mo-2.2Cu-0.9Ti	Improved on aqueous corrosion resistance in a wide variety of corrosion media, modified by Alloy 800
Others	Alloy G	Ni-22Cr-19.5Fe-6.5Mo-2Cu,Nb,Co-0.8W	Superior corrosion resistance to oxidizing environment, inferior corrosion resistant to reducing environment
	Alloy G-3	Ni-22Cr-19.5Fe-7Mo-2Cu-4Co	Improved on bending characteristics of weld joints for Alloy G
	Alloy G-30	Ni-30Cr-15Fe-5Mo-2.7W-1.7Cu-4Co	Improved on corrosion resistance in wet phosphoric acid for Alloy G
	Alloy N	Ni-16.5Mo-7Cr-4Fe	Excellent corrosion resistance to liquid fluoride
	Alloy 230	Ni-22Cr-14W-4Co-2Mo-2Fe	Excellent resistance to oxidation and nitriding, as well as high strength at high temperatures
	Alloy X	Ni-22Cr-18.5Fe-9Mo-0.6W-2Co	High strength at high temperatures and good resistance to oxidation in high temperature air
	Alloy XR	Ni-Cr-Fe-Mo-2Co	Originally developed as a structural material for high temperature gas-cooled reactors

Figure 7 Nickel-based alloy systems and their features (dotted line: reference material, P.H.: precipitation hardened). In nuclear power plants, several of these nickel-based alloys have been applied or are suitable as materials for various components, pipes, tubes, and other parts. The main applications or candidates of nickel-based alloys for various nuclear reactors are summarized in **Table 2**.

Table 2 Main applications or candidates of nickel-based alloys for nuclear reactors

Type of nuclear reactor	Alloys
BWR	600, X-750, 718, 625
PWR	600, X-750, 718, 690, 800, A286
CANDU reactor	600, X-750, 718, 690, 800
LMFBR	X-750, 718, 800
HTGR	600, X-750, 718, 625, XR

2.08.2.2 Ni–Cr–Fe and Ni–Cr–Fe–Mo Alloys

2.08.2.2.1 Chemical compositions, physical properties, and mechanical properties

The chemical compositions of typical nickel–chromium–iron and nickel–chromium–iron–molybdenum alloys are shown in [Table 3](#), together with those of other nickel-based alloys.

As described earlier, nickel is a very versatile corrosion-resistant metal. The addition of chromium confers resistance to sulfur compounds and also provides resistance to oxidizing conditions at high temperatures or in corrosive solutions, with the exceptions of nitric acid and chloride solutions. In addition, chromium confers resistance to oxidation and sulfidation at high temperatures.

Alloy 600 consists of about 76% nickel, 15% chromium, and 8% iron. The alloy is not precipitation-hardenable and can only be hardened and strengthened by cold-working. It has excellent resistance to hot halogen gases and has been used in processes involving chlorination. It has excellent resistance to oxidation and chloride SCC. It is widely applied as a structural material in many industrial fields owing to its strength and corrosion resistance.¹⁰

The thermal expansion coefficient of Alloy 600 is smaller than those of austenitic stainless steels and somewhat larger than those of ferritic steels, as shown in [Table 7](#). It is also highly resistant to sensitization in heat-affected zones during welding. The alloy and its weld metals such as Alloys 82, 132, and 182 have therefore been widely used for dissimilar metal weld joints to reduce residual stresses and strains after welding.

Alloy 601 has a higher chromium content (about 23%) than Alloy 600 and about 1.4% aluminum. The alloy is resistant to high-temperature oxidation and has good resistance to aqueous corrosion. Oxidation resistance is further enhanced by its aluminum content. The alloy has been applied to the muffles of heat-treatment furnaces and in catalytic convertors for exhaust gases in automobiles.¹¹

Alloy X-750 contains titanium, aluminum, and niobium, and is hardened by precipitation of the γ' phase as $\text{Ni}_3(\text{Ti}, \text{Al}, \text{Nb})$.¹² Alloy 718, on the other hand, contains niobium, molybdenum, titanium, and aluminum, and is hardened by the precipitation of both the γ' phase as $\text{Ni}_3(\text{Ti}, \text{Al}, \text{Nb})$ and the γ'' phase as Ni_3Nb .¹³ These alloys were developed as high creep-strength and high creep-rupture-strength materials for jet-engine blades and vanes in the 1940s. These precipitation-hardened materials have also been used in industrial gas-turbine materials. In addition, Alloy X-750 has been used as a bolting material and Alloy 718 has been applied to bellows, springs, etc. for industrial products.

Alloy 690 (UNS N06690) was developed in the late 1960s and has a higher chromium content (about 30%) than Alloys 600 and 601. It exhibits excellent resistance to many corrosive aqueous media and high-temperature atmospheres. The properties of Alloy 690 are useful in a range of applications involving nitric or nitric/hydrofluoric acid production, and as heating coils and tanks for nitric/hydrofluoric solutions used in the pickling of stainless steels, for example.¹⁴

Alloy 800 (UNS N08800) is an iron-based nickel–chromium alloy. This alloy has been compared to Alloys 600 and 690 from the view point of its corrosion resistance in many environments. It was introduced for industrial use in the 1950s as an oxidation-resistant alloy and for high-temperature applications requiring optimum creep and creep-rupture properties. Alloy 800 has been widely used as an oxidation-resistant material and is suitable for high-temperature applications due to its high resistance to σ -phase embrittlement after heating in the range of 650–870 °C.¹⁵

Alloy 825 (UNS N08825) was developed from alloy 800 by the addition of molybdenum (about 3%), copper (about 2%), and titanium (about 0.9%) for improved aqueous corrosion resistance in a wide variety of corrosive media. In this alloy, the nickel content confers resistance to chloride-ion SCC. Nickel in conjunction with molybdenum and copper gives outstanding resistance to reducing environments such as those containing sulfuric and phosphoric acids. Molybdenum also enhances its resistance to pitting and crevice corrosion. In both reducing and oxidizing environments, the alloy resists general corrosion, pitting, crevice corrosion, intergranular (IG) corrosion, and SCC. Some typical applications include various components used in sulfuric acid pickling of steel and copper, components in petroleum refineries and petrochemical

Table 3 Chemical compositions of nickel-based alloys

[illegible]

Ni-Cr-Mo-Fe	C-4	N06455 ^b	14.0–18.0	14.5–17.0	≤3.0	–	≤0.015	≤0.08	≤2.0	≤1.0	–	≤0.04	≤0.03	–	≤0.70	–	–	–	–	–	–	–
	C-22/22	N06022 ^b	20.0–22.5	12.5–14.5	2.0–6.0	2.5–3.5	≤0.015	≤0.08	≤2.5	≤0.50	≤0.35	≤0.02	≤0.02	–	–	–	–	–	–	–	–	–
	625	N06625	≥58.0	20.0–23.0	8.0–10.0	–	≤0.10	≤0.50	≤1.0	≤0.50	–	≤0.015	≤0.015	–	≤0.40	≤0.40	3.15–4.15	–	–	–	–	–
	625LCF	N06626	≥58.0	20.0–23.0	8.0–10.0	–	≤0.030	≤0.020	≤1.0	≤0.50	–	≤0.015	≤0.015	–	≤0.40	≤0.40	3.15–4.15	–	–	≤0.020	–	–
	686	N06686 ^b	19.0–23.0	15.0–17.0	≤5.0	3.0–4.4	≤0.010	≤0.08	–	≤0.75	–	≤0.04	≤0.02	–	0.02–0.25	–	–	–	–	–	–	–
Reference	59	N06059 ^b	22.0–24.0	15.0–16.5	≤1.5	–	≤0.010	≤0.10	≤0.3	≤0.5	–	≤0.015	≤0.005	≤0.50	–	0.1–0.4	–	–	–	–	–	–
	825	N08825	38.0–46.0	19.5–23.5	2.5–3.5	≥22.0	–	≤0.05	≤0.5	–	≤1.0	–	–	≤0.03	1.50–3.0	0.6–1.2	≤0.2	–	–	–	–	–
Others	G	N06007 ^b	21.0–23.5	5.5–7.5	18.0–21.0	≤1.0	≤0.05	≤1.0	≤2.5	1.0–2.0	–	≤0.04	≤0.03	1.5–2.5	–	–	1.75–2.5	–	–	–	–	–
	G-3	N06985 ^b	21.0–23.5	6.0–8.0	18.0–21.0	≤1.5	≤0.015	≤1.0	≤5.0	≤1.0	–	≤0.04	≤0.03	1.5–2.5	–	–	≤0.50	–	–	–	–	–
	G-30	N06030 ^b	28.0–31.5	4.0–6.0	13.0–17.0	1.5–4.0	≤0.03	≤0.8	≤5.0	≤1.5	–	≤0.04	≤0.02	1.0–2.4	–	–	0.30–1.50	–	–	–	–	–
	N	N10003 ^b	6.0–8.0	15.0–18.0	≤5.0	≤0.50	0.04–0.08	≤1.00	≤0.20	≤1.00	≤0.50	≤0.015	≤0.020	≤0.35	Al + Ti ≤0.50	–	≤0.010	–	–	–	–	–
	230	N06230 ^b	20.0–24.0	1.0–3.0	≤3.0	13.0–15.0	0.05–0.15	0.25–0.75	≤5.0	0.30–1.00	–	≤0.03	≤0.015	–	–	0.20–0.50	–	≤0.015	0.005–0.050	–	–	–
XR	X	N06002 ^b	20.5–23.0	8.0–10.0	17.0–20.0	0.20–1.0	0.05–0.15	≤1.0	0.5–2.5	≤1.0	–	≤0.04	≤0.03	–	–	–	–	–	–	–	–	–
	XR	^b	20.5–23.0	8.0–10.0	17.0–20.0	0.20–1.0	0.07–0.15	0.3–0.50	≤1.0	0.6–1.0	–	≤0.04	≤0.03	–	≤0.03	≤0.10	–	≤0.008	–	–	–	–

^aIncludes cobalt.^bAs remainder P.H.: precipitation hardened.

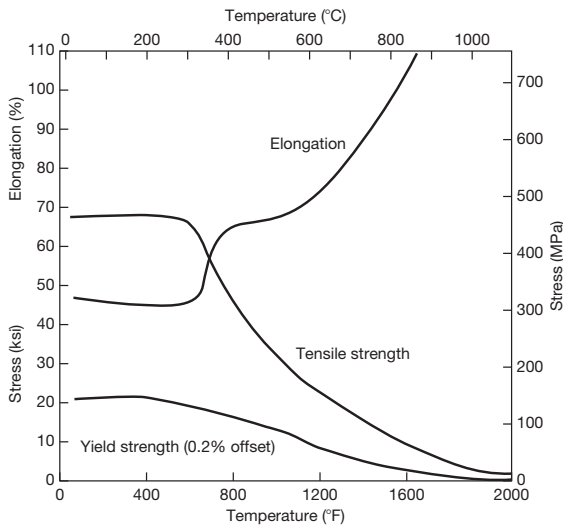


Figure 8 High-temperature tensile properties of annealed Alloy 200.

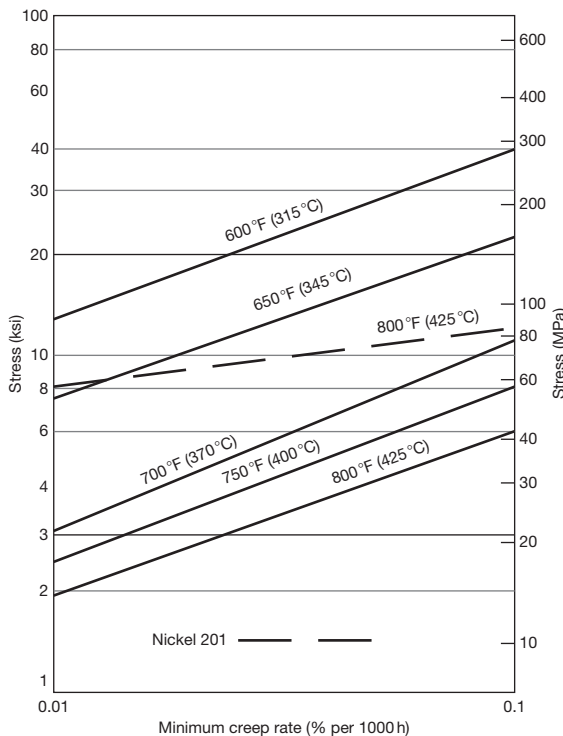


Figure 9 Typical creep strength of annealed Alloy 200.

plants (tanks, valves, pumps, agitators), equipment used in the production of ammonium sulfate, pollution control equipment, oil and gas recovery, and acid production.

Alloy A-286 (UNS S66286) is an iron-based nickel–chromium alloy with added molybdenum

and titanium. The alloy is age-hardenable to achieve superior mechanical properties. It maintains good strength and oxidation resistance at temperatures up to about 700 °C.¹⁶

The mechanical and physical properties of typical nickel–chromium–iron and nickel–chromium–iron–molybdenum alloys are shown in **Tables 4** and **5**, respectively, together with those of other nickel-based alloys.

2.08.2.2.2 Applications to nuclear power industrial fields

Alloys 600, 690, 800, X-750, and 718 have been used as materials for components and parts of nuclear power plants. These alloys are representative alloys for nuclear power plant applications.

In the *General Requirements* of the first edition of *ASME Sec. III (1963) Rules for Nuclear Vessels*, the following terms are included. “The Code rules do not cover deterioration which may occur in service as a result of radiation effects, instability of the material, or the effects of mechanical shock or vibratory loading. These effects shall be taken into account with a view to obtaining the design or the specified life of the vessel. It is recommended that the increase in the brittle fracture transition temperature due to neutron irradiation be checked periodically by means of surveillance specimens. The combined effects of fabrication, stress, and integrated neutron flux should be considered.” Consequently, materials for the pressure boundary of nuclear power plants are selected from those that have been demonstrated to have excellent properties from experience.¹⁷

Alloy X-750 was selected as the bolting and coil-spring material for water reactors (light and heavy water reactors) based on practical experience with the material in jet-engine applications as well as its excellent creep resistance (i.e., excellent resistance to stress relaxation). Wires and strips used for helical and flat springs are typically produced using Alloy X-750. **Table 9** shows an example of the design stresses for springs at elevated temperatures.¹²

Alloy A286 was also selected as a bolting material for water reactors based on similar reasons as those described for Alloy X-750.

Alloy 718 was selected as a material for springs and bellows for water reactors based on experience with the material in jet engines as well as its excellent creep resistance (i.e., excellent resistance to stress relaxation), and its high yield strength in the temperature range of up to 400 °C.

Table 4 Mechanical properties of nickel-based alloys

<i>Alloy systems</i>	<i>Alloys</i>	<i>UNS no.</i>	<i>Shape and treatment</i>	<i>Ultimate tensile strength (MPa)</i>	<i>Yield strength (0.2% offset) (MPa)</i>	<i>Elongation (%)</i>	<i>ASTM</i>
Ni	200	N02200	Seamless pipe and tube, annealed	≥379	≥103	≥40	B163
	201	N02201	Seamless pipe and tube, annealed	≥345	≥83	≥40	B163
Ni–Cu	400	N04400	Seamless tube, annealed	≥483	≥193	≥35	B163
	R-405	N04405	Annealed	≥550	≥240	≥40	B164
	K500	N05500	Rod and bar, precipitation hardened	≥1100	≥790	≥25	B865
Ni–Cr–Fe	600	N06600	Seamless tube, annealed	≥552	≥241	≥30	B163
	600M		Seamless pipe, hot worked annealed	≥586	≥241	≥30	B167
	601	N06601	Seamless tube, solution-annealed	≥552	≥207	≥30	B163
	690	N06690	Seamless tube, cold drawn (19.0 × 1.65 mm)	≥586	≥241	≥30	B163
	800	N08800	Seamless tube, annealed	≥517	≥207	≥30	B163
Ni–Cr–Fe/Ni–Cr–Fe–Mo P.H.	X-750	N07750	Bar, forge, precipitation hardened	≥1103	≥689	≥20	B637 N07752 Type1
	718	N07718	Bar, forge, precipitation hardened	≥1275	≥1034	≥12	B637
Reference	A286	S66286	Bolting materials, hardening treated	≥895	≥585	≥15	A453/A453M
Ni–Mo–Fe	B	N10001	Seamless pipe and tube, annealed	≥690	≥310	≥40	B622
	B-2	N10665	Seamless pipe and tube, annealed	≥760	≥350	≥40	B622
	B-3	N10675	Seamless pipe and tube, annealed	≥760	≥350	≥40	B622
	C-276	N10276	Plate, sheet, and strip	≥690	≥283	≥40	B575
Ni–Mo–Cr–Fe	C-4	N06455	Plate, sheet, and strip	≥690	≥276	≥40	B575
Ni–Cr–Mo–Fe	C-22/22	N06022	Plate, sheet, and strip	≥690	≥310	≥45	B575
	625	N06625	Plate, sheet, and strip, cold rolled	≥827	≥414	≥30.0	B443
	625LCF	N06626	Plate, sheet, and strip, cold rolled	971.5	525	46.0	B443
	686	N06686	Seamless pipe and tube, annealed	≥690	≥310	≥45	B622
	59	N06059	Seamless pipe and tube, annealed	≥690	≥310	≥45	B622
Reference	825	N08825	Seamless pipe and tube, cold worked and annealed	≥586	≥241	≥30	B163, B423
Others	G	N06007	Seamless pipe and tube, annealed	≥621	≥241	≥35	B622
	G-3	N06985	Seamless pipe and tube, annealed	≥621	≥241	≥40	B622
	G-30	N06030	Seamless pipe and tube, annealed	≥586	≥241	≥30	B622
	N	N10003	Plate, sheet, and strip	≥690	≥280	≥40	B434
	230	N06230	Seamless pipe and tube, annealed	≥760	≥310	≥40	B622
	X	N06002	Seamless pipe and tube, annealed	≥690	≥276	≥35	B622
	XR		Seamless pipe and tube, annealed	≥639	≥220	≥40	

P.H.: precipitation hardened.

Table 5 Physical properties of nickel-based alloys

<i>Alloy systems</i>	<i>Alloys</i>	<i>UNS no.</i>	<i>Density (g cm⁻³)</i>	<i>Melting point (°C)</i>	<i>Coefficient of thermal expansion to 100 °C (10⁶ °C⁻¹)</i>	<i>Thermal conductivity at 100 °C (W m⁻¹ °C)</i>	<i>Specific heat at 100 °C (J kg⁻¹ °C)</i>	<i>Electric resistivity at 100 °C (10⁻⁸ Ω m)</i>	<i>Young's modulus at R.T. (10³ N mm⁻¹)</i>	<i>Poisson's ratio at R.T.</i>	<i>Shear modulus at R.T. (GPa)</i>
Ni	200	N02200	8.89	1435–1446	13.3	66.5	456	130	205	0.29	79.6
	201	N02201	8.89	1435–1446	13.3	66.5	456	130	207	0.29	79.6
Ni–Cu	400	N04400	8.80	1300–1350	14.2	24	445	53.7	179	0.32	
	K-500	N05500	8.44	1315–1350	13.7	19.4	448	61.8	179	0.32	
Ni–Cr–Fe	600	N06600	8.47	1354–1413	13.3	15.9	465	104	207	0.324	80.8
	601	N06601	8.11	1360–1411	13.7	12.7	469	119	206	0.272	80.8
	690	N06601	8.13	1343–1377	14.1	13.5	471	116	211	0.289	79.3
Reference	800	N08800	7.94	1357–1385	14.4	13	460	103	197	0.339	73.4
Ni–Cr–Fe/ Ni–Cr–Fe– Mo P.H.	X-750	N07750	8.28	1393–1427	14.7	12.0	431	122	214		
	718	N07718	8.19	1260–1336	13.2	11.4	435	125	200	0.294	
Reference	A286	S66286	7.94	1370–1430	16.4	14.1	419	91.0	201		
Ni–Mo–Fe	B	N10001	9.24 ^a		10.3	12.2	389	138	217		
	B-2	N10665	9.22 ^a		10.3	12.2	373	138	217		
	B-3	N10675	9.22 ^a	1370–1418	10.6	12.2	373	137	213		
Ni–Mo–Cr–Fe	C-276	N10276	8.87 ^a	1325–1370	12.2	11.2	427	122	205	0.307	79.0
	C-4	N06455	8.64 ^a		10.8	10.1	406	125	207		
Ni–Cr–Mo–Fe	C-22/22	N06022	8.69 ^a	1351–1387	12.4	11.1	423	123	209		
	625	N06625	8.44	1290–1350	12.8	10.8	410	132	204	0.278	
	625LCF	N06626	8.44	1290–1350	12.8	11.0	429	132	208	0.28	81.4
	686	N06686	8.73 ^a	1338–1380	11.97	11.0	389	124.6	207	0.34	77
	59	N06059	8.6 ^a	1310–1360	12.2	17.2	414	126	210		
Reference	825	N08825	8.14	1370–1400	14.1	12.3	440	114	196	0.29	76
Others	G	N06007	8.30	1260–1343	13.5	10.1			200		
	G-3	N06985	8.31	1343	14.5	10.1	456				
	G-30	N06030	8.22		12.8	11.9		117	202		
	N	N10003	8.86	1300–1400	11.6	11.5	419	120	218		
	230	N06230	8.97 ^a	1301–1371	11.8	8.9	419	126	211	0.34	78.8
	X	N06002	8.23 ^a	1260–1355	13.9	11.0	461	116	205	0.33	

^aAfter ASTM B622

P.H.: precipitation hardened.

R.T. is not defined (Room Temperature)

Table 6 Thermal conductivity ($\text{W m}^{-1} \text{ } ^\circ\text{C}$) of nickel-based alloys at elevated temperatures

Temperature ($^\circ\text{C}$)	Alloy 200/201	Alloy 400	Alloy 600	Alloy 690	Alloy 800	Alloy C-22	Alloy A286
20	70.3	22.0	14.9	–	11.5	–	12.7
100	66.5	24.0	15.9	13.5	13.0	11.1	14.1
200	61.6	26.9	17.3	15.4	14.7	13.4	16.0
300	56.8	30.1	19.0	17.3	16.3	15.5	17.9
400	55.4	33.4	20.5	19.1	17.9	17.5	19.8
500	57.6	36.5	22.1	21.0	19.5	19.5	21.8
600	59.7	39.4	23.9	22.9	21.1	21.3	23.8
700	61.8	42.4	25.7	24.8	22.8	–	–
800	64.0	45.5	27.5	26.6	24.7	–	–
900	66.1	48.8	–	28.5	27.1	–	–
1000	68.2	–	–	30.1	31.9	–	–
1100	–	–	–	–	–	–	–

Table 7 Thermal expansion coefficient ($\times 10^{-6} \text{ mm}^{-1} \text{ } ^\circ\text{C}$) of nickel-based alloys at elevated temperatures

Temperature ($^\circ\text{C}$)	Alloy 200/201	Alloy 400	Alloy 600	Alloy 690	Alloy 800	Alloy C-22	Alloy A286	316 stainless steel	Carbon steel (0.23C–0.64Mn–0.11Si)
20	–	–	10.4	–	–	12.4	–	–	–
100	13.3	14.2	13.3	14.06	14.4	12.4	16.4	16.0	12.2
200	13.9	15.2	13.8	14.31	15.9	12.4	16.5	–	–
300	14.2	15.7	14.2	14.53	16.2	12.6	16.9	16.2	13.1
400	14.8	16.1	14.5	14.80	16.5	13.3	17.2	–	–
500	15.3	16.3	14.9	15.19	16.8	13.9	17.5	17.5	13.9
600	15.5	16.6	15.3	15.70	17.1	14.6	17.7	–	–
700	15.8	17.0	15.8	16.18	17.5	15.3	17.7	18.6	14.9
800	16.2	17.4	16.1	16.60	18.0	15.8	–	20.0	–
900	16.6	17.7	16.4	17.01	–	16.2	–	–	–
1000	16.9	18.1	–	17.41	–	–	–	–	–
1100	17.1	–	–	17.79	–	–	–	–	–

Table 8 Specific heat ($\text{J kg}^{-1} \text{ } ^\circ\text{C}$) of nickel-based alloys at elevated temperatures

Temperature ($^\circ\text{C}$)	Alloy 200/201	Alloy 400	Alloy 600	Alloy 690	Alloy 800	Alloy C-22	Alloy A286
20	427	427	444	450	460	–	419
100	445	445	465	471	–	423	–
200	459	459	486	497	–	444	–
300	470	470	502	525	–	460	–
400	–	–	519	551	–	476	–
500	–	–	536	578	–	485	–
600	–	–	578	604	–	514	–
700	–	–	595	631	–	–	–
800	–	–	611	658	–	–	–
900	–	–	628	684	–	–	–
1000	–	–	–	711	–	–	–
1100	–	–	–	738	–	–	–

In the case of austenitic stainless steels, SCC has often been observed in environments that include chlorides. However, high SCC resistance in chloride solutions was observed for high nickel-content alloys in the late 1950s, as indicated in [Figure 10](#).⁵

To avoid SCC in chloride-containing environments, Alloy 600 was adopted as an SG tube material, based on experience with the material used for SG tubes in the Connecticut Yankee reactor in the late 1950s. Subsequently, Alloy 600 was used

Table 9 Design stresses for springs at elevated temperatures

Temper	Method of coiling	Thermal treatment (°C h ⁻¹)	Maximum stress (MPa) for temperature (°C)																
			Up to	204–232	232–260	260–288	288–316	316–343	343–371	371–399	399–427	427–454	454–482	482–510	510–538	538–566	566–593	593–621	621–649
Helical springs																			
No.1	Cold	732/16	483	70	70	70	70	70	70	70	70	414	345	310	276	172	–	–	–
No.1 (9.7 cm)	Hot	732/16	70	70	70	70	70	70	70	448–	60–	55–	50–	45–	40–	172	–	–	–
Spring	Cold	649/4	689	100	100	621	90	586	85	–	–	–	–	–	–	–	–	–	–
Spring	Cold	1149/2 + 843/24 + 704/20	55	55	55	55	55	55	55	55	379	55	55	55	55	50	50	40	30
Flat springs																			
No.1	–	704/16	100	100	100	100	100	100	100	100	100	90	552	70	60	–	–	–	–
Spring	–	704/16	827	120	120	758	110	724	100	–	–	–	–	–	–	–	–	–	–
Spring	–	1149/2 + 843/24 + 704/20	70	70	70	70	70	70	70	70	70	70	70	70	70	70	50	40	30
Hot-finished	–	885/24 + 704/20	90	90	90	80	80	80	80	60	60	60	60	60	60	–	–	–	–
Hot-finished	–	1149/2 + 843/24 + 704/20	60	60	60	60	60	60	60	60	60	60	60	60	60	–	–	–	–

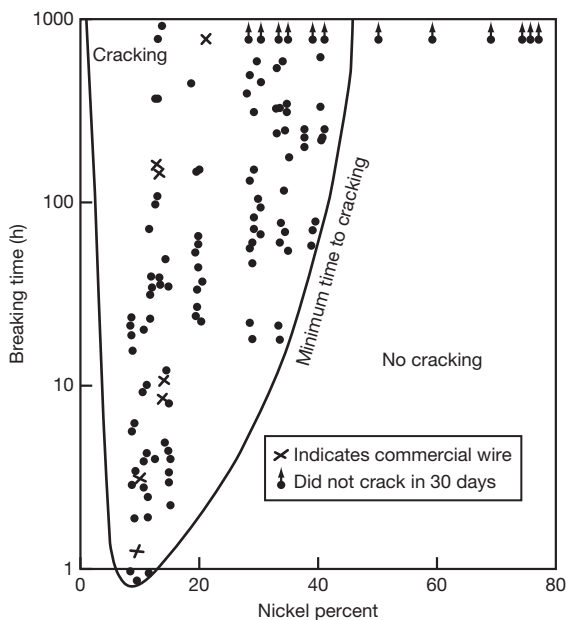


Figure 10 Effect of increasing the nickel content on the susceptibility of iron-18% chromium base wires in boiling 42% MgCl_2 .

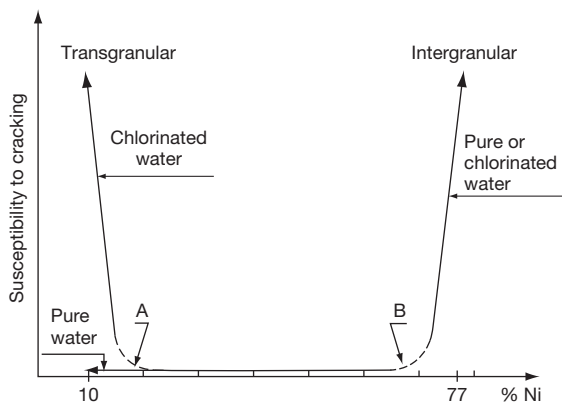


Figure 11 Schematic diagram showing the influence of nickel content on the cracking processes occurring in 18% chromium austenitic alloys, when stressed slightly above the yield point in 350 °C water (demineralized or containing 1 g l^{-1} chloride ions).

worldwide for SG tubes for PWRs and for some CANDU reactors.

Coriou reported as early as 1959 the possibility of IG stress corrosion cracking (IGSCC) in high-temperature, high-purity water for high nickel-based alloys, such as Alloys 600 and X-750, as shown in **Figures 11 and 12**.^{18,19} However, this type of IGSCC could not be reproduced by other researchers for more than 15 years. Nevertheless, IGSCC was

eventually detected in SG tubes made of Alloy 600 in the Obrigheim reactor in 1972,²⁰ and it was also detected in support pins (split pins) and flexure pins made of Alloy X-750 in the Mihama No. 3 reactor in 1978.²¹ Subsequently, IGSCC has been detected in numerous SG tubes made from Alloy 600 and support pins made of Alloy X-750. In addition, it was detected in PWR reactor-vessel internal bolts made of Alloy A286.

After these experiences, this type of IGSCC was called 'primary water stress corrosion cracking (PWSCC)'; many studies of PWSCC have been carried out. As a result of these studies, thermally treated (TT: heated at about 700 °C for more than 10 h after mill annealing) Alloy 600 was developed.²² The TT Alloy 600 was used for SG tubes as an improved IGSCC-resistant material from mill-annealed (MA) Alloy 600, toward the end of the 1970s. TT Alloy 690 was developed for SG tubes in the early 1980s as a material with excellent IGSCC resistance in PWR primary water. The thermal treatment chosen for TT Alloy 690 also consisted of heating at about 700 °C for more than 10 h after mill annealing.²³

This alloy has been and still is used for SG tubes and control rod drive mechanism (CRDM) nozzles, etc. in PWRs as an alternative material to MA Alloy 600.

In the case of conventional Alloy X-750, various heat-treatment conditions have been specified for different applications. In the case of support pins and flexure pins for PWRs, only mechanical properties such as yield, tensile strength, or hardness were specified for Alloy X-750 when used for bolts and springs. Several different heat treatments were selected by the suppliers of the material; the effects of heat-treatment conditions on PWSCC resistance are shown in **Figure 13**. Precipitation hardening at about 715 °C after solution annealing at a high temperature near 1075 °C (the so-called HTH condition) was selected for fabricating the most PWSCC-resistant Alloy X-750.²⁴ Alloy X-750 HTH has been applied as a bolting material not only for PWRs but also for BWRs due to its excellent IGSCC resistance and high strength.²⁵

However, the effects of heat treatment on IGSCC resistance have not been so clearly delineated in Alloys A-286 and 718. In particular, Alloy A-286 was replaced in many cases with Alloy X-750 HTH as a bolting material.

Alloy 800 is an iron-based nickel-chromium alloy. However, it has good IGSCC resistance in high-temperature, high-purity water and caustic solutions. A number of studies have been carried

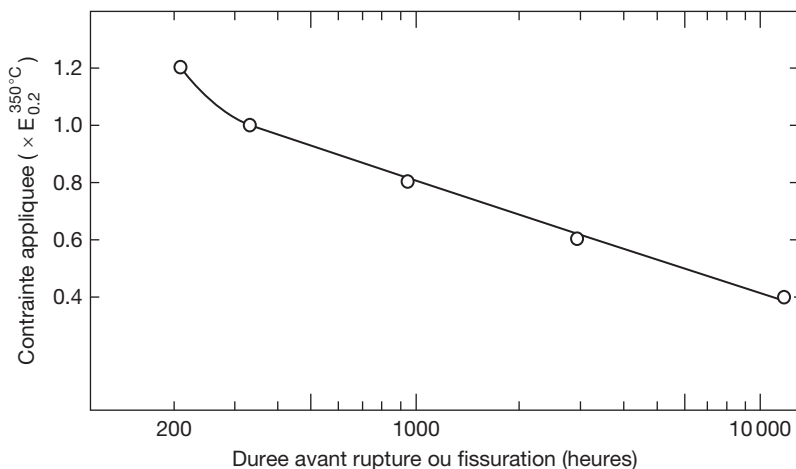


Figure 12 Relationship between applied stress and 50% mean lifetime of the experimented specimens in 350 °C water.

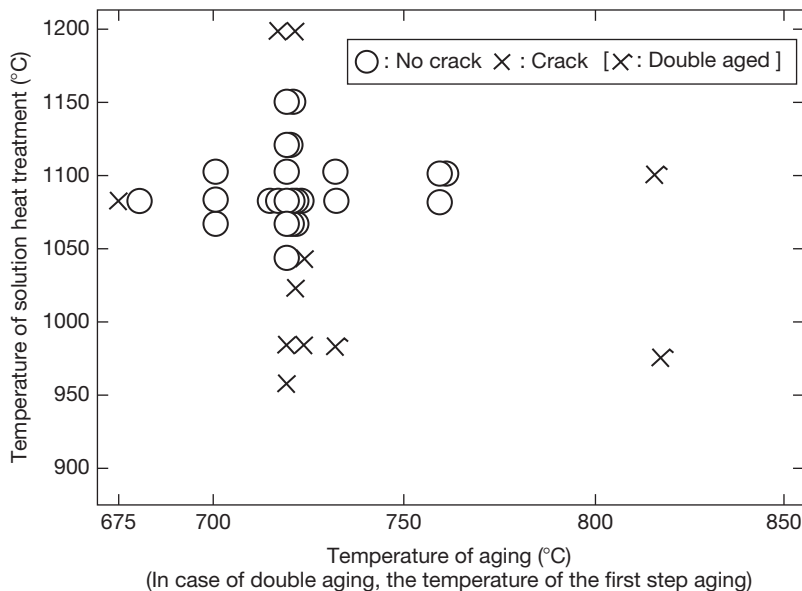


Figure 13 Effect of heat-treatment condition on the stress corrosion cracking susceptibility of Alloy X-750 in high-temperature water. (The alloys were cooled in water after solution heating.)

out to compare the IGSCC resistance of Alloys 800, 600, and 690, as shown in **Figures 14** and **15**.²⁶ Alloy 800 was selected for SG tubes in some German-designed PWRs and CANDU-type reactors.

Alloy 600M is Alloy 600 with niobium addition. The alloy was first developed for improved SCC resistance in oxidizing high-temperature water environments of BWRs.²⁷ This alloy has not been standardized yet but is specified in an ASME Code Case for nuclear applications.²⁸

2.08.2.3 Ni-Mo-Fe, Ni-Mo-Cr-Fe, and Ni-Cr-Mo-Fe Alloys

2.08.2.3.1 Chemical compositions, physical properties, and mechanical properties

The chemical compositions of typical nickel–molybdenum–iron, nickel–molybdenum–chromium–iron, and nickel–chromium–molybdenum–iron alloys are shown in [Table 3](#), along with those of other nickel-based alloys.

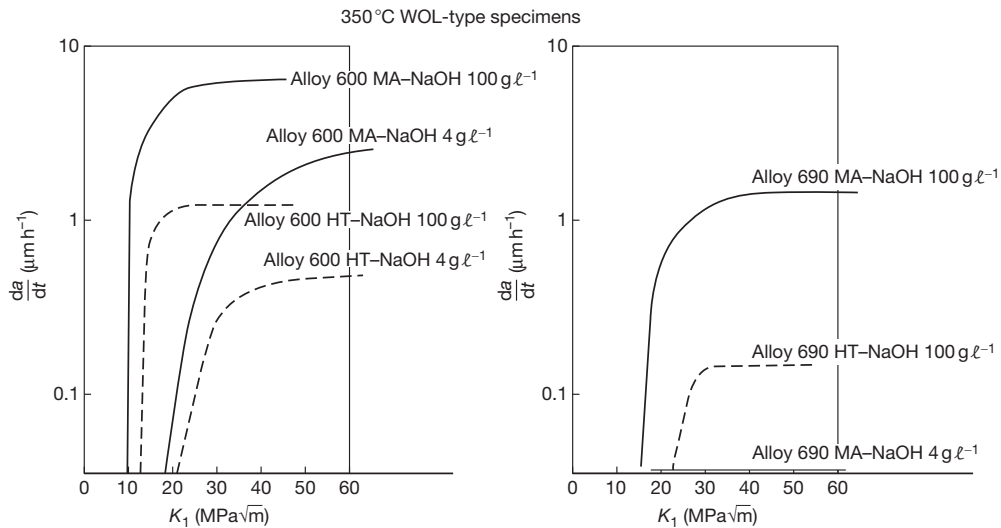


Figure 14 Stress corrosion tests in deaerated sodium hydroxide 350 °C on fracture mechanics-type specimens: comparison of Alloys 600 and 690 behavior effect of heat treatment at 700 °C for 16 h.

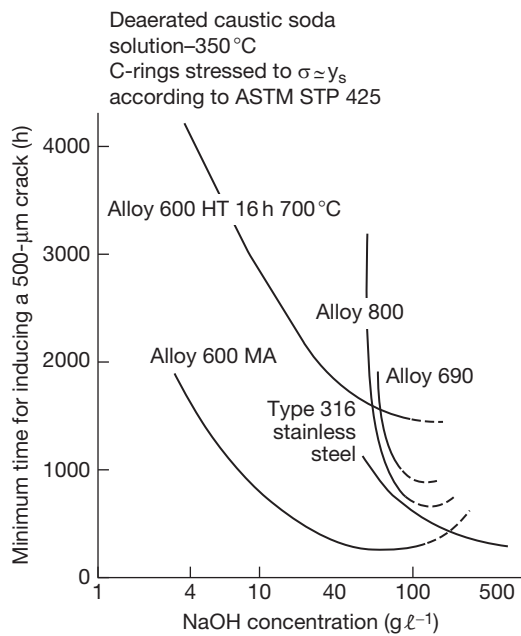


Figure 15 Resistance to stress corrosion cracking of Alloy 600 mill-annealed or heat-treated at 700 °C, Alloy 690, Alloy 800, and Type 316 stainless steel as function of sodium hydroxide concentration at 350 °C.

Nickel–molybdenum–iron alloys were originally developed as hydrochloric acid-resistant materials. They have superior resistance to reducing environments. **Figure 16** shows the effect of molybdenum content in nickel–molybdenum alloys on

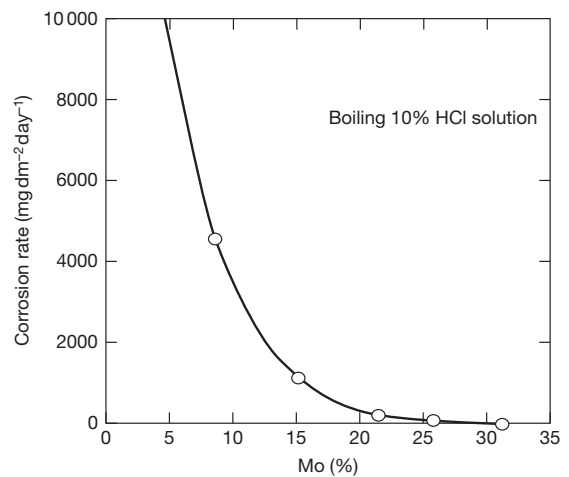


Figure 16 The effect of molybdenum content on corrosion resistance of nickel–molybdenum alloys in boiling 10% hydrochloric acid solution.

corrosion rates.²⁹ It is seen that the corrosion rate in 10% hydrochloric acid dramatically decreases with increasing molybdenum content. Commercial nickel–molybdenum alloys include about 30% molybdenum.

Alloy B (UNS N10001) (nickel-based 28% molybdenum–5% iron) is one of those rare materials which is resistant to corrosion in hydrochloric acid up to its boiling point. The alloy shows excellent corrosion resistance in reducing and oxidizing chloride solutions. However, because of its lack of chromium

content, care must be taken to avoid using this alloy in oxidizing environments.

Alloy B-2 (UNS N10665) is an advanced version of Alloy B. It has superior corrosion resistance in weld-heat-affected zones compared to Alloy B, due to reduced carbon and silicon contents and a restricted range of iron content.

Alloy B-3 (UNS N10675) was developed to minimize problems associated with the fabrication of B-2 alloy components. Alloy B-3 has excellent resistance to hydrochloric acid at all concentrations and temperatures.³⁰ It also withstands sulfuric, acetic, formic, and phosphoric acids, as well as other nonoxidizing media. Alloy B-3 has a special chemistry designed to achieve a level of thermal stability superior to that of Alloy B-2. It has been applied to similar components as Alloy B-2, but cannot be used in environments containing ferric or cupric salts because these salts may cause rapid corrosion failure.

Alloy C (UNS N10002) (nickel-based 18% chromium–16% molybdenum–5% iron–4% tungsten) is also an advanced version of Alloy B. It has superior corrosion resistance to oxidizing environments compared to Alloy B due to the added chromium. However, Alloy C is degraded after heating in the temperature range 650–1090 °C due to the precipitation of M_6C carbides and of μ phase along grain boundaries. Solution heat treatment is therefore necessary after welding in the case of this alloy.

Alloy C-276 (UNS N10276) improves upon this weakness by using reduced carbon (<0.01%) and silicon (<0.08%) contents compared to Alloy C. The alloy can be used in most cases in the as-welded state (without solution heat treatment after welding).³¹

Alloy C-4 (UNS N06455) improves upon the long-range aging characteristics of Alloy C-276 by the addition of titanium and a reduction in the iron content.³²

Alloy C-22 (same as Alloy 22) (UNS N06022) shows improved corrosion resistance in oxidizing environments due to increased chromium content (about 22%) compared to Alloy C-276 and maintains its corrosion resistance in reducing environments.³³

Alloy 625 (UNS N06625) was originally developed as a gas-turbine material. It is a typical nickel–chromium–molybdenum–iron alloy as well as a solid-solution-hardenable alloy. It has high creep-rupture strength at high temperatures, due to the added molybdenum and niobium, and high resistance to corrosion and pitting in oxidizing environments such as nitric acid due to its higher chromium (about

22%) and lower molybdenum (about 9%) content compared to Alloy C-276.³⁴ However, the corrosion resistance of the alloy in reducing environments such as hydrochloric acid and sulfuric acid is inferior to that of Alloy C-276. Alloy 625 is used where welding is required, based on the stabilization of carbon by niobium addition (about 3.5%) for preventing sensitization. Also, the alloy shows excellent SCC resistance to chloride solutions and seawater, due to its high nickel content.

Alloy 625 LCF (UNS N06626), a modified Alloy 625, shows improved low-cycle fatigue properties and cold formability for bellows applications.

Alloy 686 is very similar in composition to Alloy C-276 but where the chromium level has been increased from 16 to 21% while maintaining molybdenum and tungsten at similar levels. Alloy 686 is used for resistance to aggressive media in chemical processing, pollution control, pulp and paper manufacture, and waste management applications. This alloy contains chromium, molybdenum, and a tungsten content of around 41%. To maintain its single-phase austenitic structure, this alloy has to be solution-annealed at a high temperature of around 1220 °C followed by rapid cooling to prevent precipitation of intermetallic phases.³⁵

Alloy 59 has high chromium and molybdenum content with low iron content. This alloy has excellent resistance to general corrosion, SCC, pitting, and crevice corrosion in aggressive corrosive environment. The alloy is a nickel–chromium–molybdenum alloy without the addition of any other alloying element. This purity and balance of nickel–chromium–molybdenum is mainly responsible for its thermal stability.³⁶

Alloy 825 (UNS N08825) was developed from alloy 800 with the addition of molybdenum (about 3%), copper (about 2%), and titanium (about 0.9%) for providing improved aqueous corrosion resistance in a wide variety of corrosive media. In this alloy, the nickel content confers resistance to chloride-ion SCC. Nickel in conjunction with molybdenum and copper gives outstanding resistance to reducing environments such as those containing sulfuric and phosphoric acids. Molybdenum also aids resistance to pitting and crevice corrosion. In both reducing and oxidizing environments, the alloy resists general corrosion, pitting, crevice corrosion, IG corrosion, and SCC. Some typical applications include various components used in sulfuric acid pickling of steel and copper, components in petroleum refineries and petrochemical plant (tanks, valves, pumps, agitators), equipment used in the production of ammonium

sulfate, pollution control equipment, oil and gas recovery, and acid production.³⁷

The mechanical and physical properties of typical nickel–molybdenum–iron, nickel–molybdenum–chromium–iron, and nickel–chromium–molybdenum–iron alloys are shown in **Tables 4** and **5** respectively, along with those of other nickel-based alloys.

2.08.2.3.2 Applications to nuclear power industrial fields

Alloy 625, as a typical nickel–chromium–molybdenum–iron alloy, has been investigated for its SCC resistance in high-temperature water as an alternative material to austenitic stainless steels, from the view point of preventing sensitization. The alloy has also been studied for corrosion resistance in highly caustic solutions as a candidate material for components of supercritical light water-cooled reactors. Alloy 625 is one of the candidates for reactor-core and control-rod components in water-cooled reactors and a candidate component material for supercritical water-cooled reactors, due to its high strength, excellent general corrosion resistance, SCC resistance, and pitting resistance in high-temperature water. The alloy is also being considered in advanced high-temperature reactors because of its high allowable design stress at elevated temperatures, especially between 650 and 760 °C.

Alloy C-22 has been investigated for corrosion resistance in highly caustic solutions and concentrated chloride solutions as a candidate material for high-level radioactive waste-disposal storage containers, due to its excellent corrosion resistance in oxidizing and reducing environments.

2.08.2.4 Other Ni-Based Alloys

2.08.2.4.1 Chemical compositions, physical properties, and mechanical properties

The chemical compositions of other nickel-based alloys not already described in the previously mentioned categories are shown in **Table 3**, along with those of the alloys mentioned above.

Alloy G (UNS N06007) has excellent corrosion resistance to hot sulfuric acid and hot phosphoric acid. The alloy has superior corrosion resistance to oxidizing environments compared to Alloy C-276, due to its higher chromium content (about 22%) than that of Alloy C-276 (about 18%). On the other hand, Alloy G has inferior corrosion resistance to reducing environments such as sulfuric acid compared to Alloy C-276, due to its lower molybdenum

content (about 6.5%) than that of Alloy C-276 (about 18%). A copper content of ~2% is included in Alloy G to improve its corrosion resistance in sulfuric acid. Alloy G can be welded because of its niobium content, which stabilizes carbon. However, the alloy is highly susceptible to hot cracking during welding.

Alloy G-3 (UNS N06985) is improved in terms of the bending characteristics of welded joints due to a reduced carbon and niobium content. This alloy has a lower susceptibility to hot cracking during welding.

Alloy G-30 (UNS N06030) was originally developed to improve corrosion resistance in wet phosphoric acid. This alloy shows excellent corrosion resistance to oxidizing acids, such as nitric acid, and also to oxidizing halogen-ion-containing environments such as nitric and fluoric acid, due to its increased chromium content (about 30%).³⁸

The chromium content in this alloy leads to deleterious effects in molten fluoride. However, Alloy N shows excellent corrosion resistance to molten fluoride due to its reduced chromium content (about 7%).³⁹

Alloy 230 (UNS N06230) shows excellent resistance to oxidation and nitriding as well as high strength at high temperatures. This alloy has been applied as a heat-resistant material in industrial furnaces and gas turbines.⁴⁰

Alloy X (UNS N06002) is a solid-solution-hardened alloy owing to the presence of molybdenum. This alloy has high strength at high temperatures and good resistance to oxidation in high-temperature air.⁴¹

Alloy XR was originally developed as a structural material for high-temperature gas-cooled reactors (HTGR) and is a modified version of Alloy X. It is produced by vacuum double melting with optimized contents of manganese, silicon, and boron as intentional additives, while minimizing the aluminum, titanium, and cobalt content, as these are undesirable impurities.⁴²

The mechanical and physical properties of the above alloys are shown in **Tables 4** and **5**, respectively, together with those of other nickel-based alloys.

2.08.2.4.2 Applications to nuclear power industrial fields

Material development programs for HTGRs have been promoted in several countries since the late 1960s, including tasks for developing and qualifying materials such as nickel-based alloys for use as high-temperature structural materials. In the 1970s, the state of the art for achievable maximum service temperature for structural materials was only 750 °C for

Alloy 800; thus, shifting the practical temperature upward by about 200 °C was a technical goal.

Alloy XR has been applied as a structural material for the Japanese high-temperature engineering HTGR test reactor (HTTR). This alloy has high resistance to oxidation in high-temperature helium gas environments, and excellent creep-rupture strength up to 1000 °C. In this alloy, the coexistence of appropriate amounts of chromium and manganese helps to form a Cr_2MnO_4 spinel layer on top of the Cr_2O_3 film, which turns out to be quite stable and protective in helium-based low-oxidizing environments, even during severe thermal cycling. Figure 17⁴³ illustrates the results of long-duration corrosion tests during thermal cycling for the original and improved versions of Alloy X. An additional finding was that maintaining the boron content in the range 30–50 ppm resulted in remarkable improvement in the high-temperature strength of the base metal and the performance of welded joints.

Alloy XR is suitable for use as a structural material in ‘Generation IV Reactors.’ On the other hand, a nickel–chromium–tungsten alloy is also currently being investigated for similar applications as an advanced version of Alloy XR.

2.08.3 Fabrication of Ni-Based Alloys

2.08.3.1 Melting

In the initial development stages, melting in air was used to produce nickel–copper and nickel–chromium–iron alloys. However, subsequent to the development

of Alloys X-750 and 718 as precipitation-hardened high-strength materials for aerospace applications, a vacuum melting process in addition to a double- or triple-melting process has been applied to nickel-based alloys to minimize solidification segregation and undesirable precipitation. The double- or triple-melting process is usually selected from vacuum-induction melting, electroslag remelting, and vacuum arc remelting processes, as illustrated in Figure 18.^{44–51}

The melting process in air was mainly applied to mill-annealed Alloy 600 for SG tubes of PWRs until the 1980s. However, after the experience with IGSCC and other corrosion problems in the SG tubes of PWRs, severe quality assurance for these tubes was demanded by end users, and the melting process was changed to vacuum melting and other high-grade melting processes. Thus, TT Alloy 690 for SG tubes and other applications has been melted using the vacuum oxygen decarburization process or a double-melting process such as electroslag remelting after vacuum-induction melting.⁴⁴

2.08.3.2 Hot Forming

Austenitic alloys have inferior hot-formability characteristics compared to low-alloy steels due to the lack of softening at higher temperatures. Nickel-based alloys show even less formability than austenitic stainless steels due to their high deformation resistance at higher temperatures.

Hot-forming is basically carried out in a temperature range between the solidus temperature and the temperature at which recrystallization begins. However, nickel forms eutectic with various elements including chromium, molybdenum, silicon, titanium, aluminum, niobium, tungsten, phosphorus, sulfur, and carbon. Thus, in the case of nickel-based alloys that contain many alloying elements, heating at temperatures higher than 120 °C poses the risk of local fusion or precipitation of a secondary phase. Careful selection of the hot-forming temperature range is essential and the temperature range needs to be confirmed by high-temperature, high-speed tensile tests, high-temperature torsion tests, forging tests, etc., prior to the hot-forming process.⁵² The Ugine–Sejournet extrusion process with a glass lubricant is normally applied during hot-working of tubes and pipes, such as SG tubes. This is an expansion working process using billets with machined and drilled holes for the forged or rolled bloom.

Figure 19 illustrates the typical fabrication process of hot-finished pipes for CRDM adapter

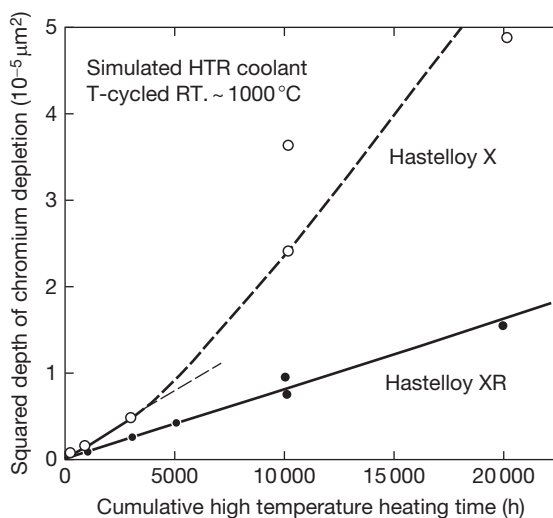


Figure 17 Long-term exposure test results of a nickel-based superalloy before and after improvement.

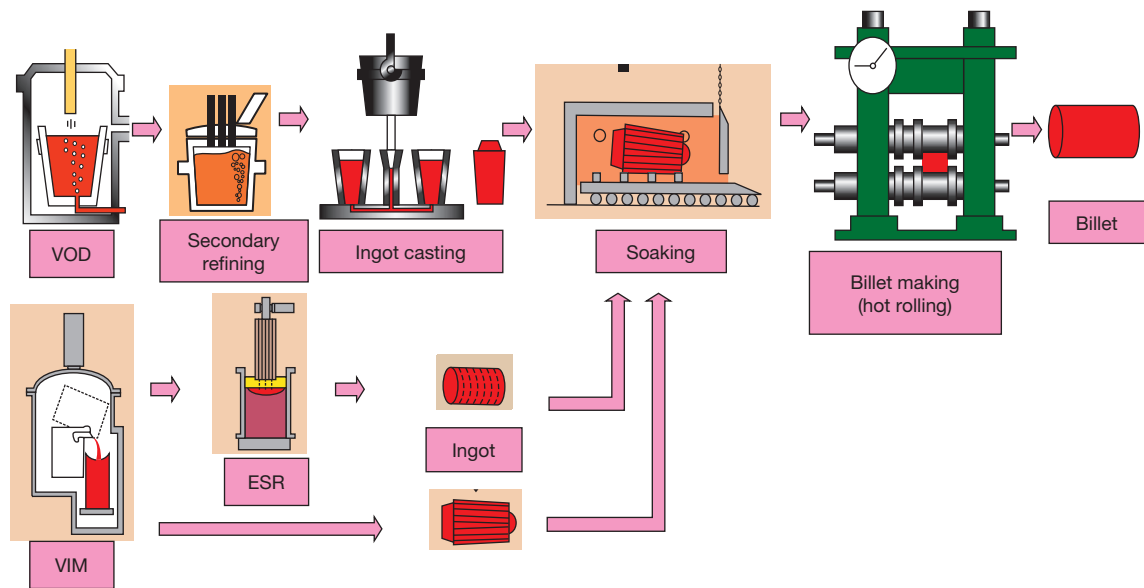


Figure 18 Typical melting process of nickel-based super alloys. VOD; Vacuum Oxygen Decarburization, VIM; Vacuum Induction Melting, ESR; Electro Slag Remelting.

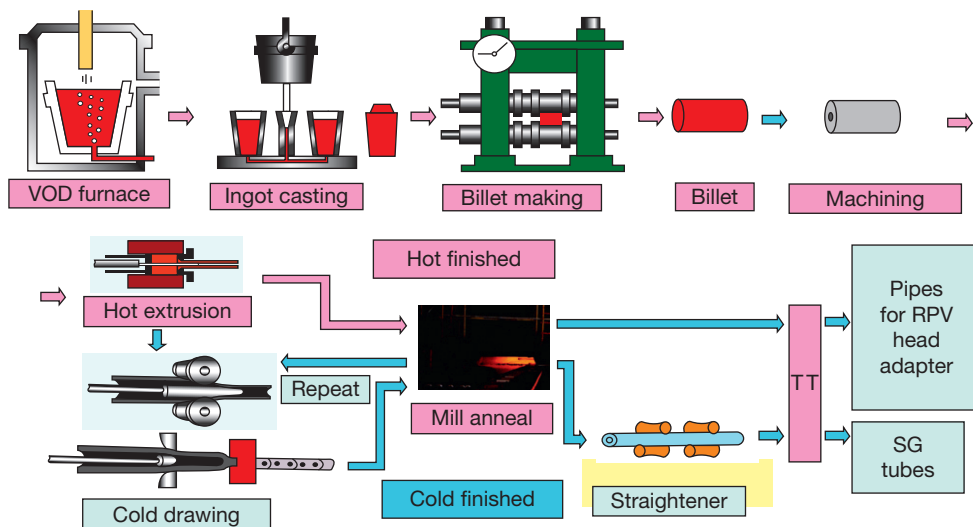


Figure 19 Typical fabricating process of piping and tubing. VOD; Vacuum Oxygen Decarburization, RPV; Reactor Pressure Vessel.

nozzles of PWRs, compared to that of cold-finished tubes for use as SG tubes.^{44,50}

2.08.3.3 Cold Forming

Cold forming can be easily applied to nickel-based alloys, except in the case of highly strengthened alloys such as precipitation-hardened Alloys X-750, 718, etc. Under severe cold-forming conditions,

intermediate and final annealing steps are needed for the products after cold forming.

The cold-forming process for the nickel–copper Alloy 400 and for Alloys 600, 690, and 800 nickel–chromium–iron alloys is typically as follows.

The bare tubes, which are hot-formed and heat-treated, are pickled using nitric and fluoric acids to remove glass and other contaminants incorporated during the hot-working and other processes, and

then finished to the desired shape by cold drawing, cold reducing, or cold rolling at ambient temperature. This cold-forming process produces small-diameter and thin-walled tubes with excellent dimensional accuracy and a fine surface finish that cannot be obtained by hot processes. However, severe or progressive die-forming operations require heavy-duty lubricants with good surface-wetting characteristics and high film strength, such as those found in metallic soaps and chlorinated or sulfochlorinated oils. However, it is very important to remove all traces of these lubricants prior to any heat treatment or welding due to the danger of carbon pickup and consequent lowering of corrosion resistance by the formation of complex carbides. Parts formed using zinc-alloy dies should also be flash-pickled to prevent liquid-metal embrittlement during heating. In the case of the fabrication of Alloys TT600 and 690 for SG tubes and other nuclear products, lubricant treatment using an oxalate film coating is recommended for the tube-drawing process.⁵²

The degree of work hardening is relatively large for nickel-based alloys. However, these alloys have somewhat higher strength and hence there is the need to have forming equipment with sufficient power commensurate with the mechanical characteristics of these alloys.

Cold drawing is a cold-forming procedure for bare tubes using dies and subsequent drawing. There are several cold-drawing methods, such as plug drawing, sink drawing, mandrel drawing, and hydraulic drawing. Mandrel drawing and hydraulic drawing allow for a high ratio of cold-working and fine surface finishes.

Cold rolling and cold reducing are applied during tube fabrication using nickel-based alloys as one of the cold-forming methods. Cold rolling can be used for high-reduction-ratio cold forming, even for nickel-based alloys with inferior workability characteristics, due to compressive forming.⁵²

Figure 19 illustrates the typical fabrication process of cold-finished tubes for SG tubes, compared with hot-finished pipes for CRDM adapter nozzles of PWRs.^{44,50}

2.08.3.4 Heat Treatment

Nickel and nickel alloys are susceptible to embrittlement by sulfur, phosphorus, lead, zinc, and some other low-melting-point metals and alloys. These materials may be present in lubricants, paints, marking crayons and inks, pickling liquids, dirt accumulated on the metal during storage, furnace slag and cinder, or temperature-indicating sticks, pellets, and

lacquers. Any foreign substances, even those that are nonembrittling, can burn into the surface of the metal at high temperatures and cause difficulty during subsequent processing. In addition, vapors produced when these substances burn are usually objectionable and can have an adverse effect on furnace and heating fixtures. It is therefore extremely important that the metal be clean before heating. Careful cleaning results in real operating economy by preventing damage to the material in subsequent operations.⁵³

Heat treatment is performed after hot-forming for hot-finished products, or after cold forming for cold-finished products. An oil, gas, or electric furnace is normally used for the heat treatment; however, a bright-annealing furnace using hydrogen gas or decomposition of ammonia gas is used for mill annealing of seamless tubes made from nickel-based alloys, for example, SG tubes of Alloys 600 and 690. A vacuum-annealing furnace is used for thermal treatment after mill annealing and polishing for TT Alloys 600 and 690, to improve SCC and other corrosion resistance properties.

The heat-treatment conditions for nickel-based alloys are selected according to the properties required. In the case of Alloy X-750, equalizing at 885 °C for 24 h, single-step aging or first-step aging at 710–735 °C followed by second-step aging at 600–650 °C after hot-forming, or solution annealing at 930–1030 °C has been applied to hot-rolled bars for bolting materials. This type of heat treatment (the so-called AH or BH condition) aims to produce high tensile strength in the material for applications at <550 °C, due to precipitation hardening by the γ' phase. Another type of heat treatment with a first-step aging at 800–850 °C for 20–24 h and a second-step aging at about 700 °C after high-temperature solution annealing at 1080–1160 °C has been applied to creep-resistant and creep-rupture-resistant materials at temperatures operating higher than 550 °C. This heat treatment aims to yield a uniform matrix, enlarge the grain size, recover any chromium-depleted zones, and eliminate precipitate-free zones near grain boundaries.

However, the heat-treatment conditions of Alloy X-750 are not suitable for SCC resistance in high-temperature water environments. The most suitable heat-treatment condition in this case is single-step aging at 700–730 °C after solution heat treatment at 1060–1100 °C in order to precipitate semicontinuous $M_{23}C_6$ carbides along the grain boundaries.²⁴ This heat treatment is specified in the American Society for Testing and Materials (ASTM) standards as B637 N07752 Type 1.

In the case of Alloys 600 and 690, a thermal treatment has been applied after mill annealing to SG tubes of PWRs and CANDU reactors and CRDM nozzles of PWRs. The objective has been to improve PWSCC resistance and IGSCC resistance in secondary side environments. The thermal treatment includes heating at about 700 °C for longer than 10 h.

2.08.3.5 Descaling and Pickling

Oxides, scales, tarnish films, or discoloration can be removed chemically or mechanically. Chemical treatment may consist of a molten caustic descaling salt treatment followed by immersion in nitric–hydrofluoric acid bath mixtures (20–25% nitric acid plus 3–5% hydrofluoric acid) at 50–70 °C. In the case of Ni–Mo alloys, since these do not contain any chromium, it is very important, indeed essential, not to leave the material in the acid bath for more than 60 s, followed immediately by a water rinse. If sulfuric–hydrochloric acid baths are used, then this precaution is not so critical for Ni–Mo alloys. Sand, shot, or vapor blasting can be used for mechanical descaling with proper care.⁵³

2.08.3.6 Grinding and Machining

The machinability of nickel–molybdenum and nickel–chromium–iron alloys is inferior to that of austenitic stainless steels. When very close tolerances are required for nickel-based alloys, grinding or machining is the preferred method. Grinding wheels must be selected carefully. Tungsten carbide and ceramic-tipped tools are recommended for machining nickel-based alloys. High-speed steel tools can also be used, although their machinability is not very good. During machining, some nickel-based alloys work-harden rapidly, generating large amounts of heat during cutting, and may weld to the cutting-tool surface, thus offering high resistance to metal removal due to their higher shear strength compared to austenitic stainless steels.⁵²

Sufficient power and rigidity of the machine, avoiding vibration during machining, sharpness of the tools, low cutting speeds, higher feed rates, and a water-based cutting-oil lubricant should all be used for machining nickel-based alloys.

2.08.3.7 Welding

For welding nickel-based alloys, cleanliness of the weld joint is the most important parameter for producing a

sound weld. Lack of thorough cleaning has accounted for most of the problems associated with welding encountered in industry, including cracking, porosity, and accelerated corrosion. The contaminants to watch out for prior to welding are carbon, oxides, sulfur, lead, phosphorous, and other elements that form low-melting-point eutectics with nickel such as arsenic, antimony, bismuth, and tin.⁵⁴ These contaminants may come from a variety of sources, including supplementary materials such as markers, tools, oils, etc.

For welding nickel-based alloys, matching filler metals have been used. However, nickel has a thermal expansion coefficient intermediate between that of austenitic stainless steels and low-alloy steels. Thus, nickel–chromium–iron Alloys 82, 182, 132, 52, and 152 have been used for dissimilar metal weld joints to minimize the residual stress and strain in the weld joints.

Shielded metal arc welding (SMAW), metal inert gas welding (MIG), submerged arc welding (SAW), metal active gas welding (MAG), flux cored arc welding (FCAW), gas tungsten arc welding (GTAW), laser beam welding (LBW), and electron beam welding (EBW) have all been applied to nickel-based alloys.

Rods for SMAW and the flux for SAW must always be used in a dry state during welding to avoid forming blow holes in the deposited weld metal. Filler metals for GTAW, MIG, MAG, and FCAW must be checked for contaminants such as stains, oils, paints, etc. to avoid blow holes and hot cracking.

2.08.3.7.1 Weldability

Nickel-based alloys are relatively easy to weld, being similar to austenitic stainless steels in that respect. However, the hot-cracking susceptibility of nickel-based alloys is greater than that of austenitic stainless steels and the fluidity of the melted metal is inferior to that of both austenitic stainless steels and carbon steels. It has been reported that the hot-cracking susceptibility of nickel-based alloys is affected by alloying elements such as niobium, titanium, and aluminum and by minor elements such as sulfur, silicon, manganese, phosphorus, etc., as shown in Figures 20 and 21.^{55,56}

2.08.3.7.2 Welding materials and example of welding condition

Typical filler materials of nickel-based alloys for MIG or MAG and weld materials of nickel-based alloys for SMAW are summarized in Tables 10 and 11, respectively. Typical welding conditions by automatic gas tungsten arc welding used for some nickel-based alloys are summarized in Table 12.^{57,58}

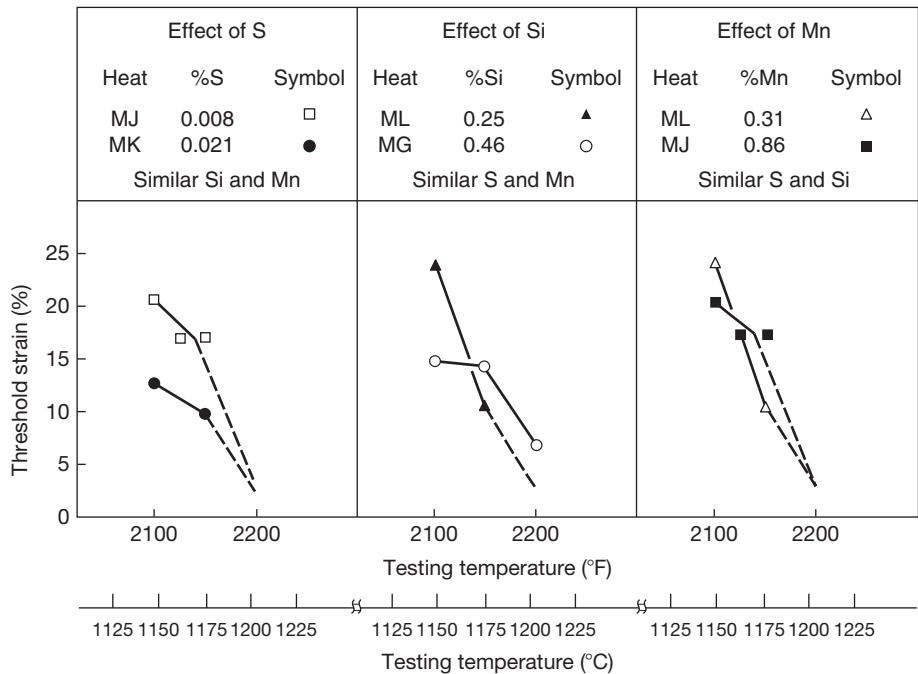


Figure 20 Effect of minor alloying element on initiation of fusion zone microcracking for Alloy X after Varestraint-type test (longitudinal bead-on-plate gas tungsten arc weld).

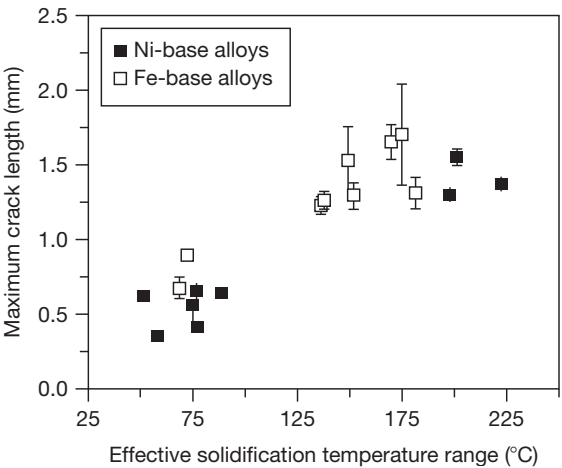


Figure 21 Maximum crack length after Varestraint test as a function of the effective solidification temperature range for niobium-bearing superalloys.

2.08.3.8 Applicable Specifications

The above-mentioned nickel-based alloys are covered by various worldwide standards organizations such as ASTM, The National Association of Corrosion Engineers (NACE), American Welding Society (AWS), American Society of Mechanical Engineering (ASME), British Standard (BS), Japanese Industrial Standards (JIS), Deutsches Institut für Normung

(DIN), International Organization for Standardization (ISO), and others. These materials are specified for various product types.

For example, rods, bars, wires, and forging stock of Alloy 690 are standardized as ASTM B/ASME SB 166, ASTM B 564/ASME SB 564, ASME Code Case N-525, ISO 9723, MIL-DTL-2481; seamless pipes and tubes of Alloy 690 are standardized as ASTM B/ASME SB 163, ASTM B 167/ASME SB 167, ASTM B 829/ASME SB 829, ASME code case 2083, N-20, N-525, ISO 6207, MIL-DTL-24803; plates, sheets, and strips of Alloy 690 are standardized as ASTM B/ASME SB 168/906, ASME N-525, ISO 6208, MIL-DTL-24802; welding products of Alloy 690 are standardized as AWS A5.14/ERNiCrFe-7, AWS A5.11/ENiCrFe-7.

2.08.4 Corrosion Resistance and Stress Corrosion Cracking Resistance

2.08.4.1 In Air and in Water

Nickel does not lose its metallic brightness and does not discolor indoors, but it does slightly discolor outdoors, and a thin adhesive sulfate corrosion film is formed.

Nickel-copper alloys also maintain metallic brightness, but they turn into a charcoal color and form an adhesive corrosion film in the presence of

Table 10 Filler metal of nickel-based alloys

Marks	Chemical compositions (%)																	Ultimate tensile strength at R.T. (MPa)	Elongation	Applicable mother metal
	C	Mn	Fe	P	S	Si	Cu	Ni	Cr	Mo	Nb + Ta	Co	Al	Ti	W	Others				
AWS A5.14	ERNiCr-3	≤0.10	2.5–3.5	≤3.0	≤0.03	≤0.015	≤0.50	≤0.50	≥67.0	18.0–22.0	–	2.0–3.0	–	–	≤0.75	–	≤0.50	≥552	≥30	Alloy 600
	ERNiCrFe-5	≤0.08	≤1.0	6.0–10.0	≤0.03	≤0.015	≤0.35	≤0.50	≥70.0	14.0–17.0	–	1.5–3.0	–	–	–	–	≤0.50	≥552	≥30	Alloy 600
	ERNiCrFe-6	≤0.08	2.0–2.7	≤8.0	≤0.03	≤0.015	≤0.35	≤0.50	≥67.0	14.0–17.0	–	–	–	–	2.5–3.5	–	≤0.50	≥552	≥30	Alloy 600
	ERNiCrFe-7	≤0.04	≤1.0	7.0–11.0	≤0.02	≤0.015	≤0.50	≤0.30	^a	28.0–31.5	≤0.50	≤0.10	–	≤1.10	≤1.0	–	≤0.50	≥552	≥30	Alloy 690
	ERNiCrMo-3	≤0.10	≤0.50	≤1.0	≤0.02	≤0.015	≤0.50	≤0.50	≥58.0	20.0–23.0	8.0–10.0	3.15–4.15	–	≤0.40	≤0.40	–	≤0.50	≥720	≥30	Alloy 625
	ERNiCrMo-2	0.05–0.15	≤1.0	17.0–20.0	≤0.04	≤0.030	≤1.0	≤0.50	^a	20.5–23.0	8.0–10.0	–	0.50–2.5	–	–	0.20–1.0	≤0.50	–		Alloy X
	ERNiCrMo-4	≤0.02	≤1.0	4.0–7.0	≤0.04	≤0.030	≤0.08	≤0.50	^a	14.5–16.5	15.0–17.0	–	≤2.5	–	–	3.0–4.5	≤0.50	≥690	≥30	Alloy C-276
	ERNiFeCr-2	≤0.08	≤0.35	^a	≤0.015	≤0.015	≤0.35	≤0.30	50.0–55.0	17.0–21.0	2.80–3.30	4.75–5.50	≤1.00	0.20–0.80	0.65–1.15	–	B ≤ 0.006	≥1138	–	Alloy 718

^aAs remainder.

Table 11 Shielded metal arc welding electrode

	Marks	C	Mn	Fe	P	S	Si	Cu	Ni	Cr	Mo	Nb + Ta	Co	Al	Ti	W	Others	Ultimate tensile strength at R.T. (MPa)	Elongation	Applicable mother metal
AWS A5.11	ENiCrFe-1	≤0.08	≤3.5	≤11.0	≤0.03	≤0.015	≤0.75	≤0.50	≥62.0	13.0– 17.0	–	1.5– 4.0	–	–	–	–	≤0.50	≥552	≥30	Alloy 600
	ENiCrFe-2	≤0.10	1.0– 3.5	≤12.0	≤0.03	≤0.02	≤0.75	≤0.50	≥62.0	13.0– 17.0	0.50– 2.50	0.5– 3.0	–	–	–	–	≤0.50	≥552	≥30	Alloy 600
	ENiCrFe-3	≤0.10	5.0– 9.5	≤10.0	≤0.03	≤0.015	≤1.0	≤0.50	≥59.0	13.0– 17.0	–	1.0– 2.5	–	–	≤1.0	–	≤0.50	≥552	≥30	Alloy 600
	ENiCrFe-7	≤0.05	≤5.0	7.0– 12.0	≤0.03	≤0.015	≤0.75	≤0.50	^a	28.0– 31.5	≤0.50	1.0– 2.5	–	≤0.50	≤0.50	–	≤0.50	≥552	≥30	Alloy 690
	ENiCrMo-3	≤0.10	≤1.0	≤7.0	≤0.03	≤0.020	≤0.75	≤0.50	≥55.0	20.0– 23.0	8.0– 10.0	3.15– 4.15	–	–	–	–	≤0.50	≥724	≥30	Alloy 625
	ENiCrMo-4	≤0.02	≤1.0	4.0– 7.0	≤0.040	≤0.030	≤0.2	≤0.50	^a	14.5– 16.5	15.0– 17.0	–	≤2.5	–	–	3.0– 4.5	≤0.50	≥690	≥30	Alloy C-276

^aAs remainder.

Table 12 Welding condition example for automatic gas tungsten arc weld

<i>Mother metal</i>	<i>No. of pass</i>	<i>Wire (dia:mm)</i>	<i>Current (A)</i>	<i>Velocity (mm min⁻¹)</i>	<i>Ar flow rate (l min⁻¹)</i>	<i>Interpass temperature (°C)</i>
Alloy 600	1	YNiCr-3	200–240	40	Torch 25	≤150
	2–6			80–120		
Alloy 625	1	YNiCrMo-3	230–260	40	Torch 25	≤150
	2–6			80–140		
Alloy C-276	1	YNiCrMo-4	60	52	Torch 10	–
Alloy X	1–15	YNiCrMo-2	130–170	50–80	Torch 15	≤150
Alloy XR	1–2	Alloy XR	60	50–100	Torch 15	≤100
Alloy 718	1	Alloy 718	60	80	Torch 15	≤100
	2		45	70		

sulfur pollutants outdoors and into a green-gray color when near a beach.

Nickel–chromium, nickel–chromium–iron, nickel–molybdenum, and nickel–chromium–molybdenum alloys do not lose their metallic brightness, and do not discolor indoors or outdoors.

Nickel has excellent corrosion resistance in natural and distilled water. Nickel and nickel-clad steels have been used for household water tanks, due to their very low corrosion rates, $<0.0005 \text{ mm year}^{-1}$.

Nickel–copper alloys also show excellent corrosion resistance in natural water and distilled water. These alloys have been applied as seamless tubes in feed water economizers in fossil-fuel electric power plants.

2.08.4.2 In Seawater and Chloride Solution

Nickel maintains its passivating oxide film in fast-flowing seawater, and its corrosion rate is $<0.125 \text{ mm year}^{-1}$. However, it becomes corroded under deposits in static seawater due to breaking down of the passive film by organic deposits.⁵⁹

Nickel–copper alloys also show excellent corrosion resistance in flowing sea water, with corrosion rates under $0.02 \text{ mm year}^{-1}$. However, they also can be corroded under deposits in static seawater by the same mechanism as for nickel. Both nickel and nickel–copper alloys show higher resistance to cavitation and erosion corrosion in seawater than copper–nickel alloys.

Nickel–chromium–iron alloys have even more outstanding corrosion resistance and can be used in water polluted with substances such as carbon dioxide, iron compounds, chloride, and dissolved oxygen. They also exhibit excellent corrosion resistance in fast-flowing seawater but are subject to pitting and crevice corrosion in slow-flowing seawater.

Nickel–chromium–molybdenum alloys have excellent SCC resistance in sea water and chloride solutions

Table 13 Crack detection time of nickel-based alloys in boiling 42% MgCl₂ solution

<i>Alloy or steel</i>	<i>Crack detection time (h)</i>
Alloy C-22	More than 1000
Alloy C-276	More than 1000
Alloy 625	More than 1000
Alloy G	More than 1000
Alloy 825	46
316L stainless steel	1–2
304 stainless steel	1–2

due to their high nickel content. **Table 13** shows SCC initiation times in a boiling magnesium chloride solution,^{31,34,37} whereas 304 and 316 stainless steels formed cracks within just 1–2 h, and Alloy 825 formed cracks in 46 h. However, SCC was not detected in Alloys 625, C-276, and C-22, even after testing for 1000 h.

SCC was not detected in Alloy G, which also shows excellent resistance to SCC in a boiling magnesium chloride solution. The SCC resistance of Alloy 825 is superior to that of 304 or 316 stainless steels, but inferior to that of Alloy G as shown in **Table 13**.

The addition of molybdenum improves the resistance of nickel-based alloys to pitting and crevice corrosion. Nickel–chromium–molybdenum alloys have excellent pitting resistance. In addition, they have higher pitting and crevice corrosion initiation temperatures, as shown in **Table 14**. They also show much better resistance compared to 316 stainless steel in strong oxidizing environments including $24\,300 \text{ ppm Cl}^-$.^{33,34,37,38}

Crevice corrosion resistance is usually evaluated by measuring the crevice repassivation potential. **Figure 22** shows the temperature dependence of the crevice repassivation potential for nickel–chromium–molybdenum alloys in a 20% NaCl solution.⁵⁹ Alloy C-276 shows a higher crevice

repassivation potential and a higher crevice corrosion resistance than Alloy 625.

By contrast, the pitting and crevice corrosion resistance of Alloy G are inferior to those of Alloy C-276 and superior to those of 316 stainless steel and Alloy 825, as shown in Table 14.

2.08.4.3 In Caustic Solutions

Nickel shows excellent corrosion resistance in caustic solutions, such as sodium hydroxide and potassium hydroxide. The corrosion rates of nickel and nickel-based alloys in sodium hydroxide are shown in Table 15.^{7,8,10,31}

Table 14 Pitting and crevice corrosion initiation temperature of nickel-based alloys

Alloy or steel	Pitting initiation temperature (°C)	Crevice corrosion initiation temperature (°C)
Alloy C-22	>150	102
Alloy C-276	150	80
Alloy 625	90	50
Alloy G-3	75	40
Alloy 825	25	≤−5
316L stainless steel	20	≤−5

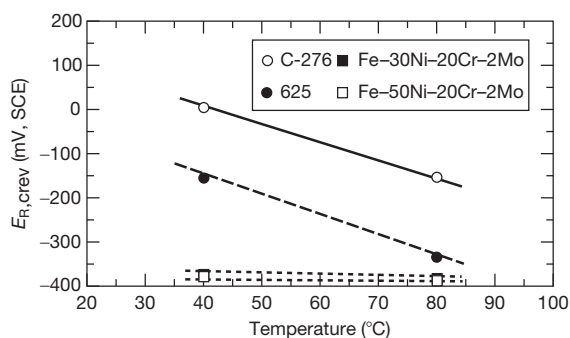


Figure 22 Temperature dependence of crevice repassivation potential ($E_{R,rev}$) in 20% NaCl solution.

Table 15 Corrosion rate of nickel and nickel-based alloys in liquid sodium hydroxide (mm year^{-1})

Alloy	Testing temperature (°C)			
	400	500	580	680
201	0.02	0.03	0.06	0.94
C	—	2.56	^a	—
400	0.05	0.13	0.45	—
600	0.03	0.06	0.13	1.69

^aSurface was swelled by oxides.

Ni shows excellent corrosion resistance to liquid sodium hydroxide at any temperature and at any concentration with water; in particular, it has an unmeasurable corrosion rate at sodium hydroxide concentrations lower than 50%. Nevertheless, Ni corrodes in sodium hydroxide in the presence of a sulfide such as sodium sulfide. Nickel–chromium–iron alloys have excellent corrosion resistance to sodium hydroxide and also high resistance to ammonium hydroxide and sulfide corrosion at high temperatures. The nickel–molybdenum alloys and Alloy C, which is a nickel–chromium–molybdenum alloy, are inferior to nickel–chromium–iron alloys with respect to corrosion in ammonium hydroxide and sulfide.

2.08.4.4 In Hydrochloride Gas, Chlorine, and Hydrofluoric Acid

Chlorine-containing gases including HCl or Cl_2 severely attack many metals. Table 16 shows the applicable temperatures for various materials in dry HCl and Cl_2 gases.^{7,8,10,30,31} Nickel can be used in hydrofluoric acid provided there is no condition of flowing in which its protective fluoride film would be removed. Nickel also can be used at temperatures higher than 500 °C, similar to Alloy 600. Nickel–chromium–iron is better as a structural alloy in this application due to its high strength compared to pure nickel. However, nickel and Alloy 600 severely corrode in HCl and Cl_2 gas in the presence of water vapor. Aeration or the presence of oxidizing chemicals will also increase corrosion rate of nickel in hydrofluoric acid.

2.08.4.5 In High-Temperature Water

Coriou reported IGSCC (PWSCC) susceptibility for nickel-based alloys and the influence of nickel content in high-temperature, high-purity water.¹⁸ It is now known, however, that this cracking susceptibility

Table 16 Maximum applicable temperature (°C) in dried HCl and Cl_2 gas

Alloy or steel	HCl	Cl_2
Alloy 201	510	538
Alloy 600	482	538
Alloy B	454	538
Alloy C	454	510
Alloy 400	232	427
316 stainless steel	427	343
304 stainless steel	399	316
Carbon steel	260	204

is very dependent on the corrosion potential, as determined by the concentration of molecular hydrogen in solution (as in PWR primary water). Subsequently, it was reported that IGSCC is affected by the chromium content, but not by the nickel content in nickel-based alloys, as shown in **Figures 23** and **24**.⁶⁰ Alloy 690 has higher resistance to PWSCC than Alloy 600, due to its higher chromium content.

Carbide precipitation along grain boundaries by thermal treatment (TT) at around 700 °C improves the PWSCC resistance for Alloys 600 and 690. In particular, $M_{23}C_6$ precipitation that is coherent with the matrix was detected along grain boundaries in the TT Alloy 690, which has excellent PWSCC resistance depending on the carbon content and the solution heat-treatment temperature. By contrast, niobium addition to Alloy 600 was found to have a poor effect on PWSCC susceptibility,⁶⁰ but improves IGSCC resistance under BWR water conditions.²⁵

2.08.4.6 In High-Temperature Gases

2.08.4.6.1 Oxidation

Nickel shows superior oxidation resistance to carbon steels and copper alloys due to the formation of a

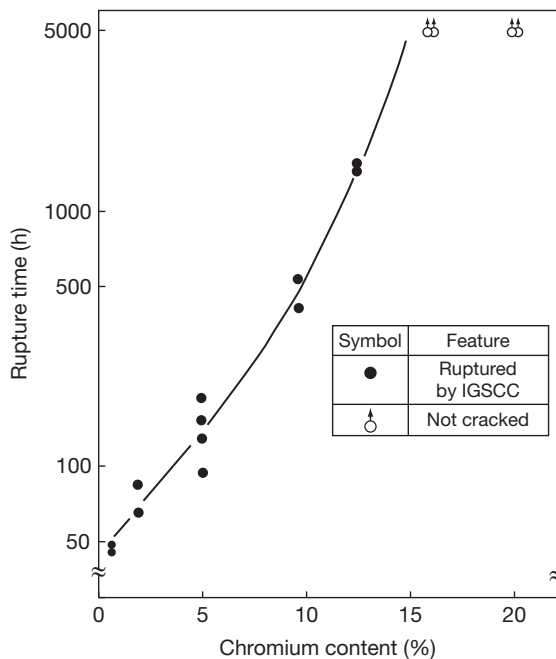


Figure 23 Effect of chromium content on the stress corrosion cracking fracture time under constant load test for solution-annealed nickel-based chromium-10% iron alloys at 360 °C in simulated pressurized water reactor primary water.

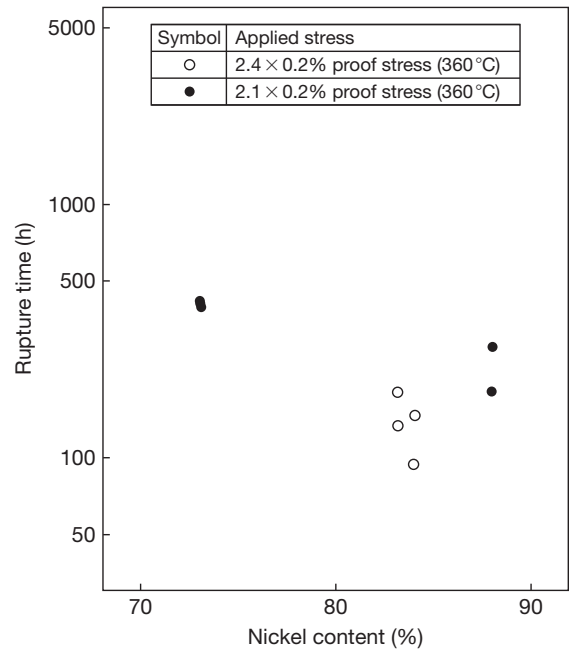


Figure 24 Effect of Ni content on the stress corrosion cracking fracture time under constant load test for solution-annealed nickel-based 5% chromium-iron alloys at 360 °C in simulated pressurized water reactor primary water.

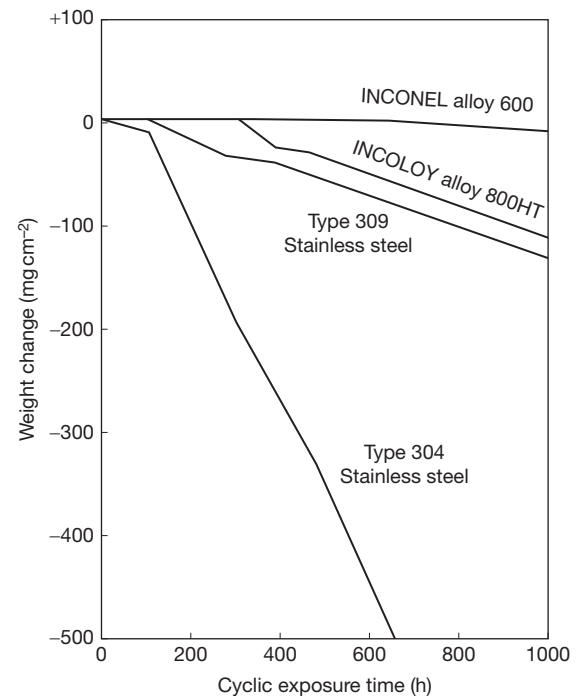


Figure 25 Repeated oxidation test results of various alloys at 980 °C in air (15 min heating, 5 min cooling).

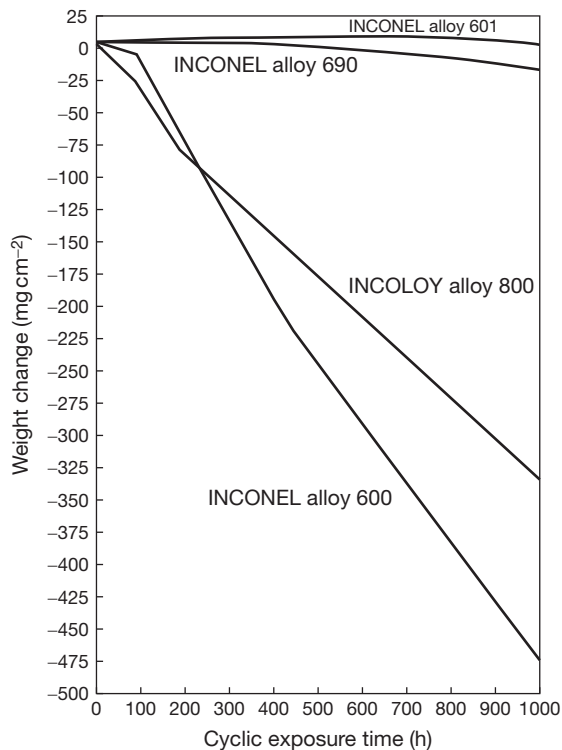


Figure 26 Repeated oxidation test results of various alloys at 1095 °C in air (15 min heating, 5 min cooling).

nickel oxide film in air or other oxidizing environments. The oxidation resistance of nickel is improved remarkably by the addition of chromium. Repeated oxidation test results for various alloys are shown in **Figures 25 and 26**.^{10,11,14} In these tests, Alloy 600 showed little weight change and was found to have better oxidation resistance than 304 or 310 stainless steels. Alloy 601 had higher oxidation resistance than Alloy 600, due to its higher chromium and aluminum contents. Alloy 690 also had higher oxidation resistance than Alloy 600 due to its higher chromium content.

2.08.4.6.2 Nitriding

Low-alloy steels are highly susceptible to nitriding in active atmospheres such as high-temperature ammonia gas. To obtain resistance to nitriding, the addition of nickel is effective. Austenitic stainless steels have higher resistance to nitriding than low-alloy steels, for example. Nickel-based alloys have significantly better resistance to nitriding. Alloy 600 shows excellent resistance to nitriding in ammonia production plant environments.

2.08.4.6.3 Sulfidation

Nickel-based alloys are highly susceptible to sulfidation. Nickel forms a eutectic with sulfur at

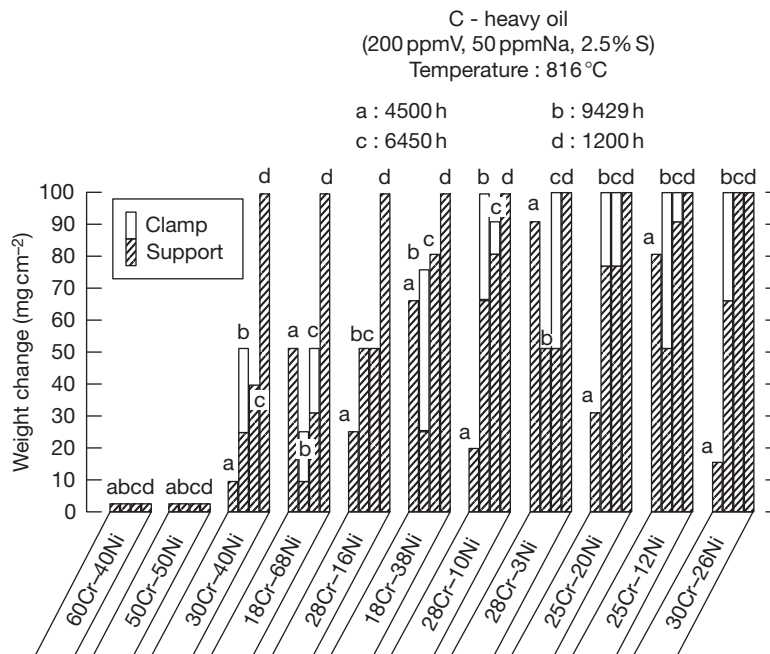


Figure 27 Hot corrosion field test results for chromium-nickel alloys.

temperatures above 645 °C and the scales on nickel lose their protective properties at higher temperatures. The addition of chromium to nickel-based alloys is effective for improving sulfidation resistance, and alloys containing higher than 20% chromium show good sulfidation resistance.

Nickel undergoes severe corrosion in combustion gases of crude petroleum. When vanadium is present in these gases, corrosion occurs due to the formation of low-temperature-melting compounds with vanadium oxides (so-called vanadium attack). When sulfur is present in crude petroleum, sulfide corrosion occurs.

50% chromium–50% nickel and 60% chromium–40% nickel alloys are rare nickel-based materials with excellent resistance to vanadium attack and sulfide corrosion. [Figure 27⁶¹](#) shows exposure test results for the supports of the super heater tubes of a fossil-fuel electric power plant. The data indicate that both alloys are indeed highly resistant to corrosion.

2.08.5 Summary

The excellent corrosion resistance and mechanical characteristics of various nickel-based alloys have been described in this chapter. In particular, typical corrosion, mechanical, other physical properties data, together with general fabrication information, have been reviewed.

Copper-based alloys have more than 5000 years of history, and iron-based alloys more than 4000 years. However, nickel-based alloys were developed only in the last 100 years or so. This very short history for nickel-based alloys means that some unknown, or uncertain, or unexpected scientific properties will be still remaining to be discovered for these alloys. Consequently, continuing and assiduous studies of nickel based alloys are plainly required (see [Chapter 4.04, Radiation Effects in Nickel-Based Alloys](#) and [Chapter 5.04, Corrosion and Stress Corrosion Cracking of Ni-Base Alloys](#)).

References

1. Bechier, P. *Annales de chimie et physique*, **1821**, 17, 573.
2. Stodart, J.; Faraday, M. *Philos. Trans. R. Soc.* **1822**, 112, 253.
3. Monell, A. U.S. Patent 811,239, Jan 1906.
4. International Nickel Co. *Nickel alloys*; 1968.
5. Copson, H. R. *Physical Metallurgy of Stress Corrosion Fracture*, Symposium on Physical Metallurgy of Stress Corrosion Fracture, (1959 Pittsburgh), LCCN: 59014890; Interscience: New York, 1959.
6. Baker, H.; Okamoto, H.; Henry, S.; *et al.* *ASM Handbook Volume 3 Alloy Phase Diagram*, 0-87170-381-5; ASM International: Materials Park, OH, 1992.
7. Technical Bulletin of Nickel 200 & 201.
8. Technical Bulletin of MONEL alloy 400.
9. Technical Bulletin of MONEL alloy K-500.
10. Technical Bulletin of INCONEL alloy 600.
11. Technical Bulletin of INCONEL alloy 601.
12. Technical Bulletin of INCONEL alloy X-750.
13. Technical Bulletin of INCONEL alloy 718.
14. Technical Bulletin of INCONEL alloy 690.
15. Technical Bulletin of INCOLOY alloy 800.
16. Technical Bulletin of INCOLOY alloy X-780.
17. ASME. Boiler and Pressure Vessel Code Section III, ASME, 9780791802694, NY, 1963.
18. Coriou, H.; Grall, L.; Le Gall, Y.; Vettier, S. In *Proceedings of 3eme Colloque de metallurgie sur la corrosion*, Saclay; North Holland: Amsterdam, 1959; pp 161–169.
19. Blanchet, J.; Coriou, H.; Grall, L.; Mahieu, C.; Offer, C.; Turluer, G. *J. Nucl. Mater.* **1975**, 55(2), 187–206.
20. Schenk, H. J. *Mater. Perform.* **1976**, 15, 25–33.
21. *Nucl. Eng. Int.* **1982**, 2.
22. Airey, G. P. *Metallography* **1980**, 13, 21–41.
23. Yonezawa, T.; Onimura, K.; Sasaguri, N.; *et al.* In *Proceedings of the Second International Symposium on Environmental Degradation of Materials in Nuclear Power Systems – Water Reactors*, Sept 9–12, 1985; American Nuclear Society: Monterey, CA, 1985; pp 593–600, 0-89448-124-X.
24. Yonezawa, T.; Onimura, K.; Sakamoto, N.; Sasaguri, N.; Nakata, H.; Susukida, H. In *Proceedings of the International Symposium on Environmental Degradation of Materials in Nuclear Power Systems – Water Reactors*, Aug 22–25, 1983; American Nuclear Society: Myrtle Beach, SC, 1983; pp 345–366, 0-915567-00-8.
25. Hosoi, K.; Hattori, S.; Urayama, V.; Masaoka, I.; Sasaki, R. In *Proceedings of the International Symposium on Environmental Degradation of Materials in Nuclear Power Systems – Water Reactors*, Aug 22–25, 1983; American Nuclear Society: Myrtle Beach, SC, 1983; pp 334–344, 0-915567-00-8.
26. Berge, P.; Donati, J. R. *Nucl. Technol.* **1981**, 55, 88–104.
27. Yamauchi, K.; Hamada, I.; Sakaguchi, Y.; *et al.* Effect of niobium addition on intergranular stress corrosion cracking resistance of Ni–Cr–Fe alloy 600. In *Proceedings of the Corrosion Cracking Program and Related Papers Presented at the International Conference and Exposition on Fatigue, Corrosion Cracking, Fracture Mechanics and Failure Analysis*, Salt Lake City, UT 1985; Vol. 2, pp 11–22.
28. ASME Boiler and Pressure Vessel Code Case, N-580-2; 2008.
29. Flint, G. N. *Metallurgia* **1960**, 62, 373; 195.
30. Technical Bulletin of HASTELLOY B-3 alloy.
31. Technical Bulletin of HASTELLOY C-276 alloy.
32. Technical Bulletin of HASTELLOY C-4 alloy.
33. Technical Bulletin of HASTELLOY C-22 alloy.
34. Technical Bulletin of INCONEL alloy 625.
35. Technical Bulletin of INCONEL alloy 625LCF.
36. Agarwal, D. C.; Corbett, R. A. *Corrosion 2000, Paper #501*; NACE International: Houston, TX, 2000.
37. Technical Bulletin of INCOLOY alloy 825.
38. Technical Bulletin of HASTELLOY G-30 alloy.
39. Technical Bulletin of HASTELLOY N alloy.
40. Technical Bulletin of HAYNES-3 alloy.
41. Technical Bulletin of HASTELLOY X alloy.
42. Tanaka, R.; Kondo, T. *Nucl. Technol.* **1984**, 66, 75–87.

43. Kondo, T. In *Proceedings on 12th International Corrosion Congress*, Sept 1993; NACE International: Houston, TX, 1993.
44. Sumitomo Metals Industries, Ltd. Steel tube works.
45. Hitachi Metals, Ltd. YSS superalloys.
46. Nippon Yakin Kogyo Co., Ltd. High-performance alloy & stainless steel.
47. Sanyo Special Steel Co., Ltd. Company profile.
48. Guide Book of Daido Special Metals, Ltd.
49. Guide Book of Kobe Steel, Ltd.
50. Guide Book of SANDVIK AB.
51. Guide Book of Nippon Welding Rod Co., Ltd.
52. Special Metals Corporation. Fabricating.
53. Huntington Alloy Products Division The International Nickel Company, Inc. Heating and pickling.
54. Huntington Alloys. JOINING, 1972.
55. Savage, W. F.; Krantz, B. M. *Weld. J.* **1966**, 45, 13S–25S.
56. Dupont, J. N.; Robino, C. V.; Marder, A. R. *Weld. J.* **1998**, 77, 417S–431S.
57. AWS Filler Metal Specifications by Material and Welding Process, A5.11/A5.11M.
58. AWS Filler Metal Specifications by Material and Welding Process, A5.14/A5.14M.
59. Noguchi, M.; Tsujikawa, S. In *Corrosion Symposium*; Japan Society of Corrosion Engineering, Tokyo, Japan, 1990.
60. Yonezawa, T.; Sasaguri, N.; Onimura, K. Effects of metallurgical factors on stress corrosion cracking of Ni-base alloys in high temperature water. In *Proceedings of the 1988 JAIF International Conference on Water Chemistry in Nuclear Power Plants*, Tokyo, Japan, Apr 19–22, 1988; pp 490–495.
61. International Nickel Co. High Chromium Cr–Ni Alloys to Resist Residual Fuel Oil Ash Corrosion.

2.09 Properties of Austenitic Steels for Nuclear Reactor Applications

P. J. Maziasz and J. T. Busby

Oak Ridge National Laboratory, Oak Ridge, TN, USA

Published by Elsevier Ltd.

2.09.1	Introduction	267
2.09.2	Properties of Unirradiated Alloys	268
2.09.2.1	General and Fabrication Behavior	268
2.09.2.2	Physical Properties	269
2.09.2.3	Mechanical Properties	270
2.09.2.4	Precipitation Behavior During Elevated Temperature Aging	273
2.09.2.5	Corrosion and Oxidation Behavior	274
2.09.3	Summary of How Properties Can Change During Irradiation	275
2.09.4	Some Examples of Advanced Alloys for FBR and ITER/Fusion Applications	279
2.09.4.1	FBR Application	279
2.09.4.2	ITER/Fusion Application	280
References		282

Abbreviations

ASTM	American Society for Testing and Materials
bcc	Body-centered cubic
BWR	Boiling water reactor
CW	Cold worked
D-T	Deuterium–tritium (fusion)
DBTT	Ductile-to-brittle transition temperature
FBR	Fast-breeder reactor
fcc	Face-centered cubic
GenIV	Generation IV reactors
HFIR	High Flux Isotope Reactor
IASCC	Irradiation-assisted stress-corrosion cracking
ITER	International Magnetic Fusion demonstration device, being constructed in Cadarache, France
LWR	Light water reactor
MFR	Magnetic fusion reactor
NIMS	National Institute for Materials Science (Japan)
ORR	Oak Ridge Research Reactor
PCA	Prime candidate alloy
PWR	Pressurized water reactor
R&D	Research and development
RIS	Radiation-induced solute segregation
SA	Solution annealed
SCC	Stress-corrosion cracking
SEM	Scanning electron microscopy

TEM	Transmission electron microscopy
UTS	Ultimate tensile strength
YS	Yield strength

2.09.1 Introduction

Austenitic stainless steels are a class of materials that are extremely important to conventional and advanced reactor technologies, as well as one of the most widely used kinds of engineering alloys. They are austenitic Fe–Cr–Ni alloys with 15–20Cr, 8–15Ni, and the balance Fe, because they have a face-centered-cubic (fcc) close-packed crystal structure, which imparts most of their physical and mechanical properties. They are steels because they contain dissolved C, typically 0.03–0.15%, and more advanced steels can also contain similar or greater amounts of dissolved N. They are stainless because they contain >13%Cr and Cr provides surface passivation for corrosion-resistance in various aqueous or corrosive chemical environments from room temperature to about 400 °C. At elevated temperatures of 500 °C and above, Cr provides oxidation resistance by the formation of protective Cr₂O₃ oxide scales. Commercial stainless steels are complex alloys, with varying additions and combinations of Mo, Mn, Si, and Ti as well as Nb to enhance the properties and behavior of the austenite parent phase over a wide range of

temperatures. They can also contain a host of minor or impurity elements, including Co, Cu, V, P, B, and S, which do not have significant effects within certain normal ranges.

Typical commercial steel grades relevant to nuclear reactor applications include types 304, 316, 321, and 347. They can be fashioned into a wide range of thick or thin components by hot or cold rolling, bending, forging, or extrusion, and many are also available as casting grades as well (i.e., 304 as CF8, 316 as CF8M, and 347 as CF8C). These steels all have good combinations of strength and ductility at both high and low temperatures, with excellent fatigue resistance, and are most often used in the solution-annealed (SA) condition, with the alloying elements fully dissolved in the parent austenite phase and little or no precipitation. The steels with added Mo (316) or stabilized with Ti (321) or Nb (347) also have reasonably good elevated temperature strength and creep resistance. Additions of nitrogen (i.e., 316LN or 316N) provide higher strength and stability of the austenite parent phase to the embrittling effects of thermal- or strain-induced martensite formation and allow this grade of steel to be used at cryogenic temperatures. It is beyond the scope of this chapter to describe in detail the physical metallurgy of austenitic stainless steels, and adequate descriptions are found elsewhere.^{1,2} The remainder of this chapter focuses on the factors that broadly affect the properties of austenitic stainless steels in specific reactor environments, and highlights efforts to develop modified steels that perform significantly better in such reactor systems. These will likely be important in enabling materials for any new applications of nuclear power.

2.09.2 Properties of Unirradiated Alloys

2.09.2.1 General and Fabrication Behavior

Without the effects of irradiation, austenitic stainless steels are fairly stable solid-solution alloys that generally remain in the metallurgical condition in which they were processed at room temperature to about 550 °C. The typical austenitic stainless steel, such as type 304, 316, 316L, or 347 stainless steel, in the SA condition (1000–1050 °C), will have a wrought, recrystallized grain structure of uniform, equiaxed grains that are 50–100 μm in diameter, particularly in products such as extruded bar or flat-rolled plates (6–25 mm thick).^{1–3} Ideally, such

products should be free of plastic strain effects and have dislocation-free grains, but for real applications, products may be straightened or bent slightly (1–5% cold strain), and thus have some dislocation substructure within the grains. Stainless steel products with heavier wall thicknesses (>50 mm) would be forgings and castings, which would have coarser grain sizes, but probably not have additional deformation. Special stainless steel products would include thin foils, sheets, or wires (0.08–0.5 mm thick), which would have much finer grain-sizes (1–10 μm diameter) due to special processing (very short annealing times) and special considerations (5–10 grains across the foil/sheet thickness).³ Typical fast-breeder reactor (FBR) cladding for fuel elements can be thin-walled tubes of austenitic stainless steel, with about 0.25 mm wall thickness, so they fall into this latter special products category. Although austenitic stainless steels are highly weldable, welding changes their structure and properties in the fusion (welded and resolidified) and adjacent heat-affected zones relative to the wrought base metal, so they may behave quite differently than the base metal, which is what was described above. The detailed behavior of welds under irradiation is beyond the scope of this chapter, so the remainder of this chapter focuses on typical wrought metal behavior.

Another important aspect of austenitic stainless steel that defines it is the stability of the parent austenite phase. The addition of nickel and elements that behave like nickel including carbon and nitrogen to the alloy causes it to have the austenite parent phase and its beneficial properties, which is also the same fcc crystal structure found in nickel-based alloys. Otherwise, the steel alloy would have the natural crystal structure of iron and chromium, which is body-centered cubic (bcc) ferrite, as the parent phase, and alloying elements that make the alloy behavior like this include molybdenum, niobium, titanium, vanadium, and silicon. A stable austenitic alloy will be 100% austenite, with no δ-ferrite formed at high temperature and no thermal or strain-induced martensite, whereas an unstable austenitic alloy may have all of these. A useful way of expressing these different phase formation tendencies at room temperature in terms of the alloy behaving more like Cr (bcc ferritic) or Ni (fcc austenitic) is a Schaeffler diagram, as shown in [Figure 1](#). The fcc austenite phase is nonmagnetic and maintains good strength and ductility even at cryogenic temperatures, with no embrittling effects of martensite formation. The bcc phase by comparison is ferromagnetic, has a little less

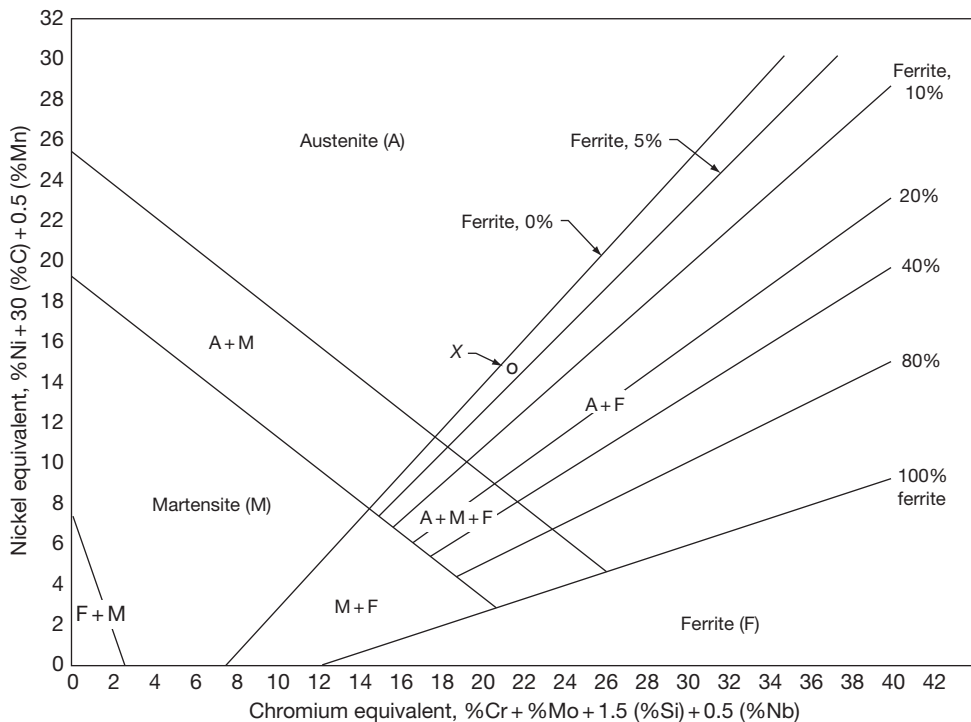


Figure 1 Schaeffler diagram showing regions of stable austenite, martensite, and delta-ferrite in austenitic stainless steels at room temperature as a function of steel alloys compositional effects acting as the equivalent of Cr or Ni. Reproduced from Lula, R. A., Ed. *Stainless Steel*; ASM International: Materials Park, OH, 1986.

ductility (less active slip systems), and has a ductile-to-brittle transition temperature (DBTT), below which the steel has low ductility and impact resistance, with a brittle fracture mode. Maintaining sufficient carbon and adding nitrogen are two ways of imparting good, stable austenite phase behavior to the common grades of austenitic stainless steels, like 304LN or 316LN.

2.09.2.2 Physical Properties

Physical properties of 300 series stainless steels tend to be fairly similar, and the typical physical properties of 316L stainless steel are given in **Tables 1** and **2**.¹⁻³ The 316L stainless steel has a density at room temperature of 8000 kg m^{-3} and a melting temperature of slightly above 1400°C (**Table 1**). The elastic (Young's) modulus at room temperature is 190–200 GPa, which is typical of a range of engineering alloys, including ferritic steels and solid-solution Ni-based superalloys. At 100°C , the coefficient of thermal expansion of 316L is about $16 \times 10^{-6} \text{ cm cm}^{-1}^\circ\text{C}^{-1}$ (**Table 2**), and values of that property may vary by up to 3–4% for types 316 and 347 steels. The 300 series stainless steels

Table 1 Basic physical properties for 316L stainless steel

Property	Value
Density	8000 kg m^{-3}
Melting temperature	$1390\text{--}1440^\circ\text{C}$
Elastic modulus	193 GPa
Shear modulus	82 GPa

Table 2 Thermal properties for 316L stainless steel

Property	Temperature range	Value
Coefficient of thermal expansion	$0\text{--}100^\circ\text{C}$	$15.9 \times 10^{-6}^\circ\text{C}^{-1}$
	$0\text{--}315^\circ\text{C}$	$16.2 \times 10^{-6}^\circ\text{C}^{-1}$
	$0\text{--}538^\circ\text{C}$	$17.5 \times 10^{-6}^\circ\text{C}^{-1}$
	$0\text{--}1000^\circ\text{C}$	$19.5 \times 10^{-6}^\circ\text{C}^{-1}$
Thermal conductivity	At 100°C	16.3 W mK^{-1}
	At 500°C	21.5 W mK^{-1}
Specific heat capacity	$0\text{--}100^\circ\text{C}$	$500 \text{ J kg}^{-1}^\circ\text{C}$

have much more thermal expansion than martensitic/ferritic steels or Ni-based superalloys, with the thermal expansion of 316L at 100°C being about

50% higher than that of type 410 ferritic steel.³ The thermal conductivity of 316L stainless steel at 100 °C is 16.3 W m K^{-1} , which is to the higher end of the range for such alloys, with type 316 or 347 steel having 15–30% lower thermal conductivity. Thermal conductivity of 300 series stainless steels is lower than that of ferritic steels or Ni-based superalloys. If the 300 series stainless steel is fully (100%) austenitic, such as 316 or 347, then it has no ferromagnetic behavior, but if it contains ferromagnetic phases (like delta-ferrite or martensite), then such steels have some degree of ferromagnetic behavior. Adding nitrogen to 316L produces fully stable austenitic phase structures.

2.09.2.3 Mechanical Properties

The general mechanical behavior properties of austenitic stainless steels at room and at elevated temperatures are described. These provide the background for their behavior in various reactor environments. The mechanical properties of the various grades of the 300 series austenitic stainless steels are fairly similar, particularly at room temperature, so available data for type 316 or 316L steel are used as representative of the group. There is more variation in properties at elevated temperatures, particularly creep-resistance and creep-rupture strength, so important properties differences are noted, particularly for steels modified with Ti or Nb which have more high-temperature heat-resistance than type 316 steel. Some effects of processing on mechanical properties are noted, but generally properties are described for material in the SA condition.

Austenitic stainless steels such as types 304, 316, and 316L have yield strength (YS – 0.2% offset) of 260–300 MPa in the SA condition at room temperature, with up to 50–70% total elongation.^{1–7} Typical YS values as a function of temperature for type 316 are shown in **Figures 2 and 3**. Other austenitic stainless steels developed for improved creep resistance at high temperatures, such as fine-grained 347HFG or the high-temperature, ultrafine precipitate-strengthened (HT-UPS) steels (**Table 3**), have very similar YS of about 250 MPa in the SA condition (typical thicker section pipes or plates), as shown in **Figure 3**. Many applications of type 304 and 316 stainless steels require a minimum YS of 200 MPa. However, small amounts of cold plastic strain, 1–5%, typical of straightening or flattening for various product forms, termed ‘mill-annealed,’ raise the YS to about 400 MPa, because austenitic stainless steels tend to have high strain-hardening rates. Large

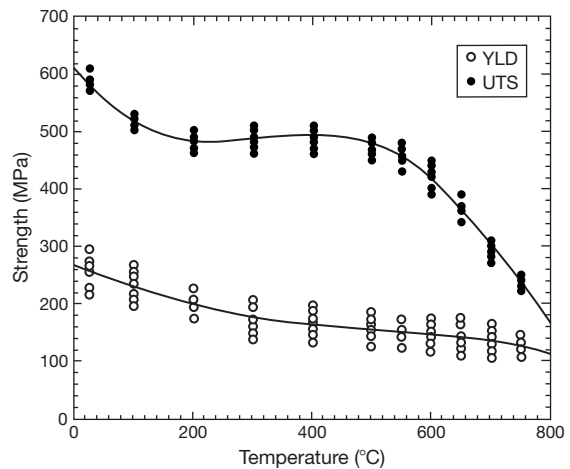


Figure 2 Plots of yield strength (YS) and ultimate tensile strength (UTS) as a function of tensile test temperature for nine heats of SA 316 austenitic stainless steel tubing tested by the National Research Institute for Metals (now NIMS) in Japan. Reproduced from Data sheets on the elevated temperature properties of 18Cr–12Ni–Mo stainless steels for boiler and heat exchanger tubes (SUS 316 HTB), Creep Data Sheet No. 6A; National Research Institute for Metals: Tokyo, Japan, 1978.

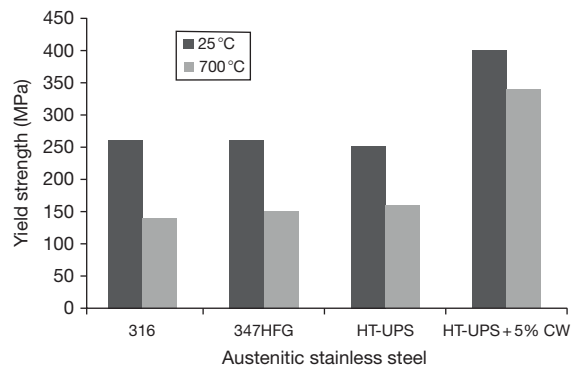


Figure 3 Comparison of yield strength (YS) at room temperature and at 700 °C for 316, 347HFG, and high-temperature, ultrafine precipitate-strengthened (HT-UPS) austenitic stainless steels, all in the solution-annealed condition, and for HT-UPS steel with 5% CW prior to testing. Adapted from Swindeman, R. W.; Maziasz, P. J.; Bolling, E.; King, J. F. *Evaluation of Advanced Austenitic Alloys Relative to Alloy Design Criteria for Steam Service: Part 1 – Lean Stainless Steels*; Oak Ridge National Laboratory Report (ORNL-6629/P1); Oak Ridge National Laboratory: Oak Ridge, TN, 1990; Teranishi, H.; et al. In *Second International Conference on Improved Coal Fired Power Plants*; Electric Power Research Institute: Palo Alto, CA, 1989; EPRI Publication GS-6422 (paper 33-1).

amounts of cold work (CW) push the YS higher, with 20–30% CW 316 having YS of 600–700 MPa,^{8,9} but with very low ductility of only 2–3%. The very

Table 3 Composition of various commercial or advanced/developmental austenitic stainless steel alloy grades and types (wt%)

Alloy	Cr	Ni	Mo	Mn	Si	C	Ti	Nb	Others
304	18–20	8–12	–	1–2	0.75	0.08	–	–	304L (0.03C), 304LN (0.03C, <0.14N)
316	16–18	10–14	2–3	2	0.75	0.08	–	–	316L (0.03C), 316LN (0.03C, <0.14N)
321	17–19	9–13	–	1–2	0.75	0.04–0.08	0.2–0.4	–	
347	17–19	9–13	–	1–2	0.75	0.04–0.08		0.4–0.8	
D9	14	15	2.3	2	1	0.05	0.25	–	D9I (0.04P, 0.005B)
PCA	14	16	2.3	2	0.4	0.05	0.24	–	0.01–0.03P
HT-UPS	14	16	2.5	2	0.4	0.08	0.3	0.1	0.5V, 0.003B, 0.05P
CF3MN	17–21	9–13	2–3	<1.5	<1.5	<0.03	–	–	<0.1N (recommended)
CF3MN (US)	17.6	12.6	2.5	3.1	0.44	0.01	–	–	0.23N

fine grain sizes found in thin-sheet and foil products made from 347 steel also tend to push ambient YS to 275–300 MPa or above.⁷ The ultimate tensile strength (UTS) of SA 316 steel at room temperature is about 600 MPa, and can be higher (600–700 MPa) for steels such as 347HFG, HT-UPS, or some of the high-nitrogen grades. The UTS of 20–30% CW 316 or other comparable steels can be 700–800 MPa at room temperature.^{4,8,9}

The impact-toughness and crack-growth resistance of SA 316 at room temperature and temperatures below 500 °C are excellent because of its high ductility and strain-hardening behavior. Charpy impact toughness values for SA 316 and 347 steel are about 150 J at 22–400 °C, and tend to stay above 100 J even at cryogenic (–196 °C) temperatures. Type 316 stainless steels also have good room-temperature fatigue resistance, exhibiting endurance limits for cyclic stresses below the YS.

At elevated temperatures, the YS of SA 316 declines with increasing temperature, reaching levels of about 150 MPa at 600–650 °C (Figure 2), and going lower at 700–800 °C. More heat-resistant steels such as 347HFG or HT-UPS steels may be slightly stronger at 700 °C, and can have YS values of 300–350 MPa in the ‘mill-annealed’ (5% CW) (Figure 3). The UTS of SA 316 remains at about 500 MPa up to 500 °C, and then declines rapidly with increasing temperature until YS and UTS approach similar values (120–180 MPa) at about 800 °C (Figure 2). More heat-resistant steel, such as 347HFG and the HT-UPS steels, can retain higher UTS values of 200–300 MPa at 800 °C. Unaged SA 316 generally have 30–60% total tensile elongation at temperatures up to 800 °C; similar steels with 20–30% CW can have 5–10% ductility until they recrystallize at temperatures of 800 °C or above.⁹

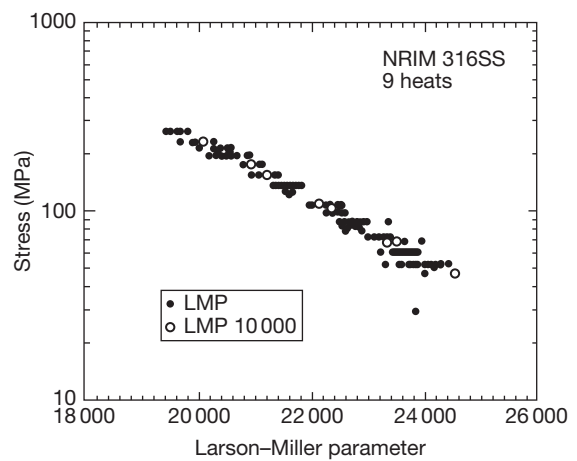


Figure 4 A plot of creep-rupture stress as a function of Larson–Miller parameter (LMP) for nine heats of SA 316 austenitic stainless steel tubing tested by the National Research Institute for Metals (now NIMS) in Japan. LMP 10 000 represents data for rupture after 10 000 h. $LMP = (T[^\circ C] + 273)(20 + \log t_r)$, where T is creep testing temperature and t_r is the creep-rupture life in hours. Reproduced from Data sheets on the elevated temperature properties of 18Cr–12Ni–Mo stainless steels for boiler and heat exchanger tubes (SUS 316 HTB), Creep Data Sheet No. 6A; National Research Institute for Metals: Tokyo, Japan, 1978.

At elevated temperatures, time-dependent deformation, or creep, becomes a concern for austenitic steels such as 304 and 316 above 500–550 °C. A Larson–Miller parameter (LMP) plot of creep-rupture strength for SA 316 is shown in Figure 4, and for 347HFG and HT-UPS steels in Figure 5. Long-term creep-rupture behavior is affected by precipitation behavior at elevated temperatures, as is described in the following section. Creep-rupture behavior (time to rupture or time to 1% strain) is far more limiting in design for high temperature integrity than tensile properties. The creep-rupture

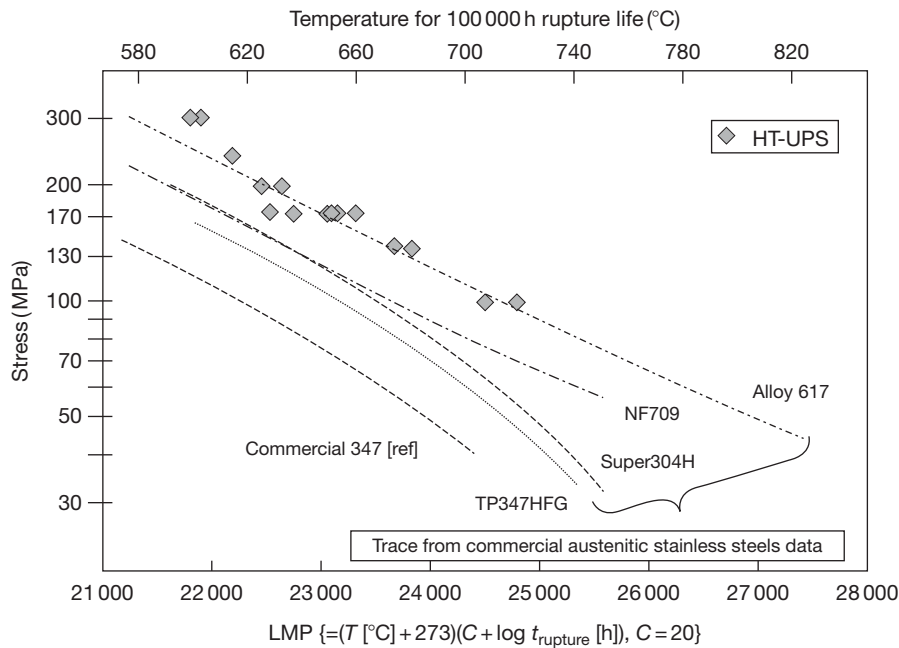


Figure 5 Creep-rupture resistance of high-temperature, ultrafine precipitate-strengthened steel compared to several commercial heat-resistant stainless steels and alloys.

strength of SA 316 in [Figure 4](#) is comparable to creep-rupture strength of 347 steel in [Figure 5](#), and both have less creep strength than 347HFG, a steel containing more Nb and C ([Table 3](#)). Types 304 and 316L steels would have less creep strength than 316 steel. By comparison, the triply stabilized (additions of Ti, V, and Nb) HT-UPS steel has outstanding creep-rupture resistance at 700–800 °C, comparable to that of the solid-solution Ni-based alloy 617. A more direct comparison of creep resistance at 700 °C and 170 MPa is shown in [Figure 6](#). For this creep-rupture condition, SA 316 ruptures after about 40 h, whereas the SA HT-UPS steel resists creep and rupture until 18 745 h.^{4,7} For elevated temperature creep behavior of heat-resistant stainless steels with additions of Ti and Nb, processing conditions are also important, including prior cold-strain and the SA temperature. The creep resistance of SA 304 and 316 steels is not affected significantly by different annealing temperatures, and both steels have less creep resistance in the 10–30% CW condition. By contrast, 347HFG and HT-UPS steels benefit dramatically from higher solution annealing temperatures (1050–1100 °C compared to 1150–1200 °C) and small amounts of CW, because these enhance the formation and stability of nano-dispersions of MC carbide precipitates, which are responsible for their high-temperature creep resistance.^{4,7,10,11}

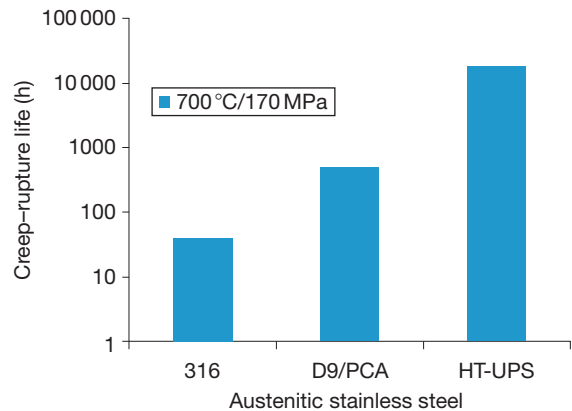


Figure 6 Direct comparison of creep-resistance of D9 and high-temperature, ultrafine precipitate-strengthened steels. Adapted from Swindeman, R. W.; Maziasz, P. J.; Bolling, E.; King, J. F. *Evaluation of Advanced Austenitic Alloys Relative to Alloy Design Criteria for Steam Service: Part 1 – Lean Stainless Steels*; Oak Ridge National Laboratory Report (ORNL-6629/P1); Oak Ridge National Laboratory: Oak Ridge, TN, May 1990; Data sheets on the elevated temperature properties of 18Cr–12Ni–Mo stainless steels for boiler and heat exchanger tubes (SUS 316 HTB), Creep Data Sheet No. 6A; National Research Institute for Metals: Tokyo, Japan, 1978; Teranishi, H.; *et al.* In *Second International Conference on Improved Coal Fired Power Plants*; Electric Power Research Institute: Palo Alto, CA, 1989; EPRI Publication GS-6422 (paper 33-1); Swindeman, R. W.; Maziasz, P. J. In *Creep: Characterization, Damage and Life Assessment*; Woodford, D. A., Townley, C. H. A., Ohnami, M., Eds.; ASM International: Materials Park, OH, 1992; pp 33–42.

2.09.2.4 Precipitation Behavior During Elevated Temperature Aging

Generally, austenitic stainless steels that have no δ -ferrite stay austenitic from room temperature up to about 550 °C, at which temperature they can start to experience the effects of thermal aging. Aging causes the alloy to decompose from a solid solution into various carbide or intermetallic precipitate phases and a more stable austenite phase. The decomposition of a quaternary Fe–Cr–Ni–Mo alloy, typical of type 316 stainless steel at 650 °C, is shown in **Figure 7**, and

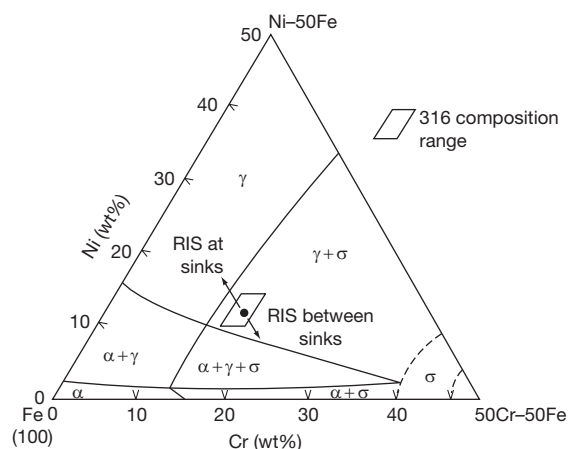


Figure 7 Fe–Cr–Ni–X phase diagram at 650 °C. X = Mo. Reproduced from Maziasz, P. J.; McHargue, C. J. *Int. Mater. Rev.* **1987**, 32(4), 190–219.

the time–temperature–precipitation (TTP) diagrams for aging of SA behavior of type 316 and 316L stainless steel at 500–900 °C are shown in **Figures 8 and 9**.^{12,13} For typical light water reactor (LWR) or fusion reactor applications, such high temperature aging behavior is not too important, but it does become important for understanding irradiation-induced or -produced precipitation behavior for FBR irradiation of components at temperatures 400–750 °C. As indicated in **Figure 8**, prolonged aging of 316 steel at 550 °C and above tend to produce precipitation of Cr-rich $M_{23}C_6$ in the matrix and along grain boundaries, while exposure at 600–750 °C eventually also produce precipitation of M_6C , Laves (Fe_2Mo), and σ ($FeCr$) phases.¹² Precipitation kinetics of these phases appears maximum at 750–850 °C, and then at temperatures above 900–950 °C, none of these phases forms. The lower C content of 316L accelerates and shifts the formation of intermetallic phases relative to 316 steel, as indicated in **Figure 9**. Additions of Ti or Nb cause the formation of MC carbides at the expense of the Cr-rich $M_{23}C_6$ carbides, depending on whether the steel is fully stabilized or not, but can also accelerate the formation of intermetallic phases, such as σ or Laves. If δ -ferrite is present in the alloy, it generally rapidly converts to σ -phase during aging. CW effects tend to accelerate the formation and refine the dispersion of carbides, but they can also significantly enhance the formation of intermetallic phases at lower temperatures, particularly in 20% CW 316.^{12–15} However, careful alloy design and compositional modification

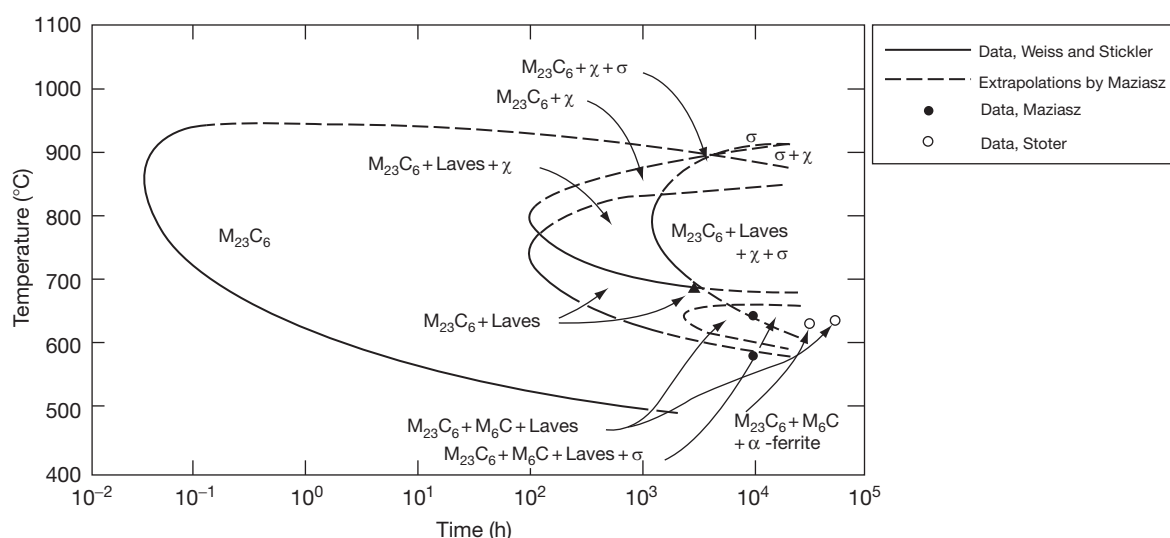


Figure 8 Time–temperature–precipitation phase (TTP) diagram for SA 316 thermally aged. Reproduced from Maziasz, P. J.; McHargue, C. J. *Int. Mater. Rev.* **1987**, 32(4), 190–219.

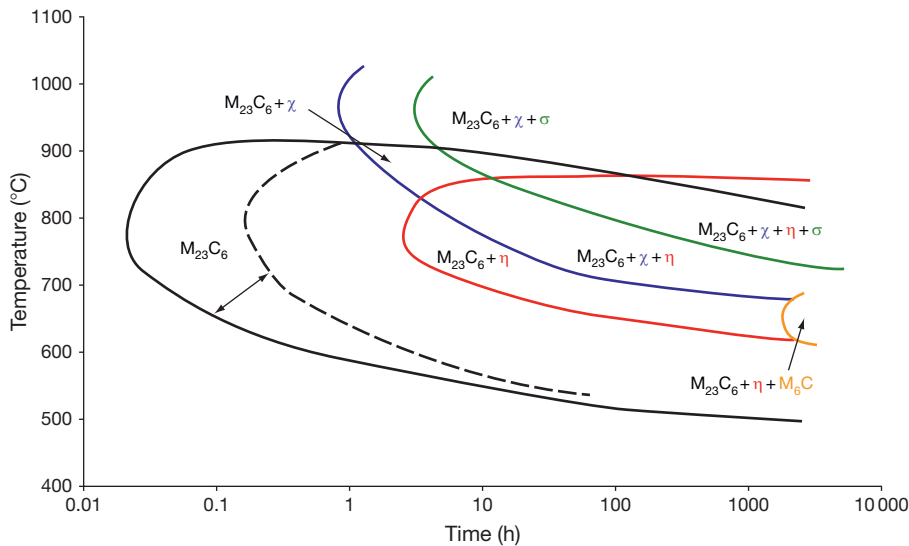


Figure 9 Time-temperature-precipitation diagram of solution-annealed 316L stainless steel during thermal aging. Dashed lines represent a lower solution anneal temperature (1090 °C vs. 1260 °C). Reproduced from Weiss, B.; Stickler, R. *Metall. Trans.* **1972**, 4, 851–866.

of certain austenitic stainless steels, such as the HT-UPS steels, can result in alloys resistant to the formation of σ -phase during aging or creep for up to 60 000 h or more. The various precipitate phases that form in 300 series austenitic stainless steels during thermal aging or creep are listed below, with some information on their nature and characteristics.^{12,14,15}

- $M_{23}C_6$ – fcc, Cr-rich carbide, that can also enrich Mo, W, and Mn, but is generally depleted in Fe, Si, and Ni relative to the 316 alloy matrix.
- M_6C – diamond-cubic phase that can be either a carbide (M_6C – filled, $M_{12}C$ – half-filled) or a silicide phase (M_5Si – unfilled), depending on how carbon fills the atomic structure. It is generally enriched in Si, Mo, Cr, and Ni relative to the 316 alloy matrix.
- MC – fcc Ti- or Nb-rich carbide. The Ti-rich MC phase can also be very rich in Mo, or V and Nb, and may contain some Cr, but tend to contain little or no Fe, Si, and Ni. The Nb-rich MC is a fairly pure carbide phase that can enrich in Ti, but does not usually contain any of the other alloying elements in the 347 or 316 alloy matrix.
- Laves – hexagonal Fe_2Mo -type intermetallic phase. Fe_2Nb and Fe_2W can also be found in steels containing those alloying additions. Phase tends to be highly enriched in Si and can contain some Cr but is generally low in Ni relative to the 316 alloy matrix.
- σ – body-centered-tetragonal intermetallic phase, consisting of mainly Cr and Fe. It can be enriched

somewhat in Mo, but is depleted in Ni relative to the 316 alloy matrix.

- χ – bcc intermetallic phase, enriched in Mo and Cr, and containing mainly Fe, and depleted in Ni relative to the 316 alloy matrix.
- $FeTiP$ or Cr_3P – hexagonal or tetragonal phosphide compounds that can be found in stainless steels containing higher levels of P. $FeTiP$ is found in the HT-UPS steels during aging.

2.09.2.5 Corrosion and Oxidation Behavior

With regard to general corrosion and oxidation, stainless steels with 16–18% Cr passivate and have good resistance to aqueous corrosion and various types of other acidic or corrosive environments at room temperature and up to about 200–300 °C.² Additions of molybdenum give type 316 better resistance to pitting and acidic attack. Effects of stress can aggravate corrosion resistance, and types 304 or 316 processed to have Cr-carbides precipitated along grain boundaries can suffer from stress-corrosion-cracking (SCC), which causes grain-boundary cracking at reduced ductility to embrittle the steel. Lower carbon steels (304LN, 316L) tend to reduce or eliminate SCC, as do the stabilized stainless steel grades such as 321 and 347, which form TiC or NbC carbides to prevent Cr-carbide precipitation at grain boundaries. Exposure to supercritical water at 300 °C and above can be very corrosive, and cause oxidation of

austenitic stainless steels.¹⁶ Generally, 300 series austenitic stainless steels have minimal oxidation in air at 500 °C and below, but oxidation and the protective behavior of chrome-oxide scales become a concern at 550–600 °C and above. Finally, 300 series steels such as types 304 and 316 tend to show little or no corrosion and behave quite well in liquid-metal sodium environments at 650 °C and below. More detailed information on austenitic stainless steels and their corrosion behavior in aqueous environments, oxidation at elevated temperatures, and behavior in liquid metals such as sodium is available in other chapters of this publication, or elsewhere.

2.09.3 Summary of How Properties Can Change During Irradiation

Other chapters in this volume present more details on the fundamental nature and aspects of the primary damage state in irradiated metals and alloys, and on the detailed effects of irradiation on mechanical properties' behavior. This chapter simply highlights some changes in microstructure caused by fission or fusion reactor neutron irradiation, and the changes in properties that they cause in 300 series austenitic stainless steels, to facilitate easy comparison to the unirradiated behavior properties described above. Various other sections of this volume deal in far more detail with the effects of irradiation in various kinds of alloys.

In LWRs at 20–250 °C, the interstitials migrate freely to sinks, while the vacancies or their clusters are relatively immobile, so this has been termed the 'low-temperature regime' of microstructural evolution in austenitic stainless steels.¹⁴ In sodium-cooled FBRs, temperatures are not lower than the sodium coolant, so they are typically 300–350 °C or above, which is termed the 'intermediate-temperature regime,' and both vacancy and interstitial defects can migrate to sinks. Transmutation-produced helium atoms are another form of primary radiation damage that varies with reactor environment (high in LWR and magnetic fusion reactor (MFR) systems, low in FBR systems). Thermal neutrons produce helium in austenitic stainless steels from boron atoms directly, and by a two-step reaction with nickel atoms.¹⁷ He/dpa ratios for LWR systems can be very high, over 100 appm He/dpa, while in mixed-spectrum fission reactors used for radiation-effects studies on materials, the ratios vary from 1 to 70 appm He/dpa. MFRs, with 14 MeV neutrons from D–T fusion

reactions, have linear He/dpa ratios of about 14 appm dpa⁻¹ in a stainless steel first-wall component. The FBR reactors with mainly fast fission neutron spectra produce very low He/dpa ratios of 0.1–0.5 appm He/dpa in austenitic stainless steels. Irradiated materials properties data discussed in the remainder of this section is mainly from LWR or mixed-spectrum fission reactor facilities used to study irradiation effects for MFR applications, so they have relatively high He/dpa ratios as well as a wide range of irradiation temperatures.

The major effects of irradiation in mixed-spectrum fission reactors, such as Oak Ridge Research Reactor (ORR) or High Flux Isotope Reactor (HFIR), on mechanical properties in the low-temperature regime are dramatic hardening (increased YS) and reduced ductility in SA and 316 and Ti-modified 316 stainless steels, and more modest hardening and ductility reduction in 20–25% CW steels. The increased YS for irradiated SA steels are illustrated in [Figure 10.18](#). The SA stainless steels have 250–300 MPa YS in the unirradiation condition, and 50% or more total elongation at room temperature and up to 250–300 °C, but irradiation increases the YS to 600–800 MPa or more, and reduces ductility to 10% or less. However, the fracture mode in this irradiation temperature regime still remains ductile.^{8,9,19} After irradiation, 20–25% CW steels have YS of 800–1000 MPa, and less ductility, but still retain ductile fracture. This is an important feature to note, and despite transmutation-produced helium levels of 1000–2000 appm, they do not embrittle, because helium and vacancy complexes are immobile in this temperature regime. However, most tensile testing results are in vacuum or air, and radiation-induced sensitization in water is not found after irradiation at 20–200 °C, but does become an embrittling factor to consider for irradiation above 300 °C.²⁰

Irradiation-induced hardening of austenitic stainless steels at room temperature to <250 °C is caused by the microstructural changes produced by irradiation in this low-temperature regime. Effects of alloy composition are small in this regime, but the effects of processing condition prior to irradiation (SA or 20–25% CW) are very large. Both SA and 25% CW steels, like 316 or Ti-modified 316, have very dense dispersions of 'black-spot' interstitial loops (2–4 nm diameter) uniformly within the grains,^{2,14,21} as illustrated for 25% CW Ti-modified steel in [Figure 11](#). However, the SA steels also have larger (10–50 nm) diameter Frank (faulted) interstitial loops and no network dislocations, whereas the 25% CW steels

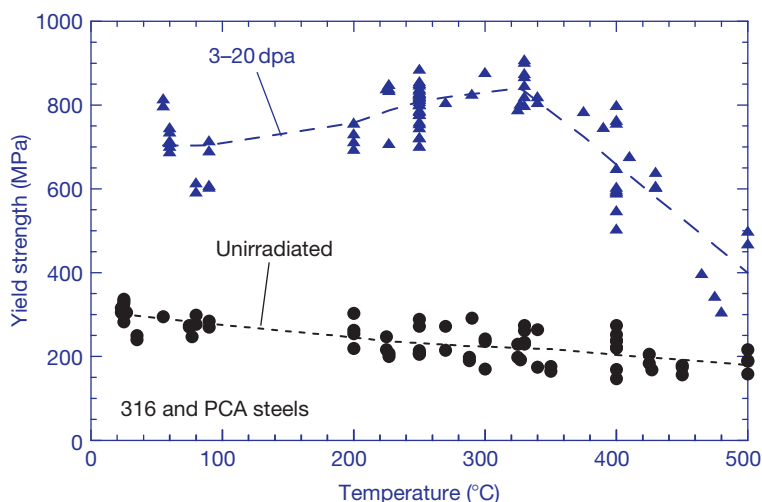


Figure 10 Yield strength as a function of irradiation temperature for SA 316 and PCA in various reactors. Reproduced from Pawel, J. E.; Rowcliffe, A. F.; Lucas, G. E.; Zinkle, S. J. *J. Nucl. Mater.* **1996**, 239, 126–131.

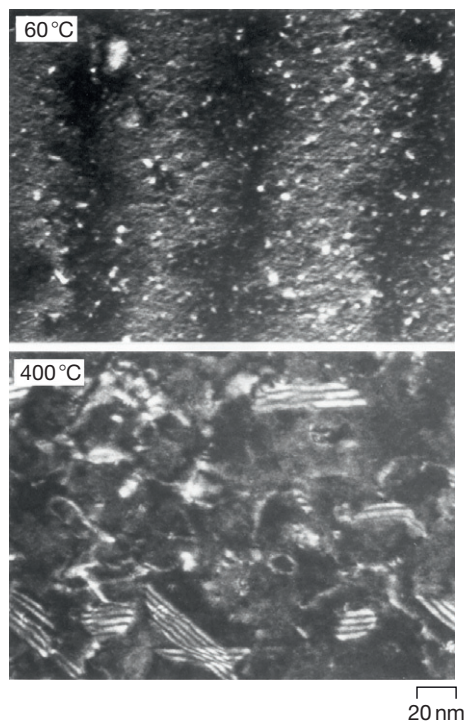


Figure 11 Transmission electron microscopy of black-dot loops in 25% CW PCA irradiated in ORR at 60 and 400°C. Reproduced from Maziasz, P. J. *J. Nucl. Mater.* **1992**, 191–194, 701–705.

have a recovered dislocation network and virtually no large Frank loops (Figure 12). These microstructural effects directly reflect the fact that interstitial defects are main point defects migrating freely to sinks in this temperature regime. Large Frank loops cannot

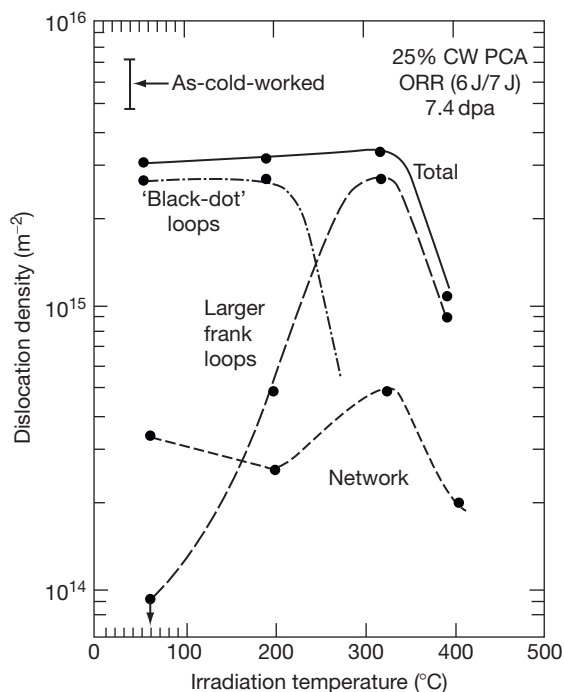


Figure 12 Plot of dislocation density versus irradiation temperature for various components of dislocation structure for 25% CW PCA irradiated in ORR at 60–400°C. Reproduced from Zinkle, S. J.; Maziasz, P. J.; Stoller, R. E. *J. Nucl. Mater.* **1993**, 206, 266–286.

nucleate and grow until the concentration of network dislocations is below some critical concentration. This also affects mechanical behavior, because the 'black-dot' and larger Frank loops are sessile until they unfault, whereas the network dislocations can

climb and glide in response to stress or as they absorb point defects.

Radiation-induced microstructural changes are definitely different at 300 °C and above. In the dislocation structure, the ‘black-dot’ loop damage clearly observed at 200–250 °C is absent at 300–330 °C, and the dislocation structure consists of larger Frank loops and networks that add up to a fairly high total dislocation density.^{14,21,22} There is now also a cavity component of the microstructure, with nanoscale helium bubbles visible at 300–330 °C, and larger voids and helium bubble visible at 400 °C, after irradiation at high He/dpa ratios in mixed-spectrum reactors (ORR, HFIR), or just voids in FBR irradiations at 350–400 °C.^{12,14,22} The appearance of cavities is a clear indication that vacancy or vacancy clusters and complexes (and helium atoms) are migrating in this temperature regime.

Tensile properties of austenitic stainless steels irradiated at 300 °C and above reflect the microstructural changes, particularly the dislocation component of the microstructure. This higher temperature regime in austenitic stainless steels is marked by stronger and more complex temperature and dose dependencies of all the microstructural components, including precipitation and micro/nano-compositional changes.^{14,22} The YS declines from the 800 MPa values at 300 °C to values of about 400 MPa at 500 °C (Figure 10), which approach the YS of unirradiated steels, because all components of the radiation-induced microstructure coarsen, and dislocation density falls by several orders of magnitude. Ductility can vary significantly, but is generally higher (>10%) at 400–500 °C, but not as high as that of unirradiated materials. However, the effects also depend on He/dpa ratio. For FBR irradiations (low He/dpa ratio, <50 dpa), total elongation can be good even at 600–650 °C, but for irradiations in mixed-spectrum reactors such as ORR or HFIR (high He/dpa ratio, >20 dpa), ductility becomes very low above 500 °C, with almost no ductility and brittle grain-boundary fracture at 600 °C due to severe grain-boundary helium embrittlement (>500–1000 appm He). For more detailed information on tensile properties after irradiation, see **Chapter 1.04, Effect of Radiation on Strength and Ductility of Metals and Alloys**.

Microstructural changes produced by irradiation at temperatures of 400 °C and above manifest the intense effects of radiation-induced solute segregation (RIS), which drive nonequilibrium flows and buildups of solute-atoms to sinks (bubbles, voids, dislocation loops and networks, and grain boundaries),

because they are coupled to the point defect flows. Such changes are important to note because prolonged aging at <550 °C produces little or no change to the as-fabricated microstructure. Undersized atoms, such as Ni and Si, strongly couple to interstitial defects, and migrate with them to all sinks. Inverse-Kirkendall effects cause fast-diffusing elements such as Cr and Mo to migrate away from sinks with vacancy fluxes diffusing toward them, whereas slow-diffusing Ni atoms build up at such vacancy sinks. The original austenitic solid-solution alloy phase then unmixes after prolonged irradiation into different kinds of micro/nano-alloys (Figure 7). Regions around the point-defect sinks (voids, loops, and grain boundaries) become enriched in Ni and Si, while the remaining alloy left behind in between such sinks is rich in Cr, and poor in Si and Ni.¹² The different micro/nano-alloy regions become unstable as dose increases, and then transform into various precipitate phases, most of which are radiation-induced or modified relative to the natural thermal precipitation that would form in austenitic alloy during aging at higher temperatures (550–650 °C).^{12,14,15} The most obvious Ni- and Si-rich radiation-induced phase is Ni₃Si γ', which forms abundantly in reactor-irradiated SA 316, as shown in Figure 13, but would not form at all in thermally aged SA 316 (Figure 12).¹⁵ Another extreme effect of such RIS, found in some FBR-irradiated steels, is the actual decomposition of the austenite parent phase into austenite shells around voids and other sinks, and ferrite regions in between.¹⁵ These effects tend to maximize at about 450–550 °C, and then all diminish with increasing irradiation temperature. At 650–700 °C, RIS effects are nearly gone and are replaced by basically thermal-aging effects with slightly enhanced kinetics due to radiation-enhanced diffusion.

In addition to the irradiation-produced mechanical properties described above, irradiation in this higher temperature regime also causes void/cavity swelling to occur. Void swelling is caused by the biased (or preferred) flows of interstitial and vacancy defects to different sinks, with more vacancies flowing to cavities (helium bubbles and voids) and more interstitials flowing to Frank loops and/or radiation-induced precipitates. An example of precipitation-enhanced void swelling in a SA 316 + Ti steel irradiated in ORR at 500 °C to 11 dpa (200 appm He) is shown in Figure 14; clearly the larger voids are directly associated with RIS-induced G-phase (Mn₆Ni₁₆Si₇) silicide particles. Formation of such voids is the direct cause of volumetric swelling in

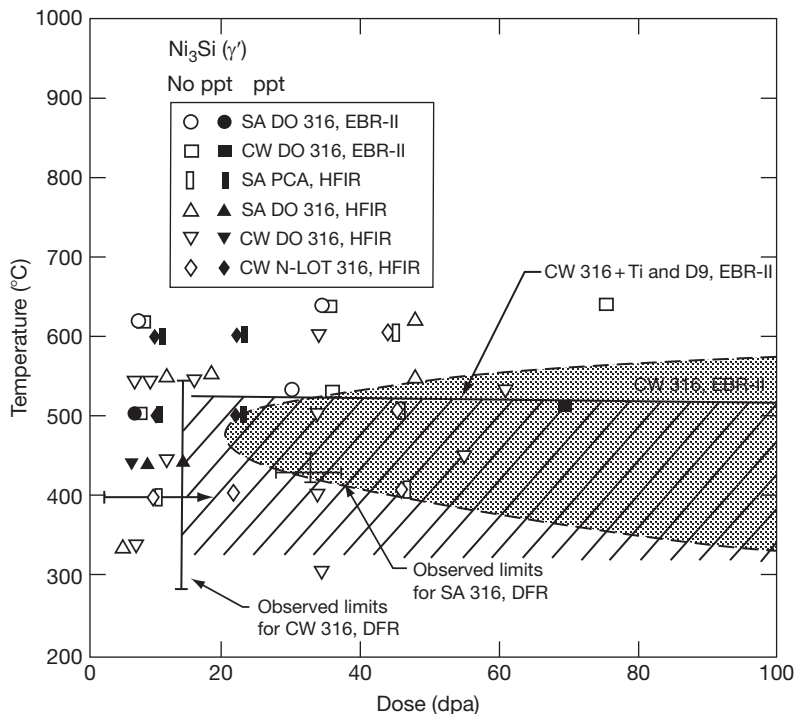


Figure 13 Radiation-induced Ni_3Si γ' formed in SA 316 as a function of dose. Reproduced from Maziasz, P. J. *J. Nucl. Mater.* **1989**, 169, 95–115.

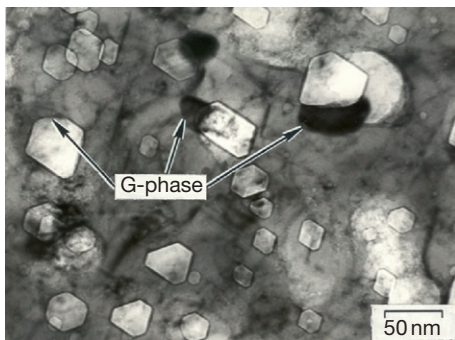


Figure 14 Transmission electron microscopy of radiation-induced voids in SA PCA steel irradiated in ORR at 500 °C to 11 dpa. Largest voids have G-phase particles attached. Reproduced from Maziasz, P. J. *J. Nucl. Mater.* **1989**, 169, 95–115.

reactor-irradiated steel, with an example of swelling of SA 316 steel as a function of dose for FBR irradiation at 420 °C shown in Figure 15.²³ For more detailed information on swelling, see **Chapter 4.02, Radiation Damage in Austenitic Steels**. Such void swelling is generally observed in various FBR or mixed-spectrum reactor environments at 400–650 °C. If very high concentrations of helium bubbles, dislocations, or precipitates become the dominant sinks for

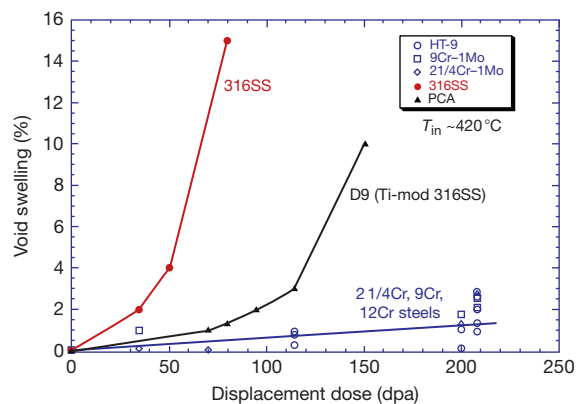


Figure 15 Swelling as a function of dose for fast-breeder reactor irradiated steels. Reproduced from Garner, F. A. In *Nuclear Materials, Part 1*; Frost, B. R. T., Ed.; *Materials Science and Technology: A Comprehensive Treatment*; Cahn, R. W., Haasen, P., Kramer, E. J., Eds.; VCH: Germany, 1994; Vol. 10A, Chapter 6, pp 419–543.

point defects, then all the radiation-induced point defects recombine at those sinks (critical radius for void growth becomes very large), and both void swelling and RIS are suppressed.^{12,14,15,22,24} Such delayed void swelling is seen for dense dispersions of Ti-rich MC carbide particles and dislocation networks

in CW Ti-modified 316 steel (D9 or prime candidate alloy, PCA), as also shown in [Figure 15](#). Very high concentrations of helium bubbles suppress void swelling at 300 °C in mixed-spectrum reactors such as ORR or HFIR (high He/dpa), but as those bubbles coarsen with increased temperature, void swelling is observed, particularly at 500–600 °C. For FBR irradiations (low He/dpa), void swelling will abate at 650–700 °C, with only tiny helium bubbles being visible at grain boundaries at high doses. However, in HFIR (high He/dpa) cavity swelling due to very large helium bubbles can still be 8–10% or more above 650 °C, with large grain-boundary cavities.¹²

One aspect of RIS effects on mechanical properties worth noting and highlighting is RIS causing grain-boundary sensitization. For specimens of 25% CW Ti-modified 316 irradiated in ORR at 330 and 400 °C to 6–7 dpa, electrochemical testing to detect grain-boundary sensitization revealed grain-boundary grooving only at 400 °C, suggesting RIS-induced sensitization due to lower Cr at the grain boundaries.²⁰ Similar ORR irradiation of SA 316 at 400 °C shows ductile fracture when tested in vacuum, but very brittle intergranular fracture when tested in oxygenated water at 300 °C ([Figure 16](#)), suggesting severe RIS-induced sensitization. In LWR systems, concerns about irradiation-assisted stress-corrosion-cracking (IASCC) at about 300 °C and <10 dpa are important for extended service,²⁵ and these data support such concerns and their connection to RIS. For more detailed information on IASCC, see [Chapter 5.12, Material Performance in Supercritical Water](#).

2.09.4 Some Examples of Advanced Alloys for FBR and ITER/Fusion Applications

2.09.4.1 FBR Application

Type 316 stainless steel was the most commonly used steel for FBR applications, and was used in the early prototype and demonstration reactors in the United States and around the world in the mid-to-late 1960s, until void swelling was discovered in 1967. As shown in [Figure 15](#), type 316 is very prone to void swelling. Alloy D9 is an advanced austenitic alloy that was developed during the US National Cladding and Duct Development Program in the 1970s and 1980s.²³ This program was designed to provide advanced materials for the liquid metal fast breeder program with a primary goal of reducing swelling at high relative to types 304 and 316 stainless steels.

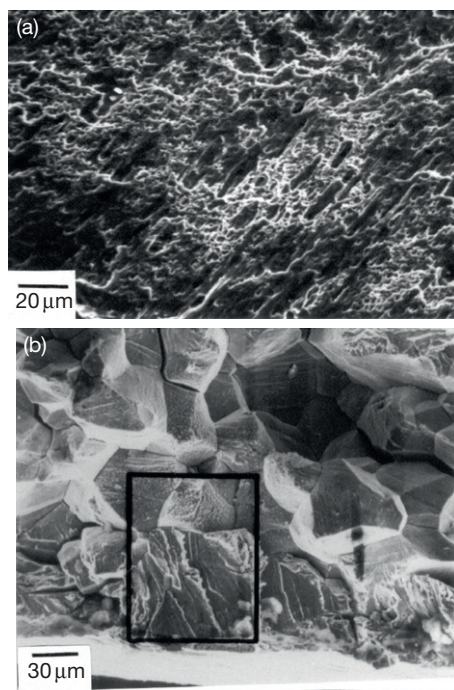


Figure 16 Fracture of SA 316 irradiated in ORR at 400 °C and 7 dpa, (a) tensile tested at a higher strain rate in vacuum at 400 °C, and (b) tensile tested at a slow strain rate in oxygenated water at 300 °C.

D9 is a Fe–15Cr–15Ni alloy with Ti added to produce TiC particles during reactor irradiation or higher temperature creep. Slight variants on this composition have been used in nuclear reactor applications in the United Kingdom, France, Germany, Japan, Russia, and most recently, India. A variant of D9 has currently been used successfully as cladding and for other components in both the Phénix and SuperPhénix reactors. The D9-type austenitic stainless steel has a clear advantage in void swelling resistance compared to 316 steel, but at high doses, voids form and swelling occurs ([Figure 15](#)). Several advanced austenitic stainless steels, including the creep-resistant HT-UPS steel, based on much more stable nano-dispersions of MC-precipitate microstructures relative to the D9-type steel may have better void swelling resistance than D9 steel.^{10,11,14,24} However, FBR irradiation data are needed on the HT-UPS steel to establish such benefits.

Currently, FBR technology in the United States is one of the advanced reactor options being considered by the Gen IV Nuclear Energy Systems Initiative.²⁶ Advanced austenitic steels like D9 have higher maximum allowable design stresses for structural

components that are in the sodium-cooled reactor compared to standard 316 steel but are not exposed to the highest radiation doses found for fuel cladding and duct components. **Figure 17** shows a comparison of the allowable stress benefits of the Ti-modified D9-type alloy, on the basis of higher values of UTS at lower temperatures and design rules that define maximum allowable stress as 33% of the UTS. At higher temperatures, creep-rupture strength is more limiting than tensile strength, so the maximum allowable stress is defined as 66% of the creep-rupture stress for rupture after 100 000 h. While creep-rupture of the D9 alloy is only modestly better than that of type 316 (**Figure 6**), the design window defined by UTS and creep-rupture properties is larger. The HT-UPS steels are austenitic stainless steels developed from the same austenitic steel alloy composition as D9, but with a combination of additions of Ti, V, and Nb rather than just Ti, and minor additions of B and P (**Table 3**). These compositional modifications to the HT-UPS steels produced unusually stable nano-dispersions of MC-carbide precipitates for much better creep-resistance than the D9 steel at 700–800 °C (**Figure 6**).^{10,11} The creep-rupture resistance and strength of the HT-UPS steels are far superior to that of 316 and 347 steels, better than that of other advanced

creep-resistant steels, such as the Nb-stabilized 347HFG, Super 304H, and NF709 austenitic stainless steels and alloys, and comparable to that of the solid-solution strengthened Ni-based superalloy, 617, as shown in **Figure 5**. The creep-resistance of the HT-UPS steel at 700 °C and 170 MPa is several orders of magnitude better than that of the D9 steel, as shown in **Figure 6**, so it should provide even larger design benefits for advanced FBR applications. Since FBR technology has recently evolved to include small, modular reactor systems as well as the more traditional larger reactor systems, advanced steels such as the HT-UPS could provide reactor designers with attractive options to improve or optimize FBR systems without dramatically increasing cost.

2.09.4.2 ITER/Fusion Application

Austenitic stainless steels are also a key component for MFR systems because of many of the properties and vast experience in fission nuclear systems described above. An important example of rapid alloy development is presented, which is part of the US contribution to the international fusion demonstration project in France, called ITER, and includes ~20% of the first wall (FW) and shield components. The ITER project could include nearly

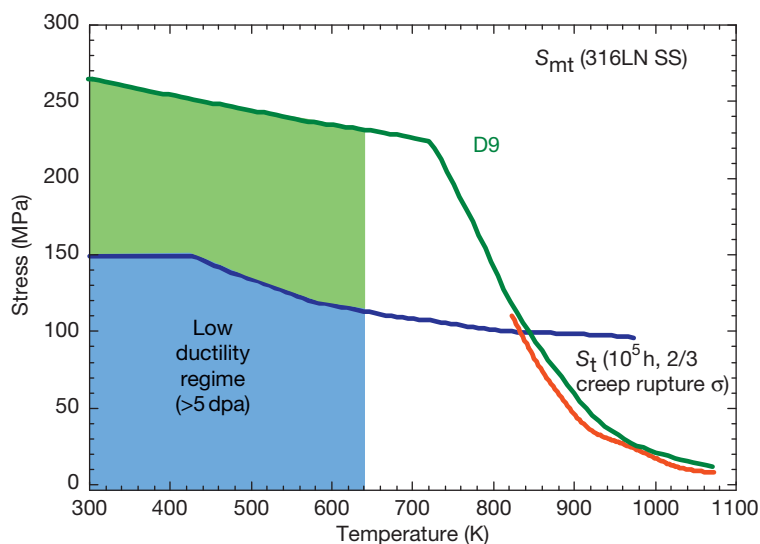


Figure 17 Design window for benefits of D9 over type 316 for fast-breeder reactor application, in terms of maximum allowable stress (S_{mt}) as a function of temperature. The blue line is 33% of the ultimate tensile strength (UTS), and the red line 66% of the creep stress for rupture at 100 000 h. The D9 steel (green lines) has higher UTS, and slightly better creep strength, which opens up the design window. The lower temperature hashed region is arbitrarily set to eliminate the low ductility regime. Reproduced from Busby, J. T.; *et al.* Candidate developmental alloys for improved structural materials for advanced fast reactors; Oak Ridge National Laboratory Report, ORNL/TM – 2008/040 (ORNL/GNEP/LTR-2008-023); Oak Ridge National Laboratory: Oak Ridge, TN, 2008.

100 modules from austenitic stainless steel (316LN-ITER Grade or – IG) each weighing $\sim 3.5T$, and 366 FW panels (SS/CuCrZr/Be). An example of the shield wall module is shown in **Figure 18**. Traditional machining of the cooling channels shown in **Figure 18** results in a loss of $\sim 30\%$ of the raw material during fabrication. A US industry manufacturing assessment indicates that casting the shield modules (including the cooling channels) results in major cost savings when compared to fabrication via welding together quarter modules machined from large forgings. However, because casting produces a large grain size, low dislocation density, and extensive segregation of alloying elements, the strength properties of such cast components are frequently inferior to those of conventionally forged and annealed components. Additional R&D has been performed²⁷ in recent years to ensure that the properties of cast 316L(N)-IG equivalent grades meet ITER Structural Design Criteria,^{28–30} which require cast steel performance that is similar to or no worse than wrought equivalent material.

On the basis of past development experience, archive material analysis, and simulations, several improvement strategies were identified as part of this effort to modify and upgrade the properties of the standard CF3MN cast stainless steel grade (which is described in more detail in Busby *et al.*²⁷) (**Table 3**). The primary strategy identified for boosting the YS was increased strengthening by additions of N and Mn; N is the most powerful solid solution strengthener (0.1 wt% should increase strength by 50 MPa). However, Mn increases are also required to raise the solubility limit of N. In addition, Mn is also an austenite stabilizer, and increases both strength and strain-hardening rate. Industrial partners were involved in the fabrication of test alloys

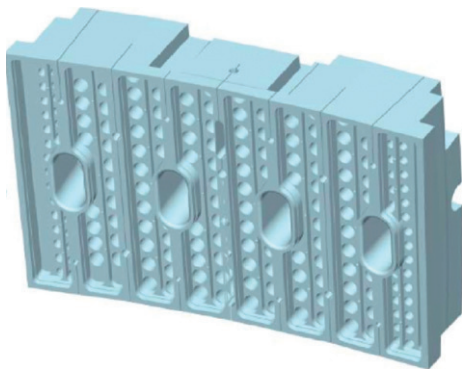


Figure 18 A schematic of an ITER fusion reactor shield wall module.

to help speed scale-up to larger test articles. Alloys with the most minor alloying additions were studied most extensively, with one alloy showing the greatest performance, which is designated CF3MN-US (**Table 3**). Mechanical testing (tensile, impact, and fracture toughness) was performed along with examinations of physical properties, porosity, weldability, and resistance to stress-corrosion cracking.

To accelerate the transition to heavy-section castings, tensile tests were conducted on both cast keel blocks and specimens cut from the larger cross-section as-cast ingots (from both the surface and center regions). These different specimen locations help illustrate the potential differences in mechanical performance. The results from room temperature testing demonstrated no systematic difference between types of specimens, locations of testing, or locations or types of specimen used.

Elevated temperature tests were also performed. The yield stress results for samples in the as-cast condition are illustrated in **Figure 19** and are compared to the minimum requirements for use in ITER applications. At all temperatures, the CF3MN-US exceeds the minimum required strength and meets the ITER acceptance criteria.

An evaluation of impact properties on the CF3MN-US was also conducted. Initial testing was performed using a drop-weight machine setup with a maximum capacity of 325 J potential energy for initial screening tests. Two tests of CM3F-US with the drop weight machine set at 325 J were performed.

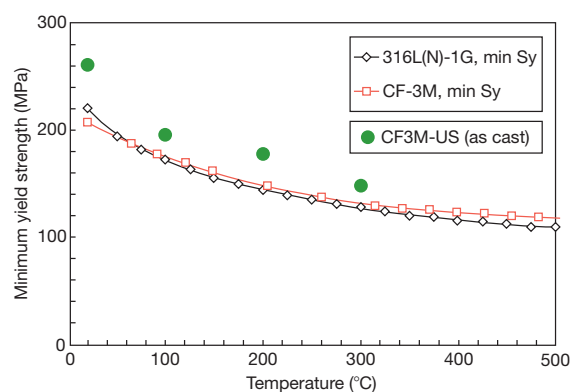


Figure 19 Tensile yield strength (YS) measurements for CF3MN-US (designated CF3M-US here) cast austenitic stainless steel compared with minimum expected values for ITER acceptance. Reproduced from Busby, J. T.; Maziasz, P. J.; Rowcliffe, A. F.; Santella, M.; Sokolov, M. Development of high performance cast stainless steels for ITER shield module applications. *J. Nucl. Mater.* as part of ICFRM-14 Proceedings, 2011.

Only one specimen at -196°C (liquid nitrogen temperature) broke. To demonstrate the excellent toughness of the materials in the temperature range of interest for the ITER shield module applications, additional testing was performed at higher temperatures. Tests were performed at room temperature (27°C), 100, 200, and 300°C , again using a drop-weight machine. All tests at all temperatures were fully ductile and very tough, and none of the specimens tested fractured. **Figure 20** shows a photograph of a Charpy specimen tested in the drop-weight machine at 300°C . It is clear that the specimen did not fracture when tested with a maximum potential energy of 270 J, so its actual impact toughness is higher than that. As indicated earlier in this section, wrought 316 and 347 steel typically have Charpy impact toughness of 100–150 J, so the CF3M-US cast stainless steels exhibit excellent impact toughness, even at the liquid nitrogen temperature (-196°C). The stated minimum impact toughness for the ITER shield module materials is 60 J, whereas the tested specimens exhibited impact toughness values ranging from 140 to 262 J at -196°C .

Finally, testing of fracture toughness properties on the CF3MN-US was performed. The 12.5-mm thick compact tension ($0.5T C(T)$) specimens were tested at room temperature and at 90 and 190°C . At least two specimens of each alloy were tested at each temperature in general accordance with the ASTM E 1820-06.³¹ As expected from the simpler Charpy

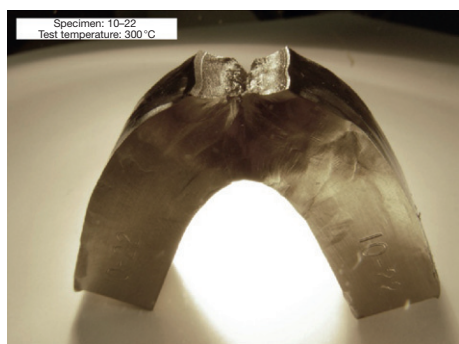


Figure 20 Photo of Charpy impact specimen of CF3MN-US tested at 300°C , with the ASTM striker and showing fully ductile fracture. The potential energy of the machine was 270 J, so the absorbed energy to break the specimens was >270 J. Typical Charpy impact values for SA 316L would be about 150 J. Reproduced from Busby, J. T.; Maziasz, P. J.; Rowcliffe, A. F.; Santella, M.; Sokolov, M. Development of high performance cast stainless steels for ITER shield module applications. *J. Nucl. Mater.* as part of ICFRM-14 Proceedings, 2011.

impact data reported previously, all alloys exhibited very high fracture toughness at all test temperatures. Moreover, none of the specimens exhibited crack extension regardless of test temperature. The value of critical J-integral, J_{1C} , was above 800 kJ m^{-2} at all tested temperatures, comparable or better than that of the equivalent wrought austenitic steel, meeting the ITER acceptance requirements.

While not shown in detail here, testing and evaluation of the most promising alloy under development, CF3MN-US, has been completed for several properties. Composition, ferrite content, microstructure, porosity, mechanical properties (tensile, impact, and fracture toughness), irradiation performance, stress-corrosion cracking performance, and weldability have all been found to meet ITER acceptance criteria. This combination of past experiences, expertise, and new tools demonstrates new opportunities for rapidly developing improved austenitic steels for advanced reactor applications such as ITER. It is also reasonable to expect that the new CF3MN-US steel may have attractive properties in either the cast or wrought condition for advanced LWR core or structural support designs and applications.

Acknowledgment

Research sponsored by the U.S. Department of Energy (DOE), Office of Nuclear Energy, for the FCRD & Gen-IV Research Program, under contract DE-AC05-00OR22725 with UT-Battelle, LLC.

References

1. Washko, S. D.; Aggen, G. In *Metals Handbook: Properties and Selection: Irons, Steels, and High-Performance Alloys*, 10th ed.; ASM International: Materials Park, OH, 1990; Vol. 1, pp 841–907.
2. Lula, R. A. Ed. *Stainless Steel*; ASM International: Materials Park, OH, 1986.
3. Data sheets for types 316 (July, 1988) and 347 (Dec, 1977) stainless steels in Aerospace Structural Materials Database, CINDAS, LLC, West Lafayette, IN, 2010.
4. Swindeman, R. W.; Maziasz, P. J.; Bolling, E.; King, J. F. In *Evaluation of Advanced Austenitic Alloys Relative to Alloy Design Criteria for Steam Service: Part 1 – Lean Stainless Steels*; Oak Ridge National Laboratory Report (ORNL-6629/P1); Oak Ridge National Laboratory: Oak Ridge, TN, 1990.
5. Data sheets on the elevated temperature properties of 18Cr–12Ni–Mo stainless steels for boiler and heat exchanger tubes (SUS 316 HTB), Creep Data Sheet No. 6A; National Research Institute for Metals: Tokyo, Japan, 1978.

6. Teranishi, H.; *et al.* In *Second International Conference on Improved Coal Fired Power Plants*; Electric Power Research Institute: Palo Alto, CA, 1989; EPRI Publication GS-6422 (paper 33-1).
7. Swindeman, R. W.; Maziasz, P. J. In *Creep: Characterization, Damage and Life Assessment*; Woodford, D. A., Townley, C. H. A., Ohnami, M., Eds.; ASM International: Materials Park, OH, 1992; pp 33–42.
8. Maziasz, P. J.; Braski, D. N. *J. Nucl. Mater.* **1986**, *141–143*, 973–977.
9. Klueh, R. L.; Maziasz, P. J. In *Influence of Radiation on Materials Properties: 13th International Symposium (Part II)*, ASTM STP 956; American Society for Testing and Materials: Philadelphia, PA, 1987; pp 207–222.
10. Maziasz, P. J. *J. Met.* **1989**, *41*, 14–20.
11. Maziasz, P. J.; Klueh, R. L.; Rowcliffe, A. F. *MRS Bull.* **1989**, *XIV*, 36–44.
12. Maziasz, P. J.; McHargue, C. J. *Int. Mater. Rev.* **1987**, *32*(4), 190–219.
13. Weiss, B.; Stickler, R. *Metall. Trans.* **1972**, *4*, 851–866.
14. Maziasz, P. J. *J. Nucl. Mater.* **1993**, *205*, 118–145.
15. Maziasz, P. J. *J. Nucl. Mater.* **1989**, *169*, 95–115.
16. Ehrlich, K.; Kony, J.; Heikinheimo, L. *J. Nucl. Mater.* **2004**, *327*, 140–147.
17. Weitman, J.; Daverhog, N.; Farvolden, S. *Trans. Am. Nucl. Soc.* **1970**, *13*, 557.
18. Pawel, J. E.; Rowcliffe, A. F.; Lucas, G. E.; Zinkle, S. J. *J. Nucl. Mater.* **1996**, *239*, 126–131.
19. Jitsukawa, S.; Maziasz, P. J.; Ishiyama, T.; Gibson, L. T.; Hishinuma, A. *J. Nucl. Mater.* **1992**, *191–194*, 771–775.
20. Inazumi, T.; Bell, G. E. C.; Maziasz, P. J.; Kondo, T. *J. Nucl. Mater.* **1992**, *191–194*, 1018–1022.
21. Maziasz, P. J. *J. Nucl. Mater.* **1992**, *191–194*, 701–705.
22. Zinkle, S. J.; Maziasz, P. J.; Stoller, R. E. *J. Nucl. Mater.* **1993**, *206*, 266–286.
23. Garner, F. A. In *Nuclear Materials, Part 1*; Frost, B. R. T., Ed.; *Materials Science and Technology: A Comprehensive Treatment*; Cahn, R. W., Haasen, P., Kramer, E. J., Eds.; VCH: Germany, 1994; Vol. 10A, Chapter 6, pp 419–543.
24. Maziasz, P. J. *J. Nucl. Mater.* **1993**, *200*, 90–107.
25. Allen, T. R.; Busby, J. T. *JOM* **2009**, *61*(7), 29–34.
26. Busby, J. T.; *et al.* Candidate developmental alloys for improved structural materials for advanced fast reactors; Oak Ridge National Laboratory Report, ORNL/TM – 2008/040 (ORNL/GNEP/LTR-2008-023); Oak Ridge National Laboratory: Oak Ridge, TN, 2008.
27. Busby, J. T.; Maziasz, P. J.; Rowcliffe, A. F.; Santella, M.; Sokolov, M. Development of high performance cast stainless steels for ITER shield module applications. *J. Nucl. Mater.* as part of ICFRM-14 Proceedings, 2011.
28. *ITER Structural Design Criteria for In-Vessel Components (ISDC)*; ITER IDoMS S74MA1 97-12-12 R0.2, Appendix A IDoMS G74MA2 98-06-26 F1; 1998.
29. Barabash, V. Proposal for procedure for the acceptance of new materials for the ITER in-vessel components; ITER document, ITER D22JZCS, Sept 2005; Vol. 1.1.
30. Barabash, V. Preliminary requirements: Cast austenitic steel for the blanket application; ITER memo, Aug 28, 2006.
31. Standard Test Method for Measurement of Fracture Toughness, Designation E 1820-06, Annual Book of ASTM Standards, Vol. 03.01.

2.10 Graphite: Properties and Characteristics

T. D. Burchell

Oak Ridge National Laboratory, Oak Ridge, TN, USA

Published by Elsevier Ltd.

2.10.1	Introduction	286
2.10.2	Manufacture	286
2.10.3	Physical Properties	290
2.10.3.1	Thermal Properties	290
2.10.3.2	Electrical Properties	293
2.10.4	Mechanical Properties	294
2.10.4.1	Density	294
2.10.4.2	Elastic Behavior	295
2.10.4.3	Strength and Fracture	297
2.10.4.3.1	Porosity	300
2.10.4.3.2	The binder phase	301
2.10.4.3.3	Filler particles	301
2.10.4.4	Thermal Shock	303
2.10.5	Nuclear Applications	303
2.10.6	Summary and Conclusions	304
References		304

Abbreviations

AE	Acoustic emission
AG	Against-grain
AGR	Advanced gas-cooled reactor
CTE	Coefficient of thermal expansion
FoM	Figure of merit
RMS	Root mean square
WG	With-grain

Symbols

<i>a</i>	Crystallographic <i>a</i> -direction (within the basal plane)
<i>b</i>	Empirical constant
<i>c</i>	Crystallographic <i>c</i> -direction
<i>C</i>	Elastic moduli
<i>C</i>	Specific heat
<i>C_p</i>	Specific heat at constant pressure
<i>E</i>	Young's modulus
<i>G</i>	Shear modulus
<i>h</i>	Planck's constant
<i>k</i>	Boltzmann's constant
<i>K_{IC}</i>	Critical stress-intensity factor
<i>K_T</i>	Thermal conductivity at temperature <i>T</i>
<i>l_a</i>	Mean graphite crystal dimensions in the <i>a</i> -direction

<i>l_c</i>	Mean graphite crystal dimensions in the <i>c</i> -direction
<i>m</i>	Charge carrier effective mass
<i>N</i>	Charge carrier density
<i>P</i>	Fractional porosity
<i>q</i>	Electric charge
<i>R</i>	Gas constant
<i>S</i>	Elastic compliance (1/ <i>C</i>)
<i>T</i>	Stress
<i>T</i>	Temperature
<i>α</i>	Coefficient of thermal expansion
<i>α</i>	Thermal diffusivity
<i>α_a</i>	Crystal coefficient of thermal expansion in the <i>a</i> -direction
<i>α_c</i>	Crystal coefficient of thermal expansion in the <i>c</i> -direction
<i>α</i>	Synthetic graphite coefficient of thermal expansion parallel to the molding or extrusion direction
<i>α_⊥</i>	Synthetic graphite coefficient of thermal expansion perpendicular to the molding or extrusion direction
<i>Δ_{th}</i>	Thermal shock figure of merit
<i>γ</i>	Cosine of the angle of orientation with respect to the <i>c</i> -axis of the crystal
<i>θ_D</i>	Debye temperature
<i>λ</i>	Charge carrier mean-free path

μ	Charge carrier mobility
ν	Poisson's ratio
ν_f	Charge carrier velocity at the Fermi surface
ρ	Bulk density
σ	Electrical conductivity
σ	Strength
σ_y	Yield strength
τ	Relaxation time
ω	Frequency of vibrational oscillations

2.10.1 Introduction

Graphite occurs naturally as a black lustrous mineral and is mined in many places worldwide. This natural form is most commonly found as natural flake graphite and significant deposits have been found and mined in Sri Lanka, Germany, Ukraine, Russia, China, Africa, the United States of America, Central America, South America, and Canada. However, artificial or synthetic graphite is the subject of this chapter.

The electronic hybridization of carbon atoms ($1s^2$, $2s^2$, $2p^2$) allows several types of covalent-bonded structures. In graphite, we observe sp^2 hybridization in a planar network in which the carbon atom is bound to three equidistant nearest neighbors 120° apart in a given plane to form the hexagonal graphene structure. Covalent double bonds of both σ -type and π -type are present, causing a shorter bond length than that in the case of the tetrahedral bonding (σ -type sp^3 orbital hybridization only) observed in diamond. Thus, in its perfect form, the crystal structure of graphite (Figure 1) consists of tightly bonded (covalent) sheets of carbon atoms in a hexagonal lattice network.¹ The sheets are weakly bound with van der Waals type bonds in an ABAB stacking sequence with a separation of 0.335 nm.

The invention of an electric furnace^{2,3}, capable of reaching temperatures approaching 3000°C , by Acheson in 1895 facilitated the development of the process for the manufacture of artificial (synthetic) polygranular graphite. Excellent accounts of the properties and application of graphite may be found elsewhere.⁴⁻⁶

2.10.2 Manufacture

Detailed accounts of the manufacture of polygranular synthetic graphite may be found elsewhere.^{2,4,7} Figure 2 summarizes the major processing steps in

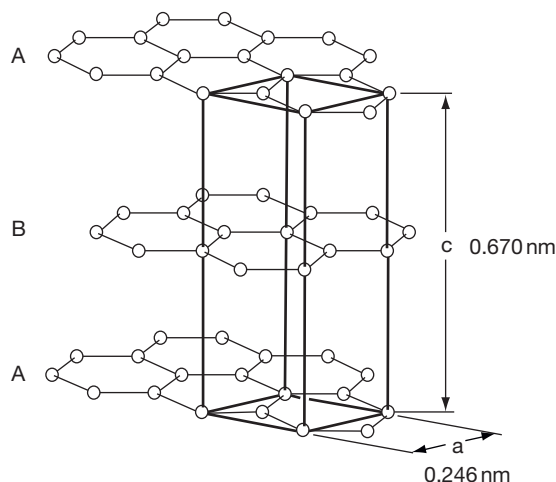


Figure 1 The crystal structure of graphite showing the ABAB stacking sequence of graphene planes in which the carbon atoms have threefold coordination. Reproduced from Burchell, T. D. In *Carbon Materials for Advanced Technologies*; Burchell, T. D., Ed.; Elsevier Science: Oxford, 1999.

the manufacture of synthetic graphite. Synthetic graphite consists of two phases: a filler material and a binder phase. The predominant filler materials are petroleum cokes made by the delayed coking process or coal–tar pitch-derived cokes. The structure, shape, and size distribution of the filler particles are major variables in the manufacturing process. Thus, the properties are greatly influenced by coke morphology. For example, the needle coke used in arc furnace electrode graphite imparts low electrical resistivity and low coefficient of thermal expansion (CTE), resulting in anisotropic graphite with high thermal shock resistance and high electrical conductivity, which is ideally suited for the application. Such needle-coke materials would, however, be wholly unsuited for nuclear graphite applications, where a premium is placed upon isotropic behavior (see Chapter 4.10, Radiation Effects in Graphite). The coke is usually calcined (thermally processed) at $\sim 1300^\circ\text{C}$ prior to being crushed and blended.

The calcined filler, once it has been crushed, milled, and sized, is mixed with the binder (typically a coal–tar pitch) in heated mixers, along with certain additives to improve processing (e.g., extrusion oils). The formulations (i.e., the amounts of specific ingredients to make a specified grade) are carefully followed to ensure that the desired properties are attained in the final products. The warm mix is transferred to the mix cylinder of an extrusion press, and

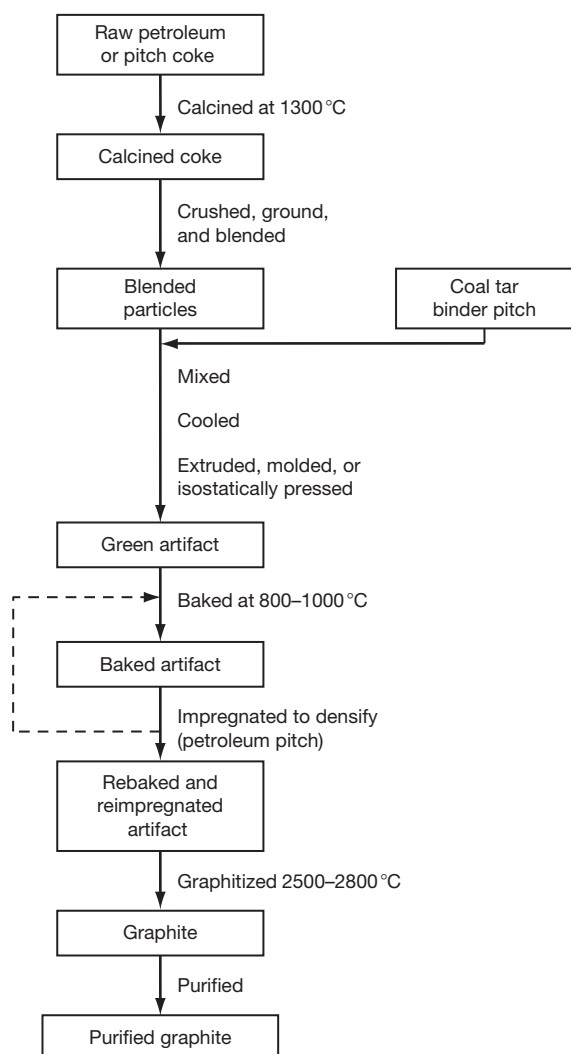


Figure 2 The major processing steps in the manufacture of nuclear graphite.

the mix is extruded to the desired diameter and length. Alternately, the green mix may be molded into the desired form using large steel molds on a vertical press. Vibrational molding and isostatic pressing may also be used to form the green body. The green body is air- or water-cooled and then baked to completely pyrolyze the binder.

Baking is considered the most important step in the manufacture of carbon and graphite. The pitch binder softens upon heating and goes through a liquid phase before irreversibly converting into a solid carbon. Consequently, the green articles can distort or slump in baking if they are not properly packed in the furnace. If the furnace-heating rate is too rapid, the volatile gases evolved during pyrolysis cannot easily diffuse out of the green body, and it may crack. If a sufficiently high temperature is not achieved, the baked carbon will not attain the desired density and physical properties. Finally, if the baked artifact is cooled too rapidly after baking, thermal gradients may cause the carbon blocks to crack. For all of these reasons, utmost care is taken over the baking process.

Bake furnaces are usually directly heated (electric elements or gas burning) and are of the pit design. The furnaces may be in the form of a ring so that the waste heat from one furnace may be used to preheat the adjacent furnace. The basic operational steps include (1) loading, (2) preheating (on waste gas), (3) gas heating (on fire), (4) cooling (on air), and (5) unloading. Typical cycle times are of the order of hundreds of hours (Figure 3). The green bodies are stacked into the furnace and the interstices filled with pack materials (coke and/or sand). Thermocouples are placed at set locations within the furnace to allow

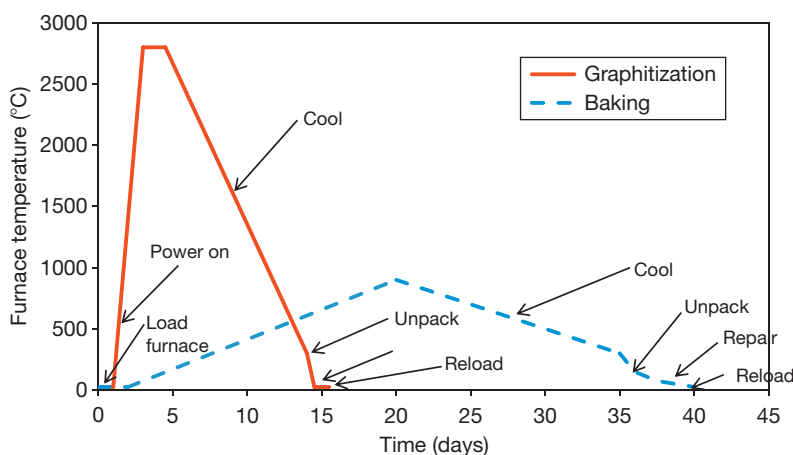


Figure 3 Typical time versus temperature cycles for baking and graphitizing steps in the manufacture of graphite.

direct monitoring and control of the furnace temperature. More modern furnaces may be of the car-bottom type, in which the green bodies are packed into saggars (steel containers) with 'pack' filling the space between the green body and the saggars. The saggars are loaded onto an insulated rail car and rolled into a furnace. The rail car is essentially the bottom of the furnace. Thermocouples are placed within the furnace to allow direct monitoring and control of the baking temperature.

The furnaces are unpacked when the product has cooled to a sufficiently low temperature to prevent damage. Following unloading, the baked carbons are cleaned, inspected, and certain physical properties determined. The carbon products are inspected, usually on a sampling basis, and their dimensions, bulk density, and specific resistivity are determined. Measurement of the specific electrical resistivity is of special significance since the electrical resistivity correlates with the maximum temperature attained during baking. Minimum values of bulk density and maximum values of electrical resistivity are specified for each grade of carbon/graphite that is manufactured.

Certain baked carbon products (those to be further processed to produce synthetic graphite) will be densified by impregnation with a petroleum pitch, followed by rebaking to pyrolyze the impregnant pitch. Depending upon the desired final density, products may be reimpregnated several times. Useful increases in density and strength are obtained with up to six impregnations, but two or three are more common. The final step in the production of graphite is a thermal treatment that involves heating the carbons to temperatures in excess of 2500 °C. Graphitization is achieved in an Acheson furnace in which heating occurs by passing an electric current throughout the baked products and the coke pack that surrounds them. The entire furnace is covered with sand to exclude air during operation. Longitudinal graphitization is increasingly used in the industry today. In this process, the baked forms are laid end to end and covered with sand to exclude air. The current is carried in the product itself rather than through the furnace coke pack. During the process of graphitization (2500–3000 °C), in simplistic terms, carbon atoms in the baked material migrate to form the thermodynamically more stable graphite lattice.

Certain graphite require high chemical purity. This is achieved by selecting very pure cokes, utilizing a high graphitization temperature (>2800 °C), or

by including a halogen purification stage in the manufacture of the cokes or graphite, either during graphitization or as a postprocessing step. Graphite manufacture is a lengthy process, typically 6–9 months in duration.

Graphite structure is largely dependent upon the manufacturing process. Graphites are classified according to their 'grain' size⁸ from coarse-grained (containing grains in the starting mix that are generally >4 mm) to microfine-grained (containing grains in the starting mix that are generally <2 μm). The forming process will tend to align the grains to impart 'texture' to the green body. The extrusion process will align the grains with their long axis parallel to the forming axis, whereas molding and vibrational molding will tend to align the long axis of the particles in the plane perpendicular to the forming axis. Thus, molded graphite has two perpendicular with-grain (WG) orientations and one against-grain (AG) orientation, whereas extruded graphite has one WG orientation (parallel to the billets long axis) and two AG orientations. Isostatically pressed graphite does not exhibit a preferred orientation. Examples of various graphite microstructures are present in **Figures 4–10**. The graphite grades shown in **Figures 4–10** have all either been used in nuclear applications or been candidates for nuclear reactor use.⁹ Grade AGOT (**Figure 4**) was used as the moderator in the earliest nuclear reactors in the United States. Pile grade A (PGA) graphite (**Figure 5**) was used as the moderator in the early air-cooled reactors and Magnox reactors in the United Kingdom.⁹ Grade NBG-18 is a candidate for the next generation of high-temperature reactors. Grade IG-110 (**Figures 7 and 8**) is the moderator material

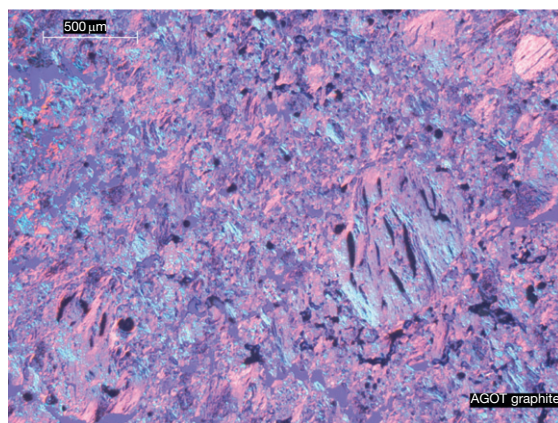


Figure 4 Grade AGOT graphite microstructure (viewed under polarized light).

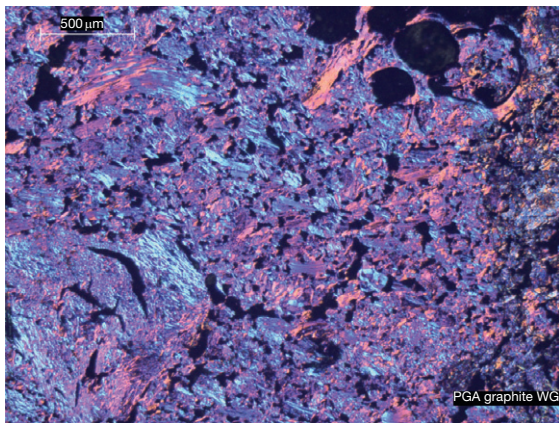


Figure 5 Grade PGA graphite (with-grain) microstructure (viewed under polarized light).

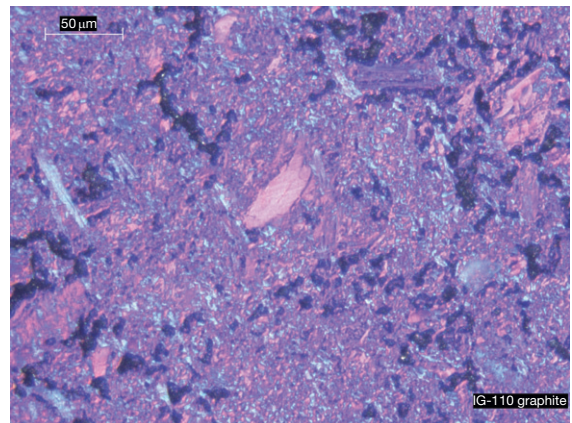


Figure 8 Grade IG-110 graphite microstructure (viewed under polarized light).

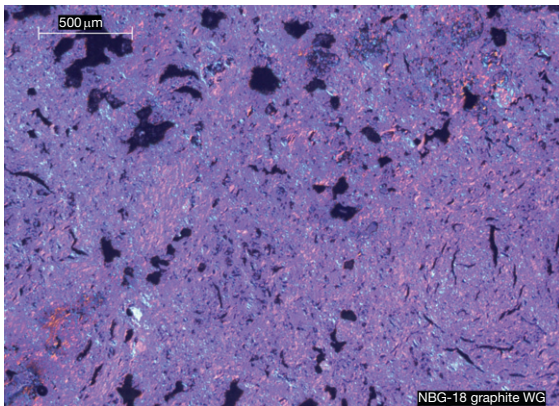


Figure 6 Grade NBG-18 graphite (with-grain) microstructure (viewed under polarized light).

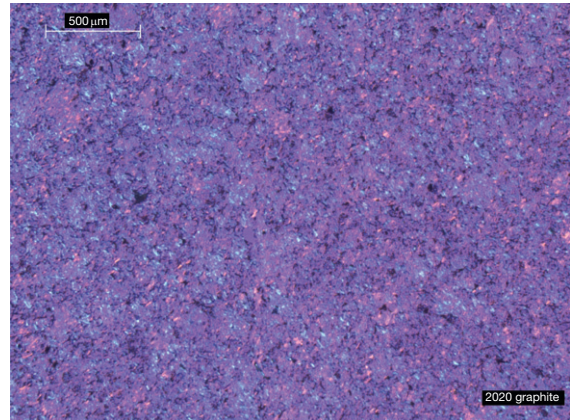


Figure 9 Grade 2020 graphite microstructure (viewed under polarized light).

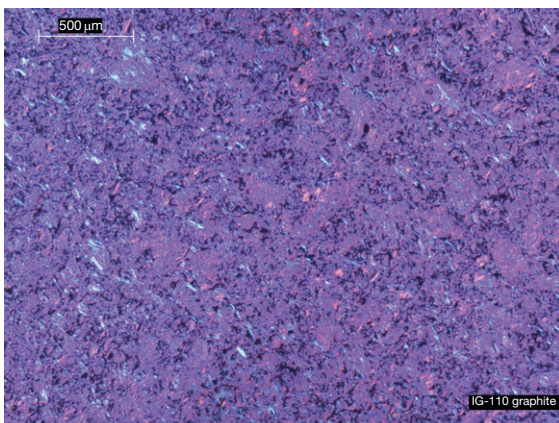


Figure 7 Grade IG-110 graphite microstructure (viewed under polarized light).

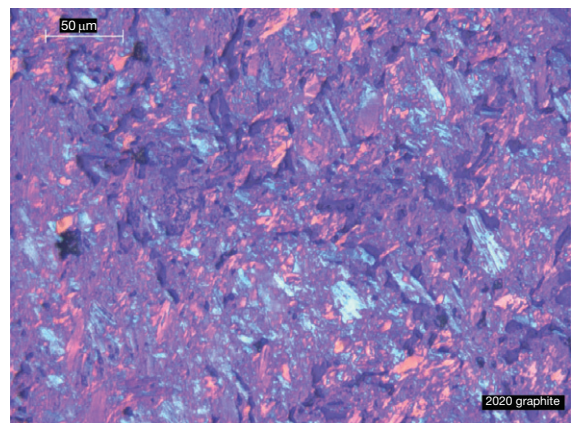


Figure 10 Grade 2020 graphite microstructure (viewed under polarized light).

in the high-temperature test reactor in Japan, and grade 2020 graphite (Figures 9 and 10) was a candidate for the core support structure of the modular high-temperature gas-cooled reactor in the United States.

A comparison of Figures 4 and 7 indicates the range of nuclear graphite textures. Figure 4 shows the structure of AGOT graphite, an extruded medium-grained, needle-coke graphite (maximum filler size ~ 0.75 mm) and Figure 7 shows the structure of IG-110 graphite, an isostatically pressed, fine-grained graphite (maximum filler size ~ 10 μ m). Similarly, grade 2020 (Figures 9 and 10) is also a fine-grained, isostatically pressed graphite. The UK graphite PGA is extruded needle-coke graphite with a relatively coarse texture (Figure 5). The large individual needle-coke filler particles (named needle coke because of their acicular structure) can clearly be distinguished in this graphite. Another dominant feature of graphite texture can easily be distinguished in Figure 5, namely porosity. Graphite single crystal density is 2.26 g cm^{-3} , while the bulk density is $\sim 1.75 \text{ g cm}^{-3}$. The difference can be attributed to the porosity that is distributed throughout the graphite structure.¹⁰ About half the total porosity is open to the surface, while the remainder is closed. In the case of PGX graphite, large pores in the structure result in relatively low strength. The formation of pores and cracks in the graphite during manufacture adds to the texture arising from grain orientation and causes anisotropy in the graphite physical properties. Three classes of porosity may be identified in synthetic graphite:

- Those formed by incomplete filling of voids in the green body by the impregnant pitch; the voids originally form during mixing and forming.
- Gas entrapment pores formed from binder phase pyrolysis gases during the baking stage of manufacture.
- Thermal cracks formed by the anisotropic shrinkage of the crystals in the filler coke and binder.

Isotropic behavior is a very desirable property in nuclear graphite (see Chapter 4.10, **Radiation Effects in Graphite**) and is achieved in modern nuclear graphite through the use of cokes¹¹ with an isotropic structure in the initial formulation.

Coke isotropy results in large measure from the optical domain structure of the calcined coke. The optical domain size is a measure of the extended-preferred orientation of the crystallographic basal planes. Essentially, the optical domain size and structure (domains are the isochromatic regions in the

coke and binder revealed when the structure is viewed at high magnification on an optical microscope under polarized light) controls the isotropy of the filler coke. Anisotropic ‘needle’ cokes have relatively large extended optical domains, whereas ‘isotropic’ cokes exhibit smaller, randomly orientated domains. The domain structure of a coke is developed during delayed coking through pitch pyrolysis chemistry (mesophase formation) and coking transport phenomena. At the atomic scale, orientation of the crystallographic structure is characterized using X-ray diffraction analysis. The crystal spacing within the graphitized artifact may be determined (the dimensions a and c in Figure 1). Moreover, the extent to which the basal planes are parallel to one another, or crystal coherence length (l_a), and the mean height over which the layers are stacked in a coherent fashion (l_c) may be defined. These two parameters, l_a and l_c (the crystal coherence lengths), define the perfection of the crystal (contained within the graphitized coke and binder) and the degree of graphitization.

An important feature of artificial graphite structure, which has a controlling influence upon the material properties, is that the structural feature dimensions span several orders of magnitude. The crystal lattice parameters are fractions of a nanometer ($a = 0.246 \text{ nm}$, $c = 0.67 \text{ nm}$). The crystallite ‘coherent domains’ or extent of three-dimensional order, l_a and l_c , are typically tens of nanometers (l_c = stack height = $15\text{--}60 \text{ nm}$ and l_a = stack width = $25\text{--}60 \text{ nm}$). The thermal microcracks between planes are typically the size of crystallites. Within the graphite, the optical domain (extended orientation of crystallites) may typically range from 5 to $200 \mu\text{m}$ and largely controls the isotropy of synthetic graphite. As discussed earlier, graphite grain size (usually refers to largest filler particles) is a manufacturing variable and is typically in the range $1 \mu\text{m}$ to 5 mm . Finally, the pore size, depending upon the category and location (pores could be within filler or binder phases) is commensurate with grain size. The largest pores (excluding thermal cracks between the crystal layers) are typically $10 \mu\text{m}$ to a few millimeters.

2.10.3 Physical Properties

2.10.3.1 Thermal Properties

The thermal behavior of a solid material is controlled by the interatomic forces through the vibrational spectrum of the crystal lattice. The properties are

generally insensitive to the spectrum details because they derive from a wide range of wavelengths in the spectrum. However, the graphite crystal is highly anisotropic because of the in-plane, strong covalent bonds and out-of-plane, weak van der Waals bonds, so the above generalizations are not necessarily applicable. Moreover, the electronic contributions to the thermal behavior must be considered at low temperatures.

A complete and comprehensive review of the thermal properties of graphite has been written by Kelly.¹² Heat energy is stored in the crystal lattice in the form of lattice vibrations. These vibrations are considered to be standing waves and thus can only have certain permitted frequencies (density of states of waves). These waves produce atomic displacements, which can be resolved so as to be parallel to the wave vector (longitudinal waves) and in two directions perpendicular to it (transverse waves).

The Debye equation thus gives the specific heat, C , as

$$C = 9R \left(\frac{T}{\theta_D} \right)^3 \int_0^{\theta_D/T} \frac{z^4 e^z}{(e^z - 1)^2} dz \quad [1]$$

where R is the gas constant ($8.314 \text{ J mol}^{-1} \text{ K}$); T , temperature; θ_D , Debye temperature; and $z = \hbar\omega/kT$, where ω , frequency of vibrational oscillations; k , Boltzmann's constant; T , temperature; and $\hbar = h/2\pi$, where h is the Planck's constant.

At low temperatures, where $(T/\theta_D) < 0.1$, z in eqn [1] is large and we can approximate eqn [1] by allowing the upper limit in the integral to go to infinity such that the integral becomes $\sim (\pi^4/15)$, and on differentiating we get

$$C = 1941 (T/\theta_D)^3 \text{ J mol}^{-1} \text{ K} \quad [2]$$

Thus, at low temperatures, the specific heat is proportional to T^3 (eqn [2]). At high temperatures, z is small and the integral in eqn [1] reduces to $z^2 dz$, hence on integrating we get the Dulong–Petit value of $3R$, that is, the theoretical maximum specific heat of $24.94 \text{ J mol}^{-1} \text{ K}$. As we are typically concerned only with the specific heat at temperatures above 10% of the Debye temperature ($0.1\theta_D$), the specific heat should rise exponentially with temperature to a constant value at $T \approx \theta_D$, the Debye temperature. The specific heat of graphite is shown in Figure 11 over the temperature range 300–3000 K. Experimental data have been shown to be well represented by eqn [3],¹³ which is applicable to all graphite.

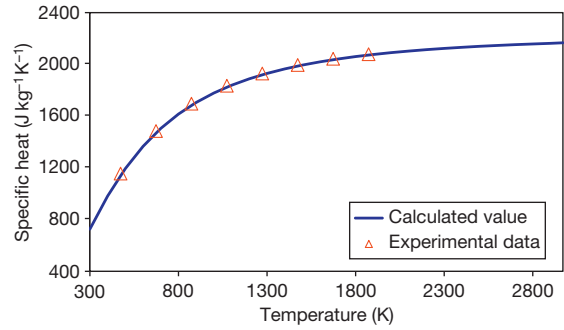


Figure 11 The temperature dependence of the specific heat of graphite, a comparison of calculated values and literature data for POCO AXM-5Q graphite. Sources: ASTM C781,¹³ data from Hust, J. G. *NBS Special Publication 260-89*; U.S. Department of Commerce, National Bureau of Standards, 1984; p 59.

$$C_p = \frac{1}{11.07 T^{-1.644} + 0.0003688 T^{0.02191}} \text{ J kg}^{-1} \text{ K} \quad [3]$$

The hexagonal graphite lattice has two principal thermal expansion coefficients¹⁴; α_c , the thermal expansion coefficient parallel to the hexagonal c -axis, and α_a , the thermal expansion coefficient of the crystal parallel to the basal plane (a -axis). The thermal expansion coefficient in any direction at an angle φ to the c -axis of the crystal is given by eqn [4]:

$$\alpha(\varphi) = \alpha_c \cos^2 \varphi + \alpha_a \sin^2 \varphi \quad [4]$$

The value of α_c varies linearly with temperature from $\sim 25 \times 10^{-6} \text{ K}^{-1}$ at 300 K to $\sim 35 \times 10^{-6} \text{ K}^{-1}$ at 2500 K. In contrast, α_a is much smaller and increases rapidly from $-1.5 \times 10^{-6} \text{ K}^{-1}$ at $\sim 300 \text{ K}$ to $\sim 1 \times 10^{-6} \text{ K}^{-1}$ at 1000 K and remains relatively constant at temperatures up to 2500 K. The thermal expansion coefficients of synthetic graphite are a function of the (1) crystal anisotropy, (2) the orientation of the crystallites (i.e., textural effects arising during manufacture), and (3) the presence of suitably oriented porosity. A billet of molded or extruded graphite would exhibit the same symmetry as the graphite crystal due to alignment of the crystallites during the forming process, with the thermal expansion coefficients α_c and α_a being replaced with α_{\parallel} (parallel to the molding or extrusion axis) and α_{\perp} (perpendicular to the molding or extrusion direction), respectively. However, the thermal expansion coefficients of polycrystalline graphites are typically significantly less than that of the graphite crystallites. Mrozowski¹⁵ was the first to associate this phenomenon with the presence of pores and cracks in the polycrystalline graphite that were preferentially aligned with the graphitic basal planes, thereby preventing the high

c -axis crystal expansion from contributing fully to the observed bulk expansion. The thermal closure of aligned internal porosity results in an increasing instantaneous and mean CTE with temperature and, significantly, an increasing strength with temperature up to temperatures of $\sim 2200^\circ\text{C}$. In high-density isotropic graphite, the CTE more closely approaches the graphite crystallite value.

Figure 12 illustrates the above thermal expansion trends. Figure 12(a) shows the expansion behavior of several graphite grades and Figure 12(b) shows the average CTE. All three graphite grades (Poco, PCEA, and IG-110) show increasing expansivity with increasing temperature due to the thermal closure of internal porosity. PCEA, the extruded grade, displays greater thermal expansion and a greater average CTE in the AG direction than in the WG direction, reflecting the preferred orientation of the filler-coke particles due to the forming process. Poco graphite is particularly high-density isotatically pressed graphite (hence the relatively large expansion and CTE). PCEA is a medium-grain extruded grade and clearly

displays different thermal expansion behavior depending upon the orientation (WG or AG). Grade IG-110 is a fine-grain, isotatically pressed grade but displays a lower density (and CTE) than Poco graphite.

Graphite is a phonon conductor of heat. Consequently, the thermal conductivity of a graphite single crystal is highly anisotropic, reflecting the different bond types within and between the carbon basal planes. In the crystallographic a -directions (within the basal plane), the atom bonding is of the primary, covalent type, whereas between the basal planes (crystallographic c -direction), the bonding is of the much weaker secondary or van der Waals type. Phonons (elastic waves) may thus travel considerably more easily in the a -direction than in the c -direction within a graphite single crystal.

Kelly¹² has reviewed the data for the thermal conductivity of natural and pyrolytic graphite (single crystal similes). The room-temperature thermal conductivity parallel to the basal planes is typically $>1000\text{ W m}^{-1}\text{ K}$, whereas perpendicular to the basal planes, the room-temperature thermal conductivity

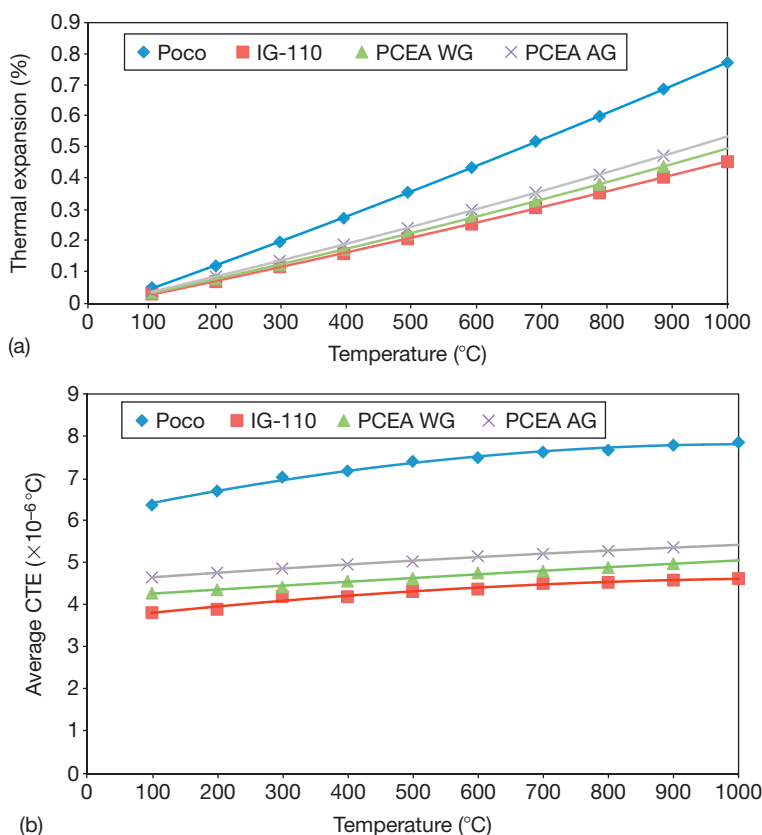


Figure 12 Thermal expansion behavior of various graphite grades (a) thermal expansion versus measurement temperature and (b) average coefficient of thermal expansion versus temperature.

is typically $<10 \text{ W m}^{-1} \text{ K}$. The thermal conductivity of graphite shows a maximum with temperature at $\sim 100 \text{ K}$. Below this maximum, the conductivity is dominated by the specific heat and varies as $\sim T^3$. At higher temperatures, above the maxima, the thermal conductivity decreases with increasing temperature due to phonon scattering. Measurements on single crystals by Smith and Rasor¹⁶ showed that the maxima in thermal conductivity parallel to the basal plane was located at $\sim 80 \text{ K}$ at a value of $2800 \text{ W m}^{-1} \text{ K}$. Nihira and Iwata¹⁷ reported the maximum thermal conductivity (perpendicular to the basal planes) for a pyrolytic graphite to be located at 75 K with a value of $\sim 20 \text{ W m}^{-1} \text{ K}$. At extremely low temperatures, that is, $T < 10 \text{ K}$, the thermal conductivity is dominated by an electronic contribution that is proportional to temperature.

The temperature dependence of the in-plane thermal conductivity is shown in **Figure 13** for various forms of pyrolytic graphites. Substantial improvements in thermal conductivity caused by thermal annealing and/or compression annealing are attributed to increased crystal perfection and increases in the size of the regions of coherent ordering (crystallites), which minimizes the extent of phonon-defect scattering and results in a larger phonon mean-free path. With increasing temperature, the dominant phonon interaction becomes phonon-phonon scattering (Umklapp processes).

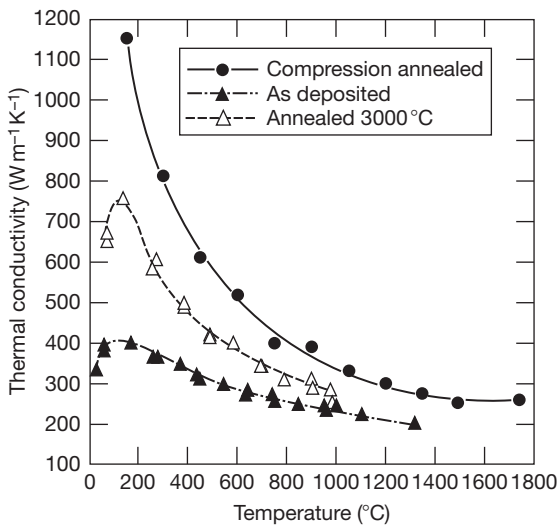


Figure 13 The temperature dependence of thermal conductivity for pyrolytic graphite in the as-deposited, annealed, and compression-annealed condition. Data from Roth, E. P.; Watson, R. D.; Moss, M.; Drotning, W. D. Sandia National Laboratory Report No. SAND-88-2057, UC-423; 1989.

Therefore, the observed reduction in thermal conductivity with increasing temperature and the convergence of the curves in **Figure 13** are attributed to the dominant effect of Umklapp scattering in reducing phonon mean-free path.

A popular method for determining the thermal conductivity of carbon and graphite is the thermal ‘flash’ technique in which a small specimen is exposed to a thermal pulse, usually from a xenon flash lamp or a laser, and the back face of the specimen observed with an infrared detector. The specimen’s thermal conductivity is then determined from the back face temperature-rise transient. The thermal conductivity (measured in $\text{W m}^{-1} \text{ K}^{-1}$) at the temperature T is calculated from the relationship

$$K_T = \alpha C_p \rho \quad [5]$$

where α is the thermal diffusivity ($\text{m}^2 \text{ s}^{-1}$), C_p is the specific heat at temperature T ($\text{J kg}^{-1} \text{ K}^{-1}$), and ρ is the density (kg m^{-3}).

Figure 14 shows data for the temperature dependence of thermal conductivity of typical near-isotropic synthetic graphite. The data were obtained using the laser-flash method over the temperature range 373–1873 K (calculated from eqn [5]) and illustrate the reduction of thermal conductivity with increasing temperature and textural effects in an extruded graphite because of filler-coke orientation.

2.10.3.2 Electrical Properties

The electrical conductivity, σ , for a given group of charge carriers can be written¹⁸ as

$$\sigma = Nq\mu = \frac{q^2 N \tau}{m} \quad [6]$$

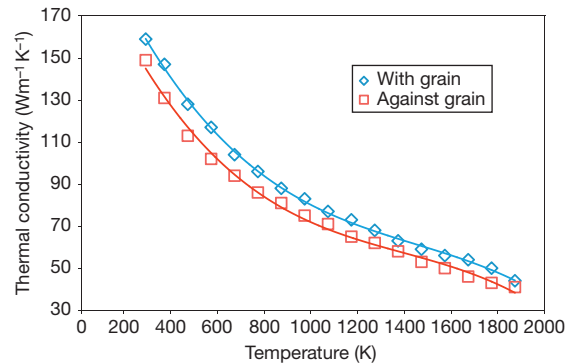


Figure 14 The temperature dependence of a typical extruded synthetic graphite in the with-grain (parallel to extrusion) and against-grain (perpendicular to extrusion) directions.

where N is the charge carrier density, q the electric charge, μ the carrier mobility, τ the relaxation time, and m is the charge carrier effective mass. The relaxation time, (τ) , is related to the carrier mean-free path, λ , and is defined as the time elapsed between two collisions, such that

$$\lambda = v_f \tau \quad [7]$$

The inverse $(1/\tau)$ in eqn [7] reflects the probability that a charge carrier will be scattered, and v_f is the charge carrier velocity at the Fermi surface. The carrier mean-free path is the distance between two scattering centers.

In synthetic graphite, the dominant charge carriers are electrons, and the dominant scattering effects are intrinsic (phonon–electron scattering) at temperatures above ~ 1000 K and extrinsic scattering (lattice defects, crystallite edges, irradiation induced defects) at temperatures below ~ 1000 K.¹⁹ In addition to electrons being scattered by defects, vacancies may act as electron traps.

The influence of intrinsic and defect scattering may be separated²⁰ using Matthiessen's rule:

$$\frac{1}{\mu_{\text{total}}} = \frac{1}{\mu_i} + \frac{1}{\mu_d} \quad [8]$$

where μ_i is the intrinsic scattering and μ_d the defect mobility. For scattering by crystallite boundaries, μ_d is approximately independent of temperature. An important parameter for characterizing scattering in graphite is the mean-free path,¹⁹ λ , which in well-ordered graphite is effectively controlled by the a -direction crystallite size, l_a .

For industrial applications of graphite, such as arc furnace electrodes and aluminum smelting cell cathode blocks, the electrical resistivity is an important parameter. Excess power consumption due to the resistance of the graphite will impact the economics of cell/furnace operations. Figure 15 shows the effect of temperature on the electrical resistivity of commercial extruded electrode grade graphite.²¹ For well-graphitized materials, the resistivity is seen to initially fall with increasing temperature, reaching a minimum at 800–1000 K, the resistivity then increases in an almost linear fashion to temperatures in excess of 1000 °C (Figure 15). The charge carrier density (eqn [6]) increases four- or fivefold over the temperature range 0–300 K.²² Consequently, the electrical resistivity also initially falls as temperature increases. However, the scattering of charge carriers (eqns [7] and [8]) is also heavily temperature-dependent. Initially, scattering is dominated by

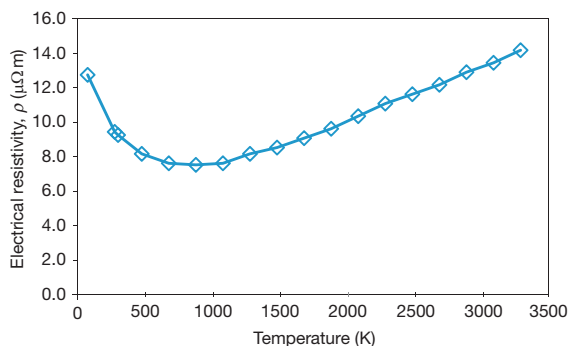


Figure 15 Temperature dependence of the electrical resistivity of a typical extruded, needle-coke grade, in the with-grain direction. Data from Page, D. J. *The Industrial Graphite Engineering Handbook*; UCAR Carbon Company: Danbury, CT, 1991.

extrinsic defects, but as the mean-free path for intrinsic scattering becomes comparable with that from defect scattering, an increase in resistivity will be observed. Thus, above ~ 1000 K, the decrease in charge carrier mobility outweighs the increase in charge carrier density, and resistivity is seen to increase in Figure 15.

Other factors may influence the electrical resistivity of synthetic graphite, such as anisotropy in the filler particle and texture (orientation and distribution of filler particle and porosity). Contributions to the overall resistivity will come from the binder phase and the interface resistance between filler-coke and binder phase. Increases in crystallinity of the graphite, through judicious selection of raw materials, or higher graphitization temperatures, will decrease the room-temperature electrical resistivity. Generally, the greater the room-temperature resistivity, the greater the temperature at which the resistivity minima occurs; the steeper the initial decrease in resistivity, the larger the magnitude of the initial drop in resistivity. Typical physical properties for several graphite grades with a range of filler-particle sizes and forming methods are shown in Table 1.

2.10.4 Mechanical Properties

2.10.4.1 Density

The bulk density of synthetic graphite varies according to the manufacturing process. Increases in density are achieved by utilizing fine filler particles (although this limits the forming size). Also, the forming method and number of impregnations can

Table 1 Physical and mechanical properties of various graphite grades with various grain sizes and forming methods

Typical properties	Graphite grade and manufacturer					
	AXF-5Q	IG-43	2020	ATJ	NBG-18	AGX
	POCO	Toyo Tanso	Mercen	GTI	SGL carbon	GTI
Forming method	Isomolded	Isomolded	Isomolded	Isomolded	Vibro-molded	Extruded
Maximum particle size (μm)	5	10 (mean)	15	25 (mean)	1600	3000
Bulk density (g cm^{-3})	1.8	1.82	1.77	1.76	1.88	1.6
Thermal conductivity ($\text{W m}^{-1} \text{K}$) (measured at ambient temperature)	85	140	85	125 (WG) 112 (AG)	156 (WG) 150 (AG)	152 (WG) 107 (AG)
Coefficient of thermal expansion (10^{-6}K^{-1}) (over given temperature range)	7.4 (20–500 °C)	4.8 (350–450 °C)	4.3 (20–500 °C)	3.0 (WG) 3.6 (AG) (at 500 °C)	4.5 (WG) 4.7 (AG) (20–200 °C)	2.1 (WG) 3.2 (AG) (at 500 °C)
Electrical resistivity ($\mu\Omega \text{m}$)	14	9.2	15.5	10.1 (WG) 11.7 (AG)	8.9 (WG) 9.0 (AG)	8.5 (WG) 12.1 (AG)
Young's modulus (GPa)	11	10.8	9.3	9.7 (WG) 9.7 (AG)	11.2 (WG) 11.0 (AG)	6.9 (WG) 4.1 (AG)
Tensile strength (MPa)	65	37	30	27.2 (WG) 23.1 (AG)	21.5 (WG) 20.5 (AG)	4.9 (WG) 4.3 (AG)
Compressive strength (MPa)	145	90	80	66.4 (WG) 67.4 (AG)	72 (WG) 72.5 (AG)	19.8 (WG) 19.3 (AG)
Flexural strength (MPa)	90	54	45	30.8 (WG) 27.9 (AG)	28 (WG) 26 (AG)	8.9 (WG) 6.9 (AG)

Data from manufacturer's literature.

WG, with-grain; AG, against-grain.

affect the density. Coarse-grain, extruded electrode graphite may have densities as low as 1.6 g cm^{-3} , whereas fine-grained, isotropic, molded, and isomolded grades can have densities exceeding 1.85 g cm^{-3} . Generally, strength and stiffness (and thermal conductivity) increase with increasing density, while electrical resistivity is reduced (Table 1). Permeability is also reduced as density increases (decreasing porosity).

2.10.4.2 Elastic Behavior

The response of synthetic graphite to a stress (its elastic behavior) is dominated by the bond anisotropy in the graphite single crystal lattice, the preferred crystal orientation, and the presence of defects (porosity) in the structure. The elastic response of the strong covalent in-plane bonds of the carbon atoms in the graphene sheets will be vastly different from the graphene sheets held in stacks with weak van der Waals forces. Definition of the stress-strain relationship for the hexagonal graphite crystal requires five independent elastic constants.²³ These constants are identified as (using a Cartesian coordinate system with the z -axis parallel to the hexagonal axis of the crystal or c -axis):

$$\begin{aligned}
 T_{xx} &= C_{11}\epsilon_{xx} + C_{12}\epsilon_{yy} + C_{13}\epsilon_{zz} \\
 T_{yy} &= C_{12}\epsilon_{xx} + C_{11}\epsilon_{yy} + C_{13}\epsilon_{zz} \\
 T_{zz} &= C_{13}\epsilon_{xx} + C_{13}\epsilon_{yy} + C_{33}\epsilon_{zz} \\
 T_{zx} &= C_{44}\epsilon_{zx} \\
 T_{zy} &= C_{44}\epsilon_{zy} \\
 T_{xy} &= 1/2(C_{11} - C_{12})\epsilon_{xy} = C_{66}\epsilon_{xy} \quad [9]
 \end{aligned}$$

where the stresses T_{lm} are defined as the force acting on the unit area parallel to the l th direction; the normal to the unit area is the m th direction. The parameters C_{ij} are the elastic moduli and their inverse S_{ij} are the elastic compliances. The various measurements of compliances made on single crystals and highly oriented pyrolytic graphites have been reviewed by Kelly¹² and are reported to be the best available estimates (Table 2).

Table 2 reports the Young's modulus parallel to the hexagonal axis of the crystal $E_c = S_{33}^{-1} \sim 36.4 \text{ GPa}$, the Young's modulus parallel to the basal planes, $E_a = S_{11}^{-1} \sim 1020 \text{ GPa}$, and the shear modulus parallel to the basal planes $G = S_{44}^{-1} = C_{44} \sim 4.5 \text{ GPa}$. The very low value of E_c results from the very weak interlayer van der Waals bonding, while the value of E_a reflects the magnitude of the in-plane (sp^2) C–C covalent bonds. Kelly¹² reviewed the literature data for

Table 2 Elastic constants of single crystal graphite

Elastic moduli (GPa)		Elastic compliances (10^{-13} Pa^{-1})	
C_{11}	1060 ± 20	S_{11}	9.8 ± 0.3
C_{12}	180 ± 20	S_{12}	-1.6 ± 0.6
C_{13}	15 ± 5	S_{13}	-3.3 ± 0.8
C_{33}	36.5 ± 1	S_{33}	275 ± 10
C_{44}	$4.0\text{--}4.5$	S_{44}	$2222\text{--}2500$

Data from Kelly, B. T. *Physics of Graphite*; Applied Science: London, 1981.

experimental values of C_{44} and noted that while many reported values are lower than those reported in [Table 2](#), the presence of glissile basal plane dislocations can reduce C_{44} by one or two orders of magnitude.

The Young's modulus, E , of the single crystal will thus depend upon orientation of the crystal to the Measurements (stress) axis. Thus, E^{-1} , may be written as a function of the angle, φ , with respect to the crystal hexagonal axis as

$$E^{-1} = S_{11}(1 - \gamma^2)^2 + S_{33}\gamma^4 + (2S_{13} + S_{44})\gamma^2(1 - \gamma^2) \quad [10]$$

where $\gamma = \cos\varphi$. Taking values for the elastic compliances from [Table 2](#), and allowing $S_{44} = 2.4 \times 10^{-10} \text{ Pa}^{-1}$, the variation of the reciprocal modulus with the angle between the measurement direction and the crystal c -axis, φ , can be calculated using [eqn \[10\]](#) ([Figure 16](#)). Also plotted in [Figure 16](#) is an approximate value of E^{-1} calculated, allowing all S_{ij} to be zero except S_{44} . The agreement between the two is good over a wide range of values of φ , clearly demonstrating the dominance of S_{44} in controlling the elastic modulus and other mechanical properties in polygranular (synthetic) graphites.

The graphite single crystal shear modulus, G (Pa^{-1}), can also be calculated¹² from the elastic compliances (S_{ij}) given in [Table 2](#) (allowing $S_{44} = 2.4 \times 10^{-10} \text{ Pa}^{-1}$) from [eqn \[11\]](#):

$$G^{-1} = S_{44} + \left(S_{11} - S_{12} - \frac{S_{44}}{2} \right) (1 - \gamma^2) + 2(S_{11} + S_{33} - 2S_{13} - S_{44})\gamma^2(1 - \gamma^2) \quad [11]$$

Values of G^{-1} as a function of φ are plotted in [Figure 17](#). The value of the crystal shear modulus at $\varphi = 0$, that is, parallel to the basal planes, is the smallest shear modulus and corresponds to C_{44} for crystal basal plane shear (weak van der Waals forces), again demonstrating the dominance of S_{44} in controlling the elastic moduli of the crystal. It is

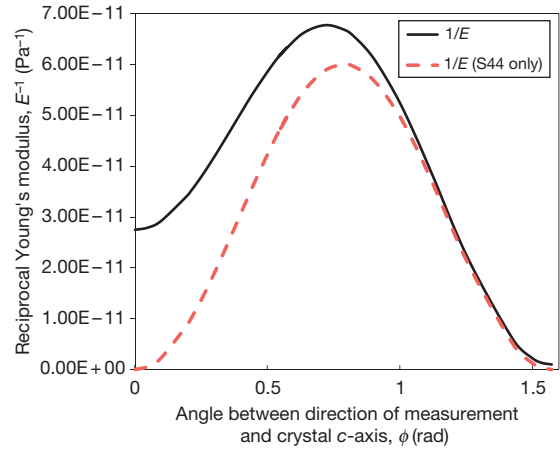


Figure 16 Variation of the reciprocal Young's modulus with angle of miss-orientation between the c -axis and measurement axis.

interesting to note that while G^{-1} displays a minimum (largest G) at $\sim\pi/4$, the reciprocal Young's modulus value displays a maximum (smallest E) at $\sim\pi/4$, reflecting the different modes of bond stretching and the different bonding nature in these cases.

The crystals in synthetic graphite are not as perfect as discussed above. Moreover, while both the filler-coke and the binder phase exhibit crystallinity, the alignment of the crystallite regions within the filler and binder is not uniform, although it may display preferred orientation because of filler-coke calcination and the formation of the synthetic artifact. Texture also arises because of the alignment of the filler particle during formation. Consequently, the single crystal values of moduli are not realized in synthetic (polygranular) graphite. Typical values of Young's modulus for synthetic graphite are given in [Table 1](#). There is considerable variation of Young's modulus with density. However, the effect of texture is clearly seen in the anisotropic values for grade AGX, 6.9 GPa (WG) and 4.1 GPa (AG), confirming the tendency of the filler grains to align on extrusion such that WG orientation displays more of the c -axis Young's moduli (0 and $\pi/2$ in [Figure 16](#)) and is thus greater than the AG value. Grades with a greater density ($\sim 1.8 \text{ g cm}^{-3}$) possess a Young's modulus value, $\sim 10 \text{ GPa}$, far less than the single crystal values (except C_{44}). Measurements of the shear modulus derived from the velocity of shear (transverse) waves propagating through the graphite give values ranging from 3 to 4 GPa for various grades all with density $\sim 1.8 \text{ g cm}^{-3}$. The values of shear modulus (WG) were slightly greater than shear modulus (AG)

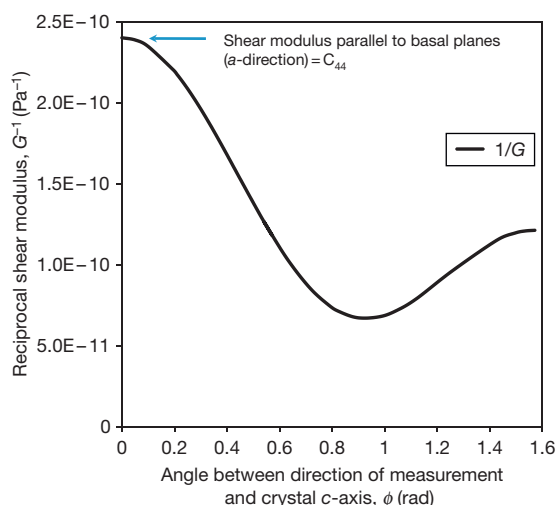


Figure 17 Variation of the reciprocal shear modulus with angle of miss-orientation between the c-axis and measurement axis.

for extruded and molded grades, as expected from the theory and textural effects. The measured values of shear modulus for synthetic graphites (3–4 GPa) are in reasonable agreement with the single crystal value of C_{44} (4–4.5 GPa) reported in Table 2. The presence of glissile basal plane dislocations would be expected to reduce the single crystal value of shear modulus substantially, but the defective nature of the crystals in synthetic graphite assures a high density of dislocation pinning sites, which will increase the value of shear modulus. For a wide range of synthetic graphites, the ratio of $E/G \sim 3$ is in agreement with previous observations.¹² In addition to the effects of texture, such as the crystal/filler preferred orientation, on the elastic moduli of synthetic graphite, the existence of porosity with a wide size, shape, and orientation distribution (refer to Section 2.10.2) makes the interpretation of the elastic properties more complicated. Typical Young's moduli for synthetic graphites range from 5 to 15 GPa (Table 1), with lower modulus being exhibited by coarser-grain graphite. The combined effect of porosity and texture in synthetic graphite causes anisotropy of the moduli, with the anisotropy ratio for Young's modulus being as large as 2. Finer-grain graphites are far more isotropic with respect to Young's modulus.

Various workers have studied the changes in the elastic compliances of single crystal graphite with temperature, as reviewed by Kelly.¹² The single crystal elastic constants decrease with increasing temperature.²³ The value of C_{33} decreases linearly

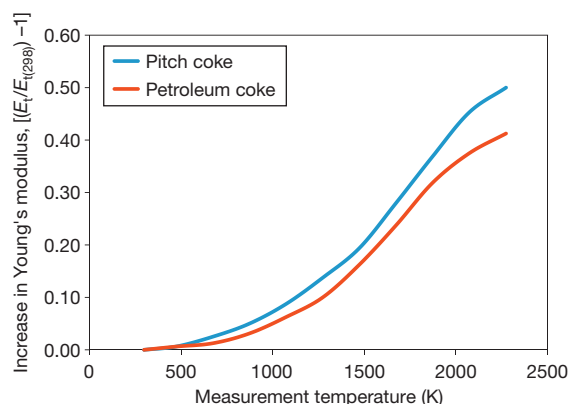


Figure 18 Typical Young's modulus increases with temperature for pitch-coke and petroleum-coke synthetic graphite. Adapted from Nightingale, R. E.; Yoshikawa, H. H.; Losty, H. H. W. In *Nuclear Graphite*; Nightingale, R. E., Ed.; Academic Press: New York, 1962.

by more than a factor of 2 over the temperature range 0–2000 K.¹² Synthetic polygranular graphite, because of the influence of texture and porosity, shows a completely different temperature dependence of their Young's moduli. The thermal closure of cracks/pores aligned along the *a*-axis (between the basal planes – the ‘Mrozowski’ cracks¹⁵) will cause an increase^{4,21,24} in Young's modulus of $\sim 50\%$ from room temperature to ~ 2300 K. Above this temperature up to ~ 3000 K, Young's modulus is reported to decrease slightly.²¹ Typical high-temperature behavior of Young's modulus is shown in Figure 18 for pitch-coke and petroleum-coke graphite.

Poisson's ratio for fine-grained isotropic graphite (ATJ) has been reported to be 0.1–0.16, and for coarser-grained extruded graphite (AGOT) 0.04–0.09, the value being dependent upon the measurement direction relative to the forming axis.²¹ In a large study of the room-temperature elastic properties of 15 graphite grades measured using the velocity of sound waves (both longitudinal and transverse), the Poisson's ratio value was seen to be between 0.17 and 0.24 for fine-grain, isotropic grades and between 0.28 and 0.32 for medium-grain, molded, or extruded grades.

2.10.4.3 Strength and Fracture

Typical compressive and tensile stress–strain curves for medium-grain, extruded graphite are shown in Figures 19 and 20, respectively. The stress–strain curve is nonlinear and typically shows hysteresis on

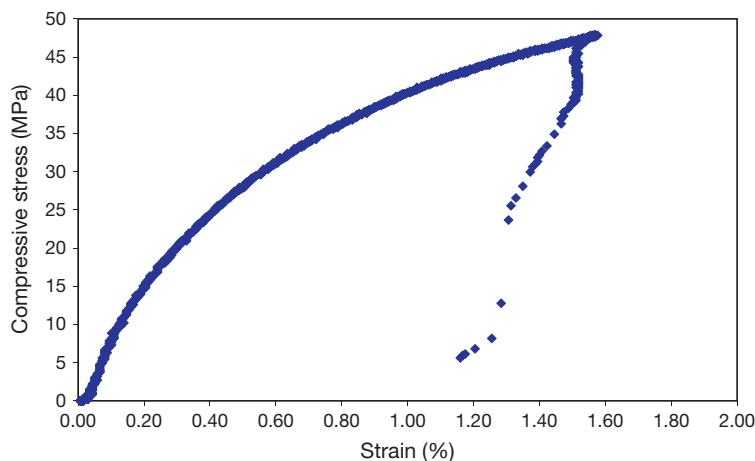


Figure 19 Typical compressive stress–strain curve for medium-grain extruded graphite (WG).

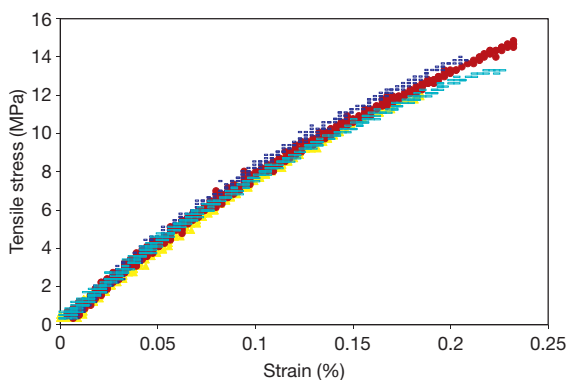


Figure 20 Typical tensile stress–strain curves for medium-grain extruded graphite (WG).

reloading after loading below the fracture stress, with a permanent set.^{12,23,25} The nonlinearity has been widely attributed to pseudo-plastic events such as basal plane shear and subcritical cracking.^{12,23–27} **Table 1** reports the tensile, flexure, and compressive strength of a range of synthetic graphites. Tensile strengths vary with texture from as low as <5 MPa for coarser-grain, extruded grades to >60 MPa for fine-grain, isotropic grades and can be >80 MPa for some isostatically molded, ultra-fine-grain and micro-fine-grain synthetic graphite. Compressive strengths range from <20 MPa to >140 MPa and typically, the ratio of compressive strength to tensile strength is in the range 2–4. Kelly¹² reports that there are two major factors that control the stress–strain behavior of synthetic graphite, namely, the magnitude of the constant C_{44} , which dictates how the crystals respond to an applied stress, and the defect/crack morphology and distribution, which controls

the distribution of stresses within the body and thus the stress that each crystallite experiences.

Generally, the strength increases as the modulus increases but is also greatly influenced by factors such as texture and density (total porosity). The strength (or Young's moduli) is related to the fractional porosity through a relationship of the form

$$\sigma = \sigma_0 e^{-bP} \quad [12]$$

where P is the fractional porosity, b is an empirical constant, and σ_0 represents the strength at zero porosity. **Figure 21** shows the correlation between flexure strength and fractional porosity for a wide range of synthetic graphite²⁷ varying from fine-grain, high-density, isomolded grades to large-grain, low-density, extruded grades. The data are fitted to an equation of the form of eqn [12] with $\sigma_0 = 179$ MPa and $b = 9.62$. The correlation coefficient, $R^2 = 0.80$. Significantly, the same flexure strength data (**Figure 22**) is better fitted when plotted against the mean filler-particle size²⁷ ($R^2 = 0.87$). In synthetic graphite, the filler-particle size is indicative of the defect size, that is, larger filler-particle graphite contains larger inherent defects. Thus, the correlation in **Figure 22** is essentially one between critical defect size and strength. The importance of defects in controlling fracture behavior and strength in synthetic polygranular graphite is well understood, and despite the pseudoplasticity displayed by graphite, it is best characterized as a brittle material with its fracture behavior described in terms of linear elastic fracture mechanics.²⁸ Synthetic graphite critical stress-intensity factor, K_{IC} , values are between 0.8 and 1.3 MPa m^{-1/2} dependent upon their texture

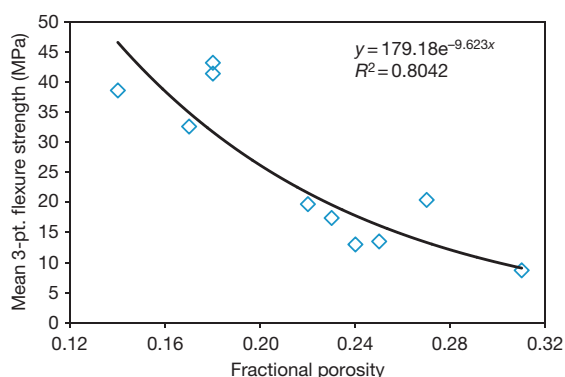


Figure 21 The correlation between mean 3-pt flexure strength and fractional porosity for a wide range of synthetic graphite representing the variation of textures. Reproduced from Burchell, T. D. Ph.D. Thesis, University of Bath, 1986.

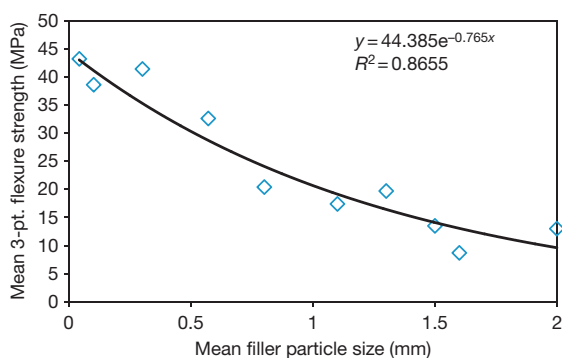


Figure 22 The correlation between mean 3-pt flexure strength and mean filler-coke particle size for a wide range of synthetic graphite representing the variation of textures. Reproduced from Burchell, T. D. Ph.D. Thesis, University of Bath, 1986.

and the method of determination.^{27–29} Such is the importance of the fracture behavior of synthetic graphite that there have been many studies of the fracture mechanisms and attempts to develop a predictive failure model.

An early model was developed by Buch³⁰ for fine-grain aerospace graphite. The Buch model was further developed and applied to nuclear graphite by Rose and Tucker.³¹ The Rose and Tucker model assumed that graphite consisted of an array of cubic particles representative of the material's filler-particle size. Within each block or particle, the graphite was assumed to have a randomly oriented crystalline structure, through which basal plane cleavage may occur. When a load was applied, those cleavage planes on which the resolved shear stress exceeded a critical value were assumed to fail.

If adjacent particles cleaved, the intervening boundary was regarded as having failed, so that a contiguous crack extending across both particles was formed. Pickup *et al.*³² and Rose and Tucker³¹ equated the cleavage stress with the onset stress for acoustic emission (AE), that is, the stress at which AE was first detected. In applying the model to a stressed component, such as a bar in tension, cracks were assumed to develop on planes normal to the axis of the principal stress. The stressed component would thus be considered to have failed when sufficient particles on a plane have cleaved such that together they formed a defect large enough to cause such a fracture as the brittle Griffith crack. Pores were treated in the Rose and Tucker model as particles with zero cleavage strength. The graphite's pore volume was used to calculate the correct number of zero cleavage strength particles in the model. Hence, the Rose and Tucker model took into account the mean size of the filler particles, their orientation, and the amount of porosity but was relatively insensitive to the size and shape distributions of both microstructural features.

Rose and Tucker applied their fracture model to Sleeve graphite, an extruded, medium-grain, pitch-coke nuclear graphite used for fuel sleeves in the British AGR. The performance of the model was disappointing; the predicted curve was a poor fit to the experimental failure probability data. In an attempt to improve the performance of the Rose and Tucker model, experimentally determined filler-particle distributions were incorporated.³³ The model's predictions were improved as a result of this modification and the higher strength of one pitch-coke graphite compared with that of the other was correctly predicted. Specifically, the predicted failure stress distribution was a better fit to the experimental data than the single grain size prediction, particularly at lower stresses. However, to correctly predict the mean stress (50% failure probability), it was found necessary to increase the value of the model's stress-intensity factor (K_{Ic}) input to $1.4 \text{ MPa m}^{1/2}$, a value far in excess of the actual measured K_{Ic} of this graphite ($1.0 \text{ MPa m}^{1/2}$). The inclusion of an artificially high value for K_{Ic} completely invalidates one of the Rose and Tucker model's major attractions, that is, its inputs are all experimentally determined material parameters. A further failing of the Rose and Tucker fracture model is its incorrect prediction of the buildup of AE counts. Although the Rose and Tucker model considered the occurrence of subcritical damage when the applied stress lay between the cleavage

and failure stresses, the predicted buildup of AE was markedly different from that observed experimentally.³⁴ First, the model failed to account for any AE at very low stresses. Second, at loads immediately above the assumed cleavage stress, there was a rapid accumulation of damage (AE) according to the Rose and Tucker model but very little according to the AE data. Moreover, the observation by Burchell *et al.*³⁴ that AEs occur immediately upon loading graphite completely invalidated a fundamental assumption of the Rose and Tucker model, that is, the AE onset stress could be equated with the cleavage stress of the graphite filler particles.

Recognizing the need for an improved fracture model, Tucker *et al.*³⁵ investigated the fracture of polygranular graphites and assessed the performance of several failure theories when applied to graphite. These theories included the Weibull theory, the Rose and Tucker model, fracture mechanics, critical strain energy, critical stress, and critical strain theories. While no single criteria could satisfactorily account for all the situations they examined, their review showed that a combination of the fracture mechanics and a microstructurally based fracture criteria might offer the most versatile approach to modeling fracture in graphite. Evidently, a necessary precursor to a successful fracture model is a clear understanding of the graphite-fracture phenomena. Several approaches have been applied to examine the mechanism of fracture in graphite, including direct microstructural observations and AE monitoring.^{34,36–38}

When graphite is stressed, micromechanical events such as slip, shear, cleavage, or microcracking may be detected in the form of AE. In early work, Kaiser³⁹ found that graphite emitted AE when stressed, and upon subsequent stressing, AE could only be detected when the previous maximum stress had been exceeded – a phenomenon named the Kaiser effect. Kraus and Semmler⁴⁰ investigated the AE response of industrial carbon and polygranular graphites subject to thermal and mechanical stresses. They reported significant AE in the range 2000–1500 °C on cooling from graphitization temperatures, the amount of AE increasing with the cooling rate. Although Kraus and Semmler offered no explanation for this, Burchell *et al.*³⁴ postulated that it was associated with the formation of Mrozowski cracks.¹⁵ In an extensive study, Burchell *et al.*³⁴ monitored the AE response of several polygranular graphites, ranging from a fine-textured, high-strength aerospace graphite to a coarse-textured, low-strength extruded graphite. They confirmed the previous

results of Pickup *et al.*,³² who had concluded that the pattern of AE was characteristic of the graphite microstructure. Burchell *et al.*³⁴ showed that the development of AE was clearly associated with the micromechanical events that cause nonlinear stress–strain behavior in graphites and that postfracture AE was indicative of the crack propagation mode at fracture. For different graphites, both the total AE at fracture and the proportion of small amplitude events tended to increase with increasing filler-particle size (i.e., coarsening texture). Ioka *et al.*⁴¹ studied the behavior of AE caused by microfracture in polygranular graphites. On the basis of their data, they described the fracture mechanism for graphite under tensile loading. Filler particles, whose basal planes were inclined at 45° to the loading axis deformed plastically, even at low stresses. Slip deformation along basal planes was detected by an increased root mean square (RMS) voltage of the AE event amplitude. The number of filler particles that deform plastically increased with increasing applied tensile stress. At higher applied stress, slip within filler particles was accompanied by shearing of the binder region. Filler grains whose basal planes were perpendicular to the applied stress cleaved, and the surrounding binder sheared to accommodate the deformation. At higher stress levels, microcracks propagated into the binder region, where they coalesced to form a critical defect leading to the eventual failure of the graphite. The evidence produced through the numerous AE studies reviewed here suggests a fracture mechanism consisting of crack initiation, crack propagation, and subsequent coalescence to yield a critical defect resulting in fracture.

A microstructural study of fracture in graphite^{27,42} revealed the manner in which certain microstructural features influenced the process of crack initiation and propagation in nuclear graphites (Figure 23); the principal observations are summarized below.

2.10.4.3.1 Porosity

Two important roles of porosity in the fracture process were identified. First, the interaction between the applied stress field and the pores caused localized stress intensification, promoting crack initiation from favorably oriented pores at low applied stresses. Second, propagating cracks could be drawn toward pores in their vicinity, presumably under the influence of the stress field around the pore. In some instances, such pore/crack encounters served to accelerate crack growth; however, occasionally, a crack was arrested by a pore and did not break free

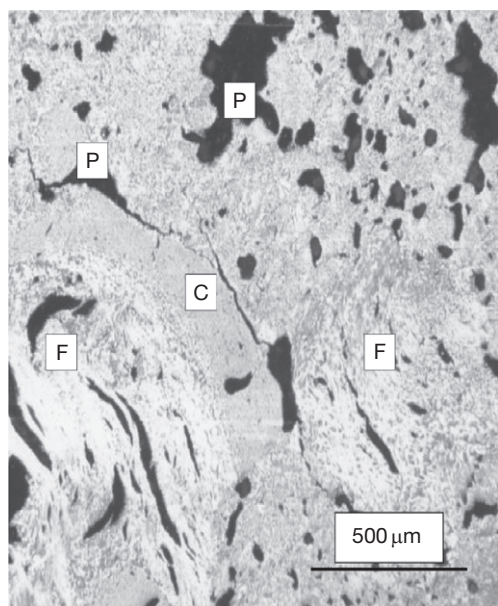


Figure 23 An optical photomicrograph of the microstructure of grade H-451 graphite revealing the presence of pores [P], coke filler particles [F], and cracks [C] that have propagated through the pores presumably under the influence of their stress fields.

until higher applied stresses were attained. Pores of many shapes and sizes were observed in the graphite microstructure, but larger, more slit-shaped pores were more damaging to the graphite.

2.10.4.3.2 The binder phase

Two arbitrarily defined types of microstructure were identified in the binder phase: (1) domains, which were regions of common basal plane alignment extending over linear dimensions $>100\ \mu\text{m}$ and (2) mosaics, which were regions of small randomly oriented pseudocrystallites with linear dimensions of common basal plane orientation of less than about $10\ \mu\text{m}$. Cleavage of domains occurred at stresses well below the fracture stress, and such regions acted as sites for crack initiation, particularly when in the vicinity of pores. Fracture of mosaic regions was usually observed only at stresses close to the fracture stress. At lower stresses, propagating cracks that encountered such regions were arrested or deflected.

2.10.4.3.3 Filler particles

Filler-coke particles with good basal plane alignment were highly susceptible to microcracking along basal planes at low stresses. This cleavage was facilitated by the needle-like cracks that lay parallel to the basal planes and which were formed by anisotropic

contraction of the filler-coke particles during the calcination process. Frequently, when a crack propagating through the binder phase encountered a well-aligned filler particle, it took advantage of the easy cleavage path and propagated through the particle. However, in contrast to the mechanism suggested by Ioka *et al.*,³⁶ the reverse process, that is, propagation of a crack initiated in the filler particle into the binder phase, was much less commonly observed.

While some of the direct observations discussed above are not in total agreement with the mechanism postulated from AE data, there are a number of similarities. Both AE and the microstructural study showed that failure was preceded by the propagation and coalescence of microcracks to yield a critical defect. However, based on the foregoing discussion of graphite-fracture processes, it is evident that the microstructure plays a dominant role in controlling the fracture behavior of the material. Therefore, any new fracture model should attempt to capture the essence of the microstructural processes influencing fracture. Particularly, a fracture model should embody the following: (1) the distribution of pore sizes, (2) the initiation of fracture cracks from stress raising pores, and (3) the propagation of cracks to a critical length prior to catastrophic failure of the graphite (i.e., subcritical growth). The Burchell fracture model^{27,43–45} recognizes these aspects of graphite fracture and applies a fracture mechanics criterion to describe steps (2) and (3). The model was first postulated²⁷ to describe the fracture behavior of AGR fuel sleeve pitch-coke graphite and was successfully applied to describe the tensile failure statistics. Moreover, the model was shown to predict more closely the AE response of graphite than its forerunner, the Rose and Tucker model. Subsequently, the model was extended and applied to two additional nuclear graphites.⁴⁵ Again, the model performed well and was demonstrated to be capable of predicting the tensile failure probabilities of the two graphites (grades H-451 and IG-110). In an attempt to further strengthen the model,⁴⁵ quantitative image analysis was used to determine the statistical distribution of pore sizes for grade H-451 graphite. Moreover, a calibration exercise was performed to determine a single value of particle critical stress-intensity factor for the Burchell model.^{28,44} Most recently, the model was successfully validated against experimental tensile strength data for three graphites of widely different texture.^{28,45,46}

The model and code were successfully benchmarked^{28,46} against H-451 tensile strength data and

validated against tensile strength data for grades IG-110 and AXF-5Q. Two levels of verification were adopted. Initially, the model's predictions for the growth of a subcritical defect in H-451 as a function of applied stress was evaluated and found to be qualitatively correct.^{28,46} Both the initial and final defect length was found to decrease with increasing applied stress. Moreover, the subcritical crack growth required prior to fracture was predicted to be substantially less at higher applied stresses. Both of these observations are qualitatively correct and are readily explained in terms of linear elastic fracture mechanics. The probability that a particular defect exists and will propagate through the material to cause failure was also predicted to increase with increasing applied stress. Quantitative validation was achieved by successfully testing the model against an experimentally determined tensile strength distribution for grade H-451. Moreover, the model appeared to qualitatively predict the effect of textural changes on the strength of graphite. This was subsequently investigated and the model further validated by testing against two additional graphites, namely grade IG-110 and AXF-5Q. For each grade of graphite, the model accurately predicted the mean tensile strength.

In an attendant study, the Burchell^{28,46} fracture model was applied to a coarse-textured electrode graphite. The microstructural input data obtained during the study was extremely limited and can only be considered to give a tentative indication of the real pore-size distribution. Despite this limitation, however, the performance of the model was very good, extending the range of graphite grades successfully modeled from a 4- μm particle size, fine-textured graphite to a 6.35-mm particle size, coarse-textured graphite. The versatility and excellent performance of the Burchell^{28,46} fracture model is attributed to its sound physical basis, which recognizes the dominant role of porosity in the graphite-fracture process (Figure 24).

Kelly¹² has reviewed multiaxial failure theories for synthetic graphite. The fracture theory of Burchell^{28,46} has recently been extended to multiaxial stress failure conditions.⁴⁷ The model's predictions in the first and fourth quadrants are reported and compared with the experimental data in Figure 25. The performance was satisfactory, demonstrating the sound physical basis of the model and its versatility. The model in combination with the Principal of Independent Action describes the experimental data in the first quadrant well. The failure envelope

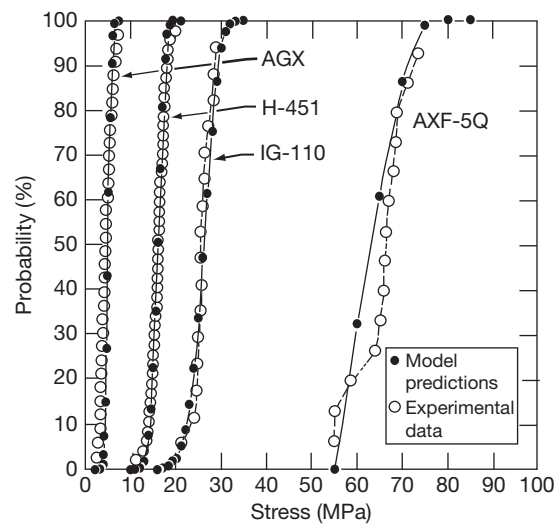


Figure 24 A comparison of experimental and predicted tensile failure probabilities for graphite with widely different textures: AGX, H-451, IG-110, and AXF-5Q. Reproduced from Burchell, T. D. *Carbon* **1996**, 34, 297–316.

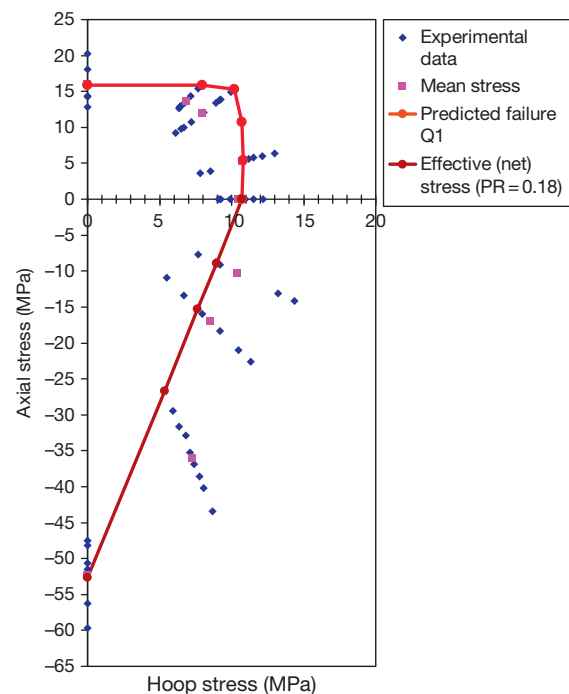


Figure 25 A summary of the Burchell model's predicted failure surface in the first (PIA) and fourth (effective stress) quadrants and the experimental data. Reproduced from Burchell, T.; Yahr, T.; Battiste, R. *Carbon* **2007**, 45, 2570–2583.

predicted by the fracture model for the first quadrant is a better fit to the experimental data than that of the maximum principal stress theory, which would be represented by two perpendicular lines through the

mean values of the uniaxial tensile and hoop strengths. The failure surface predicted by the fracture model offers more conservatism at high combined stresses than the maximum principal stress criterion. In the fourth quadrant, the fracture model predicts the failure envelope well (and conservatively) when the effective (net) stress is applied with the fracture model. Again, as in the first quadrant, the maximum principal stress criteria would be extremely unconservative, especially at higher stress ratios. Overall, the model's predictions were satisfactory and reflect the sound physical basis of the fracture model.⁴⁷

2.10.4.4 Thermal Shock

Graphite can survive sudden thermally induced loads (thermal shock), such as those experienced when an arc is struck between the charge and the tip of a graphite electrode in an electric arc melting furnace, or on the first wall of a fusion reactor. To provide a quantitative comparison of a material's resistance to thermal shock loading, several thermal shock figures of merit (Δ) have been derived. In its simplest form, the Figure of merit (FoM) may be expressed as

$$\Delta = \frac{K\sigma_y}{\alpha E} \quad [13]$$

where K is the thermal conductivity, σ_y the yield strength, α the thermal expansion coefficient, and E is the Young's modulus. Clearly, graphite with its unique combination of properties, that is, low thermal expansion coefficient, high thermal conductivity, and relatively high strain to failure (σ/E), is well suited to applications involving high thermal shock loadings. Taking property values from [Table 1](#) for Toyo Tanso IG-43 and for POCO AXF-5Q gives FoM values of $\Delta = 99\,923$ and $\Delta = 67\,875$, respectively (from [eqn \[13\]](#)). Another FoM takes account of the potential form of failure from thermally induced biaxial strains, Δ_{th} , and may be written as

$$\Delta_{th} = \frac{K\sigma_y}{\alpha E(1 - \nu)} \quad [14]$$

where K is the thermal conductivity, σ_y the yield strength, α the thermal expansion coefficient, E the Young's modulus, and ν is Poisson's ratio. Larger values of Δ_{th} indicate improved resistance to thermal shock. Using the values above and dividing by $(1 - \nu)$ from [eqn \[14\]](#) gives FoM values of $\Delta_{th} = 124\,904$ and $84\,844$ for IG-11 and AXF-5Q, respectively. The thermal shock FoM, Δ_{th} , has been reported⁴⁸ for several candidate materials for fusion reactor first wall materials (see [Chapter 4.18, Carbon as a](#)

[Fusion Plasma-Facing Material](#)). Wrought beryllium has a value of $\sim 1 \times 10^4$, pure tungsten a value of $\sim 0.5 \times 10^5$, and carbon-carbon composite material $\sim 1 \times 10^6$. If the thermal shock is at very high temperature, the material's melting temperature is a key factor. Again, graphite materials do well as they do not exhibit a melting temperature; rather they progressively sublime at a temperature higher than the sublimation point (3764 K).

2.10.5 Nuclear Applications

Many of the properties that make graphite attractive for a particular application have been discussed above. However, the following characteristics have been ascribed to synthetic, polygranular graphite⁶ and are those properties that make graphite suitable for its many applications: chemical stability; corrosion resistance (in a nonoxidizing atmosphere); non-reactive with many molten metals and salts; nontoxic; high electrical and thermal conductivity; small thermal expansion coefficient and consequently high thermal shock resistance; light weight (low bulk density); high strength at high temperature; high lubricity; easily dissolved in iron, and highly reductive; biocompatible; low neutron absorption cross-section and high neutron-moderating efficiency; resistance to radiation damage. The latter properties are what make graphite an attractive choice for a solid moderator in nuclear reactor applications.

Nuclear applications, both fission and fusion (of keen interest the reader), are described in detail in [Chapter 4.10, Radiation Effects in Graphite](#), and [Chapter 4.18, Carbon as a Fusion Plasma-Facing Material](#). Accounts of nuclear applications have also been published elsewhere.^{9,48–50} Graphite is used in fission reactors as a nuclear moderator because of its low neutron absorption cross-section and high neutron moderating efficiency, its resistance to radiation damage, and high-temperature properties. In fusion reactors, where it has been used as plasma facing components, advantage is taken of its low atomic number and excellent thermal shock characteristics.

The largest applications of nuclear graphite involve its use as a moderator and in the fuel forms of many thermal reactor designs. These have included the early, air-cooled experimental and weapons materials producing reactors; water-cooled graphite-moderated reactors of the former Soviet Union; the CO₂-cooled reactors built predominantly in the United Kingdom, but also in Italy and Japan; and helium-cooled

high-temperature reactors, built by many nations, which are still being operated in Japan and designed and constructed in China and the United States. All of the high-temperature reactor designs utilize the ceramic Tri-isotropic (TRISO) type fuel (see [Chapter 3.07, TRISO-Coated Particle Fuel Performance](#)), which incorporates two pyrolytic graphite layers in its form. Graphite-moderated reactors that were molten-salt cooled have also been operated.

2.10.6 Summary and Conclusions

Synthetic graphite is a truly remarkable material whose unique properties have their origins in the material's complex microstructure. The bond anisotropy of the graphite single crystal (in-plane strong covalent bonds and weak interplanar van der Waals bonds) combined with the many possible structural variations, such as the filler-coke type, filler size and shape distribution, forming method, and the distribution of porosity from the nanometer to the millimeter scale, which together constitute the material's 'texture,' make synthetic graphite a uniquely tailorable material.

The breadth of synthetic graphite properties is controlled by the diverse, yet tailorable, textures of synthetic graphite. The physical and mechanical properties reflect both the single crystal bond anisotropy and the distribution of porosity within the material. This porosity plays a pivotal role in controlling thermal expansivity and the temperature dependency of strength in polygranular synthetic graphite. Electrical conduction is by electron transport, whereas graphite is a phonon conductor of heat. This complex combination of microstructural features bestows many useful properties such as an increasing strength with temperature and the excellent thermal shock resistance and also some undesirable attributes such as a reduction in thermal conductivity with increasing temperature. The chemical inertness and general unreactive nature of synthetic graphite allow applications in hostile chemical environments and at elevated temperatures, although its reactivity with oxygen at temperature above $\sim 300^\circ\text{C}$ is perhaps graphite's chief limitation.

Despite many years of research on the behavior of graphite, the details of the interactions between the graphite crystallites and porosity (pores/cracks within the filler coke or the binder and those associated with the coke/binder interface) have yet to be fully elucidated at all length scales. There is more research to be done.

Acknowledgments

This work is sponsored by the U.S. Department of Energy, Office of Nuclear Energy Science and Technology under Contract No. DE-AC05-00OR22725 with Oak Ridge National Laboratories managed by UT-Battelle, LLC.

This manuscript has been authored by UT-Battelle, LLC, under Contract No. DE-AC05-00OR22725 with the U.S. Department of Energy. The US government retains and the publisher, by accepting the article for publication, acknowledges that the US government retains a nonexclusive, paid-up, irrevocable, worldwide license to publish or reproduce the published form of this manuscript, or allow others to do so, for US government purposes.

References

1. Ruland, W. *Chem. Phys. Carbon* **1968**, 4, 1–84.
2. Eatherly, W. P.; Piper, E. L. In *Nuclear Graphite*; Nightingale, R. E., Ed.; Academic Press: New York, 1962; pp 21–51.
3. *A Pathfinder-Discovery, Invention, and Industry*; The Press Scrapbook: New York, 1910.
4. Mantell, C. L. *Carbon and Graphite Handbook*; Interscience: New York, 1968.
5. Dalhaès, P. Ed. *Graphite and Precursors*; Gordon and Breach Science: The Netherlands, 2001.
6. Inagaki, M. In *Graphite and Precursors*; Dalhaès, P., Ed.; Gordon and Breach Science: The Netherlands, 2001; pp 179–198.
7. Ragan, S.; Marsh, H. J. *Mater. Sci.* **1983**, 18, 3161–3176.
8. ASTM C709. *Standard Terminology Relating to Manufactured Carbon and Graphite, Annual Book of ASTM Standards*; ASTM International: West Conshohocken, PA, 2010; Vol. 5.05.
9. Burchell, T. D. In *Carbon Materials for Advanced Technologies*; Burchell, T. D., Ed.; Elsevier Science: Oxford, 1999; pp 429–484.
10. McEnaney, B.; Mays, T. J. In *Introduction to Carbon Science*; Marsh, H., Ed.; Butterworth & Co.: London, 1989; pp 153–196.
11. ASTM Standard Specification D7219. *Annual Book of ASTM Standards*; American Society for Testing and Materials: West Conshohocken, PA, 2010; Vol. 5.05.
12. Kelly, B. T. *Physics of Graphite*; Applied Science: London, 1981.
13. ASTM Standard C781. *Annual Book of ASTM Standards*; American Society for Testing and Materials: West Conshohocken, PA, 2010; Vol. 5.05.
14. Burchell, T. D. In *Graphite and Precursors*; Dalhaès, P., Ed.; Gordon and Breach Science: The Netherlands, 2001; pp 87–109.
15. Mrozowski, S. In *Proceedings of the 1st and 2nd Conference on Carbon*; Waverley: Baltimore, MD, 1956; p 31.
16. Smith, A. W.; Rasor, N. S. *Phys. Rev.* **1956**, 104, 885.
17. Nihira, T.; Iwata, T. *Jpn. J. Appl. Phys.* **1975**, 14, 1099.
18. Issi, J.-P. In *Graphite and Precursors*; Dalhaès, P., Ed.; Gordon and Breach Science: The Netherlands, 2001; pp 45–70.

19. Kelly, B. T.; Martin, W. H.; Price, A. M.; Dolby, P.; Smith, K. *J. Nucl. Mater.* **1966**, *20*, 195–209.
20. Spain, I. L. *Chem. Phys. Carbon* **1981**, *16*, 119–322.
21. Page, D. J. *The Industrial Graphite Engineering Handbook*; UCAR Carbon Company: Danbury, CT, 1991.
22. Spain, I. L. *Chem. Phys. Carbon* **1973**, *8*, 1–150.
23. Rand, B. In *Graphite and Precursors*; Delhaès, P., Ed.; Gordon and Breach Science: The Netherlands, 2001; pp 111–139.
24. Nightingale, R. E.; Yoshikawa, H. H.; Losty, H. H. W. In *Nuclear Graphite*; Nightingale, R. E., Ed.; Academic Press: New York, 1962; pp 117–194.
25. Jenkins, G. M. *Chem. Phys. Carbon* **1973**, *11*, 189–242.
26. Brocklehurst, J. E. *Chem. Phys. Carbon* **1977**, *13*, 145–295.
27. Burchell, T. D. Ph.D. Thesis, University of Bath, 1986.
28. Romanoski, G. R.; Burchell, T. D. In *Carbon Materials for Advanced Technologies*; Burchell, T. D., Ed.; Elsevier Science: Oxford, 1999; pp 485–534.
29. Burchell, T. D.; Oku, T.; Eto, M. A comparison of fracture toughness measurement techniques as applied to nuclear graphite. In *International Conference on Carbon, "Carbone 90"*, Paris, France, July 16–20, 1990; pp 278–279.
30. Buch, J. D. ASTM Special Technical Publication 605, Pub. ASTM International: West Conshohocken, PA, USA, 1972; pp 124–144.
31. Rose, A. P. G.; Tucker, M. O. *J. Nucl. Mater.* **1982**, *110*, 186–195.
32. Pickup, I. M.; Cooke, R. G.; McEnaney, B. In *Proceedings of the 16th Conference on Carbon*, University of California, San Diego, CA; American Carbon Society, 1983; pp 406–407.
33. Burchell, T. D.; McEnaney, B.; Rose, A. P. G.; Tucker, M. O. In *Proceedings of the 17th Biennial Conference on Carbon*, Lexington, KY, 1985; pp 346–347.
34. Burchell, T. D.; Cooke, R. G.; McEnaney, B.; Pickup, I. M. *Carbon* **1985**, *23*, 739–747.
35. Tucker, M. O.; Rose, A. P. G.; Burchell, T. D. *Carbon* **1986**, *24*, 581–602.
36. Ioka, I.; Yoda, S. *J. Nucl. Mater.* **1987**, *148*, 344–350.
37. Neighbour, G.; McEnaney, B.; Philips, M. *Carbon* **1992**, *30*, 359–363.
38. Burchell, T. D.; Rose, A. P. G.; McEnaney, B. *J. Nucl. Mater.* **1986**, *140*, 11–18.
39. Kaiser, J. Ph.D. Thesis, Technische Hochschule, Munich, Germany, 1950.
40. Kraus, G.; Semmler, J. *Carbon* **1978**, *16*, 185–190.
41. Ioka, I.; Yoda, S.; Konishi, T. *Carbon* **1990**, *28*, 879–885.
42. Burchell, T. D.; Tucker, M. O.; McEnaney, B. In *Materials for Nuclear Reactor Core Application*; BNES: London, 1987; pp 95–103.
43. Burchell, T. D. In *Proceedings of IAEA Specialist's Meeting on Status of Graphite Development for Gas Cooled Reactors*, Toki-Mura, Japan, Sept 1991; IAEA: Vienna, Feb, 1993; p 49, IAEA TECDOC No. 690.
44. Burchell, T. D.; Strizak, J. P. In *Proceedings of the 21st Biennial Conference on Carbon*, Buffalo, NY, 1993; pp 687–688.
45. Burchell, T. D.; Strizak, J. P. In *Proceedings of the Carbon '94*, Granada, Spain, 1994; pp 128–129.
46. Burchell, T. D. *Carbon* **1996**, *34*, 297–316.
47. Burchell, T.; Yahr, T.; Battiste, R. *Carbon* **2007**, *45*, 2570–2583.
48. Snead, L. L. In *Carbon Materials for Advanced Technologies*; Burchell, T. D., Ed.; Elsevier Science: Oxford, 1999; pp 389–427.
49. Burchell, T. D. In *Science of Carbon Materials*; Marsh, H., Rodríguez Reinoso, F., Eds.; Universidad de Alicante, Secretariado de Publicaciones, 2000; Chapter 3, pp 117–147.
50. Burchell, T. D. Nuclear graphite and radiation effects. In *Encyclopedia of Materials Science and Technology*; Elsevier Science, 2001; pp 6309–6319.

2.11 Neutron Reflector Materials (Be, Hydrides)

S. Yamanaka and K. Kurosaki

Osaka University, Suita, Japan

© 2012 Elsevier Ltd. All rights reserved.

2.11.1	Required Properties	307
2.11.2	Beryllium	308
2.11.2.1	Introduction	308
2.11.2.2	Production and Processing Methods ¹	308
2.11.2.3	Basic Properties	308
2.11.3	Fundamental Properties of Metal Hydrides	312
2.11.3.1	Introduction	312
2.11.3.2	Production of Zirconium Hydride ²⁰	312
2.11.3.3	Lattice Parameter ²⁰	314
2.11.3.4	Elastic Modulus and Hardness ^{20,21}	314
2.11.3.5	Electronic Structure ²²	315
2.11.3.6	Electrical Conductivity ²²	316
2.11.3.7	Heat Capacity ²⁰	317
2.11.3.8	Thermal Conductivity of Metal Hydrides ²³	317
2.11.3.9	Comparison of Thermal Conductivity of Zirconium Hydride with those of the Hydrides of Titanium and Yttrium	318
2.11.3.10	Conclusion	320
2.11.4	Summary	321
References		321

Abbreviations

DOS Density of state

MO Molecular orbital

Symbols

B Bulk modulus

D Diffusivity

E Young's modulus

G Shear modulus

H Enthalpy

H_v Vickers hardness

T_m Melting temperature

T_{tr} Transformation temperature

λ Thermal conductivity

λ_{el} Electronic contribution to thermal conductivity

λ_{lat} Lattice thermal conductivity

ρ Electrical resistivity

σ Electrical conductivity

Δ_mH Enthalpy of fusion

Δ_{trs}H Enthalpy of transition

2.11.1 Required Properties

Two highly desirable properties of both neutron reflectors and moderators are efficient neutron slowing and low neutron absorption. The first requires effective slowing of neutrons over short distances, thus reducing the required volume of the reflector or moderator in the reactor core. Moreover, in a reactor core of a given shape and volume, this reduces the leakage of neutrons in the course of their slowing.

For reflectors in particular, the key requirements include a high reflectivity, a large macroscopic cross-section, and efficient neutron slowing. The reflectivity of a material is inversely proportional to its diffusion ratio (D/L), which is the ratio of its diffusivity (D) to its diffusion length (L). This ratio is generally considered to decrease as scattering becomes large in comparison with absorption. It is essential, moreover, to obtain high reflectivity without excessive thickness, and for this purpose, to use a material with a large macroscopic total cross-section. In a thermal reactor, the performance of the reflector is enhanced if it does not simply reflect the neutrons but rather slows and then reflects them,

and for this reason, the same material is often used as both reflector and moderator.

In general, materials whose nuclides have low mass number and neutron absorption may be used as moderators and reflectors. The most commonly used materials are light water (H_2O), heavy water (D_2O), and graphite (C). In addition, hydrocarbons, zirconium hydride, and other such materials are often used as moderators. Heavy water is particularly effective because of its very low absorption level. Graphite is second to heavy water in its low absorption level, is lower in cost, and has the added advantage of suitability for use at high temperatures. Beryllium is generally used as a reflector rather than as a moderator.

In addition to the aforementioned materials, there exist other candidates as neutron reflectors. For example, Commissariat à l'Energie Atomique (CEA) is studying zirconium silicide as the reflector for next generation reactors.¹ Tungsten carbide has also been used as neutron reflectors (http://en.wikipedia.org/wiki/Tungsten_carbide). For fusion reactors, various materials such as titanium carbide and boron carbide are considered as reflectors.²

This chapter outlines the basic properties of beryllium and zirconium hydride that are fundamental to their utilization as neutron reflectors and moderators in nuclear reactors.

2.11.2 Beryllium

2.11.2.1 Introduction

Apart from its use as a neutron reflector and moderator in nuclear reactors, beryllium is in strong demand for use in X-ray windows of medical and industrial equipment, acoustic speaker diaphragms, galvano mirrors for laser drilling, reflected electron guard plates in semiconductor production equipment, and various other applications. It is also widely used in the electrical and electronic industry, particularly in beryllium-copper alloys for wrought metal production and for molds and other forging tools and dies. In electronics, in particular, the need for beryllium has been growing rapidly in recent years with the trend toward lighter, thinner, and smaller electronic components. In the following sections, we outline the methods of its production and processing and discuss its basic properties.

2.11.2.2 Production and Processing Methods¹

Among the 30 or so naturally occurring ores, the most economically important is beryl, which contains

10–14% beryllium oxide (BeO). At present, the two main industrial processes used to extract BeO from beryl are the fluoride method and the sulfuric acid method. Both of these yield BeO of industrial-grade purity, which is used as a raw material for Be–Cu mother alloys, electronics manufacture, refractories, and other fields of application. For use in nuclear reactors, BeO is further purified by recrystallization or precipitation.

Metallic beryllium (Be) is produced from BeO or $\text{Be}(\text{OH})_2$ by either of two industrial processes. One involves the formation of BeF_2 followed by its thermal reduction with Mg to produce Be pebbles, and the other involves the formation of BeCl_2 followed by its electrolysis to produce Be flakes. The resulting pebbles and flakes are high in Mg and Cl_2 content, respectively, and these impurities are removed by vacuum melting.

The principal techniques of Be processing are molding by powder metallurgy, warm or hot working, and joining or welding. In hot-press sintering, which has been widely developed for Be molding, the starting material is commonly –200 mesh Be powder, which is inserted between graphite dies and then pressure molded in vacuum at high temperatures (1323 K). The resulting moldings are commonly called ‘hot-press blocks,’ and can be obtained with high integrity and near theoretical density. Other molding methods that may be employed include spark plasma sintering and cold-press sintering.

Cold working of Be at room temperature is extremely difficult because of its low elongation, and it is accordingly formed into plates, rods, or tubes by ‘warm working’ at 773–1173 K or ‘hot working’ at 1273–1373 K. In either case, the Be must be covered with mild steel or some other material and the intervening air withdrawn before it is heated, as it readily oxidizes at high temperatures.

Various methods have been developed for Be joining and welding. These include mechanical joining and resin bonding, electron-beam and diffusion welding, and brazing and soldering. Because of its high oxygen affinity, however, any process in which the Be is heated must be performed under an appropriate inert gas or vacuum.

2.11.2.3 Basic Properties

The crystal structure of Be is closed-packed hexagonal with a c/a ratio of 1.5671 and lattice parameters $a = 0.22866$ nm and $c = 0.35833$ nm.³ Table 1 shows the basic properties of Be.^{4,5} It weighs only about

two-thirds as much as aluminum (Al), and both its melting point and its specific heat capacity are quite high for a light metal. It is widely known for its high Young's modulus and other elastic coefficients. Its nucleus is small in neutron absorption cross-section and relatively large in scattering cross-section, both of which are advantageous for use as a moderator or reflector. Its superior high-temperature dynamical

properties are also advantageous for use in nuclear reactors. It emits neutrons under γ -ray irradiation and can thus be used as a neutron source. Its soft X-ray absorption is less than one-tenth that of Al, making it highly effective as a material for X-ray tube windows.

Figure 1 shows the temperature dependence of the specific heat capacities of various Be samples.³ The following equations describing the specific heat capacity of Be are reported.³

$$C_p = 11.8 + 9.12 \times 10^{-3} T$$

$$(\text{J K}^{-1} \text{g}^{-1} \text{ atom, from 600 to 1560 K})$$

$$C_p = 25.4 + 2.15 \times 10^{-3} T$$

$$(\text{J K}^{-1} \text{g}^{-1} \text{ atom, from 1560 to 2200 K})$$

Temperature dependences of the thermal expansion coefficient and the electrical resistivity of Be³ are given in Figures 2 and 3, respectively. Figure 4 shows the temperature dependence of the thermal conductivities of various Be samples.^{3,6} Be exhibits relatively high thermal conductivity values around $200 \text{ W m}^{-1} \text{ K}^{-1}$ at room temperature, and the values decrease with temperature. The effect of high-dose neutron irradiation on the thermal conductivity of Be has been investigated.^{7,8} It is reported by Chakin *et al.*⁷ that neutron irradiation at 303 K to a neutron fluence of $2 \times 10^{22} \text{ cm}^{-2}$ ($E > 0.1 \text{ MeV}$) leads to sharp decrease of thermal conductivity, in particular at 303 K, the thermal conductivity decreases by a factor

Table 1 Basic properties of Be

Crystal structure	Hexagonal
Density (near room temperature) (g cm^{-3})	1.85
Melting point (K)	1560
Boiling point (K)	2742
Heat of fusion (kJ mol^{-1})	7.895
Heat of vaporization (kJ mol^{-1})	297
Heat capacity (302 K) ($\text{J K}^{-1} \text{mol}^{-1}$)	16.443
Thermal conductivity (300 K) ($\text{W m}^{-1} \text{K}^{-1}$)	200
Thermal expansion coefficient (302 K) (K^{-1})	11.3×10^{-6}
Speed of sound (room temperature) (m s^{-1})	12870
Young's modulus (GPa)	287
Shear modulus (GPa)	132
Bulk modulus (GPa)	130
Poisson ratio	0.032
Vickers hardness (GPa)	1.67
Scattering cross-section (barn)	6
Absorption cross-section (barn)	0.009
Moderating ratio	0.0597
Diffusion ratio	0.0273

Source: *Genshiryoku Zairyou Handbook*; The Nikkan Kogyo Shimbun: Tokyo, 1952; <http://en.wikipedia.org/wiki/Beryllium>; *Rare Metals Handbook*, 2nd ed.; Reinhold: New York, NY, 1961.

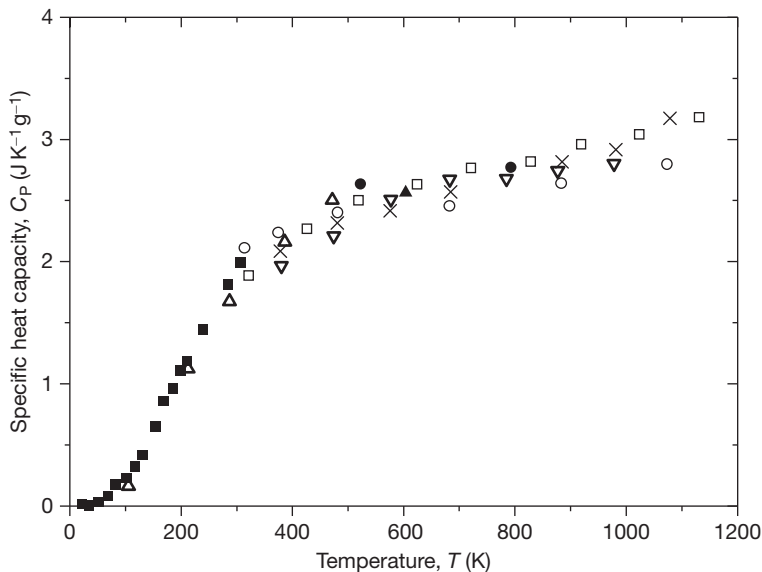


Figure 1 Temperature dependence of the specific heat capacity of various Be samples. Different marks mean different samples. Reproduced from Beeston, J. M. *Nucl. Eng. Des.* **1970**, *14*, 445.

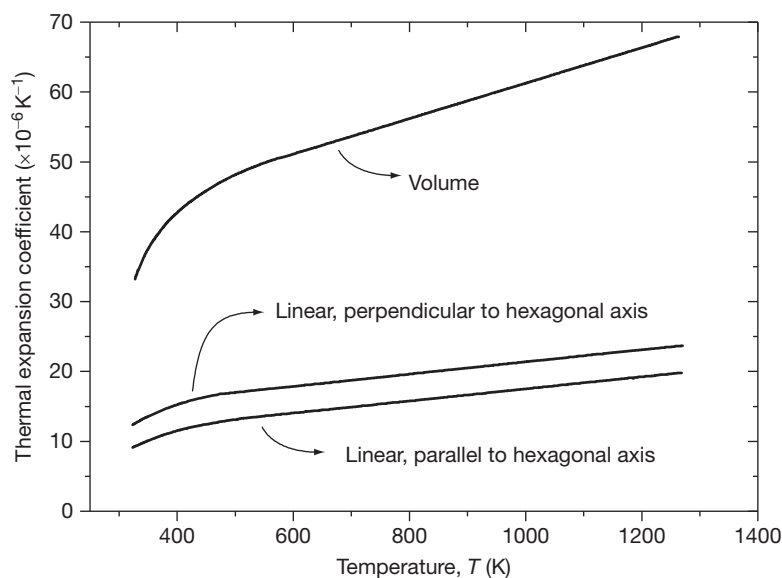


Figure 2 Temperature dependence of the thermal expansion coefficient of Be. Reproduced from Beeston, J. M. *Nucl. Eng. Des.* **1970**, *14*, 445.

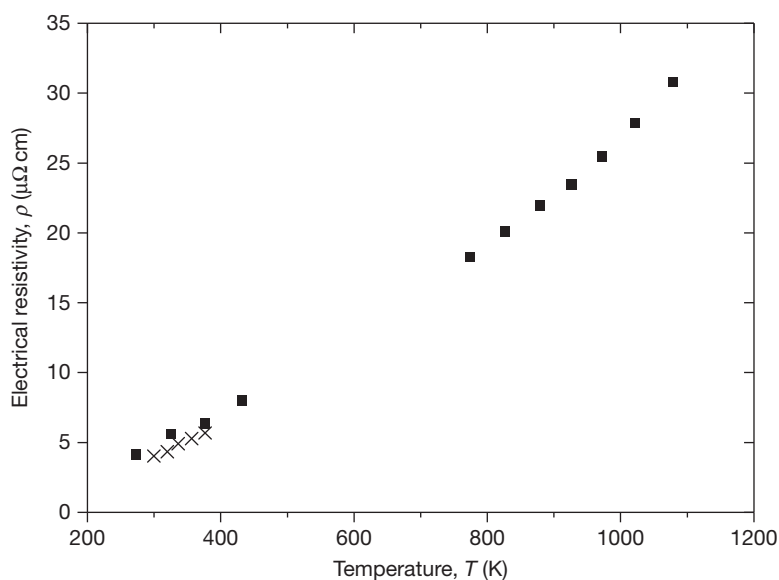


Figure 3 Temperature dependence of the electrical resistivity of Be. Different marks mean different samples. Reproduced from Beeston, J. M. *Nucl. Eng. Des.* **1970**, *14*, 445.

of five, but short-term high-temperature annealing (773 K for 3 h) leads to partial recovery of the thermal conductivity.

In addition to the data listed in [Table 1](#), the thermodynamic properties of Be have been reported recently,⁹ in which the temperatures of transformation T_{tr} and melting T_m , and the enthalpies of transformation $\Delta_{tr}H$ and melting Δ_mH are measured

by difference thermal analysis and by anisothermal calorimetry. It is reported by Kleykamp⁹ that the results for hcp–bcc transformation of Be are $T_{tr} = 1542 \pm 1$ K and $\Delta_{tr}H = 6.1 \pm 0.5$ kJ mol⁻¹ and those for the melting process are $T_m = 1556 \pm 2$ K and $\Delta_mH = 7.2 \pm 0.5$ kJ mol⁻¹.

A fine, transparent BeO film of about 10^{-6} cm thickness forms on Be in air, and it therefore retains

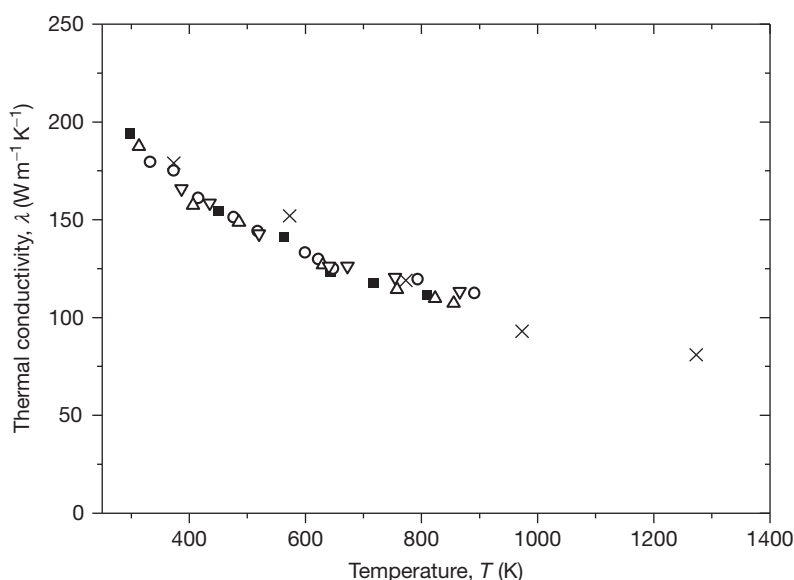


Figure 4 Temperature dependence of the thermal conductivities of various Be samples. Different marks mean different samples. Adapted from Beeston, J. M. *Nucl. Eng. Des.* **1970**, 14, 445; Chirkin, V. S. *Trans. Atom. Ener.* **1966**, 20, 107.

its metallic gloss when left standing. This results in its passivation in dry oxygen at up to 923 K, but the oxidized film breaks down at temperatures above about 1023 K and it thus becomes subject to progressive oxidation.¹⁰ It reacts with nitrogen at 1173 K or higher, forming Be_2N_3 , and with NH_3 at lower temperatures.¹⁰ Be undergoes passivation in dry CO_2 at up to 973 K, but only up to 873 K in moist CO_2 .^{11,12} Its resistance to corrosion by water varies with temperature, dissolved ion content, pH, and other factors; it is reportedly poor in water containing Cl^- (1–10 ppm), SO_4^{2-} (5–15 ppm), Cu^{2+} (0.1–5 ppm), Fe^{2+} (1–10 ppm), or other such ions.¹⁰

Among the various compounds formed by Be, BeO and Be_2C may be taken as typical. The basic properties of BeO are shown in Table 2.⁴ Its melting point and thermal conductivity are both high,¹³ its heat shock resistance is excellent, its thermal neutron absorption cross-section is small, and its corrosion resistance to CO_2 at high temperatures is also excellent. Be_2C is formed by reaction of Be or BeO with C. Its basic properties are density, 2.44 g cm^{-3} ; specific heat capacity, $41.47 \text{ J K}^{-1} \text{ mol}^{-1}$ (303–373 K); thermal expansion coefficient, $10.5 \times 10^{-6} \text{ K}^{-1}$ (298–873 K); and electric resistivity, $0.063 \text{ } \Omega \text{ m}$ (303 K). It is reportedly unstable in moist air.¹⁰

Intrinsically, BeO is an excellent moderator and reflector material in nuclear reactors. Various utilizations of BeO in reactors¹⁴ and behavior of BeO under neutron irradiation have been reported.¹⁵ Especially,

Table 2 Basic properties of BeO

Crystal structure	Hexagonal wurtzite
Density (near room temperature) (g cm^{-3})	3.02
Melting point (K)	2780
Boiling point (K)	4173
Thermal conductivity (293 K) ($\text{W m}^{-1} \text{K}^{-1}$)	281
Thermal expansion coefficient (293–373 K) (K^{-1})	5.5×10^{-6}
Electrical resistivity (1273 K) ($\Omega \text{ cm}$)	8.0×10^7
Scattering cross-section (barn)	9.8
Absorption cross-section (barn)	0.0092
Moderating ratio	0.0706
Diffusion ratio	0.0273

Source: *Genshiryoku Zaiyou Handbook*; The Nikkan Kogyo Shimbun: Tokyo, 1952; Gregg, S. J.; et al. *J. Nucl. Mater.* **1961**, 4, 46.

the effect of neutron irradiation on the thermal conductivity of BeO has been widely studied.^{16,17} Figure 5 shows the temperature dependence of the thermal conductivity of unirradiated and irradiated BeO.¹⁷ It is observed that irradiation of BeO with neutrons considerably reduces the thermal conductivity. It has also been reported that the irradiation-induced change in thermal conductivity can be removed by thermal annealing, but complete recovery is not achieved until an annealing temperature of 1473 K is reached.

One further important property of Be that must be noted is its high toxicity. The effect of Be dust, vapor, and soluble solutes varies among individuals,

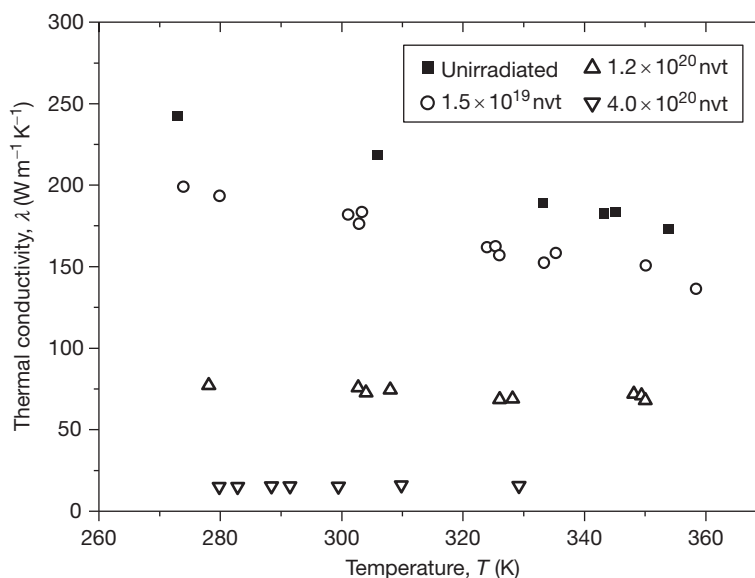


Figure 5 Temperature dependence of the thermal conductivity of unirradiated and irradiated BeO. Reproduced from Pryor, A. W.; *et al. J. Nucl. Mater.* **1964**, *14*, 208.

but exposure may cause dermatitis and contact or absorption by mucous membrane or respiratory tract may result in chronic beryllium disease, or 'berylliosis.' Maximum permissible concentrations in air were established in 1948 and include an 8-h average concentration of $2 \mu\text{g m}^{-3}$, a peak concentration of $25 \mu\text{g m}^{-3}$ in plants, and a peak concentration of $0.01 \mu\text{g m}^{-3}$ in plant vicinities.¹⁸ In relation to workplace health and safety, particular care is necessary in the control of fine powder generated during molding and mechanical processing. Dust collectors must be installed at the points of generation, and dust-proof masks, dust-proof goggles, and other protective gear must be worn during work. In Japan, Be is subject to the Ordinance on Prevention of Hazards due to Specified Chemical Substances.

2.11.3 Fundamental Properties of Metal Hydrides

2.11.3.1 Introduction

Zirconium hydride is used as a material for neutron reflectors in fast reactors. The evaluation of the thermal conductivity, elastic modulus, and other basic properties of zirconium hydride is extremely important for assessing the safety and cost-effectiveness of nuclear reactors. Metal hydrides, of which zirconium hydride is a typical example, are also very interesting because they exhibit unique properties and shed light

on some fundamental aspects of physics. As part of work on metals such as zirconium, Yanamana *et al.* have successfully created crack-free, bulk-scale metal hydrides, and systematically investigated their fundamental properties – particularly at high temperatures. Here, we present an outline of the results on the fundamental properties of zirconium hydride. [Figure 6](#) shows the zirconium–hydrogen binary phase diagram.¹⁹

2.11.3.2 Production of Zirconium Hydride²⁰

We used polycrystalline (grain size: 20–50 μm) ingots of high-purity zirconium as the starting material for producing hydrides. The main impurities present in the zirconium were O (0.25 wt%), H (0.0006 wt%), N (0.0024 wt%), C (0.003 wt%), Fe (0.006 wt%), and Cr (0.008 wt%). The hydride was generated with high-purity hydrogen gas (7 N) at a prescribed pressure, using an advanced ultra-high vacuum Sieverts instrument. Details of the instrument configuration are given in [Figure 7](#).

The procedure for synthesizing hydrides varies according to the type of metal. This is due to the phase transition, from metal to hydride that is accompanied by a massive increase in volume due to hydrogenation, and to differences in the strength of the hydride. [Figure 8](#) shows the external appearance of zirconium hydride substances produced by the author's group.

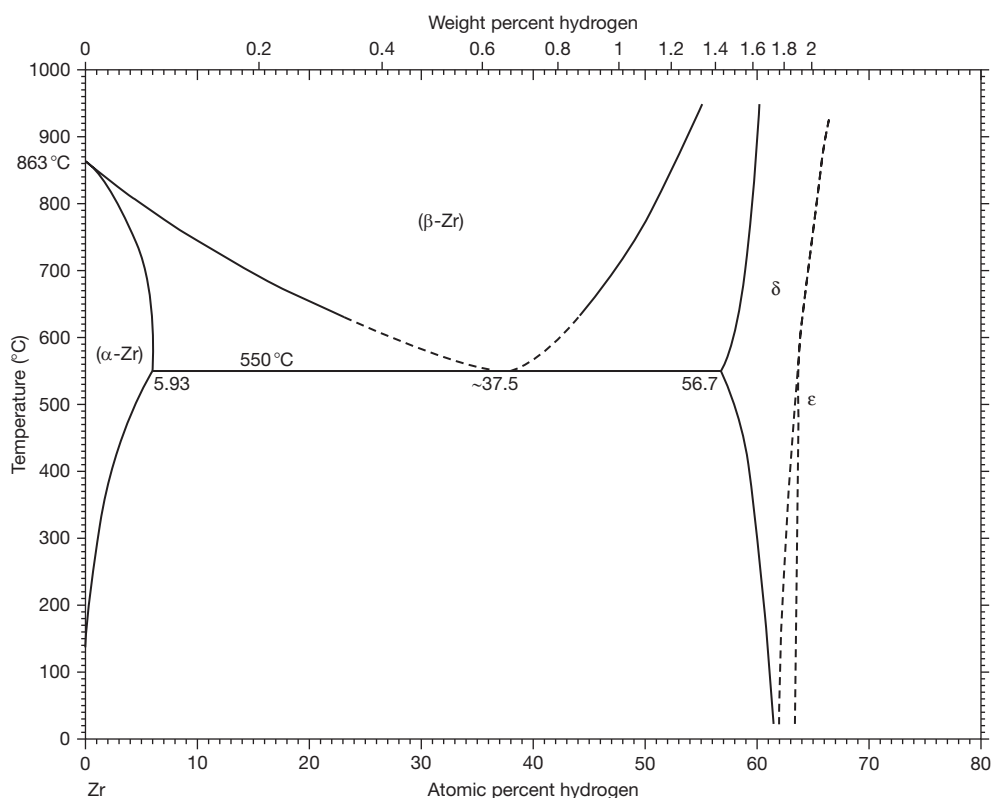
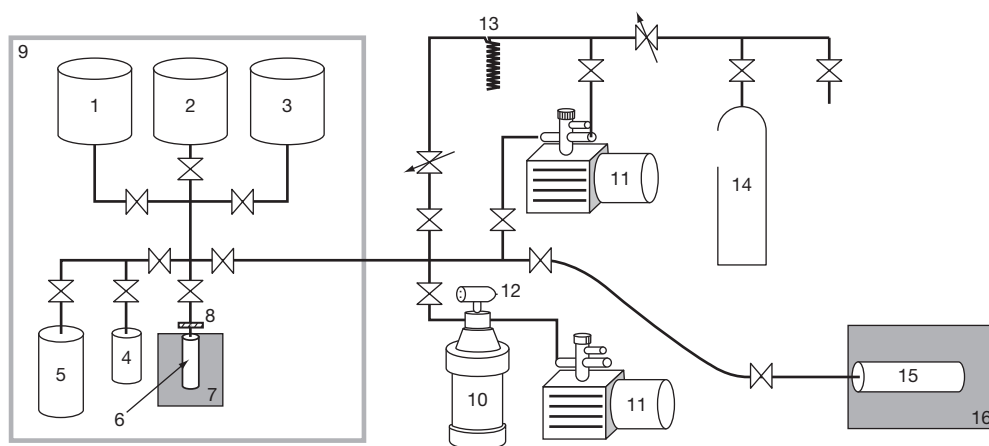


Figure 6 Binary phase diagram of the zirconium–hydrogen system. δ and ϵ represent the face-centered cubic δ -phase hydride and the face-centered tetragonal ϵ -phase hydride, respectively. Adapted from Zuzek, E.; Abriata, J. P.; San-Martin, A.; Manchester, F. D. *Bull. Alloy Phase Diagrams* **1990**, 11(4), 385–395.



- | | |
|--|---|
| 1. Absolute capacitance manometer (25 ktorr) | 9. Low temperature incubator (inner temperature: 298 K) |
| 2. Absolute capacitance manometer (1 ktorr) | 10. Turbo-molecular pump |
| 3. Absolute capacitance manometer (10 torr) | 11. Oil rotary vacuum pump |
| 4. Calibrated vessel (~50 ml) | 12. Ionization vacuum gauge |
| 5. Calibrated vessel (~500 ml) | 13. Liquid nitrogen trap |
| 6. Reactor for high pressure (steel) | 14. Compressed hydrogen gas cylinder |
| 7. Mantle heater (<723 K) | 15. Reactor for high temperature (quartz glass) |
| 8. Metal filter (pore size: 2 μ m) | 16. Electric resistance furnace (<1273 K) |

Figure 7 Schematic diagram of advanced Sieverts instrument.

2.11.3.3 Lattice Parameter²⁰

Zirconium hydride or deuteride described here was all fcc_C1 (δ) ZrH_{2-x} or ZrD_{2-x} single-phase crystals with a fluorite structure. The lattice parameters at ambient temperature of zirconium hydride or deuteride are plotted in Figure 9, as a function of hydrogen content (C_H). The lattice parameter of zirconium hydride increases slightly with increasing hydrogen content, according to the following formula:

$$a(\text{nm}) = 0.4706 + 4.382 \times 10^{-3} \times C_H(\text{H/Zr}).$$



Figure 8 Bulk-scale zirconium hydride.

2.11.3.4 Elastic Modulus and Hardness^{20,21}

Figure 10 illustrates the hydrogen content dependence of the elastic modulus of zirconium hydride or deuteride, determined using an ultrasonic pulse echo method. The elastic modulus of zirconium hydride is higher than that of the pure metal, and decreases slightly with increasing hydrogen content. The hydrogen content dependence of the elastic modulus of zirconium hydride is expressed by the following equations (E : Young's modulus, G : Shear modulus, and B : Bulk modulus):

$$E(\text{GPa}) = 187.7 - 33.28 \times C_H(\text{H/Zr})$$

$$G(\text{GPa}) = 73.59 - 14.19 \times C_H(\text{H/Zr})$$

$$B(\text{GPa}) = 130.0 - 2.329 \times C_H(\text{H/Zr})$$

Figure 11 illustrates the hydrogen content dependence of the Vickers hardness of zirconium hydride and deuteride. The graph clearly shows that the Vickers hardness of the hydride is higher than that of pure zirconium, and that it decreases slightly with increasing hydrogen content. Generalizing these results, we can conclude that increasing the hydrogen content has the effect of making zirconium hydride and deuteride plastically 'softer.' The relationship between the hardness and hydrogen content dependence for zirconium hydride is expressed by the following formula:

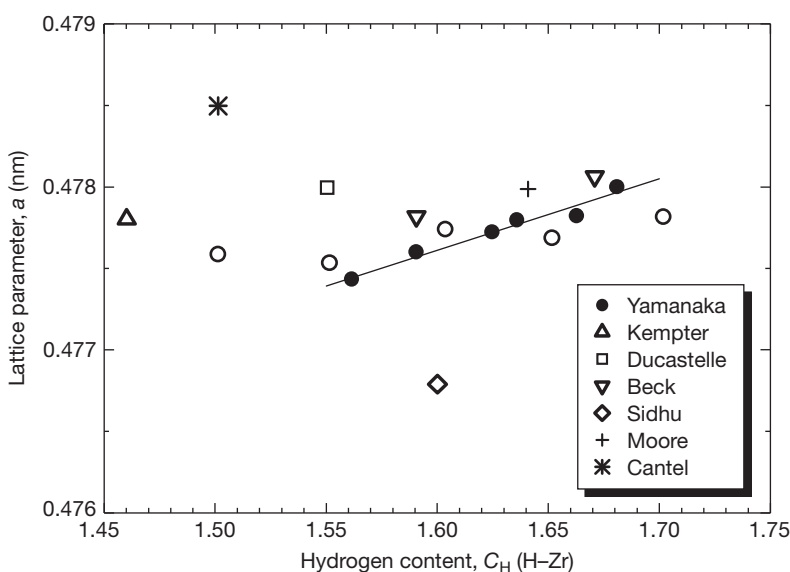


Figure 9 Hydrogen content dependence of the lattice parameter of zirconium hydride and deuteride.

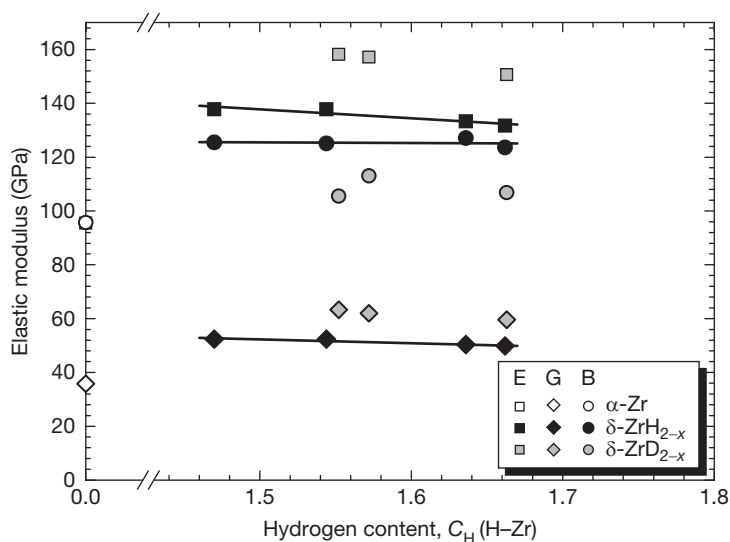


Figure 10 Hydrogen content dependence of the elastic modulus of zirconium hydride and deuteride.

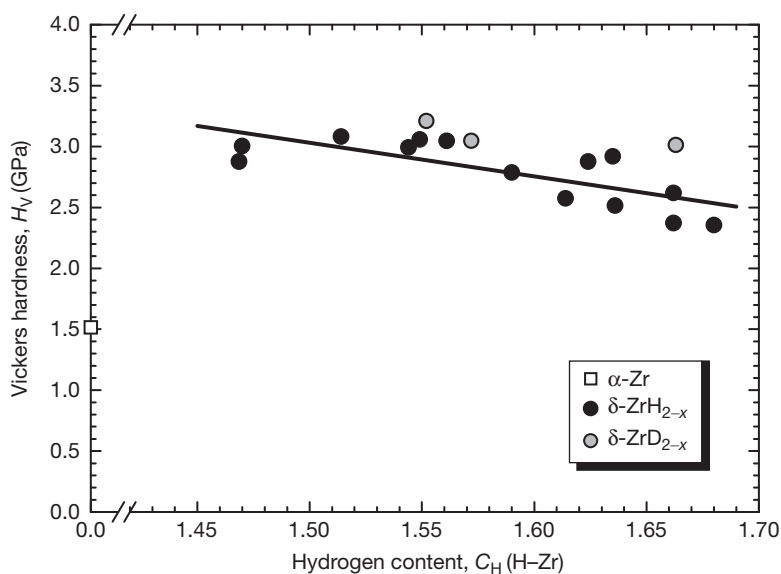


Figure 11 Hydrogen content dependence of the Vickers hardness of zirconium hydride and deuteride.

$$H_V(\text{GPa}) = 7.190 - 2.773 \times C_H(\text{H/Zr})$$

2.11.3.5 Electronic Structure²²

Figure 12 shows the density of states (DOS) of zirconium hydride, determined by DV-X α molecular orbital (MO) calculations. Here, 0 eV corresponds to the Fermi energy. The new band resulting

from the hydrogen is generated immediately below the d-band of the hydride cluster, in the region of $\sim 5\text{--}7\text{ eV}$. **Figure 13** shows the bond order of zirconium hydride. With increasing hydrogen content, there is a marked decrease in the bond order of Zr–Zr metallic bonds, whereas the bond order of Zr–H covalent bonds does not change. This reduction in bond order is likely due to a decrease in the electric charge of the matrix of Zr bonds.

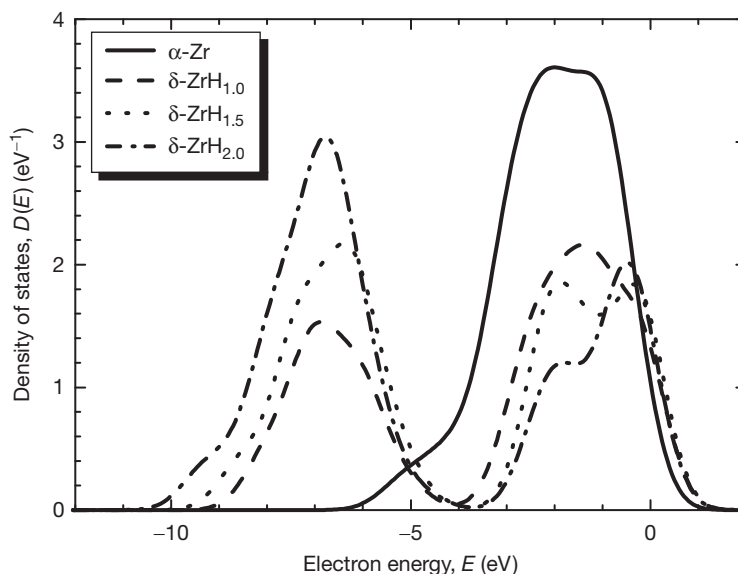


Figure 12 Hydrogen content dependence of the DOS of zirconium hydride.

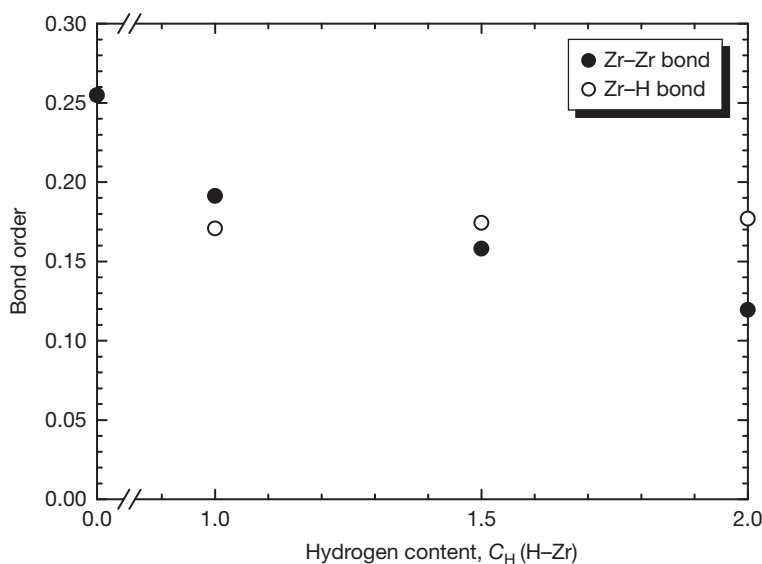


Figure 13 Hydrogen content dependence of the bond order of zirconium hydride.

Since bond order can be thought to be related to the spring constant of interatomic bonds, these results can be understood to mean that the effective spring constant of zirconium hydride, as a whole, decreases with increasing hydrogen content. This hypothesis offers a good explanation for the hydrogen content dependence of the various properties of zirconium hydride.

2.11.3.6 Electrical Conductivity²²

Figure 14 shows the temperature dependence of the electrical conductivity of zirconium hydride. In line with the behavior of most metals, electrical conductivity decreases with increasing temperature for zirconium hydride. The hydride has a lower electrical conductivity than the pure metals.

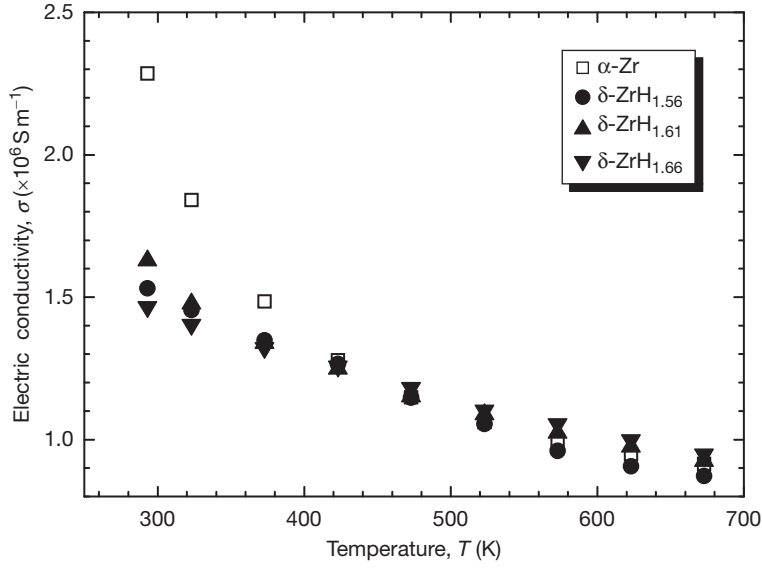


Figure 14 Temperature dependence of the electrical conductivity of zirconium hydride.

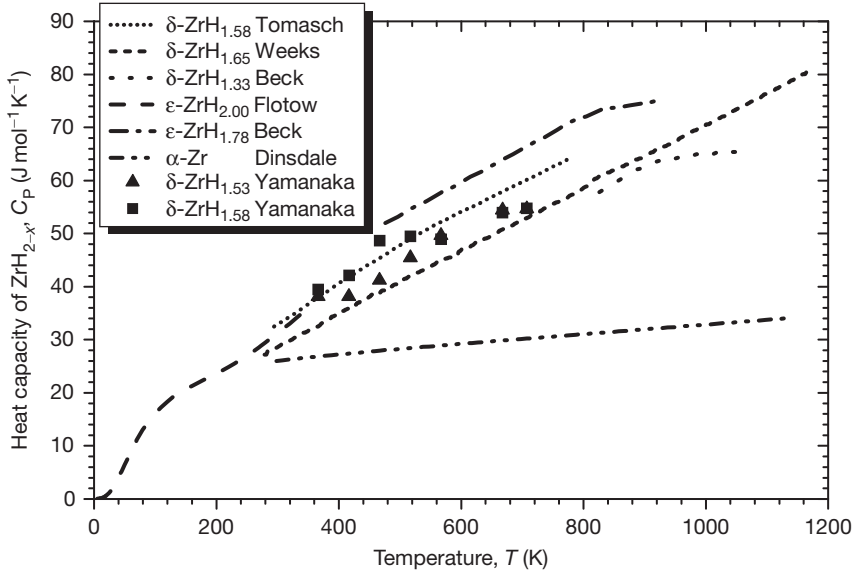


Figure 15 Temperature dependence of the heat capacity of zirconium hydride.

2.11.3.7 Heat Capacity²⁰

Figure 15 illustrates the temperature dependence of the heat capacity of zirconium hydride. It is clear that the heat capacity of the metal hydride is higher than that of the pure metal, particularly at higher temperatures. This behavior can be explained by the observation that while lattice vibrations are dominated by the acoustic mode at low temperatures, the contribution of the optical mode increases steadily as the temperature increases beyond ambient values.

2.11.3.8 Thermal Conductivity of Metal Hydrides²³

Figure 16 shows the thermal conductivity of zirconium hydride, which is seen to be almost identical to that of the pure metal, and shows no dependence on temperature.

In order to analyze the thermal conductivity results, we expressed thermal conductivity as the sum of a lattice-vibration contribution (λ_{lat}) and an electronic contribution (λ_{el}). The electronic

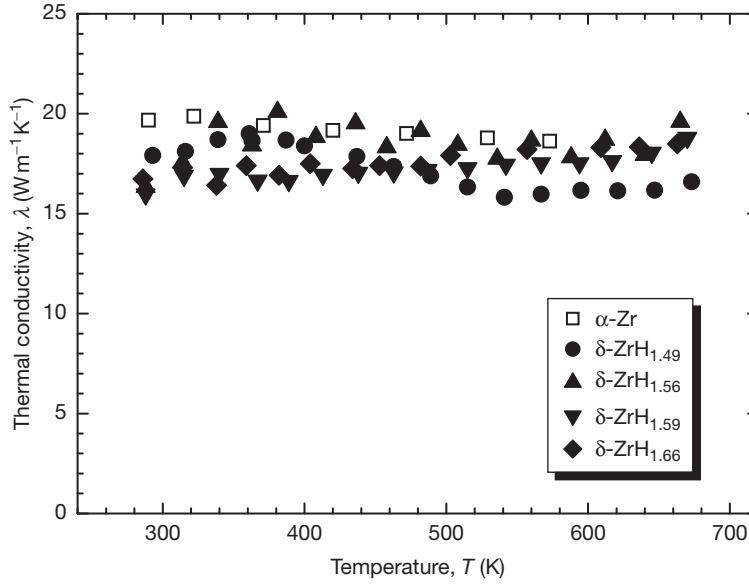


Figure 16 Temperature dependence of the thermal conductivity of zirconium hydride.

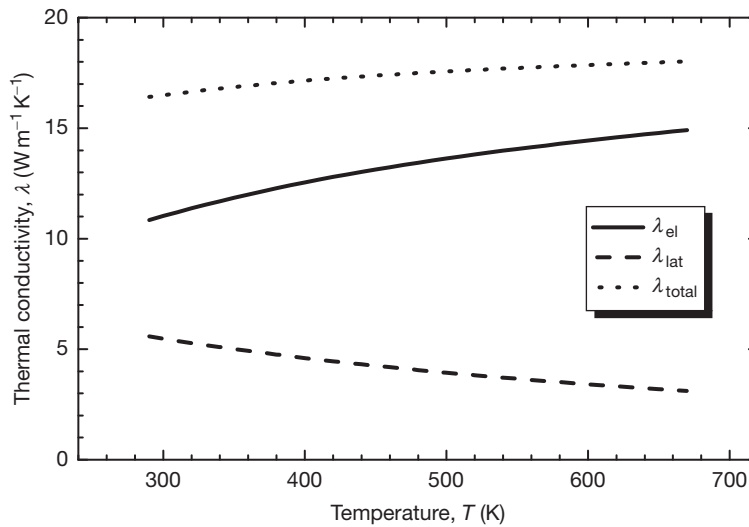


Figure 17 Temperature dependence of the lattice-vibration and electronic contributions to thermal conductivity for zirconium hydride (δ -ZrH_{1.66}).

contribution was evaluated from the Wiedemann–Franz relation as follows:

$$\lambda_{el} = L\sigma T$$

Here, L is the Lorentz constant and σ is electrical conductivity. Figure 17 plots the values of each contribution to the thermal conductivity of zirconium hydride. Here, the electronic contribution is greater than that of lattice vibrations, and the former increases with temperature, whereas the latter decreases as the temperature rises.

2.11.3.9 Comparison of Thermal Conductivity of Zirconium Hydride with those of the Hydrides of Titanium and Yttrium

Figure 18 shows the thermal conductivity of titanium hydride.²⁴ The thermal conductivity of the hydride is approximately equal to that of the pure metal, but in this case, it increases slightly with hydrogen content. Figure 19 shows the thermal conductivity of yttrium hydride.²⁵ In this case, the thermal conductivity of the hydride is higher than that of

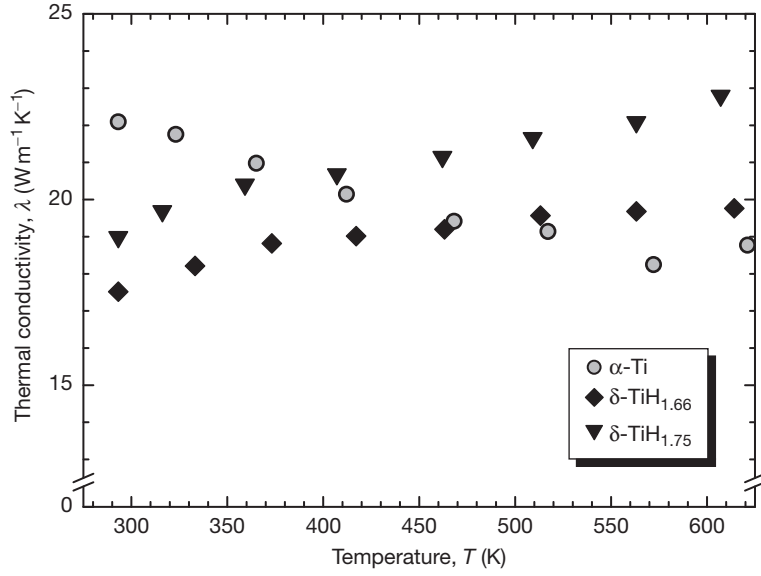


Figure 18 Temperature dependence of the thermal conductivity of titanium hydride.

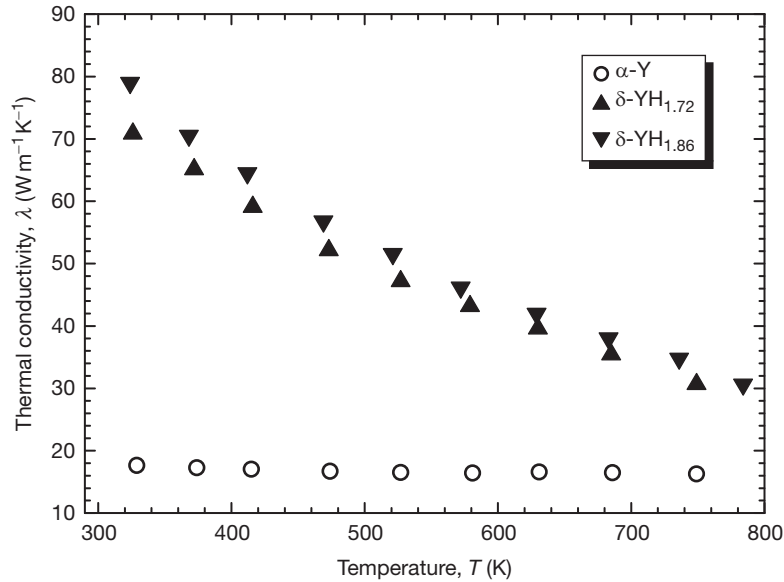


Figure 19 Temperature dependence of the thermal conductivity of yttrium hydride.

the metal, and it decreases with increasing hydrogen content. Additionally, the hydride's thermal conductivity decreases with decreasing temperature, whereas that of the metal remains more or less constant. Figure 20 plots the values of a lattice-vibration contribution and an electronic contribution to the thermal conductivity of titanium hydride. The results for titanium hydride are not much different from

those for zirconium hydride, as shown in Figure 17. However, as shown in Figure 21, the results for the case of yttrium reveal that both the lattice-vibration and electronic contributions to thermal conductivity are greater for yttrium hydride than for the pure metal. This indicates that the thermal conductivity characteristics of yttrium are different from those of zirconium and titanium.

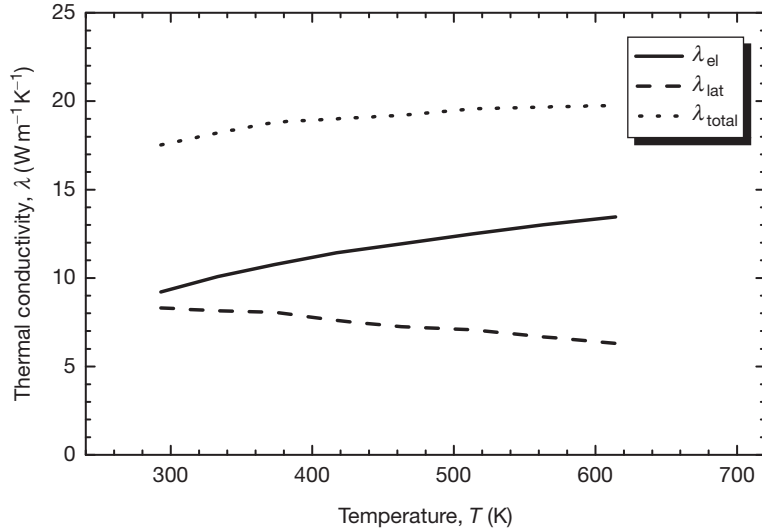


Figure 20 Temperature dependence of the lattice-vibration and electronic contributions to thermal conductivity for titanium hydride ($\delta\text{TiH}_{1.66}$).

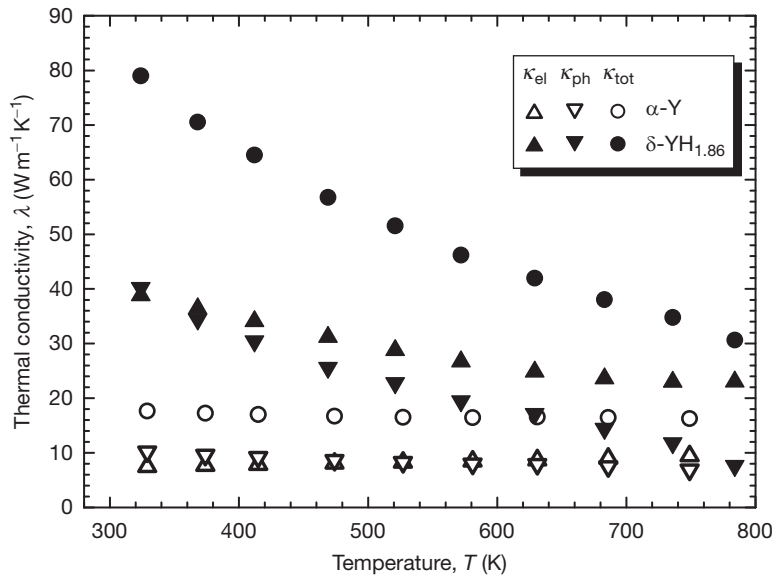


Figure 21 Temperature dependence of the lattice-vibration and electronic contributions to thermal conductivity for yttrium hydride and yttrium metal.

2.11.3.10 Conclusion

Here, we reviewed the fundamental properties of metal hydrides, focusing on zirconium hydride, which is a material used to make the neutron reflectors of fast nuclear reactors, as well as titanium hydride and yttrium hydride. We discussed the hydrogen content and temperature dependence of

the elastic modulus, hardness, electrical conductivity, heat capacity, and thermal conductivity of zirconium hydride. Values of the physical properties of zirconium hydride (δ -ZrH_{1.66}) are summarized in [Table 3](#). Such data are very important and valuable for the utilization of metal hydrides as materials for neutron reflectors in fast reactors.

Table 3 Physical properties of zirconium hydride (δ -ZrH_{1.66})

Lattice parameter (nm)	0.47782
Young's modulus (GPa)	132
Shear modulus (GPa)	50
Bulk modulus (GPa)	124
Vickers hardness (GPa)	2.67
Heat capacity (for δ -ZrH _{1.66}) (J K ⁻¹ mol ⁻¹)	39.4 (at 367 K) 54.8 (at 708 K)
Electrical conductivity ($\times 10^6$ S m ⁻¹)	1.47 (at 293 K) 0.95 (at 673 K)
Thermal conductivity (W m ⁻¹ K ⁻¹)	16.7 (at 286 K) 18.5 (at 663 K)

The data for the lattice parameter, Young's modulus, shear modulus, bulk modulus, and Vickers hardness were obtained at room temperature.

2.11.4 Summary

This chapter has provided a basic outline of neutron reflectors for nuclear reactors from the perspective of materials science, beginning with an overview of the properties required for neutron reflectors, proceeding to an outline of the production and processing methods for Be and metal hydrides as representative reflector materials, and then to a description of their basic properties. The outline of metal hydrides has focused on zirconium hydride, which is currently used mainly in fast reactors, and has described the influence of temperature and hydrogen concentration on the basic properties of zirconium hydride. The data provided in this chapter are considered to be extremely important and valuable in regard to the use of Be and zirconium hydride as neutron reflectors.

References

1. Canel, J.; Zaman, J.; Bettembourg, J.; Flem, M. Le.; Poissonnet, S. *Int. J. Appl. Ceram. Technol.* **2006**, *3*, 23.
2. Han, B.; Kim, Y.; Kim, C. H. *Fus. Eng. Des.* **2006**, *81*, 729.
3. Beeston, J. M. *Nucl. Eng. Des.* **1970**, *14*, 445.
4. *Genshiryoku Zairyou Handbook*; The Nikkan Kogyo Shimbun: Tokyo, 1952.
5. *Rare Metals Handbook*, 2nd edn.; Reinhold: New York, NY, 1961.
6. Chirkin, V. S. *Trans. Atom. Ener.* **1966**, *20*, 107.
7. Chakin, V. P.; Latypov, R. N.; Suslov, D. N.; Kupriyanov, I. B. *JAERI-Conference 2004–2006*, pp 119–127.
8. Syslov, D. N.; Chakin, V. P.; Latypov, R. N. *J. Nucl. Mater.* **2002**, *307–311*, 664.
9. Kleykamp, H. *Thermochim. Acta* **2000**, *345*, 179.
10. Tipton, C. R. *Reactor Hand Book*, 2nd edn.; Interscience: New York, 1960.
11. Gregg, S. J.; Hussey, R. J.; Jepson, W. B. *J. Nucl. Mater.* **1960**, *3*, 175.
12. Gregg, S. J.; Hussey, R. J.; Jepson, W. B. *J. Nucl. Mater.* **1961**, *4*, 46.
13. Kharlamov, A. G. *Atomnaya Énergiya* **1963**, *15*(6), 517–519.
14. Manly, W. D. *J. Nucl. Mater.* **1964**, *14*, 3.
15. Keilholtz, G. W.; Lee, J. E. Jr.; Moore, R. E.; Hamner, R. L. *J. Nucl. Mater.* **1964**, *14*, 87.
16. Cooper, M. K.; Palmer, A. R.; Stolarski, G. Z. *J. Nucl. Mater.* **1963**, *9*, 320.
17. Pryor, A. W.; Tainsh, R. J.; White, G. K. *J. Nucl. Mater.* **1964**, *14*, 208.
18. Eisenbud, M. *The Metal Beryllium*; ASM, 1995, p 703.
19. Zuzek, E.; Abriata, J. P.; San-Martin, A.; Manchester, F. D. *Bull. Alloy Phase Diagrams* **1990**, *11*(4), 385–395.
20. Yamanaka, S.; Yoshioka, K.; Uno, M.; *et al.* *J. Alloys Compd.* **1999**, *293–295*, 908.
21. Ito, M.; Setoyama, D.; Matsunaga, J.; *et al.* *J. Alloys Compd.* **2006**, *426*, 67.
22. Yamanaka, S.; Yamada, K.; Kurosaki, K.; *et al.* *J. Alloys Compd.* **2002**, *330–332*, 99.
23. Yamanaka, S.; Yamada, K.; Kurosaki, K.; *et al.* *J. Nucl. Mater.* **2001**, *294*, 94.
24. Ito, M.; Setoyama, D.; Matsunaga, J.; *et al.* *J. Alloys Compd.* **2006**, *420*, 25.
25. Ito, M.; Matsunaga, J.; Setoyama, D.; *et al.* *J. Nucl. Mater.* **2005**, *344*, 295.

2.12 Properties and Characteristics of SiC and SiC/SiC Composites

J. Lamon

CNRS/National Institute of Applied Science, Villeurbanne, France

© 2012 Elsevier Ltd. All rights reserved.

2.12.1	Introduction	324
2.12.2	β-SiC Properties²³	325
2.12.2.1	Mechanical Properties	325
2.12.2.1.1	Elastic modulus ²³	325
2.12.2.1.2	Poisson's ratio ²³	325
2.12.2.1.3	Shear modulus ²³	325
2.12.2.1.4	Hardness ²³	325
2.12.2.1.5	Fracture toughness ²³	325
2.12.2.1.6	Fracture strength	326
2.12.2.1.7	Thermal creep ²³	326
2.12.2.2	Thermal Properties²³	326
2.12.2.2.1	Thermal conductivity	326
2.12.2.2.2	Specific heat	326
2.12.2.2.3	Thermal expansion	327
2.12.3	SiC/SiC Composite	327
2.12.3.1	Fibrous Preform	327
2.12.3.2	Coating of Fibers	327
2.12.3.3	Infiltration of the SiC Matrix: The CVI Process	327
2.12.3.4	Infiltration of the SiC Matrix: The NITE Process	328
2.12.4	Properties of CVI SiC/SiC	328
2.12.5	Properties of NITE-SiC/SiC	330
2.12.6	Mechanical Behavior of CVI SiC/SiC	330
2.12.6.1	Tensile Stress–Strain Behavior	330
2.12.6.2	Damage Mechanisms	331
2.12.6.3	Ultimate Failure	333
2.12.6.4	Reliability	333
2.12.6.5	Interface Properties: Influence on the Mechanical Behavior	334
2.12.6.6	Fracture Toughness	335
2.12.6.7	Fatigue and High-Temperature Behavior	336
2.12.6.8	Thermal Shock	336
2.12.6.9	Creep Behavior	336
2.12.7	Concluding Remarks	337
References		337

Abbreviations

C/C	Carbon matrix composite reinforced by carbon fibers
C/SiC	SiC matrix composite reinforced by carbon fibers
CMC	Ceramic matrix composite
CVD	Chemical vapor deposition
CVI	Chemical vapor infiltration

LPS	Liquid phase sintering
MI	Melt infiltration
NITE	Nanopowder infiltration and transient eutectic-phase
PIP	polymer impregnation and pyrolysis
PyC	Pyrocarbon
RS	Reaction sintering
SENB	Single edge notch bending

SEP	Société Européenne de Propulsion
SiC/SiC	SiC matrix composite reinforced by SiC fibers

2.12.1 Introduction

Silicon carbide is composed of tetrahedra of carbon and silicon atoms with strong bonds in the crystal lattice. This produces a very hard and strong ceramic with outstanding characteristics such as high thermal conductivity, low thermal expansion, and exceptional resistance to thermal shock and to corrosion in aggressive environments at high temperatures. However, this implies a few inadequate characteristics for structural applications, such as low fracture toughness, high sensitivity to the presence of microstructural flaws, brittle behavior, and lack of reliability. Reinforcing with continuous SiC-based fibers allows these weaknesses to be overcome. The composite SiC/SiC that is obtained is damage tolerant, tough, and strong, and it can be insensitive to flaws and notches. The concept of composite material is very powerful. Composites can be tailored to suit end-use applications through the sound selection and arrangement of the constituents. Ceramic matrix composites (CMCs) reinforced with continuous ceramic or carbon fibers are of interest in thermostructural applications.^{1–4} They are lightweight and damage tolerant and exhibit a much greater resistance to high temperatures and aggressive environments than metals or other conventional engineering materials.

CMCs can be fabricated by different processing techniques, using either liquid or gaseous precursors. The chemical vapor infiltration (CVI) method can produce excellent SiC/SiC composites with a highly crystalline structure and excellent mechanical properties.⁵ The quality of the material obtained by the polymer impregnation and pyrolysis (PIP) method is insufficient. A novel processing technique (nanopowder infiltration and transient eutectic-phase processing, NITE) was claimed to achieve good material quality.^{5–7}

The SiC/SiC composites prepared using the CVI method and reinforced with the latest near-stoichiometric SiC fibers (such as Hi-Nicalon type S and Tyranno-SA3 fibers) appear to be promising candidates for nuclear applications^{7–12} because of their high crystallinity, high purity, near stoichiometry and radiation resistance of the β -phase of SiC, as well as excellent resistance at high temperatures to

fracture, creep, corrosion, and thermal shock. Studies on the β -phase properties suggest that CVI SiC/SiC composites have the potential for excellent radiation stability.³ CVI SiC/SiC is also considered for applications as structural materials in fusion power reactors because of low neutron-induced activation characteristics coupled with excellent mechanical properties at high temperature.^{10–12}

The CVI technique has been studied since the 1960s.^{13–19} It derives directly from chemical vapor deposition (CVD).^{13–15} In very simple terms, the SiC-based matrix is deposited from gaseous reactants on to a heated substrate of fibrous preforms (SiC).¹⁵ CVI is a slow process, and the obtained composite materials possess some residual porosity and density gradients. Despite these drawbacks, the CVI process presents a few advantages: (1) the strength of reinforcing fibers is not affected during the manufacture of the composite; (2) the nature of the deposited material can be changed easily, simply by introducing the appropriate gaseous precursors into the infiltration chamber; (3) a large number of components; and (4) large, complex shapes can be produced in a near-net shape.

Development of CVI SiC/SiC composites began in the 1980s when SEP (Société Européenne de Propulsion), Amecorm, Refractory Composites, and others began to develop equipment and processes for producing CVI components for aerospace, defense, and other applications. The development of CVI SiC/SiC composites has been inspired by the poor oxidation resistance of their predecessor CVI C/C composites. CVI SiC/SiC components have been produced and tested. SNECMA (formerly SEP) is at the forefront of this technology and has demonstrated satisfactory component performance in engine and flight tests.

The mechanical properties of SiC/SiC composites depend on the fiber–matrix interface. Pyrocarbon (PyC) has proved to be an efficient interphase to control fiber–matrix interactions and composite mechanical behavior.²⁰ But PyC is sensitive to oxidation at temperatures above 450 °C. A few versions of high-temperature-resistant CVI SiC/SiC composites have been produced. In order to protect the PyC interphase against oxidation, multilayered interphases and matrices have been developed.^{3,21} Multilayered matrices contain phases that produce sealants at high temperatures, preventing oxygen from reaching the interphase.²² This composite is referred to as CVI SiC/Si–B–C. Oxidation-resistant interphases such as BN or multilayered materials can also be coated on the fibers. An ‘oxygen getter’ can be

added to the matrix to scavenge oxygen that might ingress into the matrix (enhanced CVI SiC/SiC).

The mechanical behavior of CMCs displays several typical features that differentiate them from the other composites (such as polymer matrix composites, metal matrix composites, etc.) and from homogeneous (monolithic) materials. These features are due to heterogeneous and multiscale composite microstructure and the respective properties of the constituents (interphases, fiber, and matrix). The main characteristics of CVD SiC, CVI SiC/SiC, and NITE-SiC/SiC are reviewed in this chapter. Features of mechanical behavior of SiC/SiC are discussed with respect to microstructure, on the basis of the large amount of work done on CVI SiC/SiC.

2.12.2 β -SiC Properties²³

Silicon carbide has a myriad polytypes depending on the varied stacking of closed atomic planes.²³ Only CVD SiC material is inherently highly crystalline, pure, and stoichiometric, which is critical to irradiation stability. Much emphasis is placed on CVD SiC in this chapter, as it corresponds very closely to the matrix of CVI SiC/SiC. The reader will find further details on the SiC structure–property relationships in the excellent comprehensive review by Snead and colleagues.²³ Here the main data from Snead's paper are summarized.

Only the 3C–SiC crystal, known as β -SiC, has the sequence showing cubic symmetry out of the infinite number of variations. All the other polytypes which show noncubic symmetry are classified as α -SiC. α -SiC is formed above 2373 K and β -SiC at 1273–1873 K.

Various fabrication techniques, such as sintering, direct conversion, gas-phase reaction, and polymer pyrolysis, are currently used for the synthesis of SiC. The CVD technique is one of the most familiar gas-phase reaction methods for the synthesis of highly crystalline, stoichiometric, high-purity β -SiC.

2.12.2.1 Mechanical Properties

2.12.2.1.1 Elastic modulus²³

Generally, a dense and high-purity SiC material, for example, CVD SiC, exhibits the highest elastic modulus; however, the elastic modulus decreases with increasing porosity or impurity concentration. The elastic modulus at room temperature is conventionally expressed as an exponential function of porosity (V_p):

$$E = E_0 \exp(-CV_p) \quad [1]$$

$E_0 = 460$ GPa for CVD SiC (polycrystalline, high-purity, very dense, and pore-free SiC material) and $C = 3.57$.

No significant difference was obtained between the elastic moduli for α - and β -polycrystalline SiC or among those of hot-pressed, sintered, and CVD materials.

The elastic modulus at elevated temperatures has been empirically expressed as:

$$E = E_0 - BT \exp(-T_0/T) \quad [2]$$

with $E_0 = 460$ GPa, $B = 0.04$ GPa K⁻¹, and $T_0 = 962$ K.

2.12.2.1.2 Poisson's ratio²³

The Poisson ratio of CVD SiC with excess residual silicon yields the lowest value (~ 0.13). The highest value of 0.21 was typically obtained for pure CVD SiC. The temperature dependence is very minor.

2.12.2.1.3 Shear modulus²³

The shear modulus at room temperature of 191 GPa for CVD SiC has been determined by the four-point bending technique. This value was also derived from the elastic modulus and Poisson's ratio (ν), using the conventional formula for isotropic solids: $G = E/2(1 + \nu)$. The temperature dependence of shear modulus can be estimated from E by applying this formula.

2.12.2.1.4 Hardness²³

There appears to be no significant difference between Vicker's and Knoop hardness: $H \sim 20.7$ – 24.5 GPa has been reported for CVD β -SiC. By contrast, slightly higher values were obtained by nanoindentation. Nanoindentation is known to yield local values which depend on microstructural features. The aforementioned exponential function of porosity for elastic modulus can be extended to the hardness evaluation:

$$H_V = 27.7 \exp(-5.4V_p) \quad [3]$$

where H_V is the Vicker hardness.

Currently, there is no high-temperature data reported for high-purity CVD SiC.

2.12.2.1.5 Fracture toughness²³

Values between 2.4 and 5.1 MPa \sqrt{m} have been measured for CVD β -SiC, depending on the test technique employed and grain size. Fracture toughness of CVD SiC increases slightly at elevated temperatures. It does not exceed 6 MPa \sqrt{m} .

2.12.2.1.6 Fracture strength

As is usual with brittle ceramics, fracture data exhibit a significant scatter, as flaws that have a random distribution induce fracture. An important consequence is that the fracture stress is not an intrinsic characteristic. It is, instead, a statistical variable, which depends on several factors including the test method, the size of test specimens, and the number of test specimens.²⁴ Therefore, a universal reference value of fracture strength cannot be recommended.

It is widely accepted that the Weibull model satisfactorily describes the statistical distribution of failure strengths:

$$P = 1 - \exp \left\{ - \int (\sigma/\sigma_0)^m dV/V_0 \right\} \quad [4]$$

where P is the probability of failure, σ is the stress, σ_0 is the scale factor, m is the Weibull modulus, V is the volume of specimen, and V_0 is a reference volume (1 m^3 is generally used); m reflects the scatter in data, and σ_0 is related to the mean value of the strength.

The strength data for a given geometry and stress state can be determined using eqn [4]. However, m , σ_0 , and V_0 must be available. It is important to note that the estimate of σ_0 depends on V_0 .²⁴ It will be substantially different if $V_0 = 1 \text{ m}^3$ or 1 mm^3 . This dependence is ignored in most publications, even in the work by Snead and coworkers²³ in which a number of σ_0 values are reported. When V_0 is not given, the estimate of σ_0 is meaningless. The strength cannot be determined safely. Unfortunately, reliable σ_0 values (characteristic strength in a few papers) cannot be recommended here until the authors have completed their papers. The values of Weibull modulus of CVD SiC at room temperature reported in Snead *et al.*²³ span a large range, from 2 to 12. The following values were measured using tensile tests on CVI SiC/SiC mini-composites: $m = 6.1$, $\sigma_0 = 10.5 \text{ MPa}$ ($V_0 = 1 \text{ m}^3$).^{25,26}

2.12.2.1.7 Thermal creep²³

Primary and secondary creep deformations have been reported in the literature for CVD SiC (high-purity and polycrystalline β -SiC). Creep in SiC is highly dependent on the crystallographic orientation. The loading orientation of 45° from the CVD growth axis is the direction in which the most prominent creep strain is observed. A review of creep behaviors of stoichiometric CVD SiC has been provided by Davis and Carter.²⁷

Primary creep of CVD SiC occurs immediately upon loading and tends to saturate with time. The primary creep strain generally obeys the following relationship:

$$\varepsilon_c = A_p (\sigma/G)^n (t/\tau)^p \quad [5]$$

where A_p , p , and τ are creep parameters, and t is the time elapsed. $n = 1.63$, $A_p = 29$, $p = 0.081$, and $\tau = 0.0095 \text{ s}$ for the temperature of 1923 K . These parameters are for the loading orientation of 45° from the CVD growth axis. In severe conditions, primary creep strain in the CVD SiC can reach as high as 1%.

Steady-state creep rates for polycrystalline materials have been measured only above $\sim 1673 \text{ K}$, when the stress axis is 45° inclined from the deposition direction; temperatures as high as 2023 K are required when the stress axis is parallel to the deposition direction. The strain rate is given by a power-law creep equation:

$$d\varepsilon/dt = A_s (\sigma/G)^n \exp(-Q/k_b T) \quad [6]$$

where $A_s = 2.0 \times 10^3$, $n = 2.3$, $Q = 174 \text{ kJ mol}^{-1}$ (activation energy), σ is the applied stress, G is the shear modulus, and k_b is the Boltzmann constant.

2.12.2.2 Thermal Properties²³

2.12.2.2.1 Thermal conductivity

It is reasonable to assume that the single-crystal form of SiC, compared to the other varieties, exhibits the highest thermal conductivity. However, high-purity and dense polycrystalline CVD SiC exhibits practically the same conductivity as the single-crystal material. It is worth noting that the impurity content of the very high thermal conductivity CVD SiC materials is negligibly small, and this material has near theoretical density ($\sim 3.21 \text{ g cm}^{-3}$). The curve-fitting to the single-crystal SiC data above 300 K yields an upper limit of the thermal conductivity of SiC (in $\text{W m}^{-1} \text{ K}^{-1}$):

$$K_p = (-0.0003 + 1.05 \times 10^{-5} T)^{-1} \quad [7]$$

2.12.2.2.2 Specific heat

The temperature dependence of the specific heat can be treated in two temperature regions: a rapid increase at low temperatures (below 200 K), and a gradual increase at higher temperatures. No systematic difference can be distinguished between the structural types. The specific heat, C_p (in $\text{J kg}^{-1} \text{ K}$), over the temperature range 200 – 2400 K can be approximately expressed as

$$C_p = 925.65 + 0.3772 T - 7.9259 \times 10^{-5} T^2 - 3.1946 \times 10^7 / T^2 \quad [8]$$

The specific heat of SiC at room temperature is taken as $671 \pm 47 \text{ J kg}^{-1} \text{ K}$.

2.12.2.2.3 Thermal expansion

The coefficient of thermal expansion for β -SiC has been reported over a wide temperature range. The average value in the interval from room temperature to 1700 K is $\alpha = 4.4 \times 10^{-6} \text{ K}^{-1}$.

At higher temperatures ($T > 1273 \text{ K}$), $\alpha = 5 \times 10^{-6} \text{ K}^{-1}$

At lower temperatures ($550 < T < 1273 \text{ K}$), $\alpha = 2.08 + 4.51 \times 10^{-3} T$

2.12.3 SiC/SiC Composite

It is worth addressing the processing method first because this information is useful for a better understanding of the structure of SiC/SiC. The manufacture of long fiber-reinforced composites requires three main steps^{14,15,28,29}:

1. preparation of fibrous preform,
2. fiber coating, which provides an interface material (interphase), and
3. infiltration of the matrix.

2.12.3.1 Fibrous Preform

The preforms of SiC/SiC composites are made of refractory SiC-based continuous fibers. The latest near-stoichiometric SiC fibers (such as Hi-Nicalon type S and Tyranno-SA3 fibers) are the most appropriate for those CVI SiC/SiC foreseen for nuclear applications. These fibers exhibit high strength, high stiffness, low density, and high thermal and chemical stability to withstand long exposures at high temperatures.³⁰ Finally, the fiber diameter must be small ($< 20 \mu\text{m}$) so that the fibers can be woven easily.

The fiber preforms may consist of

1. A simple stack of unidirectional fiber layers or fabrics (1D or 2D preforms).
2. A multidirectional fiber architecture (3D preforms).

Weaving in four or five directions can also be used.

The 2D layers are stacked and kept together using a tool or using fibers in the orthogonal direction (3D preforms).

2.12.3.2 Coating of Fibers

An interface material is deposited on the fibers. This interphase acts as a deflection layer for the matrix cracks. It consists essentially of PyC, boron nitride, or

a multilayer ((PyC/SiC)_n or (BN/SiC)_n sequences). PyC-based interphases have been the subject of extensive studies and have been shown to be the most appropriate with respect to controlling crack deflection and mechanical properties. With the CVI process, the gas precursor is CH₄ for carbon, and BCl₃ and NH₃ for boron nitride. Multilayered interphases may be deposited via pulsed CVI.

2.12.3.3 Infiltration of the SiC Matrix: The CVI Process

The basic chemistry of making a coating and a matrix by CVI is the same as that of depositing a ceramic on a substrate by CVD.^{13–15} The reactions consist of cracking a hydrocarbon for deposition of carbon and cracking of methylchlorosilane for deposition of SiC. In the I-CVI process (isobaric isothermal CVI) the preform is kept in a uniformly heated chamber. Temperature and pressure are relatively low ($< 1200^\circ\text{C}$, $< 0.5 \text{ atm}$).

A few alternative CVI techniques have been proposed to increase the infiltration rate.^{15,28,29} These techniques require more complicated CVI chambers and are not appropriate to the production of large or complex shapes or a large number of pieces.

The forced CVI (F-CVI) technique was proposed in the mid-1980s.²⁹ The precursor gas is forced through the bottom surface of the preform under a pressure P_1 , and the exhaust gases are pumped from the opposite face under a pressure $P_2 < P_1$. The fibrous preform is heated from the top surface and sides, and cooled from the bottom (cold) surface. The densification times are significantly shorter when compared to I-CVI (10–24 h for a SiC matrix, a few hours for carbon), and the conversion efficiency of the precursor is relatively high. However, the technique is not appropriate for complex shapes. Only one preform per run can be processed, and complex graphite fixtures are required to generate the temperature and pressure gradients.

In order to overcome the aforementioned limitations of the F-CVI technique, alternative techniques using thermal gradients or pressure gradients have been examined for many years.¹⁵ In the thermal gradient process, the core of the fibrous preform is heated in a cold-wall reactor. The heat loss by radiation is favorable to get a lower temperature in the external surface. The densification front advances progressively from the internal hot zone toward the cold side of the preform. In the P-CVI process, the source gases are introduced during short pulses.¹⁵ The P-CVI process is appropriate for the deposition of thin films or multilayers.

2.12.3.4 Infiltration of the SiC Matrix: The NITE Process

Reaction sintering (RS), liquid phase sintering (LPS), PIP, melt infiltration (MI), and their hybrid processes are alternative options. PIP requires development of a near-stoichiometric polymer precursor. The other methods have issues in phase and uniformity control.

The NITE process is based on LPS,^{5,7,30} which has been improved owing to the progress in reinforcing fibers and availability of fine nano-SiC powders. A slurry of β -SiC nanopowders and additives is infiltrated into SiC fabrics and dried for making prepreg sheets. After the layup of the sheets, hot pressing is applied to make NITE-SiC/SiC. Small amounts of sintering aids (Al_2O_3 , Y_2O_3 , SiO_2), high temperatures (1750–1800 °C), and pressures ranging from 15 to 20 MPa are required for matrix densification. The NITE process was claimed to present great advantages such as flexibility in the shape and size of the components.⁷ The successful development of NITE is due to appropriate fiber protection and the emergence of advanced SiC fibers such as Tyranno-SA3.

2.12.4 Properties of CVI SiC/SiC

Table 1 is a complete list of the mechanical and thermophysical properties of first generation 2D CVI SiC/SiC composites reinforced with SiC Nicalon fibers of first generation.^{2,31} An average strain-to-failure of 0.3% and a tensile strength of 200 MPa have been reported. Higher strengths and strains-to-failure appear in **Tables 2** and **3**, which give the available properties measured on other generations of SiC/SiC composites reinforced with advanced Hi-Nicalon or Hi-Nicalon type S fibers.^{3,32,33} The behavior of stronger Nicalon-reinforced SiC/SiC is discussed in a subsequent section. It can be noted that the strain-to-failure can reach 1%, and the tensile strength can exceed 300 MPa. As discussed in a subsequent section, a high strain-to-failure can be obtained when the performances of the reinforcing tows and the load transfers during loading have not been impaired as a result of the processing conditions. Ideally, the strain-to-failure should coincide with that of reinforcing tows, that is, about 0.8%.

Table 1 Mechanical and thermophysical properties of 2D SiC/SiC composites reinforced with 0/90 balanced Nicalon™ fabrics

Property	Temperature		
	23 °C	1000 °C	1400 °C
Fiber content (%)	40	40	40
Specific gravity	2.5	2.5	2.5
Porosity (%)	10	10	10
Tensile strength (MPa)	200	200	150
Strain-to-failure (%)	0.3	0.4	0.5
Young's modulus (GPa)	230	200	170
Poisson's ratio			
ν_{12}	0.5		
ν_{13}	0.18		
Flexural strength (MPa)	300	400	280
In-plane compressive strength (MPa)	580	480	300
Thru-the-thickness compressive strength (MPa)	420	380	250
Interlaminar shear strength (MPa)	40	35	25
In-plane thermal diffusivity ($10^{-5} \text{ m}^2 \text{ s}^{-1}$)	12	5	5
Thru-the-thickness thermal diffusivity ($10^{-5} \text{ m}^2 \text{ s}^{-1}$)	6	2	2
In-plane coefficient of thermal expansion (10^{-6} K^{-1})	3	3	
Thru-the-thickness coefficient of thermal expansion (10^{-6} K^{-1})	1.7	3.4	
Fracture toughness ($\text{MPa}\sqrt{\text{m}}$)	30	30	30
Specific heat ($\text{J kg}^{-1} \text{ K}^{-1}$)	620	1200	
Total emissivity	0.8	0.8	0.8
In-plane thermal conductivity ($\text{W m}^{-1} \text{ K}^{-1}$)	19.0	15.2	
Thru-the-thickness thermal conductivity ($\text{W m}^{-1} \text{ K}^{-1}$)	9.5	5.7	

Source: Choury, J. J. Thermostructural composite materials in aeronautics and space applications. In *Proceedings of GIFAS Aeronautical and Space Conference*, Bangalore, Delhi, India, Feb 1989; pp 1–18; Lacombe, A.; Rougès, J. M. In *AIAA'90, Space Program and Technologies Conference'90*, Huntsville, AL, Sept 1990; The American Institute of Aeronautics and Astronautics: Washington, DC, 1990; AIAA-90-3837.

Table 2 Mechanical properties of a CVI SiC/Si-B-C composite with a self healing matrix and a multilayer reinforcement of Hi-Nicalon™ fibers, and 2D CVI-enhanced SiC/SiC composite reinforced with 0/90 five harness satin fabrics of Hi-Nicalon™ fibers

Property	Temperature	
	Room temperature	1200 °C
<i>CVI SiC/Si-B-C</i>		
Fiber type	Hi-Nicalon™ fibers	Hi-Nicalon™ fibers
Reinforcement	Plain weave	Plain weave
Density	2.3	
Porosity (%)	13	
Tensile strength (MPa)	315	
Strain-to-failure (%)	0.5	
Young's modulus (GPa)	220	
Interlaminar shear Strength (MPa)	31	23
Flexural strength (MPa)	699	620
<i>2D CVI-enhanced SiC/SiC composite</i>		
Fiber type	Hi-Nicalon™	Hi-Nicalon™
Fiber content (%)	35	35
Reinforcement	0/90 five harness satin	0/90 five harness satin
Density	2.2	2.2
Porosity (%)	10	10
Tensile strength (MPa)	324	259
Strain-to-failure (%)	0.74	0.50
Young's modulus (GPa)	207	212

Source: Bouillon, E.; Habarou, G.; Spriet, P.; *et al.* Characterization and nozzle test experience of a self sealing ceramic matrix composite for gas turbine applications. In *Proceedings of IGTI/ASME TURBO EXPO Land, Sea and Air 2002*, Amsterdam, The Netherlands, June 3–6, 2002; Power Systems Composites Datasheet.

The strain-to-failure is an interesting characteristic for CMCs for several reasons. First of all, it is not sensitive to scale effects, so that it may be regarded as an intrinsic property and so various CMCs can be compared easily. Then, it reflects the degree of damage tolerance, whereas the strength reflects the load-carrying capacity. These characteristics need to be differentiated, as most components are usually subjected to strain-controlled loading conditions.

A fracture toughness of 30 MPa√m was measured using conventional techniques designed for monolithic materials. It can be regarded as a high value when compared to monolithic SiC. However, it is

Table 3 Room-temperature properties of 2D melt infiltrated CVI SiC/SiC and 2D CVI SiC/SiC composites reinforced with Hi-Nicalon type S fibers

<i>2D melt infiltrated CVI SiC/SiC</i>	
Fiber type	Hi-Nicalon type S™
Fiber content (%)	35
Density	2.2
Tensile strength (MPa)	341–412
Strain-to-failure (%)	0.60
Young's modulus (GPa)	232–262
<i>2D CVI SiC/SiC</i>	
Fiber type	Hi-Nicalon type S™
Fiber content (%)	35
Density	2.25
Tensile strength (MPa)	305
Strain-to-failure (%)	0.60
Young's modulus (GPa)	214
45° off-axis tensile strength (MPa)	167
45° off-axis strain-to-failure (%)	0.66

Source: Morscher, G.; Pujar, V. *Int. J. Appl. Ceram. Technol.* **2009**, 6, 151–163.

worth pointing out that it represents the fracture toughness of an equivalent homogeneous material. As discussed in a subsequent section, critical stress intensity factor (K_{IC}) is not an intrinsic property, and it is not an appropriate concept for long fiber-reinforced composites. Furthermore, besides the resistance to crack propagation, damage tolerance is an important property for CMCs. It cannot be characterized by fracture toughness. This situation is new when compared to homogeneous materials. Anyway, the fracture toughness K_{IC} may be regarded as an index to compare materials. It cannot be used for design purposes for the aforementioned reasons.

Table 1 shows that CVI SiC/SiC retains its properties at high temperatures. These properties can be enhanced by using advanced fibers. Durability will be addressed in a subsequent section.

Properties vary according to factors, including preform architecture, fiber type, matrix properties, fiber–matrix bond strength, loading conditions, etc. For instance, high tensile strengths (up to 400 MPa) were obtained with Hi-Nicalon™ SiC fibers,³⁴ or with Nicalon fibers and rather strong interfaces.³⁵ Further details on microstructure versus properties are discussed in subsequent sections. The mechanical behavior of 2D CVI SiC/SiC composites exhibits features that are related to composite microstructure. Thus, it deserves special attention because it differs significantly from that of the more conventional homogeneous materials. A clear understanding will be beneficial to a sound use of CVI SiC/SiC.

Tables 3 and 4 show that the ultimate strength and Young's modulus tend to decrease under off-axis tensile conditions.³⁶ It is worth pointing out that the strain-to-failure is an invariant. It is interesting to note that in 2D CVI SiC/SiC, the directions of the principal stresses coincide with those of the fiber tows.

2.12.5 Properties of NITE-SiC/SiC

The matrix of NITE-SiC/SiC comprises polycrystalline SiC and a small amount of isolated oxides. The microstructure is highly crystalline and highly dense. Table 5 lists the typical available properties of NITE-SiC/SiC.⁷ Thermal conductivity ($\sim 30 \text{ W m}^{-1} \text{ K}^{-1}$) is quite high when compared to CVI SiC/SiC (below $15 \text{ W m}^{-1} \text{ K}^{-1}$) reinforced with either Nicalon (Table 1) or Hi-Nicalon fibers.³⁷ The high proportional stress limit is claimed to be an interesting feature.⁷ However, it is worth pointing out that it reflects a high load-carrying capacity. By contrast,

Table 4 Off-axis properties of a first generation of 2D CVI SiC/SiC reinforced with Nicalon fibers

Property	0°	20°	45°
Strain-to-failure (%)	0.3	0.3	0.3
Proportional limit (MPa)	80	70	70
Saturation stress (MPa)	150	145	145
Tensile strength (MPa)	190	170	170
Young's modulus (GPa)	220	210	210

Source: Aubard, X.; Lamon, J.; Allix, O. *J. Am. Ceram. Soc.* **1994**, 77, 2118–2126.

Table 5 Room-temperature properties of NITE-SiC composites

Property		
Fiber type	Tyranno-SA3	Tyranno-SA3
Reinforcement	UD	Cross plied
Fiber content (%)	53	51
Density	3.11	3.06
Porosity (%)	0.6	3.8
Proportional limit (MPa)	358	148
Tensile strength (MPa)	408	167
Strain-to-failure (%)	0.13	0.08
Young's modulus (GPa)	358	288
Thermal conductivity ($\text{W m}^{-1} \text{ K}^{-1}$)	32	

Kohyama, A. In *Ceramic Matrix Composites*; Krenkel, W., Ed.; Wiley-VCH: Weinheim, Germany, 2008; Chapter 15, pp 353–384, reproduced with permission.

the low strain-to-failure indicates a limited damage tolerance. The strain-to-failure does not increase after aging at high temperatures up to 1500°C . This trend is consistent with the strong fiber–matrix interactions induced by the surface roughness of Tyranno-SA3 fibers.³⁸ A comprehensive database on properties of NITE-SiC/SiC is not available. NITE-SiC/SiC has been reported to retain ultimate strength and a proportional stress limit after exposure at temperatures up to 1300°C .⁶

2.12.6 Mechanical Behavior of CVI SiC/SiC

2.12.6.1 Tensile Stress–Strain Behavior

Figures 1 and 2 summarize the typical stress–strain behavior of 2D CVI SiC/SiC composites. The behavior is initially linear under strains below 0.03%. Then,

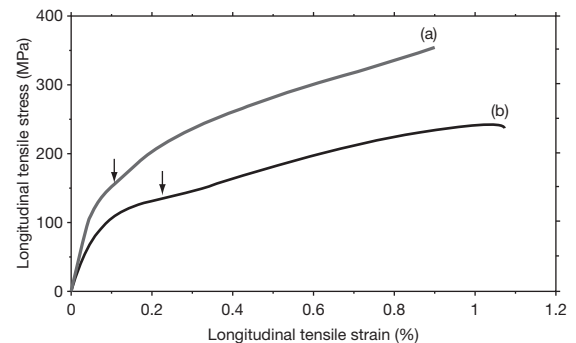


Figure 1 Typical tensile stress–strain behaviors measured on 2D SiC/SiC composites possessing PyC-based interphases and fabricated from untreated or treated Nicalon (ceramic grade) fibers: (a) strong fiber/coating interfaces and (b) weak fiber/coating interfaces.

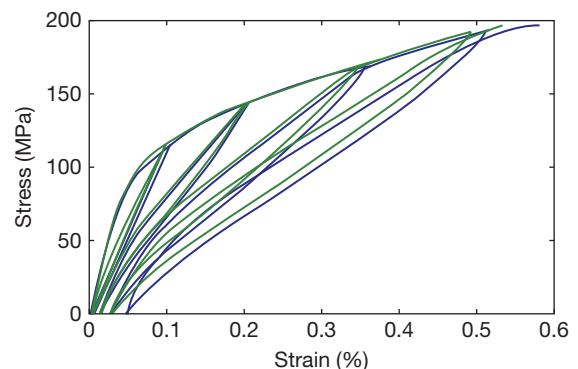


Figure 2 Typical tensile stress–strain behaviors measured on 2 different test specimens (2D SiC/SiC reinforced with Hi-Nicalon S fibers).

the nonlinear deformations result essentially from transverse cracking in the matrix (the cracks are perpendicular to fibers oriented in the loading direction). Saturation of matrix damage is indicated by the end of the curved domain marked by a point of inflection. Then the ultimate portion of the curve reflects the deformation of fibers. Fiber failures may initiate prior to ultimate fracture. Such mechanical behavior is essentially damage-sensitive.

A *damage-sensitive* stress-strain behavior is obtained when the initial contribution of the matrix to load carrying is significant. The elastic modulus of the matrix (E_m) is not negligible when compared to that of the fiber (E_f). Its contribution to the modulus of the composite (E_c) is illustrated by the mixtures law, which provides satisfactory trends for continuous fiber-reinforced composites:

$$E_c = E_m V_m + E_f V_f \quad [9]$$

where V_m is the volume fraction of matrix and V_f is the volume fraction of fibers oriented in the loading direction in a 2D woven composite.

In 2D CVI SiC/SiC composites, E_m (≈ 410 GPa) $> E_f$ (200–380 GPa), $V_m \sim V_f$ the initial contribution of the matrix to E_c is significant. Then, as it decreases when the matrix cracks, the behavior becomes controlled by the tows. The 2D SiC/SiC composites exhibit an elastic damageable behavior (Figure 3). This means that the response of the damaged material is elastic as indicated by the linear portion of the curves on reloading. Figure 4 shows the dependence of the elastic modulus on damage.

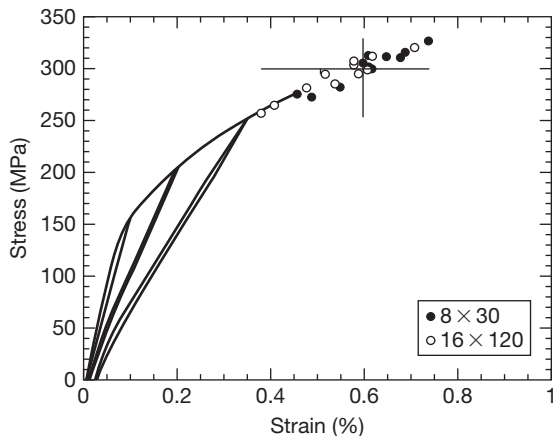


Figure 3 Stress-strain curves in tension of 2D SiC/SiC reinforced with treated Nicalon fibers. The open and filled symbols represent ultimate failure data point obtained with the specimens of volumes V_1 and V_2 , respectively.

2.12.6.2 Damage Mechanisms

The basic damage phenomena in unidirectional composites under on-axis tensile loads involve multiple microcracks or cracks that form in the matrix perpendicular to fiber direction and that are arrested by the fibers by deflection in the fiber-matrix interface. In the composites reinforced with fabrics of fiber bundles, matrix damage is influenced by a multilength scale structure.³⁹ Furthermore, 2D CVI SiC/SiC is a heterogeneous medium because of the presence of fibers, large pores (referred to as macropores) located between the plies or at yarn intersections within the plies, and a uniform layer of matrix over the fiber preform (referred to as the intertow matrix) (Figure 5). Much smaller

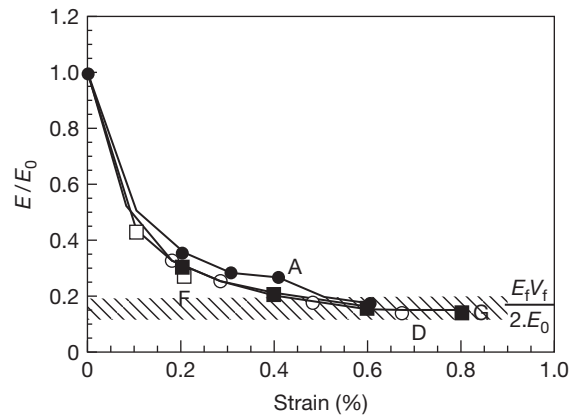


Figure 4 Relative elastic modulus versus applied strain during tensile tests on various 2D woven SiC/SiC composites reinforced with treated fibers: (A) Nicalon/(PyC₂₀/SiC₅₀)₁₀/SiC, (D) Nicalon/PyC₁₀₀/SiC, (F) Hi-Nicalon/PyC₁₀₀/SiC, (G) Hi-Nicalon/(PyC₂₀/SiC₅₀)₁₀/SiC.

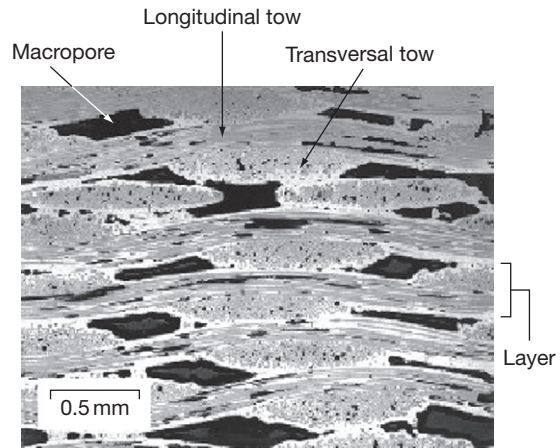


Figure 5 Micrograph showing the microstructure of a 2D CVI SiC/SiC composite.

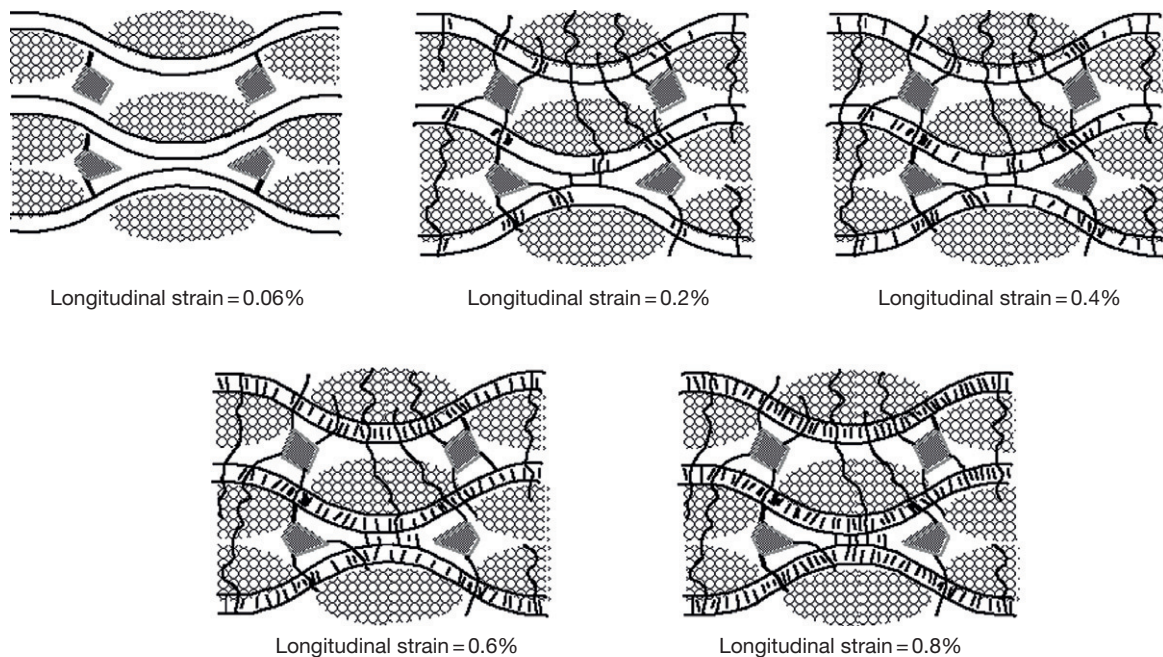


Figure 6 Schematic diagram showing matrix cracking in a 2D SiC/SiC composite during a tensile test.

pores are also present within the tows. Under on-axis tension, damage in 2D CVI SiC/SiC occurs essentially in the formation of matrix cracks perpendicular to longitudinal fiber axis and their deflection either by the tows (first and second steps) or by the fibers within the tows (third step). These steps (Figure 6) correspond to deformation increments:

Step 1: cracks initiate at macropores where stress concentrations exist (deformations between 0.025% and 0.12%);

Step 2: cracks form in the transverse yarns and in the interply matrix (deformations between 0.12% and 0.2%);

Step 3: transverse microcracks initiate in the longitudinal tows (deformations larger than 0.2%). These microcracks are confined within the longitudinal tows. They do not propagate in the rest of the composite. The matrix in the longitudinal tows experiences a fragmentation process and the crack spacing decreases as the load increases.

As mentioned earlier, the directions of principal stresses are dictated by fiber orientation rather than by the loading direction. Thus, under on-axis conditions, all the matrix cracks are perpendicular to the loading direction. Then, under off-axis tension, matrix cracks that are located in the tows are

perpendicular to fiber direction, whereas those located between the tows are perpendicular to the load direction. On-axis loading conditions are discussed later.

The resulting Young's modulus decrease illustrates the importance of damage in the mechanical behavior (Figure 4). The major modulus loss (70%) is caused by both the first families of cracks located on the outside of the longitudinal tows (deformations <0.2%). By contrast, the microcracks within the longitudinal tows are responsible for only a 10% loss. The substantial modulus drop reflects important changes in load sharing: the load gets carried essentially by the matrix-coated longitudinal tows (tow reloading). During microcracking in the longitudinal tows, load sharing is affected further, and the load becomes carried essentially by the filaments (fiber reloading). The elastic modulus reaches a minimum described by the following equation (Figure 4):

$$E_{\min} = 1/2 E_f V_f \quad [10]$$

where V_f is the volume fraction of fibers.

Equation [10] implies that the matrix contribution is negligible. At this stage, matrix damage and debonding are complete (saturation). The load is carried by fibers only. The mechanical behavior is controlled by the fiber tows oriented in the direction of loading.

2.12.6.3 Ultimate Failure

Ultimate failure generally occurs after saturation of matrix cracking. The fibers break when the applied load is close to the maximum. Matrix damage and ultimate failure thus appear to be successive phenomena.

The *ultimate failure of a tow* of parallel fibers involves two steps:

- a first step of stable failure and
- a second step of unstable failure.

During the first step, the fibers fail individually as the load increases. In the absence of fiber interactions, the load is carried by the surviving fibers only (equal load sharing). Fiber interactions cause tow weakening. The ultimate failure of a tow (second step) occurs when the surviving fibers cannot tolerate the load increment resulting from a fiber failure. At this stage, a critical number of fibers have been broken.

The *ultimate failure of a longitudinal tow coated with matrix* also involves a two-step mechanism and global load sharing when a fiber fails. In the presence of multiple cracks across the matrix and associated interface cracks, the load-carrying capacity of the matrix is tremendously reduced or eliminated. The matrix-coated tows behave like dry tows subject to the typical stress field generated by the presence of matrix cracks. The ultimate failure of a matrix-coated tow occurs when a critical number of fibers have failed. This mechanism operates in the tows within textile CVI SiC/SiC composites. The ultimate failure of the composite is caused by the failure of a critical number of broken tows (≥ 1) depending on the stress state: ~ 1 under an axial tension, > 1 in bending.

It is worth pointing out that the failure mechanism of CVI SiC/SiC composites differs from that observed in polymer matrix impregnated tows, where local load sharing prevails when a fiber fails. In these composites, the fibers fail first. Therefore, the uncracked matrix is able to transfer the loads.

2.12.6.4 Reliability

The ultimate failure of CVI SiC/SiC composites is highly influenced by stochastic features. As fibers are brittle ceramics, they are sensitive to the presence of flaws (stress concentrators) that are distributed randomly. As a consequence, the strength data exhibit significant scatter, as illustrated by [Figure 7](#).^{39,40} The figure shows that the magnitude of the strength and scatter decrease from single fibers to tows, then to infiltrated tows, and finally to woven composites.

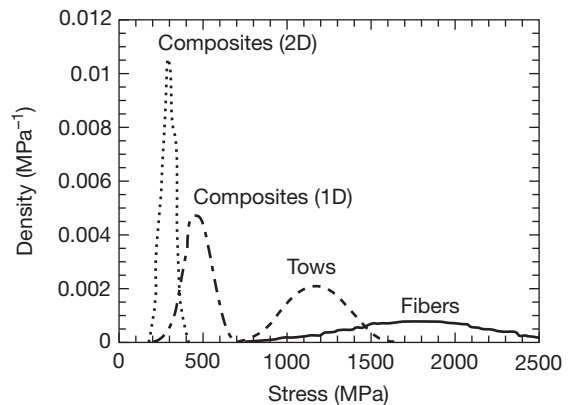


Figure 7 Strength density functions for SiC fibers (NLM 202), SiC fiber tows, SiC/SiC (1D) minicomposites, and 2D SiC/SiC composites.

As a result of the previously mentioned two-step failure mechanism, the ultimate failure of an entity is dictated by the lowest extreme of the strength distribution pertinent to its constituent: that is, tows versus filaments, infiltrated tows versus fibers, and 2D composites versus infiltrated tows. The lowest strength extremes correspond respectively to the critical number of individual fiber breaks ($\approx 17\%$ for the SiC NicalonTM fibers and for the SiC Hi-NicalonTM fibers) and to the critical number of tow failures (≥ 1). The gap between tows and SiC infiltrated tows results from the method of strength determination: the critical number of individual fiber breaks was taken into account for tow strength determination, whereas the strength of infiltrated tows and composites was underestimated because the total cross sectional area of the specimens was used.

The flaw populations are truncated during the successive damage steps, which leads to a homogeneous ultimate population of flaws.⁴⁰ This process of progressive elimination of flaws governs the trends in the ultimate failure. The tensile stress-strain curves obtained on a batch of several CVI SiC/SiC test specimens coincide quite well ([Figure 5](#)), whereas the strength data exhibit a certain scatter ([Figure 5](#)). This scatter is limited ([Figure 8](#)). Dependence of composite strength on the stressed volume is not significant ([Figure 8](#)). Furthermore, dependence on the loading conditions is not so large ([Figure 9](#)): for instance, the flexural strength is 1.15 times as large as the tensile strength^{40,41} when measured on specimens having comparable sizes ([Figure 9](#)).

The Weibull model is not appropriate to describe the volume dependence of strength data,⁴⁰ as the weakest link concept is violated. However, the

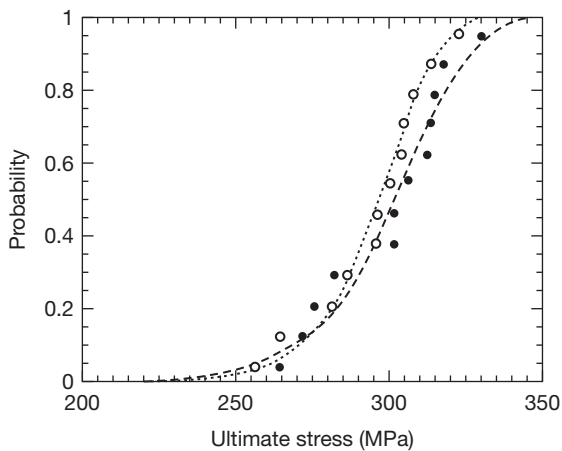


Figure 8 Scale effects in 2D woven SiC/SiC composites. Influence of specimen dimensions on ultimate failure in tension: (●) $8 \times 30 \text{ mm}^2$ and (○) $160 \times 120 \text{ mm}^2$. Reproduced from Bansal, N. P., Ed. *Handbook of Ceramics and Glasses*; Kluwer Academic: New York, 2005, with permission from Springer.

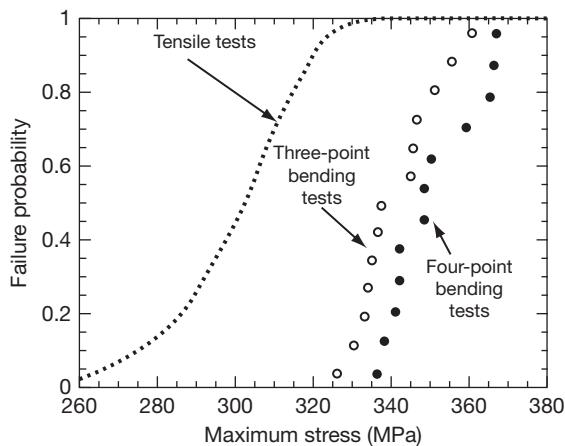


Figure 9 Strength distributions for 2D woven SiC/SiC composites tested under various loading conditions: tension, three-point bending and four-point bending. Reproduced from Bansal, N. P., Ed. *Handbook of Ceramics and Glasses*; Kluwer Academic: New York, 2005, with permission from Springer.

Weibull modulus (m) can be extracted from the statistical distribution of the strength data: m is in the range of 20–29. This value provides an evaluation of the scatter in strength data. It reflects a small scatter.

2.12.6.5 Interface Properties: Influence on the Mechanical Behavior

The fiber–matrix interfacial domain is a critical part of composites because load transfers from the matrix

to the fiber and vice versa occur through the interface. Most authors support the concept of weak interfaces to increase fracture toughness. They assign toughening to crack-bridging and fiber pullout. Weak interfaces are detrimental to the composite strength. A high strength requires that the matrix carry a part of the load. This is obtained with strong interfaces, which implies that the deflection cracks at interfaces are short and/or that significant sliding friction takes place. These latter requirements, to be met for strong composites, are therefore incompatible with the former ones for tough composites, if toughening is based solely upon crack-bridging and fiber pullout.

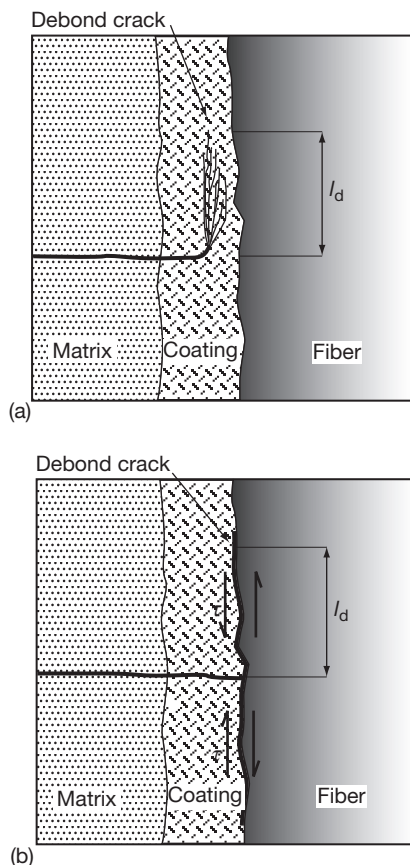
Fiber–matrix interfaces exert a profound influence on the mechanical behavior and lifetime of composites. Efforts have been directed toward optimization of interface properties. Fiber–matrix interfaces in CVI SiC/SiC composites consist of a thin coating layer ($<1\text{-}\mu\text{m}$ thick) of one or several materials deposited on the fiber (interphase). CVI SiC/SiC composites with rather strong interfaces have been obtained using fibers that have been treated in order to increase the fiber/coating bond.^{35,42} The concept of strong interfaces has been established on CVI SiC/SiC composites with PyC and multilayered (PyC/SiC)_n fiber coatings. Less interesting results have been achieved with BN interphases.⁴³ Table 6 gives the various values of the interfacial shear stresses measured using various methods on CVI SiC/SiC composites with PyC-based fiber coatings: the interfacial shear stresses range between 10 and 20 MPa for the weak interfaces, whereas they are larger than 100–300 MPa for the strong interfaces.^{43–47}

In the presence of a weak bond between the fibers and the matrix or coating, single, long interface cracks are created during matrix cracking (adhesive failure type, Figure 10). The associated interface shear stresses are low, and load transfers through the interface crack are poor. The matrix is subjected to low stresses and the volume of matrix that may experience further cracking is reduced by the presence of the long interface cracks. The matrix crack density is small. The crack spacing at saturation as well as the pull-out length tends to be long ($>100\text{ }\mu\text{m}$). Toughening results essentially from sliding friction along the cracked interfaces. However, as a result of matrix unloading due to long interface cracks, the fibers carry most of the load, which reduces the composite strength. The corresponding tensile stress–strain curve exhibits a narrow curved domain limited by a stress at matrix saturation which is distinctive of the ultimate strength (Figure 1).

Table 6 Interfacial shear stresses (MPa) measured using various methods on 2D SiC/SiC composites with PyC-based fiber coatings and reinforced with either as-received or treated fibers

SiC/C/SiC SiC/ (C/SiC) _n /SiC	Interphase	Crack spacing	Crack spacing	Tensile tests (hysteresis loops)	Tensile tests (curved domain)	Push-out tests (curved domain)	Push-out tests (plateau)
<i>Untreated fibers</i>							
2D woven	PyC (0.1)	12	8	0.7			
Microcomposites	PyC (0.1)			3	4–20		
Minicomposites	PyC (0.1)			21–115	40–80		
2D woven	PyC (0.5)			4		14–16	12–10
	(PyC/SiC) ₂			2		31	19.3
	(PyC/SiC) ₄			9		28	12.5
<i>Treated fibers</i>							
2D woven	PyC (0.1)	203	140	190			165–273
	PyC (0.5)			370			100–105
	(PyC/SiC) ₂			150			133
	(PyC/SiC) ₄			90			90

Source: Rebillat, F.; Lamon, J.; Guette, A. *Acta Mater.* **2000**, *48*, 4609–4618; Lamon, J.; Rebillat, F.; Evans, A. G. *J. Am. Ceram. Soc.* **1995**, *78*, 401–405; Lissart, N.; Lamon, J. *Acta Mater.* **1997**, *45*, 1025; Rebillat, F.; Lamon, J.; Naslain, R.; Lara-Curzio, E.; Ferber, M. K.; Besmann, T. *J. Am. Ceram. Soc.* **1998**, *81*, 965; Rebillat, F.; Lamon, J.; Naslain, R.; Lara-Curzio, E.; Ferber, M. K.; Besmann, T. *J. Am. Ceram. Soc.* **1998**, *81*, 2315–2326.

**Figure 10** Schematic diagram showing crack deflection when the fiber coating/interface is strong (a) or weak (b).

In the presence of stronger fiber/coating bonds, the matrix cracks are deflected within the coating (cohesive failure type, [Figure 10](#)) into short and branched multiple cracks. Short interphase cracks as well as improved load transfers allow further cracking of the matrix via a scale effect, leading to a higher density of matrix cracks (which are slightly opened). Sliding friction within the coating as well as multiple cracking of the matrix increases energy absorption, leading to toughening. Short interphase cracks and improved load transfers reduce the load carried by the fibers, leading to strengthening. The associated tensile stress–strain curve exhibits a wide, curved domain and the stress at matrix cracking saturation is close to the composite strength ([Figure 1](#)).

The interphase is ineffective when fiber surface is too rough, although deflection of matrix cracks occurs. Because of strong fiber–matrix interactions in the interface cracks, premature fracture of composite occurs under small strains close to the strain at proportional limit. This phenomenon is observed on CVI SiC/SiC reinforced with Tyranno-SA3 fibers.³⁸

2.12.6.6 Fracture Toughness

The CVI SiC/SiC composites develop a network of matrix cracks under load. The density of matrix cracks is enhanced by rather strong interfaces: the crack spacing may be as small as 10–20 μm whereas it is at least 10 times larger in the presence of rather

weak interfaces. Matrix cracking is an alternative mechanism of energy dissipation.

A process zone of diffused matrix microcracks is generated at the notch tip or at the tip of a preexisting main macroscopic crack. Extension of this crack results from the random failures of fiber bundles located within the process zone.³⁵ Due to the presence of a more or less large process zone associated with a jagged crack, a crack length cannot be defined and conventional concepts of fracture mechanics are not appropriate (stress intensity factor) or cannot be easily determined (strain energy release rate, \mathcal{J} -integral). Although the validity of the stress intensity factor concept to measure fracture toughness is questionable, this is an interesting characteristic for comparing CVI SiC/SiC composites to other materials. Fracture toughness values on the order of 30 MPa $\sqrt{\text{m}}$ have been measured on single edge notch bending (SENB) test specimens.^{2,31} Strain energy release rates ranging from 3 to 8 KJ m⁻² have been determined on CVI SiC/SiC composites, respectively, with weak or strong interfaces.³⁵ The corresponding values of the \mathcal{J} -integral ranges from 11 KJ m⁻² (weak interfaces) to 29 KJ m⁻² (strong interfaces).³⁵ These values are quite high. The aforementioned stress intensity factors are maintained up to at least 1400 °C.²

2.12.6.7 Fatigue and High-Temperature Behavior

During cyclic fatigue at room temperature, matrix damage is determined by the maximum stress. It is created during the first cycles. Fatigue resistance is governed by the damage of fibers and the fiber-matrix bonds. Two different fatigue behaviors have been observed: after 1000 cycles, either the elastic modulus remains constant and the specimen is running out, or it decreases until the specimen ultimately fails.⁴⁸ The modulus degradation reflects either wear at cracked interfaces⁴⁸ or growth of interface cracks. Under stresses smaller than 100 MPa, ultimate failures are generally not observed after 10⁶ cycles under tension-tension fatigue.

At high temperatures, additional phenomena activated by environment (oxidation, creep, or slow crack growth) may operate and cause the extension of initial stress-induced matrix damage and interface cracks as well as the weakening of fibers by degradation or reloading. Reloading of fibers involves changes in load sharing. If the strength of tows is exceeded by the applied stresses according to the mechanism

described previously, ultimate failure occurs. The rupture of tows dictates the lifetime.

The matrix cracks created upon loading become the pathways for the ingress of oxygen into the material. The PyC interphase is consumed, which causes fiber reloading. Creep of the SiC matrix (at very high temperatures, above 1200 °C) makes the stresses on the fiber to increase, which enhances matrix creep and further fiber reloading. Creep of fibers (at temperatures above 1200 °C) causes matrix reloading and possible matrix and interface cracking or crack propagation, leading to fiber reloading by decrease of load carried by the matrix.

Finally, the slow crack growth in fibers (at temperatures below 1100 °C) is activated by oxidation of carbon grain boundaries, leading to delayed failure.^{49,50} This phenomenon, which was observed at intermediate temperatures between 500 and 900 °C, was first referred to as the 'pest phenomenon' by a few authors. The SiC/SiC were claimed to be susceptible to degradation by oxidation embrittlement.

In order to protect the PyC interphase against oxidation, multiple coating concepts have been explored and multilayered interphases and matrices have been developed.²¹ Such multilayered matrices contain phases that produce sealants at high temperatures, causing healing of the cracks and preventing oxygen from reaching the cracks and the interphases.^{2,22,51} Lifetime is also improved with oxidation-resistant interphases such as BN or multilayers.⁵²

2.12.6.8 Thermal Shock

CVI SiC/SiC composites have been tested under thermal shock with excellent results.^{2,53} CVI SiC/SiC generally had good strength retention after thermal shock cycles involving heating up to the desired temperature and then cooling down in water at 20 °C.

2.12.6.9 Creep Behavior

CVI SiC/SiC and CVI SiC/Si-B-C composites exhibit primary creep only, even during long tests (Figures 11 and 12).⁵⁴

Creep of CMCs involves local stress transfers depending on the respective creep rates of the fiber and the matrix. Such stress transfers may lead to fiber failures or matrix cracking and debonding, and sliding at the interfaces. When the matrix is elastic and creep-resistant, fiber creep induces stress transfers from the fibers onto the matrix, which may cause matrix cracking. This creep-induced matrix damage has been observed on CVI SiC/SiC composites.⁵⁵⁻⁵⁷

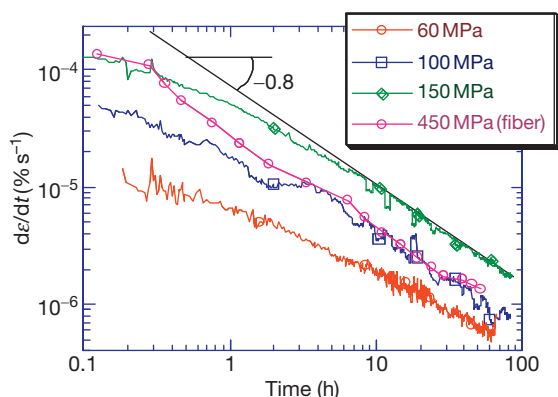


Figure 11 Creep rate curves for a damage strain $\varepsilon_0 = 0.8\%$ and for various applied constant stresses for the SiC/Si-B-C composite, and under 450 MPa at 1200 °C in argon for a Nicalon NL 202 fiber.

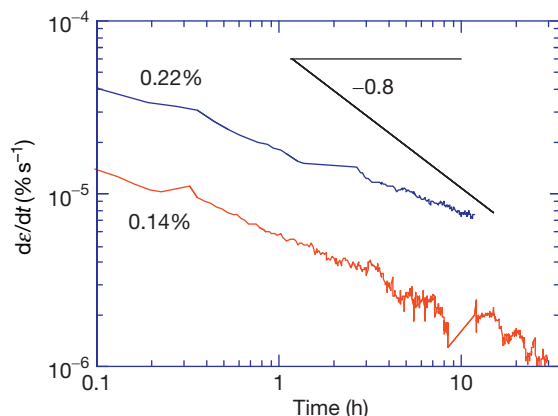


Figure 12 Creep rate curves for the SiC/SiC composite under a constant stress of 150 MPa ($\varepsilon_0 = 0.14\%$ and $\varepsilon_0 = 0.22\%$) at 1200 °C.

In CVI SiC/SiC composites, the SiC matrix is far more creep-resistant than the SiC fibers, which creep at 1100 °C.^{55,58,59}

The creep behavior of CVI SiC/SiC composites with a multilayered matrix (SiC/Si-B-C) is caused by the creep of the Nicalon SiC fibers, whatever the extent of initial damage created upon loading (Figure 11). The Si-B-C matrix is less creep-resistant and stiffer than the SiC matrix.

2.12.7 Concluding Remarks

Properties of CVD SiC, CVI SiC/SiC, and NITE-SiC/SiC have been reported and discussed. The CVI SiC/SiC composite combines the advantageous

properties of CVD SiC and the benefits of reinforcement by SiC-based continuous fibers. In particular, CVI SiC/SiC exhibits damage tolerance, limited sensitivity to flaws and notch, high load-carrying capacity, and improved reliability. As opposed to earlier generations of SiC/SiC that were reinforced with Nicalon fibers, the database for SiC/SiC reinforced with the advanced near-stoichiometric fibers is incomplete. The properties of Nicalon-reinforced SiC/SiC should provide a useful baseline. The main features of the mechanical behavior of SiC/SiC composites have been described, and the relationships between the microstructure and properties have been discussed. They have been established on CVI SiC/SiC composites reinforced with Nicalon fibers. They should be reproduced on those CVI SiC/SiC composites reinforced with near-stoichiometric Hi-Nicalon S fibers. The inherent surface roughness of Tyranno-SA3 fibers is an issue.

Precise knowledge of the mechanisms that govern the mechanical behavior is useful for proper use or design with SiC/SiC. Damage and ultimate fracture of CVI SiC/SiC involve load transfer from matrix to fibers at various length scales defined by the 2D woven structure and the tow microstructure. At high temperatures, additional load transfers are driven by the local stress relaxation induced by temperature and/or environment. The ultimate fracture and delayed failure are dictated by the tows. Scale effects and scatter in strength data are limited when compared to monolithic ceramics. Fiber-matrix interfaces and interphases play a significant role in damage tolerance and load-carrying capacity. Interfaces resistant to crack extension are beneficial to composite performances. However, this scheme is invalid when the fiber surface is rough.

Properties of CVI SiC/SiC can be tailored via engineering of the interfaces and the use of advanced fibers.

References

1. Sheppard, L. M. *Ceram. Bull.* **1990**, 69, 666–673.
2. Choury, J. J. Thermostructural composite materials in aeronautics and space applications. In *Proceedings of GIFAS Aeronautical and Space Conference*, Bangalore, Delhi, India, Feb 1989; pp 1–18.
3. Bouillon, E.; Habarou, G.; Spriet, P.; et al. Characterization and nozzle test experience of a self sealing ceramic matrix composite for gas turbine applications. In *Proceedings of IGTI/ASME TURBO EXPO Land, Sea and Air 2002*, Amsterdam, The Netherlands, June 3–6, 2002.
4. Van Roode, M. Ceramic matrix composite development for combustors for industrial gas turbines. In *The 27th Annual Cocoa Beach Conference and Exposition on*

- Advanced Ceramics and Composites*, Cocoa Beach, FL, Jan 26–31, 2003; paper ECD-S1-16-2003.
5. Hinoki, T.; Kohyama, A. *Ann. Chimie Sci. Matériaux* **2005**, 30, 659–671.
 6. Shimoda, K.; Park, J. S.; Hinoki, T.; Kohyama, A. *J. Nucl. Mater.* **2009**, 386–388, 634–638.
 7. Kohyama, A. In *Ceramic Matrix Composites*; Krenkel, W., Ed.; Wiley-VCH: Weinheim, Germany, 2008; Chapter 15, pp 353–384.
 8. Snead, L. L.; Jones, R. H.; Kohyama, A.; Fenici, P. *J. Nucl. Mater.* **1996**, 233–237, 26–36.
 9. Katoh, Y.; Snead, L. L.; Henager, C.; et al. *J. Nucl. Mater.* **2007**, 367–370, 659–671.
 10. Aiello, G. CVI SiC/SiC composites as structural components in fusion power reactors (Utilisation des composites à matrice céramique SiC/SiC comme matériau de structure de composants internes du tore d'un réacteur à fusion), Ph.D. Thesis, University of Evry, France, 2000.
 11. Fenici, P.; Scholtz, H. W. *J. Nucl. Mater.* **1994**, 212–215, 60–68.
 12. Jones, R. H.; Henager, C. H.; Youngblood, G. G.; Heinisch, H. L. *Fusion Technol.* **1996**, 30, 969–976.
 13. Chawla, K. K. *Ceramic Matrix Composites*; Chapman & Hall: London, 1993.
 14. Naslain, R.; Langlais, F. In *Tailoring Multiphase and Composite Ceramics*; Tressler, R. E., Messing, G., Pantano, G. G., Newham, R. E., Eds.; Plenum: New York, 1986; pp 145–164.
 15. Langlais, F. In *Comprehensive Composite Materials*; Kelly, A., Zweben, C., Eds.; Elsevier, 2000; Chapter 4.20, pp 611–644.
 16. Christin, F.; Naslain, R.; Bernard, C. In *Proceedings of the 7th International Conference CVD*; Sedwick, T. O., Lydin, H., Eds.; The Electrochemical Society: Princeton, NJ, 1979; p 499.
 17. Christin, F.; Naslain, R.; Hagenmuller, P.; Choury, J. J. Pièce poreuse carbonée densifiée in-situ par dépôt chimique en phase vapeur de matériaux réfractaires autres que le carbone et procédé de fabrication. French Patent 77/26979, Sept 1977.
 18. Heraud, L.; Christin, F.; Naslain, R.; Hagenmuller, P. In *Proceedings of the 8th International Conference CVD*; Blocher, J. M., et al. Eds.; The Electrochemical Society: Pennington, NJ, 1981; p 782.
 19. Fitzer, E. Chemical vapor deposition of SiC and Si₃N₄. In *Proceedings of the International Symposium on Factors in Densification and Sintering of Oxide and Non Oxide Ceramics*, Hakone, Japan, 1978; p 40.
 20. Lamon, J. In *Ceramic Matrix Composites: Fibre-reinforced Ceramics and Their Applications*; Krenkel, W., Ed.; Wiley-VCH: Weinheim, Germany, 2008; Chapter 2, pp 49–68.
 21. Lamouroux, F.; Pailler, R.; Naslain, R.; Cataldi, M. French Patent 95/14843, 1995.
 22. Forio, P.; Lamon, J. *Ceramic Trans.* **2001**, 128, 127–141.
 23. Snead, L. L.; Nozawa, T.; Katoh, Y.; Byun, T. S.; Kondo, S.; Petti, D. A. *J. Nucl. Mater.* **2007**, 371, 329–377.
 24. Lamon, J. *Mechanics of Brittle Fracture and Damage: Statistical Probabilistic Approaches* (In French: *Mécanique de la rupture fragile et de l'endommagement: Approches Statistiques-Probabilistes*); Editions Hermès-Lavoisier: Paris, France, 2007.
 25. Lissart, N.; Lamon, J. *Acta Mater.* **1997**, 45, 1025–1044.
 26. Lamon, J. *Compos. Sci. Technol.* **2010**, 70, 743–751.
 27. Davis, R. F.; Carter, C. H. *A Review of Creep in Silicon Carbide and Silicon Nitride*; Oxford University Press and Ohmsha Ltd, 1988.
 28. Bansal, N. P. Ed. *Handbook of Ceramics and Glasses*; Kluwer Academic: New York, 2005.
 29. Caputo, A. J.; Lackey, W. J.; Stinton, D. P. *Ceram. Eng. Sci. Proc.* **1984**, 6, 694–705.
 30. Nozawa, T.; Hinoki, T.; Hasegawa, A.; et al. *J. Nucl. Mater.* **2009**, 386–388, 622–627.
 31. Lacombe, A.; Rougès, J. M. In *AIAA'90, Space Program and Technologies Conference'90*, Huntsville, AL, Sept 1990; The American Institute of Aeronautics and Astronautics: Washington, DC, 1990; AIAA-90-3837.
 32. Power Systems Composites Datasheet.
 33. Morscher, G.; Pujar, V. *Int. J. Appl. Ceram. Technol.* **2009**, 6, 151–163.
 34. Bertrand, S. Lifetime of SiC/SiC minicomposites with nanometer scale multilayered interphases, Ph. D. Thesis No. 1927, University of Bordeaux, 1998.
 35. Droillard, C.; Lamon, J. *J. Am. Ceram. Soc.* **1996**, 79, 849–858.
 36. Aubard, X.; Lamon, J.; Allix, O. *J. Am. Ceram. Soc.* **1994**, 77, 2118–2126.
 37. Kowbel, W.; Bruce, C. A.; Tsou, K. L.; Patel, K.; Withers, J. C.; Youngblood, G. E. *J. Nucl. Mater.* **2000**, 283–287, 570–573.
 38. Sauder, C.; Brusson, A.; Lamon, J. *Int. J. Appl. Ceram. Technol.* **2010**, 7(3), 291–303.
 39. Lamon, J. *Compos. Sci. Technol.* **2001**, 61, 2259–2272.
 40. Calard, V.; Lamon, J. *Compos. Sci. Technol.* **2002**, 62, 385–393.
 41. McNulty, J. C.; Zok, F. W. *J. Am. Ceram. Soc.* **1997**, 80, 1535–1543.
 42. Naslain, R. *Compos. Interfac.* **1993**, 1, 253–258.
 43. Rebillat, F.; Lamon, J.; Guette, A. *Acta Mater.* **2000**, 48, 4609–4618.
 44. Lamon, J.; Rebillat, F.; Evans, A. G. *J. Am. Ceram. Soc.* **1995**, 78, 401–405.
 45. Lissart, N.; Lamon, J. *Acta Mater.* **1997**, 45, 1025.
 46. Rebillat, F.; Lamon, J.; Naslain, R.; Lara-Curzio, E.; Ferber, M. K.; Besmann, T. *J. Am. Ceram. Soc.* **1998**, 81, 965.
 47. Rebillat, F.; Lamon, J.; Naslain, R.; Lara-Curzio, E.; Ferber, M. K.; Besmann, T. *J. Am. Ceram. Soc.* **1998**, 81, 2315–2326.
 48. Rouby, D.; Reynaud, P. *Compos. Sci. Technol.* **1993**, 48, 109–118.
 49. Gauthier, W.; Lamon, J. *J. Am. Ceram. Soc.* **2009**, 92, 702–709.
 50. Gauthier, W.; Pailler, F.; Lamon, J.; Pailler, R. *J. Am. Ceram. Soc.* **2009**, 92, 2067–2073.
 51. Carrère, P.; Lamon, J. Fatigue behavior at high temperature in air of a 2D woven SiC/Si–B–C composite with a self-healing matrix. In *Key Engineering Materials*; Trans Tech: Switzerland, 1999; Vol. 164–165, pp 357–360.
 52. Bertrand, S.; Pailler, R.; Lamon, J. *J. Am. Ceram. Soc.* **2001**, 84, 787–794.
 53. Lamicq, P.; Bernhart, G. A.; Dauchier, M.; Mace, J. M. *Ceram. Soc. Bull.* **1986**, 64, 336–338.
 54. Carrère, P.; Lamon, J. *J. Eur. Ceram. Soc.* **2003**, 23, 1105–1114.
 55. Abbé, F. Flexural creep behavior of a 2D SiC/SiC composite, Ph. D. Thesis, University of Caen: Caen, France, 1990.
 56. Holmes, J. W.; Chermant, J. L. In *High Temperature Ceramic Matrix Composites*; Naslain, R., et al. Eds.; Woodhead: Cambridge, UK, 1993; pp 633–647.
 57. Evans, A. G.; Weber, C. *Mater. Sci. Eng. A* **1996**, 208, 1–6.
 58. Bodet, R.; Lamon, J.; Jia, N.; Tressler, R. *J. Am. Ceram. Soc.* **1996**, 79, 2673–2686.
 59. Sauder, C.; Lamon, J. *J. Am. Ceram. Soc.* **2007**, 90, 1146–1156.

2.13 Properties and Characteristics of ZrC

H. F. Jackson and W. E. Lee

Imperial College London, London, UK

© 2012 Elsevier Ltd. All rights reserved.

2.13.1	Introduction	339
2.13.2	Crystallographic Properties and Chemical Bonding	340
2.13.3	Thermodynamics of the Zr–C System	341
2.13.3.1	Zr–C Phase Diagram	341
2.13.3.2	Enthalpy of Formation	343
2.13.3.3	Enthalpy and Heat Capacity	343
2.13.3.4	Vaporization	346
2.13.4	Thermal Properties	347
2.13.4.1	Thermal Conductivity	347
2.13.4.2	Electrical Resistivity	350
2.13.4.3	Thermal Expansion	351
2.13.4.4	Diffusion	353
2.13.5	Mechanical Properties	355
2.13.5.1	Elastic Properties	355
2.13.5.2	Hardness	355
2.13.5.3	Strength	356
2.13.5.4	Fracture Toughness	357
2.13.5.5	Plastic Deformation	359
2.13.5.6	Creep and Stress Relaxation	361
2.13.5.7	Thermal Shock Resistance	363
2.13.6	Environmental Resistance	363
2.13.6.1	Oxidation	363
2.13.6.1.1	Oxidation products	363
2.13.6.1.2	Oxidation kinetics	364
2.13.6.1.3	Oxidation by water vapor	364
2.13.6.1.4	Summary and outlook	364
2.13.6.2	Performance Under Irradiation	365
2.13.6.2.1	Thermal neutron capture cross-section	365
2.13.6.2.2	Durability and dimensional stability under neutron irradiation	365
2.13.6.2.3	Microstructural changes under heavy ion or proton irradiation	367
2.13.6.2.4	Irradiation effects on electrical, thermal, and mechanical properties	368
2.13.7	Summary and Outlook	368
References		369

Abbreviations

fcc	Face-centered cubic
%FIMA	Percent fissions per initial actinide metal atom
CRSS	Critical resolved shear stress
CTE	Linear coefficient of thermal expansion
DBTT	Ductile-to-brittle transition temperature
dpa	Displacements per atom
DTA	Differential thermal analysis
EDX	Energy-dispersive X-ray spectroscopy

SEM	Scanning electron microscopy
TEM	Transmission electron microscopy
TRISO	Tri-structural isotropic (coated fuel particle)
XRD	X-ray diffraction

2.13.1 Introduction

Zirconium carbide, like other carbides of the transition metals of Groups IV, V, and VI, exhibits an

unusual combination of properties that are useful for refractory applications. These carbides combine the cohesive properties of covalently bonded ceramics (high melting point, high strength, and hardness) with the electronic properties of metals (high thermal and electrical conductivity). Comparative properties of the refractory transition metal carbides have been reviewed previously by Schwarzkopf and Kieffer,¹

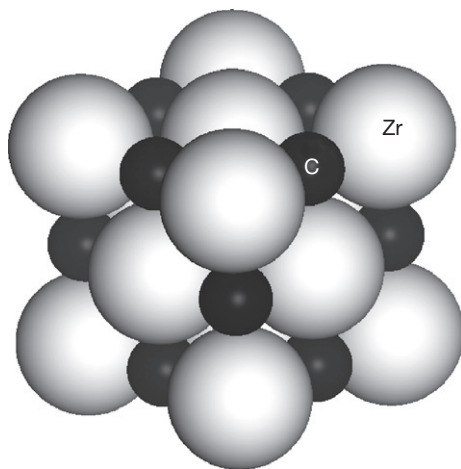


Figure 1 Rocksalt crystal structure of ZrC_x .

Storms,² Toth,³ Kosolapova,⁴ and Upadhyaya.⁵ A thorough understanding of the thermodynamic and heat transport properties of carbides is limited by a paucity of experimental data as a function of composition.

2.13.2 Crystallographic Properties and Chemical Bonding

In the Zr–C system, the monocarbide is the only intermetallic phase reported, crystallizing in the face-centered cubic NaCl structure ($Fm\bar{3}m$, space group 225) (**Figure 1**). Zr atoms form a close-packed lattice, and the smaller C atoms ($r_C = 0.48r_{Zr}$) fill the octahedral interstices.³

The ZrC_x phase exists over a wide compositional range and, as further discussed in **Section 2.13.3.1**, is stable with up to 50% vacancies on the carbon sublattice. Low-temperature ordered phases have been experimentally reported for the Ti–C, V–C, and Nb–C systems, but so far have been suggested only via thermodynamic calculations for the Zr–C system.⁶ Metallic vacancies comprise at most a few atomic percent.³

The effect of carbon vacancies on unit cell geometry has been investigated extensively (**Figure 2**),

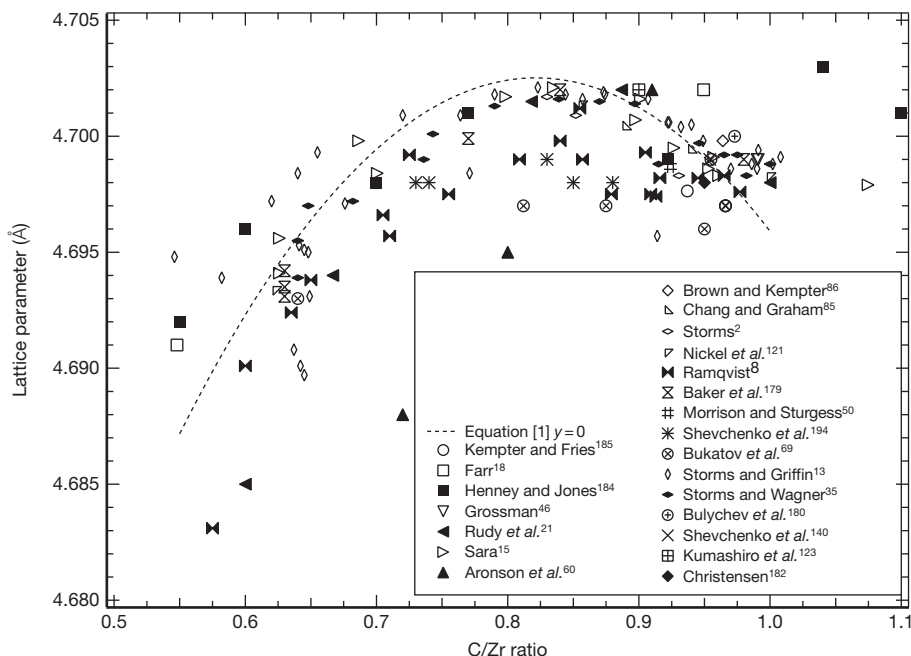


Figure 2 ZrC_x lattice parameter as a function of the carbon/zirconium ratio x .

with the relationship between room temperature lattice parameter and C/Zr ratio difficult to establish conclusively. Scatter in literature values is a common theme in the study of transition metal carbides because of the difficulty of preparing pure specimens and adequately characterizing them. Oxygen and nitrogen readily substitute for carbon in the lattice, and their presence is correlated with reduced lattice parameter. On the basis of literature values for a range of impurity contents, Mitrokhin *et al.*⁷ established a quantitative relationship between the lattice parameter of such oxycarbonitrides and carbon, as well as the oxygen–nitrogen impurity content:

$$a_{\text{ZrC}_x(\text{ON})_y} = 4.5621 - 0.2080x^2 + 0.3418x - 0.80y(1 - x) \quad [1]$$

where x is the C/Zr atomic ratio ($0.62 < x < 1$) and y is the (O + N)/Zr atomic ratio ($y < 0.3$).

In general, lattice parameter increases with C/Zr ratio, with evidence for an increase and a decrease as C content increases above approximately $\text{ZrC}_{0.8}$ toward $\text{ZrC}_{1.0}$. Ramqvist⁸ qualitatively explained the peak in lattice parameter versus C/Zr ratio as being due to competing influences on lattice size: expansion with increasing carbon content due to the increased space required to accommodate interstitials, and contraction due to the increased bond strength.

The nature of chemical bonding in ZrC_x is not fully understood, and electronic structure investigations have sought to establish the relative influences of covalent, metallic, and ionic contributions. Carbon s- and p-orbitals and zirconium d-orbitals participate in bonding and contribute to strong metal–nonmetal bonding and octahedral coordination.⁹ Other authors¹⁰ emphasize the interstitial nature of carbon in the ZrC structure and the donation of electrons from carbon to metal, strengthening Zr–Zr bonds. Lye and Logothetis¹¹ proposed that some charge transfer from carbon to metal occurs and that carbon stabilizes the carbide structure by contributing bonding states. Hollox¹² and Storms and Griffin¹³ suggest that, depending on the carbide, lattice stability decreases with increasing carbon content if antibonding states become filled; this is consistent with observed hardness and melting temperature measurements for ZrC_x . The electronic structure of ZrC must be placed in context with the properties of Groups IV, V, and VI transition metal carbides, and the interested reader is referred to the comparative reviews seen earlier.

2.13.3 Thermodynamics of the Zr–C System

2.13.3.1 Zr–C Phase Diagram

The most recent critical assessment of the Zr–C system was carried out by Fernandez-Guillermot¹⁴ and is depicted in Figure 3. The phase diagram shows the formation of a monocarbide phase which exists between 37.5 and 49.5 at.% C ($\text{ZrC}_{0.6-0.98}$ with extent of phase field temperature-dependent), melts congruently at 3700 K and 46 at.% C ($\text{ZrC}_{0.85}$), and forms a eutectic with carbon at 3200 K at 67.6 at.% C. Solid solubility of C in Zr has not been established conclusively but is estimated to be between 1 and 3 at.% C by Sara¹⁵, Rudy,¹⁶ and Kubaschewski-von Goldbeck.¹⁷ The Zr + ZrC eutectic is close to the melting temperature of bcc Zr, 2127 K, contributing to the assessment of low carbon solubility. Solubility of Zr in C is taken as nil.

Figure 4 shows the results of experimental phase diagram studies superimposed on the assessed diagram. Phase boundaries of the ZrC phase were established via ceramography by Farr,¹⁸ Sara and Doloff,¹⁹ Sara *et al.*,²⁰ Sara,¹⁵ and Rudy *et al.*,²¹ while Storms and Griffin¹³ used C and Zr activity values determined during a Knudsen effusion study. Rudy *et al.*²¹ prepared mixtures of Zr, ZrH_2 , or graphite with ZrC and determined ZrC_x solidus temperatures and ZrC –C eutectic temperature via differential thermal analysis (DTA), ceramography, or melting in a Pirani furnace. As described by Rudy and Progulski,²² the Pirani technique subjects a bar specimen with a central blackbody hole to resistance heating; melting is determined by the temperature at which liquid forms in the blackbody hole. The technique is noted to be most precise for isothermal transformations (i.e., congruent melting or eutectic), as the sample often collapses or the blackbody hole closes before the liquidus is reached. Sara¹⁵ prepared zirconium carbides having various C/Zr ratios from mixtures of ZrH_2 and graphite to determine melting temperatures and the congruent melting temperature and composition. Adelsberg *et al.*²³ performed ceramography on C–Zr diffusion couples to contribute data points to the low-carbon liquidus line; ZrC –C eutectic temperature was also determined by ceramography. Zotov and Kotelnikov²⁴ placed ZrC_x bars with a radial hole under axial loading and resistance heating; fracture of the sample at the temperature at which the hole melted determined ZrC_x solidus. For the $\text{ZrC}_{0.88}$ sample, at least, their value is

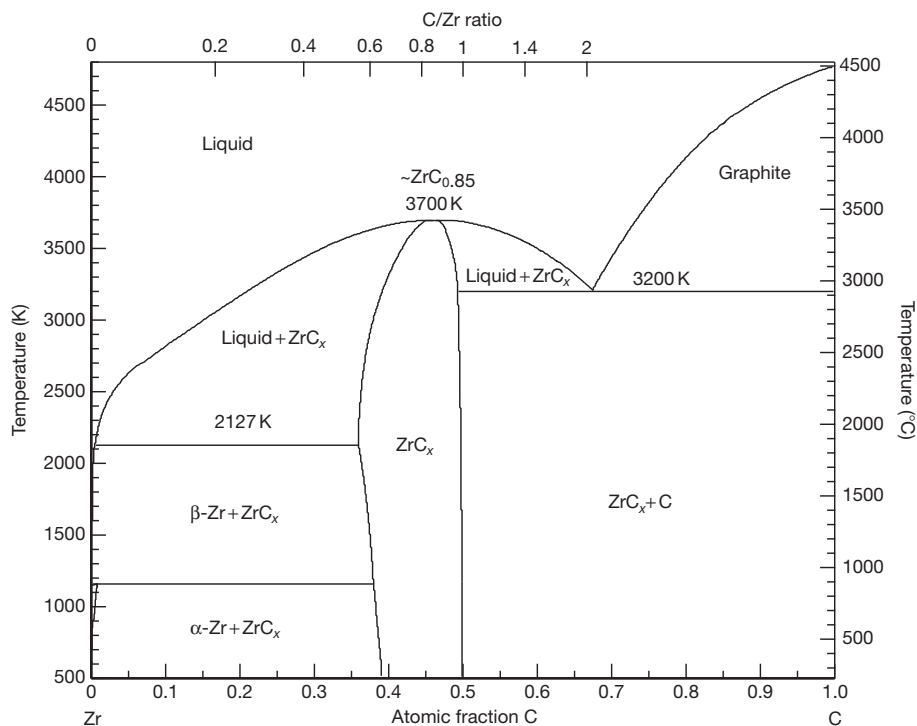


Figure 3 Zr-C phase diagram, as assessed by Fernandez-Guillermet.¹⁴

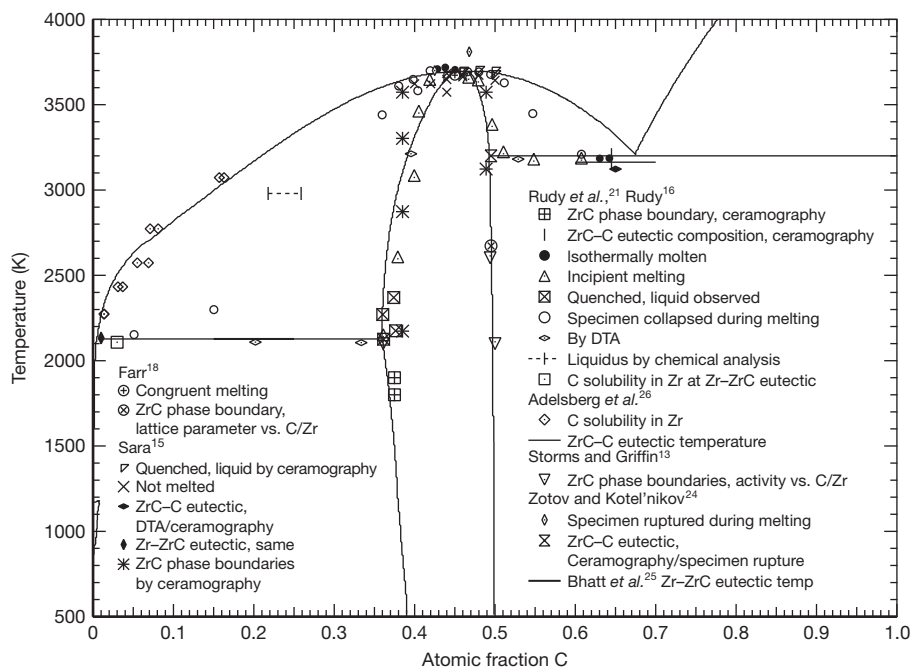


Figure 4 Experimental phase diagram studies compared with the assessed diagram.

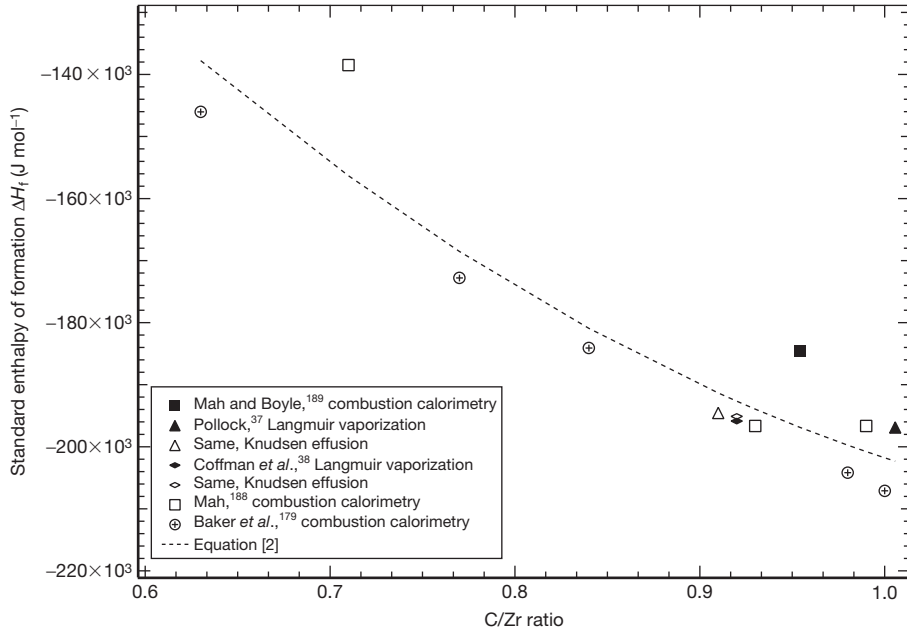


Figure 5 Standard molar enthalpy of formation of ZrC_x as a function of C/Zr ratio.

anomalously high. Heating the sample in an effusion cell, Bhatt *et al.*²⁵ determined Zr–ZrC eutectic temperature by an optical pyrometric ‘spot technique.’

2.13.3.2 Enthalpy of Formation

Other properties on which the current phase diagram is based include enthalpy of formation, enthalpy increment or heat content, specific heat capacity (C_p), and activity of C and Zr in ZrC. Standard enthalpy of formation, ΔH_f° , of ZrC_x as a function of the C/Zr ratio is plotted in Figure 5. A quadratic fit to the reviewed data is provided by

$$\Delta H_f^\circ = 2.03 \times 10^5 x^2 - 5.04 \times 10^5 x - 9.92 \times 10^4 \quad [2]$$

where x is the C/Zr ratio and ΔH_f° is in units of joules per mole. Within the compositional range, ΔH_f° is most negative at the stoichiometric composition and the recommended value is -197 kJ mol^{-1} .²⁶ Toth³ attributes this to decreasing ZrC_x bond strength with removal of C from the lattice.

2.13.3.3 Enthalpy and Heat Capacity

Enthalpy increment of ZrC_x with respect to 298 K ($H_T - H_{298}$) is plotted as a function of temperature in Figure 6 and as a function of C/Zr ratio at 1600 K in Figure 7. Storms and Griffin report the following equation to fit the experimental values of

Mezaki *et al.*,²⁷ Levinson,²⁸ Kantor and Fomichev,²⁹ and Turchanin and Fesenko³⁰:

$$H_T - H_{298} = -2.14 \times 10^4 + 56.86T - 5.46 \times 10^{-3}T^2 + 1.86 \times 10^{-6}T^3 + \frac{1.456 \times 10^6}{T} \quad [3]$$

where H is in units of joules per mole and T is absolute temperature, valid from 298 to 3200 K. From their low-temperature heat capacity measurements on $\text{ZrC}_{0.96}$, Westrum and Feick³¹ determined a value of $H_{298} - H_0$ of 5.9 kJ mol^{-1} and an entropy, $S_{298} - S_0$ of 33.3 J mol^{-1} .

Heat capacity of ZrC_x is plotted as a function of temperature in Figure 8 and as a function of C/Zr ratio at 298 K in Figure 9. Heat capacity is equal to the first derivative of enthalpy with temperature, and the function recommended by Storms and Griffin¹³ is

$$C_p = 56.86 - 0.0109T + 5.586 \times 10^{-6}T^2 - \frac{1.456 \times 10^6}{T^2} \quad [4]$$

where C_p is in units of joules per mole per kelvin.

Low-temperature heat capacity of $\text{ZrC}_{0.96}$ was measured by Westrum and Feick³¹ by adiabatic calorimetry between 5 and 350 K. No data are available for more carbon-deficient compositions, limiting efforts to quantify the entropy of mixing introduced by carbon vacancies. High-temperature drop calorimetry

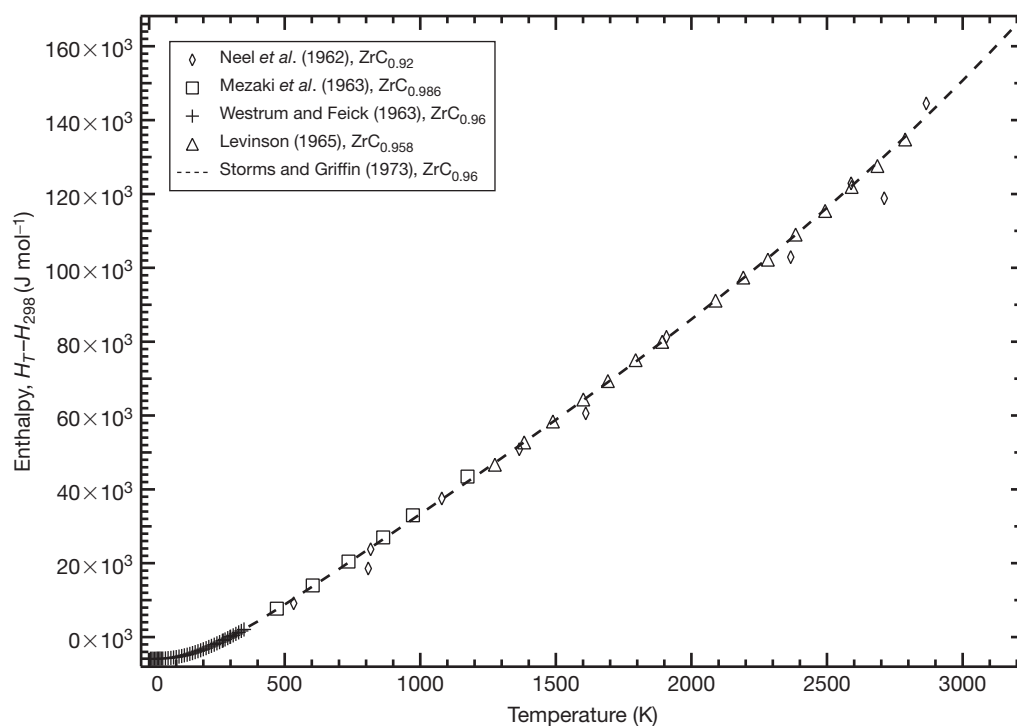


Figure 6 Enthalpy of ZrC_x as a function of temperature.

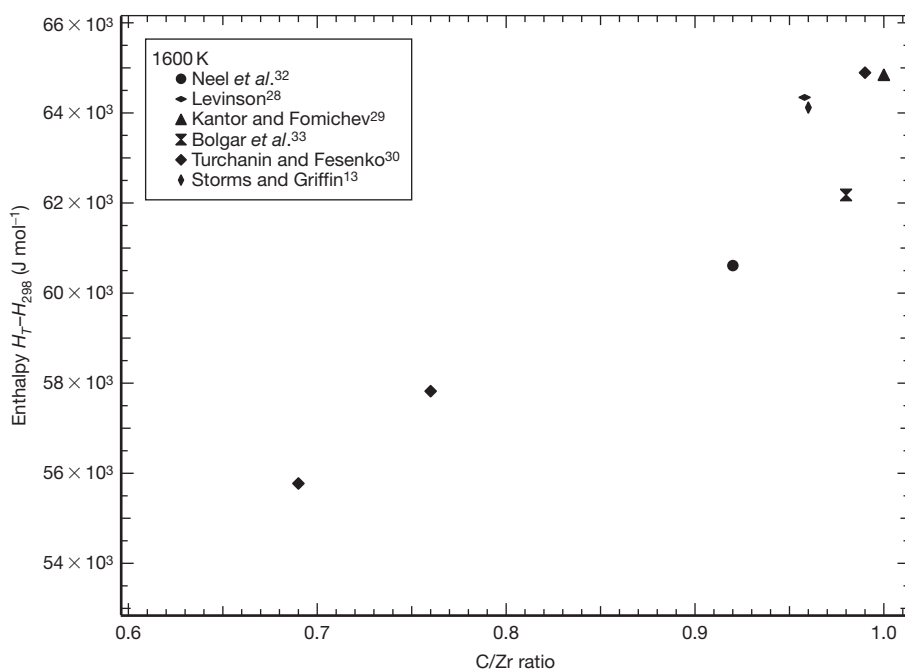


Figure 7 Enthalpy of ZrC_x at 1600 K as a function of C/Zr ratio.

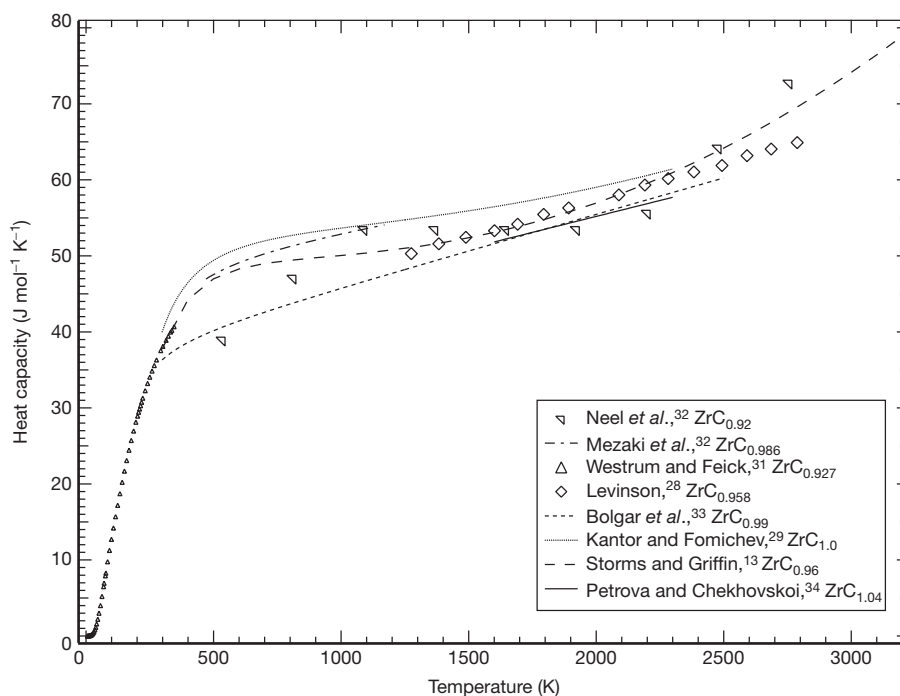


Figure 8 Heat capacity of ZrC_x as a function of temperature.

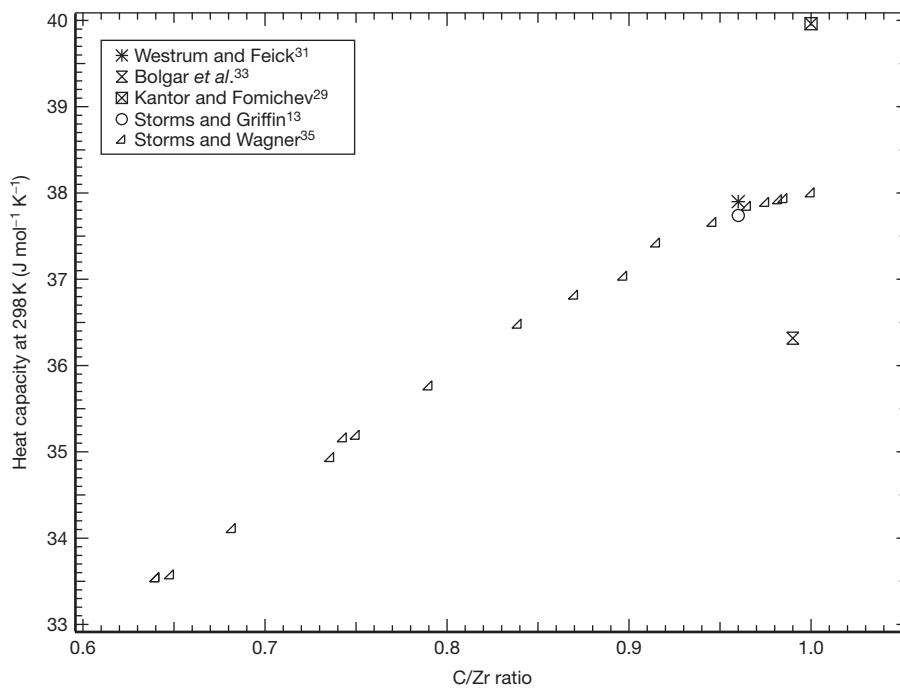


Figure 9 Heat capacity at 298 K as a function of C/Zr ratio.

measurements were made on $\text{ZrC}_{0.92-1}$ by Neel *et al.*,³² Mezaki *et al.*,²⁷ Levinson,²⁸ Bolgar *et al.*,³³ Kantor and Fomichev,²⁹ and Turchanin and Fesenko.³⁰ Petrova and Chekhovskoi³⁴ determined heat capacity, using a pulsed electric current method to measure thermal diffusivity. Storms and Wagner³⁵ used the laser flash method to measure thermal diffusivity for $\text{ZrC}_{0.64-1}$ at 300 K and estimated C_p for these compositions, using a known value for $\text{ZrC}_{0.96}$ ³¹ and by assuming a curve parallel to that established for NbC_x as a function of C/Nb ratio.³⁶ Heat capacity increases sharply between 0 and 500 K, saturates, then begins to increase more rapidly near the melting point. Both room-temperature heat capacity and high-temperature enthalpy increase with C/Zr ratio in the homogeneity range. Room-temperature heat capacity of $\text{ZrC}_{0.96}$ is $38 \text{ J mol}^{-1} \text{ K}^{-1}$.^{31,35}

2.13.3.4 Vaporization

Vapor pressures have been established by Langmuir vaporization of C-saturated ZrC and by Knudsen effusion studies of ZrC in equilibrium with graphite. These are plotted in Figure 10. Langmuir studies are internally consistent, but give higher pressures than for the Knudsen method. Pollock³⁷ and Coffman *et al.*³⁸ assumed the congruent evaporation composition

to be stoichiometric, that is, equal evaporation rates for Zr and C. However, Langmuir evaporation of $\text{ZrC}_{0.74-0.96}$ by Nikol'skaya *et al.*³⁹ found the congruently evaporating composition to lie in the range $\text{ZrC}_{0.8-0.87}$, decreasing with increasing temperature between 2300 and 3100 K. Vidale⁴⁰ computed Zr and C vapor pressures from tabulated H and S functions for Zr and C, ΔH_f° for ZrC of $-185.5 \text{ kJ mol}^{-1}$, and an estimated ΔS_f° for ZrC of $-11.3 \text{ kJ mol}^{-1} \text{ K}^{-1}$, and the trend is consistent with Langmuir data. Storms² computed Zr vapor pressure over $\text{ZrC} + \text{C}$ from thermodynamic functions derived by the author for $\text{ZrC}_{0.96}$, values in the 1963 JANAF thermochemical tables for $\text{Zr}_{(g)}$ and $\text{C}_{(s)}$, ΔH_f° for ZrC of $-196.6 \text{ kJ mol}^{-1}$, and $\Delta H_{\text{vap}}^\circ$ for ZrC of 608 kJ mol^{-1} , with the prediction consistent with Knudsen data. Evaporation rate as a function of temperature is plotted in Figure 11. Standard enthalpy of vaporization of ZrC at 298 K has been reported as $-1520 \text{ kJ mol}^{-1}$ for Langmuir studies and -805 kJ mol^{-1} for Knudsen studies.^{37,38}

Storms and Griffin¹³ coupled Knudsen effusion from TaC cells with mass spectrometry between 1800 and 2500 K to determine the Zr activity of $\text{ZrC}_{0.55-1.97}$ by comparing ion currents from pure Zr with those of the carbide. Carbon activity was obtained via a Gibbs–Duhem integration; activity of both as a function of C/Zr ratio at 2100 K is plotted

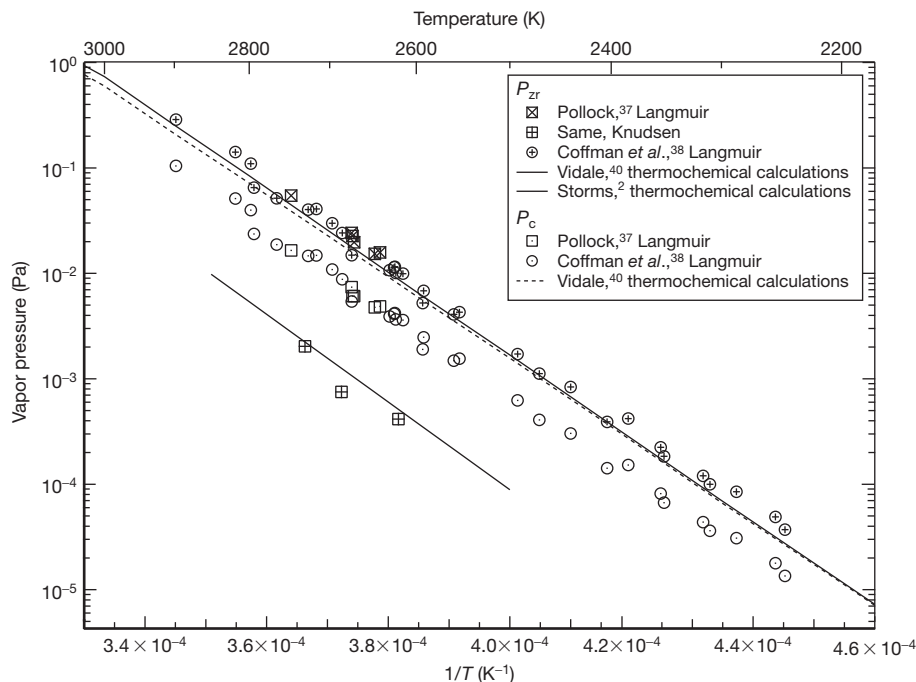


Figure 10 Vapor pressures of C and Zr as a function of temperature.

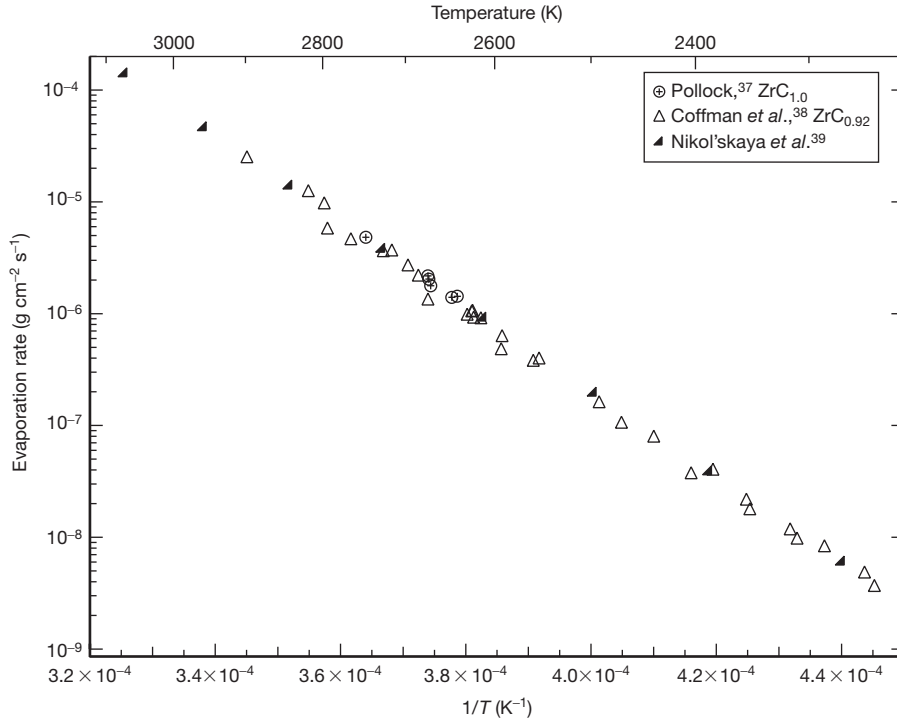


Figure 11 Langmuir rate of evaporation of ZrC_x as a function of temperature.

in [Figure 12](#). Activity of Zr exceeds that of C for carbon-deficient compositions up to the cross-over composition at 2100 K of $\text{ZrC}_{0.89}$. The change in Zr activity with C/Zr ratio is most rapid at high-carbon compositions and becomes near-constant as the composition drops below approximately $\text{ZrC}_{0.8}$. Partial standard molar enthalpies of vaporization for Zr and C as a function of C/Zr ratio are plotted in [Figure 13](#). Total enthalpies obtained by Pollock³⁷ and Coffman *et al.*³⁸ are consistent with the values of Storms and Griffin.¹³ Partial enthalpy of Zr decreases monotonically as C is removed from the lattice. Partial enthalpy of C exceeds that of Zr for most of the homogeneity range, approaching that of Zr at a composition of $\text{ZrC}_{0.99}$.

2.13.4 Thermal Properties

2.13.4.1 Thermal Conductivity

It is appropriate to discuss thermal and electrical conductivity as coupled phenomena. Thermal conductivity is considered a sum of phonon and electron contributions to conductivity. The phonon contribution to thermal conductivity should decrease with temperature, as atomic vibrations inhibit phonon

transport. The contribution to thermal conductivity due to electrons is calculated by the Wiedemann–Franz law,⁴¹ according to

$$k_e = \frac{LT}{\rho} \quad [5]$$

where k_e is the electronic thermal conductivity, L is the Lorentz constant ($2.44 \times 10^{-8} \text{ W } \Omega \text{ K}^{-2}$), T is absolute temperature, and ρ is electrical resistivity. Generally, electrical resistivity of metals increases with temperature; in transition metal carbides, electron thermal conductivity increases with temperature. At low temperatures heat is mainly conducted by phonons, which are scattered strongly by conduction electrons.^{42–44} At intermediate temperatures, both electrons and phonons contribute to thermal conductivity, but in the transition metal carbides the electronic component is dominant. Phonon scattering by carbon vacancies becomes important above about 50 K, contributing to a decrease in thermal conductivity with increasing temperature. At high temperatures, thermal conductivity increases approximately linearly with temperature. The temperature dependence of electronic thermal conductivity is plotted in [Figure 14](#); this was computed from the Wiedemann–Franz law and

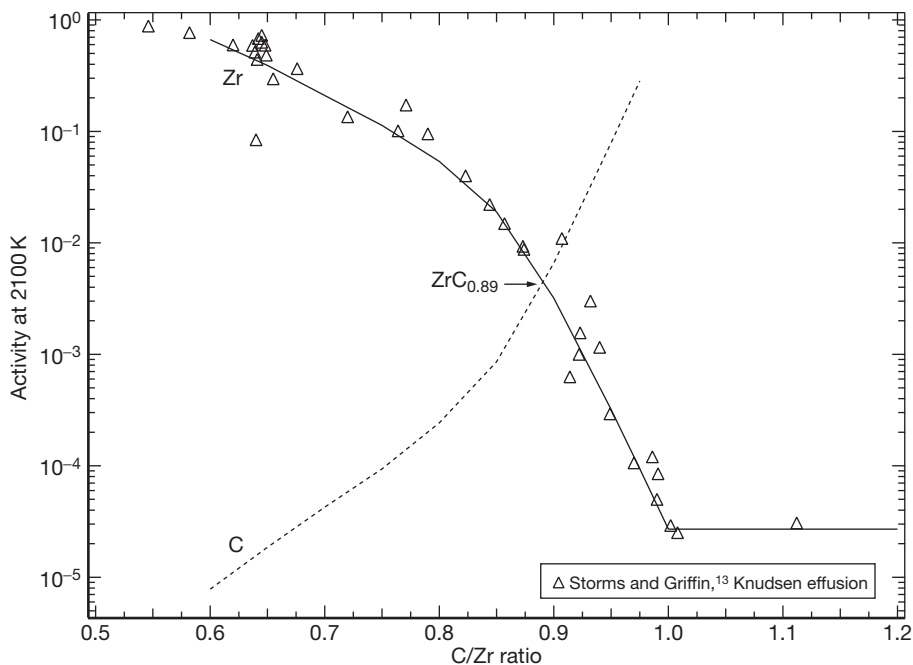


Figure 12 Activity of Zr and C in ZrC_x as a function of C/Zr ratio at 2100 K.

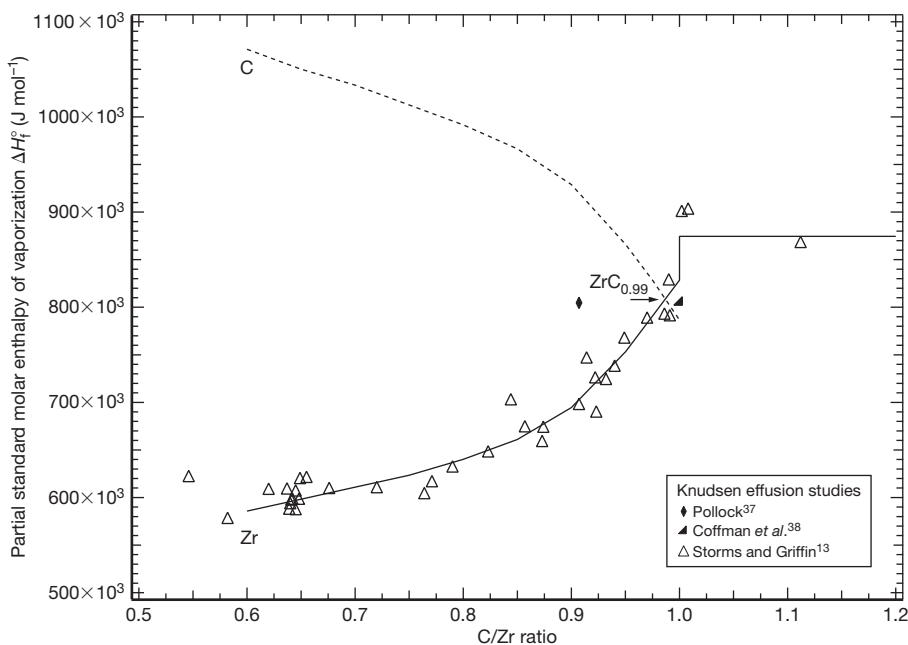


Figure 13 Partial standard enthalpies of vaporization of Zr and C as a function of C/Zr ratio.

a linear fit to the electrical resistivity measurements of Taylor⁴⁵ and Grossman⁴⁶: $\rho = 0.79T + 36.3$.

Experimental measurements of thermal conductivity of ZrC_x as a function of temperature between

1.8 and 3400 K are also plotted in Figure 14. The overall trend is a steep increase of thermal conductivity with temperature up to 50 K, followed by a slight decrease in an intermediate temperature range

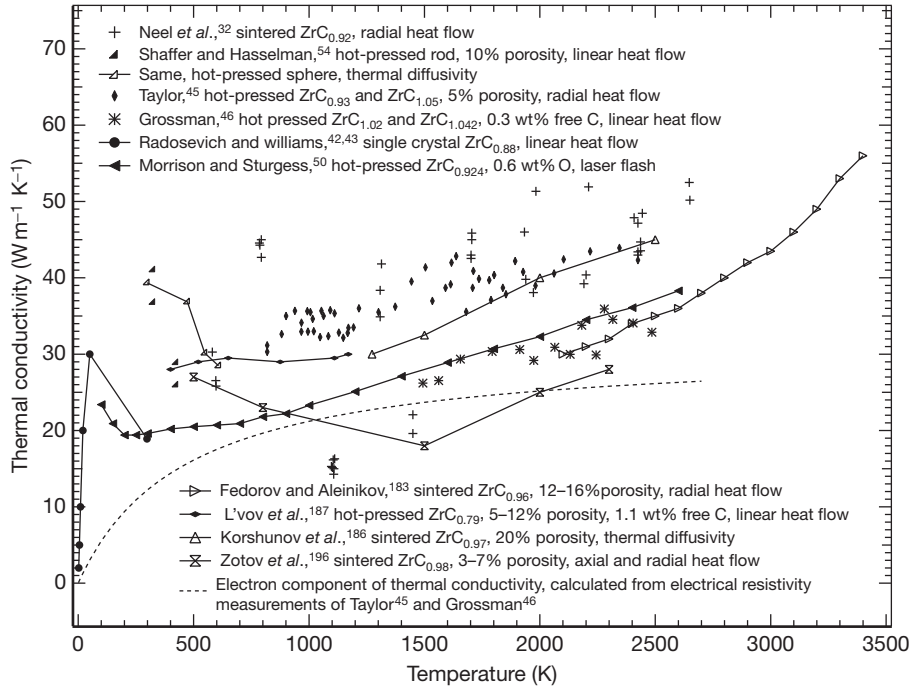


Figure 14 Thermal conductivity of ZrC_x as a function of temperature.

(up to 100–1000 K) and then a more gradual increase up to the melting temperature. Room-temperature thermal conductivity has been reported between 20 and $40 \text{ W m}^{-1} \text{ K}^{-1}$, meeting or exceeding that of Zr metal.⁴⁷ A source of experimental scatter in thermal conductivity is sample porosity, which is not always reported by authors.

Room temperature thermal conductivity is also a strong function of C/Zr ratio (Figure 15). Storms and Wagner³⁵ measured thermal diffusivity of hot-pressed $\text{ZrC}_{0.64-1}$ (0.01–0.1 wt% O) by the laser flash method,⁴⁸ computing thermal conductivity from sample density and heat capacity according to

$$k = \alpha d C_p \quad [6]$$

where k is thermal conductivity ($\text{W m}^{-1} \text{ K}^{-1}$), α is thermal diffusivity ($\text{m}^2 \text{ s}^{-1}$), d is density of the sample (kg m^{-3}), and C_p is heat capacity ($\text{J kg}^{-1} \text{ K}^{-1}$). As described in Section 2.13.3.4, C_p was available for $\text{ZrC}_{0.96}$ but not for other compositions and C_p versus x was estimated by assuming that it was parallel to that of NbC_x . A maximum room temperature thermal conductivity of $45 \text{ W m}^{-1} \text{ K}^{-1}$ occurs at near-stoichiometric compositions, with a steep drop-off as carbon atoms are removed from the lattice. Further reduction of the C/Zr ratio below approximately

$\text{ZrC}_{0.9}$ has little effect on thermal conductivity, which approaches a constant value of $10 \text{ W m}^{-1} \text{ K}^{-1}$.

From a fit to literature electrical resistivity measurements and the Wiedemann–Franz law, Storms and Wagner calculated the composition dependence of the electronic component of thermal conductivity as

$$k_e = 1.05 \times 10^3 \left(0.00382 + \frac{1}{55 + 950(1-x)} \right) \quad [7]$$

where x is the C/Zr ratio, and a Lorenz number of $3.5 \times 10^{-8} \text{ V}^2 \text{ K}^{-2}$ was used (by assuming that the thermal conductivity in the low-carbon region was entirely electronic). By taking the difference between their experimentally measured thermal conductivities and their calculated electronic thermal conductivities, Storms and Wagner expressed the phonon thermal conductivity as a function of composition by the equation

$$k_p = \frac{0.007}{(1-x)^2} \quad [8]$$

where x is the C/Zr ratio. As plotted in Figure 15, electronic thermal conductivity is dominant for highly nonstoichiometric ZrC_x , while lattice or phonon conductivity makes a larger contribution in near-stoichiometric ZrC_x . The effect of a decrease in C/Zr ratio is proposed by Avgustinik *et al.*⁴⁹ to reduce the

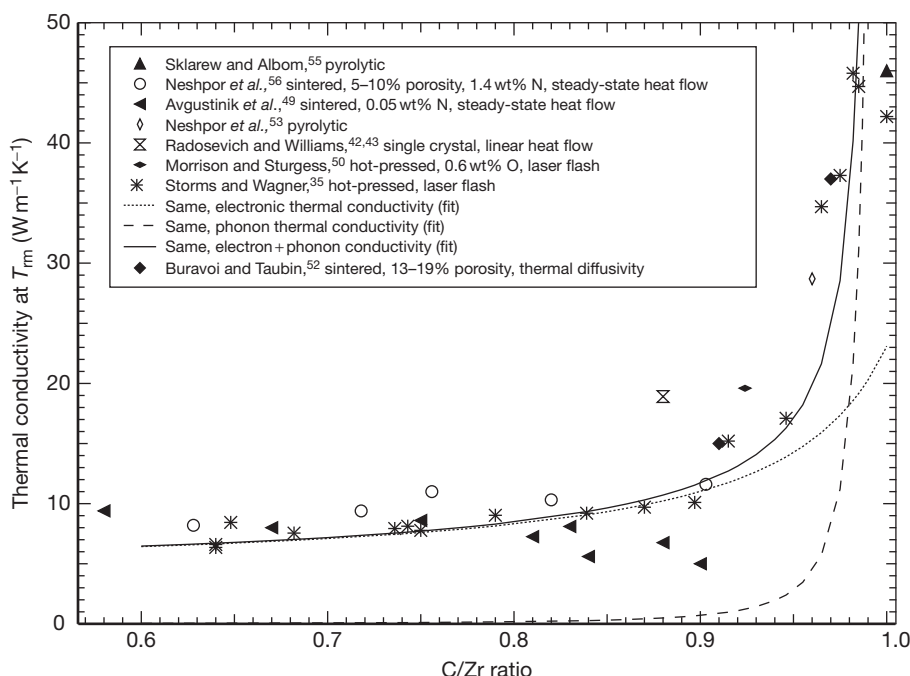


Figure 15 Room-temperature thermal conductivity of ZrC_x as a function of C/Zr ratio.

connectivity of the lattice while introducing vacancies and increasing the concentration of nonlocalized electrons. The net effect is an increase in phonon scattering and a decrease in conductivity with deviation from stoichiometry.

Storms and Wagner also studied the effect on thermal conductivity of tripling the oxygen content in $\text{ZrC}_{0.64-0.682}$ from 0.042 to 0.125–0.13 wt%. They found that thermal conductivity was affected little by varying oxygen content in the low-carbon region but asserted that 0.6 wt% O in $\text{ZrC}_{0.924}$ ⁵⁰ produced a more noticeable effect. They suggested that impurities which substitute for carbon (i.e., O or N) reduce the vacancy concentration and have the same effect on thermal conductivity as an increase in C/Zr ratio. The effect of impurities on thermal conductivity is correspondingly more pronounced for $\text{ZrC}_{0.9-1.0}$. Too few measurements of well-characterized near-stoichiometric samples are available to assess this phenomenon more conclusively.

Neshpor *et al.*⁵¹ measured room-temperature thermal conductivity of 85–95% dense sintered $\text{ZrC}_{0.6-0.9}$ containing 1.4 wt% nitrogen by a steady-state heat-flow method, repeating this study with Avgustinik *et al.*⁴⁹ after decreasing N content to 0.05 wt%. Other room-temperature measurements by heat flow or thermal diffusivity measurements^{42,49–55} are

consistent with the trend established by Storms and Wagner, but by covering only one composition, or compositions only below the drop-off at $\text{ZrC}_{0.9}$, the individual studies fail to capture the true trend.

2.13.4.2 Electrical Resistivity

Electrical resistivity of ZrC_x is plotted as a function of temperature in **Figure 16**. Room temperature resistivity ranges from 60 to 200 $\mu\Omega \text{ cm}$, depending on C/Zr ratio and microstructure. In an intermediate temperature range from approximately 100 to 2000 K, resistivity increases linearly with temperature.^{45,46,56,57} Modine *et al.*⁵⁸ measured resistivity of single crystal ZrC_x ($x = 0.89, 0.93$, and 0.98) between 4 and 1000 K. The authors deemed the data well represented by the Bloch–Grüneisen model for temperature dependence of resistivity of metals, with resistivity varying as T^5 at low temperatures (4–100 K) and linearly at intermediate temperatures. At a high enough temperature (1000–2000 K), resistivity deviates from linear behavior and tends to saturate at a constant value which decreases with C/Zr ratio. The higher-temperature measurements on single-crystal $\text{ZrC}_{0.93}$ of Hinrichs *et al.*⁵⁹ are consistent with the trend established for single crystal $\text{ZrC}_{0.93}$ at lower temperatures by Modine *et al.* (**Figure 16**).

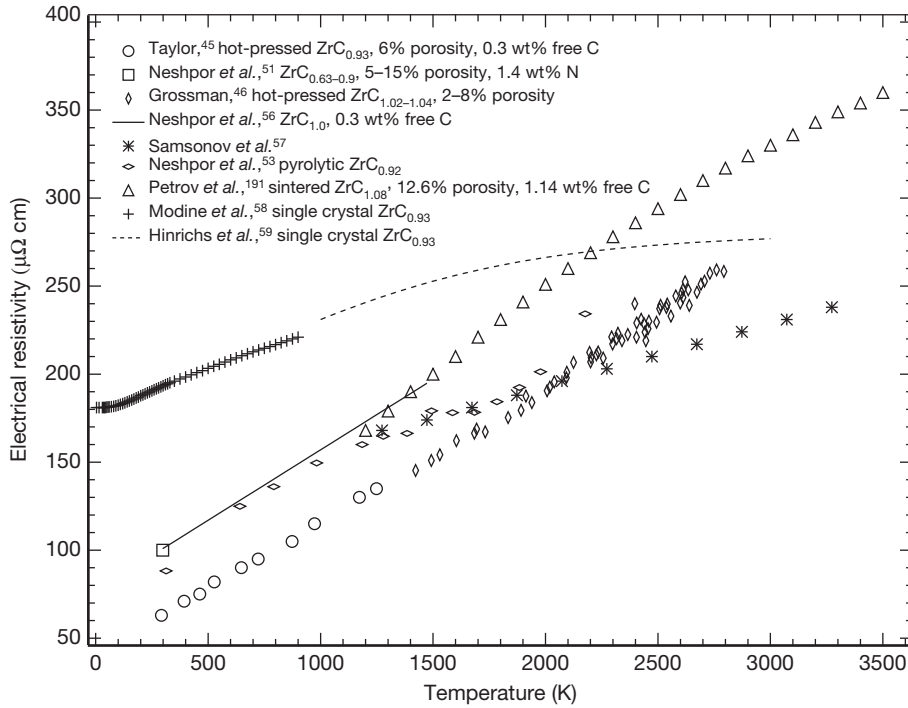


Figure 16 Electrical resistivity of ZrC_x as a function of temperature.

The resistivity of single crystals exceeds that of polycrystals up to 2200–2500 K where the former begins to saturate; resistivity of polycrystalline ZrC_x saturates only near the melting temperature, although few measurements have been made in this temperature range. The effects of free carbon and oxygen/nitrogen impurities on resistivity have not been explored. Measurements on pyrolytic ZrC_x lie in the same range as those of other polycrystalline specimens, but a detailed study of the effects of grain size, texture, porosity, and other microstructural factors on electrical resistivity is needed.

Room temperature electrical resistivity as a function of C/Zr ratio is plotted in Figure 17. Resistivity is lowest for near-stoichiometric compositions and increases with deviation from stoichiometry. A decrease in C/Zr ratio increases the concentration of carbon vacancies, which scatter conduction electrons. Storms and Wagner³⁵ fit the available experimental data to the formula

$$\rho = \frac{1}{0.00382 + \frac{1}{55 + 950(1 - x)}} \quad [9]$$

where ρ is electrical resistivity ($\mu\Omega \text{ cm}$) and x is C/Zr ratio, which is plotted in Figure 17.

2.13.4.3 Thermal Expansion

Thermal expansion has been investigated via low- and high-temperature X-ray diffraction,^{60–67} neutron diffraction,⁶⁸ and dilatometry.^{32,54,57,69–74} Elongation ($\Delta L/L_{298}$) and linear coefficient of thermal expansion (CTE) are plotted as a function of temperature with respect to 298 K in Figures 18 and 19, respectively. Elongation results are generally consistent between lattice parameter and dilatometric methods, diverging at high temperatures. Scatter is magnified on the CTE versus T curve, which is akin to the second derivative of length versus T experimental data. Elongation is fairly linear, permitting authors to report a mean CTE over various temperature ranges; slope increases slightly with temperature, consistent with an observed rising CTE with temperature. Increase in CTE is more pronounced at temperatures up to 500 K with a more modest increase at higher temperature, although more lower-temperature values are needed to fully understand this behavior. At subambient temperatures, elongation (or contraction, as the reference temperature is 298 K) is non-linear with temperature.

CTE values with respect to 298 K lie in the range $(5\text{--}7) \times 10^{-6} \text{ K}^{-1}$, but the degree of scatter

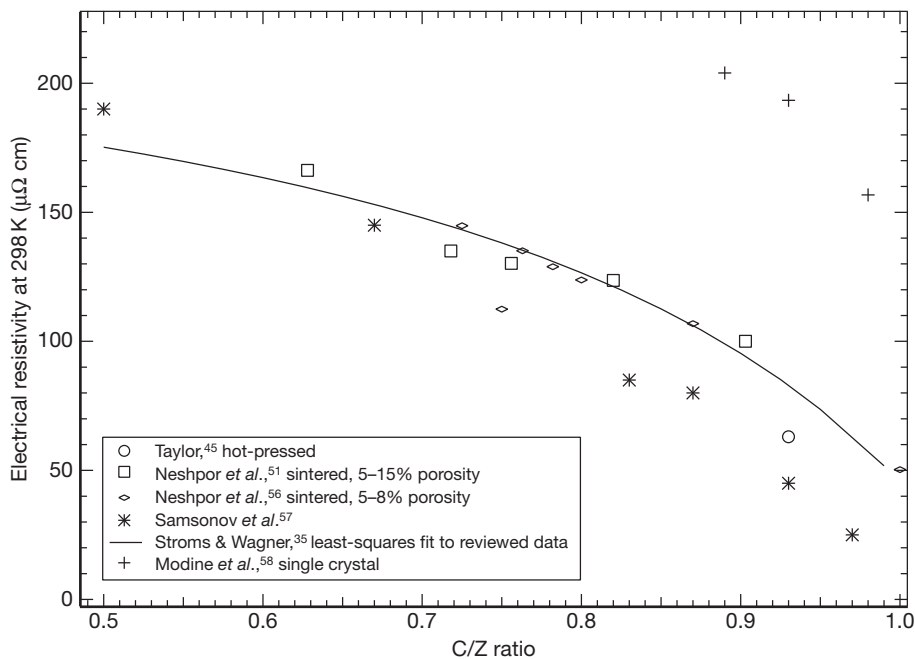


Figure 17 Room-temperature electrical resistivity of ZrC_x as a function of C/Zr ratio.

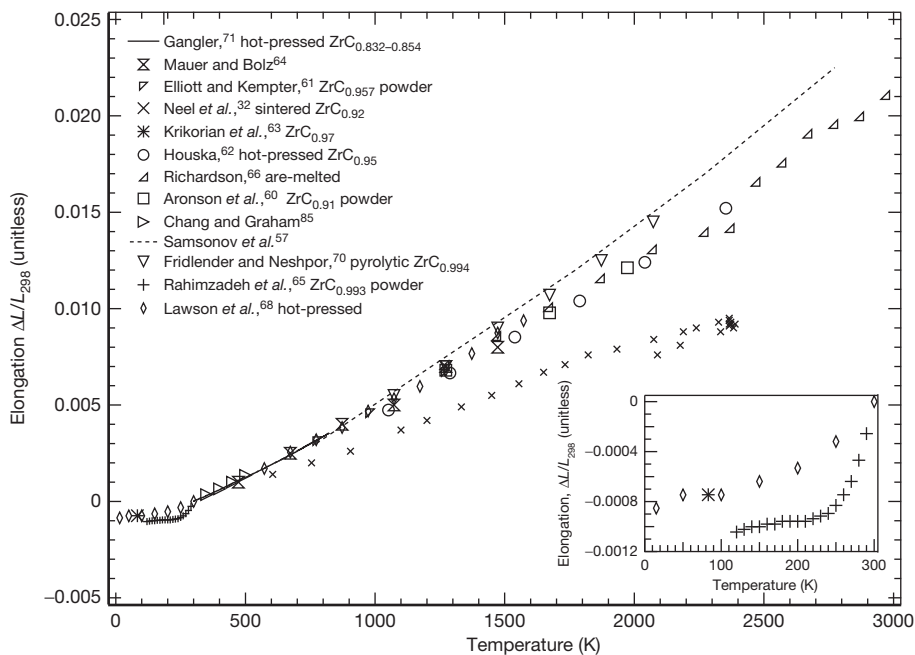


Figure 18 Elongation with respect to 298 K of ZrC_x as a function of temperature.

precludes a more precise recommended value. Thermal expansion coefficient at 1273 K as a function of C/Zr ratio is plotted in Figure 20, where a trend of increasing CTE with deviation from

stoichiometry can be seen. This composition dependence of CTE confirms the general picture of decreasing bond strength as C atoms are removed from the lattice.⁵

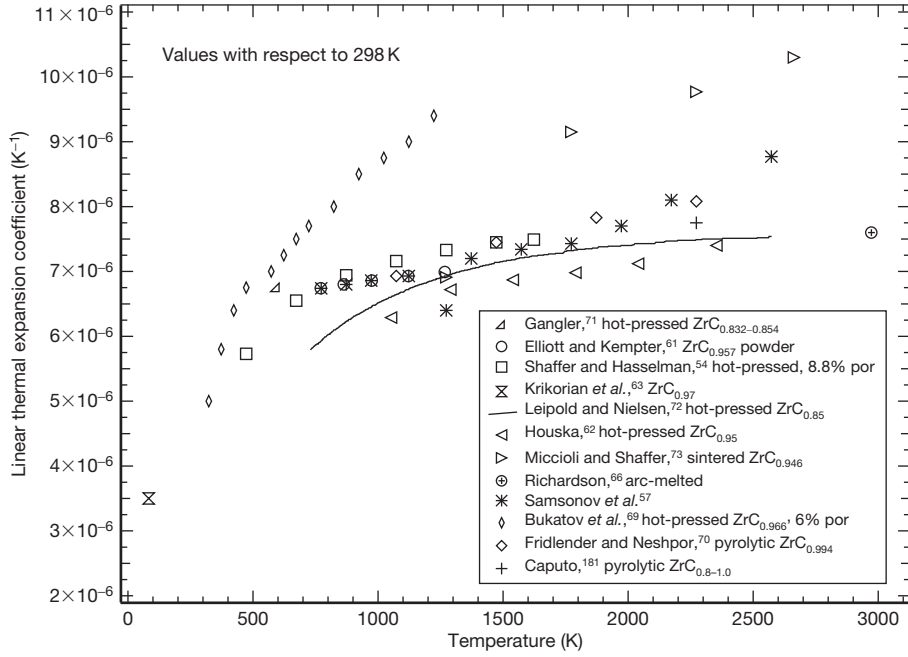


Figure 19 Linear coefficient of thermal expansion (CTE) of ZrC_x as a function of temperature.

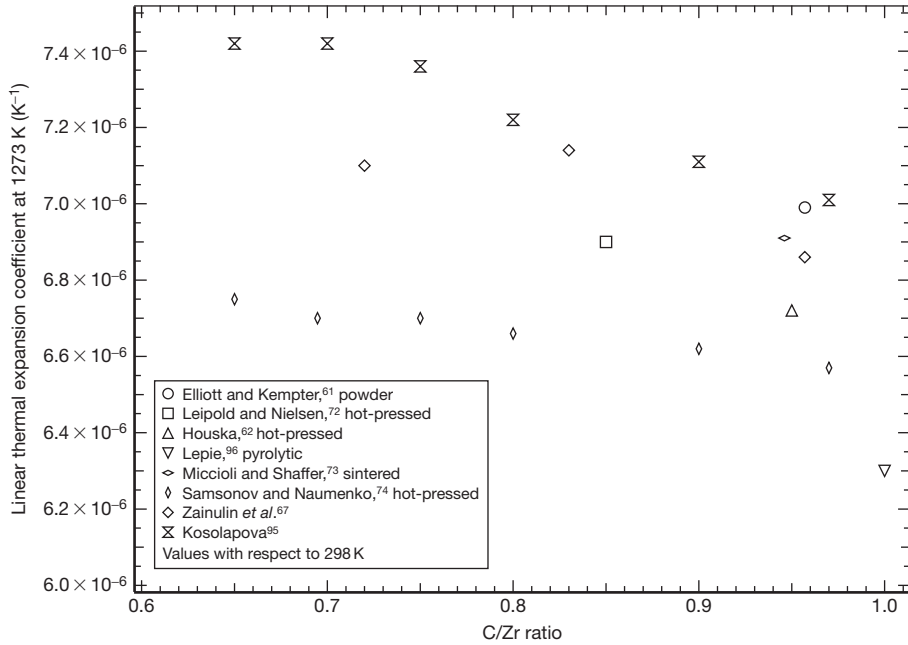


Figure 20 CTE of ZrC_x to 1273 K as a function of C/Zr ratio.

2.13.4.4 Diffusion

The results of diffusion studies are summarized in [Table 1](#). The temperature dependence of diffusion

coefficient conforms to an Arrhenius relationship, according to

$$D(T) = D_0 e^{-Q/RT} \quad [10]$$

Table 1 Diffusion parameters for ZrC

	D_0 ($\text{cm}^2 \text{s}^{-1}$)	Activation energy (kJ mol^{-1})	Temperature range (K)	$D_{1600\text{K}}$ ($\text{cm}^2 \text{s}^{-1}$)	Ref.
Diffusion of C in α -Zr	5×10^{-8}	385	898–1013	–	^a
	6×10^{-5}	134	1013–1103	–	^a
	0.002	152	873–1123	–	^b
Diffusion of C in β -Zr	0.089	133	1143–1523	4.0×10^{-6}	^b
	0.0048	112	1173–1533	1.0×10^{-6}	^c
	0.036	143	1873–2353	7.6×10^{-7}	^d
	0.37	319	1473–2173	1.4×10^{-11}	^e
	0.95	329	2273–3133	1.7×10^{-11}	^f
	332	477	1873–2353	8.9×10^{-14}	^g
Self-diffusion of C in ZrC_x	132	474	1973–2423	4.6×10^{-14}	^h
	56.4	519	2563–3123	6.5×10^{-16}	ⁱ
	14.1	456	2563–3123	1.9×10^{-14}	^j
	1030	720	2563–3123	3.3×10^{-21}	^j

^aZotov and Tsedilkin,⁷⁵ ^{14}C tracer diffusion.^bAgarwala and Paul,⁷⁶ ^{14}C tracer diffusion on Zr rod, vacuum.^cPavlinov and Bykov,⁷⁷ $\text{Zr}_4/^{14}\text{C}$ - Zr_4 diffusion couple, vacuum.^dAndrievskii *et al.*,⁷⁸ ^{14}C tracer diffusion on Zr_4 , vacuum.^eUshakov *et al.*,⁷⁹ rate of ZrC layer growth on alternating Zr_4 and graphite pellets stacked in Mo crucible, vacuum.^fAdelsberg *et al.*,²³ rate of ZrC layer growth on Zr bar melted in graphite crucible, vacuum.^gAndrievskii *et al.*,⁸⁰ ^{14}C tracer diffusion on hot-pressed $\text{ZrC}_{0.96}$, He atmosphere.^hSarian and Criscione,⁸¹ ^{14}C tracer diffusion on single crystal and arc-melted $\text{ZrC}_{0.965}$, vacuum.ⁱAndrievskii *et al.*,⁸² ^{14}C tracer diffusion on hot-pressed $\text{ZrC}_{0.85}$, Ar atmosphere.^jAndrievskii *et al.*,⁸³ ^{14}C tracer diffusion on hot-pressed $\text{ZrC}_{0.97}$ (Zr self-diffusion composition-independent from $\text{ZrC}_{0.84-0.97}$).

where T is absolute temperature, R is the gas constant, Q is the activation energy for diffusion (kJ mol^{-1}), and D_0 is a preexponential factor having the same units as D , the diffusion coefficient, ($\text{cm}^2 \text{s}^{-1}$).

Diffusion of carbon in α -Zr (hcp) and β -Zr (bcc) has been investigated through diffusion of ^{14}C tracer deposited onto Zr^{75–79} and by the rate of ZrC layer growth on Zr in contact with graphite.^{23,79}

Self-diffusion of C in ZrC_x has been determined by tracer diffusion.^{80–83} The study by Andrievskii *et al.*⁸³ provides the only reported value for self-diffusion of Zr in ZrC , which was found to be independent of C/Zr ratio. Activation energy for C self-diffusion in ZrC_x increased with decreasing C/Zr ratio, while diffusion coefficient at a given temperature increased with increasing C/Zr ratio. However, O (0.16–0.19 wt%) and N (0.27–0.55 wt%) impurity content was substantial and varied for different samples. No further studies of C self-diffusion in ZrC_x as a function of C/Zr ratio are available to clarify differences between C self-diffusion in pure ZrC_x versus oxycarbonitride phases.

Carbon and zirconium self-diffusion in ZrC is slower than the inter-diffusion of C in Zr, with correspondingly higher preexponential factors and activation energies. Pavlinov and Bykov⁷⁷ remarked that the activation energy for C diffusion in Zr was close to that of Zr self-diffusion in Zr. As for self-diffusion,

Zr diffuses much slower than C, which may be understood in terms of the interstitial nature of C in ZrC: the smaller C atom is able to diffuse via either thermal metal vacancies or interstitial sites, the latter dwarfing the former in most cases.

Matzke⁸⁴ proposed three potential mechanisms for C self-diffusion in ZrC. First, a C atom may jump along $\langle 110 \rangle$ directions to its nearest neighbor vacant C octahedral interstitial site, which, according to the author, requires a large lattice strain and the movement of two Zr atoms. Second, a C atom may jump along $\langle 111 \rangle$ directions to its nearest neighbor vacant C octahedral interstitial site via an unoccupied tetrahedral interstice, requiring lower strain energy. Third, a C atom may jump to a vacant octahedral site via a thermal metal vacancy. The author proposes that this divacancy mechanism requires the lowest energy, close to the activation energy for generation of a metal vacancy.

The operative diffusion mechanism depends on the C/Zr ratio. Upadhyaya⁵ suggested that carbon diffusion in near-stoichiometric compositions occurs via thermal metal vacancies, while jumps via tetrahedral interstices are favored at higher carbon vacancy concentration. No adequate explanations are available for the composition dependence of activation energy of C in ZrC, or the composition independence of that

of Zr. Other properties (formation enthalpy, hardness) indicate a decrease in bond strength as the C/Zr ratio decreases, which would suggest that diffusion would be enhanced as well. This stands in opposition to measured activation energies for the diffusion of C in $\text{ZrC}_{0.84-0.97}$, which increased with deviation from stoichiometry.⁸³ As for Zr diffusion, Upadaya⁵ suggested that two effects in operation when the C/Zr ratio decreases, a decrease in the energy required to form thermal metal vacancies, and an increase in the energy required for metal vacancy motion due to the decreased interatomic distance, cancel each other out.

Further discussion of diffusion mechanisms in the context of mechanical creep are considered in [Section 2.13.5.6](#).

2.13.5 Mechanical Properties

Transition metal carbides have found application in abrasive and cutting tools, where their high hardness and high melting points may be exploited. Extreme brittleness has so far limited their use in ambient-temperature structural applications, but at high temperatures, carbides have been shown to deform plastically on slip systems analogous to fcc metals. A sufficient number of independent slip systems are available so that polycrystalline ZrC can be made ductile.

2.13.5.1 Elastic Properties

Room-temperature elastic constants of ZrC_x are summarized in [Table 2](#). Chang and Graham⁸⁵ measured elastic constants of two single-crystal rods, $\text{ZrC}_{0.94}$ with [100] orientation and $\text{ZrC}_{0.89}$ with [110] orientation, by an ultrasonic method from 4 to 298 K. Constants c_{11} and c_{44} decrease, while c_{12} increases over this temperature range, none by more than a few percent. Polycrystalline isotropic elastic moduli were computed from these single crystal measurements.

Young's modulus has been measured via dynamic methods^{54,72,86-89,95} during the course of indentation⁹⁰ or loading in a four-point bend⁹¹ configuration. Typical room-temperature values for near-stoichiometric ZrC range between 380 and 420 GPa. Young's modulus as a function of temperature is plotted in [Figure 21](#) and as a function of the C/Zr ratio at room temperature in [Figure 22](#). Young's modulus decreases linearly with temperature, decreasing more rapidly above $0.5T_m$, as plastic deformation is

Table 2 Typical room-temperature elastic properties of ZrC_x

c_{11} (GPa)	472	468.2	^a
c_{12} (GPa)	98.7	99.7	^a
c_{44} (GPa)	159.3	157.3	^a
Young's modulus (GPa)	398 ± 20		^{a,b,c,d,e,f,g,h,i}
Shear modulus (GPa)	167 ± 5		^{a,d,j}
Bulk modulus (GPa)	229 ± 25		^{a,d,f,k}
Poisson's ratio	0.197 ± 0.023		^{a,d,f,j}

^aChang and Graham,⁸⁵ single crystal [100] $\text{ZrC}_{0.94}$ and [110] $\text{ZrC}_{0.89}$, respectively.

^bShaffer and Hasselman,⁵⁴ hot-pressed, 3.4% porosity.

^cLeipold and Nielsen,⁷² hot-pressed $\text{ZrC}_{0.77-0.84}$, 1.6–2.5% free C, <5% porosity.

^dBrown and Kempter,⁸⁶ hot-pressed $\text{ZrC}_{0.964}$, 3% porosity.

^eAvgustinik *et al.*,⁸⁷ sintered $\text{ZrC}_{0.95}$, 5–10% porosity.

^fBaranov *et al.*,⁸⁸ sintered $\text{ZrC}_{0.96}$, 6% porosity.

^gTravushkin *et al.*,⁸⁹ $\text{ZrC}_{0.92}$.

^hWarren,⁹⁰ sintered $\text{ZrC}_{0.95}$, 8% porosity.

ⁱZubarev *et al.*,⁹¹ die-extruded $\text{ZrC}_{1.0}$.

^jShaffer *et al.*,³² hot-pressed, 4.5% porosity.

^kAjami and MacCrone,⁹³ calculated from pressure–volume equation of state fit to high-pressure experiments of Champion and Drickamer.⁹⁴

favorable. Avgustinik *et al.*⁸⁷ found both Young's and shear moduli to decrease with decreasing C/Zr ratio, which they attribute to a corresponding decrease in the average bond strength as C is removed from the lattice.

2.13.5.2 Hardness

Typical room-temperature mechanical properties are summarized in [Table 3](#). Measurements of micro-indentation hardness of ZrC_x are prevalent in the literature. Hardness as a function of temperature is plotted in [Figure 23](#) and as a function of the C/Zr ratio at room temperature in [Figure 24](#). Room-temperature hardness ranges from 20 to 34 GPa (~ 2000 – $3300 \text{ kg}_f\text{mm}^{-2}$). Hardness decreases with increasing test temperature, dropping to approximately 0.5 GPa ($49 \text{ kg}_f\text{mm}^{-2}$) at 1800 K. Room-temperature hardness decreases with decreasing C/Zr ratio. Scatter in room-temperature measurements may be due to the variety of procedures reported (Knoop or Vickers indenter, 50–500 g load), which may not be in accordance with standard test methods.^{109,110} Hardness may be affected by sample microstructure, including porosity, grain morphology, and secondary phases. Residual stresses present in ion-beam deposited or pyrolytic ZrC coatings^{53,107} tend to inflate hardness, while free carbon reduces hardness.^{107,111}

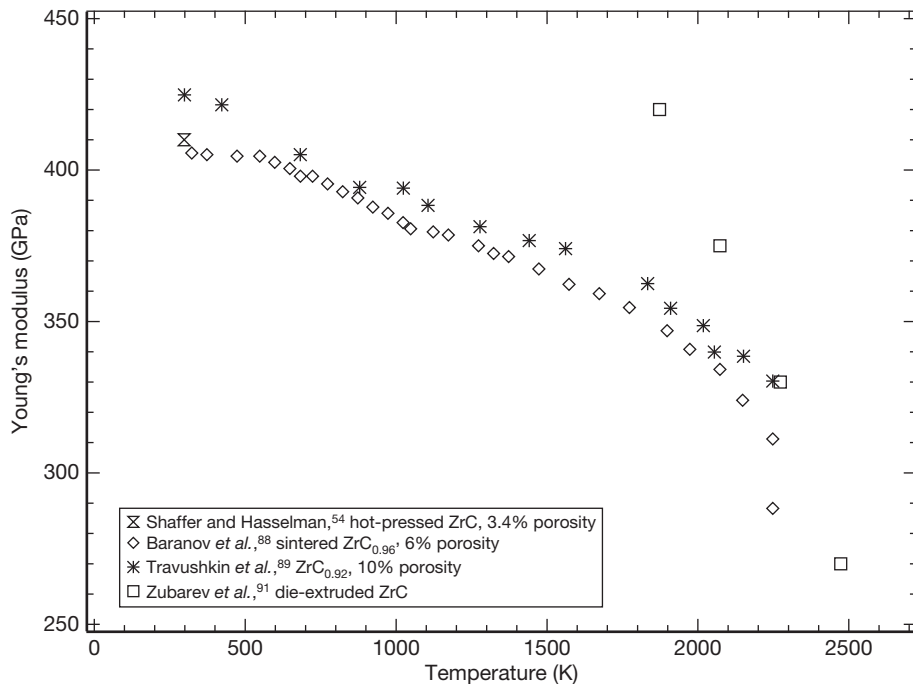


Figure 21 Young's modulus of ZrC_x as a function of temperature.

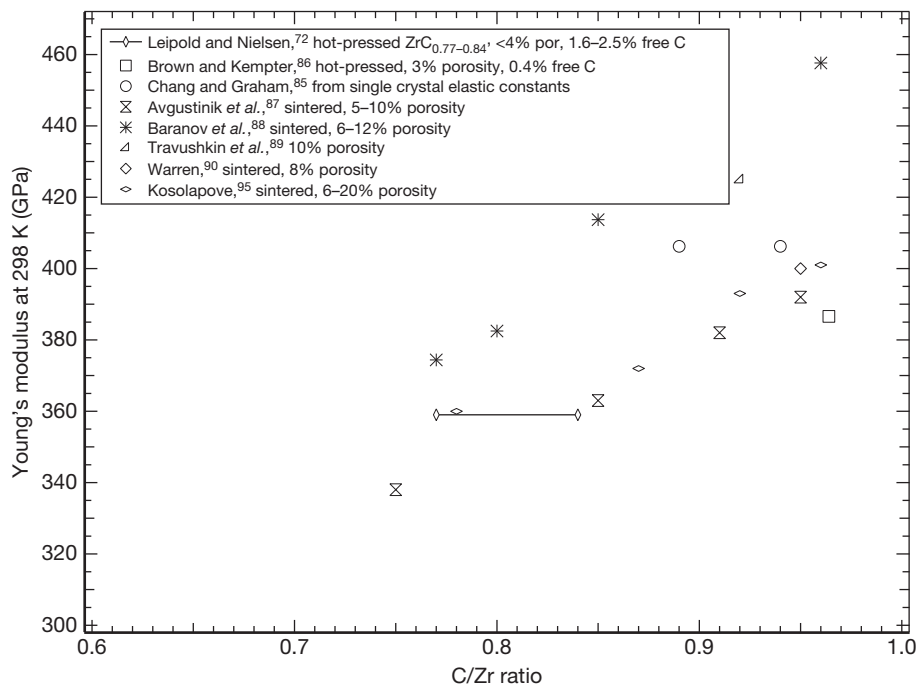


Figure 22 Room-temperature Young's modulus as a function of C/Zr ratio.

2.13.5.3 Strength

Ultimate tensile strength and bend strength are plotted as a function of temperature in **Figures 25**

and **26**, respectively. Only one room-temperature tensile strength is reported,⁹⁵ and ample scatter is evident in room-temperature bend strength. As in

Table 3 Room temperature mechanical properties of ZrC_x

Ultimate tensile strength (MPa)	105	^a
Bend strength (MPa)	100–300	^{b,c,d,e,f}
Compressive strength (MPa)	345	^c
	834	^a
Hardness (GPa)	20–34	^{a,c,d,g,h,i,j,k,l,m,n,o,p,q,r,s}
Fracture toughness, K_{IC} (MPa m ^{1/2})	1.1	^t
	2.8	^u

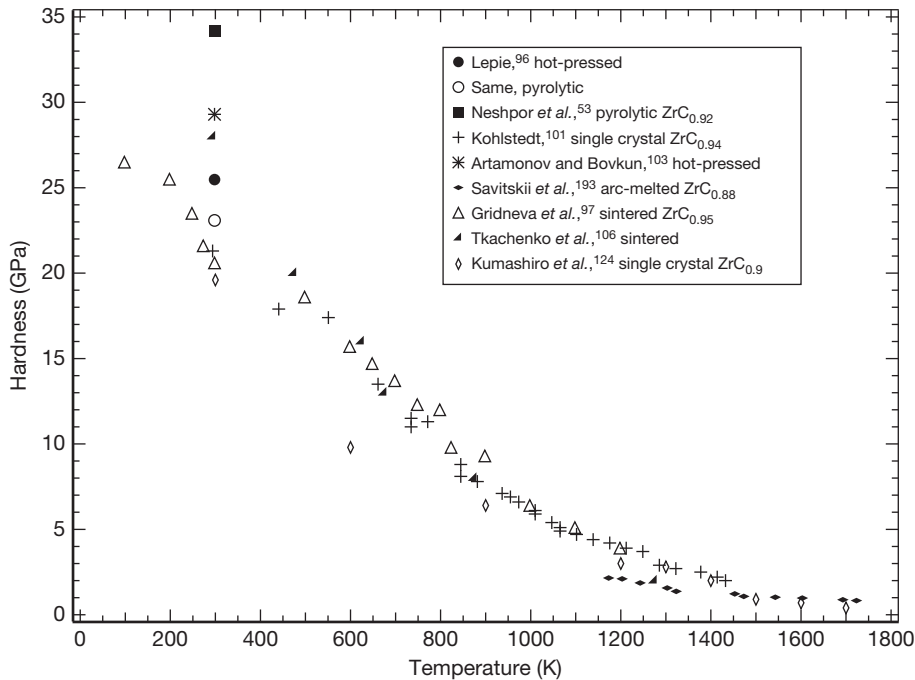
^aKosolapova.⁹⁵^bShaffer and Hasselman.⁵⁴^cLepie.⁹⁶^dGridneva *et al.*⁹⁷^eFedotov and Yanchur.⁹⁸^fLanin *et al.*⁹⁹^gNeshpor *et al.*⁵³^hRamqvist.⁸ⁱFunke *et al.*¹⁰⁰^jKohlstedt.¹⁰¹^kSamsonov *et al.*¹⁰²^lSamsonov *et al.*¹⁰^mArtamonov and Bovkun.¹⁰³ⁿAndrievskii *et al.*¹⁰⁴^oVahldiek & Mersol.¹⁰⁵^pTkachenko *et al.*¹⁰⁶^qKumashiro *et al.*¹²³^rKumashiro *et al.*¹²⁴^sHe *et al.*¹⁰⁷^tWarren.⁹⁰^uLanin *et al.*¹⁰⁸

covalent ceramics, ZrC fractures in an exclusively brittle manner below ~ 1000 K,³ by both transgranular and intergranular means. Both tensile and bend strength increase with temperature as plastic slip increases the resistance to brittle fracture. A maximum precedes a subsequent decrease in strength, due to decreasing yield strength with temperature, and failure occurs by macroscopic plastic deformation.

The effects of porosity, grain size, specimen surface condition, and impurity phases remain unexplored, with sample preparation and microstructural characteristics tending to overshadow the effects of C/Zr ratio on strength. More measurements on well-characterized samples according to standard test methods are necessary.

2.13.5.4 Fracture Toughness

Very few fracture toughness (K_{IC}) measurements are reported for ZrC. Warren⁹⁰ used a spherical steel indenter to produce ring cracks in the surface of $\text{ZrC}_{0.95}$. Using a fracture mechanics-based analysis of the surface energy and geometry of the induced Hertzian stress field under and around the indenter, the critical load to cause fracture, and the crack ring radius, he derived a K_{IC} fracture toughness of

**Figure 23** Indentation hardness of ZrC_x as a function of temperature.

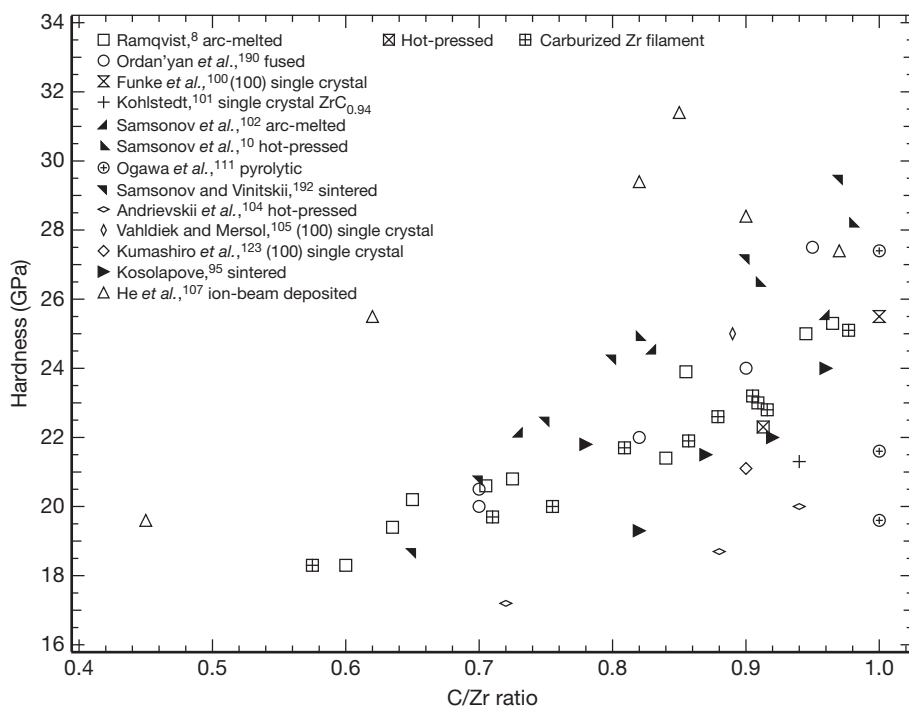


Figure 24 Room-temperature hardness of ZrC_x as a function of C/Zr ratio.

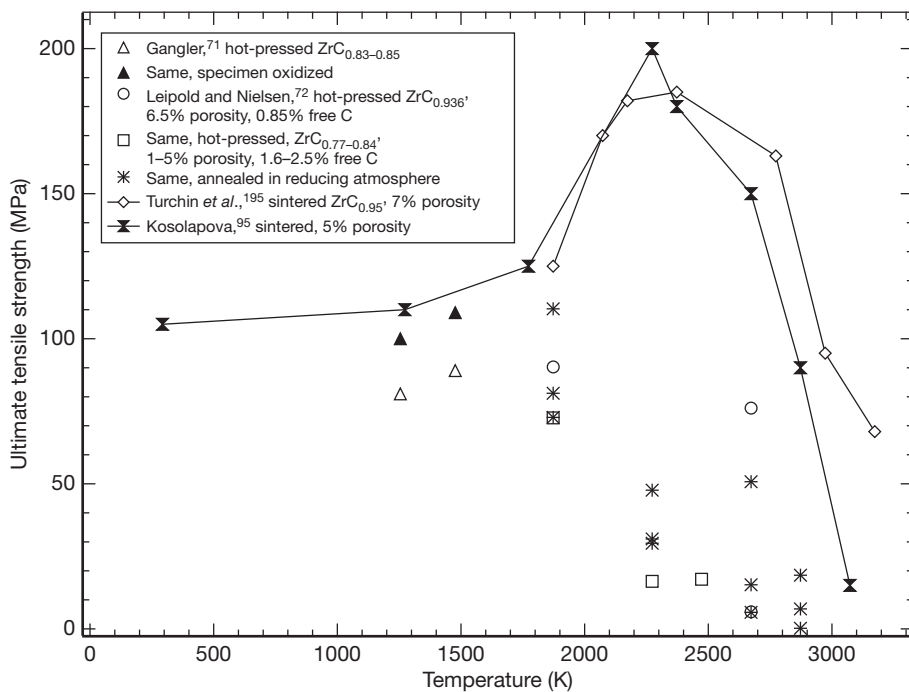


Figure 25 Ultimate tensile strength of ZrC_x as a function of temperature.

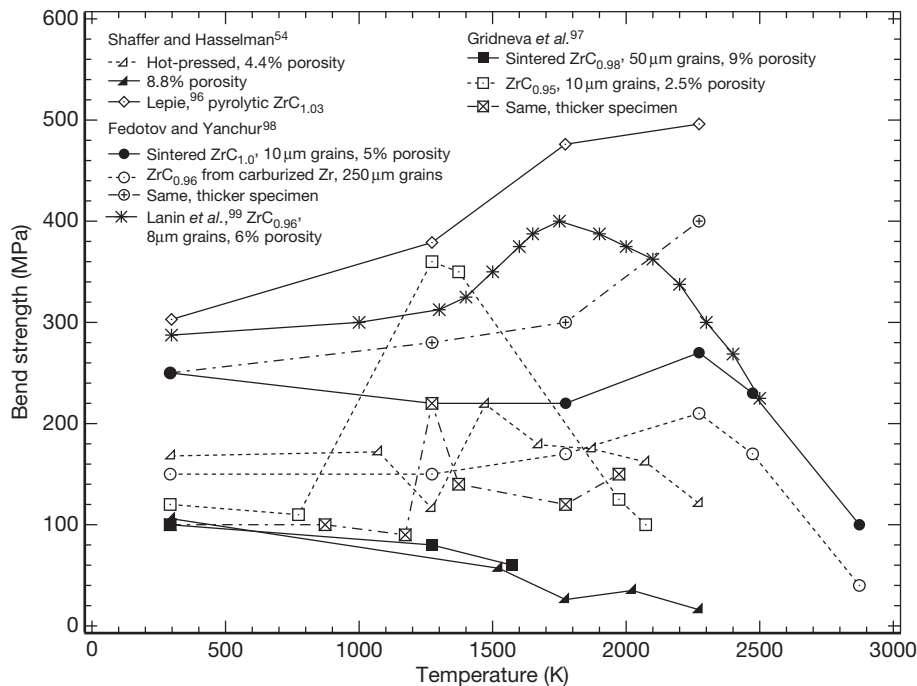


Figure 26 Bend strength of ZrC_x as a function of temperature.

$1.11 \text{ MPa m}^{1/2}$. Lanin *et al.*¹⁰⁸ reported a K_{IC} of $2.8 \text{ MPa m}^{1/2}$ based on cyclic compressive loading of notched $\text{ZrC}_{0.96}$ in air at room temperature. Toughness measurements based on cracking during Vickers indentation of magnetron-sputtered $\text{ZrC}_{0.8-1}$ thin films are also reported in the range of 1.5–2.5 $\text{MPa m}^{1/2}$.¹¹² Further study of the fracture toughness of ZrC must be undertaken, preferably according to standard tests of fracture toughness for ceramics, as the accuracy and consistency of indentation toughness results have been brought into question.¹¹³

2.13.5.5 Plastic Deformation

Though strength and fracture properties are controlled by sample processing, the elastic and plastic deformation behavior inherent to ZrC may be understood in terms of its chemical bonding. Transition metal carbides are known to be brittle at ambient temperatures but ductile at high temperatures.

The metal-like conductivity and the fcc structure of ZrC suggest that deformation along the fcc metal slip systems is possible. In fcc, the $\{111\}\langle 110 \rangle$ system corresponds to the slip of close-packed planes along close-packed directions and requires the lowest stress to form and move a dislocation. The same is assumed for the rocksalt structure.

However, many crystals with the NaCl structure are ionic, and slip along the above system is inhibited due to the energy required to overcome strong Coulombic repulsion when in the half-glide position.³ Instead, ionic rocksalt compounds prefer to slip along $\{110\}$ planes, maintaining attractive Coulombic forces. If ZrC is known to slip along $\{111\}$ planes, the degree of ionic bonding must not be large.

Even if there is no ionic prohibition to slip in ZrC, the directed nature of its covalent bonding is still an impediment to slip. Strong metal–carbon bonds in an octahedral coordination inhibit slip on close-packed $\{111\}$ planes, leading to high shear stresses required for dislocation mobility at low temperatures. The preferred mechanism of deformation is then brittle fracture, which occurs by cleavage on $\{100\}$ planes.^{12,114} Brittle fracture persists at least to 1000 K.³

At elevated temperatures, however, a ductile–brittle transition has been observed. Based on compressive loading of single-crystal $\text{ZrC}_{0.9}$,¹¹⁵ $\text{ZrC}_{0.945}$,¹¹⁶ and arc-melted $\text{ZrC}_{0.94}$,¹¹⁷ plastic yield was reported at 1172, 1353, and 1473 K. Microplasticity was reported at 1273 K, with gross plastic yield above 1773 K, as observed by fractography of tensile specimens.¹¹⁸ Transmission electron microscopy (TEM) of dislocations in $\text{ZrC}_{0.98}$ after elevated temperature compression revealed microplasticity above 1420 K.¹¹⁹

The crystallography of the slip system has been investigated. Lee and Haggerty¹¹⁶ measured the critical resolved shear stress (CRSS) in the compression of single crystal $\text{ZrC}_{0.945}$ samples grown along $\langle 100 \rangle$ and $\langle 111 \rangle$ directions, and one sample whose axis corresponded to the '0.5' orientation for $\{111\}$ $\langle 110 \rangle$ slip, indicating that one of these 12 equivalent slip systems was oriented at 45° to the crystal axis. When loaded uniaxially along the crystal axis, a maximum resolved shear stress (τ) of half of the applied stress (or 0.5σ) would be achieved, according to Schmid's law,

$$\tau = \sigma \cos \phi \cos \lambda \quad [11]$$

where ϕ and λ are, respectively, the angles separating the slip plane normal and the slip direction from the load axis. CRSS as a function of temperature for the various samples are plotted in Figure 27. The results of Williams¹¹⁵ for compression of $\langle 100 \rangle$ oriented single crystal $\text{ZrC}_{0.875}$ are consistent with those of Lee and Haggerty, plotted in the same figure.

The slip planes were identified by slip traces on the samples, while the Burgers vector was confirmed to be $1/2\langle 110 \rangle$ by diffraction contrast of dislocations, a result consistent with the TEM analysis of Britun

*et al.*¹¹⁹ Slip was induced on either $\{100\}$, $\{110\}$, or $\{111\}$ planes, depending on the crystal axis and its slip system of maximum resolved shear stress. For loading along the $\langle 100 \rangle$ direction, the maximum resolved shear stress was for the $\{110\}$ plane; for $\langle 111 \rangle$ loading, slip was along $\{100\}$ planes; and for the '0.5' oriented sample, slip was along $\{111\}$ planes. CRSS for slip along $\{100\}$ was highest, and along $\{110\}$ and $\{111\}$ was approximately equal over the temperature range where they overlapped.

Hannink *et al.*¹²² characterized the anisotropy of room-temperature Knoop hardness on the $\{100\}$ surface of single crystal $\text{ZrC}_{0.94}$, rotating the long axis of the Knoop indenter azimuthally; hardness as a function of rotation angle is plotted in Figure 28. Hardness varied sinusoidally with rotation, with a minimum occurring when the indenter was aligned along $\langle 100 \rangle$ directions, and maximum for indenter alignment with $\langle 110 \rangle$ directions. This indicated that the slip system was $\{110\}\langle 110 \rangle$, normally associated with ionic crystals. The authors also measured Vickers hardness, which exhibited anisotropy in the same sense as the Knoop measurements, but with lower amplitudes, in agreement with the results of Kumashiro *et al.*¹²³

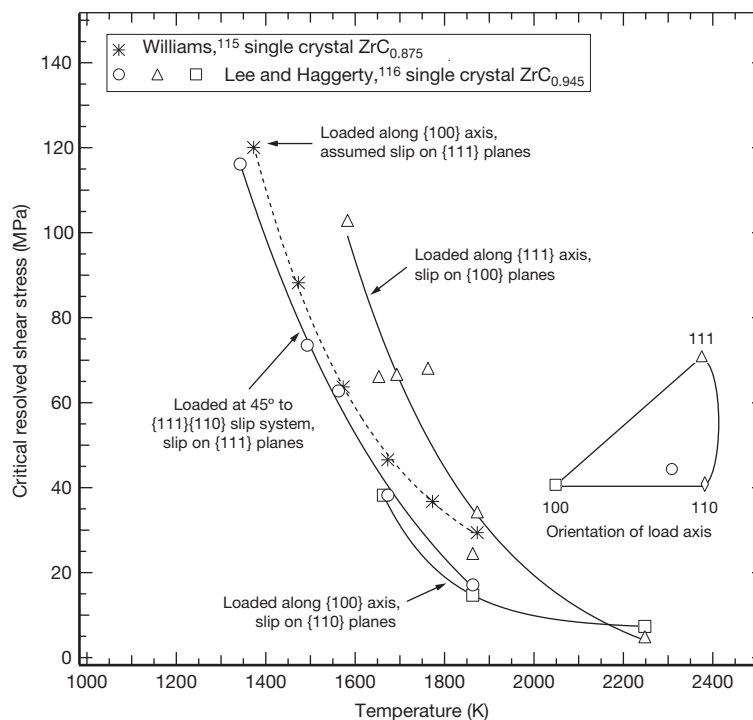


Figure 27 Critical resolved shear stress of single crystal ZrC_x loaded along different crystallographic axes as a function of temperature.

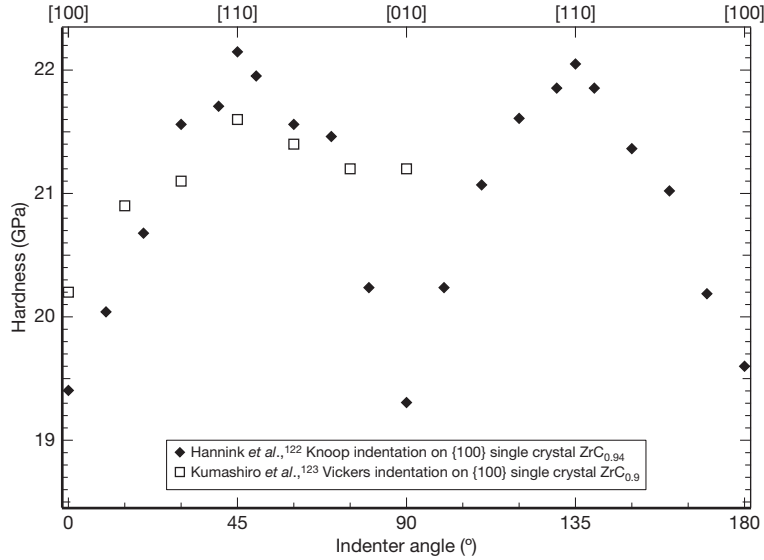


Figure 28 Room-temperature hardness of single crystal ZrC_x as a function of indenter azimuthal angle.

Hannink *et al.*¹²² suggested that the active slip system is dependent on temperature, as they observed for $\text{TiC}_{0.96}$ and $\text{VC}_{0.83}$. At ‘low’ temperatures (room temperature for TiC and ZrC, 87 K for VC), the $\{110\}\langle 110\rangle$ slip system was active, as seen by the hardness anisotropy described earlier. At higher temperatures (883 K for TiC, 623 K for VC), maximum and minimum hardness occurred respectively for indenter alignment with $\langle 100\rangle$ and $\langle 110\rangle$, which is the opposite to that observed for $\{110\}\langle 110\rangle$ slip. ‘High’ temperature slip in TiC and VC was on the $\{111\}\langle 110\rangle$ or $\{100\}\langle 110\rangle$ system. Kohlstedt¹⁰¹ proposed that covalent, directional bonding dominates at low temperatures, prohibiting slip on $\{111\}$ planes and resulting in high hardness, while at high temperatures, the degree of covalent bonding is decreased as the $\{111\}\langle 110\rangle$ slip characteristic of fcc metals is favored, resulting in the observed hardness drop with temperature.

Capacity for plastic deformation has also been observed to vary with the C/Zr ratio. A monotonic decrease in hardness with decreasing C/Zr ratio is seen in Figure 23. Although not determined for ZrC, CRSS of TiC_x was observed to decrease with decreasing C/Ti ratio.¹¹⁵ The author explains this intuitively in terms of fewer C–Ti bonds that must be broken during dislocation motion. Hollox¹² attributed these results to a decrease in the contribution made by carbon atoms to cohesion in TiC as the C/Ti ratio is reduced, further citing the band structure calculations of Lye and Logothetis¹¹ which

indicated that carbon donates electrons to and strengthens metal–metal bonds. Hollox also inferred that the DBTT might decrease as the carbon-to-metal ratio is decreased, but this has not been demonstrated conclusively.

2.13.5.6 Creep and Stress Relaxation

Two relevant thermomechanical processes in high-temperature structural applications are creep and stress relaxation. Steady-state creep deformation, or time-dependent strain under an elevated-temperature stress, has been observed for ZrC. In general, creep rate is dependent on applied stress (σ) and temperature (T) according to

$$\dot{\epsilon} = A\sigma^n \exp\left(\frac{-Q}{RT}\right) \quad [12]$$

where $\dot{\epsilon}$ is strain rate, A is a constant dependent on the material and creep mechanism, n is an exponent dependent on the creep mechanism, R is the gas constant, and Q is the activation energy of the creep mechanism. Activation energies for creep under various conditions are summarized in Table 4. Zubarev and Kuraev¹³⁰ proposed a creep mechanism map of stress normalized to shear modulus versus homologous temperature, based on compressive creep in He atmosphere of $\text{ZrC}_{1.0}$ with 14 μm grain size. The authors distinguished between different temperature–stress regimes governed by creep processes having low or high activation energies. Indeed,

Table 4 Activation energy for creep of ZrC

Temperature range (K)	Activation energy (kJ mol^{-1})	C/Zr ratio	Grain size (μm)	Ref.
1173–1373	307 308 331	0.9	sc ^d	a
1473–2073	501 \pm 19	0.94	250	b
1673–2273	460	0.945	sc ^d	c
2073–2423	314	0.76–0.84	5	d
2473–2873	837			
2450–2520	485 \pm 75	0.95	3–5	e
2400–3030	510 \pm 31	0.73	45	f
	582 \pm 33	0.75	70	
	657 \pm 40	0.84	20	
	728 \pm 44	0.895	6–65	
	678 \pm 42	0.9	16	
	703 \pm 42	0.96	8.5–17	
	761 \pm 46	0.984	30	
2423–2903	531	0.94	4.5	g
	523			
	515			
2473–3023	711 \pm 42	0.99	5–20	h

^aKumashiro *et al.*,¹²⁴ Vickers indentation in {100} surface, for (100)<001>, (110)<001>, and (111)<110> slip systems, respectively.

^bDarolia and Archbold,¹¹⁷ compression in vacuum.

^cLee and Haggerty,¹¹⁶ compression in vacuum along <111> crystal axis.

^dLeipold and Nielsen,⁷² 1–5% porosity, 1.6–2.5 wt% free carbon.

^eMiloserdin *et al.*,¹²⁵ tension, 3.4–9.8 MPa, 7% porosity.

^fSpivak *et al.*,¹²⁶ creep in He atmosphere, 4–6% porosity.

^gZubarev and Dement'ev,¹²⁷ in tension, bending, and compression, respectively, 0.96–19.6 MPa, inert atmosphere, 15–17% porosity.

^hZubarev and Shmelev,^{128,129} in tension, 0.96–73.5 MPa, Ar atmosphere, 3–5% porosity, 0.38–1.1 wt% free carbon.

ⁱSingle crystal.

the two activation energies provided by Leipold and Nielsen⁷² are attributed to a change in creep mechanism above 2423 K.

At low or intermediate temperatures (below about 1623–2473 K for ZrC, or $<0.5T_m$) and high stress relative to shear modulus, creep has a low activation energy and is controlled by the movement of dislocations. Zubarev and Kuraev¹³⁰ proposed more specific mechanisms for various regions of this overall regime, such as dislocation multiplication, cross-slip, dislocation climb, work-hardening, and gross plastic yield. The TEM analysis of Britun *et al.*¹¹⁹ supports these hypotheses, revealing intragranular dislocations and slip bands after compression of $\text{ZrC}_{0.98}$ between 1420 and 2100 K.

At high temperatures (generally >2073 K for ZrC) and intermediate or low stress, creep has a higher activation energy and is controlled by diffusion. The activation energy for creep in this regime is close to

that of bulk self-diffusion in ZrC, which is ~ 500 kJ mol^{-1} for C and ~ 700 kJ mol^{-1} for Zr, as detailed in Table 4. The diffusion rate of the lower-mobility species should be rate-limiting, so creep in this regime is usually attributed to self-diffusion of Zr. However, diffusion along grain boundaries may reduce the activation energy for creep relative to that of bulk diffusion. Diffusional mass transfer (Nabarro–Herring creep) and grain boundary sliding are suggested mechanisms,¹³⁰ with the latter confirmed by scanning electron microscopy (SEM) ceramography and not applicable to single crystals.¹³¹ Britun *et al.*¹¹⁹ also confirmed grain boundary shear and rotation by TEM ceramography of $\text{ZrC}_{0.98}$ compressed at 2100–2500 K.

The dependence of creep mechanism on grain size has been studied by Zubarev *et al.*¹³¹ Analysis of creep mechanisms among polycrystalline (14–1000 μm grain size) and single-crystal $\text{ZrC}_{1.0}$ revealed that with increasing grain size and with the single crystal, dislocation creep mechanisms occurred at lower threshold stresses, and the Nabarro–Herring and grain boundary sliding processes diminished in importance or disappeared. Free carbon has been reported to facilitate grain boundary creep.¹³¹

Creep has been studied as a function of C/Zr ratio. Creep in compression of $\text{ZrC}_{0.89-0.96}$ at 2773–2973 K¹³² showed a monotonically decreasing creep rate with decreasing C/Zr ratio. In the same work, a v-shaped trend of creep rate with C/Zr ratio was found for creep in bending of $\text{NbC}_{0.82-0.98}$ at 2273–2473 K, decreasing to a minimum creep rate at a composition of approximately $\text{NbC}_{0.85}$. They speculated that such a trend may exist for ZrC_x , but that the associated minimum existed below the compositional range they investigated. Based on creep of $\text{ZrC}_{0.75-0.98}$ between 2400 and 3030 K, Spivak *et al.*¹²⁶ found activation energy increased with increasing C/Zr ratio. This would be consistent with expectations of enhanced diffusion with an increase in C vacancies. However, their earlier work⁸³ reported activation energy for self-diffusion of Zr in ZrC as being composition-independent between $\text{ZrC}_{0.84-0.97}$, and that of C decreasing with increasing C/Zr ratio. Some hypotheses have been put forth (see Section 2.13.4.4), but further study of Zr diffusion in ZrC_x is required to explain this conclusively.

Stress relaxation, or an evolution in stress with time for a component at fixed strain, has been investigated to a lesser degree than creep. Repeated four-point bend loading of $\text{ZrC}_{0.95-1}$ (6–35 μm grains) at

1873–2273 K, with unloading at intervals, resulted in increased resistance to relaxation, via work hardening, upon subsequent loading cycles.^{91,133} The authors concluded that under these conditions slip occurs by diffusion along grain boundaries. At higher temperatures, up to 2473 K, no beneficial effects were imparted by repeated loading, and the authors concluded that no work hardening occurred. They judged stress relaxation and creep in ZrC to be controlled by different mechanisms.

2.13.5.7 Thermal Shock Resistance

Thermal shock has been evaluated qualitatively for ZrC by various means. Susceptibility to failure by thermal shock is lowered in materials with high tensile strength, low elastic modulus, low thermal expansion coefficient, and high thermal conductivity. Gangler's⁷¹ test involved cyclic heating and quenching of hot-pressed ZrC_{0.83–0.85} between a 1255 K furnace and 300 K air stream. ZrC withstood 22 cycles, though excessive oxidation was noted. Shaffer and Hasselman⁵⁴ subjected hot-pressed ZrC spheres to thermal shock on heating: room-temperature specimens were drawn rapidly into the hot zone of a tube furnace at a temperature sufficiently high to cause fracture. For ZrC this was determined to be 1725 K, and free carbon was found to improve thermal shock resistance. Lepie⁹⁶ subjected a pyrolytic ZrC–C alloy to firing in the nozzle–throat section of a solid-fuel rocket; no ill effects from the sudden exposure to the 3894 K exhaust flame were reported, and firing for 30 s at 5.5 MPa caused little erosion.

2.13.6 Environmental Resistance

2.13.6.1 Oxidation

Despite excellent refractory properties, ZrC suffers from poor oxidation resistance, with oxidation initiating in the range of 500–900 K (Table 5). The kinetics and mechanism of ZrC oxidation have been assessed in several studies, between room temperature and 2200 K, at oxygen partial pressures (P_{O_2}) between 8×10^{-4} and 101 kPa (0.79×10^{-6} and 1 atm), with the oxidation products a function of both parameters.

2.13.6.1.1 Oxidation products

Oxidation resistance is imparted by the formation of a dense, adherent oxide scale which effectively restricts oxygen access to the carbide. Since the oxides of carbon are gaseous, protection is only afforded

Table 5 Onset temperature of ZrC oxidation

Oxidation temperature (K)	P_{O_2} (kPa)	Ref.
773	0.007–101	^a
573	0.66–39.5	^b
653–673, Zr	1–40	^c
773–863, C		
575	5–50	^d
773	21	^e
973	21	^f
763, Zr	21	^g
973, C		
723–823	21	^h
658	21	ⁱ
473–573	21	^j

^aBartlett *et al.*¹³⁴

^bShimada & Ishii,¹³⁵ temperature at which sintered ZrC weight gain initiates.

^cShimada,¹³⁶ DTA peaks indicating onset of oxidation of Zr and C in single crystal ZrC, respectively.

^dRama Rao and Venugopal.¹³⁷

^eOpeka *et al.*¹³⁸

^fVoitovich and Pugach.¹³⁹

^gShevchenko *et al.*,¹⁴⁰ DTA peaks indicating onset of oxidation of Zr and C, respectively.

^hTamura *et al.*¹⁴¹

ⁱZhilyaev *et al.*,¹⁴² ZrC_xO_y ($x = 0.7–0.85$, $y = 0.15–0.25$).

^jZainulin *et al.*,¹⁴³ ZrC_xO_y ($x = 0.43–0.97$, $y = 0.09–0.36$).

by the zirconium oxide. However, low temperatures (<973 K) and P_{O_2} insufficient to oxidize C result in preferential oxidation of Zr and precipitation of amorphous carbon at the oxide–carbide interface, as detected by TEM,¹⁴⁴ Raman spectroscopy,^{145,146} and Auger electron spectroscopy.¹⁴⁷ Nonisothermal oxidation of ZrC by DTA showed two peaks, indicating the onset of appreciable Zr and C oxidation, respectively: the peak associated with Zr oxidation appeared between 653 and 763 K, while the C peak appeared at a higher temperature of 773–973 K.^{136,140}

Alternatively, the liberated C may be incorporated into the ZrO₂ lattice, stabilizing the cubic fluorite structure of ZrO₂, whereas the monoclinic structure is normally stable at room temperature. Cubic ZrO₂ nuclei absent in X-ray diffraction (XRD) were identified by electron diffraction and TEM lattice fringes by Shimada and Ishii¹³⁵ at 653–743 K. Cubic ZrO₂, with or without trace monoclinic ZrO₂, formed in the 723–1013 K range.^{134,135,143–146,148} Shimada and Ishii¹³⁵ and Tamura *et al.*¹⁴¹ also reported the metastable tetragonal ZrO₂ phase, based on XRD analysis. While XRD easily distinguishes monoclinic from tetragonal or cubic ZrO₂, the latter two are difficult to tell apart, and additional techniques such as Raman spectroscopy or electron diffraction are required for a conclusive identification.

As the oxidation temperature increases, appreciable oxidation of the precipitated or combined carbon occurs in addition to oxidation of Zr. Concurrently, the relative proportions of cubic and monoclinic ZrO_2 in the scale shift in favor of monoclinic. As carbon is more readily oxidized at higher temperatures, less carbon is available to stabilize cubic ZrO_2 and the more stable monoclinic structure forms instead. These transitions from carbon precipitation to oxidation and from cubic to monoclinic ZrO_2 are reported at temperatures higher than about 1073 K, with carbon-free, fully monoclinic ZrO_2 reported at 1473–1773 K.^{137,139–141,143,144,146,147}

The transformation may be manifested by a carbon concentration gradient with depth, either by a gradual decrease in carbon from the oxide–carbide interface to the free surface, or by the formation of distinct layers in the scale. This is consistent with observations of cubic ZrO_2 concentrated at the oxide–carbide interface and monoclinic ZrO_2 concentrated at the free surface.¹³⁹ Wavelength dispersive spectroscopy by Shimada *et al.*¹⁴⁶ detected 7–10 at.% C combined in an outer ZrO_2 scale layer, following oxidation of single-crystal $\text{ZrC}_{0.97}$ at 773–873 K, with an inner layer characterized by a steep decrease in C content with depth.

Some authors also report the formation of a ZrC_xO_y oxycarbide phase isostructural with ZrC. The ZrC_xO_y phase is reported to exist between $\text{ZrC}_{0.98}$ on the oxygen-poor side and $\text{ZrC}_{0.73}\text{O}_{0.14}$ on the oxygen-rich side.¹⁴⁹ Formation of the oxycarbide may occur as an intermediate layer between the ZrO_2 scale and carbide, by the dissolution of oxygen in ZrC,^{145,150} or by a reaction between the ZrO_2 scale and CO or CO_2 gas diffusing outward from the oxide–carbide interface.¹⁴² Limited thermodynamic data for the Zr–O–C system (see Quensanga and Dode¹⁴⁹) has hindered more thorough assessment of these hypotheses. At high temperatures in air atmosphere, formation of ZrN or $\text{ZrC}_x\text{O}_y\text{N}_z$ compounds may occur,¹³⁹ but thermodynamic data for this quaternary system is similarly limited (see Constant *et al.*¹⁵¹).

2.13.6.1.2 Oxidation kinetics

The kinetics of oxidation of ZrC is related to the nature of the oxidation products and microstructure of the oxide scale formed. In general, oxidation accompanied by the formation of a protective scale is associated with low temperatures. The oxide scale is reported to be protective and its growth to be parabolic with time, that is, controlled by diffusion of

oxygen through the cubic ZrO_2 scale.^{134,137,140,143,152} The cubic ZrO_2 structure is hypothesized to facilitate adherence of the scale to the cubic ZrC, as evidenced by high-resolution TEM of oxidized single-crystal ZrC with adherent cubic ZrO_2 crystallites face having parallel lattice fringes.¹⁴⁴

At high temperatures (and high P_{O_2} usually), oxidation is reported to be linear with time, controlled by the reaction at the oxide–carbide interface.^{134,147,152} This process is facilitated by porosity in the oxide, rupture due to CO/ CO_2 gas pressure, or cracking/delamination due to thermal expansion mismatch between the oxide and carbide,^{136,140,144,153} and interruptions in the scale allow oxygen easy access to the ZrC surface. Preferential attack of ZrC along the grain boundaries by ZrO_2 , leading to intergranular embrittlement, strengthens the case against protective oxidation of ZrC.^{154,155}

In the case of a two-layer scale on single-crystal $\text{ZrC}_{0.97}$, the inner carbon-rich scale grew parabolically, leveling out at a critical thickness (2–4 μm), above which the outer carbon-poor scale grew linearly with time.^{144,146} The inner scale was crack-free, dense, and adherent, while the outer scale was characterized by cracks and porosity. The authors proposed that scale cracking continually exposed fresh surfaces to oxygen, leading to an overall linear oxidation rate.

Oxidation behavior also depends on the pressures of volatile ZrO_x species, implicated in active oxidation. According to thermodynamic calculations by Maitre and Lefort¹⁵⁶ and Minato and Fukuda¹⁵⁷ of equilibrium pressures in the Zr–C–O and Zr–C–O–He systems, the maximum pressure of $\text{ZrO}_{(\text{g})}$ at 1600 K was predicted to be less than 10^{-9} Pa, indicating negligible active oxidation.

2.13.6.1.3 Oxidation by water vapor

One study of oxidation by water vapor is reported.¹³⁴ At 723–843 K, with $P_{\text{O}_2} > 0.5$ kPa (i.e., sufficient for surface saturation with adsorbed oxygen) and $P_{\text{H}_2\text{O}}$ 21–42 kPa, water vapor did not appreciably oxidize ZrC but did accelerate the oxidation rate in the presence of $\text{O}_{2(\text{g})}$.

2.13.6.1.4 Summary and outlook

Clearly, oxidation resistance of monolithic ZrC is compromised at temperatures above about 700 K, and its use at higher temperatures is restricted to inert or reducing atmospheres. To enable the prediction of structural component performance under accidental oxidizing conditions, it is important to

understand the effects of oxidation on mechanical properties. For instance, strength and toughness degradation must be characterized for ZrC partially oxidized to ZrO_2 and ZrC_xO_y , and failure mechanisms must be identified, such as grain boundary attack or scale rupture. Oxidation to ZrO_2 will also lower thermal conductivity, which is relevant to applications where the high thermal conductivity of ZrC is exploited, but heat transport in ZrC_xO_y must also be established.

2.13.6.2 Performance Under Irradiation

ZrC is a material of interest for next-generation nuclear fuel applications – for example, as a replacement or supplement for the SiC diffusion barrier coating in Tri-structural isotropic coated fuel particle (TRISO) coated fuel particles in high-temperature gas-cooled reactors. There are two main incentives to develop ZrC for this application. First, higher fuel operating temperatures, and thus higher efficiency of next-generation reactors, would be enabled by the higher degradation temperatures ZrC offers over SiC. There is evidence that fission product diffusion will be slower in ZrC and that ZrC is more resistant to fission product attack.¹⁵⁸ Second, its sensitivity to oxidation recommends ZrC as an effective oxygen getter, inhibiting the so-called ‘amoeba effect’ insidious in SiC-based TRISO, which involves a thermal gradient-induced diffusion of carbon and effective migration of UO_2 fuel out of its protective coating layers, in part, due to an excessive oxygen potential (see, for instance, Bullock and Kaae).¹⁵⁹

2.13.6.2.1 Thermal neutron capture cross-section

Implementation of zirconium-based components in a nuclear reactor core, in fuel cladding or advanced composite fuel coatings and matrix, is enabled by its low thermal neutron capture cross-section. Low-activation structural materials are desired, and particularly for ZrC in fuels, diversion of neutrons from fission reactions is to be avoided. The isotopic average cross-section for Zr for 0.0253 eV thermal neutrons (at room temperature) is 0.19 barn ($1.9 \times 10^{-29} \text{ m}^2$), and for C is 0.0035 barn ($3.5 \times 10^{-31} \text{ m}^2$).¹⁶⁰ Owing to similar chemistry, Zr naturally occurs together with up to 2 wt% Hf unless specially purified for nuclear reactor applications (<100 ppm Hf). The isotopic average cross-section for Hf is 106 barn ($1.06 \times 10^{-26} \text{ m}^2$), making it a very undesirable impurity in Zr for reactor applications.

2.13.6.2.2 Durability and dimensional stability under neutron irradiation

Keilholtz *et al.*¹⁶¹ irradiated hot-pressed, slip-cast, and explosion-pressed ZrC at 403–628 K (temperatures corrected by Watson and Keilholtz¹⁶²) with a fast neutron (>1 MeV) fluence of $(0.4\text{--}5.4) \times 10^{21} \text{ cm}^{-2}$, including 63–142 thermal cycles from room temperature to the irradiation temperature during the experiment, in the Oak Ridge National Laboratory’s Engineering Test Reactor. Damage due to thermal cycling alone was ruled out by out-of-pile tests. Severe fracturing of the hot-pressed and slip-cast samples were noted for fluences above $(2.5\text{--}3) \times 10^{21} \text{ cm}^{-2}$, with the explosion-pressed (containing Co or Ni binder) samples showing minor to severe damage above $1.1 \times 10^{21} \text{ cm}^{-2}$. Of the 2–3% radiation-induced volumetric swelling measured for all sample forms, 1% was accounted for by lattice parameter expansion, with the authors proposing point defect clusters and gas bubbles as causing the remainder. Helium gas is produced in carbides through fast-neutron reactions with carbon, and the authors considered the possibility of hydrogen produced by thermal neutron reactions with nitrogen impurities. Swelling increased with fluence up to $2 \times 10^{21} \text{ cm}^{-2}$, but further fluence resulted in the same or lesser degree of expansion.

Keilholtz *et al.*¹⁶³ expanded this study to irradiation at 1273–1373 K at a fluence of $2.4 \times 10^{21} \text{ cm}^{-2}$. Swelling was lower at the higher temperatures, with <1% volume expansion measured. Watson and Keilholtz¹⁶² irradiated the same materials at low temperature and fluence (338–373 K, $0.21\text{--}0.72 \times 10^{21} \text{ cm}^{-2}$), with 1.7–2.5% volume expansion reported. The irradiated samples were annealed at 973–1373 K until dimensional change ceased. Volume contracted with increasing temperature up to about 1173 K, with the degree of contraction saturating at higher temperature. Some evidence for reexpansion of slip-cast ZrC at higher temperatures was reported, but there were too few data points to determine this conclusively. The authors proposed that expansion/contraction behavior as a function of fluence was caused by atomic displacements and point defect clusters produced by initial fast neutron cascades, with subsequent cascades at higher fluence returning some displaced atoms to lattice sites. Contraction was also attributed to the annealing of defects during postirradiation heat treatment. As temperature increases, easily annealed single point defects are consumed, leaving more difficult-to-anneal defect clusters, and further contraction is limited.

These observations are consistent with the findings of Andrievskii *et al.*,¹⁶⁴ who irradiated sintered $\text{ZrC}_{0.98}$ at either 423 or 1373 K with a fast neutron fluence of $1.5 \times 10^{20} \text{ cm}^{-2}$. Lattice parameter expanded with irradiation but to a lesser degree at the higher temperature: 0.47% at 423 K versus 0.13% at 1373 K (volume increase of 1.4% vs. 0.38%). Correspondingly, density decreased after irradiation; however, the decrease was more, not less, pronounced at a higher temperature (−1.7% at 423 K vs. −2% at 1373 K). The authors propose that despite a lesser degree of lattice parameter swelling at higher temperatures, intergranular porosity increased and accelerated swelling.

Koval'chenko and Rogovoi¹⁶⁵ irradiated $\text{ZrC}_{0.98}$ at 323 K with thermal neutrons to a fluence of 1×10^{19} – $1.5 \times 10^{20} \text{ cm}^{-2}$, observing a lattice parameter expansion of 0.07–0.71% (volume expansion 0.21–2.15%) that increased with fluence. No change in the porosity or grain size of the samples was detected. Andrievskii *et al.*¹⁶⁴ attributed their lower lattice swelling to higher sample purity, as the samples of Koval'chenko and Rogovoi¹⁶⁵ had low initial lattice parameter and were likely high in O and N impurities.

Andrievskii *et al.*¹⁶⁶ considered swelling as a function of C/Zr ratio. They irradiated $\text{ZrC}_{0.7-0.94}$ at 413 K in a fast neutron of fluence of $1 \times 10^{19} \text{ cm}^{-2}$. Lattice parameter increased after irradiation for all samples, but superimposed on the expected trend of increasing lattice parameter with increasing C/Zr ratio was a more pronounced increase for samples closer to stoichiometry. Lattice parameter of $\text{ZrC}_{0.73}$ expanded by 0.04% (0.12% volume expansion), while $\text{ZrC}_{0.94}$ expanded by 0.33% (0.99% volume expansion). The authors proposed that in near-stoichiometric compositions, fast neutron-induced atomic displacements may force C atoms into tetrahedral interstitial sites, while in more nonstoichiometric compositions, C atoms may be displaced to already vacant octahedral sites. In this sense, the authors judged irradiation-induced nonstoichiometry in more carbon-deficient ZrC_x to be qualitatively similar to unirradiated nonstoichiometric ZrC_x .

ZrC has also been subjected to high-temperature heat treatment and irradiation as a 20–50 μm thick coating layer in testing of TRISO fuel having a central actinide fuel kernel coated in a porous carbon buffer layer, a dense pyrocarbon layer, a ZrC layer, and an outer pyrocarbon layer. Particles have been irradiated loose or embedded in the matrix of a fuel compact. The performance of ZrC in this

configuration is inevitably tied to that of the system as a whole, as the neighboring coatings and fuel matrix not only add structural support but also introduce the possibility of reactions among ZrC, fission products, gases, graphite, and actinides.

Reynolds *et al.*¹⁶⁷ fabricated ZrC coatings either in the standard TRISO configuration or directly on top of fissile $^{235}\text{U}\text{C}_2$ or fertile (^{232}Th , ^{233}U) O_2 kernels, the latter designed as a test of ZrC corrosion. These were irradiated at 1473 K with a fast neutron ($>0.18 \text{ MeV}$) fluence of $5 \times 10^{21} \text{ cm}^{-2}$, to a burnup of 70% fissions per initial actinide metal atom (%FIMA) for fissile and 8% FIMA for fertile particles, in the Commissariat à l'Energie Atomique's Siloe Test Reactor. Postirradiation examination revealed that the only ZrC damage was radial cracking in almost all the particles with ZrC directly atop kernels; as this configuration lacked buffer volume to accommodate fission gases, such failures were expected. ZrC in the standard TRISO configuration was crack-free. No diffusion or reactions between actinides/fission products and ZrC was evident in any configuration.

Ogawa *et al.*¹⁶⁸ fabricated TRISO particles with a 20–30 μm thick ZrC layer and UO_2 kernel and compacted these in a graphite–resin matrix at 2073 K. Irradiation by fast neutrons ($>0.18 \text{ MeV}$) under various conditions (1173–1873 K, fluence $(1\text{--}2.2) \times 10^{21} \text{ cm}^{-2}$, burnup of 1.5–4% FIMA, during 81–156 effective full-power days) was carried out in the Japan Materials Test Reactor at the Japan Atomic Energy Research Institute. Following deconsolidation of the fuel compacts to recover loose particles, ceramography showed no ZrC degradation in particles irradiated at the highest burnup, fluence, and temperature for over 135 effective full-power days. A zero particle failure rate was assessed by in-reactor monitoring of fission gas ^{85}Kr release rate during 80 effective days of irradiation at 1173 K, which was an order of magnitude smaller than that expected for a single particle rupture out of 7000 particles in this test.

Minato *et al.*¹⁶⁹ irradiated similarly prepared compacts between 1673–1923 K with a fast neutron ($>0.18 \text{ MeV}$) fluence of $1.2 \times 10^{21} \text{ cm}^{-2}$ to 4.5% FIMA burnup during 100 effective full-power days, finding a through-coating failure rate of 0.01%, that is, failure of less than one out of 2400 particles irradiated.

Some of the particles irradiated by Ogawa *et al.*¹⁶⁸ were subsequently heat treated at 1173–2273 K. Particles originally irradiated at 1173 K to a fluence of $1.2 \times 10^{21} \text{ cm}^{-2}$ and burnup of 1.5% FIMA during

80 effective days were annealed in flowing He by Minato *et al.*¹⁷⁰ at 1873 K for a total of 4500 h and by Minato *et al.*^{120,171} at 2073 K for 3000 h and at 2273 K for 100 h. *In situ* ⁸⁵Kr release monitoring showed none of the 100 particles annealed during each test ruptured. Ceramography and X-ray micro-radiography of particles from each test showed that at 1873 K, there was no thermal degradation or corrosion of ZrC coatings. At 2073 K, the ZrC coating was intact, but there was some surface roughness attributed to thermal degradation and evidence of attack along the grain boundaries. At 2273 K, all but 7 of the 100 particles showed some failed or damaged coating layers, including the ZrC layer, and evidence of reaction or interdiffusion between ZrC and U.

Interpreting the results via a thermodynamic analysis of the Zr–C–U–O system, the authors attribute deterioration of ZrC at these temperatures, at least in part, to mechanical failure of the inner pyrocarbon layer combined with oxidation of carbon by the oxygen released during the transmutation of U in UO₂. Subsequent exposure of ZrC to CO_(g) oxidizes ZrC to ZrO₂ and C and reduces the ZrC coating integrity.

Durability of ZrC is more likely to be limited by irradiation of the system contained within rather than by high-temperature degradation of ZrC alone. Ogawa and Ikawa¹⁷² subjected unirradiated TRISO particles having either UO₂ or (Th,U)O₂ kernels to annealing in He atmosphere for 1 h at 2073 K (as during fuel compact fabrication) followed by 1 h at 2173–2823 K. ZrC coatings on all (Th,U)O₂ particles were intact after 1 h at 2823 K, but durability of UO₂ particles was guaranteed only to 2373 K, with swelling noted at 2723 K and U migration out of the ZrC coating at 2773 K. ZrC grain growth and plastic deformation occurred, especially above 2723 K.

2.13.6.2.3 Microstructural changes under heavy ion or proton irradiation

Heavy ion irradiation by Kr has been used to simulate some aspects of fission neutron irradiation, such as high damage rate (up to 100 dpa). Gan *et al.*¹⁷³ irradiated TEM foils of commercial hot-pressed ZrC_{0.99} (the authors report a C/Zr ratio of 1.01, but the composition was corrected to reflect the impurity content of 1.9 wt% Hf, 0.19 wt% Ti, 0.21 wt% O, and 0.61 wt% N, considering that the metals and nonmetals substitute for Zr and C on their respective sublattices). Irradiation was conducted at 298 or 1073 K to >1 MeV Kr ions to a fluence of

$2.5 \times 10^{15} - 1.75 \times 10^{16} \text{ cm}^{-2}$ (10–70 dpa), with *in situ* TEM of microstructural evolution during irradiation. Lattice parameter swelled by 0.6–0.7% (~2% volume increase) at 10 dpa (298 and 1073 K), 0.9% (~3% volume increase) at 298 K and 30 dpa, and 7% (21% volume expansion) at 1073 K and 70 dpa. Simultaneously, precipitation of a fcc phase with 8% larger lattice parameter (5.09 Å) than the matrix (4.71 Å) was detected by ring patterns superimposed on the single-crystal ZrC electron diffraction pattern. Precipitate coarsening with temperature and fluence was observed. Energy-dispersive X-ray spectroscopy (EDX) detected no change in stoichiometry during irradiation. The authors linked the precipitate phase and the 7% lattice parameter increase at high temperature and fluence, but could not explain adequately its origin, hypothesizing that the expansion was related to Kr implantation. Cubic ZrO₂ formation is also plausible ($a \sim 5.1 \text{ Å}$). They acknowledged that the large ratio of surface area to volume in a TEM foil may permit larger lattice expansion than is possible in the bulk. Other microstructural features noted were grain boundary cracking at high fluence, defect clusters at low temperatures and fluence, and dislocation segments at high temperatures. No irradiation-induced voids or amorphization were detected.

Because of very small irradiated volume (depth <1 μm) produced by Kr ion irradiation, the authors later performed proton irradiation, asserting that protons provide a damage rate similar to the fast reactor core, with a more significant irradiated volume (depth ~30 μm), though the achievable dose is limited (~10 dpa). Gan *et al.*¹⁷⁴ subjected the same commercial hot-pressed ZrC_{0.99} to irradiation at 1073 K by 2.6 MeV protons to a fluence of $2.75 \times 10^{19} \text{ cm}^{-2}$ (1.8 dpa), subsequently preparing TEM foils. Lattice parameter change was assessed by higher order Laue zone (HOLZ) patterns in convergent beam electron diffraction, but no change within the uncertainty limit of 0.2% was detected. In contrast, when the same material was irradiated by Yang *et al.*¹⁷⁵ at 1073 K in a 2.6 MeV proton fluence of 1×10^{19} or $2.3 \times 10^{19} \text{ cm}^{-2}$ (0.7 or 1.5 dpa), XRD determined a lattice parameter expansion of 0.09% (0.27% volume expansion) for 0.7 dpa and 0.11% (0.33% volume expansion) for 1.5 dpa. Gan *et al.*¹⁷⁴ detected faulted dislocation loops on {111} planes, characteristic of irradiation of fcc metals, which were not seen for Kr irradiation. No ring pattern or precipitation was detected, as in Kr irradiation.

Gosset *et al.*^{176,177} irradiated commercial hot-pressed ZrC_{0.95} (containing <0.03 wt% O) and

sol-gel synthesized $\text{ZrC}_{0.85}\text{O}_{0.15}$ to irradiation at 298 K by 4 MeV Au ions to a fluence of 1×10^{12} – $5 \times 10^{15} \text{ cm}^{-2}$. In the carbide, XRD-determined lattice parameter expanded by 0.03–2% (0.09–6% volume expansion), increasing with fluence but saturating at about 10^{14} cm^{-2} , while the oxycarbide lattice parameter expanded by 0.05% (0.15% volume expansion), independent of fluence. In both, fine precipitates formed, identified by electron diffraction as tetragonal ZrO_2 ($a \sim 3.61 \text{ \AA}$, $c \sim 5.19 \text{ \AA}$) and identified by tilting as adherent to the sample surface. The authors concluded that high oxygen content in ZrC did not modify the nature of the ion irradiation-induced defects. Faulted dislocation loops were identified in both. No amorphization was detected by XRD.

2.13.6.2.4 Irradiation effects on electrical, thermal, and mechanical properties

The measurement of other properties of irradiated ZrC is limited and often contradictory. Some evidence for an increase in mechanical strength with irradiation is available. Andrievskii *et al.*¹⁶⁴ irradiated sintered $\text{ZrC}_{0.98}$ at 423 and 1373 K with a fast neutron fluence of $1.5 \times 10^{20} \text{ cm}^{-2}$, and found more substantial strengthening at low-temperature irradiation than at high temperature (bend strength increased by 28% vs. 4%, microhardness by 12% vs. 7.3%, and Young's modulus by 1.2% vs. no increase). Yang *et al.*¹⁷⁵ irradiated hot-pressed commercial $\text{ZrC}_{0.99}$ at 1073 K with 2.6 MeV protons to a fluence of 1×10^{19} or $2.3 \times 10^{19} \text{ cm}^{-2}$ (0.7 or 1.5 dpa), and found Vickers hardness increased after irradiation, with a slightly more pronounced increase at higher fluence (12% increase at 0.7 dpa vs. 14% increase at 1.5 dpa). Indentation toughness also increased 79% after 1.5 dpa, but scatter was large. Absent from the literature are studies of irradiation-induced creep of ZrC.

Electrical and thermal conductivity, sensitive to defect concentration, have also been studied. In general, electrical resistivity was found to increase with irradiation and thermal conductivity to degrade. Koval'chenko and Rogovoi¹⁶⁵ irradiated $\text{ZrC}_{0.98}$ at 323 K with a thermal neutron fluence of 1×10^{19} – $1.5 \times 10^{20} \text{ cm}^{-2}$, and resistivity increased by 17–167%, increasing with fluence, versus an unirradiated $60 \mu\Omega \text{ cm}$. The authors attribute the increase to point defect formation, but low initial lattice parameter suggests high O and N impurity content in any case. Following the same irradiation by Andrievskii *et al.*¹⁶⁴ described in the preceding paragraph, resistivity was found to increase, with the effect less pronounced for higher irradiation temperatures: a 481% increase was measured at 423 K, and

a 51% increase at 1373 K, versus an unirradiated $43 \mu\Omega \text{ cm}$. In unirradiated ZrC_x , resistivity increases as the C/Zr ratio decreases, and Andrievskii *et al.*¹⁶⁶ found that the increase in resistivity following irradiation at 413 K in a fast neutron fluence of $1 \times 10^{19} \text{ cm}^{-2}$ was more pronounced for compositions closer to stoichiometry. A 6% increase in resistivity was measured for $\text{ZrC}_{0.7}$ versus a 213% increase for $\text{ZrC}_{0.94}$.

Thermal conductivity was studied by David *et al.*¹⁷⁸ following irradiation at 298 K with 28.5 MeV Kr ions to a fluence of 1×10^{16} or $6 \times 10^{16} \text{ cm}^{-2}$. The authors distinguished between thermal conductivity degradation due to inelastic and elastic collisions, with inelastic damage in ZrC calculated to occur in the first $3.3 \mu\text{m}$ into the surface and elastic damage initiating at a depth where dpa increases to 20% of the maximum damage, continuing for $1.4 \mu\text{m}$ below the inelastic damage. A modulated thermoreflectance microscopy technique was employed to characterize subsurface thermal conductivity degradation. Elastic collisions were deemed considerably more damaging than inelastic, reducing thermal conductivity from $20 \text{ W m}^{-1} \text{ K}^{-1}$ before irradiation to less than $1 \text{ W m}^{-1} \text{ K}^{-1}$. In the inelastic damage region, thermal conductivity of $10 \text{ W m}^{-1} \text{ K}^{-1}$ was measured after $1 \times 10^{16} \text{ cm}^{-2}$ fluence and $5 \text{ W m}^{-1} \text{ K}^{-1}$ after $6 \times 10^{16} \text{ cm}^{-2}$ fluence.

2.13.7 Summary and Outlook

As this review has illustrated, ZrC possesses a combination of thermodynamic, thermal, and mechanical properties that are promising for nuclear fuel applications requiring high-temperature resistance and structural integrity. However, it is also clear that more data are needed. The body of mechanical property data is limited. The degree of scatter in experimental data indicates that methods for fabricating dense, pure, homogeneous, stoichiometric ZrC are not mature. Properties of ZrC are known to be affected by oxygen and nitrogen impurities, but the thermodynamics of the Zr–C–O–N system has not been elaborated. The effects of irradiation on properties and performance must be more thoroughly characterized. ZrC is stable over a large range of nonstoichiometry, which is promising for irradiation damage tolerance, but carbon vacancies are shown to cause a decrease in bond strength, reflected in decreased heat capacity and hardness and increased CTE. The introduction of lattice defects also reduces thermal and electrical conductivity. With the renewed interest in ZrC for advanced composite nuclear fuels,

much work lies ahead in building the required knowledge base in both processing and performance that will enable the nuclear community to take full advantage of ZrC as a high-temperature structural ceramic.

Chapter 1.02, Fundamental Point Defect Properties in Ceramics; Chapter 1.05, Radiation-Induced Effects on Material Properties of Ceramics (Mechanical and Dimensional); and Chapter 3.08, Advanced Concepts in TRISO Fuel.

Acknowledgments

The authors would like to thank Y. Katoh, G. Vasudevamurthy, T. Nozawa, and L. L. Snead, for early sight of their forthcoming *Journal of Nuclear Materials* review article, “Handbook of ZrC properties for fuel performance modeling.”

References

- Schwarzkopf, P.; Kieffer, R. *Refractory Hard Metals*. MacMillan: New York, 1953.
- Storms, E. K. In *The Refractory Carbides*; Margrave, J. L., Ed.; Academic Press: New York, 1967; Vol. 2.
- Toth, L. E. In *Transition Metal Carbides and Nitrides*; Margrave, J. L., Ed.; Academic Press: New York, 1971.
- Kosolapova, T. Y. *Carbides: Properties, Production, and Applications*. [Vaughan, N. B., trans.]; Plenum Press: New York, 1971.
- Upadhyaya, G. S. *Nature and Properties of Refractory Carbides*. Nova Science: Commack, NY, 1996.
- Gusev, A. I.; Rempel, A. A. *Phys. Stat. Solidi A: Appl. Res.* **1997**, 163(2), 273–304.
- Mitrokhin, V. A.; Lyutikov, R. A.; Yurkova, R. S. *Inorg. Mater.* **1975**, 11(6), 978–980.
- Ramqvist, L. J. *Annaler.* **1968**, 152(10), 517–523.
- Rundle, R. E. *Acta Crystallogr.* **1948**, 1(4), 180–187.
- Samsonov, G. V.; Naumenko, V. Y.; Ryabokon, L. P.; Verkhovurov, A. D. *Powder Metall. Metal. Ceram.* **1975**, 14(1), 44–46.
- Lye, R. G.; Logothetis, E. M. *Phys. Rev.* **1966**, 147(2), 622–635.
- Hollox, G. E. *Mater. Sci. Eng.* **1968**, 3(3), 121–137.
- Storms, E. K.; Griffin, J. *High. Temp. Sci.* **1973**, 5(44), 291–310.
- Fernandez-Guillermet, A. J. *Alloy. Compd.* **1995**, 217(1), 69–89.
- Sara, R. V. *J. Am. Ceram. Soc.* **1965**, 48(5), 243–247.
- Rudy, E. Ternary phase equilibria in transition metal–boron–carbon–silicon systems. Part V. Compendium of phase diagram data; Report no. AFML-TR-65-2; Aerojet-General Corp.: Sacramento, CA, 1969.
- Kubaschewski-von Goldbeck, O. In *Zirconium: Physico-chemical Properties of Its Compounds and Alloys*; Atomic Energy Review, Special Issue, Vol. 6, Kubaschewski, O., Ed.; International Atomic Energy Agency: Vienna, 1976.
- Farr J. Unpublished work cited by E. K. Storms. A critical review of refractories; Report no. LAMS-2674; Los Alamos Scientific Laboratory: Los Alamos, NM, 1962.
- Sara, R. V.; Doloff, R. T. Research study to determine the phase equilibrium relations of selected metal carbides at high temperatures; Report no. WADD-TR-60-143-Pt3; Union Carbide Corp.: Parma, OH, 1962.
- Sara, R. V.; Lowell, C. E.; Doloff, R. T. Research study to determine the phase equilibrium relations of selected metal carbides at high temperatures; Report no. WADD-TR-60-143-Pt4; Union Carbide Corp.: Parma, OH, 1963.
- Rudy, E.; Harmon, D. P.; Brukl, C. E. Ternary phase equilibria in transition metal boron–carbon–silicon systems. Pt. 1. Related binary systems. Vol. 2. Ti–C and Zr–C system; Report no. AFML-TR-65-2; Aerojet-General Corp.: Sacramento, CA, 1965.
- Rudy, E.; Progulski, G. Ternary phase equilibria in transition metal–boron–carbon–silicon systems. Part III. Special experimental techniques. Vol II. A pirani-furnace for the precision determination of the melting temperature of refractory metallic substances; Report no. AFML-TR-65-2; Aerojet-General Corp.: Sacramento, CA, 1967.
- Adelsberg, L. M.; Cadoff, L. H.; Tobin, J. M. *Trans. Metall. Soc. AIME* **1966**, 236(7), 972–977.
- Zotov, Y. P.; Kotel'nikov, R. B. *Russ. Metall.* **1975**(1), 148–150.
- Bhatt, Y. J.; Venkataramani, R.; Garg, S. P. *J. Less-Common Metals* **1987**, 132(2), L21–L24.
- Chase, M. W.; Davies, C. A.; Downey, J. R.; Frurip, D. J.; McDonald, R. A.; Syverud, A. N. *J. Phys. Chem. Ref. Data*; **1985**, 14(Suppl 1).
- Mezaki, R.; Jambois, T. F.; Gangopadhyay, A. K.; Margrave, J. L. In *Thermodynamic and Kinetic Studies for a Refractory Materials Program, Pt. 2*; Report no. ASD-TDR 62-204; McClaine, L. A., Ed.; Arthur D. Little, Inc: Cambridge, MA, 1963; pp 92–97.
- Levinson, L. S. *J. Chem. Phys.* **1965**, 42(8), 2891–2892.
- Kantor, P. B.; Fomichev, E. N. *High Temp.* **1967**, 5(1), 41–43.
- Turchanin, A. G.; Fesenko, V. V. *Powder Metall. Metal Ceram.* **1968**, 8(1), 67–68.
- Westrum, E. F.; Feick, G. *J. Chem. Eng. Data* **1963**, 8(2), 176–178.
- Neel, D. S.; Pears, C. D.; Oglesby, S. The thermal properties of thirteen solid materials to 5000°F for their destruction temperatures; Report no. WADD-TR-60-924; Southern Research Institute: Birmingham, AL, 1962.
- Bolgar, A. S.; Guseva, E. A.; Fesenko, V. V. *Powder Metall. Metal Ceram.* **1967**, 7(1), 31–33.
- Petrova, I. I.; Chekhovskoi, V. Y. *High Temp.* **1978**, 16(6), 1045–1050.
- Storms, E. K.; Wagner, P. *High Temp. Sci.* **1973**, 5(6), 454–462.
- Sandenaw, T. A.; Storms, E. K. *J. Phys. Chem. Solids* **1966**, 27(1), 217–218.
- Pollock, B. D. *J. Phys. Chem.* **1961**, 65(5), 731–735.
- Coffman, J. A.; Kibler, G. M.; Lyon, T. F. Carbonization of plastics and refractory materials research; Report no. WADD-TR-60-646; General Electric: Cincinnati, OH, 1963.
- Nikol'skaya, T. A.; Avarbe, R. G.; Vil'k, Y. N. In *Refractory Carbides*, [Vaughan, N. B.; trans.]; Samsonov, G. V., Ed.; Consultants Bureau: New York, 1975; pp 329–334.
- Vidale, G. In *Carbonization of Plastics and Refractory Materials Research*; Coffman, J. A., Kibler, G. M., Lyon, T. F., Eds.; General Electric: Cincinnati, OH, 1963; pp 155–178.
- Wiedemann, G.; Franz, R. *Ann. Phys.* **1853**, 165(8), 497–531.

42. Radosevich, L. G.; Williams, W. S. *Phys. Rev.* **1969**, 181(3), 1110–1117.
43. Radosevich, L. G.; Williams, W. S. *J. Am. Ceram. Soc.* **1970**, 53(1), 30–33.
44. Williams, W. S. *J. Am. Ceram. Soc.* **1966**, 49(3), 156–159.
45. Taylor, R. E. *J. Am. Ceram. Soc.* **1962**, 45(7), 353–354.
46. Grossman, L. N. *J. Am. Ceram. Soc.* **1965**, 48(5), 236–242.
47. Fink, J. K.; Leibowitz, L. J. *Nucl. Mater.* **1995**, 226(1–2), 44–50.
48. Parker, W. J.; Jenkins, R. J.; Butler, C. P.; Abbot, G. L. *J. Appl. Phys.* **1961**, 32(9), 1679–1684.
49. Avgustinik, A. I.; Golikova, O. A.; Klimashin, G. M.; Neshpor, V. S.; Ordan'yan, S. S.; Snetkova, V. A. *Inorg. Mater.* **1966**, 2(8), 1230–1233.
50. Morrison, B. H.; Sturgess, L. L. *Revue Int. Hautes Temp. Refract.* **1970**, 7(4), 351–358.
51. Neshpor, V. S.; Ordan'yan, S. S.; Avgustinik, A. I.; Khusidman, M. B. *Russ. J. Appl. Chem.* **1964**, 37(11), 2349–2354.
52. Buravoi, S. E.; Taubin, M. L. *Inorg. Mater.* **1974**, 10(2), 319–321.
53. Neshpor, V. S.; Davydov, V. S.; Ermakov, B. G.; Mogilevich, B. V. *Powder Metall. Metal Ceram.* **1967**, 6(2), 135–138.
54. Shaffer, P. T. B.; Hasselman, D. P. H. Factors affecting thermal shock resistance of polyphase ceramic bodies; Report no. WADD-TR-60-749-Pt2; The Carborundum Company: Niagara Falls, NY, 1962.
55. Sklarew, S.; Albom, M. J. Pyrolytically derived refractory materials for aerospace applications; Report no. NASA-CR-50404; The Marquardt Corp.: Van Nuys, CA, 1963.
56. Neshpor, V. S.; Airapetyants, S. V.; Ordan'yan, S. S.; Avgustinik, A. I. *Inorg. Mater.* **1966**, 2(5), 728–734.
57. Samsonov, G. V.; Paderno, I. B.; Panasiuk, A. D. *Revue Int. Hautes Temp. Refract.* **1966**, 3(2), 179–184.
58. Modine, F. A.; Foegelle, M. D.; Finch, C. B.; Allison, C. Y. *Phys. Rev. B* **1989**, 40(14), 9558–9564.
59. Hinrichs, C. H.; Hinrichs, M. H.; Mackie, W. A. *J. Appl. Phys.* **1990**, 68(7), 3401–3404.
60. Aronson, S.; Cisney, E.; Auskern, A. B. *J. Am. Ceram. Soc.* **1966**, 49(8), 456.
61. Elliott, R. O.; Kempter, C. P. *J. Chem. Phys.* **1958**, 62, 630–631.
62. Houska, C. R. *J. Phys. Chem. Solids* **1964**, 25(4), 359–366.
63. Krikorian, N. H.; Wallace, T. C.; James, L. A. *J. Electrochem. Soc.* **1963**, 110(6), 587–588.
64. Mauer, F. A.; Bolz, L. H. Measurement of thermal expansion of cermet components of high-temperature X-ray diffraction; Report no. WADC-TR-55-473; National Bureau of Standards: Washington, DC, 1955.
65. Rahimzadeh, E.; Joshi, N. R.; Singh, S. *J. Am. Ceram. Soc.* **1984**, 67(7), C139–C140.
66. Richardson, J. H. *J. Am. Ceram. Soc.* **1965**, 48(10), 497–499.
67. Zainulin, Y. G.; Alyamovskii, S. I.; Shveikin, G. P.; Gel'd, P. V. *High Temp.* **1971**, 9(3), 496–498.
68. Lawson, A. C.; Butt, D. P.; Richardson, J. W.; Li, J. *Philos. Mag.* **2007**, 87(16), 2507–2519.
69. Bukatov, V. G.; Rymashevskii, G. A.; Fedorov, V. B. *Inorg. Mater.* **1971**, 7(3), 457–458.
70. Fridlender, B. A.; Neshpor, V. S. *High Temp.* **1976**, 14(5), 847–850.
71. Gangler, J. J. *J. Am. Ceram. Soc.* **1950**, 33(12), 367–375.
72. Leipold, M. H.; Nielsen, T. H. Mechanical and thermal properties of hot-pressed zirconium carbide tested to 2600°C; Report no. NASA-TR-32-452; Jet Propulsion Laboratory: Pasadena, CA, 1963.
73. Miccioli, B. R.; Shaffer, P. T. B. *J. Am. Ceram. Soc.* **1964**, 47(7), 351–356.
74. Samsonov, G. V.; Naumenko, V. Y. *High Temp.* **1970**, 8(5), 1022–1024.
75. Zotov, V. S.; Tsedilkin, A. P. *Phys. Metals Metallogr.* **1979**, 47(2), 344–348.
76. Agarwala, R. P.; Paul, A. R. *J. Nucl. Mater.* **1975**, 58(1), 25–30.
77. Pavlinov, L. V.; Bykov, V. N. *Phys. Metals Metallogr.* **1965**, 19(3), 73–76.
78. Andrievskii, R. A.; Zagryazkin, V. N.; Meshcheryakov, G. Y. *Phys. Metals Metallogr.* **1966**, 21(1), 140–143.
79. Ushakov, B. F.; Zagryazkin, V. N.; Panov, A. S. *Inorg. Mater.* **1972**, 8(11), 1690–1693.
80. Andrievskii, R. A.; Ereemeev, V. S.; Zagryazkin, V. N.; Panov, A. S. *Inorg. Mater.* **1967**, 3(12), 2158–2164.
81. Sarian, S.; Criscione, J. M. *J. Appl. Phys.* **1967**, 38(4), 1794–1798.
82. Andrievskii, R. A.; Klimenko, V. V.; Khromov, Y. F. *Phys. Metals Metallogr.* **1969**, 28(2), 115–120.
83. Andrievskii, R. A.; Khromov, Y. F.; Alekseeva, I. S. *Phys. Metals Metallogr.* **1971**, 32(3), 664–667.
84. Matzke, H. *Solid State Ionics* **1984**, 12(1), 25–45.
85. Chang, R.; Graham, L. J. *J. Appl. Phys.* **1966**, 37(10), 3778–3783.
86. Brown, H. L.; Kempter, C. P. *Phys. Status Solidi* **1966**, 18(1), K21–K23.
87. Avgustinik, A. I.; Ordan'yan, S. S.; Fishchev, V. P. *Inorg. Mater.* **1973**, 9(7), 1039–1041.
88. Baranov, V. M.; Knyazev, V. I.; Korostinm, O. S. *Strength Mater.* **1973**, 5(9), 1074–1077.
89. Travushkin, G. G.; Knyazev, V. I.; Belov, V. S.; Rymashevskii, G. A. *Strength Mater.* **1973**, 5(5), 639–641.
90. Warren, R. *Acta Metall.* **1978**, 26(11), 1759–1769.
91. Zubarev, P.; Kuraev, A.; Maskae, A.; Astakhova, E.; Bessarabov, A. *Strength Mater.* **1994**, 26(1), 63–69.
92. Shaffer, P. T. B.; Hasselman, D. P. H.; Chaberski, A. Z. Factors affecting thermal shock resistance of polyphase ceramic bodies; Report no. WADD-TR-60-749-Pt1; The Carborundum Company; Niagara Falls, NY, 1961.
93. Ajami, F. I.; MacCrone, R. K. *J. Less-Common Metals* **1974**, 38(2–3), 101–110.
94. Champion, A. R.; Drickamer, H. G. *J. Phys. Chem. Solids* **1965**, 26(12), 1973–1975.
95. Kosolapova, T. Y. Ed. *Handbook of High Temperature Compounds*; Hemisphere: New York, 1990.
96. Lepie, M. P. *Trans. Br. Ceram. Soc.* **1964**, 63(8), 431–449.
97. Gridneva, I. V.; Mil'man, Y. V.; Rymashevskii, G. A.; Trefilov, V. I.; Chugunova, S. I. *Powder Metall. Metal Ceram.* **1976**, 15(8), 638–645.
98. Fedotov, M. A.; Yanchur, V. P. *Inorg. Mater.* **1976**, 12(3), 421–425.
99. Lanin, A. G.; Zubarev, P. V.; Vlasov, K. P. *Atomic Energy* **1993**, 74(1), 40–44.
100. Funke, V. F.; Pshenichnyi, I. V.; Kruglov, V. N.; Kharkhardin, E. D. *Inorg. Mater.* **1973**, 9(12), 2151–2155.
101. Kohlstedt, D. L. *J. Mater. Sci.* **1973**, 8(6), 777–786.
102. Samsonov, G. V.; Stepanchuk, A. N.; Pritulyak, A. S.; Shlyuko, V. Y.; Adamovskii, A. A.; Mashonkina, T. V. *Powder Metall. Metal Ceram.* **1974**, 13(9), 735–738.
103. Artamonov, A. Y.; Bovkun, G. A. In *Refractory Carbides* [Vaughan, N. B.; trans.]; Samsonov, G. V., Ed.; Consultants Bureau: New York, 1975; pp 371–376.
104. Andrievskii, R. A.; Klimenko, V. V.; Mitrofanov, V. I.; Poltoratskii, N. I. *Powder Metall. Metal Ceram.* **1977**, 16(6), 423–426.

105. Vahldiek, F. W.; Mersol, S. A. *J. Less-Common Metals* **1977**, 55(2), 265–278.
106. Tkachenko, Y. G.; Ordan'yan, S. S.; Yurchenko, D. Z.; Yulyugin, V. K.; Bovkun, G. A.; Unrod, V. I. *Inorg. Mater.* **1979**, 15(4), 704–708.
107. He, X.-M.; Li, S.; Li, H.-B.; Li, H.-D. *J. Vacuum Sci. Technol. A* **1998**, 16(4), 2337–2344.
108. Lanin, A. G.; Sokolov, V. A.; Egorov, V. S. *Strength Mater.* **1984**, 16(1), 101–107.
109. ASTM Standard C1326. Standard test method for Knoop indentation hardness of advanced ceramics. ASTM International: West Conshohocken, PA, 2008.
110. ASTM Standard C1327. Standard test method for Vickers indentation hardness of advanced ceramics. ASTM International: West Conshohocken, PA, 2008.
111. Ogawa, T.; Ikawa, K.; Iwamoto, K. *J. Nucl. Mater.* **1976**, 62(2–3), 322–324.
112. Chen, C.-S.; Liu, C.-P.; Tsao, C. Y. A. *Thin Solid Films* **2005**, 479(1–2), 130–136.
113. Quinn, G. D.; Bradt, R. C. *J. Am. Ceram. Soc.* **2007**, 90(3), 673–680.
114. Williams, W. S.; Schaal, R. D. *J. Appl. Phys.* **1962**, 33(3), 955–962.
115. Williams, W. S. *J. Appl. Phys.* **1964**, 35(4), 1329–1338.
116. Lee, D. W.; Haggerty, J. S. *J. Am. Ceram. Soc.* **1969**, 52(12), 641–647.
117. Darolia, R.; Archbold, T. F. *J. Mater. Sci.* **1976**, 11(11), 283–290.
118. Turchin, V. N.; Rymashevskii, G. A.; Lanin, A. G. In *Refractory Carbides* [Vaughan, N. B.; trans.]; Samsonov, G. V., Ed.; Consultants Bureau: New York, 1975; 247–249.
119. Britun, V. F.; Erin, O. N.; Lanin, A. G.; Turchin, V. N. *Powder Metall. Metal Ceram.* **1992**, 31(12), 1054–1058.
120. Minato, K.; Fukuda, K.; Sekino, H.; Ishikawa, A.; Oeda, E. *J. Nucl. Mater.* **1998**, 252(1–2), 13–21.
121. Nickel, H.; Inanc, O.; Lucke, K. Z. *Metall.* **1968**, 59(12), 935–940.
122. Hannink, R. H. J.; Kohlstedt, D. L.; Murray, M. J. *Proc. R. Soc. London A: Math. Phys. Sci.* **1972**, 326(1566), 409–420.
123. Kumashiro, Y.; Nagai, Y.; Kato, H.; Sakuma, E.; Watanabe, K.; Misawa, S. *J. Mater. Sci.* **1981**, 16(10), 2930–2933.
124. Kumashiro, Y.; Nagai, Y.; Kato, H. *J. Mater. Sci. Lett.* **1982**, 11(1), 49–52.
125. Miloserdin, Y. V.; Naboichenko, K. V.; Laveikin, L. I.; Bortsov, A. G. *Strength Mater.* **1972**, 4(3), 302–305.
126. Spivak, I. I.; Andrievskii, R. A.; Klimenko, V. V. *Powder Metall. Metal Ceram.* **1973**, 12(3), 212–214.
127. Zubarev, P. V.; Dement'ev, L. N. *Strength Mater.* **1973**, 5(8), 61–64.
128. Zubarev, P. V.; Shmelev, A. G. *Strength Mater.* **1980**, 12(2), 142–148.
129. Zubarev, P. V.; Shmelev, A. G. *Strength Mater.* **1980**, 12(3), 264–268.
130. Zubarev, P. V.; Kuraev, A. B. *Phys. Metals Metallogr.* **1992**, 73(6), 643–646.
131. Zubarev, P. V.; Kuraev, A. B.; Lanin, A. G.; Turchin, V. N.; Erin, O. N.; Burkhanov, G. S.; et al. *Phys. Metals Metallogr.* **1992**, 73(6), 647–649.
132. Zubarev, P. V.; Dement'ev, L. N. *Inorg. Mater.* **1977**, 13(7), 988–991.
133. Zubarev, P.; Kuraev, A. *Strength Mater.* **1994**, 26(2), 132–136.
134. Bartlett, R. W.; Wadsworth, M. E.; Cutler, I. B. *Trans. Metall. Soc. AIME* **1963**, 227(2), 467–472.
135. Shimada, S.; Ishii, T. *J. Am. Ceram. Soc.* **1990**, 73(10), 2804–2808.
136. Shimada, S. *Solid State Ionics* **2002**, 149(3–4), 319–326.
137. Rama Rao, G. A.; Venugopal, V. *J. Alloy Compd.* **1994**, 206(2), 237–242.
138. Opeka, M. M.; Talmy, I. G.; Wuchina, E. J.; Zaykoski, J. A.; Causey, S. J. *J. Eur. Ceram. Soc.* **1999**, 19(13–14), 2405–2414.
139. Voitovich, R. F.; Pugach, E. A. *Powder Metall. Metal. Ceram.* **1973**, 12(11), 916–921.
140. Shevchenko, A. S.; Lyutikov, R. A.; Andrievskii, R. A.; Terekhova, V. A. *Powder Metall. Metal. Ceram.* **1980**, 19(1), 48–52.
141. Tamura, K.; Ogawa, T.; Fukuda, K. *J. Nucl. Mater.* **1990**, 175(3), 266–269.
142. Zhilyaev, V. A.; Zainulin, Y. G.; Alyamovskii, S. I.; Shveikin, G. P. *Powder Metall. Metal. Ceram.* **1972**, 11(8), 632–636.
143. Zainulin, Y. G.; Zhilyaev, V. A.; Alyamovskii, S. I.; Shveikin, G. P. *Inorg. Mater.* **1976**, 12(2), 239–240.
144. Shimada, S. *Solid State Ionics* **2001**, 141–142, 99–104.
145. Shimada, S.; Inagaki, M.; Suzuki, M. *J. Mater. Res.* **1996**, 11(10), 2594–2597.
146. Shimada, S.; Nishisako, M.; Inagaki, M.; Yamamoto, K. *J. Am. Ceram. Soc.* **1995**, 78(1), 41–48.
147. Belluci, A.; Gozzi, D.; Kimura, T.; Noda, T.; Otani, S. *Surf. Coat. Technol.* **2005**, 197(2–3), 294–302.
148. Dufour, L. C.; Simon, J.; Barret, P. *Comptes Rendus Seances l'Acad. Sci. C: Sci. Chim.* **1967**, 265(3), 171–174.
149. Ouensanga, A. H.; Dode, M. *J. Nucl. Mater.* **1976**, 59(1), 49–60.
150. Matskevich, T. L.; Kazantsev, A. P. *Sov. Phys. Tech. Phys.* **1982**, 27(4), 477–480.
151. Constant, K.; Kieffer, R.; Ettmayer, P. *Monatshefte Chemie/Chem. Month.* **1975**, 106(4), 823–832.
152. Kuriakose, A. K.; Margrave, J. L. *J. Electrochem. Soc.* **1974**, 111(7), 827–831.
153. Berkowitz-Mattuck, J. B. Kinetics of oxidation of refractory metals and alloys at 1000–2000°C, Part II; Report no. ASD-TDR-62-203; Arthur D. Little, Inc: Cambridge, MA, 1962.
154. Berkowitz-Mattuck, J. B. *J. Electrochem. Soc.* **1967**, 114(10), 1030–1033.
155. Janowski, K. R.; Carnahan, R. D.; Rossi, R. C. Static and dynamic oxidation of ZrC; Report no. TDR-669; Aerospace Corp.: El Segundo, CA, 1966.
156. Maitre, A.; Lefort, P. *Solid State Ionics* **1997**, 104(1–2), 109–122.
157. Minato, K.; Fukuda, K. *Response of Fuel, Fuel Elements, and Gas Cooled Reactor Cores Under Accidental Air or Water Ingress Conditions*; Report no. IAEA-TECDOC-784; IAEA: Vienna, Austria, 1995; pp 86–91.
158. IAEA. Fuel performance and fission product behaviour in gas cooled reactors; Report no. IAEA-TECDOC-978; International Atomic Energy Agency: Vienna, Austria, 1997.
159. Bullock, R. E.; Kaae, J. L. *J. Nucl. Mater.* **1983**, 115(1), 69–83.
160. Holden, N. E. In *CRC Handbook of Chemistry and Physics*, 89th ed.; Lide, D. R., Ed.; CRC Press/Taylor and Francis: Boca Raton, FL, 2009.
161. Keilholtz, G. W.; Moore, R. E.; Osborne, M. F. *Nucl. Applic.* **1968**, 4(5), 330–336.
162. Watson, G. M.; Keilholtz, G. W. In *Fuel and Materials Development Program. Quarterly Progress Report for Period Ending 30 September 1969*; Report no. ORNL-4480; Patriarca, P., Rucker, D. J., Eds.; Oak Ridge National Laboratory: Oak Ridge, TN, 1970; pp 245–255.
163. Keilholtz, G. W.; Moore, R. E.; Dyslin, D. A. In *Fuels and Materials Development Program. Quarterly Progress Report for Period Ending 30 September 1968*; Report no. ORNL-4350; Patriarca, P., Harms, W. O.,

- Eds.; Oak Ridge National Laboratory: Oak Ridge, TN, 1969; pp 139–145.
164. Andrievskii, R. A.; Vlasov, K. P.; Shevchenko, A. S.; *et al. Inorg. Mater.* **1978**, 14(4), 530–533.
 165. Koval'chenko, M. S.; Rogovoi, Y. I. *Inorg. Mater.* **1973**, 9(2), 290–292.
 166. Andrievskii, R. A.; Savin, V. I.; Markin, V. Y.; Spravtsev, V. T.; Shevchenko, A. S. *Inorg. Mater.* **1978**, 14(4), 526–529.
 167. Reynolds, G. H.; Janvier, J. C.; Kaae, J. L.; Morlevat, J. P. *J. Nucl. Mater.* **1976**, 62(1), 9–16.
 168. Ogawa, T.; Fukuda, K.; Kashimura, S.; *et al. J. Am. Ceram. Soc.* **1992**, 75(11), 2985–2990.
 169. Minato, K.; Ogawa, T.; Sawa, K.; *et al. Nucl. Technol.* **1999**, 130(3), 272–281.
 170. Minato, K.; Ogawa, T.; Fukuda, K.; *et al. J. Nucl. Mater.* **1995**, 224(1), 85–92.
 171. Minato, K.; Ogawa, T.; Fukuda, K.; Sekino, H.; Kitagawa, I.; Mita, N. *J. Nucl. Mater.* **1997**, 249(2–3), 142–149.
 172. Ogawa, T.; Ikawa, K. *J. Nucl. Mater.* **1981**, 99(1), 85–93.
 173. Gan, J.; Meyer, M. K.; Birtcher, R. C.; Allen, T. R. *J. ASTM Int.* **2006**, 3(4), 358–364.
 174. Gan, J.; Yang, Y.; Dickerson, C. A.; Allen, T. R. *J. Nucl. Mater.* **2009**, 389(2), 317–325.
 175. Yang, Y.; Dickerson, C. A.; Swoboda, H.; Miller, B.; Allen, T. R. *J. Nucl. Mater.* **2008**, 378(3), 341–348.
 176. Gosset, D.; Dolle, M.; Simeone, D.; Baldinozzi, G.; Thome, L. *Nucl. Instrum. Methods Phys. Res. B* **2008**, 266(12–13), 2801–2805.
 177. Gosset, D.; Dolle, M.; Simeone, D.; Baldinozzi, G.; Thome, L. *J. Nucl. Mater.* **2008**, 373(1–3), 123–129.
 178. David, L.; Gomes, S.; Carlot, G.; *et al. J. Phys. D: Appl. Phys.* **2008**, 41(3), 035502.
 179. Baker, F. B.; Storms, E. K.; Holley, C. E. *J. Chem. Eng. Data* **1969**, 14(2), 244–246.
 180. Bulychiev, V. P.; Andrievskii, R. A.; Nezhevenko, L. B. *Powder Metall. Metal. Ceram.* **1977**, 16(4), 273–276.
 181. Caputo, A. J. *Thin Solid Films* **1977**, 40(1–3), 49–55.
 182. Christensen, A. N. *Acta. Chem. Scand.* **1990**, 44, 851–852.
 183. Fedorov, V. B.; Aleinikov, I. N. *High Temp.* **1971**, 9(5), 984–985.
 184. Henney, J.; Jones, J. W. S. Ternary phases in the zirconium–carbon–oxygen system; Report no. AERE-R 4619; Atomic Energy Research Establishment: Harwell, UK, 1964.
 185. Kempter, C. P.; Fries, R. J. *Anal. Chem.* **1960**, 32(4), 570.
 186. Korshunov, I. G.; Zinov'ev, V. E.; Gel'd, P. V.; Chernyaev, V. S.; Borukhovich, A. S.; Shveikin, G. P. *High Temp.* **1973**, 11(4), 803–805.
 187. L'vov, S. N.; Lesnaya, M. I.; Vinitskii, I. M.; Naumenko, V. Y. *High Temp.* **1972**, 10(6), 1196–1198.
 188. Mah, A. D. Heats of formation of zirconium carbide and hafnium carbide; Report no. BM-RI-6518; US Bureau of Mines: Berkeley, CA, 1964.
 189. Mah, A. D.; Boyle, B. J. *J. Am. Chem. Soc.* **1955**, 77(24), 6512–6513.
 190. Ordan'yan, S. S.; Kudryasheva, L. V.; Avgustinik, A. I. *Inorg. Mater.* **1971**, 7(12), 2179–2182.
 191. Petrov, V. A.; Chekhovskoi, V. Y.; Sheindlin, A. E.; Nikolaeva, V. A.; Fomina, L. P. *High Temp.* **1967**, 5(6), 889–893.
 192. Samsonov, G. V.; Vinitskii, I. M. In *Refractory Compounds Handbook* [Shaw, K.; trans.]; Plenum Press: New York, 1980.
 193. Savitskii, E. M.; Kul'bakh, A. A.; Evstyukhin, N. A. In *Refractory Carbides* [Vaughan, N. B.; trans.]; Samsonov, G. V., Ed.; Consultants Bureau: New York, 1975; pp 361–365.
 194. Shevchenko, A. S.; Andrievskii, R. A.; Kalinin, V. P.; Lyutikov, R. A. *Powder Metall. Metal. Ceram.* **1970**, 10(1), 71–73.
 195. Turchin, V. N.; Emel'yanov, A. B.; Rymashevskii, G. A.; Lanin, A. G. *Powder Metall. Metal. Ceram.* **1980**, 19(1), 24–27.
 196. Zotov, Y. P.; Kotel'nikov, R. B.; Kakushadze, L. E.; Migunov, L. V.; Galiakbarov, Z. G. *Russ. Metall.* **1974**(6), 59–64.

2.14 Properties of Liquid Metal Coolants

V. Sobolev

Belgian Nuclear Research Centre SCK-CEN, Mol, Belgium

© 2012 Elsevier Ltd. All rights reserved.

2.14.1	Introduction	374
2.14.2	General Properties	375
2.14.3	Characteristic Temperatures, Pressures, and Heats	375
2.14.3.1	Melting Line	376
2.14.3.2	Boiling Line	377
2.14.3.3	Critical Point	378
2.14.4	Thermodynamic Properties	379
2.14.4.1	Density and Thermal Expansion	380
2.14.4.2	Sound Velocity and Compressibility	380
2.14.4.3	Surface Tension	382
2.14.4.4	Heat Capacity and Enthalpy	383
2.14.4.5	Equation of State	384
2.14.4.5.1	Low pressures	384
2.14.4.5.2	High pressures	385
2.14.5	Transport Properties	385
2.14.5.1	Viscosity	385
2.14.5.2	Electric Conductivity	386
2.14.5.3	Thermal Conductivity	387
2.14.6	Conclusions	389
References		390

Abbreviations

CTE	Coefficient of thermal expansion
EOS	Equation of state
(e)	Eutectic
GEN IV	Generation IV reactor systems
GIF	Generation IV International Forum initiative
LFR	Lead-cooled fast reactor
LM	Liquid metal
SFR	Sodium-cooled fast reactor
VdW	Van der Waals
WFL	Wiedemann–Franz–Lorenz
WPFC	Working Party on Fuel Cycle

Symbols

a_p	Isobaric thermal diffusivity
C_p	Isobaric molar heat capacity
C_v	Isochoric molar heat capacity
H	Enthalpy
L_0	Lorentz number; $2.45 \times 10^{-8} \text{ W } \Omega \text{ K}^{-2}$
M_a	Molar mass

p	Pressure
p_c	Critical pressure
p_0	Normal atmospheric pressure
p_s	Pressure of saturated vapor
R	Universal gas constant; $8.314 \text{ J mol}^{-1} \text{ K}^{-1}$
r	Specific electrical resistivity
$r_{M,0}$	Specific electrical resistivity at normal melting temperature and normal atmospheric pressure
T	Temperature
$T_{B,0}$	Boiling temperature at normal atmospheric pressure
T_c	Critical temperature
$T_{M,0}$	Melting temperature at normal atmospheric pressure
u	Sound velocity
$u_{M,0}$	Sound velocity at normal melting temperature and normal atmospheric pressure
V_a	Molar volume
α_p	Isobaric volumetric coefficient of thermal expansion
β_s	Adiabatic (isentropic) compressibility

β_T	Isothermal compressibility
$\Delta H_{B,0}$	Enthalpy of boiling at normal atmospheric pressure
ΔH_e	Enthalpy of evaporation
$\Delta H_{M,0}$	Enthalpy of melting at normal atmospheric pressure
η	Dynamic viscosity
λ	Thermal conductivity
λ_e	Electronic thermal conductivity
$\lambda_{M,0}$	Thermal conductivity at normal melting temperature and normal atmospheric pressure
ρ	Density
ρ_c	Critical density
$\rho_{M,0}$	Density at normal melting temperature and normal atmospheric pressure
σ	Surface tension
$\sigma_{M,0}$	Surface tension at normal melting temperature and normal atmospheric pressure
ν	Kinematic viscosity

2.14.1 Introduction

Liquid metals (LM), such as sodium (Na), lead (Pb), and lead–bismuth (Pb–Bi) eutectic (e), are considered as potential coolants for the fast spectrum nuclear reactors of the next generation.¹ In the period 1960–1980, a lot of studies were performed for the creation of adequate databases of thermophysical properties of Na in the frameworks of development, construction, and operation of liquid metal (cooled) fast breeder reactors LMFBR in the United States, European Union, and in the former USSR.² Most of these results were collected later and published in review reports and handbooks.^{3–11} Since that time, the interest for fast reactors with Na coolant increased significantly worldwide, especially after the launch of the Generation IV International Forum (GIF) initiative,¹ where the sodium fast reactor (SFR) is considered as the main candidate for future nuclear power plants, which can be used for both electricity production and transuranium elements (TRU) incineration – a way for closing the nuclear fuel cycle. In the GIF documents, the lead-cooled fast reactor (LFR – cooled by Pb or Pb–Bi) is considered as the second candidate.¹ An interest to use Pb and Pb–Bi(e) in the civil power reactors appeared mainly after communications in open literature about the preliminary design studies on BREST¹² and SVBR¹³ reactors in the Russian

Federation. LFR systems are now considered in few other countries: PBWFR,¹⁴ SLPLFR,¹⁵ and CANDLE¹⁶ in Japan, PEACER¹⁷ and BORIS¹⁸ in Korea, SSTAR¹⁹ in the United States, and ELSY^{20,21} in the European Union. At present, the available data on thermophysical properties of Pb and Pb–Bi(e) in the temperature range of interest are still incomplete and often contradictory. This complicates the design calculations and the prediction of the normal and abnormal behavior of nuclear installations where they will be used. Intensive studies have been performed in different countries aiming at better understanding of their properties needed for design and safety analysis of the nuclear installations. Recently, a review of the Na properties was performed in Argonne National Laboratory²²; compilations with the recommendations for the properties of Pb and Pb–Bi(e) were prepared by the WPFC (OECD) Expert Group on Heavy Liquid Metals Technology^{23,24} and for all three LM of interest by expert groups of the IAEA.^{25,26}

This chapter gives a brief review of the compilations and recommendations developed for the main thermophysical properties of Na, Pb, and Pb–Bi(e), which include melting temperature, boiling temperature, critical point parameters, saturated vapor pressure, melting and boiling enthalpies, surface tension, density, thermal expansion, adiabatic and isothermal compressibility, speed of sound, heat capacity at constant pressure and at constant volume, enthalpy, electrical resistivity, viscosity, and thermal conductivity. The properties of these coolants were measured in many laboratories but mainly at normal atmospheric pressure and at relatively low temperatures (except for Na). In general, the reliability of the data is satisfactory; however, a large uncertainty still exists in some properties of Pb and Pb–Bi(e). A set of correlations for the estimation of the main properties of Na, Pb, and Pb–Bi(e), as a function of temperature and pressure, is proposed based on the previous reviews and new results that appeared in open literature. For the prediction of the missing properties at high temperatures and pressures, relevant equations of state (EOS), based on the proven physical models and available experimental data, were indicated. Taking into account that the critical parameters for the considered metals are not yet well defined with adequate precision, the EOS validation at high temperatures and pressures is still a problem.

In **Section 2.14.2**, general properties of liquid Na, Pb, and Pb–Bi(e) at a temperature of 400 °C, which is within the typical temperature range of coolant in SFR and LFR, are compared.

Characteristic temperatures (melting, boiling, and critical), and the enthalpies of melting and boiling are given in [Section 2.14.3](#). Thermodynamic properties are reviewed in five subsections of [Section 2.14.4](#). [Section 2.14.5](#) is devoted to transport properties. Conclusions are formulated in [Section 2.14.6](#). Compatibility of structure materials with liquid sodium and lead alloys is considered in [Chapter 5.13, Material Performance in Sodium](#) and [Chapter 5.09, Material Performance in Lead and Lead-bismuth Alloy](#), respectively.

2.14.2 General Properties

Almost all main thermophysical properties of liquid Na, Pb, and Pb–Bi(e) (such as density, thermal expansion, compressibility, heat capacity, surface tension, sound velocity, and compressibility) are measured with satisfactory precision in the region close to normal melting temperature. An exception is the saturated vapor pressure, which is rather small at these temperatures to be measured with high precision. The aforementioned parameters of liquid Na, Pb, and Pb–Bi(e), calculated with the recommended correlations given below for normal atmospheric pressure and at the typical mean temperature 400 °C (673 K) of the normal operation of the considered LM coolants in a Gen IV reactor, are compared in [Table 1](#).

The main advantages of Na coolant in comparison with Pb and Pb–Bi(e) are the lower density and viscosity and the higher other transport coefficients (electrical conductivity and thermal conductivity); its disadvantages are higher compressibility, high saturation vapor pressure, and lower surface tension. More detailed information about the thermophysical properties of liquid Na, Pb, and Pb–Bi(e) is given in the following sections.

The pressure diapason of the normal operation of the LM coolants in nuclear installations usually ranges from 0.1 to 1–1.5 MPa and the temperature diapason is between 300 °C (573 K) and 600 °C (873 K). Under accidental conditions, the coolant temperature can locally increase up to the fuel melting temperature, and the local coolant pressure can increase up to the cladding failure limit. Therefore, coolant properties have to be known within larger temperature and pressure ranges. For the development of an EOS of the LM coolants needed for the correct extension of the properties' recommendations to higher temperatures and pressures, their critical parameters (temperature, pressure, and density) should be known.

2.14.3 Characteristic Temperatures, Pressures, and Heats

A temperature range of the normal operation of a liquid metal coolant is usually determined by its melting and boiling temperatures. Under accidental conditions, it can even be close to the critical point region. The melting temperature increases very weakly with pressure, but the boiling temperature increases rapidly, so the temperature range is larger at the higher pressures.

The melting temperatures of the chemically pure Na, Pb–Bi(e), and Pb were measured with high precision at normal atmospheric pressure.^{3–30} However, the difference between the values coming from different sources sometimes reaches a few tenths of degree of Celsius (a few tenths of Kelvin) for Na and Pb, and a few degrees for Pb–Bi(e). This dispersion is mainly explained by the presence of impurities in the samples.³⁰ Moreover, for Pb–Bi(e), supplementary uncertainties exist due to a possible deviation from the eutectic composition (currently, most of the

Table 1 Thermophysical parameters of Na, Pb, and Pb–Bi(e) at normal atmospheric pressure and temperature 673.15 K (400 °C)

Parameter	Units	Na	Pb	Pb–Bi(e)
Density	kg m ⁻³	856.0	10 578	10 194
Isobaric volumetric coefficient of thermal expansion	10 ⁻⁵ K ⁻¹	27.5	12.1	12.7
Adiabatic compressibility	10 ⁻¹² Pa ⁻¹	209	29.6	33.5
Isobaric heat capacity	J mol ⁻¹ K ⁻¹	29.5	30.4	29.8
Surface tension	10 ⁻³ N m ⁻¹	166	450	395
Saturated vapor pressure	Pa	5.2 × 10 ¹	2.8 × 10 ⁻⁵	3.0 × 10 ⁻⁵
Dynamic viscosity	10 ⁻³ Pa s	0.27	2.23	1.51
Electric resistivity	10 ⁻⁸ Ω m	21.3	98.7	123.2
Thermal conductivity	W m ⁻¹ K ⁻¹	72.6	16.6	13.1

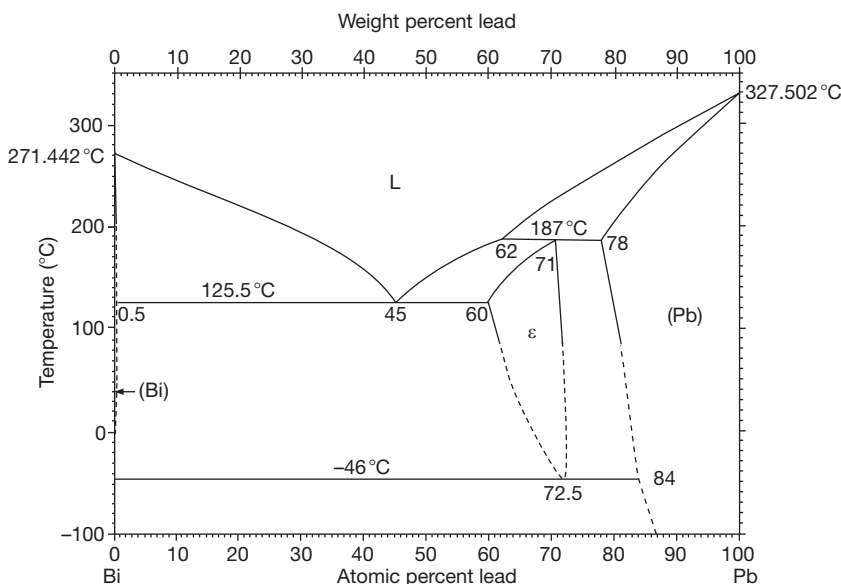


Figure 1 Phase diagram of the Pb–Bi system. Reproduced from Gokcen, N. A. *J. Phase Equil.* **1992**, *13*, 21–32.

researches fix it at 45.5 wt% Pb + 55.5 wt% Bi^{24,31}; see **Figure 1**) and due to a possible presence of metastable phases.^{24,32} For the technically pure metals, the best estimated values of the melting temperature ($T_{M,0}$) for the considered metals at the standard atmospheric pressure are 371.0 ± 0.1 K for Na, 600.6 ± 0.1 K for Pb, and 398 ± 1 K for Pb–Bi(e).^{9,24–34}

In 1999, Stølen and Grønvold³⁵ performed the critical assessment of the available data on the enthalpy of melting ($\Delta H_{M,0}$) of pure metals, used as enthalpy standards, at the standard atmospheric pressure. The values recommended by them for Na and Pb are 2.60 ± 0.03 and 4.78 ± 0.03 kJ mol^{−1}, respectively. For the Pb–Bi(e) melting enthalpy, the analysis of the available data was performed in Sobolev and Benamati²⁴ and Sobolev,³⁴ where the mean value of 8.04 ± 0.06 kJ mol^{−1} of three more reliable sources Bogoslovskaja *et al.*,²⁵ Kirillov *et al.*,²⁶ Cevolani³⁶ was recommended, which is adopted in this work.

The boiling temperatures of these LM were measured with a lower precision than their melting temperatures. The uncertainty ranges from 10 to 20 K for Pb and Pb–Bi(e)²⁴ and about 1–2 K for Na.^{22,27,30} The selected ‘best estimate’ values of the normal boiling temperatures ($T_{B,0}$) of Na, Pb, and Pb–Bi(e) are 1155 ± 2 K, 2021 ± 3 K, and 1927 ± 16 K, respectively.

The available data on the enthalpy of boiling of Na were analyzed in Fink and Leibowitz²² and Kirillov *et al.*,²⁶ and the selected recommended value

of $\Delta H_{B,0(\text{Na})} = 97.4 \pm 0.1$ kJ mol^{−1} is recommended for the standard atmospheric pressure. The literature values on the boiling latent heat of Pb at normal atmospheric pressure were reviewed in Sobolev and Benamati.²⁴ The difference <3% was found between the maximum and minimum reported values: $\Delta H_{B,0(\text{Pb})} = 177.9 \pm 0.4$ kJ mol^{−1}. In the same compilation,²⁴ the mean value of 178 ± 1 kJ mol^{−1} of only three available sources^{25,26,36} was recommended for the latent heat of boiling of LBE at normal pressure.

The most probable values of the melting and boiling temperatures, together with the latent enthalpies of the melting and boiling of Na, Pb–Bi(e), and Pb at normal atmospheric pressure, recommended earlier, and the operation temperature ranges of these liquid metal coolants, are presented in **Table 2**.

2.14.3.1 Melting Line

At pressures below 6 GPa, the melting temperatures of Na, Pb, and Pb–Bi(e) increase monotonically with decreasing rate with pressure. The melting temperature of Na increases from 371 K at an atmospheric pressure up to 507–522 K when pressure increases up to 3 GPa^{37–39}; the melting temperature of Pb increases from 600.6 to 795–815 K at the same pressure increase.^{38,40} For Pb, the rate of the melting temperature increase of 0.0792 K MPa^{−1} in the pressure range of 15–200 MPa, 0.0671 K per 1 MPa in the range of 0.8–1.2 GPa, and an increase of 5.4 K for the pressure increase from 2 to 3 GPa, were cited in Hofmann.²⁸

Table 2 Characteristic temperatures and temperature ranges of liquid Na, Pb–Bi(e), and Pb at normal atmospheric pressure

	$T_{M,0}$ (K)	$\Delta H_{M,0}$ (kJ mol ⁻¹)	$T_{B,0}$ (K)	$\Delta H_{B,0}$ (kJ mol ⁻¹)	$T_{B,0} - T_{M,0}$ (K)
Na	371.0 ± 0.1	2.60 ± 0.03	1155 ± 2	97.4 ± 0.1	784 ± 2
Pb–Bi(e)	398 ± 1	8.04 ± 0.06	1927 ± 16	178 ± 1	1529 ± 17
Pb	600.6 ± 0.1	4.78 ± 0.03	2021 ± 3	177.9 ± 0.4	1420 ± 4

Table 3 Coefficients of the correlation [1] for the pressure dependence of the melting temperatures (in K) of Na, Pb, and Pb–Bi(e)

Parameter	Unit	Na	Pb	Pb–Bi(e)
$T_{M,0}$	K	371.0	600.6	398
b_{T_M}	K GPa ⁻¹	59.5	71.94	46.7
c_{T_M}	K GPa ⁻²	-3.9	-1.546	-

The eutectic point of Pb–Bi(e) is shifted to lower Pb contents and higher melting temperature with pressure. The eutectic temperature increases from 398 K at normal atmospheric pressure to ~422 K at pressure 0.75 GPa and to ~481 K at 1.8 GPa.⁴¹

In the pressure range of 0.1 MPa–3 GPa, the parabolic function can be used for the description of the pressure dependence of the melting temperatures of Na, Pb, and Pb–Bi(e), (Table 3):

$$T_M(p) = T_{M,0} + b_{T_M}(p - p_0) + c_{T_M}(p - p_0)^2 \quad [1]$$

The melting temperatures of Na and Pb as functions of pressure up to $p = 6$ GPa and up to 1.8 GPa for Pb–Bi(e), are presented in Figure 2. At higher pressures, a more complicated behavior of the melting temperatures of the considered metals in the function of pressure is observed.^{39,42}

2.14.3.2 Boiling Line

The saturated vapor pressure is a very important parameter of LM coolants for safety estimations. It is directly related to the latent heat of evaporation. The boiling temperature increases (with the decreasing rate) when pressure increases. At low pressures, where the vapor behaves as a perfect gas and the evaporation enthalpy (ΔH_e) is practically constant, it follows from the Clausius–Clapeyron equation that temperature dependence of the saturated vapor pressure is about exponential:

$$p_s(T) = p_{s,\infty} \exp(-\Delta H_e/RT) \quad [2]$$

$R = 8.314 \text{ J mol}^{-1} \text{ K}^{-1}$ is the universal gas constant.

Equation [2] can provide approximate values for equilibrium-saturated vapor pressures over a wide range of temperature due to the relatively small variation of ΔH_e with temperature at low pressures. At high pressures, closer fits of the experimental results can be obtained by adding supplementary temperature-dependent terms:

$$\ln(p_s(T)) = A + \frac{B}{T} + C \ln(T) + DT \quad [3]$$

Very often this correlation is used without the last term.

Evaluation of data on the temperature dependence of the saturation vapor pressure of sodium in a wide range of temperatures was performed many times^{3,8,43,44} and correlations of type [3] were proposed that can describe the temperature dependence of the Na saturation pressure in a wide temperature range with an uncertainty of 1–25%. In the recent compilation of IAEA,²⁶ a polynomial of the fifth order was proposed for the saturation pressure of Na constructed on the bases of the recommended data presented in Bystrov *et al.*,¹¹ Browning and Potter,⁴⁴ and Vargaftik and Voljak.⁴⁵ In the review of Fink and Leibowitz,²² a detailed analysis of previous compilations was performed and a correlation of type [3] proposed in Browning and Potter⁴⁴ was selected, which allows to calculate the Na saturated vapor pressure with an uncertainty of <3% in the temperature range from 864 K to the region close to $T_{c(\text{Na})}$. The uncertainty increases at lower temperatures and reaches 24% at $T = 400$ K. This correlation is recommended for high temperatures in the current work and its coefficients are given in Table 4.

Not many data exist on the saturation vapor pressure of lead. In 1973, they were reviewed by Hultgren *et al.*,⁵ who analyzed different sources and presented a table with the recommended data in the temperature range of 298.15–2100 K. Later, Kubaschewski and Alcock⁴⁶ reanalyzed the available data on the Pb saturation vapor pressure and proposed a correlation of type [3]. In more recent compilations^{23,27,33,47,48} and in the present work, the simpler correlation of type [2] or the correlation of type [3] with the coefficients from

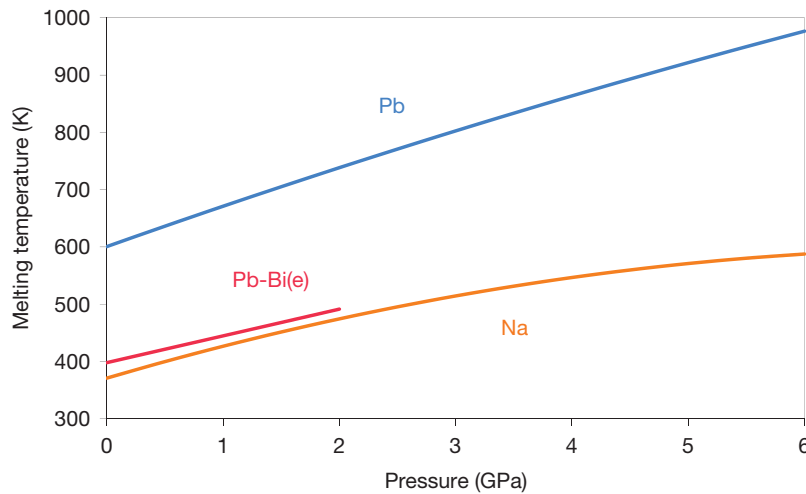


Figure 2 Melting temperature versus pressure.

Table 4 Coefficients of the correlation [3] for the temperature dependence of the saturated vapor pressure (in MPa) of Na, Pb, and Pb-Bi(e)

Parameter	Unit	Na	Pb	Pb-Bi(e)
$T_{M,0}$	K	371.0	600.6	398
$T_{B,0}$	K	1155	2021	1927
A	ln(MPa)	11.9463	16.7488	21.9575
B	K	-12633.73	-23325	-24053
C	—	-0.4672	-0.985	-1.6402
$D \times 10^{-4}$	K ⁻¹	—	—	3.3274

Kubaschewski and Alcock⁴⁶ are recommended for the saturated vapor pressure of lead (see Table 4).

Data on the saturated vapor pressure of Pb-Bi(e) are very limited in number^{49–51} and in the temperature range (508–1023 K), and a larger dispersion exists between them, especially at lower temperatures. Therefore, they can be described with correlation [2]. Nevertheless, in order to take into account the formation of Bi₂ molecules in the Pb-Bi vapor phase, Morita *et al.*⁵² proposed to use a four-term correlation [3] for temperature interval 700–2000 K. The coefficients are included in Table 4; the coefficient D was corrected to obtain $T_B = 1927$ K at $p_s = 0.101\,325$ MPa (1 atm).

At low temperatures, the saturated vapor pressure of the considered LM can be estimated with the same or better uncertainty with eqn [2]; the coefficients recommended in the compilations^{33,34} for Na, Pb, and Pb-Bi(e) are given in Table 5.

Figure 3, in which the saturated vapor pressure is plotted as a function of temperature, illustrates the

Table 5 Coefficients of the correlation [2] for the temperature dependence of the saturated vapor pressure of Na, Pb, and Pb-Bi(e)

Parameter	Unit	Na	Pb	Pb-Bi(e)
$T_{M,0}$	K	371.0	600.6	398
$T_{B,0}$	K	1155	2021	1927
$p_{s,\infty}$	10 ⁹ Pa	4.43	5.76	12.2
ΔH_e	kJ	102.6	184.0	187.5

correlation [2] for Na, Pb-Bi(e), and Pb in the temperature range of $T_{M,0}$ to $T_{B,0}$.

It should be noticed that for Na and Pb, the uncertainty of this correlation is about 7–10% when the temperature is 50–100 °C higher than normal melting temperature and lower than normal boiling temperature. The uncertainty increases rapidly beyond this interval, at lower and higher temperatures. For Pb-Bi(e), the uncertainty of this correlation is about 10% at temperatures higher than 1500 K; however, it becomes more than 50% when temperature decreases below 1000 K.^{24,34} At lower temperatures, the saturated pressure is too low to be measured correctly. The values of ΔH_e presented in Table 5 are slightly higher but in satisfactory agreement with $\Delta H_{B,0}$ presented in Table 2.

2.14.3.3 Critical Point

A great uncertainty still exists in the critical temperatures, pressures, and densities of the LM of interest. These parameters are very important for the development of EOS and the extension of the

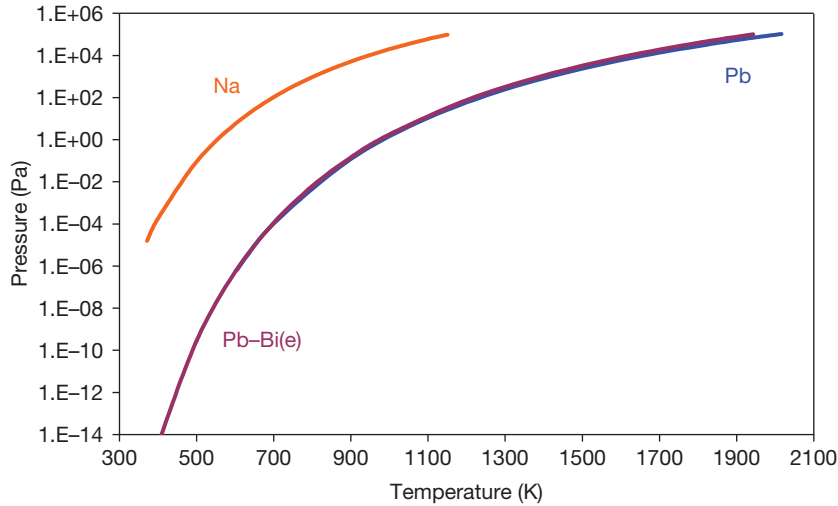


Figure 3 Saturated vapor pressure of Na, Pb, and Pb-Bi(e) ($p \leq p_{\text{atm}}$).

Table 6 Critical parameters of Na, Pb, and Pb-Bi(e)

Parameter	Unit	Na	Pb	Pb-Bi(e)
T_c	K	2500 ± 12	5000 ± 200	4800 ± 500
ρ_c	kg m^{-3}	220 ± 20	3250 ± 100	2200 ± 200
p_c	MPa	25.6 ± 0.4	180 ± 30	160 ± 70

properties' recommendations to higher temperatures and pressures.

With satisfactory precision they were determined only for sodium. The available experimental data and theoretical estimations for the critical parameters of Na were reviewed in 1985 by Ohse *et al.*,³⁰ who recommended $T_{c(\text{Na})} = 2497 \pm 18$ K, $p_{c(\text{Na})} = 25.22 \pm 0.60$ MPa, and $\rho_{c(\text{Na})} = 211 \pm 2$ kg m^{-3} . Later, Fink and Leibowitz²² extended this review by including the results of new studies and analyses from Thurnay⁵³ and Petiot and Seiler⁵⁴ and suggested to use $T_{c(\text{Na})} = 2503.7 \pm 12$ K, $p_{c(\text{Na})} = 25.64 \pm 0.40$ MPa, and $\rho_{c(\text{Na})} = 219 \pm 20$ kg m^{-3} . In the recent compilation of IAEA,²⁶ the Na critical parameters are reproduced from the earlier review.³⁰ The rounded within uncertainty values from the review of Fink and Leibowitz²² are recommended in the present compilation (see Table 6).

A lot of studies were performed to determine the critical point of lead, but the obtained results show a large variation. In 1990, Pottlacher and Jäger⁵⁵ published a summary of experimentally determined and theoretically estimated parameters for the critical point of lead available in the literature as of that date. They considered 16 sets of data as well as their

own estimations based on the experimental results obtained using the pulse-heating technique. Their summary shows that the experimental and theoretical data on the critical temperature of lead lie within the range of 3584–6000 K, while their own estimation yields $T_{c(\text{Pb})} = 5400 \pm 400$ K. For the Pb critical pressure and density, they recommend $p_{c(\text{Pb})} = 250 \pm 30$ MPa and $\rho_{c(\text{Pb})} = 3200 \pm 300$ kg m^{-3} . Morita *et al.*⁵⁶ analyzed the previous and later publications using different methods to estimate the critical parameters of lead. The IAEA compilation²⁶ suggests to use $T_{c(\text{Pb})} = 5000 \pm 200$ K, $p_{c(\text{Pb})} = 180 \pm 30$ MPa, and $\rho_{c(\text{Pb})} = 3250 \pm 100$ kg m^{-3} with the reference to the handbook of Babichev *et al.*⁵⁷ These values give good compromise and they were selected in the present compilation (see Table 6).

Only theoretical estimations were found in the open literature for the critical parameters of Pb-Bi(e).^{24,52,56,58} Based on these studies and on the conclusions of the report,³⁴ the following values and uncertainties are recommended for the critical temperature, pressure, and density of Pb-Bi(e): $T_{c(\text{Pb-Bi})} = 4800 \pm 500$ K, $p_{c(\text{Pb-Bi})} = 160 \pm 70$ MPa, and $\rho_{c(\text{Pb-Bi})} = 2200 \pm 200$ kg m^{-3} . The recommended values of the critical parameters of Na, Pb, and Pb-Bi(e) are summarized in Table 6.

2.14.4 Thermodynamic Properties

The main thermodynamic properties of the considered LM (such as density, thermal expansion, heat capacity, enthalpy, surface tension, sound velocity,

and compressibility) are measured with satisfactory precision in the region close to normal melting temperature. (An exception is the saturated vapor pressure, which is well measured for Na, but not so well for the other two LM: Pb and especially for Pb–Bi(e) at low temperatures – see [Section 2.14.3.2](#).)

2.14.4.1 Density and Thermal Expansion

The temperature and pressure dependence of density allows directly the construction of a thermal EOS. At normal atmospheric pressure, the density was measured better than other properties for all three liquid metal coolants of interest. For Na and Pb, the experimental data are available from normal melting point up to normal boiling point^{7–11,22–26} and even up to higher temperatures⁵⁹; for Pb–Bi(e), the upper temperature limit is about 1300 K,²⁴ that is more than 600 K below its normal boiling point.

At normal atmospheric pressure (p_0), the temperature dependence of the density (ρ) of most of normal LM can be described with an uncertainty of 1–3% by a linear correlation:

$$\rho(T, p_0) = \rho_{M,0} - A_{\rho,0}(T - T_{M,0}) \quad [4]$$

where $\rho_{M,0}$ is the density at normal melting temperature and $A_{\rho,0}$ is a constant.

The isobaric volumetric coefficient of thermal expansion (CTE) is, by definition, expressed through the density as follows:

$$\alpha_p(T, p) \equiv -\frac{1}{\rho(T, p)} \left(\frac{\partial \rho(T, p)}{\partial T} \right)_p \quad [5]$$

Substitution of ρ in eqn [5] by correlation [4] yields for CTE at normal atmospheric pressure:

$$\alpha(T, p_0) = \frac{1}{\frac{\rho_{M,0}}{A_{\rho,0}} + T_{M,0} - T} \quad [6]$$

Sometimes, more complicated correlations are used to estimate a liquid metal density on the saturation line at high temperatures in the region close to the critical point.^{22,59}

Recent reviews of literature data on the thermophysical properties of liquid Na,²² Pb, and Pb–Bi(e)^{24,26,34} show that the uncertainty of correlation [4] at normal atmospheric pressure is about 0.3–3% for Na and 0.7–0.8% for Pb and Pb–Bi(e) in the aforementioned temperature ranges. The recommended coefficients³⁴ of the correlations [4] and [6] are given in [Table 7](#), and the density and the isobaric

Table 7 Coefficients of the correlations [4] and [6] for the temperature dependence of density and the isobaric volumetric coefficient of thermal expansion of liquid Na, Pb, and Pb–Bi(e) at normal atmospheric pressure

Parameter	Unit	Na	Pb	Pb–Bi(e)
$T_{M,0}$	K	371.0	600.6	398
$\rho_{M,0}$	kg m ^{−3}	927.0	10 671	10 550
$A_{\rho,0}$	kg m ^{−3} K ^{−1}	0.235	1.2795	1.293

volumetric CTE of Na, Pb, and Pb–Bi(e) are presented as a function of temperature in [Figures 4](#) and [5](#), respectively.

Densities of the liquid metal coolants of interest monotonically decrease with temperature due to the increase of the interatomic distances caused by thermal expansion; the CTE increases with temperature due to reduction of the interatomic forces with the distance.

2.14.4.2 Sound Velocity and Compressibility

The velocity of the propagation of sound (u) in Na, Pb, and Pb–Bi(e) was mainly measured at normal atmospheric pressure and at temperatures below 1773 K for Na, <1423 K for Pb, and <1073 K for Pb–Bi(e).^{7,33,34,60–64} It decreases with temperature due to decreasing interatomic interactions. In the temperature range limited by the normal melting and boiling temperatures, the temperature dependence of the sound velocity in Na, Pb, and LBE is almost linear and can be presented as follows:

$$u(T, p_0) = u_{M,0} - A_{u,0}(T - T_{M,0}) \quad [7]$$

The recommended values of the sound velocity at the normal melting temperature $u_{M,0}$ and the coefficients $A_{u,0}$ of eqn [7] for liquid Na, Pb, and Pb–Bi(e) are given in [Table 8](#) and their sound velocities as a function of temperature are presented in [Figure 6](#).

Experimental results at higher temperatures were found only in a few publications. For Na, the measurements of the sound velocity were performed in the temperature range from $T_{M,0}$ up to 1773 K, and a parabolic function was proposed in Fink and Leibowitz⁷ to take into account its deviation from the linear temperature dependence. In Mustafin and Shaikhiev,⁶³ it was shown that the sound velocity in the liquid Pb can also deviate from the linear temperature dependence at high temperatures.

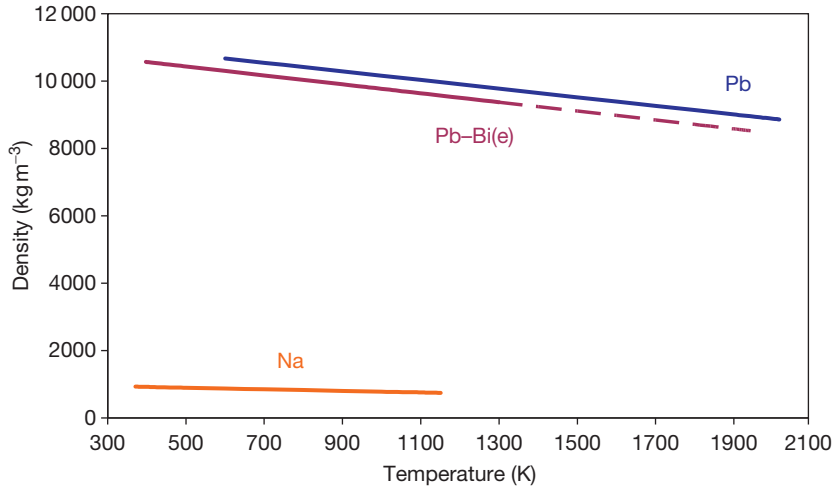


Figure 4 Density of liquid Na, Pb-Bi(e), and Pb at normal atmospheric pressure.

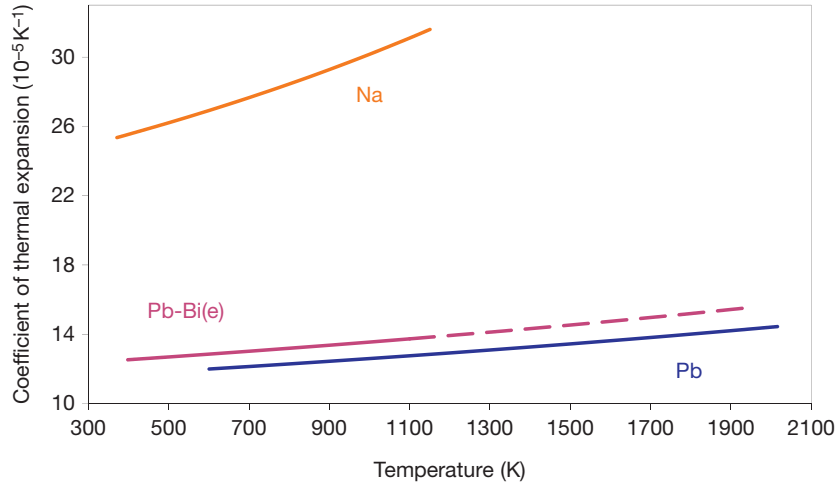


Figure 5 Isobaric volumetric coefficient of the thermal expansion of liquid Na, Pb-Bi(e), and Pb at normal atmospheric pressure.

Table 8 Coefficients of the correlation [7] for the temperature dependence of sound velocity in liquid Na, Pb, and Pb-Bi(e) at normal atmospheric pressure

Parameter	Unit	Na	Pb	Pb-Bi(e)
$T_{M,0}$	K	371.0	600.6	398
$u_{M,0}$	ms^{-1}	2526	1805	1771
$A_{u,0}$	$\text{ms}^{-1} \text{K}^{-1}$	0.5313	0.2463	0.212

The adiabatic (isentropic) compressibility β_S can be deduced from the results of the measurements of the sound velocity and density:

$$\beta_S \equiv \frac{1}{\rho} \left(\frac{\partial \rho}{\partial p} \right)_S = \frac{1}{\rho u^2} \quad [8]$$

The adiabatic compressibility of the liquid Na, Pb, and Pb-Bi(e), at normal atmospheric pressure, calculated with formula [8] and correlations [4] and [7], and using the parameters given in **Tables 7** and **8**, are presented in **Figure 7** as a function of temperature.

The isothermal compressibility can be expressed through the adiabatic compressibility (β_S), the isobaric molar heat capacity (C_p , see **Section 2.14.4.4**), the density (ρ), and the isobaric volumetric CTE (α_p , see **Section 2.14.4.1**):

$$\beta_T = \beta_S + \frac{M_a \alpha_p^2 T}{\rho C_p} \quad [9]$$

where M_a is the molar mass.

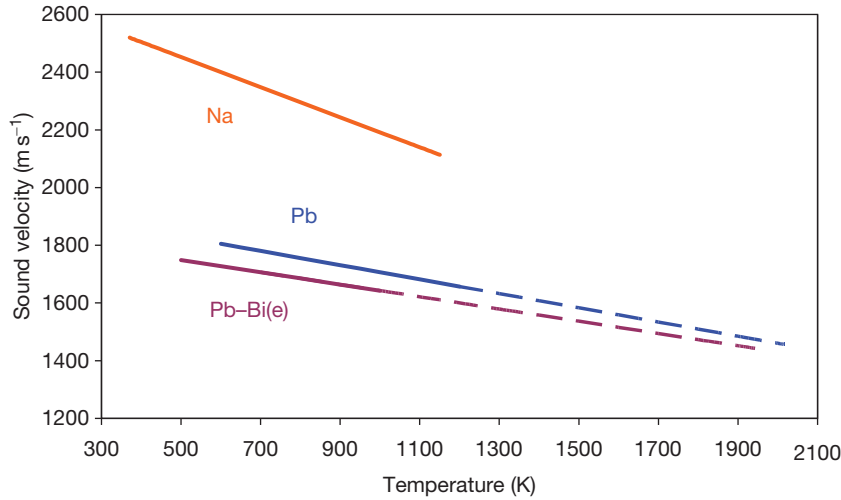


Figure 6 Ultrasound velocity in liquid Na, Pb-Bi(e), and Pb at normal atmospheric pressure.

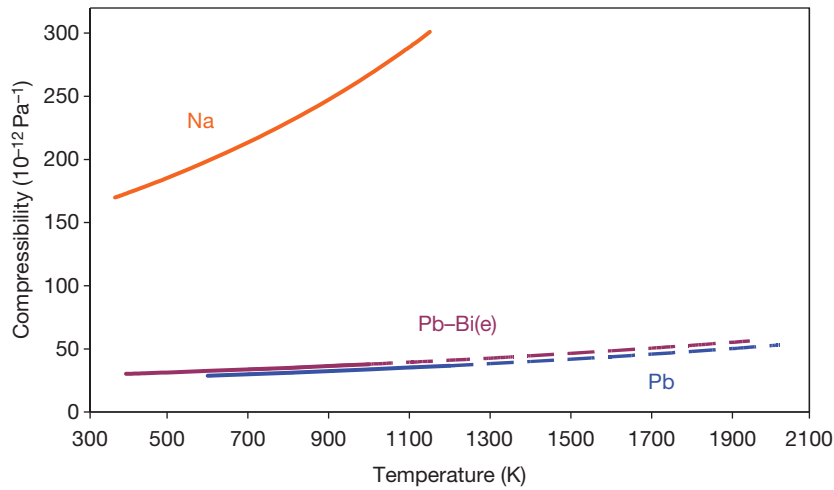


Figure 7 Adiabatic compressibility of liquid Na, Pb-Bi(e), and Pb at normal atmospheric pressure.

2.14.4.3 Surface Tension

The surface tension is a measure of the cohesive energy of atoms and correlates with the latent heat of evaporation. The surface tension of normal liquids should decrease linearly with temperature and becomes zero at critical temperature, where the difference between liquid and gas phases disappears. In accordance with Eötvös' law (cited in Iida and Guthrie²⁷), it can be presented as follows:

$$\sigma(T) = k_{\sigma} V_a^{-2/3} (T_c - T) \quad [10]$$

where V_a is the molar volume and k_{σ} is a constant, which is about the same for normal LM.

Considering liquid Na, Pb, and Pb-Bi(e) as normal liquids, a linear correlation can be recommended for the description of the temperature dependence of their surface tension:

$$\sigma(T, p_0) = \sigma_{M,0} - A_{\sigma,0} (T - T_{M,0}) \quad [11]$$

The experimental data on the surface tension of sodium were reviewed by Golden and Tokar,³ Allen,⁶⁵ Fink, and Leibowitz.²² In 1993, Keene⁶⁶ reviewed many data on the surface tension of pure metals (including Na and Pb) at normal atmospheric pressure and concluded that the linear temperature dependence is valid for most LM in the temperature range from normal melting to normal boiling

point. The available recommendations on the surface tension of Pb and Pb–Bi(e) were summarized by Sobolev and Benamati.²⁴ The surface tension of liquid Na, Pb, and Pb–Bi(e) is well measured at normal atmospheric pressure from temperatures close to their melting points up to 1100–1300 K. In this temperature range, a variation of $\pm(3\text{--}6)\%$ exists between values given by different sources. At higher temperatures, the scatter of the experimental results increases significantly. The coefficients of correlation [11] for these LM, recommended in the report³⁴ and adopted in this work, are given in Table 9, and the calculated surface tension of liquid Na, Pb, and Pb–Bi(e) at normal atmospheric pressure is presented in Figure 8 as a function of temperature.

2.14.4.4 Heat Capacity and Enthalpy

In spite of difficulties existing in the measurement of the heat capacity of LM, it was measured with a good precision for liquid Na at normal atmospheric pressure – the recommendations from different sources differ for $<1\%$ in the temperature range from normal melting point up to normal boiling

Table 9 Coefficients of the correlation [11] for the temperature dependence of the surface tension of liquid Na, Pb, and Pb–Bi(e) at normal atmospheric pressure

Parameter	Unit	Na	Pb	Pb–Bi(e)
$T_{M,0}$	K	371.0	600.6	398
$\sigma_{M,0}$	10^{-3}N m^{-1}	195	458	416.7
$A_{\sigma,0}$	$10^{-3}\text{N m}^{-1}\text{K}^{-1}$	0.0966	0.113	0.0799

point at normal atmospheric pressure.^{7,10,67} Higher uncertainty is observed at higher pressures and temperatures and on the saturation line.⁶⁸ The heat capacity of liquid Pb was satisfactorily measured only at temperatures up to about 1400 K^{5,24,48} and with a precision $\sim 5\%$. At higher temperatures, the available experimental data often give contradictory results. The heat capacity values for liquid Pb in a large range of temperatures at normal atmospheric pressure were estimated by Gurvich and Veyts⁶⁹ with theoretical models benchmarked on the existing experimental results. Available data on the heat capacity of Pb–Bi(e) are very limited.^{70–72} In order to describe the temperature dependence of LM heat capacity, often the following correlation is used:

$$C_p(T, p_0) = a_{C_p} + b_{C_p} T + c_{C_p} T^2 + d_{C_p} T^{-2} \quad [12]$$

The recommended coefficients of correlation [12] for liquid Na were taken from the compilation of IAEA,²⁶ for Pb from Gurvich and Veyts,⁶⁹ and for Pb–Bi(e), they were deduced in Sobolev³⁴ on the basis of a review of the existing data and recommendations; the coefficients are given in Table 10. The uncertainty is about $\pm 1\%$ for Na and $\pm(5\text{--}7)\%$ for Pb and Pb–Bi(e) at temperatures up to $T = 1100\text{--}1400$ K; the uncertainty increases at higher temperatures where no experimental data were found for Pb and Pb–Bi(e) in the literature.

The calculated with correlation [10] isobaric heat capacities of liquid Na, Pb, and Pb–Bi(e) are presented in Figure 9 versus temperature.

The isochoric heat capacity can be estimated using correlations for the isobaric heat capacity (C_p),

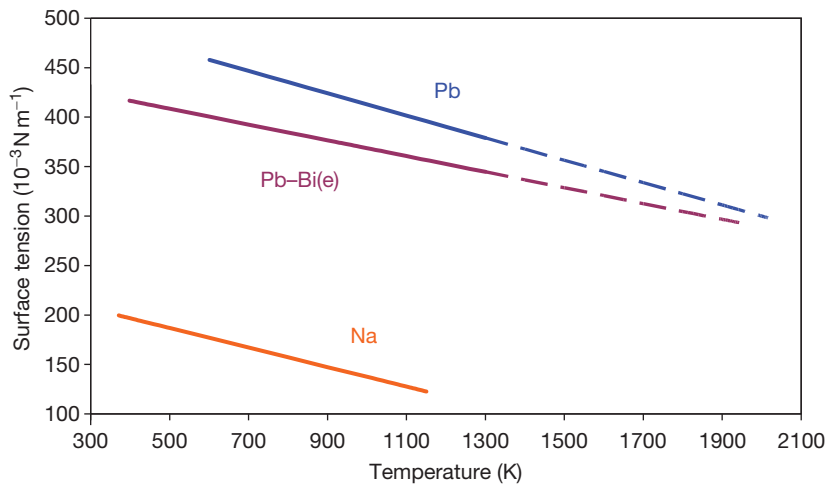
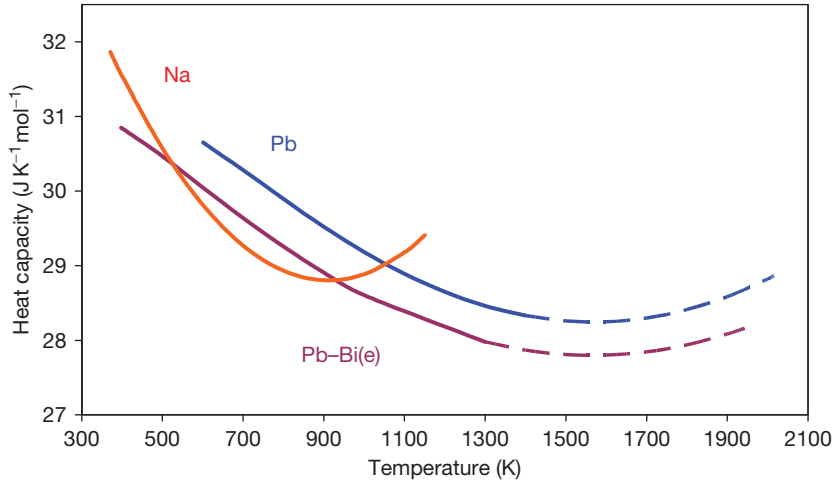


Figure 8 Surface tension of Na, Pb–Bi(e), and Pb at normal atmospheric pressure.

Table 10 Recommended coefficients of correlation [12] for the temperature dependence of the molar isobaric heat capacity of liquid Na, Pb, and Pb–Bi(e) at normal atmospheric pressure

	$a_{C_p} (JK^{-1} mol^{-1})$	$b_{C_p} (JK^{-2} mol^{-1})$	$c_{C_p} (JK^{-3} mol^{-1})$	$d_{C_p} (JK^2 mol^{-1})$
Na	38.12	-1.9493×10^{-2}	1.024×10^{-5}	-6.9×10^4
Pb–Bi(e)	34.30	-8.20×10^{-3}	2.6×10^{-6}	-9.5×10^4
Pb	36.50	-1.020×10^{-2}	3.2×10^{-6}	-3.158×10^5

**Figure 9** Isobaric heat capacity of Na, Pb–Bi(e), and Pb at normal atmospheric pressure.

the isothermal compressibility (β_T), the density (ρ), and the isobaric volumetric CTE (α_p):

$$C_V = C_p - \frac{M_a \alpha_p^2 T}{\rho \beta_T} \quad [13]$$

The molar enthalpy (H) of LM as a function of temperature at the given pressure can be presented as a sum of the LM enthalpy at the melting point $H(T_M, p)$ and the LM enthalpy increment caused by temperature increase $\Delta H(T - T_M, p)$, which is expressed through an integral of the isobaric heat capacity over temperature:

$$\begin{aligned} H(T, p) &= H(T_M, p) + \Delta H(T - T_M, p) \\ &= H(T_M, p) + \int_{T_M}^T C_p(T, p) dT \\ &= H(T_M, p) + a_{C_p}(T - T_M) + \frac{b_{C_p}}{2}(T^2 - T_M^2) \\ &\quad + \frac{c_{C_p}}{3}(T^3 - T_M^3) + d_{C_p} \left(\frac{1}{T_M} - \frac{1}{T} \right) \end{aligned} \quad [14]$$

The temperature dependence of $\Delta H(T - T_{M,0})$ for liquid Na, Pb, and Pb–Bi(e), calculated with

formula [14] at normal atmospheric pressure, is shown in [Figure 10](#).

2.14.4.5 Equation of State

During the past years, considerable progress has been achieved in the development of empirical, semi-empirical, and mechanistic EOS for fluids. Simple thermal EOS is frequently used in engineering practice, which relates the main TD variables pressure, temperature, and volume (or density): $F(p, T, \rho) = 0$, which is equivalent to $\rho = \rho(T, p)$ considered in [Section 2.14.4.1](#). Knowledge of the temperature and pressure dependence of one of the thermodynamic potentials (e.g., enthalpy H) allows to construct the caloric EOS: $H = H(T, p)$.

2.14.4.5.1 Low pressures

At low pressures, the simplest approach to construct a simple thermal EOS is to use available information on temperature and pressure dependence of density:

$$\rho(p, T) \approx \int_{T_0}^T \left(\frac{\partial \rho}{\partial T} \right)_p dT + \int_{p_0}^p \left(\frac{\partial \rho}{\partial p} \right)_T dp \quad [15]$$

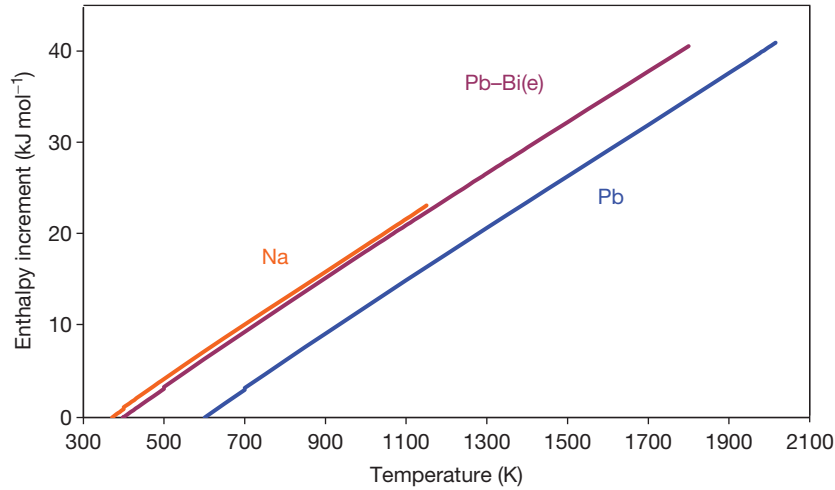


Figure 10 Enthalpy increase with temperature for liquid Na, Pb–Bi(e), and Pb at normal atmospheric pressure.

The first term on the right-hand side is described by eqn [5] in Section 2.14.4.1. The effect of pressure can be estimated using the information on the sound velocity, thermal expansion, and heat capacity, with the following thermodynamic relationship:

$$\left(\frac{\partial \rho}{\partial p}\right)_T = \left(\frac{1}{u^2(T)} + \frac{M_a T \alpha_p^2(T)}{C_p(T)}\right) \quad [16]$$

The results of the calculation of the pressure coefficient [16] for liquid Na, Pb, and Pb–Bi(e) show³⁴ that it is rather small: the density correction does not exceed 0.04% per 1 MPa of pressure for Na and 0.01% per 1 MPa for Pb and Pb–Bi(e) in the temperature range of the normal operation of these coolants in Gen IV reactors. Thus, at normal operation pressures of these reactors (0.1–2.0 MPa), the thermal EOS developed at normal atmospheric pressure can be used for design estimations.

2.14.4.5.2 High pressures

The results presented earlier are valid only for the liquid phase and under condition that thermodynamic coefficients do not depend on pressure. In order to take into account the pressure dependence of the LM thermodynamic parameters, different thermal EOS were developed and applied to LM. Two main directions were followed with more success: the generalization of the well-known EOS of Van der Waals (VdW) and the use of statistical mechanics and intermolecular potentials for EOS development.

The generalized three-parameter VdW EOS was used by Martynyuk⁷³ to find the critical parameters

of many pure metals (including Na and Pb). Morita and Fischer⁷⁴ proposed a modification for the EOS of Redlich and Kwong⁷⁵ to describe a metal vapor with dimer and monomer molecules and applied it for Na coolant. Later, this approach was extended by Morita *et al.* to Pb–Bi(e)⁵² and to Pb.⁵⁶ A simple EOS for liquid phase was developed by Srinivasan and Ganesan⁷⁶ based on the concept of the internal pressure of liquids and applied to sodium. Later, it was used by Azad⁵⁸ for the calculation of the critical temperatures of Pb and Pb–Bi(e).

Eslami⁷⁷ applied a perturbed hard-sphere-chain EOS developed by Song *et al.*⁷⁸ to calculate the density of liquid Na and Pb on the saturation line up to very high pressures.

Comparison of different approaches shows that better results in large temperature and pressure ranges can be obtained with the modified Redlich and Kwong EOS⁷⁴ and with the perturbed hard-sphere-chain EOS.⁷⁸

2.14.5 Transport Properties

The most important transport properties of liquid metal coolants are viscosity, thermal conductivity, and electric resistance.

2.14.5.1 Viscosity

Accurate and reliable data on the viscosity of LM are not abundant. Some discrepancies between experimental data can be attributed to the high reactivity of metallic liquids, to the difficulty of taking

precise measurements at elevated temperatures. All three LM: Na, Pb, and Pb–Bi(e), are believed to be Newtonian liquids and the temperature dependence of their dynamic viscosity (η) is usually described by an Arrhenius-type equation:

$$\eta(T, p) = \eta_{\infty}(p) \exp(E_{\eta}(p)/RT) \quad [17]$$

where E_{η} is the activation energy of motion for normal viscous flow and η_{∞} – the asymptotic value of η at $T \rightarrow \infty$. In a large temperature range, a more complicated formula is often used for more precise fitting of the experimental results on LM dynamic viscosity:

$$\eta(T, p) = \frac{A_{\eta}}{T^n} \exp(E_{\eta}(p)/RT) \quad [18]$$

where A_{η} and n are constants.

The viscosity of liquid Na at normal atmospheric pressure was well measured in the liquid range from normal melting point to normal boiling point at normal atmospheric pressure^{3,6–8,11,22,26,79}; the variation in the most reliable recommendations does not exceed $\pm 5\%$.³⁴

Data on the viscosity of Pb and Pb–Bi(e) were reviewed in Sobolev and Benamati²⁴ and Imbeni *et al.*⁴⁸; it was measured up to about 1270 K for

lead⁷⁹ and up to 1180 K for Pb–Bi(e).⁸⁰ A good agreement exists among the different sets of experimental data and the values calculated by means of the empirical equations reported in different publications. In the temperature range from $T_{M,0}$ to 1270 K, the viscosity of liquid Pb can be described with the Arrhenius-type eqn [17] with uncertainty of $\pm 5\%$. A higher variation (7–10%) exists between the values and recommendations given by different sources for Pb–Bi(e).

The recommended coefficients of correlation [17] are given in Table 11, and the calculated temperature behavior of the dynamic viscosity of liquid Na, Pb, and Pb–Bi(e) is presented in Figure 11.

In engineering hydrodynamics, the kinematic viscosity (ν) is also often used, which is a ratio of the liquid dynamic viscosity to the density:

$$\nu(T, p) = \frac{\eta(T, p)}{\rho(T, p)} \quad [19]$$

The kinematic viscosities of liquid Na, Pb, and Bi versus temperature at normal atmospheric pressure, calculated with formula [19], and the recommended correlation for their dynamic viscosities and densities presented earlier, are presented in Figure 12.

Table 11 Coefficients of the correlation [17] for the temperature dependence of the dynamic viscosity of liquid Na, Pb, and Pb–Bi(e) at normal atmospheric pressure

Parameter	Unit	Na	Pb	Pb–Bi(e)
$T_{M,0}$	K	371.0	600.6	398
$\eta_{\infty,0}$	10^{-3} Pa s	0.0844	0.455	0.494
$E_{\eta,0}$	J	6500	8888	6270

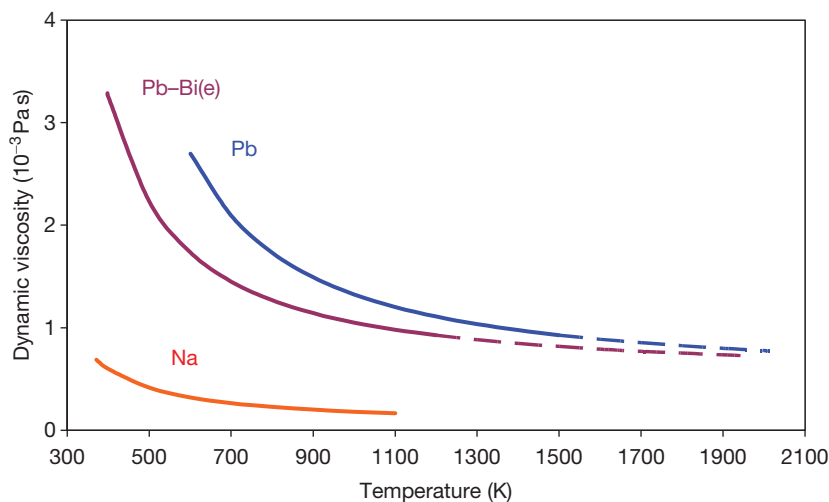


Figure 11 Dynamic viscosity of liquid Na, Pb–Bi(e), and Pb at normal atmospheric pressure.

2.14.5.2 Electric Conductivity

Metals are characterized by a very low electrical resistance, which increases with temperature and about doubles as a consequence of melting. In general, the electrical resistivity of LM increases, when impurities enter the melt. However, in the case of a liquid

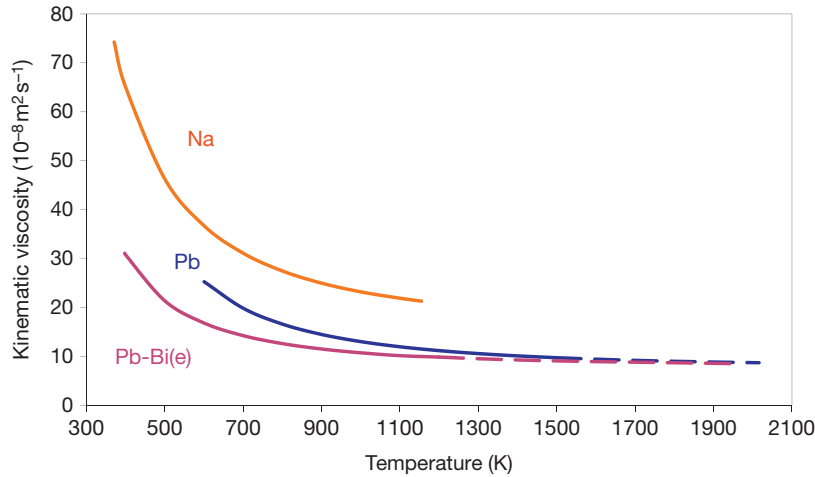


Figure 12 Kinematic viscosity of liquid Na, Pb-Bi(e), and Pb at normal atmospheric pressure.

alloy system that is composed of polyvalent components' the resistivity sometimes shows a negative deviation from the additivity of the components' resistivities. The electrical resistivity of LM with rare exceptions (such as Na) increases almost linearly with temperature below the boiling temperature; at high temperatures close to the boiling point, it can increase more rapidly. In many cases, the parabolic function can be used:

$$r(T, p) = r_M + A_r(T - T_M) + B_r(T - T_M)^2 \quad [20]$$

In 1985, the data on the electric resistivity of liquid Na were estimated by Ho and James.⁸² Later, Bretonnet⁸³ reviewed different sources to obtain correlations for the electric resistivity of many pure LM and found that a linear function could be used in most cases. However, for Na, the use of a parabolic function was proposed, which describes its electric resistivity with an uncertainty <4% in the temperature range from normal melting to normal boiling point.³⁴

The electric resistivity of liquid lead at normal atmospheric pressure was measured rather well from the melting point up to about 1300 K. In this temperature range, it can be described with a linear function with an uncertainty <2%.³⁴ The precision of data obtained at high temperatures is lower, and they indicate a more rapid increase of the Pb electric resistivity with temperature.⁸⁴ Only a few reliable data sources exist on the electric resistivity of Pb-Bi(e), which are limited to a temperature of 1073 K.^{25,70,85} The difference between these sources is about 7–8%.

The coefficients of correlation [20] for liquid Na, Pb, and Pb-Bi(e), at normal atmospheric pressure, taken from Sobolev,³⁴ are presented in Table 12;

Table 12 Coefficients of the correlation [20] for the temperature dependence of the electrical resistivity of liquid Na, Pb, and Pb-Bi(e) at normal atmospheric pressure

Parameter	Unit	Na	Pb	Pb-Bi(e)
$T_{M,0}$	K	371.0	600.6	398
$r_{M,0}$	$10^{-8} \Omega \text{ m}$	9.69	95.3	110.0
$A_{r,0}$	$10^{-8} \Omega \text{ m K}^{-1}$	0.02917	0.0471	0.048
$B_{r,0}$	$10^{-8} \Omega \text{ m K}^{-2}$	3.093×10^{-5}	–	–

Figure 13 illustrates the temperature dependence of the calculated electrical resistivities.

2.14.5.3 Thermal Conductivity

The experimental determination of the thermal conductivity of LM is very difficult because of the problems related to convection and to wetting, therefore large discrepancies exist between different sets of data. The high thermal conductivity of LM is mainly due to free electrons. A simple theoretical relation exists for pure metals between electrical and thermal conductivities, known as the Wiedemann–Franz–Lorenz (WFL) law:

$$\lambda_e = L_0 T / r \quad [21]$$

where λ_e is the electronic thermal conductivity, r is the electrical resistivity, and $L_0 = 2.45 \times 10^{-8} \text{ W } \Omega \text{ K}^{-2}$ is the Lorenz number.

With reasonable uncertainties, this law has been confirmed for many LM, taking into account the fact that the contribution of phonons to the thermal conductivity of the metals of interest is small. Therefore, the approximate prediction of the thermal

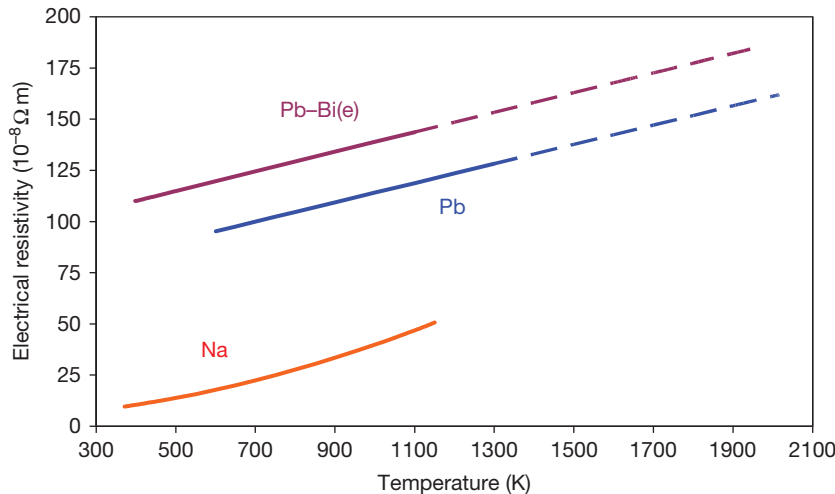


Figure 13 Electric resistivity of liquid Na, Pb-Bi(e), and Pb at normal atmospheric pressure.

conductivity of LM and several alloys is possible by combining WFL law and the existing, reliable values of the electrical resistivity.

Valuable recommendations for the thermal conductivity of Na, Pb, and Pb-Bi(e) based on the available at this time experimental data were published by Touloukian *et al.*⁸⁶ in 1970 and for Na by Cook and Fritsch⁸⁷ in 1985. Later, Mills *et al.*⁸⁸ took the first publication as the starting point and reestimated recommendations for the thermal conductivity of many LM. Fink and Leibowitz²² examined the recommendations from various assessments for the thermal conductivity of liquid Na and concluded that significant differences (up to $\pm 15\%$) exist over the range of experimental data (371–1500 K). Available data on the thermal conductivity of liquid Pb and Pb-Bi(e) were also analyzed by Sobolev *et al.*^{23,24} in the temperature range from $T_{M,0}$ to 1300 K. It was found that all data on the Pb thermal conductivity were in good agreement close to the melting temperature; however, they differed in the temperature dependence and some of them were in serious contradiction with WFL law. These anomalies were explained by the effects of impurities, oxidation and by not relevant experimental conditions and techniques. In an effort to find a physically reasonable compromise between the available data and taking into account the WFL law, the linear correlation was recommended for the thermal conductivity of a pure liquid, which allows to describe the most reliable data with the maximum difference of $\pm 15\%$ in the temperature range of $T_{M,0}$ –1300 K. At present, few experimental

Table 13 Coefficients of the correlation [22] for the temperature dependence of the thermal conductivity of liquid Na, Pb, and Pb-Bi(e) at normal atmospheric pressure

Parameter	Unit	Na	Pb	Pb-Bi(e)
$T_{M,0}$	K	371.0	600.6	398
$\lambda_{M,0}$	$\text{W m}^{-1} \text{K}^{-1}$	86.7	15.8	9.35
$A_{\lambda,0}$	$\text{W m}^{-1} \text{K}^{-2}$	0.0466	0.011	0.01434
$B_{\lambda,0}$	$\text{W m}^{-1} \text{K}^{-3}$	–	–	2.305×10^{-6}

data are available on the thermal conductivity of liquid Pb-Bi(e). A nonnegligible difference exists between different recommendations at lower temperatures. The parabolic function can describe the temperature dependence of the Pb-Bi(e) thermal conductivity up to 1100 K with an uncertainty of 10–15%. The WFL law can be used for an estimate of the Pb-Bi(e) thermal conductivity with the same precision. In the report,³⁴ the following correlation was used to describe the temperature dependence of the thermal conductivities of liquid Na, Pb, and Pb-Bi(e) at normal atmospheric pressure:

$$\lambda(T, p_0) = \lambda_{M,0} + A_{\lambda,0}(T - T_{M,0}) + B_{\lambda,0}(T - T_{M,0})^2 \quad [22]$$

The parameters of this correlation are presented in Table 13. In Figure 14, the recommended values of the thermal conductivity of liquid Na, Pb, and Pb-Bi(e) are presented as a function of temperature.

In nonstationary thermal calculations, the thermal diffusivity is often used, which is defined as follows:

$$a_p(T, p) \equiv \frac{\lambda(T, p)M_a}{\rho(T, p)C_p(T, p)} \quad [23]$$

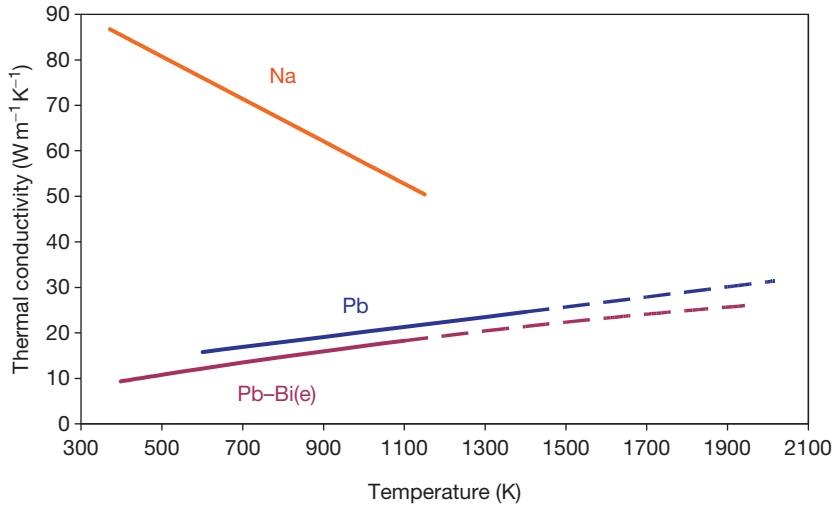


Figure 14 Thermal conductivity of liquid Na, Pb-Bi(e), and Pb at normal atmospheric pressure.

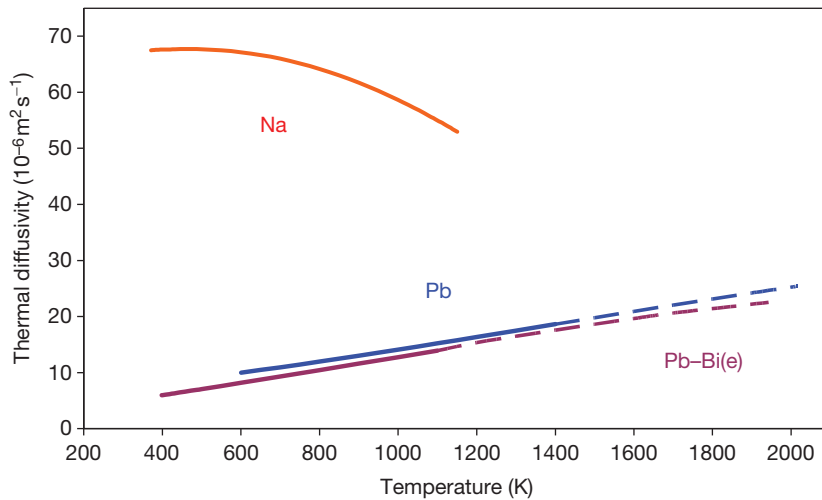


Figure 15 Thermal diffusivity of liquid Na, Pb-Bi(e), and Pb at normal atmospheric pressure.

The thermal diffusivities of the considered LM calculated at normal atmospheric pressure with the recommended correlations presented earlier are presented in [Figure 15](#).

2.14.6 Conclusions

For liquid Na, Pb, and Pb-Bi(e), the experimental data and correlations for the prediction of their thermophysical parameters of interest are available in the temperature region of the normal operation of nuclear installations. In spite of the fact that most of the properties were mainly measured at atmospheric

pressure and some of them have not yet been determined with the needed accuracy, the proposed recommended correlations can be used for the predesign calculations of Gen IV nuclear installations with these coolants.

The simplified EOS can be applied for the prediction of the effect of pressure far away from the critical point in the pressure and temperature range typical for normal and abnormal operation of new generation power nuclear reactors with LM coolants. However, for the prediction of the properties of the Pb and Pb-Bi(e) coolants at higher temperatures and pressures, which can be potentially reached under accidental conditions, the existing

EOS can be used with utmost care. In order to improve the precision of EOS, the critical parameters of Pb and Pb–Bi(e) should be determined with lower uncertainty.

Acknowledgments

This work was supported by funds of the SCK-CEN project MYRRHA and by the EURATOM FP6 projects ELSY and IP EUROTRANS.

References

1. *A Technology Roadmap for Generation IV Nuclear Energy Systems*. USDOE Nuclear Energy Research Advisory Committee and the Generation IV International Forum, 2002; GIF-002-00.
2. *Fast Reactor Facilities in Russia and Former Soviet Union*. Argonne National Laboratory, International Nuclear Safety Centre: Argonne, IL, 1995.
3. Golden, G. H.; Tokar, J. V. *Thermophysical Properties of Sodium*; Report of Argonne National Laboratory, ANL-7323; National Bureau of Standards: Springfield, 1967.
4. Shpil'rain, E. E.; Yakimovitch, K. A.; Toskij, E. E.; Timrot, D. L.; Fomin, V. A. *Thermophysical Properties of Alkali Metals*; Standard Press: Moscow, 1970.
5. Hultgren, R.; Desai, P. D.; Hawkins, D. T.; et al. *Selected Values of the Thermodynamic Properties of the Elements*; Wiley: New York, NY, 1973.
6. Vargaftik, N. B. *Tables on Thermophysical Properties of Liquids and Gases*; Wiley: New York, NY, 1975.
7. Fink, J. K.; Leibowitz, L. *Thermophysical Properties of Sodium*; Report of Argonne National Laboratory, ANL-CEN-RSD-79-1; ANL: Argonne, IL, 1979.
8. Thurnay, K. *Thermophysical Properties of Sodium in the Liquid and Gaseous States*; Report of Kernforschungszentrum Karlsruhe GmbH, KfK 2863; KfK: Karlsruhe, 1981.
9. Ohse, R. L. Ed. *Handbook of Thermodynamic and Transport Properties of Alkali Metals*; International Union of Pure and Applied Chemistry, Blackwell Scientific: Boston, MA, 1985.
10. Cordfunke, E. H. P.; Konings, R. J. M. *Thermochemical Data for Reactor Materials and Fission Products*; North Holland/Elsevier Science: New York, NY, 1990.
11. Bystrov, P.; Kagan, D. N.; Krechetova, G. A.; Shpil'rain, E. E. In *Liquid-Metal Coolants for Heat Pipes and Power Plants*; Kirilin, V. A., Ed.; Hemisphere: New York, NY, 1990 (Translated from Russian; Bystrov, P. M.; Kagan, D. N.; Krechetova, G. A.; Shpil'rain, E. E. In *Liquid Metal Coolants of Heat Pipes and Power Plants*; Kirilin, V. A., Nauka, M., Eds.; 1988.)
12. Orlov, V. V.; Leonov, V. N.; Sila-Novitskij, A. G.; Smirnov, A. G.; Filin, A. I.; Tsikunov, V. S. In *Proceedings of the International Conference on Heavy Liquid Metal Coolants in Nuclear Technology – HLMC'98*, Obninsk, Russian Federation, Oct 5–9, 1998; SSC RF – IPPE: Obninsk, 1999; Vol. 2, pp 462–469.
13. Zrodnikov, A. V.; Toshinskii, G. I.; Grigor'ev, O. G.; et al. *Atom. Energ.* **2004**, 97, 528–533.
14. Takahashi, M.; Uchida, S. *Bull. Res. Lab. Nucl. Reactors* **2006**, 30, 206–212.
15. Nakazima, T.; Rivai, A. K.; Hata, K.; Dostal, V.; Takahashi, M. Study plan for material corrosion test in lead and bismuth eutectic at high temperature. In *Proceedings of the Fourteenth International Conference on Nuclear Engineering – ICONE 14*, Miami, FL, July 17–20, 2006; Paper 89420.
16. Sekimoto, H.; Ryu, K.; Yoshimura, Y. *Nucl. Sci. Eng.* **2001**, 139, 306–317.
17. Lim, J. Y.; Kim, M. H. *Progr. Nucl. Energ.* **2007**, 49, 230–245.
18. Yu, Y. H.; Son, H. M.; Lee, I. S.; Suh, K. Y. Optimized battery-type reactor primary system design utilizing lead. In *Proceedings of the International Conference on Advances in Nuclear Power Plants – ICAPP'06*, Reno, NV, June 4–8 2006; Paper 6148.
19. Sienicki, J. J.; Moiseyev, A. V. SSTAR lead-cooled, small modular fast reactor for deployment at remote sites – system thermal hydraulic development. In *Proceedings of the International Conference on Advances in Nuclear Power Plants – ICAPP'05*, Seoul, Korea, May 15–19, 2005; Paper 5426.
20. Cinotti, L.; Smith, C. F.; Sienicki, J. J.; et al. The potential of LFR and ELSY project. In *Proceedings of the International Congress on Advances in Nuclear Power Plants – ICAPP'07*, Nice, France, May 13–18, 2007; Paper 7585.
21. Cinotti, L.; Locatelli, G.; Ait Abderrahim, H.; et al. Lead fast reactor. In *Proceedings of the Conference on EU Research and Training in Reactor Systems – FISA 2006*, Luxembourg, Mar 13–16, 2006; Luxembourg, Document EUR 21231, FISA 2006, European Commission.
22. Fink, J. K.; Leibowitz, L. *Thermodynamic and Transport Properties of Sodium Liquid and Vapour*; Report of Argonne National Laboratory, ANL/RE-95/2; ANL: Argonne, IL, 1995.
23. Sobolev, V. J. *Nucl. Mater.* **2007**, 362, 235–247.
24. Sobolev, V.; Benamati, G. In *Handbook on Lead-Bismuth Eutectic Alloy and Lead Properties, Materials Compatibility, Thermal Hydraulics and Technologies*; Fazio, C., Ed.; OECD: Paris, France, 2007; Chapter 2, pp 25–99, NEA No. 6195. (The updated version is in preparation and planned to be published in the end of 2011.)
25. Bogoslovskaja, G.; Kirillov, P. L.; Kupitz, J. et al. Eds. *Comparative Assessment of Thermophysical and Thermohydraulic Characteristics of Lead, Lead-Bismuth and Sodium Coolants for Fast Reactors*; IAEA: Vienna, 2002; IAEA-TECDOC-1289.
26. Kirillov, P. L.; Bobkov, V. P.; Fokin, L. R.; Popov, V. V.; Rumiantsev, V. N.; Savvatimsky, A. I. Eds. *Thermophysical Properties of Materials for Nuclear Engineering: A Tutorial and Collection of Data*; IAEA-THPH: Vienna IAEA, 2008.
27. Iida, T.; Guthrie, R. I. L. *The Physical Properties of Liquid Metals*; Clarendon Press: Oxford, UK, 1988.
28. Hofmann, W. *Lead and Lead Alloys*; Springer: New York, Berlin, 1970.
29. Gale, W. F.; Totemeier, T. C. Eds. *Smithells Metals Reference Book*, 8th ed.; Elsevier: Amsterdam, 2004.
30. Ohse, R. W.; Babelot, J. F.; Magill, J.; Tetenbaum, M. In *Handbook of Thermodynamic and Transport Properties of Alkali Metals*; Ohse, R. W., Ed.; International Union of Pure and Applied Chemistry, Blackwell Scientific: Boston, MA, 1985; Chapter 6.1, pp 329–347.
31. Gokcen, N. A. *J. Phase Equil.* **1992**, 13, 21–32.
32. Sklyarchuk, V.; Plevachuk, Yu.; Gerberth, G.; Eckert, S. *J. Phys. Conf. Ser.* **2007**, 79, 012019.
33. Sobolev, V.; Schuurmans, P.; Benamati, G. *J. Nucl. Mater.* **2008**, 376, 358–362.

34. Sobolev, V. *Database of Thermophysical Properties of Liquid Metal Coolants for GEN-IV*; Report of SCK-CEN BLG-1069; SCK-CEN: Mol, Belgium, 2010.
35. Stølen, S.; Grønvold, F. *Thermochim. Acta* **1999**, *327*, 1–32.
36. Cevolani, S. *Review of the Liquid Lead-Bismuth Alloy Physical Properties*; Report of ENEA, DT.SBD.00004; ENEA: Brasimone, 1998.
37. Ponyatovskiy, Y. G. *The Melting Points of Lithium and Sodium Under Pressures up to 30,000 kg/cm²*; Report of Defense Technical Information Center, Accession Number AD0261833; DTIC: Fort Belvoir, VA, 1961.
38. Mirwald, P. W.; Kennedy, G. C. *J. Phys. Chem. Solids* **1976**, *37*, 795–797.
39. Zha, C. S.; Boehler, R. *Phys. Rev. B* **1985**, *31*, 3199–3201.
40. Akella, J.; Ganguly, J.; Grover, R.; Kennedy, G. *J. Phys. Chem. Solids* **1973**, *34*, 631–636.
41. Ponyatovsky, E. G.; Rabinkin, A. G. *Fiz. Met. Metalloved.* **1970**, *30*, 606–613.
42. Gregoryanz, E.; Degtyareva, O.; Somayazulu, M.; Hemley, R. J.; Mao, H.-K. *Phys. Rev. Lett.* **2005**, *94*, p 4, 185502.
43. Hicks, W. T. *J. Chem. Phys.* **1963**, *38*, 1873–1979.
44. Browning, P.; Potter, P. E. In *Handbook of Thermodynamic and Transport Properties of Alkali Metals*; Ohse, R. W., Ed.; International Union of Pure and Applied Chemistry, Blackwell Scientific: Boston, MA, 1985; Chapter 6.2, pp 349–358.
45. Vargaftik, N. V.; Voljak, L. D. In *Handbook of Thermodynamic and Transport Properties of Alkali Metals*; Ohse, R. W., Ed.; International Union of Pure and Applied Chemistry, Blackwell Scientific: Boston, MA, 1985; Chapter 6.6.1, pp 535–576.
46. Kubaschewski, O.; Alcock, C. B. In *Metallurgical Thermochemistry*, 5th ed.; Pergamon Press: Oxford, UK, 1979.
47. Cheynet, B.; Dubois, J. D.; Milesi, M. *Donnees thermodynamiques des elements chimiques, Techniques de L'Ingénieur, Matériaux métalliques*. No. M153, Form M64, 1996.
48. Imbeni, V.; Martini, C.; Masini, S.; Palombarini, G. Stato dell'arte sulle proprietà chimico-fisiche del Pb e Pb–Bi. Parte I. Proprietà di Pb, Bi, Li, Na, in Studio di un acceleratore superconduttivo di protoni di grande potenza e studio di un sistema sottocritico da esso sostenuto per il bruciamento dei residui radioattivi; Report of ENEA, DT-EUB-00001; ENEA: Bologna, 1998.
49. Tupper, R. B.; Minushkin, B.; Peters, F. E.; Kardos, Z. L. In *Proceedings of the International Conference on Fast Reactors and Related Fuel Cycles*, Kyoto, Japan, Oct 28–Nov 1, 1991; Westinghouse Electric: Madison, WI, 1991; Vol. 4, pp 5.6–1–5.6–9.
50. Orlov, Y. I. *Presentations for the Seminar on the Concept of Lead-Cooled Fast Reactor*, Cadarache, France, Sept 22–23, 1997; CEA: Cadarache, 1991.
51. Ohno, S.; Miyahara, S.; Kurata, Y. *J. Nucl. Sci. Technol.* **2005**, *42*, 593–599.
52. Morita, K.; Maschek, W.; Flad, M.; et al. *J. Nucl. Sci. Technol.* **2006**, *43*, 526–536.
53. Thurnay, K. *Nucl. Sci. Eng.* **1982**, *82*, 181–189.
54. Petiot, F.; Seiler, J. M. *High Temp. High Press.* **1984**, *16*, 289–293.
55. Pottlacher, G.; Jäger, H. *Int. J. Thermophys.* **1990**, *11*, 719–729.
56. Morita, K.; Sobolev, V.; Flad, M. *J. Nucl. Mater.* **2007**, *362*, 227–234.
57. Babichev, A. P.; Babushkin, N. A.; Bratkovsky, A. M.; et al. In *Reference Book*; Grigoriev, I. S., Meilikhov, E. Z., Eds.; Energoatomizdat: Moscow, 1990; (in Russian).
58. Azad, A. M. *J. Nucl. Mater.* **2005**, *341*, 45–52.
59. Shpil'rain, E. E.; Yakimovich, K. A.; Fomin, V. A.; Skovorodjko, S. N.; Mozgovo, A. G. In *Handbook of Thermodynamic and Transport Properties of Alkali Metals*; Ohse, R. W., Ed.; International Union of Pure and Applied Chemistry, Blackwell Scientific: Boston, MA, 1985; Chapter 6.3.3, pp 435–469.
60. Beyer, R. T.; Ring, E. M. In *Liquid Metals*; Beer, S. Z., Ed.; Marcel Dekker: New York, NY, 1972; pp 411–430.
61. Beyer, R. T. In *Handbook of Thermodynamic and Transport Properties of Alkali Metals*; Ohse, R. W., Ed.; International Union of Pure and Applied Chemistry, Blackwell Scientific: Boston, MA, 1985; Chapter 6.5.1, pp 525–528.
62. Greenberg, Y.; Yahel, E.; Ganor, M.; et al. *J. Non-Crystalline Solid* **2008**, *354*, 4094–4100.
63. Mustafin, G. M.; Shaikhiev, G. F. *Russ. J. Phys. Chem.* **1983**, *45*, 421–423.
64. Stremousov, V. I.; Solomin, B. A. *Zh. Fiz. Khimii* **1975**, *XLIX*(8), 1972–1974; (in Russian).
65. Allen, B. J. In *Handbook of Thermodynamic and Transport Properties of Alkali Metals*; Ohse, R. W., Ed.; International Union of Pure and Applied Chemistry, Blackwell Scientific: Boston, MA, 1985; Chapter 6.8, pp 691–700.
66. Keene, B. J. *Int. Mater. Rev.* **1993**, *38*, 157–192.
67. Cox, J. D.; Wagman, D. D.; Medvedev, V. A. *CODATA Key Values for Thermodynamics*; Hemisphere: New York, NY, 1989.
68. Fink, J. K.; Leibowitz, L. In *Handbook of Thermodynamic and Transport Properties of Alkali Metals*; Ohse, R. W., Ed.; International Union of Pure and Applied Chemistry, Blackwell Scientific: Boston, MA, 1985; Chapter 6.3.2, pp 411–434.
69. Gurvich, L. V.; Veyts, I. V. In *Thermodynamic Properties of Individual Substances*, 4th ed.; Hemisphere: New York, NY, 1991; Vol. 2, Part 2.
70. Miller, R. R. In *Liquid Metals Handbook*, 2nd ed.; Lyon, R. N., et al. Ed.; Report of Atomic Energy Commission, NAVEXOS P-733; AEC: Washington, DC, 1952; pp 38–102.
71. Kutateladze, S. S.; Borishanskii, V. M.; Novikov, I. I.; Fedinskii, O. S. *Liquid-Metal Heat Transfer Media*; Cons. Bur: New York, NY, 1959. (Translated from Russian journal *Atomnaya Energiya*, **1958** (Suppl. 2).)
72. Hultgren, R.; Desai, P. D.; Hawkins, D. T.; Gleiser, M.; Kelley, K. K. *Selected Values of the Thermodynamic Properties of Binary Alloys*; ASM: Metals Park, OH, 1973.
73. Martynyuk, M. M. *Russ. J. Phys. Chem.* **1998**, *72*, 13–16. (Translated from *Zhu. Fiz. Khimii*, **1998**, *72*, 19–22.)
74. Morita, K.; Fischer, E. A. *Nucl. Eng. Des.* **1998**, *183*, 177–191.
75. Redlich, O.; Kwong, J. N. S. *Chem. Rev.* **1949**, *44*, 233–244.
76. Srinivasan, G. M.; Ganesan, S. *J. Nucl. Mater.* **1983**, *114*, 108–110.
77. Eslami, H. *J. Nucl. Mater.* **2005**, *336*, 135–139.
78. Song, Y.; Lambert, S. M.; Prausnitz, J. M. *Ind. Eng. Chem. Res.* **1994**, *33*, 1047–1057.
79. Lucas, L. D. *Techniques de l'Ingénieur, Matériaux métalliques*; No. M153, Form M66, Paris, 1984; Edition T.I.
80. Kaplun, B.; Shulaev, V. M.; Linkov, S. P.; Vartanov, Yu. D. *Teplofizicheskie svoystva veshestv i materialov*; Kutateladze Institute of the Thermophysics of the USSR Academy of Science: Novosibirsk, 1979; pp 105–109 (in Russian).
81. Shpil'rain, E. E.; Yakimovich, K. A.; Fomin, V. A.; Skovorodjko, S. N.; Mozgovo, A. G. In *Handbook of Thermodynamic and Transport Properties of Alkali Metals*;

- Ohse, R. W., Ed.; International Union of Pure and Applied Chemistry, Blackwell Scientific: Boston, MA, 1985; Chapter 7.3, pp 753–784.
82. Ho, C. Y.; James, H. M. In *Handbook of Thermodynamic and Transport Properties of Alkali Metals*; Ohse, R. W., Ed.; International Union of Pure and Applied Chemistry, Blackwell Scientific: Boston, MA, 1985; Chapter 7.1, pp 703–734.
83. Bretonnet, J. L. *Techniques de l'Ingénieur, Matériaux métal-liquides*; No. M153, Form M69, Paris, 1988; Edition T.I.
84. Banchila, S. N.; Filippov, L. P. *High Temp. (USSR)* **1973**, *11*(3), 602–605. (Translated from *Teplofizika Vysokikh Temperatur*, **1973**, *11*(6), 1301–1305.)
85. Plevachuk, Yu.; Sklyarchuk, V.; Eckert, S.; Gerbeth, G. *J. Nucl. Mater.* **2008**, *373*, 335–342.
86. Touloukian, Y. S.; Powel, R. W.; Ho, C. Y.; Klemens, P. G. *Thermophysical Properties of Matter*; IFI/Plenum: New York/Washington, 1970; Vol. 1.
87. Cook, J. G.; Fritsch, G. In *Handbook of Thermodynamic and Transport Properties of Alkali Metals*; Ohse, R. W., Ed.; International Union of Pure and Applied Chemistry, Blackwell Scientific: Boston, MA, 1985; Chapter 7.2, pp 329–347.
88. Mills, K. C.; Monaghan, B. J.; Keene, B. J. *Int. Mater. Rev.* **1996**, *41*, 209–242.

2.15 Uranium Oxide and MOX Production

T. Abe and K. Asakura

Japan Atomic Energy Agency, Tokai-mura, Ibaraki, Japan

© 2012 Elsevier Ltd. All rights reserved.

2.15.1	Introduction	394
2.15.2	Summary of Oxide Characteristics	395
2.15.2.1	Thermal and Mechanical Properties of Oxides	395
2.15.2.1.1	Basic properties	395
2.15.2.1.2	Oxide powder	395
2.15.2.1.3	Sintered oxide pellet	396
2.15.2.2	Nuclear Characteristics of Uranium and Plutonium Isotopes	398
2.15.3	Fuel Design^{2,27–29}	399
2.15.3.1	Fuel Rod Design	399
2.15.3.1.1	Basic structural design	399
2.15.3.1.2	Fuel rods for LWRs	399
2.15.3.1.3	Fuel rods for CANDU reactors and AGRs	400
2.15.3.1.4	Fuel rods for FBRs	400
2.15.3.1.5	Fissile content of oxide pellets	400
2.15.3.2	Fuel Assembly Design	401
2.15.3.2.1	PWR UO ₂ fuel assembly	401
2.15.3.2.2	BWR UO ₂ fuel assembly	402
2.15.3.2.3	VVER fuel assembly	402
2.15.3.2.4	CANDU reactor fuel	402
2.15.3.2.5	AGR fuel	402
2.15.3.2.6	LWR MOX fuel assembly	402
2.15.3.2.7	FBR fuel assembly	403
2.15.4	Uranium Oxide Production	404
2.15.4.1	Uranium Oxide Powder Production	404
2.15.4.1.1	ADU process	404
2.15.4.1.2	AUC process ³⁷	405
2.15.4.1.3	Dry process ³⁸	406
2.15.4.2	UO₂ Pellet Production	407
2.15.4.2.1	Powder preparation	407
2.15.4.2.2	Pelletizing	408
2.15.4.2.3	Dewaxing and sintering	408
2.15.4.2.4	Finishing and inspecting	408
2.15.4.3	Burnable Poison-Doped Fuel Production⁴³	408
2.15.5	MOX Production	408
2.15.5.1	Plutonium Powder Production	409
2.15.5.1.1	Oxalate precipitation method	409
2.15.5.1.2	Microwave heating denitration method	409
2.15.5.2	MOX Pellet Production	410
2.15.5.2.1	Belgium	410
2.15.5.2.2	France	411
2.15.5.2.3	Germany	412
2.15.5.2.4	Japan	414
2.15.5.2.5	United Kingdom	415
2.15.5.2.6	Developments for future systems	416
2.15.6	Rod Fabricating and Assembling	418
2.15.6.1	LWR UO₂ and MOX Fuels	418

2.15.6.1.1	Rod fabrication	418
2.15.6.1.2	Assembly fabrication	418
2.15.6.2	Fast Spectrum Oxide Fuel Reactors	419
2.15.7	Outlook	420
References		420

Abbreviations

ABWR	Advanced boiling water reactor
ADU	Ammonium diuranate
AGR	Advanced gas cooled reactor
ATALANTE	Atelier Alpha et Laboratoires d' Analyses des Transuraniens et d' Etudes de retraitement, France
AUC	Ammonium uranyl carbonate
AUPuC	Ammonium uranyl plutonyl carbonate
BN	Belgonucléaire, Belgium
BNFL	British Nuclear Fuels plc, United Kingdom
BWR	Boiling water reactor
CANDU	CANadian Deuterium Uranium reactor
CFCa	Complexe de Fabrication de Cadarache, France
COCA	Cobroyage (co-milling) Cadarache
COEX	CO-EXtraction
DNB	Departure from nucleate boiling
DOVITA	Dry reprocessing, Oxide fuel, Vibropac, Integral, Transmutation of Actinides
FBR	Fast breeder reactor
FR	Fast reactor
HTR	High-temperature reactor
HWR	Heavy water reactor
IDR	Integrated dry route
ITU	Institute for Transuranium Elements, Germany
JAEA	Japan Atomic Energy Agency, Japan
LEFCA	Laboratoire d' Etudes et de Fabrications experimentales de Combustibles nucleaires Avances, France
LWR	Light water reactor
MA	Minor actinide
MH	Microwave heating denitration
method	method
MH-MOX	Microwave heating denitrated MOX powder
MIMAS	Micronized master blend
MOX	Mixed oxide of uranium and plutonium
O/M ratio	Oxygen-to-metal ratio

OCOM	Optimized CO-Milling
PCI	Pellet-cladding interaction
PCMI	Pellet-cladding mechanical interaction
PFFF	Plutonium Fuel Fabrication Facility, Japan
PFPF	Plutonium Fuel Production Facility, Japan
PVA	Polyethylene glycol or polyvinyl alcohol
PWR	Pressurized water reactor
R&D	Research and development
RIAR	Research Institute of Atomic Reactors, Russia
SBR	Short binderless route
SCK-CEN	Studiecentrum voor Kernenergie – Centre d' Etude de l' énergie Nucléaire, Belgium
SEM	Scanning electron microscope
tHM	Tons of heavy metal
TIG	Tungsten inert gas
UKAEA	United Kingdom Atomic Energy Authority, United Kingdom
VHTR	Very high-temperature reactor
VVER	Vodo-Vodyanoi Energetichesky Reaktor (Russian type PWR)
% TD	Theoretical density ratio

Symbols

A	Mass number
D_{Pu}	Diffusion coefficient of plutonium
σ_a^{fast}	Fast neutron absorption cross-section
$\sigma_a^{thermal}$	Thermal neutron absorption cross-section
σ_f^{fast}	Fast neutron fission cross-section
$\sigma_f^{thermal}$	Thermal neutron fission cross-section

2.15.1 Introduction

Almost all the commercial nuclear power plants operating currently utilize uranium oxide fuel. These reactors, sometimes referred to as Generation II or Generation III reactors, produce ~15% of the world's

electricity supply. Production of the uranium oxide fuel required for these reactors is a mature industry and it annually requires more than 68 000 tU.¹

Fuel design differs according to the reactor types, which include the advanced gas cooled reactors (AGRs), pressurized water reactors (PWRs), boiling water reactors (BWRs), PWRs developed in the former Soviet Union (Vodo-Vodyanoi Energetichesky Reaktor, VVERs), and CANadian Deuterium Uranium (CANDU) reactors. There are some differences in the production processes to fit each fuel design.

Plutonium utilization within the closed fuel cycle is essential to utilize natural uranium resources efficiently. Plutonium recycling demonstrations have been conducted in light water reactors (LWRs) and heavy water reactors (HWRs).² Industrial utilization of MOX in LWRs has commenced in some countries.

The use of MOX in fast neutron reactors has many attractive features. Plutonium breeding in fast breeder reactors (FBRs) leads to drastically increased energy output from uranium resources. Nuclide transmutation by fast neutrons to incinerate minor actinides (MAs) has the potential to reduce the long-term radio-toxicity of spent nuclear fuel.

2.15.2 Summary of Oxide Characteristics

2.15.2.1 Thermal and Mechanical Properties of Oxides

The starting material for oxide fuel production is oxide powder. It is fed to a powder preparation process and then to a pelletizing process to get powder compacts, which are called green pellets. The green pellets undergo a dewaxing and sintering process to get sintered oxide pellets. Certain characteristics of the oxide powder and the sintered pellets are very important for fuel production. A brief summary of their important characteristics is presented in this section. As a comprehensive review of the characteristics of actinide oxide has been given in **Chapter 2.02, Thermodynamic and Thermophysical Properties of the Actinide Oxides**, most of the data presented here are those dealt with in **Chapter 2.02, Thermodynamic and Thermophysical Properties of the Actinide Oxides**.

2.15.2.1.1 Basic properties

2.15.2.1.1.1 Crystal structure

The phase diagrams and crystal structures of uranium oxide and MOX have been described in Sections 9.1.1, 9.1.2, and 9.1.3. These oxides exhibit

the fluorite or CaF_2 structure. MOX is a substitutional solid solution in which U-cations of UO_2 , as MOX base material, are substituted for Pu-cations. There is complete substitutional solid solubility between UO_2 and PuO_2 . As mentioned in **Section 9.1.2.7**, phase separation into two fcc phases occurs in MOX with a plutonium content exceeding 30% in the hypostoichiometric region.

Uranium oxide can become a hyperstoichiometric type oxide (UO_{2+x}) at room temperature while MOX can become both a hyperstoichiometric type and a hypostoichiometric type ($\text{MO}_{2\pm x}$) oxide at room temperature. This is because uranium can exist in an oxide as ions with valences of 4+, 5+, and 6+ and plutonium can exist in an oxide as ions with valences of 3+ and 4+ due to the oxygen potential in the atmosphere. Therefore, the oxygen-to-metal (O/M) ratio regions in which the single phase MOX exists vary according to the plutonium content of MOX.

2.15.2.1.1.2 Oxygen potential

Oxygen potential is an important property for controlling certain properties related to oxide fuel fabrication such as variations in density and O/M ratio.

As mentioned in **Section 9.1.4.3.2**, the oxygen potentials of uranium oxide and MOX increase with an increase in temperature and plutonium content. In addition, these potentials increase with an increase in O/M ratio and they increase rapidly, especially near the stoichiometric region (refer to **Figures 22 and 23** in **Section 9.1.4.3.2**). In the case of $(\text{U}, \text{Gd})\text{O}_{2-x}$, the oxygen potential increases with an increase in Gd content.^{3,4}

2.15.2.1.2 Oxide powder

2.15.2.1.2.1 Flowability

In pellet fabrication, powder flowability is one of the most important characteristics that determine the productivity of the fabrication process. It is well known that blended powders have very poor powder flowability, just after milling.⁵ Therefore, the milled powder is granulated or mixed with a powder having good flowability to ensure uniform die filling and good compaction behavior.⁵⁻⁷ Carr indices are a well-known method to evaluate powder flowability of dry solids.^{8,9} The powder flowabilities of microwave heating denitrated MOX (MH-MOX) powder and ammonium diuranate (ADU) powder have been evaluated on the basis of Carr indices both before and after granulation.^{10,11}

2.15.2.1.2.2 Effective thermal conductivity

The temperature of MOX powder increases by self heat generation of plutonium by α -decay when the powder is kept in the fuel fabrication process. In a MOX fuel fabrication plant, the temperature increase in MOX powder should be prevented because the excessive temperature increase of MOX powder may possibly cause changes in powder characteristics (e.g., O/M ratio variation), degradation of additives (e.g., lubricant agents), and overheating of equipment in the fabrication process. An example of a preventive measure against the temperature increase of MOX powder is the use of a storage vessel that has radiator plates.

The effective thermal conductivity of MOX powder is important for estimating its temperature distribution. The effective thermal conductivity of a powder can be defined as the combination of thermal conductivities of powder particles and the atmospheric gas because the volume fraction of the atmosphere gas in the total volume is large. In addition, particle shapes, mean particle size, specific surface area, and O/M ratio of powder particles influence the effective thermal conductivity of the powder.¹² Figure 1 shows the effective thermal conductivities of various MOX powders as functions of O/M ratio and bulk density.¹²

2.15.2.1.3 Sintered oxide pellet

2.15.2.1.3.1 Sintering process

During the sintering process, MOX powder compacts are subjected to high temperature for a few hours

under a controlled atmosphere to improve their mechanical strength. The powder compact is composed of individual grains separated by 35–50 vol.% porosity. During sintering, the following major changes commonly occur: an increase in grain size, and changes in pore shape, pore size, and pore number. In the early stages of sintering, the powder particles begin to mutually bond. In the middle stage, grain growth, disappearance of pores, and formation of closed pores occur. The pellet densification proceeds according to the shape change from a point contact to a face contact between grains. In the last stage, disappearance of the closed pores occurs. The diffusion of uranium, plutonium, and oxygen, the evaporation–condensation process of their compounds, the grain growth process, the pore migration process, and the pore disappearance processes are important for understanding the process of sintering. To obtain pellets with high mechanical strength and density, it is desirable to eliminate as much porosity as possible.

Diffusion coefficients of these elements are needed for evaluating the sintering behavior (e.g., volume shrinkage in the fuel fabrication technology). Section 9.1.6.1 shows that the oxygen self diffusion coefficients of actinide oxides increase with increasing deviation from stoichiometry near the stoichiometric region and that the diffusion coefficients of cations in hyperstoichiometric actinide oxides increase drastically with deviation from stoichiometry. It was shown that the diffusion coefficient of plutonium in $(U_{0.8}Pu_{0.2})O_{2\pm x}$ has the lowest value near the stoichiometric region and it increases significantly with an increase in deviation from stoichiometry¹³ (see Figure 2).

Vapor species of oxide fuel and its vapor pressure are required to assess the redistribution of elements, pore migration, and fuel restructuring. The O/M ratio dependencies of vapor pressures in the vapor species of uranium oxide, plutonium oxide, and MOX are shown in Figures 26 and 27 of Section 9.1.5. The vapor pressures of each of these species have a large dependency on the O/M ratio and their behavior is different in each vapor species.

Temperatures used during dewaxing and sintering are very important factors in the fabrication process. The Hüttig and Tamman temperatures, which are defined as the start temperatures for surface diffusion and volume diffusion of powder particles, respectively, are provided for establishing temperatures for dewaxing and sintering. These temperatures can be easily calculated using melting point temperature.

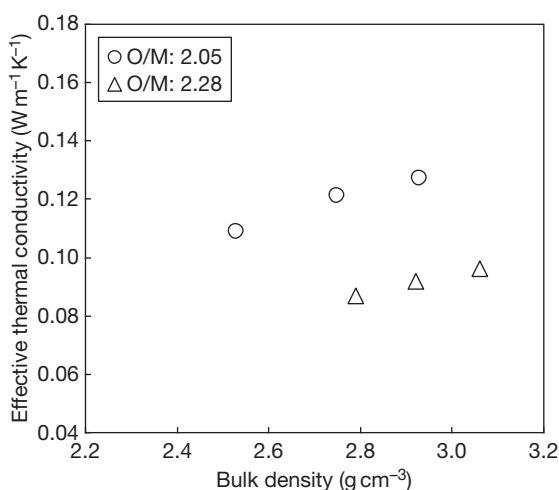


Figure 1 Effective thermal conductivities of mixed oxide of uranium and plutonium powders. Reproduced from Takeuchi, K.; Kato, M.; Sunaoshi, T.; Aono, S.; Kashimura, M. *J. Nucl. Mater.* **2009**, 385, 103–107.

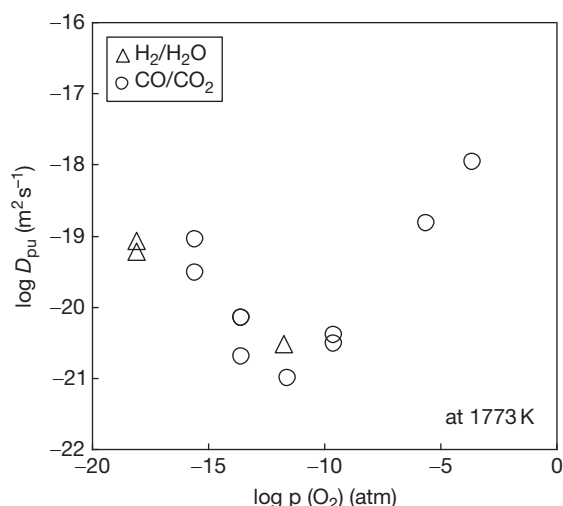


Figure 2 Dependence of Pu-diffusion coefficient, D_{Pu} , in $(U_{0.8}Pu_{0.2})O_{2\pm x}$ on oxygen partial pressure at 1773 K. The oxygen partial pressure was controlled using H_2/H_2O mixed gas and CO/CO_2 mixed gas. The high oxygen partial pressures correspond to $MO_{2.07}$, the low oxygen partial pressures correspond to $MO_{1.92}$. Reproduced from Matzke, H. J. *J. Nucl. Mater.* **1983**, 114, 121–135.

2.15.2.1.3.2 Effects of O/M ratio on physical properties of sintered oxide pellet

Most of the physical properties of oxide fuel such as lattice parameter, diffusion coefficient, and thermal conductivity are affected by the O/M ratio.

The lattice parameter is needed for calculation of the theoretical density (TD) ratio in the fuel fabrication process. The thermal expansion coefficient, which is defined as the temperature dependency of the lattice parameter, is also an important thermophysical property in fuel design when the variation in heat transport between the fuel and the cladding tube by thermal expansion of the fuel pellets and the stress to the cladding tube by fuel pellets under irradiation are evaluated.

The lattice parameters and thermal expansion coefficients of actinide dioxides are summarized in Table 2 in Section 9.1.3.1. As mentioned in Section 9.1.3.1.2, the dependency of the lattice parameter of stoichiometric mixed oxides on their chemical composition usually obeys Vegard's law. The lattice parameter of MOX fuel decreases with an increase in the plutonium content. In the hypostoichiometric region, the lattice parameter of MOX fuel increases with a decrease in O/M ratio. In addition, Leyva *et al.*¹⁴ showed that the lattice parameter of $(U, Gd)O_2$ decreases with an increase in Gd content.

As mentioned in Section 9.1.3.1.2, Vegard's law is applied to the evaluation of lattice parameters as a function of composition and temperature in many cases (refer to Figure 13 in Section 9.1.3.1.2). It means that the thermal expansion coefficient of MOX fuel is independent of plutonium content. Martin¹⁵ showed that the thermal expansion coefficient of MOX fuel tends to increase with an increase in deviation from stoichiometry in the hypostoichiometric region.

The melting point of oxide fuel is one of the most important thermophysical properties for fuel design and performance analyses. As the chemical composition and the O/M ratio of the oxide fuel change the melting point of the fuel itself, fuel design and performance analysis should be done in consideration of not only the chemical composition at the time of fuel fabrication but also its variation subsequent to nuclear transmutation during reactor operation. In addition, the melting point is also used in the estimation of sintering temperature, as mentioned before.

Section 9.1.2 shows that the melting point of uranium oxide has its largest value near the stoichiometric region and the melting point decreases with an increase in deviation from stoichiometry (refer to Figure 1 in Section 9.1.2.1). Further, the melting point of stoichiometric MOX decreases with an increase in plutonium content (refer to Figure 7 in Section 9.1.2.7). In the hypostoichiometric MOX, the melting point of MOX fuel increases with a decrease in O/M ratio.¹⁶ Beals *et al.*¹⁷ studied the UO_2 – $GdO_{1.5}$ system at high temperatures and showed that the melting point of Gd bearing UO_2 decreases with an increase in Gd content.

During reactor operation, the heat generated in the oxide fuel pellets flows from the central high temperature region to the low temperature periphery of the pellets, and consequently thermal equilibrium is achieved in the pellets. To evaluate the temperature distribution when thermal equilibrium is reached, thermal conductivity is one of the most important thermophysical properties. As thermal conductivity is a function of O/M ratio, density, chemical composition, and so on, the variation in chemical composition that occurs during reactor operation should be noted, along with the evaluation of the melting point, as mentioned before.

As mentioned in Section 9.1.6.2, thermal conductivities of oxide fuel decrease with an increase in temperature up to 1600–1800 K but increase with an increase in temperature beyond this range

(refer to Figures 33 and 34 in **Section 9.1.6.2**). The factors which heavily influence the thermal conductivity are O/M ratio and fuel density. Thermal conductivity decreases significantly with an increase in deviation from stoichiometry and with a decrease in density. In addition, the thermal conductivity of a gadolinium-bearing uranium oxide decreases significantly with an increase in Gd content.^{18,19}

2.15.2.1.3.3 Solubility in nitric acid solution

When the nuclear fuel cycle is considered, the dissolution of oxide fuel is the essential first step in

aqueous reprocessing. The solubility and dissolution rate of oxide fuel in nitric acid solution are important parameters related to the capabilities of the reprocessing process. Generally, it has been supposed that the dissolution of MOX fuel decreases with an increase in the plutonium content. The maximum plutonium content of MOX driver fuel for fast reactors has been limited to about 30%, from the viewpoint of solubility in nitric acid solution.

There have been many studies on the solubility of oxide fuel in nitric acid solution.^{20–23} From the results of these studies, it has been supposed that the factors affecting the dissolution rate of MOX are the fuel fabrication conditions (homogeneity of the admixture of UO₂ and PuO₂, sintering conditions and plutonium content, etc.) and the fuel dissolution conditions (nitric acid concentration, solution temperature, dissolution time, etc.) (see **Figure 3**).

2.15.2.2 Nuclear Characteristics of Uranium and Plutonium Isotopes

Plutonium is an isotopically composition-variable material and the variation is attributable to its generation reaction in LWR fuel, the initial uranium enrichment and burn-up of the LWR fuel, and so forth. It needs various methodologies and much prudence in its handling because its nuclear properties differ noticeably from one isotope (nuclide) to another. **Table 1**^{24,25} summarizes the principal nuclear properties of typical nuclides in MOX fuel, including uranium isotopes. A material with high content of ²³⁸Pu is more calorific owing to its decay mode (α) and short life. Therefore, the content of ²³⁸Pu would be the limiting factor for handling batch sizes in a fabrication process. ²⁴¹Pu, which also has a short life, causes alteration in the isotopic composition even during a relatively short period, for example, during storage after fuel

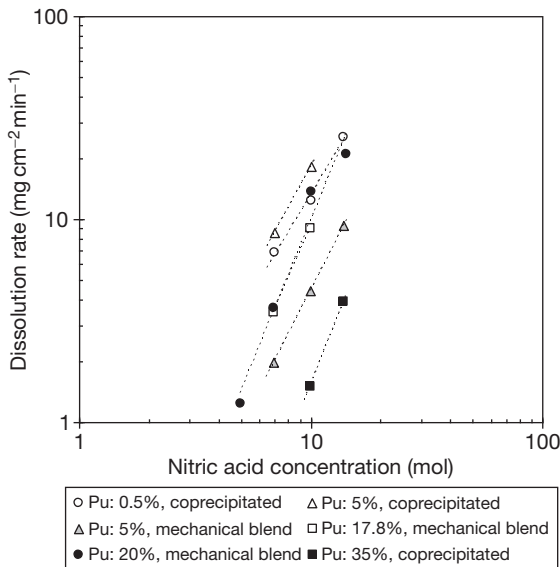


Figure 3 Dissolution rate of mixed oxide of uranium and plutonium with various Pu contents as a function of the nitric acid concentration. Reproduced from Oak Ridge National Laboratory. Dissolution of high-density UO₂, PuO₂, and UO₂–PuO₂ pellets in inorganic acids, ORNL-3695; Oak Ridge National Laboratory: Oak Ridge, TN, 1965.

Table 1 Half lives and typical reaction cross sections of isotopes in MOX fuel

Nuclide	Half life (year)	Cross-section (barn, 10 ^{–28} m ²)				Specific power from decay (W kg ^{–1})
		$\sigma_a^{thermal}$	$\sigma_f^{thermal}$	σ_a^{fast}	σ_f^{fast}	
²³⁵ U	7.04E+08	684	585	2.49	1.95	8.7E–05
²³⁸ U	4.47E+09	2.7	1.20E–05			1.2E–05
²³⁸ Pu	87.74	558	17.9			820
²³⁹ Pu	2.41E+04	1018	747	2.3	1.83	2.8
²⁴⁰ Pu	6564	289	5.90E–02			10.2
²⁴¹ Pu	14.35	1374	1012	2.86	2.45	12.4

Source: Shibata, K.; *et al. J. Nucl. Sci. Technol.* **2002**, 39, 1125–1136; Hori, M. *Kiso Kousokuro Kougaku (Basic Fast Reactor Engineering)*; The Nikkan Kogyo Shimbun: Tokyo, 1993 (in Japanese).

fabrication but before loading into a reactor. Besides the above, neutron reaction cross-sections are completely different in isotopes and reactor types. Taking such variations in the cross-sections into consideration, MOX fuel is prepared, in view of plutonium content, to secure sufficient in-core reactivity.²⁶

The nuclear characteristics of uranium and plutonium are needed for the evaluation of radiation exposure during the fuel fabrication process. In particular, the short life of a nuclide merits attention with regard to exposure to radiation. All isotopes listed in **Table 1** are α -emitters, especially ^{238}Pu , which has highly significant α -radioactivity. ^{241}Am , which is adjunct to ^{241}Pu , is also a strong α -emitter. These two nuclides also give off strong γ -ray emissions following their α -decay. The major sources of neutrons are the even- A (mass number) plutonium isotopes such as ^{238}Pu , ^{240}Pu , and ^{242}Pu because of their high probability for spontaneous fission. In addition, especially in oxide fuels such as MOX fuel, α -particle bombardment of oxygen isotopes is an important factor that determines neutron emission. ^{238}Pu and ^{241}Am have a higher specific (per unit mass) influence on this reaction than other nuclides because of their large α -ray emission rates, as mentioned above. In addition, these two nuclides have a somewhat higher Q -value (α -ray energy) for decay and this increasingly affects the neutron production rate.

Turning to the topic of safeguards, the large neutron yield by spontaneous fission from the MOX fuel is utilized for a neutron coincidence counting method for inventory verification. This method uses the fact that neutrons from spontaneous fission or induced fission are essentially emitted simultaneously. This measurement can be made in the presence of neutrons from room background or (α , n) reactions because these neutrons are noncoincident, or random, in their arrival times. The detection signals of these neutrons are analyzed and plutonium isotopes are determined by their quantity.

Burnable poison suppresses initial fuel reactivity during fuel life and compensates fuel reactivity with the gradual reduction in burnable poison with burn-up. Consequently, the fuel burn-up reactivity is lowered and this lowered reactivity leads to an extended operation cycle period. Burnable poison is often mixed into oxide fuel. Gadolinium is a typical one; it has a variety of stable and substable isotopes and some of them ($^{155,157}\text{Gd}$) have large thermal capture cross-sections. They are used in the form of a sesqui-oxide compound, gadolinia, in oxide fuel.

2.15.3 Fuel Design^{2,27-29}

2.15.3.1 Fuel Rod Design

2.15.3.1.1 Basic structural design

In LWRs and FBRs, a number of fuel rods are formed into a fuel assembly. The fuel rod is a barrier (containment) for fission products; it has a circular cross-section that is suited for withstanding the primary pressure stress due to the external pressure of the coolant and the increase in internal pressure by fission gas release. An axial stack of cylindrical fuel pellets is encased in a cladding tube, both ends of which are welded shut with plugs. A gas plenum is located at the top part of the rod, in most cases, to form a free space volume that can accommodate internal gas. Helium gas fills the free space at atmospheric pressure or at a given pressure. A hold-down spring, located in the gas plenum, maintains the fuel stack in place during shipment and handling. UO_2 insulator pellets are inserted at both ends of the fuel stack, in some fuel designs, to thermally isolate metallic parts such as the end plug and the hold-down spring.

2.15.3.1.2 Fuel rods for LWRs

Table 2 summarizes LWR fuel rod design specifications.³⁰ LWR UO_2 fuel rods contain dense low-enrichment UO_2 pellets in a zirconium alloy cladding; they are operated at a low linear heat rate with centerline temperatures normally below 1400°C . The fuel pellets of the VVER have a small central hole (1.2–1.4 mm in diameter).

Fission gas release is low under these conditions and no large gas plenum is needed. Burnable absorber fuel rods containing $\text{UO}_2\text{--Gd}_2\text{O}_3$ pellets are located in some part of the fuel assemblies of LWRs to flatten reactivity change throughout the reactor operation cycle.

Great efforts have been made in LWR fuel rod design in order to achieve the following good performance features: high burn-up, long operation cycle, good economy, and high reliability. Toward achieving these ends, many modifications have been made, such as the development of high-density UO_2 pellets, axial blankets for reducing neutron leakage, ZrB_2 integral burnable absorber, high Gd content $\text{UO}_2\text{--Gd}_2\text{O}_3$ pellets, corrosion-resistant cladding materials, and optimization of helium pressure and plenum length in the rod designs.

LWR MOX fuel rods contain MOX pellets that have a low plutonium content. As the plutonium concentration is low, their irradiation behavior is similar to that of LWR UO_2 fuel rods. No additional

Table 2 Summary of fuel rod design specifications for LWRs and CANDU reactors

Reactor type	PWR	BWR	VVER	CANDU
Fuel assembly type	Mitsubishi 17 × 17	GNF 9 × 9A	TVS-2M	AECL 28-element
No. of fuel rod per assembly	264	66+(8) ^a	312	28
Rod length (mm)	3856	4090 (2600) ^a	3988	493
Rod diameter (mm)	9.5	11.2	9.1	15
Pellet material	UO ₂	UO ₂	UO ₂	UO ₂
Pellet diameter (mm)	8.19/0	9.6/0	7.6/1.2	14/0
Pellet density (g cm ⁻³)	97% TD	97% TD	10.4–10.7	10.6
Clad material	MDA ^b /Zirlo	Zry-2 (Zr-liner)	Zr-1% Nb	Zry-4
Clad thickness (mm)	0.57	0.71	0.63	0.4
Average discharge burn-up (MWd kgHM ⁻¹)	55	45	60	8

^aPartial length rod.^bMitsubishi developed alloy.Source: Tarlton, S., Ed. *Nucl. Eng. Int.* **2008**, 53, 26–36.

problems are apparent, with the possible exception of higher gas release and therefore an increase in rod internal pressure at high burn-up. Power degradation with burn-up is less in the MOX fuel than in UO₂ fuel because of the neutronic properties of the plutonium isotopes and thus MOX fuel is irradiated at higher power later in its life, releasing more fission gases. In addition, the slightly lower thermal conductivity of MOX may give rise to higher fuel temperatures, resulting in higher fission gas release. Design changes, such as lowering the helium filling pressure, increasing the plenum volume, and/or decreasing the fuel stack length in the rod, are applied to accommodate higher gas release in MOX fuel rods.

2.15.3.1.3 Fuel rods for CANDU reactors and AGRs

CANDU reactors and AGRs generally have fuel rod design specifications similar to those of LWRs. The CANDU reactors use natural uranium oxide or slightly enriched uranium oxide contained within a thin Zircaloy clad, and design burn-up is lower than that of LWRs. In AGR fuel rods, uranium dioxide pellets, enriched to about 3%, are encased in a stainless steel clad. Fuel bundles of both the reactors have circular, cylindrical shapes to fit in the pressure tube of CANDU reactors or in the graphite sleeve of AGRs. The fuel rod diameter differs according to the number of fuel rods per bundle. Typical CANDU fuel rod design specifications for a 28-rod bundle are presented in Table 2.³⁰ The overall fuel rod lengths of both the reactor types

are much shorter than those of LWRs in order to fit their fuel assembly design which enables on-load refueling.

2.15.3.1.4 Fuel rods for FBRs

FBR fuel rods contain MOX pellets having high plutonium content, with the exception of Russian FBRs, BN-350, and BN-600 in which high enrichment UO₂ fuel pellets have been mostly used. Fuel pellets of less than 8 mm diameter are encased in a stainless steel cladding; they operate at a high linear heat rate with centerline temperatures of around 2000 °C or higher. Under these conditions, fission gas release is typically high (>80%) and a very large plenum is included to limit gas pressure. The gas plenum is located at the bottom of the rod in some fuel designs, aimed at minimizing plenum length, thanks to the lower gas temperature at the bottom of the rod. Upper and lower sections of the depleted UO₂ pellets are included for breeding. Pellet-smear density is set not to exceed a criterion that is formulated as a function of burn-up to avoid fuel-cladding mechanical interaction at high burn-up; high-density annular pellets or low-density solid pellets are used; the former lower the fuel centerline temperature allowing a higher linear heat rate.³¹

2.15.3.1.5 Fissile content of oxide pellets

The same U enrichment is used throughout a given PWR fuel assembly, but the core usually contains several levels of enrichment arranged to give uniform power distribution. In contrast, BWR fuel rods have

several axial segments with different enrichments and a BWR fuel assembly has several different rods with different enrichments. Thus, there are a variety of UO_2 pellets with different U enrichments depending on reactor design; the enrichments are within 5% which is due to the limits of fuel fabrication facilities and fuel shipments.

For current LWR MOX fuels, depleted uranium (0.2–0.3% ^{235}U), which is obtained in the form of tails from the enrichment process, is coupled with plutonium because there are economic incentives to concentrate as much plutonium in as few fuel assemblies as possible as it conserves the expensive fabrication cost of MOX fuel. As the quality of plutonium, from a neutronic aspect, varies with the isotope composition of plutonium, the specification of the plutonium content of LWR MOX fuel is affected by the quality of plutonium. Total plutonium concentrations of 7.5% are considered to be equivalent to U enrichments of 4.0–4.3% for the current usual plutonium that is recycled from spent LWR UO_2 fuel.²

To determine plutonium content of FBR MOX fuel, equivalent ^{239}Pu ($^{239}\text{Pu}/(\text{U} + \text{Pu})$) is used. The actual plutonium content for a given batch is obtained by a calculation that uses the neutronic equivalent coefficient of each isotope and the isotope composition of plutonium to be used for the batch. ^{241}Am , a daughter product of ^{241}Pu , is considered in the calculation as well. The specification for equivalent ^{239}Pu ($^{239}\text{Pu}/(\text{U} + \text{Pu})$) is relatively low for a large size core; equivalent ^{239}Pu is 12–15% for the SUPERPHENIX (1200 GWe),²⁸ 14–22% for MONJU (280 GWe).

2.15.3.2 Fuel Assembly Design

2.15.3.2.1 PWR UO_2 fuel assembly

Figure 4³² shows an example of a PWR fuel assembly. PWRs have 197–230 mm square, ductless assemblies that traverse the full 2635–4550 mm height of the core. They comprise a basic support structure of unfueled zirconium alloy guide tubes attached to the top- and bottom-end fittings, an array of 14×14 to 18×18 fuel elements (minus the number of guide tubes), and several axially spaced grids that hold the array together. About half of the assemblies have rod control clusters attached at their upper end; these consist of 18–24 slender stainless-steel-clad absorber rods of AgInCd alloy or B_4C , individually located in the guide tubes. The absorber rods are withdrawn for startup and are repositioned after

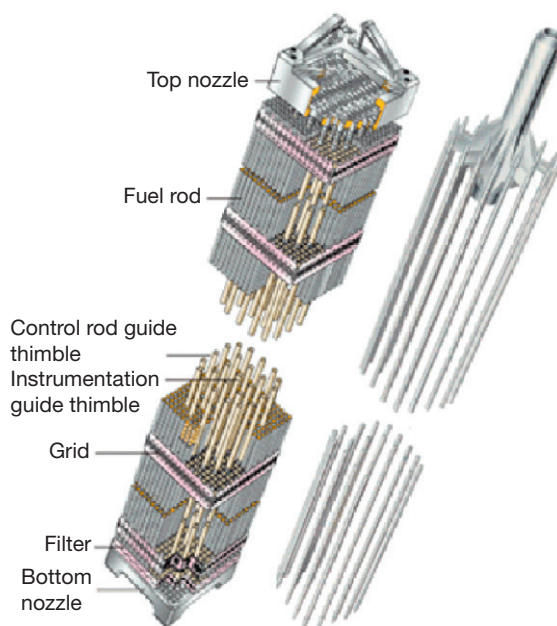


Figure 4 Example pressurized water reactor fuel assembly design of the $17 \times 17 - 24$ type with a fuel assembly averaged U enrichment of 3.9%. Reproduced from <http://www.mhi.co.jp/en/index.html>.

refueling; the reactor is controlled at power by altering the concentration of an absorber (boric acid) in the coolant. The bottom-end fitting is located on the core grid plate and the assembly is spring loaded against a hold-down system to compensate for differential expansion or growth during irradiation.

Fine control is obtained by incorporating a burnable poison like Gd_2O_3 in some of the elements, in which it is admixed with UO_2 in the core region, and with the upper and lower sections of natural UO_2 . By minimizing power changes in this manner, the incidence of pellet-clad interaction (PCI) failures can be kept to very low, acceptable values. Various improvements in fuel assembly design have been adopted. To improve reliability, for instance, debris filtering was adopted in the structural design of the bottom part of the fuel assembly, the grid structure design was modified against fretting corrosion, and an intermediate flow mixer grid was added to enhance the margin to depart from nucleate boiling (DNB). Zirconium alloy grids for better neutronics, optimized distribution of fissile and fertile materials, and a burnable poison to improve fuel cycle economy and to extend reactor cycle length were all introduced for economy in the current assembly designs, as also the removable top nozzle to reduce operation and maintenance costs.

2.15.3.2.2 BWR UO_2 fuel assembly

Figure 5³⁰ shows some examples of BWR fuel assemblies. BWRs have 110–140 mm square full-core height assemblies which, unlike their PWR counterparts, are contained within thick-walled channel boxes of zirconium alloy. They contain arrays of 6×6 to 10×10 fuel elements, usually with eight elements acting as tie rods that screw into upper and lower tie plates. Some of the element positions are occupied by unfueled water-filled tubes (called water rods) or water channels and are used to control local flux peaking. Element separation is maintained by grid spacers that are attached to the water rods and evenly distributed along the entire length. The square duct is attached to a top-end fixture, relative to which the remainder of the subassembly may slide. The bottom-end fitting has a mechanized orifice to control flow in the subassembly and this is located in the core grid plate. The upper end fixture has a handle for loading and unloading against which the hold-down bars rest to prevent levitation.

There are no absorber elements in BWR assemblies and reactor control is achieved by having cruciform-shaped absorber blades throughout the core which move vertically in the clearance between

sets of four subassemblies. Power peaking is minimized on the local scale by having fuel elements with different enrichments and burnable poisons (generally Gd_2O_3) dispersed within each assembly. Various fuel design improvements have been adopted, such as a debris-filtering structure for better reliability, optimized distribution of water channels, fissile material with partial length fuel rods and burnable poison use to improve fuel cycle economy and to extend reactor cycle length.

2.15.3.2.3 VVER fuel assembly

Figure 6³⁰ shows an example of a VVER fuel assembly. The VVER uses hexagonal fuel assemblies of 3200–4690 mm length and 145–235 mm width. The assembly is used such that it is contained in a hexagonal shroud, but shroudless assemblies are available for the VVER-1000.³⁰

2.15.3.2.4 CANDU reactor fuel

Figure 7³⁰ shows an example of a CANDU fuel bundle. Twelve fuel bundles fit within each fuel channel that is horizontally aligned in the reactor core.

2.15.3.2.5 AGR fuel

AGR fuel assemblies typically have 36 rods contained within a graphite sleeve. Twenty fuel assemblies are placed in a skip inside a flask.

2.15.3.2.6 LWR MOX fuel assembly

Plutonium recycling has so far been limited to partial loading in LWR cores. A primary design target of the MOX fuel assembly is compatibility with the UO_2 standard fuel assembly. In the neutronic design for partial loading of LWR cores, significant thermal neutron flux gradients at the interfaces between the MOX and UO_2 fuel assemblies have to be considered. The increase in thermal neutron flux in the direction of an adjacent UO_2 assembly is addressed by a gradation in the plutonium content of the MOX fuel rods at the edges and corners of the fuel assembly. There are three typical rod types for PWR MOX fuel assemblies. Optimized BWR fuel assemblies are more heterogeneous: wider water gaps and larger water structures within a BWR fuel assembly result in MOX fuel assembly designs with an increase in the number of different rod types. Examples of MOX fuel assembly designs are shown in Figure 8.² There are plans for recycling weapons grade plutonium in PWRs in the United States.³³

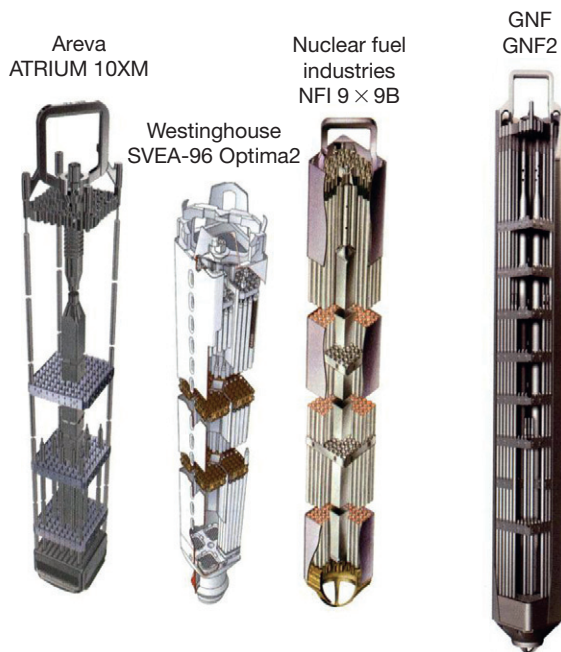


Figure 5 Example boiling water reactor fuel assemblies. Reproduced from Tarlton, S., Ed. *Nucl. Eng. Int.* **2008**, 53, 26–36.

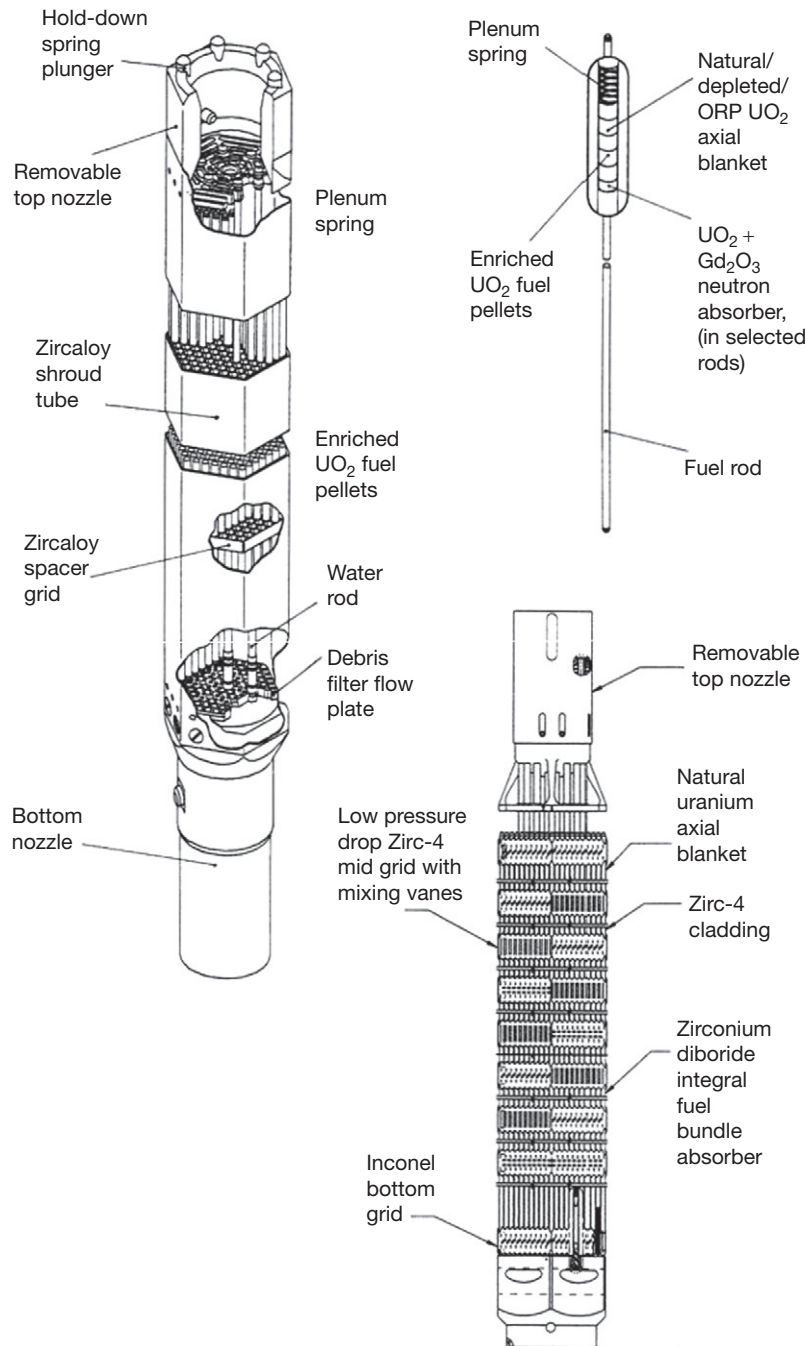


Figure 6 Example Westinghouse VVER-1000 fuel assembly. Reproduced from Tarlton, S., Ed. *Nucl. Eng. Int.* **2008**, 53, 26–36.

The 100% MOX cores permit an increase in the amount of plutonium under irradiation at a reduced level of heterogeneity of the core. An advanced boiling water reactor (ABWR) to be constructed in Ohma, Japan, will be the first plant with an in-built 100% MOX core capability.

2.15.3.2.7 FBR fuel assembly

Figure 9² shows an example of an FBR fuel assembly. FBR fuel assemblies have a hexagonal fuel rod arrangement with small gaps provided by a wire spacer, helically wound around each of the fuel pins or by hexagonal grid spacers. The fuel bundle is

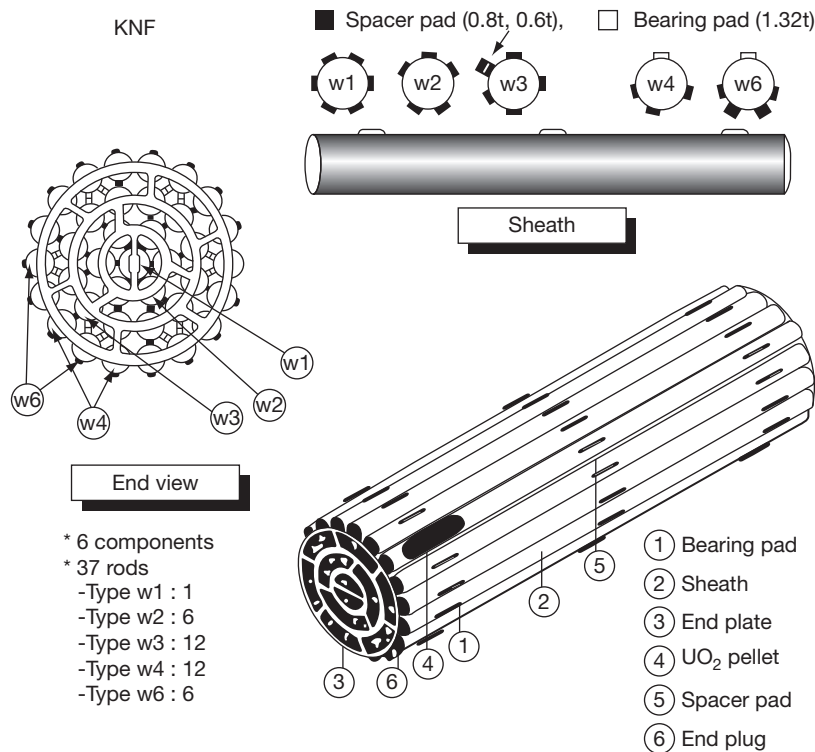


Figure 7 Example CANadian Deuterium Uranium reactor fuel assembly. Reproduced from Tarlton, S., Ed. *Nucl. Eng. Int.* 2008, 53, 26–36.

encased in a wrapper tube, in order to form a sodium flow channel for efficient cooling and to prevent fuel failure propagation during an accident.

Austenitic or ferritic steels or nickel alloys are selected as materials for structural components because of their good compatibility with sodium and their ability to cope with high temperatures and high levels of fast neutron exposure. These features of FBR fuel assembly design result from the unique design requirements of the FBRs, including the hard neutron energy spectrum, compact core size, high power density, high burn-up, high temperature, and plutonium breeding. The fuel structure and actual fuel design vary with the reactor scale, design targets, and the design methodology. Table 3 summarizes the fuel assembly design specifications of the SUPERPHENIX, BN-600, and MONJU.³⁴

2.15.4 Uranium Oxide Production

Uranium oxide has become the primary fuel for the nuclear power industry today. As of April 2010, there

are some 438 commercial nuclear power reactors operating in 30 countries, with a total capacity of 374 000 MWe.¹ Most of these reactors are of the LWRs, AGRs, or the CANDU reactor types, and they are fuelled with sintered pellets of UO₂ containing natural or slightly enriched uranium.

2.15.4.1 Uranium Oxide Powder Production

Prior to UO₂ pellet fabrication, the enriched uranium feed, UF₆, is converted to UO₂ powder. Although a number of conversion processes have been developed, only three are used on an industrial scale today. Two of these are wet processes: ADU and ammonium uranyl carbonate (AUC) and the third is a dry process.

The selected conversion process and its process parameters strongly influence the characteristics of UO₂ powder and the resulting UO₂ pellets.

2.15.4.1.1 ADU process

The ADU process has been widely used for many years. It uses ADU as an intermediate product in

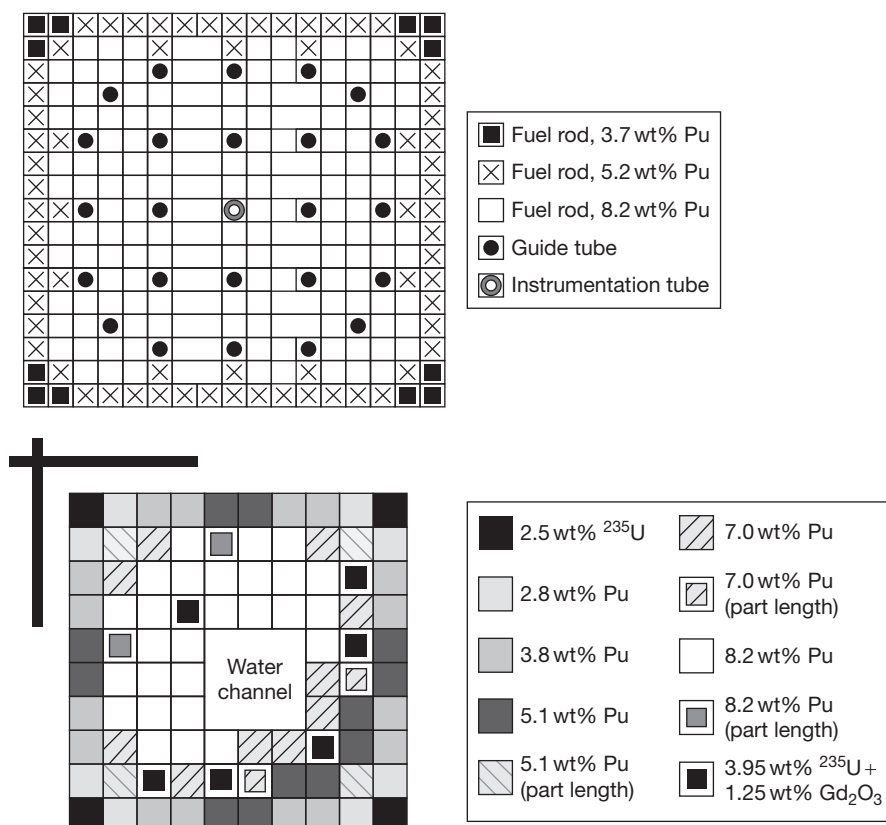
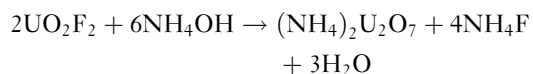
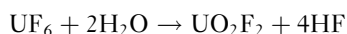
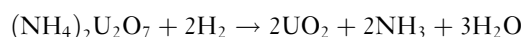


Figure 8 Example light water reactor mixed oxide of uranium and plutonium fuel assemblies. The upper is pressurized water reactor design of the $17 \times 17 - 24$ type with a fuel assembly averaged plutonium concentration of 7.2% Pu. The lower is boiling water reactor design of the $10 \times 10 - 9\text{Q}$ type with a fuel assembly averaged plutonium concentration of 5.4 wt% Pu. Reproduced from IAEA. *Status and Advances in MOX Fuel Technology*; Technical Reports Series No. 415; IAEA: Vienna, 2003.

a two-step process. First, UF_6 is vaporized and injected into an ammonia solution. UF_6 hydrolyzes and precipitates as ammonium diuranate $(\text{NH}_4)_2\text{U}_2\text{O}_7$. The ADU precipitate is collected on filters and dried to get the ADU powder.



Secondly, the ADU powder is calcined and then reduced to UO_2 with hydrogen.

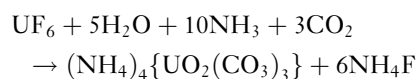


The properties of the resulting UO_2 are strongly dependent on the processing parameters of precipitation,

calcinations, and reduction and equally on material contents, and reacting temperatures. For example, the amount of NH_3 is critical in the precipitation step: too much will yield gelatinous ADU which is difficult to filter; if there is too little then the resulting UO_2 powder will be difficult to press and sinter into pellets.

2.15.4.1.2 AUC process³⁷

In Europe, the AUC process is widely used for fabricating UO_2 fuels. The precipitation of AUC is done in a precipitator, filled with demineralized water. The vaporized UF_6 , CO_2 , and NH_3 are added as gases through a nozzle system. Reaction occurs according to the following equation:



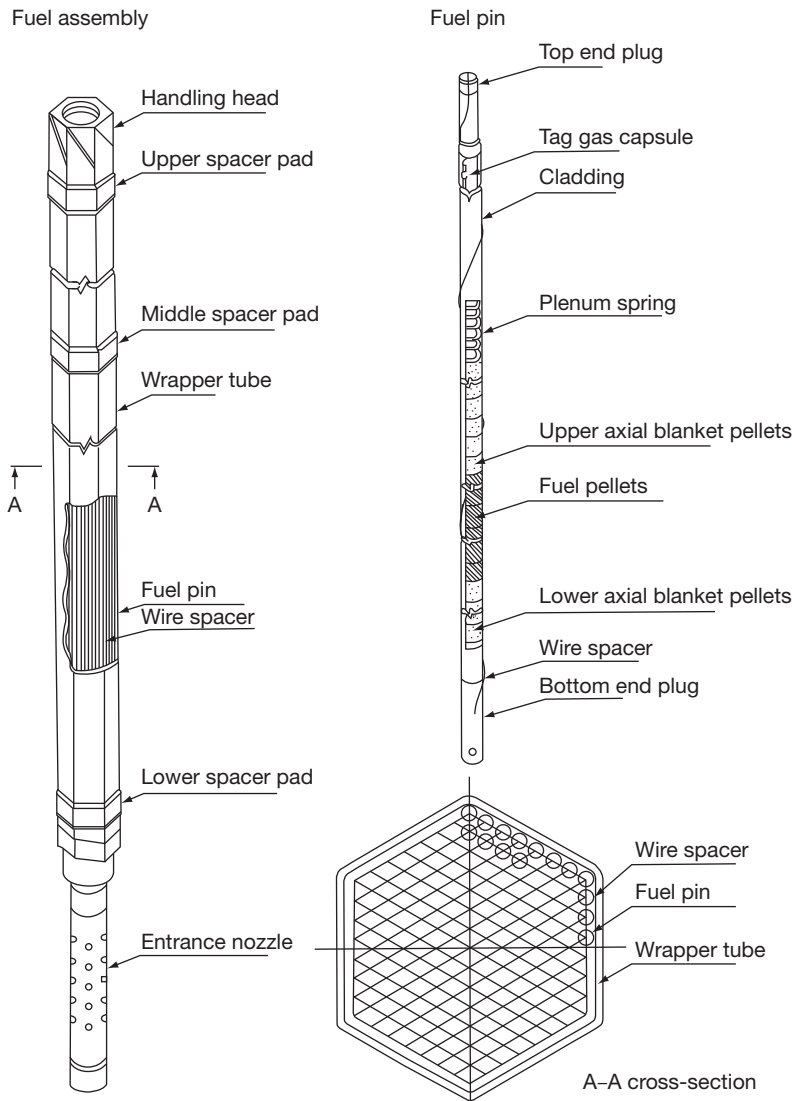
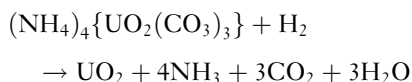


Figure 9 Example fast breeder reactor mixed oxide of uranium and plutonium fuel assembly design of MONJU. Reproduced from IAEA. *Status and Advances in MOX Fuel Technology*; Technical Reports Series No. 415; IAEA: Vienna, 2003.

The AUC precipitates in the form of yellow single crystals. The grain size depends on the precipitation conditions. Instead of UF_6 , uranyl nitrate solution can also be used as a feed material.

The AUC precipitate is filtrated and washed with a solution of ammonium carbonate and methyl alcohol. Then, the AUC powder is pneumatically transferred to a fluidized-bed furnace, decomposed, and reduced to UO_2 with hydrogen according to the following equation.



The transformation of AUC to UO_2 gives rise to desirable UO_2 powder properties: it is free-flowing and has a high sintering activity.

The resulting UO_2 powder is made chemically stable by a slight oxidation to about $\text{UO}_{2.10}$.

2.15.4.1.3 Dry process³⁸

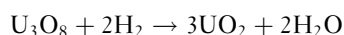
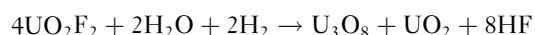
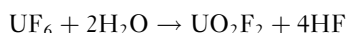
The dry process was developed in the late 1960s and is widely used today. UF_6 is vaporized from steam or hot-water-heated vaporizing baths, and vaporized UF_6 is introduced into the feed end of a rotating kiln. Here, it meets and reacts with superheated steam to give a plume of uranyl fluoride (UO_2F_2). UO_2F_2

Table 3 Summary of fuel assembly design data of SUPERPHENIX, BN-600 and MONJU

Reactor name	SUPERPHENIX	BN-600	MONJU
No. of fuel rods per assembly	271	127	169
Assembly length (mm)	5400	3500	4200
Assembly width (mm)	173	96	110.6
Rod length (mm)	2700	2445	2813
Rod diameter (mm)	8.5	6.9	6.5
Pellet material	MOX	UO ₂	MOX
Pellet diameter (OD/ID) (mm)	7.14/1.8	5.95/1.6	5.4/0
Pellet density (g cm ⁻³)	95.5% TD	10.4	85% TD
Clad material	17% Cr–13% Ni stainless steel	16% Cr–15% Ni stainless steel	PNC316
Clad thickness (mm)	0.56	0.4	0.47
Average discharge burn-up (MWd kgHM ⁻¹)	60 (achieved)	60 (achieved)	80 (target)

Source: IAEA. Fast Reactor Database 2006 Update, IAEA-TECDOC-1531; IAEA: Vienna, Austria, 2006.

passes down the kiln where it meets with a counter-current flow of steam and hydrogen and is converted to UO₂ powder. The reaction sequence follows the equations below.



The UO₂ powder resulting from dry processes is of low bulk density and fine particle size. Therefore, granulation before pressing and the employment of a pore former process are usual during the pellet fabrication process.

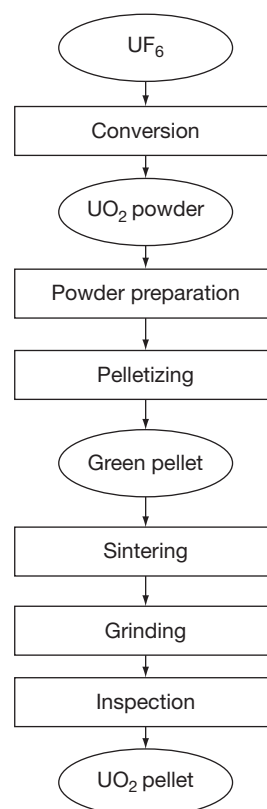
A dry process has preferable advantages: the process is simple and the equipment is compact; the criticality limitation is less required; and liquid waste treatment is not necessary.

2.15.4.2 UO₂ Pellet Production

The flow sheet for UO₂ pellet production is shown in Figure 10. The UO₂ pellet fabrication process consists of mixing the UO₂ powder with additives such as binder, lubricant and pore former materials, granulating to form free-flowing particles, compaction in an automatic press, heating to remove the additives, sintering in a controlled atmosphere, and grinding to a final diameter. The process varies slightly according to the nature of the starting UO₂ powder.

2.15.4.2.1 Powder preparation

In the pelletizing process, UO₂ powder must be filled easily and consistently into dies. UO₂ powder from the AUC process is free-flowing and can be pressed

**Figure 10** Flow sheet for UO₂ pellet production.

without granulation. Usually it is mixed with a small amount of U₃O₈ to control the density and pore distribution of the pellets. The fine particle size of the integrated dry route (IDR) powders prevents them from being free-flowing when produced; these powders are therefore prepressed into briquettes, fractured, sieved to produce granules, and a dry

lubricant added. ADU powder is slurried with a solvent and a volatile binder such as polyethylene glycol or polyvinyl alcohol, spray dried and sieved to size. The obtained material flows freely and will consistently fill pellet dies but an extra operation is required to remove the binder. Additives known as pore formers are often included to give uniform final density: 95–97% TD for LWR UO_2 and MOX, and 85–95% TD for FBR MOX fuel pellets. The pore former will decompose in the dewaxing process to leave closed pores that are stable in-reactor.

2.15.4.2.2 Pelletizing

The prepared UO_2 powder is pressed into green pellets in reciprocal or rotary presses at 150–500 MPa. The density of green pellets reaches 50–60% TD. Pellets are normally fabricated with dished ends and/or chamfered edges. The dishes compensate for radial variation in thermal expansion in-reactor, and the chamfers reduce the pellet–cladding mechanical interaction (PCMI). In VVERs and some fast reactors, pellets are made with a central hole to reduce fuel centerline temperatures. The pressing actions of the dies and the punches are carefully controlled to obtain a homogeneous local density distribution in the green pellet and to prevent defects in the green pellet. Two typical LWR UO_2 pellets are shown in Figure 11.

2.15.4.2.3 Dewaxing and sintering

The volatile additives such as binders, lubricants and pore formers (if used) are removed from the green pellets by heating at 600–800 °C in a furnace for several hours. The additives will decompose into harmless gases at low temperature. This dewaxing process is generally done as the first step of the sintering process. The green pellets are then sintered in a reduction atmosphere at 1600–1800 °C for times that are based on control samples from previous batches, but are typically 3–10 h. U_3O_8 powder, mixed with the

original UO_2 powder, can also be used to control the final product density.³⁹

The properties of UO_2 fuel pellets such as thermal conductivity, gas bubble mobility, and creep rate influence fuel performance in-reactor. These properties are affected by the grain size and the porosity distribution of the pellets. Early LWR fuel pellets had a small grain size (2–3 μm), but the requirement for greater fission gas retention by large grain fuel has led to the current use of 10–20 μm grain size material. As higher burn-ups become required, greater fission gas retention in the fuel pellets may be expected in the future. The grain size of UO_2 pellets can be increased by controlling the sintering conditions or by using sintering additives such as Al_2O_3 , SiO_2 , TiO_2 , Nb_2O_5 , or Cr_2O_3 .^{40–42}

2.15.4.2.4 Finishing and inspecting

As-sintered pellets have an hour-glass shape because of the internal density distribution generated during pressing, and the diameter of the pellet must be accurate at 10 μm . Also, from the viewpoint of gap conductance, the pellet surface must be smooth. Therefore, pellets are ground by a centerless grinding machine.

After grinding, pellets are inspected to check their diameter, length, density, and appearance; inspections are almost completely automated except for appearance. Analyses for their uranium enrichment, impurities, and microstructures are also done.

2.15.4.3 Burnable Poison-Doped Fuel Production⁴³

The fabrication process of the gadolinia-doped fuel is almost the same as that of the UO_2 fuel. The gadolinia-doped fuel fabrication line must be separated from the UO_2 fuel to prevent gadolinium from contaminating the UO_2 fuel fabrication line.

2.15.5 MOX Production

The utilization of plutonium in reactors is essential for the establishment of the nuclear fuel cycle. It is already being used in LWRs and research and development (R&D) has been continued to utilize plutonium more efficiently in FBRs. MOX fuel is often selected as FBR fuel because of its excellent burn-up potential, high melting point, and relative ease of commercial fabrication and also because LWR fuel fabricators already have extensive experience with UO_2 fuel fabrication. Furthermore, oxide fuel has good irradiation stability, and proven safety

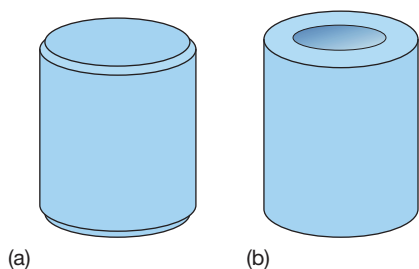


Figure 11 Typical light water reactor UO_2 pellets. Pellet with (a) chamfer and (b) dish.

response using a negative Doppler coefficient that mitigates over-power transients.^{42,43} These advantages must be weighed against the disadvantages of oxide fuel, such as lower thermal conductivity that leads to fuel structuring and enhanced swelling,⁴⁴ reduced compatibility with sodium,^{45–47} low fissile atom density, and the presence of two moderating atoms per one metal atom. Based on a balance between the advantages and disadvantages, various fabrication processes for MOX fuels, including the conversion processes for plutonium oxide, were developed more than 40 years ago and are still applied. Major processes utilized in the conversion of plutonium oxide and MOX fuel production are summarized here. Their details have been described in the literature.^{2,6,27,29,42,48}

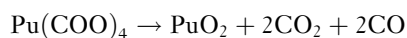
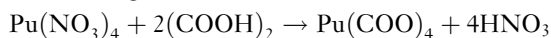
Plutonium emits α -particles with energies higher than 5 MeV, and all operations from powder handling to end plug welding after pellets are loaded into a cladding tube are carried out in glove boxes. In order to prevent plutonium inhalation accidents during fuel fabrication, these glove boxes have an airtight structure and their interiors are continuously kept at negative pressure. Furthermore, as described in Section 39.2.2, gamma and neutron shielding is required for these glove boxes to reduce radiation exposure.⁴⁹

2.15.5.1 Plutonium Powder Production

Plutonium is extracted from spent fuels in the reprocessing plants in the form of plutonium nitrate. In order to utilize extracted plutonium for MOX fuel production, plutonium nitrate is converted to oxide powder by three methods: one is an oxalate precipitation method; the other two methods involve coconversion with uranium, the ammonium uranyl plutonyl carbonate (AUPuC) conversion method, and the microwave heating denitration method (MH method). The AUPuC conversion method is described in Section 39.5.2.3 as part of the AUPuC fuel fabrication process.

2.15.5.1.1 Oxalate precipitation method

In the oxalate precipitation method, the plutonium oxide powder is prepared from plutonium nitrate by the following two reactions.⁵⁰



Oxalate acid, $\text{H}_2(\text{COOH})_2$, is added to plutonium nitrate solution at about 60 °C, and the temperature

maintained until the precipitation reaction (1) is completed. The plutonium oxalate precipitate is filtered and then dried in air. Dried plutonium oxalate is calcined in a furnace at temperatures from 350 to 650 °C. It has been reported that reaction (2) begins below 100 °C and is completed at around 350 °C.⁵⁰ The characteristics of the obtained PuO_2 powder vary depending upon the precipitation and calcination conditions, that is, the precipitation temperature, addition rate of oxalate acid to plutonium nitrate, oxalate acid concentration, and calcination temperature. This PuO_2 powder is commonly utilized as a feed material for MOX fuel production in the world. The microstructure and characteristics of PuO_2 powder prepared by the oxalate precipitation method have also been explained elsewhere.⁵¹

2.15.5.1.2 Microwave heating denitration method

To increase the proliferation resistance of plutonium, a coconversion method of adding plutonium nitrate and uranyl nitrate to a mixed oxide powder was developed in Japan. In the MH method, about 7 l of a mixed solution of uranyl nitrate and plutonium nitrate with a concentration of about 250 g l⁻¹ of heavy metal, is fed into a denitration vessel. The diameter and height of this silicon nitride vessel are about 50 and 6 cm, respectively. After microwave irradiation (2450 MHz, 16 kW), $\text{PuO}_2 + \text{UO}_3$ is formed, and then this product is calcined to $\text{PuO}_2 + \text{U}_4\text{O}_9 + \text{U}_3\text{O}_{8x}$ in air for 2 h at 750 °C. Subsequently, this mixture is reduced to $\text{PuO}_2 + \text{UO}_2$ (MH-MOX) powder under an atmosphere of N_2 –5% H_2 mixed gas, at the same temperature used for calcination.⁵² The obtained MH-MOX powder has sufficiently good powder characteristics to allow fabrication of MOX pellets of more than 95% TD.^{52,53} Full details of the MH method have been given elsewhere.^{53–56} With the MH method, the generation of radioactive liquid waste containing plutonium is reduced compared with other conversion processes.

Figure 12 shows microstructures which were observed by scanning electron microscopy (SEM) at 10 000-fold magnification, in the PuO_2 powder (A) prepared by the oxalate precipitation method and MH-MOX powder (B). The microstructures of MH-MOX powder and UO_2 powder (prepared by the ADU process) calcined at various temperatures have been reported in Asakura *et al.*⁵²

Examples of the characteristics of PuO_2 and MH-MOX powders are shown in Table 4.

The values vary depending on the conversion conditions described above.

2.15.5.2 MOX Pellet Production

In the beginning stages of R&D for MOX fuel production, many kinds of manufacturing techniques were investigated. In the 1960s, the pellet route was adopted for all the pilot plants in Belgium, France, Germany, the United Kingdom, and Japan.^{2,48} The two types of MOX fuel for LWRs and FBRs have quite different characteristics, affecting both the fabrication process and the quality requirements. These characteristics are summarized in the following points⁶:

- The plutonium content of FBR fuel is several times higher than that of LWR fuel.
- The smear density of FBR fuel has to be lower than that of LWR fuel because the former has to be used at higher temperature and for higher burn-up.
- The higher plasticity of FBR fuel, resulting from the higher irradiation temperature, justifies less

restrictive specification tolerances and quality requirements, than for LWR fuel.

- The uniformity in plutonium isotopic composition within a batch of fuel assemblies is a key performance-related quality for LWR fuel, while it is rather unimportant for FBR fuel.

On the basis of these points, various kinds of processes were developed to fabricate MOX pellets for FBRs and LWRs. The MOX pellet fabrication processes that have been adopted in several countries are described below.

2.15.5.2.1 Belgium

In Belgium, the micronized master blend (MIMAS) process was developed by Belgonucleaire (BN) in the early 1980s based on the experiences acquired in the reference fabrication process developed earlier and commercially used in the 1970s at BN's Dessel plant.² The reference process consisted of a single blending of PuO_2 powder with free-flowing UO_2 powder and this blending resulted in a blend with adequate flowability to feed the pelletizing press.⁶ As MOX pellets fabricated by the reference process could not satisfy the preprocessor's new requirement, which was that MOX pellets had to be soluble in a nitric acid solution, BN had to improve the solubility of MOX pellets in the nitric acid solution. In order to improve their solubility, the MIMAS process was introduced in the Dessel plant. **Figure 13** shows the flow sheet for the MIMAS process.

In the MIMAS process, suitable amounts of PuO_2 powder, UO_2 powder, and dry recycled scrap powder are prepared to get a 60 kg MOX master blend powder with 30% plutonium concentration. The master blend powder is ball milled to obtain a homogeneous distribution of plutonium. In the second blending, force-sieved (i.e., micronized) master blend powder is diluted with the free-flowing UO_2 powder and

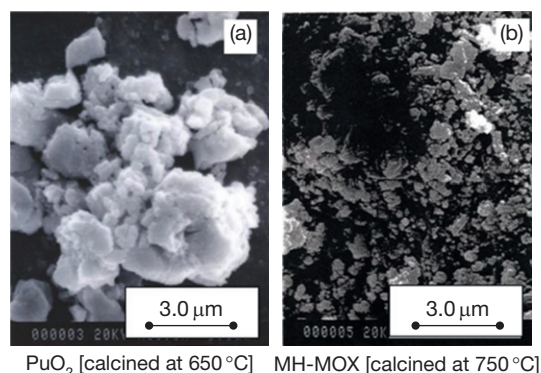


Figure 12 Microstructures of PuO_2 and MH-MOX powders observed by scanning electron microscope.

Table 4 Characteristics of PuO_2 and MH-MOX powders

	<i>PuO_2 powder prepared by the oxalate precipitation method</i>	<i>MH-MOX powder prepared by the microwave heating denitration method</i>
Calcination temperature and atmosphere	650 °C in air	750 °C in air
Reduction temperature and atmosphere	–	750 °C in $\text{N}_2 + 5\% \text{H}_2$
BET specific surface area ($\text{m}^2 \text{g}^{-1}$)	15.35	3.70
Average particle size (μm)	4.60	4.28
Bulk density (g cm^{-2})	2.66	2.20
Tap density (g cm^{-2})	3.56	3.40

additional dry recycled scrap to form 80 kg of the final blended MOX powder with the desired plutonium concentration.⁶ In this step, it is very important to obtain uniform distribution of master blend in free-flowing UO_2 powder. This final blended MOX powder is pelletized into green pellets using a pressing machine with multiple punches and a reciprocating mechanism. Approximately 10–12 green pellets can be pressed simultaneously. These green pellets are sintered at about 1700°C under a reduced atmosphere of $\text{Ar} + \text{H}_2$ mixed gas, after dewaxing. Not only does the intimate contact between the micronized UO_2 and PuO_2 powders provide adequate interdiffusion during sintering and therefore enhanced solubility, but also the larger contact area between the more abundant fine powder and the free-flowing UO_2 powder results in a more heterogeneous MOX structure than in the earlier reference process. This is apparent in measurements such as the α -autoradiograph of a transverse section of a MOX pellet prepared by the MIMAS process, given by Lippens *et al.*⁵⁷

During the 1990s, the Dessel plant accounted for over 60% of the world's production of MOX fuel.⁴⁹ However, MOX fuel fabrication was terminated in 2006. Now, this plant is undergoing preparative work for its decommissioning.

2.15.5.2.2 France

In France, the Complexe de Fabrication de Cadarache (CFCa) started operation in 1962, on a pilot scale, for developing FBR fuel. The Cobroyage

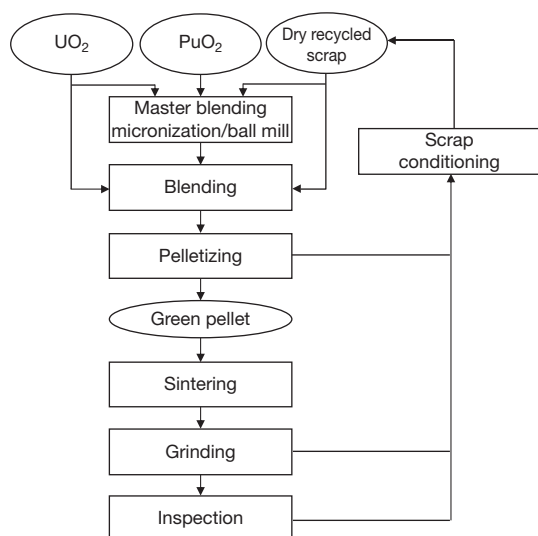


Figure 13 Flow sheet for the micronized master blend process.

(co-milling) Cadarache (COCA) process was developed there in the 1970s to fabricate MOX pellets for FBRs using two fuel fabrication lines.

Figure 14 shows the flow sheet for the COCA process. It utilizes an optimized ball mill as a blender and involves the forced extraction of the lubricated micronized powder through a sieve. This results in free-flowing granules which are suitable for feeding at the pelletizing step.⁴⁹ In the COCA process, the lubricant and the porogen, which is a pore former to control pellet density, are added to the force-sieved powder.⁵¹ One of the two FBR fuel fabrication lines in CFCa was switched to a LWR fuel fabrication line which introduced the LWR fuel fabrication technology developed by BN. This LWR fuel fabrication line started producing PWR fuel in 1990.⁶ MOX fabrication at CFCa was stopped in 2005 because of seismic safety issues and the facility is now undergoing preparative work for its decommissioning.

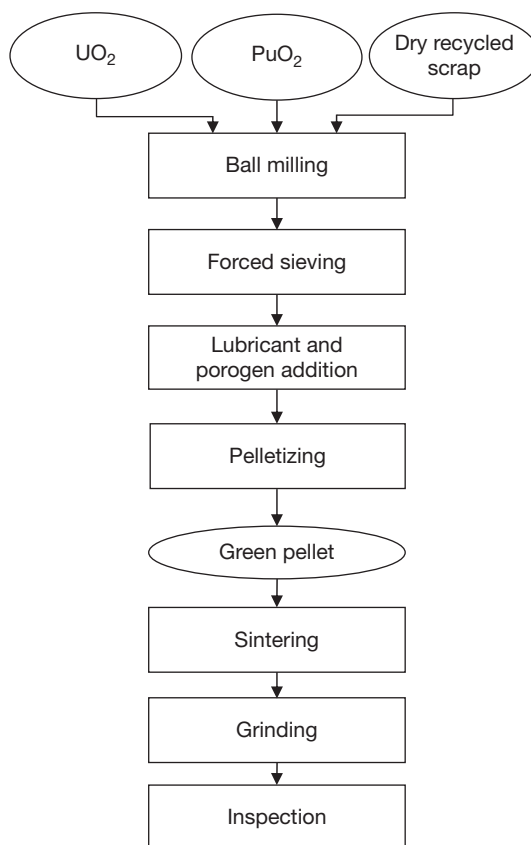


Figure 14 Flow sheet for the Cobroyage (co-milling) Cadarache process.

In 1985, the construction of the MELOX plant at Marcoule was started; it had an annual production capability of 100 tons of heavy metal (tHM) for PWR fuel which was decided on the basis of operational experiences with the MIMAS process obtained at CFCa and it started MOX fuel production in 1995. Gradually, its licensed annual production capability was expanded and it reached 195 tHM as of April 2007; MOX fuel fabrication for BWRs was also covered during this expansion. The process adopted in the MELOX plant is called the advanced MIMAS process and its flow sheet is shown in **Figure 15**. The accumulated MOX fuel production at the MELOX plant reached 1426 tHM at the end of 2008. The features of this process are given below.

In order to utilize up to 50% of dry recycled scrap powder in the master blend powder and to achieve excellent homogeneity and uniformity of PuO_2 as well, a new ball mill was developed for the first blending step.⁶ This mill uses three-dimensional movement and U–Ti alloy balls. For the second blending, a high capacity (640 kg) blender consisting of a conical screw mixer with a double envelope cooling system was adopted.^{6,49} In order to achieve MOX fuel production on a large scale, complete automation was implemented in the production line. Similar to the original MIMAS process invented in BN, three kinds of feed powders, PuO_2 powder, UO_2 powder, and dry recycled scrap powder, are ball milled to obtain the master blend powder with about 30% plutonium

concentration. The force-sieved master blend powder is diluted with the free-flowing UO_2 powder, prepared by the ADU process or the AUC process and additional dry recycled scrap powder using the high capacity conical screw mixer. This free-flowing diluted powder is pelletized into green pellets using a pressing machine with multiple punches and a reciprocating mechanism. Approximately 10–14 green pellets can be pressed simultaneously. The green pellets are sintered in a continuous-type sintering furnace consisting of a dewaxing part and a sintering part. After dry centerless grinding of sintered pellets, the exterior of all pellets are inspected.

A mapping image of plutonium, acquired by X-ray microanalysis of a transverse section of a MOX pellet prepared by the advanced MIMAS process, was reported by Oudinet *et al.*⁵⁸ In the MIMAS process, a two-step blending method is utilized to obtain the desired plutonium content in the pellets, as described above. This results in the presence of two or three phases in the transverse section of a sintered pellet. The MOX pellets prepared with UO_2 powder from the ADU process show three phases, plutonium rich clusters, a coating phase and a UO_2 phase on their transverse sections while those prepared with UO_2 powder from the AUC process show two phases, plutonium rich clusters and a UO_2 phase.^{58,59} The MOX pellets manufactured by the short binderless route (SBR) and Japan Atomic Energy Agency (JAEA) processes in which a one-step blending method is adopted to obtain the desired plutonium concentration of pellets show a single homogeneous phase on their transverse sections, and are different from pellets fabricated by the MIMAS process.^{51,60} The MOX pellets currently manufactured in the MELOX plant are reported to have a mean grain size of 5.8 μm .⁶¹

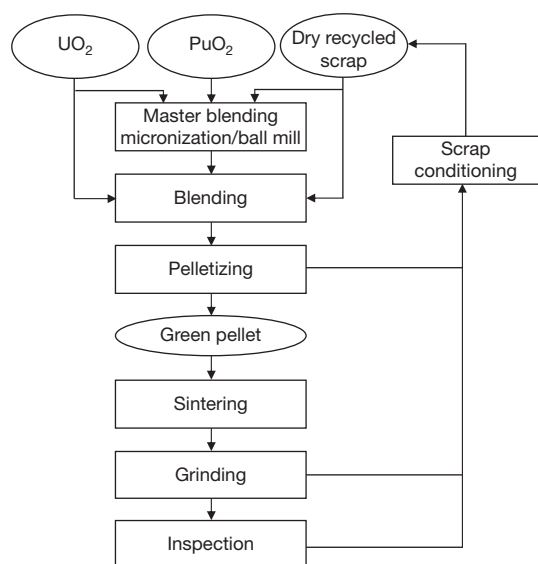


Figure 15 Flow sheet for the advanced micronized master blend process.

2.15.5.2.3 Germany

Two MOX pellet fabrication processes were developed in Germany, the Optimized CO-Milling (OCOM) process and the AUPuC process.^{7,62}

The OCOM process was developed by Alkem and uses UO_2 powder, PuO_2 powder, and recycled scrap powder as feed materials. The manufactured MOX pellets are made fully soluble in nitric acid by optimizing the co-milling of the three powders. In the OCOM process, two different MOX pellet fabrication routes can be taken as shown in **Figure 16**.

In the first route (left half of **Figure 16**), three powders are prepared to achieve specified plutonium concentrations required for the fuel to be used in

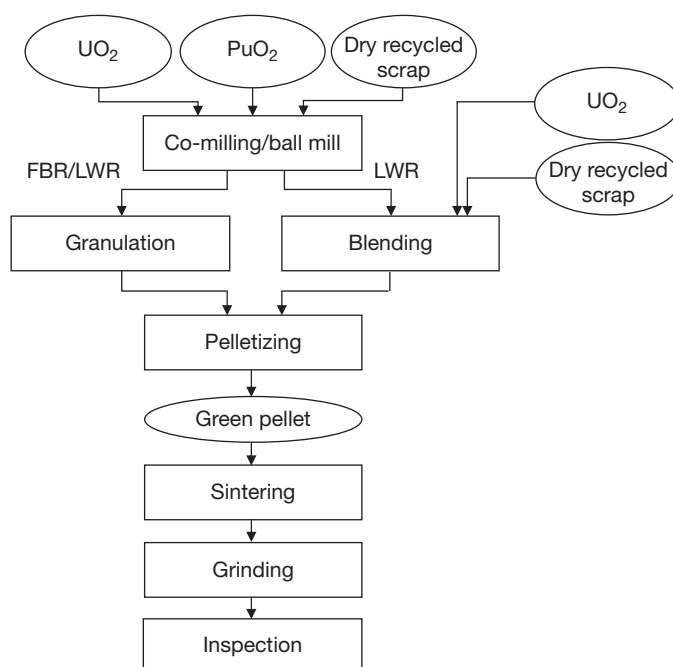
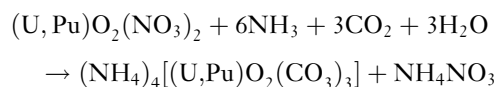


Figure 16 Flow sheet for the Optimized CO-Milling process.

FBRs and LWRs. The powders are co-milled to obtain a homogeneous distribution of plutonium, and the milled powder is pressed into green pellets after granulation. The second route (right half of [Figure 16](#)) is used to fabricate MOX pellets for LWRs; it effectively introduces the master blend concept into the process for better economy.⁷ This means that a mixture containing ~30% plutonium is made from UO_2 powder and PuO_2 powder, and this mixture is then milled using the OCOM milling process. The MOX powder that results from the milling process is no longer free-flowing. By mixing this master blend with the eight- to tenfold amount of free-flowing UO_2 powder to obtain the required plutonium content for LWR MOX fuel, a feed powder is obtained with sufficient flowability for direct pelletizing. An issue requiring special attention for this route is the homogeneity of the plutonium distribution; two powders of very different physical properties have to be mixed together to obtain the desired plutonium content. One powder is the master blend of PuO_2 and UO_2 , which after milling consists of a powder with very fine nonflowing grains and having a high tendency to self-agglomerate, while the second part is the free-flowing UO_2 powder prepared by the AUC process with its rather coarse grains.⁷ The mixing of the two powder components and preventing their segregation during further processing steps

require special attention and expertise. The green pellets prepared by the two routes are sintered in a reducing atmosphere after dewaxing. A typical α -autoradiograph of a transverse section of an LWR pellet manufactured by the OCOM process has been reported by Roepennack *et al.*⁶² The density and appearance of sintered pellets are inspected after centerless grinding.

The AUPuC process ([Figure 17](#)⁷) was developed as a coprecipitation process based on the AUC process. The AUPuC process uses plutonium in the form of a nitrate solution. NH_3 and CO_2 gases are introduced into a mixed solution of plutonium nitrate and uranyl nitrate with a concentration of about 400 g l^{-1} of heavy metal at first, and then tetraammonium tricarbonat dioxo urinate/plutonate is precipitated by the following reaction.⁷



The precipitated AUPuC is filtered and directly reduced at $\sim 750^\circ\text{C}$ in an atmosphere of hydrogen gas. The obtained MOX powder with about 30% plutonium concentration is utilized as the master blend and is the same as in the OCOM process. The homogeneity of plutonium in the master blend is much better in the AUPuC process than in the

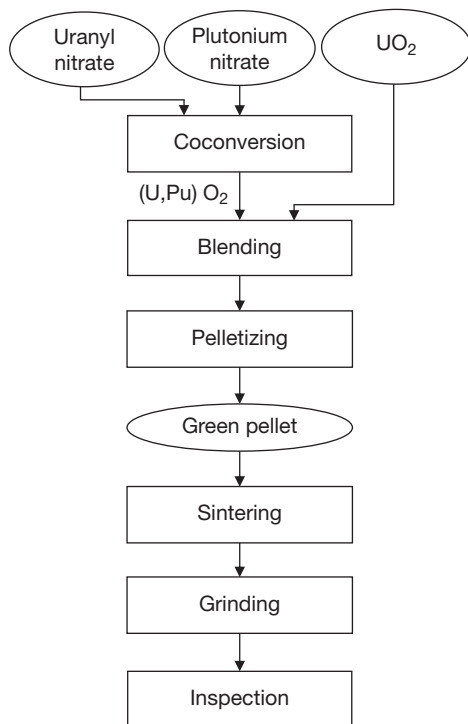


Figure 17 Flow sheet for the ammonium uranyl plutonyl carbonate process.

OCOM process because solid solutions have already formed during precipitation in the AUPuC process. This coconverted powder is also diluted like the master blend by the free-flowing UO₂ prepared by the AUC process and recycled MOX powder so that the final blended MOX powder has the desired plutonium concentration. This final blended MOX powder flows easily, just as in the OCOM process, and it is pressed into green pellets by a rotary pressing machine without granulation.⁴³ The steps after pelletizing are the same as those in the OCOM process. A typical α -autoradiograph of a transverse section of a LWR pellet manufactured by the AUPuC process has also been reported by Krellmann.⁷

On the basis of the above processes, Siemens constructed the MOX fuel fabrication facility in Hanau as a dual purpose (FBR and LWR) facility and started operation in 1972. After reaching an effective capacity of 20–25 tHM per year of LWR fuel in the 1987–1991 period, it was shut down, as a result of a contamination incident in 1991.⁶ This plant was subsequently decommissioned. On the same site, Siemens constructed a larger plant with an annual capacity of 120 tHM for LWRs.⁷ However, this plant was abandoned before starting operation

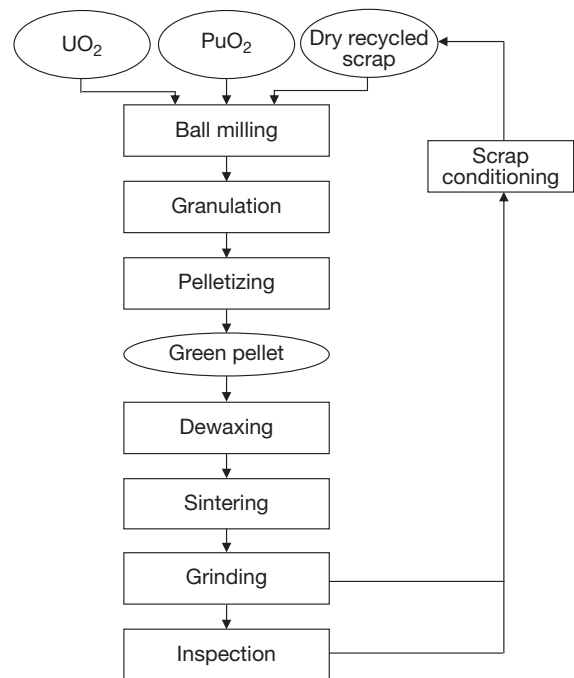


Figure 18 Flow sheet for the Japan Atomic Energy Agency process.

because Siemens never received an operating license from the local government.

2.15.5.2.4 Japan

Early in the 1960s, comprehensive R&D programs concerning MOX fuel were started in Japan and they resulted in the JAEA process that was adopted by the Plutonium Fuel Fabrication Facility (PFFF) which started operation in 1972. The PFFF used local control equipment to fabricate MOX fuel for the advanced thermal reactor FUGEN,⁶³ and the experimental fast reactor JOYO on an engineering scale. Following the completion of the Plutonium Fuel Production Facility (PFPP) in 1987, MOX fuel fabrications for JOYO and the prototype FBR MONJU have been conducted in PFPP since 1988. MOX fuel fabrication for FUGEN in PFFF was completed in 2001. Now, this plant is undergoing preparative work for its decommissioning.

Figure 18 shows the flow sheet of the JAEA process utilized in the PFPP. Two kinds of plutonium, either PuO₂ powder prepared by the oxalate precipitation or the MH-MOX powder, can be used in the JAEA process to fabricate FBR MOX pellets.

In this process, three feed powders, UO₂ prepared by the ADU process, PuO₂ or MH-MOX powder,

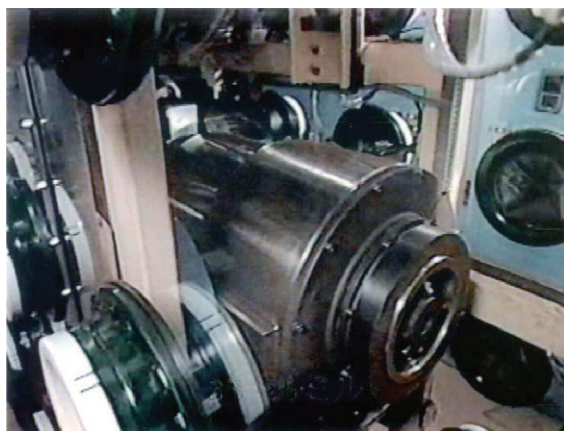


Figure 19 The ball mill used in the Plutonium Fuel Production Facility.

and dry recycled scrap powder, are prepared to get the plutonium concentration specified by the fuel specifications in the mixed powder. The feed powders are ball milled to get a homogeneous distribution of plutonium in the sintered MOX pellets. This mill pot has a silicon rubber lining on its inner surface to enhance the charging and discharging of powders by automated operation. About 40 kg of powder can be charged in this ball mill. A photograph of the ball mill is shown in [Figure 19](#).

Similar to the milled powder in the SBR process (see [Section 39.5.2.5](#)), this powder must be granulated to provide a free-flowing property.^{51,52} After mixing zinc stearate (binder) and Avicel (microcrystalline cellulose; pore former) with the milled powder, this powder mixture is roughly pressed into tablets at pressures of around 200 MPa and the tablets are then crushed into granules of sizes that make them free-flowing. These granules are pelletized into green pellets at pressures of around 500 MPa followed by the addition of zinc stearate as lubricant. Normally, these green pellets are sintered at about 1700 °C for 4 h under an atmosphere of Ar + 5% H₂ mixed gas after dewaxing at about 800 °C for 2 h under the same atmosphere as used in the sintering.⁶⁴ A ceramograph of a transverse section of a sintered MOX pellet prepared by the JAEA process is shown in [Figure 20](#). This MOX pellet was fabricated under specifications for pellets to be loaded in the MONJU outer core.

After centerless grinding, the diameter, geometrical density, and appearance of each sintered pellet are inspected. An inspection device to check pellet density and appearance is shown in [Figure 21](#); it is installed in the PFPF. Details of the JAEA process

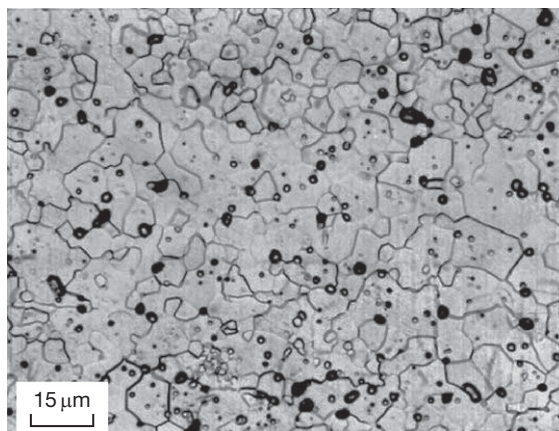


Figure 20 Ceramograph of a transverse section of a sintered mixed oxide of uranium and plutonium pellet for MONJU fuel prepared by the Japan Atomic Energy Agency process (plutonium content: 30.8 wt%, density: 84.84% theoretical density, mean grain size: 3.9 μm).

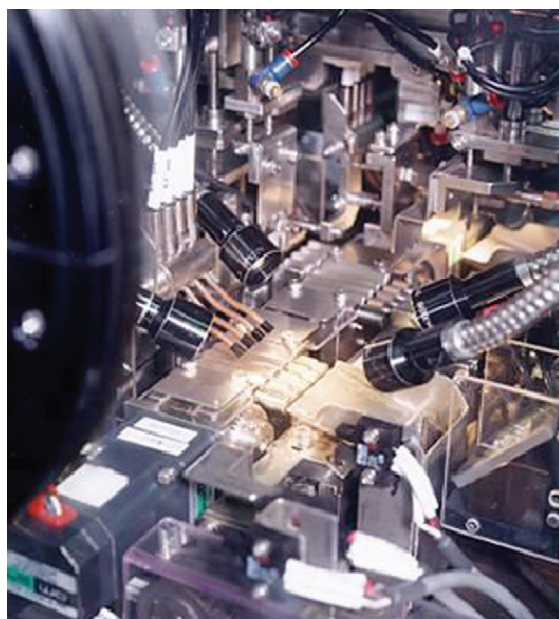


Figure 21 Inspection device for pellet density and appearance.

and its fuel fabrication technologies have been previously reported in the literature.^{64,65}

2.15.5.2.5 United Kingdom

In the United Kingdom, over the past 25 years, extensive work has been carried out on the manufacture of MOX fuel under the support of the UK Fast Reactor Development Program.⁵¹

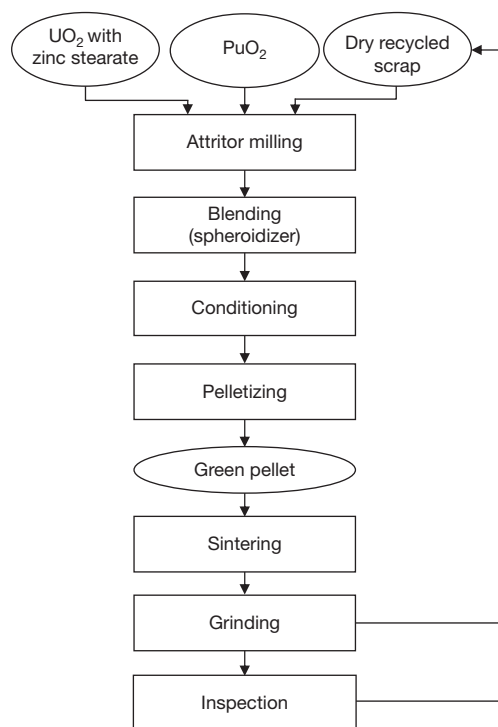


Figure 22 Flow sheet for short binderless route process.

Based on these experiences, the SBR process was developed by the British Nuclear Fuels plc (BNFL) to fabricate MOX pellets for LWRs. The process was originally developed in the 1980s by BNFL-UKAEA (United Kingdom Atomic Energy Authority). **Figure 22** shows the flow sheet for the SBR process.

In the SBR process, three kinds of feed materials, PuO_2 powder prepared by the oxalate precipitation method, UO_2 powder prepared by the ADU process, and dry recycled scrap powder are prepared to get the desired plutonium concentration in the initially mixed powder. These powders are milled completely using an attritor mill (a photograph is shown in MacLeod and Yates⁵¹), an off-the-shelf mill widely used in the pharmaceutical industry. The attritor mill provides good blends with a homogenized plutonium distribution in a short blending time and can be operated continuously.⁶ The milled MOX powder must be granulated in order to provide a free-flowing, dust-free feed to the pelletizing press to ensure uniform die filling and good compaction.⁵¹ In the milling step, the lubricant and Compo pore former are added in order to control the pellet density and obtain characteristics similar to those of the UO_2 pellets produced by BNFL from IDR UO_2 powder.⁶⁶ In order to condition

the milled MOX powder to form granules prior to pelletizing and sintering, a spheroidizer is introduced instead of the precompaction granulation equipment commonly used.⁶ The spheroidizer is used in a powder agglomeration process and was invented by SCK•CEN (Studiecentrum voor Kernenergie – Centre d'Etude de l'énergie Nucléaire) in the 1970s to fabricate a fuel kernel, the pit of coated particles fuelling high temperature reactors.⁶

In the SBR process, the binder that is commonly used in the conventional MOX fuel manufacturing process is not used. As a result, the dewaxing step of the green pellets prior to sintering is not needed and the process is similar to the current UO_2 fuel fabrication process in this respect. The processing time is short and the equipment can be stacked so that the powder can be discharged by gravity from the feed dispensing and dosing glove box through the processing equipment into the hopper of the pelletizing press. The simple sequence of one attritor mill and one spheroidizer, utilized in the Manufacturing Demonstration Facility, was made more sophisticated for the Sellafield MOX Plant by the addition of one homogenizer and one more attritor mill.⁶⁸ This expansion allowed the size of the powder lot to be increased from 50 kg MOX to 150 kg MOX with additional benefits such as reducing the number of quality control points and operating with a larger quantity of fuel with uniform plutonium isotopic composition.⁶ After conditioning in the spheroidizer, the powder is pelletized into green pellets using a hydraulic multipunch press, and then green pellets are sintered at temperatures of up to 1750 °C under an atmosphere of Ar + 4% H_2 mixture gas without heat treatment in a dewaxing furnace.⁶⁷ An automatic pellet inspection system is adopted for monitoring each pellet diameter, pellet surface, and end surfaces after centerless grinding.⁵¹ The MOX pellets produced by the SBR process have a mean grain size of about 7.4 μm with a standard deviation of 0.6 μm , and mean pore diameter is about 5 μm .⁶⁸

2.15.5.2.6 Developments for future systems

In order to improve the economical aspects of MOX pellet fabrication and to extend the fabrication process to MOX pellets containing MAs, various R&D programs have been started especially in France, Germany, Japan, and Russia.

In France, several coconversion processes have been developed and combined with the development of reprocessing processes. One typical coconversion process, called the CO-EXtraction (COEX) process,

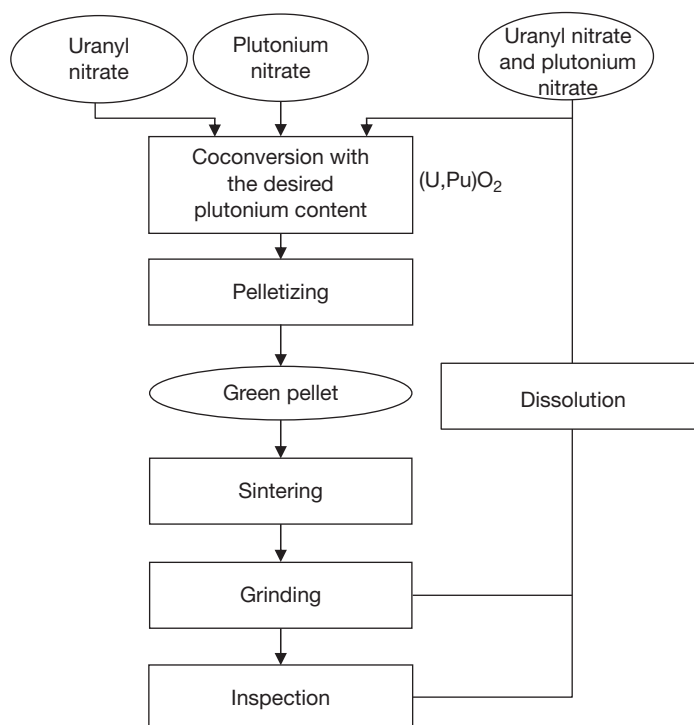


Figure 23 Flow sheet for the short process.

has been developed at the ATALANTE (Atelier Alpha et Laboratoires d'Analyses des Transuraniens et d'Etudes de Retraitement).^{61,69} In this, a mixture of uranyl and plutonium nitrate solutions containing MAs is coconverted to MOX powder following the oxalate precipitation method. According to the results of COEX pellet fabrication tests in the MELOX test chain, MOX pellets produced by the COEX process have mean grain size larger than 6 μm . These are compatible with current MOX manufacturing values obtained in the MELOX.⁶¹ In parallel with the above development, fuel fabrication processes have also been developed in the ATALANTE and LEFCA (Laboratoire d'Etudes et de Fabrications Experimentales de Combustibles Nucleaires Avances).

In Germany, basic R&D concerning fabrication processes for MOX fuel bearing MAs have been carried out at the Institute for Transuranium Elements (ITU).⁷⁰ One of the fuel irradiation test programs carried out by ITU was the SUPERFACT experiment. In this experiment, SUPERFACT fuels bearing Np or Am were fabricated by the sol-gel method and they were irradiated in various fast reactors.^{70,71}

In Japan, a simplified MOX pellet fabrication process, the short process, has been developed on the

basis of the MH method, for the above purposes. The flow sheet for this process is shown in **Figure 23**. A 300 g scale laboratory test of the short process has been successfully completed.⁷²

In the short process, three different solutions, uranyl nitrate, plutonium nitrate, and a nitrate solution in which rejected MOX pellets are dissolved, are mixed to obtain the desired plutonium content in the final mixed solution. Then, the mixed solution is converted to the MH-MOX powder with desired plutonium content by the MH method. This converted MH-MOX powder is tumbling-granulated after adding an adequate amount of water as a binder to improve its flowability. The tumbling-granulated MH-MOX powder is calcined at 750 °C in air and reduced to MH-MOX powder at 750 °C under an atmosphere of $\text{N}_2 + 5\% \text{ Ar}$ mixed gas. The MH-MOX powder so obtained is directly pressed into green annular pellets using a die-wall lubrication method. These are then sintered without heat treatment in the dewaxing furnace because the amount of organic compounds contained in the green pellets is controlled at a lower value than that in pellets prepared by the conventional MOX fuel fabrication process. Sintered MOX pellets are ground by a centerless grinder, and subsequently, the geometrical



Figure 24 Photograph of annular mixed oxide of uranium and plutonium pellets prepared by the short process (outer diameter: ~ 7 mm, height: ~ 8 mm, diameter of center hole: ~ 2 mm).

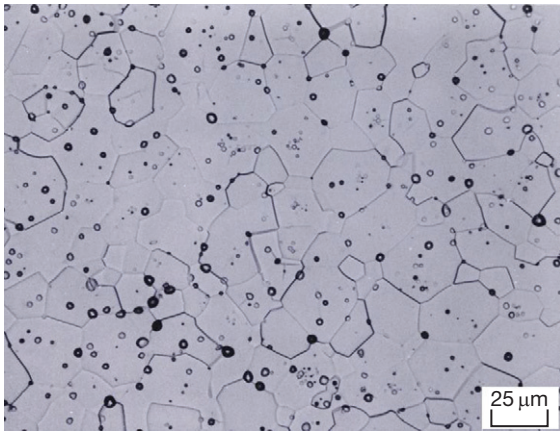


Figure 25 Ceramograph of a transverse section of a mixed oxide of uranium and plutonium pellet prepared by the short process (plutonium content: 30.0 wt%, density: 96.72% theoretical density, mean grain size: 14 μm).

density and appearance of each pellet are inspected. The MOX pellets rejected at the inspections are dissolved in nitric acid and used as part of the final blending solution as shown in Figure 23. Figure 24 shows a photograph of annular MOX pellets prepared by the short process. A ceramograph of a pellet prepared by the short process is shown in Figure 25.

The MOX pellets manufactured by the short process have a larger mean grain size than those manufactured by the other processes such as the SBR, MIMAS, JAEA, and COEX processes. The development of a series of small scale (kg scale) test devices was started in 2007.⁷³ In parallel with this work, JAEA has an irradiation test program for MOX pellets bearing MAs, to understand their irradiation behavior. In this program, MOX pellets bearing the MAs, Am, and Np were prepared by the JAEA process and irradiated in the JOYO. These irradiated pellets were subjected to postirradiation examinations and the results obtained have been reported in Maeda *et al.*^{74,75}

In Russia, RIAR (Research Institute of Atomic Reactors) has proposed the demonstration program

concept DOVITA (Dry reprocessing, Oxide fuel, Vibropac, Integral, Transmutation of actinides) and many R&D activities related to them have been carried out. From this program, vibro-packing technology has been applied to load MOX granules into a cladding tube.^{76,77}

2.15.6 Rod Fabricating and Assembling

2.15.6.1 LWR UO_2 and MOX Fuels

The LWR fuel designs are described in Section 39.3.2. There are some differences in the fuel assembly fabrication process between PWRs and BWRs. On the other hand, there is no major difference between UO_2 and MOX with respect to the fuel assembly fabrication. As an example, the flow sheet of PWR fuel assembly fabrication is shown in Figure 26.

2.15.6.1.1 Rod fabrication

The fabrication of LWR fuel rods involves the introduction of fuel pellets and a spring into the cladding tube, followed by welding of the end plugs and the cladding tube. For PWRs, the rods are filled with helium at a higher pressure than for BWRs. For this purpose, the top plug has a hole through which the fuel rod is pressurized, and then the hole is arc-welded. The fuel rods are inspected for surface contamination, dimensions, appearance, plug welds, leak tightness, and uranium enrichment. The fabrication and inspection operations are highly automated and use advanced inspection technologies, such as an X-ray image digitizing system.

2.15.6.1.2 Assembly fabrication

The PWR fuel assembly consists of fuel rods, grids, the top nozzle, the bottom nozzle, the instrumentation tube, and guide tubes. First, the skeleton assembly is made, which is an assembly of the instrumentation tube and the grids. Then, the fuel rods and the guide tubes are inserted into the skeleton assembly. Finally, the top nozzle and the bottom nozzle are mounted on the guide tubes by screws.

The BWR fuel assembly consists of fuel rods, water rods, grid spacers, the upper tie plate and the lower tie plate. First, the water rods, grid spacers, and the lower tie plate are assembled. Then, fuel rods are inserted into grid spacers and tie rods are connected to the lower tie plate. Finally, the upper tie plate is mounted and connected to the tie rods with screws.

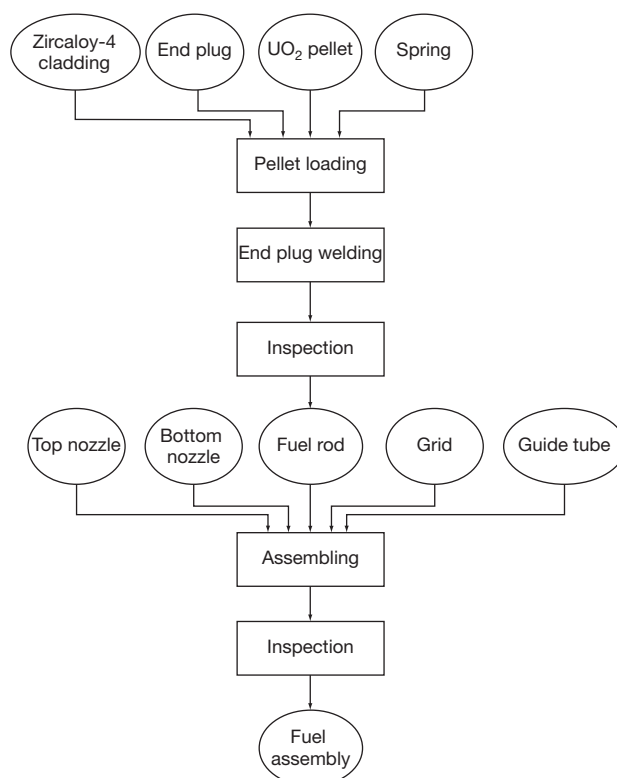


Figure 26 Flow sheet for pressurized water reactor fuel assembly fabrication.

The dimensions and appearance of the fuel assemblies are inspected and the BWR fuel assembly is attached to the channel box before loading it into a reactor.

2.15.6.2 Fast Spectrum Oxide Fuel Reactors

As described in [Section 2.15.3.2.7](#), two types of pin spacing for fuel assemblies, the grid type and the wire type, have been adopted for all FBRs. The wire type is more widely used except those for the Dounreay Fast Reactor in UK.³⁴ Here, the rod fabrication and assembly are described taking a wire spacer type fuel assembly from the MONJU as an example.

The lower end plug is TIG-welded (tungsten inert gas-welded) to a cladding tube made of SUS 316 based alloy; this is done outside the PFPE. Cladding tubes with lower end plugs are then transferred to PFPE along with blanket pellets of depleted UO_2 and the other cold components such as plenum sleeves and plenum springs. After adjusting the column length of MOX pellets and measuring their weight, they are loaded into each cladding tube

with the other components; this is done in a glove box under a helium gas atmosphere. Then, an upper end plug is TIG-welded to the cladding tube. In this welding, the position of the weld electrode is adjusted automatically using image analysis. [Figure 27](#) shows photographs of a welding torch installed in the glove box and an image display showing the position of the weld electrode.

Decontamination of the fuel rod surface is carried out prior to a contamination check. The fuel rods which pass the contamination check are brought from the glove box and are sent to the helium leak test to certify tightness of the welded part. An X-ray check of the welded part to confirm its soundness is also carried out prior to wrapping a spacer wire around the fuel rod. Finally, each fuel rod is checked for its weight, straightness, gap between spacer wire and fuel rod, γ -ray spectrum from Am in the MOX pellets, and general surface appearance. Next, 169 fuel rods are transferred to the automated assembly station where 15 layers of fuel rods, consisting of 8–15 rods in each layer, are prepared at first. The layers of fuel rods are fixed to the entrance nozzle one by one to get a hexagonal cross-section. This bundle of 169

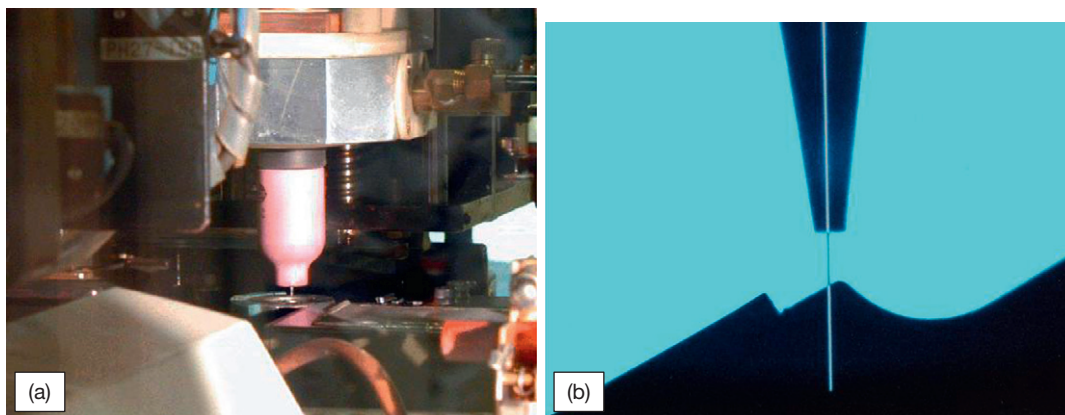


Figure 27 Photographs of (a) a welding torch and (b) an image display showing the position of the weld electrode.

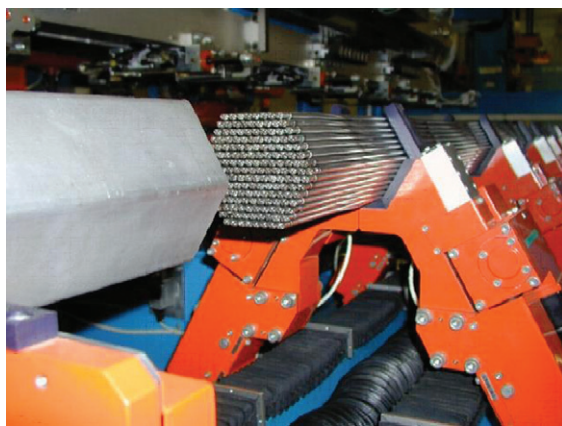


Figure 28 Photograph of assembling station.

fuel rods is inserted into a wrapper tube, and then this wrapper tube is TIG-welded to the entrance nozzle.

Figure 28 shows a photograph of a bundle being inserted into a wrapper tube at the assembly station. The completed fuel assembly is then moved to an inspection station to confirm its straightness, twist, distance between opposite outer surfaces and appearance through automatic and remote operations.

2.15.7 Outlook

Oxide fuels are one of the most popular selections for fast reactor fuel systems, metallic fuels being the other.⁷⁸ The basis of this popularity can be largely attributed to the great successes achieved in fabrication and operation of LWR oxide fuels.⁴² Nowadays, LWR operators are seeking ever higher burn-ups of their fuel to attain an economical advantage for LWRs compared to other power plants burning coal

and natural gas. However, the current fuel design has reached its limit at an estimated burn-up of $\sim 80 \text{ GWd tU}^{-1}$.²⁹ In addition, LWRs produce outlet coolant water at a maximum temperature of $\sim 320^\circ\text{C}$; this limits the efficiency of converting heat to electricity to $\sim 33\%$ and precludes its use as process heat for H_2 production.²⁹ The above disadvantages in LWRs based on UO_2 fuel may possibly be overcome by the very high temperature reactor (VHTR). The VHTR is fueled by tiny fuel particles embedded in graphite and are cooled by helium (see **Chapter 3.06, TRISO Fuel Production**). Certain R&D projects still remain to introduce the VHTR commercially, in place of LWRs.

For next generation fuel systems that need to burn MAs and process the fuel in a manner that never yields pure plutonium, modifications will be required to minimize waste generation, maximize safety, and maintain operation economics.⁴² At present, oxide fuels have a higher potential for use in next generation reactor systems than other fuels because a wealth of data has been accumulated for oxide fuels such as fuel fabrication, irradiation behavior, and reprocessing. As time is still needed to switch from LWRs to FBRs, other fuel systems still have a chance to be the next generation fuel systems through development of innovative technologies.

References

1. World Nuclear Power Reactors 2007–2009 and Uranium Requirements, World Nuclear Association, Apr 2009; <http://www.world-nuclear.org/info/reactors.html>.
2. IAEA. *Status and Advances in MOX Fuel Technology*; Technical Reports Series No. 415; IAEA: Vienna, Austria, 2003.

3. Une, K.; Oguma, M. *J. Nucl. Mater.* **1983**, *115*, 84–90.
4. Une, K.; Oguma, M. *J. Nucl. Mater.* **1985**, *131*, 88–91.
5. MacLeod, H. M.; Yates, G. *Nucl. Technol.* **1993**, *102*, 3–17.
6. Bariot, H.; Van Vliet, J.; Chiarelli, G.; Edwards, J.; Nagai, S.; Reshetnikov, F. In *MOX Fuel Cycle Technologies for Medium and Long Term Deployment*, Vienna, Austria, May 17–21, 1999; IAEA: Vienna, Austria, 2000; pp 81–101.
7. Krellmann, J. *Nucl. Technol.* **1993**, *102*, 18–28.
8. Carr, R. L., Jr. *Chem. Eng.* **1965**, Jan 18, 163–168.
9. ASTM International. *Standard Test Method for Solid Characteristics by Carr Indices*, ASTM D 6393-99; ASTM International: West Conshohocken, PA, 2006.
10. Asakura, K.; Kato, Y.; Furuya, H. *Nucl. Technol.* **2008**, *162*, 265–275.
11. Asakura, K.; Takeuchi, K.; Makino, T.; Kato, Y. *Nucl. Technol.* **2009**, *167*, 348–361.
12. Takeuchi, K.; Kato, M.; Sunaoshi, T.; Aono, S.; Kashimura, M. *J. Nucl. Mater.* **2009**, *385*, 103–107.
13. Matzke, H. J. *J. Nucl. Mater.* **1983**, *114*, 121–135.
14. Leyva, A. G.; Vega, D.; Trimarco, V.; Marchi, D. *J. Nucl. Mater.* **2002**, *303*, 29–33.
15. Martin, D. G. *J. Nucl. Mater.* **1988**, *152*, 94–101.
16. Kato, M.; Morimoto, K.; Sugata, H.; Konashi, K.; Kashimura, M.; Abe, T. *J. Alloys Compd.* **2008**, *452*, 48–53.
17. Beals, R. J.; Handwerk, J. H.; Wrona, B. J. *J. Am. Ceram. Soc.* **1969**, *52*, 578–581.
18. Fukushima, S.; Ohmichi, T.; Maeda, A.; Watanabe, H. *J. Nucl. Mater.* **1982**, *105*, 201–210.
19. Hirai, M. *J. Nucl. Mater.* **1990**, *173*, 247–254.
20. Oak Ridge National Laboratory. Dissolution of high-density UO_2 , PuO_2 , and UO_2 - PuO_2 pellets in inorganic acids, ORNL-3695; Oak Ridge National Laboratory: Oak Ridge, TN, 1965.
21. Oak Ridge National Laboratory. Preparation and properties of actinide oxides, ORNL-4272; Oak Ridge National Laboratory: Oak Ridge, TN, 1968.
22. Lerch, R. E. Dissolution of mixed oxide fuel as a function of fabrication variables, HEDL-SA-1935; US/United Kingdom Information Exchange on Dissolution of Nuclear Fuel: Windscale, UK, Oct 16, 1979.
23. Crofts, J. A.; Douglas, J. A. M.; Weatherley, L. R.; Wilkinson, K. L. In *Proceedings of a Symposium Sponsored by the Society of Chemical Industry*, Dounreay, UK, May 15–18, 1979; Society of Chemical Industry: London, 1980; pp 149–168.
24. Shibata, K.; et al. *J. Nucl. Sci. Technol.* **2002**, *39*, 1125–1136.
25. Hori, M. *Kiso Kousokuro Kougaku (Basic Fast Reactor Engineering)*; The Nikkan Kogyo Shimbun: Tokyo, 1993 (in Japanese).
26. Nakae, N. *J. Nucl. Sci. Technol.* **2006**, *43*, 361–366.
27. Cahn, R. W.; Haasen, P.; Kremer, E. J., Eds. *Materials Science and Technology*, Vol. 10A: *A Comprehensive Treatment*; VCH (Verlagsgesellschaft mbH): Weinheim, Germany, 1994.
28. Bailly, H.; Menessier, D.; Prunier, C., Eds. *The Nuclear Fuel of Pressurized Water Reactors and Fast Reactors*; CEA: Paris, 1999.
29. Olander, D. *J. Nucl. Mater.* **2009**, *389*, 1–22.
30. Tarlton, S., Ed. *Nucl. Eng. Int.* **2008**, *53*, 26–36.
31. Lawrence, L. A.; Jensen, S. M.; Hales, J. W.; Kamesky, R. A.; Makenas, B. J. In *International Conference on Reliable Fuels for Liquid Metal Reactors*, Tucson, AZ, Sept 7–11, 1986; ANS (American Nuclear Society): La Grange Park, IL, 1986; pp 3–62–3–74.
32. <http://www.mhi.co.jp/en/index.html>.
33. Department of Energy, National Nuclear Security Administration. In *Amended Record of Decision for the Surplus Plutonium Disposition Program*, 67 FR 76, Apr 19, 2002; Office of the Federal Register: Washington, DC, 2002.
34. IAEA. *Fast Reactor Database 2006 Update*, IAEA-TECDOC-1531; IAEA: Vienna, Austria, 2006.
35. Assman, H.; Becker, M. *Trans. Am. Nucl. Soc.* **1979**, *31*, 147–148.
36. Heal, T. J.; Littlechild, J. E. *Trans. Am. Nucl. Soc.* **1978**, *28*, 326–328.
37. Assman, H.; Bairiot, H. Technical Report Series No. 221; IAEA: Vienna, Austria, 1983; pp 161–166.
38. Hirai, M.; Hosokawa, T.; Yuda, R.; et al. In *Proceedings of the International Topical Meeting on LWR Fuel Performance*, Portland, OR, Mar 2–6, 1997; ANS (American Nuclear Society): La Grange Park, IL, 1997.
39. Bourgeois, L.; Dehaudt, Ph.; Lemaignan, C.; Hammou, A. *J. Nucl. Mater.* **2001**, *297*, 313–326.
40. Harada, Y. *J. Nucl. Mater.* **1997**, *245*, 217–223.
41. Assmann, H.; Peehs, M.; Roepenack, H. *J. Nucl. Mater.* **1988**, *153*, 115–126.
42. Burkes, D. E.; Fielding, R. S.; Porter, D. L.; Meyer, M. K.; Makenas, B. J. *J. Nucl. Mater.* **2009**, *393*, 1–11.
43. Kittel, J. H.; Frost, B. R. T.; Mustelier, J. P.; Bagley, K. Q.; Crittenden, G. C.; Van Dievoet, J. *J. Nucl. Mater.* **1993**, *204*, 1–13.
44. Boltax, A. In *Materials Science and Technology: A Comprehensive Treatment*; Cahn, R. W., Haasen, P., Kremer, E. J., Eds.; VHC: New York, 1994; Vol. 10B, pp 341–390.
45. Mignanelli, M.; Potter, P. E. In *Proceedings of the BNES International Conference, Science and Technology of Fast Reactors Safety*, Guernsey, UK, May 12–16, 1986; British Nuclear Energy Society: London, 1986; Vol. 1, pp 53–57.
46. Mignanelli, M.; Potter, P. E. *Thermochim. Acta* **1988**, *129*, 143–160.
47. Strain, R. V.; Bottcher, J. H.; Ukai, S.; Arai, Y. *J. Nucl. Mater.* **1993**, *204*, 252–260.
48. OECD NEA. *Management of Separated Plutonium – The Technical Options*; OECD NEA: Paris, 1997.
49. Haas, D.; Vandergheynst, A.; Lorenzelli, R.; Nigon, J. L. *Nucl. Technol.* **1994**, *106*, 60–82.
50. Cleveland, M. J. *The Chemistry of Plutonium*; ANS (American Nuclear Society): La Grange Park, IL, 1979.
51. MacLeod, H. M.; Yates, G. *Nucl. Technol.* **1993**, *102*, 3–17.
52. Asakura, K.; Kato, Y.; Furuya, H. *Nucl. Technol.* **2008**, *162*, 265–275.
53. Koizumi, M.; Ohtsuka, K.; Isagawa, H.; Akiyama, H.; Todokoro, A. *Nucl. Technol.* **1983**, *61*, 55–70.
54. Oshima, H. *J. Sci. Technol.* **1989**, *26*(1), 161–166.
55. Kato, Y.; Kurita, T.; Abe, T. *J. Sci. Technol.* **2004**, *41*(8), 857–862.
56. Kato, Y.; Kurita, T.; Abe, T. *Trans. Jpn. Nucl. Soc.* **2005**, *4*(1), 77–83 (in Japanese).
57. Lippens, M.; Van Loon, C.; Ketels, J. In *The IAEA Technical Meeting on Properties and Materials for Water Reactor Fuel Elements and Methods of Measurement*, Vienna, Austria, Oct 13–16, 1986; IAEA: Vienna, Austria, 1986; pp 69–76.
58. Oudinet, G.; Munuz-Viallard, I.; Aufore, L.; et al. *J. Nucl. Mater.* **2007**, *375*, 86–94.
59. Garcia, P.; Bouloré, A.; Guérin, Y.; Trotabas, M.; Goeuriot, P. In *Proceeding of International Meeting on Light Water Reactor Fuel Performance*, CD-ROM, Park City, UT, Apr 10–13, 2000; ANS (American Nuclear Society): Park City, UT, 2000.
60. Asakura, K.; Takeuchi, K. *J. Nucl. Mater.* **2005**, *348*, 165–173.

61. Castelli, R.; Gervais, T.; Favel, D.; Ytoumel, B. In *Proceedings of Global 2009. The Nuclear Fuel Cycle: Sustainable Option & Industrial Perspectives*, Paris, France, Sept 6–11, 2009; SFEN (French Nuclear Society): Paris, 2009; pp 103–107.
62. Roepennack, H.; Shhlemmer, F. U.; Schlosser, G. J. *Nucl. Technol.* **1986**, *77*, 175–186.
63. Okita, T.; Aono, S.; Asakura, K.; Aoki, Y.; Ohtani, T. In *MOX Fuel Cycle Technologies for Medium and Long Term Deployment*, Vienna, Austria, May 17–21, 1999; IAEA: Vienna, Austria, 2000; pp 109–117.
64. Asakura, K.; Yamaguchi, T.; Ohtani, T. *J. Nucl. Mater.* **2007**, *357*, 126–137.
65. Asakura, K.; Aono, S.; Yamaguchi, T.; Deguchi, M. In *Fuel Cycle Technologies for Medium and Long Term Deployment*, Vienna, Austria, May 17–21, 1999; IAEA: Vienna, Austria, 2000; pp 119–126.
66. Swedish Nuclear Powder Inspectorate (SNPI). *Models for MOX Fuel Behavior*, A selective review; SNPI: Stockholm, Sweden, 2006.
67. Edwards, J.; Brown, C.; Marshall, S.; Connell, M.; Thompson, H. In *The Fifth International Conference on Recycling, Conditioning and Disposal – RECOD 98*, Nice, France, Oct 25–28, 1998; SFEN (French Nuclear Society): Paris, 1999; pp 182–190.
68. IAEA. *Recycling of Plutonium and Uranium in Water Reactor Fuel*; Edwards, J., Crimoldby, R. D., Marshall, S. J., Stratton, R. W., Eds.; BNFL Supply of MOX Fuel Assemblies to the Beznau 1 PWR of NOK, IAEA-TECDOC-941; IAEA: Vienna, Austria, 1995; pp 57–67.
69. Grandjean, S.; Arab-Chapelet, B.; Robisson, A. C.; *et al.* Synthesis of mixed actinide compounds by hydrometallurgical co-conversion methods. In *Proceedings of Global 2007, Advanced Nuclear Fuel Cycles and Systems*, Boise, ID, Sept 9–13, 2007; pp 98–105.
70. Fernandez, A.; McGinley, J.; Somers, J.; Walter, M. *J. Nucl. Mater.* **2009**, *392*, 133–138.
71. Prunier, C.; Boussard, F.; Koch, L.; Coquerelle, M. *Nucl. Technol.* **1997**, *119*, 141–148.
72. Asakura, K.; Takeuchi, K.; Makino, T.; Kato, Y. *Nucl. Technol.* **2009**, *167*, 348–361.
73. Ito, M.; Funasaka, H.; Namekawa, T. In *European Nuclear Conference (ENC) 2007*, Brussels, Belgium, Sept 16–20, 2007; ENC: Brussels, 2007.
74. Maeda, K.; Sasaki, S.; Kato, M.; Kihara, Y. *J. Nucl. Mater.* **2009**, *385*, 178–183.
75. Maeda, K.; Sasaki, S.; Kato, M.; Kihara, Y. *J. Nucl. Mater.* **2009**, *389*, 78–84.
76. Herbig, R.; Rudolph, K.; Lindau, B.; Skiba, O. V.; Maershin, A. A. *J. Nucl. Mater.* **1993**, *204*, 93–101.
77. Bychkov, A. V.; Skiba, O. V.; Mayorshin, A. A.; *et al.* Burning of minor actinides in fuel cycle of the fast reactor: DOVITA programme-results of the 10 year activities. In *Proceedings of Actinide and Fission Product Partitioning and Transmutation. 7th Information Exchange Meeting*, Jeju, Republic of Korea, Oct 14–16, 2002; pp 295–307.
78. Burkes, D. E.; Fielding, R. S.; Porter, D. L.; Crawford, D. C.; Meyer, M. K. *J. Nucl. Mater.* **2009**, *389*, 458–469.

2.16 Burnable Poison-Doped Fuel

K. Hesketh

UK National Nuclear Laboratory, Preston, UK

© 2012 Elsevier Ltd. All rights reserved.

2.16.1	Introduction	423
2.16.2	Control of Neutron Multiplication Factor in Nuclear Reactors	424
2.16.3	Comparison of Burnable Poisons	425
2.16.3.1	Boron	425
2.16.3.2	Gadolinium	427
2.16.3.3	Erbium	429
2.16.3.4	Dysprosium	429
2.16.3.5	Comparison of Burnable Poisons	431
2.16.4	Burnable Poison Materials Property Requirements	433
2.16.5	Materials Characteristics of Integral Burnable Poisons	434
2.16.6	Effect of Burnable Poisons on Fuel and Core Operating Parameters	436
2.16.7	Burnable Poison Engineering Design Process and Economics	437
2.16.8	Future Developments	438
References		438

Abbreviations

AGR	Advanced gas reactor
BWR	Boiling water reactor
CANDU	Canadian designed heavy water cooled and moderated reactor
Dy₂O₃	Dysprosium oxide (dysprosia)
Er₂O₃	Erbium oxide (erbia)
Gd₂O₃	Gadolinium oxide (gadolinia)
GWd/tHM	Gigawatt-days per tonne of initial heavy metal
IFBA	Integral fuel burnable absorber
IMF	Inert matrix fuel
k	Neutron multiplication factor
LWR	Light water reactor
PWR	Pressurized water reactor
RBMK	Russia designed graphite moderated water cooled reactor
UO₂	Uranium dioxide (urania)
VVER	Russian designed PWR

2.16.1 Introduction

Burnable poisons or burnable absorbers perform a very valuable function in nuclear fuels. They are materials, such as boron, gadolinium, erbium, or dysprosium, which in their unirradiated state have a high

propensity for neutron absorption, but which transform into ones that absorb very little after capturing a neutron. By this means, the neutron multiplication factor can be controlled in the reactor throughout the lifetime of the fuel with less reliance on insertion of neutron-absorbing control rods or other control mechanisms.

The first application of burnable poisons was actually for an early submarine reactor design. It was discovered that control rods would be insufficient on their own to control the neutron multiplication factor for the specified refueling cycle time of the core and burnable poisons were used for supplementary control. Today, burnable poisons are used extensively in commercial light water reactors (LWRs), comprising western pressurized water reactors (PWRs) and the Russian equivalent denoted VVERs and boiling water reactors (BWRs). LWRs are by far the most numerous of the 436 commercial reactors currently (2009) in operation. The UK's advanced gas-cooled reactors (AGRs) also rely heavily on burnable poisons. The other reactor types in commercial operation (Canadian designed heavy water cooled and moderated reactor (CANDU), Russian designed graphite moderated water cooled reactors (RBMKs), and the UK Magnox reactors) do not normally use burnable poisons at present, though there is an advanced fuel bundle design available for CANDU reactors that do use them.

2.16.2 Control of Neutron Multiplication Factor in Nuclear Reactors

A nuclear reactor operating at a steady power has a neutron multiplication factor of precisely 1.0. In this state, each fission event yields on average one further fission reaction to maintain the chain reaction. If the multiplication factor is <1.0 , the nuclear chain reaction will die away quickly, while if >1.0 , the chain reaction will build up exponentially. A definition of the neutron multiplication factor, usually denoted k , is:

$$k = \frac{\text{(No. of neutrons born in generation } j\text{)}}{\text{(No. of neutrons born in generation } j - 1\text{)}}$$

In a reactor operating in the steady state, it is possible to maintain k extraordinarily close to 1 using the inherent negative feedback effects, so that the power output precisely matches the amount of thermal energy extracted from the reactor; thermal power production from the reactor in excess of that removed by the turbine generator raises the temperature of the reactor, and temperature feedback effects reduce the multiplication factor to establish a new balance between reactor output and thermal load.

Some reactors are operated on-load, meaning that fuel can be inserted during full power operation. In such a reactor, it is theoretically possible to start the reactor with just sufficient fissile material (such as ^{235}U) so that k just marginally exceeds 1.0 at full power. As the fissile material is depleted (burns up), fresh fuel is added to compensate and a corresponding quantity of spent fuel is discharged.

However, on-load refueling is not practical in all reactors; many are designed such that access to the fuel is possible only with the reactor shut down and such reactors operate with batch refueling. This means that the reactor is shut down periodically (typically every 12–24 months) and a fraction of the fuel replaced (with an equivalent amount of the highest burnup fuel discharged). In between refueling shutdowns, the reactor operates with no change in the fissile inventory, except for those changes due to fuel depletion and the buildup of fission products and transuranic elements through neutron captures. The next refueling occurs when the fissile content is depleted to the point where, with all control absorbers removed from the core, the reactor is just capable of maintaining $k = 1.0$ at full power.

It is useful to note the concept of reactivity at this point, which is a dimensionless quantity usually measured in units of per cent mill or 10^{-5} . It is

defined by

$$\rho = 10^5 [(k - 1)/k] \text{pcm}$$

A reactor that is just critical has a reactivity of zero and is in steady-state operation. Positive reactivity corresponds to a reactor where the neutron flux and power output are increasing with time, while conversely, negative reactivity corresponds with decreasing flux and power. Control rod insertion is said to cause a decrease in reactivity, while their withdrawal is said to increase reactivity.

The upper curve in [Figure 1](#) illustrates the variation of k with irradiation for a typical PWR fuel assembly with an initial ^{235}U enrichment of 4.45 wt% and no burnable poison. At low irradiation, k is around 1.3, while by the time the fuel has reached its discharge burnup of ~ 55 Gigawatt-days per tonne (1 Gigawatt-days is a convenient unit of thermal energy output for nuclear fuel equivalent to $8.64 \times 10^{13} \text{ J ton}^{-1}$; the mass refers to 1 ton of initial heavy metal and the unit is usually abbreviated GWd/tHM), k for the assembly is lower than 1.0. Thus, by the time the fuel is ready for discharge, it is incapable of sustaining a chain reaction by itself. However, the core always contains a mix of fresh fuel in its first cycle of irradiation along with highly irradiated fuel and the fresh fuel effectively donates excess neutrons to the high irradiation fuel such that for the core as a whole, $k = 1.0$.

Batch refueling causes a problem, however, because if the core is capable of attaining $k = 1.0$ at the end of the cycle, then by implication, the uncontrolled k must exceed 1.0 at earlier times. In principle of course, control rods can be inserted to control the excess multiplication factor, but in practice, there are limitations: First, the control rods have a limited effectiveness and more might be required than is practical within the engineering constraints. Second, inserting control rods distorts the spatial distribution of neutron flux and power within the core, causing localized power peaking that might easily exceed the acceptable performance limits of the fuel. Some means is therefore needed to supplement the control rods.

To an extent, PWRs are able to achieve this with boron as boric acid dissolved in the coolant. This soluble absorber approach has its limitations as well, as will be seen later, and soluble absorber is not an option for most other reactor types. Burnable poisons are used to fill this reactivity control gap. The lower curve in [Figure 1](#) illustrates how a burnable poison (in this case, 24 fuel rods per assembly consisting of 6 wt% Gd_2O_3 in UO_2 with a ^{235}U enrichment of

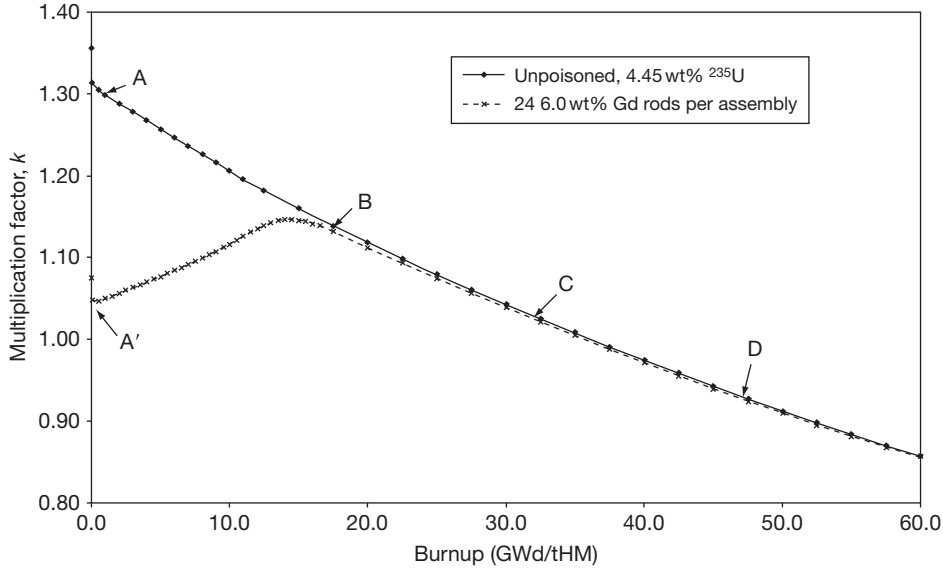


Figure 1 Variation of multiplication factor in a pressurized water reactor with fuel irradiation in GWd/tHM: 4.45 wt% enriched pressurized water reactor assembly with no burnable poison and with 24 poisoned fuel rods containing 6 wt% Gd_2O_3 .

4.45 wt%) might be used to control the excess reactivity of fresh fuel by holding down the multiplication factor in low burnup fuel assemblies. Consider, for example, a 3-batch fueling scheme in which the core is made up of equal quantities of fuel assemblies in their first, second, and third irradiation cycles. At the start of the fuel cycle, the first cycle assemblies will have zero burnup, corresponding to points A and A' unpoisoned and poisoned, respectively. Similarly, the second and third cycle assemblies will correspond to points B and C. The multiplication factor of the unpoisoned core will be $k_1 = [k(A) + k(B) + k(C)]/3$ at the start of the cycle. At the end of the cycle, the three assembly types will have burned up to points B, C, and D and k will be $k_2 = [k(B) + k(C) + k(D)]/3 = 1.0$. The difference in reactivity between the start and end of the cycle is $k_1 - k_2 = [k(A) - k(D)]/3$. For the poisoned assembly, the corresponding difference is

$$k'_1 - k'_2 = [k(A') - k(D)]/3.$$

Since $k(A') < k(A)$, the change in multiplication factor during the cycle is considerably reduced. Ideally, the burnable poison material is depleted during the fuel cycle such that there is none left at the end of the first irradiation cycle indicated; any residual poison material left at the end of the cycle means that the cycle will end prematurely or will require an increased initial ^{235}U loading if the cycle length is to be preserved, both of which equate to an economic

penalty. The small gap between the poisoned and unpoisoned curves in [Figure 1](#) represents just such a residual poison penalty.

2.16.3 Comparison of Burnable Poisons

There are three burnable poison materials in common use in current fuel assembly designs, and they are boron, gadolinium, and erbium. There is also an advanced fuel design for CANDU reactors (called the CANFLEX bundle) that uses dysprosium burnable poison, but it has yet to be used on a commercial scale. They all have one or more isotopes with a large neutron capture cross-section that, following a neutron capture, are transformed into isotopes with small cross-sections.

2.16.3.1 Boron

Natural boron consists of the two isotopes ^{10}B and ^{11}B at 19.9% and 80.1% natural abundance, respectively.^{1,2} ^{10}B has a thermal neutron capture cross-section (meaning the neutron absorption cross-section for a neutron moving with 0.0256 eV kinetic energy) of 3837 barns² (where a barn is a convenient unit of area 10^{-28} m^2). Following a neutron capture, it is transmuted to ^7Li and ^4He , both of which have very low neutron absorption cross-sections. For some applications, for example, where it is difficult to incorporate

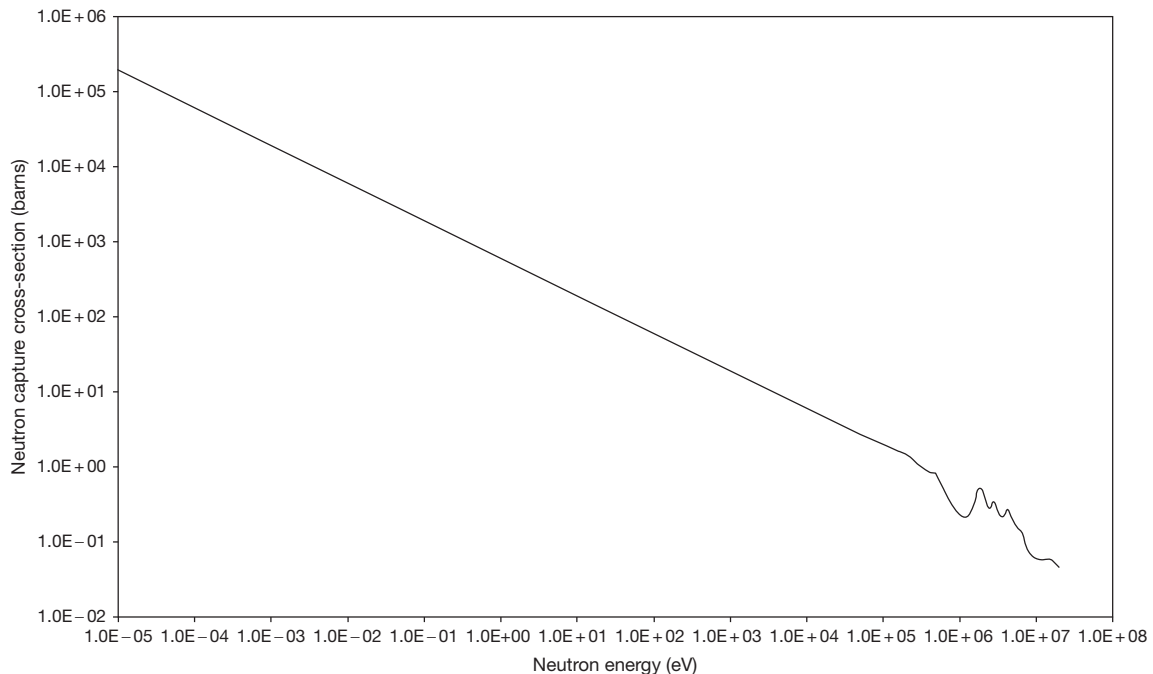


Figure 2 Neutron capture cross-section of ^{10}B in barns (10^{-28} m^2) as a function of neutron kinetic energy in electron volts.

sufficient quantity of ^{10}B as natural boron, isotopically enriched ^{10}B is available commercially. The neutron capture cross-section of ^{10}B decreases smoothly with increasing neutron energy (Figure 2), so that slow moving (thermal) neutrons are the most likely to be absorbed. (To be strictly accurate, the cross-section shown in Figure 2 is the cross-section for neutron capture, followed by transmutation to ^7Li and ^4He ; the true neutron capture cross-section of ^{10}B is actually very small and is insignificant relative to the $^{10}\text{B} \rightarrow ^7\text{Li} + ^4\text{He}$ reaction.)

Early applications of boron burnable poisons in PWRs used natural boron in borosilicate glass rods that fitted into the control rod guide tubes of assemblies not positioned under a control rod location, as illustrated in Figure 3. Such a design is called a discrete burnable poison rod. It has the advantage that the burnable poison material does not need to be incorporated in the fuel, and can therefore be manufactured separately. Also, the precise number of poison rods can be fine-tuned before the fuel assembly is loaded in the core. Such discrete poison rods are now seldom used because the stainless steel outer clad and other structural components continue to absorb neutrons after all the ^{10}B is depleted; this represents a parasitic absorption penalty that costs the utility because a higher initial enrichment of ^{235}U is needed to compensate. This effect is made worse because the

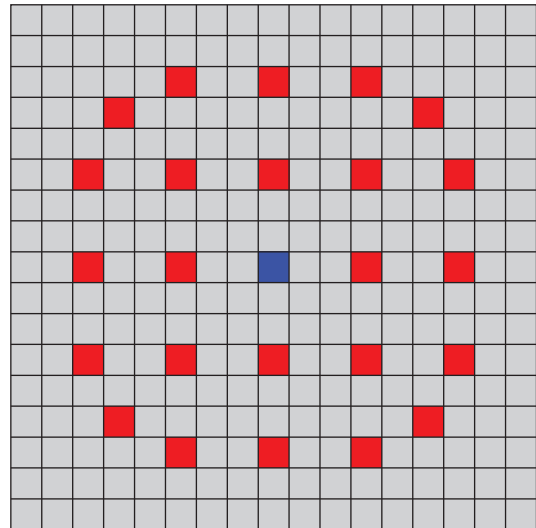


Figure 3 Locations of discrete burnable poison rods (red squares) in the control rod guide tubes of a pressurized water reactor assembly. Gray squares represent fuel rods. The central blue square is the instrumentation tube.

poison rods also displace water, reducing moderation in the fuel assembly and further decreasing the multiplication factor. Another disadvantage is that discrete poison rods constitute an additional source of intermediate level waste that adds to waste management costs.

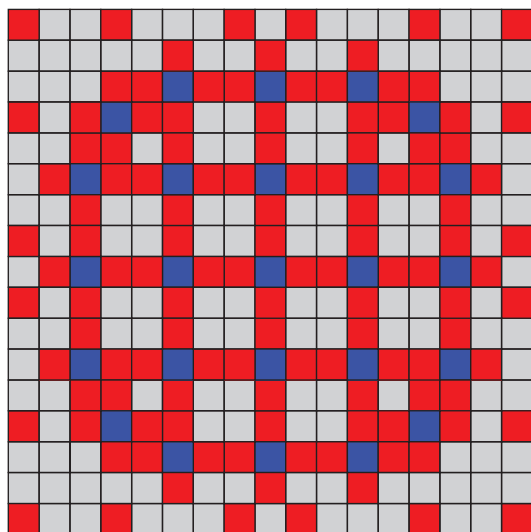


Figure 4 Typical distribution of integral fuel burnable absorber (ZrB_2) rods (red squares) in a pressurized water reactor assembly. Gray squares represent fuel rods. The central blue square is the instrumentation tube, the other blue squares being control rod guide tubes.

An alternative to discrete boron burnable poison rods is to incorporate a boron compound with the fuel rods themselves. The so-called integral fuel burnable absorber (IFBA) is used in many commercial PWRs in the United States. It consists of a thin coating of zirconium diboride (ZrB_2), which is applied to the surface of some of the UO_2 fuel pellets in the fuel assembly. Since zirconium has a very low capture cross-section and there is no structural material, IFBA has practically zero residual absorption penalty. A disadvantage is that the application of the coating adds an extra process in fuel manufacture and since it is hygroscopic, manufacturing needs to take place under a dry atmosphere in glove boxes. **Figure 4** illustrates a typical distribution of IFBA fuel rods in a PWR assembly.

2.16.3.2 Gadolinium

Gadolinium is now the most commonly used burnable poison in commercial reactors. Natural gadolinium consists of the isotopes 152, 154, 155, 156, 157, 158, and 160, with abundances of 0.2%, 2.18%, 14.8%, 20.47%, 15.65%, 24.84%, and 21.86%, respectively.^{1,2} Of these, ^{155}Gd and ^{157}Gd have extraordinarily high thermal neutron capture cross-sections of 61 000 and 254 000 barns, respectively (**Figure 5**). This means that gadolinia can effectively suppress the neutron multiplication factor at even a very low concentration.

However, gadolinia is usually concentrated spatially rather than dispersed to take advantage of spatial self-shielding^{3,4}; when concentrated into a small number of fuel rods, for example, thermal neutrons entering the poisoned fuel rod are absorbed near the surface because of the high cross-section. ^{155}Gd and ^{157}Gd atoms near the center of the fuel rod see virtually zero thermal neutron flux, and are thereby shielded from neutron captures. Self-shielding thereby limits the initial multiplication effect of lumped gadolinium and extends the depletion time for ^{155}Gd and ^{157}Gd . Self-shielding has the effect that the initial reaction rate is proportional to the surface area, while the time to deplete the ^{155}Gd and ^{157}Gd is proportional to the ratio of surface area to volume. It allows the nuclear designer flexibility in controlling both the initial absorption effect and the depletion rate independently.

Gadolinium is usually incorporated in fuel assemblies in the form of gadolinia/uranium $\text{Gd}_2\text{O}_3/\text{UO}_2$ fuel pellets, with properties only slightly different from those of conventional UO_2 pellets and a virtually identical manufacturing route. **Figures 6** and **7** show typical distributions of $\text{Gd}_2\text{O}_3/\text{UO}_2$ fuel rods in PWR and BWR fuel assemblies, respectively. Gadolinia rods offer the nuclear designer flexibility in choosing the optimal combination of initial reactivity worth and poison depletion rate. There is a residual absorption penalty that, though less than that for discrete burnable poison rods, could in theory be reduced by using gadolinium enriched in ^{157}Gd . **Figure 8** shows the radial distribution of ^{157}Gd atoms as a function of time. The self-shielding effect is evident in that the depletion proceeds from the outside in shells, usually likened to peeling an onion. ^{155}Gd behaves similarly, though on a slower timescale because of its smaller cross-section.

Gadolinia is used routinely in the UK's AGRs, but in a different form to that used in LWRs. AGR fuel elements incorporate discrete absorber cables containing gadolinia Gd_2O_3 powder in a stainless steel tube. These are located on a support structure within the outer graphite sleeve, with provision for up to three cables each at the bottom, middle, and top of the element, giving a maximum of nine cables per element. The complete AGR fuel assembly, called a stringer, consists of eight fuel elements stacked on top of one another, and at the interfaces between elements, the absence of fuel causes the thermal neutron flux and thermal power production to peak. This is because the thermal neutron flux is determined by the balance between the source of thermal neutrons slowing

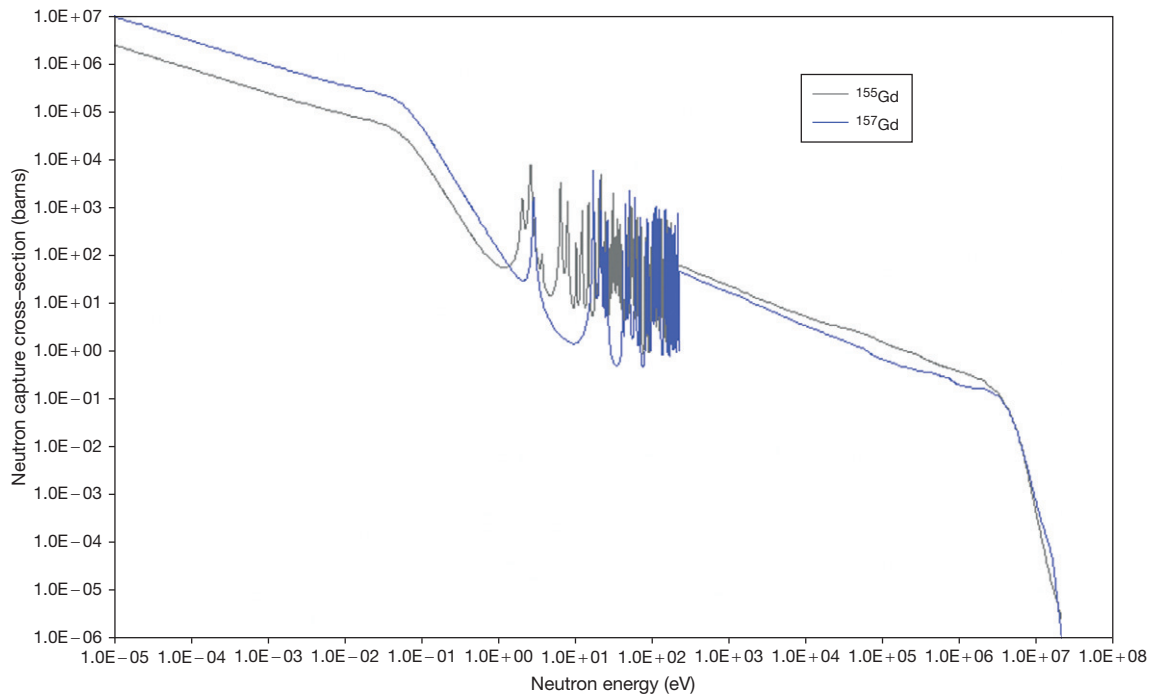


Figure 5 Neutron capture cross-section of ^{155}Gd and ^{157}Gd in barns (10^{-28} m^2) as a function of neutron kinetic energy in electron volts.

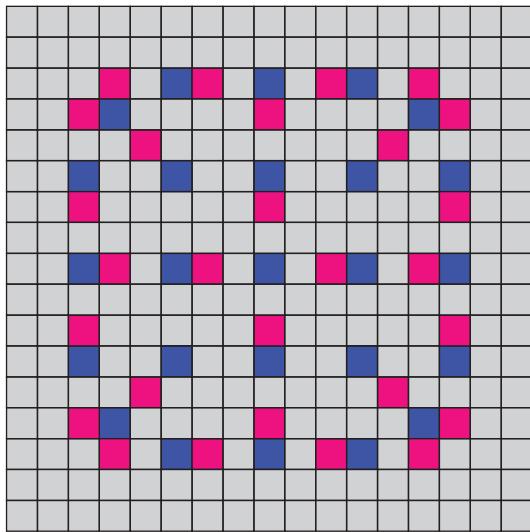


Figure 6 Typical distribution of $\text{UO}_2/\text{Gd}_2\text{O}_3$ burnable poison rods (pink squares) in a pressurized water reactor fuel assembly. Gray squares represent unpoisoned fuel rods. The central blue square is the instrumentation tube, the other blue squares being control rod guide tubes.

down in the moderator and their removal by (principally) the nuclear fuel. Where fuel is absent, the balance shifts to produce a higher thermal flux. The gadolinia cables are used to counter this

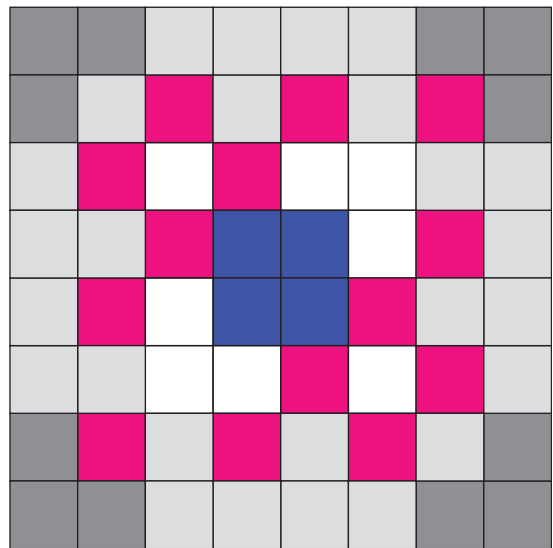


Figure 7 Typical distribution of $\text{UO}_2/\text{Gd}_2\text{O}_3$ burnable poison rods (pink squares) in a boiling water reactor fuel assembly. Red squares represent $\text{UO}_2/\text{Gd}_2\text{O}_3$ rods, the gray squares represent unpoisoned fuel rods and the blue squares represent the water channels.

deleterious axial heterogeneity, helping to reduce flux peaking in the axial gaps between fuel elements.

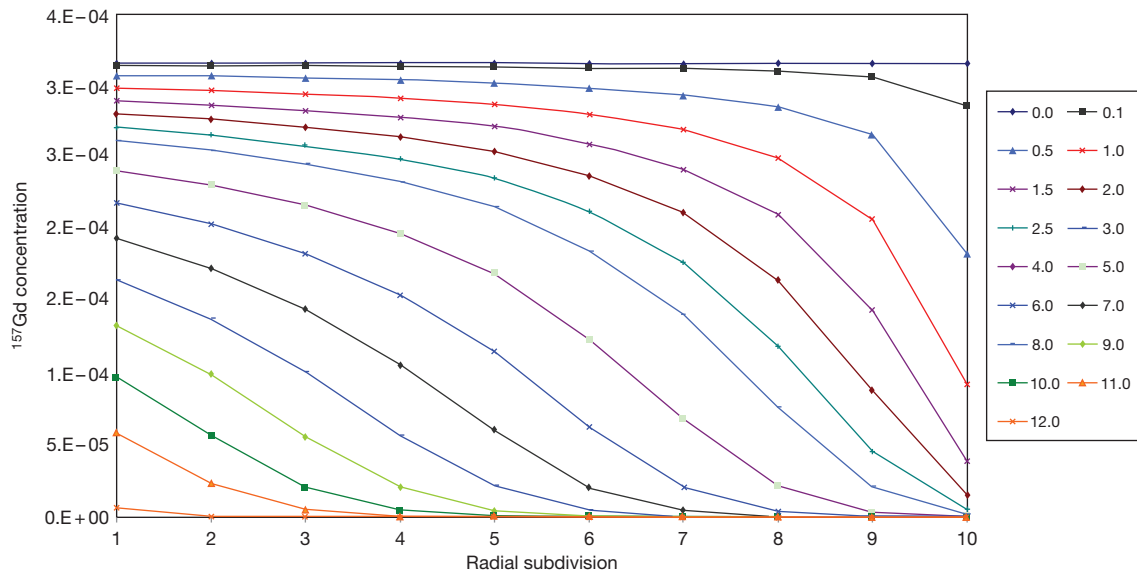


Figure 8 Radial distribution of ^{157}Gd versus burnup across a gadolinia poisoned fuel rod (subdivision 10 represents the outside of the fuel pellet) as a function of burnup from 0.0 to 12.0 GWd ton^{-1} . The radial distribution is initially uniform, but with increasing burnup, depletion takes place from the outside toward the center of the fuel rod.

2.16.3.3 Erbium

Erbium is a less commonly used burnable poison material, but has been used in some commercial PWRs and is potentially useful for specialized applications. Natural erbium consists of the isotopes 162, 164, 166, 167, 168, and 170 with abundances of 0.14%, 1.61%, 33.6%, 22.95%, 26.8%, and 14.9%, respectively.² The thermal neutron capture cross-sections are modest however, ^{167}Er having the highest thermal cross-section of 700 barns and the others all less than 20 barns, which makes erbium characteristically slow to deplete in reactor and causes it to have a high residual absorption penalty. It is normally deployed in the form of erbia/urania $\text{Er}_2\text{O}_3/\text{UO}_2$ fuel pellets in selected fuel rods.

Unlike boron, erbium acts as a resonant absorber, meaning that there are resonance peaks in the absorption cross-section plotted against incident neutron kinetic energy (Figure 9). Erbium is therefore able to mimic the negative fuel temperature feedback mechanism due to resonance absorptions in ^{238}U , which could theoretically be helpful in the so-called inert matrix fuel (IMF) designs currently being considered to irradiate and destroy the minor actinides Np, Am, and Cm. Destruction of the minor actinides is more efficient if the fuel does not contain any ^{238}U , which would generate fresh ^{239}Pu through fertile captures. IMF therefore uses matrix materials such as cerium, zirconium, and

yttria which dilute the nuclear materials, but which contribute little to neutron captures.

2.16.3.4 Dysprosium

Natural dysprosium contains a mix of seven stable isotopes 156, 158, 160, 161, 162, 163, and 164 with natural abundances of 0.06%, 0.10%, 2.34%, 18.9%, 25.5%, 24.9%, and 28.2%, respectively. The low abundance of ^{156}Dy and ^{158}Dy are such that only the latter five make a significant contribution to neutron capture in a dysprosium poison rod. ^{164}Dy has the highest thermal capture cross-section (Figure 10) and combined with 28.2% initial abundance, it dominates the overall neutron capture rate. On capturing a neutron, ^{164}Dy changes to ^{165}Dy , with a small cross-section. The presence of the 160, 161, 162, and 163 isotopes, each of which has a small but nevertheless significant neutron capture cross-section, causes dysprosium to have a high residual absorption penalty. Moreover, the residual absorption does not burn out because for all the isotopes, a neutron capture event generates the next higher dysprosium isotope and a significant residual cross-section remains.

The first application of dysprosium burnable poisons is likely to be in advanced CANDU heavy water moderated reactors. A new fuel design consisting of a bundle of 42 fuel rods arranged in three annular rings around a central uranium oxide/dysprosium

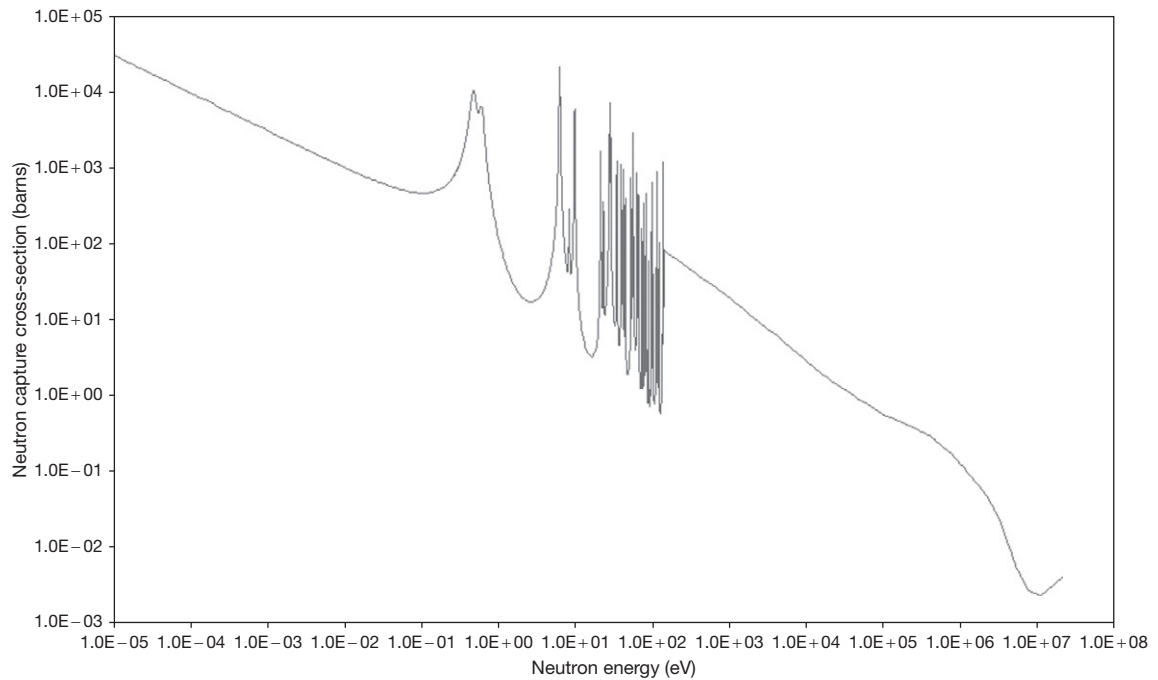


Figure 9 Neutron capture cross-section of ^{167}Er in barns (10^{-28} m^2) versus neutron kinetic energy in electron volts.

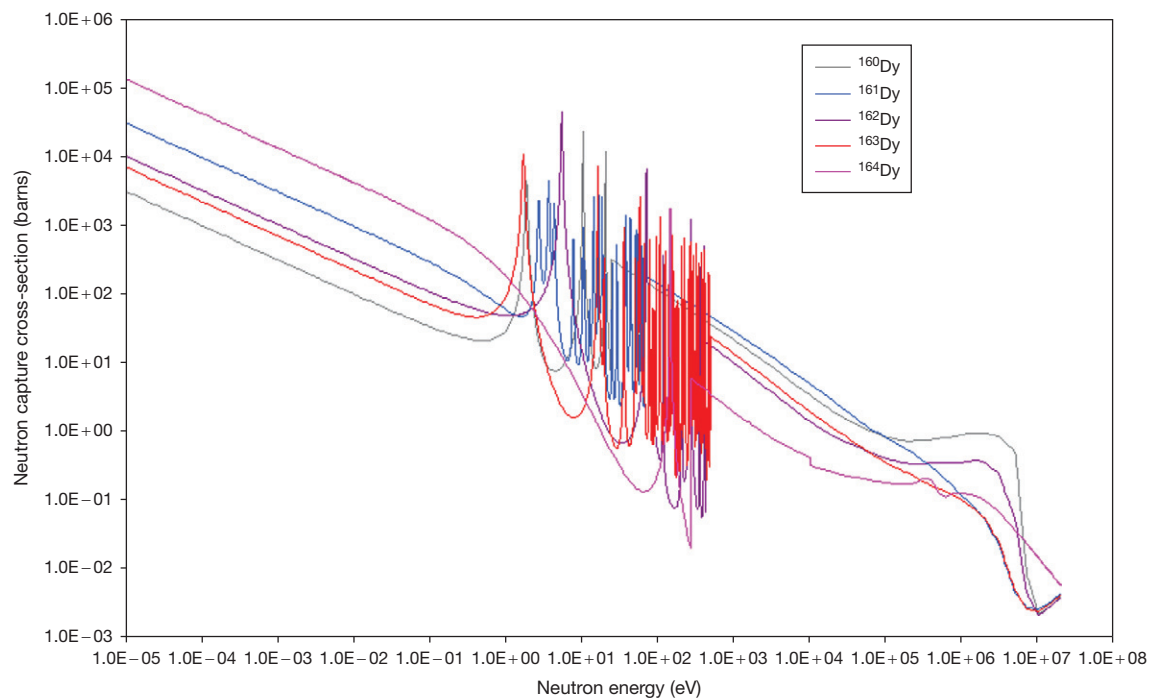


Figure 10 Neutron capture cross-section of naturally occurring Dy isotopes in barns (10^{-28} m^2) versus neutron kinetic energy in electron volts.

oxide ($\text{UO}_2/\text{Dy}_2\text{O}_3$) poison rod. The dysprosium plays an important role in helping to ensure a more negative void reactivity coefficient and more negative total power reactivity coefficient, as well as controlling the neutron flux shape across the core, while maximizing the power density of the reactor (which in turn has a direct impact on the economics of reactor operation). The void coefficient is the reactivity change in response to steam void formation in the core. The power coefficient is the change in reactivity following a perturbation to reactor power. Both of these coefficients are important in ensuring that the inherent response of the reactor in transient conditions is safe. The presence of a persistent neutron absorber, such as dysprosium, helps to remove thermal neutrons in the presence of steam void and thereby helps to maintain a negative void coefficient.

2.16.3.5 Comparison of Burnable Poisons

The ideal burnable poison is one in which the neutron capture cross-section of the neutron-absorbing nuclides is high, while the capture cross-section of the nuclide created by neutron capture is zero or close to zero. In this case, the residual absorption penalty would be zero. A large cross-section is advantageous because in the absence of self-shielding effects, the burnout rate of the poison material is proportional to the cross-section;

if the cross-section is very large, it gives the designer the option of being able to engineer a rapid burnout rate. Moreover, if the cross-section is extremely high, as is the case for gadolinia, the designer also has the option of being able to control the burnout rate by taking advantage of the self-shielding effect. Self-shielding can be used to delay the initial burnout rate, and then when the poison material nears full depletion, the remaining reactivity hold-down can be made to burn out very quickly, leaving very little residual poison effect.

It is instructive to compare the different burnable poison types to see how closely the common types approach this ideal, and **Figure 11** shows a graphical comparison of the behavior of boron, gadolinium, and erbium in a PWR. Dysprosium has been omitted because it has not been used in LWRs and its application in advanced CANDU reactors does not lend itself to meaningful comparison here.

The dark gray curve in **Figure 11** (gray diamonds) shows the neutron multiplication factor k for an unpoisoned PWR fuel assembly containing 268 fuel rods with 4.0 wt% initial enrichment. This is very similar to the corresponding curve in **Figure 1**, with the multiplication factor decreasing with burnup and with a slight flattening of the gradient at higher burnups.

The light blue curve (open squares) shows the corresponding multiplication factor curve for an identical assembly, with the same 4.0 wt% initial

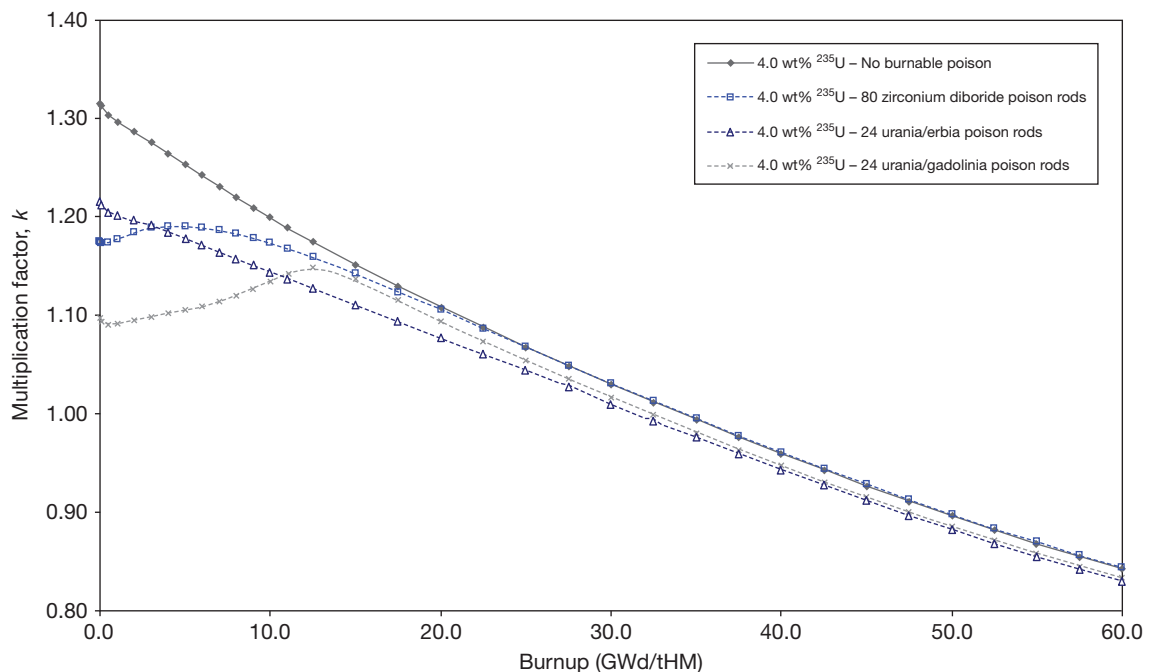


Figure 11 Multiplication factor of different burnable poisons as a function of fuel irradiation in GWd/tHM.

enrichment, but this time, 80 of the 268 fuel rods are coated with a thin layer of zirconium diboride, with a linear density of ^{10}B (i.e., the mass of ^{10}B per meter of fuel rod) typical of that used in commercial PWR assemblies. The multiplication factor starts off much lower (1.17 compared with 1.31 for the unpoisoned assembly) and the difference represents the initial reactivity hold-down. The gradient is initially positive because the burnout rate of the ^{10}B exceeds the rate at which ^{235}U is consumed and a maximum is reached at about 5.0 GWd ton^{-1} . This is typical of zirconium diboride and characteristically causes the critical boron concentration to increase with burnup in the first part of the fuel cycle. This rapid burnout occurs because there is no self-shielding with ^{10}B and the burnout rate is proportional to the concentration of ^{10}B remaining. At about 20 GWd ton^{-1} , the ^{10}B is completely depleted, and thereafter, the poisoned assembly actually has a very slightly higher multiplication factor than its unpoisoned equivalent. The reason for this is because zirconium diboride has virtually zero residual absorption, making it practically the ideal burnable poison in this respect, combined with the spectral history effect that causes the poisoned assembly to have a slightly higher concentration of ^{239}Pu than the unpoisoned reference. Early on in the irradiation, when the ^{10}B still remains, the thermal neutron flux is slightly depressed relative to the fast flux, an effect known as spectral hardening. This slightly enhances the rate at which ^{238}U fertile captures occur, resulting in a corresponding increase of ^{239}Pu . The effect is subtle, but has a small beneficial impact on the multiplication factor at higher burnups and at the end of the operating cycle.

With respect to residual absorption, zirconium diboride is undoubtedly the best performer. However, as will be seen in the following section, the ^{10}B produces helium gas, which has an impact on internal pressurization of fuel rods. Also, zirconium diboride provides very little scope for the nuclear designer to adjust the initial burnout rate of the ^{10}B because of the lack of self-shielding. For example, the nuclear designer might wish to adjust the initial hold-down of zirconium diboride and this can be achieved by increasing or decreasing the number of zirconium diboride rods in the assembly, or by varying the thickness of the coating. However, this will not affect the depletion rate of the ^{10}B , because there is no self-shielding and each ^{10}B nucleus sees the full neutron flux almost as though it was in complete isolation of other ^{10}B atoms. The result is that the peak multiplication factor will still occur at or very close to 5.0 GWd ton^{-1} , even though the designer typically

might wish to delay that point. This relative inflexibility is one of the reasons why gadolinia burnable poison is preferred by some PWR fuel vendors, despite it being disadvantaged by a noticeable residual absorption penalty.

The light gray curve in [Figure 11](#) shows the multiplication factor behavior of a PWR fuel assembly containing 24 urania/gadolinia fuel rods (with 6.0 wt% Gd_2O_3) and 240 unpoisoned UO_2 rods, with a uranium enrichment of 4.0 wt% throughout. The initial reactivity hold-down approaches twice that of the zirconium diboride case, even though there are only 24 gadolinia rods compared with 80 zirconium diboride rods for the earlier case. The very high thermal cross-sections of ^{155}Gd and ^{157}Gd ([Figure 5](#)) are the reason for this: unlike the zirconium diboride rods, which are partially transparent to thermal neutrons, the gadolinia rods absorb virtually all thermal neutrons whose track takes them toward the gadolinia rods. Each individual gadolinia rod therefore has a correspondingly higher hold-down effect than a zirconium diboride rod and generally a small number of gadolinia rods (typically not more than 24 per assembly) is all that is needed to meet the design requirements.

The self-shielding effect is evident in [Figure 11](#) in the slow reduction of the reactivity hold-down in the gadolinia case. Although the thermal cross-sections of ^{155}Gd and ^{157}Gd are extremely high, the self-shielding effect slows the burnout rate such that the multiplication factor peaks much later than the zirconium diboride case, at about $12.0 \text{ GWd ton}^{-1}$ burnup. In LWRs, this equates to roughly a full power year of operation and is ideal for controlling excess reactivity in an 18-month or longer fuel cycle. The burnout rate can be adjusted by increasing the concentration of Gd_2O_3 up or down as required, while the initial hold-down effect can be controlled almost independently by adjusting the number of gadolinia rods. It is this independent control capability that gives gadolinia a significant advantage over zirconium diboride, despite gadolinia having a notable residual absorption penalty.

This is evident in [Figure 11](#), where it can be seen that at high burnups, the multiplication factor for the gadolinia case never quite recovers to that of the unpoisoned case but tracks parallel and a little lower. The residual absorption is due to continuing neutron absorption from the even gadolinium isotopes that are present in the gadolinia rods on initial loading (and which are subsequently added to by the ^{156}Gd and ^{158}Gd produced from neutron captures in ^{155}Gd and ^{157}Gd). This represents a direct economic

penalty for the utility because a higher initial enrichment needs to be specified if the cycle length is to be held constant, which implies a higher cost for uranium ore procurement and the associated conversion and enrichment services. However, in practice, this direct economic penalty is often outweighed by the indirect operational cost savings that long fuel cycles can offer a utility and this is why gadolinia has become so prevalent. This discussion has all been in the context of PWRs. As explained further in **Section 37.4**, the flexibility offered by gadolinia is even more beneficial in BWRs and is the reason why gadolinia poisons have been universally adopted in BWRs.

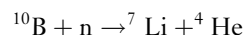
The comparison between the gadolinia case and the unpoisoned case in **Figure 11** is not quite fully representative, because the calculations underlying **Figure 11** have been deliberately simplified to aid interpretation. The presence of the gadolinia in the 24 poisoned rods displaces some UO_2 and therefore reduces the ^{235}U loading of the assembly. Some of the apparent residual absorption penalty in **Figure 11** is accounted for by this modeling simplification. In reality, it is usual for the ^{235}U enrichment in the gadolinia rods to be set slightly lower than in the unpoisoned rods for reasons that are explained in **Section 37.3**. This has a larger impact on the initial ^{235}U loading in the assembly and it may be necessary for the designer to specify a slightly higher ^{235}U enrichment in the unpoisoned rods in order to retain the same overall initial fissile loading as the unpoisoned equivalent. Even if the initial fissile is equivalent, the gadolinia case will have a slightly lower multiplication factor at high burnups because of the residual absorption effect.

The final curve in **Figure 11** corresponds to a PWR fuel assembly with 24 urania/erbia fuel rods (containing 6.0 wt% erbia), with 240 unpoisoned rods and a uniform ^{235}U enrichment of 4.0 wt%. As can be seen, the erbia rods have a smaller initial hold-down effect than the gadolinia equivalent, even though the hold-down per rod is larger than that of zirconium diboride. Compared with ^{155}Gd and ^{157}Gd , the thermal capture cross-section of ^{167}Er (**Figure 9**) is relatively modest and this is why the initial hold-down is lower. The relatively small cross-section of ^{167}Er causes the burnout rate to be very slow, even though it is not affected by self-shielding to the same extent as gadolinia. The burnout is incomplete even at 20 GWd ton^{-1} (corresponding to approaching 2 years' operation), so that there is a significant residual burnable poison penalty, larger than that of gadolinia. The slow burnout rate means that erbia is best suited to very long refueling cycles with a duration of 24 months or so.

Although erbia does allow the designer some flexibility to adjust the initial hold-down effect by varying the number of rods, the burnout rate does not lend itself to the same degree of control available with gadolinia. The combination of high residual absorption and less controllable burnout rate has made erbia more of a niche product, offered by some fuel vendors as an option that is to some extent aimed at product differentiation, with claimed advantages for very long refueling cycles.

2.16.4 Burnable Poison Materials Property Requirements

Any burnable poison material needs to meet a number of important materials property requirements if it is to be used in nuclear fuel. Such materials must be physically stable under high-temperature conditions, they must not be susceptible to corrosion in the harsh chemical environment, and they must be compatible with the other materials present in nuclear fuel, such as UO_2 , Zircaloy, stainless steel, and the coolant materials water, steam, or gas as appropriate to the reactor type. The burnable poison materials must also be well behaved under the intense neutron irradiation and gaseous releases must be accommodated. This latter consideration is particularly important for boron, because the neutron absorption leads to helium production through the reaction



If used in discrete poison rods, there must be sufficient free volume to accommodate the helium release without overpressurization. With IFBA, the helium released accumulates in the plenum volume provided to accommodate the gaseous fission products and adds to the end-of-life rod internal pressure.

Additionally, burnable poisons must be designed so that there is no possibility that the poison material could melt or slump out of the active core in an accident scenario or in any way interfere with the insertion of control rods. The migration of absorber material away from the active core would add reactivity during the accident scenario that could potentially worsen the consequences of an accident.

The zirconium diboride coating thickness used in IFBA fuel is thin enough that there is only a very small temperature drop across it and virtually no impact on fuel temperatures and fuel behavior, apart from the higher internal gas pressure due to helium generation noted earlier. In contrast, the

presence of a second ceramic phase in the fuel pellets, as is the case for gadolinia, erbia, and dysprosia, does have an impact on fuel pellet behavior, as discussed in the next section.

2.16.5 Materials Characteristics of Integral Burnable Poisons

For integral burnable poisons (gadolinia, erbia, and dysprosia), the poison material is intimately mixed with the UO_2 fuel, and it is important that the materials properties of the fuel/poison matrix are not too far removed from those of pure UO_2 . Intermixing UO_2 with another ceramic oxide usually has the effect of decreasing the thermal conductivity. For a given fuel rating, this leads to somewhat elevated fuel pellet center temperatures, with consequent implications for fuel melting, fission gas release, and other fuel behavior parameters.

For this reason, the fuel properties of urania/gadolinia and urania/erbia fuel have been investigated very carefully.⁵⁻⁹ The main parameters of interest are the thermal expansion coefficient, heat capacity, fuel melting point, and thermal conductivity, which have been extensively measured to ensure that the thermal performance of the fuel/poison matrices remains acceptable. In this respect, the performance of urania/gadolinia and urania/erbia as fuels is very similar, which might be expected, since

gadolinium and erbium are closely related rare earth elements and form oxides with the same structure. Other properties of the fuel that may be affected by the gadolinia or erbia phase include the UO_2 grain size (which decreases with gadolinia or erbia fraction) and the fuel diffusivity (which affects fission gas release). However, this is a small effect that does not have a significant impact on fuel behavior.

The thermal expansion coefficients of gadolinia and erbia are both compatible with that of UO_2 and there are no significant implications for fuel behavior. The concentrations of gadolinia used today range up to a maximum of about 8.0 wt%. At these concentrations, the melting point is decreased by just a few tens of degrees, which is relatively insignificant compared with the $\sim 2600^\circ\text{C}$ melting point of UO_2 . Erbia has a similar effect, but because the design concentrations of typically 2–3 wt% are lower, the overall impact is a reduction of the order of 10°C .

Similarly, the thermal properties of UO_2 are affected when gadolinia or erbia is intermixed. Figures 12–14 show the variation in linear expansion coefficient, heat capacity, and thermal conductivity in urania/gadolinia as a function of temperature and gadolinia content. These data are recommendations made by IAEA⁵ and are intended to be used here only for illustration. For details of the experimental data underlying these recommendations, the reader is referred to IAEA-TECDOC-1496 or the original sources cited therein.

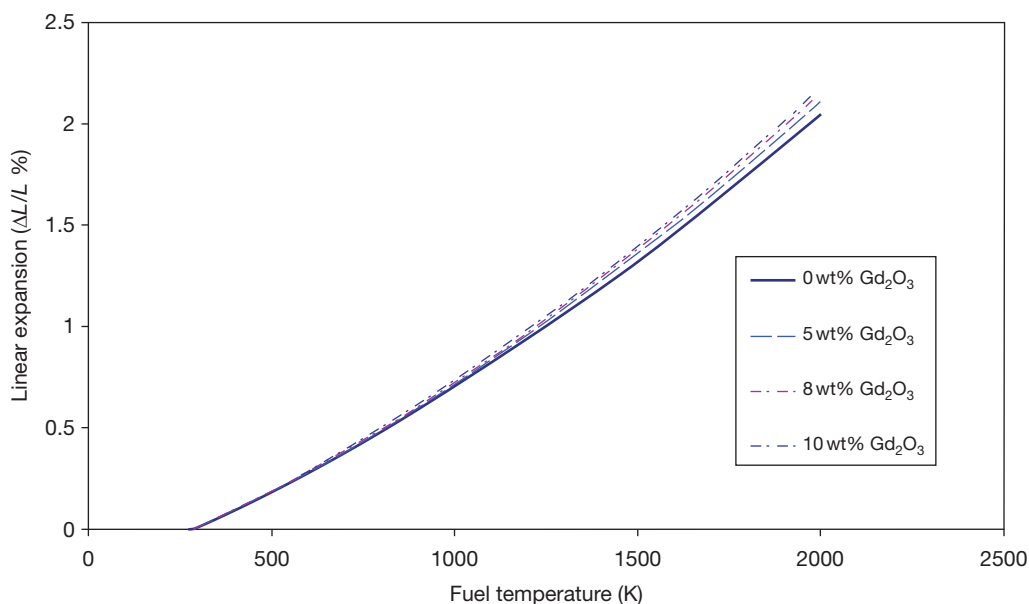


Figure 12 Linear expansion of urania/gadolinia fuel versus temperature and gadolinia concentration.

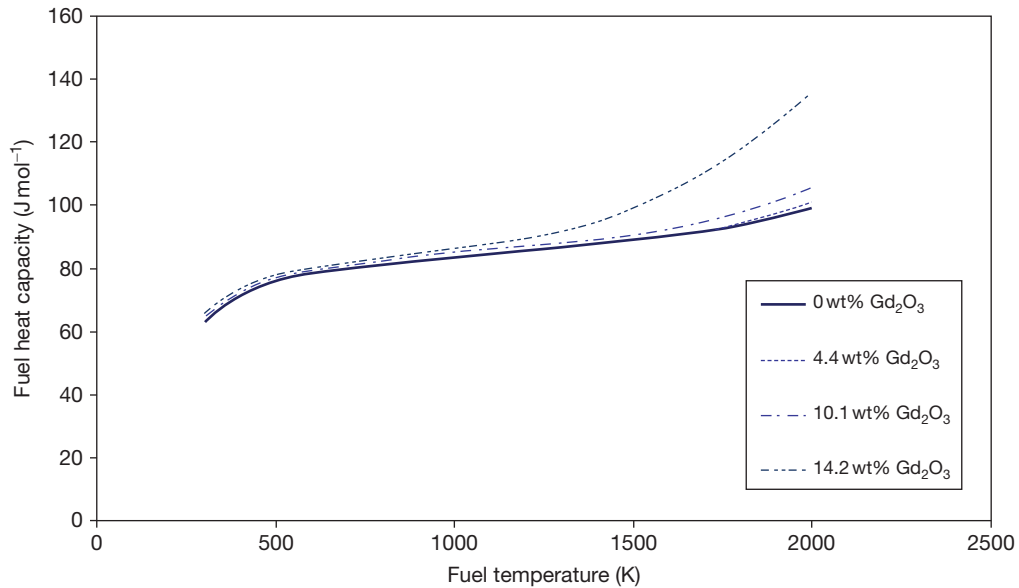


Figure 13 Heat capacity of urania/gadolinia fuel versus temperature and gadolinia concentration.

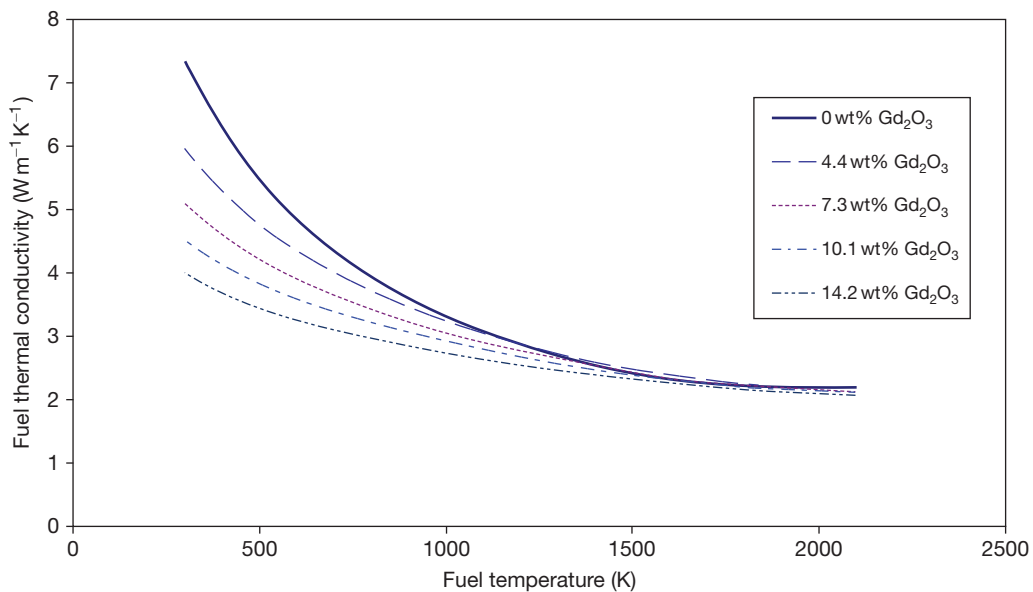


Figure 14 Thermal conductivity of urania/gadolinia fuel versus temperature and gadolinia concentration.

Recommended materials properties data are not as readily available for urania/erbia fuel, but [Figure 15](#) illustrates one evaluation of the thermal conductivity that has been published in the open literature (see Kim *et al.*⁸). This illustrates that the thermal properties of urania/erbia are similar to those of urania/gadolinia, weight for weight. However, since lower concentrations of erbia are required for practical applications (because of the slower depletion of

erbia compared with gadolinia), the depression of the thermal conductivity is less significant.

Much of the data for gadolinia and erbia fuels used by industry are regarded as being proprietary information and are therefore not made available in open publications.

While the absorbing nuclides are still present, the change in thermal properties caused by the poison material is not a concern, because the fission

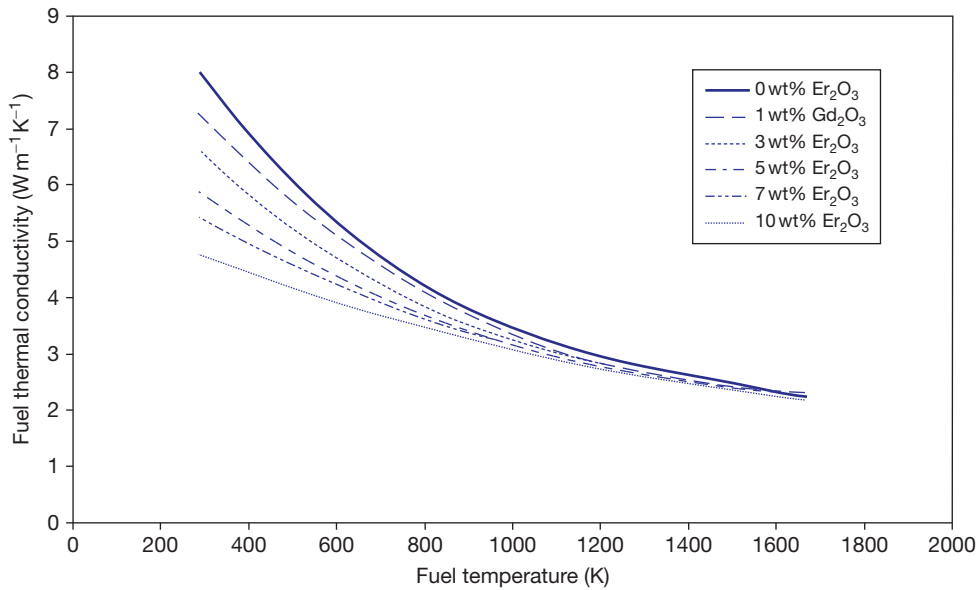


Figure 15 Thermal conductivity of urania/erbium fuel versus temperature and erbium concentration.

power produced in the fuel rods containing the poison material is depressed to the point where these rods are far from being limiting. However, a problem may occur when the poison material is fully depleted because the poisoned fuel rods will then increase in power and possibly become limiting. Indeed, because the poison material initially holds down the fission power in the poisoned rods, the fissile material is initially depleted more slowly than in the rest of the assembly and this can cause the poisoned rods to become the highest power rods in the entire assembly. This is undesirable, since the thermal conductivity is depressed and the fuel center temperature elevated. Furthermore, the materials properties of two-phase ceramics such as urania/gadolinia or urania/erbium may not be known with the same degree of precision as for the urania phase on its own, and it may be necessary to apply larger uncertainties in the fuel behavior assessments that feed into the reactor safety case.

The remedy is simple and involves reducing the ^{235}U enrichment in the poisoned rods relative to the remaining rods in the assembly. When the poison material is fully depleted, the power in the poison rods is reduced because of the reduction in fissile content. Since the two rod types are invariably fabricated in different facilities, this approach does not cause any difficulties in the fabrication logistics. There is a slight additional enrichment cost for the entire assembly, but this is not very significant. Fuel

vendors have been able to demonstrate that this approach ensures that the poisoned rods are never the limiting ones and that the materials properties uncertainties for the two-phase poison fuels do not affect the safety case.

2.16.6 Effect of Burnable Poisons on Fuel and Core Operating Parameters

Burnable poisons affect the operating characteristics of the core by reducing the excess reactivity control requirements, reducing power peaking in fresh fuel assemblies, and by modifying the reactivity feedback coefficients. BWRs have the most stringent requirements for reactivity control, since in the absence of burnable poison, an excessive amount of control rod insertion would be required, especially if the reactor is operating with long fuel cycles (18 months or more). Control rod insertion in power operation is undesirable as it distorts the radial and axial neutron flux distributions, increasing the core power peaking factor (the ratio of peak power to average power in the core). Burnable poisons allow a much more uniform flux distribution and a lower peaking factor. A further deleterious effect of control rod insertion is that fuel rods near the control rods operate at reduced powers and can be subject to a rapid power ramp when the control rods are removed. This can lead to fuel failures, which burnable poisons help to avoid.

PWRs have a smaller reactivity control requirement than BWRs because of the use of boron dissolved in the coolant. PWRs typically operate with 1000–1500 ppm of boric acid in the coolant at the start of a fuel cycle, ramping gradually to zero by the end of the cycle. This can control as much as 15 000 pcm of excess reactivity. However, even this is insufficient for long fuel cycles, and more boric acid cannot be added indefinitely due to the need to maintain a negative moderator temperature coefficient and also for other reasons such as the need to carefully control the acidity of the coolant.

An increase in water temperature in a PWR normally reduces reactivity because the water is also the moderator and the fuel assembly design is such that reducing moderation reduces the density of thermal neutrons available to propagate the chain reaction. The presence of boron has the opposite effect, however, because when the temperature of the water increases, the density decreases, and with it the density of ^{10}B atoms decreases. At a high-enough concentration of boric acid (usually ~ 1500 ppm), the effect of changing absorption outweighs that of moderation and the moderator temperature coefficient becomes positive. This sets an upper limit to the reactivity hold-down that is achievable with soluble boron and burnable poisons are now routinely used to supplement soluble boron.

The presence of burnable poisons in a fuel assembly needs to be accounted for in the thermal-hydraulic and fuel thermomechanical performance design assessments. For discrete burnable poisons, it is important to ensure that there is sufficient cooling to remove the heat production that accompanies neutron captures in the poison material. As noted in **Section 37.3**, the fuel thermal conductivity is the material property that is the most affected and has to be carefully taken into account in any thermomechanical simulations of the individual fuel rods. It is dependent on the total concentration of gadolinia or erbia and has the same effect irrespective of whether the neutron-absorbing isotopes are still present or have been burned up.

Some additional physical phenomena are relevant in the first phase of irradiation. One important physical effect results from the strong resonance absorption of neutrons within a fuel rod. Resonance absorption effects distort the radial power profile across the fuel pellets and lead to a different radial temperature gradient at low burnups. Another effect is that the low fuel temperatures lead to reduced in-pile densification and delayed cracking of the fuel at beginning-of-life.

As these issues are very difficult to measure experimentally, thermomechanical simulations usually rely on radial power profiles that are precalculated using neutron transport codes. Densification effects are difficult to model and usually neglected in the thermomechanical models, or allowed for by applying a reduced swelling rate. Existing fuel relocation models may need to be refined in order to simulate delayed cracking. The overall effect of these physical mechanisms, however, disappears after the burnable poison is consumed (which typically occurs before the end of the first cycle of irradiation cf. **Figure 1**). For example, the time of closure of the fuel-to-cladding gap is hardly affected at all. Moreover, fission gas release in the later phases of irradiation is similar to that of nonpoisoned fuel and is consistent with experiments where the fission gas diffusion coefficient in gadolinia fuels was judged to be independent of the Gd_2O_3 content. Also, no differences have been found between the temperature dependence of the fission gas diffusion coefficient in gadolinia fuels and nonpoisoned UO_2 fuels.

2.16.7 Burnable Poison Engineering Design Process and Economics

The engineering design process starts with the utility defining its preferred refueling interval (usually between 12 and 24 months depending on the grid demand profile) and the average load factor expected. This in turn determines the excess reactivity at the beginning of the cycle and the difference between this and the reactivity hold-down capability of the control rods and soluble poison (if applicable) defines the reactivity hold-down requirement for burnable poisons. The nuclear designer must then set the number and location of burnable poisons to meet this requirement. The next step is to adjust the burnable poison loading in each location such that the poison material is nearly completely depleted by the end of the cycle. For IFBA poisons, this may involve choosing to use enriched ^{10}B , while for gadolinia, it will involve choosing the optimum initial concentrations (usually in the range 4–8 wt% gadolinia). This is usually an iterative process carried out as part of the core design; it involves finding the fuel assembly loading pattern that best meets the design and safety constraints. Clearly, a compromise is required between the nuclear designer's ideal, which might demand different numbers of poison rods in each assembly and different

initial poison concentrations, and the manufacturing constraints, which demand as simple a solution as possible.

The initial choice of burnable poison is usually dictated by the manufacturing capabilities of the fuel supplier. The IFBA design requires a major capital investment in the fuel manufacturing plant, while gadolinia rods usually have to be manufactured in a dedicated facility to avoid inadvertent contamination of the main fuel production lines (where even a few ppm of gadolinia contamination can cause fuel to go out of specification). These capital costs and the associated operational costs are passed on to the utility as part of the fuel fabrication price and appear as an indirect cost to the utility. Depending on the burnable poison type, there may also be a residual absorption penalty. For a given cycle length, this will increase the initial enrichment requirement of the fuel, which the utility sees as a direct cost.

Though large in absolute terms, relative to the overall generating costs of a commercial reactor, they are not so important. The benefit to the utility comes through being able to extend the fuel cycle length as much as possible. For a fixed refueling and maintenance outage time, the overall electrical output can be increased if the time between refueling outages is extended. Since fuel costs typically only represent around 20% of the overall generating cost (with capital and finance accounting for about 60%), the penalty on the fuel cost is easily outweighed by even a modest increase in output. Therein lies the main benefit and justification of burnable poisons. Absorption of neutrons is generally regarded as a thing to be avoided in reactor design and operation, but burnable poisons are usually important in allowing reactor operations to be optimized. Even relatively small incremental improvements in reactor operations are very often sufficient to offset the negative aspects of burnable poisons, such as residual neutron absorption.

2.16.8 Future Developments

Utility requirements are tending to become ever more demanding as they attempt to extend cycle lengths further and further and at the same time demand increased fuel discharge burnup. If this trend continues,

it is likely that burnable poisons will be used even more extensively and with ever-increasing sophistication (which usually means more heterogeneous distribution of the poison material radially and axially within the fuel assemblies). The use of enriched ^{10}B , already available commercially, is likely to increase and there may also arise a demand for isotopically enriched gadolinia and erbia. These developments are likely to increase the pressure on fuel manufacturers to develop automated fabrication lines that can more easily deal with more complicated burnable poison loadings, and on the developers of nuclear design codes to more easily accommodate very heterogeneous burnable poison loadings through a higher level of automation. Since there are only around 90 naturally occurring elements in the Periodic Table, the number of candidate burnable poison materials is virtually exhausted and it is unlikely that any new ones will emerge (see [Chapter 2.09, Properties of Austenitic Steels for Nuclear Reactor Applications](#), [Chapter 2.15, Uranium Oxide and MOX Production](#) and [Chapter 2.19, Fuel Performance of Light Water Reactors \(Uranium Oxide and MOX\)](#)).

References

1. Chart of the Nuclides, Forschungszentrum Karlsruhe, Dec 1998.
2. Emsley, J. *The Elements*, 2nd ed.; Oxford University Press: Oxford, 1991.
3. Duderstadt, J. J.; Hamilton, L. J. *Nuclear Reactor Analysis*; Wiley: New York, 1976; pp 551–554.
4. Graves, H. W., Jr. *Nuclear Fuel Management*; Wiley: New York, 1979; Section 5.5.
5. IAEA-TECDOC-1496. Thermophysical Properties Database of Materials for Light Water Reactors and Heavy Water Reactors; IAEA: Vienna, 2006; ISBN 92-0-104706-1, ISSN 1011-4289, IAEA 2006.
6. IAEA-TECDOC-844. Characteristics and Use of Urania-Gadolinia Fuels; IAEA: Vienna, 1995; ISSN 1011-4289, IAEA 1995.
7. Fiero, I. B.; Jonsson, A.; Pati, S. R.; Pirek, R. C.; Van Saun, P. A. Status of Erbium Burnable Absorber Development at ABB Combustion Engineering Nuclear Fuel. In *Proceedings of the 1994 International Topical Meeting on Light Water Reactor Fuel Performance*, American Nuclear Society: La Grange Park, IL, 1994; ANS; pp 667–673.
8. Kim, S.-H.; Kim, Y.-G.; Kim, H.-S.; Na, S.-H.; Lee, Y.-W.; Suhr, D.-S. *J. Nucl. Mater.* **2005**, *342*, 119–124.
9. Hirai, M.; Davies, J. H.; Williamson, R. J. *Nucl. Mater.* **1995**, *226*, 238–251.

2.17 Thermal Properties of Irradiated UO₂ and MOX

D. Staicu

European Commission, Joint Research Centre, Institute for Transuranium Elements, Karlsruhe, Germany

© 2012 Elsevier Ltd. All rights reserved.

2.17.1	Introduction: Importance of Thermal Conductivity	440
2.17.2	Parameters Determining the Thermal Conductivity	442
2.17.2.1	Parameters Acting at the Mesoscopic Scale	442
2.17.2.1.1	Porosity and grain boundaries	443
2.17.2.1.2	Precipitates of insoluble fission products	443
2.17.2.2	Parameters Acting at the Atomic Lattice Scale	443
2.17.2.2.1	Soluble fission products	444
2.17.2.2.2	Volatiles and fission gases	444
2.17.2.2.3	Point defects created by radiation damage	445
2.17.2.2.4	Stoichiometry	445
2.17.2.2.5	Additives in UO ₂ (Pu, Gd, Cr)	445
2.17.2.3	Global Parameters	445
2.17.2.3.1	Irradiation temperature	445
2.17.2.3.2	Plutonium distribution (MOX microstructure)	445
2.17.2.3.3	Microstructure	446
2.17.2.3.4	Burnup	446
2.17.2.4	Necessary Reduction of the Number of Parameters	446
2.17.3	Specific Heat of Irradiated Fuel	447
2.17.4	Thermal Conductivity of Fuels with Simulated Burnup Effects	447
2.17.5	Thermal Conductivity Determined from In-Pile Measurements	448
2.17.6	Thermal Conductivity Out-of-Pile Measurement on Irradiated Fuel	448
2.17.6.1	Measurement Procedure and Analysis of the Results	449
2.17.6.1.1	Underlying mechanisms of the recovery	450
2.17.6.1.2	Autoirradiation effects	451
2.17.6.2	Summary of the Main Experimental Results	451
2.17.6.3	NFI (1997–2005)	453
2.17.6.4	Baron and NFIR (1998–2004)	455
2.17.6.5	HBRP (2004)	456
2.17.6.6	A Correlation for UO ₂ and MOX	458
2.17.7	Comparison of the Results Obtained Using Different Models	460
2.17.8	Conclusions	463
References		463

Abbreviations

DPA	Displacements per atom
EOL	End of life
ERV	Elementary representative volume
FP	Fission product
HBRP	High Burnup Rim Project
HBS	High burnup structure
LWR	Light water reactor
MOX	Mixed oxide (U,Pu)O ₂
NFI	Nuclear Fuel Industries
NFIR	Nuclear Fuel Industry Research

PNNL	Pacific Northwest National Laboratory
SIMFUEL	Simulated high burnup fuel
TD	Theoretical density

Symbols

bu	Burnup (MWd kg HM ⁻¹)
C_p	Specific heat (J g ⁻¹ K ⁻¹)
λ₉₅	thermal conductivity normalized to 5 vol.% porosity (W m ⁻¹ K ⁻¹)

T	Temperature (K)
T_{ann}	Annealing temperature (K)
T_c	Temperature (°C)
T_{irr}	Irradiation temperature (K)
x	Deviation from stoichiometry
λ	Thermal conductivity (W m ⁻¹ K ⁻¹)
ρ	density (kg m ⁻³)

2.17.1 Introduction: Importance of Thermal Conductivity

Knowledge of the thermal conductivity of the fuel of a nuclear reactor is required for the prediction of fuel performance during irradiation, in particular for the determination of the temperature distribution and of the fission gas release. The principal objectives of this chapter are to give elements useful to understand the phenomena causing the degradation of the thermal conductivity during irradiation and to provide guidance for the interpretation and comparison of in-pile or out-of-pile measurements, especially as a function of burnup and for samples having different irradiation temperatures, in-pile histories, and microstructures. The importance of such studies is more significant when the discharge burnup of the fuel is increased and with the formation of the high burnup structure (HBS), because these two parameters have a significant impact on the thermal conductivity. More details on the performance of LWR UO₂ fuel can be found in **Chapter 2.19, Fuel Performance of Light Water Reactors (Uranium Oxide and MOX)**. The impact of the introduction of plutonium or additives (Gd, Cr, etc.) in standard UO₂ also requires assessment (see also **Chapter 2.16, Burnable Poison-Doped Fuel**). Uranium–plutonium mixed oxide (MOX) fuel represents a significant fraction of the nuclear fuel used in commercial light water reactors (LWRs). The industrial processes used for the production of MOX fuel are based on the mixing of a few percent of plutonium oxide with UO₂. The different microstructures that can be obtained are mainly characterized by the degree of homogeneity of the plutonium distribution. The impact of the introduction of plutonium in UO₂ and the different microstructures therefore need to be considered because the presence of Pu in the UO₂ lattice will reduce the thermal conductivity. UO₂ fuel with increased grains size is produced by doping with chromium oxide, with the objectives of reducing the pellet–cladding interaction

by an increased viscoplasticity and of reducing fission gas release.

This section mainly deals with LWR fuel because the data available for fast reactor fuel are extremely inadequate. The specific heat of the fuel is also affected by irradiation. This parameter is required for the investigation of fuel performance during transients and also for the calculation of the thermal conductivity from thermal diffusivity measurements. The evolution of the thermal conductivity as a function of burnup is nonlinear, and numerous approaches and approximations are used, leading to a large number of publications on this subject. This is not the case for the specific heat which generally obeys the law of mixtures. The thermal expansion, melting temperature, and oxygen potential of the fuel are also important for fuel performance studies, but they are not addressed in this section.

The thermal conductivity distributions as a function of the radial position in a pellet for two temperature profiles (central temperatures of 1000 and 1500 K) and for burnups of 0 (fresh fuel) and 40 MWd kg HM⁻¹ calculated with the equation of Ronchi *et al.*¹ are shown in **Figure 1**. A large temperature gradient exists over the small distance between the pellet center and the pellet rim, inducing large variations in the conductivity. It can be seen that the conductivity decreases with temperature and burnup.

Under steady-state irradiation conditions and assuming a purely radial heat transfer, the temperature distribution $T(r)$ in a fuel pellet is given by eqn [1] and depends on the thermal conductivity $\lambda(r, T)$ and volumetric heat generation rate $q(r)$.

$$\frac{1}{r} \frac{d}{dr} \left(r \lambda(r, T) \frac{dT(r)}{dr} \right) + q(r) = 0 \quad [1]$$

The local thermal conductivity $\lambda(r, T)$ depends on the radial position and local temperature. The local heat generation rate requires information on the fission cross sections and depends on the radial distribution of the thermal neutron flux and of the fissile isotopes. This distribution changes during irradiation as a result of the consumption of the initial fissile isotopes and the production of fissile Pu.

From the point of view of heat transfer, both fresh and irradiated fuels are heterogeneous materials (e.g., due to the presence of the porosity). However, fresh fuels can be considered as homogeneous, even the heterogeneous MOX, and an effective or equivalent thermal conductivity can be defined. This is because the size of the pores and the plutonium-rich

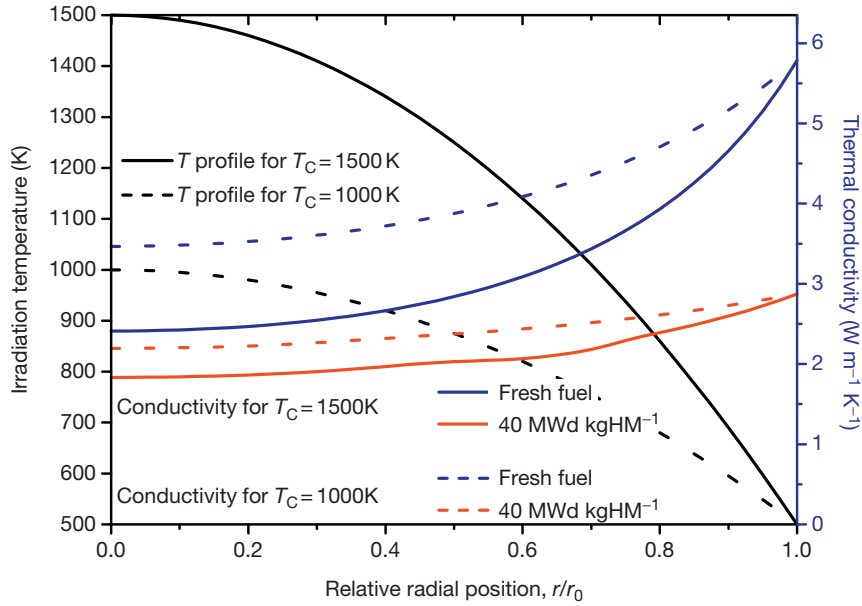


Figure 1 Thermal conductivity distribution¹ as a function of the radial position in a pellet, for two temperature profiles and for burnups of 0 (fresh fuel) and 40 MWd kg HM⁻¹.

agglomerates is small (compared with the dimensions of the pellet) and has a uniform distribution as required by fuel fabrication specification. (See also **Chapter 2.15, Uranium Oxide and MOX Production** for more information on the uranium oxide and MOX production). The heterogeneity is higher in irradiated fuel because irradiation induces the formation of numerous elements and compounds, bubbles, pores, etc., with concentrations depending on the radial position.

The definition of the effective thermal conductivity of a heterogeneous material such as irradiated fuel is not straightforward. The different scales that may be considered for the heat transfer are shown in **Figure 2**, where m is the microscale corresponding to the size of the larger heterogeneities, L is the mesoscale corresponding to the elementary representative volume (ERV), and M is the macroscale corresponding to the pellet radius. The thermal conductivities of the matrix and of the inclusions are noted λ_m and λ_i , respectively. If the separation of scales is verified,² $M \gg L \gg m$ and the equivalent thermal conductivity λ_{eq} is defined from the mean temperature gradient $\langle \nabla T \rangle$ and the mean density of the heat flux $\langle \varphi \rangle$ within the ERV: $\lambda_{eq} = -\langle \varphi \rangle / \langle \nabla T \rangle$.

The equivalent thermal conductivity λ_{eq} can be evaluated from the conductivity and the geometric distribution of the constituents on the basis of the following assumptions:

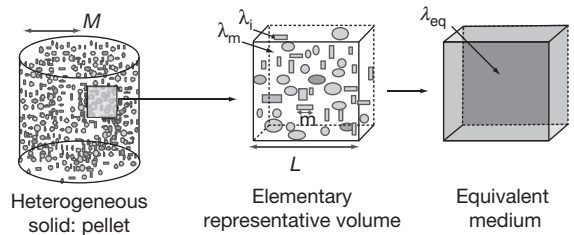


Figure 2 Notion of separation of scales: an elementary representative volume exists for the heat transfer, with $M \gg L \gg m$.

1. If the equivalent conductivity is evaluated over a volume V , and there exists a value of V beyond which the value of the conductivity no longer varies as V is increased, this volume is the ERV.
2. The medium is statistically homogeneous: the statistical distribution of the phases does not depend on the position within the material, and the equivalent conductivity is the same irrespective of the position of the ERV.
3. The dimensions of the material are large compared with the dimensions of the ERV.
4. Steady-state heat transfer is assumed. For transient heat transfer, homogenization is inappropriate, and the real microstructure has to be considered.
5. The medium is opaque to thermal radiation.

6. Fourier's law applies within the ERV and in the entire medium.
7. No mass transfer is involved.
8. No internal heat sources exist.

The first three criteria, relating to the microstructure, are not perfectly met for irradiated fuel. A rigorous homogenization is therefore not possible because the thermal conductivity depends on the radial position in the pellet as a result of the radial distribution of burnup and the irradiation temperature. However, a local homogenization is usually made by assuming that over a small radial position interval, the characteristics of the fuel are constant and allow the measurement or calculation of an effective thermal conductivity. For standard irradiated fuels, the unit cell required for homogenization has dimensions of about 1 mm³, considering that the biggest heterogeneities are pores of size up to 100 μm. However, burnup and irradiation temperature are not constant over a radial interval of 1 mm, and therefore this unit cell is not rigorously suited for homogenization. Homogenization can be accomplished in a more rigorous way in the case of disc fuels obtained during test irradiations, if uniform burnup and irradiation temperature profiles are obtained. This homogenization allows an average temperature field to be calculated. Local temperature variations exist, for instance, because of plutonium-rich zones or a particular local arrangement or shape of the pores.

The criteria 4–6 are met for irradiated fuel. The seventh criterion can be considered as met because the effect of mass transfer is negligible for LWR fuels: some elements migrate as a result of the gradients in the pellet, but the heat transferred by this mechanism is small when compared to conduction. The eighth criterion is not met when the effective thermal conductivity is deduced from in-pile temperature measurements. The internal heat sources should not be considered when the effective thermal conductivity of heterogeneous fuels is evaluated, for instance from finite-element temperature calculations.

The thermal properties of irradiated fuels are investigated in pile by temperature measurements and out of pile by thermal diffusivity measurements. Theoretical studies exist for the effect of some single parameters. Direct out-of-pile measurements on irradiated fuel samples appear more reliable because of the well-defined and optimized measurement parameters, although the in-pile conditions cannot be completely reproduced (temperature gradient, fission rate, etc.). Therefore, in-pile determinations

are indispensable, even though the deduction of the thermal conductivity from eqn [1] is less accurate. The published correlations range from empirical formulae to more sophisticated models integrating explicitly and semiempirically the effect of some parameters. A new correlation is often a combination of different existing approaches, for instance, fresh fuels results, out-of-pile experiments on simulated or real irradiated samples, and correlations obtained from in-pile temperature measurements.

No consensus exists on the most reliable correlation and usually, fuel performance codes incorporate a number of correlations, leaving it to the user to select which is the most appropriate for a specific case. For instance, the FEMAXI-6 code³ includes about 10 thermal conductivity correlations for irradiated UO₂. Before presenting the most representative results, the different burnup effects that have an impact on the thermal conductivity are discussed individually.

2.17.2 Parameters Determining the Thermal Conductivity

The composition, atomic structure, and microstructure of an irradiated fuel are complex and evolve during irradiation. Because the thermal conductivity depends on each of these characteristics, a large number of parameters are required to determine its value. At the mesoscopic scale, the main relevant parameters are the microstructure (porosity, grains size, fission gas bubbles, and plutonium or additives distribution) and the eventual precipitates. The parameters acting at the microscopic (atomic) scale are plutonium and the additives that are dissolved in the lattice, the soluble and insoluble fission products (fission products) and fission gases dispersed as atoms, radiation damage (interstitials, vacancies), stoichiometry, and fission density. A scheme summarizing some of these parameters is presented in Figure 3. The radiation effects in UO₂ are described with more detail in Chapter 2.18, Radiation Effects in UO₂.

2.17.2.1 Parameters Acting at the Mesoscopic Scale

The effect of the parameters acting at the mesoscopic scale can be assessed using solutions of the heat equation obtained for particular microstructures, for instance, a matrix containing inclusions.

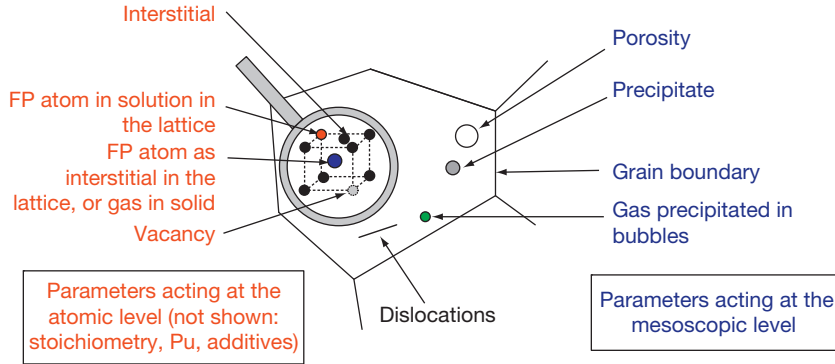


Figure 3 Some parameters affecting thermal conductivity.

2.17.2.1.1 Porosity and grain boundaries

The porosity existing in fresh fuels evolves during irradiation and has a strong impact on the heat transfer in the pellet because of its low thermal conductivity as compared to the solid. The porosity is assumed to have identical effects on the fresh and irradiated fuels and therefore the same correction formulae are used. This assumption is valid when the shape of the pores is similar and the pore volume fractions are comparable (i.e., around 5 vol%). In order to analyze the effect of parameters other than the porosity, its effect is normalized to 0 or 5 vol% by converting the measurements obtained for samples with different porosity levels. Irradiation-induced pore-size distribution changes have a small effect, but the pore shape can play a larger role if the pores are not spherical and oriented. The correction formulae are derived from composite material formulae giving the effective conductivity of a matrix containing inclusions,⁴ often simplified by attributing zero conductivity to the pores. Loeb⁵ introduced the effect of temperature to take into account the radiative heat transfer in the pores. The influence of the complex pore shape observed in irradiated fuel was investigated by Bakker using the finite-elements technique applied to realistic microstructures obtained by image analysis.⁶ Limiting this presentation to a recent recommendation, the thermal conductivity can be normalized to 5% porosity using the formula of Brandt and Neuer as recommended by Fink⁷ (eqn [2]).

$$\lambda_{95}(T) = \frac{1 - 0.05f(T)}{1 - Pf(T)} \lambda_p(T) \quad [2]$$

where $f(T) = 2.6 - 0.5T/1000$ and P is the porosity fractional volume.

2.17.2.1.2 Precipitates of insoluble fission products

Precipitates are formed by fission products that are insoluble in the UO₂ lattice (see Chapter 2.20,

Fission Product Chemistry in Oxide Fuels). They form oxide inclusions (such as BaZrO₃ or SrZrO₃) or metallic inclusions (Mo, Ru, Tc, Rh, Te, Pd, Sn, Cd, Sb, Ag, etc.) and their influence on the effective thermal conductivity can be evaluated by the formulae obtained for composite materials⁸: for instance, the Maxwell–Eucken equation.⁹ As the volume fraction of inclusions is small, this simple model gives results of sufficient accuracy. The inventory and volume fraction of the precipitates can be calculated from the number of moles created at a given burnup. For illustration purposes, the Maxwell–Eucken formula was applied at a fixed temperature assuming a UO₂ matrix with a thermal conductivity of 4 W m⁻¹ K⁻¹ containing inclusions with thermal conductivities of 0 (pores), 2 and 10 (ceramic precipitates), and 100 (metallic precipitates) W m⁻¹ K⁻¹. As shown in Figure 4, the effect of the precipitates on the thermal conductivity varies linearly with their volume fraction, which is proportional to the burnup, bu . If the coefficients a and b are used to describe this proportionality, we have $k = a - b \times bu$; the negative burnup dependence is introduced because the fuel thermal conductivity globally decreases with burnup. Usually, the thermal conductivity is approximated by the $1/(A + BT)$ formula, where A and B describe the phonon scattering mechanisms. Therefore, one obtains the formula $A + BT = (1/a)/(1 - b/a \times bu)$ and if $b/a \times bu$ is small, we have $A + BT = 1/a + (b/a^2 \times bu) - (b^2/a^3 \times bu^2) + \dots$. At a fixed temperature T , the A and B coefficients depend in a linear or quadratic way on the burnup. This kind of dependence is often found in thermal conductivity correlations.

2.17.2.2 Parameters Acting at the Atomic Lattice Scale

The fission products that form a solid solution with UO₂ and the point defects influence the thermal

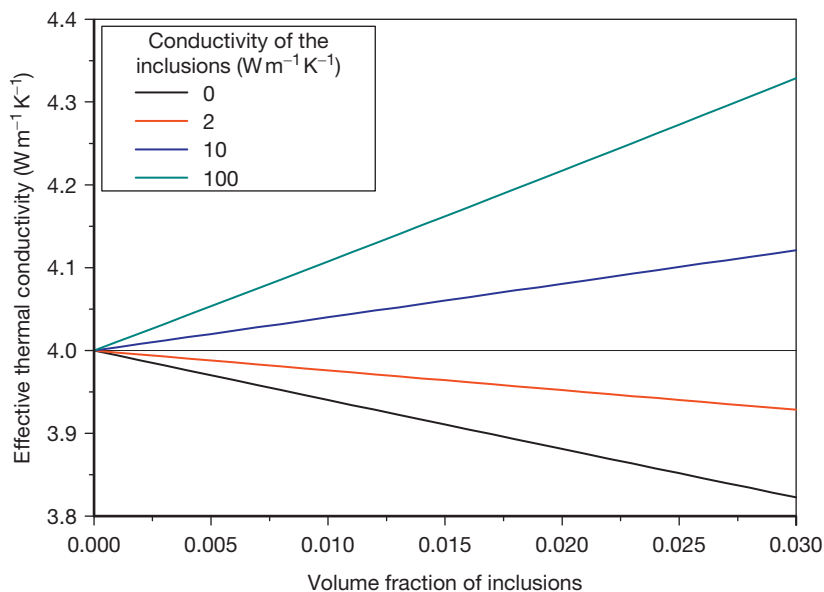


Figure 4 Effective thermal conductivity for a solid composed of a matrix of conductivity $4 \text{ W m}^{-1} \text{ K}^{-1}$ containing inclusions of conductivities 0, 2, 10, and $100 \text{ W m}^{-1} \text{ K}^{-1}$, determined with the model of Maxwell.⁴

conductivity at the atomic scale. Their effect on the thermal conductivity is interpreted in terms of phonon scattering and is described by the formula $\lambda = 1 / (A + BT)$.⁸ The constant A can be expressed as the sum of the thermal resistance due to phonon scattering by substitutional atoms or point defects (impurities, interstitial atoms, vacancies) using the expression obtained by Ambegaoker.¹⁰ The main parameters are the Debye temperature, the mean phonon velocity, and the phonon diffusion cross section of the defects. Extended defects such as grain boundaries scatter phonons by limiting their mean free path. The product BT corresponds to the intrinsic lattice thermal resistivity caused by phonon–phonon scattering. The value of B can be evaluated from a simplified model by Leibfried and Schlömann,¹¹ but the information available on the physical and thermodynamic data of UO₂ is not sufficiently accurate. Therefore, B is usually obtained empirically from the measured thermal resistivity slopes.

2.17.2.2.1 Soluble fission products

Actinides, rare earths, and transition metals can form mixed oxides with UO₂ or (U,Pu)O₂. Examples of these elements are the fission products Zr, Ce, Nd, Ba, La, Pr, Sr, Sm, Y, Rb, Te, Pu, Np.¹² Their solubility limits determined for binary systems are never reached in the case of irradiated fuel, and these elements can be completely or partially dissolved in the

fuel matrix. When such solid solutions are formed, these atoms act as phonon scattering centers as a result of the differences in bonding potential, ionic radii, or mass between the impurities and the substituted atoms (U or Pu). The total scattering coefficient can be evaluated from the differences in atomic mass and ionic radii¹³ and from the Grüneisen constant, which represents the strain generated in the lattice by the difference in ionic radius and is usually treated as an empirical parameter obtained from experimental data.^{14–17}

2.17.2.2.2 Volatiles and fission gases

Insoluble or volatile fission products (Kr, Xe, Cs, Te, I, etc.) are partially dispersed as interstitials and induce static displacements of host lattice atoms U or Pu from their mean lattice sites. In that case, their effect can be interpreted with the same equations as for the dissolved fission products. The fission gas, thermodynamically insoluble in the matrix, is initially injected into the lattice and may precipitate into bubbles. Since collisions with fission fragment recoil cascades tend to re-inject gas into the lattice, for temperatures below about 1100 K, a fraction of the gas is kept in dynamical solution. At higher temperatures, most of the gas precipitates into bubbles or pores or can be released from the pellet. The simultaneous mechanisms of gas diffusion, precipitation, and release can be described by reaction-rate

equations¹⁸ to calculate the partitioning of the gas in the different states starting from a number of kinetic (gas creation rate, diffusion coefficient, and resolution rate) and structural (grain size, radii, and concentrations of the bubbles) parameters. The entire irradiation history of the sample and, when laboratory annealing is involved, the applied temperature program, have to be considered.

2.17.2.2.3 Point defects created by radiation damage

The perturbations of the crystal lattice due to the displacement of atoms, that is point defects (interstitials, vacancies) and extended defects (defects clusters, dislocations, voids), contribute to the degradation of the thermal conductivity by scattering or limiting the mean free path of the phonons. This perturbation at the atomic scale is of the same nature as for soluble fission products and is also interpreted in terms of phonon scattering centers. Two aspects introduce uncertainties into the prediction of the effect of radiation damage: the concentration is difficult to calculate as a function of the irradiation conditions and the effect on the thermal conductivity is nonlinear (saturation occurs). Because of the large number of displacements produced by fission, the point defect concentration is expected to saturate early, probably before a burnup of 1 MWd kg HM⁻¹, the saturation level depending on temperature. Supplementary radiation damage of a dynamical nature is present only in pile because of the fission spikes and its concentration depends on the fission rate; it disappears immediately when irradiation stops.

2.17.2.2.4 Stoichiometry

Stoichiometry has a major effect on the thermal conductivity of fresh fuels.¹⁹ UO₂ is generally stoichiometric when introduced in pile and the O/U ratio of UO₂ irradiated under LWR conditions remains close to 2.00 up to a burnup of 100 MWd kg HM⁻¹.^{20–22} This parameter is, however, difficult to define for an irradiated fuel because of the complex chemical composition. Also, the effect of the oxygen defects due to the nonstoichiometry can be expected to be reduced because of the large number of oxygen defects created by irradiation.

2.17.2.2.5 Additives in UO₂ (Pu, Gd, Cr)

The addition of Pu, Gd, or Cr to UO₂ reduces the thermal conductivity of the fresh fuel. These additives may form solid solutions with UO₂ or be present as precipitates. The perturbation decreases with

burnup because of the other burnup effects, as observed for (U,Gd)O₂ by Sonoda *et al.*,²³ for (U,Pu)O₂ by Fujii *et al.*²⁴ and Staicu *et al.*,²⁵ and for Cr by Caillot *et al.*²⁶

2.17.2.3 Global Parameters

Because of the complex characteristics of the irradiated fuel, the thermal conductivity is often deduced from correlations using global parameters summarizing the state of the fuel: for instance, the burnup and the irradiation temperature. Some fuel characteristics are implicitly taken into account. For instance, the grain size is a parameter having a small impact on the conductivity of fresh fuels but a large impact on the conductivity of irradiated fuels. This is because grain boundaries are sinks for point defects and therefore a smaller grain size induces reduced concentrations of point defects.

2.17.2.3.1 Irradiation temperature

The irradiation temperature has an impact on the state of the fuel. During long irradiations, temperature has an effect on the microstructure of the fuel and on the concentration of radiation damage accumulated. During a short annealing (transient or laboratory annealing), the effect is mainly restricted to the radiation damage concentration change and to the redistribution of some fission products: precipitation of atoms that were distributed as single atoms and formation of fission gas bubbles. However, the definition of this parameter is vague because the irradiation temperature at a given radial position is not constant throughout the irradiation and the real relevant parameter is the irradiation temperature history. The out-of-pile measurements must be interpreted by considering the irradiation temperature at end of life (EOL).

2.17.2.3.2 Plutonium distribution (MOX microstructure)

The fresh fuel plutonium concentration and distribution (homogeneous or heterogeneous microstructure) and the induced variations in the local stoichiometry are supplementary parameters for MOX fuels. The plutonium concentration decreases with burnup whereas it increases in UO₂. Therefore, the differences observed in fresh fuels linked to the plutonium effect can be expected to decrease with burnup, at least for homogeneous MOX fuels. In heterogeneous MOX, the microstructure may have an enhanced impact because of the presence of Pu-rich

agglomerates in which the burnup is much higher than in the matrix. However, recent studies showed that this effect is in fact negligible.^{27,28}

2.17.2.3.3 Microstructure

The microstructure of the fuel is linked to the presence of additives and porosity, voids, and fission gas bubbles, their concentrations changing with the radial position. Other parameters concern the fuel matrix itself: the densification at the beginning of life and the grain size evolution. The effect of porosity and voids can be approximated by applying a factor to the matrix conductivity, determined for instance by the formula of Maxwell giving the effective thermal conductivity λ_{eq} of a medium constituted by a matrix of conductivity λ_m containing a small volume fraction v_f of inclusions having a conductivity λ_f (eqn [3]). This approximation is obtained only when $\lambda_m \gg \lambda_f$, and is therefore not usable for ceramic or metallic precipitates. Approximate formulae, validated for porosity in nuclear fuels, were proposed by Brandt and Neuer.²⁹

$$\lambda_{eq} = \lambda_m \frac{\lambda_f + 2\lambda_m + 2v_f(\lambda_f - \lambda_m)}{\lambda_f + 2\lambda_m + v_f(\lambda_m - \lambda_f)} \underset{\text{if } \lambda_m \gg \lambda_f}{=} \lambda_m \frac{2(1 - v_f)}{2 + v_f} \quad [3]$$

The macroscopic cracking and fracture of the pellet are heterogeneities that cannot be taken into account for the definition of an equivalent thermal conductivity because their size is not small compared to the size of the pellet. Cracking can be separated into radial and tangential, the latter decreasing the apparent thermal conductivity.

Extensive microstructure changes take place with the formation of the HBS starting from the periphery of the pellet for discharge burnups higher than about 40 MWd kg HM⁻¹ or local burnups higher than about 60 MWd kg HM⁻¹. This structure is characterized by a reduced grain size, an increase in porosity, and a depletion of fission gas from the UO₂ matrix.^{30,31}

2.17.2.3.4 Burnup

The fuel burnup reflects the proportion of fissioned atoms and is the most commonly used parameter for the interpretation of thermal conductivity degradation. In principle, this parameter integrates the phenomena that do not depend on the irradiation conditions, that is, the concentration of nonvolatile fission products. In practice, it is often the only parameter of the correlations and is used to account for (almost) all irradiation effects. Some particular effects exist at low burnup: the fast buildup of irradiation damage, and at high burnup: the formation of the HBS.

2.17.2.4 Necessary Reduction of the Number of Parameters

The fuel thermal conductivity changes during irradiation as a result of fission and high operating temperatures; the chemical composition, lattice structure, and microstructure evolve in a complex and correlated manner. The fuel microstructure and state result from the irradiation history (transients generate cracking, shutdown periods result in autoirradiation at low temperatures, etc.). A complete and three-dimensional knowledge of the fuel characteristics is required for the prediction of the thermal conductivity. The number of parameters is large and it is difficult to isolate and model their effects individually. Furthermore, many parameters act in a coupled manner: that is, the impact of the individual parameters is not the sum of the individual effects. Therefore, no purely theoretical model is available and semiempirical correlations are built from the interpretation of experimental results by selecting the most influential parameters, the effect of the others being implicitly included when the models are adjusted to measurement results.

Two categories of parameters can be distinguished: first, the parameters that depend on burnup but not on irradiation conditions. The burnup is a global parameter that integrates all the effects which are proportional or related to it only, for instance, the concentration of soluble fission products or precipitates. Second, the parameters are those that depend on burnup and irradiation temperature history. This is the case for radiation damage, for the state of fission products that are present as isolated atoms and can precipitate, or for the distribution of volatile fission products between the states dynamically dissolved, precipitated in bubbles or pores, or released.

The proposal of a model implies a reduction in the number of parameters remaining, for instance, only the burnup or a second parameter summarizing the effect of the irradiation history, such as the irradiation temperature¹ or the lattice parameter,³² assuming that these parameters describe, with sufficient precision, the state of the fuel.

The general expression of the heat conduction used for irradiated fuels is similar to the one adopted for the fresh fuel (eqn [4]). It includes the lattice conduction mechanism by phonons, empirically represented by $1/(A + BT)$ and largely dominant up to temperatures of about 1600 K, and the high-temperature contribution attributed to the electron vacancy pair mobility, usually represented by adding an expression of the form Ce^{bT} . This last contribution

cannot be accurately quantified because of the lack of measurements at high temperatures.

$$\lambda = \frac{1}{A + BT} + C e^{DT} \quad [4]$$

The quantity $1/A + BT$ applies only to perturbations at the atomic scale, that is, the effects of soluble fission products, and to point defects (radiation point defects, nonstoichiometry, dynamically dissolved atoms and fission gases). It is not rigorous for precipitates and porosity, as the effect of these parameters is macroscopic and described by composite materials formulae derived from the solution of the Fourier law. In practice, this formalism is often applied, including the effect of all the parameters. Fuel variants, such as (U,Gd)O₂, UO₂ doped with Cr, or MOX, are modeled on the basis of UO₂, with supplementary parameters describing the effect of the additive.

2.17.3 Specific Heat of Irradiated Fuel

Specific heat is an important parameter for the transient behavior studies where the temperature variations are linked to the variations of reactor power. Also, it is required for the calculation of thermal conductivity from thermal diffusivity. Only a very limited number of studies are available and the specific heat of irradiated fuel is not yet fully clarified. The effects of soluble fission product elements added to fresh UO₂ were quantified, for instance, by Verall and Lucuta,³³ Matsui *et al.*,³⁴ and Takahashi and Asou.³⁵ No large burnup effect was found because the specific heat obeys the law of mixtures (Neumann–Kopp law) and because only a limited fraction of the fresh fuel heavy metal atoms change nature during irradiation.

Specific heat measurements for irradiated fuel by calorimetric techniques show an exothermic effect during the first heatup of the sample linked to the recombination of radiation damage and to fission products redistribution. The apparent specific heat is lower than for annealed samples because of the heat effect, as observed by Gomme *et al.*³⁶ and Yagnik and Turnbull.³⁷ A similar effect is observed for (U,Pu)O₂ samples damaged by autoirradiation.³⁸ This means, for instance, that during fast power increases, the temperature will increase faster than predicted using the fresh fuel-specific heat. For the intrinsic specific heat (i.e., measured on annealed

samples), no significant difference was found when compared with fresh fuel. Similar results were obtained by direct measurements of specific heat on irradiated fuels by laser flash, reported by Ronchi *et al.*¹ for UO₂ and by Sonoda *et al.*²³ for (U,Gd)O₂. Therefore, the specific heat of irradiated fuel is generally assumed to be equal to that of the fresh fuel.

2.17.4 Thermal Conductivity of Fuels with Simulated Burnup Effects

The changes in the fuel thermal conductivity were quantified in simulated high burnup fuel (SIMFUEL) in which additives are introduced in UO₂.³⁹ Some additives are soluble in the lattice and other precipitate as second phases. The advantage of this approach is that the samples are easy to prepare and handle. Single effects can be studied, but the main disadvantage is that only part of the burnup effects can be simulated. This approach was used, for instance, by Ishimoto *et al.*¹⁵ for UO₂ and (U,Gd)O₂ and by Kang *et al.*⁴⁰ for UO₂. Hartlib *et al.*⁴¹ simulated the effects of fission products in MOX fuel and evaluated the decrease in thermal conductivity, and this work was used by Philipponneau to obtain a thermal conductivity correlation for the irradiated fast reactor MOX.⁴²

The most complete work on simulated burnup effects was published by Lucuta *et al.*,³⁹ who proposed a formula in a form of factors contributing to the degradation of the thermal conductivity λ_0 of unirradiated UO₂ (eqn [5]).

$$\lambda_{95} = \lambda_1(bu)\lambda_2(p)\lambda_3(x)\lambda_4(r)\lambda_0 \quad [5]$$

In this formula, $\lambda_1(bu)$ is the burnup dependence, containing the effect of dissolved fission products as derived from measurements on SIMFUEL, and the effect of precipitates, assessed theoretically with composite materials formulae, including a correction reflecting that precipitation takes place at high temperature. $\lambda_2(p)$ accounts for the porosity and bubbles contribution, based on the Maxwell–Eucken formula for composite materials. $\lambda_3(x)$ refers to the effect of nonstoichiometry and was assessed from SIMFUEL measurements results, but this factor is generally not used as the fuel is assumed to be stoichiometric. $\lambda_4(r)$ describes the radiation damage effect presuming that recovery takes place progressively in the range 600–1200 K. This model was used in some fuel performance codes⁴³ but was replaced⁴⁴ because its predictions were found to be too high.

2.17.5 Thermal Conductivity Determined from In-Pile Measurements

The fuel thermal conductivity can be deduced from a measurement of the temperature history at the pellet center with a thermocouple during irradiation. The determination is done for different values of the reactor power and assuming that the coolant temperature and the fuel-cladding gap conductance are known. In order to suppress the uncertainties linked to the heat transfer in the fuel-cladding gap, some rig designs include simultaneous central and off-central temperature measurement positions. The fuel center temperature is linked in an integral way to the radial profiles of the thermal conductivity and the heat production (eqn [1]).

The advantages of this approach are that the determination includes the effect of the dynamical damage created by the fission rate. Also, in contrast to out-of-pile measurements usually carried out a few years after the end of the irradiation, the measurement is not perturbed by the out-of-pile auto-irradiation damage accumulated during storage. The disadvantages include the uncertainties linked to the fuel-cladding heat transfer and the fact that it is an integral measurement only, not local. Also, the criteria for the definition of an equivalent thermal conductivity are not perfectly fulfilled because the heat sources are not homogeneously distributed within the material; the heat production is a function of the radius, and in MOX fuel, it is concentrated in the Pu-rich agglomerates.

The main result was obtained by the Halden Reactor Project. The thermal conductivity of irradiated UO₂ (eqn [6]) is given by Wiesenack.⁴⁵ A recent adaptation (eqn [7]) was cited by Lanning *et al.*,⁴⁴ including the effect of gadolinia. T_C is the current temperature in °C, bu is in MWd kg UO₂⁻¹, gad is the weight fraction of gadolinia, and ϑ is the lower value between T_C and 1650 °C.

$$\lambda_{95} = \frac{0.1148 + 3.05 \times 10^{-3} bu + 2.475 \times 10^{-4}}{(1 - 3.3 \times 10^{-3} bu) T_C} + 0.0132e^{0.00188 T_C} \quad [6]$$

$$\lambda_{95} = \frac{1}{0.1148 + 1.1599 gad + 4 \times 10^{-3} bu + 2.475 \times 10^{-4} (1 - 3.3 \times 10^{-3} bu) \vartheta + 0.0132e^{0.00188 T_C}} \quad [7]$$

Lee *et al.*⁴⁶ proposed to adapt the correlation to take into account the increased porosity in the HBS (eqn [8]) by using a formula for composite materials derived from a one-dimensional heat transfer approximation made by Kampf and Karsten.⁴⁷ In eqn [8], λ_0 is the conductivity of the fully dense matrix, λ_p is the conductivity of the pores, and P_{rim} is the volume fraction of pores in the HBS.

$$\lambda_{rim} = \lambda_0 \left\{ 1 - P_{rim}^{2/3} \left[1 - \frac{1}{1 + P_{rim}^{1/3} \left(\frac{\lambda_0}{\lambda_p} - 1 \right)} \right] \right\} \quad [8]$$

Wiesenack *et al.*⁴⁸ proposed an adaptation for MOX fuel also using eqn [8] and considering a matrix with low Pu content of conductivity λ_0 and Pu-rich inclusions of conductivity λ_p . The thermal conductivity of the matrix is obtained by assuming that the effect of the plutonium is proportional to its concentration, while the conductivity of the Pu-rich inclusions is obtained with the correlation of Phillipponeau for fresh fuel.⁴²

The Halden Reactor Project also developed an adaptation of their correlation for MOX fuel, based on fuel center temperature measurements. As cited and adapted by Lanning *et al.*,⁴⁴ this formula is obtained by multiplying the phonon term of the formula for UO₂ as given by eqn [7] by the factor 0.92.

The conductivities for UO₂ (eqn [6]), (U_{0.95}Gd_{0.05})O₂ (eqn [7]), and LWR MOX (eqn [7] multiplied by 0.92) fuels are plotted in Figure 5 as a function of burnup. It can be seen that the conductivity of UO₂ and (U_{0.95}Gd_{0.05})O₂ converge with increasing burnup. The constant ratio between the UO₂ and MOX thermal conductivities is a matter of discussion. Convergence between UO₂ and MOX was proposed by other authors, for instance, from in-pile central temperature measurements by Fujii *et al.*,²⁴ who made the analysis with the assumption that the burnup degradation for MOX is slightly lower than that of UO₂. Other correlations were obtained on the basis of in-pile measurements, for instance,⁴⁹ using a database of central temperature measurements combined with the radiation damage term derived by Lucuta *et al.*³⁹

2.17.6 Thermal Conductivity Out-of-Pile Measurement on Irradiated Fuel

In this technique, the irradiated fuel samples are small discs or disc fragments with irregular shape and are not suitable for direct measurements of

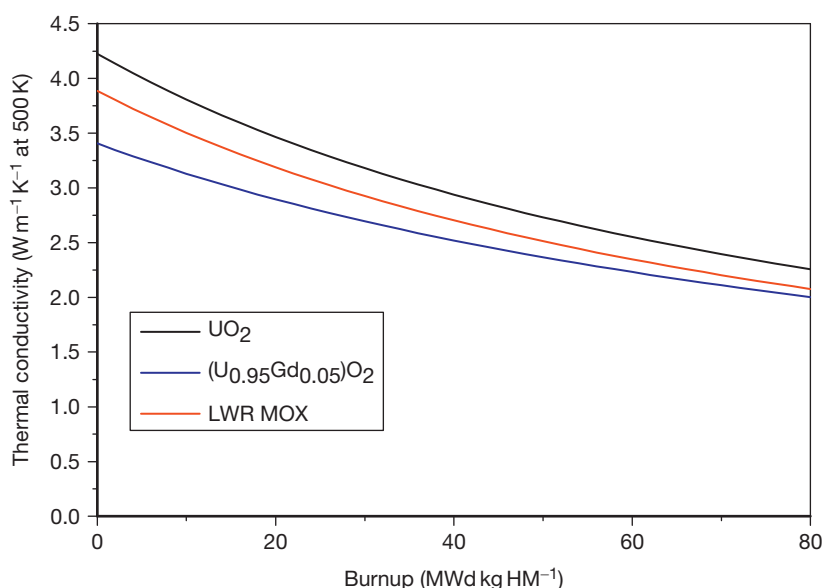


Figure 5 Thermal conductivities of UO₂,⁴⁴ (U_{0.95}Gd_{0.05})O₂,⁴³ and LWR MOX⁴³ predicted by models based on in-pile measurements. Irradiation temperature 500 K.

thermal conductivity. Out-of-pile measurements of the thermal diffusivity are carried out using shielded laser flash devices, specially designed and constructed for irradiated nuclear fuel, for instance, at AEA technology,³⁶ at NNFD,⁵⁰ and at ITU.⁵¹ The samples are discs or fragments of a disc having plane and parallel faces, with a thickness of about 1 mm, and with diameters or lateral dimensions between 3 mm and the pellet diameter. The sample is first heated up to the measurement temperature. Then, one face receives a heat pulse produced by a laser and the temperature rise at the opposite face is recorded as a function of time to deduce the thermal diffusivity. The thermal conductivity $\lambda(T) = \rho(T)C_p(T)\alpha(T)$ is then calculated from the thermal diffusivity $\alpha(T)$, the specific heat $C_p(T)$, and the density $\rho(T)$.

The advantages of this technique are that it is a direct measurement not requiring assumptions about other parameters and a uniform temperature of the sample; samples can be chosen free of cracks, measurements can be made at different radial positions, and annealing studies can be carried out to investigate the radiation damage recovery. Some experimental difficulties arise because of the delicate sample preparation procedure and their brittleness. From the point of view of the relevance in terms of in-pile behavior, drawbacks include the absence of a thermal gradient in the sample (the irradiation temperature has a unique and different value in each

radial position) and the absence of the dynamical damage produced and maintained in-pile by fission. Because of the supplementary damage created during storage, the interpretation requires an analysis of autoirradiation effects and annealing of in-pile damage. These drawbacks are avoided when the thermal conductivity is evaluated in pile using thermocouples, but then supplementary uncertainties arise because of the integral nature of such measurements.

2.17.6.1 Measurement Procedure and Analysis of the Results

A typical experiment usually starts at a low temperature (300–500 K) and thermal diffusivity measurement cycles are recorded with increasing maximum temperatures. An increase in thermal diffusivity is observed after the annealing cycles, the magnitude of which depends on the maximum temperature reached. Therefore, a typical thermal diffusivity measurement does not result in a unique curve as a function of temperature but in a series of curves obtained by increasing the maximum measurement temperature. Even after high temperature annealing, recovery is only partial because some burnup effects remain, and the value corresponding to unirradiated UO₂ is not obtained. The typical evolution of the thermal conductivity during successive annealing cycles is presented in [Figure 6](#) for a sample having a

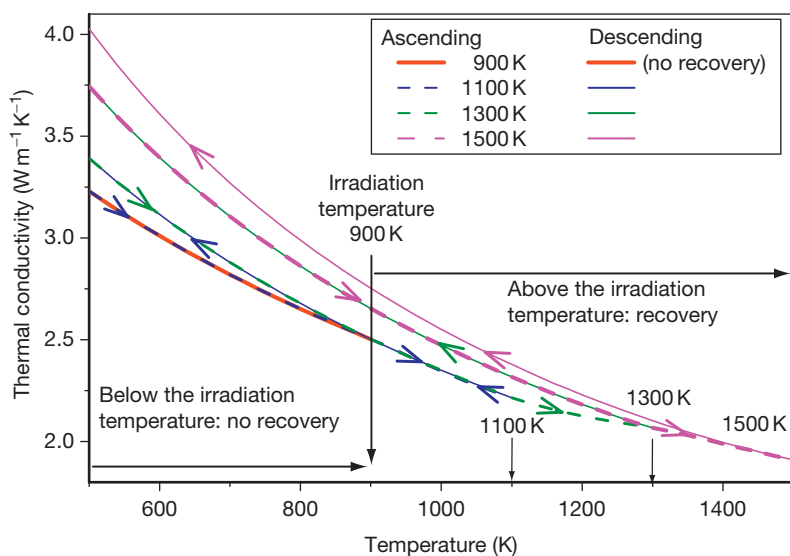


Figure 6 Thermal conductivity of a UO_2 sample with a burnup of $30 \text{ MWd} \cdot \text{kgHM}^{-1}$ and an irradiation temperature of 900 K, measured during four successive out-of-pile annealing cycles with increasing maximum temperatures. As autoirradiation damage was not present, recovery begins after the irradiation temperature is exceeded.

burnup of $30 \text{ MWd kg HM}^{-1}$ and an irradiation temperature of 900 K.¹

The in-pile microstructure and radiation damage concentration result from an equilibrium between the defect creation rate due to fission and their recombination or migration rates which depend on temperature. The point defect equilibrium concentration corresponds to the saturation level at the irradiation temperature. For out-of-pile measurements below the irradiation temperature, the damage concentration is lower compared to that of samples that would have been irradiated at this temperature, and the microstructure is different. This is particularly obvious for samples where the HBS has formed, this structure having properties different from the unstructured fuel. For out-of-pile measurements above the irradiation temperature, it is not clear whether the damage concentration is higher or lower compared to a sample that would have been irradiated at these temperatures. Thus, only the measurements at the irradiation temperature represent the in-pile state of the fuel, as discussed by Bayer and Lanning.⁵² This statement assumes that autoirradiation effects can be neglected: for instance, if the measurement takes place immediately after the irradiation or if the fuel α -activity is low. The effect of the autoirradiation can be quantified by measuring the magnitude of the recovery at temperatures below the irradiation temperature. In the absence of autoirradiation effects, no recovery will take place, as illustrated in **Figure 6**.

When the experimental measurements are interpolated by the $1/(A + BT)$ equation, a clear distinction exists between the ascending temperature regimes, where recovery takes place and therefore A and B change during the measurement as some characteristics of the sample being measured change, and the descending temperature regimes, where A and B have constant values.

Generally, the samples are resistant to fracture up to the irradiation temperature and then they may fracture or lose fragments. Fracture resistance at higher temperatures depends on the burnup and microstructure of the sample (high burnup samples are less resistant), but also has a stochastic nature linked to the existence of cracks.

2.17.6.1.1 Underlying mechanisms of the recovery

The annealing cycles measurement procedure is used to investigate the recovery mechanisms and also to accumulate sufficient data that will be used later to deduce the thermal conductivity at the irradiation temperature, this temperature being not necessarily known at the moment when the measurements are done or is to be assessed using the experimental results.

Most of the recovery is due to a decrease in the concentrations of point defects, voids, and dislocations (recombination or precipitation). As discussed by Ronchi *et al.*,¹ a contribution is also due to the redistribution of fission product atoms,

for instance, the precipitation of isolated atoms or the formation of fission gas bubbles from dynamically dissolved atoms present at the end of the irradiation. The mechanisms responsible for the out-of-pile annealing behavior are not fully described by a quantitative interpretation. Their investigation is, however, important for the understanding of the relation between the irradiation temperature and the in-pile state of the fuel. Studies of α -doped fuels have shown that the recovery takes place in different steps as a function of the annealing temperature. The different annealing stages and the nature of the related defects were shown to be identical in autoirradiated and reactor-irradiated fuels;³⁸ these stages are the oxygen vacancy/interstitial recombination (oxygen Frenkel pairs) at 600–800 K, the recombination of uranium vacancy/interstitial clusters at 800–1000 K, dislocation loop formation, and precipitation of bubbles near 1200 K.

Annealing time, that is, the hold time of the sample at the annealing temperature, was not found to have a measurable effect on the thermal diffusivity as observed by Ronchi *et al.*¹ and Carrol *et al.*⁵³ However, this result is not necessarily general, because the thermal diffusivity is not measured during the stabilization of the measurement temperature which is relatively long, and the annealing durations are limited for practical reasons.

2.17.6.1.2 Autoirradiation effects

The thermal diffusivity values obtained during laboratory measurements, performed a few years after the end of the irradiation, are not the same as the EOL values since they include the effect of supplementary damage produced by autoirradiation during storage. The impact of autoirradiation depends on the storage time, the initial enrichment of the fuel, and the burnup. Quantitative studies on fresh α -doped fuels have provided correlations between the autoirradiation dose and the thermal conductivity degradation, and have shown that the effect of radiation damage on the thermal conductivity saturates at a lower displacements per atom (DPA) value than other properties, for instance, the lattice parameter.³⁸ These studies are, however, not directly applicable to irradiated fuels, because such fuels are already damaged when autoirradiation begins, and the extent of this initial damage is not yet quantified in terms of damage concentrations.

Three characteristic thermal conductivity curves can be distinguished (Figure 6):

1. The first curve represents the conductivity measured on increasing the temperature up to the

irradiation temperature. During this stage, only damage produced by the out-of-pile autoirradiation is annealed.

2. The recovered conductivity is given by the curve obtained during the descending temperature measurement made after this annealing. This corresponds to the first part of the second curve, when the measurement begins at low temperature and continues up to temperatures higher than the irradiation temperature. During this stage, the damage produced in pile is progressively annealed above the irradiation temperature.
3. The third curve represents the conductivity of the sample after annealing at the maximum measurement temperature.

This interpretation supposes that the damage produced by autoirradiation can be clearly distinguished and separated from that produced in pile. In fact, both are of a similar nature but are produced at different temperatures.

In pile, damage that can be removed at temperatures lower than the irradiation temperature is immediately healed. At EOL, a sample can be assumed to have a concentration of radiation damage corresponding to the saturation level at the irradiation temperature. This damage is annealable only at temperatures higher than the irradiation temperature. During storage, the damage concentration increases and reaches the saturation levels at the storage temperature. As autoirradiation produces damage of identical nature to in-pile damage, part of this damage can recover at temperatures below the irradiation temperature, and part at temperatures above it. This last contribution requires supplementary modeling work.

2.17.6.2 Summary of the Main Experimental Results

Two categories of approaches can be distinguished: studies on fuel irradiated under standard conditions with irradiation temperature and burnup gradients existing between the pellet center and periphery; and studies of special irradiations, where almost uniform irradiation temperature and burnup are obtained.

Recent experimental results obtained on standard fuels are summarized in Table 1. Measurement on UO₂ were published by Carrol and coworkers,^{36,53} Ohira and Itagaki,⁵⁵ Hirai,⁵⁰ Nakamura,⁵⁷ Minato *et al.*,⁵⁸ Amaya *et al.*,⁵⁹ and Walker *et al.*⁶¹ Amaya *et al.*⁵⁹ also investigated (U,Gd)O₂ with a burnup of 43.5 and 50.7 MWd kg HM⁻¹. Only a limited number of

Table 1 Some out-of-pile thermal diffusivity measurements from which the thermal conductivity of irradiated fuel has been determined

Author and reference	Year	Fuel	Irradiation	Burnup (MWd kg HM ⁻¹)	Meas. temp. range (K)	Comment
Yamamoto <i>et al.</i> ⁵³	1993	(U _{0.82} Pu _{0.18})O ₂ FBR	Standard	8, 19, 35	850–1900	No burnup degradation observed
Carrol <i>et al.</i> ⁵²	1994	UO ₂	Standard	40	670–1670	Two samples, two runs each
Gomme <i>et al.</i> ³⁵	1997	UO ₂	Standard	61	670–1794	One cycle
Ohira and Itagaki ⁵⁴	1998	UO ₂	Standard	39		Irradiation with a temperature escalation at 1270 K and then 18 days at 573 K
Hirai ⁴⁹						Two or more cycles per sample
Baron, ³¹ Yagnik ⁵⁵	1998 2000	UO ₂ (U,Gd)O ₂	Capsule	28, 39, 63, 80 21, 47	300–1900	
Nakamura ⁵⁶	1998	UO ₂	Standard	63	Three or four cycles	
Minato <i>et al.</i> ⁵⁷	2001	UO ₂ (U,Gd)O ₂	Capsule	18, 39 39	380–1780	Two cycles
Amaya <i>et al.</i> ⁵⁸	2002	UO ₂ same as Hirai ⁴⁹ (U,Gd)O ₂	Standard	39, 60 43, 50	465–1890	Three cycles
Ronchi <i>et al.</i> ¹ Kinoshita <i>et al.</i> ⁵⁹	2004	UO ₂	Capsule	34, 52, 76, 92	500–1500	Ten samples
Walker <i>et al.</i> ⁶⁰	2006	UO ₂	Standard	102	500–1100	Two samples, three radial positions
Staicu <i>et al.</i> ²⁵	2007	(U,Pu)O ₂ LWR	Standard	33	500–1550	Three radial positions
Cozzo <i>et al.</i> ⁶¹	2008	(U,Pu)O ₂ LWR	Standard	19, 44	500–1500	Three radial positions
Sonoda <i>et al.</i> ²³	2008	UO ₂ same as Ronchi <i>et al.</i> ¹ (U,Gd)O ₂	Capsule	32, 53, 86, 96 32, 53	500–1500	Summary of HBRP results

publications are available for MOX fuel. Yamamoto *et al.*⁵⁴ made measurements on FBR MOX with 17.7 wt% Pu and burnups of 8, 19, and 35 MWd kg HM⁻¹ and did not observe a clear burnup dependence. This surprising behavior might be due to the large degradation of conductivity in the fresh fuel because of the high Pu content, and also to measurement uncertainties. Yamamoto also measured the recovery behavior of a very low burnup fuel (0.5 MWd kg HM⁻¹) of high Pu content (28.8 wt%). Measurements were published for homogeneous LWR MOX with burnups of 35⁽²⁵⁾ and 44 MWd kg HM⁻¹⁽⁶²⁾ and for heterogeneous MOX with burnups of 23 and 44 MWd kg HM⁻¹.⁶² A comparison between the MOX of homogeneous and heterogeneous microstructures for the burnup of 44 MWd kg HM⁻¹⁽⁶²⁾ showed no significant difference. Also, no difference between irradiated UO₂ and MOX was observed at the burnups of 35 and 44 MWd kg HM⁻¹.⁶² The studies on standard

fuel are the most relevant but the effect of individual parameters is difficult to assess and usually only a small number of samples is considered, making the development of a thermal conductivity model problematic.

In the special irradiation NFIR (Nuclear Fuel Industry Research) and HBRP (High Burnup Rim Project), the samples were placed in metallic capsules to have an almost uniform irradiation temperature (Table 1). A flat burnup profile was achieved by a high enrichment of ²³⁵U: 25.8% for HBRP and 19.8% for NFIR.⁶³ These irradiations involve a large number of samples of different burnups and irradiation temperatures, making them more suitable for the development of models. Despite the absence of a temperature gradient and of mechanical constraint induced by the cladding, comparative studies have shown good agreement between standard and special irradiation data.^{1,61}

and also between the NFIR and HBRP data.⁶³ NFIR results were published by Baron³² for UO_2 with burnups of 28, 39, 63, and 80 MWd kg HM^{-1} and by Yagnik⁵⁶ for UO_2 (similar to Baron³²) and $(\text{U}_{0.9}\text{Gd}_{0.1})\text{O}_2$ for the burnups of 21 and 47 MWd kg HM^{-1} . HBRP results were published by Kinoshita *et al.*,⁶³ Ronchi *et al.*,¹ and Sonoda *et al.*²³ for UO_2 with burnups of 34, 52, 76, and 92 MWd kg HM^{-1} and different irradiation temperatures, and by Sonoda *et al.*²³ for $(\text{U}_{0.95}\text{Gd}_{0.05})\text{O}_2$ with burnups of 33 and 53 MWd kg HM^{-1} .

Results obtained by Carrol *et al.*,⁵³ Hirai,⁵⁰ Minato *et al.*,⁵⁸ and Baron³² for UO_2 at a burnup of about 40 MWd kg HM^{-1} are shown in Figure 7. The experimental points include the results of annealing cycles made to observe the out-of-pile recovery. The thermal conductivity measured at 500 K ranges from about 2.8 to 4.8 $\text{W m}^{-1} \text{K}^{-1}$. This scatter is due to the differences in the experimental procedure (out-of-pile annealing history) and the irradiation temperatures, which are not always reported or considered as parameters. Such scatter is also observed for the results obtained by Ohira and Itagaki,⁵⁵ Nakamura,⁵⁷ Amaya *et al.*,⁵⁹ and Baron³² for UO_2 at a burnup of about 60 MWd kg HM^{-1} , shown in Figure 8. Compared with the measurements at about 40 MWd kg HM^{-1} (Figure 7), a clear decrease is observed: for instance, at 500 K, the thermal conductivity at a burnup of 60 MWd kg HM^{-1} ranges from 2.1 to 4.0 $\text{W m}^{-1} \text{K}^{-1}$.

Some results for $(\text{U,Gd})\text{O}_2$ by Amaya *et al.* (6.4 at.% Gd),⁵⁹ Yagnik (10 at.% Gd),⁵⁶ and Sonoda *et al.* (5 at.% Gd)²³ are shown in Figure 9. The measurements of Yagnik show a clear degradation between the burnups of 21 and 47 MWd kg HM^{-1} . The thermal conductivity results of Amaya at burnups of 43.5 and 50.7 MWd kg HM^{-1} are in the same range as those of Yagnik at 21 and 47 MWd kg HM^{-1} , whereas the measurements of Sonoda at 52 MWd kg HM^{-1} are significantly lower.

The plots in Figures 7–9 illustrate the relatively wide range of thermal conductivity values obtained for a given burnup and temperature. In this context, the modeling assumptions used for the interpretation of the experimental results have a significant influence on the predicted in-pile thermal conductivity. The main models developed from out-of-pile results will be presented in the subsequent sections.

2.17.6.3 NFI (1997–2005)

Ohira and Itagaki⁵⁵ proposed the ‘NFI’ (Nuclear Fuel Industries) model (eqn [9], Table 2) for the thermal conductivity, based on experimental results for an UO_2 fuel with about 61 MWd kg HM^{-1} . A linear dependence of the parameter A on burnup was assumed for the effect of fission products in solution, $f(bu)$, and the effect of radiation damage

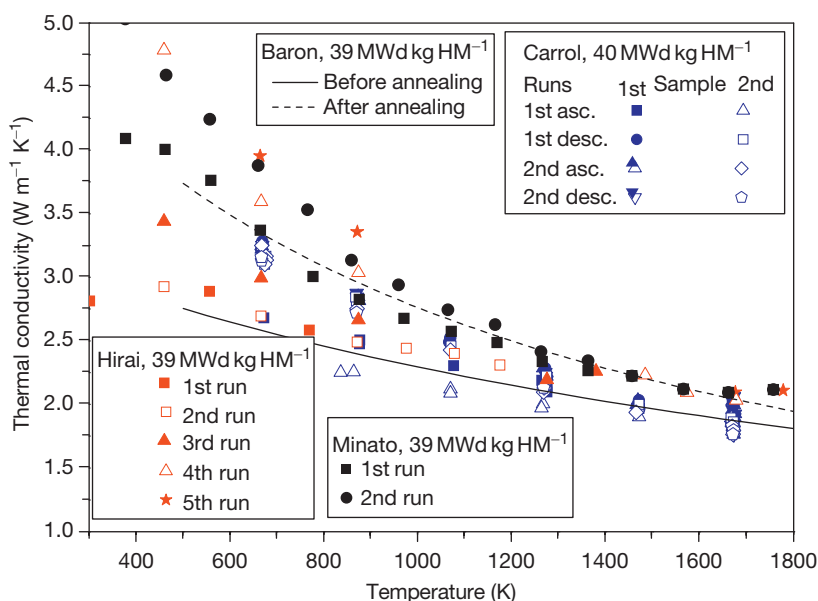


Figure 7 Comparison of the thermal conductivity data published by Carrol *et al.*⁵² Hirai,⁴⁹ Minato *et al.*,⁵⁷ and Baron³¹ for UO_2 with a burnup of about 40 MWd kg HM^{-1} (95% TD).

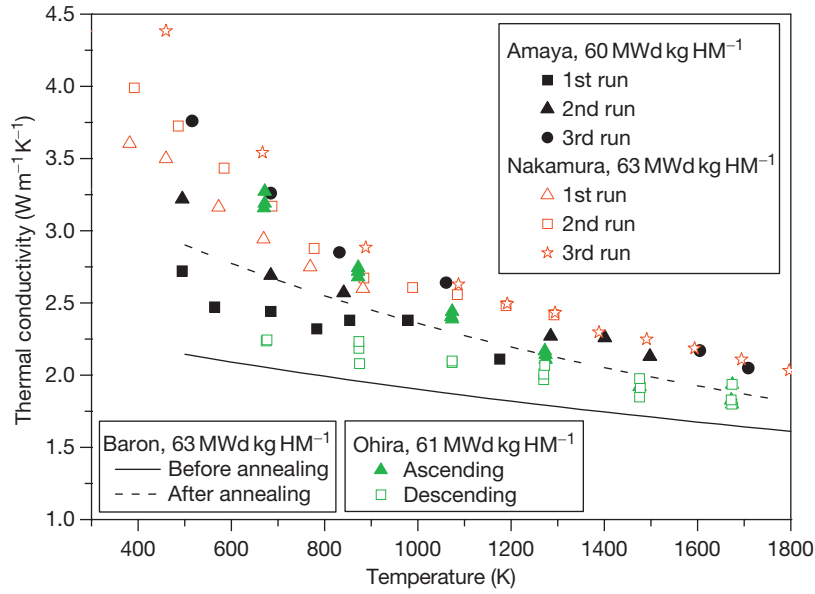


Figure 8 Comparison of the thermal conductivity data published by Ohira and Itagaki,⁵⁴ Nakamura,⁵⁶ Amaya *et al.*,⁵⁸ and Baron³¹ for UO_2 with a burnup of about $60 \text{ MWd kg HM}^{-1}$ (95%TD).

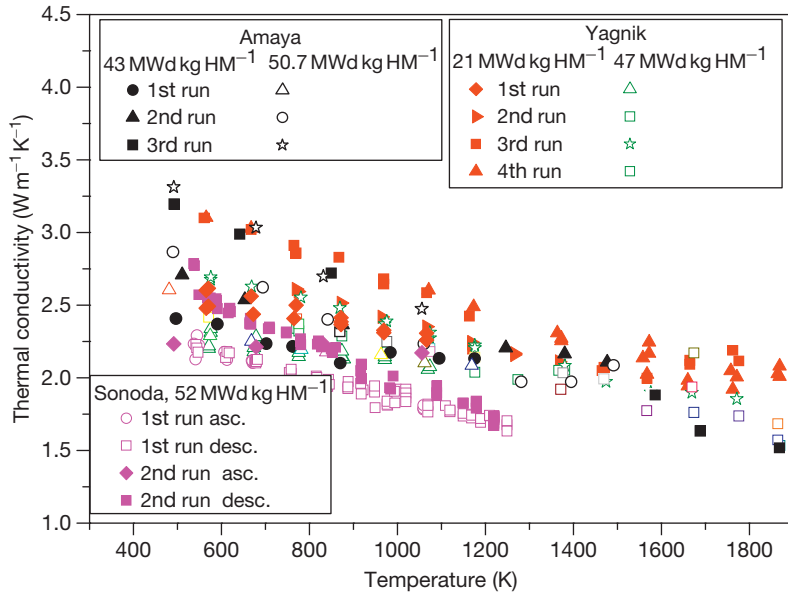


Figure 9 Comparison of the thermal conductivity data for $(\text{U,Gd})\text{O}_2$ published by Yagnik,⁵⁵ Amaya *et al.*,⁵⁸ and Sonoda *et al.*²³ (95%TD).

was modeled as increasing slowly with burnup (proportional to $bu^{0.28}$) and to be progressively annealed when temperature increases, as described by $b(T)$.

$$\lambda_{95} = \frac{1}{A + BT + f(bu) + g(bu)b(T)} + CT^2 + DT^4 \quad [9]$$

Lanning *et al.*⁴⁴ modified this model to obtain eqn [10] and verified it against the experimental results of Carroll *et al.*⁵³ and Ronchi *et al.*¹ and also introduced the effect of gadolinia assuming a similar effect as observed for fresh fuels by Massih *et al.*⁶⁴

Table 2 Constants of the NFI and NFI-based models (eqns [9]–[11])

$a = 1.1599$	$A = 0.0452 \text{ mK W}^{-1}$
Gd : weight fraction of gadolinia	$B = 2.46 \times 10^{-4} \text{ mK W}^{-1} \text{ K}^{-1}$
$f(bu) = 0.00187bu$: effect of FPs in solution in the matrix	$C = -5.47 \times 10^{-9} \text{ W m K}^3$
$g(bu) = 0.038bu^{0.28}$ effect of irradiation defects	$D = 13520 \text{ K}$
$h(T) = 1/(1 + 396 \exp(-6380/T))$: annealing of irradiation defects	$E = 3.5 \text{ E9 W K m}^{-1}$
$x = 2.00 - O/M$ (O/M is the oxygen-to-metal ratio)	$F = 16361 \text{ K}$
$A(x) = 2.85x + 0.035 \text{ mK W}^{-1}$	$C_{\text{mod}} = 1.5 \times 10^9 \text{ W K m}^{-1}$
$B(x) = (2.86 - 7.15x) \times 10^{-4} \text{ m W}^{-1}$	

The Duriez-modified NFI model (eqn [11]) was proposed by Pacific Northwest National Laboratory (PNNL) for MOX fuels.⁴⁴ It is a combination of the fresh MOX fuel model of Duriez¹⁴ and the modified NFI model (eqn [10]) for irradiated UO₂, incorporating a modification of the high-temperature term of Duriez (C_{mod}). The constants $A(x)$, $B(x)$, and D are those proposed by Duriez for fresh MOX and x is the deviation from stoichiometry (i.e., $x = 2 - O/M$). This model was verified by PNNL using in-pile fuel central temperature measurements.

$$\lambda_{95} = \frac{1}{A + a \text{ gad} + BT + f(bu) + (1 - 0.9e^{-0.04bu})g(bu)b(T) + \frac{E}{T^2}e^{-F/T}} \quad [10]$$

$$\lambda_{95} = \frac{1}{A(x) + B(x)T + f(bu) + (1 - 0.9e^{-0.04bu})g(bu)b(T) + \frac{C_{\text{mod}}}{T^2}e^{-D/T}} \quad [11]$$

2.17.6.4 Baron and NFIR (1998–2004)

Using NFIR experimental results for UO₂ up to a burnup of 80 MWd kg HM⁻¹, Baron³² proposed a correlation in which thermal recovery during the out-of-pile annealing is accounted for by using the variation of the lattice parameter ξ (in Å) as a marker of the matrix damage evolution (eqn [12] and Table 3). Comparison with experimental results shows good agreement, but the application of the correlation is possible only when the lattice parameter is known. For this reason, approximate formulae for A_0 and B_0 for the conductivity before recovery were deduced from the original plots: $A_0 = -3.422 \times 10^{-5}bu^2 + 7.792 \times 10^{-3}bu + 4.645 \times 10^{-2}$, $B_0 = 1.328 \times 10^{-8}bu^2 - 2.292 \times 10^{-6}bu + 2.123 \times 10^{-4}$. The correlation includes the effect of Pu and Gd. The effects of these two additives were obtained from fresh fuel measurements and also from NFIR results for irradiated gadolinia fuel.³²

Table 3 Constants in the Baron model eqn [12]

$A_0 = 0.044819 + 0.005bu + 20(\xi - 5.4702) \text{ mK W}^{-1}$	$D = -4.302 \times 10^{10} \text{ W K m}^{-1}$
$B_0 = (2.12^a - 0.0125bu - 70(\xi - 5.4702)) \times 10^{-4} \text{ m W}^{-1}$	$W = 1.41^a - 1.6 \times 10^{-19} \text{ J}$
$A_1 = 4$	$k = 1.38 \times 10^{-23} \text{ J K}^{-1}$
$A_2 = 0.611$	ξ lattice parameter in Å
$A_3 = 11.081$	bu : burnup in MWd.t _U ⁻¹
$B_1 = 0.8$	Gd : gadolinium weight content
$B_2 = 9.603 \times 10^{-4}$	x : absolute value of stoichiometric deviation
$B_3 = -1.768 \times 10^{-2}$	q : plutonium weight content
$C = 5.516 \times 10^9$	

^aValue modified using the plots in the original paper: Baron, D. Fuel thermal conductivity: A review of the modeling available for UO₂, (U,Gd)O₂ and MOX fuel. In *Proceedings of OECD/NEA Seminar on Thermal Performance of High Burn-up LWR Fuel*, Cadarache, France, March 1998; p 129.

Table 4 Constants of the thermal conductivity model described by eqn [13] (SI units)

Parameter	Value	Parameter	Value
A_1	0.09592	B_1	0.00025
A_2	0.00614	B_2	0.00000181 ^a
A_3	-0.000014	B_3	0.00000027 ^a
A_4	0.0026	B_4	-0.01268763
A_5	0.1197	C	0.0132
A_6	0.01214167	D	0.00188
A_7	0.000540625	Gd	Gd weight content
A_8	-0.00005182292		

^aSigns changed to correct the original values.

$$K = \frac{1}{A_0 + A_1x + A_2g + A_3g^2 + (B_0(1 + B_1q) + B_2g + B_3g^2)T_k + \frac{C + DGd}{T_k^2}e^{-W/KT_k}} \quad [12]$$

An updated correlation for UO₂ and (U,Gd)O₂ (eqn [13] and Table 4) was derived by Yagnik from the NFIR thermal conductivity results obtained on samples irradiated below 800 °C.⁶⁵ This correlation takes into

account the thermal recovery observed during laboratory measurements. The lattice thermal conductivity before and after thermal recovery is given by λ_{start} and λ_{end} , respectively, and the temperature dependence of the fission products redistribution and radiation damage recovery is given by the coefficient F . The burnup, bu , is in MWd kg HM⁻¹ and T is in °C.

$$\lambda_{95}(bu) = (1 - F)\lambda_{\text{start}} + F\lambda_{\text{end}} + \lambda_{\text{el}} \quad [13]$$

with

$$\lambda_{\text{start}} = \frac{1}{A_1 + A_2 bu + A_3 bu^2 + (B_1 - B_2 bu)T(^{\circ}\text{C})}$$

$$\lambda_{\text{end}} = \frac{1}{A_1 + A_4 bu + (B_1 - B_3 bu)T(^{\circ}\text{C})}$$

$$\lambda_{\text{el}} = Ce^{DT(^{\circ}\text{C})}$$

$$F = 0.5 \left(1 - \tanh \left(\frac{T(^{\circ}\text{C}) - 900}{150} \right) \right)$$

For (U,Gd)O₂ the same formula is used, replacing the coefficients A_1 and B_1 by:

$$A'(Gd) = (A_5 + A_6 Gd + A_7 Gd^2 + A_8 Gd^3) \times 0.26e^{28.5875/(bu+19.8085)} \text{ and } B'(Gd) = B_1 e^{B_4 Gd}$$

In this correlation, no information on the irradiation temperature or on the out-of-pile autoirradiation is explicitly taken into account. The temperature

dependence of the coefficient F can be used to reconstruct experimental results obtained for different annealing temperatures (Figure 10). Starting with an irradiated sample, F is calculated up to the first annealing temperature during the ascending temperature phase, and then kept constant during the descending phase. For the second annealing cycle, F is kept at the value used in the first cycle up to the first annealing temperature, and then F is recalculated when this temperature is exceeded. Then, for the evaluation during the descending temperature phase, F is kept at the value corresponding to the highest temperature reached in the second cycle. According to eqn [13], most of the out-of-pile recovery takes place in the range from 900 to 1500 K. This temperature range for recovery appears to be relatively high and may be related to the irradiation temperature of the samples, which is specified only as being below 800 °C.

2.17.6.5 HBRP (2004)

UO₂ and (U,Gd)O₂ samples were irradiated in the framework of the HBRP which comprised a matrix of four burnups and four irradiation temperatures.⁶⁰ The samples were in the form of 1-mm-thick discs, irradiated at constant, controlled temperature (~750–1500 K) and up to different burnups in the range from 34 to 96 MWd kg HM⁻¹.⁶³

Kitajima *et al.*⁶⁰ derived a first correlation (eqn [14]) summarizing the HBRP thermal

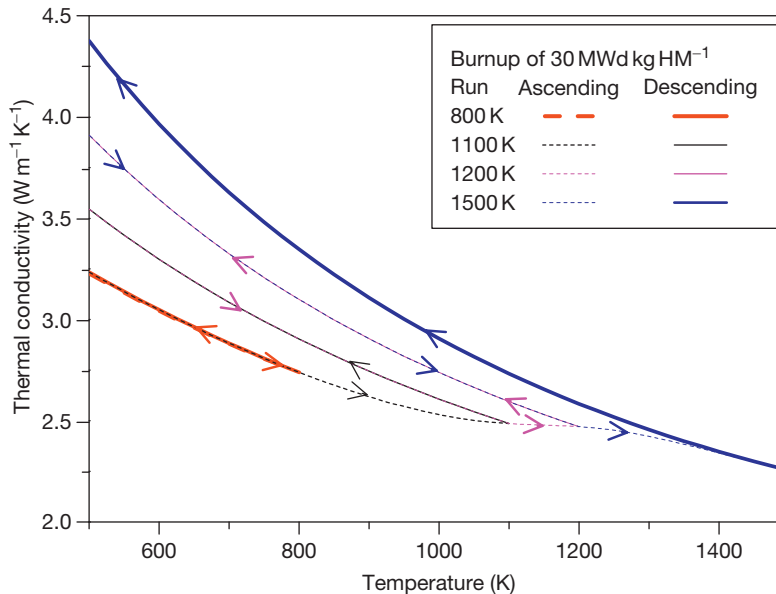


Figure 10 Thermal conductivity during out-of-pile annealing cycles as predicted by the Nuclear Fuel Industry Research correlation for a burnup of 30 MWd kg HM⁻¹.

Table 5 Parameters of the thermal conductivity model of Kitajima *et al.*⁵⁹

$T < 1273$ K	$T > 1473$ K	$1273 \leq T \leq 1473$ K; linear interpolation between the conductivities in the two temperature regions
$A = 40 + 4.12bu$	$A = 40 + 1.74bu$	
$bu < 50$ $B = 0.22$	$B = 0.22 + 0.0003bu$	
$50 < bu < 80$ $B = 0.447 - 0.00453bu$		
$80 < bu$ $B = 0.084$		

Source: Kinoshita, M.; Sonoda, T.; Kitajima, S.; *et al.* High Burnup Rim Project (III): Properties of rim-structured fuel. In *Proceedings of the 2004 ANS International Meeting on LWR Fuel Performance*, Orlando, Florida 2004; p 207.

conductivity results and including the effect of the HBS structure formation (Table 5). A slight increase of the conductivity normalized to 100% TD was observed after its formation, attributed to the matrix damage recovery and to the transfer of the gas atoms to the pores.

$$\lambda = \frac{1}{A + BT} + \lambda_e \quad [14]$$

where λ_e is the electronic contribution to the conductivity.

Ronchi obtained a second model based on the HBRP results.¹ Three temperatures are taken into account: the irradiation temperature, T_{irr} which summarizes the state of the fuel at EOL; the out-of-pile annealing temperature, T_{ann} , which indicates how much damage was recovered; and the temperature, T , at which the thermal conductivity is measured. The thermal diffusivity was measured during annealing cycles with maximum temperatures lower and higher than the irradiation temperatures when the samples did not fragment.

The phonon thermal conductivity (normalized to 5 vol% porosity) is expressed by

$$\lambda = (A(T_{irr}, T_{ann}, bu) + B(T_{irr}, T_{ann}, bu)T)^{-1} \quad [15]$$

where T is the instant application temperature (300–1500 K); T_{irr} is the irradiation temperature (700–1450 K); T_{ann} is the maximum temperature (700–1450 K) reached during out-of-pile annealing; and bu is the local fuel burnup, in MWd kg HM⁻¹ (up to 100).

The different contributions to the degradation of the thermal conductivity were quantified. The coefficient A , as given by eqn [16], is the sum of the fresh fuel value, 0.046 m K W⁻¹; the contribution of nonvolatile and volatile fission products, $\Gamma(bu, GIS)$ (GIS is the fraction of volatile fission products present as dispersed atoms in the fuel matrix); the autoirradiation damage, $\delta A_{Auto}(T_m, bu)$; and the in-pile radiation damage, $\delta A_{EOL}(T_m, bu)$.

$$A(T_{irr}, T_{ann}, bu) = 0.046 + \Gamma(bu, GIS) + \delta A_{Auto}(T_m, bu) + \delta A_{EOL}(T_m, bu) \quad [16]$$

The temperature $T_m = \max(T_{irr}, T_{ann})$ takes into account the irreversible recovery taking place when the irradiation temperature is exceeded. The damage state of the fuel corresponds to that at EOL as determined from T_{irr} but as soon as T_{irr} is exceeded during the measurement, the damage state is determined by T_{ann} .

The effect of autoirradiation damage produced between EOL and the time of the measurements is determined by measuring the recovery during measurements up to the irradiation temperature. This autoirradiation effect was found to be present in all samples, independently of the irradiation temperature and burnup. This means that the values of A at EOL were always lower than those measured in laboratory. A compensation was applied, but it is not discussed here.¹ The effect of parameters that are not sensitive to temperature was assessed from the results obtained after laboratory annealing. These are the soluble fission products (whose effect was analyzed with the phonon scattering formulae based on the evaluation of the phonon scattering cross section Γ) and the nonvolatile fission products (metallic and ceramic precipitates, the effect of which was analyzed by using the theory of the effective conductivity of composite materials). The effect of these parameters on the coefficients A and B was found to be proportional to the burnup and therefore could not be discerned from the experimental results. This effect was integrated in the parameter Γ as a linear burnup effect (eqn [17]). Gaseous and volatile fission products present in a frozen atomic state also contribute to the phonon scattering, and their effect is therefore included in the phonon scattering cross section Γ . Its maximum amplitude was deduced by analyzing the evolution of the conductivity due to the HBS formation. The temperature and microstructure dependence were interpreted by determining the

thermodynamic state of the fission gas, calculated with a diffusion/precipitation/release model¹⁸ predicting the fraction of gas dynamically dissolved (gas in solid (GIS)) and precipitated (gas in bubbles). The latter state was found to depend both on temperature and grain size, and this last parameter accounts for the effect of rim restructuring. This effect was integrated in the parameter Γ , which depends on bu and GIS as shown in eqn [17].

$$\Gamma(bu, GIS) = 9.02 \times 10^{-4} bu GIS + 1.74 \times 10^{-3} bu + 7.51 \times 10^{-3} \quad [17]$$

An approximate expression of GIS needed for evaluating eqn [17] is given by eqn [18]. The numerator takes into account the irradiation temperature and the burnup, which are indicators for HBS formation, taking into account the precipitation of a fraction of the fission gas inventory at that transition. The denominator represents the formation of gas bubbles and fission product inclusions that takes place at high irradiation or annealing temperatures, independently of the microstructure.

$$GIS(bu, T_{irr}, T_{ann})$$

$$= \frac{1 - 0.9 \left[1 + \exp\left(\frac{T_{irr} - 950}{30}\right) \right]^{-1} \left[1 + \exp\left(\frac{73 - bu}{2}\right) \right]^{-1}}{\left[1 + \exp\left(\frac{T_{irr} - 1350}{200}\right) \right] \left[1 + \exp\left(\frac{T_{ann} - 1350}{200}\right) \right]} \quad [18]$$

The contribution of in-pile radiation damage to the thermal conductivity deterioration was quantified from the measured magnitude and temperature dependence of the recovery for measurement temperatures higher than T_{irr} . The in-pile radiation damage could be investigated in samples that did not fragment. These generally are characterized by low burnup and low irradiation temperatures. After subtracting the out-of-pile autoirradiation effect, a conductivity recovery in the form of a decrease of the coefficient A was observed. No significant recovery was observed below 800 K. The recovery took place in two stages: between 800 and 1000 K and between 1200 and 1350 K. The variation of A due to the change in the effective concentration of irradiation defects at EOL, δA_{EOL} , was found to be proportional to burnup and can be expressed by eqn [19], with $T_m = \max(T_{irr}, T_{ann})$.

$$\delta A_{EOL}(T_m, bu) = \frac{bu}{850} \left[\left(1 + \exp\left(\frac{T_m - 950}{25}\right) \right)^{-1} + \left(1 + \exp\left(\frac{T_m - 1300}{35}\right) \right)^{-1} - 0.0525 \right] (\text{mK W}^{-1}) \quad [19]$$

In agreement with the experimental results, the effect of in-pile and out-of-pile thermal annealing of irradiation defects for a given temperature is equivalent in eqn [19], so that $\delta A_{EOL}(T_{irr}, bu)$ is calculated by the same function, replacing T_{irr} by T_{ann} when $T_{ann} > T_{irr}$.

The variation of the coefficient B was analyzed using the same methodology but is not presented here. A factor was also introduced in the original formulae in order to extrapolate the values to fresh fuel, but it is not discussed here since it is not based on measured data.

The thermal conductivity at EOL as a function of burnup for different irradiation temperatures (obtained with $T = T_{irr} = T_{ann}$) is shown in Figure 11. In this model, the formation of the HBS induces a large decrease in the fission gas concentration dissolved in the matrix and has a positive effect on the lattice thermal conductivity (i.e., normalized to 5 vol% porosity) as seen for the curves for irradiation temperatures of 300, 600, and 900 K in Figure 11. When the burnup further increases, the degradation continues, as a result of the accumulation of fission products.

2.17.6.6 A Correlation for UO₂ and MOX

Systematic studies of unirradiated MOX fuel¹⁴ have shown that the thermal conductivity is significantly lower than that of UO₂ and that the effects of the Pu concentration (in the range 3–15 wt%) and microstructure were insignificant. Investigations were performed by comparing the experimental results available for irradiated UO₂ and MOX fuels with different microstructures and burnups in the range 0.4–100 MWd kg HM⁻¹.^{1,25,38,61,62} A model for the comparison between fuels with different burnups and irradiation conditions is required. Starting from the Ronchi model for UO₂,¹ a simplified version was derived for purposes of comparison. The parameters that have to be included in such a correlation are the burnup and irradiation temperature. The irradiation temperature is required to describe the increase in thermal conductivity observed when moving from the periphery to the pellet center, in regions with almost constant burnup.²⁵ The only measurements that are to be considered are those obtained after annealing at the irradiation temperature and measured during the descending temperature phase. The measurements obtained during the ascending temperature phase up to the irradiation temperature were not

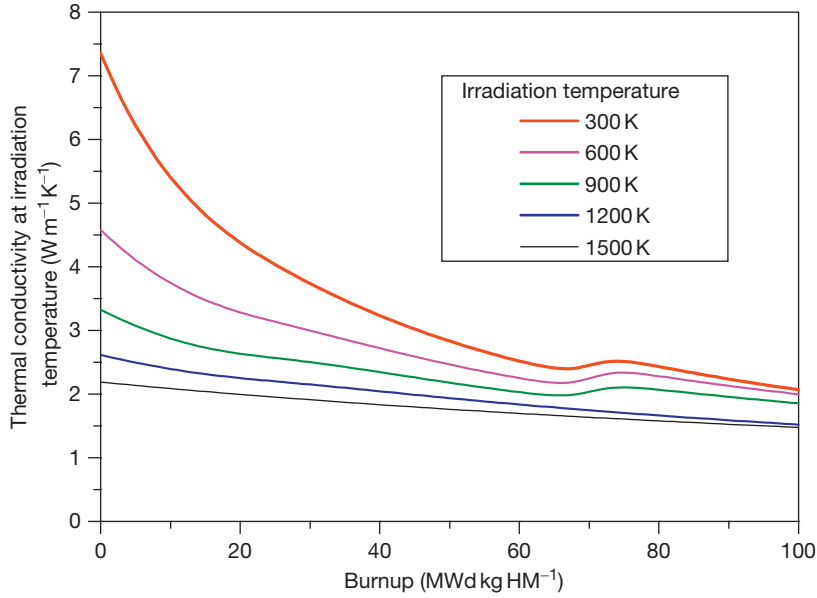


Figure 11 Thermal conductivity as a function of burnup for different irradiation temperatures according to the model of Ronchi *et al.*,¹ evaluated at the irradiation temperature (at end of life and for 95% TD).

considered because annealing takes place progressively during such a measurement run. The out-of-pile damage, due to autoirradiation, is assumed to be annealed at this temperature. In order to investigate the differences or similarities between irradiated UO₂ and MOX, the correlation was fitted to three different datasets: UO₂ alone, MOX alone, and UO₂ and MOX together.

As a preliminary approach, a formula including the effect of the burnup only is investigated: $\lambda = 1/(A + BT)$ with A and B depending linearly on burnup: $A = A_1 + A_2 bu$ and $B = B_1 + B_2 bu$ (where bu is the burnup in MWd kg HM⁻¹). As the formula is validated only for measurements up to 1500 K, no high-temperature contribution is introduced. The extrapolation to zero burnup has to be considered carefully when such a simple formula is used, because of the rapid degradation in thermal conductivity occurring at very low burnups, linked to the buildup of radiation damage. Preliminary tests have shown that the parameters A_1 and B_1 cannot have the values corresponding to fresh fuel. This is well demonstrated by the experimental results obtained for UO₂ fuel with the very low burnup of 0.4 MWd kg HM⁻¹(38): the degradation of the thermal conductivity at this burnup is much higher than that predicted by a formula valid up to 100 MWd kg HM⁻¹. The extrapolation to zero burnup requires introducing a supplementary term in the correlation.

The 0.4 MWd kg HM⁻¹ sample was therefore not used, and the next lowest burnup sample has a burnup of 23 MWd kg HM⁻¹. The four free parameters A_1 , A_2 , B_1 , and B_2 were evaluated by a least-squares method and it was shown that it is not justified to propose distinct correlations for UO₂ and MOX. The obtained correlation corresponds to the following values of the parameters:

$$A_1 = 0.11906 \text{ mK W}^{-1}; A_2 = 0.002617 \text{ mK W}^{-1};$$

$$B_1 = 2.5974 \times 10^{-4} \text{ m W}^{-1}; B_2 = -8.726 \times 10^{-7} \text{ m W}^{-1}.$$

As both samples with low and high irradiation temperatures were considered in this study, the results given by such a correlation cannot provide an optimum prediction for each particular sample. In a second correlation, the irradiation temperature dependence was introduced using a formula already proposed,¹ based on a two-step annealing of radiation damage in the temperature range 500–1500 K: the first at 950 K and the second at 1300 K. The thermal conductivity (normalized to 5% porosity) is expressed (eqn [20]) as $\lambda = (A(bu, T_{\text{irr}}) + B(bu, T_{\text{irr}})T)^{-1}$, where T is the measurement temperature (300–1500 K), T_{irr} is the irradiation temperature (600–1500 K), and bu is the burnup (23–100 MWd kg HM⁻¹).

$$A(bu, T_{\text{irr}}) = A_1 + A_2 bu + A_3 bu f(T_{\text{irr}}) \text{ and}$$

$$B(bu, T_{\text{irr}}) = B_1 + B_2 bu + B_3 bu f(T_{\text{irr}}) \quad [20]$$

with

$$f(T_{\text{irr}}) = \left(1 + \exp\left(\frac{T_{\text{irr}} - 950}{25}\right)\right)^{-1} + \left(1 + \exp\left(\frac{T_{\text{irr}} - 1300}{35}\right)\right)^{-1}$$

The results of the parameter estimation process show that the average interpolation error for UO₂ and MOX fuels is lower than in the previous case, but all the qualitative observations remain valid. It is confirmed that it is not justified to propose separate correlations for the UO₂ and MOX fuels. The correlation is defined by (in SI units):

$$A_1 = 0.1088; A_2 = 1.664 \times 10^{-3}; A_3 = 8.371 \times 10^{-4};$$

$$B_1 = 2.932 \times 10^{-4}; B_2 = -5.548 \times 10^{-7};$$

$$B_3 = -7.189 \times 10^{-6}$$

The interpolation error was therefore reduced by introducing the irradiation temperature as a parameter in the correlation, and the predictions for samples with high irradiation temperatures were particularly improved. The interpolation error might be reduced further by introducing supplementary parameters, such as the presence of the rim structure. However, if the uncertainties in the experimental thermal conductivities are taken into account (about 10% for irradiated fuel), the average error of 7.4% obtained with the present correlation is already acceptable.

2.17.7 Comparison of the Results Obtained Using Different Models

The available models range from correlations built from in-pile or out-of-pile measurements to combinations of models or results. The thermal conductivity predictions for UO₂ obtained with the three approaches presented in this chapter are compared for the burnups of 30 (Figure 12) and 80 (Figure 13) MWd kg HM⁻¹ in the temperature range from 500 to 1500 K. The model of Lucuta³⁹ was obtained from measurements on simulated irradiated fuels, and the model of the Halden Reactor Project⁴⁵ was derived from in-pile central temperature data. The models published from out-of-pile measurements by NFI (Ohira and Itagaki⁵⁵ and Lanning *et al.*⁴⁴), by NFIR (Baron³² and Yagnik *et al.*⁶⁵), by HBRP (Ronchi *et al.*¹), and by the correlation for UO₂ and MOX accounting for differences in irradiation temperature (eqn [20]) were selected. The calculations were done at the irradiation temperature, that is, without taking into account out-of-pile recovery during annealing at higher temperatures. For the models considering only one temperature, that is, the measurement temperature, it was assumed to be equivalent to the irradiation temperature.

The model of Lucuta predicts the weakest degradation with burnup compared with both out-of-pile and in-pile measurements; this degradation is

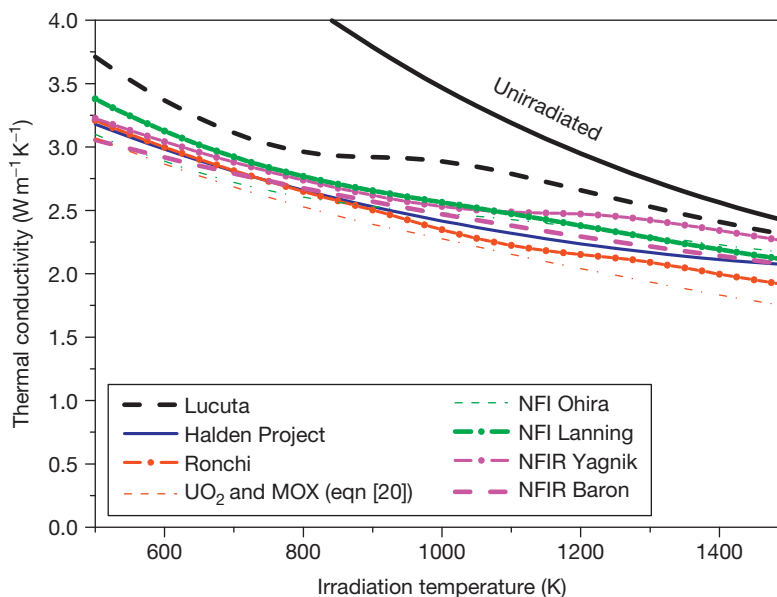


Figure 12 Thermal conductivity at 95% TD as a function of temperature at a burnup of 30 MWd kg HM⁻¹ according to different models.

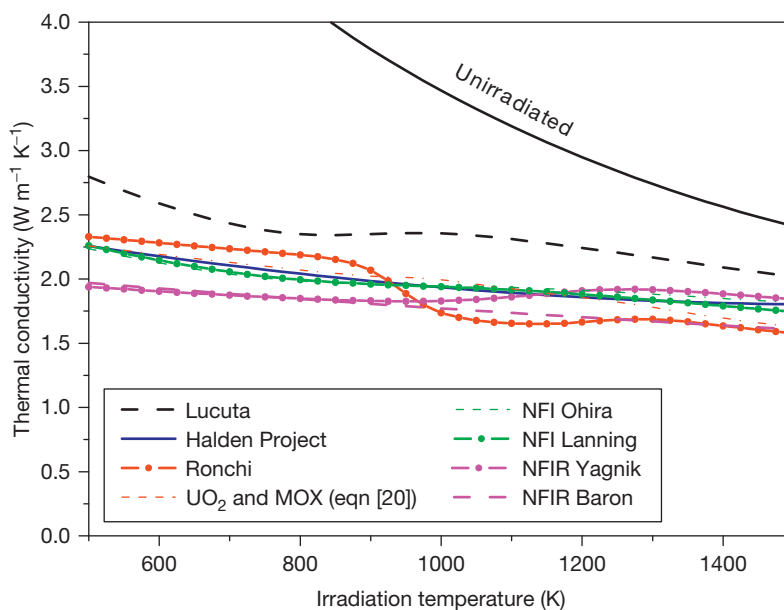


Figure 13 Thermal conductivity at 95% TD as a function of temperature at a burnup of $80 \text{ MWd kg HM}^{-1}$ according to different models.

considered too low by Ohira and Itagaki⁵⁵ and Lanning *et al.*⁴⁴ This model is therefore not considered in the following discussion. However, Minato *et al.*⁵⁸ found that this model was in good agreement with their experimental results.

The model of the Halden Reactor Project and the models obtained from out-of-pile measurements give predictions that are in the same range. Some scatter exists, due to the differences in the nature and number of samples used: no model was produced using samples covering the entire burnup and irradiation temperature range considered. At the burnup of $30 \text{ MWd kg HM}^{-1}$ (Figure 12), the scatter is moderate at low temperatures and increases with temperature. This increase reflects the reduced number of samples available for high irradiation temperatures. To our knowledge, only the correlations of Ronchi and ‘ UO_2 and MOX’ consider samples with irradiation temperature up to 1500 K and these correlations give the lowest predictions at high temperatures. At the burnup of $80 \text{ MWd kg HM}^{-1}$ (Figure 13), the scatter between the different models is of about 20%, independent of the temperature. The model of Ronchi shows the positive effect of HBS formation: it predicts the highest values for low irradiation temperatures. For both burnup values, it is noteworthy that even correlations obtained from almost similar experimental results do not give identical predictions as a result of the different approaches and aims of the authors.

Differences exist in the analysis of the out-of-pile annealing cycles (i.e., the selection of the data used from the large number of data produced by such cycles), taking into account or not the irradiation temperature and in the mathematical form adopted, which reflects the phenomena included such as the HBS formation or the out-of-pile annealing behavior.

The thermal conductivity as a function of burnup for an irradiation temperature of 700 K is plotted in Figure 14. It can be seen that the scatter is high at low and high burnup. At low burnup, this is explained by the lack of samples and the fact that a simple formula valid at intermediate and high burnups cannot be extrapolated to zero burnup, where the degradation of the thermal conductivity is much faster. At high burnup, the scatter is due to the reduced number of samples and the brittleness of the samples that complicates the measurements.

The thermal conductivities of $(\text{U,Gd})\text{O}_2$ and MOX fuels follow the same trend as UO_2 in terms of burnup degradation. The main difference between the models is how the ratio between the conductivity of the fuel with an additive and UO_2 changes with burnup. For MOX fuel, the ratios obtained with the models of Lanning (Duriez-NFI⁴⁴), Baron,³² ‘ UO_2 and MOX’ (eqn [20]), and the Halden Project⁴⁵ are shown in Figure 15. Only the Halden Project formula and the ‘ UO_2 and MOX’ correlations are based on experiments; the Lanning and Baron correlations are derived

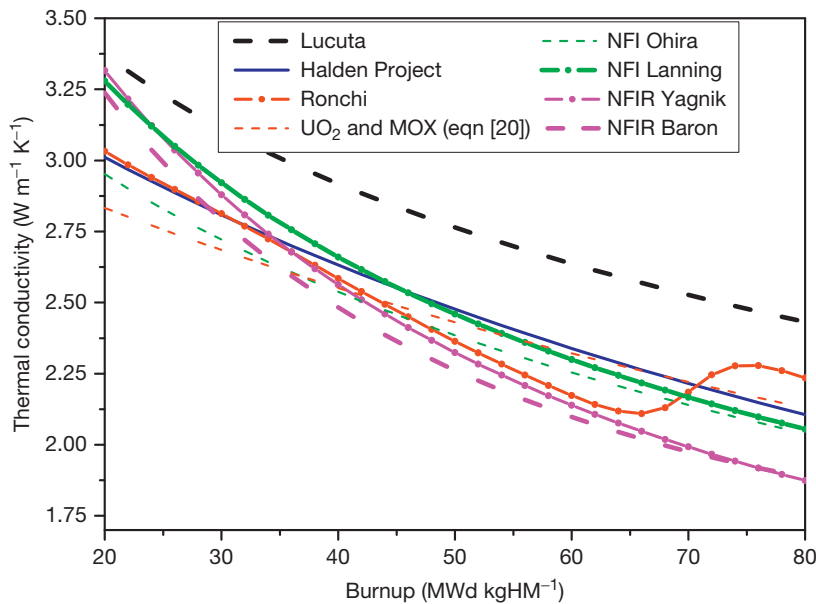


Figure 14 Thermal conductivity at 95% TD as a function of burnup at an irradiation temperature of 700 K according to different models.

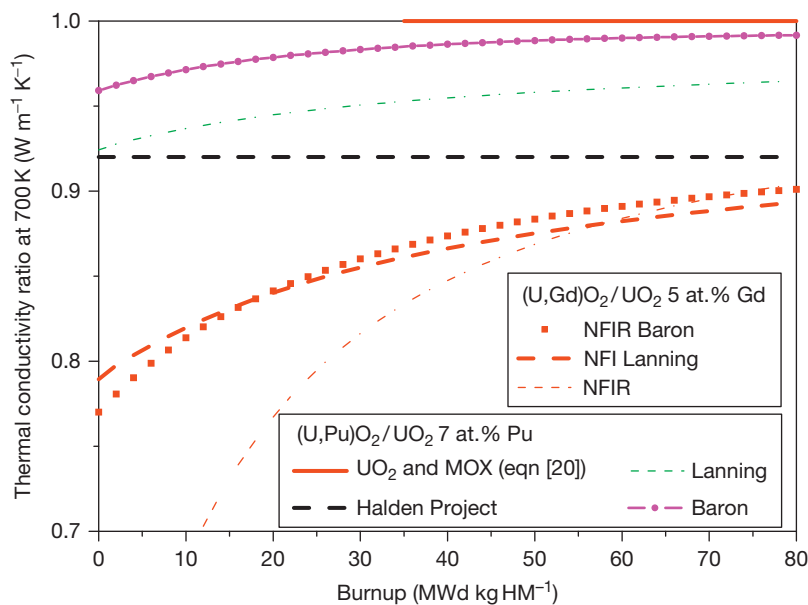


Figure 15 Ratio of the conductivities of the $(\text{U,Gd})\text{O}_2$ and mixed oxide fuels to that of UO_2 as a function of burnup.

from measurements on unirradiated fuel. The ' UO_2 and MOX' correlation predicts a ratio of 1 for burnups higher than $32 \text{ MWd kg HM}^{-1}$, as observed in out-of-pile measurements.

The ratio is larger for the $(\text{U,Gd})\text{O}_2$ fuels but is also predicted to decrease with burnup, as illustrated in Figure 15 with the models of Baron,³² NFI

modified by Lanning *et al.*,⁴⁴ and NFIR.⁶⁵ The HBRP results, which were not used to derive a correlation, have shown a ratio decreasing with burnup and reaching a value around 1 at the burnup of about $80 \text{ MWd kg HM}^{-1}$.²³ Therefore, both for $(\text{U,Gd})\text{O}_2$ and MOX fuels, as well as for the Cr-doped fuel,²⁶ the degradation observed for the fresh fuels as compared

with standard UO₂ decreases with burnup and can be expected to become negligible after a certain burnup value, depending on the kind and initial concentration of the additive: for equal initial concentrations, the effect of Pu is weaker and will also disappear earlier than the effect of Gd. This is due to the consumption of Pu in the MOX and to the buildup of Pu in standard UO₂ as the burnup increases.

2.17.8 Conclusions

UO₂ is the most studied nuclear fuel, with characterization results accumulated since more than 50 years. Investigations are also conducted to assess the high burnup effects and the impact of additives such as Pu, Gd, and Cr. Experimental and theoretical studies of the influence of microstructure on the thermal conductivity of fresh and irradiated MOX fuels are conducted using UO₂ as a reference. The addition of a few percent of Pu in UO₂ lowers the thermal conductivity of the fresh fuel but does not significantly influence the thermal conductivity at intermediate and high burnups. Recent studies have also shown that the effect of the MOX microstructure is negligible. As a result, a common correlation was proposed for irradiated UO₂ and MOX.⁶² Further studies will be needed, linked to the increase of the discharge burnup, made possible by increase of the enrichment of UO₂ fuel and of the plutonium content of MOX fuel. For MOX fuel, the Pu content in fresh fuel will further be increased because of the degradation of the isotopic composition of the Pu obtained from reprocessing of spent high-burnup UO₂. Other developments are necessary, aimed at improving the precision and validity domain of the correlations: extrapolation down to zero burnup, effect of the HBS, and in-pile and out-of-pile annealing of the radiation damage due to temperature variations.

The choice of an appropriate correlation or approach depends on the needs, between the simple formulae describing only the average expected degradation with burnup or more complex formulae adapted to precise studies taking into account irradiation conditions (average irradiation temperature at EOL or irradiation temperature history).

Because of the nature of irradiated fuel, the precision that can be reached for the thermal conductivity is limited, and fluctuations linked to the uncertainties on the irradiation conditions will remain. Only a complete integration of the irradiation history in the model can lead to a perfect prediction, assuming

that the effect of each parameter can be quantified, which is not the case currently. High-temperature data are almost nonexistent because of the brittleness of the samples: in particular, high-burnup fuel samples irradiated under normal conditions are hardly resistant to out-of-pile annealing at temperatures higher than the irradiation temperature. The prediction of the thermal conductivity at very high temperatures ($T > 1500$ K) is therefore not straightforward.

Purely theoretical studies are not found in the literature because of the complex structure and composition of irradiated fuel, and only semiempirical studies are possible at present: the mathematical formulation is chosen from theoretical considerations and the coefficients are fitted to experimental results. Theoretical studies exist only for single effects, such as the porosity and pore shape⁶ or the effect of the microstructure of MOX fuels.⁴⁸

References

1. Ronchi, C.; Sheindlin, M.; Staicu, D.; Kinoshita, M. *J. Nucl. Mater.* **2004**, 327, 58.
2. Quintard, M.; Whitaker, S. *Chem. Eng. Sci.* **1993**, 48, 2537–2564.
3. Suzuki, M.; Saitou, H. *Light Water Reactor Fuel Analysis Code FEMAXI-6 (Ver. 1)*; Report JAEA-Data/Code 2005-003; Feb 2006.
4. Maxwell, J. C. *A Treatise on Electricity and Magnetism*, 3rd ed.; Dover: New York, 1954; pp 435–441.
5. Loeb, A. L. *J. Am. Ceram. Soc.* **1954**, 37, 96.
6. Bakker, K.; Konings, R. J. M. *Nucl. Technol.* **1996**, 115, 91–99.
7. Fink, J. K. *J. Nucl. Mater.* **2000**, 279, 1.
8. Lucuta, P. G.; Matzke, H. J.; verall, R. A. *J. Nucl. Mater.* **1994**, 217, 279–286.
9. Eucken, A. *Forsch. Gebiete Ingenieur* **1932**, B-3, 6–21.
10. Ambegaoker, Y. *Trans. Am. Nucl. Soc.* **1966**, 9, 488.
11. Leibfried, G.; Schlömann, E. *Nachr. Akad. Wiss. Göttingen. Math. Physik.* **1954**, KI 2-A, 71–93.
12. Kleykamp, H. *J. Nucl. Mater.* **1985**, 131, 221–246.
13. Abeles, B. *Phys. Rev.* **1963**, 131, 507.
14. Duriez, C.; Alessandri, J. P.; Gervais, T.; Philipponneau, Y. *J. Nucl. Mater.* **2000**, 277, 143.
15. Ishimoto, S.; Hirai, M.; Ito, K.; Korei, Y. *J. Nucl. Sci. Technol.* **1994**, 31, 796.
16. Fukushima, S.; Ohmichi, T.; Maeda, A.; Hanada, M. *J. Nucl. Mater.* **1983**, 116, 287–296.
17. Murti, P. S.; Mathews, C. K. *High Temp. High Press.* **1990**, 22, 379–390.
18. Syros, C.; Sakellariadis, J.; Ronchi, C. *J. Nucl. Mater.* **1989**, 168, 65–69.
19. Martin, D. G. *J. Nucl. Mater.* **1982**, 110, 73–94.
20. Une, K.; et al. *J. Nucl. Sci. Technol.* **1991**, 28, 409.
21. Matzke, H. J. *J. Nucl. Mater.* **1994**, 208, 18.
22. Spino, J.; Peerani, P. *J. Nucl. Mater.* **2008**, 375, 8–25.
23. Sonoda, T.; Kameyama, T.; Sasahara, A.; et al. Clarification of rim structure effects on properties and behaviour of LWR UO₂ fuels and gadolinia doped fuels. In *Proceedings of the 2007 International LWR Fuel*

- Performance Meeting, San Francisco, CA, Sept 30–Oct 3, 2007; Paper 1026.
24. Fujii, H.; Teshima, H.; Kanasugi, K.; Sendo, T. *J. Nucl. Sci. Technol.* **2006**, 43, 998.
 25. Cozzo, C.; Staicu, D.; Pagliosa, G.; Papaioannou, D.; *et al.* *J. Nucl. Mater.* **2010**, 400, 213–217.
 26. Caillot, L.; Noirot, J.; Pontillon, Y.; Valin, S. TANOXOS: An analytical irradiation program aiming at understanding the behaviour of various doped UO₂ fuels. In *Proceedings of the 2006 International LWR Fuel Performance Meeting*, Salamanca, Spain, Oct 22–26, 2006.
 27. Staicu, D.; Cozzo, C.; Papaioannou, D.; Konings, R. J. M.; Walker, C. T. Thermal conductivity of fresh and irradiated MOX fuel: Influence of microstructure. In *Proceedings of Top Fuel 2009*, Paris, France, Sept 6–10, 2009; Paper 2107.
 28. Staicu, D.; Baron, D. Discussion about the main parameters affecting the thermal conductivity of LWR UO₂ and MOX fuels. In *Proceedings of the International meeting on LWR Fuel Performance*, Orlando, FL, Sept 26–29, 2010.
 29. Brandt, R.; Neuer, G. *J. Non-Equilib. Thermodyn.* **1976**, 1, 3.
 30. Spino, J.; Vennix, K.; Coquerelle, M. *J. Nucl. Mater.* **1996**, 231, 179–190.
 31. Walker, C. T. *J. Nucl. Mater.* **1999**, 275, 56–62.
 32. Baron, D. Fuel thermal conductivity: A review of the modeling available for UO₂, (U,Gd)O₂ and MOX fuel. In *Proceedings of OECD/NEA Seminar on Thermal Performance of High Burn-up LWR Fuel*, Cadarache, France, Mar 1998; p 129.
 33. Verall, R. A.; Lucuta, P. G. *J. Nucl. Mater.* **1996**, 228, 251.
 34. Matsui, T.; Arita, Y.; Naito, K. *J. Nucl. Mater.* **1992**, 188, 205.
 35. Takahashi, Y.; Asou, M. *J. Nucl. Mater.* **1993**, 201, 108.
 36. Gomme, R. A.; Carrol, J. C.; Shaw, T. L. *High Temp. High Press.* **1998**, 30, 135–140.
 37. Yagnik, S.; Turnbull, J. A. Specific heat and density of high burnup fuel. In *Proceedings of the 2006 International LWR Fuel Performance Meeting*, Salamanca, Spain, Oct 22–26, 2006.
 38. Staicu, D.; Wiss, T.; Rondinella, V. V.; Hiernaut, J. P.; Konings, R. J. M.; Ronchi, C. *J. Nucl. Mater.* **2010**, 397, 8–18.
 39. Lucuta, P. G.; Matzke, H.; Hastings, I. J. *J. Nucl. Mater.* **1996**, 232, 166.
 40. Kang, K. H.; Moon, H. S.; Song, K. C.; Yang, M. S.; Lee, S. H.; Kim, S. W. *Int. J. Thermophys.* **2007**, 28, 1595–1606.
 41. Hartlib, S. M.; Hough, A.; Waite, M. P.; Hall, A. R. Hanoell Report AERE-R 7325; 1973.
 42. Philipponneau, Y. *J. Nucl. Mater.* **1992**, 188, 194–197.
 43. Lanning, D. D.; Beyer, C. E.; Painter, C. L. FRAPCON-3: Modifications to Fuel Rod Material Properties and Performance Models for High Burn-up Application; NUREG/CR-6534; 1997.
 44. Lanning, D. D.; Beyer, C. E.; Geelhood, K. J. Report NUREG/CR-6534; PNNL-11513. 2005; Vol. 4.
 45. Wiesenack, W. Assessment of UO₂ conductivity degradation based on in-pile temperature data. In *Proceedings of ANS International Meeting on LWR Fuel Performance*, Portland, OR, 1997; p 507.
 46. Lee, B. H.; Koo, Y. H.; Sohn, D. S. *J. Nucl. Sci. Technol.* **2001**, 38, 45–52.
 47. Kampf, H.; Karsten, G. *J. Nucl. Technol.* **1970**, 9, 228.
 48. Wiesenack, W.; Lee, B. H.; Sohn, D. S. *Nucl. Eng. Technol.* **2005**, 37, 317–326.
 49. Bernard, L. C.; Jacoud, J. L.; Vesco, P. *J. Nucl. Mater.* **2002**, 302, 125–134.
 50. Hirai, M.; Amaya, M.; Wakashima, Y.; *et al.* Thermal diffusivity measurements of irradiated UO₂ pellets. In *IAEA TCM on Advances in Pellet Technology for Improved Performance at High Burn-up*, Tokyo, Japan, Oct 26–Nov 1, 1996; IAEA-TECDOC-1036.
 51. Sheindlin, M.; Halton, D.; Musella, M.; Ronchi, C. *Rev. Scient. Instrum.* **1998**, 69, 1426.
 52. Beyer, C. E.; Lanning, D. D. Review of fuel thermal conductivity data and models. In *Proceedings of the OECD/NEA Seminar on Thermal Performance of High Burn-up LWR Fuel*, Cadarache, France, Mar 1998.
 53. Carrol, J.; Gomme, R.; Leech, N. A. Thermal diffusivity measurements on unirradiated archive fuel, and fuel irradiated in the Halden IFA-558 experiment. In *Enlarged Halden Programme Meeting*, Bolkeshjo, Norway, Oct 30–Nov 4, 1994.
 54. Yamamoto, K.; Hirokawa, T.; Yoshikawa, K.; Morozumi, K.; Nomura, S. *J. Nucl. Mater.* **1993**, 204, 85–92.
 55. Ohira, K.; Itagaki, N. Thermal conductivity measurements of high burnup UO₂ pellet and a benchmark calculation of fuel center temperature. In *Proceedings of the ANS International Meeting on LWR Fuel Performance*, Portland, OR, Mar 2–6, 1997; p. 541.
 56. Yagnik, S. Thermal conductivity recovery phenomenon in irradiated UO₂ and (U,Gd)O₂. In *Proceedings of the ANS Topical Meeting on LWR Fuel Performance*, Park City, UT, Apr 10–13, 2000.
 57. Nakamura, J. Thermal diffusivity of high burn-up UO₂ pellet irradiated at HBWR. In *Thermal Performance of High Burn-up LWR Fuel*, Cadarache, France, OECD, Mar 3–6, 1998.
 58. Minato, K.; Shiratori, T.; Serizawa, H.; *et al.* *J. Nucl. Mater.* **2001**, 288, 57–65.
 59. Amaya, M.; Hirai, M.; Sakurai, H.; *et al.* *J. Nucl. Mater.* **2002**, 300, 57.
 60. Kinoshita, M.; Sonoda, T.; Kitajima, S.; *et al.* High Burnup Rim Project (III): Properties of rim-structured fuel. In *Proceedings of the 2004 ANS International Meeting on LWR Fuel Performance*, Orlando, FL, 2004; p 207.
 61. Walker, C. T.; Staicu, D.; Sheindlin, M.; Papaioannou, D.; Goll, W.; Sontheimer, F. *J. Nucl. Mater.* **2006**, 350, 19–39.
 62. Staicu, D.; Cozzo, C.; Pagliosa, G.; Papaioannou, D.; Bremier, S.; *et al.* *J. Nucl. Mater.* **2011**, 412, 129–137.
 63. Kinoshita, M.; Sonoda, T.; Kitajima, S.; *et al.* High Burnup Rim Project (II): Irradiation and examination to investigate rim-structured fuel. In *Proceedings of the ANS Topical Meeting on LWR Fuel Performance*, Park City, UT, Apr 9–13, 2000.
 64. Massih, A. R.; Persson, S.; Weiss, Z. *J. Nucl. Mater.* **1992**, 188, 323–330.
 65. Yagnik, S.; Rashid, Y.; Dunham, R.; Montgomery, R. In *Fuel Analysis and Licensing Code: FALCON MOD01; Volume 1: Theoretical and Numerical Bases*; EPRI: Palo Alto, CA, 2004; 1011307.

2.18 Radiation Effects in UO_2

T. Wiss

European Commission, Joint Research Centre, Institute for Transuranium Elements, Karlsruhe, Germany

© 2012 Elsevier Ltd. All rights reserved.

2.18.1	Introductory Remarks	465
2.18.2	The Slowing Down of Energetic Projectiles in UO_2	466
2.18.2.1	Main Processes	466
2.18.2.1.1	Nuclear energy losses	466
2.18.2.1.2	Electronic energy losses	467
2.18.2.2	Main Damage Sources	468
2.18.2.2.1	Energy loss and displacements produced by neutrons	468
2.18.2.2.2	Energy loss and displacements produced by (β , γ)-decays	468
2.18.2.2.3	Energy loss and displacements produced by α -decays	469
2.18.2.2.4	Impact of fission fragments	469
2.18.2.3	Range of Different Projectiles in UO_2	471
2.18.3	Basic Effects of Radiation Damage	471
2.18.3.1	Point Defects Formation	472
2.18.3.2	Modeling of Point Defects	472
2.18.3.3	Extended Defects	473
2.18.3.3.1	Ionic configurations of dislocations in UO_2	473
2.18.3.3.2	Prismatic loops	474
2.18.3.3.3	Void nucleation and growth	474
2.18.4	Radiation Effects in UO_2 Fuels	475
2.18.4.1	Change in Bulk Physical Properties	476
2.18.4.2	The High Burnup Structure (HBS)	477
2.18.5	Conclusions	479
References		479

Abbreviations

FBR	Fast breeder reactor
FPS	Fission products
HFP	Heavy fission product
LFP	Light fission product
LWR	Light water reactor
pka	Primary knock-on atom
SEM	Scanning electron microscope
SRIM	Stopping and range of ions in matter
TEM	Transmission electron microscope

2.18.1 Introductory Remarks

The macroscopic, observable, and often technologically crucial results of exposure of solids to energetic particles are collectively known as *radiation effects*. The primary microscopic events that precede the appearance of gross changes in the solid are called *radiation damage*. This branch of the physics attempts

to predict not only the number and the configuration of the point defects (vacancies and interstitial atoms) produced by the bombarding particles but also their evolution toward extended defects resulting from their coalescence.

UO_2 is today's most commonly used fuel material in nuclear power reactors. Nuclear fuels have to operate safely for years under severe conditions of radiation damage. Heat production from the nuclear fuel which is used to generate electricity ensues mostly from the slowdown of the fission products (FPs), that is, high-energy heavy ions and also from their further radioactive decay, most frequently by γ - or β -decay. The heat dissipated in the lattice of the crystalline material constituting the conventional nuclear fuels is a primary effect from the energy losses of the fission fragments by nuclear or electronic interactions on the atoms constituting the fuel. As a direct consequence, there are also defects created along the path of the fission fragments leading to modification of the physical properties of the fuel.

In addition to the fission process, damage is also created by α -decay, particularly in the fuel containing strong α -emitters (minor actinides), and also from β - and γ -decay of the FPs.

In this chapter, basic processes on energy losses are given and stopping power and range of various ions/particles defined for the specific case of UO_2 . The radiation damage produced by the passage of these ions/particles is conceptually described. The impact of defect creation on the physicochemical properties of UO_2 is then described with particular emphasis on its use as nuclear fuel. Fuel operating conditions are taken into account in addition to concomitant effects of damage sources when discussing the overall behavior of UO_2 during irradiation and also during (long-term) storage (see **Chapter 1.03, Radiation-Induced Effects on Microstructure**).

Uranium dioxide has been extensively studied and an exhaustive list of publications related to the radiation effects is impossible. The reader is referred to more detailed publications covering UO_2 properties by Belle,¹ radiation damage processes in UO_2 by Lemaignan,² or processes of damage in nuclear fuel by Olander,³ for example.

The physical processes of radiation damage had started soon after the discovery of radioactivity by Henri Becquerel in 1896. There was very soon interest in how particles from radioactive decay were slowed down in matter. Marie Curie has stated, “les rayons alpha sont des projectiles susceptibles de perdre de leur vitesse en traversant la matière” (α rays might lose part of their speed while traveling through matter).⁴ J. Thomson, N. Bohr, and E. Rutherford⁵ were pioneers in studying the effect of particles interactions with matter. The development of ion accelerators allowed extensive studies on radiation damage in all types of materials. Linked to the use of the Monte Carlo code stopping and range of ions in matter (SRIM) for the estimation of energy loss, range, and damage, the description of the main processes of particles/ions interactions with matter is given.⁶ The investigation of irradiated fuel being more difficult, numerous studies were performed on ion-irradiated UO_2 in order to understand the basic mechanisms of damage evolution.

2.18.2 The Slowing Down of Energetic Projectiles in UO_2

In the context of physical processes occurring in nuclear fuels involving energy dissipation, all types

of radiations should be considered. When the conditions are met for a fission to occur, about 200-MeV energy is dissipated in the fuel lattice. Most of this high energy is carried by the FPs that cover the mass range from 75 to 160, that is, elements between Ga and Dy. The FPs fall into two groups: the light ones, typically Kr, with about 100 MeV energy, and the heavy ones, typically Ba, with about 70 MeV energy. Intense neutron fluxes, produced by the fission reactions themselves, with energies ranging from eV to MeV are necessary to sustain the controlled nuclear chain reaction. An intense β -, γ -radiation field is also present because most FPs are radioactive with different decay energies and very different half-lives. Additionally, α -decay occurs in the original actinides, and even more so, in the case of large amounts of ‘minor actinides,’ for example, Np, Am, and Cm that are formed by successive neutron capture during the operation of the fuel. The α -decay has to be accounted for not only during reactor irradiation (at elevated temperature), but also during storage before and after reactor irradiation, that is, under conditions where thermally activated damage recovery is largely or fully absent.

In terms of energy releases, two major processes have to be considered, that is, inelastic collisions and ballistic (elastic) collisions depending on the type of projectile and its characteristics such as energy and mass. In given conditions, both processes can occur simultaneously in different proportions. The next paragraphs summarize these aspects with particular emphasis on the UO_2 nuclear fuel.

2.18.2.1 Main Processes

Energetic charged particles interact independently with the nuclei and the electrons in a solid. Basically, the energy loss of a charge particle can occur by four processes:

- Inelastic collisions with an electron (main process of energy loss producing excitation and ionization).
- Inelastic collisions with a nucleus (Bremsstrahlung and coulombic excitation).
- Elastic collisions with a nucleus (Rutherford diffusion).
- Elastic collisions with an electron.

2.18.2.1.1 Nuclear energy losses

When the energy of a given particle/ion is sufficiently low, elastic collisions with nuclei occur. The main process called Rutherford diffusion is the result of the transfer of kinetic energy from the

impinging particle/ion to a target atom. The resulting effects (described more extensively in the next paragraphs) are the displacements of atoms from their regular lattice site. If such a knock-on atom has gained sufficient kinetic energy from the collision, it can itself generate a new collision and hence displacement. The energy necessary to displace an atom from its lattice site is called displacement energy and its values in UO₂ are 20 and 40 eV for oxygen and uranium atoms, respectively.⁷ If the total energy from an incident particle is high enough, the succession of such collision displacement produces collision cascades. **Figure 1** shows such a collision cascade produced by a recoil nucleus during an α -decay (the energy is typically 100 keV). The cascade has been calculated with SRIM2003.⁶ The ‘size’ of the knock-on atoms represents the energy transferred during the collisions. The green spheres are uranium and the blue spheres oxygen. In a collision cascade, the typical energy transferred is 50 eV but some collisions with a large cross-section can produce energy transfer of a few kiloelectron volt, which explains the formation of subcascades. The resulting displaced atoms either recombine or leave permanent defects, which is discussed in another section.

2.18.2.1.2 Electronic energy losses

Electronic energy losses and their effects have been extensively described. Different concepts have

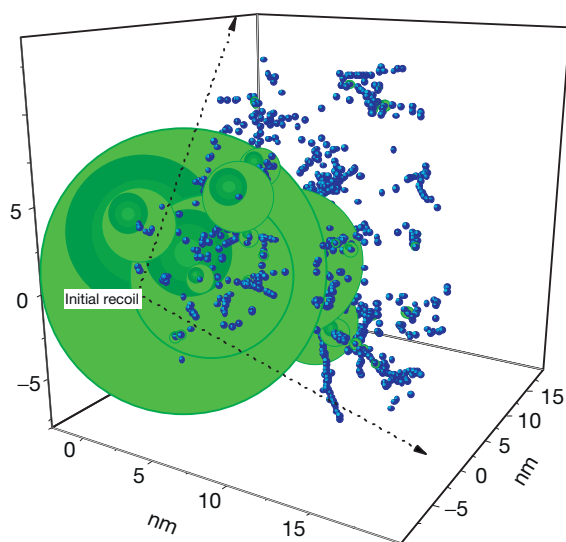


Figure 1 Collision cascade produced by a recoil nucleus during an α -decay (the energy is typically 100 keV). The cascade has been calculated with SRIM2003. With permission of the European communities. © European Atomic Energy Community.

been proposed to explain the formation of ion tracks in matter by the slowing down of swift heavy ions in the electronic stopping power regime. The ‘ionic spike’ model for insulators of Fleischer *et al.*⁸ assumes a high ionization rate of the lattice-atoms surrounding the path of the incoming ion, which leads to a local explosion due to high Coulomb repulsions. However, it has been shown that the electronic stopping power threshold deduced from the etching of several insulators cannot be scaled by the parameters governing this model, but can rather be related to the thermal conductivity of the material. This leads many authors to reconsider the thermal-spike model. The basic assumption in the thermal-spike model originally proposed by Seitz and Koehler⁹ is that around the trajectory of the high-energy ion a high-temperature region is formed in the material. The maximum temperature reached in a cylinder around the ion trajectory may surpass the melting point T_m of the material, as for example, in UO₂ (with $T_m = 3150$ K). In a model revisited by Toulemonde *et al.*,¹⁰ thermodynamic parameters of UO₂ have been taken into account to calculate the radius of observed ion tracks in UO₂. This model takes into account that energetic ions transfer their energy in a first step to the target electrons and then to the lattice via electron–phonon interactions leading to a heating of the lattice. It is assumed that the effect of the electron–phonon coupling can be described by the parameter λ , the mean diffusion length of the energy deposited on the electrons.

This parameter is linked to the electron–phonon coupling constant, g , by the relation $\lambda^2 = D_e \tau_a$, where $\tau_a = C_e/g$ is the mean electron–phonon interaction time, C_e is the specific heat of the electrons ($D_e \sim 2 \text{ cm}^2 \text{ s}^{-1}$ and $C_e \sim 1 \text{ J cm}^{-3} \text{ K}^{-1}$), and D is the electron diffusivity. As suggested by Baranov *et al.*,¹¹ we shall consider these values of C_e and D_e to be constant as the hot electrons in the conduction band of an insulator will behave as in metals. Using different values of λ as parameter, the track radius was calculated as a function of (dE/dx) . For a value of $\lambda = 6 \text{ nm}$, **Figure 2** shows the calculated lattice temperature as a function of time and radial distance from the ion path for a U ion of 11.4 MeV u^{-1} in UO₂. The peak temperature of the spike increases to its maximum value within a very short time of 10^{-13} s and then it decreases and the spike broadens as a result of heat conduction.¹² A similar calculation for 173 MeV Xe ions with $(dE/dx) = 29.1 \text{ keV nm}^{-1}$ also shows a good correlation between measured and calculated track radii, demonstrating, at least for the few values of dE/dx studied here, that this model can

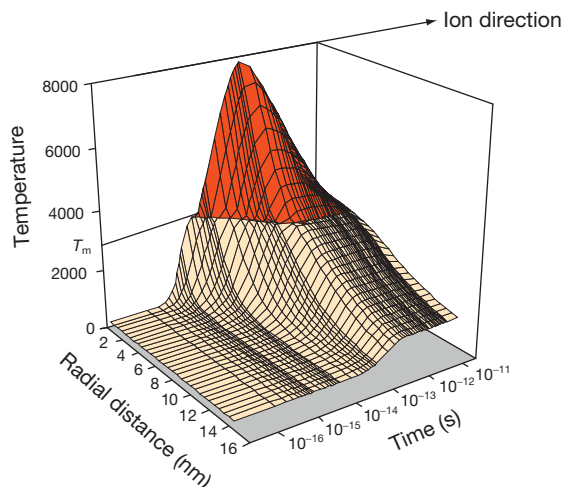


Figure 2 Calculated evolution of the UO₂ radial temperature distribution along a track in UO₂ as a function of time. The calculations are for 11.4 MeV u⁻¹ U ions in the first nm of the target, that is, $dE/dx = 60 \text{ keV nm}^{-1}$ with $\lambda = 6 \text{ nm}$ and a melting temperature of $T_f = 3150 \text{ K}$. Reproduced from Wiss, T.; *et al. Nucl. Instrum. Methods Phys. Res. B* **1997**, 122, 583.

be successfully applied to UO₂. The present results thus add further evidence to the existence of thermal-spike effects produced by fission fragments in UO₂. The previous evidence was as follows: (1) transmission electron microscopy (TEM) observations of a fission-spike induced phase change in U₄O₉ needles existing in UO_{2+x} (this transformation occurs at $T = 1150^\circ\text{C}$),¹³ (2) fission-enhanced diffusion of U in UO₂ can only be explained by thermal and pressure effects of fission spikes,¹⁴ and (3) the same is true for the observed fission gas resolution (destruction of fission gas bubbles) due to passing FPs.¹⁵

Recently, the formation of a dislocation cell structure in fluorite (CeO₂) due to electronic excitation and the motion of dislocations caused by overlapping energetic heavy ion tracks was presented in Sonoda *et al.*¹⁶ and more recently for UO₂ in Sonoda *et al.*¹⁷ The drastic changes of surface morphology and inner structure in UO₂ indicate that the overlapping of ion tracks will produce point defects, enhance the diffusion of point defects and dislocations, and form the subgrains at relatively low temperature. These findings have been used to describe the mechanism of the high-burnup structure (HBS) formation in nuclear fuel as summarized in Section 2.18.4.2.

In another model, the formation of ion track in UO₂ has been described by the propagation of a pressure wave created along the path of an energetic fission fragment under specific conditions of geometry.

It is shown that a large fraction of the fission fragment electronic losses is converted into strong shock waves whose passage in the solid is too fast for producing atomic displacements, but can release high energies by unloading on free surfaces. The consequent matter displacements have been shown to have important effects on the structural properties of the nuclear fuel. Surface tracks could be explained by the expelling of material when this pressure wave reaches the surface.¹⁸

2.18.2.2 Main Damage Sources

2.18.2.2.1 Energy loss and displacements produced by neutrons

In nuclear reactors, three types of neutrons are considered: the thermal neutrons with energy $E > 1 \text{ eV}$ (0.025 eV), the epithermal neutrons with $1 \text{ eV} < E < 10 \text{ keV}$, and the fast ones with $E > 10 \text{ keV}$. In the energy domain where neutrons from fission are emitted, only elastic collisions and capture are considered. The energy loss by the neutrons in the moderator is the *sine qua non* condition for a controlled fission reaction chain to occur while the remaining fast neutrons (not thermalized) produce damage in the fuel and on the structure materials.

A neutron of mass $m = 1$ and of energy E_n , while passing through a medium of mass M_1 , will occasionally collide (mean free path $\sim 1 \text{ cm}$) with a lattice atom, imparting to it an energy (depending on the impact parameters) up to a *maximum* energy given by

$$E_{\max} = \frac{4mM_1}{(m + M_1)^2} E_n \quad \text{or} \quad \sim \frac{4E_n}{M_1} \quad \text{for} \quad M_1 \gg m$$

The *maximum* pka (primary knock-on atom) energies for a neutron of energy $E_n = 1 \text{ MeV}$ are thus for UO₂ 17 keV for U, and 250 keV for O, but most interactions with neutrons will lead to a smaller energy transfer.

The *minimum* neutron energy to produce one displacement is given by $E_{\max} = E_d$, where E_d is the displacement energy (e.g., 20 eV for O and 40 eV for U in UO₂).⁷ Hence,

$$E_n^{\min} \sim 0.1 \text{ keV}$$

Thermal (low-energy) neutrons thus do not produce direct displacements.

2.18.2.2.2 Energy loss and displacements produced by (β , γ)-decays

For β -decays of the FPs in nuclear fuels, the energy distribution is a continuum with $E_{\beta\max}$ (typically $2.6 \text{ keV} < E < 10.4 \text{ MeV}$). The e^- and e^+ produce

ionization and excitation along their path and the nuclear scattering is very large. Rutherford scattering cross-section is proportional to $(M_1/m_0)^2$ and the cross-section ratio $\sigma_{e^-}/\sigma_{p^+} = 4 \times 10^6$.

In fact, σ can be extremely large and target e^- have to be considered.

Electrons can also produce isolated displaced atoms if their energy is high enough. The minimum energy, E_e^{\min} , to displace a lattice atom is given by

$$E_d = 2 \frac{m_0}{M} \frac{E_e^{\min}}{m_0 c^2} (E_n^{\min} + 2 m_0 c^2)$$

where m_0 is the electron mass, M the mass of the displaced atom, and c the velocity of light. β -decay thus causes very few, isolated point defects.

The emission of photons, γ , and also X-rays in nuclear fuel will be neglected in this section. Heating effects and ionization are anyhow produced but their consequences compared to the other damage sources during operation of nuclear fuel, for example, are negligible.

2.18.2.2.3 Energy loss and displacements produced by α -decays

The α -decay has two damaging sources:

- a He-ion (α -particle) of ~ 5.5 MeV, with mainly electronic stopping, producing about 200 displacements, most of them as largely isolated defects at the end of its range of some 10–20 μm
- a heavy recoil atom, for example, ^{237}Np in the decay of ^{241}Am which receives a recoil energy E due to conservation of momentum, $ME = mE_\alpha$, hence typically ~ 100 keV (or 91 keV in the decay of ^{241}Am).

These recoil atoms show predominantly nuclear stopping and produce a dense collision cascade with typically ~ 1500 displacements within a short distance of ~ 20 nm. Defect clustering can occur, stabilizing the damage.

In general, ions passing through matter lose energy via one of the two processes, either by direct collisions with the atoms of the matter (elastic collisions) or by dissipating their energy on the electrons (inelastic collisions), thereby giving rise to nuclear energy loss $(dE/dx)_n$ leading directly to displaced atoms, or ionizations (electronic energy loss $(dE/dx)_e$), respectively. Any given radiation source can exhibit these two types of energy loss. The case of α -decay in UO₂ is partially included in Figure 1, showing a displacement cascade produced by the recoil atom of the decay of ^{238}Pu , that is, ^{234}U . Figure 3 shows the energy loss of the α -particle which is predominantly

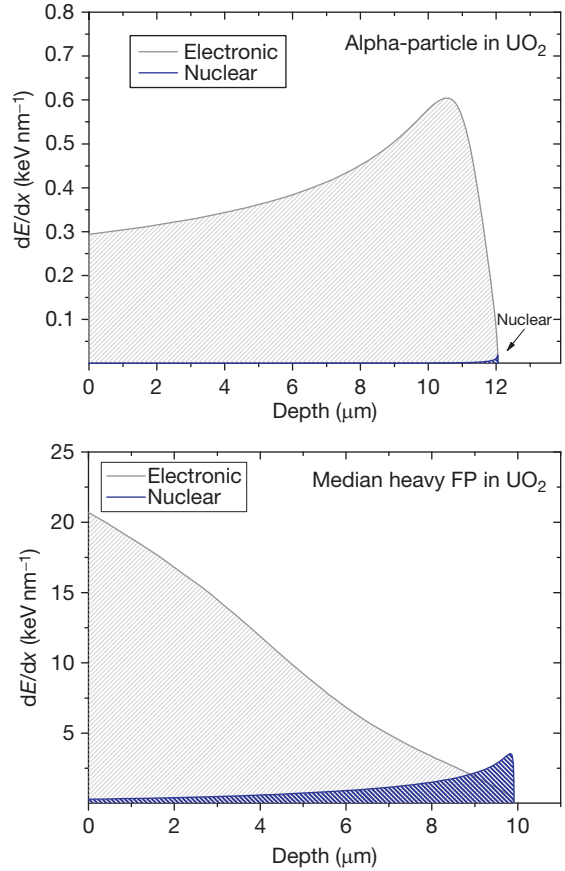


Figure 3 Electronic energy loss (dashed lines) and nuclear energy losses (black area) of a typical α -particle (upper part) and of a median fission product (lower part) in UO₂. © European Atomic Energy Community.

electronic by comparison with the recoil nucleus (see also Table 1).

The effects of α -damage in UO₂ have been studied for decades either by external irradiations with α -particles or heavy ions simulating the recoil nucleus¹⁹ or by doping UO₂ with strong α -emitters (e.g., ^{238}Pu).^{20–22} The formation of point defects and their evolution into extended defects, and also the consequences on the UO₂ lattice (e.g., lattice swelling) and on the modification of thermophysical properties have been assessed.²³ The studies on α -damage also at determining the long-term evolution of spent nuclear fuel during storage and more specifically what has to be expected from its integrity or behavior against corrosion on contact with water.^{24–26}

2.18.2.2.4 Impact of fission fragments

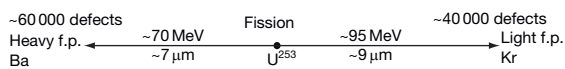
Fission produces two FPs (plus two to three neutrons). These FPs fall into two groups, the light

Table 1 Displacements induced in UO₂ by different damaging sources

	Energy (keV)	Range (μm)	Fraction of energy lost by elastic (nuclear)/inelastic collisions (electronic)	Number of defects formed (N)
Light fission product	$\sim 95\,000$	9	0.03/0.97	40 000
Heavy fission product	$\sim 70\,000$	7	0.06/0.94	60 000
α -particle	5500	15	0.01/0.99	200
Recoil atom	95	0.02	0.90/0.10	1500

Source: © European Atomic Energy Community.

ones (light fission products (LFPs), typically Mo or Kr with ~ 95 MeV energy) and the heavy ones (Heavy fission products (HFPs), typically I or Ba with ~ 70 MeV energy). Further typical values (for the case of UO₂) are given in **Table 1** and in the sketch below: range, number of defects produced, etc. The exact values depend on the substance used (e.g., displacement energy, E_d , atomic number, density, etc.). Because of the high-energy deposition rate, typically $20\text{--}30\text{ keV nm}^{-1}$, a locally (over-) heated track (fission spike or thermal spike) may be formed. Such fission tracks are visible in TEM in many materials. Most of the energy deposition is by electronic energy loss, in particular for the more energetic LFPs. This, in addition to causing local heating up to or above the melting point, can cause the formation of additional defects and/or rearrangement of existing defects. An extreme case is the destruction of preexisting fission gas bubbles by the passage of a fission spike, known to occur in the conventional nuclear fuel, UO₂.



The following is a short description of the sequence of events in the fission spike:

- Primary phase or ballistic phase – the passage of the fission fragment – is very short but it defines the initial size and shape of the spike. Most Frenkel defects are produced by secondary collision cascades. The deposited Coulomb energy is dissipated into local heating through electronic interactions with recoiling ions to produce a thermal spike.
- Second or quenching phase – recombination of vacancies and interstitials occurs when the spike comes to thermal equilibrium. An interstitial-rich outer zone and a vacancy-rich inner zone form. The hydrostatic pressure field originally created by the molten core of the spike – contributing to the separation of interstitials from the vacancies of

the Frenkel pairs formed in the primary phase – is replaced by compressive stresses in the outer zone and dilatational stresses in the core.

- Third or track annealing phase – more recombination occurs, and some vacancy clusters are stabilized by fission gases forming embryos for later bubbles.

The processes in these three phases are repeated many times all through the fuel volume in a homogeneous fuel. All of such a fuel is affected after a rather short time, the level of one displacement per atom (dpa) being typically reached within <1 day. The consequences are a significant fission-enhanced diffusion, fission-enhanced creep, resolution of fission gas from bubbles, etc.

Figure 3 shows the large difference in electronic energy loss, $(dE/dx)_e$, between the α -particles and the FPs. The energy loss curves show the electronic stopping only, that is, the ionization part, with high values of $18\text{--}22\text{ keV nm}^{-1}$ at the point of fission (full ion energy) for the case shown, that is, UO₂. The nuclear part, that is, the displacement damage part, peaks at the end of the range ($\sim 1\text{ keV nm}^{-1}$) and is very small (but still present) at the point of fission ($\sim 0.1\text{ keV nm}^{-1}$). The ratio of nuclear to electronic stopping is always low for those high energies, but it varies between 1:180 at the fission site and some 1:3 toward the end of the range, or even $<1:1$ at the very end.

The recoil atoms of the α -decay and the high defect density produced by their slowing down are not included in **Figure 3** below because of the large difference in range: about 1500 displacements are formed along a very short track of only $\sim 20\text{ nm}$, as shown in **Figure 1**.

Figure 4 shows the energy loss of a typical light fission fragment as a function of the energy of the fragment. In this figure, the energy displayed covers a range beyond fission energy to show that when increasing the energy above the energy corresponding to the coulombic barrier, the energy loss decreases.

This is to contribute to the fact that the fission fragment is fully ionized and that when increasing energy the velocity also increases, reducing the energy transfer for a given unit length. Two energy losses can indeed correspond to two different ion energies.

The energy losses in UO₂ for different projectiles can result in the formation of defects in different proportions as a function of their nature. The ballistic effects can be easily converted into a certain number of instantaneous defects formed (although instantaneous recombination are not easy to quantify). The electronic energy losses result generally in less quantifiable effects for a single projectile. The next paragraphs will give more insights on these phenomena.

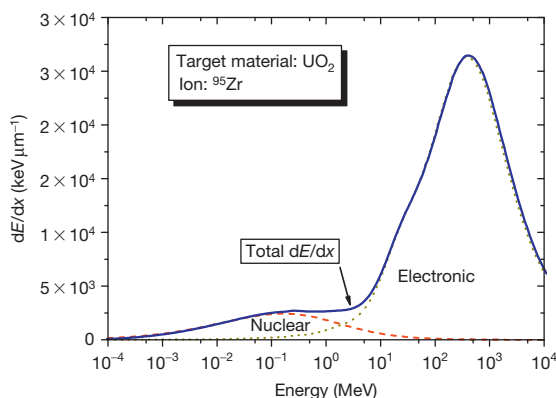


Figure 4 Energy loss of a typical light fission product as a function of its energy. © European Atomic Energy Community.

2.18.2.3 Range of Different Projectiles in UO₂

Because of numerous collisions with energy transfer to the target atoms, a given ion or particle will have a defined trajectory with a given length. From the energy losses, either elastic or inelastic, the range of a given particle can be determined. Whereas the high energetic particles/ions experience only a few scattering events (low cross-section for nuclear scattering) and hence almost do not deviate from their original direction, the low energetic ones might experience high angle scattering. This is shown in **Figure 5** for the case of FPs or α -particles having an almost straight path in a material in contrast to the α -recoil shown in **Figure 1**.

As a function of the mass of the particle/ion, it can be noticed that the range decreases with increasing mass and is directly correlated to the charge of the ions at a certain energy. When the ions are fully ionized at a certain energy, hence at a given speed, the energy loss decreases and the range proportionally increases again. This phenomenon can be observed in **Figure 6** for the heavier ions (Kr, Zr, Xe) showing an inflexion in their range above 100 MeV, corresponding to their nearly full ionization.

2.18.3 Basic Effects of Radiation Damage

During the slowing down of a particle/ion in a target, the history of the particle has to be followed by finding out the energy loss of the particle, its range, and the

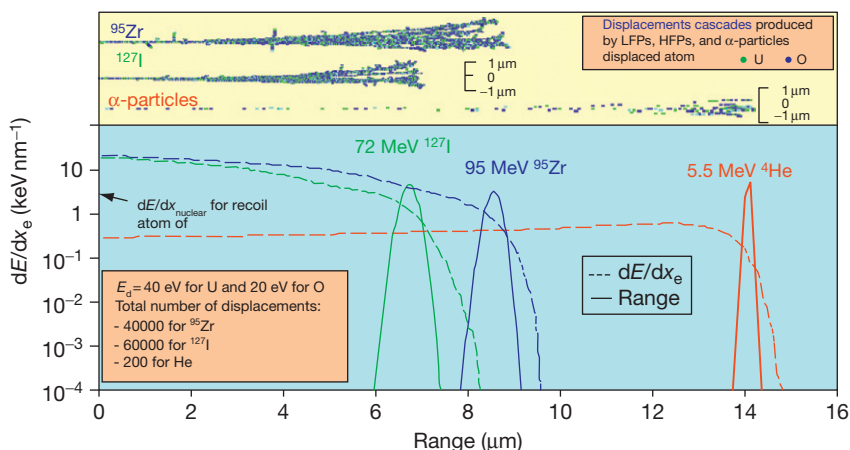


Figure 5 Range and energy loss (electronic) of different projectiles in UO₂. The upper inset shows the straggling and the cascades produced from several projectiles, all having a normal incidence relative to the surface. Color version of the original that can be found in Sickafus, K.; Kotomin, E. A.; Uberuaga, B., Eds. *Radiation Effects in Solids*; NATO Science series; Springer: Dordrecht, 2007; Vol. 235.

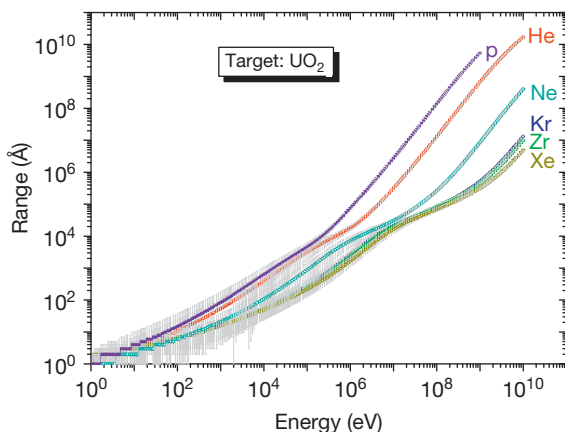


Figure 6 Range of different ions and protons (p) in UO_2 as function of their energies. © European Atomic Energy Community.

interactions with the media it is passing through. As interactions, one has to primarily consider the displacements, recombination, ionization, and excitations in order to assess the radiation damage buildup. Additionally, complexes can be formed between different kinds of point defects; for example, point defects can be arranged to give rise to line defects.

2.18.3.1 Point Defects Formation

Contrary to the perfect lattices, all real crystals contain defects differentiated according to their dimension. The defects in a crystal can be triggered by the different kinds of damage processes as described in the previous sections. The one-dimensional defect is called a point defect, implying that it involves only one atom surrounded by an otherwise perfect lattice. However, the presence of a point defect may affect the properties of its nearest neighbors and, by elastic or electric interactions, a sizable spherical region of the lattice around the defect. Two point defects are intrinsic to the material, meaning that they form spontaneously in the lattice without any external intervention. These two are the vacancy and the self-interstitial, shown schematically in **Figure 7** and referenced (d) and (c), respectively. The vacancy is simply an atom missing from a lattice site, which would be occupied in a perfect lattice.

The defects referenced (a) and (h) in **Figure 7** show the two basic mechanisms by which a foreign or impurity atom exists in the crystal lattice of a host element. Large impurity atoms, usually of the same category as the host atoms (e.g., Pu in UO_2), replace the host atoms on regular lattice positions. These are called substitutional impurities. The structure of

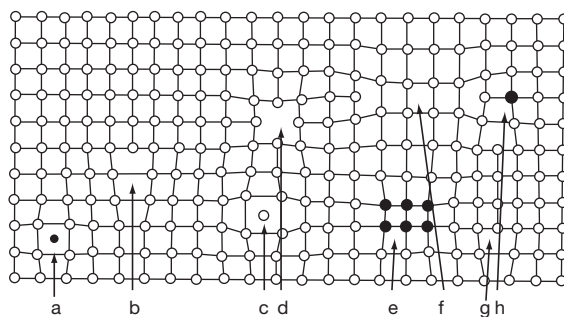


Figure 7 Various crystal lattice defects: (a) interstitial impurity atom, (b) edge dislocation, (c) self-interstitial atom, (d) vacancy, (e) precipitate of impurity atoms, (f) vacancy-type dislocation loop, (g) interstitial-type dislocation loop, (h) substitutional impurity atom, an atom lodged in a position between normal lattice atoms; that is in an interstice. The qualification 'self' indicates that the interstitial atom is the same type as the normal lattice atoms. © European Atomic Energy Community.

the lattice is not disturbed; only the identities of the atoms occupying the lattice sites are different. Small atoms that are also chemically dissimilar from the host atoms occupy interstitial positions and do not appreciably distort the surrounding host crystal (e.g., He in UO_2). They are termed interstitial impurities.

Self-interstitials and vacancies occur naturally in ionic crystals as well as in elemental solids.

However, because in UO_2 the cations (U) and anions (O) carry electrical charges (+4 and -2 respectively) vacancy and interstitial formation are not independent processes. To create a vacancy on the anion sublattice by moving the anion to the surface, for example, would leave the surface negatively charged and the interior around the vacancy with a net positive charge. This violation of local electrical neutrality prevents such a process. Similar arguments apply to cation vacancies or self-interstitials of ionic type. In UO_2 , two anion vacancies need to be created for each cation vacancy, forming a Schottky trio. However, the dominant point defects in ideally pure stoichiometric UO_2 are anion Frenkel defects, O^{2-} vacancies and O^{2-} interstitials.²⁷

2.18.3.2 Modeling of Point Defects

Electronic structure calculations by *ab initio* techniques enable us to determine quantities inaccessible to experiments because of either the too-small length scale or the impossibility in isolating the contribution of a given factor to the studied physical properties (see **Chapter 1.08, *Ab Initio* Electronic Structure Calculations for Nuclear Materials**). In particular,

ab initio calculations allow the study of separately different types of point defects in a solid and to determine for each of them its stability (formation energy) or its influence on the crystal structure (atom relaxation around the defect, swelling of the crystal). Many works have recently contributed to assessing the energy associated with these different defects in UO_2 as well as in nonstoichiometric UO_{2+x} .^{28,29} The study of the primary damage state (e.g., point defects caused by an α -decay in UO_2) is essential to understand how the material ages. Molecular dynamics (MD) simulations have also been successfully applied to model this phenomenon in various materials used in nuclear science applications³⁰ (see **Chapter 1.09, Molecular Dynamics**). In a recent thesis,³¹ simulation techniques based on empirical potentials have been used, focusing in a first stage on pure uranium dioxide to describe the behavior of point defects and also the estimation of elastic and melting properties. It could be, for example, determined that simple defects such as interstitials occupy the large empty zone 4b in the unit cell. However, for positive deviation from stoichiometry, Willis determined that oxygen interstitials tend to cluster, which have a binding energy of about $1.7 \pm 0.6 \text{ eV}$.³² The structure that best fitted experimental neutron diffraction patterns is a 2:2:2 cluster, consisting of two interstitials and two oxygen atoms displaced from their regular lattice position, creating two additional interstitials and two vacancies. This is illustrated in

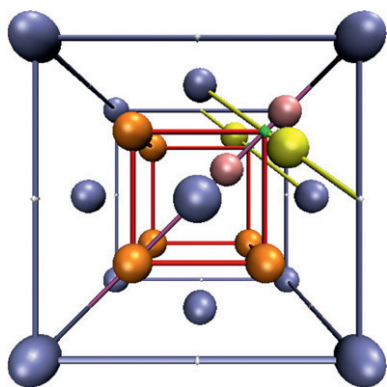


Figure 8 Structure of the Willis cluster. Both oxygen interstitials (in purple) occupy 4b sites corresponding to a displacement from the 4b site of $\sim 1.1^\circ \text{Å}$ in a $\langle 110 \rangle$ direction (purple lines). In addition, two oxygen atoms (in yellow) are displaced by $\sim 1.33^\circ \text{Å}$ from their regular lattice (green octahedrons) positions, in a $\langle 111 \rangle$ direction (yellow line), to 32f sites (reprinted from Govers, K. Atomic scale simulations of noble gases behavior in uranium dioxide. In *Faculté des sciences appliquées*; Université Libre de Bruxelles: Bruxelles, 2008).

Figure 8.³¹ Yakub *et al.*²⁹ have studied the formation and stability of different types of clusters in hyperstoichiometric UO_{2+x} , including Willis's 2:2:2 interstitial dimers as well as cuboctahedral tetra- and pentamers under static and dynamic conditions based on a partly ionic model. A 'free hopping approximation' for small polarons has been proposed and implemented in a molecular dynamic simulation computer code.²⁹ Lattice parameter and other equilibrium properties of UO_{2+x} were calculated and compared with existing experimental data in a wide range of temperature and stoichiometry.²⁹

The modeling of radiation damage has also been used to predict the evolution of some microstructural aspects like the evolution of gas (helium) bubbles exposed to dense cascades from the α -recoil nucleus³³ and also the mobility of the defects has been used to model the diffusion of gas.³⁴

The formation of point defects and their study by modeling via *ab initio* and MD consider the oxygen behavior which is the very fast diffusing specie in UO_2 but nevertheless has impact on many of the macroscopic properties as it has to be accounted that it affects notably the transport properties.

2.18.3.3 Extended Defects

Once point defects start diffusing within the solid, they can interact with each other and form extended defects (linear, planar, or three-dimensional defects) so as to reduce the total energy. The following extended defects must be considered:

- Dislocation-type defects: In general, dislocation-type defects are loops which can exhibit edge, screw, and mixed dislocation character within a single loop, or can be prismatic (interstitial- or vacancy-type dislocation loop). The latter is a direct consequence of production and diffusion of interstitials and vacancies of the U and O sublattices. The former is a plastic deformation under external loading and is not a direct product of the fission process.
- Voids: These are formed by vacancies absorption and are more stable than vacancy loops.

2.18.3.3.1 Ionic configurations of dislocations in UO_2

The geometry of slip in a single crystal is fully defined by the slip system, which designates the slip plane (reticular plane in which surface atomic density is maximum) and the slip direction (reticular direction in which linear atomic density is maximum).

The dislocation is generally a mixture of screw and edge components in the shape of a loop. However, important deformation properties, such as the creep rate and the yield stress (or usually called the critical resolved shear stress), are controlled primarily by the edge components of the dislocation. Consequently, the nature of edge dislocations in UO_2 has received the most attention in the literature. In 1960, Rapperport and Huntress³⁵ examined the macroscopic slip of UO_2 monocrystals deformed in compression between 700 and 1900 °C. The most active slip system, highlighted by the analysis of slip trace and the Laue stereotypes, is $\{100\}\langle 110\rangle$. The planes $\{110\}$ and $\{111\}$ become active when the temperature increases, the slip direction remaining $\langle 110\rangle$. The planes $\{111\}$ are often activated by cross-slip. In 1963, Ashbee³⁶ confirmed these results, by means of TEM observations, and defined the Burgers vector as $a/2 \langle 110\rangle$. The distance $a/2 \langle 110\rangle$ effectively corresponds to the shortest period of the fluorite network. Primary slip planes in UO_2 are not the densest ones, that is, $\{111\}$ planes as classically observed in fcc metals. The most important slip system in UO_2 is the one which rather confers on the crystal a minimum electrostatic energy rather than a minimum elastic energy. The easy slip along $\{100\}\langle 110\rangle$ tends to minimize the intense repulsive force between cations. The anions then screen during such translations. The ionic configurations of dislocations in UO_2 have been investigated by Evans and Pratt³⁷ in order to identify the peculiarities that may influence the deformation characteristics of this material.

Ashbee³⁶ has observed dissociated dislocations in partial dislocations. However, these stacking faults might have been identified in nonstoichiometric UO_2 because of the TEM observation conditions, which induced a local reduction of the oxide. These excess uranium ions could stabilize stacking faults according to calculations based on an ionic model.³⁸ The same calculations showed that the stacking-fault energy was much too high to consider the dissociation of dislocations into partial dislocations in UO_2 .

2.18.3.3.2 Prismatic loops

Another type of loop is called a prismatic loop. This type is fundamentally different from the shear loop; the only features the two types have in common are their circular shape and their ability to expand or contract radially. Figure 9 shows a TEM micrograph of a UO_2 sample having cumulated 10^{-5} dpa α -damage. Prismatic dislocation loops are clearly visible in this sample. A study of the function of the α -damage has shown that the loops grow in size and

concentration.^{23,39} Corresponding to the two types of point defects, vacancies, and interstitials, there are two types of prismatic loops. The interstitial loop consists of a disk-shaped layer of atoms formed by assembling free interstitial atoms from the bulk solid. The atom-layer agglomeration is thermodynamically more stable than the same number of atoms dispersed in the lattice as self-interstitials. Interstitial loops form only in solids bombarded by high-energy radiation (e.g., fission fragments) because only this environment produces sufficient quantities of self-interstitials. In common with the interstitial loop, the periphery of the vacancy loop is a circular edge dislocation with a Burgers vector perpendicular to the plane of the loop. However, the Burgers vectors of the two types are of opposite sign. By definition, an interstitial loop grows/shrinks by absorption of interstitials/vacancies, whereas the vacancy loop grows/shrinks by absorption of vacancies/interstitials. However, vacancy loops shrink by self-interstitial atom absorption at all temperatures and shrink by vacancy emission at high temperatures. This means that vacancy loops are intrinsically unstable at all temperatures. Rather than forming loops in the shape of a disc, vacancy condensation results in voids, which are in turn a perfect trap for gas atoms (see next paragraph and Figure 9).

2.18.3.3.3 Void nucleation and growth

Because of preferential absorption of self-interstitials at dislocations, a slight excess of vacancies is left in the solid to first nucleate and then grow voids (a void does not contain gas). Voids, as well as prismatic loops, can nucleate homogeneously or heterogeneously. Homogeneous nucleation refers to the buildup of small clusters by chance encounters of individual point defects executing random walks in

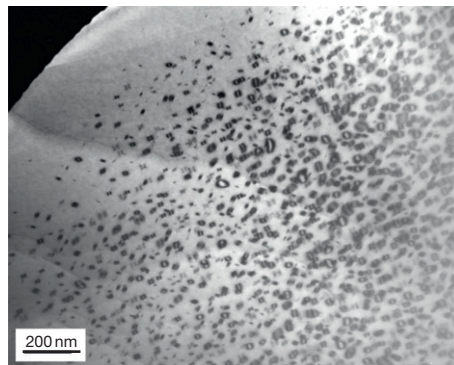


Figure 9 Transmission electron micrograph of a 10 wt% ^{238}Pu -doped UO_2 (2.4 dpa) annealed at 1100 K.
© European Atomic Energy Community.

the solid. The stability of these clusters relative to the individual point defects of which they are composed (i.e., voids contain vacancies and perhaps gas atoms, whereas loops contain interstitials) is the driving force for nucleation.

None of the structural features of the solid is needed to cause agglomeration of the point defects. Heterogeneous nucleation refers to the appearance of voids on distinct structural features of the solid. These features can be preexisting gas bubbles, incoherent precipitate particles, or dislocations. The depleted zone created in the collision cascade can also act as heterogeneous nucleation sites for void formation. The latter is considered to be the most important nucleation mechanism in irradiated UO_2 fuels.

Nucleation and growth are often treated as sequential steps in the overall process of void formation. During the nucleation period, the number density of cavities increases with time, but the sizes remain small. During the growth period that follows, the number density stabilizes and the void size increases with time. The void is assumed to be spherical and its growth is controlled by diffusion of vacancies and interstitials from the bulk of the solid to the void surface. In most situations, gas atoms will stabilize the voids/cavities. **Figure 9** shows a TEM micrograph of a heavily α -damaged (U, Pu) O_2 sample where voids have formed by diffusion of vacancies and stabilized by the radiogenic helium. The pending interstitial loops formed as shown in **Figure 10** have been annealed.

2.18.4 Radiation Effects in UO_2 Fuels

Most electricity-producing nuclear power stations use uranium dioxide (UO_2) as fuel, enriched in

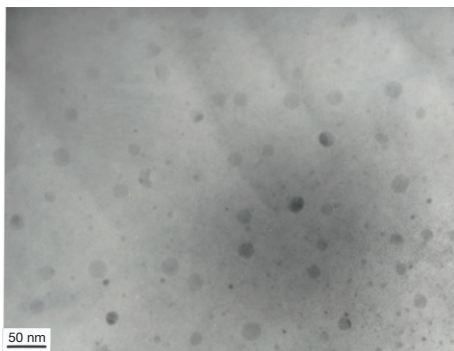


Figure 10 Transmission electron micrograph of 10 wt% ^{233}U -doped UO_2 showing the presence of prismatic loops resulting from the α -damage. © European Atomic Energy Community.

^{235}U between 5% and 7% typically, and some also use MOX (mixed oxide) fuel, that is, UO_2 with about 5% of PuO_2 replacing the UO_2 . The fuel consists of sintered pellets of about 1 cm in diameter. These pellets are used to produce long stacks that are sheathed in tubes (cladding) of a Zr alloy.

Uranium dioxide fuel is subjected to all the radiation and damaging sources for about 5 years, covering γ - and X-rays, neutrons, electrons, fission fragments, and α -decaying elements. During this period, FPs grow in and change both chemical and physical properties. Any treatment of damage effects has to allow for such changes that occur even in the absence of damage buildup. The most interesting damage effect in UO_2 fuel at high burnup (expressed in GWd tU^{-1} or in percent fissions of the heavy metal atoms) is polygonization, the formation of about 10^4 small submicrometer grains from each original UO_2 grain. Polygonization is the term used to describe the rearrangement of those dislocations formed in the earlier stage of irradiation that do not annihilate one another into walls of dislocations, forming low-energy ‘subboundaries’ and perfect but slightly misaligned subgrains.

A well-known consequence of accumulated radiation damage is damage-induced phase changes, most notably amorphization (or metamictization) of originally crystalline matter, or polygonization, also named grain subdivision – a process that transforms a typical grain of an originally well-crystallized ceramic into thousands of small grains in the submicron range. Polygonization occurs in some nuclear fuels, including UO_2 .

When discussing damage accumulated by fission, or to a lesser extent, by radioactive decay, one has to consider the simultaneous change in chemistry. Each fission, besides producing the above 100 000 displacements, also produces two fission products: new chemical elements between Ga and Dy, including volatile elements such as Br, I, Kr, Xe, Cs, etc., accumulating to often more than 10 at.% at the end of life of the nuclear fuels, or in α -decay, daughter atoms, for example, Np in the decay of Am and He atoms formed in addition to the displacements; the He atoms may precipitate into bubbles, thus causing the specimens to swell. Similarly, in β -decay, new elements are formed. For example, Cs, a high-abundance fission product, decays into Ba with another valence state and a different chemical behavior. Therefore, we deal with complex phenomena that explain why interest is still high in understanding damage effects and mechanisms in not only new but

also conventional nuclear fuels, despite the large amount of work devoted to this subject in the past five decades.

2.18.4.1 Change in Bulk Physical Properties

The effects caused by atomic displacements are rather complex and depend on the relative sink strengths of a given material for interstitials and vacancies and on the temperature. A majority of the Frenkel pairs recombine in a short time. The defects that survive migrate through the crystal lattice where they cluster to form extended defects like dislocation loops and dislocation networks or are absorbed in grain boundaries, gas bubbles, or precipitates, which act as sinks. An important effect of radiation damage is the volume increase of the crystal lattice, leading to macroscopic swelling of the fuel material. For example, at room temperature α -damage in UO_2 doped with ^{238}Pu leads to a distinct increase of the volume, saturating rapidly, when an equilibrium between formation and annealing of defects is attained (Figure 11).

In this case, the ingrowth or the change in the lattice parameter of UO_2 doped with ^{238}Pu is reflecting the evolution of radiation damage. Accumulation of radiation damage can also lead to damage-induced phase transformation, most notably amorphization (or metamictization) of originally crystalline matter. When discussing damage accumulated by fission, or to a lesser extent, by radioactive decay, one has to consider the simultaneous change in chemistry. Each

fission, besides producing the above-mentioned 100 000 displacements, also produces two FPs, often accumulating to more than 10 at.% at the end of life of the nuclear fuels. The FPs include gaseous elements like Kr and Xe, and volatile elements such as Br, I, Cs, etc. As most of the FPs decay by β -particle emission, new elements are formed. For example, Cs, a highly abundant FP, decays to Ba with another valence state and a different chemical behavior. Further, gaseous helium is formed by the α -decay of short-lived actinides that are formed, for example, ^{241}Am that decays to ^{237}Np . The α -decay results in displacements in the lattice and the He atoms may precipitate into bubbles, thus causing the fuel to swell. Thus, we deal with complex phenomena that explain why it is very important to understand damage effects and mechanisms, not only in new but also in conventional nuclear fuels, despite the large amount of work devoted to this subject in the past five decades. The understanding of the basic processes involved in the damage buildup could also help to predict the long term behavior of UO_2 (nuclear fuel) during storage (interim or long term).

UO_2 does not become amorphous under any damage source. Fission damage and the ingrowth of FPs can eventually cause polygonization, that is, both single crystals and sintered specimens are transformed into a material consisting of very small grains of about 0.1–0.3 mm grain size. In UO_2 fuel, about 10^{-4} subgrains are formed from each original UO_2 grain. Polygonization is the term used to describe the rearrangement of those dislocations formed in the earlier stage of irradiation that do not annihilate one another into walls of dislocations, forming low-energy ‘subboundaries’ and perfect but slightly misaligned subgrains. This phenomenon was already observed in early test irradiations and was called grain subdivision. It received renewed attention in the 1980s when power reactors increased the fuel burnup.

Between 130 and 1000 °C, the diffusion of U and Pu is completely athermal, that is, independent of temperature. The results have been explained by the formation of thermal spikes along the trajectory of the fission fragments in combination with a pressure gradient. Because of the high-energy deposition rate, a locally (over) heated track (fission spike or thermal spike) may be formed. Such fission tracks are seen in TEM in thin UO_2 foils and with the replica technique at UO_2 surfaces but not in TEM samples prepared from the bulk.^{12,13} This indicates that the threshold for the formation of observable tracks must be close to the energy loss value of FPs,

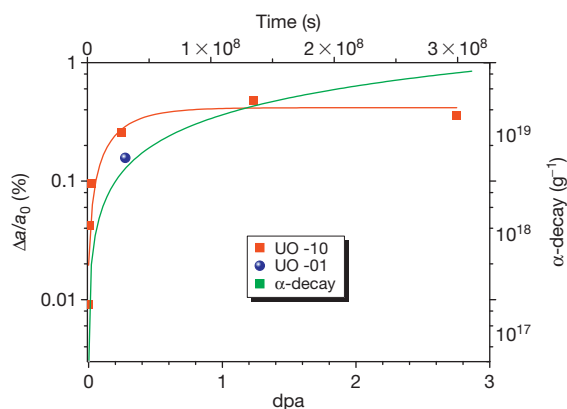


Figure 11 Lattice parameter evolution as function of accumulated α -damage for two UO_2 samples doped with 0.1 (UO-01) and 10 wt% of ^{238}Pu (UO-10), respectively. The green curve indicates the corresponding α -dose (right scale). © European Atomic Energy Community.

that is, 18–22 keV nm⁻¹. An extreme case of fission spikes interacting with the fuel matrix is the destruction of preexisting fission gas bubbles by a fission spike that is passing by. The phenomenon is called ‘resolution’ of fission gas and was known for about 40 years. It was explained by the above-mentioned hydrostatic pressure component¹⁵ of the thermoelastic stress field of the fission spike interacting with the bubbles. The pressure gradients also serve to explain the surprisingly high U and Pu diffusion coefficients. To decrease these gradients, the highly mobile uranium interstitials are pushed away from the spike axis, thus increasing the U diffusion to values higher than those calculated for atomic mixing and thermal-spike effects alone. Like diffusion, in-pile creep of UO₂ was shown to be athermal and fission enhanced below 1273 K as well.⁴⁰

Mechanical properties can also vary as a function of damage cumulating in UO₂. **Figure 12** shows the evolution of the Vickers hardness as function of accumulated damage for the two α -doped compounds. The two materials accumulate decay damage at a rate differing by two orders of magnitude. The combined data for the two materials span over six orders of magnitudes of damage, providing insight on different stages of radiation damage accumulation. The initial trend for the UO₂ doped with 0.1 wt% of ²³⁸Pu shows essentially no clear changes of the hardness. A relatively sharp transition occurs around 10⁻² dpa, indicating that this is a threshold level at which the accumulation of microscopic defects produces evident macroscopic changes. This level of damage corresponds to spent fuel at discharge from the reactor or during the first months/years of cooling.

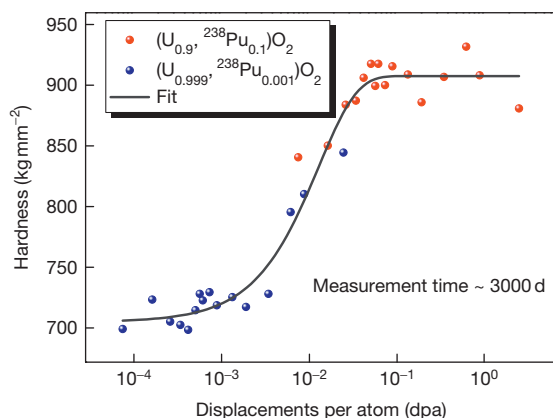


Figure 12 Hardness evolution for two α -doped materials expressed as a function of accumulated damage (dpa).

© European Atomic Energy Community.

In spite of the different decay rates, the evolution of the hardness shows an essentially continuous evolution independently from the time necessary to reach a given dpa level. This important finding is confirmed by other types of analysis: for instance, microstructure analysis by TEM revealed that the damage accumulation pattern up to a few dpa is characterized by the production of dislocation loops as shown in **Figure 10**.

2.18.4.2 The High Burnup Structure (HBS)

In the late 1950s, it was observed that a strong capture by ²³⁸U of neutrons in the resonance range occurs at the periphery of the nuclear fuel leading to the production of ²³⁹Np and therefore of ²³⁹Pu.⁴¹ The consequence of the increase of the fissile density is a local increase of the burnup. Typically, the area concerned by this phenomenon is the annular outer part of the fuel pellet of about 200 nm thickness, representing about 8% of the fuel volume (with average 60 MWd kgU⁻¹ burnup). The local enrichment then decreases almost exponentially toward the center of the fuel. The original grains with size of around 10 μ m in typical light water reactor (LWR) fuels tend to subdivide into thousands of smaller grains with sizes of about 100–200 nm. This restructuring of the grains is associated with the formation of a local porosity that can reach values above 20%. The coarsened micrometric size porosity contains almost all of the fission gases. For power reactors, this phenomenon has been observed in the 1980s. Two structures, rounded grains at open surfaces and (bulk) polyhedral grains, have been identified in the high-burnup region of the fuel.⁴² The formation of smaller grains at open surfaces (e.g., pores) shows a fractal appearance with the smaller grains having a size of <10 nm as can be seen in **Figure 13**.

The surface reorganization has been observed by scanning electron microscopy^{43,44} and is accompanied by a bulk restructuring that is also observable by scanning electron microscopy and is mostly investigated by TEM.⁴⁵ The fuel transforms by a subdivision process in polyhedral grains surrounding pores. The newly formed tiny grains are often found to be slightly disoriented (a few degrees).⁴⁶ A recent observation of a memory effect of the original grains structure supports this assumption.⁴⁷ **Figure 14** shows a TEM micrograph of a high-burnup UO₂ fuel sample (100 GWd t⁻¹) showing the formation of the HBS and the reminiscence of the original grain boundaries. It was also observed that the HBS develops randomly inside grains and not at grain boundaries.

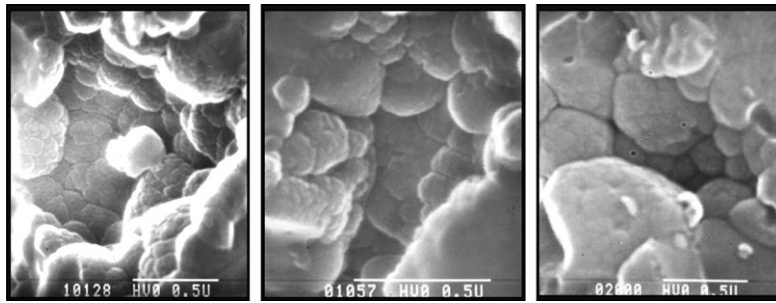


Figure 13 Secondary electron image of a restructured UO_2 fuel showing the occurrence of rounded-shaped subgrains inside pores. © European Atomic Energy Community.

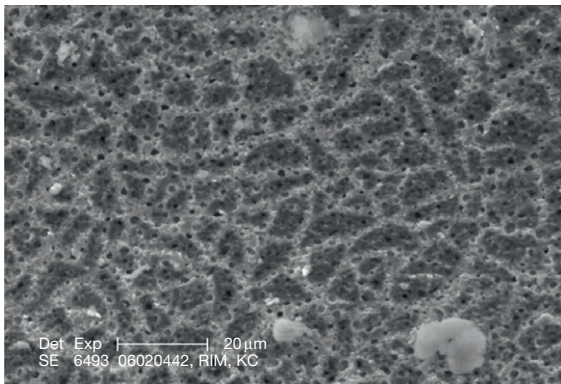


Figure 14 Transmission electron micrograph of a high-burnup UO_2 fuel sample (100 GWd t^{-1}) showing the formation of the high-burnup structure and the reminiscence of the original grain boundaries. © European Atomic Energy Community.

The exact mechanisms responsible for the formation of the HBS are still under investigation. The formation of defects in combination with the presence of the fission gases appears to play a key role in the process and several scenarios have been suggested.⁴⁸

Nogita and Une^{49,50} proposed a formation mechanism of the HBS that is directly related to the accumulation of radiation damage. Tangled dislocation networks are formed by the inhomogeneous accumulation of dislocations after the development of interstitial-type dislocation loops. At the same time, intragranular FPs gas bubbles are formed by the clustering of vacancies and of fission gases Xe and Kr. With increasing burnup, tangled dislocations are organized into subdivided grains with high angle boundaries.⁴⁹ Then, some of them are recrystallized, sweeping out small intragranular bubbles. In this approach, recrystallization refers to a series of steps, that is, formation of subgrains, growth of the

subgrains into recrystallization nuclei, and growth of the recrystallized grains. In line with this, Spino *et al.*⁵¹ have tentatively attributed the formation of the HBS to the local start of recrystallization around pores (characteristic of the HBS). This interpretation has been opposed by the results of the High Burnup Rim Project (HBRP) in which a set of irradiated UO_2 disks of different burnup and temperature were analyzed extensively.⁵² On the basis of the results of this project Matzke⁵³ concluded that (1) there is no instantaneous recrystallization due to the accumulation of gas and radiation damage, (2) an increased temperature is needed for recrystallization, and (3) if occurring, recrystallization does not necessarily sweep gases. The latter three facts disagree with the formation mechanisms proposed by Nogita and Une.

TEM observations of HBRP samples⁵⁴ showed that in the HBS the initial grains are subdivided and not recrystallized. Figure 15 shows a TEM image of a restructured UO_2 fuel sample. The subdivided grains with sizes as small as 50 nm for some of them are clearly visible. The subdivision process proceeds further with increasing burnup as recently observed by the scanning electron microscope (SEM) examination of a very high-burnup specimen.⁴⁷ Sonoda *et al.*⁵⁴ thus concluded that the restructuring is initiated by the accumulation and mutual interaction of (1) radiation damage including point defects and dislocations, (2) FPs including gas bubbles and metal particles, (3) stored energy caused by electronic excitation and nuclear collision which may cause radiation-enhanced diffusion of interstitials and vacancies, and (4) the growth of dislocation loops.

In spite of the different views on its formation mechanism, there is now agreement that the HBS has a high fission gas retention capacity. In particular, the HBS does not evolve toward an open system of interconnected channels, even when porosity reaches very high values (e.g., 35% in a fast breeder reactor

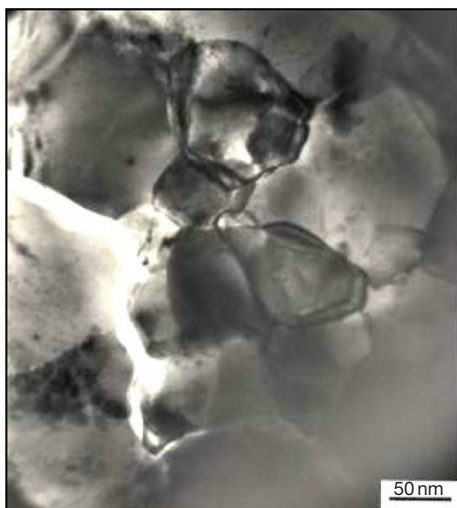


Figure 15 Transmission electron microscopy bright field micrograph showing the high-burnup structure in a fuel sample with 96 MWd kg^{-1} irradiated at 530°C . © European Atomic Energy Community.

(FBR) fuel, 50% in a PWR MOX agglomerate).⁵⁵ As a technological spin-off of this result, the HBS could be considered to effectively retain the fission gases occluded in pores up to relatively high local burnups ($>300 \text{ MWd kgHM}^{-1}$) because only at these burnup values porosity fractions >0.3 may be reached, for which incipient pore interconnection might just appear. A consequence of the influence of HBS on thermal conductivity is that the high-burnup fuel will run cooler in the reactor than would be assumed from its thermal conductivity versus porosity behavior at low burnup, leading to lower fission gas release.

2.18.5 Conclusions

Radiation damage in UO_2 has been extensively studied for more than 50 years. The studies cover single effects from various damage sources and combined effects in, for example, irradiated nuclear fuels. UO_2 is the most commonly used fuel in nuclear reactors and a thorough knowledge of its behavior under irradiation is extremely important to ensure a safe exploitation of this energy production source. The safety and economic issues have especially triggered the research on the microstructural evolution of the fuel at high burnup.

The second practical issue related to the understanding of the damage formation in UO_2 lies in the forecast of its long-term behavior. The spent fuel that

will be disposed off will not be in equilibrium because of radioactive decay for millenaries. The α -damage will impact the long-term properties of the spent fuel and the comprehension of the mechanisms of damage formation will help to predict its behavior.

References

1. Belle, J. In *Uranium Dioxide: Properties and Nuclear Applications*; Handbooks, N. R., Ed.; United States Atomic Energy Commission: Washington, DC, 1961.
2. Lemaignan, C. *Science des Matériaux pour le Nucléaire*; Collection Génie Atomique: EDP Sciences.
3. Olander, D. *Fundamental Aspects of Nuclear Fuel Elements*; Office of Public Affairs Energy Research and Development Administration: U.S. Department of Commerce, Springfield, VA, 1976.
4. Curie, M. P. *Compt. Rendus* **1900**, 130, 76.
5. Rutherford, E.; Owens, R. B. *Trans. R. Soc. Can.* **1899**, 2, 9–12.
6. Ziegler, J. F.; Biersack, J. P.; Littmark, U. *The Stopping and Range of Ions in Solids*; Pergamon: Oxford, 1985.
7. Soullard, J.; Alamo, A. *Radiat. Eff.* **1978**, 38, 133.
8. Fleischer, R. Price, P.; Walker, R. Eds. *Nuclear Tracks in Solids*; University of California Press: Berkeley, CA, 1975.
9. Seitz, F.; Koehler, J. *Solid State Phys.* **1956**, 2, 305.
10. Toulemonde, M.; Paumier, E.; Dufour, C. *Radiat. Eff. Solids* **1993**, 126, 205.
11. Baranov, I. A.; Martynenko, Y. V.; Tsepelevitch, S.; Yavlinskii, Y. N. *Sov. Phys. Usp.* **1988**, 31, 1015.
12. Wiss, T.; Matzke, H.; Trautmann, C.; Klaumünzer, S.; Toulemonde, M. *Nucl. Instrum. Meth. Phys. Res. B* **1997**, 122, 583.
13. Ronchi, C. *J. Appl. Phys.* **1973**, 44, 455.
14. Matzke, H. *Radiat. Eff.* **1983**, 75, 317.
15. Blank, H.; Matzke, H. *Radiat. Eff.* **1973**, 17, 57–64.
16. Sonoda, T.; Kinoshita, M.; Chimi, Y.; Ishikawa, N.; Sataka, M.; Iwase, A. *Nucl. Instrum. Meth. Phys. Res. B* **2006**, 250, 254–258.
17. Sonoda, T.; Kinoshita, M.; Ishikawa, N.; Sataka, M.; Iwase, A.; Yasunaga, K. *Nucl. Instrum. Meth. Phys. Res. B* **2010**, 268, 3277–3281.
18. Ronchi, C.; Wiss, T. *J. Appl. Phys.* **2002**, 92(10), 5837–5848.
19. Matzke, H.; Meyer, O.; Turos, A. *Radiat. Eff. Defects Solids* **1991**, 119–121, 885–890.
20. Weber, W. *Radiat. Eff.* **1984**, 83, 145–156.
21. Weber, W. J. *J. Nucl. Mater.* **1981**, 98(1–2), 206–215.
22. Weber, W. J. *J. Nucl. Mater.* **1983**, 114(2–3), 213–221.
23. Staicu, D.; Wiss, T.; Rondinella, V. V.; Hiernaut, J. P.; Konings, R. J. M.; Ronchi, C. *J. Nucl. Mater.* **2010**, 397, 8–18.
24. Rondinella, V. V.; Matzke, H.; Cobos, J.; Wiss, T. *Mater. Res. Soc. Symp. Proc.* **1999**, 556, 447–454.
25. Rondinella, V. V.; Cobos, J.; Wiss, T.; Staicu, D. Studies on spent fuel alterations during storage and effects on corrosion behaviour. In *Proceedings of the 10th International Conference on Environmental Remediation and Radioactive Waste Management, ICEM'05*, Glasgow, UK, 2005.
26. Rondinella, V. V.; Wiss, T.; Hiernaut, J. P.; Staicu, D. *ICEM'07: The 11th International Conference on Radioactive Waste Management and Environmental Remediation*, Oud Sint-Jan Hospital Conference Center, Bruges, Belgium. 2007.

27. Lidiard, A. J. *Nucl. Mater.* **1966**, 19, 106.
28. Freyss, M.; Petit, T.; Crocombette, J.-P. *J. Nucl. Mater.* **2005**, 347(1–2), 44–51.
29. Yakub, E.; Ronchi, C.; Staicu, D. *J. Nucl. Mater.* **2009**, 389(1), 119–126.
30. Freyss, M.; Vergnet, N.; Petit, T. *J. Nucl. Mater.* **2006**, 352(1–3), 144–150.
31. Govers, K. Atomic scale simulations of noble gases behaviour in uranium dioxide. In *Faculté des sciences appliquées*; Université Libre de Bruxelles: Bruxelles, 2008.
32. Willis, B. T. M.; Chem, J. *Soc. Faraday Trans.* **1987**, 2, 1073.
33. Parfitt, D. C.; Grimes, R. W. *J. Nucl. Mater.* **2008**, 381, 216–222.
34. Govers, K.; Lemehov, S.; Verwerft, M. *J. Nucl. Mater.* **2008**, 374(3), 461–472.
35. Rapperport, E. J.; Huntress, A. M. *Deformation Modes of Single Crystal Uranium Dioxide from 700 °C to 1900 °C*; U.S. Atomic Energy Commission: Washington, DC, 1960; pp 1–29.
36. Ashbee, K. H. G. Stacking faults in uranium dioxide. In *Proceedings of the Royal Society of London*, 1964; Vol. 280, pp 37–46.
37. Evans, A. G.; Pratt, P. L. *Philos. Mag.* **1969**, 20, 1213–1237.
38. Lefebvre, J. M.; Soullard, J.; Gaboriaud, R. J.; Grilhe, J. *J. Nucl. Mater.* **1976**, 60, 59–65.
39. Jonnet, J.; Van Uffelen, P.; Wiss, T.; Staicu, D.; Re'my, B.; Rest, J. *Nucl. Instrum. Meth. Phys. Res. B Beam Interact. Mater. Atoms* **2008**, 266(12–13), 3008–3012.
40. Brucklacher, D.; Dienst, J. *J. Nucl. Mater.* **1972**, 42, 285.
41. Klein, D.; Baer, W.; Smith, G. G. *Nucl. Sci. Eng.* **1958**, 3, 698.
42. Lozano, N.; Desgranges, L.; Aymes, D.; Niepce, J. C. *J. Nucl. Mater.* **1998**, 257, 78–87.
43. Matzke, H.; et al. *J. Nucl. Mater.* **1989**, 166, 165.
44. Une, K.; Nogita, K.; Kashibe, S.; Imamura, M. *J. Nucl. Mater.* **1992**, 188, 65.
45. Une, K.; Nogita, K.; Shiratori, T.; Hayashi, K. *J. Nucl. Mater.* **2001**, 288, 20–28.
46. Ray, I. L. F.; Matzke, H.; Thiele, H.; Kinoshita, M. *J. Nucl. Mater.* **1997**, 245, 115–123.
47. Hiernaut, J. P.; et al. *J. Nucl. Mater.* **2008**, 377(2), 313–324.
48. Rondinella, V. V.; Wiss, T. *Mater. Today* **2010**, 13, 24–32.
49. Nogita, K.; Une, K. *Nucl. Instrum. Meth. Phys. Res. B* **1994**, B91, 301.
50. Nogita, K.; Une, K. *J. Nucl. Mater.* **1995**, 226, 302.
51. Spino, J.; Baron, D.; Coquerelle, M.; Stalios, A. D. *J. Nucl. Mater.* **1998**, 256(2–3), 189–196.
52. Kinoshita, M.; et al. High Burnup Rim Project: (III) properties of rim-structured fuel. In *Proceedings of the 2004 International Meeting on LWR Fuel Performance*, ANS: Orlando, FL, 2004.
53. Matzke, H. *J. Nucl. Mater.* **1999**, 270, 49–54.
54. Sonoda, T.; et al. *Nucl. Instrum. Meth. Phys. Res. B Beam Interact. Mater. Atoms* **2002**, 191(1–4), 622–628.
55. Noirot, J.; Desgranges, L.; Lamontagne, J. *J. Nucl. Mater.* **2008**, 372(2–3), 318–339.

2.19 Fuel Performance of Light Water Reactors (Uranium Oxide and MOX)

D. D. Baron

Electricité De France, Moret-sur-Loing, France; Commissariat à l'Energie Atomique et aux Energies Alternatives, Cadarache Nuclear Centre, France

L. Hallstadius

Westinghouse Electric Sweden AB, Västerås, Sweden

© 2012 Elsevier Ltd. All rights reserved.

2.19.1	Introduction	482
2.19.2	Experience on Oxide Fuel in LWRs	483
2.19.2.1	History of Development	483
2.19.2.2	Fuel Elements Design	484
2.19.2.2.1	The fuel pellets	485
2.19.2.2.2	The fuel rod cladding	487
2.19.2.2.3	Use of additives in the fuel	487
2.19.2.2.4	The fuel rod assemblies	488
2.19.2.3	LWR Operating Conditions	488
2.19.2.3.1	PWR normal operating conditions	488
2.19.2.3.2	BWR normal operating conditions	490
2.19.3	Behavior at Beginning of Life	491
2.19.3.1	Basic Irradiation Effects	491
2.19.3.2	Thermal Aspects	492
2.19.3.3	Mechanical Aspects	495
2.19.3.3.1	Base irradiation	495
2.19.3.3.2	Transient conditions	498
2.19.3.4	Material Microstructure and Chemistry	500
2.19.4	Consequences of Burnup Accumulation	501
2.19.4.1	Burnup	501
2.19.4.2	Low Temperature Restructuring (HBS)	502
2.19.4.3	Behavior of the Gaseous and Volatile Fission Products	504
2.19.4.4	Evolution of the Oxygen Potential	508
2.19.4.5	Evolution of the Properties	509
2.19.5	Limiting Phenomena	510
2.19.6	Conclusions	512
References		512

Abbreviations

ASTM	American Society for Testing and Material (International Normalization)
BWRs	Boiling water reactor
CEA	Commissariat à l'Energie Atomique
EDF	Electricité De France
EPMA	Electron probe micro analysis
FBR	Fast breeder reactors
GCR	Gas Cooled Reactors
HBEP	High Burn-up Effect Program
HBRP	High Burn-up Rim Project

HBS	High burnup structure
HPWR	Heavy Pressurized Water Reactor
IAEA	International Atomic Energy Agency
ITU	Institute for Transuranium Elements
LWR	Light water reactors
MOX	Mixed oxides fuel
NFIR	Nuclear Fuel Industry Research group
NXO	New Cross over Project
PCI	Pellet-cladding interaction
PCMI	Pellet-cladding mechanical interaction
PWR	Pressurized water reactor

RIA	Reactivity insertion accident
RMBK	Russian High Power Chanel-type Reactor
SEM	Scattering electron microscopy
TEM	Transmission electron microscopy
XRD	X-ray diffraction
Zyr2	Zirconium 2 alloy (with Nickel)

2.19.1 Introduction

Historically, mainly because of their very simplified and sage design, pressurized water reactors (PWRs) and boiling water reactors (BWRs) are representing the two designs most commonly used for electricity production for the last 50 years. In 2009, 436 reactor units are operated worldwide, out of which 57% are PWR, and 22% are BWR. Altogether, 345 (79%) are therefore light water reactor (LWR) units (Figure 1).

These LWR units are mainly loaded with uranium dioxide (UO_2) with an average enrichment ranging between 3.5% and 5% in isotope 235 (natural uranium contains only 0.72% of this isotope). However, Europe and Japan have now experienced the recycling of plutonium for more than 20 years, introduced in mixed oxides (MOX, $(\text{U,Pu})\text{O}_2$), mostly manufactured by a two-stage powder mixing process. In the LWR designs, purified light water with controlled pH plays the roles of both moderator and coolant, flowing up from the bottom to the top of the core. The BWR design allows the water to achieve bulk boiling, starting near the bottom of the core, with a primary circuit pressurization fixed at about 7 MPa. In the PWR design, the water is highly pressurized to around 15.5 MPa to avoid any bulk boiling all along the fuel assembly height, or only very local nucleate boiling

around the hot spots. At a pressure of 15.5 MPa, the water boiling temperature is around 345 °C. A typical maximum temperature in normal operation is 326 °C at the core exit, compared to somewhat <290 °C in a BWR.

Since the very first introduction in the gas-cooled reactors (GCRs) in the 1960s (MAGNOX reactors), the uranium dioxide fuel is probably the most well known and optimized material, accounting for the tremendous volume of oxides irradiated since 50 years, the important experimental programs conducted worldwide (mainly in the 1960s, 1970s, and 1980s), and the large amount of survey programs. The thermal domain of the fuel in the LWR is different from the fast breeder reactors (FBRs) or the HPWRs (heavy pressurized water reactors) with temperatures ranging only from 500 to 1200 °C in normal operation. In terms of burnups, it has been demonstrated that UO_2 fuels are able to achieve 100 MWd kgM^{-1} local pellet average in LWR. In 2009, the batch average discharge burnups agreed by the safety authorities range up to 70–75 MWd kgM^{-1} , that is, what is technically achievable within the generally accepted 5% enrichment limit. Figure 2 shows the evolution of the average fuel discharge burnup worldwide.

The optimal discharge burnup depends on technical and economical aspects, which obviously evolve with time.¹ However, more recently, in the framework of a closed fuel cycle including spent fuel reprocessing and MOX fuel reloading, it was estimated that 52 MWd kgM^{-1} (batch average) could be an optimum in order to avoid a too significant degradation of the isotopic composition of the reprocessed plutonium in MOX fuels. Indeed, the higher the discharge burnup of the reprocessed spent fuel, the higher is the proportion of nonfissile plutonium isotopes, curium, and americium.²

This chapter deals with the basic knowledge and state of the art on LWR fuel thermal and mechanical behavior: survey programs, main assembly and rod designs, and operating conditions and trends in the future developments. The main phenomena occurring in the LWR oxide fuels are described, focusing on the irradiation conditions and on the long-term effects of irradiation on material properties and microstructure evolution. Control of the fuel cladding integrity, that is, fuel reliability, is then discussed.

For general information on LWR oxide fuel's behavior and performances, we recommend Olander³ and Bailly *et al.*⁴

Types of NPP in the world

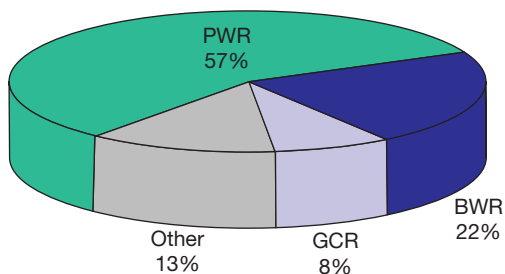


Figure 1 Distribution of the reactor designs in the nuclear electricity production. www.icjt.org/an/tech/jesvet/jesvet.htm. © ICJT 2001.

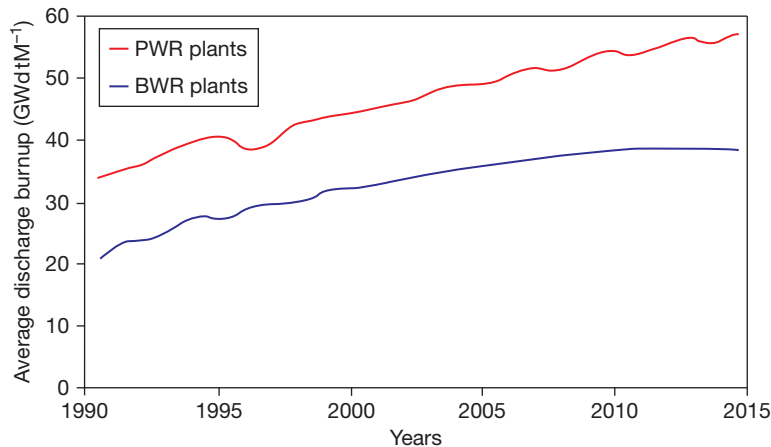


Figure 2 Evolution of the average fuel oxide discharged burnup from 1990 to 2015 for pressurized water reactor and boiling water reactor (projection after 2008).

2.19.2 Experience on Oxide Fuel in LWRs

2.19.2.1 History of Development

After the Second World War, engineers began to develop methods to use nuclear energy for propulsion and the generation of electricity. On 20 December 1951, the experimental breeder reactor-I (EBR-I) produced the first electricity in Idaho,⁵ powering electric lightbulbs under the leadership of Walter Zinn. This was the first electricity produced with nuclear energy, followed by the advent of the nuclear submarines. PWR design was first developed for the submarine application but was soon adopted for commercial energy. Zirconium alloys were first used because of the minimal interaction of zirconium with thermal neutrons, allowing a higher reactivity of the core and a reduction of the core size to reach criticality. In the United States, the first nuclear plant to go on the commercial electricity grid was the Shippingport unit, built in Pennsylvania by the federal government's Atomic Energy Commission and admiral Rickover's navy organization. The plant was able to produce 150 MWe. The first full power commercial PWR was designed by Westinghouse and built for the Yankee Atomic Power Corporation at Rowe, MA, producing 250 MWe; it was in operation from 1958 to 1991. In the meantime, the Argonne National Laboratory had developed the BWR concept. In 1960, Common Edison started to operate the first commercial BWR at Dresden, IL, designed and built by General Electric, with a production capability of 250 MWe.

Other concepts were developed at the same time by other countries such as GCRs in France and

United Kingdom (MAGNOX), HPWRs in Canada, and RBMK in Russia. The 1950s and 1960s were the first period for the utilities to get acquainted with operating nuclear plants. Encouraged by the first successes and facing a large increase in electricity consumption, utilities started to look for larger nuclear production. After the 1973 oil crisis, the motivation was the highest for countries having little or no domestic fossil fuel production. At this time, several of these countries invested heavily in nuclear electricity production, for example, France, Belgium, Japan, and Sweden. Because of the simplicity of the concepts, and probably also due to the large experience acquired with nearly 100 units in the United States, LWR designs were chosen to produce nuclear electricity at a larger scale. The main nuclear plant providers for PWR were Westinghouse, Combustion Engineering, and Babcock & Wilcox, and for BWR, General Electric. Westinghouse and General Electric gave licenses to several European and Japanese companies. This is the main reason for the consistency of most of the LWR fuel designs.

Westinghouse was first providing PWR units with an electric power generation level of about 900 MWe. The 1300 MWe level was achieved at the end of the 1970s and 1450 MWe level in the 1990s. The change of scale was mainly obtained by an increase in the number of fuel assemblies as well as their length. However, enlarging the core imposed adaptations in the core management and the mode of operation to guarantee the radial core stability.

In the 1970s, based on the large US acquired experience, the LWR fuel was already quite optimized to achieve maximum assembly burnup of 35 MWd kgM⁻¹

in normal operation, with a PWR core management by third of the core. A large research investment has since been made worldwide, mainly to increase the discharge burnup and optimize the nuclear fuel cycle. Programs were initiated to:

- Improve the UO_2 fuel density stability, leading to preferred powder manufacturing processes: The Integrated Dry Route developed by BNFL, and the wet routes, ammonium diuranate (ADU) and ammonium uranyl carbonate (AUC).
- Limit the risk of rod failure by pellet-clad mechanical and chemical interaction, by improving the plant operation management.
- Limit the risk of failure by migrating fragments in the primary circuit, adding a filter at the assembly bottom end.
- Justify the load follow operating conditions imposed when nearly 80% of the electricity production is nuclear (France and Belgium).
- Limit the fuel rod bow and the PWR fuel assembly deformation, to facilitate assembly reloading and avoid gap pitching between fuel rods; modification of the spacer grids and mixing grids to increase the assembly rigidity.
- Reducing BWR assembly bow by optimizing the materials used for the channel box, as well as fine-tuning the manufacturing processes.
- Increase the batch discharge burnup up to 60 or 70 MWd kgM, $^{-1}$ which requires a detailed understanding of material properties and microstructure evolution with irradiation, in particular, the behavior of the gaseous and volatile fission product species in UO_2 .
- More generally, improve the material knowledge and modeling, and our insights into the mechanical assembly and rod structure behavior under irradiation.

In order to cope with the needs to increase the operational margins and flexibility, an evolution in the fuel material composition was investigated:

- By adding ‘burnable’ neutron-absorbing elements to limit the core reactivity at the beginning of life (gadolinium, erbium, or boron).
- By adding chemical species such as niobium, chromium, and aluminosilicates to increase the grain size and delay the fission gas release during normal operation and/or accidental power transients. Such additives can also influence the viscous properties at medium temperatures, that is, the pellet-cladding mechanical interaction (PCMI) behavior.

Moreover, a large number of research projects have been focused, mainly since the 1980s, on the recycling of plutonium. The particular behavior of these heterogeneous MOX will be described in this chapter as well, focusing on their specificities.

In terms of international research projects, since the 1970s, the classification can be made in several large categories: power ramps (PCI/PCMI in usual power transient or for more severe accidents), fission gas behavior and high burnup structure (HBS), fuel chemistry, fuel properties evolution with burnup (conductivity specific heat, mechanical properties, swelling, and densification, fuel stability), cladding behavior (in-pile and out-of-pile creep, growth, corrosion, and hydrogen pickup). Major reference programs are given in [Table 1](#).

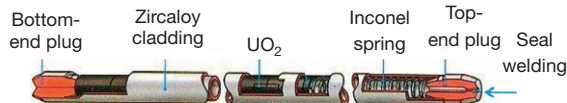
2.19.2.2 Fuel Elements Design

The PWR and BWR fuel assembly designs have progressively evolved with time. However, these evolutions approached maturity in the 1970s with 17×17 square mesh structures for most PWR fuel and in the 1990s for BWR with 10×10 lattices. The more recent evolutions were mainly focused on the rigidity of the structure PWR, enhancing the neutron economy BWR, and fuel reliability, for example, protection against migrating objects (‘debris’) and increasing the margin against pellet-cladding interaction (PCI) failure BWR. Materials have also evolved to facilitate increasing burnups and help reduce geometric deformation during operation. LWRs are able to operate currently with MOX fuel in order to recycle plutonium. Europe and Japan have now irradiated such MOX fuel at a large scale in PWR units.¹⁶

The fuel rod is a zirconium alloy tube, containing fuel cylinders (‘pellets’) piled to form the fuel stack, with a remaining upper volume called plenum at the top (see [Figure 3](#)), to allow fuel stack elongation and accommodation of the released gaseous and volatile fission products. The fuel stack is typically maintained during handling operation by a spring placed in the plenum. The fuel rod is closed at both ends by sealed end plugs after filling it with a neutral gas (helium) with a pressure ranging from 1 to 34.5 bar (0.3–3.45 MPa), depending on the design. The PWR fuel rods are pressurized to partly counterbalance the primary circuit pressure (14–15.5 MPa for PWR vs. 7 MPa for BWR) and to delay creep down of the cladding. However, the initial pressure has been progressively reduced with increasing discharge burnups (general trend in the core management), in particular with

Table 1 List of the main international programs conducted on LWR fuel between 1970 and 2010

Project	References	Period	Subject
OVER-ramp	[6]	1977–1983	PCI/PCMI
SUPER-ramp	[7]	1980–1983	
DOE/Petten	[8]	1983–1984	
TRIBULATION		1984–1987	Fuel rod behavior after an accidental transient
HBEP	[9]	1979–1988	Fission gas release at high burnup and high burnup fuel transformation (HBS)
	[10]		
HBC	Several progress reports	1987–1994	Fuel chemistry
NFIR I	Large number of proprietary reports	1982–1988	Global fuel behavior at high burnup
ROPE-I	http://www.nea.fr/abs/html/nea-1722.html	1986–1993	BWR rod overpressure experiments
ROPE-II	http://www.nea.fr/abs/html/nea-1723.html	1991–2008	PWR rod overpressure experiment
NFIR II	Large number of proprietary reports	1988–1994	Fuel rod behavior under irradiation – fuel and cladding properties
NFIR III	Large number of proprietary reports	1992–1999	Fuel rod behavior under irradiation – fuel and cladding properties
HBRP	[11–14]	1994–2002	High burnup structure (HBS or RIM)
NFIR IV	Large number of proprietary reports	1998–2004	Fuel rod behavior under irradiation – fuel and cladding properties
HBRP_NT	[15]	2002–2007	High burnup structure (HBS or RIM)
NFIR V	Large number of proprietary reports	2004–2010	Fuel rod behavior under irradiation – fuel and cladding properties – fuel dispersion
NXO	Ongoing	2006–2009	Multiscale approach of HBS
F-BRIDGE	Ongoing	2008–2012	Acquisition of basic data for modeling and multiscale approach
SCIP	Studsvik, near closure	2004–2009	PCI/PCMI and hydrogen-assisted cladding failure modes
SCIP 2	Studsvik, about to start	2009–2014	Continuation of SCIP, focusing on pellet behavior


Figure 3 Fuel rod scheme.

MOX fuel, to avoid exceeding the pressure criterion at end of life. The initial pressure has been between 1.5 and 2 MPa for the more recent PWR fuel fabrications. The initial helium pressure is usually 0.2–0.8 MPa for BWR fuels. **Table 2** provides the main characteristics of fuel rods. PWR data are given for the 17×17 design, which is the most common. For BWRs, the standard has evolved over 8×8 and 9×9 to a 10×10 lattice.

2.19.2.2.1 The fuel pellets

Fuel pellets are shaped from uranium dioxide by a pressing process and then sintered at high temperature (e.g., 1740 °C) in controlled atmosphere for several hours (see **Chapter 2.15, Uranium Oxide and MOX Production**). Manufacturing conditions have been pragmatically optimized during the 1960s and

1970s. These processes lead to a ceramic material containing an initial porosity ranging from 3 to 7% of the volume (**Figure 4**). When necessary, pore formers are used. The final density is ranging from 10.2 to 10.7 g cm⁻³, the UO₂ theoretical density being 10.96 g cm⁻³. The average grain size ranges usually between 8 and 20 μm. The fuel pellets are generally designed with end dishes for core physics aspects and chamfers to facilitate the introduction into the tubing. Dishes are needed for counterbalancing the in-pile hour-glassing of pellets, essentially induced by the steep radial temperature gradient.

The industrial MOX fuel fabrication is generally done by a two-step mixing process firstly developed by Belgonucleaire, and improved more recently to better homogenize the plutonium distribution. A first blend called master blend is performed, mixing plutonium oxide with depleted uranium oxide. In the present fabrications, the plutonium content in this first mixture is close to 30%. In a second step, this master blend is mixed again with depleted uranium oxide to obtain the targeted average plutonium content, between 6 and 10%. After grinding and then pressing,

Table 2 Main fuel rod characteristics for current PWR and BWR plants

<i>Fuel rod characteristics</i>	<i>PWR 17 × 17</i>	<i>BWR 8 × 8</i>	<i>BWR 10 × 10</i>
Fuel rod outer diameter (10^{-3} m)	9.45	12.30	9.6–9.8
Fuel rod inner diameter (10^{-3} m)	8.347	10.68	9.0–9.2
Cladding wall thickness (μ m)	570	810	Around 600
Cladding material	Zirconium alloy	Zry-2	Zry-2
Pellet diameter (10^{-3} m)	8.19	10.4	8.2–8.5
Pellet length (10^{-3} m)	10–12	10.4	Around 10
Fuel	UO ₂	UO ₂	UO ₂
Possible neutron absorbent additives	Gd, Er, B	Gd	Gd
Initial ²³⁵ U enrichment (%)	3.2–5	3.2–5	3.2–5
Theoretical density (kg m^{-3})	10950	10950	10950
Fuel initial porosity (%)	4.5–7	4.5–7	4.5–7
Fuel initial relative density	0.93–0.955	0.93–0.955	0.95–0.98



Figure 4 UO₂ manufacturing.

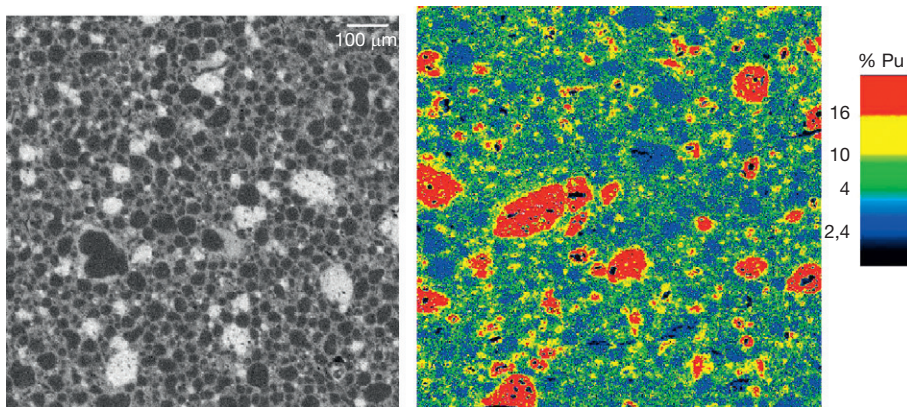


Figure 5 Plutonium concentration imaging in a fresh mixed oxides fuel.

the ‘green’ pellets are sintered in a neutral atmosphere, slightly added with vapor. This aims to reach a 2.000 stoichiometry. The final material is obviously heterogeneous as shown in the electron probe microanalysis (EPMA) picture in [Figure 5](#). The average grain size is smaller than in UO₂ fuels, particularly in the

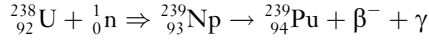
rich plutonium agglomerates. For detail on this and alternative fabrication routes (see [Chapter 2.15, Uranium Oxide and MOX Production](#)).

The isotopic composition of the plutonium (²³⁸Pu, ²³⁹Pu, ²⁴⁰Pu, ²⁴¹Pu, ²⁴²Pu, ²⁴¹Am, ²⁴²Cm) depends upon the final discharge burnup of the reprocessed

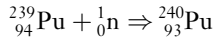
fuel. The isotopes ^{240}Pu , ^{242}Pu , and ^{241}Am are neutron absorbers. They degrade the fissile quality of the plutonium.

The plutonium production in-pile is as follows:

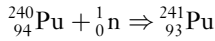
^{239}Pu production by neutron absorption and β -decay (^{239}Pu half-life 24 000 years, ^{239}Np half-life 2.36 days)



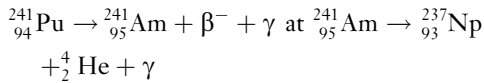
^{240}Pu production by neutron absorption (^{240}Pu half-life, 6563 years)



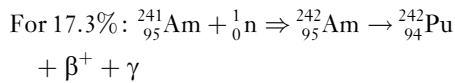
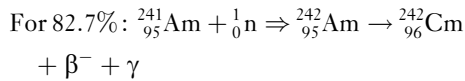
^{241}Pu production by neutron absorption (^{241}Pu half-life, 14 years)



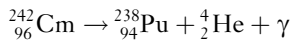
^{241}Am production by β -decay (^{241}Am half-life, 432 years)



^{241}Am production by neutron absorption (^{242}Am half-life, 16.02 h), then ^{242}Cm (half-life 160 days) and ^{242}Pu (half-life 3.76×10^5 years) by β -decay β^- or β^+



^{238}Pu production by α -decay (^{238}Pu half-life, 87.74 years)



All these isotopes produce α -emitters. Their decay properties are given in [Table 3](#).

The longer the MOX fuel is stored, the larger is the americium content. The production of Helium in MOX fuel is much higher than in UO_2 fuel. It cannot be neglected in the fuel rod behavior simulation, as far as helium release participates in the increase of the fuel rod inner pressure during irradiation.

2.19.2.2.2 The fuel rod cladding

The cladding material is a zirconium alloy, traditionally Zircaloy-2 for the BWR fuel rods and Zircaloy-4 for PWR. The main difference is the presence of nickel in Zircaloy-2 and not in Zircaloy-4. For Zr-4 in a PWR, the tin content is an important parameter to control the corrosion rate in-pile (see [Chapter 2.07, Zirconium Alloys: Properties and Characteristics](#)). To reduce corrosion and hydrogen pickup, the Zircaloys have evolved, and new advanced alloys were developed over the last 30 years. For PWR cladding, the main change in alloy composition is the addition of niobium and the reduction of the tin content. Another important parameter for the cladding final microstructure and its mechanical properties (strength, creep, irradiation growth) is the final heat treatment, which varies between materials and manufacturers. Depending on the final anneal, the material obtained is stress relieved (SRA or CW, cold worked), partially recrystallized, (pRXA) or fully recrystallized (RXA).

Since control rods are deployed during normal operation of a BWR, and movements of those control rods lead to significant and rapid changes of local power, PCI is a significant mode of rod failure for BWR fuel, relatively common through industry history. Modern BWR cladding is therefore equipped with a liner barrier of a dilute Zr alloy at the inner wall to protect against this failure mode.

2.19.2.2.3 Use of additives in the fuel

A number of rods in a fuel assembly usually incorporate a burnable neutron absorber, which is typically either boron, with boron-10 the active isotope, or gadolinium

Table 3 Decay characteristics for the different isotopes

Isotopes	half-life (years)	Decay constant (s^{-1})	Activity per gram of Pu (Bq)	Decay product	Mode	Decay energy (MeV)	Energy (W/g Pu)
^{238}Pu	87.74	$2.505\text{E} - 10$	$6.340\text{E} + 11$	^{234}U	α	5.593	$5.679\text{E} - 01$
^{239}Pu	24 110	$9.116\text{E} - 13$	$2.297\text{E} + 09$	^{234}U	α	5.245	$1.930\text{E} - 03$
^{240}Pu	6563	$3.349\text{E} - 12$	$8.405\text{E} + 09$	^{236}U	α	5.140	$6.919\text{E} - 03$
^{241}Pu				^{241}Am	β^-	0.021	$1.287\text{E} - 02$
	14.35	$1.532\text{E} - 09$	$3.828\text{E} + 12$	^{237}U	α	5.140 (0.025%)	
^{242}Pu	375 000	$5.861\text{E} - 14$	$1.459\text{E} + 08$	^{238}U	α	4.984	$1.164\text{E} - 04$
^{241}Am	432.2	$5.086\text{E} - 11$	$1.271\text{E} + 11$	^{237}Np	α	5.638	$1.148\text{E} - 01$

where gadolinium 155 and 157 are the burnable neutron poisons (see **Chapter 2.16, Burnable Poison-Doped Fuel**). These serve to limit the core reactivity at the beginning of the life, and furthermore

- For PWR, to limit the effluent production by using excessive boric acid volume in the primary circuit.
- For BWR, to extend the lives of control rods that would otherwise need to be deployed to control excess reactivity.

New fuels were developed with additives such as niobium, chromium, and aluminosilicates to increase the as-fabricated fuel grain size, and consequently, reduce the fission gas release kinetics. Such additives can simultaneously provide other benefits, for example, higher density, reduced densification, and a better PCI behavior.

2.19.2.2.4 The fuel rod assemblies

The fuel rods are bundled into fuel assemblies (**Figure 6**). The main characteristics of the fuel

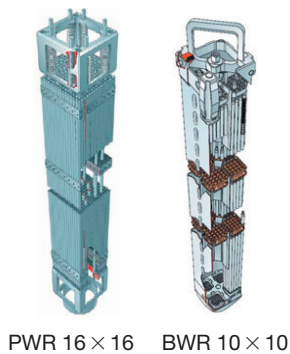


Figure 6 Fuel rod assemblies. Pictures from Westinghouse Electric Company.

assemblies, representative of typical current designs, are given in **Table 4**.

For both LWR types, the fuel assemblies are square-meshed structures. In PWR, the number of fuel rods per assembly has evolved between the 1960s and the 1970s. The 12×12 became 14×14 , and the 15×15 became 17×17 , retaining the same outer dimensions. One design even uses an 18×18 lattice. The fuel rod external diameter decreased from 1.051 to 0.951 cm to improve the core physics design and decrease the fuel centerline temperature, however, maintaining a constant assembly power. The original 15×15 assembly had a zirconium box like that of BWR fuel. It has later been eliminated to facilitate the thermohydraulic cross flow between the fuel assemblies, and thus reduce the risk to reach locally the critical heat flux leading to a departure of the nucleate boiling (DNB).

The BWR assembly has evolved over 8×8 and 9×9 lattices to the modern 10×10 mesh design. The fuel assembly is equipped with a channel box made from a zirconium alloy, providing mechanical and thermohydraulic insulation from neighboring assemblies. This feature has facilitated large improvements in key performance parameters over the years, for example, by means of the above-mentioned evolution of the lattice mesh, and by adding internal structures such as water rods or a water cross.

2.19.2.3 LWR Operating Conditions

2.19.2.3.1 PWR normal operating conditions

The LWR fuel rods are designed to operate in normal operation at medium heat rate, ranging from 15 to 25 kW m^{-1} ($150\text{--}250 \text{ W cm}^{-1}$). In 17×17 or 16×16 designs, these linear heat rates lead to a fuel centerline temperature not exceeding $1000\text{--}1200^\circ\text{C}$.

Table 4 Main fuel core characteristics for current PWR and BWR plants

Power plant type (MWe)	PWR 900	PWR 1300	PWR 1400	Typical BWR
Number of fuel assemblies in the core	157	193	214	700–900
Type of assembly	17×17	17×17	17×17	10×10
Number of water rods	25	25	25	
Number of fuel rods per assembly	264	264	264	91–96
Total number of fuel rods in the core	41 448	50 952	56 496	63 000–86 000
Primary circuit coolant and moderator	Light water	Light water	Light water	Light water
Primary circuit pressure (bar)	155	155	155	~70
Feed coolant temperature	285	285	285	
Average coolant temperature ($^\circ\text{C}$)	300	300	300	~286
Assembly length (m)	4.00	4.50	4.50	~4
Active fuel length (m)	3.66	4.268	4.268	~3.7

This is fundamentally different from the FBR fuel (see **Chapter 2.21, Fuel Performance of Fast Spectrum Oxide Fuel**) regarding the fission gas release, with a low activation in base irradiation of the gas thermal diffusion. Another aspect for the PWR fuel is a very uniform neutron spectrum condition all along the assembly height as far as the moderator (primary circuit water which plays the role of coolant as well) stays in liquid phase at all axial levels. The inlet core coolant temperature is typically around 285 °C and the elevation from the bottom to the top is around 40 °C. This temperature elevation has a slight effect on the moderator efficiency. When local boiling occurs, it stays much localized at the fuel rod cladding surface. The water saturation temperature value at a pressure of 15.5 MPa is 345 °C and the maximum core outlet temperature in normal operation is around 320 °C. The fuel assembly pressure drop is around 1.5 MPa.

The maximum axial power at the beginning of the core cycle is located at the bottom and skips quickly to the upper part of the assembly as irradiation proceeds. It results in an axial profile with a peaking factor ranging between 1.08 and 1.2. The control rods are never deeply inserted in base operations. **Figures 7 and 8** below show typical average power history for a standard UO₂ fuel rod irradiated for five

annual cycles and for a standard MOX fuel irradiated for four annual cycles, respectively. The power generated in the fuel rod, highest during the two first cycles, generally decreases with time as UO₂ reactivity decreases with burnup (fissile atoms consumption). In the MOX fuel, the global reactivity is not decreasing so fast. The power rate during the second and third cycles is close to the first cycle power rate. The fourth cycle depends upon the localization of the MOX assembly. Due to their highest production of fast neutrons, the MOX assemblies are managed so as to avoid a localization that is too close to the core vessel. **Figure 9** is an example of the final burnup axial profile obtained by γ -scanning. A drop of the scan is observed at each pellet-to-pellet interface, as far as cesium axial diffusion is not activated (centerline temperatures have not exceeded 1200 °C).

France has a high proportion of nuclear electricity production (about 80%), and therefore, a certain number of the Electricité De France (EDF) nuclear reactors are involved in following the electricity demand. These are usually operating in load follow (daily cycles, decreasing the power to 30% or 50% of its nominal value during the night) and frequency control (instantaneous adaptation to the grid in a range $\pm 5\%$ around the nominal power). Semi-absorbent control rods (so-called ‘gray rods’) are

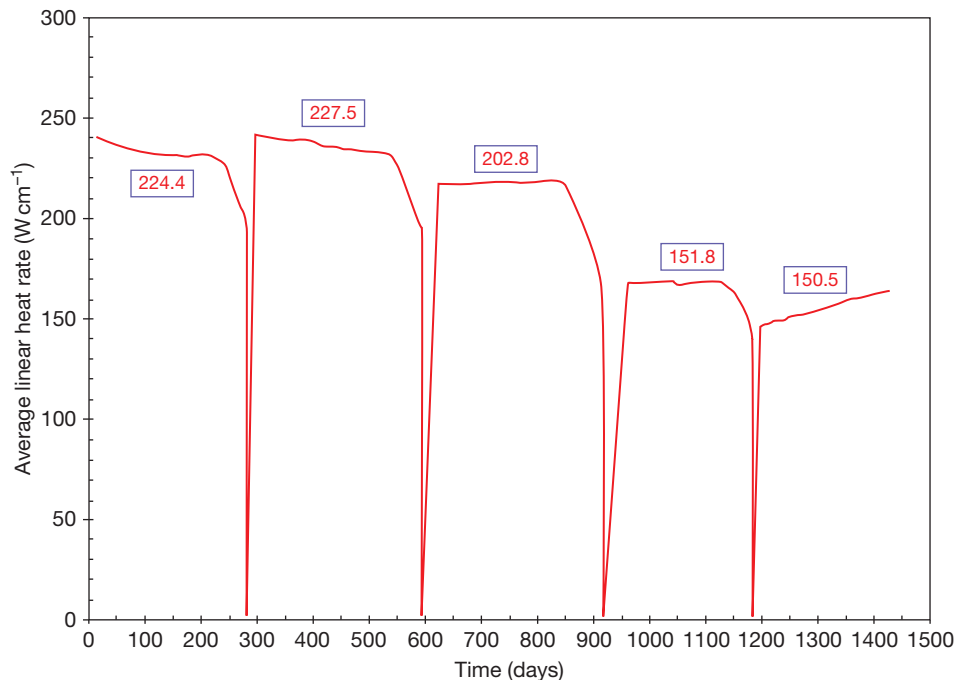


Figure 7 Evolution of the linear heat rate in base irradiation for standard pressurized water reactor UO₂ fuel.

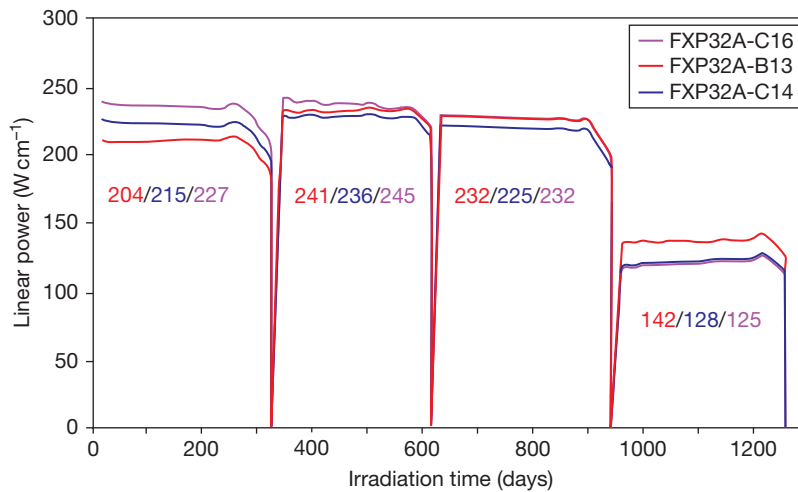


Figure 8 Evolution of the linear heat rate in base irradiation for standard pressurized water reactor mixed oxides fuel.

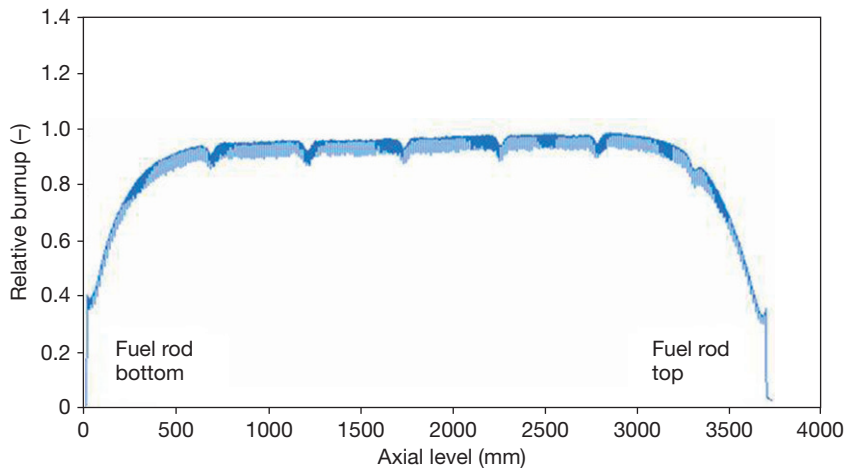


Figure 9 Final burnup axial profile for a pressurized water reactor fuel rod.

inserted to perform these power variations. Such semi-absorbent control rods allow limiting the ^{135}Xe isotope shadow effects. It was demonstrated that the power cycling had only a slight influence on the overall final fuel performance even if the local power cycling can be higher than the average power variations.

2.19.2.3.2 BWR normal operating conditions

One major difference between the core physics in a BWR reactor compared to a PWR reactor, apart from the lower system pressure, is the effect of the relative void volume in the boiling water, increasing from the bottom to the top of the assemblies. This void induces a significant neutron submoderation resulting in a PWR-like spectrum at the bottom of the core and a

harder spectrum in the upper part. This leads to significantly more generation of fissile nuclides in the upper part, and hence, an axial power profile that depends on the burnup of the fuel assembly (Figure 10).

Net boiling, starting near the bottom of the core, leads to a constant coolant temperature of around 286°C , that is, significantly less than in the upper parts of a PWR core. The core power is controlled using cruciform control blades, inserted between fuel assemblies, which are equipped with channel boxes. This leads to a more nonuniform power distribution, both radially and axially, than for a PWR, where usually all control rods are withdrawn during operation and core power is controlled using boron in the

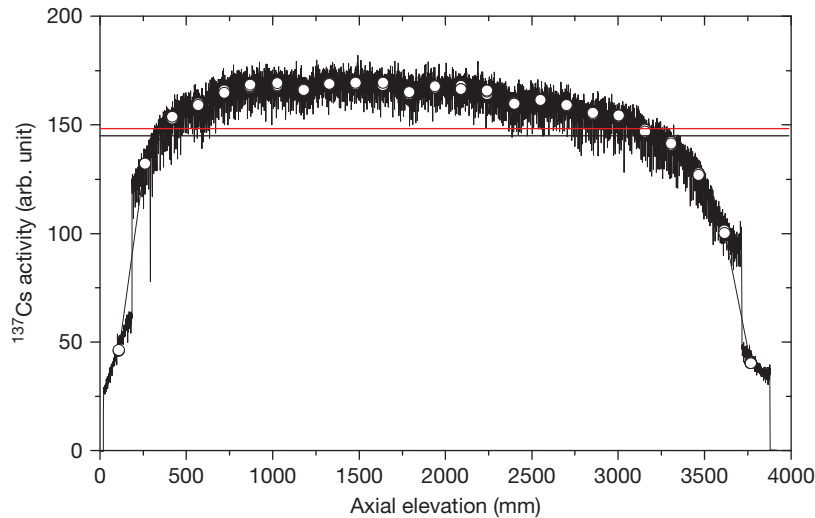


Figure 10 Example of an axial profile for a high burnup boiling water reactor fuel rod. Note that the rod has low-enrichment zones ('blanket zones') at both ends, for increased neutron economy.

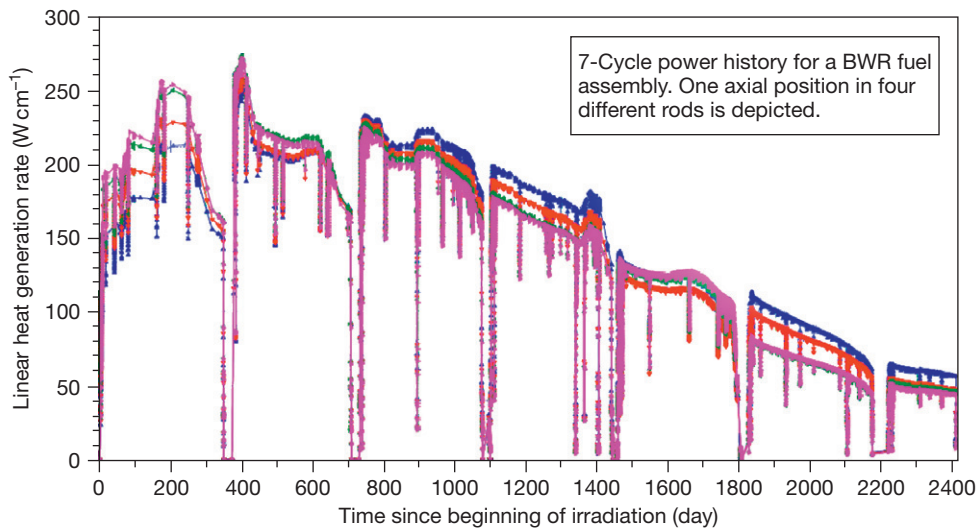


Figure 11 Example of a boiling water reactor power history. Courtesy of KKL.

coolant. The influence of control rods is evident from [Figure 11](#), where we see a significant difference between individual fuel rods and axial locations during parts of the operating history.

2.19.3 Behavior at Beginning of Life

For the overall LWR fuel rod simulation, see also [Chapter 3.19, Oxide Fuel Performance Modeling and Simulations](#), dealing with the computational simulation.

2.19.3.1 Basic Irradiation Effects

First, one has to keep in mind that as soon as the irradiation of the fuel starts, the fuel pellets are evolving to accommodate the in-pile conditions. For this, there are two energy sources:

- The local temperature
- The fission energy

For the portion of fuel operating at temperatures lower than 800 °C (pellet periphery), the second source is predominant. On the other hand, in the pellet center,

the temperatures are high enough to activate diffusion mechanisms driven by Brownian mobility. The fission energy is mostly transmitted to the fission fragments in the form of kinetic energy. The average energy is about 60–140 MeV. Then the fission fragments are progressively slowed down, transferring their kinetic energy to the surrounding material, mainly by external atomic electronic layer friction at high energy and then progressively by cascades colliding when energy is decreasing. These cascades induce creation of Frenkel pairs or Schottky defects (U or Pu + 2 Oxygen). Most of these defects are recovered quickly. Soullard¹⁷ has evaluated in his Ph.D. work that about 26 500 uranium vacancy–interstitial Frenkel pairs are created per fission and 72 700 oxygen vacancy–interstitial pairs. This means that in a standard fuel operating around 220 W cm⁻¹, each heavy atom (U or Pu) is displaced almost 0.4 times a day. Due to its lower weight, the number is three times higher for oxygen atoms. This has obvious consequences for the local physical properties of the material as far as these properties are very sensitive to the deviation from stoichiometry. Since the fuel material is a ceramic, Frenkel defects are electrically charged. The oxygen is then redistributed in a way reflecting electrical symmetries, preferring the formation of the specific octahedral position over tetrahedral position in the cubic structure.¹⁸

Defect recovery is influenced by fission cascades as well as the local temperature and the local fission density energies. In the external part of the fuel pellet, the temperature is not high enough to activate an atomic diffusion. However, the cascades allow a partial recovery. In a first phase, the overall balance leads to a stabilization of the lattice parameter after a few days of irradiation¹⁹ with the formation and accumulation of dislocation loops. At high burnup, this population of dislocation loops is progressively tangling and clustering,²⁰ leading to a material transformation described later in this chapter. At the pellet center, the temperature allows a quasitotal recovery of the irradiation defects.

2.19.3.2 Thermal Aspects

Generally speaking, the heat equation to solve is as follows:

$$\rho C_p(T) \frac{\partial T}{\partial t} - \text{div}(k(T) \overline{\text{grad}} T) = S(r) \quad [1]$$

where $C_p(T)$ is the local heat capacity of the material (J kg⁻¹ K⁻¹), T is the local temperature (K), $k(T)$

is the local thermal conductivity of the material (W kg⁻¹ K⁻¹), and $S(r)$ is the local power generation (W kg⁻¹).

In normal operation, and still more, in accidental conditions, the radial temperature gradient is predominant, compared to the axial gradient. For engineering applications, the problem can be solved by a one-dimensional finite element calculation, along a radius considering the fuel rod as an axisymmetric structure. The conductivity integral can then be written as follows:

$$\rho(r, T, t) C_p(r, T) \frac{\partial T(r, t)}{\partial t} - \lambda(r, T) \frac{1}{r} \frac{\partial}{\partial r} \left(r \frac{\partial T(r, t)}{\partial r} \right) = S(r, t) \quad [2]$$

If $\overline{P_V}(t)$ is the average volumetric power in the fuel pellet and $f(r, t)$ the radial power profile, it gives:

$$\begin{aligned} & \rho(r, T, t) C_p(r, T) \frac{\partial T(r, t)}{\partial t} \\ & - \lambda(r, T) \frac{1}{r} \frac{\partial}{\partial r} \left(r \frac{\partial T(r, t)}{\partial r} \right) \\ & = f(r, t) \times \overline{P_V}(t) \end{aligned} \quad [3]$$

In steady-state conditions, the equation can be reduced:

$$- \lambda(r, T) \frac{1}{r} \frac{\partial}{\partial r} \left(r \frac{\partial T(r)}{\partial r} \right) = f(r) \times \overline{P_V} \quad [4]$$

In the cladding, the second term is null. Nevertheless, solving of the fuel rod heat transfer problem is not limited to the standard basic equation. To evaluate the temperature field in the nuclear fuel rod, several phenomena are to be accounted for in the evaluation of the temperature performance (Figure 12; see also Chapter 3.19, Oxide Fuel Performance Modeling and Simulations):

- *The radial power generation in the pellet*²¹: The radial power generation is not uniform, due to the self-shielding effect of the ²³⁸U isotope in the neutron epithermal energy domain. In this domain, the ²³⁸U capture cross-section presents very high values for certain neutron incident energies (resonances). For these energies, the capture probability becomes very high when entering the fuel after slowing down in the moderator. This capture produces a transmutation of ²³⁸U to ²³⁹Np, which very quickly becomes ²³⁹Pu by β -decay. The plutonium production is therefore higher in the fuel rim than in the rest of the pellet. Plutonium buildup

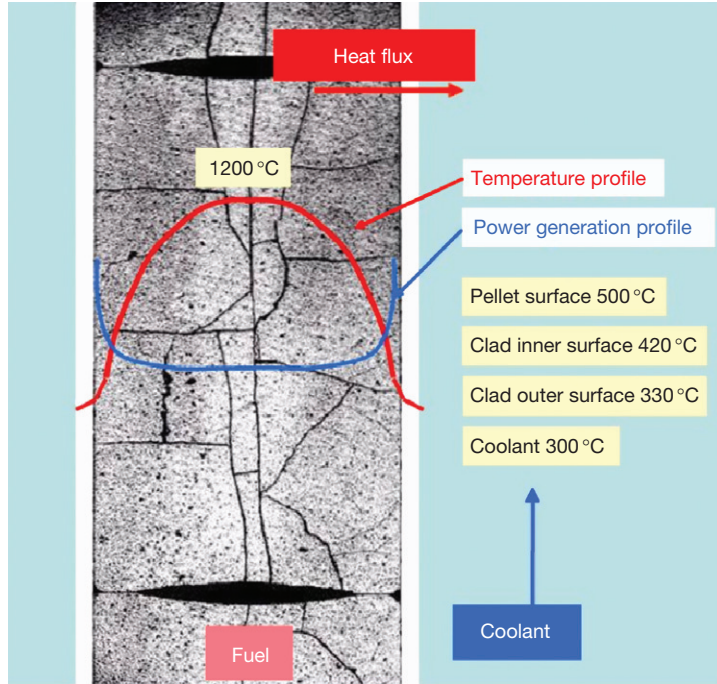


Figure 12 Temperature profile in light water reactor fuel during base irradiation.

occurs mainly in the rim and progressively participates in the energy production since ^{239}Pu is a fissile isotope; at the same time the ^{235}U concentration is decreasing. The consequence is a progressive shift toward the radial periphery of the power generation, which is beneficial as it decreases the center-line temperature for the same overall pellet power generation. An example of the evolution of the radial plutonium profile is given in [Figure 13](#), for three average pellet burnup values. This evolution depends obviously upon the initial pellet enrichment. The radial depletion first increases and then stabilizes as plutonium progressively contributes to the power generation. In a UO_2 fuel pellet, the lower is the initial enrichment in ^{235}U , the higher is the plutonium contribution to the power generation. Another power generation component is the γ -energy deposition due to photons from the surrounding fuel rods. This deposition can be considered uniform along the radius. The radial power generation in the MOX fuel is evaluated in the same way, accounting for the different isotopic composition of this particular fuel. Generally, radial depression is not so high in MOX fuel compared to UO_2 . Nevertheless, the same plutonium buildup is observed in the rim due to the

^{238}U self-shielding. Concerning the axial power distribution, it is generally considered uniform all along the pellet length.

- *The heat transfer between water coolant and cladding wall:* The heat transfer along a heated wall is somewhat complex depending upon the local water state: liquid, local nucleate boiling, formation of a vapor film, bulk boiling, or vapor.²² The water coolant flowing from the bottom to the top of the rod increases its average enthalpy along the cladding.

The calculation of the temperature drop between the cladding wall and the water coolant is given by:

$$\Delta T = \frac{\text{Plin}}{2\pi R_{\text{out}} H_{\text{film}}} \quad [5]$$

where Plin is the local linear power (W m^{-1}), R_{out} is the cladding outer diameter, and H_{film} is the limit layer conductance ($\text{m}^2 \text{W}^{-1} \text{K}^{-1}$), which depends upon the local regime: forced convection, boiling incipience, partial developed nucleate boiling, bulk boiling, critical heat flux, and vapor.^{23–25} In a PWR, the critical flux corresponds to the DNB regime and the formation of a local and stable insulator vapor film, preventing the total evacuation of the heat flux. In this situation, the subcooled fuel rod segment can

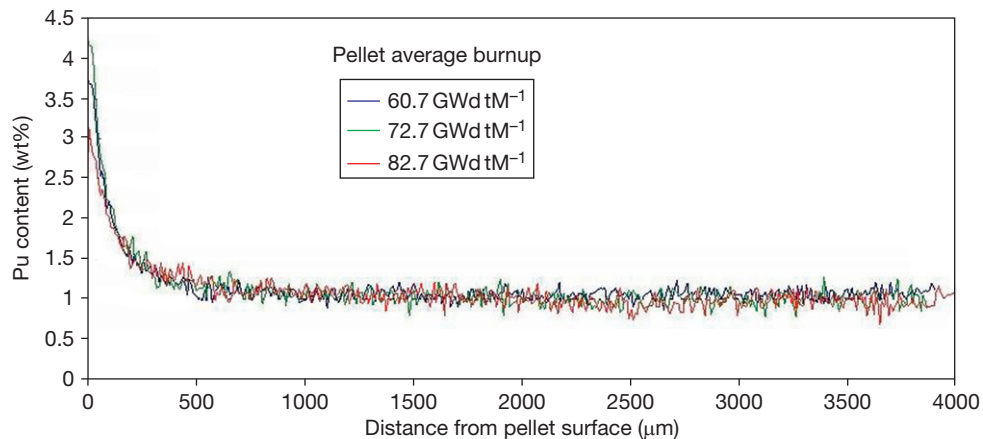


Figure 13 Electron probe microanalysis plutonium radial profile for three different average pellet burnup.

melt. In a BWR, exceeding the critical heat flux leads to dry-out, a condition where the cladding surface is cooled only by flowing steam. The surface temperature increases by several hundred degrees, and after some time, failure can follow by enhanced cladding creep and/or corrosion. The core management specifications and the reactor protections are obviously designed to avoid reaching such a situation at any location and at any time in the core.

- *The heat transfer through the cladding:* The heat transfer through the cladding is an easier task, resumed to the heat transfer through a metallic material layer. However, an oxidation reaction occurs with coolant water at the cladding surface, with the formation of a ceramic zirconia layer, that is, ZrO_2 . Since the heat conductivity of the oxide layer is much lower than that of the metal, the evolution of the oxide layer must be accounted for in the heat transfer analysis. Furthermore, the corrosion rate increases with temperature, that is, at the surface of the metal. Thus, there is a positive feedback between oxide layer thickness and growth, in particular in a PWR with its somewhat higher temperature regime. One design criterion sets a limit on the zirconia layer thickness corresponding to a maximum cladding (metal) wall thickness reduction of 10% (based on ASTM recommendations), corresponding to around 100 μm of oxide.

On the internal cladding wall, a thin zirconia layer can also develop after close contact with the fuel, that is, at medium-to-high burnup levels. This layer, however, never exceeds 10 μm because it is mainly based on a recoil implantation, and is very dense. Most of the time, this corrosion layer is therefore neglected in the heat transfer calculation.

- *The heat transfer in the pellet–cladding interface:* In the evaluation of the radial heat transfer, this part is the delicate point, since the temperature drop through the gap between the fuel pellets and the cladding depends on the gap width, which in turn depends upon the fuel pellet and cladding differential thermal and irradiation-driven expansion/contraction. Moreover, the fuel pellets have, first, no reason to be properly centered within the cladding, and second, cannot be considered as perfect cylinders since they crack into several pieces as soon as they are first heated (Figure 12). Therefore, when the gap is still open, calculations must account for fuel pellet fragments, partially in contact with the cladding and for heat transfer through a gas layer evolving in its composition with burnup. When the gap starts to close, the material surface roughness maintains a minimal gas layer, as long as no chemical interaction occurs. There are then three components in the gap conductance: the convection transfer, the radiative transfer, and the contact conduction. For the light gases such as helium or hydrogen, an extrapolation correction is added to the convection transfer to account for the capability of the gas to penetrate into the fuel. Empirical models are used to account for the pellet fragmentation to evaluate the fraction of the pellet surface in contact with the cladding.²⁶ In some particular conditions, when the fuel pellet temperature exceeds 1200 °C in the center, cesium or molybdenum transport can occur toward the gap with the formation of [U, O, Pu, Cs, Mo, Zr] compounds in the gap. These compounds are viscous above 400 °C.²⁷ Formed when the gap is firmly closed, they are usually neglected in the gap conductance calculation.

- The heat transfer in the fuel pellet:** The heat transfer along the fuel pellet radius is usually evaluated without considering any eventual radial crack. It can be justified by the slight temperature drop introduced, compared to the relatively large uncertainty in the fuel local power (often more than 10%). However, in one particular experiment (project High Burn-up Chemistry) involving annular pellets, the multiplication of such cracks due to a grain separation at the annulus surface led to a quick gas release, and hence, to a 500 °C increase of the centerline temperature at constant power.²⁸ There are two components of the ceramic conductivity: a phonon component dominant up to 2000 K, decreasing with temperature, and an electronic component increasing with temperature and dominant above 2000 K. The local fuel conductivity depends, in decreasing order, upon the temperature, the local porosity (volume and shape mainly), the oxygen potential (oxygen defects), the local burnup (fission products in solution, mainly number of point defects and density of dislocations), and probably weakly on the plutonium content up to 25%.^{29,30} These aspects are more detailed in **Chapter 2.17, Thermal Properties of Irradiated UO₂ and MOX**. The fuel conductivity decreases with burnup as shown in **Figure 14**. However, about 30% of this degradation is related to irradiation defects, which can be recovered during a local temperature increase.³¹

The Thermal conductivity of MOX fuel measured on fresh fuel is known to be about 8% lower than equivalent UO₂ fuel. However, for an average plutonium content not exceeding 15%, it is demonstrated that the degradation is not related to the plutonium content but more to the modification of the overall local

oxygen sublattice. Moreover, accounting for an equivalent degradation of the UO₂ fuel conductivity as soon as irradiation proceeds, due to the perturbation of the oxygen sublattice, it can be considered that the initial MOX fuel in-pile conductivity is close to the UO₂ conductivity. Then, the heterogeneity of the MOX fuel leads to a differential degradation between the phases with burnup, which must be accounted for.

The evolution of the heat capacity of UO₂ was studied within the Nuclear Fuel Industry Research group (NFIR III) project.³² The main conclusion was that the heat capacity is not strongly influenced by the burnup as such. However, in the cold parts of the fuel pellets, the accumulation of irradiation defects can lead to a strong exothermic behavior in case of sudden temperature increase (out of pile experiments). Nevertheless, after an experimental conducted by the UK Atomic Energy Agency within the third Nuclear fuel Industry Research Program (NFIR III), it was concluded that the observed phenomena cannot have any measurable impact for in-reactor studies. At this time, these conclusions are considered available for MOX fuel as well.

2.19.3.3 Mechanical Aspects

2.19.3.3.1 Base irradiation

The mechanical aspect is dominated by the interaction between a metallic cladding and fragmented ceramic fuel pellets. Originally, due to fabrication constraints, there is a remaining gap between the two materials to facilitate the introduction of the fuel stack in the tube. As soon as irradiation starts, the fuel pellets are fragmented in the radial axial direction, first in two pieces, then four, and so on,³³ as power increases (**Figure 15**). This fragmentation allows relaxing the energy induced by the thermal strain as soon as the cracking limit is achieved. This energy release tends to propel the fragments toward the cladding. This is called fragment delocalization. The consequence is that the apparent gap is reduced. At the beginning of life, the number of radial cracks range from 6 to 8 and 3 to 4 in the axial direction (**Figure 12**). The second and third generation of cracks is obviously of more random type than the first generation.

Then, as irradiation proceeds, the fragments are forced toward the center by the cladding creep down due to the coolant pressure (7–15.5 MPa, minus the internal gas pressure). Progressively, after maybe 100–200 days with a kinetics depending on many parameters (initial gap, power history, fuel, and cladding

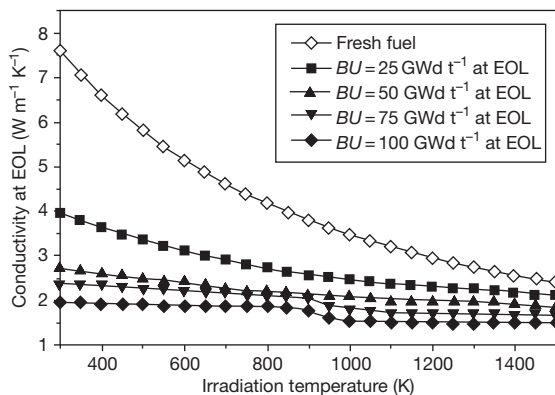


Figure 14 Evolution of the intrinsic UO₂ fuel thermal conductivity with burnup.

behavior), the cladding comes in hard contact with the fuel pellet fragments. Because of the very rough fragment surfaces, the relocation of the fragments, being pushed toward the center by cladding creep down, is resisted by their mutual interaction.³⁴ The repetitive movement of the fragments with the core power oscillations leads to a progressive wear of the fragment surfaces, which are then easier to relocate as shown in the French experiment 'RECOR'.³⁵ This period corresponds to a smooth pellet-cladding interaction.

Another aspect is the consequence of the steep radial temperature gradient in the fuel pellets, which leads to an 'hour-glassing' of the cylinder-shaped pellets (Figure 16). This hour-glassing effect is very locally amplified in the presence of the end 'dishing.' The consequence is a nonuniform gap closure along the pellet length with an earlier closure at pellet ends. Consequently, the pellet-cladding interaction starts at pellet-pellet interfaces, leading to the specific bamboo

shape observed on the cladding outer diameter axial profile (Figure 17). It is also called primary ridging. If total gap closure is not achieved, it can generate an axial rotation of the fragments (relocation). When hard contact is achieved all along the pellets, the maximum primary ridges measured range from 8 to 10 μm . The height obviously depends upon the pellet length, the fuel temperature gradient, and the eventual existence of end dishing in the design of the pellets. During a power ramp, if fuel temperature is locally high enough, gas swelling can occur, inducing an extra deformation of the pellet, which can be observed on spent fuel rods by the formation of secondary ridges at mid-pellet, sometimes actually more pronounced than the primary ridges at pellet ends (see Chapter 3.22, Modeling of Pellet-Cladding Interaction).

The fuel material is a porous ceramic obtained by powder pressing and then sintering at high temperature (generally in the range 1700–1800 °C).

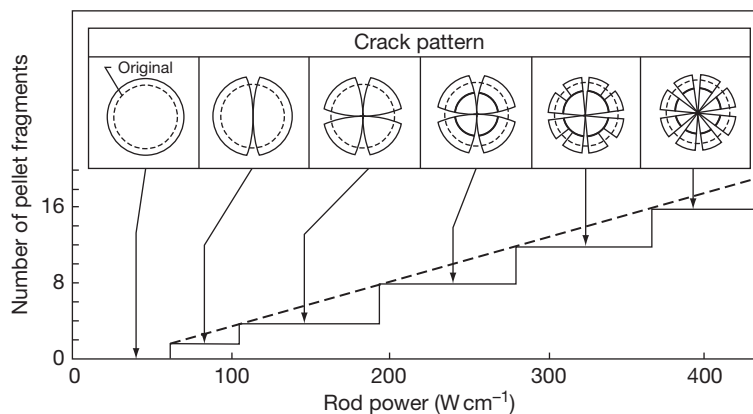


Figure 15 Changes in crack pattern during rise to power. Reproduced from Oguma, M. *Nucl. Eng. Des.* **1983**, 76, 35–45.

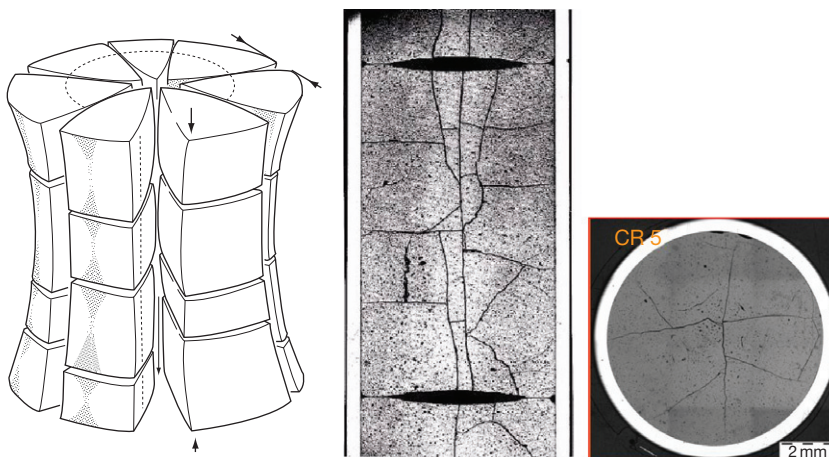


Figure 16 Pellet hour-glassing (theoretical fragmentation).

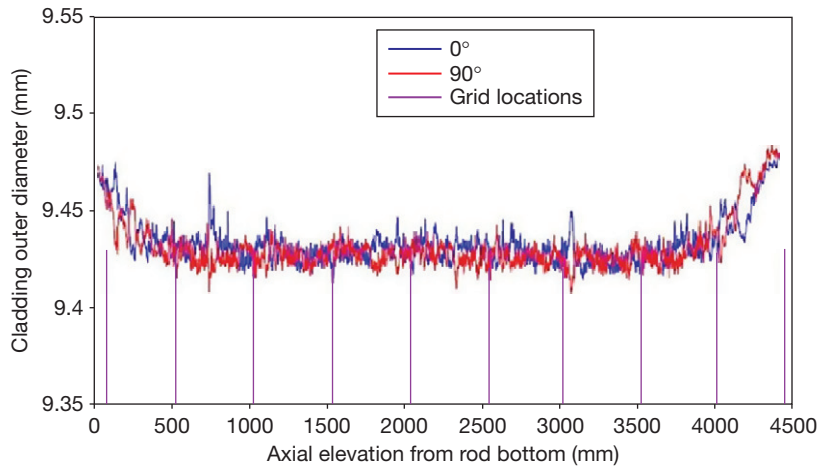


Figure 17 Fuel rod cladding diameter profile after irradiation, showing hour-glassing and a beginning mid-pellet ridge.

During the base irradiation, the fuel temperature is low enough not to activate additional thermal sintering. On the other hand, nonthermal sintering activation is possible. As addressed in [section 2.19.3.1](#) (and see [Chapter 2.18, Radiation Effects in UO₂](#)) a large number of atoms are displaced for each fission event. This energy is high enough to eliminate part of the remaining small porosity by reimplantation of vacancies from the pores to the bulk. This allows an in-pile sintering of the fissile material, which is called ‘densification.’³ Densification follows a logarithmic evolution with time. Simultaneously, the fuel material is swelling due to several phenomena: the accumulation of nonsoluble species, the accumulation of single or complex defects, the creation of new cells in the lattice, and the formation of precipitates. The combination of densification and swelling phenomena results in an increase of the density at beginning of life, and then a global swelling of the material. The maximum density and the kinetics depend upon the fuel powder used (e.g., spherical or nonspherical grains) and the manufacturing techniques (e.g., pressure for compaction, use of pore former). In LWR fuel, the fuel volumetric swelling rate is typically about 0.67% per at.%. For higher temperatures (>1200 °C), an additional swelling component is driven by the gas bubbles coalescence. This is called the gas swelling mechanism (see also [Chapter 3.20, Modeling of Fission-Gas-Induced Swelling of Nuclear Fuels](#)). We shall see further in this chapter that gas swelling can also be observed at high burnup and low temperature. Once again, in MOX fuel, all these

phenomena described here are induced in a heterogeneous manner, due to the multiphase character of the fuel material.

In base irradiation, the combination of cladding creep down and fuel swelling leads to a progressive contact, until the pellets are in hard contact with the cladding. This process stabilizes when the cladding outward creep rate balances the fuel pellets swelling. At this stage, cladding conditioning is reached locally. When a significant contact pressure has been established, interpenetration of species, mainly oxygen, occurs by fission recoil. In post irradiation examinations, one can detect the formation of zirconium oxide spots at the interface, at positions where the contact was strongly established during operation ([Figure 18](#)). With the propagation of such strong contact to all the interface, the zirconium oxide layer also propagates, and the species implantation as well, creating an effective chemical bonding between the two materials with [U, Pu, Zr, O, Cs, Mo] compounds. If the power then decreases suddenly, the gap is no longer able to reopen between the cladding and the fuel. This induces stress and cracks within the fuel pellet periphery. Hence, the reopening of the gap is indeed within the pellet itself.

On the other hand, when the initial gap has not been entirely closed, there is a combination of bonded spots and free sliding at the interface, with friction conditions in intermediate location. This has no effect during base operation but can induce strong shear strain on the cladding in case of a transient (see [Chapter 3.22, Modeling of Pellet–Cladding Interaction](#) on PCMI). Moreover, the presence of

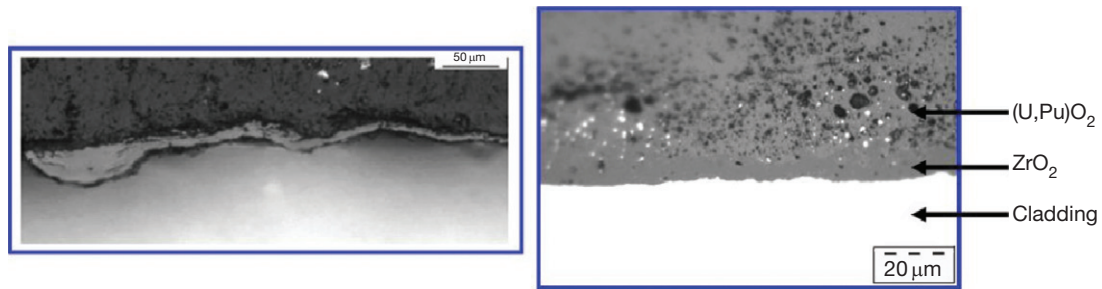


Figure 18 Zirconium oxide and complex phase formation on the cladding inner surface.

zirconium oxide spots can have a negative effect regarding the risk to failure, playing a role equivalent to an incipient crack.

2.19.3.3.2 Transient conditions

There are two families of transients to be considered (see also [Chapter 3.22, Modeling of Pellet–Cladding Interaction](#)):

- Normal transients, related, for example, to the controlled daily operation load follow in a PWR with a maximum core power rise rate of $3\% \text{ mn}^{-1}$ ($0.5 \text{ kW m}^{-1} \text{ mn}^{-1}$), or control rod shuffling in a BWR, leading to high local power increase rates. The local power along the fuel rods can vary in a wider range than the mean core power, mainly due to the effect of the control rods (in particular in a BWR) and the xenon delayed neutron absorption (^{135}Xe neutrons absorption) inherent to the control rod or blades withdrawal.
- The accidental transients with the possibility for the fuel rods to sustain a linear power increase rate of $10 \text{ kW m}^{-1} \text{ mn}^{-1}$ (class 2 accident) or an even higher rate, around $100 \text{ kW m}^{-1} \text{ mn}^{-1}$ in case of a reactivity insertion accident (RIA, class 4). When an abnormal core transient is detected by the protection chains, all emergency shutdown rods/blades are automatically inserted. In accidental conditions, immediately before the scram, fuel rods can be locally subject to a rapid and short transient with a maximum power depending upon their remaining reactivity ($40\text{--}50 \text{ kW m}^{-1}$). For the class 2 accident category, the fuel rods design and operating restraints are established to avoid any cladding failure. The reactor can then be restarted as soon as the origin of the transient is identified and remedied. The RIA accident is quite different, in that the assumption is made that a control rod assembly/blade is ejected/dropped and no more able to control the local reactivity.

During a fast power increase, the main mechanical loading of the cladding is related to the differential thermal expansion between the fuel and the cladding. Fuel and cladding have a similar thermal expansion coefficient but their temperatures are very different. The cladding remains within the range of $350\text{--}400^\circ\text{C}$, while a range $850\text{--}1250^\circ\text{C}$ is applicable for the fuel stack average temperature. The temperature gradient in the fuel ranges from 175 to $375^\circ\text{C mm}^{-1}$. This has several consequences:

- The hour-glassing phenomenon is amplified.
- The radial cracks in the fuel pellets are opening in the hoop (circumferential) direction, inducing a hoop shear stress on the cladding inner surface.
- The central part of the pellet passes from a purely elastic behavior to a viscoplastic behavior. In some cases, fuel material is able to flow in the axial direction, filling partly or totally the dishing.
- Fission gases are able to move quickly and precipitate in intergranular and then intragranular bubbles, leading to a massive gas swelling and to a possible resintering process under the induced compressive stress.

The PCI/PCMI processes, well analyzed in the GONCOR analytical experiment performed in the SILOE reactor,³⁶ is the following:

1. During a power rise, the thermal expansion of the pellet is straining the cladding. The level of the final hoop stress induced on the cladding depends upon the status of the gap previous to the ramp. When the contact is already established prior to the ramp (conditioned situation), the maximum stress is achieved. Due to the pellet hour-glassing, the initial stress is higher at the pellet-to-pellet interface than at mid-pellet. At this stage, several possibilities are to be considered: the closure is achieved only locally at pellet ends, the gap closure is total, or an intermediate

situation involving friction. The initial ovality of the cladding and the presence of a radial crack both favor a strain localization/concentration on the cladding inner surface.

2. The end of the ramp is the critical period for inducing a potential cladding failure. Some volatile and corrosive species such as iodine, cadmium, or bromine, released by the fuel pellets during the ramp, can lower the resistance of the clad material to stress-corrosion cracking (SCC) and help induce incipient cracks (① in Figure 19). If the local strain is high enough, the crack can propagate (②) with a rate proportional to the power 9 of the stress intensity factor K_{ISCC} of the material. Initially, propagation is also facilitated by the presence of corrosive species, for example, iodine, but if/when the effective stress (σ_{real}) becomes higher than the ultimate stress of the cladding, a ductile shear causes crack propagation throughout the cladding (③). Often the first, SCC-driven part of the propagation is mainly intergranular.
3. The increase of the hoop stress of the cladding induces creep-out of the tubing, which gradually relaxes the stress. The stress relaxation is amplified by fuel creep in the central, hot, and viscous part of the pellets. At the same time, the fission gases start to precipitate in bubbles in the hottest part of the pellet $>1100^\circ\text{C}$, inducing a swelling of the material. As the gas swelling proceeds, it increases the hydrostatic strain in the fuel material and then accelerates the axial creep toward the dishes. The creep tends to a resintering of the hottest part of the pellet. Nevertheless, the fuel swelling leads to an increase of the pellet diameter. The GONCOR experiment has shown that the

kinetics of all these processes are quicker at the pellet ends than at mid-pellet probably because the interaction stress is achieved earlier and is higher at the pellet end (effect of hour-glassing).

4. Finally, the swelling kinetics lead within 20 mn to the formation of secondary ridges at mid-pellet, which are larger than the primary ridges with heights ranging between 40 and 60 μm .

Figure 20 summarizes the process described above. The largest risk of PCI failure occurs within a few minutes after the ramp initiation and the failure is most likely to happen at the pellet-to-pellet interface (second drawing). There is no relationship to the final height of the secondary ridges (fourth draw). The code simulations account also for the fragment relocation.^{37–39}

The RIA accident is a quasiadiabatic process accounting for the ramp rate and its overall duration (1 mn maximum). No diffusion processes or creep strains are involved due to the short duration. Cladding failure can be achieved by a quasiuniform strain applied by the fuel on the cladding, exceeding the ultimate strain capability. The sudden change in the dimension of the fuel pellets is due to the quick thermal expansion, a reversed radial power generation, and the induction of grain separation provoked by the increase of the pressure of the fission gases accumulated in the grain boundaries. The main question is not how the pellets are loading the cladding

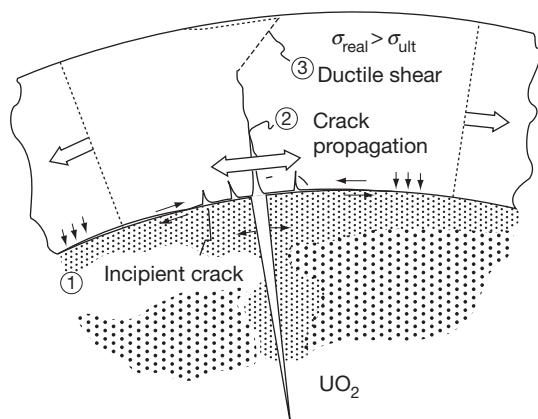


Figure 19 Mechanisms leading to leading failure.

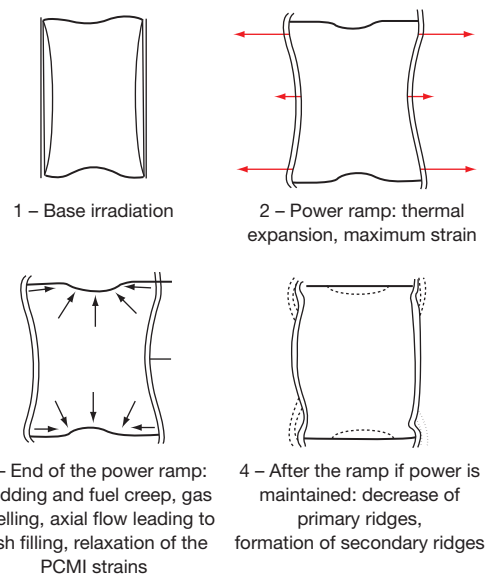


Figure 20 Summary of the process induced by the power ramp.

tube, but whether the cladding material is able to sustain the near-instantaneous strain. The RIA international projects have shown that the fuel enthalpy leading to clad failure is decreasing with the irradiation level of the material. Looking closer, it was demonstrated that the oxide thickness was the main parameter, probably because it is associated with hydrogen pickup. Hydrogen can reduce the strength and ductility of the cladding, in particular when the hydrides are reoriented in the radial direction. With modern, carefully optimized cladding materials, the hydrogen pickup is highly reduced, compared to earlier variants.

2.19.3.4 Material Microstructure and Chemistry

The temperature range of a fuel pellet in normal operation is within a range of 500–1200 °C. These temperatures are not high enough to initiate any grain growth. On the other hand, during accidental transient, the temperatures can reach 2000 °C at the pellet center. The grain growth mechanism then activated is an equiaxial growth.⁴⁰ In most conditions of operations, activation of columnar grain growth with the formation of a central hole is not likely to occur such as in FBR fuels.

A great variety of fission products are produced by the fission, covering a large part of the Mendeleyev table. The fission yields for each species are related to the fissile isotope concerned: ^{235}U or ^{239}Pu mainly. **Figure 21** shows that the yield distribution is ‘camel back shaped’ with two maxima.

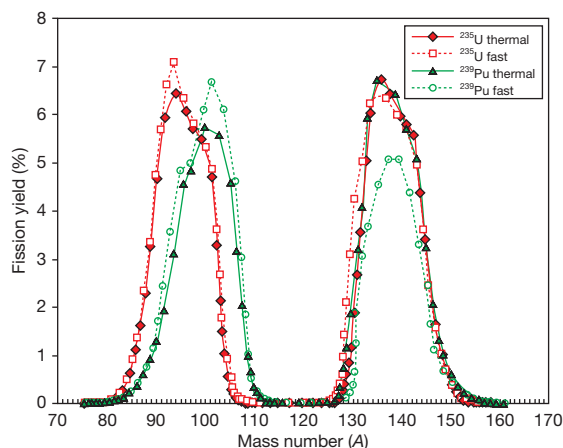


Figure 21 Fission yields for ^{235}U and ^{239}Pu .

The fission typically leads, indeed, to the appearance of two fragments in a mass ratio about 1/3–2/3. The highest production is for zirconium, molybdenum, xenon, cerium, and neodymium with a yield higher than 10% of the overall fission products. Nearly 20 species are over the 1% value and are easy to detect after irradiation using EPMA analysis. The yield of these species is slightly different between ^{235}U and ^{239}Pu with a higher production of xenon for ^{239}Pu .

The stabilization of the fission products after slowing down by ionization, and then collision cascades, depends upon their chemical affinities and their size. In terms of localization, the EPMA allows characterizing $1\ \mu\text{m}^3$ volumes, which gives no indication on an eventual heterogeneity at a lower scale. Moreover, most of the fission products are nonstable isotopes continuously decaying after their creation into other chemical species. The evidence then depends upon the decay chain; some local and temporary association of species is likely to happen. The fission products can roughly be divided in four groups,⁴¹ however, with a variability depending upon the local temperature and partial oxygen pressure:

- The fission products in solution in UO_2 , meaning that they are located in the UO_2 lattice replacing a uranium or plutonium atom. These are typically Rb, Sr, Y, Zr, Nb, Te, Cs, Ba, La, Ce, Pr, Nd, Pm, Sm, and Eu.
- The fission products able to form isolated ceramic precipitates, such as Rb, Sr, Zr, Nb, Mo, Cs, and Ba.
- The fission products forming metallic precipitates, such as Mo, Tc, Ru, Rh, Pd, Ag, Cd, In, Sn, and Sb.
- And finally, the gaseous and volatile fission products, able to diffuse and precipitate in bubbles when the local temperature is exceeding their respective threshold diffusion energy: Xe, Kr, Br, and I.

Figure 22 summarizes these chemical affinities in the Mendeleyev table. Obviously, this description is simplified and the reality is a bit more complex since various fission products are able to react with each other to form compounds depending upon their chemical equilibrium diagrams versus temperature. Some of these compounds, such as CsI , can be volatile. Others such as Cs_2UO_4 are stable up to 800 °C and viscous above 400 °C.²⁷ Cesium and Molybdenum are mobile in the temperature gradient when the local temperature exceeds 1200 °C. In that case, these species move generally toward the pellet

minimum displacement rate per heavy atom is once every two days and once a day for oxygen. However, the crystal structure is maintained. Due to transmutation, the local material has limited relationship with the initial fuel material and the average chemical composition depends on radial location. Moreover, as soon as the fuel starts irradiation, the oxygen sublattice is modified. Most of the physical properties are sensitive to oxygen sublattice defects. Therefore, all these processes have to be accounted for in the evaluation of the local properties.

For MOX fuels, due to the heterogeneity in the plutonium distribution (see **Chapter 2.15, Uranium Oxide and MOX Production**), and therefore, power generation, one must account for the different phases in the material evolution:

- Rich plutonium agglomerates
- UO_2 particles with low plutonium content
- Intermediate phases

Experiencing different fission densities, this leads to a differential evolution of the phase parameters, mainly local burnup (as shown in **Figure 23**), dislocation density, chemical composition, gas, and metallic precipitates.

Implantation processes because of recoil nevertheless tend to reduce slightly the heterogeneity between the phases. The heterogeneity brings a non-uniformity in the fission products distribution, and therefore, has an effect on the overall material properties. Moreover, the high burnup transformation (**Section 2.19.4.2**) starts earlier in the plutonium agglomerates due to their higher burnup, for a same average pellet burnup.

2.19.4.2 Low Temperature Restructuring (HBS)

When thermal recovery is not sufficiently efficient, the accumulation of defects at high burnup can lead to the instability of the crystalline structure, initiating a restructuring driven by the energy stored in the material. In the cold regions of the fuel, operating at temperatures lower than 800–900 °C, no thermal diffusion should usually be expected. However, a non-thermal phenomenon was demonstrated in the 1980s in the first LWR high burnup fuels.⁴³ It was then widely studied during the next 20 years. To be correct, it must be mentioned that a first observation was already reported by Bleiberg *et al.*⁴⁴ in the 1960s in FBR fuels.

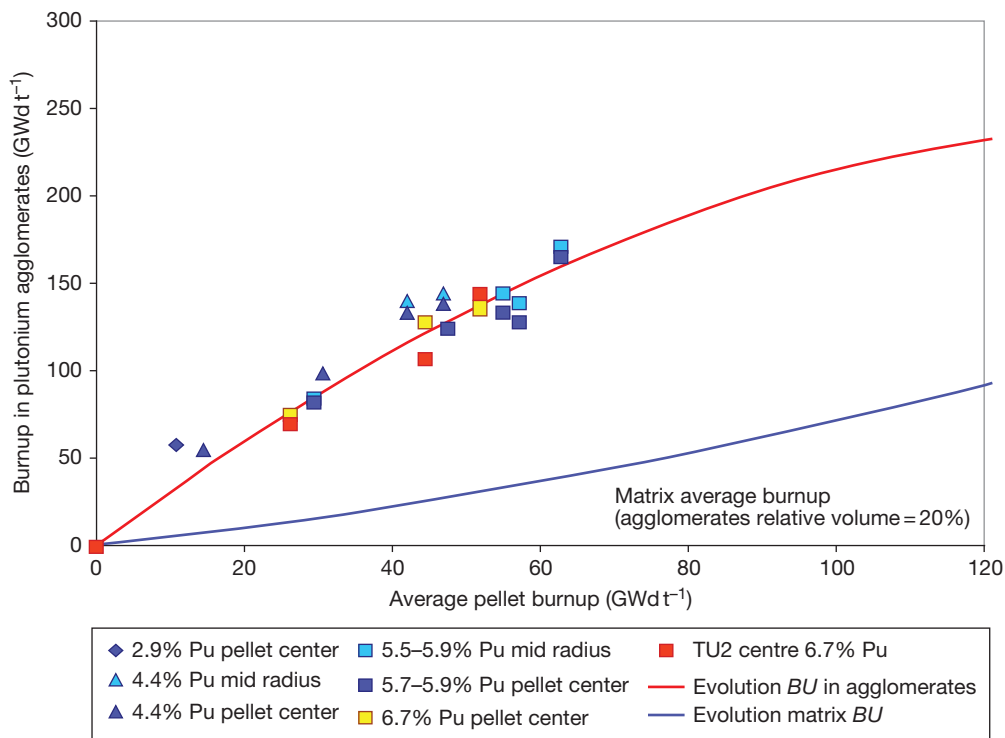


Figure 23 Mixed oxides fuels – evolution of the phase burnup assuming two phases: agglomerates rich in plutonium spread in a UO_2 matrix.

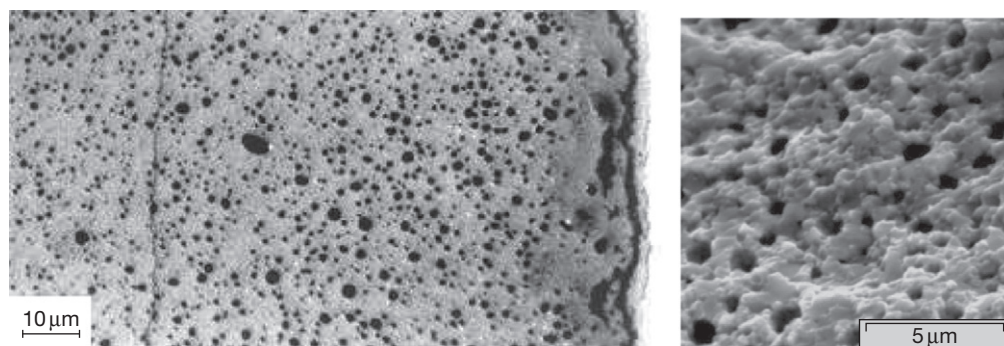


Figure 24 High burnup structure transformation with the apparition of a micrometric and dense porosity, accompanied by a grain subdivision.

A low temperature transformation is observed beyond a local burnup evaluated around 55–60 MWd kgM⁻¹, with the appearance of a micrometric and dense porosity, generally accompanied by a grain subdivision (Figure 24), with average nanograin size ranging from 200 to 500 nm. This phenomenon was firstly called ‘Rim effect’ since it started in the neutron self-shielded part of the fuel pellet (radial periphery).

The more recent state of understanding is described by Baron *et al.*,⁴⁵ but a large number of good publications are focused on the analysis of the phenomenon,^{11,19,42,46–49} or more recently by multi-scale approach.⁵⁰ As a complement to the national survey programs, HBS was investigated in several international parametric experimental studies, mainly the following projects: High Burn-up Effect Program (HBEP),¹⁰ High Burn-up Rim Project (HBRP),^{11,51–53} HBRP_NT,¹⁵ and some new projects such as New Cross over Project (NXO)⁵⁰ and F-Bridge.⁵⁴ Simplifying, the HBS transformation can be considered evolving into four phases, as follows:

- **Phase 1:** Construction of a periodic network. It initiates as soon as the irradiation is started. In order to understand the very beginning of the process, two scales must be considered, nanometric scale with the construction of an entangled dislocation network,²⁰ and micrometric scale with the construction of a periodic network of planar defects, often observed on optical and scattering electron microscopy (SEM) pictures with sizes ranging between 1.5 and 2 μm.
- **Phase 2:** Loss of gas detection in EPMA characterization. The gas starts to precipitate in 10–100-nm-sized bubbles, which grow progressively. At this stage, the apparent xenon diffusion coefficient has increased.

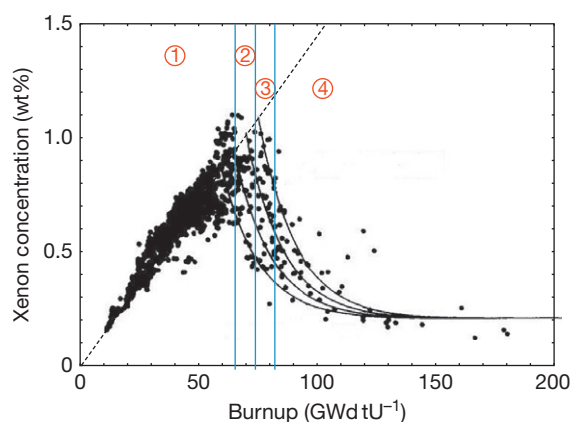


Figure 25 Electron probe microanalysis xenon detection versus local burnup in pressurized water reactor UO₂ fuel pellets. Reproduced from Lassmann, K.; Walker, C. T.; Van de Laar, J.; Lindström, F. J. *Nucl. Mater.* **1995**, 226, 1–8.

- **Phase 3:** The 10–100-nm-sized bubbles are growing to finally achieve micrometric sizes, trapping more and more gases. At the end of the process, EPMA is no more able to detect more than 20% of the created gases, which are however still retained in the fuel (Figure 25).
- **Phase 4:** Grain subdivision propagation. It really starts when the micrometric porosity is already well underway, inducing a polygonization process⁵⁵ favored by the defect-cleaning of the crystal. It was demonstrated that the final bubble density has an influence on the subdivision kinetic process.

Several models were developed and published to simulate HBS transformation during the last 15 years.^{56–61} They are obviously still improving with the evolution of the comprehension of the mechanisms involved at the atomic scale.

Obviously all this material restructuring has a strong effect on the material properties and the structural interactions. The increase of the relative porosity volume degrades the material conductivity but increases the viscosity and reduces the mean grain size. On the other hand, the intragranular irradiation defect-cleaning improves the fuel intrinsic thermal conductivity.⁶² The presence of viscous phases on the grain boundary can be expected, which also improves the material overall viscosity in a pellet-cladding interaction scenario. All these aspects are understood to explain the demonstrated good behavior of high burnup fuel rods regarding PCI/PCMI in accidental ramps. The HBS structure also has a very particular behavior regarding the fission gas release processes,⁶³ showing a metastable behavior for normal operating temperature, and a very distinct temperature threshold around 1500 K, beyond which the HBS bubble content is quickly released.

In MOX fuel, the HBS transformation appears earlier during the second year of irradiation, due to the higher burnup in the Pu-rich agglomerates as shown in [Figure 26](#). The rich agglomerates exhibit a large micrometric porosity when the rest of the material is still not restructured. It was demonstrated from EPMA and SIMS analysis that the gases are still trapped in the bubbles such as in the UO₂ rim. However, in some rare cases, agglomerates can also release most of the gases when it is crossed by a crack. This phenomenon is related to the fact that the recoil distance is of the same order as the crack distance, the crack being an efficient sink for the fission products. The HBS transformation can occur deeply within

the pellet, toward the mid-radius, depending upon the radial temperature profile in base irradiation.

For higher pellet average burnup, all phases are concerned by the fuel restructuring in the pellet rim as is the case in UO₂ fuels. The main difference is the presence of restructured agglomerates deep within the pellet radius. This particularity obviously gives a sensitivity of these MOX fuels to the thermal fission gas release during transients.

2.19.4.3 Behavior of the Gaseous and Volatile Fission Products

The fission gas release and the fuel gaseous swelling mechanisms are extensively described by Olander,³ and in [Chapter 3.22, Modeling of Pellet–Cladding Interaction](#) and [Chapter 4.01, Radiation Effects in Zirconium Alloys](#). The last International Atomic Energy Agency (IAEA) seminar focused on this subject was held in Cadarache (France) in 2000.⁶⁴

The behavior of gaseous and volatile fission products is one of the major concerns in the LWR fuel design, as it affects the dimensional stability of the fuel and the evolution of the rod inner pressure. Moreover, some volatile fission products such as cesium, iodine, and tellurium are aggressive for the Zircaloy fuel rod cladding, that is, can help induce a PCI failure. Xenon has the largest fission yield, for uranium as well as for plutonium, that is, about 30% of the overall fission products. Krypton has a fission yield a decade lower than xenon. Both are considered non-soluble in the fuel matrix and need a trivacancy (one metallic atom and two oxygen) to accommodate their

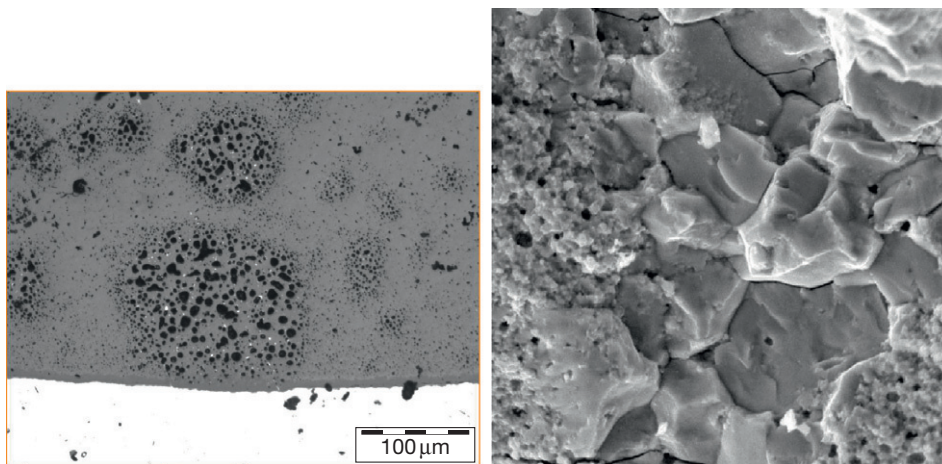


Figure 26 Mixed oxides fuels – high burnup structure restructuring firstly in the plutonium-rich agglomerates optical image on the left and MEB fractography on the right.

volume, inducing however a local deformation of the lattice. In order to relax the internal energy, the trend for these gaseous fission products is to migrate and precipitate in traps such as bubbles or grain boundaries. The higher the temperature, the faster is the diffusion. The bubble's behavior is not fully understood up to now. A fraction of the fission products precipitate (solid and gaseous). These precipitates are initiation points for nanobubble formation and growth, enabled by a flow of vacancies. These bubbles become traps for the gaseous fission products, moving both by thermal diffusion and nonthermal processes; they recoil when the atom is produced directly by the fission event or ejection when the kinetic energy is transferred by colliding processes. These nonthermal processes can also knock out partly the gas located inside a bubble or even destroy a tiny bubble. This is called the resolution process.

At low temperature, the activation of nonthermal processes are dominating, filling slowly and progressively the grain boundaries with all kinds of fission products (not only gaseous) and leading to a low level gas release from the fuel by percolation along the grain boundaries or recoil processes close to the free surfaces. This fission gas release level is strongly related to the level of the open porosity (ratio of the surfaces to the volume). The instantaneous fission gas release fraction can be calculated by the following equation⁶⁵:

$$\frac{R}{B} = \frac{1}{4} \frac{S_g}{V} \mu_f + \frac{S_t \mu_f \alpha_U \dot{F}}{V 4 \lambda N_U} \quad [7]$$

where $\frac{R}{B}$ is the instantaneous fission gas release: ratio release to birth, S_g geometrical surface of the fuel

pellet (m^2), S_t developed fuel pellet surface (m^2), V pellet volume (cm^3), μ_f average fission fragment free path (m), α_U number of fission fragments, N_U number of uranium atoms per volume unit (m^{-3}), \dot{F} instantaneous fission density (fission $m^{-3} s^{-1}$), and λ decay constant for the considered species.

Note that the first term represents the recoil phenomenon, independent of the decay constant λ , and the second term the knockout process, inversely dependent on the decay constant.

At higher temperature (above $800^\circ C$), thermal diffusion starts dominating as evidenced in [Figure 27](#). At intermediate temperatures, the major process is an atomic diffusion of gases. However, vacancies are moving faster than the gas atoms, contributing to bubble formation and growth, both within the grains and on grain boundaries. Bubbles are efficient traps for gas atoms, but grain boundaries are also efficient sinks, even if a small fraction can eventually return through the grain surface by knockout processes (a few microns).

Grain boundaries are efficient traps, not only for gases but also for solid fission products and vacancies. These elements mechanically weaken the grain boundaries and pins the bubbles. Tiny bubbles first appear and grow. This can be seen in [Figure 27](#) (left SEM image on a smoothly polished surface) where bubbles are aligned mainly along the grain boundaries. The right picture in [Figure 27](#) is a SEM observation of a fractured surface showing a large bubble precipitation on the grain surfaces.

Bubbles are then able to interconnect, progressively building tunnel-like mazes eventually able to open to the edge of the fuel grains, allowing the available gases in the grain boundaries to escape.⁶⁶

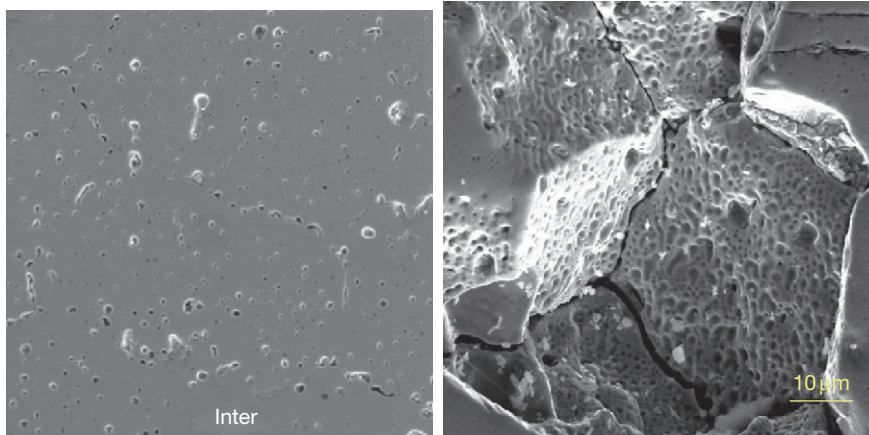


Figure 27 Bubble formation and coalescence at grain boundaries.

In **Figure 27** (right picture) this bubble coalescence is evidenced by the appearance of oblate bubbles on the grain surfaces. The growth and coalescence of bubbles induces a gaseous swelling of the material as long as the gases are not efficiently released.

In a simplified approach, the Fick equation can be used to describe gas diffusion within the grains. It includes five components corresponding to five separate mechanisms:

- Gas isotope yield
- Atomic gas diffusion
- Isotope decay
- Gas trapping in bubbles
- Gas resolution from bubbles

$$\frac{\partial C}{\partial t} = \gamma \dot{F} + \frac{1}{r^2} D \frac{\partial}{\partial r} r^2 \left(\frac{\partial C}{\partial r} \right) - \lambda C - \sum_j g_j C + \sum_j b_j M_j \quad [8]$$

where C is isotope concentration at time t and radius r (mol m^{-3}), r radius in the grain (m), \dot{F} instantaneous fission density ($\text{fission m}^{-3} \text{s}^{-1}$), λ decay constant for the considered species (s), g_j trapping efficiency for type j trap, b_j resolution coefficient from type j trap, M_j gas concentration in type j trap (mol m^{-3}), and D gas diffusion coefficient ($\text{m}^2 \text{s}^{-1}$).

The xenon diffusion coefficient in the fuel matrix under irradiation is usually described with three terms representing the temperature contribution, the nonthermal mechanisms (recoil and knockout)

and the influence of the vacancies creation under irradiation (mixed term)^{67–69} (**Figure 28**):

$$D_{\text{Xe}} = D_{\text{th}} + D_{\text{ath}} + D_{\text{mix}} \quad [9]$$

The thermal contribution is:

$$D_{\text{th}} = 7.6 \times 10^{-10} \exp \left[-\frac{35225}{T} \right] \quad [10]$$

The pure nonthermal contribution is:

$$D_{\text{ath}} = 6.10^{-40} \dot{F} \quad [11]$$

With a mixed term for vacancies:

$$D_{\text{mix}} = 1.39 \times 10^{-24} \frac{\sqrt{\dot{F}}}{2} \exp \left[-\frac{13870}{T} \right] \quad [12]$$

In the simplified approaches, the gas behavior on grain boundaries is not directly described. The diffusion equation is solved in a theoretical sphere, the radius of which decreases with burnup, as grain boundaries progressively open due to gas and fission products accumulation.^{70,71} The minimum value is reached when it becomes equivalent to the local average grain size of the material. In steady-state conditions, the solution of the differential equation gives³:

$$f = \frac{3D}{\lambda a^2} \left[\left(\frac{\lambda a^2}{D} \right)^{1/2} \coth \left(\frac{\lambda a^2}{D} \right)^{1/2} - 1 \right] \quad [13]$$

where a is the radius of the Booth sphere (m) and f is the fraction of fission gases released.

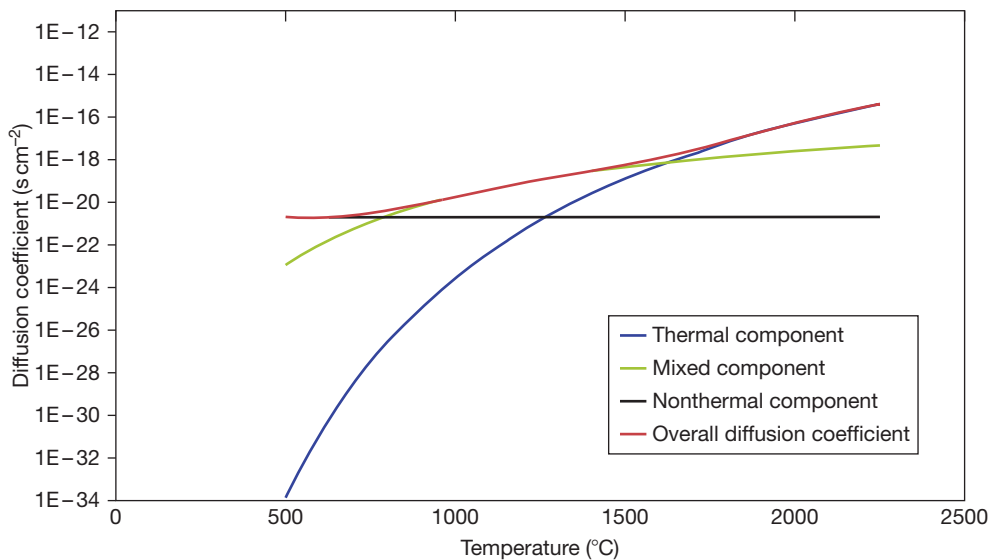


Figure 28 Turnbull diffusion coefficient.

Assuming $\left(\frac{\lambda a^2}{D}\right)^{1/2} \gg 1$, then it comes:

$$f = 3 \left(\frac{D}{\lambda a^2} \right)^{1/2} \quad [14]$$

It shows that the gas thermal diffusion is reversely proportional to $\lambda^{1/2}$.

More advanced models now exist such as the MARGARET model by the Commissariat à l'Énergie Atomique (CEA), describing in detail all the different processes within the grains and in the grain boundaries, involving atomic gas diffusion and bubble growth and coalescence in order to accurately simulate fuel swelling and fission gas release.⁷² Experimental characterizations combining mainly SIMS analysis and EPMA are still being improved in order to validate these models in terms of gas repartition between matrix and bubbles and between the inside of the grains and the grain boundaries. Attempts are also being made to experimentally evaluate the gas pressure in bubbles as a function of their size.

Fission gas release remains generally quite low during LWR base operating conditions (see Figure 29) as long as the centerline temperature does not exceed the Vitanza *et al.*⁷³ threshold power. The 'Vitanza curve,' also called 'Halden threshold,' is an experimental curve originally used to monitor the Halden reactor irradiations. For a given fuel rod burnup, it gives the linear heat generation rate (kW m^{-1}) for which the fission gas release level exceeds 1% of the fission gas produced.

The thermally activated release is indeed a threshold mechanism. Beyond this threshold, fission gas release increases by about 3% per 100 °C on the fuel centerline temperature. The empirical Vitanza curve has a meaning for burn-up ranging from 0 to 60 GWJ tM^{-1} , as long as fuel restructuring (HBS formation) stays limited and the fuel fragmentation is also limited.

Even if gases are not released, they progressively accumulate in the grain boundaries as burnup proceeds, weakening them. They are directly available for release in case of grain boundary separation such as during RIA transients. This grain separation is provoked by sudden power variations inducing large local micrometric stress fields. Thermally speaking, in UO_2 fuels, the centerline temperature is however always close or slightly over the temperature for which thermal diffusion starts, mainly during the first two years of operation.

Obviously, the fission gas release fraction in an LWR fuel rod can reach higher values in case of accidental transients, with a maximum of 50% at power levels around 500 W cm^{-1} . Such power levels are not achievable at high burnup because of the reactivity decrease.^{9,10}

MOX fuels generally exhibit a higher fission gas release in base operating conditions or during accidental transients due to the fact that their activity is still high at high burnup (Figure 30). However, the heterogeneity slows down the fuel conductivity degradation and therefore the fission gas release rate increases with burnup. The HBS structure in the agglomerates and the specific behavior of the

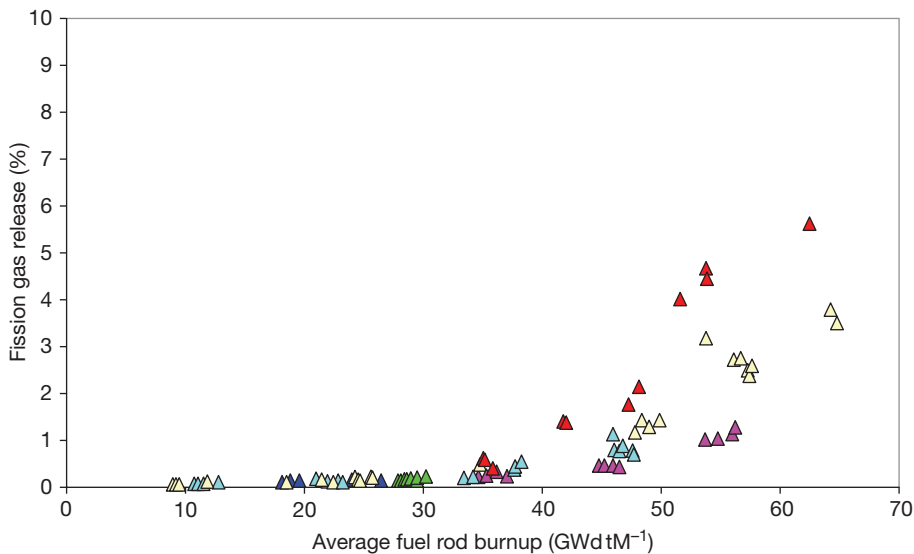


Figure 29 Fission gas release in UO_2 -pressurized water reactor fuel rods during normal operating conditions.

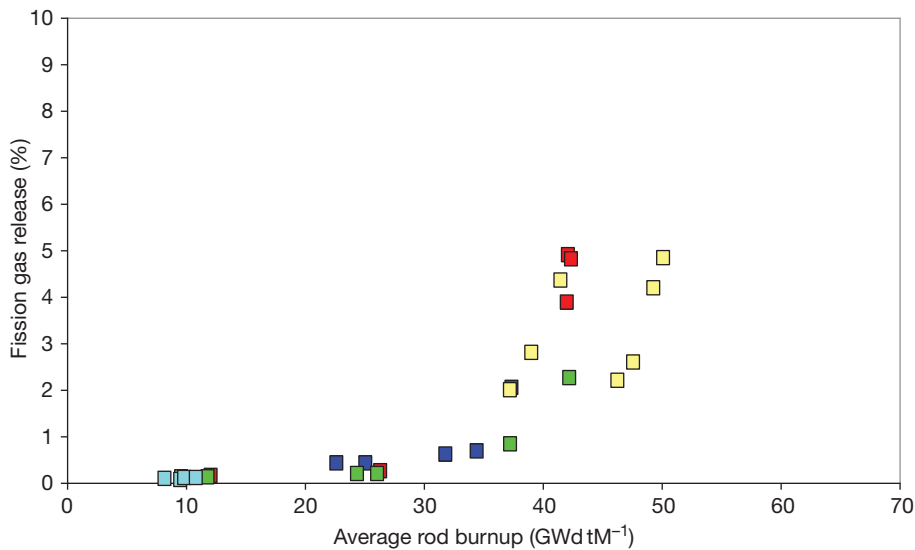


Figure 30 Fission gas release in mixed-oxides-fuel-pressurized water reactor fuel rods during normal operating conditions.

restructured material gives a higher sensitivity to the temperature of the MOX fuel compared to UO_2 . The restructured phases tend to release 80% of the gas as soon as the local temperature passes beyond a threshold temperature evaluated from Knudsen cell evaluation in a range of 1100–1300 °C.^{45,63} In UO_2 fuel, the rim region never reaches this temperature during normal or incidental transients. This is obviously the same for the MOX rim region. On the other hand, the restructured agglomerates located at mid-radius can be concerned. This is the reason for the sensitivity of MOX fuel with temperature regarding fission gas release.

We have earlier mostly spoken of usual volatile and gaseous fission products. In UO_2 fuels, helium production during irradiation is low enough to be neglected. For MOX fuel, due to the high α -production, it cannot be ignored any more with regard to the evolution of the gas pressure in the free volumes. During irradiation, a large number of heavy isotopes are issued from capture or fission, decays producing one or several α -emission. Due to the presence of higher isotopes range in MOX fuels (plutonium 239, 240, 241, 242, americium, and curium), these fuels exhibit a high α -emission, even out of pile (see Section 2.19.2.2.1). In fact, there are three modes of helium production:

- 68% is α -decay of heavy actinides (^{238}Pu for 4%, ^{244}Cm for 21%, ^{242}Cm for 75%)
- 25% is (n, α) reactions on ^{16}O
- 7% is ternary fissions (fission combined with an α -decay)

The helium behavior in the fuel during irradiation is slightly different of xenon or krypton due to its very small size which does not interact strongly with the fuel lattice. Helium can infuse easily in the fuel material, in the existing pores and bubbles, and in the grain boundaries. There is obviously no difference between the helium produced and the initial helium pressurized during fuel rod fabrication. During transient, helium is released faster than the heavy noble gases. This requires a specific modeling of the helium behavior in the simulation of the MOX fuels.

2.19.4.4 Evolution of the Oxygen Potential

Uranium or plutonium fission produces fission fragments and releases two oxygen atoms. Most of these oxygen atoms are able to recombine with the fission products when they stabilize in the fuel matrix. This is not the case for the gaseous atoms (about 30% of the fission products), and in particular, the noble gases which tend to precipitate. This is also true for the noble metals. Depending upon the considered species, in the operating temperature range, they can be mono-, bi-, tri-, or quadrivalent. Moreover, more complex oxides can be formed with molybdenum, barium, cesium, etc. Figure 31 shows the equilibrium oxygen potentials for different metal/metal-oxide mixtures.⁴²

This leads to a quite slow, global increase of the oxygen potential as burnup proceeds.^{42,74,75} The oxygen potential ($\Delta G(\text{O}_2)$) data for LWR fuel is

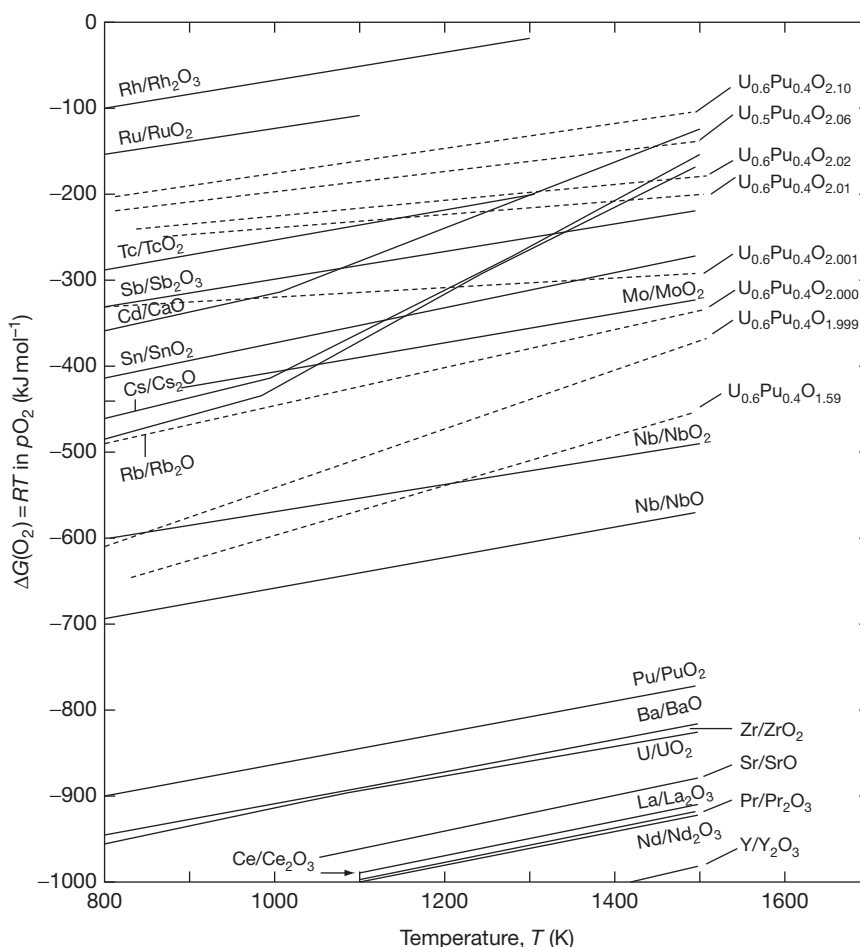


Figure 31 Free energy formation of the main fission products oxides compared to $U_{0.6}Pu_{0.4}O_{2+x}$, for various x values. $U_{0.6}Pu_{0.4}O_{2+x}$ phase is here considered representative of the fuel state at high burn-ups. It shows that Cs, Rb, and Mo oxidation depends upon the fuel oxygen potential. Reproduced from Spino, J.; Peerani, P. *J. Nucl. Mater.* **2008**, 375, 8–25.

generally measured by the EMF method. The data analyzed by Spino *et al.* shows that at a burnup higher than 80 MWd kgM^{-1} up to 100 MWd kgM^{-1} , the UO_2 fuel tends to become slightly hyperstoichiometric (Figure 32). The maximum O/M ratios potentially achieved at 100 MWd kgM^{-1} would range only between 2.001 and 2.002, accounting for an initial O/M in fabrication between 2.000 and 2.005. The causes for this relative hyperstoichiometric shift are attributed to the stagnation of the oxygen uptake by the cladding and the stagnation of the molybdenum oxidation. These conclusions are obviously very dependent upon the power history of the LWR fuel. For more details, fission product chemistry is described more extensively in Chapter 2.20, Fission Product Chemistry in Oxide Fuels.

2.19.4.5 Evolution of the Properties

Most of the physical properties of the fuel change as irradiation proceeds. This is mainly due to the modification of the oxygen sublattice, the lattice defect accumulation, and the incorporation of many fission products. When burnup increases, despite the high mobility of the atoms by colliding cascades, the fuel matrix accumulates lots of defects and fission products, which are more or less restored depending upon the fuel local temperature (for more details see Chapter 2.18, Radiation Effects in UO_2). The fuel porosity also evolves locally by densification (resintering processes) or gas precipitation. Due to metallic and ceramic precipitations, the material becomes a multiphase system. Moreover, the grain

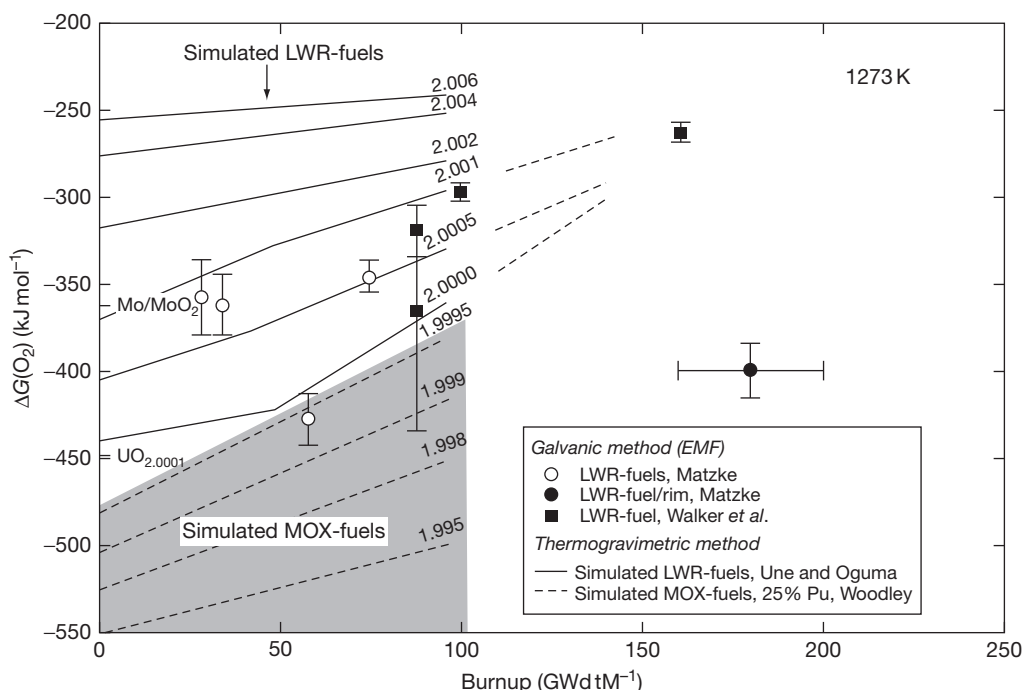


Figure 32 Compilation of oxygen potential versus burn-up. The oxygen potential found for irradiated fuel is consistent with nearly stoichiometric simulated LWR and MOX fuels. Reproduced from Spino, J.; Peerani, P. *J. Nucl. Mater.* **2008**, 375, 8–25.

boundaries are drastically modified with the accumulation of bubbles and fission products. All these factors lead to a global modification of the physical and mechanical properties of the fuel material. Fuel conductivity and heat capacity are described in **Chapter 2.17, Thermal Properties of Irradiated UO_2 and MOX**. Concerning the fuel mechanical properties, a lot of data have been acquired for fresh fuel. Compressive tests or three-point bending tests have allowed developing thermal creep models. Such mechanical testing cannot be performed on irradiated fuel because of the fuel fragmentation and the steep radial gradient in the properties. Only micro-hardness tests were performed since 1994, mainly by Institute for Transuranium Elements (ITU).⁷⁶ New techniques are proposed in the ITU hot laboratories in collaboration with EDF R&D to assess these properties⁷⁷: focused acoustics operating at 230 MHz for the local elastic properties and microindentation in controlled atmosphere from room temperature up to 1200 °C.

The fuel density evolves with the fuel densification and solid swelling and with the gaseous swelling. **Figure 33** shows a gradual decrease of the density with burnup. The reality is that in LWR, the density decrease follows roughly the solid swelling rate up to

55 MWd kg⁻¹ and then accelerates as soon as gas precipitates, mainly in the rim region or at the pellet center.

2.19.5 Limiting Phenomena

Concerning the limiting phenomena, some criteria are established for the UO_2 fuel design. Engineering must demonstrate that all sensible parameters stay within the criteria at any time from the loading to the reprocessing or during the fuel assembly storage as well. The performance limiting phenomena are:

1. *Cladding oxidation and hydriding*: Concerning the ZrO_2 formation at the cladding surface, the criterion is initially related to the ASTM criterion of a maximum cladding wall thickness reduction of 10%, which corresponds to an oxide thickness of the order of 100 μm . (The zirconia density is lower than the Zircaloy density: 6.6 g cm⁻³ compared to 7.7 g cm⁻³.) Another aspect is to avoid the zirconia's spalling, which could induce local cold points at the cladding surface leading to hydrogen accumulation by diffusion and a mechanical weakening. The second aspect of corrosion is the hydrogen pickup, leading to precipitation of hydrides near

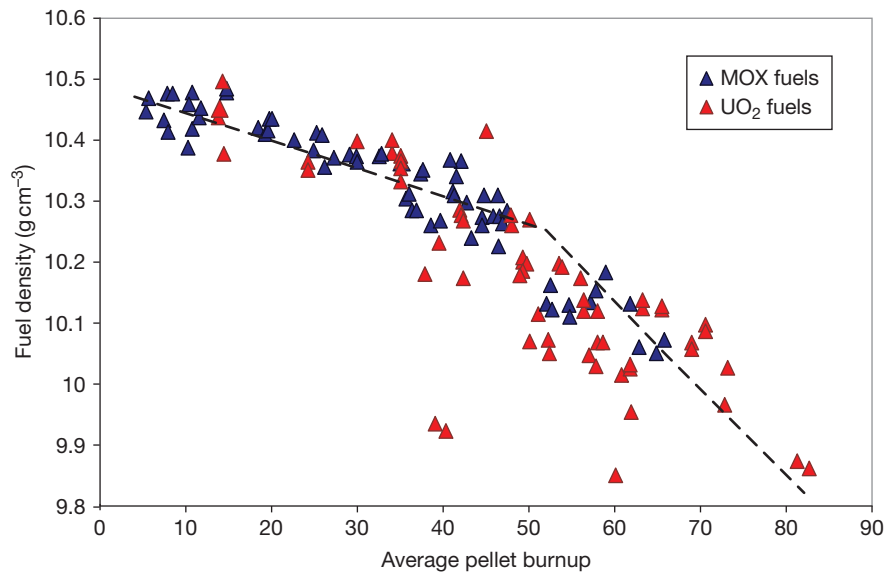


Figure 33 Evolution of the average fuel density with burnup.

grain boundaries, usually in the hoop direction. Hydrides can degrade the mechanical properties of the cladding, in particular, when there is a radial reorientation of the hydrides.

2. *Fuel rod internal pressure:* Reopening of the radial gap between the fuel stack and the cladding must be avoided to ensure at any time the heat transfer to the coolant. Otherwise, fuel overheating and excessive fission gas release can occur, ultimately leading to fuel failure. The original criterion required that the gas inner pressure must never exceed the outer coolant pressure. This criterion is quite conservative and has usually been replaced by a 'nonlift-off' criterion, that is, the radial creep-out of the cladding, driven by gas pressure in excess of the system pressure, must never exceed the expansion rate of the pellet associated with increasing burnup. Thus, the nonlift-off criterion ensures that the pellet-cladding gap does not open at high burnup. Experiments have shown that a large overpressure of the gas (considerably more than 5.0 MPa) is needed to initiate the reopening.
3. *Cladding wear:* The criterion on cladding wear at the contact between grid spring and dimples and the fuel rod is often also related to the ASTM criterion of a maximum cladding wall thickness reduction of 10%. Experience shows that considerably more wear is technically acceptable, that is, it will not cause failure due to local weakening of the cladding wall.
4. *Cladding elongation and assembly bow:* During irradiation, the nonisotropic character of the Zircaloy material and the preferential migration of vacancies and interstitial in specific lattice planes drive an overall cladding axial growth, activated by the neutron fast flux. This can lead to fuel rod bow with pitch reduction between the rods, reducing thermal margins. Differential elongation of guide tubes in a PWR assembly can lead to an overall assembly bow, problematic for assembly reloading, and affecting local power in fuel rods at the assembly periphery. For BWR fuel, the same mechanism can cause fuel channel deformation, 'channel bow,' leading to local thermal margin reduction, interference with control rod operation, as well as other issues. These phenomena are closely surveyed, and improvements in design and material have been, and are being, introduced to mitigate.
5. *Power to melt:* In LWR reactors, the use of uranium dioxide or MOX allows a comfortable power to melt margin. The uranium dioxide melting temperature is 2850 °C for UO₂ and quite similar for MOX fuels. This temperature decreases slowly with burnup due to the dilution with a large number of fission products. It however remains above 2750 °C. To achieve such temperatures, the linear heat rate must reach 700 W cm⁻¹, not realistic with the fuel initial reactivity. At very high burnup, above 50 MWd kg⁻¹, due to the fuel thermal conductivity decrease, the power to melt was evaluated around 600 W cm⁻¹.

within the High Burn-up Chemistry Project. This criterion is verified at any time of the irradiation.

6. *Pellet-clad (mechanical) interaction (PCI/PCMI)*: There is no imposed safety criterion on this aspect. The risk of failure by PCI/PCMI is a complex process with a maximum risk when the fuel pellet to clad gap starts to close firmly and the reactivity of the fuel is still high, that is, in the 30 MWd kg⁻¹ U range. The process is outlined in [Section 2.19.3.3.2](#). This risk is mainly monitored by the pellet fragments behavior able to induce a shear strain on the cladding and by the chemical interaction kinetic at the interface.

The control blade operation at power typical for a BWR creates a more severe PCI/PCMI challenge than in a PWR. Therefore, typical BWR fuel features a cladding liner, that is, a thin layer of a dilute, very ductile Zr alloy on the inside of the cladding. Such a liner creates a substantial additional margin to PCI failure.

2.19.6 Conclusions

The performance of uranium dioxide or MOX fuels in LWR nuclear reactors is very well established. These fuels have demonstrated a very good behavior during irradiation, favored by their high melting temperature, giving large operating temperature margins. Some progress is still needed in the characterization of the mechanical properties of irradiated fuel samples. Experimentally, this is a tricky problem to solve, accounting for the drastic fuel pellet fragmentation and the steep radial gradient in the nuclear fuel properties evolution. Microindentation and focused acoustic techniques, able to characterize micrometric-sized fields on irradiated fuel samples, are now potentially available in the ITU hot laboratories.

Due to the mild operating conditions compared to FBR reactors, the uranium dioxide matrix retains most of the fission products, even at very high burnup, up to 300 MWd kgM⁻¹.⁴⁸ The local fuel power variability is higher in BWR than in PWR, due to an axial gradient in the neutron spectrum and control blade operation. For these reasons, BWR fuel has evolved with the use of a PCI liner barrier. The addition of minor quantities of softening elements to the fuel (chromium, niobium, alumino-silicates) is expected to increase PCI margins in both BWR and PWR fuel. Moreover, these additives favor manufacturing large grain fuels in order to delay

the release of corrosive volatile fission products during power transient. The new and improved zirconium alloys first introduced in the 1980s allowed achieving higher discharge burnups due to a reduction of the cladding oxidation and hydrogen pickup.

As the use of uranium dioxide is universal, very efficient international projects such as NFIR, SCIP, HBEP, HBRP, and HRP, etc., have provided the modelers in the past with useful basic data or brought good insights for mechanisms' comprehension. With the incredible progress in computer capability and the large improvement in the knowledge base regarding the mechanisms involved in the fuel during irradiation, very efficient tools are now available for fuel design. Modeling is still in progress, shifting progressively to multiscale approaches, or fundamental atomic calculations to evaluate parameters not attainable, up to now, by experimental characterization (see [Chapter 1.08, *Ab Initio* Electronic Structure Calculations for Nuclear Materials](#); [Chapter 1.10, Interatomic Potential Development](#); [Chapter 1.11, Primary Radiation Damage Formation](#); [Chapter 1.12, Atomic-Level Level Dislocation Dynamics in Irradiated Metals](#); [Chapter 1.13, Radiation Damage Theory](#); [Chapter 1.14, Kinetic Monte Carlo Simulations of Irradiation Effects](#); [Chapter 1.15, Phase Field Methods](#); [Chapter 1.16, Dislocation Dynamics](#); [Chapter 1.17, Computational Thermodynamics: Application to Nuclear Materials](#); and [Chapter 1.18, Radiation-Induced Segregation](#)).

References

1. Odelli, O.; Edsinger, K. Optimum cycle length and discharge burnup for nuclear fuel – comprehensive study for BWRs and PWRs, phase 1: Results achievable within the 5% enrichment limit; EPRI Technical Report 1003133; 2001.
2. Gauld, I. C.; Parks, C. V. Review of technical issues related to predicting isotopic compositions and source terms for high-burn-up LWR fuel; NUREG/CR-6701 ORNL/TM-2000/277.
3. Olander, D. R. Fundamental aspects of nuclear reactor fuel elements, TID-26711-P1; Technical Information Center, Office of Public Affairs, Energy Research and Development Administration, 1976.
4. Bailly, H.; Menessier, D.; Prunier, C. *The Nuclear Fuel of Pressurized Water Reactors and Fast Reactors*; Collection du Commissariat à l'Energie Atomique, Lavoisier: Paris, 1999.
5. Reynolds, A. B. *Bluebells and Nuclear Energy*; Cogito Books: Madison, WI, 1996; ISBN: 0-944838-63-451353705.
6. Stüdsvik, X. The Studsvik OVERRAMP Project; EPRI Report NP-3007, Research Project 1026-1; Apr 1983.

7. Djurle, S. Final Report of the SUPERRAMP Project; STSR-33; Stüdsvik, Dec 1984.
8. Lavake, J. C.; Gaertner, M. High Burn up PWR Ramp Test Program (DOE); Final Report DOE/ET/34030-10; Dec 1984.
9. Barner, J. O.; Cunningham, M. E.; Freshley, M. D.; Lanning, D. D. High Burnup Effects Program – Summary Task 2; HBEP-45; Battelle Pacific Northwest Laboratories, 1985.
10. Barner, J. O.; Cunningham, M. E.; Freshley, M. D.; Lanning, D. D. High Burnup Effects Program – Final Report; HBEP-61; Battelle Pacific Northwest Laboratories, 1990.
11. Kinoshita, M.; *et al.* HBRP – Final Report; Mar 2001.
12. Kinoshita, M.; Matsumura, T.; Kameyama, T.; Kitajima, S.; Kolstad, E.; Matzke, H. High Burnup Rim Project, Irradiation Program to Study Rim Structure Formation – Outline and Preliminary Analysis. In *EHPG Meeting*, Bolkesjo 10/31–11/4; 1994.
13. Sonoda, T.; Matzke, H.; Kinoshita, M. High Burnup Rim Project (IV) Threshold Burn Up of Rim Structure Formation. In *EHPG Meeting*, Loen, Norway, May 1999.
14. Kinoshita, M.; Kameyama, T.; Kitajima, S.; Matzke, H. *J. Nucl. Mater.* **1998**, 252, 71–78.
15. Kinoshita, M.; Kameyama, T. HBRP_NT – Final Report No. 2; Juillet, 2005.
16. Blanpain, P.; Arslan, M.; Porsch, D.; Mollard, P.; Castelli, R.; Goll, W. AREVA advanced MOX fuel assembly design and manufacturing. In *2008 Water Reactor Fuel Performance Meeting*, Seoul, Korea, Oct 19–23, 2008.
17. Soullard, J. Contribution à l'étude des défauts de structure dans le bioxyde d'Uranium. Ph.D. Work Presented on Oct 8, 1976; faculté des Sciences de Poitiers, Report CEA-R-4882 CEN Fontenay-aux-roses.
18. Garrido, F. Crystallochemistry of anion-excess fluorite-type uranium oxides. In *4th NXO Meeting, Accelerator and Computer Science to Study Fission Irradiation on Fuel Materials*, Tokyo University, Tokyo, Japan, Nov 13–14, 2007.
19. Spino, J.; Papaioannou, D. *J. Nucl. Mater.* **2000**, 281, 146–162.
20. Nogita, K.; Une, K. *Nucl. Instrum. Methods Phys. Res. B* **1994**, 91, 301–306.
21. Lassmann, K.; Walker, C. T.; van de Laar, J. *J. Nucl. Mater.* **1998**, 255, 222–233.
22. Nukiyama, S. *J. Jpn. Soc. Mech. Eng.* **1934**, 37, 367.
23. Mac Adams, W. H. *Heat Transmission*; McGraw-Hill: New York, 1954.
24. Kreith, F.; Bohn, M. S. *Principles of Heat Transfer*; West: Eagan, MN, 1993.
25. Marshall, T. D.; Youchison, D. L.; Cadwallader, L. C. *Fusion Technol.* **2001**, 39(2), 849–855.
26. Mac Donald, P. E.; Weissman, J. *Nucl. Technol.* **1976**, 31, 357.
27. Berton, J. P.; Baron, D.; Coquerelle, M. Chemical stability and physical properties of caesium uranates. In *IAEA TCM*, Tokyo, Japan, Oct 29–Nov 1, 1996.
28. Baron, D.; Couty, J. C. A simulation of the temperature overshoot observed at high burn-up in annular fuel pellets. In *IAEA TCM on Water Reactor Fuel Element Modelling at High Burn-up and Its Experimental Support*, Windermere, Sept 19–23, 1994.
29. Lucuta, P. G.; Matzke, H.; Hastings, I. J. *J. Nucl. Mater.* **1996**, 232, 166–180.
30. Baron, D. About the modelling of the fuel thermal conductivity degradation at high burn-up, accounting for recovering processes with temperature. In *IAEA TCM on Thermal Performance of (High Burn-up) LWR Fuel*, Cadarache, France, Mar 2–6, 1998.
31. Gomme, R. A.; Yagnik, S. Understanding of thermal diffusivity recovery with thermal annealing; EPRI TR 111068; Oct 1998.
32. Gomme, R. A.; Yagnik, S. Specific heat measurements and post-test characterization of irradiated and unirradiated urania and gadolinia doped fuel; EPRI Report TR 1000946; Dec 2000.
33. Oguma, M. *Nucl. Eng. Des.* **1983**, 76, 35–45.
34. Callu, C.; Baron, D.; Ruck, J. M. EDF fragment relocation model based on the displacement of rigid bodies. In *International Conference on CANDU Fuel*, Toronto, Canada, Sept 21–25, 1997.
35. Caillot, L.; Delette, G.; Julien, B.; Couty, J. C. Impact of pellet fragmentation on pellet-cladding interaction in a PWR fuel rod: Results of the RECOR Experimental Programme. In *14th International Conference on Structural Mechanics in Reactor Technology (SMIRT 14)*, Lyon, France, Aug 17–22, 1997.
36. Garcia, Ph.; Struzik, C.; Agard, M.; Louche, V. *Nucl. Eng. Des.* **2002**, 216, 183–201.
37. Garcia, Ph.; Moyné, M. Modelling the steady state and transient mechanical behaviour of fuel rods. In *14th International Conference on Structural Mechanics in Reactor Technology (SMIRT 14)*, Lyon, France, Aug 17–22, 1997.
38. Helfer, T.; Garcia, Ph.; Ricaud, J. M.; *et al.* Modelling the effect of oxide fuel fracturing on the mechanical behaviour of fuel rods. In *NEA-IAEA Seminar on Pellet-Clad Interaction in Water Reactor Fuels*, Aix-en-Provence, France, Mar 9–11, 2004.
39. NEA-IAEA. In *Seminar Proceedings on Pellet-Clad Interaction in Water Reactor Fuels*, Aix-en-Provence, France, Mar 9–11, 2004; NEA/OCDE Seminar Proceedings.
40. Ainscough, J. B.; Oldfield, B. W.; Ware, J. O. *J. Nucl. Mater.* **1973**, 49, 117–128.
41. Kleykamp, H. *J. Nucl. Mater.* **1985**, 131, 221–246.
42. Spino, J.; Peerani, P. *J. Nucl. Mater.* **2008**, 375, 8–25.
43. Baron, D. Abnormal porosity buildup in the fuel periphery at high burnup. In *9th HBEP Review*, Wengen, Switzerland, Jun 9, 1986.
44. Bleiberg, M. L.; Berman, R. M.; Lustman, B. In *Proceedings Symposium on Radiation Damage in Solids and Reactor Materials*; IAEA: Vienna, 1963; pp 319–428.
45. Baron, D.; Kinoshita, M.; Thevenin, Ph.; Largenton, R. *Nucl. Eng. Technol.* **2009**, 41(2), 199–214.
46. Spino, J.; Baron, D.; Coquerelle, M.; Stalios, A. D. *J. Nucl. Mater.* **1998**, 256, 189–196.
47. Lozanno, N.; Desgranges, L. *J. Nucl. Mater.* **1998**, 257, 78.
48. Spino, J.; Baron, D.; Papaioannou, D.; Ray, I. Rim formation and fission gas behaviour: Some structural remarks. In *IAEA/NEA Seminar on Fission Gas Behaviour in Water Reactor Fuels*, Cadarache, France, Sept 26–29, 2000.
49. Noirot, J.; Desgranges, L.; Lamontagne, J. *J. Nucl. Mater.* **2007**, 372, 318–339.
50. Kinoshita, M.; Yasunaga, K.; Sonoda, T.; *et al.* *Nucl. Instrum. Methods Phys. Res. B* **2009**, 267, 960–963.
51. Kinoshita, M. High Burnup Rim Project, (II) Progress of irradiation and preliminary analysis. In *Proceedings of Enlarged HPG Meeting*, Loen, Norway, May 19–24, 1996; HPR-347, OECD Halden Reactor Project.
52. Kinoshita, M.; Kitajima, S.; Kameyama, T.; Matsumura, T.; Kolstad, E.; Matzke, H. High Burnup Rim Project, Progress of irradiation and preliminary analysis. In *Proceedings, 1997 International Topical Meeting on Light Water Reactor Fuel Performance*, Portland, OR, Mar 2–6, 1997; pp 530–535.

53. Kinoshita, M.; Sonoda, T.; Kitajima, S.; *et al.* In *Proceedings of International Conference on LWR Fuel Performance*, Apr 9–14, 2000; ANS: Park City, UT, 2000; pp 590–603.
54. F-Bridge Project, Basic Research for Innovative Fuel Design for GEN IV Systems, Annexe1 – Description of the Work, Seventh Framework Programme Euratom, European Commission, 2008.
55. Matzke, H.; Kinoshita, M. *J. Nucl. Mater.* **1997**, *247*, 108–115.
56. Baron, D.; Hermitte, B.; Piron, J. P. An attempt to simulate the porosity build-up in the rim at high burn-up. In *IAEA TCM on Advances in Pellet Technology for Improved Performance at High Burn-up*, Tokyo, Japan, Oct 28–Nov 1, 1996.
57. Kinoshita, M. *J. Nucl. Mater.* **1997**, *248*, 185–190.
58. Likhanskii, V. V.; Khoruzhii, O. V.; Sorokin, A. A. Physical model of rim-layer formation in UO_2 fuels. In *International Workshop on the High Burn-up Structure in Nuclear Fuels*, ITU, Karlsruhe, Jun 28–30, 2004.
59. Rest, J. *J. Nucl. Mater.* **2004**, *326*, 175–184.
60. Rest, J. *J. Nucl. Mater.* **2005**, *346*, 226–232.
61. Khvostov, G.; Novikov, V.; Medvedev, A.; Bogatyr, S. Approaches to modeling of high burn-up structure and analysis of its effects on the behaviour of light water reactor fuels in the START-3 fuel performance code. In *2005 Water Reactor Fuel Performance JNS-ENS-ANS Meeting*, Paper 1104, Kyoto, Oct 2–6, 2005.
62. Ronchi, C.; Sheindlin, M.; Staicu, D.; Kinoshita, M. *J. Nucl. Mater.* **2004**, *327*, 58.
63. Hiernaut, J. P.; Wiss, T.; Colle, J. Y.; *et al.* *J. Nucl. Mater.* **2008**, *377*, 313–324.
64. NEA-IAEA. In *Seminar Proceedings on Fission Gas Behaviour in Water Reactor Fuels*, Cadarache, France, Sept 26–29, 2000; NEA/OCDE Seminar Proceedings.
65. Lewis, B. J. *J. Nucl. Mater.* **1986**, *148*, 28–42.
66. Walker, C. T.; Knappik, P.; Mogensen, M. *J. Nucl. Mater.* **1988**, *160*, 10–23.
67. Turnbull, J. A.; Friskney, C. A.; Findlay, J. R.; Johnson, F. A.; Walter, A. J. *J. Nucl. Mater.* **1982**, *107*, 168–184.
68. Rest, J.; Hofman, G. L. In *Fundamental Aspects of Inert Gases in Solids*; Donnelly, S. E., Evans, H. H., Eds.; Plenum: New York, 1991; p 443.
69. Harding, J. H.; Martin, D. G. *J. Nucl. Mater.* **1989**, *166*, 223–226.
70. Booth, A. H. A method of calculation of fission gas diffusion from UO_2 fuel and its application to the X-2-F loop test; Canadian Report CRCD-721; Sept 1957.
71. Booth, A. H.; Rymer, G. T. Determination of the diffusion constant of fission xenon in UO_2 crystals and sintered compacts; Canadian Report, AECL-692; Aug 1958.
72. Noirot, L. In *MARGARET an Advanced Mechanistic Model of Fission Gas Behavior in Nuclear Fuel – Water Reactor Fuel Performance Meeting*, Kyoto, Japan, Oct 2005.
73. Vitanza, C.; Kolstad, E.; Graziani, U. In *Proceedings of ANS Topical Meeting – Fission Gas Release from UO_2 Pellet Fuel at High Burn-up, Light Water Reactor Fuel Performance*, Portland, OR, 1979; ANS: La Grange Park, IL, 1979; pp 361–366.
74. Matzke, H. *J. Nucl. Mater.* **1994**, *208*, 18.
75. Matzke, H. *J. Nucl. Mater.* **1995**, *223*, 1.
76. Spino, J.; Cobos-Sabate, J.; Rousseau, F. *J. Nucl. Mater.* **2003**, *322*, 204–216.
77. Baron, D.; Masson, R.; Gatt, J. M.; Spino, J.; Laux, D. Evolution of the nuclear fuel mechanical properties with burn-up: An Extensive European Experimental Program. In *2005 Water Reactor Fuel Performance JNS, ENS-ANS Meeting*, Kyoto, Japan, Oct 2–6, 2005.

2.20 Fission Product Chemistry in Oxide Fuels

B. J. Lewis and W. T. Thompson

Royal Military College of Canada, Kingston, ON, Canada

F. C. Iglesias

Candesco Corporation, Toronto, ON, Canada

© 2012 Elsevier Ltd. All rights reserved.

2.20.1	Introduction	516
2.20.1.1	General Characteristics of Thermal and Fast Reactor Fuels	518
2.20.1.1.1	Plutonium distribution	518
2.20.1.1.2	Radial dependence of fuel stoichiometry after irradiation	518
2.20.1.2	Fission Product Classifications in Irradiated Fuels	518
2.20.2	Chemical State of Fission Products in Irradiated Oxide Fuels	522
2.20.2.1	Experimental Techniques	523
2.20.2.1.1	Electron probe microanalyzer	523
2.20.2.1.2	Laser-induced breakdown spectroscopy	524
2.20.2.1.3	Auger electron spectroscopy	524
2.20.2.1.4	Secondary ion mass spectrometry	524
2.20.2.1.5	Elastic recoil detection	525
2.20.2.1.6	X-ray techniques	525
2.20.2.2	Postirradiation Observations	526
2.20.2.2.1	Volatile fission products	526
2.20.2.2.2	Distribution and segregation of fission products	527
2.20.2.2.3	Reaction of fission products with the Zircaloy cladding	528
2.20.2.2.4	Oxygen in the Zircaloy cladding	528
2.20.3	Thermodynamic Modeling Methods	529
2.20.3.1	Gibbs Energy of Formation and Minimization Techniques	529
2.20.3.2	Uranium–Oxygen Binary System	529
2.20.3.3	Phase Diagram Studies of Fission Products in Oxide Fuels	533
2.20.3.3.1	Solutes in UO_2	534
2.20.3.3.2	Noble metals	535
2.20.3.3.3	Nonfluorite oxide phases	535
2.20.3.3.4	‘Other’ metallic phases (UPd_3 – URh_3 – URu_3)	536
2.20.3.3.5	Establishing the fuel inventory for equilibrium calculations	537
2.20.3.3.6	Validation experimentation	537
2.20.4	Defective Fuel Behavior	537
2.20.4.1	Fuel Oxidation Phenomena	538
2.20.4.2	Aqueous Fuel and Fission Product Behavior	538
2.20.5	High-Temperature Fuel and Fission Product Behavior in Accident Condition	541
2.20.6	Conclusion	544
References		544

Abbreviations

AES	Auger electron spectroscopy
CANDU	Canada Deuterium Uranium
CCD	Charge-coupled device
CEA	Commissariat à l’Energie Atomique
EAC	Environmental-assisted corrosion
EDS/EDX	Energy dispersive X-ray spectroscopy

EPMA	Electron probe microanalyzer
ERD	Elastic recoil detection
ESCA	Electron spectroscopy for chemical analysis
FBR	Fast breeder reactor
FLHT	Full-length high temperature
FP	Fission product

FPT	Fission product tests
HI	Horizontal induction
JAEA	Japan Atomic Energy Agency
LIBS	Laser-induced breakdown spectroscopy
LIF	Laser-induced fluorescence
LOFT	Loss-of-Fluid Test
LWR	Light water reactor
NRA	Nuclear reaction analysis
ORNL	Oak Ridge National Laboratory
PBF	Power Burst Facility
PIXE	Particle-induced X-ray emission
PWR	Pressurized water reactor
SCC	Stress corrosion cracking
SFD	Severe Fuel Damage
SIMS	Secondary ion mass spectrometry
ST	Source Term
STEP	Source Term Experiments Project
TMI	Three Mile Island
VEGA	Verification Experiments of radionuclides Gas/Aerosol
VI	Vertical Induction
WDS	Wavelength dispersive X-ray spectroscopy
XPS	X-ray photoelectron spectroscopy
XRD	X-ray diffraction
XRF	X-ray fluorescence

2.20.1 Introduction

In the present generation of nuclear power reactors, including the light water reactor (LWR) and the heavy water moderated CANDU reactor, the uranium dioxide fuel is in the form of ceramic pellets that are encased in Zircaloy (see **Chapter 2.19, Fuel Performance of Light Water Reactors (Uranium Oxide and MOX)**). A mixed oxide fuel $U_{1-\gamma}Pu_{\gamma}O_2$ (where $\gamma \sim 0.2$) has also been used with stainless steel cladding for the liquid-metal-cooled fast breeder reactors (FBRs) (see **Chapter 2.21, Fuel Performance of Fast Spectrum Oxide Fuel**). As the UO_2 and (U, Pu) O_2 oxide fuels are burned, a large number of fission products are produced. The irradiated oxide fuel forms a multicomponent system consisting of more than 40 main fission product elements as summarized in **Table 1**.^{1,2} These elements are collected into representative groups that exhibit similar chemical and physical behavior in irradiated fuel (see **Table 2**). The fission products may be distributed among several

phases, depending on the temperature, pressure, and composition (burnup) of the fuel–element system. The chemical state will also influence the physical properties of the fuel (**Chapter 2.17, Thermal Properties of Irradiated UO_2 and MOX**), including the thermal conductivity, swelling, creep, and incipient melting point, as well as the release behavior of the fission products from the fuel matrix because of their relative volatility both under normal operating conditions and during transients.³ Gaseous fission products (xenon and krypton) released to the fuel-to-clad gap and plenum regions strongly influence the thermal conductance in the fuel-to-clad gap, internal gas pressure, and eventual stresses on the cladding. In addition, the knowledge of the chemical states of the fission products in irradiated fuels and the conditions that cause them is of importance in interpreting the postirradiation examinations of the discharged fuel, and long-term spent fuel storage and reprocessing.^{4,5}

The chemical state of the fuel and fission products can be determined from out-of-pile release experiments, dissolution experiments, postirradiation and metallographic examination (e.g., γ -scanning, mass spectrometry, and a number of microanalysis techniques including laser-induced, nuclear, X-ray, secondary ion, and Auger electron) (**Section 2.20.2**),^{1,4,6–11} and thermochemical computations^{12–15} (**Section 2.20.3**). The thermochemical computations implicitly assume that the system is in thermodynamic equilibrium. However, during and after irradiation, the chemistry of the fuel–fission product system is complicated by several phenomena in which (1) the fission product concentrations increase gradually with irradiation, (2) the chemical properties of the fission products change after irradiation due to radioactive β -decay, (3) the oxygen chemical potential of the fuel changes with fuel burnup and the related production of fission products that can alter the oxygen-to-metal ratio of the fuel, and (4) axial and radial temperature gradients that can affect the distribution of the elements into phases, thereby leading to compositional gradients with material transport by thermal diffusion processes.^{2,5,16,17} There can be substantial migration of some elements, particularly the volatile fission products, that can contribute to a gradient in the oxygen chemical potential in the pellet. Equilibrium calculations can be used only as a basis for the estimation of the chemical state, which requires as an added complexity a material transport analysis into the calculation requiring numerical data for the heat of transport of all elements and some compounds that are not well

Table 1 Inventories of the main fission products and actinides in oxide fuel and their expected segregation tendencies

Element	Abundance after 1 year cooling			Segregation tendency ^c	Segregation form ^c
	CANDU (g per t of U) for a burnup of 290 MWh per kilogram of U ^a	Fast neutron fission in oxide fuel (g per t of (U, Pu,f.p.)O ₂) for a burnup of 1% ^b			
		U ²³⁵	Pu ²³⁹		
Se	18			(Like Te?)	(Like Te?)
Br	7			Strong	Uncertain
Kr	101	120	60	Pronounced	Elemental bubbles
Rb	94	130	60	Strong	Oxide (inclusions?)
Sr	246	260	100	Slight	Oxide
Y	126	180	60	None	
Zr	1080	1000	650	Slight	Oxide (inclusions?)
Mo	1140	890	790	Strong	Metallic particles and oxide
Tc	288	220	210	Strong	Metallic particles (and oxide?)
Ru	871	480	800	Strong	Metallic particles (and oxide?)
Rh	235	130	230	Strong	Metallic particles
Pd	511	110	580	Strong	Metallic particles
Ag	42	8	80	Strong	Metallic particles
Cd	32	8	35	Strong	Metallic particles (and oxide?)
Sn	19	32	35	Strong	Metallic particles (and oxide?)
Sb	7	14	14	Strong	Metallic particles
Te	176	140	170	Strong	Metallic or oxide (inclusions?)
I	91	80	100	Strong	Uncertain
Xe	1930	1050	1150	Pronounced	Elemental bubbles
Cs	901	960	950	Strong	Oxide (inclusions?)
Ba	447	390	310	Strong	Oxide (inclusions?)
La	409	290	260	None	
Ce	882	690	630	None	
Pr	378	340	260	None	
Nd	1240	980	870	None	
Pm	78	90	110	None	
Sm	246	140	220	None	
Eu	46	20	40	None	
Gd	35			None	
Np	51			None	
Pu	5250			None	
Am	34			None	

^aFor fuel used in the Bruce Nuclear Generating Station. Taken from Hocking, W. H.; Duclos, A. M.; Johnson, L. H. *J. Nucl. Mater.* **1994**, 209, 1–26.

^bTaken from Kleykamp, H. *J. Nucl. Mater.* **1985**, 131, 221–246.

^cBased on extensive studies of LWR and FBR fuel and limited studies on CANDU fuel. Hocking, W. H.; Duclos, A. M.; Johnson, L. H. *J. Nucl. Mater.* **1994**, 209, 1–26.

known.¹⁸ Moreover, in the case of failed fuel pins during normal operating conditions, the ingress of water for water-cooled thermal reactors or sodium for FBRs into the element can result in further reactions with the fuel and fission products (Section 2.20.4).^{19,20} The cladding can participate in reactions with the fission products delaying their release into the fuel-to-clad gap or into the coolant system with the

possibility of fuel rod failure.²¹ Moreover, the corrosive behavior of the fission products in the fuel-to-clad gap can affect fuel performance, possibly leading to fuel failure as a consequence of environmentally assisted stress corrosion cracking (SCC) during power ramping maneuvers (see Chapter 3.22, Modeling of Pellet–Cladding Interaction).^{22–24} The fission products, fuel, and cladding can also interact among themselves, as

Table 2 Chemical grouping of fission product elements

Group	Chemical group name	Elements
1	Noble gases	Xe, Kr
2	Halogens	I, Br
3	Alkali metals	Cs, Rb
4	Tellurium group	Te, Se, Sb
5	Alkaline earths	Sr, Ba
6	Noble metals	Ru, Mo, Pd, Rh, Tc
7	Rare earths	La, Nd, Eu, Y, Ce, Pr, Pm, Sm, Zr, Nb

well as with the surrounding structural materials, during high-temperature reactor accident conditions (see **Chapter 2.23, Behavior of LWR Fuel During Loss-of-Coolant Accidents**), leading to the possibility of fuel dissolution and material relocation (**Section 2.20.5**).^{11,25–30}

2.20.1.1 General Characteristics of Thermal and Fast Reactor Fuels

In a thermal reactor such as the AREVA 1300 MWe pressurized water reactor (PWR), the high-pressure coolant (~ 15.5 MPa) enters the cladding and assembly structures at a temperature of 283°C and exits at 325°C , yielding a maximum external cladding temperature of 350°C .³¹ These coolant conditions can lead to significant corrosion at the external surface of the cladding. The PWR oxide fuel typically operates at an average linear power rating of 17.0 – 17.5 kW m^{-1} . For these cladding temperatures and fuel ratings, the fuel has a centerline temperature lower than 1850°C that leads only to small fuel restructuring and low fission gas release.³¹ The fuel will reside in the reactor for three or more cycles, for a given cycle of 12–18 months, reaching a fuel burnup of ~ 35 – 50 GWd tU^{-1} . In contrast, CANDU fuel operates at much higher fuel ratings of up to 63 kW m^{-1} but for considerably shorter fuel burnups of 7.5 GWd tU^{-1} to limit the internal fission gas pressure below that of the coolant pressure so that sheath liftoff does not occur for the collapsible sheathing design. The fuel centerline temperature in CANDU fuel can therefore reach temperatures over 2000°C .

In the SUPERPHENIX FBR, the fuel has a much higher power density of $\sim 200\text{ W cm}^{-2}$, which is 2–3 times greater than for water reactor rods, where the linear fuel ratings can reach 47 kW m^{-1} .³¹ The liquid sodium coolant is at a lower pressure of ~ 0.2 MPa with a much higher temperature of 400°C at the bottom of the pin cluster and can reach over 600°C

at the exit of the maximum-rated pin. The neutrons have a higher energy spectrum with a total neutron flux that can reach $6 \times 10^{15}\text{ n cm}^{-2}\text{ s}^{-1}$. For these higher coolant temperatures and linear power ratings, the fuel centerline temperature can reach in excess of 2000°C , which can result in large fuel restructuring and relatively high internal fission-gas pressure.

2.20.1.1.1 Plutonium distribution

^{239}Pu is produced from the capture of epithermal neutrons in the resonances of ^{238}U with subsequent β -decay. Other Pu isotopes are also formed, but their contribution to the overall fission yield is small. **Figure 1** presents measurements of Pu across a pellet cross-section for a thermal reactor pin. It is seen that Pu is uniformly distributed in the interior of the fuel, whereas its concentration increases steeply at the fuel surface because of enhanced neutron capture in this region. The high surface concentration affects the radial power generation in the fuel rod. This result is of particular importance for natural-uranium fuelled reactors. This so-called ‘skin effect’ should be taken into account for a proper analysis of the radial temperature distribution in fuel rods.

2.20.1.1.2 Radial dependence of fuel stoichiometry after irradiation

The oxygen potential of fuel during irradiation can be estimated from the oxidation states of the fission products, sheath, and clad impurities (see **Sections 2.20.1.2** and **2.20.3**). It is estimated from calculations up to 5 at.% burnup that there is an increase in the O/M ratio of about 0.0013 per at.% burnup.¹⁷ However, measurement of oxygen diffusion into the Zircaloy cladding (see **Figure 2**) shows that such excess oxygen can diffuse into the Zircaloy cladding, resulting in a fuel stoichiometry with an O/M ratio very close to 2.00.¹⁷ In addition, changes in UO_2 pellet stoichiometry during storage in air, that is, prior to fuel rod fabrication for periods of up to 32 years, show no increase in the stoichiometric deviation.³²

2.20.1.2 Fission Product Classifications in Irradiated Fuels

The intrinsic mobility of fission products will depend on the charge state of the atomic species that migrate by volume diffusion through the lattice of the fuel. When fission product atoms reach a free surface, they may form thermodynamically favored compounds.

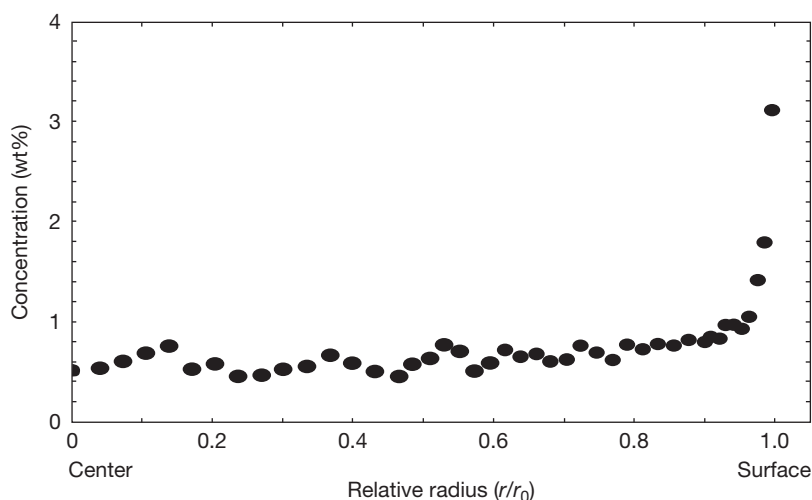


Figure 1 Diametral concentration profile of Pu across a fuel rod. Modified from Walker, C. T.; Bremier, S.; Portier, S.; Hasnaoui, R.; Goll, W. *J. Nucl. Mater.* **2009**, 393, 212–223.

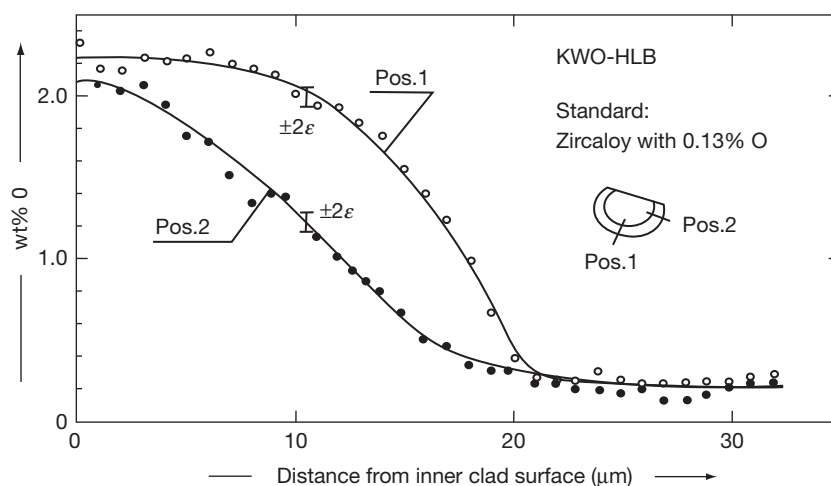


Figure 2 Oxygen concentration in function of distance from the sheath inner surface. Modified from Kleykamp, H. *J. Nucl. Mater.* **1979**, 84, 109–117.

The chemical form will determine the subsequent gas-phase mass transport (i.e., vaporization). The release of fission products is also determined by the solubility of the fission products in the UO_2 lattice. During irradiation, the noble gases are distributed dynamically between a fission-induced solution within the oxide lattice and their nucleation and precipitation into intragranular and intergranular bubbles. The chemical state of the fission products can therefore be classified into the following main groups on the basis of numerous elemental analyses of irradiated LWR and FBR fuels (see [Table 1](#) and [Figure 3](#))^{2,5}:

1. fission gases and other volatile fission products: Kr, Xe, Br, and I;
2. fission products forming metallic precipitates: Mo, Tc, Ru, Rh, Pd, Ag, Cd, In, Sn, Sb, and Te;
3. fission products forming oxide precipitates: Rb, Cs, Ba, Zr, Nb, Mo, and Te;
4. fission products dissolved in the fuel matrix: Sr, Zr, Nb, and the rare earths Y, La, Ce, Pr, Nd, Pm, and Sm.

There are continuous transitions between the four groups as the critical concentration conditions for

A
T
B

I A	II A													III B	IV B	V B	VI B	VII B	
Li	Be													B	C	N	O	F	Ne
Na	Mg	III A	IV A	V A	VI A	VII A		VIII		I B	II B	Al	Si	P	S	Cl	Ar		
K	Ca	Sc	Ti	V	Cr	Mn	Fe	Co	Ni	Cu	Zn	Ga	Ge	As	Se	Br	Kr		
Rb	Sr	Y	Zr	Nb	Mo	Tc	Ru	Rh	Pd	Ag	Cd	In	Sn	Sb	Te	I	Xe		
Cs	Ba	La	Hf	Ta	W	Re	Os	Ir	Pt	Au	Hg	Tl	Pb	Bi	Po	At	Rn		
Fr	Ra	Ac	Ce	Pr	Nd	Pm	Sm	Eu	Gd	Tb	Dy	Ho	Er	Tm	Yb	Lu			
			Th	Pa	U	Np	Pu	Am	Cm	Bk	Cf	Es	Fm	Md	No	Lr			

Volatile fission product

Metallic precipitates (alloys)

Ceramic precipitates (oxides)

Oxides dissolved in the fuel

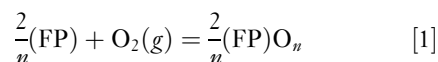
Figure 3 The chemical state of the fission products in oxide fuels. Adapted from Kleykamp, H. J. *Nucl. Mater.* **1985**, 131, 221–246.

new phase development are surpassed because of increased burnup.

Since the process of fission by its nature contributes to an increase in the moles of elements of metal, M , in relation to the virtually fixed number of moles of oxygen, O , the O/M ratio slowly increases during burnup. The different elements have widely varying ability to associate with oxygen. This matter is captured in the diagram in [Figure 4](#) attributed to Ellingham, originally developed in support of understanding metallurgical processing practices. The diagram gives the standard Gibbs (free) energy of isothermal formation of oxides from pure metal (or element) and oxygen gas at one atmosphere pressure as a function of temperature. To permit easy comparison of the relative affinity for oxygen, all oxide formation reactions on the diagram are based on one mole of O_2 instead of the more usual convention of one mole of oxide. In this way, recognition is given to the different number of moles of oxygen in the formula mass when comparing, for example, the relative ability of a comparable quantity of O_2 to react with U (1 mol) or La ($4/3$ mol) to form UO_2 (1 mol) or La_2O_3 ($2/3$ mol). The lowest lines on the Ellingham diagram are thus associated with the elements (rare earths or lanthanides, Ln) that form the most stable of oxides. By comparison, elements associated with lines near the top of the diagram, such as Pd , are not strongly reactive with oxygen and may, when heated to temperatures that pass through the top of the diagram ($\Delta G \geq 0$), not combine with oxygen at all.

The reaction of metal with oxygen is sensitive to the concentration or partial pressure of oxygen.

The equilibrium oxygen pressure for the reaction involving a typical fission product may be written as³³



where (FP) and $(\text{FP})O_n$ denote the fission product element and its oxide, respectively. The valence of the fission-product cation in the oxide form is $2n$. The equilibrium constant for the above equation yields the oxygen partial pressure:

$$pO_2 = \exp\left(\frac{\Delta G_p}{RT}\right) \quad [2]$$

where R is the ideal gas constant and ΔG_p is the standard Gibbs energy of formation of the fission-product oxide per mole of oxygen at 1 atm pressure at temperature T . At 1500 K, PdO has a standard Gibbs energy of formation of $+50 \text{ kJ mol}^{-1}$ of O_2 , and yields a pO_2 (where pure oxide and pure metal can coexist) of 50 atm, whereas for La_2O_3 with a standard Gibbs energy of formation of -960 kJ mol^{-1} of O_2 , the equilibrium pO_2 is $\sim 10^{-35}$ atm. The equilibrium partial pressure of oxygen therefore provides an equivalent means to discuss relative oxide stabilities. From [eqn \[2\]](#), it is apparent that ΔG_p and $RT \ln pO_2$ are equivalent, and the latter is sometimes called the (relative) oxygen (chemical) potential.

With burnup, the liberated oxygen will associate with U , Pu , and La but may not be in sufficient supply to combine with Pd , and other elements, near the top of the Ellingham diagram.

In terms of oxygen potential, if the Gibbs energy of formation of the given fission product lies below

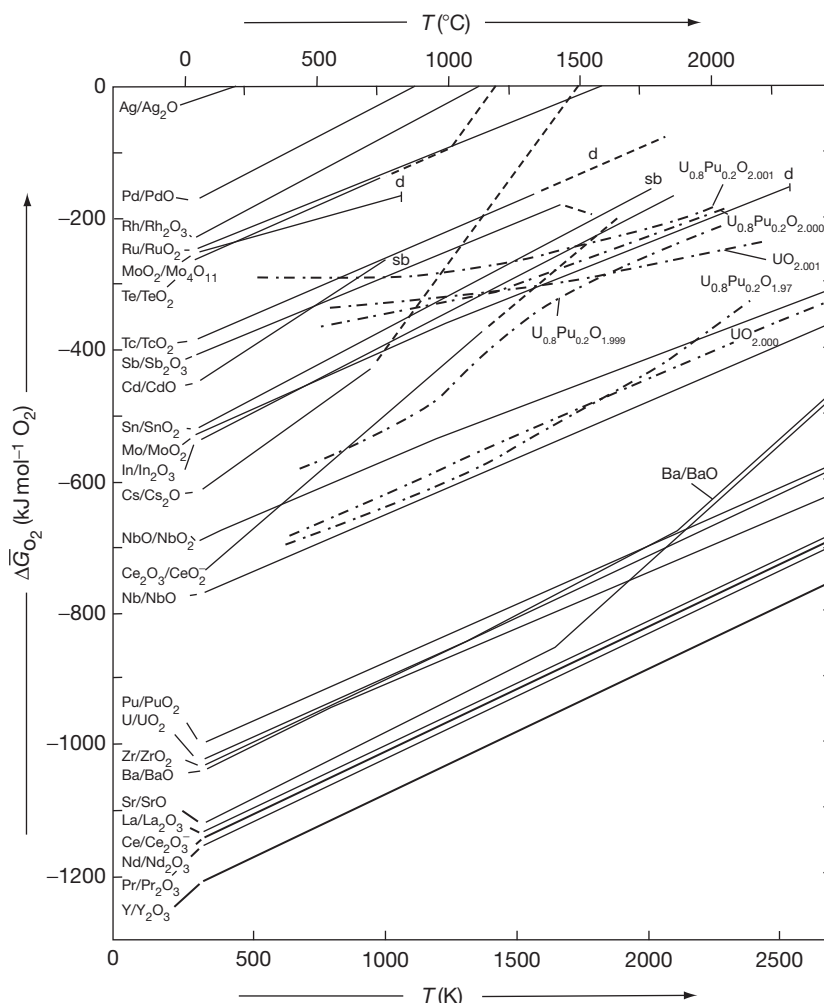


Figure 4 Relative partial molar Gibbs free energies of oxygen of the fission product oxides and of UO_{2+x} , and $\text{U}_{0.8}\text{Pu}_{0.2}\text{O}_{2 \pm x}$; d: oxide decomposes; sb: oxide sublimes. Modified from Kleykamp, H. *J. Nucl. Mater.* **1985**, 131, 221–246.

the fuel oxygen potential, as shown in **Figure 4**, the element will be capable of associating with oxygen in the fuel matrix and an oxide of that fission product can be said to form; if the fission product point is above the chemical potential in the fuel, the fission product will exist as an element in the fuel (in a separate metallic phase). Thus, Pd should be found as a metal, and La as an oxide as depicted in **Figure 3**. In the case of molybdenum, the Gibbs energy of formation of MoO_2 is very close to the lowest value of the oxygen potential that can be expected in irradiated fuel and the fission product may be present as an oxide dissolved to some small extent in the fuel matrix (as MoO_2) or as an element in a metallic inclusion phase with Pd and other elements (Tc, Ru, Rh).³⁴ Under certain conditions of high oxygen

potential not normally encountered, a mixed oxide phase with uranium may also appear, that is, UMoO_6 . Molybdenum therefore provides an important buffering capability on the oxygen potential in oxide fuel,² or equivalently, a means of inferring what the oxygen potential may have been in postirradiation examination of irradiated fuel. A summary of the chemical destiny of fission products is given in **Table 3**.

The fission-product oxides can dissolve in the fluorite structure of the fuel matrix by replacing a uranium or plutonium cation on the normal lattice site. When a 4+ valence fission product (e.g., Zr^{4+}) enters the lattice, there is no change in the electrical neutrality of the crystal; the Zr^{4+} replaces a position otherwise occupied by U^{4+} . However, if the charge of

Table 3 Probable chemical and physical states of fission products in mixed-oxide fuels^a

<i>Chemical group</i>	<i>Physical state</i>	<i>Probable valence</i>
Zr and Nb	Oxide in fuel matrix; some Zr in alkaline earth oxide phase	4+
Rare earths	Oxide in fuel matrix	3+
Ba and Sr	Alkaline earth oxide phase	2+
Mo	Oxide in fuel matrix or element in metallic inclusion	4+ or 0
Ru, Tc, Rh, and Pd	Elements in metallic inclusion	0+
Cs and Rb	Elemental vapor or separate oxide phase in cool regions of fuel	1+ or 0
I and Te	Elemental vapor; I may be combined with Cs and Csl	0 or 1–
Xe and Kr	Elemental gas	0

^aFor near stoichiometric fuels. Reproduced from Olander, D. R. *Fundamental Aspects of Nuclear Reactor Fuel Elements*; TID-26711-P1, Technical Information Centre, US Department of Energy, 1976.

the fission-product cation is lower than the host U^{4+} ion (as with a rare earth or lanthanide oxide of the form M_2O_3 with a charge of 3+), the site occupancy of the lattice is altered to achieve electrical neutrality. In this case, oxygen anion vacancies are created. On the other hand, under sufficiently oxidizing conditions, some 4+ uranium ions may oxidize to 5+ or 6+, giving rise to vacancies in the cation lattice. Elements that readily substitute in size for uranium in the uraninite structure, such as the actinides and rare earths, are expected to remain atomistically dispersed with the host matrix.² The alkaline earth cations Ba^{2+} and Sr^{2+} have large ionic radii and therefore form a separate oxide phase generally in combination with other elements. Sr is (partially) soluble in the UO_2 lattice, whereas Ba does not dissolve in the fuel matrix. In the local presence of sufficient zirconium, the stable forms of the oxides are the zirconates, $BaZrO_3$ and $SrZrO_3$. Fission products that have limited solubility in UO_2 will segregate to the grain boundaries and eventually to the void space within the element (Table 1). Up to several percent of the noble gas inventory of xenon and krypton can typically be found in the fuel-to-cladding gap, depending on the fuel irradiation history. These volatile species can be segregated into numerous microscopic bubbles at the grain boundaries.^{10,35}

The so-called ‘white inclusions’ are detected in postirradiation studies of UO_2 and $(U, Pu)O_2$ fuels. These metallic precipitates, known as the ϵ -phase, which are composed of Mo, Tc, Rh, Ru, and Pd, form a quinary alloy that crystallizes (given the proportions involved) in most cases in a close packed hexagonal structure. In addition, a ‘gray oxide phase,’ containing different combinations of Ba, Cs, Zr, Mo, U, and possibly other elements (rare earths or lanthanides Ln), for example, with a composition of $Ba(U, Pu, Zr, Ln, Mo)O_3$, has also been observed

for higher power/burnup LWR and FBR fuels.² The same fission products as well as less abundant ones (Te, Sr, I, Sn, Sb) have also been detected in deposits formed on the fuel cladding and/or within a central void under extreme conditions.^{2,6,9,12}

Although the conventional Ellingham diagram in Figure 4 provides a quite useful means to assess whether the fission product exists as an oxide or metal for the given oxygen potential, this approach does not take into consideration the possibility of more complex oxide fission product phases (e.g., $BaZrO_3$ and Cs_2MoO_4). Another computationally intensive methodology, that of Gibbs energy minimization (Section 2.20.3), is required. This technique provides a means to determine the chemical speciation of the fission products and their effect on the fuel oxygen potential with burnup. This computation is complicated by a continually changing fission product concentration, diffusion, and oxygen potential with irradiation and decay, as well as by very steep temperature gradients within the fuel (see Section 2.20.1). However, this type of analysis if pursued can account for (1) the O–U system (including nonstoichiometry); (2) soluble fission products; (3) noble metals (Mo, Rh, Pd, Ru, and Tc); (4) zirconate, uranate, and molybdate phases; (5) second metal solid solution $U(Pd-Rh-Ru)_3$; and (6) volatile species within the inert gas phase (see Figure 5).

2.20.2 Chemical State of Fission Products in Irradiated Oxide Fuels

It is difficult to perform direct measurements on irradiated fuel samples to ascertain the chemical state of the fission products. A combination of indirect methods are therefore more commonly used, including an observation of measured deposition

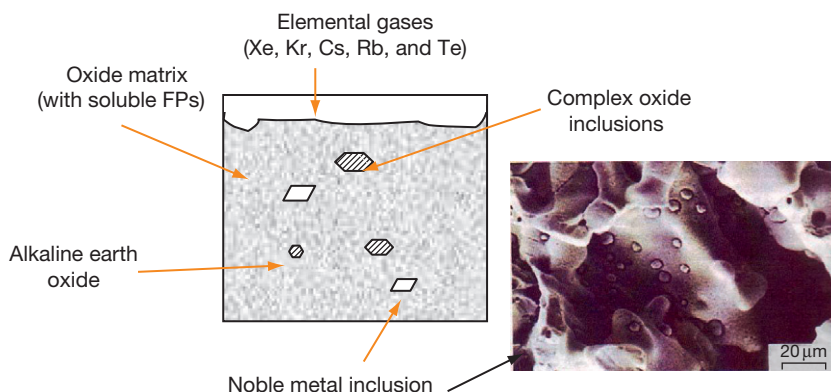


Figure 5 Schematic of irradiated fuel. The photograph shows a secondary electron image of the metallic Mo-Tc-Ru-Rh-Pd precipitates on the surface of the central void of a fast breeder reactor mixed-oxide pin at a local burnup of 6.4%. Adapted from Olander, D. R. *Fundamental Aspects of Nuclear Reactor Fuel Elements*; TID-26711-P1, Technical Information Centre, US Department of Energy, 1976.

patterns or phase changes, as well as experiments performed in hot-cells under strict environmental control. Nevertheless, the chemical state of some particular elements remains elusive and thermodynamic analysis becomes an important tool for such assessments. A description of the more common techniques employed, and major observations from these investigations, are detailed in **Sections 2.20.2.1** and **2.20.2.2**, respectively.

2.20.2.1 Experimental Techniques

Postirradiation examination techniques initially involved ceramography and optical inspection. Gamma scanning was also used to determine the fission product axial and radial distribution. Further improvements were achieved with the introduction of software that made possible absorption and emission tomography to determine fission product redistributions in fuel cross sections and entire pins. Microsampling of irradiated fuel pellets via dicing or drilling also permitted the use of analytical and radiochemical chemistry to help identify some of the fission-product compounds.

A significant improvement involved the replacement of microsampling with various analytical electron and ion optical methods. In addition, the evolution of scanning electron microscopy, X-ray diffraction (XRD), laser and nuclear microanalysis, secondary ion microanalysis, and Auger electron analysis permitted a high level of accuracy for the determination of the fission product concentration and spatial location. These various techniques are briefly reviewed in the following sections.

2.20.2.1.1 Electron probe microanalyzer

Electron probe microanalyzer (EPMA) is a tool to determine the chemical composition of small volumes of solid materials. This technique is similar to scanning electron microscopy, where sample volumes of $10\text{--}30\text{ }\mu\text{m}^3$ can be investigated. The concentration of elements from boron to plutonium can be measured at levels as low as 100 ppm. An electron beam promotes the emission of X-rays at a characteristic frequency, which are detected by an electron microprobe. The size of the electron beam determines the trade-off between resolution and the scan time. Low-energy electrons are produced from a tungsten filament cathode and accelerated by a positively biased anode plate to 10–30 keV. The anode plate has a central aperture and electrons that pass through it are collimated and focused by a series of magnetic lenses and apertures. The resulting $\sim 1\text{-}\mu\text{m}$ -diameter electron beam may be displaced across the sample or used in a spot mode resulting in phonon excitation (heat), cathodoluminescence (visible light fluorescence), continuum X-ray radiation (bremsstrahlung), characteristic X-ray radiation, secondary electrons (plasma production), backscattered electron production, and Auger electron production. When applied to noble gas analysis for fuel samples, EPMA has a drawback of being insensitive to gas retained at grain boundaries or trapped in large bubbles or pores within the fuel.³⁶

The characteristic X-rays can be used for chemical analysis. Specific X-ray wavelengths are counted, either by wavelength dispersive spectrometry (WDS) (see **Figure 6**) or by energy dispersive X-ray spectroscopy (EDS). WDS utilizes Bragg diffraction from

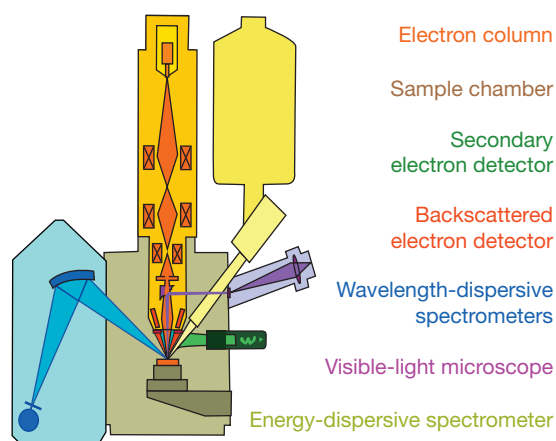


Figure 6 Schematic for wavelength dispersive spectrometry analysis.

crystals for the selection of X-rays of particular wavelengths, which are directed to gas-flow or sealed proportional detectors. In contrast, EDS uses a solid-state semiconductor detector to accumulate X-rays of all wavelengths produced from the sample.³⁶

The chemical composition is determined by comparing the intensities of the characteristic X-rays from the sample material with intensities of known composition (standards). The counts must be corrected for matrix effects (i.e., absorption and secondary fluorescence). Although electron probes have the ability to analyze most elements, they are unable to detect the lightest ones (i.e., H, He, and Li).

EPMA has been used with quantitative image analysis for the determination of noble gas retention in fuel grains at the RisØ National Laboratory,³⁶ as well as analysis of deposits on the fuel cladding.⁶

2.20.2.1.2 Laser-induced breakdown spectroscopy

In laser-induced breakdown spectroscopy (LIBS), a laser is focused onto a small area at the surface of a specimen, where it ablates a very small amount of material in the range of nanograms to picograms. This process generates a plasma plume at temperatures in excess of 100 000 K. During data collection, typically after local thermodynamic equilibrium is established, plasma temperatures range from 5000 to 20 000 K. At these high temperatures, the ablated material dissociates (breaks down) into excited ionic and atomic species. The plasma then emits a continuum of radiation and within a very small timeframe, expands at supersonic velocities and cools. At this point, characteristic atomic emission lines of the

elements can be observed. The delay between the emission of continuum radiation and characteristic radiation is of the order of 10 μ s so that it is necessary to temporally gate the detector.

Because all elements emit light of characteristic frequencies at high temperatures, LIBS can detect all elements in principle, limited only by the power of the laser as well as the sensitivity and wavelength of the spectrograph and detector. In practice, detection limits are a function of (1) the plasma excitation temperature, (2) the light collection window, and (3) the line strength of the viewed transition. The LIBS technique is very similar to a number of other laser-based analytical techniques, including Raman spectroscopy and laser-induced fluorescence (LIF). In fact, current devices now combine these techniques into a single instrument, allowing a characterization of the atomic, molecular, and structural properties of the specimen.

This technique is essentially nondestructive with an average power density of <1 W radiated onto the specimen. One of the major advantages of this technique is its ability to depth profile a specimen. It can also remove surface contamination and is very practical as a rapid technique for high-volume analyses.

Since LIBS requires only optical access to the specimen, fiber optics can be employed for remote analyses providing a technique that is noninvasive, noncontact, and applicable as a stand-off method when coupled to an appropriate telescopic apparatus. As such, it has found application for irradiated fuel material. The accuracy of LIBS is typically better than 10% with detection limits of 1–30 ppm by mass.

LIBS and other associated techniques have been specifically used for carbon analysis of irradiated carbide fuel pins.^{37,38}

2.20.2.1.3 Auger electron spectroscopy

Auger electron spectroscopy (AES) involves the analysis of electrons emitted from an excited atom after a series of internal relaxation events. It has become a practical and straightforward characterization technique for probing chemical and compositional surface environments. The typical setup for AES is shown in Figure 7.

Applications of AES include the determination of the oxygen concentration distributions in oxidized Zircaloy samples and microchemical studies of irradiated fuel.³⁹

2.20.2.1.4 Secondary ion mass spectrometry

Secondary ion mass spectrometry (SIMS) is a technique to analyze the composition of solid surfaces

by sputtering the surface of the specimen with a focused primary ion beam and analyzing the ejected secondary ions (see [Figure 8](#)). These secondary ions are measured with a mass spectrometer to determine the elemental, isotopic, or molecular composition of the surface. In particular, because SIMS can analyze the isotopic composition, this tool is useful for studies that require this special capability.^{40,41} SIMS is the most sensitive surface analysis technique capable of detecting elements at the level of parts per billion.

2.20.2.1.5 Elastic recoil detection

Elastic recoil detection (ERD) is a nuclear technique for elemental depth profile analysis in thin films. An energetic ion beam is directed at the sample, where

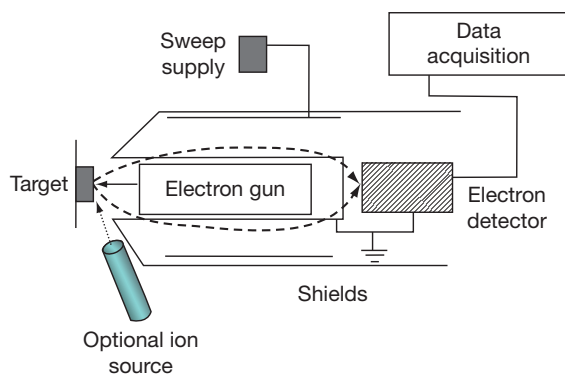


Figure 7 Typical Auger electron spectroscopy experimental setup.

there is interaction with the atoms of the sample. The incident energetic ions have sufficient energy to cause a recoil of the atoms that can be detected. For example, a 200 MeV Au beam can be used with a gas ionization detector. A 35 MeV Cl (or 50 MeV I) beam is often used with a time-of-flight detector, which is good for light elements (or transition metals). ERD is also often done using a relatively low-energy (2 MeV) ^4He beam specifically to depth profile hydrogen. Similar methods to ERD are nuclear reaction analysis (NRA) and particle-induced X-ray emission (PIXE).

2.20.2.1.6 X-ray techniques

These are a family of nondestructive analytical techniques that reveal information about the crystallographic structure, chemical composition, and physical properties of materials. These techniques are based on observation of the scattered intensity of an X-ray beam hitting a sample as a function of incident and scattered angle, polarization, and wavelength (or energy).

2.20.2.1.6.1 X-ray diffraction

XRD involves the elastic scattering of X-rays from structures that have a long-range order. Powder diffraction (XRD) is a technique used to characterize the crystallographic structure, crystallite size (grain size), and preferred orientation in polycrystalline or powdered solid samples. Powder diffraction is commonly used to identify unknown substances by comparing diffraction data against a known database.

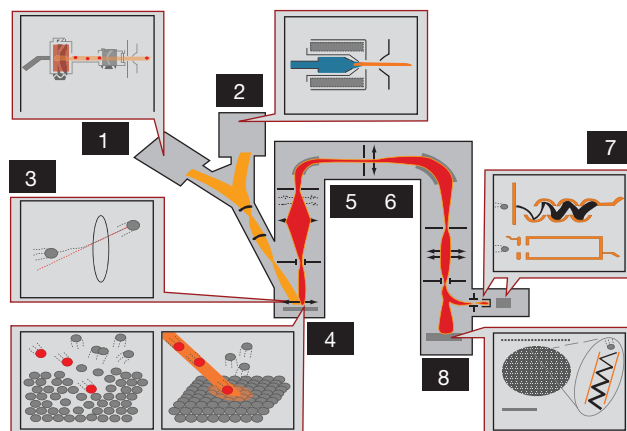


Figure 8 Typical schematic of a dynamical secondary ion mass spectrometry instrument. High-energy ions are supplied by an ion gun (1 or 2) and focused on to the target sample (3), which ionizes and sputters some atoms off the surface (4). These secondary ions are then collected by ion lenses (5) and filtered according to atomic mass (6), then projected onto an electron multiplier (7, top), Faraday cup (7, bottom), or charge-coupled device screen (8).

It may also be used to characterize heterogeneous solid mixtures to determine the relative abundance of crystalline compounds and, when coupled with lattice refinement techniques, such as Rietveld refinement, can provide structural information on unknown materials. X-ray pole figure analysis enables one to determine the distribution of crystalline orientations within a crystalline thin-film sample. Studies of the reaction of zircaloy with fission products have made use of this technique.²¹

2.20.2.1.6.2 X-ray fluorescence

X-ray fluorescence (XRF) is the emission of characteristic 'secondary' (or fluorescent) X-rays from a material that has been bombarded by high-energy X-rays or γ -rays. The phenomenon is widely used for elemental analysis and chemical analysis. In principle, the lightest element that can be analyzed is beryllium ($Z=4$), but due to instrumental limitations and low X-ray yields for the light elements, it is often difficult to quantify elements lighter than sodium ($Z=11$).

2.20.2.1.6.3 X-ray photoelectron spectroscopy

X-ray photoelectron spectroscopy (XPS) is a surface chemical analysis technique, involving quantitative spectroscopy under ultra-high vacuum conditions, for the measurement of the elemental composition, empirical formula, chemical state, and electronic state of the elements that exist within a material. XPS spectra are obtained by irradiating a material with a beam of X-rays while simultaneously measuring the kinetic energy and the number of electrons that escape from the top surface layer ($\sim 1\text{--}10\text{ nm}$) of the material. XPS is also known as electron spectroscopy for chemical analysis (ESCA). XPS detects all elements with an atomic number (Z) of 3 (lithium) and above. Detection limits for most of the elements are in the range of parts per thousand, although limits of parts per million (ppm) are possible for surface layers using a long collection time (overnight). This technique has been used for microchemical studies of fuel.

2.20.2.1.6.4 Energy dispersive X-ray spectroscopy

EDS is used for the elemental analysis or chemical characterization of a sample. To stimulate characteristic X-rays from a specimen, a high-energy beam of charged particles such as electrons or protons (see ERD), or a beam of X-rays, is focused onto the sample. The incident beam may excite an electron in an inner shell, ejecting it from the shell and creating an electron hole. An electron from an outer shell

can fill in this hole with the emission of an X-ray. The number and energy of the X-rays emitted from a specimen can be measured by an energy dispersive spectrometer to determine the elemental composition of the specimen.

EDS is often contrasted with its spectroscopic counterpart, WDS (wavelength dispersive X-ray spectroscopy). WDS differs from EDS in that it uses the diffraction patterns created by light-matter interaction as raw data. WDS has a much finer spectral resolution than EDS. In WDS, only one element can be analyzed at a time, while EDS provides a complete spectrum of all elements. Studies of the chemical form of fission products have been performed using EDS for the fuel and cladding.^{21,26}

2.20.2.2 Postirradiation Observations

In-pile measurements are difficult to interpret because of the many chemical reactions that can occur with the release of fission products. For such interpretation, other supporting tests are performed in hot-cells or in the laboratory with irradiated or unirradiated fuel specimens. Under these experimental conditions, there is better control, where more complex and accurate measurement equipment can be used.

As mentioned, the initial UO_2 or $(\text{U, Pu})\text{O}_2$ fuel will change during irradiation to a multiphase system with the production of fission products. In general, as mentioned earlier, irradiated fuel displays five identifiable phases: (1) fuel-fission product oxide solid solutions, (2) perovskite oxides known as the 'gray phase,' (3) metallic inclusions, (4) phases rich in Pd and Te, and (5) metallic actinide-noble metal compounds at low oxygen partial pressures.²

This section describes the major behavior characteristics of fission products, fissionable material, and possible fission product reactions with the clad.

2.20.2.2.1 Volatile fission products

Since noble or inert gases are by nature nonreactive, the Kr and Xe isotopes can be easily measured by γ -spectroscopy methods, depending on their half-life. Medium- and long-lived isotopes can be determined from in-pile experiments with correction for decay due to transport to the detector station. In-cell tests allow of a direct γ -measurement, with relatively low background, thereby permitting observations of the shorter-lived isotopes. In-reactor experiments, in which the gap inventories are swept away from the fuel to γ -detectors, have been performed to obtain information on short-lived fission product release

behavior of volatile isotopes either directly or by measuring their decay daughters in the gas flow or on charcoal cold traps.

Noble gases are mainly released from the UO_2 matrix by diffusion from the fuel grains to the grain surfaces where they precipitate into grain boundaries bubbles (see **Chapter 3.19, Oxide Fuel Performance Modeling and Simulations** and **Chapter 3.20, Modeling of Fission-Gas-Induced Swelling of Nuclear Fuels**). Tunnels form on grain edges after bubble interconnection, resulting in a release into the fuel-to-clad gap. Some of these tunnels are observed in ceramographs at room temperature if they do not collapse during cool down. Very small amounts of noble gas isotopes can also be directly released from the pellet surfaces into the gap by recoil and knock-out processes, or produced by the decay of bromine and iodine isotopes that are already in the gap region or have deposited on pellet and clad surfaces. **Figure 9** shows the Xe concentration (wt%) distribution for three fuel rods irradiated to burnups between 3.7 and 4.3 at.% for linear power of 22, 36, and 43 kW m^{-1} .

Xe release occurs at the central region of the pellet where the highest temperatures were achieved during irradiation.^{17,42} The fractional release from the fuel depends on the stoichiometry of the UO_2 where higher releases occur at higher stoichiometric deviations.⁷ In hot-cell experiments, where irradiated fuel specimens were subjected to temperature ramps, an initial burst of noble gas is observed followed by a significantly lower release rate. This burst arises from a release of noble gases from the grain boundaries, whereas the slower release occurs from diffusion in the fuel grains.^{43,44}

Recently, the Xe concentration distribution in a single UO_2 grain has been reported.³⁶ This distribution is consistent with a diffusional release process.

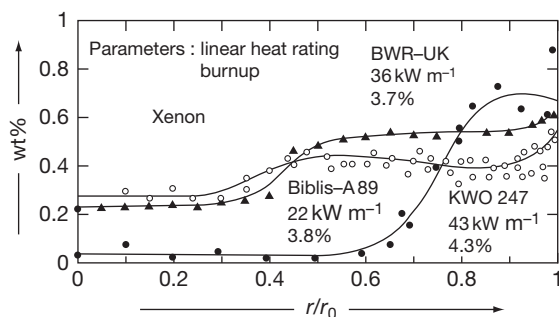


Figure 9 Xe concentration as a function of the relative pellet radius in pressurized water reactor. Modified from Kleykamp, H. J. *Nucl. Mater.* **1985**, 131, 221–246.

Measurements at the Harwell Laboratory have shown that the gas release depends on the heating rate with a maximum release resulting between 10 and 20 K s^{-1} . This observation suggests that the migration of fission gases is a complicated process, involving an interaction between the gas atoms and bubbles within the UO_2 grains and on the grain boundary surfaces.^{44,45}

Volatile fission products shown in **Figure 3** are released from the fuel matrix similar to that of the noble gases. In addition, Cs isotopes can be considered as part of this group if the fuel temperatures are higher than 1600 K. In particular, migration of cesium from the fuel to the pellet surface is consistently reported on axial γ -scans (with high concentrations at the pellet-to-pellet interfaces). In some in-pile and in-cell experiments, the fractional release of these volatile isotopes is very difficult to distinguish from the fractional releases of the noble gases. Other studies, however, suggest that Te and I may be released significantly faster than that of the noble gases.^{46–48}

The presence of some compounds (i.e., CsI) in the gap is well supported by experimental evidence.^{11,17} What is not clear is whether the CsI has already formed before reaching the gap or if it is formed in the gap at low burnups (<0.5 at.%).^{7,25} In FBR, the presence of Mo and Cs compounds was determined in the fuel-to-clad region with EDX.⁴⁹ Also, the iodine volatility can be significantly affected by the oxidation state of Mo.²⁸

Volatile fission products in the gap can react among themselves, resulting in a changing chemical speciation. At normal operation temperatures, the reaction kinetics for formation and radiolytic decomposition may dominate the abundance of some chemical species.¹¹ In the case of Cs, I, and Zr (see **Section 2.20.2.2.3**), the kinetics of formation/decomposition of CsI and Zr iodides are possible factors in the mechanism of SCC. Other compounds are also expected to be present in the gap as suggested from thermodynamic calculations; however, the confirmation of their existence requires further experimentation.

2.20.2.2.2 Distribution and segregation of fission products

Fission products can be segregated because of their migration to specific locations (i.e., grain boundaries or pellet surfaces). The neutron flux inside a pellet decreases from the surface to the center (self-shielding) and the fission events in the pellets follow this distribution. In particular, the fission events per unit volume are the highest at the pellet surface. In this region,

the fission of ^{239}Pu provides an additional contribution of fission products (see [Section 2.20.1.1.1](#)). The noble gases will segregate into bubbles that populate the grain boundaries.

Metallic inclusions are commonly observed in ceramographs from irradiated samples. They are formed by isotopes of Mo, Tc, Ru, Rh, Pd, Ag, Cd, In, Sn, Sb, and Te.^{3,8} These inclusions are found at the surface of the grain boundaries and are associated, in general, with grain boundary bubbles. Under certain conditions, these precipitates inhibit the movement of the grain boundary bubbles (i.e., bubble pinning). A thermodynamic-based estimation of some possible compounds is detailed in [Section 2.20.3.3.2](#).

Despite the low releases associated with these inclusions, under certain environmental conditions (highly oxidizing or reducing), some of the components of these precipitates can be oxidized or reduced forming other compounds of higher volatility that can be released from the fuel matrix. Examples of this behavior are for the cases of Ru and Ba. Under reducing conditions, the Ru release is very limited; however, Ru release is much faster in steam and even more so in air (probably as RuO_4 and/or RuO_3).^{50,51} Nb behavior is similar to Ru.²⁹ Ba exhibits a different behavior, in which very small quantities of Ba are released in oxidizing conditions (steam or air) probably because of the low volatility of the oxide. On the other hand, significant releases of Ba were measured under reducing conditions.²⁹

Furthermore, under accident conditions in which UO_2 oxidation occurs, these precipitates can be carried by UO_2 aerosols that are formed by fuel grain boundary oxidation.²⁹ However, if the conditions are such that UO_2 volatilization is possible (UO_3 formation), these precipitates can be left on the remaining fuel surfaces.²⁹ Finally, an understanding of this complex behavior can be guided only by thermodynamic assessments that require a knowledge of the enthalpy of formation of possible fission product compounds such as RuO_2 ,⁵² BaZrO_3 , BaMoO_4 , and SrMoO_4 (see [Section 2.20.3](#)).⁵³

In addition, Cs, Ru, Te, and Ba have been consistently found at the cracks in the pellet and on the clad inner surface. A surface enrichment of these fission products is common, whereas Cd, Mo, Sr, and I have been occasionally detected.¹ Despite the fact that the total extent of segregation appears to depend on the irradiation history, the relative abundance of individual segregates show significant variation. This variability could be attributed to the slight differences in initial fuel stoichiometry, which can have a major

effect on the chemistry of some elements (Te, Mo, Cd) as well on thermal diffusion rates.¹ Furthermore, a widespread distribution of segregated fission products, in particular Cs, was observed along the length of the inner surface of the clad.⁶ Even more diverse element segregation was observed at the ends of the fuel rods where high levels of Ba, Sr, Te, I, and Cd were found relative to that of Cs. These findings are consistent with the premise that the fission products migrate in the hotter central region of the pellet and then radially toward the clad at the pellet-to-pellet interfaces.³⁹ In mixed oxides containing considerable Si impurities, agglomeration of these elements without fuel constituents were deposited at the fuel crack openings.⁵⁴

2.20.2.2.3 Reaction of fission products with the Zircaloy cladding

Fission products will deposit on the inner surface of the clad.³⁹ Some of these species can diffuse into the clad, while others can attack the clad forming cracks that can later progress with the formation of through-wall cracks. Oxygen will diffuse into the cladding and contribute to its oxidation state. Recent measurements have shown deposits of Sr, Cs, Pu, and Am.⁵⁵

The corrosion behavior of Zircaloy by Te was reported with a duplex corrosion layer consisting of zirconium telluride and zirconium oxide for an oxygen potential less than -500 kJ mol^{-1} . Zirconium telluride is absent for oxygen potentials over -430 kJ mol^{-1} .²¹ Te can diffuse into the clad and after the segregation of the Sn during Zircaloy oxidation, can combine to form tin telluride (see [Section 2.20.5](#)).²⁶

The reaction between fission product(s) and the cladding can lead to so-called environmental-assisted corrosion (EAC) (or SCC). In this mechanism, fission products such as Cs, Cd, or I can attack the clad inducing crack initiation, which then progress through the clad thickness by intragranular and transgranular cracking modes. Fractographic studies indicate that the most probable species responsible for this crack formation is iodine. Zr atoms can be removed from the crack tip by the formation of several zirconium iodides. This mechanism has not been fully investigated. It has been suggested that the necessary reactive iodine in the gap can be produced by radiolysis of CsI due to fission fragment recoil from the fuel surface.²²

2.20.2.2.4 Oxygen in the Zircaloy cladding

The oxidation of Zircaloy in steam was recognized early as an important source of heat during postulated accidents. Parabolic rate correlations have been developed from isothermal oxidation tests. Also, more

sophisticated theoretical models, based on the assumption that oxygen diffusion is the controlling mechanism for this phenomenon, have been developed.⁵⁶ During the oxidation process, the Sn in the oxide phase is precipitated in a series of concentration beads in a plane parallel to the oxide surface. This observation indicates that precipitation occurs at a particular oxygen concentration in the oxide phase.

The heat of the oxidation reaction in steam is -616 kJ mol^{-1} at 298 K and in air $-1100 \text{ kJ mol}^{-1}$ at 298 K.⁵⁷ This difference is reconciled by the amount of energy required to decompose the H_2O molecules. Recently, isothermal experiments performed in air have shown that oxidation rates in the temperature range between 700 and 1500 K are considerably faster than for steam at the same temperature.⁵⁷ More experimental work is required however to understand the kinetic behavior during temperature transients and the effect of steam preoxidation.

2.20.3 Thermodynamic Modeling Methods

When many elements are involved in possible reactions, particularly when more than one phase may arise, the broad thermodynamic judgments made using the Ellingham diagram are inadequate and may even lead to false conclusions in view of the simplifying assumptions that must necessarily be made. A more general and computationally intensive methodology, involving Gibbs energy minimization, is required (Section 2.20.3.1). This approach, which retains the cornerstone principles of the Ellingham diagram, involves the systematic redistribution of elements among the many possible compounds in such a way as to preserve the number of moles of each element in a closed system. For each possible distribution, at the chosen temperature and pressure, the Gibbs energy change is computed relative to the previous distribution. This process continues until the Gibbs energy is no longer significantly reduced. Considerable computational advantage arises from the recognition that the Gibbs energy is not an absolute function; only differences in Gibbs energies are significant and must be preserved.⁵⁸

2.20.3.1 Gibbs Energy of Formation and Minimization Techniques

Figure 10 illustrates the concept of Gibbs energy minimization (see Chapter 1.17, Computational Thermodynamics: Application to Nuclear

Materials) applied to the U–O system at 2000 K and 1 atm pressure. The overall proportion of O to U atoms corresponds to an atom fraction of O of 0.714 arbitrarily selected for discussion purposes. Five different compounds of U and O are shown. Pure U and O are off the compositional scale to the left and right, respectively. The vertical lengths of the line segment for each compound express the Gibbs energy per gram atom instead of mole so that the graphical concept of the lever rule in capturing the proportion of any two compounds that satisfy the overall atom fraction of O (0.714) can be retained. In the case of nonstoichiometric UO_{2+x} , the Gibbs energy is shown as a function of composition. The iterative approach in finding pairs of phases with progressively lower Gibbs energy eventually ends when U_3O_8 is found to coexist with UO_{2+x} . No other combination gives rise to a lower Gibbs energy and the composition of UO_{2+x} (atom fraction O) is given by the point of tangency of the line projecting to U_3O_8 . For the final iteration, the tangent line is horizontal and the point of tangency corresponds to the minimum on the curve for UO_{2+x} as a consequence of reassigning the numerical value for Gibbs energy for the elements during this process of minimization. The Gibbs energy separating any species from the lowest tangent line ΔG (when scaled up to a per mole basis) gives the chemical potential.

The minimization procedure outlined earlier is lengthier when many elements are involved but not excessively so. This methodology is approximately linearly proportional to the number of elements and the number of possible compounds. Therefore, even with over 50 elements possibly existing in 1000 or more chemical species or phases, the method of Gibbs energy minimization can be practically applied.

The Gibbs energy minimization technique can be extended even further through the theory of irreversible processes (i.e., nonequilibrium thermodynamics),⁵⁹ which yields a fundamental interrelation of the thermodynamic state variables with the thermodynamics of the system including the Soret and Dufour effects as well as phase stability. The latter methodology has been applied to account for noncongruent melting of hyperstoichiometric uranium dioxide.⁶⁰

2.20.3.2 Uranium–Oxygen Binary System

Following the methodology in Section 2.20.3.1, a thermodynamic treatment of the complete U–O system with particular emphasis on the location of the UO_{2+x} – U_4O_9 phase boundary and the behavior

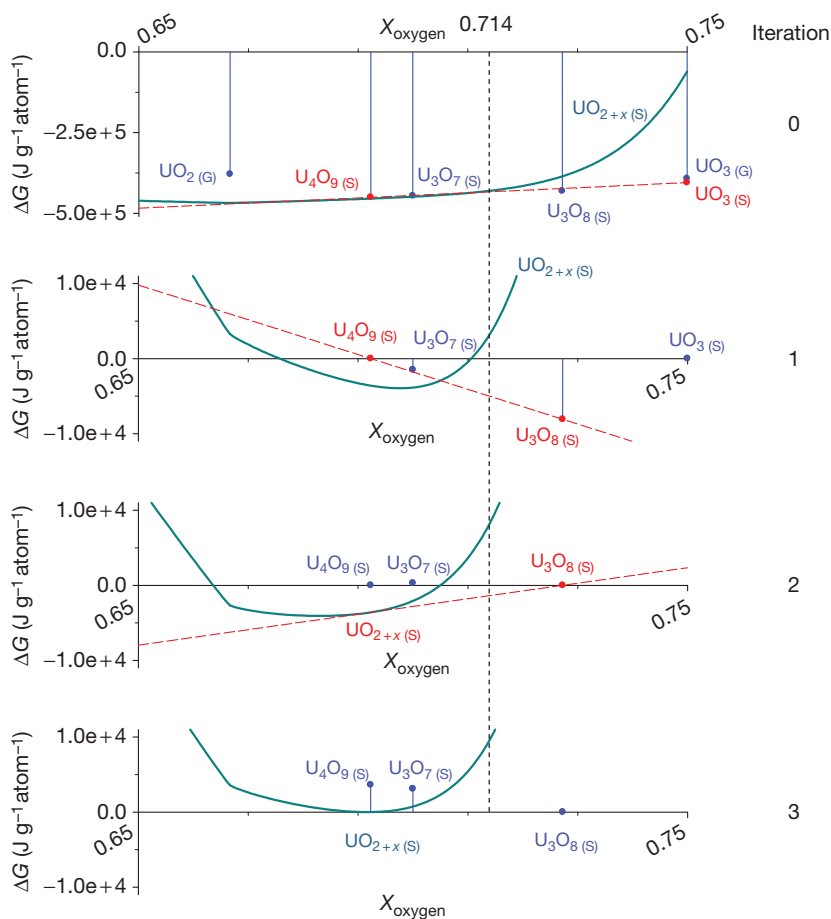


Figure 10 Illustration of algorithm employed in the computation of chemical equilibrium of the U–O system at 2000 K, 1 atm. The atom fraction of O is arbitrarily set to 0.714.

of $p\text{O}_2$ over the entire range of UO_{2+x} (652–3100 K) can be developed (see also **Chapter 2.02, Thermodynamic and Thermophysical Properties of the Actinide Oxides**).^{20,61}

There are various approaches to the modeling of the UO_{2+x} . This phase can be regarded as a solid solution of UO_2 and UO_3 , noting the equivalence

$$\text{UO}_{2+x} = \{(1-x)\text{UO}_2 + x\text{UO}_3\} \quad [\text{I}]$$

When the component oxides conceptually dissolve, the entropy of mixing is approximately given by the ideal expression near the middle of **Figure 11**. This is based on random molecular mixing. However, UO_{2+x} is actually an ionic crystal with the fluorite structure. The ideal mixing process therefore involves the distribution of cations of uranium and anions of oxygen over the allowed positions in this structure.

The nonstoichiometry arises because all the uranium cations do not have the same charge. On the

premise that only U^{4+} ions and U^{6+} ions exist, the conceptual mixing process involves a random distribution of U^{4+} and U^{6+} cations within a regular arrangement of O^{2-} anions. However, a certain fraction, v , of the cationic lattice sites must be vacant for charge neutrality reasons if the fluorite structure is to be maintained. This vacancy fraction is related to the value of x in UO_{2+x} by the simple formula given in the lower part of **Figure 11**. When the entropy of mixing expression is developed for U^{4+} , U^{6+} , as well as vacancies distributed over the allowed cationic sites, an additional term is involved in the expression of the entropy of mixing. This expression is given near the top of **Figure 11**. We now inquire as to the significance of this distinction in expressing the Gibbs energy of mixing needed for computations of phase equilibrium.

The Gibbs energy of mixing involves two terms: an ideal baseline term and a departure term called

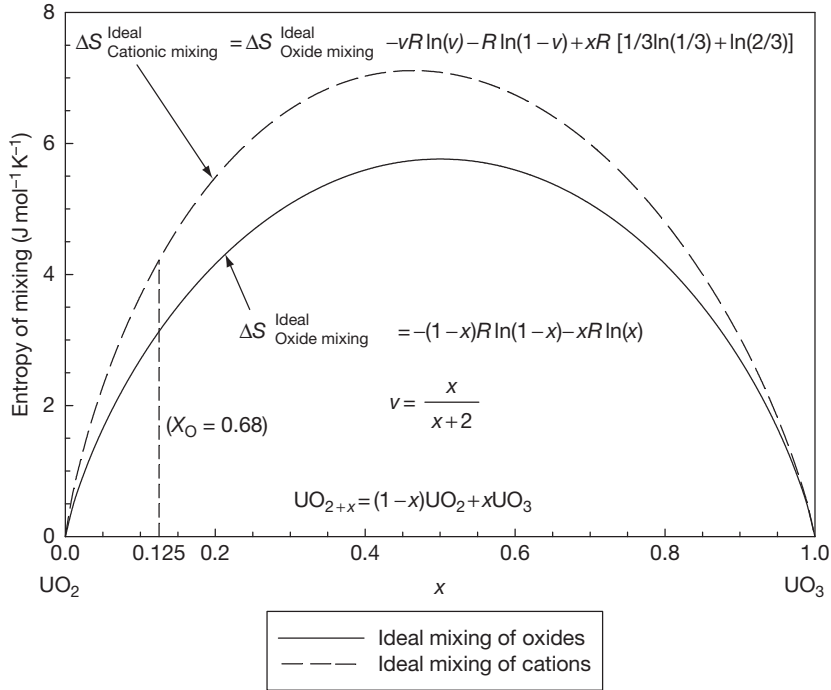


Figure 11 Comparison of entropy calculations illustrating the significance of vacancies (v) in the crystalline structure of UO_{2+x} .

the excess Gibbs energy. The ideal Gibbs energy of mixing is

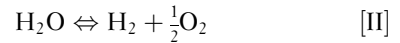
$$\Delta G_{\text{Cationic mixing}}^{\text{Ideal}} = -T\Delta S_{\text{Cationic mixing}}^{\text{Ideal}} \quad [3]$$

where $\Delta S_{\text{Cationic mixing}}^{\text{Ideal}}$ is the ideal entropy of mixing.

The actual Gibbs energy recognizes deviations from random distribution in the actual entropy of mixing as well as the heat effects when the conceptual dissolution of the component oxides occurs. The departure term, or excess Gibbs energy, is essentially an adjustment expression to experimental data involving, typically, a short series in the concentration variable with temperature-dependent coefficients. In the case of the U–O system, the Gibbs energy of mixing of UO_2 and UO_3 is illustrated by the shaded drooping feature in **Figure 12**. Note the very small contribution to the droop contributed by the ideal term using either of the expressions in **Figure 11**. The projection of the tangent line (at an atomic fraction O of 0.68) to pure oxygen gives the equilibrium partial oxygen pressure at this composition by the formulation evident on the figure. This information is carried over to **Figure 13** and is shown in relation to many independent experimental measurements.^{62–69} Repetition of this process permits the placement of lines of constant partial oxygen pressure over the UO_{2+x} field in

Figure 14(a). The same technique produces the UO_3 partial pressure isobars in **Figure 14(b)**.

Isobaric lines of O_2 and UO_3 partial pressure can be added to the phase diagram as shown in **Figure 14**. Since the partial oxygen pressure in the UO_{2+x} field is very low, it is more useful to express this partial pressure as the equivalent $\text{H}_2/\text{H}_2\text{O}$ proportion, using the temperature dependent equilibrium constant for the process:



An expression can therefore be derived relating the hydrogen-to-steam partial pressure ratio for the LWR system, temperature T (in K), and the equilibrium stoichiometric deviation x_e ²⁰:

$$\begin{aligned} \log\left(\frac{p_{\text{H}_2}}{p_{\text{H}_2\text{O}}}\right) &= 5706.8 + 0.1245T - 5.482 \\ &\times 10^{-6}T^2 + \frac{4\,296\,016}{T} - 1550.95\log(T) \\ &- \frac{1\,772\,730\log(T)}{T} - \frac{155\,930\,360}{T^2} \\ &+ \log\left(\frac{1-x_e}{x_e}\right) - 0.9158x_e - 16.08x_e^2 \\ &+ 75.15x_e^3 - 251.51x_e^4 \end{aligned} \quad [4]$$

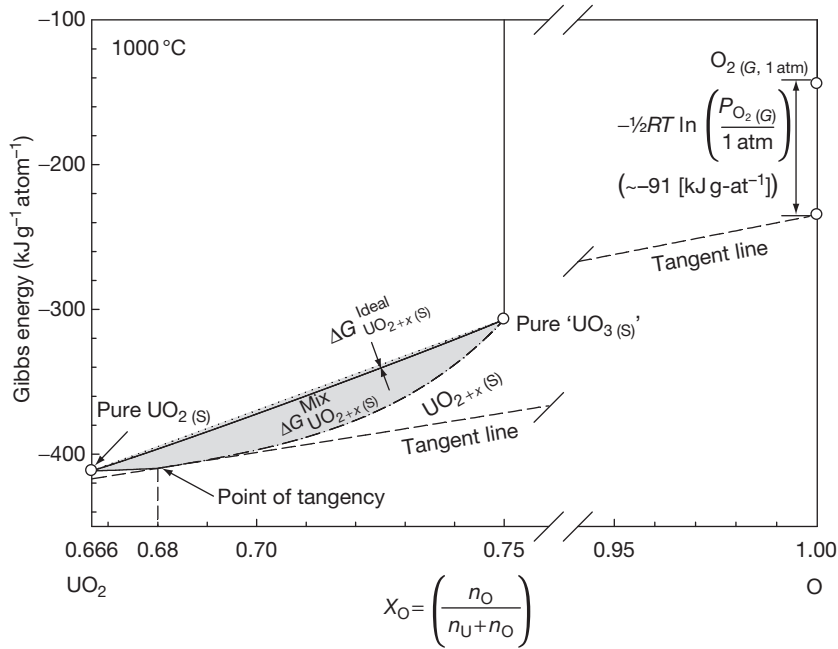


Figure 12 Illustration of the computation of partial oxygen pressure in equilibrium with UO_{2+x} . The composition is at an atomic fraction of oxygen atoms of $X_{\text{O}} = 0.68$. The tangent projection on the left relates to [Figure 13](#).

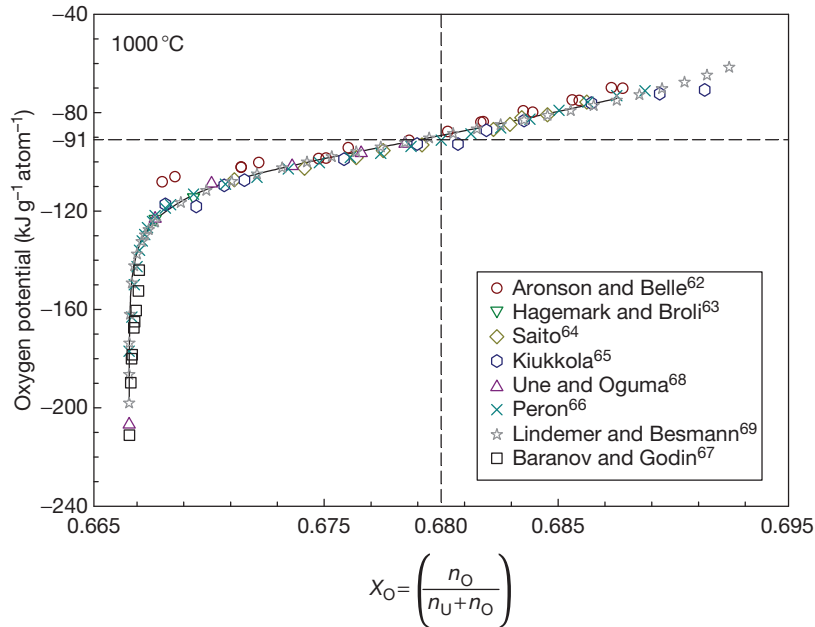


Figure 13 Chemical potential of oxygen versus atomic fraction of oxygen at 1000 °C.

[Equation \[4\]](#) is in excellent agreement with the thermodynamic treatments of Lindemer–Besmann⁶⁹ and Blackburn.⁷⁰ Similarly, for the CANDU system, using the properties for heavy water, the $(\text{D}_2/\text{D}_2\text{O})$ variation of the UO_{2+x} nonstoichiometry is²⁰

$$\log\left(\frac{p_{\text{D}_2}}{p_{\text{D}_2\text{O}}}\right) = \log\left(\frac{p_{\text{H}_2}}{p_{\text{H}_2\text{O}}}\right) + 1.76985$$

$$-\frac{333.783}{T} - 0.488145\log(T) \quad [5]$$

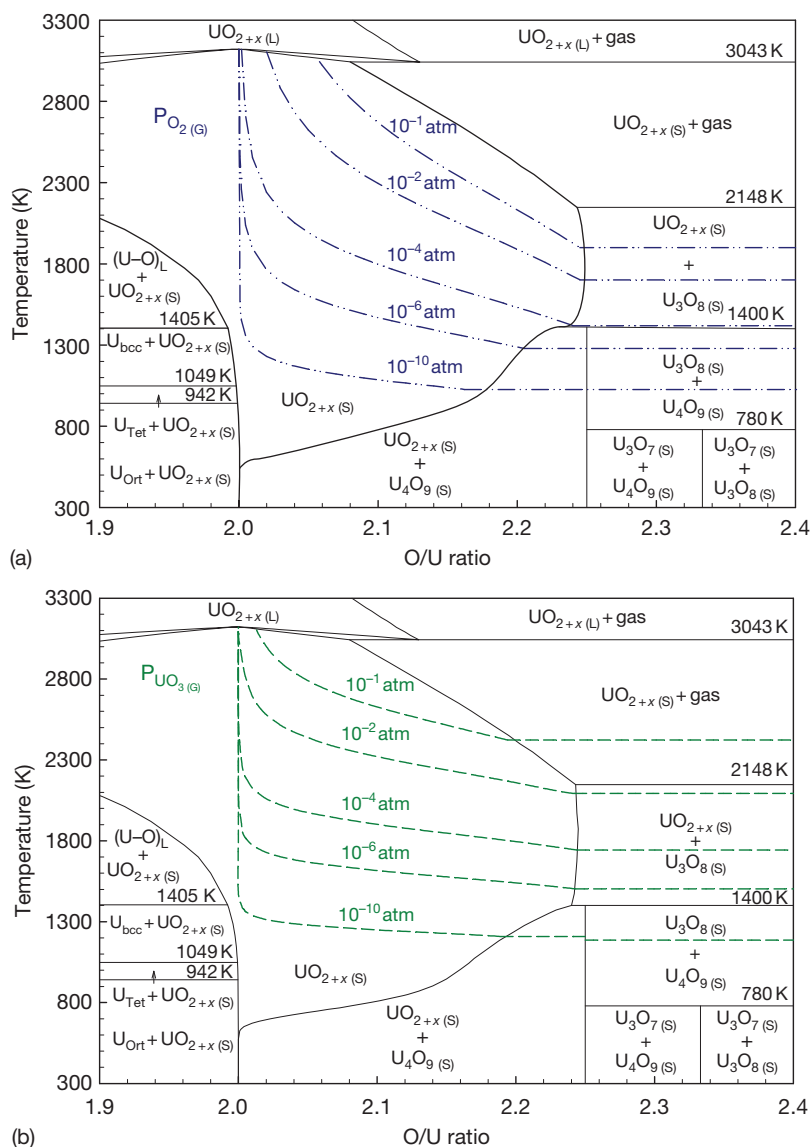


Figure 14 Calculated U–O binary phase diagram with isobaric lines of (a) oxygen and (b) UO_3 partial pressure.

These expressions are shown as they relate to the U–O phase diagram in [Figure 15](#) and indicate that there is little difference for the prediction of the atmospheric oxygen potential between light and heavy water. It is noteworthy that the constant ratio lines pinch about the 2:1 ratio for the O:U proportion at temperatures below about 500 °C. This implies that contact of steam with UO_2 below 500 °C imparts very little disturbance to the UO_2 stoichiometry; higher temperatures are required to create a significantly hyperstoichiometric UO_2 . [Equations \[4\] or \[5\]](#) can be used, for example, to estimate fuel hyperstoichiometry arising from the

penetration of steam/heavy water vapor through the cracks in the fuel pellets of defective elements ([Section 2.20.4](#)).²⁰

2.20.3.3 Phase Diagram Studies of Fission Products in Oxide Fuels

Thermodynamic models can be developed using Gibbs energy minimization ([Section 2.20.3.1](#)) to account for the influence of the fission products on the fuel oxygen potential with burnup.⁷¹ The development of a complete thermodynamic model and thermochemical database for irradiated fuel, encompassing the complex

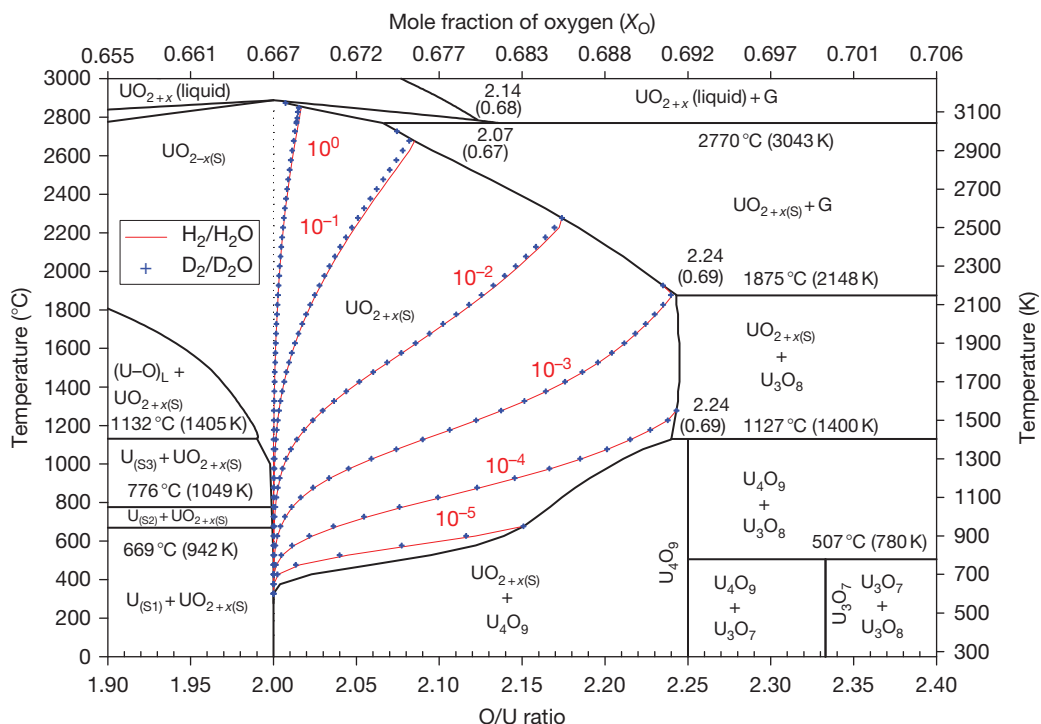


Figure 15 Calculated U–O binary phase diagram with lines of constant H_2/H_2O and points of constant D_2/D_2O ratios as calculated from eqns [4] and [5].

Table 4 Oxides (grouped by O/M proportion) included as solutes in UO_2

M_2O	MO	M_2O_3	MO_2
Cs_2O	SrO	Ce_2O_3	CeO_2
Rb_2O	BaO	Dy_2O_3	MoO_2
		Ho_2O_3	NbO_2
		La_2O_3	NpO_2
		Nd_2O_3	PuO_2
		Pr_2O_3	TeO_2
		Sm_2O_3	ZrO_2
		Y_2O_3	

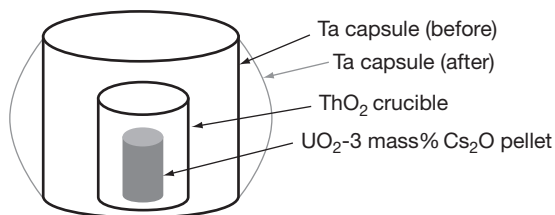


Figure 16 Schematic diagram of Cs_2O 'solubility' experiment.

U–O system, and the fission product and actinide components, as briefly described in Sections 2.20.3.3.1–2.20.3.3.4, is detailed in Corcoran.⁷²

2.20.3.3.1 Solutes in UO_2

Table 4 shows the various oxides contained in Figure 5 that can be found as solutes in uranium dioxide. Kleykamp⁷³ has reviewed data for 12 oxides dissolved in UO_2 . In a typical experiment involving, for example, Cs_2O , two samples of near stoichiometric powdered UO_2 ($O/U = 2.003$) were mixed with Cs_2O inside a thoria crucible. These crucibles were sealed within separate tantalum capsules, as shown in

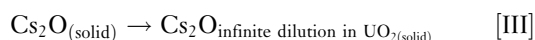
Figure 16. Each assembly was annealed at either 1273 or 2173 K for 8 h. The experiment at the lower temperature did not attain thermodynamic equilibrium,² but the results at 2173 K yielded the following observations: (1) the internal pressure of the Ta capsule was estimated to be 200 bar from the wall curvature; (2) a tantalum oxide layer deposited on the inner walls of the Ta capsule; and (3) the level of dissolved Cs in the pellet was 0.08 mol% Cs_2O .

This experiment does not give the solubility of Cs_2O directly, that is, Cs_2O dissociates, oxygen combines with Ta, and a high Cs vapor pressure causes the capsule to swell. All of these factors must be

Table 5 Thermodynamic data for selected solute oxides in UO_2

Oxide	Solubility in UO_2 (mol%)	Temperature (K)	Excess Gibbs energy (w.r.t. solid) (J mol^{-1})	Cations per formula mass
Cs_2O		2173	230	2
La_2O_3	69	523	$-2686 + 8.505T$	2
La_2O_3	50	1523		2
Pr_2O_3	55	1523	$-4268 + 8.505T$	2
Nd_2O_3	68	1523	$-7714 + 8.505T$	2
PuO_2	Miscible		0	1
NpO_2	Miscible		0	1

considered in extracting the required thermodynamic data for Cs_2O dissolved in a UO_2 solid solution. The inferred Gibbs energy change for



as well as for other oxides is given in Table 5. Note that the number of moles of foreign solute cations per formula mass is also given. When the Gibbs energy of mixing equations is formulated, the mole fractions of the solute oxide are based on a formula mass containing only one mole of the metal. Solubility data along with the inferred Gibbs energy changes for selected lanthanide sesquioxides also appear in Table 5.

The behavior of PuO_2 in relation to its dissolution in UO_2 may be inferred from the phase diagrams in Figure 17.^{74,75} Although there is a divergence on the melting of pure PuO_2 , all studies indicate complete miscibility of PuO_2 in UO_2 in both the solid and liquid phases.^{76,77} In general, considering the uncertainties that put into question even such a basic matter as the melting temperature of PuO_2 , the lens-like topology of the binary phase diagram is taken as sufficient evidence to justify the ideal mixing assumption.

A similar treatment was applied to the UO_2 – NpO_2 binary system, using melting data taken from Belyaev⁷⁸ and Chikalla.⁷⁹ Owing to their ideal mixing assumption, the partial excess Gibbs energy for both PuO_2 and NpO_2 , as shown in Table 5, is set to zero. Generally, for other oxide solutes such as ZrO_2 , ideal solution behavior is not sufficient. In the case of UO_2 – ZrO_2 , a complete model for the binary system incorporating the three crystal structures of ZrO_2 has been developed.⁷²

2.20.3.3.2 Noble metals

The presence of noble metal inclusions (the so-called ‘white’ or ‘five metal’ inclusions) in irradiated fuel is well documented.^{5,80–85} Thermodynamic models for these inclusions have been developed.^{15,86} The insufficiency of oxygen to combine with the chemically more

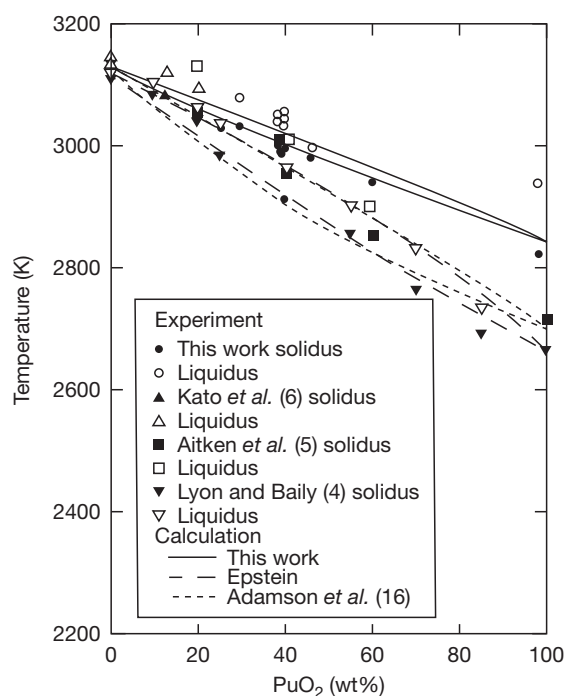


Figure 17 UO_2 – PuO_2 phase diagram. The solid symbols correspond to the solidus and the open symbols to the liquidus. Modified from Kato, M.; Morimoto, K.; Sugata, H.; Konashi, K.; Abe, T. *J. Nucl. Mater.* **2008**, 373, 237–245.

noble metallic fission products creates an alloy phase of Pd, Rh, Ru, Mo, and Tc. Four calculated isothermal ternary phase diagrams are shown in Figure 18. The triangles are arranged so that Rh–Pd, Rh–Ru, and Pd–Ru binary edges on the central triangle are common to the edges of the surrounding three ternary systems involving Mo. Figure 19 illustrates how the central ternary system is related to its binary subsystems.

2.20.3.3.3 Nonfluorite oxide phases

Separate oxide phases are known to appear in irradiated fuel.⁸⁷ Oxide inclusions of the type $(\text{Ba}, \text{Sr})(\text{U}, \text{Pu}, \text{Zr}, \text{Mo})\text{O}_3$ form a ‘gray’ phase with a perovskite

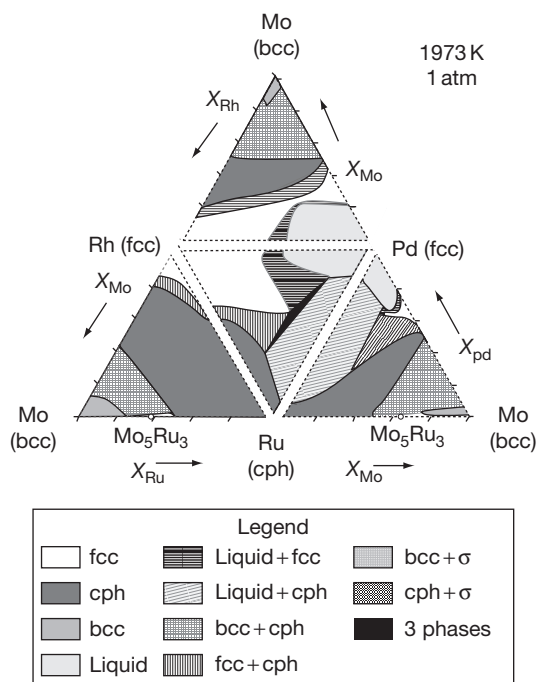


Figure 18 Noble metal phase diagram at 1973 K showing the faces of the tetrahedron unfolded onto a plane. fcc, face-centered cubic; cph, closed packed hexagonal; bcc, body-centered cubic. Modified from Kaye, M. H.; Lewis, B. J.; Thompson, W. T. *J. Nucl. Mater.* **2007**, 366, 8–27.

structure, and result because of the extremely limited solubility of BaO and SrO in actinide oxides. The presence of zirconium generally leads to the formation of zirconates.

Four distinct minor solid oxide phases and one liquid oxide phase can be considered for the thermodynamic model¹³: (1) (Rb/Cs) zirconate solid – (Rb, Cs)₂ZrO₃; (2) (Sr/Ba) zirconate solid – (Sr, Ba)ZrO₃; (3) (Rb/Cs) uranate solid – (Rb, Cs)₂UO₄; (4) (Sr/Ba) uranate solid – (Sr, Ba)UO₄; and (5) (Rb/Cs) molybdate liquid – (Rb, Cs)MoO₄. Ideal mixing is assumed for the chemically similar cations (shown in brackets). The mixing treatments recognize the number of moles of ions contributed to the solid solution in relation to the formula mass of the oxide components. Computations show that the appearance of Cs in combination with Mo, Zr, or U in condensed phases does not preclude Cs existing also in the vapor phase or as a dissolved oxide in UO₂ + x₂.

2.20.3.3.4 'Other' metallic phases (UPd₃-URh₃-URu₃)

Postirradiation examination of FBR fuels has shown the presence of (U, Pu)Pd₃ particles.^{88,89} It should be noted that similar metallic inclusions of URu₃ and URh₃ may also be possible.^{90,91} This potential phase

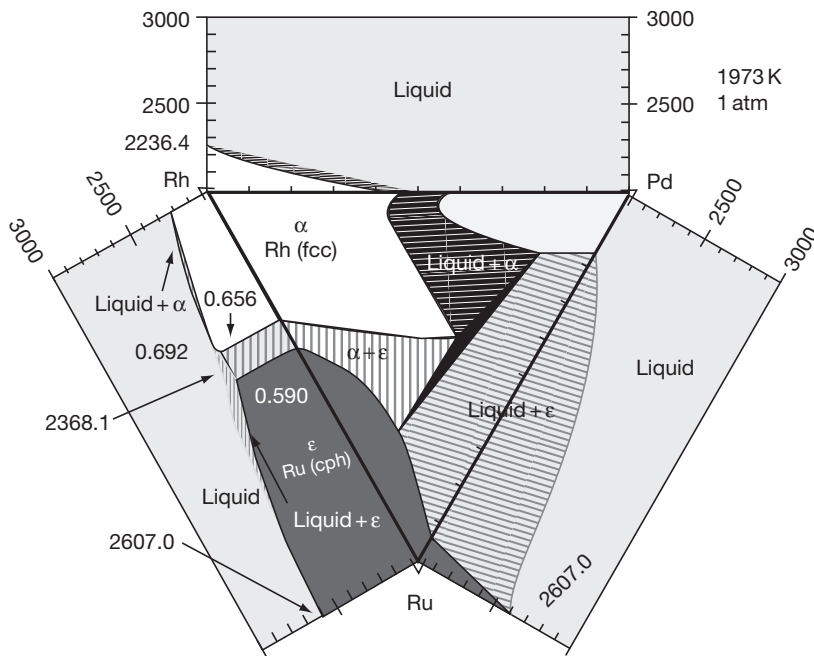


Figure 19 Noble metal phase diagram bounded by the binary diagrams for the Rh-Pd, Pd-Ru, and Rh-Rh subsystems. Modified from Kaye, M. H.; Lewis, B. J.; Thompson, W. T. *J. Nucl. Mater.* **2007**, 366, 8–27.

can be considered to be a solution of the three solids UPd_3 , URh_3 , and URu_3 ,¹³ the data for which can be derived from Cordfunke and Konings.⁹² The ideal mixing of Pd, Rh, and Ru recognizes three atoms per mole of each component in the formulation.

2.20.3.3.5 Establishing the fuel inventory for equilibrium calculations

The fission product inventory for any particular fuel, at a given burnup, may be generated by the ORIGEN-2 (now SCALES-5) code,⁹³ for the inventory of 63 elements. The greater part of these elements is present in very small concentrations. To simplify the calculations, most free energy minimization calculations typically consider less than ~ 20 elements, the most important ones being ranked both by relative concentration (e.g., Pu, Zr, and Mo) and by the radiological consequences (e.g., I, Cs, Xe, and Ru). In addition, oxygen and hydrogen can be added to the thermodynamic calculation to allow for the possible presence of steam in the event of a cladding breach. A stand-alone Gibbs energy minimizer technique is currently being developed on the basis of an extension of the leveling technique discussed in Section 2.20.3.2 to consider the large number of elements and compounds required for irradiated fuel analysis.^{94,95} This method promises the possibility of handling nuclear fuel systems with virtually any number of components especially after parallelization of the programming structure.

2.20.3.3.6 Validation experimentation

As evident in Figures 11 and 15, the U–O fission product system is complex in terms of the number of components and potential phases. One means of validation of a thermodynamic model putting emphasis on

the effects of fuel oxidation is illustrated in the apparatus shown in Figure 20. This equipment is capable of electrometrically converting some of the hydrogen in an Ar–H₂ mixture to water vapor, using a solid oxide electrolyte (not unlike a high-temperature fuel cell).^{96,97} The partial oxygen pressure in the Ar–H₂–H₂O gas mixture so produced is detected in a similar solid oxide cell from its open circuit voltage (EMF). The prepared gas mixture, with a known oxygen partial pressure, then passes over the heated nuclear fuel sample or artificially produced simulated fuel. The extent to which the sample oxidizes as it reacts with the H₂O vapor (thereby producing hydrogen) is monitored in a down stream electrochemical cell that coulometrically converts all the hydrogen to water vapor. Virtually complete conversion is assured using another open-circuit solid-state cell detecting the partial oxygen pressure. A feedback loop from that open circuit cell (oxygen probe) using a potentiostat regulates the current to ‘coulometrically titrate’ the hydrogen with oxygen. The time integrated current associated with the ‘titration’ provides a measure of the oxygen pickup by the sample associated with exposure to a known oxygen partial pressure. Although this relationship is well known for UO_{2+x} , it is influenced by the presence of fission products that, as discussed earlier, have vastly different abilities to combine with oxygen. These measurements can therefore provide a test for the nuclear fuel treatments such as detailed in Sections 2.20.3.3.1–2.20.3.3.4.⁷²

2.20.4 Defective Fuel Behavior

With the occurrence of defective fuel, coolant can enter the element and react with the oxide fuel and

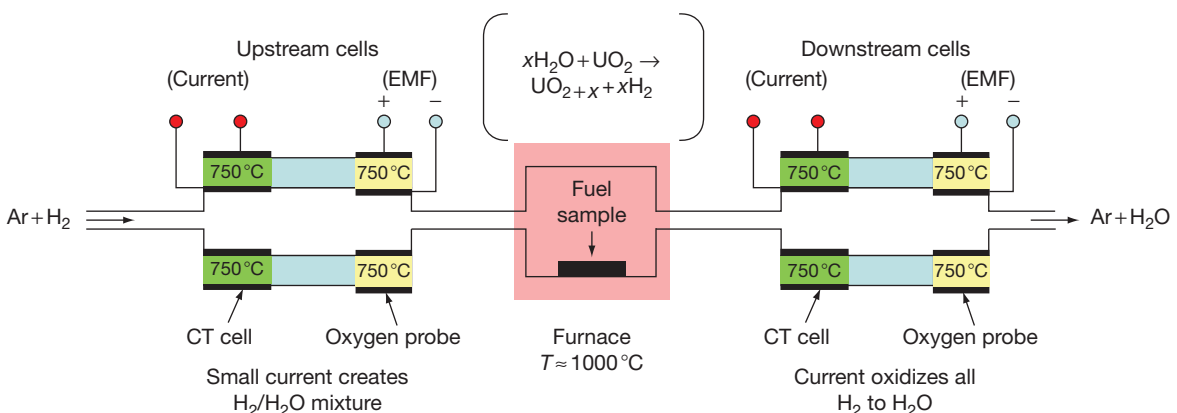


Figure 20 Schematic diagram of coulometric titration (CT) apparatus.

cladding. It is important to understand fuel oxidation phenomena with defective fuel operation since the hyperstoichiometric fuel has a reduced thermal conductivity and a lower incipient melting temperature, which can affect the thermal performance of the fuel rod and possibly lead to fuel centerline melting.²⁰ In addition to fuel oxidation phenomena, fission products (i.e., notably the volatile species of noble gas and iodine) will be released into the primary coolant.^{98–100} Moreover, the fission product diffusivity is enhanced with continued fuel oxidation.^{10,100,101} Thermochemical models (Section 2.20.3) can be employed to predict the equilibrium state of the oxidized fuel (i.e., fuel oxygen potential) for defective fuel analysis (Section 2.20.4.1). The understanding of the aqueous chemistry of the fuel and fission product system is needed to assess the potential for the leaching of fission products from defective fuel during reactor shutdown as well as the impact of defective fuel storage in the water bays (Section 2.20.4.2).

2.20.4.1 Fuel Oxidation Phenomena

With the knowledge of the equilibrium stoichiometry deviation x_e in eqns [4] or [5], the kinetics of fuel oxidation can be described where the fuel oxidation reaction will cease when the stoichiometry deviation x in UO_{2+x} reaches the equilibrium value.^{102,103} Consequently, interstitial transport of oxygen in the defective element for the stoichiometry deviation x can be determined from the mass balance equation²⁰:

$$\frac{\partial x}{\partial t} = \vec{\nabla} \left(D \left(\nabla x + x \frac{Q}{RT^2} \nabla T \right) \right) + \sigma_f \alpha \sqrt{p_{\text{H}_2\text{O}}} (x_e - x) \quad [6]$$

Here σ_f is the surface area of cracks per unit volume of fuel for the cracked fuel pellet, D is the chemical diffusion coefficient for the oxygen interstitials, Q is the effective molar heat of transport, α is the rate coefficient for the surface exchange of oxygen at the fuel/atmosphere interface,¹⁰² and $p_{\text{H}_2\text{O}}$ is the partial pressure of H_2O . Using eqn [6], the oxygen-to-uranium (O/U) ratio and its distribution within the pellets can therefore be predicted as a function of the post defect residence time. This computation involves the simultaneous consideration of the gas phase transport of hydrogen and steam in the fuel-to-clad gap and fuel cracks, and the heat transfer in the fuel pellets accounting for the dependence of thermal conductivity on the degree of fuel oxidation.²⁰ The O/U radial profiles

predicted using eqn [6] are in good agreement with measurements obtained from commercial defective fuel elements of the oxygen-to-metal (O/M) ratio, using a coulometric titration technique (Section 2.20.3.3.6).²⁰

The oxygen partial pressure calculations in eqns [4] and [5] are applicable only for fresh fuel, whereas, with irradiation, fission products and actinides are produced. The fission product elements may form compounds with oxygen that will affect the oxygen potential within the fuel. The advantage of the more general Gibbs energy minimization approach described in Section 2.20.3 is that the U–O phase diagram model can be extended to include fission products and actinides, in comparison with earlier correlations of oxygen potential (e.g., the Lindemer and Besmann treatment⁶⁹) to assess the impact of fuel burnup. For instance, as shown in Figure 21, for a typical discharged burnup of ~ 175 MWh per kilogram of U for CANDU fuel reacting in the presence of increasing amounts of moles of steam, such calculations show that the effect of fission products on the fuel oxygen potential is small for the expected hydrogen-to-steam partial pressure ratio in Figure 15. This result is also consistent with the work of Park *et al.*,¹⁰⁴ which shows little change in the oxygen potential of intact fuel from 0 to 5 at.% burnup. Burnup effects can therefore be neglected for the prediction of x_e in eqns [4] or [5].²⁰

2.20.4.2 Aqueous Fuel and Fission Product Behavior

‘Iodine-spiking’ phenomenon can occur on reactor shutdown when the temperature in the fuel-to-clad gap drops below the steam saturation temperature, permitting liquid water to dissolve the soluble iodine species in the gap.^{105–107} To better understand the fission product leaching behavior during reactor shutdown, a further thermodynamic analysis can be performed assuming that either a vapor or aqueous phase is present in the fuel-to-clad gap (Table 6). The fission products that readily dissolve in the water and are subsequently washed out of the fuel-to-clad gap from a defective element during shutdown or startup operation include Cs (Cs^{+}), Mo (MoO_4^{2-}), iodine (I^{-}), and Rb (Rb^{+}), while the fission products that are not expected to wash out are Zr, Ba, La, (and other Ln), Rh, Ru, Sr, Tc, and Te. It is for this reason that the concentration of La is used to infer the burnup of the fuel during postirradiation examination. The presence of Zr, Ba, La, Rh, Ru, Sr, and

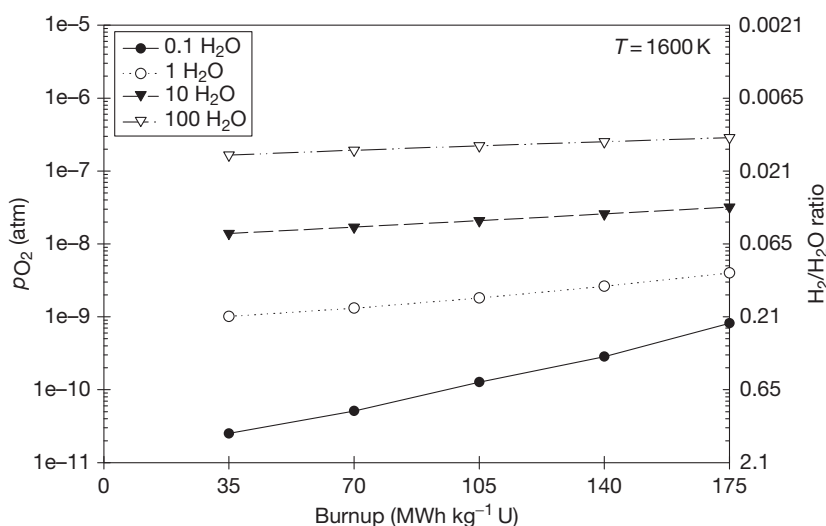


Figure 21 Oxygen partial pressure for various amounts (moles) of steam for a typical CANDU fuel element with burnup.

Table 6 Fission product inventory modes of formation with only a vapor phase and an aqueous phase present in the fuel-to-clad gap

Fission product	Vapor phase present in the fuel-to-clad gap		Aqueous phase present in the fuel-to-clad gap		
	Solid	Vapor	Solid	Vapor	Aqueous
Xe (10% Kr)	No formation	Entire inventory	No formation	Entire inventory	No formation
Cs	Cs ₂ MoO ₄ CsI	No formation	No formation	No formation	Cs[+]
Mo	MoO ₂ (in UO _{2+x}) Cs ₂ MoO ₄ Rb ₂ MoO ₄	No formation	MoO ₂ (in UO _{2+x})	No formation	MoO ₄ [2-]
Zr	SrZrO ₃ ZrO ₂	No formation	SrZrO ₃ ZrO ₂	No formation	No formation
I	CsI	No formation	No formation	No formation	I[-]
Ba	BaUO ₄	No formation	Ba(OH) ₂ BaUO ₄	No formation	No formation
Rb	Rb ₂ MoO ₄	No formation	No formation	No formation	Rb[+]
La	La ₂ O ₃ (in UO _{2+x})	No formation	La ₂ O ₃ (in UO _{2+x})	No formation	No formation
Rh	hP2 – noble metal inclusion	No formation	hP2 – noble metal inclusion	No formation	No formation
Ru	hP2 – noble metal inclusion	No formation	hP2 – noble metal inclusion	No formation	No formation
Sr	SrZrO ₃	No formation	SrZrO ₃	No formation	No formation
Tc	hP2 – noble metal inclusion	No formation	hP2 – noble metal inclusion	No formation	No formation
Te ^a	TeO ₂ (in UO _{2+x})	No formation	TeO ₂ (in UO _{2+x})	No formation	No formation

^aFindings are subject to further investigation.

hP2, hexagonal – primitive (with two atoms in the unit cell).

Tc in the coolant is therefore evidence of fuel debris in the coolant system. These predictions are in qualitative agreement with the observed leaching behavior in in-reactor loop experiments¹⁰⁸; however, in contrast to the thermodynamic prediction, which suggests that Te remains as TeO₂ dissolved in the

UO_{2+x}, the loop experiments indicate that Te is released out of high power defected fuel elements during shutdown conditions. This matter warrants further inquiry since the washout of ¹³²Te becomes an important issue when determining the ¹³²I coolant activity behavior on shutdown.¹⁰⁰

Spent defective fuel bundles are eventually stored for long periods (i.e., several years) in water bays at $\sim 30^\circ\text{C}$. The water bays are oxygenated since they are open to the air surface and are therefore virtually in equilibrium with the air. The thermodynamic treatment described in Section 2.20.3 can be further applied to understand the fuel oxidation behavior in the storage bays. In this case, the diagrams of Pourbaix originally developed to better understand aqueous corrosion phenomena are helpful. The diagrams of redox potential, E_h , versus pH are an important method for understanding aqueous chemical behavior.¹⁰⁹ The redox potential is the conventional electrometric way of expressing the oxidizing ability of the solution in place of

giving the oxygen partial pressure at a particular pH. The uranium Pourbaix diagram at 298 K, covering the range of redox potential pertinent to fuel oxidation behavior, is shown in Figure 22(a). The details of the diagram development via Gibbs energy minimization are given in Lewis.¹¹⁰ The data for UO_2 , U_4O_9 , U_3O_7 , and U_3O_8 are the same as those used for the U–O binary phase diagram in Figure 14. Placed on the diagram for reference are dashed lines (a) and (b) corresponding to redox potentials associated with hydrogen and oxygen saturation (at 1 atm partial pressure), respectively. This methodology provides a means to assess fuel oxidation behavior of defective fuel during long-term storage in the fuel bays.

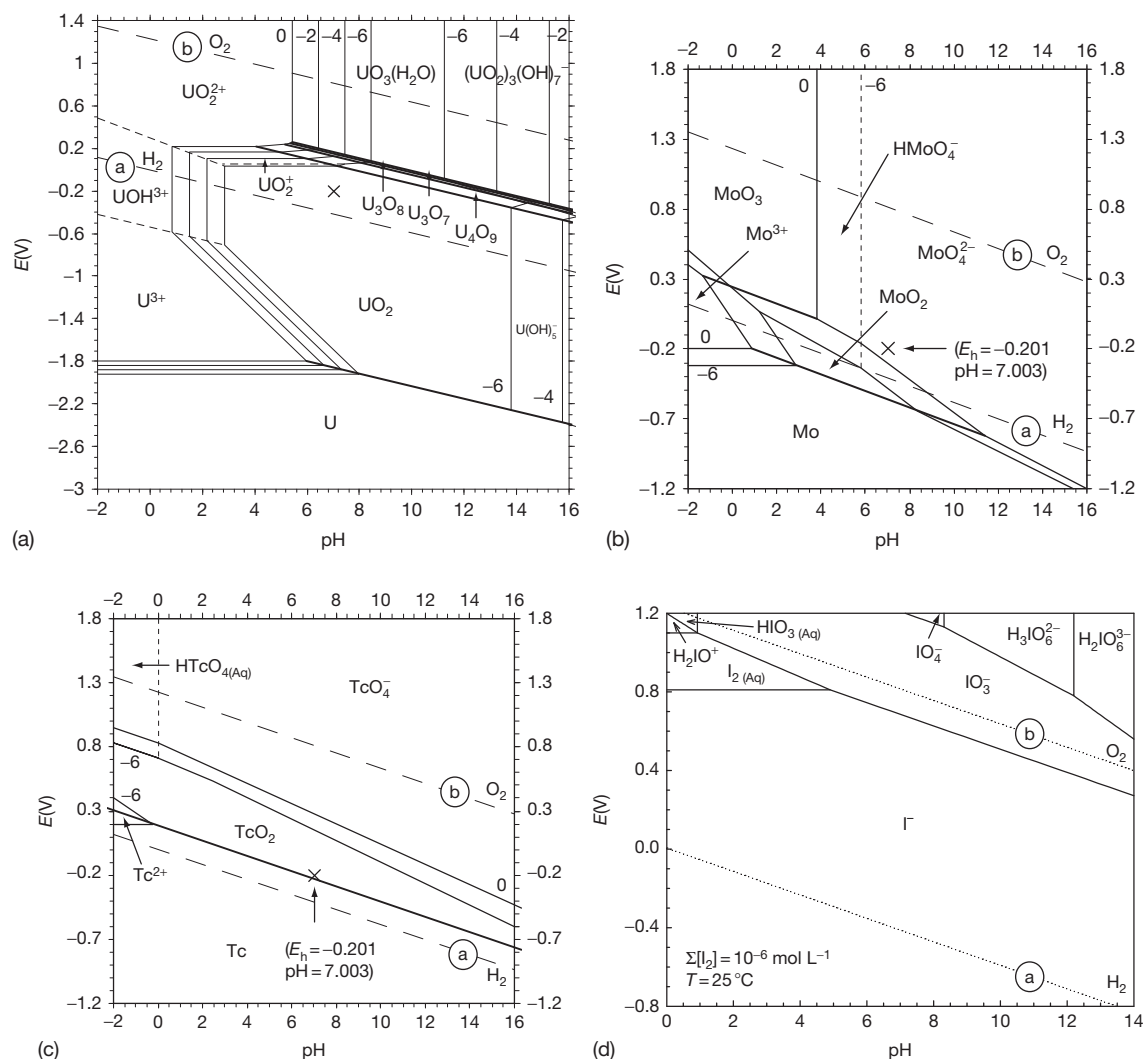


Figure 22 Computed Pourbaix diagrams at 298.15 K for (a) U–H₂O, (b) Mo–H₂O, (c) Tc–H₂O, and (d) I–H₂O. (d) Modified from Ticknor, K. V.; Cho, Y. H. *J. Radioanal. Nucl. Chem.* **1990**, *140*, 75–90.

Furthermore, similar diagrams can also be developed to better understand the aqueous behavior and leaching of such fission products as Mo and Tc (Figure 22(b) and 22(c), respectively).¹¹⁰ In the case of iodine, as shown in Figure 22(d), the diagram has been reconstructed from the work of Ticknor and Cho.¹¹¹ Note that solid iodine does not appear as a field in Figure 22(d) since the concentrations for the aqueous species fields were constructed for 10^{-6} molar. Since the redox potential of the water will be controlled by the UO_2 water reactions shown in Figure 22(a), the condition marked by x in Figure 22(a) (established by independent computations) can be used to locate the relevant field in Figure 22(b)–22(d). For example, for CANDU coolant conditions during reactor shutdown, Mo would be expected to oxidize principally to MoO_4^{2-} ions, while the concentrations for the aqueous species of Tc would be undetectable. Thus, if Tc were detected in the coolant water phase, it could arise (since there is an absence of dissolved oxygen) only as a result of the decay of Mo.¹¹⁰ In the case of iodine, it is evident from Figure 22(d) that I^- is, practically speaking, the only water-soluble iodine species at any pH in the absence of air. The IO_3^- field of stability is only reached near conditions of air saturation (near line (b)).

Experiments conducted in aerated water for ~ 20 days at $\sim 200^\circ\text{C}$ with uranium dioxide fuel specimens have indicated that fuel oxidation can occur via (1) solid-state diffusion to U_3O_7 (similar to dry oxidation), (2) oxidative dissolution and precipitation of U(VI) as $\sim(\text{UO}_3) \cdot 0.8\text{H}_2\text{O}$, and (3) back-reduction of dissolved U(VI) on the $\text{UO}_2/\text{U}_3\text{O}_7$ surface to form U_3O_8 .¹¹² These species are consistent with the computed Pourbaix diagram in Figure 22(a) that shows the dissolution/precipitation product $\text{UO}_3(\text{H}_2\text{O})$.

2.20.5 High-Temperature Fuel and Fission Product Behavior in Accident Condition

To better understand the integral effects of fission product release under degraded core conditions, numerous in-pile experiments have been conducted (e.g., Source Term (ST) tests, Source Term Experiments Project (STEP) tests, Power Burst Facility (PBF) Severe Fuel Damage (SFD) tests, Full Length High-Temperature (FLHT) tests, Loss-of-Fluid Test Facility (LOFT) Fission Product (FP-2) test, and the Phebus Fission Product Tests (FPT)), including an examination of core material following the Three

Mile Island Unit 2 (TMI-2) accident.^{29,113,114} In addition, out-pile annealing tests conducted at high temperatures with spent fuel samples in various environments provided an additional opportunity to study single-effects behavior (e.g., Horizontal Induction (HI) and Vertical Induction (VI) test series at the Oak Ridge National Laboratories (ORNL), the Heva and Vercors test series at the Commissariat à l'Energie Atomique (CEA), and the Verification Experiments of radionuclides Gas/Aerosol release (VEGA) program at the Japan Atomic Energy Agency (JAEA)).^{29,115} Typical results from these various experiments are summarized in Table 7. Details of the various in- and out-pile experiments are given in Lewis.²⁹

The fission product releases from the in-pile PBF tests (i.e., SFD-ST (steam-rich), SFD 1–1 (steam-starved), and SFD 1–4 (steam-starved)), and Phebus FPT-1 test (steam-rich) are compared with those in the TMI-2 accident shown in Table 7.^{29,116,117} These results indicate very low release fractions for cerium and the actinides (typically $<0.01\%$); ruthenium, strontium, and antimony generally $<1\%$; barium less than a few percent; molybdenum up to 50%; similar volatile release behavior of iodine, cesium, and noble gases up to $\sim 90\%$; and tellurium between 1% and 83%. These findings are also consistent with those observed for annealing experiments. However, there is a difference for the barium release between the in-reactor Phebus FPT-0 and FPT-1 experiment ($\sim 1\%$) and the HI, VI, and Vercors annealing tests ($>40\%$) (see Table 8).¹¹⁸ This difference is thought to be attributed to (1) the short duration of the temperature escalation in the in-pile tests, where there is no 'high-temperature plateau' as in the annealing tests but rather a temperature escalation due to the formation of a molten pool in the Phebus experiment; and (2) the presence of a significant amount of ZrO_2 in the fuel melt ($\sim 47\text{ mol}\%$) as well as small amounts of iron oxide in the in-reactor test which can reduce the volatility of Ba.¹¹⁸ Moreover, thermochemical calculations suggest that the Ba vapor pressure is reduced in the solidus–liquidus transition zone as shown in the U–Ba–O phase diagram ($\sim 2400\text{--}3100\text{ K}$).¹¹⁸ Release rates of volatile fission products were large during the temperature escalations in the PBF SFD 1–1 and 1–4 tests and the Phebus FPT-0 test. In the Phebus FPT-0 test, the highest mass flow rates of aerosol and fission products (i.e., ^{131}I , ^{139}Xe , ^{140}Xe , ^{90}Kr , and ^{92}Kr), as well as structural materials (such as tin, silver, and indium), were observed at a peak temperature of $\sim 2770\text{ K}$. The oxygen potential plays an important role, principally in

Table 7 Comparison of fission product release fractions from in- and out-pile experiments and TMI-2^a

Element and experimental conditions	Fission product release fractions (%)									
	PBF experiments			Phebus		TMI-2	Annealing ORNL and VI tests			
	SFD-ST	SFD 1-1	SFD 1-4	FPT-0	FTP-1		VI-3	VI-5	Vercors-4	Vercors-5
T_{\max} (K)	2800	2800	2800	~2870	2500	2800	2700	2720	2570	2570
Atmosphere	H ₂ O	H ₂ O	H ₂ O	H ₂ O/H ₂	H ₂ O/H ₂	H ₂ O/H ₂	H ₂ O	H ₂	H ₂	H ₂ O
Pressure (MPa)	6.9	6.8	6.95	0.2	0.2	5–15	0.1	0.1	0.1	0.1
Heating method	Fission	Fission	Fission	Fission	Fission	Decay	Anneal	Anneal	Anneal	Anneal
No. rods/length (m)	32/0.9	32/0.9	28/1.0	20/1.0	20/1.0	36816/4.0	1/0.2	1/0.2	1/0.08	1/0.08
Krypton, xenon	50	2.6–9.3	23–52	96	77	54	100	100	86	87
Iodine	51	12	24	100	87	55	79	70	87	93
Cesium	32	9	39–51	84	84	55	100	100	93	93
Tellurium	40	1	3	100	83	6	99	82	100	>98
Barium	1.1	0.6	0.8	1	1		30	76	80	55
Strontium	0.002		0.88			0.1				
Antimony			0.13	62	31	0.16	99	18	97	98
Ruthenium	0.03	0.02	0.007	4	1	0.5	5	0	7	6
Cerium	0.0002	0.009	0.013			0.01				
Europium			0.08			<0.1				
Zirconium/niobium					<1					
Molybdenum				No data	56		77	2	47	92
Actinides			<0.001		<1					
Zirconium oxidized (%)	75 ^b	28	38 ^b	85	68	45 ^b				
Fuel melted (%)	15	16	18	50	20	45				
Test environment	Steam-rich	Steam	Steam-starved	Steam-rich	Steam-rich	Steam-rich	Steam-rich	Steam-starved	Steam-starved	Steam-rich
Fuel burnup (GWd tU ⁻¹)	Trace	Trace	29–42	Fresh	23	3	44	47	38	38

^aTaken from Lewis, B. J.; Dickson, R.; Iglesias, F. C.; Ducros, G.; Kudo, T. *J. Nucl. Mater.* **2008**, 380, 126–143.^bTest bundle inventory (core inventory for TMI-2) from Cronenberg, A. W. *Nucl. Technol.* **1992**, 97, 97.

Table 8 Conditions and Ba release data for ORNL (HI and VI) and CEA (HEVA, VERCORS, and VERCORS HT) annealing tests and Phebus tests^a

Test	Temperature (K)	Duration (min)	Atmosphere	Ba release (%)
HI-4	2200	20	H ₂ O	<1
HI-5	2025	23	H ₂ O	<1
VI-2	2300	60	H ₂ O	19
VI-3	2700	20	H ₂ O	30
VI-4	2440	20	H ₂	27
VI-5	2720	20	H ₂	76
Heva-4	2270	7	H ₂ O + H ₂	6
Heva-6	2370	30	H ₂	27
Vercors-1	2130	17	H ₂ O + H ₂	4
Vercors-4	2570	30	H ₂	80
Vercors-5	2570	30	H ₂ O	55
Vercors HT-1	3070	7	H ₂	49
Phebus FPT-0	~2700	–	H ₂ O/H ₂	1
Phebus FPT-1	~2500	–	H ₂ O/H ₂	1

^aTaken from Lewis, B. J.; Dickson, R.; Iglesias, F. C.; Ducros, G.; Kudo, T. J. *Nucl. Mater.* **2008**, 380, 126–143.

the release characteristics of the low-volatile fission products. Only small releases of barium and strontium are observed in the steam experiments of [Table 7](#) as the prevailing atmosphere typically hindered the formation of the more volatile metallic species but favored low-volatility oxides and hydroxides²⁷; in fact, releases for these species occurred in the Phebus FPT-0 test during the temperature escalation phase when hydrogen generation was at a maximum.¹¹⁹ This observation is consistent with the in-pile ST experiments, where higher releases of several percent for barium and strontium, and up to 15% for europium, were observed in a reducing environment which would promote more volatile forms of these species.¹²⁰ These results are also seen in the VI, Heva, and Vercors annealing tests.^{121,122} Since ruthenium–ruthenium oxide has the highest oxygen potential of all fission products (see [Figure 4](#)), the higher-volatile oxides cannot form for the given steam–hydrogen mixtures of the experiments shown in [Table 7](#) or in the TMI-2 accident.

As indicated in [Table 7](#), the tellurium release is dependent on the extent of Zircaloy oxidation, where large releases occur when the Zircaloy cladding is nearly completely oxidized. Although tellurium is released from the fuel on heating, it will chemically react with the Zircaloy cladding and become trapped ([Section 2.20.2.2.3](#)).^{7,26,123,124} During Zircaloy oxidation, the tin constituent in the cladding is segregated as a thin band in the zirconium oxide layer, which advances with the metal–oxide interface, because of the lower solubility of Sn in the oxide than in the metal (and its placement relative to Zr on the Ellingham

diagram shown in [Figure 4](#)). After complete oxidation, there is a production of elemental tellurium and zirconium oxide from the reaction of zirconium telluride with oxygen; however, as a consequence of the tin segregation process, an enhanced formation of SnTe ultimately leads to a release of tellurium. A SnTe compound has in fact been observed by Collins *et al.* under accident conditions.¹²⁵ Only at high oxygen partial pressures, which are above the equilibrium value of Sn/SnO₂, as shown in [Figure 4](#), will tellurium be released in its elemental form. This delayed release behavior for tellurium has been observed in numerous annealing experiments.¹²⁶ Significant tellurium release occurred in the Phebus FPT-0 and FPT-1 tests because of the extent of cladding oxidation. Although antimony, like tellurium, is readily released from the fuel during heating in a severe accident, a lower release is observed since the antimony most likely sequesters in metallic melts (as it alloys with other metals such as nickel and silver).

In [Table 7](#), comparison of the volatile releases for the comparable tests, PBF SFD 1–1 and 1–4, indicates that the release is enhanced in high-burnup fuel compared to trace-irradiated fuel because of the presence of grain boundary tunnels that serve as pathways for gaseous release. Enhanced release rates (due to fuel morphology) occur primarily during the initial heating, while this difference diminishes afterwards (i.e., above ~2200 K), where releases are now dominated by dissolution of the fuel by the molten Zircaloy cladding. Moreover, in [Table 7](#), fuel release is low for the given conditions of the integral

experiments and the TMI-2 accident since just a small amount of hydrogen will significantly lower the oxygen partial pressure, thereby affecting the partial pressures of the uranium-bearing vapor species (e.g., UO_3).^{27,127}

With the occurrence of fuel liquefaction, the release of fission products will be governed by atom and bubble migration in the melt. Although this migration mechanism is faster than diffusion in the solid fuel, a release enhancement is not necessarily observed in the integral tests because of the noncoherent nature of the melt progression. As seen in TMI-2, decay heat from the fission products trapped in the ceramic blockage resulted in the formation of a molten pool. The release of fission gases and volatile fission products residing in this molten pool can be further delayed since they must nucleate into bubbles, and then coalescence and grow in the liquid medium by Brownian motion and buoyancy-biased motion, before they can rise to the pool surface for eventual release.¹²⁸ Gas bubbles can also be trapped at the interface between the pool and the crust that surrounds the pool. The oxygen potential of the molten pool will influence the fission product chemical form, that is, the presence of iron oxides in the melt of the TMI-2 establishes a lower limit of about -120 kJ mol^{-1} at 2800 K so that fission products such as lanthanum, cerium, and strontium should exist as an oxide (i.e., La_2O_3 , Ce_2O_3 , or CeO_2 , and SrO) that is soluble in the $(\text{U}, \text{Zr})\text{O}_2$ ceramic, whereas ruthenium and antimony would be present as metals immiscible in the ceramic melt. Although iodine and cesium are identified as volatile fission products, only small fractions (3–10%) have been observed in previously molten ceramics in the PBF SFD experiments and the TMI-2 reactor.

2.20.6 Conclusion

The physical chemistry of oxide fuels is an exceedingly daunting technical matter in view of the number of elements and potential phases involved, not to mention the complications of conducting experiments at high temperatures with radioactive systems. Moreover, the elemental composition of the fuel is changing with time and the chemical speciation is influenced by exposure to steam or coolant water in the event of a clad failure or other materials in the case of a reactor accident. Nevertheless, advances by those referenced in computational methodologies rooted in numerical modeling linked

to Gibbs energy minimization and related phase field theory are making possible substantial and exciting progress.

Acknowledgments

The authors acknowledge the assistance of M. Piro in the preparation of the chapter.

References

- Hocking, W. H.; Duclos, A. M.; Johnson, L. H. *J. Nucl. Mater.* **1994**, 209, 1–26.
- Kleykamp, H. *J. Nucl. Mater.* **1985**, 131, 221–246.
- Cordfunke, E. H. P.; Konings, R. J. M. *J. Nucl. Mater.* **1988**, 152, 301–309.
- Kleykamp, H. *J. Nucl. Mater.* **1990**, 171, 181–188.
- Kleykamp, H. *Nucl. Technol.* **1988**, 80, 412–422.
- Sah, D. N.; Viswanadham, C. S.; Kumar, S.; Roy, P. R. *Nucl. Technol.* **1989**, 85, 136.
- Johnson, I.; Johnson, C. E. *J. Nucl. Mater.* **1988**, 154, 67–73.
- Kleykamp, H. *J. Nucl. Mater.* **1989**, 167, 49–63.
- Cubiciotti, D.; Sanecki, J. E. *J. Nucl. Mater.* **1978**, 78, 96.
- Matzke, H. *J. Radiat. Eff.* **1980**, 53, 219–242.
- Gittus, J. H.; Mathews, J. R.; Potter, P. E. *J. Nucl. Mater.* **1989**, 166, 132–159.
- Ball, R. G. J.; Burns, W. G.; Henshaw, J.; Mignanelli, M. A.; Potter, P. E. *J. Nucl. Mater.* **1989**, 167, 191–204.
- Thompson, W. T.; Lewis, B. J.; Corcoran, E. C.; et al. *Int. J. Mater. Res.* **2007**, 98(10), 1004–1011.
- Potter, P. E. *J. Nucl. Mater.* **2009**, 389, 29–44.
- Kaye, M. H.; Lewis, B. J.; Thompson, W. T. *J. Nucl. Mater.* **2007**, 366, 8–27.
- Imoto, S. *J. Nucl. Mater.* **1986**, 140, 19–27.
- Kleykamp, H. *J. Nucl. Mater.* **1979**, 84, 109–117.
- Kleykamp, H. *J. Nucl. Mater.* **2005**, 344, 1–7.
- Kleykamp, H. *J. Nucl. Mater.* **1997**, 248, 209–213.
- Higgs, J. D.; Lewis, B. J.; Thompson, W. T.; He, Z. *J. Nucl. Mater.* **2007**, 366, 99–128.
- Arima, T.; Masuzumi, T.; Furuya, H.; Idemitsu, K.; Inagaki, Y. *J. Nucl. Mater.* **2002**, 301, 90–97.
- Sidky, P. S. *J. Nucl. Mater.* **1998**, 256, 1–17.
- Jacques, P.; et al. *J. Nucl. Mater.* **1999**, 264, 239–248.
- Jacques, P.; et al. *J. Nucl. Mater.* **1999**, 264, 249–256.
- Cronenberg, A. W.; Osetek, D. J. *J. Nucl. Mater.* **1987**, 149, 252–260.
- de Boer, R.; Cordfunke, E. H. P. *J. Nucl. Mater.* **1997**, 240, 124–130.
- Lewis, B. J.; Corse, B. J.; Thompson, W. T.; et al. *J. Nucl. Mater.* **1998**, 252, 235–256.
- Sunder, S. *Nucl. Technol.* **2003**, 144, 259.
- Lewis, B. J.; Dickson, R.; Iglesias, F. C.; Ducros, G.; Kudo, T. *J. Nucl. Mater.* **2008**, 380, 126–143.
- Lewis, B. J.; Iglesias, F. C.; Dickson, R. S.; Williams, A. *J. Nucl. Mater.* **2009**, 394, 67–86.
- Bailly, H.; Ménessier, D.; Prunier, C. *The Nuclear Fuel of Pressurized Water Reactors and Fast Reactors: Design and Behaviour*, Commissariat à l'Énergie Atomique; Lavoisier: Paris, France, 1999.
- Kato, M.; Komeno, A.; Uno, H.; et al. *J. Nucl. Mater.* **2009**, 393, 134–140.

33. Olander, D. R. *Fundamental Aspects of Nuclear Reactor Fuel Elements*; TID-26711-P1; Technical Information Centre, US Department of Energy, 1976.
34. Nicoll, S.; Matzke, H. J.; Grimes, R. W.; Catlow, C. R. *J. Nucl. Mater.* **1997**, *240*, 185–195.
35. Thomas, L. E.; Beyer, C. E.; Charlot, L. A. *J. Nucl. Mater.* **1992**, *188*, 80–89.
36. Mogensen, M.; Bagger, C. J. *J. Nucl. Mater.* **1993**, *199*, 85–101.
37. Johnson, C. E.; Steidl, D. V.; Crouthamel, C. E. In *Proceedings of the Conference on Fast Reactor Fuel Element Technology*, New Orleans, LA, 1971; p 603.
38. Graczyk, D. G.; Bandyopadhyay, G.; Gehl, S. M.; Hughes, J. P.; Goodspeed, H. T. *Laser Microsampling Method for Determination of Retained Fission Gas in Irradiated Nuclear Fuels*; Report ANL79-86; 1979.
39. Do, T.; Irving, K. G.; Hocking, W. H. *J. Nucl. Mater.* **2008**, *383*, 34–40.
40. Walker, C. T.; Bremier, S.; Portier, S.; Hasnaouri, B.; Goll, W. *J. Nucl. Mater.* **2009**, *393*, 212–223.
41. Desgranges, L.; Pasquet, B.; Valot, CH.; Roure, I. *J. Nucl. Mater.* **2009**, *385*, 99–102.
42. Viswanathan, U. K.; Sah, D. N.; Rath, B. N.; Anantharaman, S. *J. Nucl. Mater.* **2009**, *392*, 454–551.
43. Une, K.; Kashibe, S. *J. Nucl. Sci. Technol.* **1990**, *27*, 1002–10016.
44. Small, G. J. In *IAEA Specialists Meeting on Water Reactor Fuel Element Computer Modelling in Steady State, Transient and Accident Conditions*, Preston, Sept 1988; Paper IAEA-TC-657/4.3.
45. Matthews, J. R.; Small, G. J. In *IAEA Specialists Meeting on Water Reactor Fuel Element Computer Modelling in Steady State, Transient and Accident Conditions*, Preston, Sept 1988; Paper IAEA-TC-657/4.1.
46. Hiernaut, J. P.; Wiss, T.; Rondinella, V. V.; et al. *J. Nucl. Mater.* **2009**, *392*, 34–438.
47. Shirsat, A. N.; Ali, M.; Kolay, S.; Datta, A.; Das, D. *J. Nucl. Mater.* **2009**, *392*, 16–21.
48. Mansouri, M. A.; Olander, D. R. *J. Nucl. Mater.* **1998**, *254*, 22–33.
49. Tourasse, M.; Boidron, M.; Pasquet, B. *J. Nucl. Mater.* **1992**, *188*, 49–57.
50. Auvinen, A.; Brillant, G.; Davidovich, N.; et al. *Nucl. Eng. Des.* **2008**, *238*, 3418–3428.
51. Iglesias, F. C.; Hunt, C. E. L.; Garisto, F.; Cox, D. S. In *Proceedings of the ICHMT Conference on Fission Products Transport Process in Reactor Accidents*, Dubrovnik, Yugoslavia, May 22–26, 1989; Hemisphere: New York, 1990; p 187.
52. Cordfunke, E. H. P.; Konings, R. J. M. *J. Nucl. Mater.* **1989**, *167*, 205–212.
53. Saha, R.; Babu, R.; Nagarajan, K.; Mathews, C. K. *J. Nucl. Mater.* **1989**, *167*, 271–277.
54. Maeda, K.; Sasaki, S.; Kato, M.; Kihara, Y. *J. Nucl. Mater.* **2009**, *385*, 178–183.
55. Rudisill, T. S. *J. Nucl. Mater.* **2009**, *385*, 193–195.
56. Baker, L.; Just, L. C. Studies of metals water reactions at high temperatures – III Experimental and theoretical studies of the zirconium–water reaction; Technical Report ANL-6548 May; Argonne National Laboratory, 1962.
57. Duriez, C.; Dupont, T.; Schmet, B.; Enoch, F. *J. Nucl. Mater.* **2008**, *380*, 30–45.
58. Pelton, A. D.; Thompson, W. T. *Prog. Solid State Chem.* **1975**, *10*(Pt 3), 119–155.
59. De Groot, S. R.; Manzur, P. *Non-Equilibrium Thermodynamics*; Dover: New York, 1984.
60. Welland, M. J.; Thompson, W. T.; Lewis, B. J.; Manara, D. *J. Nucl. Mater.* **2009**, *385*, 358–363.
61. Chevalier, P. Y.; Fischer, E.; Cheynet, B. *J. Nucl. Mater.* **2002**, *303*, 1.
62. Aronson, S.; Belle, J. *J. Chem. Phys.* **1958**, *29*, 151–158.
63. Hagemark, K.; Broli, M. *J. Inorg. Nucl. Chem.* **1966**, *28*, 2837.
64. Saito, Y. *J. Nucl. Mater.* **1974**, *51*, 112.
65. Kiukkola, K. *Acta Chem. Scand.* **1962**, *16*, 327.
66. Perron, P. O. *Thermodynamics of Non-Stoichiometric Uranium Dioxide*; Report AECL-3072; Atomic Energy of Canada Ltd., 1968.
67. Baranov, V. G.; Godin, Y. G. *At. Energy Engl. Transl.* **1980**, *51*, 633.
68. Une, K.; Oguma, M. *J. Nucl. Mater.* **1982**, *110*, 215.
69. Lindemer, T. B.; Besmann, T. M. *J. Nucl. Mater.* **1985**, *130*, 473–488.
70. Blackburn, P. E. *J. Nucl. Mater.* **1973**, *46*, 244–252.
71. Eriksson, G.; Thompson, W. T. *CALPHAD* **1989**, *13*(4), 389–400.
72. Corcoran, E. C. Ph.D. Thesis, Royal Military College of Canada, Kingston, ON, 2009.
73. Kleykamp, H. *J. Nucl. Mater.* **1993**, *206*, 82–86.
74. Lyon, W. L.; Baily, W. E. *J. Nucl. Mater.* **1967**, *22*, 332–339.
75. Kato, M.; Morimoto, K.; Sugata, H.; Konashi, K.; Abe, T. *J. Nucl. Mater.* **2008**, *373*, 237–245.
76. Kleykamp, H. *J. Nucl. Mater.* **2001**, *294*, 8–12.
77. Philipponeau, T. Fast Reactor European Collaboration Data Sheet, 1990.
78. Belyaev, Y. u. I. *Radiokhimiya* **1983**, *25*, 791–794.
79. Chikalla, T. D.; McNeilly, C. E.; Bates, J. L.; Rasmussen, J. J. In *Int. Col. on the Study of Crystalline Transformation at High Temperature Above 2000 K*, Odeillo, France, 1971.
80. Kleykamp, H.; Paschoal, J. O. A.; Pejsa, R.; Thümmel, F. *J. Nucl. Mater.* **1985**, *130*, 426–433.
81. Kleykamp, H.; Vincenzini, P., Eds. *High Tech Ceramics*; Elsevier Science: Amsterdam, 1987; pp 2769–2798.
82. Muromara, T.; Adachi, T.; Takeishi, H.; Yoshida, Z.; Yamamoto, T.; Ueno, K. *J. Nucl. Mater.* **1988**, *151*, 318–326.
83. Prussin, S. G.; Olander, D. R.; Lau, W. K.; Hansson, L. *J. Nucl. Mater.* **1988**, *154*, 25–37.
84. Lucuta, P. G.; Verrall, R. A.; Matzke, H. J.; Palmer, B. J. *J. Nucl. Mater.* **1991**, *178*, 48–60.
85. Yamanaka, S.; Kurosaki, K. *J. Alloys Compd.* **2003**, *353*, 269–273.
86. Kaye, M. H.; Thompson, W. T.; Lewis, B. J.; Sunder, S.; O'Connor, R. In *7th International Conference on CANDU Fuel*, Kingston, ON, 2001.
87. Imoto, S. *J. Nucl. Mater.* **1986**, *140*, 19–27.
88. Ewart, F. T.; Taylor, R. G.; Horspool, J. M.; James, G. *J. Nucl. Mater.* **1976**, *61*, 254–270.
89. Itaki, T.; Kono, K.; Tachi, H.; Yamonouchi, S.; Yuhara, S.; Shibahara, I. *J. Atomic Energy Soc. Japan* **1985**, *27*, 435–449.
90. Chandrasekhariah, M. S. *J. Nucl. Mater.* **1985**, *130*, 366–374.
91. Kurosaki, K.; Uno, M. *J. Alloys Compd.* **1998**, *271–273*, 641–644.
92. Cordfunke, E. H. P.; Konings, R. J. M. *Thermochemical Data for Reactor Materials and Fission Products*; Elsevier Science: Amsterdam, 1990.
93. Oak Ridge National Laboratory, SCALES–5, Radiation Safety Information Computational Center, 2005.
94. Piro, M. H. A.; Thompson, W. T.; Lewis, B. J. A self standing Gibbs energy minimization procedure to solve chemical equilibrium in multielement multiphase nuclear materials. In *10th International Conference on CANDU Fuel*, Ottawa, ON, Oct 5–8, 2008.

95. Piro, M. H.; Welland, M. J.; Lewis, B. J.; Thompson, W. T.; Olander, D. R. Development of a self-standing numerical tool to compute chemical equilibria in nuclear materials. In *Top Fuel, Light Water Reactor Fuel Performance Conference*, Paris, France, Sept 6–10, 2009.
96. Verrall, R. A.; He, Z.; Mouris, J. J. *Nucl. Mater.* **2005**, *344*, 240–245.
97. Corcoran, E. C.; Kaye, M. H.; Akbari, F.; *et al.* In *International LWR Fuel Performance Meeting*, San Francisco, CA, 2007.
98. Lewis, B. J. *J. Nucl. Mater.* **1988**, *160*, 201–217.
99. Lewis, B. J.; MacDonald, R. D.; Ivanoff, N. V.; Iglesias, F. C. *Nucl. Technol.* **1993**, *103*, 220–245.
100. Lewis, B. J.; El-Jaby, A.; Higgs, J.; *et al.* *J. Nucl. Mater.* **2007**, *366*, 37–51.
101. Killeen, J. C.; Turnbull, J. A. An experimental and theoretical treatment of the release of ^{85}Kr from hyperstoichiometric uranium dioxide. In *Proceedings of the Workshop Chemical Reactivity of Oxide Fuel and Fission Product Release*, Gloucestershire, England, Apr 7–9, 1987; Central Electricity Generating Board, 1987; p 387.
102. Cox, D. S.; Iglesias, F. C.; Hunt, C. E. L.; O'Connor, R. F.; Barrand, R. D. High temperature oxidation behaviour of UO_2 in air and steam. In *Proceedings of the International Symposium on High-Temperature Oxidation and Sulphidation Process*, Hamilton, ON, Aug 26–30, 1990.
103. Abrefah, J.; de Aguiar Braid, A.; Wang, W.; Khalil, Y.; Olander, D. R. *J. Nucl. Mater.* **1994**, *208*, 98.
104. Park, K.; Yang, M. S.; Park, H. S. *J. Nucl. Mater.* **1997**, *247*, 116–120.
105. Lewis, B. J.; Duncan, D. B.; Phillips, C. R. *Nucl. Technol.* **1987**, *77*, 303–312.
106. Lewis, B. J.; Iglesias, F. C.; Postma, A. K.; Steininger, D. A. *J. Nucl. Mater.* **1997**, *244*, 153–167.
107. Bishop, W. N. *Iodine Spiking*; EPRI NP-4595; Electric Power Research Institute, 1986.
108. Da Silva, R. L.; McCracken, D. R.; Monserrat, K. J. *Adv. Ceram.* **1985**, *17*, 107–120.
109. Pourbaix, M. *Atlas of Electrochemical Equilibria in Aqueous Solutions*; Pergamon: New York, 1966.
110. Lewis, B. J.; Thompson, W. T.; Akbari, F.; Morrison, C.; Husain, A. J. *Nucl. Mater.* **2005**, *340*, 69–82.
111. Ticknor, K. V.; Cho, Y. H. *J. Radioanal. Nucl. Chem.* **1990**, *140*, 75–90.
112. Taylor, P.; Wood, D. D.; Owen, D. G.; Park, G. I. *J. Nucl. Mater.* **1991**, *183*, 105.
113. Hobbins, R. R.; Petti, D. A.; Hagrman, D. L. *Nucl. Technol.* **1993**, *101*, 270.
114. Wright, R. W.; Hagen, S. J. L. In *The Phebus Fission Product Project*; Krischer, W., Rubinstein, M. C., Eds.; Elsevier Applied Science: New York, 1992; p 49.
115. Iglesias, F. C.; Lewis, B. J.; Reid, P. J.; Elder, P. J. *Nucl. Mater.* **1999**, *270*, 21.
116. Cronenberg, A. W. *Nucl. Technol.* **1992**, *97*, 97.
117. Dubourg, R.; Faure-Geors, H.; Nicaise, G.; Barrachin, M. *Nucl. Eng. Des.* **2005**, *235*, 2183–2208.
118. Dubourg, R.; Taylor, P. *J. Nucl. Mater.* **2001**, *294*, 32–38.
119. Hanniet, N.; Repetto, G. Phebus PF, FPT0 – Final Report, CD Version, Suntech 10/99.
120. Allen, M. D.; Stockman, H. W.; Reil, K. O.; Grimley, A. J.; Camp, W. J. ACRR Fission Product Release Tests ST-1 and ST-2. In *Proceedings of the International Conference on Thermal Reactor Safety*, Avignon, France, Oct 2–7, 1988; Vol. 5.
121. Osborne, M. F.; Lorenz, R. A. *Nucl. Saf.* **1992**, *33*, 344.
122. Andre, B.; Ducros, G.; Leveque, J. P.; Maro, D.; Osborne, M. F.; Lorenz, R. A. *Nucl. Technol.* **1996**, *114*, 23.
123. Bowsher, B. R.; Dickinson, S.; Gomme, R. A.; Jenkins, R. A.; Nichols, A. L.; Ogden, J. S. The interaction of zircaloy cladding with fission product tellurium released during a severe reactor accident. In *Proceedings of the Workshop on Chemical Reactivity of Oxide Fuel and Fission Product Release*, Gloucestershire, England, Apr 7–9; Central Electricity Generating Board: Berkeley, Gloucestershire, 1987; p 455.
124. De Boer, R.; Cordfunke, E. H. P. *J. Nucl. Mater.* **1995**, *223*, 103.
125. Collins, J. L.; Osborne, M. F.; Lorenz, R. A. *Nucl. Technol.* **1987**, *77*, 18.
126. Lewis, B. J.; Andre, B.; Ducros, G.; Maro, D. *Nucl. Technol.* **1996**, *116*, 34.
127. Olander, D. R. *J. Nucl. Mater.* **1999**, *270*, 187.
128. McClure, P. R.; Leonard, M. T.; Razani, A. *Nucl. Sci. Eng.* **1993**, *114*, 102.

2.21 Fuel Performance of Fast Spectrum Oxide Fuel

Y. Guerin

Commissariat à l'Energie Atomique, Cadarache, St Paul Lez Durance, France

© 2012 Elsevier Ltd. All rights reserved.

2.21.1	Introduction	548
2.21.2	Experience with Oxide Fuel in Fast Reactors	548
2.21.2.1	History of Development	548
2.21.2.2	Fuel Element Design	549
2.21.2.3	Operating Conditions	550
2.21.2.4	Main Objectives and Requirements of Fast Oxide Fuel Development	551
2.21.3	Behavior at Beginning of Life	552
2.21.3.1	Temperature Distribution in Oxide Pellets	552
2.21.3.1.1	Thermal conductivity of oxide fuel	552
2.21.3.1.2	Temperatures inside the fuel rod	552
2.21.3.2	Fuel Restructuring	553
2.21.3.2.1	Pellet cracking	553
2.21.3.2.2	Formation of columnar grains and central hole	553
2.21.3.2.3	Grain growth	554
2.21.3.3	Redistribution of Fuel Constituents	554
2.21.3.3.1	Oxygen redistribution	555
2.21.3.3.2	Plutonium redistribution	556
2.21.3.3.3	Redistribution of minor actinides	557
2.21.3.4	Geometrical Evolution	558
2.21.3.4.1	Gap closure	558
2.21.3.4.2	Evolution of fuel stack length	559
2.21.4	Consequences of Fission	559
2.21.4.1	Formation of Fission Products and MA	559
2.21.4.2	Chemistry of Fission Products	560
2.21.4.2.1	Fission products in solid solution	561
2.21.4.2.2	Fission products forming oxide precipitates	561
2.21.4.2.3	Fission products forming metallic precipitates	561
2.21.4.2.4	Volatile fission products	562
2.21.4.2.5	Gaseous fission products	562
2.21.4.3	Evolution of O/M Ratio and Oxygen Potential	563
2.21.4.4	Migration of Fission Products	564
2.21.4.4.1	Radial migration	564
2.21.4.4.2	Evolution of fuel to cladding gap: JOG formation	564
2.21.4.4.3	Axial migration	566
2.21.4.5	Behavior of Fission Gases	567
2.21.4.5.1	Formation of fission gases	567
2.21.4.5.2	Fission gas release	567
2.21.4.6	Fuel Swelling	569
2.21.5	Limiting Phenomena	569
2.21.5.1	Margins to Fuel Melting	570
2.21.5.1.1	Temperature field in the oxide fuel	570
2.21.5.1.2	Nominal situation and case of control rod withdrawal	571
2.21.5.2	Fuel Cladding Mechanical Interaction	571
2.21.5.2.1	Limit burnup due to FCMI during steady-state operation	571
2.21.5.2.2	FCMI due to power increases	572
2.21.5.2.3	FCMI due to cesium accumulation	572

2.21.5.3	Fuel Cladding Chemical Interaction	573
2.21.5.3.1	Early-in-life corrosion	573
2.21.5.3.2	Intergranular corrosion	574
2.21.5.3.3	Corrosion at high burnup	574
2.21.5.3.4	Corrosion at fissile–fertile interface	575
2.21.6	Cladding Failure	575
2.21.7	Summary and Outlook	576
References		577

Abbreviations

CW	Cold worked
DND	Delayed neutron detector
dpa	Displacement per atom
EPMA	Electron probe microanalysis
FCCI	Fuel cladding chemical interaction
FCMI	Fuel cladding mechanical interaction
FFTF	Fast Flux Test Facility
FP	Fission product
HBS	High burnup structure
JOG	Joint oxyde gain (oxide cladding joint)
LBE	Lead bismuth eutectic
LWR	Light water reactor
MA	Minor actinides
NTP	Normal temperature
O/M ratio	Oxygen to metal ratio
ODS	Oxide dispersion strengthened
PFR	Prototype Fast Reactor
PWR	Pressurized water reactor
R&D	Research and development
RE	Rare earth (or lanthanide)
SA	Solution annealed
SEM	Scanning electron microscope
TD	Theoretical density

2.21.1 Introduction

Despite some disadvantages, such as its low density of heavy atoms, its poor thermal conductivity, and its chemical reaction with sodium, mixed oxide fuel (U,Pu)O₂ is the fuel that has been used most in fast reactors FRs worldwide. This is due to its advantageous properties such as high melting point, with no allotropic changes, excellent stability, and an excellent behavior under irradiation, in particular, a swelling rate much lower than the other fuels.

Oxide fuel is contemplated as a reference fuel in several fast reactor systems of Generation IV, in particular, sodium-cooled fast reactors and LBE (lead bismuth eutectic)-cooled reactors. Nevertheless,

experience on the behavior of oxide fast fuel has been gained essentially in sodium fast reactors and, consequently, this chapter addresses mainly this type of fuel.

This chapter recalls first some generalities on fast oxide fuels: existing experience, main design of fuel pins, operating conditions, requirements, and main objectives of fuel development. Then, the main phenomena occurring in fast oxide fuels are described, focusing first on behavior at the beginning of life and high-temperature effects such as fuel restructuring, radial redistribution of fuel constituents, and geometrical evolution. The behavior of fission products is described, with the consequences on thermochemistry of oxide pellets such as the evolution of O/M ratio, as well as on fuel swelling or fission gas release. The main potential-limiting phenomena are presented, addressing thermal, mechanical, and chemical life-limiting mechanisms. The behavior of in-pile failed pins is briefly recalled before concluding the chapter.

General information on fast oxide fuel behavior and performance can also be found in Olander,¹ Lambert,² Guérin,³ Millet,⁴ Martin,⁵ and Pelletier.⁶

2.21.2 Experience with Oxide Fuel in Fast Reactors

2.21.2.1 History of Development

The first fast breeder reactors, built in the 1950s in the United States and in the United Kingdom, used metallic fuel (plutonium and uranium), as metals offer the highest heavy metal density and therefore the highest breeding ratio. Because of dimensional instability due to swelling and growth, metal fuels could hardly achieve high burnup. By the 1960s, mixed uranium and plutonium oxide (U,Pu)O₂ was known to be highly radiation tolerant and began to be considered as a reference fuel for fast reactors. Extensive studies were also carried out on mixed carbide and nitride fuels (U,Pu)C and (U,Pu)N, which have a better breeding ratio than oxide, thanks to their density, which lies between the oxide and the metal fuel.

The experimental fast reactor built in the 1960s and 1970s largely used mixed oxide as a reference fuel. This was the case in Rapsodie (France, 1967), BOR 60 (USSR, 1968), KNK II (Germany, 1972), JOYO (Japan, 1978), and FFTF (USA, 1980). As irradiation of oxide fuels in these reactors was highly successful, all the prototype or commercial fast reactors built in the 1970s later chose oxide as reference fuels (Table 1). Consequently, mixed oxide is the fast fuel, experience of which is by far the largest available. Several hundreds of thousands of oxide fuel pins have been successfully irradiated worldwide in fast reactors (e.g., 180 000 in Phénix, 98 000 in Prototype Fast Reactor (PFR), 63 000 in Fast Flux Test Facility (FFTF)). Along with driver fuels, a great number of experimental

fuel pins have been irradiated, in order either to test new fuel pin designs or new materials, or to test behavior in off-normal conditions, including accidental situations. These experiments provided a solid background of knowledge on the behavior of oxide fuel and a large database for the validation of models and fuel performance codes.

2.21.2.2 Fuel Element Design

Table 1 provides the main characteristics of fuel elements in prototype and commercial fast reactors. Despite the scatter in the values of the different parameters, these fuel elements refer to rather similar fuel concepts.

Table 1 Main characteristics of standard fuel pins irradiated in the prototype and commercial fast reactors ($p > 200$ MWth)

	BN350	Phénix	PFR	BN600	FFTF ^a	Super-Phénix	MONJU
First criticality	1972	1973	1974	1979	1980	1985	1994
Thermal power (MWth)	750	563	600	1470	400	3000	714
Electric power (MWe)	350 ^b	250	250	600	–	1200	280
Type of fuel	UO ₂	(U,Pu)O ₂	(U,Pu)O ₂	UO ₂	(U,Pu)O ₂	(U,Pu)O ₂	(U,Pu)O ₂
No. of subassemblies (inner/outer core)	109/117	55/48	28/44	209/160	28/45	193/171	108/90
No. of pins per assembly	127	217	325	127	217	271	169
Type of spacer	Wire	Wire	Grids	Wire	Wire	Wire	Wire
Length of pin (m)	1.8	1.793	2.25	2.445	2.38	2.7	2.813
Height of fissile column (m)	1.06	0.85	0.914	1.0	0.914	1.0	0.93
Lower fertile column length (m)	0.4	0.3	0.45	0.4	–	0.3	0.35
Upper fertile column length (m)	0.57	0.31	0.45	0.4	–	0.3	0.3
Clad outer diameter (mm)	6.9	6.55	5.8	6.9	5.84	8.5	6.5
Clad thickness (mm)	0.4	0.45	0.38	0.4	0.38	0.565	0.47
Helical wire diameter (mm)		1.15			1.42	1.2	1.32
Pellet diameter (mm)		5.42				7.14	5.4
Fuel clad diametral gap (mm)		0.23			0.14	0.23	0.16
Central hole diameter (mm)	0	0	1.5	0		2.0	0
Fissile atoms/(U + Pu) (%) (inner core/outer core)	17/26	18/23	22/28	17/26	20/25	15/22	16/21
Fuel density (% TD)	95	95.5	97	95	91	95.5	85
Smeared density (%)	75	88	78	77	86	83	80
Plenum volume (cm ³)	8	13	14	21	19	43	28
Maximum linear power (W cm ^{−1})	400	450	420	472	413	470	360
Peak cladding temperature (°C)	570	650	670	700	660	620	675
Maximum neutron flux (10 ¹⁵ n cm ^{−2} s ^{−1})	7	7.1	7.6	7.7	7	6	6.0
Maximum burnup (at.%)	9.0	16.9	23.5	11.8	24.5	Not relevant	Not relevant
(GWd t ^{−1})	65	144	200				
Maximum dose (dpa)	60	156	155	90		–	–

Source: IWGFR. LMFBR plant parameters. In *International Working Group on Fast Reactors*; International Atomic Energy Agency: Vienna, 1991; IWGFR/80; IAEA-TECDOC. *Status of Liquid Metal Cooled Fast Reactor Technology*; International Atomic Energy Agency: Vienna, 1999; IAEA-TECDOC-1083.

P means power.

^aFFTF is usually classified as an experimental reactor rather than a prototype reactor. But from a fuel point of view, irradiation of fuel pins in FFTF is rather prototypic.

^bIncluding 200 MWe for desalting water.

The fuel pin is a long cylinder (2–3 m long, 5–10 mm diameter), clad in a steel tube (~ 0.4 – 0.6 mm thick) closed in both ends by welded plugs, preventing direct contact between the radioactive material and the sodium coolant. The cladding serves as a first safety barrier and is designed to keep its integrity and tightness in nominal and off-normal conditions.

The oxide fissile column (~ 1 m long) consists of a stack of conventionally pressed and sintered pellets with an outer diameter slightly smaller than the inner diameter of the clad, providing a gap (~ 100 μm radial gap) between fuel and cladding needed for the fabrication. Depending upon the design, both full pellets and annular pellets (with a central hole between 1.5 and 2 mm) have been used. Other concepts have also been tested (especially in United Kingdom and Russia), where pellets are replaced by a vibropacked piling-up of fuel particles, which may be either spheres produced by sol–gel, or fuel particles obtained by a pyrometallurgical process. (In the pyrometallurgical process, spent fuel is dissolved in molten salt and oxide is extracted by electrolysis.)

UO_2 axial blankets (0.3–0.5 m long) made with natural or depleted uranium are placed at the lower and upper ends of the fissile column. The trend in the future might be to suppress the use of these fertile columns. But, other concepts of fuel pins have also been tested, as the axially heterogeneous fuel pin in which a short fertile column is located in the middle of the fissile column, in order to decrease the reactivity loss rate.⁷

Two gas plenums are located at both ends of the fuel pin, providing free volume for the released fission gases and limiting the internal pressure induced by fission gas release. Typically, the volumes of the plena and of the fissile column are about the same. The largest plenum is preferably located at the bottom end of the fuel pin, as it is the colder place in the fuel pin, thus mitigating the gas pressure increase. At the end of fabrication, fuel pins contain helium gas under 1 atm. Helium has been chosen because of its high thermal conductivity in order to improve the heat transfer through the gap between the fuel and the cladding at the beginning of life.

In the upper plenum, a stainless steel spring maintains the fuel column during fabrication, transportation, and handling stages.

Fuel subassemblies consist of a bundle of hexagonally packed fuel pins (~ 100 – 300 pins in each subassembly).

Around each pin, a steel wire (~ 1 – 1.5 mm diameter), helically wrapped around the cladding, and

attached to the end plugs, ensures regular spacing of the pins and sodium mixing. In some reactors, such as PFR and KNK II, grids replace the helical wire and ensure the spacing function.

Parallel rails make up a bottom grid to which the lower plugs of fuel pins are attached.

The bundle of fuel pins is contained in a steel hexagonal wrapper tube, which has essentially two functions: it forms the cooling channel and allows coolant flow to be adjusted, thanks to a depressor system located in the bottom nozzle. With the top and the bottom nozzle to which it is connected by welding and crimping, it forms the mechanical structure of the subassembly, allowing handling and positioning in the reactor core.

The core of the reactor consists of the piling-up of a great number of subassemblies (~ 100 – 400). The diameter of the core is about 1–2 m in prototypic reactors, up to 4 m in commercial reactor. The core is typically 1 m high, or a little less in prototypic reactors.

Fuel pellets are generally mixed oxide ($\text{U,Pu}\text{O}_2$) (with the exception of Russian reactors where they are made of uranium oxide) with a plutonium content between 15% and 30%. The plutonium content is higher in the outer core than in the inner core in order to compensate the decrease of neutron flux at the periphery of the reactor core.

The oxide pellets, fabricated by powder metallurgy (ball milling, pressing, and sintering), contain several volume percentages of porosity that will help accommodate fuel swelling: pellet densities of as-fabricated fuel lie generally around 95% of theoretical density, but may lower down to 85% (Table 1). As-fabricated pellets may be either solid pellets (orthocylinders) or annular pellets.

Mixed oxide fuel is hypostoichiometric: O/M ratio (where M denotes U + Pu) of as-fabricated pellets lies typically in the range 1.93–1.99.

2.21.2.3 Operating Conditions

Fuel pins of fast reactors are designed to operate at a high linear heat generation rate: between ~ 400 and 500 W cm^{-1} , about twice higher than standard linear power in light water reactors (LWRs). As the fast reactor fuel pin diameters are generally smaller than classical rod diameters of LWRs, the power density and heat fluxes are much higher in fast reactors than in LWRs. For example, in a Phénix fuel pin at 450 W cm^{-1} , the power density in the pellet reaches almost 2000 W cm^{-3} and the heat flux in the gap between fuel and cladding is 260 W cm^{-2} , whereas

in a pressurized water reactor (PWR), these values are about 400 W cm^{-3} and 80 W cm^{-2} .

Due to the low height to diameter ratio of the fast reactor cores, the axial profile of neutron flux and linear heat rate is rather peaked, with a maximum to mean ratio in the range 1.2–1.3.

The linear heat rate of the fuel pins, which depends on the position in the core, decreases continuously due to depletion of fissile materials with the burnup. The higher the initial plutonium content, the higher the decrease rate.

The sodium coolant is not pressurized, but its weight induces a few bars of pressure in the bottom part of the fuel bundle. Sodium enters the bottom part of the core at about 400°C or slightly lower, and the average coolant temperature above the core is typically about 550°C . Locally, the temperatures may be higher and fuel pins for fast reactors are designed to withstand maximum cladding temperatures above 600°C (typically between ~ 620 and 650°C).

The neutron flux is very intense ($\sim 7 \times 10^{15} \text{ n cm}^{-2} \text{ s}^{-1}$ in the core center) and the neutrons have high energy. Consequently, the metallic materials in the subassembly (cladding, wire, and wrapper tube) suffer high damage, more than 100 dpa (displacement per atom) at high burnup. This was one of the main challenges in the development of fast reactors: qualifying metallic materials able to withstand such high damage while keeping to a certain extent, their dimensional stability and suitable mechanical properties.

The mean residence times of fuel subassemblies lie in the range 400–800 days. The mean length of a reactor cycle is typically around 100 days. Even if some shuffling is possible, fuel subassemblies remain in the same zone (inner or outer core) during their whole life.

2.21.2.4 Main Objectives and Requirements of Fast Oxide Fuel Development

In order to reduce fuel cycle costs, the main objective of oxide fuels R&D for fast reactors has been to reach high burnup, typically around 150 GWd t^{-1} , about twice the burnup achieved in LWRs. First experimental results demonstrated that the oxide fuel is able to reach very high burnups: in Rapsodie, for example, a burnup above 25 at.% ($\sim 240 \text{ GWd t}^{-1}$) had been achieved in the 1970s. The main difficulty has been to reach high burnups for oxide fuel pins irradiated in representative conditions, which means

with high damage dose on the cladding, while complying with all reliability and safety requirements. Table 1 gives some indications on the maximum burnups that have been achieved in the different prototypic reactors. Altogether, about 10 000 oxide fuel pins have reached a burnup of 15 at.-%.

The main requirements and design criteria are the following:

- Guaranteeing the absence of fuel melting, both in nominal conditions and during off-normal events. This criterion must be fulfilled with a high confidence level, that is, taking into account all uncertainties. It has been the main factor limiting the linear heat generation rate of fuel pins.
- Keeping cladding integrity and fuel pin tightness. The probability of cladding failure in nominal conditions must remain low ($\sim 10^{-5}$) in order to guarantee a low activity of sodium coolant. Experience showed that the main cause of failure in fast reactor oxide pins was related to excessive clad deformation because of steel swelling. This was the main factor limiting the increase of in-reactor lifetime and fuel burnup. In fact, the limitation was not on burnup but on the maximum dose the steel material could withstand. Indeed, other causes of fuel failures have also to be taken into account, in particular, loadings due to mechanical interaction between fuel and cladding, or reduction of clad ductility or strength due either to irradiation embrittlement or a decrease in the width of sound material due to fuel cladding chemical interaction (FCCI).
- Cooling of the fuel pin bundle must be ensured up to high burnup in all operating conditions. Again, clad and wire deformations induced by steel swelling appeared to be the main limitation as they alter the bundle thermal-hydraulics, eventually leading to local overheating.
- Loading and unloading of subassemblies have to be guaranteed, which induces a limitation on the deformation of the hexagonal wrapper tubes. Swelling induces an increase in the flat to flat width of the wrapper tubes and also, in the periphery of the reactor core, a bowing of subassemblies due to a swelling gradient. In addition, the small inner pressure of sodium (a few bars) may induce deformation of the wrapper flats by irradiation creep.

Demonstration of fuel compliance to the various requirements is done with the help of fuel performance codes, which take into account all the known phenomena and which have been developed and validated against experimental results.

2.21.3 Behavior at Beginning of Life

2.21.3.1 Temperature Distribution in Oxide Pellets

Most phenomena occurring inside oxide fuel pellets are thermally activated, and a good knowledge of the thermal field inside the fuel stack is of paramount importance.

2.21.3.1.1 Thermal conductivity of oxide fuel

Thermal conductivity of oxide fuel is the key property to calculate the temperatures in the fuel pellets and it has received much attention. (U,Pu)O₂ oxide fuel is an ionocovalent material with a rather poor thermal conductivity, in the range of 2–3 W m⁻¹ K⁻¹ in the operating temperature range for an as-fabricated oxide 100% dense. At low temperatures, up to about 1800 K heat migrates by a phonon mechanism, while at higher temperatures, electronic conductivity is predominant. The correlation used for thermal conductivity λ of oxide has generally the following form: the first term applying to phonon conduction λ_{ph} and the second term λ_e predominant at high temperatures refer to electronic conduction with a possible contribution of heat transfer by radiation

$$\lambda = \lambda_{ph} + \lambda_e = \frac{1}{a + bT} + \frac{d}{T^2} \exp\left(-\frac{Q}{T}\right)$$

where the coefficient a accounts for phonon scattering by point defects of the lattice and the bT term stands for the contribution from the anharmonic interaction between phonons.

In addition, conductivity of the oxide decreases with the porosity p (about 14% decrease for a porosity of 5%). λ also decreases sharply as the O/M ratio decreases. As oxide fuels used in fast reactors are hypostoichiometric, this deviation from stoichiometric compositions brings an additional drop of the conductivity at the beginning of life.

Last but not the least, thermal conductivity decreases during irradiation as a consequence of fission products and irradiation-induced point defects. Nevertheless, this last effect is partly compensated by an increase in O/M ratio resulting from fission (see [Section 2.21.4.3](#)). See [Chapter 2.17, Thermal Properties of Irradiated UO₂ and MOX](#) for more details on thermal conductivity.

2.21.3.1.2 Temperatures inside the fuel rod

The heat produced inside the fuel pellet flows toward the coolant through the gas gap and the cladding. As the external cladding temperature T_{ec} is known,

the inner temperature T_{ic} is deduced from the heat equation in the cladding:

$$T_{ic} - T_{ec} = \frac{P_l}{2\pi\lambda_c} \ln\left(\frac{r_{ec}}{r_{ic}}\right)$$

where P_l is the linear power, λ_c is the thermal conductivity of the cladding, and r_{ec} and r_{ic} are the external and the internal cladding radii.

The heat flux flowing through the gas gap between the fuel and the cladding is proportional to the difference between the surface temperature T_s of the fuel pellet and the cladding inner temperature T_{ic} :

$$T_s - T_{ic} = \frac{1}{b} \frac{P_l}{2\pi r}$$

where r is the pellet radius. The heat transfer coefficient b is the sum of three terms:

$$b = b_c + b_R + b_{cond}$$

- b_{cond} : conductive heat transfer coefficient is linked to the width of the gap and to the gas conductivity. This is why the pins are filled with helium that is the inert gas with the highest thermal conductivity. The heat transfer from fuel to gas and from gas to cladding introduces an additional resistance term that needs to be taken into account. As long as the gap is open, conduction plays a predominant role.
- b_R : radiative heat transfer coefficient. As a T^4 term intervenes in this coefficient, the contribution of radiation to heat transfer is generally very low in nominal irradiation conditions.
- b_c : contact or solid–solid heat transfer coefficient, different from 0 when the gap is closed, is linked to contact pressure and to roughness of the fuel and cladding surface.

Inside the fuel pellet, the radial flux depression can be disregarded in fast reactors. In the case of a solid pellet, the heat equation may be simply written:

$$\int_{T_s}^{T_c} \lambda dT = \frac{P_l}{4\pi}$$

where T_c and T_s are the center and the surface temperatures of the fuel pellet, and λ is the fuel thermal conductivity.

Examples of typical radial temperature profiles are given in [Figure 1](#) for a linear power of 450 W cm⁻¹. Center temperature may exceed 2000 °C, with a thermal gradient reaching several thousands of kelvins per centimeter. These very high operating

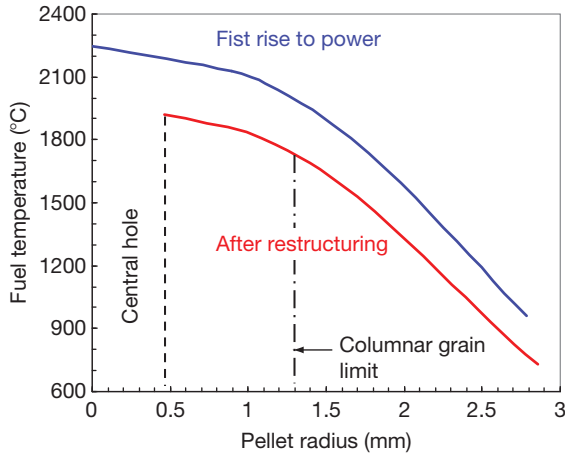


Figure 1 Radial temperature profile in oxide pellet calculated in a Phénix pin (at first rise to power and after restructuring and central hole formation).

temperatures, much higher than in oxide fuel irradiated in thermal reactors, will induce several phenomena specific of oxide behavior in fast spectrum and considerable changes of microstructure during the initial irradiation period.

2.21.3.2 Fuel Restructuring

2.21.3.2.1 Pellet cracking

The radial temperature gradient in the fuel induces internal stresses since the center tends to expand more than the periphery. In a plane strain approximation, the hoop and the axial stresses σ_θ and σ_z at the surface of the pellet are tensile stresses given by:

$$\sigma_\theta = \sigma_z = \frac{E\alpha}{2(1-\nu)}(T_c - T_s)$$

with E being Young's modulus (~ 168 GPa at 1000°C), α the thermal expansion coefficient ($\sim 10 \times 10^{-6}$), and ν the Poisson ratio (~ 0.31).

At low temperatures, under about 1400°C , the oxide is brittle, with a rupture stress of about 130 MPa. A 100°C difference between T_c and T_s is sufficient to induce tensile stresses at the periphery of the pellet of about 120 MPa, which means that oxide fuel pellets start to crack at the very beginning of the first power rise when linear power is still 10% of full power. Pellet cracking is the first phenomenon occurring in the fuel pellet at the beginning of life. At the end of power rise, the central area of oxide pellets becomes ductile, but many radial and axial cracks have already been formed.

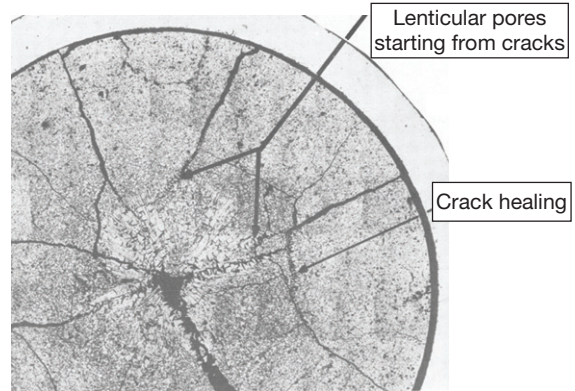


Figure 2 Micrograph of an oxide pellet irradiated at start-up of Rapsodie for 4 h at 380 W cm^{-1} .

2.21.3.2.2 Formation of columnar grains and central hole

Because of the very high temperatures and steep temperature gradients, spectacular changes in the microstructure occur in a short time, during the first hours and days at full power. Figure 2 gives an example of this restructuring effect.

In the central area of the pellets, that is, at very high temperatures ($\geq 2000^\circ\text{C}$), pores tend to a disk shape, a few micrometers thick ($\sim 5\text{--}10 \mu\text{m}$) with a diameter of several tens of micrometers ($\sim 50\text{--}100 \mu\text{m}$), the axis of symmetry oriented in the thermal gradient: they are called 'lenticular pores.' Between the hot and the cold faces of these lenticular pores, the thermal gradient $(dT/dx)_p$ is greater than the gradient $(dT/dx)_f$ in the neighboring fuel

$$\left(\frac{dT}{dx}\right)_p = \frac{\lambda_f}{\lambda_p} \left(\frac{dT}{dx}\right)_f$$

λ_f/λ_p , the ratio of fuel thermal conductivity to the conductivity of gas contained in the pores, is much higher than 1. The gas contained in these pores is a mixture of helium that has been filled in the pin during the fabrication, with small amounts of fission gases (xenon and krypton) and spurious gases (essentially CO) arising from impurities.

The pressure of the fuel vapor in equilibrium with the oxide is higher on the hot side of the lenticular pore than on its cold side. This difference in vapor pressures induces an evaporation–condensation mechanism: matter evaporating from the hot face and condensing on the cold face travels down the thermal gradient, inducing an inverse displacement of the lenticular pores that climb the thermal gradient toward the center of the pellet.

The displacement velocity of the pore v_p is an increasing function of the temperature gradient $(dT/dx)_p$, the oxide vapor pressure (and therefore the temperature), and the diffusion rate D_g of the oxide molecules through the gas contained in the pores. D_g decreases with the pressure in the pores (a few atmospheres) and the atomic mass of the gas.

$$v_p = A \frac{D_g}{T^3} \exp\left(-\frac{\Delta H_v}{kT}\right) \left(\frac{dT}{dx}\right)_p$$

where ΔH_v is the vaporization enthalpy.

The oxide vapor condenses on the cold side in a nearly single crystal way. While moving toward the pellet center, the lenticular pores destroy the initial fuel microstructure and leave behind them a dense fuel ($\sim 97\%$ TD) in very elongated crystal grains (>1 mm long by a few tens of micrometer width) called ‘columnar grains’ that appear clearly in metallographs (see [Figure 2](#)). The grain boundaries of these columnar grains are delineated by trails of small spherical pores ($\sim 1 \mu\text{m}$) that have been left from the periphery of the large lenticular pores during their migration.

The emergence of these lenticular pores at the center of the pellet leads to the formation of a central hole in as-fabricated full pellets. The cracks’ volume of the central area and a fraction of the pellet initial porosity and of the initial gap are thus transferred toward the central hole. During the first stage of the process, cracks are the main source giving rise to lenticular pores, and migration of these pores is the main mechanism for healing the cracks.

At very high temperatures ($\geq 2000^\circ\text{C}$), this migration of lenticular pores by vapor transport is a very efficient mechanism to form columnar grains and central void: a large part of this fuel-restructuring process has taken place in a few hours. At lower temperatures in the range $1800\text{--}2000^\circ\text{C}$, even if lenticular pores are not systematically observed, elongated grains may be formed resulting from grain growth and migration in the thermal gradient of spherical pores. This migration can occur either by vapor transport (as lenticular pores) or by volume diffusion in the oxide surrounding the pore.

The displacement velocity of the pores varies very rapidly with temperature, and the columnar grains only form at high temperatures above $\sim 1800^\circ\text{C}$. This external limit of the columnar grains, that is, the frontier between columnar grains and equiaxed grains, is often used to deduce thermometric information, assuming that the observed microstructural

changes can be correlated to a fixed temperature. This assumption is not fully rigorous, as not only temperature but also temperature gradient and time play a role in these restructuring mechanisms, and the temperature at a given radius is continuously evolving as a consequence of gap closure and restructuring effects. Nevertheless, this assumption gives an approximation and helps in validating the thermal calculations of the fuel performance codes: the higher the temperature, the greater the diameters of the central hole and of the columnar grains.

In the case of annular pellets, these restructuring mechanisms occur in a similar way, inducing an enlargement of the initial central hole at all levels with high linear heat rates ($\geq 350 \text{ W cm}^{-1}$). These mechanisms are also efficient in the case of vibro-compacted fuel: the vibropacked microstructure disappears from the central area, and a central hole and columnar grains appear quite similar to those observed in full pellets.⁸

One of the main consequences of this restructuring is a decrease in the center temperature resulting from two effects: the geometry change, especially when a full pellet is transformed into an annular pellet, and the slight decrease of porosity with a positive effect on fuel thermal conductivity.

2.21.3.2.3 Grain growth

Micrographs of the irradiated oxide fuel reveal an increase in grain size in a ring outside the columnar grain region, for temperatures of about $1300\text{--}1800^\circ\text{C}$. This grain growth results from the displacement of grain boundaries induced by a reduction of the energy linked to surface tension of the boundaries; smaller grains disappear to the benefit of larger ones.

This grain growth mechanism, which also occurs during out-of-pile annealing of the oxide pellets, has a faster kinetic in reactor, at least at low burnup, because of irradiation-enhanced diffusion. However, at high burnup, grain boundaries are blocked by an accumulation of intergranular gas bubbles.

2.21.3.3 Redistribution of Fuel Constituents

Because of the high temperatures and of the very large temperature gradients, radial redistributions of constituents have been systematically observed. These redistributions are made possible by vapor transport, thanks to radial cracks and interconnected porosity, which provide easy paths for transport, allowing communication between the hot and the

cold areas of the fuel pellets. Migration of components also occurs in the solid phase by thermal diffusion; the driving forces for radial migration obey the laws of irreversible thermodynamics.

2.21.3.3.1 Oxygen redistribution

The as-fabricated oxide pellets to be used as fuel in fast reactors are always hypostoichiometric with an initial O/M typically in the range 1.93–2.00. Some experiments have shown that in the early stages of irradiation, oxygen is redistributed radially, migrating down the thermal gradient, thus bringing the composition close to stoichiometry near the periphery, whereas the O/M ratio becomes very low in the hottest area. This oxygen redistribution occurs without affecting the mean O/M ratio of the pellets. Most of these experiments have been performed in out-of-pile tests, but a few results were obtained from in-pile experiments. Figure 3, for example,⁹ shows the local O/M values as a function of pellet radius for different initial O/M ratios. These local O/M ratios were deduced from lattice parameters measured on the oxide powder taken out of concentric rings microdrilled in irradiated pellets. These pellets were extracted from fuel rods with different initial O/M ratio irradiated in thermal reactor to very low burnup, then quenched at the end of irradiation in order to avoid oxygen redistribution during cooling.

Because of the high oxygen diffusion rate, this radial redistribution of oxygen occurs very rapidly during the first power rise, as it may be concluded from the experiments on pins equipped with a thermocouple in the central hole.

Studies of this phenomenon have been carried out mainly in the 1960s and 1970s. Several mechanisms have been proposed to explain this redistribution.

2.21.3.3.1.1 Oxygen migration by vapor transport

One of the first proposed models is based on the assumption that oxygen is transported in a gaseous mixture of CO and CO₂^{10,11} (it could be also a mixture of H₂ and H₂O). The carbon is provided by the fuel, as there is always some parts per million of carbon as an impurity in the oxide and may volatilize as CO or CO₂ at operating temperatures. The model assumes that radial cracks and interconnected porosity provide pathways for vapor transport: as a result, the partial pressures of CO and of CO₂ are constant over the pellet radius, and the ratio CO/CO₂ is constant in the pellet despite the temperature gradient. Thermodynamic considerations require that all along the radius, oxygen pressure corresponding to the ratio $P_{\text{CO}}/P_{\text{CO}_2}$ is in equilibrium with the local oxygen potential $\Delta G(\text{O}_2)$ of the fuel. As $\Delta G(\text{O}_2)$ is a function of T and O/M, such an equilibrium implies that the O/M varies along the radius as a result of oxygen migrating down the thermal gradient.

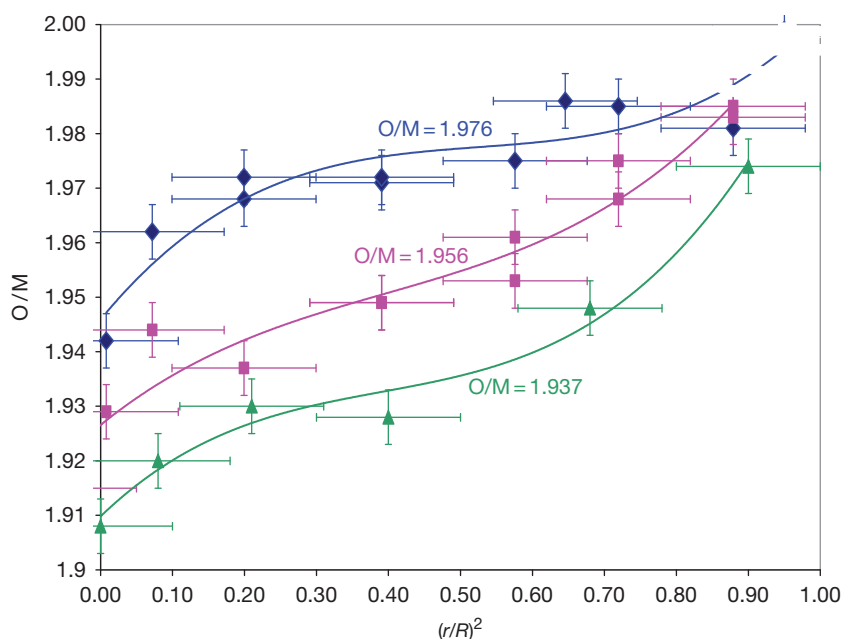


Figure 3 O/M radial profiles measured in irradiated (U,Pu)O₂ fuel for various initial O/M ratios.⁹

Such a model allows predicting an oxygen redistribution profile in reasonable agreement with the experiments. This mechanism of vapor transport certainly exists, but it alone cannot explain the oxygen redistribution.

- At low temperatures in the periphery of the pellets ($\sim 1000^\circ\text{C}$), the partial pressure of CO_2 in equilibrium with the fuel is very low and the transport mechanism would require a very long time, while experiments have shown it is a very fast phenomenon.
- Thermal diffusion of oxygen in the solid is rapid and the chemical driving forces due to a nonuniform distribution would induce oxygen migration that would strongly reduce the extent of oxygen redistribution.

2.21.3.3.1.2 Oxygen migration in solid phase

These models^{12–14} are based upon the theory of irreversible thermodynamics and on the observation in laboratory experiments that oxygen redistribution can occur even in fully dense mixed oxide with no pathways for gas transport. See **Chapter 3.21, Matter Transport in Fast Reactor Fuels**. By thermal diffusion, oxygen vacancies climb the thermal gradient and accumulate in the hot central region inducing a decrease of the O/M in this area. Chemical diffusion of oxygen counterbalances this effect and an equilibrium is rapidly found corresponding to the radial oxygen redistribution profile.

Several equations and models have been proposed to calculate this oxygen redistribution. One of the simple ones is the following¹²: in a thermal gradient, the value of x in $(\text{U,Pu})\text{O}_{2-x}$ should vary locally with the temperature T according to:

$$\ln x = \frac{Q^*}{RT} + K$$

Q^* , the characteristic heat of transport, is determined empirically; for slightly hypostoichiometric oxide, the proposed values for Q^* are about -125 kJ mol^{-1} ; for other O/M values, Q^* is a function of the deviation from stoichiometry and of the Pu content.

This oxygen redistribution has several consequences:

- The center temperature decreases slightly, as the increase in the O/M ratio in the periphery improves the fuel thermal conductivity in the region that experiences the highest thermal flux.
- The oxygen potential at the pellet surface also increases slightly, with potentially adverse effects on the corrosion of the cladding.

- Diffusion coefficients of many species depend upon the O/M ratio and will be affected by oxygen redistribution.
- In case of clad failure, the extent of reaction between the fuel and sodium will be enhanced, as this reaction occurs with fuels with a high O/M ratio and requires a source of oxygen.

2.21.3.3.2 Plutonium redistribution

Microprobe examinations performed on irradiated oxide pellets generally exhibit a plutonium enrichment in the central area near the central hole, and a slight plutonium depletion in a ring located near the periphery of columnar grains. Contrary to oxygen redistribution, the plutonium redistribution does not affect the whole radius but only the central hot region ($T \geq 1800^\circ\text{C}$), a consequence of much slower actinide diffusion as compared to oxygen diffusion. **Figure 4** gives an example of such plutonium redistribution measured at high burnup, but a major part of this redistribution had occurred at the beginning of life. Pu content varies from about 20% at the periphery of columnar grains up to about 30% near the central hole.

This plutonium redistribution starts at the very beginning of irradiation: recently, electron probe microanalysis (EPMA) measurements have been performed on oxide pins that had been irradiated only 10 min and 24 h at full power (430 W cm^{-1}) and a significant Pu redistribution could already be observed.¹⁵

As for the oxygen redistribution, several mechanisms and models have been put forward to explain such actinide migration under thermal gradient, the key processes being again vapor transport and solid diffusion.^{13,16,17}

2.21.3.3.2.1 Plutonium redistribution by vapor transport

An obvious mechanism of plutonium redistribution is directly linked to the mechanisms of fuel restructuring and especially the evaporation–condensation phenomenon. The evaporation is not congruent: above slightly hypostoichiometric oxide (for O/M in the range ~ 1.95 – 2.00), the partial pressure of UO_3 is much higher than the other actinide oxide species (see **Chapter 2.02, Thermodynamic and Thermophysical Properties of the Actinide Oxides**). The actinide oxide vapor in equilibrium with the solid is, therefore, enriched in uranium, and in a temperature gradient, UO_3 will preferentially evaporate from the hot zone, resulting in plutonium enrichment in the hot area and condense in

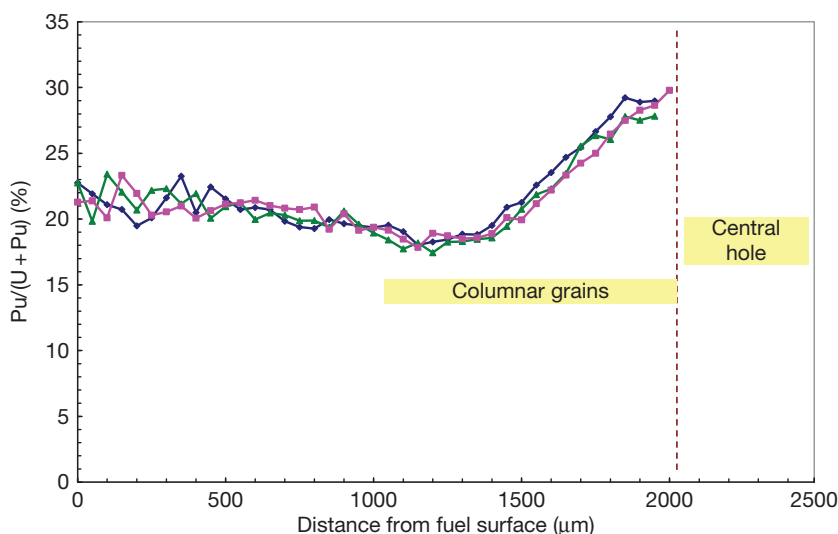


Figure 4 Plutonium radial profile measured by electron probe microanalysis on oxide pellets irradiated in Phénix at 15 at. %.

colder area where the vapor pressure becomes too low to have significant effects.

The radial migration of lenticular pores by evaporation–condensation is one of the mechanisms responsible for this Pu redistribution, nevertheless with a limitation on its efficiency. As soon as the lenticular pore starts to migrate up the temperature gradient, the hot side of the pore is highly enriched in Pu while the cold side is depleted.¹⁸ As the velocity of the pore is much higher than the rate of plutonium diffusion, the narrow zone with excess plutonium on the hot side is pushed ahead of the migrating pore and evaporation on the pore’s hot side affects an oxide with Pu content much higher than the average value.

Vapor transport may also occur, thanks to the radial cracks and open porosity as long as these pathways remain open.

For very low O/M ratios (≤ 1.94), PuO becomes the actinide oxide species with the highest partial pressure. Consequently, the plutonium redistribution is reversed and a Pu depletion can be observed near the central hole of highly hypostoichiometric oxides, but this occurs for O/M ratios at the limit of the O/M range generally considered to be used in commercial fast reactors.

2.21.3.3.2.2 Plutonium redistribution by solid diffusion

As for oxygen redistribution, according to irreversible thermodynamics, a temperature gradient applied to a mixed oxide will induce a flux of atoms. The causes of thermal diffusion are the differences of

the lattice energies of the fuel components in the temperature gradient. Migration of plutonium can be described using again Q^* the heat of transport of plutonium in the solid. The flux \mathcal{J}_{Pu} of Pu atoms is given by the equation:

$$\mathcal{J}_{\text{Pu}} = -D \left[\frac{\partial c}{\partial r} + c(1 - c) \left(\frac{Q^*}{RT^2} \right) \left(\frac{\partial T}{\partial r} \right) \right]$$

where D is the diffusion coefficient of Pu and c is the volumetric concentration of Pu. Q^* is determined empirically from Pu redistribution measured on irradiated fuel pellets or in laboratory experiments. A large range of values (from -35 to -240 kJ mol^{-1}) have been published in the literature, the negative sign indicates that Pu migrates up the thermal gradient.

The main consequence of this plutonium redistribution is a small decrease in the margin to fuel melting for two reasons. The first small effect related to the Pu-enriched area near the central hole is a slight increase in the power generation at a place more distant from the coolant, which slightly increases the center temperature. The second and more significant consequence is a decrease in the fuel melting temperature due to the increase in Pu/M: for example, when Pu content rises from 20 to 30%, solidus temperature decreases by about 50°C .

2.21.3.3.3 Redistribution of minor actinides

In Generation IV systems, recycling of minor actinides (MA) (i.e., mainly americium and neptunium, and possibly curium) is envisaged in order to decrease the amount of long-lived radionuclides going to waste.

It is even a prerequisite in many countries. This could be done either in a homogeneous way, diluting a few percentages of MA in the driver fuel or in a heterogeneous way, dedicating for this recycling specific subassemblies to be irradiated either in the core or in the radial blanket. **Chapter 2.02, Thermodynamic and Thermophysical Properties of the Actinide Oxides** addresses the main properties of these actinide oxides.

In case of homogeneous recycling, the question arises as to how a few percentages of Am or Np will behave at beginning of life and how redistribution processes will affect them. Recently, the Japanese experiment Am1 provided answers to this question.^{15,19} Several MOX fuel pins, with about 30% Pu, two O/M ratios (1.98 and 1.95), and various contents of MA (2% Am + 2% Np or several Am contents up to 5%) were irradiated in the experimental reactor JOYO at a linear heat rate of 430 W cm^{-1} during short times (either 10 min or 24 h). **Figure 5** shows an example of the results as measured by EPMA: americium redistributes as plutonium with a strong enrichment in the hot area (Am content rises from 2 to 3% near the central hole), while neptunium profiles exhibit no radial redistribution. The authors explain these results by vapor transport: for slightly hypostoichiometric oxides, the UO_3 vapor pressure is higher than the vapor pressures of both Pu- and Am-bearing gas species. However, these gas pressures are still known with rather high uncertainties, and the radial stability of Np is not yet explained; studies in this field are under progress.

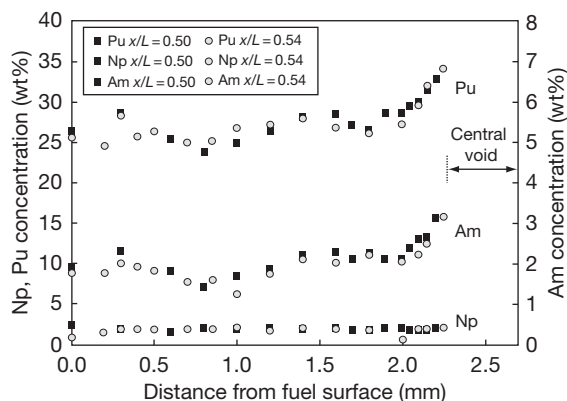


Figure 5 Radial profiles of Pu, Am, and Np in a $(\text{U}_{0.672}\text{Pu}_{0.288}\text{Am}_{0.02}\text{Np}_{0.02})\text{O}_{1.98}$ irradiated 24 h at 432 W cm^{-1} . Reproduced from Maeda, K.; Sasaki, S.; Kato, M.; Kihara, Y. *J. Nucl. Mater.* **2009**, DOI: 10.1016/j.jnucmat.2009.01.010.

2.21.3.4 Geometrical Evolution

2.21.3.4.1 Gap closure

Although the thermal expansion coefficient is lower in oxide fuel than in austenitic stainless steel cladding (typically about 10×10^{-6} in oxide vs. 17×10^{-6} in steel), the temperatures in the fuel pellets are much higher than in the cladding and induce a higher thermal expansion in the fuel pellet. The gap size under hot conditions is therefore smaller than the initial gap size: for example, in a Phénix pin, the diametrical gap size under hot conditions becomes about $150 \mu\text{m}$ for an initial value of $230 \mu\text{m}$.

Postirradiation observations of fast reactor pins irradiated at low burnup show that the fuel clad gap, as observed at room temperature, decreases rapidly until it is completely closed. At high linear powers ($\geq 400 \text{ W cm}^{-1}$), gap closure is completed after a burnup of about 1% or even less, while at lower linear powers, in particular, close to the bottom and top of fuel columns, gap closure needs more time (several atomic percentage). This gap closure results from several mechanisms: relocation of pellet fragments and axial creep of the fuel stack intervene in a very short time (a few hours), while the effects of fuel gaseous swelling need longer time and some burnup to accumulate.

- Fuel pellets are broken into several fragments at the end of first rise to power. Due to vibration in the pins, each fragment can move with respect to the others in a stochastic manner, resulting in a small average displacement of matter toward the cladding. This mechanism called ‘fuel relocation’ is probably responsible for a small but significant fraction ($\sim 20\%$) of the gap closure. As the cracks are healed in the central area, this mechanism can occur each time the reactor is shut down, but with smaller extent than the first time.
- Under the effect of the force exerted on the fuel column by the spring located in the upper part of the pin, plus the proper weight of the fuel stack, an axial compression creep occurs in the oxide especially near the peak power node (see **Section 2.21.3.4.2**). Consequently, this induces an additional diameter expansion of fuel pellets ($\sim 20 \mu\text{m}$), which slightly contributes to gap closure.
- However, the main cause of gap closure is probably the gaseous swelling of the fuel. At high temperatures ($\geq 1300^\circ\text{C}$), fission gas bubbles can grow and coalesce, generating large rates of gaseous swelling. Spurious gas due to carbon impurities can also contribute to this swelling at beginning

of life. However, this large swelling rate can hardly be measured because it is a dynamic swelling: in the hot central area, these gas bubbles rapidly migrate toward the central hole, gas is released, and the unique observable consequence of this gas swelling and sweeping is an overall displacement of the oxide from the center toward the periphery.

With a large gap, the difference of temperature between the outer pellet and the inner cladding may reach several hundreds of degrees centigrade; therefore, this gap closure induces a large decrease in fuel temperatures (see [Figure 1](#)).

2.21.3.4.2 Evolution of fuel stack length

At the first rise to full power, due to thermal expansion, both lengths of fuel column and pin cladding increase. As the temperatures are much higher in the oxide fuel than in the cladding steel, the axial dilatation is higher in the fuel than in the cladding. For rapid rise to power, as it has been seen, thanks to the hodoscope in some CABRI experiments, the fuel length can increase by about 2% (fuel hottest regions pilot axial expansion), while clad increase does not exceed 1%. (The hodoscope in CABRI is a neutron radiograph device allowing instantaneous scan of the whole length of the fuel column.) However, at the beginning of irradiation, as a result of the load of the spring at the top of the fuel column and also due to proper weight of the fuel stack, the hottest area of the fuel creeps, and the fuel stack length decreases by several millimeters. Gap closure induces a decrease in fuel temperatures and therefore an additional decrease in fuel length.

At the time of gap closure for initially dense fuels, the increase in fuel column length is generally a few millimeters higher than the increase in cladding length. After gap closure, fuel is mechanically and chemically anchored on the cladding. Measurements of lengths at high burnup show that fuel length evolution does not depend on burnup, but is directly related to clad length evolution induced by steel swelling. In case of large clad swelling (e.g., with nonstabilized austenitic 316 grades), clad elongation stretches the fuel column, opening interpelllets at the level of highest clad swelling. In case of low clad swelling (e.g., with stabilized austenitic grades or ferritic/martensitic steels), fuel elongation remains quite low; fuel is squeezed in the cladding and is generally too soft to be able to induce significant loadings and axial deformation in the cladding.

2.21.4 Consequences of Fission

For economic reasons, the main objective of oxide fuels in fast reactors is to achieve very high burnup; 15 at.% or even more is typically considered as a reference target. Each fission of actinide atom gives birth to two new atoms, the fission product, which means that at the end of irradiation, 15% of the initial actinide atoms (U and Pu) have disappeared and 30% new atoms are present in the fuel.

Such a large change obviously induces considerable consequences on the overall behavior of the fuel pin. All physical and chemical properties of oxide fuel will continuously evolve during its lifetime in the reactor; in particular, fission products will induce a decrease of thermal conductivity as well as a decrease of melting point, thus reducing the margin to fuel melting. Most phenomena occurring in the fuel pins will be a direct consequence of these fission products. This is the case for solid and gaseous swelling, resulting in fuel cladding mechanical interaction (FCMI) as well as fission gas release inducing an increase of the gas pressure inside the pins. This is also true for all the types of corrosion and the so-called FCCI where in fact oxide fuel alone could not have any harmful effect. The chemical state of the fission product also influences the residues from the dissolution of spent fuel in nitric acid during reprocessing.

This large amount of fission products is one of the specificities of fast oxide fuel, along with the fact that high temperature and steep temperature gradient induce not only radial but also axial migration of certain categories of these fission products. All these effects depend upon the chemical state of the fission product, which is influenced by the oxygen potential of the fuel, and which in turn determines the fate of the two oxygen atoms that are liberated by each fission, thus controlling the evolution during irradiation of the oxygen potential inside the fuel pins.

2.21.4.1 Formation of Fission Products and MA

In fast oxide fuel, as in all types of fuels, the fission of plutonium creates two fission products: a light fission product and a heavy fission product. Statistically, the mass numbers of created nuclides are distributed on the classical two maxima curve. With fission of ^{239}Pu , the position of the first maximum (the light fission product) is shifted toward slightly heavier atoms as compared to fission of ^{235}U .

Most newly created atoms are unstable and generally short-lived radionuclides. From the fuel performance point of view, we consider essentially the nuclides with rather long half-lives (≥ 1 day) and the total quantity of a chemical element, which can gather several radioisotopes. For example, cesium that plays an important role in fuel behavior comes from three main nuclides: ^{133}Cs , ^{135}Cs , and ^{137}Cs . ^{137}Cs is a decay product of the very short-lived ^{137}Xe (3.9 min), while the precursor of ^{133}Cs is ^{133}Xe with a longer half-life (5.3 days). In the hot central area of the fuel pellets, this ^{133}Xe has time to escape the fuel and reach the plena before decaying into ^{133}Cs . Consequently, γ -spectrometric observations often show at the extremities of fuel column peaks of ^{134}Cs that are not associated with corresponding peaks of ^{137}Cs . This ^{134}Cs is in fact a neutron activation product of ^{133}Cs that was formed in the plena by decay of ^{133}Xe and which condensed on the nearest oxide cold spot (ends of either fissile or fertile stacks).

Table 2 gives an example of elemental yields of the main fission product. They are the average values calculated with the Darwin code system for an oxide fuel (U,Pu) O_2 (23% initial Pu content, 70% ^{239}Pu) irradiated up to 10 at.% in Phénix core 1. The exact values are slightly dependent on initial isotopic composition, burnup, and neutron flux spectrum. They are gathered into several categories according to their physical and chemical states inside the fuel pellet. **Figure 6** shows how they are distributed in the Mendeleev table.²⁰

In addition to the fission product, another type of new atoms is generated during irradiation in a reactor by the transmutation of actinides nuclides that capture a neutron and create a new atom with higher atomic number, essentially, neptunium, americium, and curium, called ‘MA,’ as they are at low contents when compared to the major actinides uranium and plutonium. This mechanism, which is very efficient in thermal flux, does not introduce great changes in fast flux as the fission cross-section is much higher than the capture cross-section. In the example of the Phénix fuel, which has been used for the calculation of the fission product yields (**Table 2**), the increase of MA between 0 and 15 at.% is:

Neptunium	0	→0.07% HM (heavy metal)
Americium	0.18	→0.27% HM
Curium	0	→0.03% HM

Table 2 Elemental yields of fission products in a Phénix fuel pin at 10 at. %

	<i>Element</i>	<i>Yield (% fission products per fission)</i>	<i>Total (% per fission)</i>
Fission products in solid solution	Y	1.9	45
	La	5.6	
	Ce	11.4	
	Pr	4.8	
	Nd	15.5	
	Pm	1.2	
	Sm	3.4	
	Eu	0.6	
Fission products forming oxide precipitates	Gd	0.4	52
	Rb	1.5	
	Cs	20.1	
	Sr	3.6	
	Ba	6.8	
	Zr	19.2	
	Nb	0.2	
Fission products forming metallic precipitates	Mo	21.3	75
	Tc	5.5	
	Ru	22.0	
	Rh	5.8	
	Pd	13.8	
	Ag	1.3	
	Cd	1.0	
	In	0.1	
	Sn	0.5	
	Sb	0.2	
	Te	3.5	
Gases and volatile fission products	He ^a	0.8	28
	Kr	1.8	
	Xe	23.6	
	Br	0.1	
	I	1.7	

^aHelium is produced by ternary fissions ($\sim 0.2\%$ of fissions), α -decay of some actinide isotopes (especially ^{142}Cm), and reaction with oxygen ($^{16}\text{O} + ^1_0\text{n} \rightarrow ^{13}\text{C} + ^4_2\text{He}$) of neutrons with high energy (> 2.3 MeV).

This evolution of MA contents, especially the small production of curium, has an influence on the fuel cycle, but the consequences on in-pile fuel performance are minor and generally discarded.

2.21.4.2 Chemistry of Fission Products

The role the fission products play on the behavior of the fuel pins depends directly upon their physical and chemical state, which depends on the local values of temperature and oxygen potential and on the thermodynamics properties of fission product species.²⁰

I A II A		III B IV B V B VI B VII B															
H																	He
Li	Be																
Na	Mg	III A	IV A	V A	VIA	VII A	VIII		I B	II B							
K	Ca	Sc	Ti	V	Cr	Mn	Fe	Co	Ni	Cu	Zn	Ga	Ge	As	Se	Br	Kr
Rb	Sr	Y	Zr	Nb	Mo	Tc	Ru	Rh	Pd	Ag	Cd	In	Sn	Sb	Te	I	Xe
Cs	Ba	La	Hf	Ta	W	Re	Os	Ir	Pt	Au	Hg	Tl	Pb	Bi	Po	At	Rn
Fr	Ra	Ac															
			Ce	Pr	Nd	Pm	Sm	Eu	Gd	Tb	Dy	Ho	Er	Tm	Yb	Lu	
			Th	Pa	U	Np	Pu	Am	Cm	Bk	Cf	Es	Fm	Md	No	Lr	

Fission products in solid solution

Fission products forming oxide precipitates

Fission products forming metallic precipitates

Gases and volatile fission products

Figure 6 Distribution of main fission product in the periodic table.

2.21.4.2.1 Fission products in solid solution

Yttrium and all the rare earth (RE) fission products (La, Ce, Pr, Nd, Pm, Sm, Eu) are largely miscible in the oxide matrix. The RE atoms occupy an actinide site in the crystal lattice, and therefore can hardly migrate; in postirradiation examination of safety test, their axial distribution, as observed by γ -scanning (e.g., on ^{140}La or ^{154}Eu), gives good information on the axial movements of oxide fuel. A large fraction of zirconium and a smaller fraction of strontium and niobium are also dissolved in the fuel oxide; the remaining part of these fission product forms precipitated oxides. Some other fission products (such as Ba, Cs, or Te) are slightly miscible with mixed oxide, but only in small quantities.

These fission products in solid solution induce a decrease of the oxide thermal conductivity and a slight decrease of the lattice parameter. They also have an influence on the chemical properties of the fuel; for most of RE oxides, the valence in the oxide phase is 3, while the valence of the U or Pu atoms is 4. This results in a trend to increase the oxygen potential with the burnup even at a constant O/M ratio (in irradiated fuels, M stands for U + Pu + FP in solution).

2.21.4.2.2 Fission products forming oxide precipitates

From a thermodynamics point of view, barium and zirconium must be in an oxidized form, but barium has a limited solubility in the phase $(\text{U,Pu})\text{O}_2$ because

of the large ionic radius of Ba^{2+} . They precipitate therefore in the form of a perovskite structure phase BaZrO_3 that appears on optical metallographies at high burnup as gray inclusions. Other fission products may be partly dissolved into this perovskite phase: Sr and Cs may substitute with Ba; U, Pu, Mo, and some RE (especially cerium that is a decay product of ^{140}Ba) may occupy the Zr site of the perovskite lattice. The oxide precipitates are finally compounds of the type $(\text{Ba,Sr,Cs})(\text{Zr,U,Pu,Mo,RE})\text{O}_3$.

2.21.4.2.3 Fission products forming metallic precipitates

On the metallographs of fuel irradiated at high burnup, white inclusions are systematically observed (Figure 7), the higher the burnup and the temperature, the larger these precipitates. They are generally several micrometers in size, up to $10\mu\text{m}$ in the columnar grain region. In some cases, in pins that have experienced high central temperatures, large particles ($\sim 1\text{ mm}$) of metallic precipitates may form in the central hole, demonstrating the capacity of these metallic elements to migrate radially and even axially. The presence of such ingots can be detected on γ -scanning, especially on the ruthenium (^{103}Ru and ^{106}Ru).

In most cases, EPMA on these precipitates shows essentially five elements: Mo, Ru, Tc, Rh, and Pd. They are the five ‘noble metal’ fission products with the highest yield (see Table 2). This five-metal phase crystallizes in a hexagonal structure and melts



Figure 7 Metallography of an oxide fuel irradiated in Phénix at 13 at.% showing central hole (fuel pellet was initially a solid pellet), columnar grains, white metallic precipitates at the periphery of columnar grains and a joint oxyde gain (see Section 2.21.4.4.2) between fuel and cladding.

slightly below 2000 °C, which means that in reactors, these precipitates can be liquid in the hot central area, explaining how large ingots may form in the central hole. For Ru, Tc, and Rh, all the created fission products are probably located in these metallic precipitates. It is not the case for molybdenum: depending upon the burnup and the initial O/M ratio, the main part of created Mo may be found either in the metallic precipitates or in oxidized phases as a result of the evolution of oxygen potential (see Section 2.21.4.3).

At high burnups, in addition to these classical ‘noble metal’ precipitates, another type of metallic precipitates is observed with a different composition: EPMA reveals essentially the presence of palladium and tellurium with traces of tin, antimony, and sometimes plutonium. These precipitates, predominantly found in the periphery between the fuel surface and the cladding, result from the high vapor pressure of palladium but they can also be found in hotter parts of the fuel.

2.21.4.2.4 Volatile fission products

Volatile fission products are the fission products that are in solid or liquid phase at temperatures at the periphery of the pellets, but a large part of the compounds they form are in gaseous state in the hot temperatures area and especially in the columnar

grain region. These volatile fission products, essentially cesium, tellurium, and iodine, play a crucial role in the fuel pin performance, for they may migrate radially and axially and buildup at some places in the periphery where they may have a corrosive effect on the steel cladding (see Section 2.21.5.3). They may also induce local clad deformations, for example, on the UO₂ blanket at each end of the fuel column (see Section 2.21.5.2).

Cesium forms several compounds, the stability of which depends on the oxygen potential $\Delta G(\text{O}_2)$.^{21–23} For low values of oxygen potential (e.g., $\Delta G(\text{O}_2) \approx -500 \text{ kJ mol}^{-1}$) likely to exist at beginning of irradiation in hypostoichiometric oxides, the most stable compounds from a thermodynamic point of view are in increasing order CsI, Cs₂Te, and Cs₂UO₄ or Cs₂MoO₄ (depending on the temperature and oxygen potential). The yields of iodine and tellurium are much lower than the amount of cesium ($\sim 9\%$ for I and 32% for Te); therefore, at low burnup and low $\Delta G(\text{O}_2)$, all the iodine and tellurium should be associated in stable cesium compounds. The real situation is more complex and strongly affected by radial and axial migration of volatile fission products, resulting in relative fractions that can be locally quite different from the average relative fission yields. Postirradiation examinations hardly found the compounds CsI and Cs₂Te, which are most stable from thermodynamic calculations.

At higher oxygen potentials ($\Delta G(\text{O}_2) \geq -400 \text{ kJ mol}^{-1}$), likely to occur at high burnup, the respective stabilities change: the most stable compounds become CsI and Cs₂MoO₄; therefore, the Cs₂Te compound may dissociate and the activity of tellurium may sharply increase with potential consequence on FCCI (see Section 2.21.5.3). The cesium molybdate Cs₂MoO₄ melts at 942 °C and has a high vapor pressure (10^{-4} atom at melting temperature), which results in radial migration of cesium and molybdenum that leave the central area to accumulate at the periphery, contributing to the formation of a layer between the fuel pellet and the cladding (see Section 2.21.4.4).

2.21.4.2.5 Gaseous fission products

The noble gas xenon and krypton play a crucial role in fuel behavior as they are insoluble in the oxide fuel, precipitate as intragranular and intergranular bubbles inducing local swelling, and are finally released in the fuel pin plenum, significantly increasing the gas pressure inside the pins (see Section 2.21.4.5).

2.21.4.3 Evolution of O/M Ratio and Oxygen Potential

As a result of fission, two oxygen atoms are released for every heavy atom destroyed. These liberated oxygen atoms may combine with fission products but a large fraction of these fission products (especially noble metals and rare gas) do not accept oxygen. On an average, the two fission products that were produced for every fission are not efficient enough to combine with the two liberated oxygen atoms, at least as long as the $(\text{U,Pu})\text{O}_{2-x}$ fuel remains hypostoichiometric. The excess oxygen dissolves in the fuel matrix where it increases the O/M ratio; fission may therefore be regarded as an oxidizing process.

The oxidation state of fission products can be roughly assessed in the following way:

In the early stage of irradiation of an initially hypostoichiometric fuel $(\text{U,Pu})\text{O}_{2-x}$, molybdenum is essentially in a metallic state and a large part of zirconium, alkali metals, and alkaline earths are in solution in the matrix oxide. In these conditions, less than one atom (out of the two fission products) consumes oxygen and the sum of the average valences of the two fission products is about 3–3.3 (to be compared to the mean valence of the fissioned Pu atom, which was near 4). Consequently, the oxide O/M ratio (M stands for U + Pu + fission product dissolved in the matrix) increases at a rate of about 0.003–0.005 per at.%, inducing an increase of the oxygen potential of the fuel. This remains valid as long as the molybdenum is in the metallic state.

When burnup increases, an increasing fraction of alkaline and alkaline earths form second phases, and when $(\text{U,Pu})\text{O}_2$ approaches stoichiometric composition, the oxygen potential in the fuel reaches values

where molybdenum starts to oxidize as MoO_2 (where Mo is tetravalent) or Cs_2MoO_4 (where Mo is hexavalent). This effect appears clearly when analyzing the Mo content in the metallic precipitates of the central region of the pellet by EPMA (Figure 8).^{24,25} With initial O/M ratios of about 1.97–1.98, Mo is predominantly in the metallic state up to a burnup threshold between 5 and 10 at.% (depending on the initial O/M). A sharp decrease of the Mo content inside the metallic inclusions appears at this burnup threshold: Mo migrates outside the metallic precipitates and at higher burnup, Mo is predominantly in oxidized state.

Therefore, at high burnup (≥ 10 at.%), because of the oxidation of molybdenum, the average valence of the two fission products reaches a value of about 4. Fission products appear able to consume the two oxygen atoms liberated by each fission. Due to uncertainties in the chemical state of the different fission products, it is not possible to determine whether there is still an evolution of O/M ratio at a much slower rate, allowing the fuel to enter into the hyperstoichiometric or hypostoichiometric range. Thanks to the buffer role of molybdenum, it is likely that at high burnup, the fuel remains at an O/M ratio not far from 2.00.

This O/M evolution of course induces an increase in the oxygen potential. During the early stage of irradiation, the plutonium valence steadily rises from its as-fabricated value toward the limiting value of 4. This increase in oxygen potential has been demonstrated experimentally: $\Delta G(\text{O}_2)$ of fuels irradiated in Phénix up to 11 at.% have been measured by an electrolytic cell.²⁶

The results (Figure 9) clearly show the increase of $\Delta G(\text{O}_2)$, which is associated to an increase of

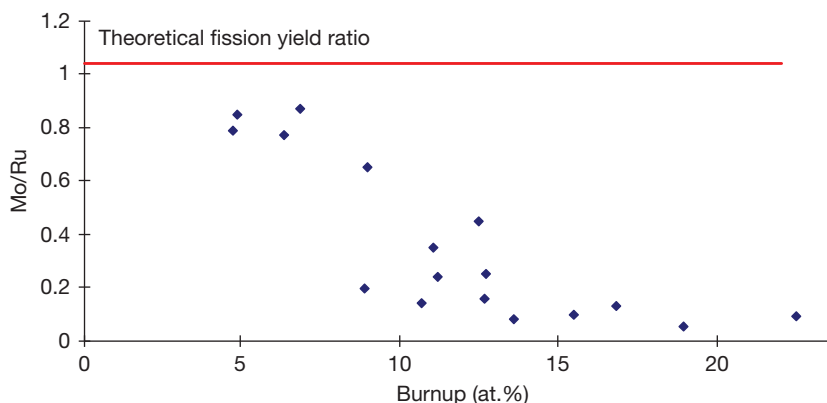


Figure 8 Evolution with burnup of the Mo content in metallic precipitates in columnar grain region of different Phénix fuel pins with initial O/M of about 1.98.

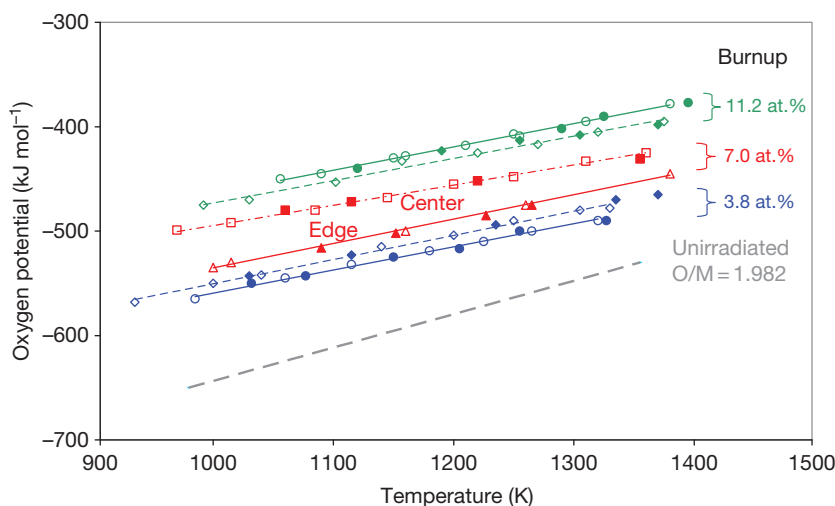


Figure 9 Evolution with burnup and temperature of the oxygen potential of fast reactor fuels irradiated in Phénix. Reproduced from Matzke, H.J.; Ottaviani, J. P.; Pellotiero, D.; Rouault, J. J. *Nucl. Mater.* **1988**, 160, 142.

O/M ratio at low burnup. But, even at high burnup, when the O/M ratio remains more or less close to 2.00, the oxygen potential still slightly increases. The introduction in the matrix oxide of RE atoms that are generally trivalent induces an increase of the oxidation state of the remaining actinide cations.

The increase of O/M ratio has a beneficial effect on the thermal conductivity; it partially compensates, at least at low burnup, the thermal conductivity degradation induced by irradiation. But the increase of $\Delta G(\text{O}_2)$, which reaches high values ($\geq 400 \text{ kJ mol}^{-1}$), has a deleterious effect on FCCI (see [Section 2.21.5.3](#)).

2.21.4.4 Migration of Fission Products

2.21.4.4.1 Radial migration

The volatile fission products (Cs, Te, I) have no stable compounds allowing them to remain in the hot regions of the pellets. Above a threshold temperature of about 1200°C , they behave more or less like gas and a fraction of them migrates down the thermal gradient and condensates in the colder area at the periphery of the pellets; in the hot columnar grain region, this radial migration is almost complete. Radial migration concerns not only the fission products classified as volatiles but also some other fission products with high vapor pressure or that may form compounds with high vapor pressures. The metallic fission product palladium has high vapor pressure (10^{-2} Pa at 1500 K) and partially escapes pellet central zone migrating toward outer zone.⁵⁰ At high

burnup, oxide fuel reaches high oxygen potential and molybdenum transforms into oxidized forms, some of them, especially Cs_2MoO_4 and MoO_3 , having high vapor pressure, which explains how Mo migrates to pellet periphery, forming one of the joint oxyde gain (JOG) components. Similar behavior is found for some barium and cadmium compounds.

2.21.4.4.2 Evolution of fuel to cladding gap: JOG formation

At low burnup, between the fuel pellet outer surface and the cladding inner surface, there is a gap filled with gas (helium at the beginning of life, then rapidly a mixture of helium and fission gases when gas release has started). The gap width progressively decreases due to fuel swelling; after a small burnup (a few at.%), the gap is practically closed at least in the region of peak power node. However, even after gap closure, there remains a residual gap a couple of micrometers wide due to surface roughness. At high burnup, radial micrographs show a reopening of the gap (see [Figure 10](#) giving the evolution of gap width measured in MONJU type pins irradiated in JOYO); however, this gap is no longer filled with gas, but with fission product compounds.

All the fission products migrating toward the cold region of the pellet accumulate first in the oxide fuel, and then escape the fuel and accumulate between the fuel and the cladding where they form a bonding layer (called JOG, joint oxyde gain). At high burnup, this JOG reaches a diameter width of about $150 \mu\text{m}$ in unstrained pins, still larger, up to $300 \mu\text{m}$, in pins

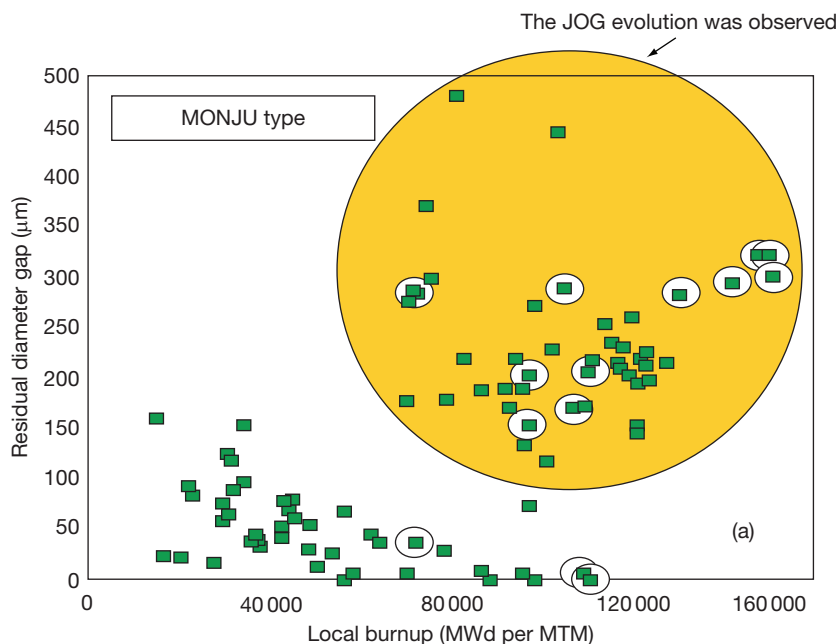


Figure 10 Evolution with burnup of fuel-to-cladding residual gaps in the MONJU type fuel pins. Reproduced from Inoue, M.; Maeda, K.; Katsuyama, K.; Mondo, K.; Hisada, M. *J. Nucl. Mater.* **2004**, 326, 59–73.

with high swelling claddings.^{27–29} The JOG appears first in the upper half of the fissile column where the fuel surface temperature is the higher; then it evolves progressively toward the lower part.

As revealed by EPMA observations (Figure 11), this JOG contains predominantly the elements molybdenum, cesium, and oxygen. Other fission products in smaller quantities are also observed in this layer: barium (but no zirconium), as well as palladium, tellurium, and cadmium. Generally, when the JOG is well defined, neither uranium nor plutonium is detected inside. In the upper part of the fuel column where some cladding corrosion has taken place, some cladding elements (Fe, Ni, Cr) can be found.

The exact composition of JOG is not well known, and it varies axially and even azimuthally according to local temperatures, oxygen potential, and piling up of fission products after radial and axial migration. According to EPMA observations and thermodynamics calculations, the main component of JOG is probably cesium molybdate Cs_2MoO_4 , but a great number of other volatile fission product compounds contribute to the formation of this layer. At high burnup, this JOG plays a crucial role in fuel pin behavior.

- The thermal conductivity of cesium molybdate Cs_2MoO_4 has been measured by the laser flash

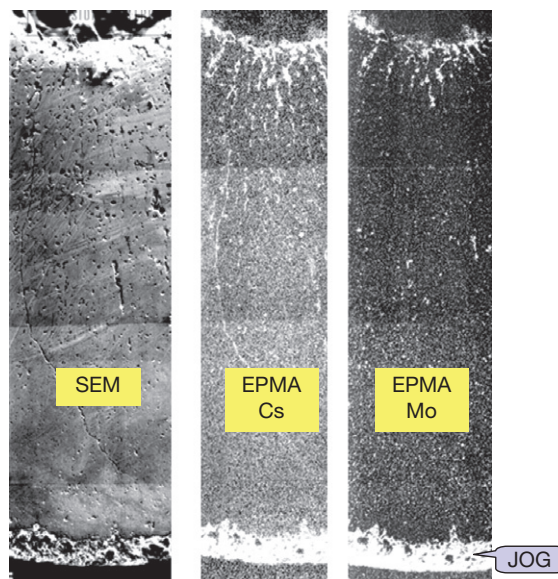


Figure 11 X-ray images by electron probe microanalysis on the joint oxide gain in a Phénix pin irradiated at 13.6 at. %.

method and lies in the range $0.3\text{--}0.5 \text{ W m}^{-1} \text{ K}^{-1}$ at operating temperatures,³⁰ a value 5–10 times lower than the thermal conductivity of $(\text{U,Pu})\text{O}_2$, but much higher than the thermal conductivity of xenon. Therefore, the heat transfer between the

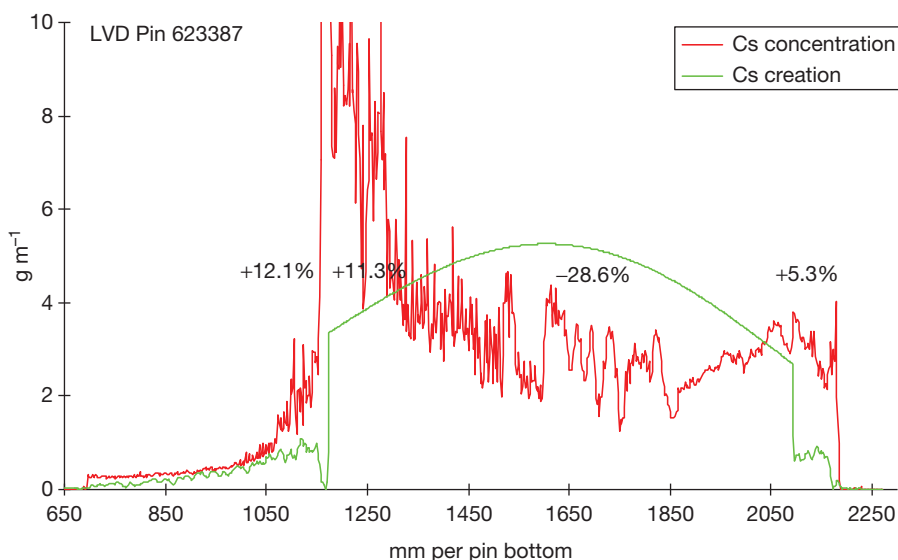


Figure 12 γ -Scanning of cesium in a PFR pin irradiated at very high burnup (23 at. %).

fuel and the cladding is much better through this JOG than through an equivalent gap filled with fission gases, but not as good as in case of a closed gap when the oxide fuel is in contact with the cladding. The layer is probably not dense and uniform everywhere; in the hottest regions of the JOG, some fission product compounds might migrate by evaporation condensation, leaving behind voids that locally deteriorate the heat transfer.

- From a mechanical point of view, the JOG acts as a buffer. At nominal operating temperatures, most fission product compounds in the JOG are viscous (even liquids for some of them). In case of FCMI, the fission product compounds in the JOG at the level of maximum pressure can be axially extruded, thus relieving the stresses induced in the cladding.
- At high burnup in pins clad with low swelling steels, JOG formation is associated with a decrease of pellet diameter. The release outside the oxide matrix of a considerable fraction of fission products induces a sharp decrease of the matrix swelling,³¹ and consequently, a decrease of pellet diameter giving place for JOG to form between fuel outer and cladding inner surfaces. However, the overall volume of oxide matrix plus JOG remains more or less constant.
- Fission products in the JOG play a predominant role on FCCI and on the resulting strong corrosion (see Section 2.21.5.3).

2.21.4.4.3 Axial migration

The volatile fission products migrate down the thermal gradient not only radially but also axially. This axial migration starts at beginning of life: the species iodine and tellurium that are created in the hot part of the pellets, the part which undergoes thermal restructuring, escape the oxide matrix toward the central hole (thanks to pore migration). Then, they migrate and escape the central hole through inter-pellet spaces, especially those located at both ends of the central hole; axial γ -scanning on pins irradiated during some days shows this axial migration appears as peaks of tellurium and iodine at the lower and upper ends of the central hole. In certain circumstances, the piling-up of these corrosive species may induce an intergranular clad corrosion (see Section 2.21.5.3.1).

At high burnup, large axial migration of cesium appears on the γ -scanning. In extreme cases, a minimum on the cesium axial profile can be found at peak power node level, that is, at the place of maximum of cesium creation³² (see, e.g., in Figure 12 the cesium profile in a PFR fuel pin irradiated at 23 at. %).

This cesium migration results from vaporization – condensation process of all compounds likely to be formed (Cs_2Te , CsI , Cs_2MoO_4 , etc.) in hot regions, which migrate toward the colder region radially and also axially. After JOG formation, some evaporation – condensation may occur in the JOG itself; but also every FCMI, for example during power increase, will induce in the JOG an axial extrusion of highly viscous

fission product compounds, which will leave the peak power level zone and migrate toward the extremities of the fuel column ([Figure 12](#)).

2.21.4.5 Behavior of Fission Gases

Fission gases are not soluble in oxide and their behavior in nuclear fuels is a topic that has been generating a huge amount of studies for several decades, and a great number of papers have been published in literature predominantly addressing gas behavior in oxide fuels for LWRs. A great difference between LWR fuels and fast reactor oxide fuel has to be kept in mind:

- In LWR rods, the fuel is operating at low temperatures (typically between 500 and 1000 °C) and the rods are designed with a small plenum taking into account the observation that, in nominal cases, a small fraction of created gas is released outside the fuel pellets in the plenum (typically $\leq 10\%$). Therefore, at high burnup, the ceramic matrix must retain a significant amount of fission and gas release may be a limiting factor, as it induces large inner pressure in the rods.
- On the contrary, in fast reactor oxide fuel pins, because of the high temperatures and high burnups, large gas releases are generally observed; typically, 80–90%. (Indeed, design calculations generally assume a release of 100%.) The design of the rods has to consider this large release, and oxide pins for fast reactors are designed with a large plenum (about the same volume as the fuel column). Therefore, gas release in fast oxide fuel pins is not a limiting factor. Nevertheless, gas behavior plays a considerable role in fuel performance as it influences thermal behavior and fuel swelling.

2.21.4.5.1 Formation of fission gases

The gaseous fission products are primarily rare gases xenon and krypton in various isotopic forms: ^{129}Xe , ^{131}Xe , ^{132}Xe , ^{134}Xe , ^{136}Xe and ^{83}Kr , ^{84}Kr , ^{85}Kr , ^{86}Kr . Helium is also produced in oxide fuel by ternary fissions, (n, α) reaction on oxygen, and predominantly during irradiation by α -decay of some actinide isotopes, mainly ^{242}Cm plus ^{138}Pu , and ^{241}Am .

The elemental yields of these gases are ~ 0.23 atom per fission for xenon, 0.02 atom per fission for krypton, which corresponds to a production of Xe + Kr of about $0.21 \text{ cm}^3(\text{NTP}) \text{ g}^{-1}$ per at.%. The exact values depend on the neutron flux spectrum, on the isotopic composition of plutonium, and on its evolution with burnup. The fission gas yield in a

fast reactor (~ 0.25 (Xe + Kr) per fission) is lower than that in a thermal reactor (~ 0.31 (Xe + Kr) per fission), because ^{135}Xe decays to ^{135}Cs within 9.2 h and is not counted as a gas in fast spectrum. In thermal spectrum, the capture cross-section of ^{135}Xe is so high (10^6 barns) that, before decaying into cesium, ^{135}Xe mostly transmutes into ^{136}Xe , which is almost stable.

The production of helium in (U,Pu)O₂ fuels is about 0.01 atom per fission ($\sim 0.01 \text{ cm}^3(\text{NTP}) \text{ g}^{-1}$ per at.%). As the fuel pins are initially filled with helium, the influence of this small helium production on the behavior of standard fuels remains low, but He production is much higher in fuels with MA, especially with americium, and in such pins, He behavior must be taken into account.

2.21.4.5.2 Fission gas release

The behavior of fission gases is complex. Given their very low solubility in oxide fuel, fission gases will tend to diffuse within the grains and precipitate as small intragranular bubbles (some nanometers). Fission fragments can resolute the precipitated gas. Bubbles grow by trapping gas atoms and vacancies; they coalesce when two bubbles meet; they migrate randomly and up the thermal gradient (by vaporization–condensation, surface diffusion, or volume diffusion, depending on temperature and bubble size). Most gas reaches grain boundaries either by atomic diffusion or by migration of intragranular bubbles. On the grain boundaries, gases precipitate as elongated intergranular bubbles, which grow and interconnect, finally allowing venting of the gas toward the plenum through open porosity and interlinked intergranular bubbles. These different phenomena are detailed in [Chapter 3.19, Oxide Fuel Performance Modeling and Simulations](#) and [Chapter 3.20, Modeling of Fission-Gas-Induced Swelling of Nuclear Fuels](#) dealing with modeling of oxide fuel and fission gas.

Puncture tests of irradiated fast fuel pins allow the determination of the overall gas release in the plenum. As an example, [Figure 13](#) gives the fractional release, as a function of burnup, of Phénix pins irradiated in nominal conditions. Even at very low burnup, a significant gas release is already observed (~ 30 – 50%); the gases created in the columnar grain region are almost completely released during restructuring. The fractional release increases with burnup and, at high burnup, it levels at about 80% in unstrained pins, and 90% in pins with large clad deformation. The results clearly indicate that fission gas release is driven by burnup and fuel thermal level.³³

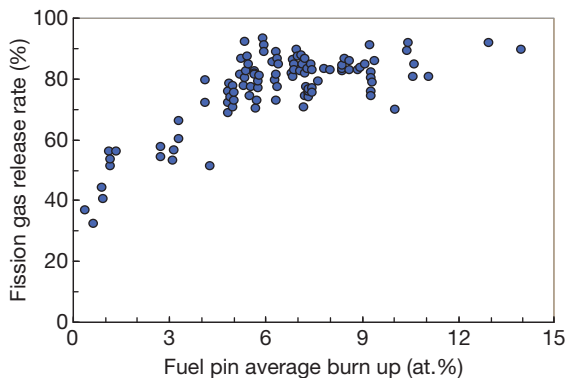


Figure 13 Evolution with burnup of global fission gas release in Phénix pins.

Microprobe analysis gives information on the radial profile of xenon; sublimation or dissolution of irradiated pellets at several levels of a fuel pin gives the axial profile of occluded fission gases. At moderate burnup (≤ 7 at.%), gas release is essentially a thermally activated mechanism; the release is almost complete above $\sim 1400^\circ\text{C}$ and very low below $\sim 1000^\circ\text{C}$. Therefore, the fractions of gas release are directly related to the parameters governing the temperature field inside the oxide fuel: initial density and O/M ratio of the pellets, fuel to cladding gap size, linear heat rate, clad deformation that may increase the gap width, etc.

At a threshold burnup of about 7–9 at.%, the microstructure changes at the periphery of the pellets; the grains (initially $\sim 10\ \mu\text{m}$) subdivide into small grains ($\sim 1\text{--}2\ \mu\text{m}$) and a precipitation of bubbles occurs (see **Figure 14**).

This transformation is quite similar to the restructuring observed, at about the same burnup but at lower temperatures, at the periphery of pellets irradiated in LWRs and known as ‘Rim effect’ or ‘high burnup structure (HBS).’ At about the same burnup, the JOG is formed (see **Section 2.21.4.4**). Results of sublimations (**Figure 15**) show that, at a given level of fuel pins irradiated under steady-state conditions, the amount of gas occluded in fuel pellets increases with burnup up to a burnup threshold ($\sim 5\text{--}8$ at.%) and suddenly drops at about the same time as JOG forms and fuel restructures at the periphery. This drop may be partly due to fuel overheating induced by clad swelling, but this probably means also that, at high burnup, even the low-temperature region of fuel pellets releases a fraction of its fission gases; oxide cannot accumulate fission gas beyond a certain level. (Contrary to what happens in the HBS zone of LWR fuels, where most fission

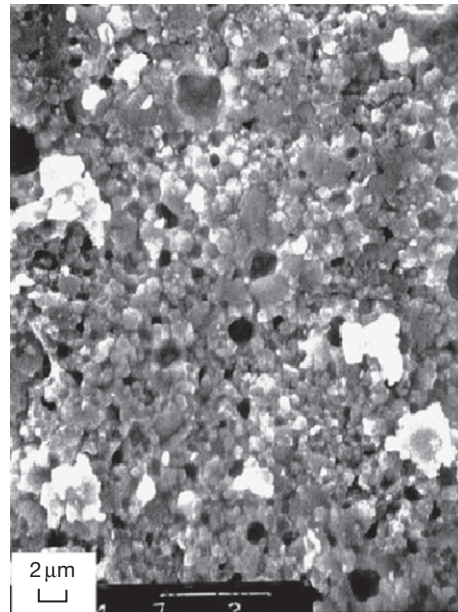


Figure 14 Fractograph by scanning electron microscope of a porous rim structure at the periphery of a mixed oxide fuel pellet irradiated in a fast reactor at $97\ \text{GWd t}^{-1}$. Reproduced from Maeda, K.; Katsuyama, K.; Asaga, T. *J. Nucl. Mater.* **2005**, 346, 244–252.

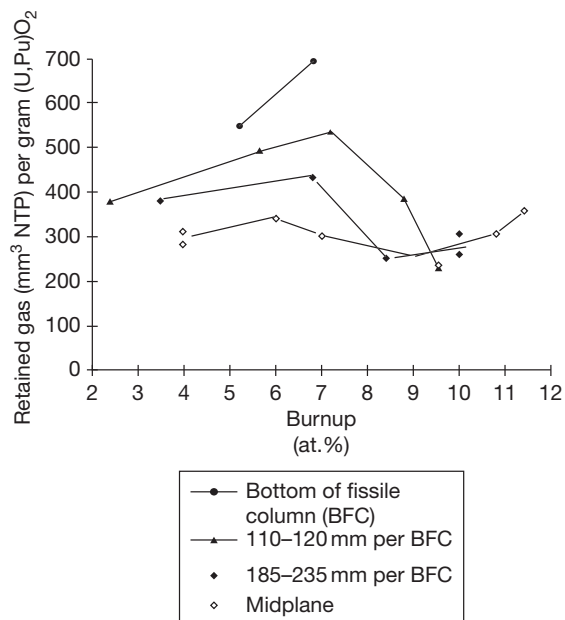


Figure 15 Evolution with burnup of gas retention in Phénix fuel pins. Reproduced from Mélis, J. C.; Plitz, H.; Thetford, R. *J. Nucl. Mater.* **1993**, 204, 212–216.

gases are still present after restructuring. But the temperatures in the outer zone of fuel pellets are typically 700–1000 °C in fast oxide fuel, much higher than in LWR fuel where the HBS zone undergoes temperatures of about 450–650 °C.)

2.21.4.6 Fuel Swelling

Burnup induces an increase in the number of atoms inside the fuel. 10 at.% burnup corresponds to 10% increase in the total number of atoms (heavy atoms + fission products). As a direct consequence of this increase, a fuel swelling is observed; its volume increases with burnup. The two atoms created by each fission occupy more space than the initial Pu atom.

Density measurements carried out on irradiated fuel pellets give access to this overall volume change. Hydrostatic densities of irradiated fuels show a linear decay with a slope of about 0.7% per at.%. After correction of the mass of gas released by the fuel, a swelling rate of about 0.6% per at.% can be inferred from this density slope. This swelling rate, which seems to remain constant up to high burnup (20%), integrates all the effects: volume change of oxide matrix, volume of metallic phase and oxide phase, volume of JOG at high burnup, and contribution from gaseous swelling. It is an average value, and significant variations may be encountered due to radial and axial migrations of fission products. Especially cesium, which displays large radial and axial migrations, plays a considerable role on fuel swelling, and a strong relationship may be established between local swelling and cesium amount; swelling is lower than expected at levels where cesium profile is depleted (see [Figure 12](#)).

Two different types of swelling are often considered: the solid swelling due to fission products in solid state and the gaseous swelling. The respective contributions of each type of fission product to the fuel solid swelling can be assessed considering the volume V_i occupied by each family of fission product and reporting it to the atomic volume of the plutonium V_{Pu} ¹:

- Fission products in solid solution are in substitution to the actinide atoms ($V_i/V_{Pu} = 1$). At high temperatures as it is the case in fast oxide fuel, the lattice parameter slightly decreases with burnup ($\sim -0.007\%$ per at.%).
- Fission products pertaining to the ‘noble metal’ family have an atomic volume lower than actinide atom ($V_i/V_{Pu} \sim 0.36$).

- The same occurs for volatile fission products whose average volume gives about ($V_i/V_{Pu} \sim 0.76$).
- On the contrary, fission products forming oxide precipitates have a larger volume ($V_i/V_{Pu} \sim 1.74$).

Taking into account the elemental yield of each fission product family (see [Table 2](#)), a solid swelling rate of about $0.3(\pm 0.15)\%$ per at.% can be inferred from the aforementioned values. This rate is slightly lower than the swelling deduced from density measurements; fission gases bring an additional contribution to the swelling rate.

In steady-state conditions, at high burnup, as most fission gases have already been released, and as fuel swelling is constrained by the cladding, the gaseous swelling rate is low. (This is one of the great advantages of oxides over other ceramic fuels as carbide or nitride or metallic fuels, which have a much higher swelling rate, due to gaseous swelling, inducing strong loadings to the cladding in the case of ceramic fuels.) However, during any situation when oxide fuel is no longer in mechanical interaction with its cladding, the gaseous swelling rate may considerably increase.³⁴ This occurs, for example at beginning of life, when gaseous swelling contributes to gap closure. This happens also in case of large clad deformation due to steel swelling: because of temperature increase and pressure drop induced by the reopening of the gap, gaseous swelling strongly increases, which helps to avoid a too large reopening of the fuel-to-cladding gap.

2.21.5 Limiting Phenomena

Let us first recall that during the past decades, cladding deformation due to swelling of austenitic stainless steel has been the main limiting factor for the performance of oxide fuel pins in fast reactors. Experience on in-pile behavior of fast fuel pins has been mainly achieved with pin claddings in austenitic stainless steels, and the limit burnup was determined by an excessive clad deformation due to swelling of the clad material, induced by the high fluence of fast neutrons and high irradiation dose (>100 dpa). Evolutions of steel composition and metallurgical state (316 in solution annealed (SA) or cold worked (CW) state, then CW 316 Ti and 15/15 Ti) progressively allowed increasing the burnup and dose beyond 100 dpa. But, the main cause of failure in these pins remained associated to large clad swelling generating large clad deformation ($>5\%$ diametral) and interaction between

pins in the bundle. Large swellings (≥ 6 vol%) were also generally associated with embrittlement of the clad material.

Other types of alloys with higher resistance to swelling have been tested, especially nickel alloys, such as Inconel 706 (F and US), or Nimonic PE16 (UK) and ferritic–martensitic steels, such as EM12 (F) or HT9 (US). The most promising alloys that are currently considered for the future are the ferritic–martensitic steels reinforced by a nanodispersion of oxide precipitates: ODS alloys (oxide dispersion strengthened). This steel behavior under irradiation damage is described in other parts of this volume (see [Chapter 4.02, Radiation Damage in Austenitic Steels](#); [Chapter 4.03, Ferritic Steels and Advanced Ferritic–Martensitic Steels](#); and [Chapter 4.08, Oxide Dispersion Strengthened Steels](#)).

Besides this limitation due to clad behavior, the oxide fuel itself may bring some limitations related to thermal, mechanical, and chemical behavior.

2.21.5.1 Margins to Fuel Melting

Many experimental results have shown that fuel melting can occur in a fuel pin without inducing a clad failure. It is generally considered that, provided there is enough volume to accommodate thermal expansion, a significant fraction of molten fuel in the oxide pin (up to $\sim 20\%$ depending on burnup and initial smeared density) would not induce any apparent harmful consequence. For example, in FFTF, the experiment DEA-9 has demonstrated that a once-molten fuel (melting up to half the pellet radius at beginning of life) was able to reach high burnup.³⁵

Nevertheless, in order to keep a large margin to any uncontrolled phenomenon such as axial movements of fissile nuclides, fuel licensing requires guaranteeing the absence of fuel melting in all the nominal operating situations. As the nominal oxide temperatures are high, and as all the uncertainties have to be taken into account, this conservative requirement induces a strong constraint on the maximum linear heat rating achievable.

2.21.5.1.1 Temperature field in the oxide fuel

The temperature at first rise to full power is often the highest center temperature achieved during the life-time of oxide fuel in reactor, especially in solid pellets. The phenomena occurring at beginning of life induce globally a sharp decrease (several hundreds of degrees) in this temperature.

- Radial redistribution of oxygen improves fuel thermal conductivity in the periphery, where thermal flux is the highest.
- Fuel restructuring decreases fuel porosity; and formation of the central hole (or enlargement of the central hole in case of annular pellets) decreases the center temperature.
- Gap closure has the strongest effect: thanks to the enhancement of fuel to cladding heat transfer, fuel temperatures may decrease by several hundreds of degrees.

At higher burnup, the general trend is to increase the fuel temperature for the following reasons:

- Xenon has a much lower thermal conductivity than helium; thus, release of fission gases induces a degradation of the conductivity of the gases in the gap, with a deleterious effect on the heat transfer between fuel and cladding.
- As an effect of burnup, fuel thermal conductivity is continuously decreasing; all defects and fission products act as diffusion centers for phonon.
- In case of clad deformation, at medium or high burnup, the tendency is to reopen the gap, inducing a degradation of the fuel to cladding heat transfer.
- The JOG formation may either degrade the heat transfer in case of good contact between fuel and cladding, or improve it in case of gap reopened by clad deformation.

This general trend to temperature increase with burnup is partly compensated by the continuous decrease of linear heat rating in most of the fuel pins as evident from past experience worldwide. Typically, linear heat rates at peak power node were above 400 W cm^{-1} at the beginning of life and around 300 W cm^{-1} at high burnup. As a result, it was generally calculated that the maximum center temperature of the fuel was seen at the very beginning of life, even if the center temperature at end of life was not far from this maximum value.

This is likely to change in the future: in order to increase the safety characteristics and especially to limit excess reactivity of the core of sodium-cooled fast reactor of Generation IV design, the trend is to use large diameter pins with lower plutonium content allowing an internal breeding compensating the plutonium consumption.³⁶ As a result, the linear heat rate remains almost constant during the whole in reactor life. Therefore, the maximum temperature will probably occur at end of life, which has to be taken into account for the choice of linear power of the fuel pins.

2.21.5.1.2 Nominal situation and case of control rod withdrawal

In fast oxide driver fuel pins, typical maximum center temperatures lie in the range 2000–2200 °C for nominal conditions, up to 2400 °C in some cases. The solidus temperature of as-fabricated (U,Pu)O_{2.00} is 2744 °C for a Pu content of 20% and 2696 °C for 30% Pu. This melting temperature of oxide decreases with deviation from stoichiometry (~ -50 °C for MO_{1.95} as compared to MO_{2.00}), and decreases also with burnup (~ -34 °C for 10 at.% burnup).

Therefore, when the center temperature is calculated with nominal values of the parameters and on a best-estimate basis, the margin to fuel melting reaches several hundreds of degrees centigrade. However, when taking into account all the uncertainties on fabrication parameters (cladding and pellet diameter, pellet density, O/M, Pu content), on fuel properties (thermal conductivity), and operating conditions (linear heat rating, cladding temperature), the resulting uncertainty on the maximum center temperature is rather high (~ 100 °C for one standard deviation). Moreover, this absence of fuel melting must remain guaranteed even during some off-normal situations such as control rod withdrawal, when linear heat rating may increase 10–15% before reactor undergoes a scram.

At high burnup, the center temperatures are calculated with higher uncertainties because of degradation of thermal conductivity, uncertainties on the heat transfer across the JOG, and activation of mechanisms such as gaseous transient swelling during power increase. In order to validate code calculations, several experiments have been performed, either on pins instrumented with a thermocouple inside the central hole, or on pins irradiated at high linear heat rating in order to generate a limited fuel melting. The radius of molten fuel is used to validate calculations. For example, the JOG1 and the JOG2 tests were power-to-melt experiments (up to 770 W cm⁻¹, 20% molten fuel) performed in CABRI on Phénix pins irradiated up to 15 at.%.³⁷ Results of postirradiation examination showed a decrease of JOG width at peak power node due to axial extrusion toward fuel column ends of the viscous compounds of fission products filling the JOG. Such experiments provide data enabling to validate the models of heat transfer across the JOG and the mechanism of gaseous transient swelling in the central part of the pellets. Before melting occurs, this transient swelling may reduce the central hole diameter at a rate depending on the kinetics of

power rise and amount of occluded fission gas. This results in a decrease of the power-to-melt, as a consequence of central hole reduction and increased porosity in the central region.

2.21.5.2 Fuel Cladding Mechanical Interaction

In the early days of development of fast oxide fuel, fuel cladding mechanical interaction (FCMI) was considered as a mechanism likely to induce strong limitations both on burnup and on operating conditions. Indeed, in other families of fast fuels and especially in carbide and nitride fuels, FCMI revealed to be a major limiting factor and the predominant cause of fuel pin failure; this is due to the high swelling rate of these fuels and to their low creep rate. In oxide fuel pins, thanks to the low swelling rate of oxide and to its high fuel creep rate related to its high temperature, FCMI does not play such a crucial role; it has nevertheless to be taken into account both in the fuel pin design and in the operating conditions.

2.21.5.2.1 Limit burnup due to FCMI during steady-state operation

During irradiation, the oxide fuel swells at about 0.6% per at.% (see Section 2.21.4.6). Consequently, the volume of a fuel that reaches a burnup of 15 at.% has increased by about 9%. As the temperature is much higher in the oxide than in the cladding, fuel thermal expansion is larger than cladding expansion and this consumes 1–2% of the initial free volume. Postirradiation examination shows that, as a consequence of fission gas behavior, a porosity of several percentages always remains in the pellet. When designing the fuel pin, a free volume has to be managed, which considers fuel swelling, thermal expansion, and residual porosity.

Several experimental programs and calculations have been carried out worldwide in order to determine the optimized smear density of fuel pins as a function of target burnup and to analyze the potential risks of clad strain and damage induced by FCMI, for example, Gatesoupe *et al.*,³⁸ Biancheria *et al.*,³⁹ Levine *et al.*,⁴⁰ Dienst *et al.*⁴¹ It appeared that very high smear densities ($\geq 90\%$), and especially narrow fuel-to-cladding gaps, should be avoided; in such pins, FCMI may induce additional clad strain.

For intermediate smear density (between 85% and 90%), the situation is not straightforward: driver fuel pins of Phénix and FFTF, which were in this family (88% for Phénix, 86% for FFTF), have been

able to reach high burnups (beyond 15 at.%) without reaching a limit due to consumption of available free volume for accommodation of fuel swelling. But, in most cases, these pins had clads with steels undergoing irradiation swelling, which provided additional free volume at high burnup. From immersion density measurements on clad and analysis of clad deformation, it was deduced that clad deformations are mainly due to steel swelling and that plastic deformation of clad (the part of deformation that is not due to swelling) results essentially from irradiation creep of steel induced by the inner pressure of fission gases.

One can also refer to the results of fuel pins irradiated in PFR⁴²: despite rather high smear density (86% and 88%) and low clad swelling (diameter clad deformation of the nickel alloy PE16 was less than 1%), very high burnups were achieved (23 and 19 at.%). And the FCMI contribution to clad deformation remained small and localized in the lower part of fuel column where a strong accumulation of cesium is observed (see [Figure 12](#)).

In fuel pins with annular pellets and clad with irradiation swelling, the diameter of the central hole at high burnup is generally larger than its initial value. In case of clads with very low swelling, a small decrease of the central hole diameter may be observed in the lower and the upper parts of the fuel column, this diameter nevertheless remaining very close to its fabrication value.⁴²

In fast oxide fuels, this benign effect of FCMI during steady-state operation is a consequence of the following points:

- low swelling rate of oxide (as compared to carbide or metal fuels);
- high fuel temperature that allows high creep rates. Even in the outer part of pellets, thermal creep and irradiation creep in oxide fuels relieve the FCMI stresses induced by fuel swelling. As long as a central hole is available, calculations account for a hoop stress not exceeding a couple of MPa induced in the cladding by FCMI during steady-state operation;
- JOG formation and axial migration of cesium and other fission product compounds. Swelling rate of (U,Pu)O₂ itself is lower than 0.6% per at.%; and volume increase due to JOG formation can hardly strain the clad as the fission product compounds of the JOG have no real mechanical strength.

Nevertheless, despite these encouraging results, designers do not rely on axial migration of cesium to relieve FCMI stresses. For commercial reactors

with high burnup targets (15 or 20 at.%), it is nowadays considered that reliable fuel pins should be designed with smear density not exceeding 85%. This low smear density may be achieved by using either annular pellets or highly porous oxide pellets. Low density of pellets has adverse effects on thermal behavior and on in-reactor stability of the fuel stack. This is why fuel pins of latest commercial fast reactors have been designed with annular pellets.

2.21.5.2.2 FCMI due to power increases

Nevertheless, in some cases, the consequences of FCMI should be seriously considered. Each time the linear heat rate of a fuel pin is increased, the differential fuel cladding expansion induces additional stresses in the cladding. For high linear heat rates, thanks to high temperatures, these stresses remain low; but if the power increase occurs after an extended period at reduced power, fuel temperatures at the beginning of power ramp are too low to permit high thermal creep rates and fuel irradiation creep has not enough time to relieve FCMI stresses. In such a case, high stresses may be induced in the clad, exceeding the elastic limit and generating permanent clad strain and a risk of pin failure in case of clad embrittlement.

To prevent any risk in such a situation, highly brittle irradiated clad material should be excluded; and the rate of power increase should be limited, relying on calculations by fuel performance codes.

2.21.5.2.3 FCMI due to cesium accumulation

In many pins irradiated to high burnup, diameter profilometries reveal small cladding deformation peaks at the level of UO₂ insulator pellets, or in front of first pellets of the axial blankets, at each end of the fuel column. These deformation peaks, clearly associated to cesium accumulation on γ -scanning profiles, result from swelling of fertile UO₂ due to reaction with cesium, forming cesium uranate Cs₂UO₄ or Cs₂U₄O₁₂ for high oxygen potentials,^{20,43} or from filling up of the gap at this level by fission product compounds. As fertile UO₂ is much colder than fissile (U,Pu)O₂ and has generally no central hole, this volume increase results in clad strain as there is no possibility for swelling accommodation inside the oxide.

Similar observation of a local cladding distension has also been observed in the fuel column at the level of cesium accumulation. It may be observed either near the ends of the fuel stack, in places where linear heat rates and fuel temperatures are low, or at the level of FCCI where high volume increase is induced

not only by accumulation of fission product compounds but also by reaction products resulting from clad corrosion (see [Section 2.21.5.3](#)).

2.21.5.3 Fuel Cladding Chemical Interaction

Fuel cladding chemical interaction (FCCI) is a general term for all types of chemical reaction resulting in a corrosion of the cladding inner surface. Indeed, the (U,Pu)O₂ fuel itself does not directly react with the cladding, but it provides the oxygen needed for some of the reactions. It was demonstrated in out-of-pile test that the volatile fission products, tellurium and cesium, are the corrosive species able to overcome the passivation of stainless steel and therefore to induce clad corrosion.

FCCI appears as one of the potential life-limiting factors for high burnup fuel elements. Many studies have been carried out worldwide in order to understand and model this phenomenon: a large number of nondestructive examinations (especially eddy current which allows to localize the clad corrosion and assess its magnitude on a great number of irradiated pins), thorough destructive examinations (especially EPMA to determine the corrosion products resulting from the reaction), thermodynamics studies, out-of-pile tests, and specific irradiation programs.

Although a qualitative understanding of corrosion mechanisms has been achieved, it is not yet possible to give a complete physical description of FCCI and to predict corrosion depths in every circumstance. In fact, there is not only one corrosion mode, several types of reactions and mechanisms are possible, occurring at different stages of irradiation, sometimes successively in the same pin, and resulting in different attack features. The occurrence of one or another mechanism depends upon local conditions: clad and oxide temperatures, temperature gradient across the fuel-to-cladding gap, oxygen potential, and relative amounts of the different corrosive species (Te, Cs, I) and other fission products (especially Mo) involved in the equilibrium of the main chemical reactions. These local quantities of fission products depend not only on their respective yield; they result from their radial and axial migration, and their local buildup is related to the different chemical reactions likely to occur between fission product compounds, fuel, and cladding components.

The equilibrium of these different reactions is very sensitive to local conditions and determines the activity of corrosive species. This explains why a

large scatter of corrosion depths may be observed in similar fuel pins, and why a great variety of FCCI features have been observed. Local conditions depend on initial characteristics (such as O/M ratio) and operating conditions (such as linear heat rate), and evolve during pin time-life in reactor (e.g., clad deformation modifies fuel surface temperature and therefore oxygen potential).

We present hereafter some of the main types of FCCI effects.

2.21.5.3.1 Early-in-life corrosion

In a few cases, irradiated oxide fuel pins exhibited severe intergranular corrosion on the inner cladding surface, which could be observed at very low burnup (after one or two weeks of irradiation).^{4,5} Such attack occurred essentially in highly rated pins ($\geq 450 \text{ W cm}^{-1}$ at beginning of life), and it induced clad failures in some cases, especially in solid pellet fuel pins irradiated in Rapsodie after up rating into Fortissimo.

Out-of-pile tests on corrosion by cesium and tellurium and thermochemical evaluation reveal that an intergranular attack of stainless steel claddings may occur when the Cs/Te ratio is lower than 2.^{44,45} In such a case, Te activity is no longer buffered by formation of the very stable compound Cs₂Te and free tellurium is available for fission product-induced liquid metal embrittlement. As Cs fission yield is about 6 times higher than Te yield, such a low Cs/Te ratio is generally hardly found at moderate or high burnup.

However, at beginning of life, the Cs/Te ratio is much lower than the equilibrium value because of the effect of radioactive decay chains; during the first week of irradiation, Te may be locally in excess. In pins irradiated under high linear heat rates, and therefore generating high fuel temperatures, tellurium and iodine generated in the columnar grain zone escape from the oxide fuel and build up on the cladding. γ -Scanning on such pins shows peaks of tellurium and iodine in front of oxide interpelllets at the top and the bottom ends of the central hole.⁴ If the oxygen potential and the clad temperature are high enough, an intergranular attack of stainless steel may occur probably by formation of chromium telluride at grain boundaries with a regeneration process of the small quantity of tellurium.

In order to prevent this early-in-life corrosion, one solution successfully applied in Rapsodie and Phénix is to limit the linear heat rate during the first days of irradiation, thus reducing escape and

accumulation of corrosive fission products while Te is in excess. The use of annular pellets also seems to reduce this risk of early-in-life corrosion.

2.21.5.3.2 Intergranular corrosion

Intergranular corrosion has been also observed in a lot of oxide pins at moderate burnups, and again associated with high fuel temperatures related to high linear heat rates, low fuel density, or vibro-packed oxide fuels. Such a corrosion mode is probably linked to high-temperature gradients across the fuel-to-cladding gap, enabling the cesium pressure in equilibrium with cesium uranate formation on the fuel surface to become higher than the cesium partial pressure required for cesium chromate formation on the cladding inner surface.⁴⁶ In order to prevent this corrosion mode, very high fuel surface temperatures should be avoided. Another way is to reduce the oxygen potential by using low O/M ratio, but with adverse effects on fuel temperatures.

Vibropacked oxide fuel pins exhibited such an intergranular corrosion when irradiated at a high linear heat rate. This occurred especially in vibro-packed fuel pins irradiated in the experimental reactor DFR (Dounreay fast reactor).⁴⁷ To avoid this corrosion in vibropacked oxide fuel pins irradiated in Russia, several percentages of uranium metal powder are added to the fissile mixed oxide in order to decrease the oxygen potential.⁸

2.21.5.3.3 Corrosion at high burnup

Clad corruptions observed at high burnups appear generally as a rather uniform broad-front layer sometimes preceded by a small intergranular attack; it may reach considerable depth. The Phénix pins irradiated at high burnup give typical examples of this FCCI mode. Clad corruptions are located in the upper third of the fissile stack and affect a large clad surface; several tens of millimeters long and more or less azimuthally uniform. As an example, **Figure 16** shows one of the largest corruptions observed in Phénix pins, up to 200 μm deep.

During nondestructive examination, such corrosion may be detected and localized by eddy currents. It is often associated to cesium accumulation seen on the γ -scanning, and in some cases, but rarely, to small deformation peaks (cf. **Section 2.21.5.2.3**).

Burnup plays a crucial role in the development of this corrosion, which is directly linked to the amount of created corrosive species, which is also linked to the high oxygen potential needed for this corrosion to occur. A minimum clad temperature is necessary;



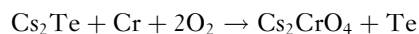
Figure 16 Metallography showing a large clad corrosion observed in a Phénix pin irradiated at 17 at. %.

this is why corrosion is not observed in the lower half of the fuel column.

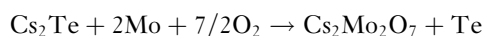
Cladding strain plays an indirect role; most extensive corrosion has been observed in pins clad with austenitic stainless steels (as 316 Ti or 15/15 Ti), which exhibited at high burnup (and high dose) a swelling bump in the lower half of the fuel column. This clad deformation induces locally an overheating of the oxide fuel, which favors an axial migration of volatile fission products from the region with high fuel temperature (lower part) to colder areas (upper part with small clad strain), thus locally enhancing the quantity of corrosive species. Consequently, low swelling cladding materials such as ferritic steel are likely to be less susceptible to clad corrosion than austenitic stainless steel, but this has yet to be extensively demonstrated at high burnup.

The mechanism of this corrosion involves essentially tellurium and cesium^{4,48} and needs local conditions where Cs_2Te compound can split and high tellurium activity may develop. Many types of reactions of Cs and Te with oxide fuel, fission product compounds, and clad components are likely to occur depending upon relative amounts of constituents, local conditions of temperatures, and oxygen potential.⁴⁹ Among these different reactions, the two probably play a crucial role in clad corrosion:

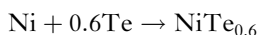
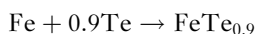
- Reaction with cladding components



- Reaction with JOG components



These reactions need oxygen potential higher than -400 kJ mol^{-1} , which are likely to occur at high burnup. The liberated tellurium reacts with clad constituents, forming iron and nickel telluride:



2.21.5.3.4 Corrosion at fissile–fertile interface

A similar type of corrosion has also been observed at the upper end of the fissile column in front of the interface between fissile pellets and fertile pellets. Although localized and affecting a much smaller volume than the former type of FCCI, this corrosion may also reach locally significant depths, up to $200 \mu\text{m}$. The mechanisms at work are probably the same as the previous type, but the local conditions are different: low fuel temperature with high oxygen potential, high clad temperature, and as Cs and Te reached this area after a long axial migration, their relative amounts may be quite different from their relative fission yield.

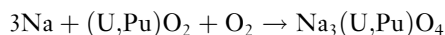
2.21.6 Cladding Failure

Although still under development, oxide fuel pins irradiated in fast reactors have demonstrated a high reliability, with a relatively small number of in-reactor clad failures (e.g., 15 pin failures with sodium ingress in Phénix, out of 180 000 irradiated fuel pins, 23 failures in PFR, 12 in FFTF, out of 64 000 oxide fuel pins), the major part on experimental fuel pins.

In case of clad failure of an oxide fuel pin in sodium-cooled fast reactors, the first effect of the loss of tightness is a release of fission gases in the coolant. Reactors equipped with monitoring of fission gas above the coolant can detect this first stage of pin failure. The second step is sodium ingress inside the fuel pin, followed by an exchange of sodium between inside and outside the fuel pin. All fast reactors are equipped with a delayed neutron detector (DND), which detects the delayed neutrons released by some of the fission products escaping the fuel pin. This allows monitoring the evolution of the clad failure, as the DND signal is related more or less to the surface of fuel in contact with sodium. Some experimental and prototypic reactors have also used a gas-tagging system in order to detect failures and identify the responsible subassembly. In this method,

a mixture of stable isotopes of a rare gas is added to the plenum of fuel pins, one different mixture for each subassembly.

The crucial point is the incompatibility of mixed oxide and sodium. $(\text{U,Pu})\text{O}_2$ reacts with sodium to form sodium uranoplutonate^{50–53}:



This reaction takes place at the periphery of the pellets (see an example in Figure 17) and requires an oxygen supply. As sodium coolant is very clean (1 or 2 ppm of oxygen), oxide fuel supplies the oxygen needed for the reaction. Consequently, the O/M ratio of the fuel decreases, and the reaction is stopped when the oxygen potential is low enough for the aforementioned reaction to reach equilibrium. For a low burnup fuel with a Pu content of 20%, this O/M equilibrium is about 1.96 at 750°C . The quantity of oxygen that can be supplied by the fuel and therefore the magnitude of the reaction increases with plutonium content and with burnup. A stoichiometric UO_2 does not react with pure sodium, as there is no oxygen to feed the reaction.

Due to the radial temperature gradient, this reaction induces a radial migration of oxygen, which migrates down the thermal gradient. With an O/M of about 1.96 at the limit between oxide fuel and the peripheral sodium uranoplutonate layer, the O/M at the center of the pellet becomes very low, reaching values around 1.90.

When clad breaches occur at high burnup, the reaction progresses from the pellet periphery toward the pellet center by an intergranular front; the rate

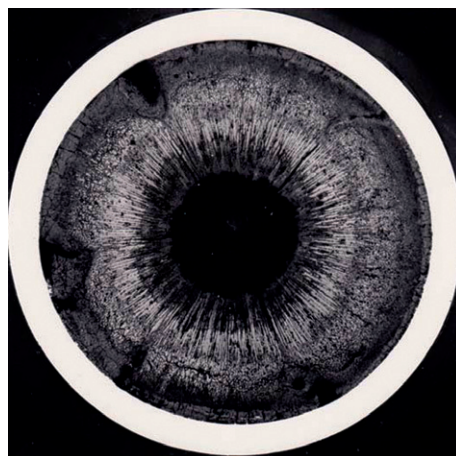


Figure 17 Macrograph of a failed Phénix pin showing a wide layer of sodium uranoplutonate.

of oxide sodium reaction is higher at the grain boundary. The sodium uranoplutunate layer reaches a thickness of several hundreds of micrometers. The main consequences of this reaction are:

- An increase in fuel temperature due to the decrease of thermal conductivity induced by the decrease in O/M ratio. The sodium uranoplutunate layer also has a lower thermal conductivity than the oxide fuel (about a factor 3 lower).
- An increase in global fuel volume induced by the formation of uranoplutunate (which has a density about half the oxide density) and by the thermal expansion of oxide fuel due to reduction and subsequent heating of the fuel.

As a result of the reaction of sodium with the oxide fuel, the volume expansion of the fuel induces a strain in the cladding, with a risk of propagating the initial clad breach or developing a new breach; a secondary failure. The sizes of primary and secondary failure depend greatly on the cause of the primary failure and of the ductility of the clad. Large clad failures (up to several hundreds of millimeters of axial extension) are found with embrittled clad materials.

The main consequence of clad failure is a release of fission products in the coolant; the fission gases that had been previously released in the pin plenum and a fraction of the volatile fission products such as cesium (typically 15–40%). Cesium is soluble in sodium and sodium replaces cesium in most cesium compounds of the periphery (cesium uranates and molybdates). These releases of fission products not only depend upon the size of the failure but also on irradiation conditions in particular; power variations induce a peak of fission product release by favoring sodium movements between inside and outside the fuel pin, and by modifying the fuel thermal regime.

Indeed, in most failure cases, there was no significant release of fissile material in the coolant. In practice, the fuel sodium reaction product was found to form a scab over the breach site, allowing operation in steady-state conditions for a considerable time without significant contamination of the primary coolant. But in order to guarantee they will avoid any release of fissile atoms, reactor operators have to determine a threshold of the DND signal beyond which the reactor is shut down and the subassembly with the failed pin is discharged. The time between DND failure detection and reactor scram may vary in a large range (from a few minutes to more than 100 days) depending upon the cause of

rupture, the embrittlement of the clad, and the operating conditions. The shortest times have been observed in case of failure of high burnup rods, with brittle claddings occurring during power transients. This time is typically a question of hours or days, and generally the reactor has generally to be stopped before the next planned shutdown. This means that each pin failure causes a specific shutdown and stops the reactor for several days, the time needed to unload the failed subassembly and to load a new one.

The main consequences of rod failures are, therefore, a pollution of the sodium coolant by radioactive nuclides and a decrease in the load factor of fast reactors. High reliability of fuel pins, with a failure rate of 10^{-5} or lower, is therefore a strong objective in the development of oxide fuel.

2.21.7 Summary and Outlook

Oxide fuel for fast reactors has proved to be a mature, quite reliable, and very robust fuel concept. The low conductivity of mixed oxide may appear as a weakness of this fuel as it induces a limitation of linear heat generation. However, thanks to its high operating temperature and related high creep rate, fuel loadings to the cladding remain low, and oxide fuel pins have demonstrated an ability to reach extremely high burnup.

Experience achieved in the past decades on oxide fuel behavior in fast reactors paves the way to face the new challenges of the next generation of reactors for Generation IV systems. Even if other types of fuel (such as carbide, nitride, or metals) are seriously considered, if advantages and drawbacks of the different fuels are still weighed, it is likely that the first prototypes of this new generation will use oxide as it is the most mature fuel among the various candidates.

All phenomena occurring in fast oxide fuel are relatively well understood and modeled. However, it might be useful in the future to improve the accuracy of code predictions, in particular regarding the thermal margin to fuel melting at high burnup or the consequences of FCCI. This will imply developing quantitative modeling of thermochemical phenomena, such as JOG formation or clad corrosion, which may be quite complex as these mechanisms involve not only thermodynamics but also considerable radial and axial migration of a great number of fission product compounds. (See also [Chapter 2.14, Properties of Liquid Metal Coolants](#); [Chapter 2.17,](#)

Thermal Properties of Irradiated UO_2 and MOX; Chapter 3.19, Oxide Fuel Performance Modeling and Simulations; and Chapter 3.21, Matter Transport in Fast Reactor Fuels).

Acknowledgments

The author wishes to thank M. Pelletier, J.P. Piron, and J. Noirot (CEA) for the critical review of the manuscript.

References

- Olander, D. R. *Fundamental Aspects of Nuclear Reactor Fuel Elements*; Report No. TID-26711-P1; Technical Information Center, Office of Public Affairs, Energy Research and Development Administration: Oak Ridge, TN, 1976.
- Lambert, J. D. B.; Strain, R. In *Materials Science and Technology – A Comprehensive Treatment, Volume 10 A – Nuclear Materials*; Frost, B. R. T., Ed.; VCH: New York, 1994; pp 108–190.
- Guérin, Y. In *The Nuclear Fuel of Pressurized Water Reactors and Fast Reactors*; Bailly, H., Ménéssier, D., Prunier, C., Eds.; Collection du Commissariat à l'Energie Atomique; Lavoisier: Paris, 1999; pp 77–158.
- Millet, P.; Ratier, J. L.; Ravenet, A.; Truffert, J. In *The Nuclear Fuel of Pressurized Water Reactors and Fast Reactors*; Bailly, H., Ménéssier, D., Prunier, C., Eds.; Collection du Commissariat à l'Energie Atomique. Lavoisier: Paris, 1999; pp 437–529.
- Martin, P.; Pelletier, M.; Every, D.; Buckthorpe, D. *Nucl. Technol.* **2008**, *161*, 35–43.
- Pelletier, M. Les performances du combustible. *Revue Générale Nucléaire – Le réacteur Phénix: bilan de 35 ans de fonctionnement*. n 1 Janvier – Février 2009.
- Pages, J. P.; Brown, C.; Steinmetz, B.; Languille, A. Development of the axially heterogeneous fuel concept in Europe. In *Proceedings of the International Conference on Fast Reactors and Related Fuel Cycles*, Kyoto, Japan, 1991; Vol. 1, 6.2-1.
- Gratchyov, A. F.; Skiba, O. V.; Tsykanov, V. A.; et al. *J. Nucl. Sci. Technol.* **2007**, *44*(3), 504–510.
- Conte, M.; Gatesoupe, J. P.; Trotabas, M.; Boivineau, J. C.; Cosoli, G. Study of the thermal behaviour of LMFBR fuel. In *Proceedings International Conference Fast Breeder Reactor Fuel Performance*, Monterey, 1979; pp 301–319.
- Rand, M. H.; Roberts, L. E. J. In *Symposium Proceedings in Thermodynamics*; IAEA: Vienna, 1965; Vol. 1, STI/PUB/109.
- Rand, M. H.; Markin, T. L. In *Symposium Proceedings on Thermodynamics of Nuclear Materials*; IAEA: Vienna, 1967; STI/PUB/162.
- Aitken, E. A. *J. Nucl. Mater.* **1969**, *30*, 62.
- Bober, M.; Schumacher, G. *Adv. Nucl. Sci. Technol.* **1973**, *7*, 495–564.
- Sari, C.; Schumacher, G. *J. Nucl. Mater.* **1976**, *61*, 192–202.
- Tanaka, K.; Miwa, S.; Sato, I.; et al. *J. Nucl. Mater.* **2009**, *385*, 407–412.
- Olander, D. *J. Nucl. Mater.* **1973**, *49*, 21–44.
- Clement, C. F.; Finniss, M. W. *J. Nucl. Mater.* **1978**, *75*, 193–200.
- Guarro, S.; Olander, D. R. *J. Nucl. Mater.* **1975**, *57*, 136–144.
- Maeda, K.; Sasaki, S.; Kato, M.; Kihara, Y. *J. Nucl. Mater.* **2009**, DOI: 10.1016/j.jnucmat.2009.01.010.
- Kleykamp, H. *J. Nucl. Mater.* **1985**, *131*, 221–246.
- Lindemer, T. B.; Besman, T. M.; Johnson, T. E. *J. Nucl. Mater.* **1981**, *100*, 178–226.
- Adamson, M. G.; Aitken, E. A.; Lindemer, T. B. *J. Nucl. Mater.* **1985**, *130*, 375–392.
- Kleykamp, H.; Paschoal, J. O.; Pejsa, R.; Thummier, F. *J. Nucl. Mater.* **1985**, *130*, 426.
- Tourasse, M.; Boidron, M.; Pasquet, B. Effect of clad strain on fission product chemistry in Phénix pins at high burnup. In *Symposium Proceedings on Materials Chemistry 92*, Tsukuba, 1992; p 13.
- Sato, I.; Furuya, H.; Arima, T.; Idemitsu, K.; Yamamoto, K. *J. Nucl. Mater.* **1999**, *273*, 239–247.
- Matzke, H.; Ottaviani, J. P.; Pellotier, D.; Rouault, J. *J. Nucl. Mater.* **1988**, *160*, 142.
- Tourasse, M.; Boidron, M.; Pasquet, B. *J. Nucl. Mater.* **1992**, *188*, 49.
- Inoue, M.; Maeda, K.; Katsuyama, K.; Mondo, K.; Hisada, M. *J. Nucl. Mater.* **2004**, *326*, 59–73.
- Maeda, K.; Tanaka, K.; Asaga, T.; Furuya, H. *J. Nucl. Mater.* **2005**, *344*, 274–280.
- Ishii, T.; Mizuno, T. *J. Nucl. Mater.* **1997**, *247*, 82–85.
- Maeda, K.; Asaga, T. *J. Nucl. Mater.* **2004**, *327*, 1–10.
- Roche, L.; Pelletier, M. Modeling of the thermomechanical and physical processes in FR fuel pins using the Germinal code. IAEA-SM-358/25. In *Proceedings of International Symposium on MOX Fuel Cycle Technologies for Medium and Long-Term Deployment*, Vienna, Austria, May 17–21, 1999.
- Maeda, K.; Katsuyama, K.; Asaga, T. *J. Nucl. Mater.* **2005**, *346*, 244–252.
- Zimmermann, H. *Fission Gas Behavior in Nuclear Fuels*; European Applied Research Report; Harwood: London, 1979; Vol. 1(1), pp 127–138.
- Baker, R. B.; Leggett, R. D. *International Conference on Fast Breeder Reactor Fuel Performance*; ANS: La Grange Park, IL, 1979; p. 258.
- Renault, C.; Rouault, J.; Anzieu, P. Status and perspective of fuel developments for fast neutron reactors of 4th generation. In *Proceedings of RRFM International Conference*, 2009.
- Méris, J. C.; Piron, J. P.; Roche, L. *J. Nucl. Mater.* **1993**, *204*, 188–193.
- Gatesoupe, J. P.; Guérin, Y.; Courtois, C.; Truffert, J. Fuel cladding mechanical interaction – Observation and analysis. In *Proceedings International Conference Fast Breeder Reactor Fuel Performance*, Monterey, 1979; pp 246–257.
- Biancheria, A.; Roth, T. S.; Nayak, U. P.; Boltax, A. Fuel-cladding mechanical interaction in fast reactor fuel rods. In *Proceedings International Conference Fast Breeder Reactor Fuel Performance*, Monterey, 1979; pp 513–535.
- Levine, P. J.; Nayak, U. P.; Schwallie, A. L.; Boltax, A. Irradiation performance of WSA-3, -4, and -8 mixed-oxide fuel pins in grid-spaced assemblies. In *Proceedings International Conference Fast Breeder Reactor Fuel Performance*, Monterey, 1979; pp 143–154.
- Dienst, W.; Guérin, Y.; Gatesoupe, J. P.; Müller-Lyda, I. *J. Nucl. Mater.* **1980**, *91*, 73–84.
- Naganuma, M.; Koyama, S.; Asaga, T.; et al. High burnup irradiation performance of annular fuel pins irradiated in fast reactor PFR IAEA-SM-358/24. In *Proceedings of*

*International Symposium on MOX Fuel Cycle**Technologies for Medium and Long-Term Deployment*, Vienna, Austria, May 17–21, 1999.

43. Fee, D. C.; Johnson, C. E. *J. Nucl. Mater.* **1981**, 99, 107–116.
44. Adamson, M. G.; Aitken, E. A. *J. Nucl. Mater.* **1985**, 132, 160–166.
45. Pulham, R. J.; Richards, M. W. *J. Nucl. Mater.* **1990**, 171, 319–326; **1990**, 172, 47–53; **1990**, 172, 206–219; **1990**, 172, 304–313; **1992**, 187, 39–42; **1994**, 209, 122–127; **1995**, 223, 180–185.
46. Götzmann, O. In *Proceedings of the BNES Conference on Fast Reactor Core and Fuel Structural Behavior*, London, 1990; pp 1–8.
47. Yates, G.; Linekar, G. A. B. Fuel/clad chemical interaction in PFR fuel pins. In *Proceedings International Conference on Materials for Nuclear Reactor Core Applications*, Bristol, Oct 1987; BNES, pp 329–333.
48. Ratier, J. L. Phénomènes de corrosion des gaines d'éléments combustibles de réacteurs à neutrons rapides. In *Conference EUROCORR*, Epsöo, Finland, Jun 4, 1992.
49. Ball, R. G. J.; Burns, W. G.; Henshaw, J.; Mignanelli, M. A.; Potter, P. E. *J. Nucl. Mater.* **1989**, 167, 191–204.
50. Mignanelli, M. A.; Potter, P. E. *J. Nucl. Mater.* **1984**, 125, 182.
51. Lorenzelli, R.; Athanassiadis, T.; Pascard, R. *J. Nucl. Mater.* **1985**, 130, 298.
52. Pillon, S. Etude des diagrammes de phases U–O–Na et U, Pu–O–Na. Thesis Université des Sciences et Techniques du Languedoc. Rapport CEA-R-5489; 1989.
53. Kleykamp, H. *Assessment of the Physico-Chemical Properties of Phases in the Na–U–Pu–O System*. Kernforschungszentrum Karlsruhe Report; KFK 4701; 1990.

2.22 Transient Response of LWR Fuels (RIA)

T. Fuketa

Japan Atomic Energy Agency, Tokai-mura, Ibaraki, Japan

© 2012 Elsevier Ltd. All rights reserved.

2.22.1	Introduction	579
2.22.1.1	Background	579
2.22.1.2	Reactivity Insertion Events in LWRs	580
2.22.2	Sequence of Fuel Rod Behavior During a Reactivity-Initiated Accident	580
2.22.3	Cladding Failure	582
2.22.3.1	Failure Modes	582
2.22.3.2	Thermal Failure: Brittle Fracture and Rod Burst	584
2.22.3.3	Mechanical Failure: PCMI Failure	586
2.22.4	Fuel Fragmentation and Mechanical Energy Generation	590
2.22.5	Fission Gas Release	590
2.22.6	MOX Effect	591
2.22.7	Summary	592
References		593

Abbreviations

ATR	Advanced thermal reactor, 'Fugen'
BORAX	Boiling Water Reactor Experiment
BWR	Boiling water reactor
CEA	Commissariat à l'énergie atomique, France
DBA	Design basis accident
DNB	Departure from nucleate boiling
FGR	Fission gas release
FP	Fission product
INL	Idaho National Laboratory, USA
IRSN	Institut de Radioprotection et de Sûreté Nucléaire, France
JAEA	Japan Atomic Energy Agency
LWR	Light water reactor
MIMAS	Micronized master blend
MOX	Mixed oxide
NSRR	Nuclear Safety Research Reactor
OECD/NEA	Nuclear Energy Agency, Organization for Economic Co-operation and Development
PBF	Power burst facility
PCMI	Pellet-cladding mechanical interaction
PIRT	Phenomena identification and ranking tables
PWR	Pressurized water reactor
RDA	Rod drop accident
REA	Rod ejection accident
RIA	Reactivity-initiated accident
RXA	Recrystallization annealed

SBR	Short binderless route
SPERT	Special power excursion reactor test
SPERT/	Special power excursion reactor test in
CDC	the capsule driver core facility
SRA	Stress-relieved annealed

2.22.1 Introduction

2.22.1.1 Background

A possible power excursion was a primary concern in the very beginning stage of developing power-producing reactors. In the first nuclear reactor CP-1, a person on the floor physically withdrew a control rod. If the reaction threatened to grow out of control he could reinsert the control rod, and another control rod would also insert itself automatically if the reaction reached a certain preset level. In case of emergency, another person, who stood on the balcony with an axe, would cut a rope and release another emergency control rod into the pile. The last line of defense consisted of a 'liquid control squad' that stood on a platform, ready to flood the pile with a cadmium salt solution. The first nuclear reactor was equipped with multiple and diverse control systems.¹ A number of test reactors, such as the Boiling Water Reactor Experiment (BORAX) I–V and the Special Power Excursion Reactor Test (SPERT), were constructed in Idaho, United States, in order to experimentally determine reactor kinetics and to demonstrate the

self-limiting characteristics in light water reactors (LWRs). In July 1954, the BORAX-I facility was destroyed during the final experiment with a rapid withdrawal of a control rod. Fuel plate fragments were scattered to a distance of 60–90 m. On January 3, 1961, the famous SL-1 accident occurred. The improper withdrawal of the main control rod caused the accident at the Stationary Low Power Reactor No. 1, known as the SL-1, located at the National Reactor Testing Station, Idaho, USA. The accident resulted in three fatalities and extensive damage to the reactor core.² A recent analysis concluded that the core power level reached nearly 20 GW in just 4 ms, precipitating the reactor accident and steam explosion.³ One could naturally expect that destructive forces may be triggered and generated by fuel failure and melting. It is not necessary to destroy a whole core in order to study fuel failure and its consequences; a fuel crash test inside a rigid capsule or loop, such as the SPERT program in the capsule driver core facility (SPERT/CDC), had been initiated. Although the test programs⁴ in United States, SPERT/CDC and Power Burst Facility (PBF) in Idaho National Laboratory (INL), were terminated in 1970 and in 1980, respectively, the Nuclear Safety Research Reactor (NSRR) program of Japan Atomic Energy Agency (JAEA) started in 1975 and has performed ~1200 tests until now. The French IRSN (Institut de Radioprotection et de Sûreté Nucléaire) also started tests in 1993 by using a sodium loop in the CABRI reactor of the Commissariat à l'énergie atomique (CEA). Tests in a newly constructed water loop in the CABRI are to be performed by IRSN under the Nuclear Energy Agency, Organization for Economic Co-operation and Development (OECD/NEA) program.

2.22.1.2 Reactivity Insertion Events in LWRs

A control rod ejection or drop can occur by mechanical failure of the control rod drive mechanism or its housing, and the reactivity of the core can rapidly increase due to decreasing neutron absorption. Since the reactivity insertion rates and the resulting power transients are much larger for these events than for other accident scenarios, the control rod ejection and drop belong to design basis accidents (DBAs) in LWRs. This means that they are postulated, credible accidents with low probability that are used to establish the design basis for the reactor and to define safety limits for its operation.⁵

The design basis reactivity accident in pressurized water reactors (PWRs) is the rod ejection accident

(REA). This accident is caused by mechanical failure of a control rod mechanism housing, such that the coolant pressure ejects a control rod assembly completely out of the core. The consequence of the rod ejection is a rapid positive reactivity addition, which results in a core power excursion with large localized relative power increase.⁶ On the other hand, the design basis reactivity accident in boiling water reactors (BWRs) is the rod drop accident (RDA).⁷ The initiating event for this accident is the separation of a control rod blade from its drive mechanism. The separation is assumed to take place when the blade is fully inserted in the core, and the detached blade remains stuck in this position until it suddenly becomes loose and drops out of the core in a free fall. The rod ejection is also slower in RDAs than in REAs. For this reason, and because of the coarser core lattice (lower ratio of fissile to nonfissile core material) for BWRs in comparison with PWRs, the power surge is generally somewhat slower in RDAs than in REAs. In addition to the REA and RDA, inadvertent changes in coolant/moderator temperature and/or void fraction may add reactivity to the core. Since the moderator temperature coefficient and void coefficient can have both positive and negative sign, scenarios for reactivity addition through moderator temperature and void effects vary significantly between reactors.

2.22.2 Sequence of Fuel Rod Behavior During a Reactivity-Initiated Accident

Anticipated sequence of fuel behavior during a reactivity-initiated accident (RIA) is schematically presented in **Figure 1**.⁸ As shown in the figure, the rapid increase in power leads to nearly adiabatic heating of fuel pellets, which immediately deform by solid thermal expansion. The pellet expansion leads to a direct contact between the pellet and the cladding inner surface (a closure of the gap between pellet and cladding), and pellet-cladding mechanical interaction (PCMI) leads to rapid and biaxial mechanical loading of the cladding tube. In the case of high-burnup fuels, the pellet-cladding gap (P-C gap) becomes narrow or closed during the normal operation, so the loading to the cladding occurs instantly. At this early stage of the transient, the cladding material remains at a fairly low temperature (at an initial temperature), and the thrust imposed by the expanding fuel pellets may therefore cause a partially brittle mode⁹ of cladding failure. This low-temperature failure mode

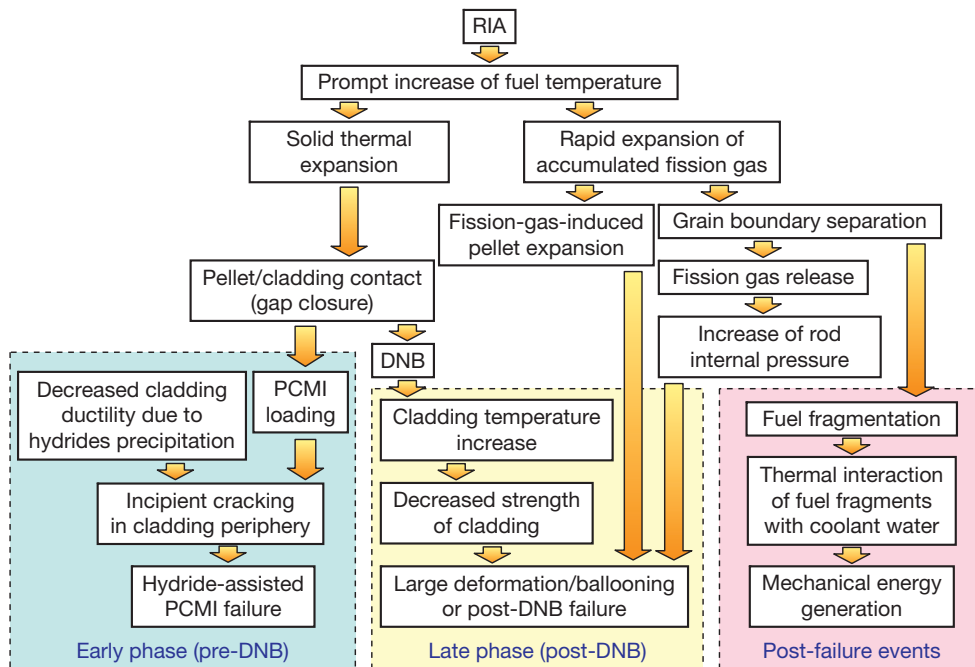


Figure 1 Sequence of fuel behavior during a reactivity-initiated accident.

is commonly observed in pulse-irradiation tests^{10–12} on high-burnup fuel rods. Hydride precipitation in high-burnup fuel cladding, in particular, plays an important role¹³ in the cladding failure, and incipient cracking due to the hydride precipitation in cladding periphery and stress concentration at the tip of the incipient crack result in through-wall cracking in the cladding tube. This failure mode in high-burnup fuels is called as ‘hydride-assisted PCMI failure’⁴ and is further described in [Section 2.22.3.3](#).

At a later stage of the transient, heat transferred from the pellets brings the cladding to such a high temperature that a departure from nucleate boiling (DNB) occurs. In this stage, experience from pulse-irradiation tests shows that the cladding material can remain at high temperature for up to about 15 s, until rewetting takes place. This fairly long period at elevated temperature may lead to cladding ballooning and rupture, or ‘rod burst,’ in cases where significant pressure differences exist across the cladding wall. As indicated in the figure, rapid expansion of fission gas accumulated in pellet grain boundaries leads to grain boundary separation over an extensive volume of the pellets, and transient release of the fission gas increases the internal pressure loading. Another mode of high-temperature failure may occur during rewetting of the overheated cladding tube since thermal stresses under the abrupt quenching may cause brittle

fracture and disruption of the cladding material. This ‘brittle fracture’ is imminent if the clad tube is embrittled by high-temperature oxidation during the film-boiling phase. Rod burst and brittle fracture are further explained in [Section 2.22.3.2](#).

Finally, if the energy deposited in the fuel is significantly high, the fuel pellets may melt. Pellet melting generally leads to cladding failure and violent thermal interaction between molten fuel pellets and the coolant, causing pressure pulses in the coolant. Since the fissile content becomes low at a high burnup, the possibility of the pellet melting in high-burnup fuels is very low even taking into account a reduction of the melting point due to burnup. However, thermal interaction between nonmolten fuel fragments and the coolant may occur, as indicated in the rightmost column of [Figure 1](#). The above-mentioned grain boundary separation in fuel pellets leads to fuel fragmentation, and the coherent thermal interaction between the fragmented pellets and the coolant results in mechanical energy generation. The fuel fragmentation and resulting mechanical energy generation are further discussed in [Section 2.22.4](#).

Although fuel enthalpy during an RIA reaches higher level for relatively fresh fuels, concerns have been concentrated particularly on high-burnup fuel behavior for the last few decades. The extended operational exposure that accompanies high burnup causes

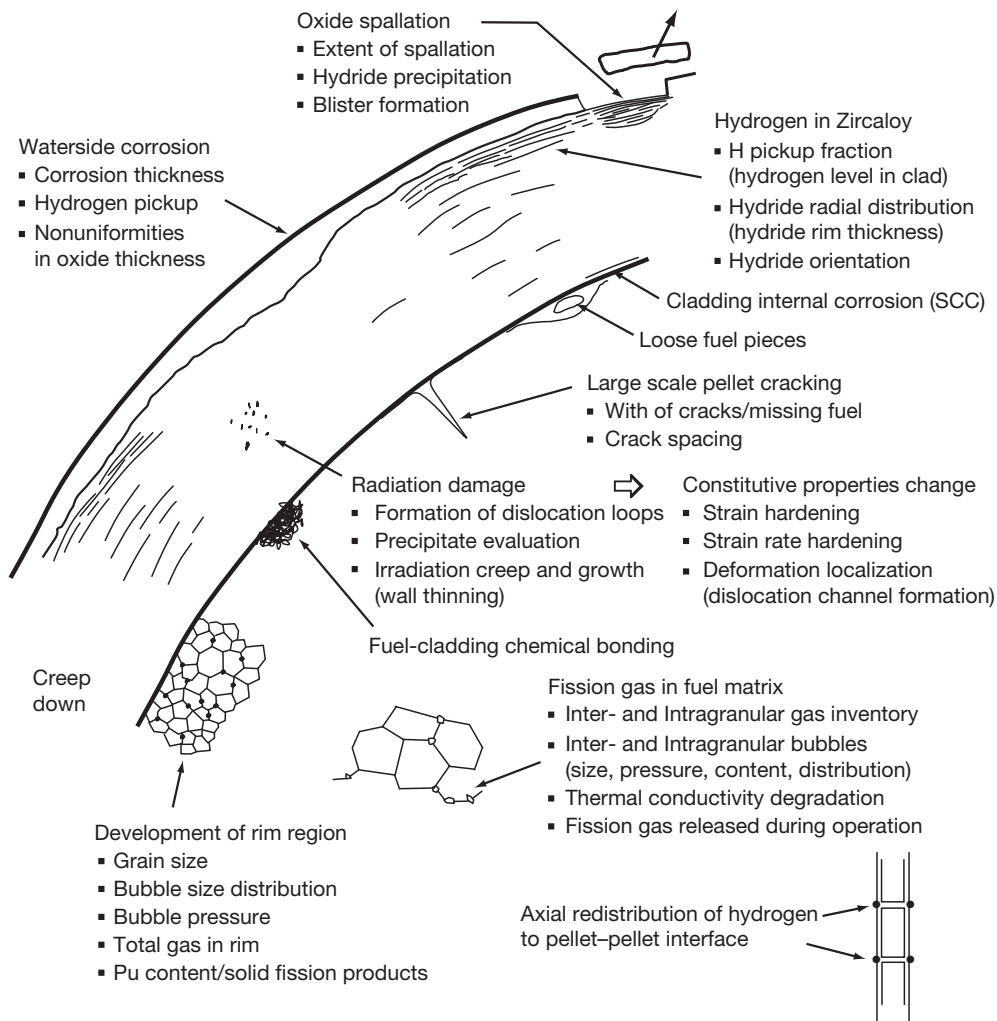


Figure 2 Processes during normal operation leading to initial conditions at high burnup.

changes to the fuel and cladding, and these changes, as illustrated in Figure 2,¹⁴ can be considered as initial conditions for an accident. There are many changes that occur to the fuel and the cladding as a result of prolonged exposure to the irradiation field present in a reactor core as well as to the corroding environment and high temperature. The combination of high temperature, radiation damage, transmutation, mechanical stresses, and chemical reactions causes the microstructure of cladding and fuel to evolve considerably during reactor exposure. These changes in microstructure, microchemistry, and macroscopic characteristics of pellet and cladding are responsible for the changes in material behavior observed at high burnup. These changes are very complex and difficult to predict mechanistically. Of the many changes to the fuel and cladding, it is

important to discern which are of greatest importance in determining fuel rod behavior during an RIA. The processes that occur during an RIA and may result in cladding failure are illustrated in Figure 3.¹⁴

2.22.3 Cladding Failure

2.22.3.1 Failure Modes

The processes of three different failure modes are shown in Figure 4. After the onset of an RIA, REA in PWRs or RDA in BWRs, fuel temperature increases promptly, and fuel pellets expand rapidly. The fuel pellets then contact with the inner wall of the cladding and push it from inside. If the cladding has decreased ductility due to corrosion and subsequent hydrogen absorption during normal operations, it may fail due

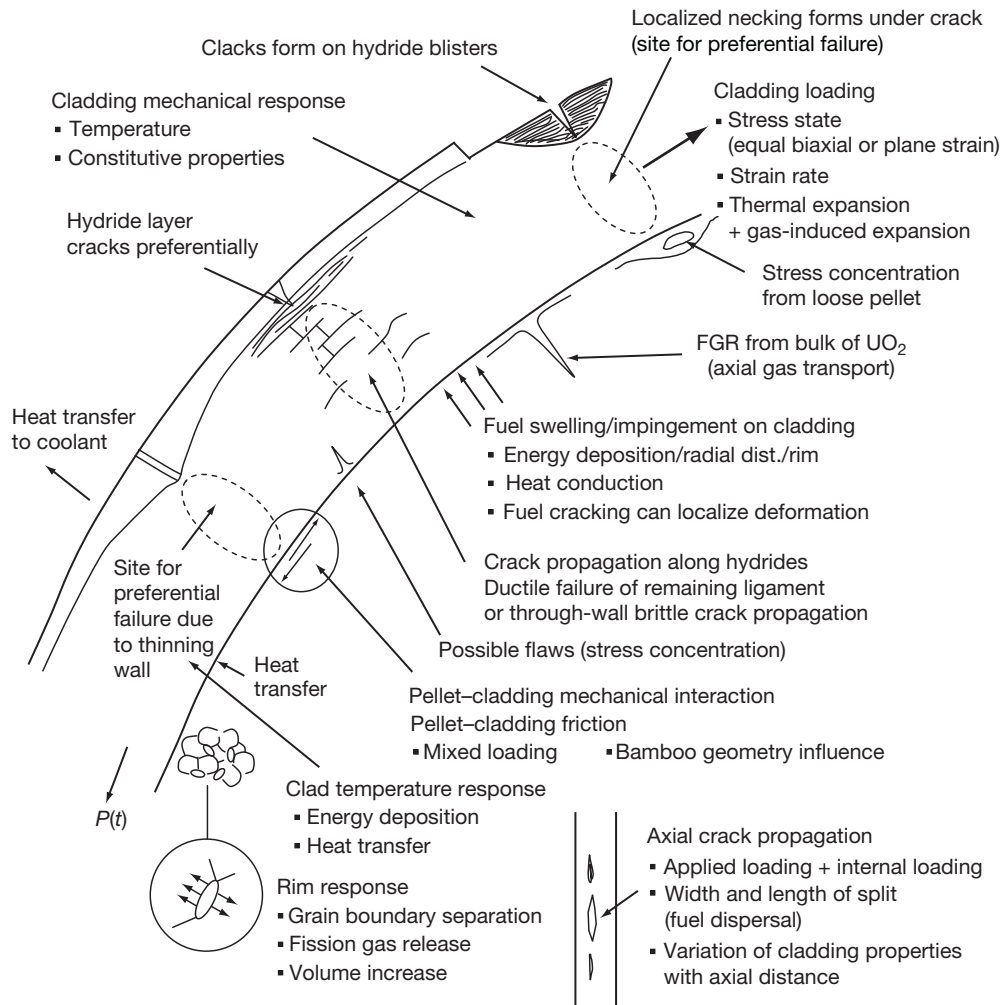


Figure 3 Phenomena during a reactivity-initiated accident leading to cladding failure.

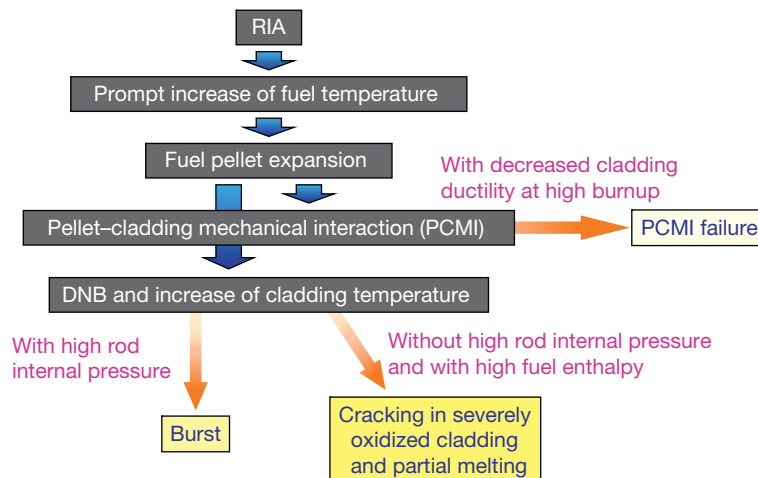


Figure 4 Cladding failure modes in a reactivity-initiated accident.

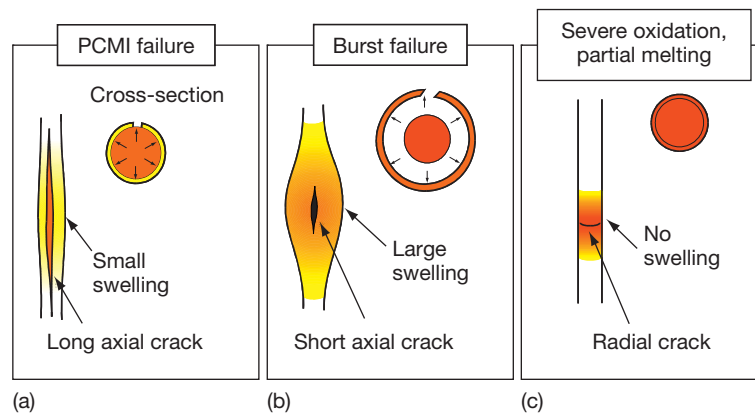


Figure 5 Schematic diagram of failed rods.

to PCMI, (see also **Chapter 5.03, Corrosion of Zirconium Alloys**). This 'PCMI failure' occurs only in a very early stage of the transient, and the cladding temperature remains low at the time of failure. Post-failed cladding has a long axial crack and its deformation is limited as illustrated in **Figure 5(a)**.

If the cladding is ductile enough to survive the stage of the PCMI loading and fuel enthalpy continues to increase, cladding temperature becomes higher after an occurrence of DNB. If the rod internal pressure is higher than the external pressure, the cladding gets ballooned due to the decreased yield stress of the cladding at the high temperature. The ballooned cladding may be ruptured, and the fuel enthalpy at the time of the rod burst is determined as a function of rod internal–external pressure difference and cladding temperature. Failed cladding in this case has a short axial crack in the ballooned region, as shown in **Figure 5(b)**.

If the internal pressure in the rod is not high and fuel enthalpy reaches much higher values, the cladding may fracture due to severe oxidation and partial melting. This 'brittle fracture' (or 'melt failure'¹⁵) can occur in a late phase of the transient, and the fuel enthalpy at the time of failure is relatively high. The failed rod has a radial crack as shown in **Figure 5(c)**.

2.22.3.2 Thermal Failure: Brittle Fracture and Rod Burst

The two failure modes of rod burst and brittle fracture described in the previous section are categorized as thermal failure and can occur only after an occurrence of DNB. The Japanese regulatory criteria regarding the thermal failures are based on NSRR experiments performed with unirradiated, fresh test

fuel rods. Brittle fracture was observed in baseline experiments of the early phase of the NSRR program. The failure is principally caused by cladding embrittlement and the fracture generally occurs at the time of quench. The cracking is enhanced by the thinning of the cladding wall. The duration of stable film boiling is several seconds to tens of seconds in the tests, and this is not sufficient to cause the cladding to become embrittled. Post-test rods showed that the cladding wall near the cracked portion became thin with melting. In the baseline tests, where the cracking occurred cladding melt was observed. Molten cladding moved to other locations inside the cladding, probably under gravity or by forces due to boiling. The variation of the wall thickness and the oxidation ratio along the axial direction in the cladding indicate that the oxygen pickup becomes relatively high in the thinner region. The cladding becomes more brittle in the thinner regions of the wall and cannot withstand axial tensile stress upon quenching. Accordingly, Ishikawa and Shiozawa¹⁵ named this type of failure 'cladding melt failure' instead of 'cladding brittle fracture' in their review paper.

As for the burst type of cladding failure, a series of NSRR experiments¹⁶ had been conducted with unirradiated, prepressurized fuel rods. The cladding ballooning is initiated at the point of the highest temperature, and once the ballooning starts, it progresses rapidly. The rupture occurs at the point of ballooning initiation due to the extremely high strain rate. In the experiment, the burst split was located nearest to the thermocouple, which indicated the highest temperature at the time of the peak pressure but the lowest temperature at the time of the rod burst. Transient histories of the rod internal pressure during the experiments show a typical response in

the case of prepressurization of 2.0 MPa. As shown in **Figure 6**, Saito *et al.*¹⁶ characterized those into the following four phases:

Phase I: Rapid increase in accordance with the initiation of the power burst. Rod pressure increased from the rapid thermal expansion of the fuel pellet, which coincided with the fuel heatup caused by rapid energy insertion. During this period, the increase in the temperature of the

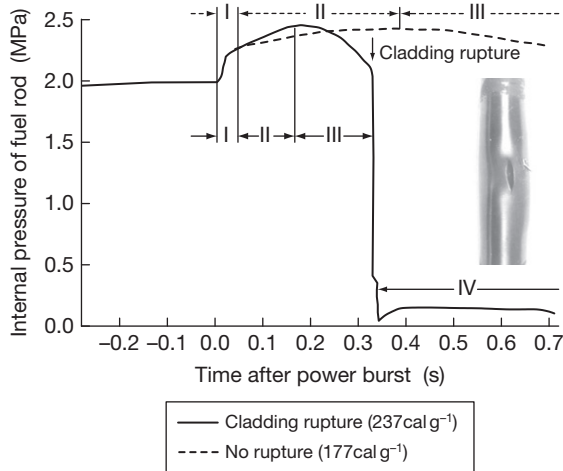


Figure 6 Transient histories of the rod internal pressure during experiments with prepressurized rods.

fill gas was thought to be negligibly small because of the almost adiabatic heating up of the fuel.

Phase II: Gradual increase up to maximum value for several hundred milliseconds after the initiation of the power burst, depending on energy depositions, initial rod pressures, etc. Rod pressure increased as a result of the increase of gap gas temperature until the ballooning of the cladding became significant.

Phase III: Gradual decrease until rod rupture or until equilibrium was reached if the rod did not fail. The ballooning of the cladding became significant. Rod pressure decreased in accordance with the ballooning.

Phase IV: Sudden drop to coolant pressure if the rod ruptured. The rod pressure continued to decrease in accordance with the decrease in the temperatures of the fuel pellet and fill gas if the rod did not fail.

A threshold of the thermal failures was defined in terms of the peak fuel enthalpy and rod internal–external pressure difference, as shown in **Figure 7**. The dashed line in the figure is a failure threshold derived from the NSRR experiments with a single test pin. When the pressure difference was below 0.6 MPa, cladding fractured with partial melting at a peak fuel enthalpy of 212 cal g^{-1} (0.89 kJ g^{-1}) or

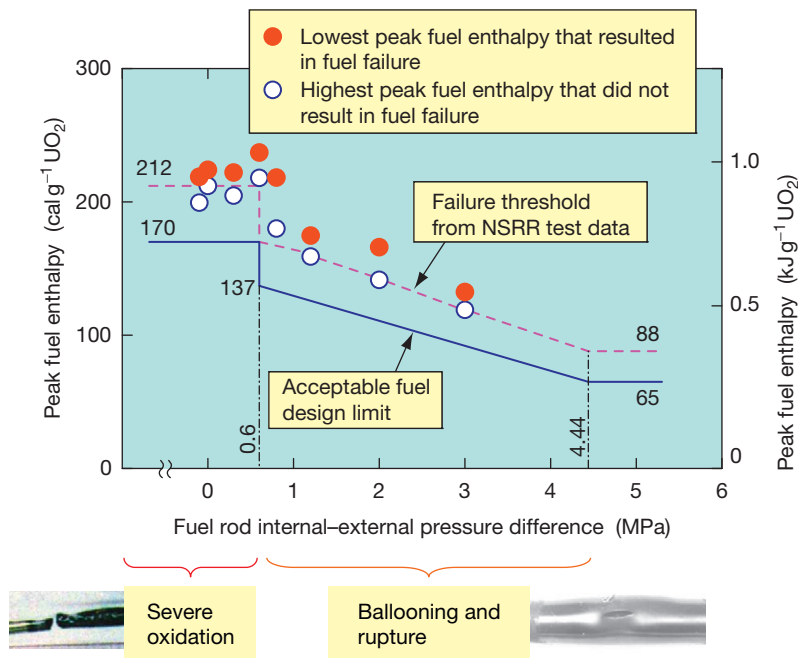


Figure 7 Threshold of the thermal failures in terms of peak fuel enthalpy and rod internal–external pressure difference.

higher. Above the difference of 0.6 MPa, the failure changes to the burst mode and the threshold decreases with pressure elevation. When the peak fuel enthalpy did not exceed 88 cal g^{-1} (0.37 kJ g^{-1}), DNB did not occur and therefore the rod did not experience thermal failures. Since thermal failures are strongly affected by the cooling conditions of the rod, the single-pin experiments give a less conservative threshold. In another test series with a rod bundle geometry, 15% reduction of the failure threshold appears due to decreased cooling. With 15% reduction and 10 cal g^{-1} (42 J g^{-1}) margin, the acceptable fuel design limit was determined as the solid line of Figure 7.

Rod ballooning was observed also in some experiments with irradiated test fuels, but no post-DNB failure occurred so far. Figure 8 shows the residual hoop strain of post-test rods as a function of peak fuel enthalpy. In the test TK-1, the residual strain reached ~25%, and photographs in Figure 9 show radial relocation of the pellet.⁸

2.22.3.3 Mechanical Failure: PCMI Failure

As stated previously, a long axial crack appears in rods failed as a result of PCMI loading. Figure 10 shows a horizontal cross section in the vicinity of a crack generated in an HBO-1 rod.¹⁰ A brittle fracture appears in the peripheral region of the cladding, where dense hydride clusters have precipitated, and propagates to the inside with a ductile nature. The failure initiation is obviously influenced by the radially localized hydride layer, that is, hydride rim, and

so it is called 'hydride-assisted PCMI failure'.^{8,13,17}

The HBO-1 rod was sampled from the second highest span, where the hydrogen concentration in the cladding was the highest in axial distribution, but the radially averaged hydrogen concentration was ~400 ppm at the most. However, the local hydrogen concentration in the cladding peripheral region well exceeded 2500 ppm, as shown in Figure 11.¹³ Incipient cracking occurs in this peripheral region due to the highly concentrated hydride clusters. Figure 12 illustrates the incipient cracks and the occurrence of stress concentration at a tip of the incipient cracks. The incipient cracks penetrate the oxide layer, and a layer with high concentrations of hydride precipitates, called the 'hydride rim.' The stress concentration at a tip of the incipient cracks drives the crack propagation to the inner part. Since the oxide layer has a negligibly low tensile stress, the thickness of the hydride rim controls the stress intensity factor. The hydride rim forms only in stress-relieved annealed (SRA) cladding, but the hydride-assisted PCMI failure occurs also in rods with recrystallization annealed (RXA) cladding. In the RXA cladding, the length of peripheral and radially oriented hydrides may control

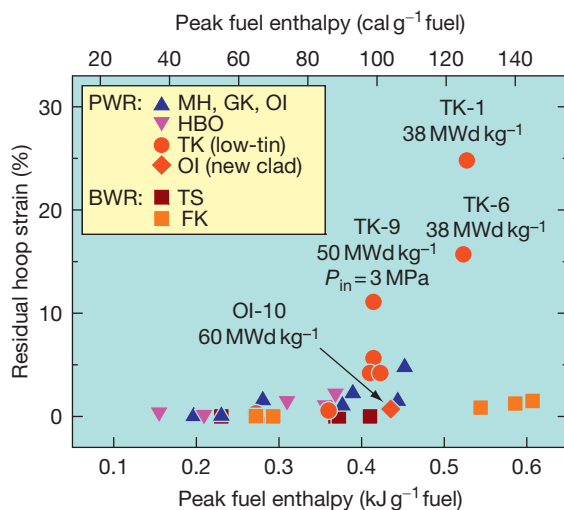


Figure 8 Residual hoop strain of post-test rods as a function of peak fuel enthalpy.

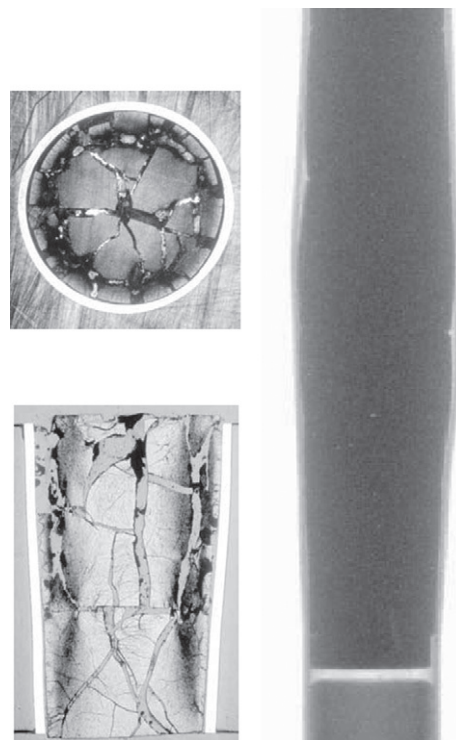


Figure 9 Post-test appearances of the TK-1 rod resulting in a large deformation.

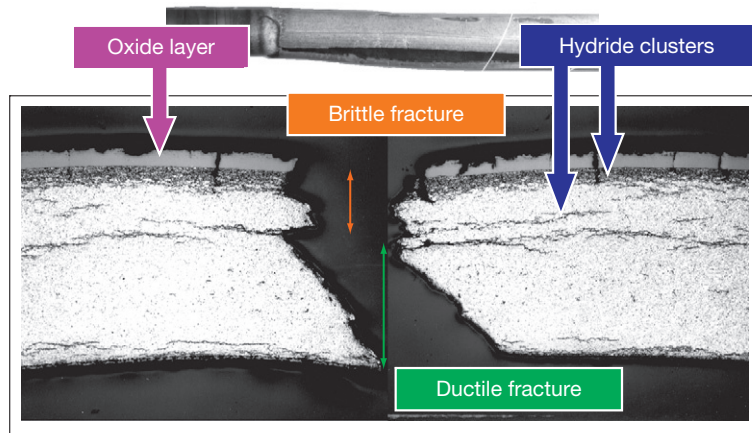


Figure 10 Crack generated in the Nuclear Safety Research Reactor experiment HBO-1 with a high-burnup pressurized water reactor fuel.

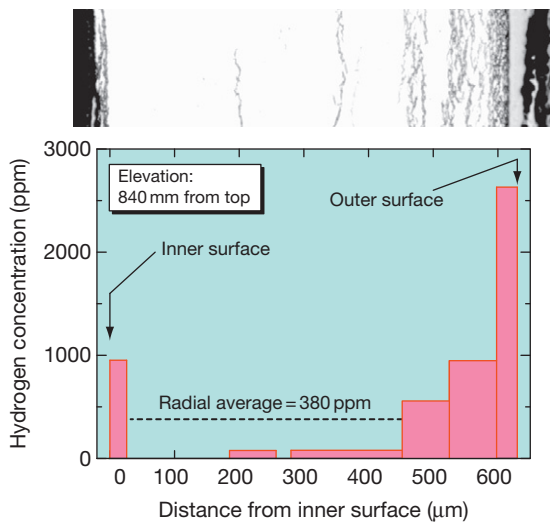


Figure 11 Radial profile of hydrogen concentration in the HBO sibling rod.

the stress intensity factor. **Figure 13**¹⁸ compares roles of the hydride rim in the SRA cladding and the radially oriented hydrides in the RXA cladding on incipient cracking. Fuel enthalpy at failure depends accordingly on the orientation of hydrides as well as on the amount of hydride precipitation.^{18–20}

Figure 14¹² shows the peak values of the residual hoop strain of the cladding during the NSRR room-temperature tests with PWR fuels. The nearly straight line in this figure indicates the strain level achievable only by the thermal expansion of the pellet. Tests in which DNB did not occur generally resulted in PCMI-induced strains. When DNB occurs during the transient, the large cladding deformation is caused

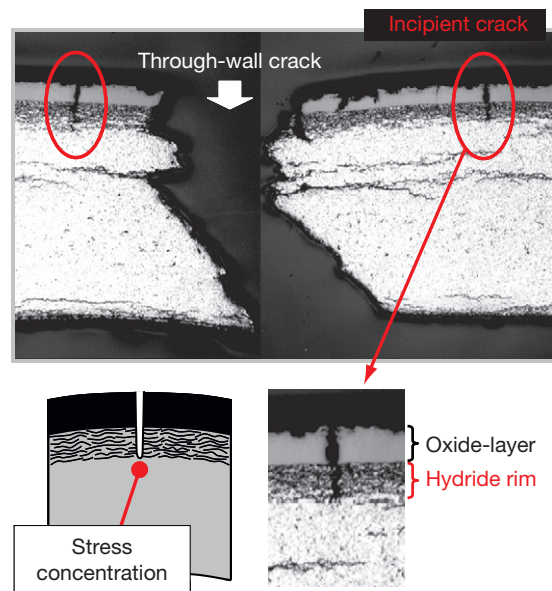


Figure 12 Stress concentration at the tip of an incipient crack.

by the increase of the rod internal pressure in combination with the decreased yield stress of the cladding at elevated temperatures. In the phase of the PCMI, the deformation is driven only by solid thermal expansion of the fuel pellets.¹²

This hydride-assisted PCMI failure occurs only in the early stage of the transient when the cladding surface temperature remains in the same level as at the onset of the event. If the cladding survives this early phase, the behavior proceeds to the late phase, post-DNB process; then, cladding temperature

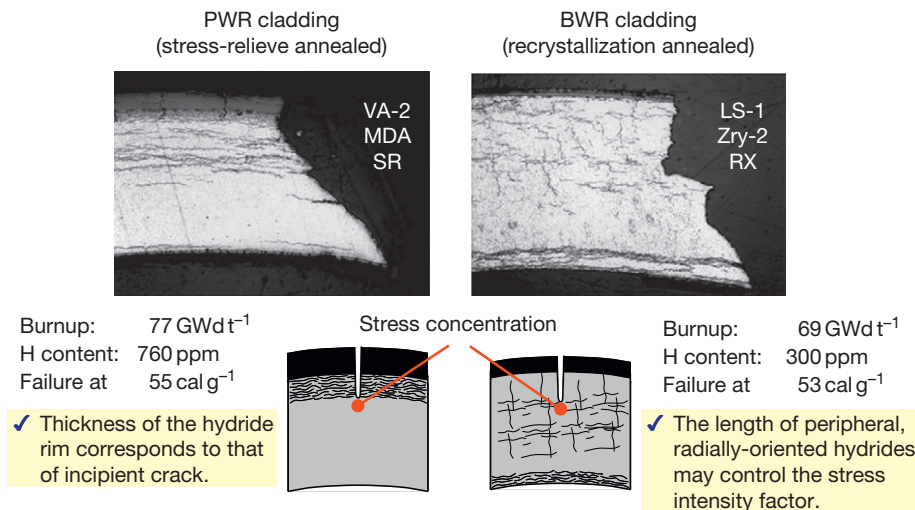


Figure 13 Influence of hydride morphology.

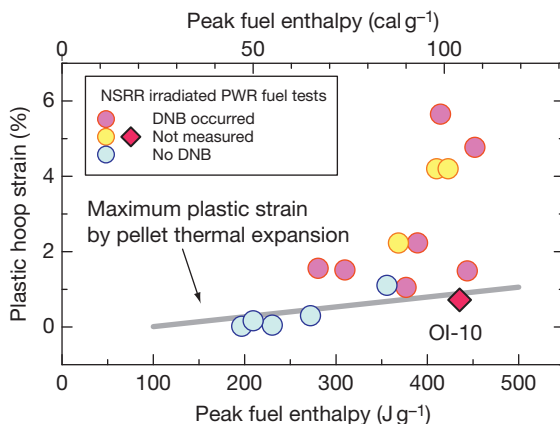


Figure 14 Cladding residual hoop strain in post-test fuel rods as a function of peak fuel enthalpy.

increases rapidly and the ductility of the cladding increases. The data shown in **Figure 14** suggests that the cladding deformation was caused by the solid thermal expansion of pellets and that fission-gas-induced pellet expansion was negligible in this early phase. The fission-gas-induced expansion is caused by thermal expansion of fission gas accumulated in fuel grain boundaries, and may have an important role on loading cladding only in the late phase.

Figure 15¹² shows the data of fuel enthalpy increases at failure as a function of burnup of tested fuel segments. A step-function-like failure threshold, defined in 1998 by Nuclear Safety Commission of Japan, is shown in the figure. The enthalpy increase at a time of failure in the test OI-11 on a rod with ZIRLO cladding was much higher than those

observed in previous tests with Zry-4 cladding in the same burnup, about 60 MWd kgU⁻¹. The higher failure energy in the test OI-11 reflects the better performance of the new cladding materials in terms of corrosion, the thinner oxides, and, accordingly, the lower hydrogen content generated during irradiation in the PWR. It can be therefore concluded that rods with improved corrosion resistance have larger safety margin against PCMI failure than conventional Zry-4 rods. Although the burnup of the tested rod is much higher, 71 MWd kgU⁻¹, in the test VA-1, the enthalpy increase at failure was 64 cal g⁻¹ (0.27 kJ g⁻¹) and remained at the same level comparing the data obtained in 50–60 MWd kgU⁻¹. The result suggests that high-burnup structure (rim structure) in the pellet periphery does not have a strong effect on the reduction of the failure threshold because the PCMI load is produced primarily by solid thermal expansion.

Since the failure threshold formulated as a function of burnup cannot reflect any improvements in the fuel design, some proposals have been made to describe the threshold with a different parameter. **Figure 16**¹⁸ shows data of fuel enthalpies at failure from experiments on PWR fuels with SRA cladding as a function of the cladding oxide layer thickness. The fuel enthalpy at failure correlates closely with the thickness of the hydride rim, and the amount of hydrogen introduced into the metal during the corrosion process is proportional to the oxide thickness. Accordingly, the fuel enthalpy at failure correlates well with the oxide layer thickness. It can be seen that the thinner oxide in the OI-11 results in higher enthalpy at failure even with the high burnup of

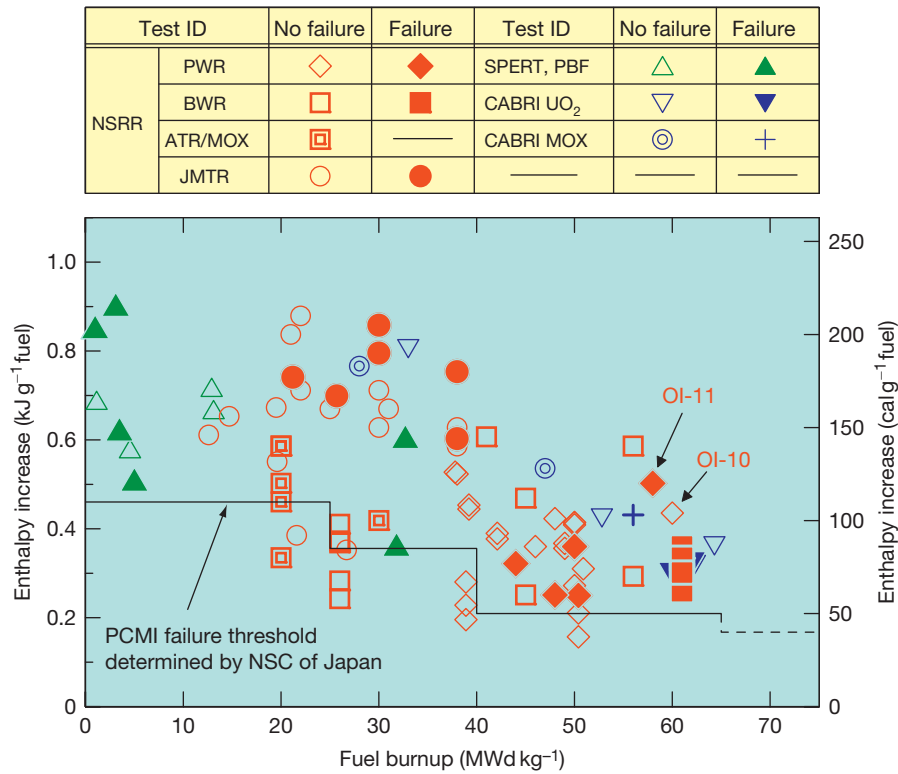


Figure 15 Burnup-dependent pellet-cladding mechanical interaction failure threshold.

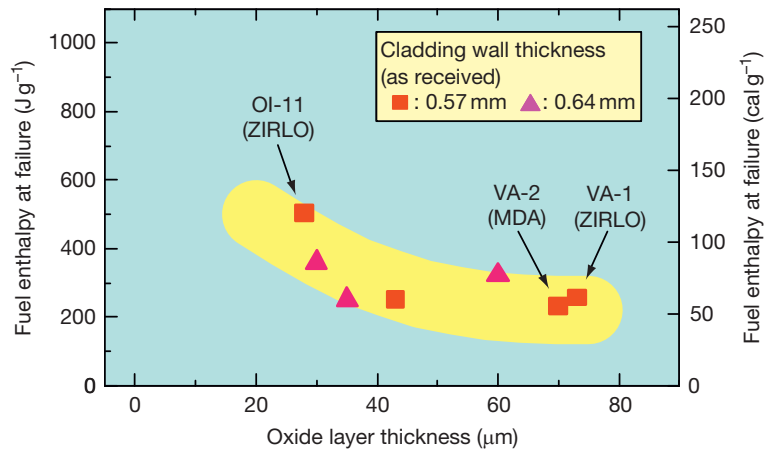


Figure 16 Fuel enthalpy at failure as a function of oxide layer thickness.

58 MWd kgU⁻¹. Although the ZIRLO-sheathed rod tested in the VA-1 had a thick oxide layer of 73 μm, the enthalpy at failure remained 64 cal g⁻¹ (0.27 kJ g⁻¹), which was at the same level as with an oxide thickness of 40 μm. The formulation of the threshold as a function of oxide thickness may offer

an improvement in establishing an RIA failure threshold particularly for fuel designs with advanced cladding materials.¹² However, there is room for further improvement, since the formulation does not account for the other factors, for example, hydride distribution and orientation.

2.22.4 Fuel Fragmentation and Mechanical Energy Generation

Fuel fragmentation and mechanical energy generation^{21,22} occur when the peak fuel enthalpy exceeds 285 cal g^{-1} (1.19 kJ g^{-1}) in the NSRR experiments with a fresh, single pin. Higher fuel enthalpy correlates with higher mechanical energy generated, as shown in Figure 17. Partial melting of pellets was always observed. In order to avoid incipient pellet melting, the Japanese regulatory guideline defined the absolute limit of maximum fuel enthalpy as 230 cal g^{-1} (0.96 kJ g^{-1}) in 1984. It is generally known that pellet melting occurs at the lower temperature due to burnup, additives such as gadolinium, and Pu in mixed oxide (MOX) fuels. It was accordingly required that the reduction of the melting point be taken into account for the absolute limit, and the Nuclear Safety Commission of Japan reexamined burnup effects on RIA fuel behaviors and issued a regulatory report in 1998. As for the effect of burnup on the melting point, the report noted that the assumption of no reduction up to 30 MWd kg^{-1} and $3.2 \text{ deg MWd}^{-1} \text{ kg}^{-1}$ reduction above 30 MWd kg^{-1} was acceptable. It has been suggested that the assumption is overly conservative, but data regarding the melting point at higher burnup are very limited at the moment.

In NSRR experiments with high-burnup PWR and BWR fuels, which resulted in fuel failure, fuel pellets were dispersed from the rod and were

recovered as fragmented particles from capsule water after the experiment. A cross-sectional view and scanning electron microscopy images of the fragmented debris²³ are shown in Figure 18.⁸ The appearance indicates that the collected fuel particles have not melted during the experiment, as can be expected from the low maximum fuel temperature (below $\sim 2100 \text{ K}$ in this case) during pulse irradiation. Although the fragmented particles remained in the solid phase, significant mechanical energy generation was observed in these experiments. The estimation of mechanical work due to the release and expansion of internal gas from the rod shows that the gas does not have enough potential to produce this level of mechanical energy. With the extreme assumption that all gas inside the rod reaches the maximum fuel temperature, gas internal energy is only limited, which is well below the mechanical energy generated. This suggests that rapid steam generation due to coherent thermal interaction of the dispersed fuel fragments with the coolant water is the primary source of mechanical energy generated during the test. The postulated heat flux in this thermal interaction was compared with those in separate-effects experiments with powder fuels,²⁴ which corroborated that the heat flux in this process is realistic. In the current Japanese safety guideline, the mechanical energy generated in PCMI failure is evaluated with a formula identical to that for mechanical energy produced by pellet melting.

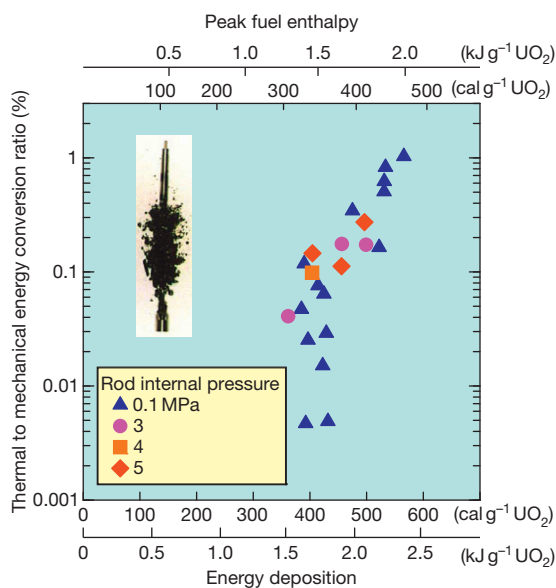


Figure 17 Mechanical energy generation due to pellet melting.

2.22.5 Fission Gas Release

After the pulse-irradiation experiments, rod-average fission gas release was measured for the test rods by rod puncture and gas analysis. The data are shown in Figure 19⁸ as a function of the peak fuel enthalpy. Except for HBO-2, -3, and -4, the higher fission gas release correlates with the higher peak fuel enthalpy. In HBO-2, -3, -4, and TK-1, the fission gas release reached $\sim 20\%$, and this corresponds to all the fission gas accumulated in grain boundaries being released during these experiments. Rapid expansion of fission gas in grain boundaries causes grain boundary separation, which then results in fission gas release and fuel fragmentation. The experiments with high fission gas release resulted in large rod deformation, except in HBO-2, -3, and -4. This indicates the significant role of fission gas in rod deformation. In HBO-2, -3, and -4, DNB did not occur and cladding temperatures remained low. (A transient signal from

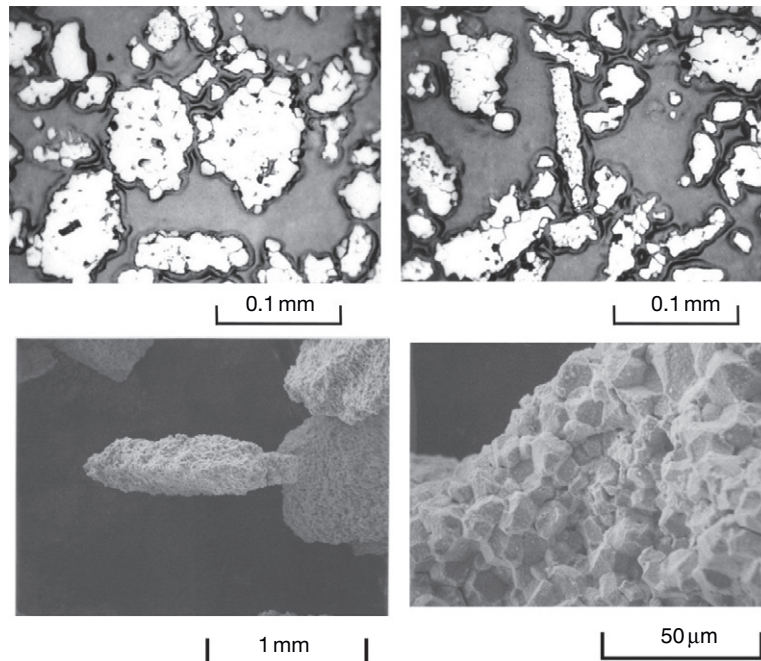


Figure 18 Fuel particles collected after a Nuclear Safety Research Reactor experiment with a high-burnup fuel resulting in pellet-cladding mechanical interaction failure.

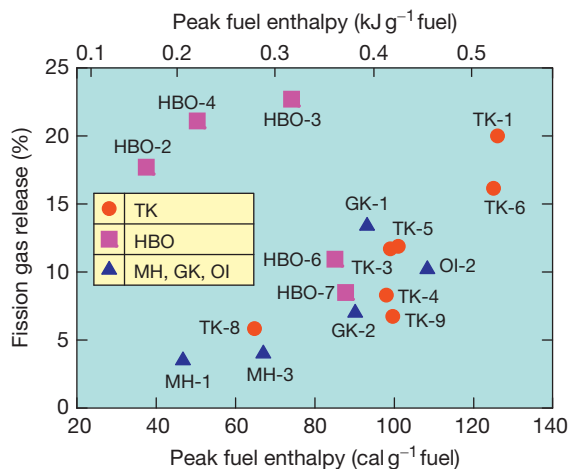


Figure 19 Fission gas release from pressurized water reactor/ UO_2 fuel pellets to rod plenum as a function of peak fuel enthalpy.

the thermocouple in HBO-3 showed ~ 670 K at maximum, but the duration of stable film boiling was very short and must have been limited to the local area.) Therefore, the significant role of fission gas in rod deformation appears only at high temperatures where cladding ductility is enhanced.

2.22.6 MOX Effect

As stated previously, results from a series of the NSRR experiments on high-burnup LWR fuels show that the heavier corrosion of cladding during operations in nuclear power plants and, in turn, the larger hydrogen absorption in cladding result in fuel failure at the lower enthalpy under RIA conditions. In particular, the thickness of the hydride rim that appeared in high-burnup PWR fuel cladding, that is, peripheral layer of the cladding containing dense hydride clusters, well correlates with fuel enthalpy at failure. Fuel enthalpies at failure in the two recent MOX tests BZ-1 and BZ-2²⁵ are consistent with the tendency derived from number of tests on UO_2 fuels, and indicate that no MOX effects appear due to the PCMI failure. The threshold of fuel failure due to PCMI only depends on the cladding state, with the PCMI loading dependent only on the pellet thermal expansion. Accordingly, the same failure limit is applicable to UO_2 and MOX fuels. Since the temperature escalation in an RIA is the most severe in the peripheral region of the pellet, plutonium agglomerates uniformly distributed over MOX pellets may have weaker or negligible effect on the PCMI loading than in a high-burnup fuel structure.

On the other hand, data regarding the fission gas release indicate a possible MOX effect. The fission gas releases during PWR fuel experiments are plotted in **Figure 20** as a function of peak fuel enthalpy. Data from NSRR experiments on advanced thermal reactor (ATR)/MOX fuels²⁶ and REP-Na experiments^{11,27,28} performed in the sodium loop of the French CABRI reactor are included in the figure. It can be seen that the fission gas releases of PWR fuels correlate with the maximum increase of fuel enthalpy. The ATR/MOX fuels have a homogeneous microstructure similar to that in short binderless route (SBR)/MOX fuels, and the fission gas releases from the ATR fuels remain in the same level as those from UO_2 fuels. The micronized master blend (MIMAS)/MOX fuels tested in the REP-Na experiments and the most recent test BZ-3, on the other hand, show larger fission gas releases. In particular, the fission gas release of 39.4% in the test BZ-3 is significantly large in comparison with those in tests on UO_2 fuels, even if one takes into consideration the fact that the initial fuel enthalpy of 70 J g^{-1} (17 cal g^{-1}) in the experiment started from a coolant condition of 281°C . The highest fission gas release among each UO_2 fuel ranged from 20 to 30% in the previous NSRR experiments, and it is generally accepted that the fission gas release achievable in an RIA-simulating test corresponds to the total amount of accumulated fission gas in the grain boundaries. In the MIMAS procedure, a mother blend of uranium/plutonium MOX is added to natural or depleted UO_2 , (see also **Chapter 2.15, Uranium Oxide and MOX**

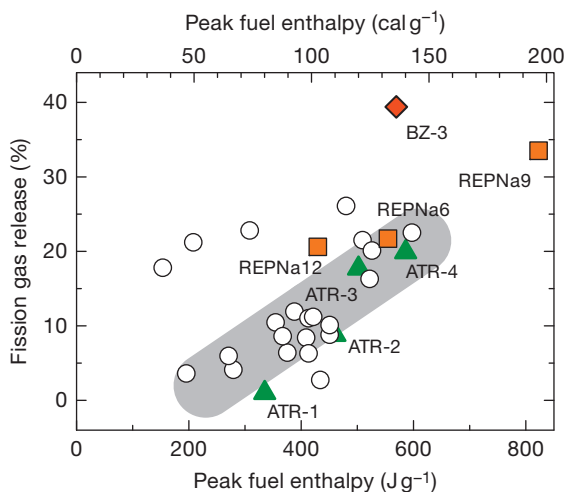


Figure 20 Fission gas release from pressurized water reactor/mixed oxide fuel pellets to rod plenum as a function of peak fuel enthalpy.

Production). Pelletizing and sintering of this powder mixture creates a heterogeneous final product with MOX (U, Pu) O_2 agglomerates embedded in the matrix of natural or depleted UO_2 . During operation cycles in a nuclear power plant, the fission occurs in the agglomerates which reach very high burnups compared to that averaged over the pellet. In the MIMAS/MOX fuels, a large amount of fission gas is accumulated in the Pu agglomerates, and in turn gives the large fission gas release during the RIA transient. It should be noted that further investigation is needed regarding gas inventories in the grain boundaries and in the Pu agglomerates in order to gain a better understanding of the fission gas release from MOX fuels, (see also **Chapter 2.19, Fuel Performance of Light Water Reactors (Uranium Oxide and MOX)**).

2.22.7 Summary

Considerable effort has been made in the past decade to produce experimental data in support of the definition of fuel safety limits for a variety of fuel designs and considering the effect of burnup. In particular, tests have been performed in specialized laboratories to address the fuel safety limits at conditions representative of the design-basis RIA. In addition to assessing the effect of burnup, the main focus of these tests has been on the safety performance of different fuel and cladding types. Specialized test reactors have been and are being used to characterize the fuel response to power transient conditions representative of potential RIA, which are postulated to occur in power reactors. The main objective of these tests was and is to assess the fuel failure limit (and possibly also the limit for fuel dispersal), as well as to gain a better understanding of burnup effects on fuel behavior in RIA conditions.²⁹

Two failure modes can be observed with relatively low burnup fuel rods. Both occur after cladding temperature escalation due to an occurrence of DNB. In cases with a high rod internal pressure, ballooning and rupture is the mode, and the failure threshold in terms of fuel enthalpy depends on the pressure. In the case with a low internal pressure, fuel fails as a result of severe oxidation of cladding in combination with a partial melting at a relatively high enthalpy level. Fuel fragmentation and mechanical force generation are observed with a very high fuel enthalpy resulting in partial melting of pellets.

A pre-DNB failure, that is, PCMI failure, is observed with high-burnup PWR and BWR fuel rods.

Test rods with a thicker oxide layer and higher hydrogen concentration failed at a lower fuel enthalpy. These results indicate that the critical factor is whether cladding has enough ductility to survive until the cladding temperature reaches a certain level. The hydride rim, that is, a radially localized hydride layer, in PWR/SRA cladding and radially oriented hydride clusters in BWR/RXA cladding have important roles in failure of high-burnup fuels. In experiments resulting in PCMI failure, fuel fragmentation and mechanical energy generation were observed as events post failure. Collected fuel particles were not previously molten. These results indicate coherent thermal interaction between the particles and coolant water. Grain boundary separation was observed over an extensive area of post-test fuel pellets. This separation can cause large fission gas release and post-failure fragmentation. PCMI load can be explained only by solid thermal expansion of pellets.

Continued experimentation is needed to confirm several of the existing observations, in particular regarding the effect of corrosion and consequent hydrogen pickup, including the behavior of different cladding alloys. As to the fuel type, more data are needed to confirm the behavior of MOX fuel as compared with UO_2 fuel. Additive UO_2 fuel testing on selected compositions will also be required for the licensing of such fuel types. The role of fission gas at the early stage of the transient also remains an important pending question.

It is highly recommended to read also the section on the modeling of RIA in **Chapter 3.19, Oxide Fuel Performance Modeling and Simulations** and a state-of-the-art report⁵ published recently.

References

1. The Manhattan Project; An Interactive History, www.cfo.doe.gov/me70/manhattan, Office of History and Heritage Resources, U.S. Department of Energy.
2. Nuclear Incident at the SL-1 Reactor, Idaho Operations Office, U.S. Atomic Energy Commission, IDO-19302; 1962.
3. "Supercritical", System Failure Case Studies, Vol. 1, Issue 4, National Aeronautics and Space Administration, 2007.
4. Meyer, R.; McCardell, R.; Chung, H.; Diamond, D.; Scott, H. *Nucl. Saf.* **1996**, 37(4), 271–288.
5. *Nuclear Fuel Behaviour Under Reactivity Initiated Accident Conditions*; State-of-the-art Report, Nuclear Energy Agency, Organisation for Economic Co-operation and Development, NEA No. 6847; 2010.
6. Diamond, D.; Bromley, B.; Aronson, A. Studies of the rod ejection accident in a PWR; Technical Report W-6382; Brookhaven National Laboratory: Upton, NY, 2002.
7. Gómez, A.; García, P.; Ortego, A.; Montalvo, C.; Collazo, I.; Mata, P. Analysis of a reactivity initiated accident (RIA) in confrontes NPP, cold and hot conditions with RETRAN-3D. In *Water Reactor Fuel Performance Meeting*, Kyoto, Japan, Oct 2–6, 2005; pp 767–781.
8. Fuketa, T.; Sasajima, H.; Sugiyama, T. *Nucl. Technol.* **2001**, 133, 50–62.
9. Chung, H.; Kassner, T. *Nucl. Eng. Des.* **1998**, 186, 411–427.
10. Fuketa, T.; Mori, Y.; Sasajima, H.; Ishijima, K.; Fujishiro, T. Behavior of high burnup PWR fuel under a simulated RIA condition in the NSRR. In *CSNI Specialist Meeting on Transient Behaviour of High Burnup Fuel*, Cadarache, France, Sept 12–14, 1995; 1996; pp 59–85, OECD/GD(96)197.
11. Schmitz, F.; Papin, J. *J. Nucl. Mater.* **1999**, 270, 55–64.
12. Fuketa, T.; Sugiyama, T.; Nagase, F. *J. Nucl. Sci. Technol.* **2006**, 43(9), 1080–1088.
13. Fuketa, T.; Nagase, F.; Ishijima, K.; Fujishiro, T. *Nucl. Saf.* **1996**, 37(4), 328–342.
14. Boyack, B.; *et al.* Phenomenon identification and ranking tables (PIRTs) for rod ejection accidents in pressurized water reactors containing high burnup fuel; NUREG/CR-6742, LA-UR-99-6810; U.S. Nuclear Regulatory Commission: Washington, DC, 2001.
15. Ishikawa, M.; Shiozawa, S. *J. Nucl. Mater.* **1980**, 95, 1–30.
16. Saito, S.; Ishijima, K.; Shiozawa, S.; Iwata, K. *J. Nucl. Sci. Technol.* **1982**, 19(4), 289–306.
17. Meyer, R. *Nucl. Technol.* **2006**, 155, 293–311.
18. Sugiyama, T.; Umeda, M.; Fuketa, T.; Sasajima, H.; Udagawa, Y.; Nagase, F. *Ann. Nucl. Energ.* **2009**, 36, 380–385.
19. Tomiyasu, K.; Sugiyama, T.; Fuketa, T. *J. Nucl. Sci. Technol.* **2007**, 44(5), 733–742.
20. Udagawa, Y.; Suzuki, M.; Sugiyama, T.; Fuketa, T. *J. Nucl. Sci. Technol.* **2009**, 46(10), 1012–1021.
21. Tsuruta, T.; Ochiai, M.; Saito, S. *J. Nucl. Sci. Technol.* **1985**, 22(9), 742–754.
22. Fuketa, T.; Fujishiro, T. *Nucl. Eng. Des.* **1994**, 146, 181–194.
23. Fuketa, T.; Sasajima, H.; Mori, Y.; Ishijima, K. *J. Nucl. Mater.* **1997**, 248, 249–256.
24. Sugiyama, T.; Fuketa, T. *J. Nucl. Sci. Technol.* **2000**, 37(10), 877–886.
25. Fuketa, T.; Sugiyama, T.; Umeda, M.; Sasajima, H.; Nagase, F. Behavior of LWR/MOX fuels under reactivity-initiated accident conditions. In *Paper 2083, Top Fuel 2009*, Paris, France, Sept 6–10, 2009.
26. Sasajima, H.; Fuketa, T.; Nakamura, T.; Nakamura, J.; Kikuchi, K. *J. Nucl. Sci. Technol.* **2000**, 37(5), 455.
27. Papin, J. The CABRI research program for study of reactivity-initiated accidents; Scientific and Technical Report 2002; Institut de Radioprotection et de Sûreté Nucléaire: France, 2002.
28. Papin, J.; Cazalis, B.; Frizonnet, J.; *et al.* *J. Nucl. Technol.* **2007**, 157, 230–250.
29. Vitanza, C.; Fuketa, T. *EUROSAFE Tribune* **2009**, 16, 13–17.

2.23 Behavior of LWR Fuel During Loss-of-Coolant Accidents

F. Nagase

Japan Atomic Energy Agency, Tokai-mura, Ibaraki, Japan

© 2012 Elsevier Ltd. All rights reserved.

2.23.1	Loss-of-Coolant Accident Conditions and Main Fuel Behavior in an LOCA	595
2.23.2	Phase Transition	596
2.23.3	Plastic Deformation of Cladding During Heat-up	596
2.23.4	Oxidation of Cladding	598
2.23.5	Embrittlement of Cladding	600
2.23.5.1	Ductile–Brittle Condition	600
2.23.5.2	Effect of Cooling History	602
2.23.5.3	Enhancement by Hydrogen Absorption	602
2.23.5.4	Fracture of Embrittled Cladding	603
2.23.6	Effect of High Burnup on Fuel Behavior	604
2.23.7	Outlook	607
References		607

Abbreviations

ANL	Argonne National Laboratory
ECCS	Emergency core cooling system
ECR	Equivalent cladding reacted
JAEA	Japan Atomic Energy Agency
LOCA	Loss-of-coolant accident
LWR	Light water reactor
TEM	Transmission electron microscopy

2.23.1 Loss-of-Coolant Accident Conditions and Main Fuel Behavior in an LOCA

The loss-of-coolant accident (LOCA) is one of the possible accidents for light water reactors (LWRs). An LOCA is caused by a break in the reactor coolant pressure boundary. The automatic emergency shutdown system of the reactor will be initiated to stop the fission reaction, but the temperature of the reactor core continues to rise due to stored heat, loss of coolant, and radioactive decay in the fuel. The cladding temperature has been analyzed to monitor the change during an LOCA as schematically illustrated in [Figure 1](#). The cladding temperature may reach over 1000 °C, though the peak clad temperature depends on reactor type, accident scenario, and fuel burnup. During the heat-up, the cladding plastically deforms

(balloon and rupture) due to decrease of the system pressure outside the fuel rod and decrease in cladding strength. The phase structure of Zircaloy transforms from α to $\alpha + \beta$ above about 800 °C, and to β above about 1000 °C. The cladding reacts with steam or coolant at high temperatures, and an oxide (ZrO_2) layer is formed on the surface of the cladding (see also [Chapter 2.07, Zirconium Alloys: Properties and Characteristics](#)). In addition, absorbed oxygen stabilizes the α -phase and a layer of α -phase with a high content of oxygen ($\alpha\text{-Zr(O)}$) begins to grow on the β -phase underneath the oxide layer. The oxide and $\alpha\text{-Zr(O)}$ layers are brittle, and the base metal (β -phase) becomes less ductile by the oxygen absorption, (see also [Chapter 5.03, Corrosion of Zirconium Alloys](#)).

The emergency core cooling system (ECCS) is immediately operated to cool and reflood the reactor core. However, severely oxidized cladding may shatter when the hot fuel rod is quenched back to low temperatures on the reflooding.

Ballooning of the cladding may block the coolant flow channel. Shattering of severely oxidized cladding and extensive degradation of fuel rods may result in the loss of coolable geometry of the reactor core. Therefore, this chapter mainly describes phase transition, plastic deformation during heat-up, oxidation, and embrittlement of the cladding since the cladding behavior is very important to evaluate and confirm the safety of LWRs in an LOCA.

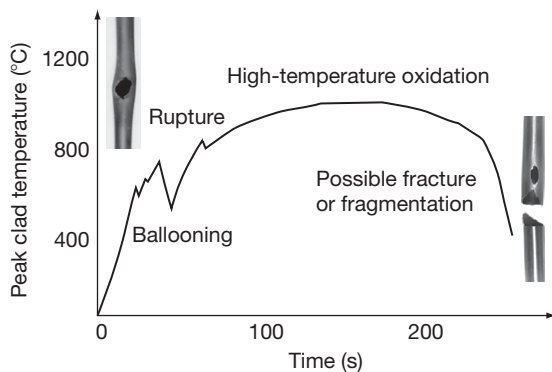


Figure 1 Analysis of cladding temperature change during a loss-of-coolant accident.

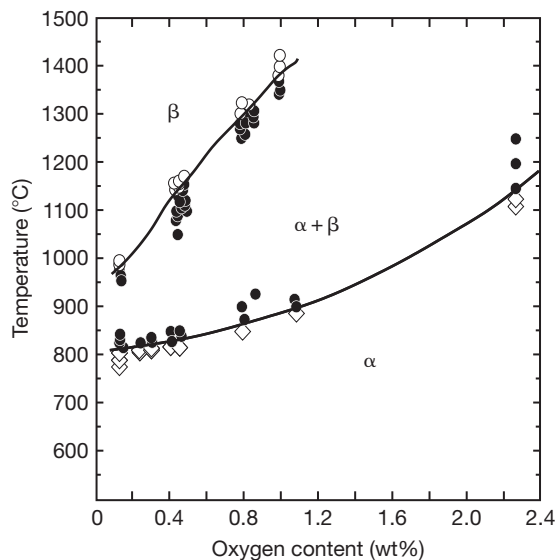


Figure 2 Pseudo-binary phase diagram of the Zircaloy–oxygen system. Reproduced from Chung, H. M.; Kassner, T. F. *J. Nucl. Mater.* **1979**, *84*, 327–339.

2.23.2 Phase Transition

Pure zirconium transforms from the hexagonal-close-packed α -phase to the body-centered cubic β -phase at $\sim 860^\circ\text{C}$. Zirconium alloys generally contain β -stabilizing elements such as Fe, Cr, and Nb, and the phase transition takes place over a temperature interval ($\alpha + \beta$ -phase temperature region). Accordingly, the α -phase partly transforms to the β -phase above about 800°C and completely to the β -phase at about 1000°C in Zircaloy. [Figure 2](#) shows the pseudo-binary phase diagram of Zircaloy–oxygen system.¹ The phase transition temperatures become

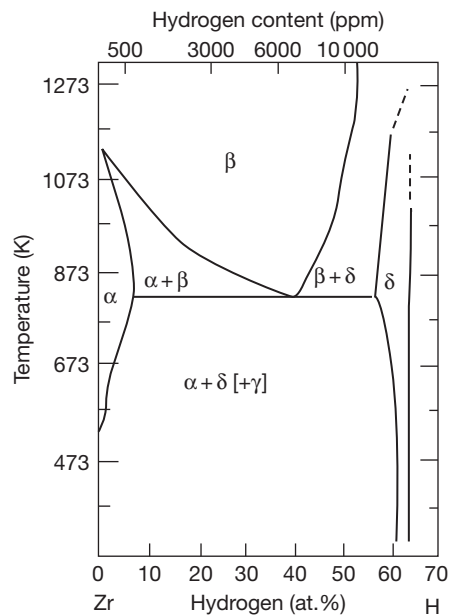


Figure 3 Binary phase diagram of the zirconium–hydrogen system. Adapted from Zuzek, E.; Abriata, J. P.; San-Martin, A.; Manchester, F. D. *Bull. Alloy Phase Diagrams* **1990**, *11*(4), 385–395.

higher with increasing oxygen concentration. It is well known that the cladding absorbs a part of hydrogen generated by corrosion of the cladding during the reactor service. [Figure 3](#) shows the binary phase diagram of the zirconium–hydrogen system.² The delta and gamma phases are hydrides. The delta phase is stable and generally observed as zirconium hydride. The gamma hydride is meta-stable and it coexists with the delta hydride after the material is cooled very rapidly. Solid solubility of hydrogen in zirconium is very low, and δ -hydrides precipitate in the α -phase for a wide range of temperature and hydrogen concentration. Once the β -phase appears above 550°C in the α -phase of highly hydrided zirconium, the solid solubility of hydrogen drastically increases and several hundred parts per million of hydrogen that is absorbed during the reactor service can be in solid solution.

2.23.3 Plastic Deformation of Cladding During Heat-up

In an LOCA the rod pressure becomes higher than the system pressure of the reactor due to a break of the coolant pressure boundary. Creep strength of Zircaloy rapidly falls with the temperature.

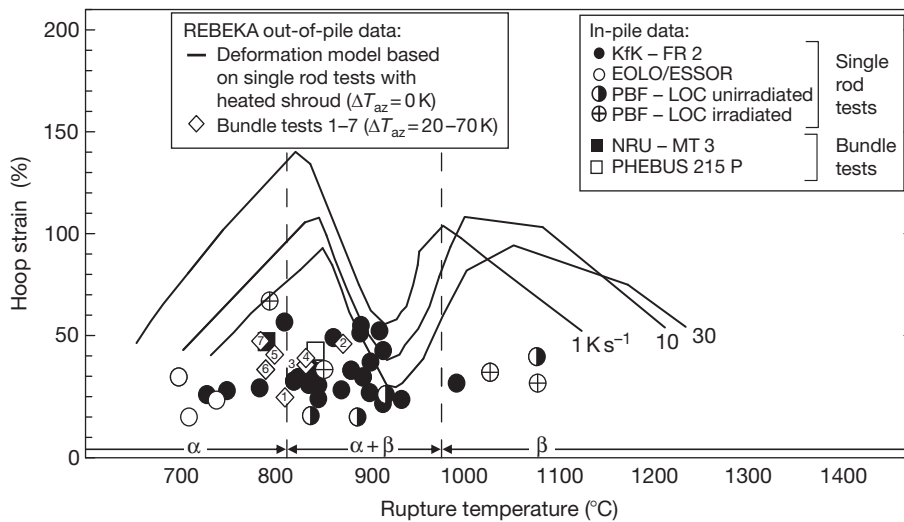


Figure 4 Relation between hoop strain and temperature at rupture. Reproduced from Erbacher, F. J. *Nucl. Eng. Des.* 1987, 103, 55.

Therefore, the cladding plastically deforms in the radial direction (ballooning) during the heat-up and may finally rupture. **Figure 4** shows the relation between the hoop strain and temperature at rupture.³ Zircaloy transforms from the α -phase to the β -phase over the temperature interval of the $\alpha + \beta$ -phase. The β -phase has creep properties different from those of the α -phase,⁴⁻⁶ and the $\alpha + \beta$ -zirconium alloys exhibit superplastic behavior.⁷ Therefore, the hoop strain is strongly dependent on the phase structure of the Zircaloy at rupture. It is maximum at temperatures near the $\alpha/(\alpha + \beta)$ -phase boundary, minimum in the higher temperature range of the $\alpha + \beta$ -phase region, and again a second maximum from the $\alpha + \beta$ -phase boundary to the lower temperature range of the β -phase region. The temperature dependence of the hoop strain at rupture is also affected by heat-up rate, azimuthal temperature gradient which occurs in the fuel bundle, free volume in the fuel rod, and the heating method in experiments. The hoop strain at rupture generally decreases as the heat-up rate and azimuthal temperature gradient increase.³

During the last decades, the in-service period of the LWR fuel has been increased steadily. The burnup extension of the fuel should be continued for the efficient use of nuclear fuel resources and reduction of radioactive waste. A thicker corrosion layer is formed on the outer surface and a larger amount of hydrogen is absorbed in the fuel cladding at higher burnups, (see also **Chapter 5.03, Corrosion**

of Zirconium Alloys). It is known that the precipitated hydrides reduce ductility of Zircaloy cladding. It is also shown that hydrogen in solid solution reduces the elastic modulus, yield stress, and tensile strength of α - and $\alpha + \beta$ -zirconium and titanium.^{8,9} Consequently, the rupture stress and temperature may reduce because of the preexisting hydrogen in the high-burnup cladding.¹⁰

Recent investigations on the Zr-H-O ternary system showed that both the $\alpha/\alpha + \beta$ -phase boundary and the $\alpha + \beta/\beta$ -boundary shift to lower temperatures as the hydrogen concentration increases.¹¹ Investigations regarding hydrogen effects on the creep behavior have shown that hydrided cladding samples exhibit lower creep resistance.¹² Therefore, the hoop strain at rupture can be changed by the hydrogen absorption, and that of the high-burnup fuel cladding should be evaluated taking account of the hydrogen effects.

Large plastic deformation of the cladding in the radial direction results in blockage of the coolant channels between fuel rods in a fuel bundle. The subsequent reduction of the coolability was a key question in 1970s. Fuel bundles or simulated bundles of 650–3900 mm long ($3 \times 3-8 \times 8$ arrays) were heated in steam environments with test conditions to obtain maximum deformation.¹³⁻¹⁷ **Figure 5** shows an example of the bundle experiments.¹⁴ It was shown that coolability could be maintained even if 90% of the coolant channel, much higher than expected in commercial reactors, was blocked by the deformed cladding.

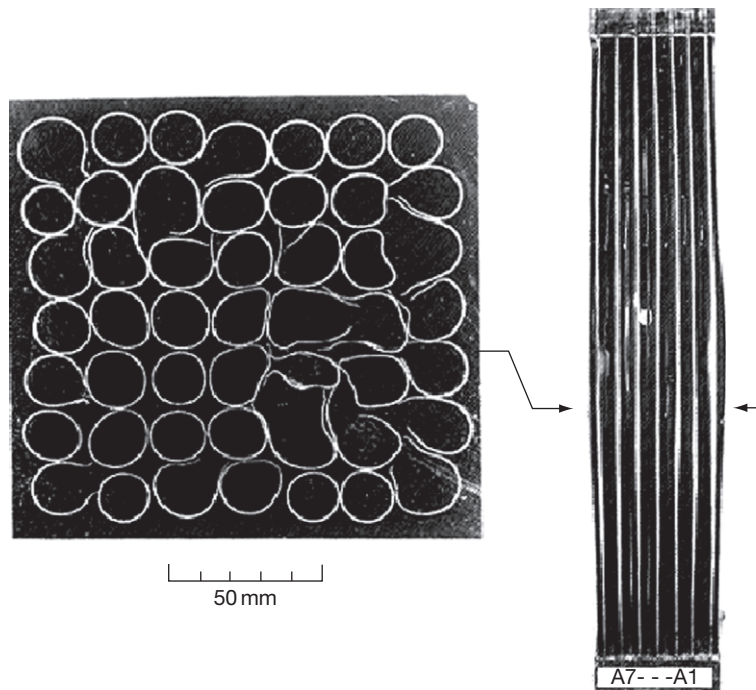


Figure 5 Posttest appearance and radial cross-section of a test bundle. Reproduced from Kawasaki, K.; Hashimoto, M.; Otomo, T.; Furuta, T.; Uetsuka, H. *J. Nucl. Sci. Technol.* **1983**, 20(3), 246–253.

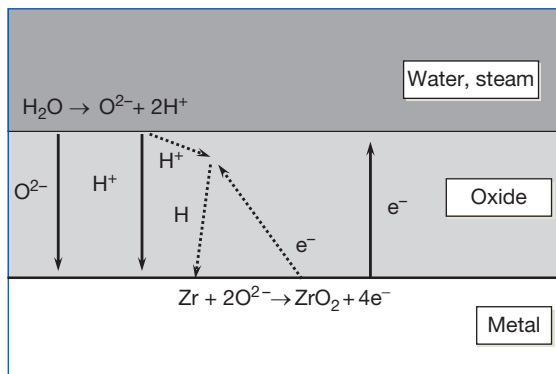
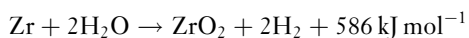


Figure 6 Zirconium–water reaction.

2.23.4 Oxidation of Cladding

Zirconium, the main component of the cladding material, reacts with water. The reaction is described by the following chemical equation:



Elemental reactions as well as migration of the atoms, ions, and electrons in the reaction are schematically shown in [Figure 6](#). Oxygen generated at the surface

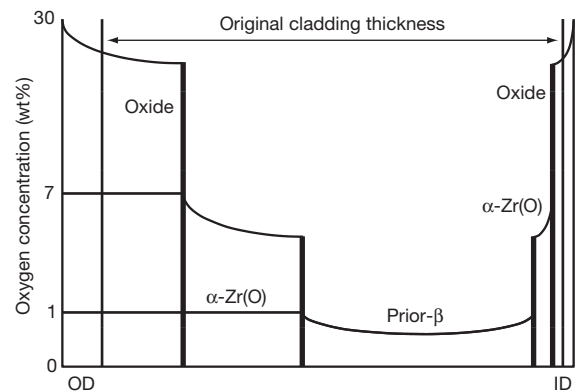


Figure 7 Radial profile of oxygen in oxidized Zircaloy cladding. Reproduced from Leistikow, S.; Schanz, G. Comprehensive presentation of extended Zircaloy-4 steam oxidation results (600–1600 °C), OECD-NEA-CSNI/IAEA specialists meeting on water reactor fuel safety and fission product release in off-normal and accident conditions, Risö, 1983.

by the reaction diffuses into the internal part of the cladding. According to the gradient of oxygen concentration ([Figure 7](#)),¹⁸ an oxide (ZrO_2) layer and a layer of α -phase with a high content of oxygen ($\alpha\text{-Zr(O)}$) grow on the β -phase during oxidation above about 1000 °C as shown in [Figure 8](#). The β -phase

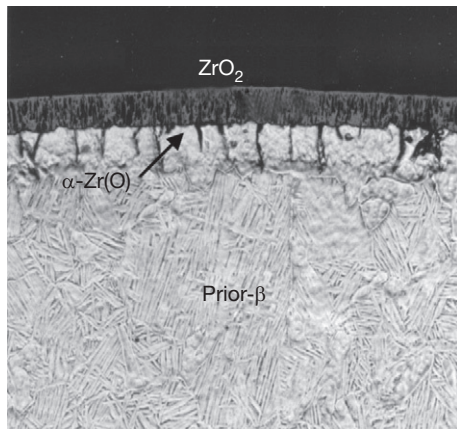


Figure 8 Radial cross-section of Zircaloy cladding oxidized at 1100 °C.

transforms back into the α -phase during cooling and quenching with higher rates. The microstructure after the fast cooling is quite different from the initial as-fabricated microstructure. Thus, the α -phase is called 'prior- β -phase' or 'transformed β -phase' and shows the basket-wave (Widmanstätten) structure.

The oxide layer and the α -Zr(O) layer are brittle. Therefore, ductility of the cladding is controlled by thickness and ductility (oxygen content) of the prior- β -phase layer. Hydrogen is generally swept away under steam-flow conditions that are normally expected in the reactor core. However, a large amount of hydrogen is absorbed in the cladding if the partial pressure of hydrogen is high under stagnant steam conditions and 'breakaway' oxidation conditions.^{19,20} Once the breakaway oxidation occurs, the oxidation rate significantly increases. The mechanism of the breakaway oxidation has not been always clarified. However, the oxide layer has laminar structures and radial cracks, and the oxidation occurs near the $\alpha + \beta$ -phase temperature region for a longer time (at 500–1050 °C for >3600 s). Therefore, it may be connected with phase transitions and the subsequent stress generated in the oxide layer.

The cladding oxidation is very important for safety in terms of the following issues:

- The cladding is embrittled when severely oxidized.
- The oxidation is an exothermic reaction which is a source of the core heating.
- The oxidation generates hydrogen which may be a source of explosion inside the containment vessel.

Hence, oxidation kinetics has been extensively studied to increase the accuracy of the safety analysis. Oxidation of zirconium alloys is controlled by

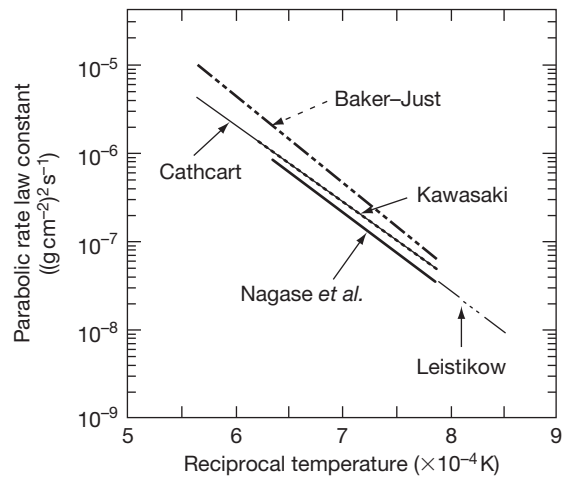


Figure 9 Temperature dependence of the parabolic rate constant in the oxidation of Zircaloy cladding.

diffusion of oxygen in the oxide layer and it obeys a parabolic rate law above about 1000 °C. Namely, the oxidation is described by the following equation.

$$\Delta w^2 = K \times t$$

where Δw is the reaction amount (weight increase or oxide layer growth), K is the reaction rate constant, and t is the oxidation time, (see also **Chapter 5.03, Corrosion of Zirconium Alloys**).

Figure 9 compares the temperature dependences of the reaction rate constant, which were obtained by various researchers,^{21–25} for the oxidation of Zircaloy cladding in the temperature range above 1000 °C. The reaction rate exponentially increases with the temperature, and therefore the temperature dependence is described by an Arrhenius-type equation:

$$K = A \exp(-Q/RT)$$

where A is a preexponential factor, Q is the activation energy in J mol^{-1} , T is the temperature in K, and R is the gas constant ($8.314 \text{ J mol}^{-1} \text{ K}^{-1}$).

The oxidation is very fast above 1200 °C, and the cladding of 0.6 mm thickness completely transforms to the oxide and the α -Zr(O) layers at 1200 °C within about 1800 s or at 1300 °C within 900 s. The figure shows that the reaction rates agree very well except for the Baker-Just equation. It is known that the Baker-Just equation overestimates the reaction, but the equation is often used for the safety analysis to obtain conservative results. The temperature dependence of the oxidation rate constant shows discontinuities at about 1000 and 1500 °C. It is considered

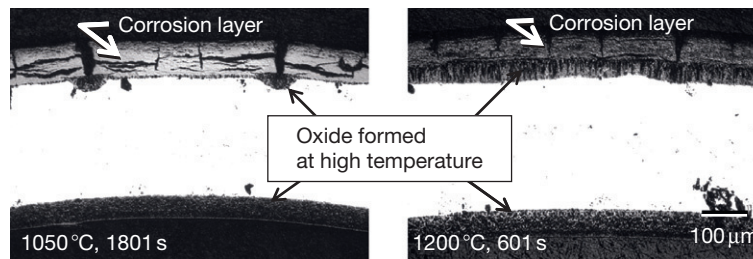


Figure 10 Radial cross-sections of pre-corroded cladding after oxidation at 1050 and 1200 °C.

that the discontinuities are related to the phase structure changes of oxide from monoclinic to tetragonal and from tetragonal to cubic, respectively. The oxidation obeys a cubic rate law for longer term oxidation at temperatures below 1000 °C.^{25,26}

In the oxidation test with corroded cladding, it was observed that no additional oxidation is observed for shorter times, an additional oxide is locally formed at cracked positions of the corrosion layer for longer times, and finally the high-temperature oxide grows uniformly beneath the corrosion layer (Figure 10).²⁷ These results show that the corrosion layer has a protective effect for the high-temperature oxidation, that high-temperature oxidation initiates at cracks in the corrosion layer, and that this barrier effect is maintained until an additional oxide layer by high-temperature oxidation is uniformly formed beneath the corrosion layer. The protective effect becomes smaller for longer times and at higher temperatures. It has been observed that fine cracks are generated in the corrosion layer due to ballooning during the heat-up phase and the oxide is uniformly formed beneath the corrosion layer even in the shorter period. Therefore, the protective effect of the corrosion layer is not expected in actual LOCA conditions where the cladding balloons.²⁸

Influence of hydrogen on the oxidation kinetics has been also studied. The oxidation kinetics can be changed by prehydrogenating and the effect is different depending on oxidation temperature, time, and hydrogen concentration. However, the effect is so small (<5%) in the realistic conditions (<800 ppm and <300 s) that it can be actually neglected in the safety evaluation.^{29,30}

2.23.5 Embrittlement of Cladding

On rewetting of the cladding by ECCS water, the vapor film of the steam collapses at the overheated cladding surface before the transition to nucleate

boiling, which results in sudden change in heat transfer. It is said that the phenomenon takes place in the temperature range of 450–600 °C and a large thermal shock is induced. If the cladding is severely oxidized at temperatures above 1000 °C, the embrittled cladding may be fragmented by the thermal shock. Fragmented cladding and pellet pieces may block the coolant flow channel and harm coolability of the reactor core in case the fragmentation occurs extensively. There is also a risk of fragmentation even after quenching due to hydraulic, seismic, handling, and transport forces.

In order to determine conditions for cladding embrittlement and fracture on quenching, experiments have been performed at research institutes of the United States, Europe, and Japan in 1970s and 1980s.

2.23.5.1 Ductile–Brittle Condition

Figure 11 shows the historically most famous results which indicated ductile–brittle conditions as a function of the oxidation amount.³¹ Zircaloy-4 cladding tubes were oxidized from both the outer and inner surfaces in steam and quenched from the oxidation temperatures (927–1315 °C). Ring-like specimens were cut from the oxidized cladding tubes and were either compressed slowly or squashed by impact loading at 23–1000 °C. After the tests, broken pieces of the ring were assembled back to determine the degree of brittleness. The results are categorized into four: total ductility, higher ductility with one to three fractures, lower ductility with four fractures, and zero ductility. In Figure 11, the ductility of the oxidized cladding specimens is shown relevant to deformation temperature and fraction of the prior-β-phase layer in the total thickness of the oxidized cladding. The ductility decreases as the fraction of the prior-β-phase layer and the decrease in deformation temperature. The dashed line on the left side of the figure indicates the zero-ductility boundary for

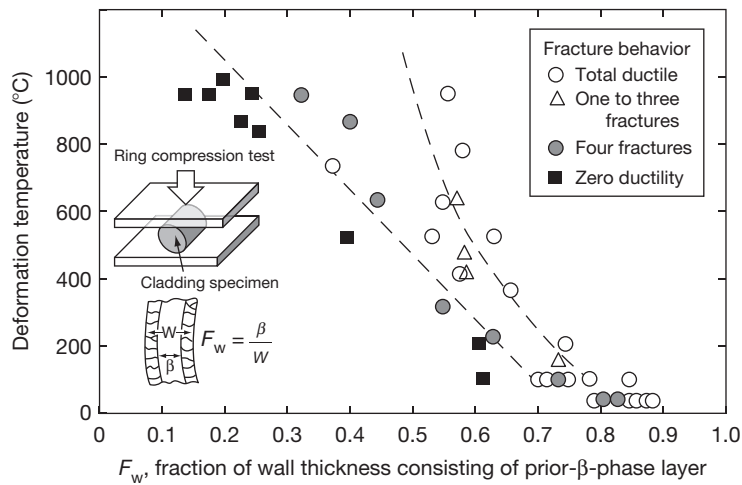


Figure 11 Ductile–brittle conditions of the oxidized cladding examined by ring compression test. Reproduced from Hobson, D. O.; Rittenhouse, P. L. Embrittlement of Zircaloy clad fuel rods by steam during LOCA transients; ORNL-4758; Oak Ridge National Laboratory, Jan 1972.

the oxidation temperatures of $<1204^{\circ}\text{C}$. The United States has established the safety criteria on cladding embrittlement based on the ‘zero-ductility’ condition determined from [Figure 11](#) and other experimental data which were available at that time.^{32,33} It is defined in the LOCA criteria that

The calculated total oxidation of the cladding shall nowhere exceed 0.17 times the total cladding thickness before oxidation. Total oxidation means the total thickness of cladding metal that would be locally converted to oxide if all the oxygen absorbed by and reacted with the cladding locally were converted to stoichiometric zirconium dioxide.

The ‘total oxidation’ is generally expressed as the equivalent cladding reacted (ECR). The Baker–Just equation on oxidation rate²¹ was used to derive the 17% ECR criterion. Thus, the equation must be used to determine the degree of total oxidation and compare with the safety limit.

Although the cladding embrittlement is basically related to the prior- β -fraction, the correlation is not applied to the oxidation above about 1200°C . Hence, the maximum allowable temperature is also defined in the safety criteria.

The calculated maximum fuel element cladding temperature shall not exceed 2200°F (1204°C).

The cladding embrittlement above about 1200°C is considered to be caused by the drastic increase of oxygen solubility in Zircaloy.³³ Details of the safety criteria are different from country to country;

however, the bases of these criteria are essentially the same as those of the United States.

In the recent work at Argonne National Laboratory (ANL) in the United States, unirradiated and irradiated ring specimens were compressed at a low displacement rate after oxidation at high temperatures.³⁴ The compression of the cladding specimens was performed at room temperature or at 135°C . Tests were interrupted following first significant load drop ($>30\%$) and specimens were removed from the testing machine and examined under a microscope to determine whether the sample failed with a single through-wall crack along the whole length of the sample or with multiple cracks. If a single through-wall crack is found, the posttest diameter will be measured in the loading direction and the permanent displacement will be determined. If the permanent strain is $<1\%$, the specimen will be classified as brittle. If multiple cracks are found, the offset displacement and strain from the load–displacement curve will be used. The specimen was classified as brittle when the permanent strain (offset strain) was $<2\%$ in this case. They calculated the overestimation in evaluating the permanent strain from the load–displacement curves and concluded that, to compensate for this overestimation of offset strain, a limiting offset strain of 2% was to be set in the determination of the ductile-to-brittle transition. In other words, there is reasonable confidence that samples with $\geq 2\%$ offset strain are ductile. For samples with offset strains $<2\%$, it is not clear whether they are ductile or brittle.

There seems to be no clear common definition on what is an acceptable residual ductility from the ring-compression test. In general, the residual ductility decreases rapidly in a relatively narrow ECR interval, and the critical ECR may be derived by extrapolating the fall in residual ductility to zero or 2% limit on offset strain or 1% limit on permanent strain.^{31,34,35} Another definition of ductile–brittle transition has been proposed with the use of the strain energy per millimeter of specimen length spent during the compression test up to the formation of the first through crack.³⁶

2.23.5.2 Effect of Cooling History

Both cooling rate during the slow cooling process and quench temperature have effects on postquench ductility of the oxidized cladding. In an experiment by the JAEA (Japan Atomic Energy Agency) with unirradiated Zircaloy-4 cladding, specimens were oxidized in steam at 1100 or 1200 °C, cooled at a rate from 2 to 7 °C s⁻¹, and finally quenched from temperatures ranging from 800 to 1100 °C.³⁷ Postquench ductility was evaluated by ring-compression test, and microscopic properties were examined by metallurgical examination, hardness test, and oxygen analysis. The phase diagram shows that oxygenated Zircaloy is separated into the oxygen-rich α -phase and oxygen-depleted β -phase when cooled from the β -phase to the $\alpha + \beta$ -phase temperature region. As a result of the experiment, morphology and area fraction of oxygen-rich α -phase in the prior- β -phase layer changed depending on the cooling history. With decrease in the quenching temperature, area fraction of α -phase region in the cross-section obviously increased and postquench ductility reduced. Since the ductility of the α -phase region with higher oxygen content is so low, it can be the preferential path for crack propagation, and increase in the area fraction of α -phase region possibly decreases the resistance for fracture. On the other hand, the area fraction was nearly constant irrespective of the rate of the slow cooling, and, consequently, effect of the cooling rate on the postquench ductility was negligible in the examined temperature range.

The postquench ductility effect of cooling scenario was investigated in Brachet *et al.*³⁸ with prehydrided, unirradiated cladding. They used a direct quench and a quench after furnace cooling to 800, 700, and 600 °C from 1200 °C. They also included a specimen furnace cooled to room temperature. The cladding had the highest ductility after cooling to 700

and 600 °C before quench. Direct quench or quench from 800 °C results in a relatively brittle behavior and furnace cooling to room temperature leads to more brittle behavior than quench from 700 and 600 °C. Microstructural studies have shown that the oxygen concentration in the prior- β -phase is quite uniform for the directly quenched specimens and that a separation between α - and prior- β -phases has occurred in the specimen cooled from 800 °C. In the specimens quenched from 700 and 600 °C, the oxygen concentration is again more uniform but a precipitation of iron and chromium-rich particles has occurred in subgrain boundaries. In the specimen furnace cooled to room temperature, relatively large hydride plates have precipitated, which probably explains its embrittlement relative to the specimens furnace cooled to 700 and 600 °C.

2.23.5.3 Enhancement by Hydrogen Absorption

The cladding ruptures during the heat-up. Once the cladding ruptures, steam enters the rod from the opening and oxidizes the inner surface of the cladding. Hydrogen generated by the oxidation is stagnant and the partial pressure of hydrogen increases inside the rod. Consequently, a significant amount of hydrogen is absorbed by the cladding.³⁹ Since the partial pressure is low at the outer surface under the tested condition, hydrogen is not absorbed from the outer surface under steam-flow conditions. **Figure 12** shows the axial changes in the amount of hydrogen absorbed by the ruptured cladding during the high-temperature oxidation in steam.¹⁰ Hydrogen profiles generally show peaks (<3000 ppm for <30% ECR) at positions about 30–50 mm away from the rupture position. As suggest by the figure, the cladding ductility axially changes and it is embrittled at positions where the oxidation and hydriding is significant.⁴⁰

Hydrogen absorbed during in-service corrosion also decreases the ductility of the oxidized cladding. In transmission electron microscopy (TEM) examinations of oxidized and hydrided cladding,³⁹ a large number of fine δ -hydrides smaller than 1 nm were observed on the boundaries of α -grains in the prior- β -phase region. Such distribution and concentration of brittle hydrides in wide areas of the cross-sections should enhance embrittlement of oxidized cladding. It has been also reported that $\alpha/\alpha + \beta$ - and $\alpha + \beta/\beta$ -phase boundaries in the Zr–O binary system shift to lower temperature and higher oxygen concentration with an increase in hydrogen concentration.¹¹ The shifts of

the phase boundaries can increase the oxygen concentration in the α -grain of the prior- β -phase region of the oxidized cladding.

2.23.5.4 Fracture of Embrittled Cladding

It is considered that thermal shock on reflooding has possibly the greatest impact on the fuel in an LOCA.

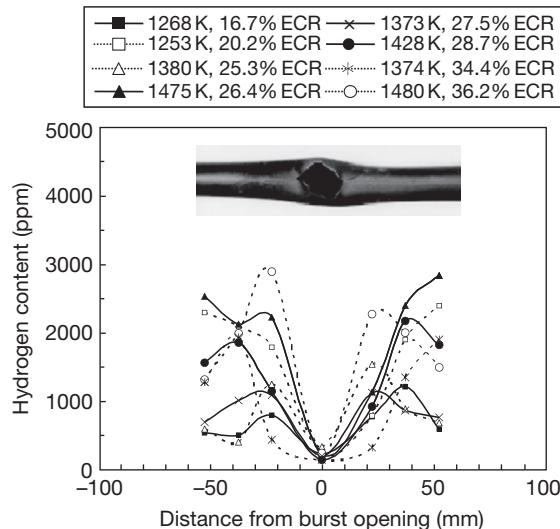


Figure 12 Axial hydrogen profiles in ruptured and oxidized cladding. Reproduced from Nagase, F.; Fuketa, T. *J. Nucl. Sci. Technol.* **2005**, 42(2), 209–218.

In addition, the cladding is embrittled not only by oxidation but also by hydriding from the inner surface. Therefore, ‘quench test’ of ruptured and oxidized cladding has been performed with short test rods, simulating the whole LOCA sequences such as ballooning, rupture, double-sided oxidation including secondary hydriding, thermal shock by reflooding, and possible axial loading. The tests are performed in Japan, Korea, and the United States,^{10,40–42} and the obtained data are used to judge the fuel integrity during an LOCA in Japan. **Figure 13** shows a schematic of the test rod and apparatus that are used at the JAEA.¹⁰ The test is generally conducted with isothermal oxidation period at predetermined temperatures at various times as shown in **Figure 14**. The test rod is heated at a rate of 3–10 °C. Sufficient amount of steam is introduced prior the heat-up to oxidize the cladding. During the heating up to the temperature for isothermal oxidation, the specimen normally ruptures. The test rod is isothermally oxidized at temperatures from 800 to 1300 °C for various times. The cladding is allowed to cool down in the steam flow to about 700–800 °C when quenching starts by flooding the specimen with water. The test rod is quenched under nonrestrained or restrained condition to simulate the axial loading that may be generated by friction or lockup between the fuel rods and the grid spacers in bundle geometry. Since the cladding, which axially expands during the heat-up and isothermal oxidation phases,

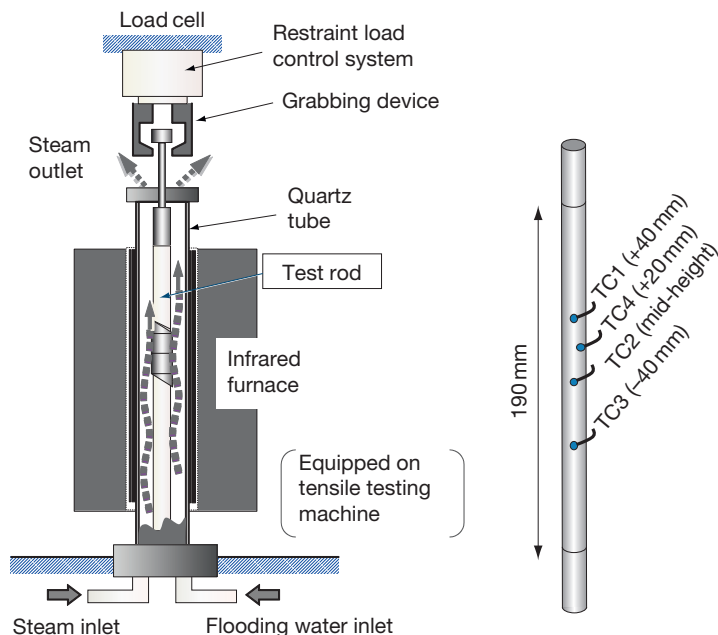


Figure 13 Schematic illustration of test rod and apparatus for quench test.

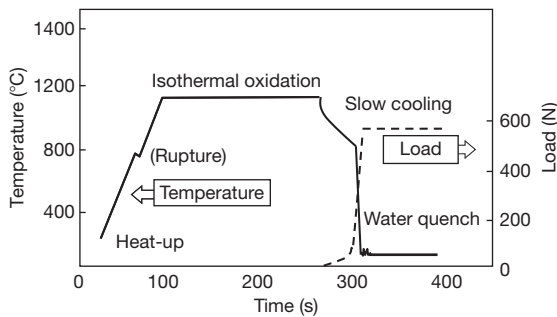


Figure 14 Typical temperature history in quench test.

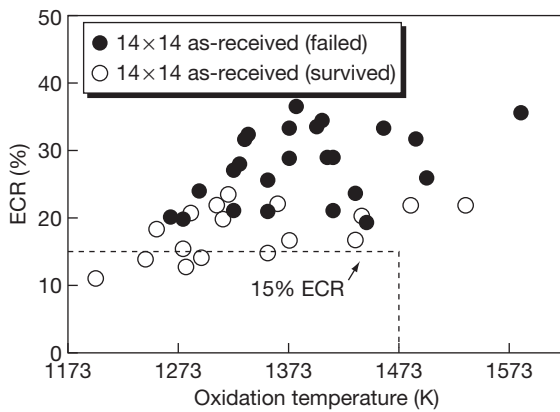


Figure 15 Fracture map relevant to oxidation amount and temperature which obtained by quench tests under fully restrained conditions with 14×14 PWR cladding. Reproduced from Uetsuka, H.; Furuta, T.; Kawasaki, S. *J. Nucl. Sci. Technol.* **1983**, 20(11), 941–950.

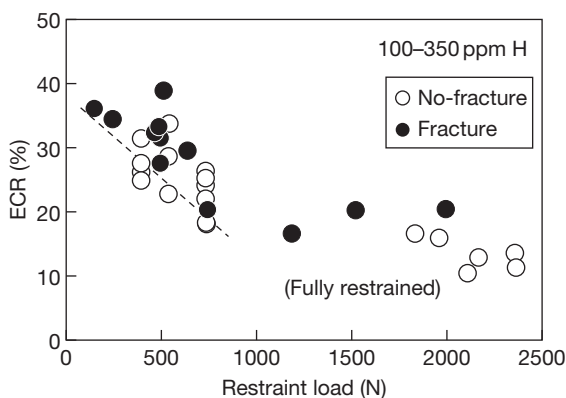


Figure 16 Influence of restraint load on fracture condition. Reproduced from Nagase, F.; Fuketa, T. *J. Nucl. Sci. Technol.* **2005**, 42(2), 209–218.

shrinks during the cooling and quenching phases, axial tensile load is generated in the cladding if it is restrained.

Figure 15 shows a fracture map obtained by the thermal shock tests with unirradiated pressurized water reactor (PWR) (Zircaloy-4) cladding.⁴⁰ Depending primarily on the oxidized fraction of the cladding thickness, a part of claddings sustained circumferential cracking and fractured into two pieces during the quench. The figure shows that fracture occurred at higher oxidations. The fracture boundary lies at about 20% of ECR, which is sufficiently higher than the safety limit, even under very severe fully restrained conditions. **Figure 16** shows the influence of the restraint load on fracture conditions. The reduction of the threshold with increase in restraint load is evident in figure.¹⁰

2.23.6 Effect of High Burnup on Fuel Behavior

Corrosion, hydrogen absorption, and neutron irradiation become more pronounced in the fuel cladding with increase in fuel burnup. In an LOCA, the cladding experiences temperatures much higher than the operation temperature. Therefore, irradiation damage possibly recovers during the early stage of the temperature transient, and influence of the high neutron dose is not expected on the fuel behavior. The influence of pronounced corrosion and hydrogen absorption is likely the main concern of cladding embrittlement under LOCA conditions. Since corrosion and hydriding are the key factors that limit the life of the fuel also for the normal use, industries have been making great efforts to develop new cladding alloys with higher corrosion resistance to achieve higher burnup. As a result, the new alloys such as ZIRLO, M5, MDA, NDA, HiFi alloy, E110, and E635 (**Table 1**) have been developed, and most of them are being actually used in the high-burnup fuel. Changes of alloy components may alter the cladding behavior under LOCA conditions. Therefore, behavior of the new cladding alloys under LOCA conditions has been carefully examined to conform to the safety requirements.

As described in **Section 2.23.3**, it was clarified that corrosion and hydriding have effects on the oxidation kinetics of cladding though the effects are small or negligible under realistic conditions. The oxidation kinetics of the alloys is generally very similar to that of the conventional Zircaloy. The oxidation of the Nb-containing alloys may be slightly slower at temperatures below 1000 °C.²⁷

Ring-compression tests of oxidized specimens were conducted with unirradiated and irradiated

Table 1 Nominal composition of commercial cladding alloys

	<i>Zircaloy-2</i>	<i>Zircaloy-4</i>	<i>ZIRLO</i>	<i>M5</i>	<i>E110</i>	<i>E635</i>	<i>MDA</i>	<i>NDA</i>	<i>HiFi</i>
Sn	1.45	1.3–1.45	0.75–1.1			1.2	0.8	1.0	1.45
Nb				1.0	1.0	1.0	0.5	0.1	
Fe	0.14	0.21	0.1	0.038	0.009	0.35	0.2	0.27	0.4
Cr	0.10	0.10					0.1	0.16	0.10
Ni	0.06							0.01	0.06
Zr	Balance	Balance	Balance	Balance	Balance	Balance	Balance	Balance	Balance

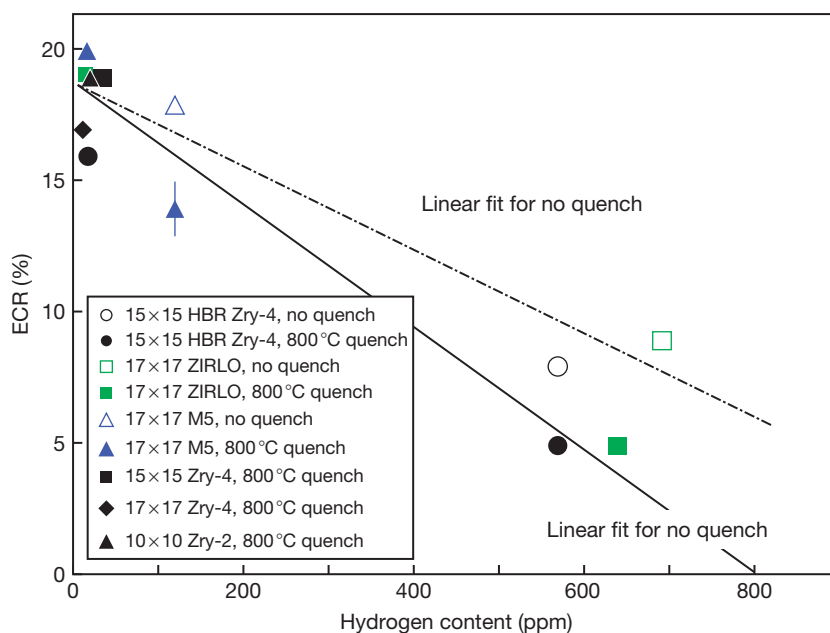


Figure 17 Results of ring compression tests of oxidized high burnup fuel cladding (63–70 GWdt⁻¹, 700 ppm of hydrogen); equivalent cladding reacted was calculated with the oxidation rate equation determined by Cathcart-Pawel. Reproduced from Billone, M.; Yan, Y.; Burtseva, T.; Daum, R. Cladding embrittlement during postulated loss-of-coolant accidents; NUREG/CR-6967 (ANL-07/04); July 2008.

cladding that had been sectioned from high-burnup fuel rods (63–70 GWdt⁻¹) at the ANL.³⁴ The results of the tests are summarized in Figure 17. It was indicated that hydrogen produces the main burnup effect on embrittlement, and embrittlement threshold (the permanent strain <2%, see Section 2.23.5.1) obviously decreases with the hydrogen content. In addition, embrittlement of the cladding is dependent on cooling conditions. As a consequence, for high-burnup Zircaloy-4 and ZIRLO with higher hydrogen content (<700 ppm), post-LOCA embrittlement thresholds are bounded by 8–9% (no quench) and 5% (quench at 800°C), respectively, which is much lower than the current US safety limit. For high-burnup M5 with lower hydrogen content (<150 ppm), the embrittlement threshold is bounded by 18% (no quench) and 14% (quench at 800°C).

At ANL, specimens of the new alloys have been tested in the same equipment, which makes the results intercomparable with regard to the performance of the different alloys.³⁴ The results are summarized in Table 2. One of the first discoveries in that research was that the embrittlement threshold for unirradiated conventional Zircaloy (Zr–1.4%Sn) is not fixed at exactly 17% as defined in the US regulations. Three different manufacturing quantities of Zircaloy-4 exhibit thresholds from 15.6% to 19%. The base alloy compositions of M5 and E110 are nominally the same (Zr–1%Nb); however, they exhibit very different embrittlement thresholds. Zircaloy-2 and ZIRLO showed embrittlement thresholds (19%) that are very similar to the other modern cladding materials manufactured with similar techniques. Consequently, the variations in embrittlement threshold

Table 2 Variation of embrittlement threshold (percent equivalent cladding reacted) for unirradiated zirconium-alloy cladding materials oxidized in steam at 1200 °C

Alloy and geometry	Vintage	Embrittlement threshold ^a
Zircaloy-4, 15 × 15	Conventional	15.6
Zircaloy-4, 17 × 17	Current, low tin	17
Zircaloy-4, 15 × 15	Current, low tin	19
Zircaloy-2, 10 × 10	Current, Zr liner	19
ZIRLO, 17 × 17	Current, standard tin	19
M5, 17 × 17	Current	20

^aECR based on oxidation rate equation derived by Cathcart-Pawel.

Source: Billone, M.; Yan, Y.; Burtseva, T.; Daum, R., Cladding embrittlement during postulated loss-of-coolant accidents; NURG/CR-6967 (ANL-07/04); July 2008.

are caused mainly by differences in the manufacturing process rather than specific alloy composition.

A comparative study with E110 and Zircaloy-4⁴³ showed that the oxidation kinetics is generally very similar for the two alloys and the results for Zircaloy-4 agreed well with other published results. However, the oxide scales on the E110 alloy had a very heterogeneous appearance with a multilayer character and tended to flake. Ring-compression tests of oxidized specimens showed that the E110 alloy had lost its ductility at about 6% ECR while the ductility of Zircaloy-4 was gradually reduced to zero at about 18% ECR. A high hydrogen pickup fraction, 15–70% was seen in E110 for the temperature range 900–1050 °C where the pickup fraction in Zircaloy-4 was ~2–5%. It is considered that the significant hydrogen absorption during the oxidation was associated with the formation of the multilayer oxide scale and that the higher hydrogen pick up decreased the embrittlement threshold of E110.

To obtain base information on the fracture of a high-burnup fuel in an LOCA, thermal shock tests were performed by varying sample and test conditions with prehydrided unirradiated cladding samples.¹⁰ These tests were performed to complement the tests with irradiated cladding, which are limited in number. Short test rods, fabricated with claddings having a wide range of hydrogen concentrations (about 100–1450 ppm), were heated, isothermally oxidized at about 1000–1250 °C in steam flow, and quenched in flooding water. Axial shrinkage of the rods during the quench was restrained, controlling the maximum restraint load. Test rods ruptured during the heat-up phase, and slight hydrogen concentration effects were

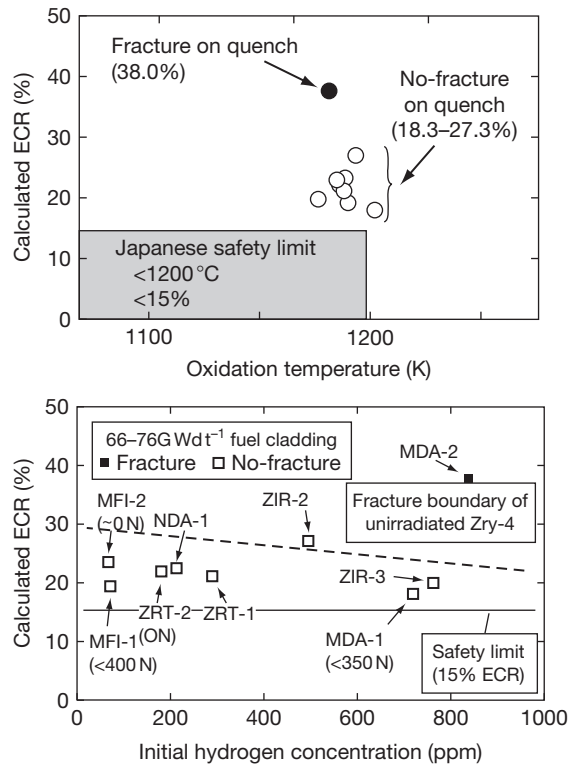


Figure 18 Fracture map from quench tests of high burnup fuel cladding ($66\text{--}77\text{ GWd t}^{-1}$, $<840\text{ ppm}$ of hydrogen); equivalent cladding reacted was calculated by the Bake-Just equation. Reproduced from Nagase, F.; Chuto, T.; Fuketa, T. *J. Nucl. Sci. Technol.* **2009**, 46(7), 763–769.

seen on rupture temperature and strain as expected and described in Section 2.23.3. The fracture/no-fracture threshold of the oxidized fraction decreases with the initial hydrogen concentration. Consequently, the fracture threshold is higher than 20% ECR even under the restraint condition, irrespective of the hydrogen concentration. This is sufficiently higher than the limit in the LOCA criteria.

Recently, the thermal shock tests simulating LOCA conditions were successfully performed with high-burnup fuel cladding ($66\text{--}77\text{ GWd t}^{-1}$, $<840\text{ ppm}$ of hydrogen) at the JAEA.²⁸ The cladding alloys were MDA, ZIRLO, M5, NDA, and Zircaloy-2. The cladding samples were oxidized at temperatures from about 1190 to 1210 °C and the oxidation amounts from about 18% to 38% ECR. The effects of high burnup are inconsiderable in terms of oxidation, ballooning, and rupture behavior. Two fracture maps are shown in Figure 18: one is relevant to the extent of oxidation and the oxidation temperature, and the

other is relevant to the extent of oxidation and hydrogen concentration. The fracture/no-fracture boundary is not reduced significantly by the high burnup and the use of new alloys in the examined burnup range, although it may be somewhat reduced with prehydrogenating during the reactor operation, as observed in the unirradiated Zircaloy-4 cladding. In other words, the fracture boundary of the high-burnup cladding is sufficiently higher than the limit in the LOCA criteria, possibly in the burnup range up to about 80 MWd kg⁻¹ and/or up to about 840 ppm of hydrogen.

Change in fuel pellet temperature is relatively small in an LOCA, and it has been considered that the fuel pellets do not have an important role in the degradation of integrity of the fuel rod or safety of the reactor. However, it was recently pointed out that it is not always true for high-burnup fuel.⁴⁴ High burnup and repeated thermal cycles cause cracking of the fuel pellets, and the cracked pellets may fragment on rod rupture. The major concern here is that the fuel fragments may axially relocate toward the ballooned region from the upper positions and be released from the rupture opening. Integral in-pile LOCA tests were conducted in the Halden reactor to measure the extent of fuel relocation into the ballooned region and evaluate its possible effect on cladding temperature and oxidation.⁴⁴ Although relocation has been observed in some of the conducted tests, further testing is necessary in order to draw a general picture of this phenomenon.

2.23.7 Outlook

Extensive investigations have been made and extensive data obtained on the fuel behavior under LOCA conditions since the 1970s. However, as-fabricated materials were used in the most performed tests. There are many changes that occur to the fuel pellet and cladding as a result of prolonged exposure to the irradiated field in a reactor core and to the corroding environment as well as high temperature. Although the fuel pellet and cladding have been developed to improve the performance, its main purpose is the improvement for the normal operation condition. Therefore, more investigations are required to better understand the behavior of the high-burnup fuel under accidental conditions.

In the field of the safety evaluation, discussions are made on test methodologies to evaluate cladding integrity and embrittlement under LOCA conditions.

The traditional methods may be too conservative since they were developed and adopted at a time when loading conditions applied to the fuel during accidents were not sufficiently analyzed. It is expected that efforts will be made to select or develop test methodologies taking account of loading conditions in the actual situations and appropriate safety margin.

References

1. Chung, H. M.; Kassner, T. F. *J. Nucl. Mater.* **1979**, *84*, 327–339.
2. Zuzek, E.; Abriata, J. P.; San-Martin, A.; Manchester, F. D. *Bull. Alloy Phase Diagrams* **1990**, *11*(4), 385–395.
3. Erbacher, F. J. *Nucl. Eng. Des.* **1987**, *103*, 55.
4. Hardy, D. G. High temperature expansion and rupture behaviour of Zircaloy tubing. In *Topical Meeting on Water Reactor Safety*, Salt Lake City, UT, 1973; pp 254–273.
5. Hunt, C. E. L.; Foote, D. E. High temperature strain behaviour of Zircaloy-4 and Zr-2.5Nb fuel sheaths. In *Zirconium in the Nuclear Industry: Third International Symposium*, ASTM STP 633, 1976; pp 50–65.
6. Chung, H.; Garde, A.; Kassner, T. Deformation and rupture behavior of Zircaloy cladding under simulated loss-of-coolant conditions. In *Zirconium in the Nuclear Industry: Third International Symposium*, ASTM STP 633, 1976; pp 82–97.
7. Kearns, J. J.; McCauley, J. E.; Nichols, F. A. *J. Nucl. Mater.* **1976**, *61*, 169–184.
8. Yamanaka, S.; Kuroda, M.; Setoyama, D. *Trans. Atom. Energ. Soc. Jpn.* **2002**, *1*(4), 323, text in Japanese.
9. Senkov, O. N.; Jonas, J. J. *Metall. Mater. Trans. A* **1996**, *27A*, 1869.
10. Nagase, F.; Fuketa, T. *J. Nucl. Sci. Technol.* **2005**, *42*(2), 209–218.
11. Setoyama, D.; Yamanaka, S. *Trans. Atom. Energ. Soc. Jpn.* **2003**, *2*(4), 452, text in Japanese.
12. Bouffieux, P.; Rupa, R. Impact of hydrogen on plasticity and creep of unirradiated Zircaloy-4 cladding tubes. In *Zirconium in the Nuclear Industry: Twelfth International Symposium*, ASTM STP 1354, 2000; pp 399–422.
13. Chapman, R. H.; Crowley, J. L.; Longest, A. W.; Hofmann, G. Zirconium cladding deformation in a steam environment with transient heating. In *Zirconium in the Nuclear Industry: Fourth Conference*, ASTM STP 681, 1979; pp 393–408.
14. Kawasaki, K.; Hashimoto, M.; Otomo, T.; Furuta, T.; Uetsuka, H. *J. Nucl. Sci. Technol.* **1983**, *20*(3), 246–253.
15. Wiehr, K.; Erbacher, F. J.; Harten, U.; Just, W.; Schaeffner, P. Untersuchungen zur Wechselwirkung zwischen aufblähenden Zircaloy-Hüllen und einsetzender Kernnotkühlung (REBEKA-programm), Kernforschungszentrum Karlsruhe, Report KfK-3450; 1984.
16. Loftus, M. J.; Hochreiter, L. E.; Lee, N.; McGuire, M. F.; Wenzel, A. H.; Valkovic, M. M. PWR FLECHT SEASET 21-rod bundle flow blockage task data and analysis report NRC/EPRI/Westinghouse; Report No. 11, NUREG/CR-2444 (EPRI/NP-2014); 1982.
17. Ihlea, P.; Rust, K. *Nucl. Eng. Des.* **1987**, *99*, 223–237.
18. Chung, H. *Nucl. Eng. Technol.* **2005**, *37*(4), 327–362.
19. Leistikow, S.; Schanz, G. Comprehensive presentation of extended Zircaloy-4 steam oxidation results

- (600–1600 °C), OECD-NEA-CSNI/IAEA specialists meeting on water reactor fuel safety and fission product release in off-normal and accident conditions, Risö, 1983.
20. Schantz, G.; Leistikow, S. In *ANS/ENS Topical Meeting on Reactor Safety Aspects of Fuel Behavior*; American Nuclear Society: Sun Valley, CA, 1981.
 21. Baker, L.; Just, L. C. Studies of metal-water reaction at high temperatures. III: Experimental and theoretical studies of the zirconium-water reaction, ANL-6548, Argonne National Laboratory, 1962.
 22. Pawel, R. E.; Cathcart, J. V.; McKee, R. A. *J. Electrochem. Soc.* **1979**, 126(7), 1105–1111.
 23. Kawasaki, S.; Furuta, T.; Suzuki, M. *J. Nucl. Sci. Technol.* **1978**, 15(8), 589–596.
 24. Leistikow, S.; Schanz, G. *Werkst. Korros.* **1985**, 36, 105–116.
 25. Nagase, F.; Otomo, T.; Uetsuka, H. *J. Nucl. Sci. Technol.* **2003**, 40(4), 213–219.
 26. Westerman, R. E. *J. Electrochem. Soc.* **1964**, 111, 140.
 27. Chuto, T.; Nagase, F.; Fuketa, T. *Nucl. Eng. Technol.* **2009**, 41(2), 163–170.
 28. Nagase, F.; Chuto, T.; Fuketa, T. *J. Nucl. Sci. Technol.* **2009**, 46(7), 763–769.
 29. Portier, L.; Bredel, T.; Brachet, J. C.; Maillot, V.; Mardon, J.; Lesbros, A. Influence of long service exposures on the thermal-mechanical behavior of Zy-4 and M5 alloys in LOCA conditions. In *Zirconium in the Nuclear Industry: Fourteenth International Symposium*, ASTM STP 1467; ASTM: Stockholm, 2004; pp 896–920.
 30. Nagase, F.; Otomo, T.; Tanimoto, M.; Uetsuka, H. In *2000 International Topical Meeting on Light Water Reactor Fuel Performance*; American Nuclear Society: Park City, UT, 2000.
 31. Hobson, D. O.; Rittenhouse, P. L. Embrittlement of Zircaloy clad fuel rods by steam during LOCA transients; ORNL-4758; Oak Ridge National Laboratory, Jan 1972.
 32. Hesson, J. C.; Ivins, R. O.; Wilson, R. E.; Nishio, K.; Barnes, C. Jr. Laboratory simulations of cladding-steam reactions following loss-of-coolant accidents in water-cooled power reactors; ANL-7609; Argonne National Laboratory, Jan 1970.
 33. Pawel, R. E. *J. Nucl. Mater.* **1974**, 50, 247–258.
 34. Billone, M.; Yan, Y.; Burtseva, T.; Daum, R. Cladding embrittlement during postulated loss-of-coolant accidents; NUREG/CR-6967 (ANL-07/04); July 2008.
 35. Yegorova, L.; Liooutov, K.; Jouravkova, N.; *et al.* NUREG/IA-0211002C IRSn-194, NSI RRC KI 3188, US NRC, Mar 2005.
 36. Hozer, Z.; Györi, C.; Matus, L.; Horvath, M. *J. Nucl. Mater.* **2008**, 373, 415–423.
 37. Udagawa, Y.; Nagase, F.; Fuketa, T. *J. Nucl. Sci. Technol.* **2006**, 43(8), 844–850.
 38. Brachet, J.; Vandenberghe-Maillot, V.; Portier, L.; *et al.* *J. ASTM Int.*; **2008**, 5(5), Paper JAI101116.
 39. Uetsuka, H.; Furuta, T.; Kawasaki, S. *J. Nucl. Sci. Technol.* **1981**, 18(9), 705–717.
 40. Uetsuka, H.; Furuta, T.; Kawasaki, S. *J. Nucl. Sci. Technol.* **1983**, 20(11), 941–950.
 41. Chung, H. M.; Kassner, T. F. Embrittlement criteria for Zircaloy fuel cladding applicable to accident situations in light-water reactors, Summary Report; NUREG/CR-1344 (ANL-79-48); Jan 1980.
 42. Kim, J. H. Korea deformation and thermal quench behavior of HANA claddings in LOCA condition, Sep 2008; WRFPM, paper 1030.
 43. Böhmert, J.; Dietrich, M.; Linek, J. *Nucl. Eng. Des.* **1993**, 147, 53–62.
 44. OECD/NEA State-of-the-Art Report, Nuclear fuel behavior in loss-of-coolant accident (LOCA) conditions, 2009; p 120.

2.24 Behavior of Fast Reactor Fuel During Transient and Accident Conditions

J. Papin

Institut de Radioprotection et de Sûreté Nucléaire, St Paul Lez Durance, France

© 2012 Elsevier Ltd. All rights reserved.

2.24.1	Introduction	610
2.24.2	The Study of Oxide Fuel Behavior Under Transient and Accident Conditions of Sodium Fast Reactors	610
2.24.2.1	General Objectives	610
2.24.2.2	Overview of the Main Accident Scenarios Considered	611
2.24.2.2.1	Control-rod withdrawal accident	611
2.24.2.2.2	Local blockage of a subassembly	611
2.24.2.2.3	The unprotected loss of flow accident	611
2.24.2.3	The Research Approach Relative to Fuel Accident Behavior	612
2.24.3	The Fuel Behavior Under Slow Power Transients	613
2.24.3.1	The CABRI Data Base for Slow Power Transients Study	615
2.24.3.2	Fuel Melting	615
2.24.3.2.1	Influence of fuel smear density on melting occurrence (power-to-melt)	616
2.24.3.2.2	Cavity formation and in-pin fuel motion	618
2.24.3.3	Pin Thermomechanical Behavior	618
2.24.3.3.1	Low smear density fuel	618
2.24.3.3.2	High smear density fuel	619
2.24.3.4	Postfailure Fuel Behavior	620
2.24.3.4.1	Molten fuel ejection conditions with low mass melt fraction	620
2.24.3.4.2	Consequences of molten fuel ejection at low mass melt fraction	621
2.24.3.5	Fission Gas Behavior Summary	622
2.24.4	The Fuel Behavior Under Unprotected Loss of Flow Accident	623
2.24.4.1	The Experimental Simulation for the Study of the ULOF Primary Phase	623
2.24.4.2	Fuel Pin Behavior up to Failure	624
2.24.4.2.1	Fuel temperature increase and thermal expansion	624
2.24.4.2.2	Fuel pin mechanical behavior and pin failure conditions	624
2.24.4.3	Postfailure Phenomena	626
2.24.4.4	In-Pin Fuel Motion	628
2.24.5	Fuel Behavior as Consequence of a Complete Loss of Coolant in a Subassembly	629
2.24.5.1	The Degradation of the Faulted Subassembly	629
2.24.5.2	The Mechanisms of the Hexcan Melt-Through	630
2.24.5.3	The Propagation of the Molten Materials	631
2.24.6	Conclusion	632
References		633

Abbreviations

BFC	Bottom of fissile column
CDA	Core-disruptive accident
CRWA	Control rod withdrawal accident
DBA	Design basis accident
DND	Delayed neutron detection

EFR	European fast reactor
FCI	Fuel-coolant interaction
FCMI	Fuel clad mechanical interaction
LOF	Loss of flow
Pn	Nominal power
PWR	Pressurized water reactor
SA	Subassembly

SFR	Sodium fast reactor
TD	Theoretical density
TIB	Total instantaneous inlet blockage
TOP	Transient over power
ULOF	Unprotected loss of flow
UTOP	Unprotected transient over power

2.24.1 Introduction

Since the start of the fast reactor studies, fuel behavior under transient and accident conditions has been a major safety concern with special attention given to the possible fuel melting occurrence and subsequent events. In effect, fast reactor cores under nominal operating conditions are not in the most reactive configuration and are thus highly sensitive to any fuel compaction effect that might result from fuel motion (for instance, due to melting) with the potential risk of prompt-critical events and mechanical energy release to the vessel structure. For sodium-cooled fast reactors, such potential risk is also linked to the positive reactivity feedback (in some core regions), of the sodium void effect that can generate fast power transients in the event of loss of core cooling and coolant boiling (with associated fuel pin damage and disruption).

Among the different types of fuel possibly implemented in the fast reactors (oxide, metal, nitride, carbide), the mixed oxide fuel (U,Pu)O₂ is the most largely used one. The past experience gained from operation since the 1970s of several experimental, prototype, and commercial size reactors with sodium as coolant (for instance, RAPSODIE, PHENIX, SUPERPHENIX in France, KNK-II in Germany, JOYO, MONJU in Japan, BN-350–600 in Russia, DFR, PFR in United Kingdom, EBR II and FFTF in the United States) has provided a comprehensive knowledge on this type of fuel. Moreover, the mixed oxide fuel is also anticipated at least for the first operating phases of the future industrial prototypes within Generation IV development, with, however, a higher burn-up target objective. Therefore, this chapter addresses the accident behavior of mixed oxide fuel in sodium-cooled fast reactors.

The chapter first recalls some general points related to the study of fast reactors fuel accident behavior: objectives, main accident scenarios considered as reference for safety assessment of sodium-cooled fast reactors and related R&D approach. Then, the main phenomena occurring in the irradiated oxide fuel pins under different accident conditions are described, focusing on the fuel pin behavior up to failure and

onset of pin degradation: fuel melting, mechanical loading of the cladding and failure mechanisms, fission gas behavior and molten fuel ejection into the coolant channel. The phenomena related to the late phase of the accidents with extended degradation of the fuel pins, of the subassembly or of the whole core are not detailed but only mentioned for completeness.

2.24.2 The Study of Oxide Fuel Behavior Under Transient and Accident Conditions of Sodium Fast Reactors

2.24.2.1 General Objectives

As for all types of reactors, the evaluation of fuel behavior under transient and accident conditions is an important part of the safety studies and assessment of the sodium fast reactors.

Many transients and potential initiators of accident sequences are considered and classified within design basis accidents or in the severe accident domain, according to their frequency of occurrence and to the severity of their consequences with regard to potential radiological releases to the environment (physical protection objective).

In the case of accidents within design basis for which radiological releases below stringent limit values have to be guaranteed, a precise quantification of the fuel transient behavior is needed in order to be able to check the compliance of the key parameters with the design limits and safety criteria, and also to evaluate the margins relatively to these design limits. For instance, with regard to fuel element, slow power transients during operation with protection insured by the emergency shut-down systems, should not lead to pin failure: to follow this requirement, criteria on maximal clad temperature and on the absence of fuel melting inside the pin are settled in order to guarantee pin integrity in such operational transients (the fuel element design is defined with the objective to withstand such transients all along its life) and computational tools are used to demonstrate the fulfillment of the requirement.

In case of severe accidents (design extension conditions), the study and evaluation of the fuel behavior and associated consequences are also needed in view of:

- The establishment of appropriate measures for prevention, management of the accident, and minimization of its consequences (for instance, implementation of improved detection, mitigation, and passive systems).

- The examination of the efficiency of the implemented measures.

These considerations are the basis for the safety research and development studies that were initiated since the start of fast reactor development with oxide fuel (from around 1960).

2.24.2.2 Overview of the Main Accident Scenarios Considered

For sodium fast reactors, with regard to the risk of local or generalized core melting, three main types of transient and accident scenarios are considered as references for the study of fuel transient and accident behavior:

- the slow power transient representative of one control-rod withdrawal (local fault),
- the loss of cooling due to blockage of a subassembly (local fault), and
- the unprotected loss of flow (ULOF) accident that might lead to a core disruptive accident (CDA, generalized accident).

Through the study of these scenarios (local, global accidents) that consider extreme conditions and consequences, the phenomenology of other accident sequences, due to less severe transients or to other initiators leading to similar phenomena, is also addressed.

2.24.2.2.1 Control-rod withdrawal accident

Slow power transients due to control-rod withdrawal are the most common transients occurring during reactor operation as they are used for regulation of the core power by the operators. In case of an inadvertent control-rod withdrawal due to inadvertent operator action together with a postulated dysfunction of the various protection systems, this transient might lead to severe consequences. For instance, in the French Superphenix reactor, the unprotected control-rod withdrawal accident (CRWA) has been identified as one of the most likely initiating events for a core melt accident (probability was evaluated to 3.9×10^{-6} per year). It is characterized by a slow power increase (about 1–3% Pn/s, Pn: nominal power) and may lead to partial fuel melting inside the pins of the subassemblies surrounding the control rod. In case of an adventitious clad failure of one of those fuel pins (for instance, due to an initial defect), molten fuel ejection, even at low melt fraction of 10–20%, and pin-to-pin failure propagation leading to whole subassembly degradation might take place

and result in core melting extension and critical events. The consequences of such an accident depend on the reactor core size, mode of control-rod operation, and respective detection capabilities: in the case of a large core, local core effects of overpower may be more pronounced than in a small core in which global overpower can be early detected by usual control systems leading to power shut down.

2.24.2.2.2 Local blockage of a subassembly

Local blockage formation in a fuel assembly due to ingress of some external material into the bundle may lead to pin failure with subassembly degradation and melting, depending on the nature and geometry of the blocked zone. As a bounding case of the different types of subassembly blockages (local, total but progressive), the hypothetical total instantaneous inlet blockage (TIB) of a subassembly at nominal power has been postulated as potential initiator for a core melt accident in the frame of EFR (European fast reactor) studies. Owing to the complete and fast loss of flow in the faulted subassembly, the usual detection systems are not operating in due time (outlet temperature increase in a subassembly, delayed neutron detection (DND)) so that core power cannot be shut down early. The accident is characterized by overheating and melting of the fuel pins, degradation of the Subassembly (SA), wall failure, and possible propagation of molten materials into neighboring subassemblies and further extension of the melting process. The main safety issue is the risk of propagation of the accident beyond the neighboring subassemblies that might lead to critical events and generalized core melting.

It should be noted that for the Fermi-1 reactor, subassembly blockage caused by a piece coming loose from the Zr core catcher in the reactor vessel led to a core melt accident on October 5, 1966. Since then, recommendation to design inlet nozzles preventing blockage formation was made (no axial flow).

2.24.2.2.3 The unprotected loss of flow accident

The ULOF accident is considered to be the result of loss of primary pump flow due to potential initiating events such as electrical break-down without reactor scram. The first phase (some seconds), leads to sodium flow reduction (kinetics depending on pump inertia characteristics) and to associated power reduction linked to reactivity feedback; thereafter (some seconds later), the power to flow ratio increases so that sodium temperature reaches sodium saturation

level (boiling onset). Due to the positive 'sodium void effect' in the central core regions, the ULOF leads to sodium boiling and channel voiding and may result in a CDA with a primary core power excursion (TOP, transient over power) that initiates generalized core degradation: fuel melting, clad failure and/or melting, fuel ejection into coolant with possible thermodynamic interaction, molten materials motion, fuel dispersal and relocation into the channels, and possible mechanical energy release. Beyond the primary excursion, recompaction phenomena, formation of large molten pools with melting of the subassembly walls may occur (transition phase) and lead to a secondary power excursion (recriticality events); then an expansion phase due to fuel or sodium vapor bubble may cause significant mechanical energy release to the structures (and potential consequences on sodium spray fire after ejection into the containment vessel).

It is to be underlined that although this accident is initiated by a loss of coolant flow, it may rapidly evolve toward a fast reactivity insertion accident; therefore, it also addresses the similar phenomenology resulting from an uncontrolled passage of gas bubbles inside the core which may lead to a fast power transient (UTOP, unprotected transient over power) linked to sodium void positive reactivity feedback. In addition, it can also be noticed that the phenomena occurring beyond the primary excursion phase (transition phase, . . .) have close links with the propagation of a local fault accident to neighboring subassemblies due to fuel melting.

The ULOF accident phenomenology also has close links with another loss of flow accident that is considered as potentially leading to core damage: the so-called 'LIPOSO' (DBA accident for Superphenix), caused by the break of one of the pipes between the primary pumps and the diagrid. Such an event leads to a rapid loss of flow (down to half nominal value within about 1 s) inside the core and to sodium and clad temperature increase in the outlet of the subassemblies together with a slight power increase. In case of a late detection by outlet sodium temperature increase, the main safety concerns are the risk of sodium voiding due to sodium boiling occurrence or to clad failure with potential fission gas escape, phenomena that are also addressed in the ULOF sequence.

2.24.2.3 The Research Approach Relative to Fuel Accident Behavior

Since the start of sodium fast reactor studies, the investigation of fuel accident behavior has been

performed through in-pile experimental programs that used oxide fuel pins submitted to typical transient conditions as compared to reactor (neutron heating mode, thermo-fluid conditions of sodium flow, fuel and clad temperatures, slow or fast power transients) and thus allowed a close simulation of the involved phenomena (although most of the reactors with transient test capabilities provided only tests under thermal or epithermal neutron spectrum).

In particular, during transients, the fuel accident evolution is governed by thermal and mechanical effects intimately coupled with fission gas and solid fission product behavior so that only neutron heating mode is able to provide a reliable simulation of the events.

Moreover, the initial state of the irradiated fuel before the accident, is determined by the thermo-mechanical and physicochemical phenomena (see **Chapter 2.21, Fuel Performance of Fast Spectrum Oxide Fuel**) that occurred during in-reactor normal operation and resulted in structural and mechanical changes in both fuel and cladding materials; those changes (i.e., fission gas accumulation and release, cladding swelling and embrittlement, pellet-clad gap size variation and composition, etc.), depending on temperature level and burn-up evolutions, may jeopardize the ability of the fuel pins to withstand thermal and/or mechanical loads as consequence of design basis accidents and influence the phenomena during severe accidents, and cannot be simulated without the use of realistic irradiated fuel pins.

General information on fast oxide pin designs, assembly designs, and on fast oxide fuel behavior and performance during in-reactor operation can be found in **Chapter 2.21, Fuel Performance of Fast Spectrum Oxide Fuel**.

Among the experimental programs, the TREAT¹ program (United States) was firstly dedicated to the study of fast power transients as consequences of ULOF and later addressed slow power ramps; the SLSF² program (United States), the German programs MOL-7B and MOL-7C in BR2 reactor,^{3,4} and the SCARABEE⁵ program (France) addressed the loss of cooling phenomena (flow blockage, loss of flow).

The most comprehensive contribution to fuel behavior studies comes from the CABRI test programs that were carried out as a common research program by the French IRSN (Institut de Radioprotection et de Sûreté Nucléaire, formerly IPSN) in conjunction with the French CEA (Commissariat à l'Energie Atomique) and the German Forschungszentrum Karlsruhe (now Karlsruher Institut für Technologie) as Senior Partners over the period 1973–2001, within a large international

collaboration in part time with the United Kingdom, US/DOE, and US/NRC and with an important contribution from Japan. The first experiments (single pin geometry) were dedicated to fast UTOP and ULOF simulations using fresh fuel or low irradiated fuel pins; then, the data base was extended to industrial pins irradiated in Phenix and PFR reactors at different burn-up levels (up to 12 at%) and with various pellet geometry (solid, annular pellets), and to slow power transients. It is to be noted that the length of the fast reactor fuel columns (in the range of 0.85–1 m) being close to CABRI core height (0.8 m), allows a direct use in the CABRI⁶ facility without any need of reconditioning (unlike Pressurized Water Reactor (PWR) fuel rods). Moreover, the hodoscope device used in both TREAT and CABRI facilities and measuring fuel motion during transients (and also initial and final pin states) provides a quantified understanding of the fuel pin behavior.⁷

In relation with the experimental programs, computational tools were continuously developed in the different countries and used for analysis of the tests and evaluation of the consequences of the studied accidents of fast reactors. The fuel performance codes such as TOSURA, GERMINAL^{8,9} were developed and provide the state of the fuel after irradiation as initial fuel conditions at the beginning of an accident sequence. The accident codes PHYSURAC, PHYSURA-Grappe, SURFASS (France), PAPAS-2S (Japan), CASAS (Germany), SAS-4A, and SIMMER II (United States) were developed and used; since the 1990s, the SAS-4A code was further developed through a close collaboration between France, Germany, and Japan and the SIMMER III and IV codes (respectively two and three-dimensional modeling) were developed by Japan¹⁰ and are now largely used in the Sodium Fast Reactor (SFR) community (i.e., France, Germany¹¹).

2.24.3 The Fuel Behavior Under Slow Power Transients

In a fast neutron reactor, an inadvertent control-rod withdrawal generates a linear power increase of about 1% Pn/s in the pins located close to the control rod; this results from the reactivity insertion typically below few cents per second balanced by the negative reactivity feedback due to fuel thermal effect (Doppler effect, axial fuel expansion).

Fast reactor fuel pins operate at high linear generation rate (in the range of 40–50 kW m⁻¹, i.e., above standard values of light water reactor fuel) and with

an axial power profile of cosine shape leading to a peaking factor of 1.2–1.3. In case of mixed oxide fuel with low thermal conductivity, this results in high operating temperature (around 2300 K at the center and 1000 K in periphery of the fuel pellet, (see **Chapter 2.21, Fuel Performance of Fast Spectrum Oxide Fuel**) and in possible fuel melting occurrence under transient overpower. It is to be noted that although metallic fuel is characterized by much lower steady-state operating temperature due to its higher thermal conductivity, its relative margin to melting is similar to oxide with $T(\text{nominal average})/T_{\text{melt}}$ around 80%.¹²

Moreover, in spite of high fission gas release rate observed with irradiated fuel due to high operation temperature (60–80% fractional release at moderate to high burn-up level and mainly from the hottest center zone), power increase and subsequent high temperature also activate fission gas-related phenomena¹³ that influence thermal and mechanical pin behavior such as:

- intragranular gas migration toward grain boundary related to thermal gradient,
- gas bubble growth due to coalescence, vacancy diffusion (and migration for intergranular bubbles),
- fission gas-induced fuel swelling driven by transient evolution of hydrostatic fuel pressure and bubble pressure versus temperature,
- saturation and interconnection of grain boundary bubbles leading to additional gas release to the free volumes.

The present understanding of irradiated fuel pins behavior under such slow power ramps mainly refers to the outcomes of the CABRI tests.^{14–17} According to the safety concerns, the objectives were to determine the power corresponding to fuel-melting occurrence ('power-to-melt'), the failure mechanisms with evaluation of the margin-to-failure (margin-to-failure is given by the difference between power level at which pin failure is expected and power level of an emergency reactor scram), and the possibility and conditions of molten fuel ejection into sodium channel in case of an adventitious clad failure with low fuel-melting fraction.

It can be underlined that under slow power transients, fuel heat generation and heat removal by the sodium coolant are almost in thermal equilibrium: these 'quasi' steady-state conditions allow the evaluation of the power level at which fuel melting occurs. These conditions then may serve for definition of the operating power limit as fuel melting onset is a first step prior to pin degradation.

Table 1 Main characteristics of the irradiated fuel pins used in the slow power transients performed in the CABRI experimental programs (CABRI-2, FAST, RAFT)

Fuel pin	Ophelie-6	Scarabix (Superphenix type)	Viggen-4 (Phenix type)
Pellet geometry	Annular pellets	Annular pellets	Solid pellets
Cladding: ϕ inner/outer diameter $\times 10^{-3}$ m (as fabricated values)	7.5/8.65	7.37/8.5	5.65/6.55
Fuel: ϕ inner/outer diameter $\times 10^{-3}$ m (as fabricated values)	2.0/7.27	2.0/7.13	0.0/5.42
Fuel smear density (%TD, %theoretical density)	82.9	82.8	88
Maximum burn-up (at%)	4.9	6.4	11.5
Cladding material (stainless steel)	316 CW	15–15 Ti CW	15–15 Ti CW

Table 2 Main characteristics of the slow power transient tests performed in the CABRI experimental programs

Tests	Objective	Power transient	Main results
E9 (Ophelie-6 pin)	Power-to-melt and margin-to-failure of a low smear density fuel (annular pellet)		No pin failure, large melting extension (average mass melt fraction ~57%)
E9 bis (Ophelie-6 pin)	Cladding with reduced thickness at peak power node (to promote failure and possible ejection)		No pin failure, large melting extension (average mass melt fraction: 40–50%)
E12 (Viggen-4 pin)	Power-to-melt and margin-to-failure of a high smear density fuel at high burn-up		Pin failure with limited fuel melting extension (average mass melt fraction around 10%)
BCF1 (Viggen-4 pin)	Influence of the power ramp rate on power-to-melt and on margin-to-failure of a high smear density fuel		Pin failure with limited fuel melting extension (average mass melt fraction ~10%), no influence of power ramp rate on melting and failure conditions (from comparison to E12 test result)
PFX (Scarabix pin)	Power-to-melt of an annular fuel pellet (Superphenix type)		No pin failure, melting onset power level

Continued

Table 2 Continued

Tests	Objective	Power transient	Main results
PF1 (Scarabix pin)	Power-to-melt of an annular fuel pellet (Superphenix type)		No pin failure, average mass melt fraction $\sim 10\%$
MF2 (Scarabix pin)	Margin-to-failure of an annular fuel pellet (Superphenix type)		No pin failure, large melting extension (maximum fractional melting radius $R_m/R_0 > 80\%$)
RB1 (Scarabix pin with notch)	Fuel ejection in case of an adventitious pin failure with 10% average mass melt fraction		Imposed pin failure, no fuel ejection with $\sim 10\%$ average mass melt fraction
RB2 (Scarabix pin with notch)	Fuel ejection in case of an adventitious pin failure with 20% average mass melt fraction		Imposed pin failure, molten fuel ejection with $\sim 20\%$ average mass melt fraction

2.24.3.1 The CABRI Data Base for Slow Power Transients Study

Industrial oxide fuel pins of various designs and irradiated in the Phenix reactor were submitted to slow power transients; the main characteristics of both the fuel pins and tests are respectively summarized in [Tables 1 and 2](#).

More details on the pins characteristics are given in Charpenel *et al.*¹⁴ and Fukano.^{15,16}

2.24.3.2 Fuel Melting

Fuel-melting occurrence depends on pin thermal behavior that is governed by thermal conductivity

and heat exchange between fuel and clad through the pellet-clad gap and on melting temperature, most of these factors being function of burn-up level and of irradiation history.

In effect, melting temperature of oxide fuel depends on fuel composition (PuO_2 fraction), on burn-up level and on deviation from stoichiometry: the higher the values of these parameters, the lower the melting temperature.¹⁸

Fuel thermal conductivity depends on temperature, O/M ratio, porosity, and burn-up (see [Chapter 2.17, Thermal Properties of Irradiated \$\text{UO}_2\$ and MOX](#) and reference Carbajo¹⁸ for more information). Heat exchange through pellet-clad gap is a function of the evolution of the gap thickness and of its composition

(at peak linear rating close to 40 kW m^{-1} , gap closure occurs at around 1 at% burn-up, gap composition is linked to fission gas release under irradiation and transient). At burn-up higher than 7 at%, the formation, of a bonding layer of fission products compounds inside the gap (so called 'JOG,' see **Chapter 2.21, Fuel Performance of Fast Spectrum Oxide Fuel**) may also influence the thermal behavior under slow power transients but uncertainty still exists on its impact.

2.24.3.2.1 Influence of fuel smear density on melting occurrence (power-to-melt)

With low smear density fuel, a significant effect of the retained fission gas on the degradation of fuel thermal performance at overpower conditions has been highlighted by the existing data base.

Such effect was derived from the striking results of the E9 and E9 bis tests indicating earlier onset of fuel melting (detected by in-pin fuel motion, thanks to the hodoscope measurement) and larger melting extension than initially predicted; for instance, in the E9 test, the power at fuel melting onset was 73 kW m^{-1} in the CABRI neutron flux, while initially predicted at 85 kW m^{-1} (it is, however, to be noted that due to the thermal spectrum of CABRI reactor causing a radial flux depression, these values need to be corrected by calculation for evaluation of the power-to-melt under a flat radial power profile as in fast neutron conditions).

In effect, due to irradiation, rare gases (Xe, Kr) are precipitated in intra- and intergranular bubbles. When

fuel temperature increases during the slow power transient, and depending on the fission gas radial retention profile, the following main mechanisms take place:

- migration of intragranular gas toward grain boundary due to diffusion and linked to thermal gradient,
- intergranular gas bubble growth due to vacancy diffusion (relaxation of overpressure caused by temperature increase and migration from intragranular gases),
- transient fission gas-induced swelling of the solid fuel from intergranular and porosities gases,
- together with high-temperature plastic fuel creep into free volumes.

This may lead to central hole reduction and to increase of the macroscopic fuel porosity with subsequent reduction of the thermal conductivity and thus higher fuel temperature in the center that results in a lower power at melting onset. The consequences of this mechanism were enhanced in E9 and E9bis tests due to the low power level ($2/3 \text{ Pn}$) at the end of irradiation of the Ophelie pins in the Phenix reactor that led to a high retention of fission gases (intragranular) in the equiaxed zone of the fuel pellet with potential for migration to the grain boundary (intergranular gas and porosity) and fuel swelling during thermal transient.

This significant gas retention over a 1 mm thick zone (from the pellet periphery) is illustrated by **Figure 1** showing the radial profile of the Xenon mass as given by microprobe measurements

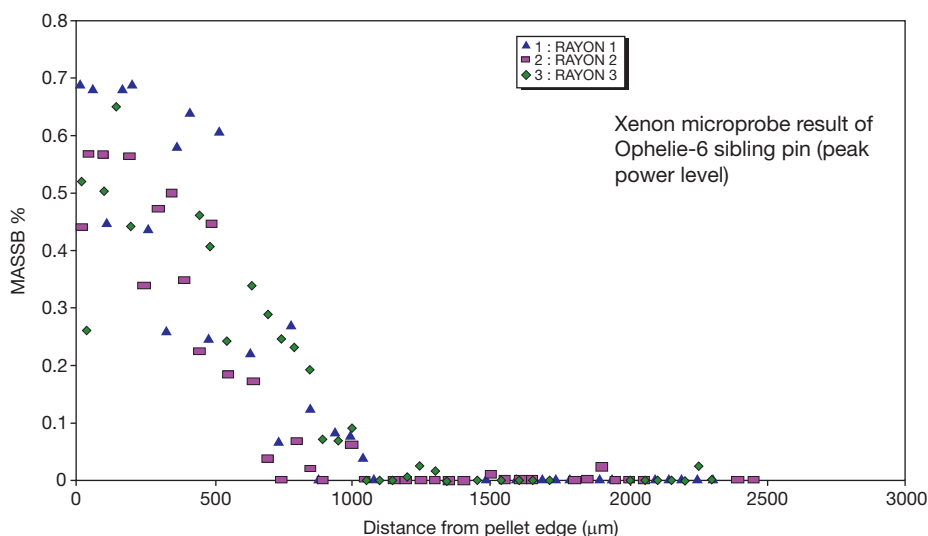


Figure 1 Xenon radial profile from the microprobe examinations d on Ophelie-6 sibling pin (axial level close to peak power location) illustrated by the Xenon mass percentage relatively to the total fuel mass of the microprobe sample (y-axis) versus distance from pellet edge (x-axis).

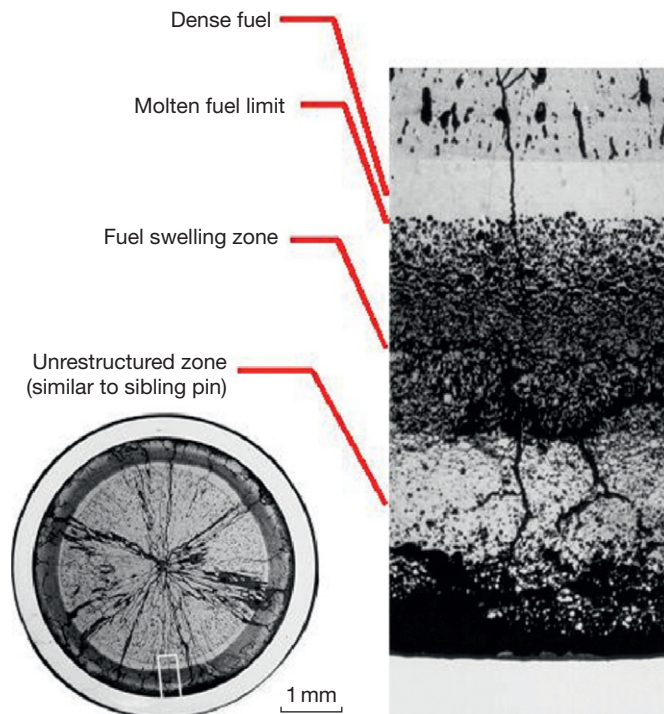


Figure 2 Radial cut micrograph of CABRI E9 test. Reproduced from Charpenel, J.; Lemoine, F.; Sato, I.; Stuwe, D.; Pfrang, W. *Nucl. Technol.* **2000**, 130, 252–271.

(representing the intragranular gas) at the peak power level of the Ophelie sibling pin.

As an example, the micrography of a radial cut of the E9 test pin in the [Figure 2](#) exhibits a decrease of fuel density and fuel fragmentation in the unmolten zone of the fuel pellet due to the slow power transient.

The impact of the fission gas-induced swelling on the fuel microstructure evolution and degradation of fuel thermal conductivity generated the need of improved physical modeling in calculation tools that provided consistent analysis of the data base. In particular, simulation of this mechanism also allowed a correct determination of the power-to-melt of the Scarabix pins from the PFX experiment (78 kW m^{-1} under CABRI neutron flux). Such effect was also the basis for the limitation of the operating power of the Superphenix reactor in order to fulfill the requirement of no fuel melting during a control-rod withdrawal event.

Uncertainty still exists on fuel creep properties at high temperature (close to melting) and on high burn-up impact as almost no data is available for annular fuel type beyond 6.4 at% and submitted to slow power transient (for instance, thermal and mechanical effect of the JOG layer under slow power transient).

With high smear density fuel (solid pellet design) and even at a high burn-up of 12 at% as in the Viggen-4 pin tests, fission gas-induced swelling has a limited effect on degradation of fuel thermal behavior as compared to low smear density fuel, since less free volume is available for porosity increase and reduction of thermal conductivity. In addition, the thermal effect of JOG during transient is also lowered as the high potential for fuel-clad mechanical interaction (FCMI) of high smear density fuel leads to axial extrusion of the viscous compounds of this layer.

So, it can be stated that the fission gas retention (including radial distribution and form) due to in-reactor irradiation together with the fuel pellet smear density (or pellet design) play a major role on fuel melting occurrence during slow power transients. This stresses the high importance of the irradiated fuel state before the accident transient (so called ‘T0 state’). In particular, it is underlined that with low smear density fuel, operation at low power level leading to a high quantity of retained gases in the intermediate zone of the pellet may induce low power-to-melt in case of control-rod withdrawal transient.

In the future, as low smear density fuel type is anticipated (especially with regard to mechanical aspects, see [Section 2.24.3.3](#)) together with high

burn-up objectives, attention should be paid on fission gas retention and radial location with potential evolution of microstructure and on high burn-up impact on power-to-melt.

2.24.3.2.2 Cavity formation and in-pin fuel motion

Fuel melting firstly occurs in the pellet center and leads to the formation of an internal cavity filled with molten fuel and fission gases initially retained inside the fuel.

The cavity is pressurized (some tenths of MPa) by the high temperature gases and acts as a compressible volume. The gradual evolution of the cavity depends on both radial and axial fuel melting extension and also on axial fuel relocation into the available free volume as a consequence of pressure built-up within the fuel–gas mixture (foam).

According to pellet geometry, molten fuel firstly moves through the central hole (created by irradiation or by design) toward the blanket pellets in case of solid fertile pellets, or toward the plenum in case of hollow fertile pellets. This fuel motion (fuel squirting) is governed by the following parameters:

- the pressure difference between the foam and the trapped gases in the central hole or in the plena,
- the size of the central hole that influences drag forces,
- the viscosity of the molten fuel and gas mixture, function of the fuel enthalpy,
- the freezing mechanism of the fuel when in contact with cold pellets.

Under slow power ramps, and in case of annular pellets, in-pin fuel motion has been evidenced in all the tests, even when low mass melt fraction is reached (CABRI PFX, PF1 tests). In those transients with slow melting kinetics, the in-pin motion evolution is closely related to the gradual supply of molten fuel at liquidus enthalpy that spreads over several seconds; such time scale is consistent with the observed segregation of metallic fission products (in case of fast transients, fission products are dragged with the fuel on a time scale of 100 ms).

Figure 3 shows for the E9 test, the upward motion of the molten fuel inside the central hole of intact pellets up to the top of fissile length with central hole filling. The axial motion is limited by the solid fertile pellets. In some cases, penetration above fertile may occur through available paths (as for instance, in E9bis test with fragmented fertile pellets before test).

In-pin molten fuel motion, in providing additional volume to the molten fuel mixture, leads to reduced cavity pressurization and acts as a mitigating effect for clad mechanical loading. No significant impact on reactivity feedback (negative) is expected from this in-pin motion as long as it remains limited to fissile height of the fuel pins (and also due to the small mass involved in case of the withdrawal of a single control rod).

2.24.3.3 Pin Thermomechanical Behavior

The pin thermomechanical behavior depends on fuel and clad materials properties, temperature, and burn-up level.

The in-reactor irradiation tends to reduce the ductility of the cladding material but 15–15 Ti CW cladding material, as used in the Phenix and Super-Phenix reactors, nevertheless revealed residual ductility at a high dose rate (90 dpa) corresponding to burn-up of 12 at% (total elongation of 4–2% in the range of 700–800 °C under low strain rate, from tensile tests on Viggen-4 cladding).

Under slow power transients, clad mechanical loading may result from fuel thermal expansion (linked to temperature increase), fission gas-induced swelling (burn-up effect) and molten cavity pressurization after fuel melting onset (if any).

2.24.3.3.1 Low smear density fuel

Within the present data base (CABRI, TREAT), low smear density fuel up to medium burn-up demonstrated high margin-to-failure and its ability to withstand high overpower conditions. Indeed, in spite of large radial extension of fuel melting (for instance, 0.86 R/R0 in E9 test), no or very limited and local clad plastic deformation was obtained due to the transient and therefore no pin failure (only a slight deformation of 0.13% in MF2 test with 15–15 Ti CW steel was obtained). **Figure 4** shows as an example, in E9 test, the large radial extension of fuel melting along the pin and the absence of clad deformation due to transient (initial clad deformation is due to high irradiation swelling of stainless steel cold worked 316).

Such behavior is linked to the potential of low smear density fuel for mitigation of clad loading by axial in-pin motion and related limited cavity pressure built-up. Moreover, under slow power transients, no contribution of cesium (volatile fission product) on the cavity pressurization could be evidenced consistently with Cs migration in radial direction toward unmolten zone (posttest analysis of E9-E9bis tests). Therefore, it is suggested that pin failure of low

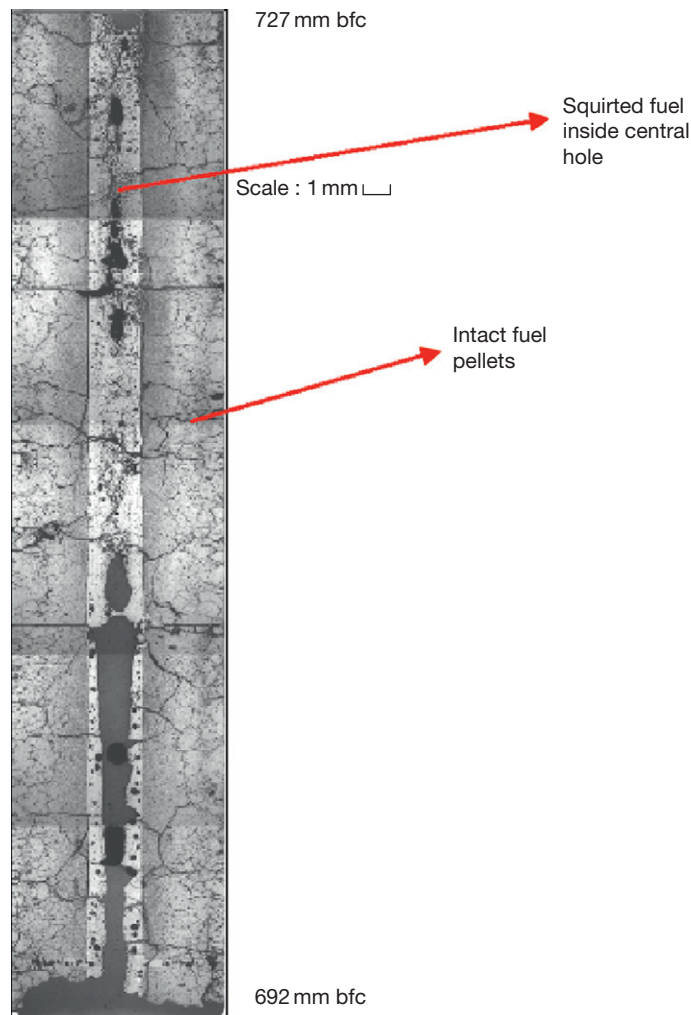


Figure 3 Axial cut of CABRI E9 test in the upper part of the fissile column showing in-pin molten motion inside the central hole and freezing of molten fuel on the intact pellets (bfc: bottom of fissile column). Reproduced from Charpenel, J.; Lemoine, F.; Sato, I.; Stuwe, D.; Pfrang, W. *Nucl. Technol.* **2000**, 130, 252–271.

smear density fuel up to intermediate burn-up, can only result from high overpower as compared to nominal value, with large melting extension and uniform pressure from cavity or from plenum, and reduced strength of the cladding due to significant clad temperature increase. In such a situation, pin failure is likely to occur in the upper part of the fissile column that is the level of maximum clad temperature under almost steady-state conditions of slow power transients (such failure mode was evidenced in some TREAT experiments¹⁶).

These points however hold for low to intermediate burn-up oxide fuel pins (up to 6.4 at %). For low smear density fuel at higher burn-up or with different fuel types, attention should be given to the potential

occurrence of FCMI (Fuel-clad Mechanical Interaction) under transients, due to solid fuel pressurization and swelling before fuel melting onset. For instance, the operation period at reduced power level that leads to high fission gas inventory or the high intergranular gas retention at the periphery of the high burn-up fuel pellets, may promote FCMI loading.

2.24.3.3.2 High smear density fuel

With high smear density fuel, mechanical loading can be high enough to cause significant clad straining or even failure due to combined contribution of both mechanisms:

- FCMI from solid fuel pressurization and swelling; in particular, strong FCMI is likely with high

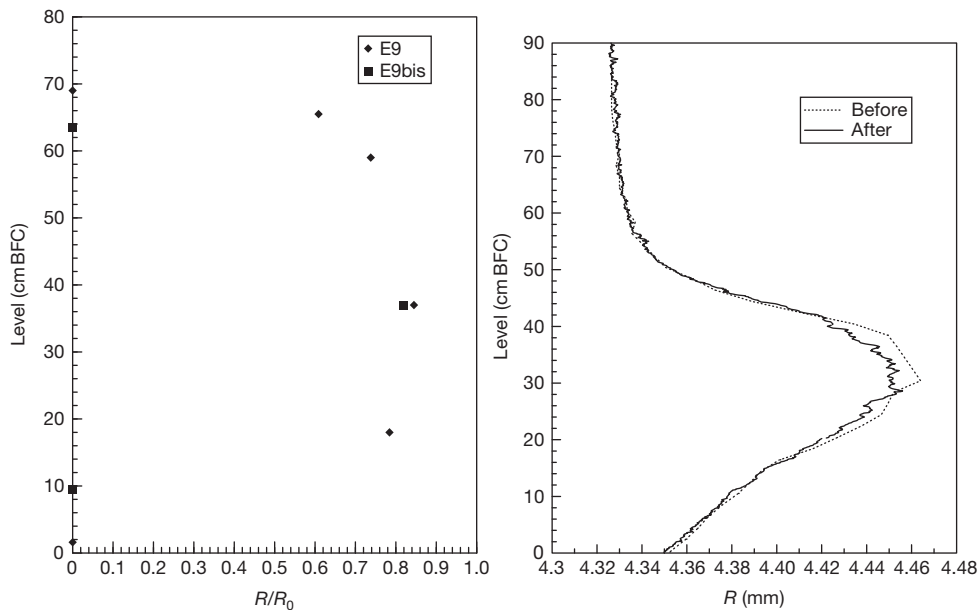


Figure 4 Radial extension of fuel melting along fissile length in E9 and E9bis tests (right) and clad outer diameter before and after E9 test showing no deformation due to transient (left).

burn-up fuel in which significant gas quantity is retained at grain boundary and porosity, in the outer zone of the pellet with fine grain structure, similarly to the rim zone of light water reactor fuel.^{19,20}

- Cavity pressurization depending on the amount of retained gas after irradiation.

In effect, in the CABRI E12 test pin that failed at 81 kW m^{-1} (power, however, much greater than end of life level of 31 kW m^{-1}) at the level 0.6 m from bottom of fissile length where clad temperature at failure level is in the range of 983–1013 K (710–740 °C) and with a limited radial extension of the molten cavity (molten mass fraction of 10%), an additional plastic deformation of 0.6% in the lower part due to transient (see Figure 5) is obtained: this confirms that FCMI highly contributed to clad loading and failure in addition to cavity pressure.

On this basis, it can be stated that high smear density fuel has lower margin-to-failure than low smear density fuel. In addition, it is demonstrated that the pin failure threshold of high smear density fuel is not affected by the average power ramp rate in the range of 0.9–2.8%P0/s (from E12 and BCF1 tests).

In case of high burn-up fuel, large internal clad corrosion layer (made of Cs, oxygen, steel components) with reduction of the gap might lead to an increased FCMI; however, the corrosion level is

located in the upper part of the pin that is not the zone of maximum FCMI loading and no impact of this corrosion feature has been evidenced from the present slow power transient data base. Nevertheless, with future fuel designs and depending on operation conditions, attention should be paid on the risk of possible fuel-cladding chemical interaction occurrence close to the maximum mechanical loading zone.

2.24.3.4 Postfailure Fuel Behavior

2.24.3.4.1 Molten fuel ejection conditions with low mass melt fraction

The possibility and conditions of molten fuel ejection into flowing sodium is a safety concern (see Section 2.24.2.2) within the investigation of consequences of slow power transients and in case of an adventitious pin failure with low mass melt fraction.

In case of high smear density fuel and high burn-up level, evidence of molten fuel ejection at mass melt fraction of 10% (corresponding to an areal melt fraction of 20–30% at the axial peak) is brought from failure of E12 and BCF1 test pins with the following points:

- as a result of the limited molten area, a thick shell of solid fuel is present in the outer pellet zone characterized by a high fission gas retention and

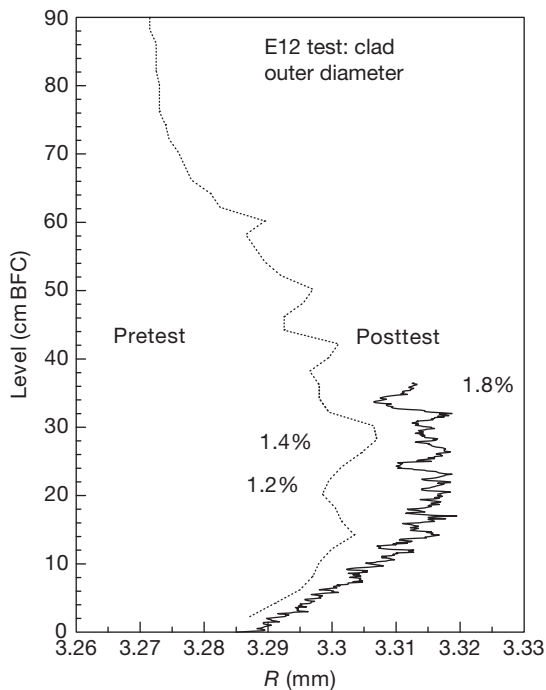


Figure 5 Clad outer diameter before and after E12 test showing a 0.6% permanent deformation due to transient, in the lower part of the test pin. Reproduced from Charpenel, J.; Lemoine, F.; Sato, I.; Stuwe, D.; Pfrang, W. *Nucl. Technol.* **2000**, 130, 252–271.

high concentration of intergranular gases and pores (typical of high burn-up structure),

- under slow transients, molten fuel is highly mobile as its enthalpy is close to liquidus value that induces low viscosity; together with high cavity pressure, this enables penetration of molten fuel through the cracks in the porous solid shell potentially inducing a release of molten fuel outside the pin and contact with sodium,
- a complete voiding of the molten cavity occurs due to its high pressure.

For low smear density fuel, pin failure with a low melt fraction is unlikely in a deterministic manner; so, the investigation of the low melt fraction leading to fuel ejection in case of an adventitious clad failure required a specific approach through the simulation of an initial clad defect that is designed to fail at a given molten mass fraction. This could be performed by the use of a machined slot on the irradiated cladding of Scarabix pins, covered with a fusible material whose melting is initiated at peak power level by a small cladding temperature increase without any modification of the molten fuel fraction.

The detailed analysis of these RB1 and RB2 tests suggested that molten fuel ejection at low melt fraction is possible if the following conditions are simultaneously fulfilled:

- the melting radius reaches the limit of the solid fuel cracked zone which provides free paths for the highly mobile fuel liquid fuel,
- the cavity pressure is higher than coolant pressure (sodium pressure is about 0.2–0.4 MPa).

In terms of molten mass fraction and in case of low smear density fuel at moderate burn-up (6.4 at%), this corresponds to a threshold for molten fuel ejection to be expected between 10 and 18%. However, the validity of extrapolation of these conditions to higher burn-up fuel is not assured.

In addition, as pressure cavity is driving the fuel ejection, influence of fuel smear density is also outlined (lower fuel ejection rate with low smear density fuel as compared to solid fuel under similar low melt fraction).

2.24.3.4.2 Consequences of molten fuel ejection at low mass melt fraction

Fuel ejection into a sodium channel leads to sodium flow divergence in the first milliseconds with acceleration of sodium slugs and to voiding of the sodium channel as a result of:

- volume displacement of liquid sodium linked to fuel ejection and liquid sodium thermal expansion to a lower extent,
- fuel–coolant thermodynamic interaction (so called FCI) due to the contact of high-temperature fuel droplets (above 3100 K) with liquid sodium (at temperature between 670 and 820 K) and high heat exchanges leading to sudden vaporization of the sodium with pressure increase in the interaction zone,
- expansion of fission gases inside the solid fuel (due to release of clad constraint) and gas release from plena through the rip site.

In case of high burn-up fuel, fission gas release from the solid outer fuel zone with high gas retention under intergranular form (as derived from E12 test) contributes to a sustained flow divergence.

Furthermore, the impact of molten fuel ejection rate, in relation with cavity pressure, on sodium-voiding extension is highlighted by the **Figure 6** showing a smaller voiding effect with annular fuel (RB2 test) than with solid fuel (E12 and BCF1 tests).

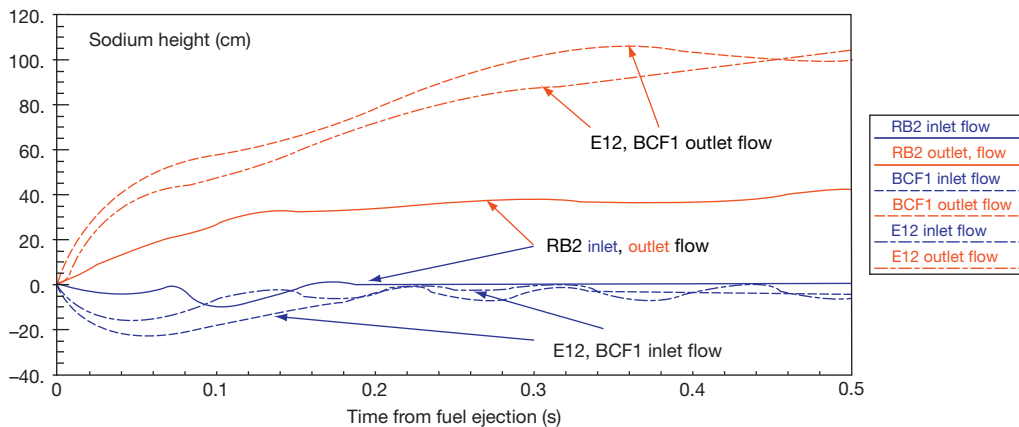


Figure 6 Sodium channel voiding extension after clad failure in the slow transient CABRI tests E12, BCF1, RB2 (from outlet and inlet flows measurements, origin of voiding is the failure location in each test).

After fuel ejection, molten fuel is rapidly relocated due to freezing in the channel (no significant axial motion) and fuel accumulations are created.

Considering reactor conditions under slow power transients, such consequences of pin failure and fuel ejection at low mass melt fraction underline the potential risk of propagation of the pin degradation inside the subassembly depending on:

- the molten fuel contact with the cladding of the neighboring pins that are also partially molten and may lead to further pin-to-pin failure,
- the kinetics of blockage of the subassembly due to molten fuel freezing,
- the FCI amplitude that might enhance sodium voiding and clad melting of other pins, and generate mechanical effects linked to pressure peaks,
- the performance of detection devices for the accident (DND, noise sensors, etc...),
- the capability of cooling down one (or several) subassembly(ies) containing the failed pin(s) taking into account the detection and power shut-down times, and the stored energy due to overpower.

2.24.3.5 Fission Gas Behavior Summary

The above paragraphs clearly underlined the major role of fission gases on fuel pin behavior under slow power transients during the whole accident sequence in relation with the fuel smear density, burn-up level and fission gas retention.

Fission gas retention and distribution (radial) govern fission gas-induced fuel swelling in solid fuel (from intergranular and porosity gas) due to temperature increase. This fission gas-induced fuel

swelling is accompanied by solid fission products swelling but to clearly isolate and quantify this contribution from the one of the fission gases is difficult.

Fission gas-induced fuel swelling mainly acts on:

- power-to-melt of low smear density fuel through evolution of fuel microstructure and degradation of thermal performance,
- clad loading of high smear density fuel; at high burn-up level (due to outer gas rich zone with grain boundary gas) it may cause clad failure.

Fission gas retained in the molten fuel affects cavity pressure and in-pin fuel motion with impact on clad mechanical loading, and molten fuel ejection in case of pin failure.

Fission gas release inside the pin may lead to sustained voiding of the sodium after pin failure, if any (depending on the amount of available gas); it may also generate pin failure by pressure loading of the cladding at high temperature level, if no significant FCMI clad loading is at work.

For these reasons, the conditions of fuel pin irradiations are very important as they determine the amount, location (axial–radial profiles), form (intra–intergranular gas) of the retained and released gases inside the pins with potential impact on the phenomena. In particular, operating conditions at low power level (beyond some tens of days) followed by a slow power ramp up to a certain overpower level, might promote significant fission gas-induced fuel swelling and related consequences.

However, the fission gas-related transient mechanisms are complex, intimately coupled with thermal and

mechanical behavior of oxide fuel at high temperature (not well known) and with irradiated cladding mechanical properties. No direct and accurate measurement of fission gas-induced mechanisms is presently possible and their kinetics is not known, so that simulation of these phenomena is not yet very precise in the available accident computer tools. For the future SFR fuels, attention should be given to these phenomena in view of knowledge and modeling improvements.

2.24.4 The Fuel Behavior Under Unprotected Loss of Flow Accident

The ULOF accident in sodium fast reactors has been worldwide studied for a long time because of its potential severe consequences such as prompt-critical events occurrence and risk of mechanical energy release to the vessel structure (cf. [Section 2.24.2.2.3](#)).

As described in [Section 2.24.2.2.3](#), the phenomenology of the ULOF sequence can be considered along two main phases:

- The primary phase concerns the first consequences of the global loss of core cooling, starting at nominal power: sodium temperature increase, sodium boiling occurrence in the hottest part of the core and in the upper part of the fissile length due to forced convection (or at the peak power level in case of rapid flow reduction rate, below ~ 3 s halving time); then, development of the channel voiding inside the fissile zone with positive reactivity feedback causes a subsequent fast overpower transient so called 'primary excursion'; from there, fuel melting, pin failure/degradation, molten fuel ejection, FCI, fuel motion with associated reactivity feedback may occur with potential for a mechanical energy release.
- The late phase concerns the extended core degradation (transition phase) and the possible evolution toward more severe events: compaction effects with secondary power excursion, fuel dispersal, and mechanical energy release; the evolution of the accident during this phase is highly dependent on the core state at the end of the primary phase; for instance, if a significant fuel mass is definitively ejected out of the fissile zone at that time, the probability of prompt-critical events may be reduced.

However, the late phase of a ULOF accident with extended core degradation is not discussed in the following as it addresses multiphase multicomponents

thermohydraulic system intimately coupled with neutron physics (which is out of scope of the article).

The present section will focus on the fuel pin behavior during the first phase of the accident (primary phase) that allows the quantification of the mechanical energy release due the transient overpower (TOP) and the evaluation of the impact of the mitigating events against reactivity insertion.

The present understanding of irradiated fuel pin behavior under fast power transients is mainly based on the outcomes from in-pile experimental programs: TREAT (up to 1987) and on the extensive data base from the several CABRI programs (up to 2001) that provided data for simulation tools development (see [Section 2.24.2.3](#)).

It is also underlined that in the reactor case, the whole accident sequence (also during the primary phase) is driven by the total reactivity coming from different contributions (positive, negative feedbacks) depending on the core design and the transient evolution. These different contributions to the reactivity versus time are important and must be taken into account in the computational tools in view of reliable simulations. During the primary phase, the main reactivity contributions are:

- the sodium voiding in the central core regions generally acting as a positive feedback and dominant effect,
- the Doppler effect, the fuel axial expansion (both due to the fuel temperature increase during the transient), and the core structure dilatation (design dependent) giving a negative feedback (although not compensating the void reactivity in case of sodium boiling extension),
- the molten steel motion if any, as a positive feedback,
- the dominant impact of the fuel motion, especially due to molten fuel motion after pin failure; any axial motion toward the zone of high neutron flux results in a positive feedback, conversely, any fuel ejection out of the fissile zone has a negative feedback.

2.24.4.1 The Experimental Simulation for the Study of the ULOF Primary Phase

In the ULOF sequence and at the time of the transient overpower onset, all the sodium channels in the core are not in the same thermohydraulic state: largely voided due to boiling extension in the center, partially voided or still filled with liquid sodium in the other regions, as function of the size and design of the core. So the fuel pins in the different channels

undergo the power pulse impact at different clad temperature levels and thus with different mechanical resistance and failure conditions (if any).

In the in-pile experiments, for instance, in the CABRI programs,⁶ these conditions are simulated by using single or several irradiated fuel pins cooled by a sodium flow under initial nominal power and by applying a loss of flow reduction followed by a power pulse triggered at different times corresponding to various thermal conditions of the cladding. The other main parameters investigated through the CABRI data base are:

- various designs of the irradiated fuel pins (solid, annular pellets, different smear densities) including industrial fuel pins (from Phenix and Superphenix designs),
- burn-up levels (different values in the range 0–12.7 at%),
- energy injection of the TOP (range of $0.8\text{--}2 \times 10^6 \text{ J kg}^{-1}$) and energy injection rates (fast: $10\text{--}20 \times 10^6 \text{ J kg}^{-1} \text{ s}^{-1}$, medium: $1\text{--}5 \times 10^6 \text{ J kg}^{-1} \text{ s}^{-1}$) as illustrated in Figure 7.

Detailed information on the ULOF data base and on the understanding can be found in Cranga,²¹ Fukano,²² Haessler,²³ Sato,^{24,25} Struwe,²⁶ and Wright.¹

2.24.4.2 Fuel Pin Behavior up to Failure

As a result of power transients, some phenomena that are already described in Section 2.24.3 for slow power transients also occur during ULOF sequence, however, with a different time constant. In the following, the main specific impacts of loss of flow combined with fast transients are underlined.

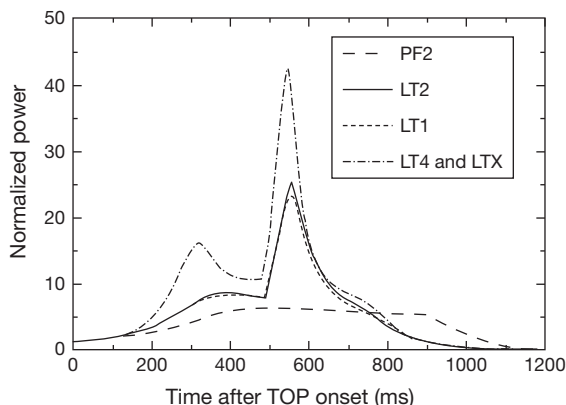


Figure 7 Examples of medium overpower transients of the CABRI unprotected loss of flow data base.

2.24.4.2.1 Fuel temperature increase and thermal expansion

In the ULOF accident, the fuel temperature evolution is mainly governed by the time of TOP occurrence and related energy injection (depending on the core neutron characteristics).

The first consequence is fuel thermal expansion. In the radial direction, thermal fuel expansion causes the gap closure (if it was not already closed due to high burn-up) and increase of pellet-clad heat exchange as a function of contact pressure. At high burn-up, no thermal impact of the presence of the JOG could be evidenced from the data base in those conditions. The axial thermal fuel expansion was found to be significant, even when restrained by clad constraint (due to closed pellet-clad gap) probably because of the JOG presence (the JOG layer is in fact squeezed toward pin ends due to high contact pressure). Fuel axial expansion may amount to about $2\text{--}3 \times 10^{-2} \text{ m}$ during TOP, depending on the injected energy. This effect, in reducing the fuel mass inside the fissile zone, produces a negative reactivity feedback, that is however not sufficient to stop the energy injection.

In case of a delayed TOP after onset of sodium boiling, a first significant fuel temperature increase may take place after clad dry-out (due to drastic reduction of heat exchanges from the clad to sodium) and is then followed by the TOP effect. During the LOF phase, the axial fuel expansion is limited (of the order of $4 \times 10^{-3} \text{ m}$).

Under ULOF/TOP conditions, fuel melting is reached as a result of the significant fuel temperature increase. It is to be noted that in such fast power transients, the impact of fuel smear density on fuel thermal performance is not significant (on the contrary to the slow power transient behavior) because significant fuel swelling has no time to take place. A molten cavity is formed from the center of the pellets (highest fuel temperature location); under the high and fast energy injection and when clad temperature is lower than 1200 K, the cavity pressure from the mixture of molten fuel and fission gases (see Section 2.24.3.2.2) is higher than in slow power ramps as a result of high cladding strength (related to high strain rate) and of fast extension of the melting zone.

2.24.4.2.2 Fuel pin mechanical behavior and pin failure conditions

The basic mechanisms driving the pin mechanical behavior are similar to those already described in Section 2.24.3.3 for slow power transients; however,

in the ULOF/TOP sequence, their importance highly depends on the energy injection rate and on the clad temperature level at the time of maximum loading. Moreover, pin failure conditions have a significant impact on the follow-on of the accident as they determine the potential for molten fuel relocation and associated reactivity feedback.

Similarly to slow power transients, no significant impact of the presence of the JOG layer (high burn-up fuel) is evidenced on the pin mechanical behavior under fast TOP (due to axial extrusion).

The present understanding of the data base allows identifying the three dominant mechanisms responsible for pin failure or onset of pin degradation during ULOF/TOP accident, in addition to fuel thermal expansion:

- Molten cavity pressure loading is dominant under high-energy injection rate (fast energetic TOP, $10\text{--}20 \times 10^6 \text{ J kg}^{-1} \text{ s}^{-1}$) with clad temperatures below 1200 K and results in burst type failure. Cavity pressurization is increasing with fission gas retention of the molten zone and with fuel smear density. Moreover, due to fast kinetics, the gaseous swelling mechanism in solid fuel is limited before melting onset and does not participate to the clad mechanical loading.
- FCMI loading with contribution of fission gas-induced swelling (from intergranular gases and porosities) is dominant when energy injection rate is moderate ($1\text{--}5 \times 10^6 \text{ J kg}^{-1} \text{ s}^{-1}$) or slow (see Section 2.24.3.3). FCMI due to fission gas swelling is enhanced with high burn-up fuel due to its significant inventory of grain boundary gases in the periphery of the pellets (rim zone) and also with high smear density fuel. This is highlighted by the CABRI-2 tests E2 and E3 using high-burn-up high smear density fuel (Viggen-4 fuel, see Section 2.24.3) that resulted in pin failure at a low enthalpy level (peak enthalpy) with a limited fuel melting extension and thus a limited cavity pressure (Figure 8). FCMI loading due to fission gas-induced fuel swelling may also result from reactor operation at reduced power that enhances fission gas retention inside fuel. With high clad temperature (in the range of 970–1170 K), larger fuel swelling is expected as a result of the reduced cladding strength; in such conditions and according to clad mechanical properties of irradiated stainless steel (as those already used: 15–15 Ti CW, for instance), FCMI failure potential may be increased due to low clad failure strain.

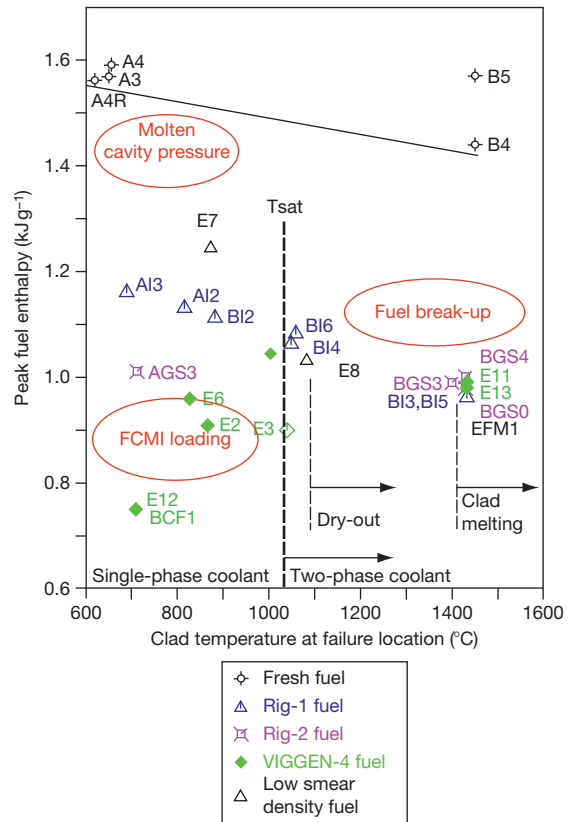


Figure 8 Peak fuel enthalpy versus clad temperature in some CABRI tests with different fuel pins (Rig-1, Rig-2, Viggen-4 fuel, respective burn-up of 1, 2.9, and 12 at%, solid pellet; Ophelie-6 pin, 4.9 at%, low smear density fuel). Enthalpy values calculated by SAS-4A code version from D. Struwe, KIT.

- In case of a delayed TOP after loss of flow, the high clad temperature ($T > 1300 \text{ K}$) and the reduced cladding strength allow significant fuel swelling to occur and result in fuel ‘break-up’ when fuel temperature is close to melting onset. It is underlined that this mechanism (clearly identified from the hodoscope measurements) is independent of the total injected energy, of fuel smear density, and of burn-up (except for fresh fuel in which very low gas quantity prevents from fuel swelling) as shown in Figure 8. The high amplitude of fuel swelling in these conditions may also lead to loss of clad integrity before clad melting (clad melting temperature around 1660 K) and to gas blow-out from the plenum, before fuel break-up.

When failure occurs due to cavity pressurization or FCMI loading and according to clad temperature axial profile, failure site is located above the peak

power level, at around 2/3 of fissile length; when fuel pin break-up mode is at work, the onset of pin disruption occurs close to peak power level. These points are important with regard to reactivity feedback linked to further fuel motion. Moreover, when pins fail at a low fuel enthalpy level (FCMI loading), multiple failure sites may also exist if a significant amount of energy is injected after first failure.

As a general feature, the low smear density fuel shows a tendency to lower FCMI potential due to the available free volume for fuel swelling accommodation and to a reduced cavity pressure loading after fuel melting onset (if any). This is clearly outlined in the conditions of TOP with high cladding strength (clad temperature below 1200 K) by the two CABRI tests LT2 and E6, performed under similar conditions: high burn-up level (~ 12 at%), cladding material (15–15 Ti CW) and close pure TOP transients (no clad undercooling). No failure occurred with annular fuel pellet (LT2, 79% TD (theoretical density) fuel) while solid pellet fuel pin resulted in failure (E6, 88% TD fuel). It can be noted that in the unfailed LT2 Quasar pin with annular fuel, the design of the hollow fertile pellets, in providing a direct flow path for molten fuel from fissile zone to the upper and lower plena, also contributed to the reduction of the cavity pressure after melting.

Nevertheless, considering transient fission gas behavior (fuel swelling), FCMI loading may be significant even with low smear density fuel²² due to:

- clad decreased strength caused by an undercooled overpower transient (for instance, with local undercooling),
- high fission gas-induced fuel swelling linked to high burn-up fuel occurring before fuel melting onset (before cavity formation and occurrence of fuel squirting).

In addition, in case of hollow pellet, cavity pressure is not significant before large fuel melting extension is reached and is also reduced by in-pin fuel motion. This is reflected by the high failure enthalpy threshold in the CABRI E7 test (Ophelie-6 pin, annular pellets) under fast energy injection (**Figure 8**).

The **Figure 8** presents the peak fuel enthalpy (calculated value) versus clad temperature at failure location for most of the CABRI tests that led to pin failure and shows the different domains of clad-loading types and main tendencies according to the above description. The general trend of failure enthalpy decreasing with temperature is consistent with mechanical properties of irradiated cladding.

During an ULOF sequence, the loss of clad integrity due to clad melting only (with draining of molten clad) may occur in case of a delayed TOP after sodium boiling occurrence (depending on the core neutron characteristics) and if no fuel break-up is to occur (low burn-up). On the other hand, when fuel break-up occurs, intimate mixing of fuel and cladding leads to steel melting as confirmed by the transfer of metallic fission products from fuel to steel (seen on γ -scanning measurements).

These points clearly underline the impact of several parameters on the mechanical pin behavior under ULOF/TOP accident (loading and failure mechanisms) such as: irradiation history (burn-up level, fission gas retention), oxide fuel smear density, clad temperature, and transient conditions.

The modeling developed in the different simulation tools reflects the phenomena, the conditions and tendencies but uncertainty exists on failure prediction that has to be taken into account when applied to reactor calculations.

2.24.4.3 Postfailure Phenomena

The basic postfailure phenomena are similar to those described in **Section 2.24.3.4** (slow TOP): fuel ejection into channel coolant, FCI, fuel pin degradation and fuel relocation. However, in comparison to slow TOP conditions, they are characterized by more energetic power transients, different channel conditions at failure (liquid sodium, partially or totally voided channel), different fuel enthalpy level at failure and the fact that additional energy injection may occur after the first failure of the pin.

It is clearly outlined that the fuel ejection rate and mode depend on the fuel enthalpy level at failure time (based on the hodoscope measurements from the experimental data base). Fuel ejection rate is increased with high fuel enthalpy (from cavity pressure loading) while at low enthalpy level (due to FCMI loading), first fuel ejection is limited by pressure loss through failure rip and fuel accumulation at failure site including solid fragments from outer fuel shell. When failure occurs in a partially voided channel (high clad temperature) and at low enthalpy level, radial extrusion of solid outer fuel zone into the coolant is the dominant mode of fuel pin disruption.

In all cases, the contact of molten fuel with liquid sodium leads to FCI with related fast sodium vaporization and pressure peaks (see **Figure 9**). As a result, fast channel voiding (illustrated on **Figure 10**) and

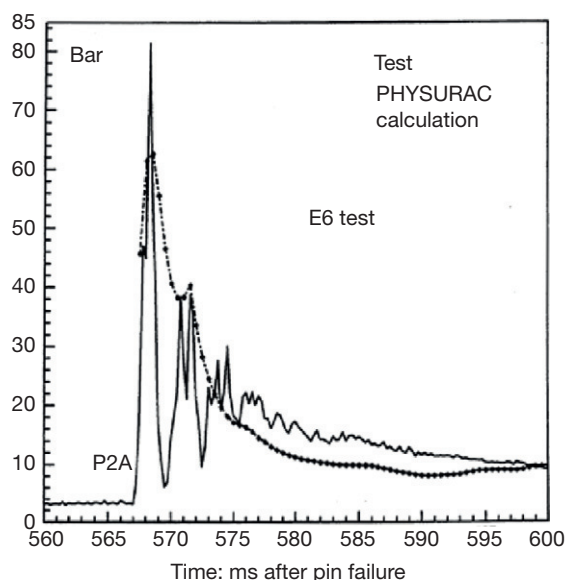


Figure 9 Sodium channel outlet pressure as a consequence of fuel-coolant interaction after pin failure in the E6 CABRI test (experiment, PHYSURAC calculation).

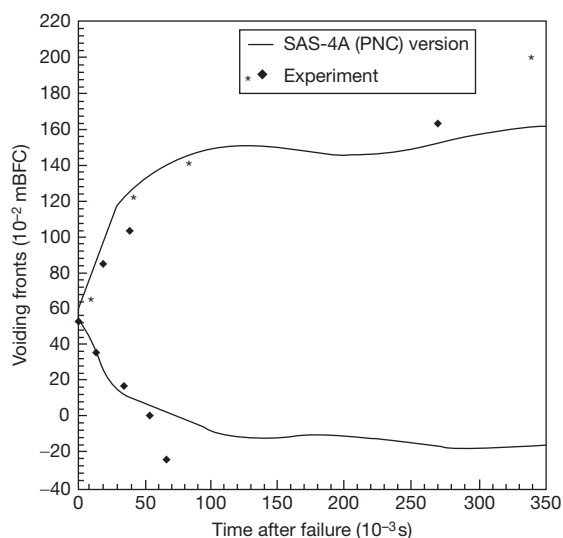


Figure 10 Sodium channel voiding as a consequence of fuel-coolant interaction in the E6 CABRI test (experiment, SAS-4A calculation).

liquid sodium slug displacement occur with mechanical energy release.

Mechanical energy release reaches maximum values when FCI occurs in a liquid sodium channel and is lower when the channel is partially voided due to compressible zone; it increases with ejected fuel mass and enthalpy. Based on the measurements in the different CABRI test conditions, the mechanical to

thermal energy ratio due to FCI is estimated to 0.7% during the first phase of sodium voiding (5 ms) and to 0.1% during the total duration of sodium expulsion: this value tends to indicate a low probability of a significant mechanical energy release due to FCI as a result of fuel ejection into sodium channel after pin failure. However, this result holds for oxide fuel. In the event of use of different fuel type in future SFR, consequences of FCI have to be checked with regard to energetic potential (for instance with carbide fuel).

In case of highly irradiated fuel, and independently of thermal-hydraulic conditions of the sodium channel at failure time, a significant amount of fission gas can be released from plena and from external parts of the fuel pellets and contribute to a sustained voiding after failure with, however, no major impact on molten fuel entrainment.

The major outcomes from the research studies devoted to ULOF/TOP concern fuel motion and relocation after pin failure. Indeed, it is clearly underlined that axial fuel dispersal and axial relocation occurring after failure is limited. The main mechanisms governing the fuel dispersal are the following:

- the freezing of the molten fuel above and below the fissile length due to bulk freezing on the leading edge (evidenced from dedicated tests²⁷) and intimate steel and fuel mixing in case of failure at high fuel enthalpy; this results in the formation of upper and lower fuel accumulations;
- in case of failure at low enthalpy level, the high viscosity of the oxide fuel under melting (fuel enthalpy between solidus and liquidus state) prevents an extended motion and the accumulation of solid fuel fragments ('chunk jamming') limits the further penetration of the foamy fuel (gas and fuel mixture).

Figure 11 illustrates the final state of the relocated fuel in several CABRI tests simulating ULOF/TOP sequences with highly irradiated fuel pins (Viggen-4 pins, 12 at%) and shows the limited extension of relocated fuel out of the fissile zone in relation with the enthalpy level at failure or clad temperature at failure level (increasing from E6 to E11 test).

The total ejected fuel mass due to primary excursion remains lower than 20–30% of the initial fuel mass in all cases (a higher value could be obtained in case of a delayed TOP after LOF with degradation of short upper fertile zone due to molten fuel contact). These findings are consistent with the results obtained in bundle geometry (TREAT results, CABRI tests performed in 3 pins bundle).

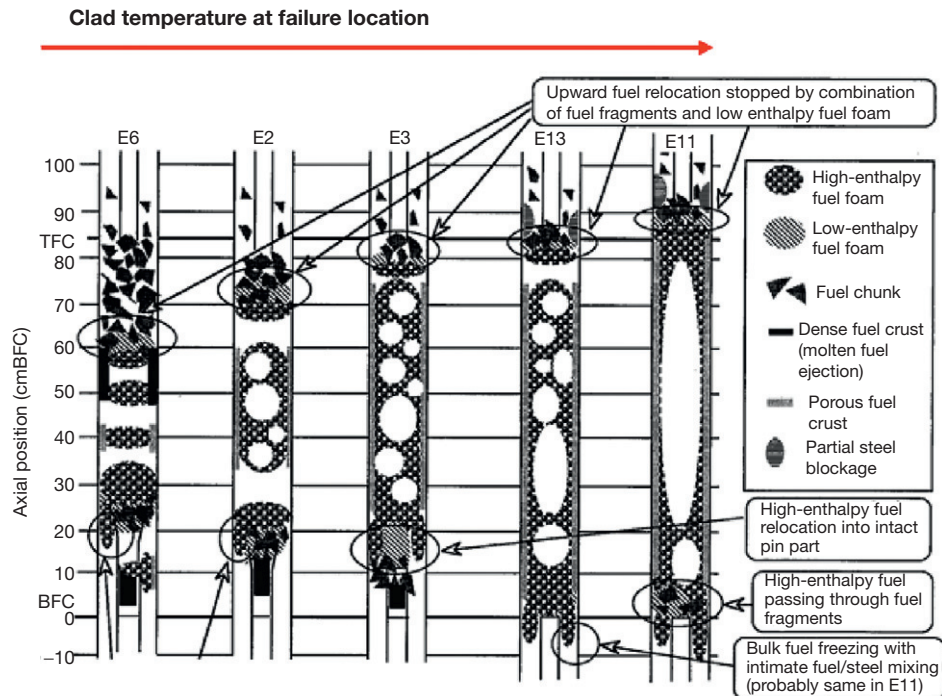


Figure 11 Fuel relocation state at the final state of CABRI tests with high burn-up fuel (Viggen-4 pins) (white zone = materials voided zone).

When applied to reactor calculations, the present understanding and results underline that fuel dispersal at the end of the primary excursion in a ULOF accident (in spite of negative reactivity feedback) is not sufficient to prevent the occurrence of any further critical event and that the evolution of the accident toward transition phase cannot be avoided.

In addition to prevention of ULOF accidents, reduction of the risk of occurrence of critical events during the ULOF accident sequence should be the main goal for future SFR design studies.

2.24.4.4 In-Pin Fuel Motion

In-pin fuel motion is considered during ULOF due to its potential consequences on reactivity feedback.

With annular pellets, in-pin motion of molten fuel is governed by the same mechanisms as described in [Section 2.24.3.2.2](#) for slow power transients. So, its occurrence mainly depends on injected energy (molten fuel enthalpy and viscosity) and on clad strength (temperature <1200 K). The amplitude of the in-pin fuel motion is mainly limited by the freezing mechanism (bulk freezing at the front); due to

fuel freezing when in contact with colder zones, fertile pellets with a central hole do not allow significant additional in-pin motion. Velocity of the in-pin molten fuel motion (derived from tests) has been evaluated to be of the order $6\text{--}9\text{ m s}^{-1}$ (faster than in slow power transients) and leads to penetration above and below the fuel melting front as shown in [Figure 12](#).

Under fast power transients and when the clad temperature is higher than 1200 K, occurrence of in-pin motion of molten fuel is limited as pin failure occurs before any significant motion of molten fuel (especially if FCMI loading results in failure). When the overpower transient occurs in reactor conditions, the majority of the subassemblies sodium channels are partially or totally voided so that pin failures mostly occur with high clad temperature; the in-pin motion of molten fuel is thus limited and the expected mitigating effect of annular pellet design against reactivity insertion is low and has to be evaluated as a function of pins and core designs.

Another type of in-pin motion has also been evidenced from the data base: the displacement of some intact pellets from the upper and lower parts of the fissile length toward the center with potential

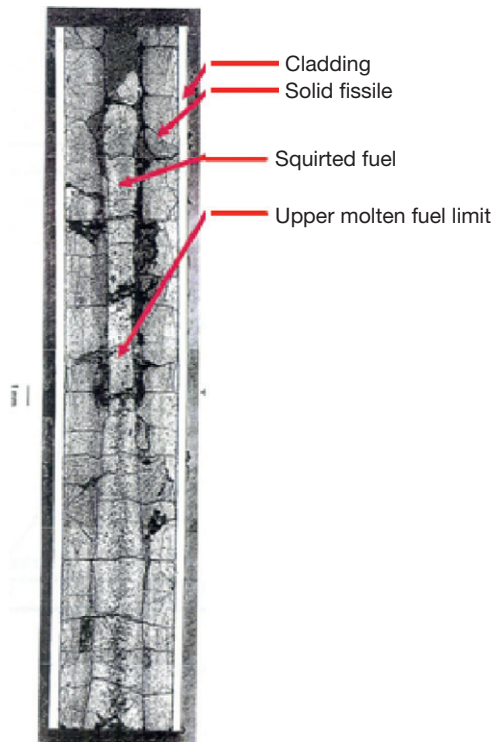


Figure 12 In-pin molten fuel motion in the central hole of annular pellets, due to fast transient overpower (upper part of the fuel pin in CABRI PF2 test, annular pellet). PF2 axial cut: 700–735 mm from bottom of fissile length.

for reactivity insertion in addition to the TOP due to sodium voiding. This phenomenon occurs with solid fuel pellet, at the end of the power transient (after pin failure). Such a motion is driven by the pressure difference between the plena and the disrupted zone and is made possible by the release of the clad constraint on the lower and upper pellets linked to the clad temperature increase at these levels. This stub motion is increased with high burn-up fuel but is, however, limited in amplitude (some centimeters) and velocity ($<1 \text{ m s}^{-1}$) and should not lead to significant increase of reactivity in reactor conditions.

2.24.5 Fuel Behavior as Consequence of a Complete Loss of Coolant in a Subassembly

The hypothetical TIB of a subassembly at nominal power is considered as a bounding case of other subassembly blockage accidents in some reactors studies (see [Section 2.24.2.2.2](#)).

The complete and fast loss of coolant prevents the early accident detection by the usual systems (measurement of the sodium temperature at the outlet of the subassembly, DND). As a consequence, there is no power shut down at the early stage of the accident sequence and the fuel pins are rapidly degraded by overheating with propagation of molten material to the surrounding subassemblies. The main safety concern of TIB is the risk of evolution of the accident toward local critical events and subsequently toward a generalized core melting.

The present knowledge related to this accident sequence, refers to the subassembly blockage studies and to the in-pile SCARABEE experimental program.^{3–5,28–33} In the SCARABEE experiments, the TIB accident was simulated by the rapid closure of an inlet sodium valve in a bundle geometry (19, 37 pins) with fresh fuel pins (fissile length of 0.6 m) at nominal power (average pin power of $35 \times 10^3 \text{ W m}^{-1}$).

2.24.5.1 The Degradation of the Faulted Subassembly

As a consequence of the undercooling of the subassembly, the fuel pin transient evolution is mainly governed by thermal effects with the following rapid scenario as illustrated on [Figure 13](#):

- sodium boiling, clad dry-out, and clad melting at the level of maximum power, in the center of fissile length (absence of forced convection, cosine power profile);
- draining of the molten cladding (sodium vapor velocity is not sufficient for upwards entrainment), formation of a tight steel blockage in the lower cold part and accumulation of liquid steel around intact fuel pellets;
- fuel melting occurrence and mixing with molten steel leading to a local boiling pool that expands over the fissile length with formation of an upper steel blockage.

This degradation phase lasts over 14–16 s assuming nominal power conditions.

It is underlined that as in the ULOF sequence, no significant fuel mass is ejected out of the fissile length, even if small FCIs contribute to the fuel relocation in the upper part. This results in a confined pool with power generation and thus implies high thermal fluxes (value of the order of $15\text{--}20 \times 10^6 \text{ W m}^{-2}$ in a reactor case) toward the external wall (hexagonal stainless steel structure named “hexcan”). These fluxes are maintained at a high level even after power shut

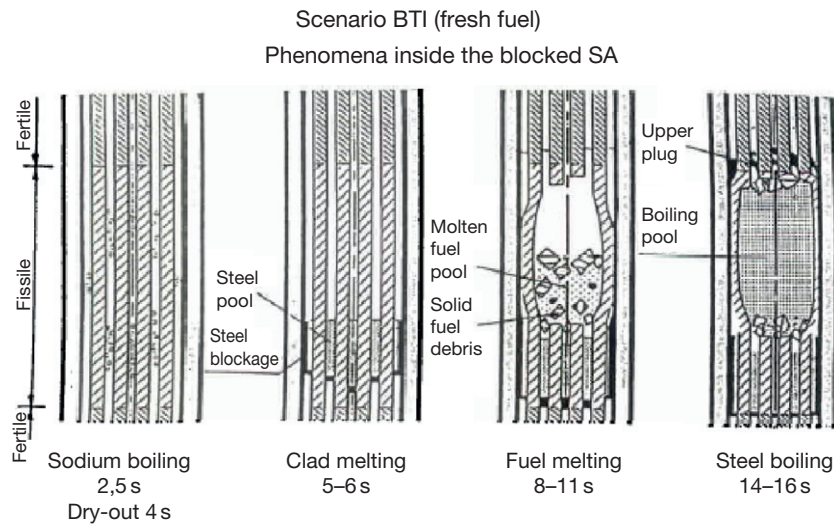


Figure 13 Scenario of the subassembly degradation under total instantaneous inlet blockage accident with fresh fuel, as deduced from posttest examinations of the SCARABEE test series. Reproduced from Kayser, G.; Charpenel, J.; Jamond, C. *Nucl. Sci. Eng.* **1998**, 128, 144–185.

down, with subsequent risk of hexcan melt-through. No significant pressurization of the boiling pool due to steel vapor could be evidenced (under pressure of the order of 0.1 MPa, the steel vapor temperature is closed to fuel melting temperature).

Under the TIB conditions, the impact of irradiation is not well known and the above scenario of degradation might differ with irradiated fuel pins on the following points: improved detection capability (by DND) from the faulted subassembly (i.e., before the propagation of the accident to the surrounding subassemblies), molten pool formation with early mixing of fuel and steel owing to the fuel break-up mode (see [Section 2.24.4.2.2](#)), axial fuel ejection due to high fission gas blow-out after clad melting, high pressurization of the molten materials pool with influence on the propagation phenomena.

The degradation phase and pool formation may also differ in case of use of different oxide fuel element with axial zones of different power levels (as, for instance, with axial heterogeneous fuel column).

2.24.5.2 The Mechanisms of the Hexcan Melt-Through

After the degradation of the fuel pins in the faulted subassembly, the contact of liquid fuel with the hexcan wall (externally cooled by sodium under natural convection in the intersubassembly gap) generates a

fuel crust that acts as a thermal insulating layer between the pool and the hexcan wall (due to low thermal conductivity of the oxide fuel). Inside the molten or boiling pool, the thermal exchanges are governed by natural convection and the presence of steel inside the pool is a major point for the efficiency of the radial heat transfer.

Several mechanisms for the hexcan melt-through were evidenced from the data base:

- thermal erosion of the cooled wall due to steel melting just under the fuel crust; molten steel is then drained away (below or through the cracks of the crust), fuel crust is broken and allows a new contact of liquid fuel with the wall of reduced thickness; this process leads to a rapid erosion of the wall unless an efficient cooling is provided;
- flux disequilibrium between the high heat flux from molten pool and the heat removal from the external cooling of the hexcan;
- mechanical deformation of the hexcan walls due to high temperature and/or to FCI pressure loading, that may lead to a loss of cooling (by the intersubassembly gap);
- jet or projections of molten materials on the wall, as a result of pressure event, may initiate local erosion of the wall.

Whatever the mechanism involved, when a boiling pool exists in reactor conditions, heat fluxes

toward the wall are so high that the hexcan melt-through of both the blocked and neighboring subassemblies will rapidly occur (time delay of 1 s to some seconds).

For future SFRs with new materials anticipated for the subassembly walls, the global mechanical behavior

of the hexcan at high temperature level (above 1400 K) with related loss of mechanical strength has to be further considered due to the potential consequences on the global scenario (creep mechanism and risk of compaction effect).

2.24.5.3 The Propagation of the Molten Materials

The hexcan melt-through initiates the propagation of the molten material⁵ in the intersubassembly gap or in the neighboring subassemblies.

The propagation of molten materials inside the subassembly gap is very limited by the formation of a resistant steel blockage (from the steel wall) that prevents further penetration of the materials (evidenced from the Scarabee PI-A test, [Figure 14](#)).

The melt propagation in the neighboring subassembly (cooled by nominal sodium flow, Scarabee PV-A test, [Figure 15](#)), occurs step by step due to mild FCI events and pressure peaks. These events break the steel accumulation formed on the intact pins (clad under melting) and allow progression of the melt in a symmetrical way inside the neighboring subassemblies with rapid formation of a blockage at the inlet of these subassemblies.

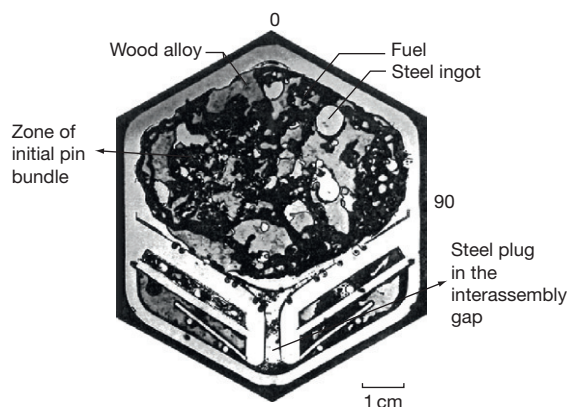


Figure 14 Propagation in the intersubassembly as a result of a total instantaneous inlet blockage accident: experimental simulation in the SCARABEE PI-A test. Reproduced from Kayser, G.; Charpenel, J.; Jamond, C. *Nucl. Sci. Eng.* **1998**, 128, 144–185.

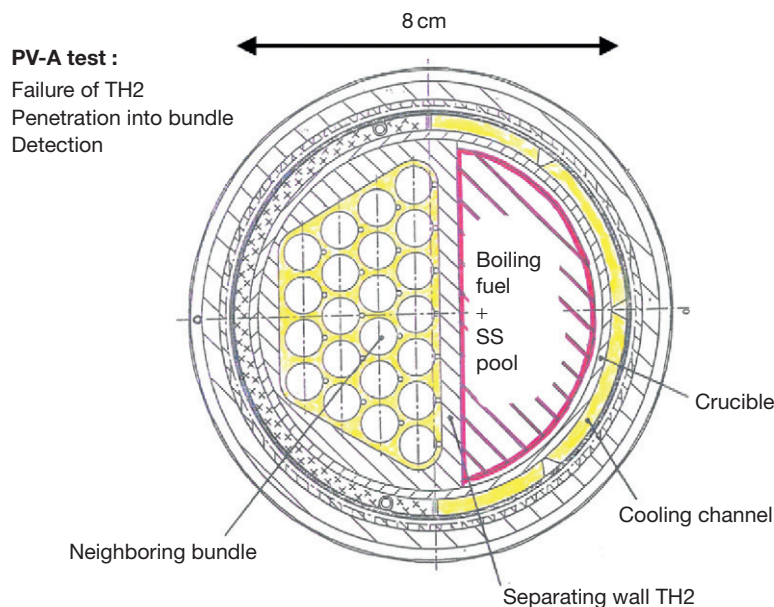


Figure 15 Propagation of a boiling pool in a neighboring subassembly as a result of a total instantaneous inlet blockage accident: experimental simulation in the SCARABEE PV-A test. Reproduced from Kayser, G.; Charpenel, J.; Jamond, C. *Nucl. Sci. Eng.* **1998**, 128, 144–185.

However, neither axial fuel ejection out of the fissile zone nor energetic events due to FCI were evidenced. It is underlined that such propagation conditions are characterized by the emission of a strong delayed neutron signal that corresponds to the first significant and reliable detection capability of the accident in case of fresh fuel.

The identified degradation and propagation mechanisms in the TIB accident with fresh oxide fuel clearly outline that the short-term scenario of the accident is globally governed by thermal effects (a simple modeling could therefore be used for translation to reactor conditions in a first step).

Moreover, as the degradation of the faulted subassembly inevitably leads to the propagation into the neighboring subassemblies, the prevention of further propagation of the accident beyond the six neighboring subassemblies relies on the detection capability (short time response is needed, some seconds, along with efficiency and reliability). For future SFR, attention should be focused on the impact of irradiated fuel on the scenario (not yet addressed), on the mechanical behavior of subassembly walls at high temperature and on the capability for an early detection of the accident.

With regard to the risk of large propagation with potential occurrence of critical events and core melting, long-term behavior also needs to be evaluated. The related phenomenology (molten-boiling pool, propagation) is close to that of the late phase of an ULOF or to the propagation phase of an unprotected CRWA and is described by the SIMMER III tool.^{10,11}

2.24.6 Conclusion

Fuel behavior under transient and accident conditions is a major safety concern for fast reactors in relation with possible fuel melting occurrence and potential risk of prompt-critical events leading to significant mechanical energy release.

The present overview focused on oxide fuel behavior (as the most widely used for SFR up to now) and addressed typical reference scenarios that are considered within the safety assessment such as: slow power transients, ULOF and total blockage of a subassembly.

Thanks to the in-pile experimental data base, reliable knowledge on the phenomena occurring with industrial irradiated fuel pins under various representative transient conditions was provided and allowed a consistent understanding. This past experience

stands as valuable guidelines to orient the innovative aspects of future SFR fuel development toward search for improved safety and reduction of recriticality potential.

The main phenomena have been identified and the influence of the key parameters on fuel accident behavior has been highlighted.

In particular, under slow power transients, low smear density fuel has evidenced a high margin for pin failure but a possible degradation of thermal performance linked to high fission gas retention that underlines the important impact of the burn-up level and of the irradiation history.

Under fast power transients in the ULOF/TOP sequence, the possible mitigating effect of annular fuel with regard to in-pin molten fuel motion and related negative reactivity feedback is not assured; the degradation mechanisms due to the primary power excursion result in a limited fuel discharge that does not prevent for further risk of critical events occurrence.

In a TIB accident, the risk of propagation of the molten materials from the faulted subassembly beyond the surrounding subassemblies highly depends on the efficiency and time response of the detection systems; impact of irradiated fuel and long-term cooling of the degraded zone should be evaluated.

Modeling of fuel transient behavior has been developed for these various transient conditions and provides a reasonable description of the accident scenarios. Such modeling concerns a wide range of phenomena that are intimately coupled together or dealing with degraded geometry: fuel and clad thermomechanical and fission gas transient behavior, failure mechanisms, postfailure events, FCI, molten pools formation and evolution, etc. However, the present modeling suffers from uncertainties that limit predictive capability to other conditions (higher burn-up, other fuel types, etc.). More accurate modeling will be needed in the future, in order to insure that design limits are not overpassed in case of design basis accidents.

Moreover, it is underlined that for future SFR, objectives of improved safety together with performance goals will induce design strategies to limit accident consequences (prevention, mitigation systems) and implementation of high-performance materials and new fuel types. Therefore, such evolution will call for additional knowledge and data base in view of development and validation of the computational tools that are needed for a robust safety approach and assessment.

Acknowledgments

The author is very thankful to Y. Guérin and M. Pelletier from CEA for their thorough review of the manuscript and valuable comments. Deep acknowledgments are also expressed to D. Struwe from KIT (Germany) and to I. Sato from JAEA (Japan), for their detailed review and comments, as long-standing partners of common safety research programs on SFR. Many thanks are also expressed to V. Georgenthum and G. Brillant from IRSN, for their critical review of the manuscript.

References

- Wright, A. E.; Dutt, D. S.; Harrison, L. J. In *Proceedings of the International Fast Reactor Safety Meeting*, Snowbird, UT, Aug 12–16, 1990; American Nuclear Society: La Grange Park, IL, 1990; Vol. II, p 233.
- Thompson, D. H.; et al. SLSF local fault safety experiment P4-summary and conclusions. In *Proceedings of the International Topical Meeting on Fast Reactor Safety*, Knoxville, TN; American Nuclear Society: La Grange Park, IL, 1985; p 129.
- Peppler, W.; Will, H. *Nucl. Eng. Des.* **1988**, *110*, 73.
- Schleisiek, K.; et al. *Nucl. Sci. Eng.* **1998**, *128*, 93–143.
- Kayser, G.; Charpenel, J.; Jamond, C. *Nucl. Sci. Eng.* **1998**, *128*, 144–185.
- Marquie, C.; Nervi, J. C.; Gonnier, C.; Serre, F.; Döderlein, C. SURA: A test facility to investigate the safety of LMFBR and PWR fuels. In *Proceedings of the International Symposium on Research Reactor Utilisation*, Lisbon, Portugal, 1999.
- Baumung, T.; Lumpkin, A. H. Fuel Motion Measurement with the CABRI Hodoscope. In *Proceedings of the International Conference on Science and Technology of Fast Reactor Safety*, Guernsey, UK, May 12–16, 1986; Vol. I, p 141.
- Melis, J. C.; Piron, J. P.; Roche, L. *J. Nucl. Mater.* **1993**, *204*, 188–193.
- Roche, L.; Pelletier, M. Modeling of the thermomechanical and physical processes in FR fuel pins using the Germinal code; IAEA-SM-358/25. In *Proceedings of International Symposium on MOX Fuel Cycle Technologies for Medium and Long-Term Deployment*, Vienna, Austria, May 17–21, 1999.
- Yamano, H.; Tobita, Y.; Fujita, S.; Mashek, W. *Ann. Nucl. Energy* **2009**, *36*, 337–343.
- Maschek, W.; Rineiski, A.; Flad, M.; et al. The SIMMER safety code system and its validation efforts for fast reactor application. In *Proceedings of the PHYSOR 2008*, Interlaken, Switzerland, Sept 14–19, 2008.
- Wigeland, R.; Cahalan, J. Fast reactor fuel type and reactor safety performance. In *Proceedings of Global 2009*, Paris, France, Sept 6–11, 2009.
- Olander, D. R. *Fundamental Aspects of Nuclear Reactor Fuel Elements*; TID-26711-P1. Technical Information Center, Office of Public Affairs, Energy Research and Development Administration, 1976.
- Charpenel, J.; Lemoine, F.; Sato, I.; Struwe, D.; Pfrang, W. *Nucl. Technol.* **2000**, *130*, 252–271.
- Fukano, Y.; Charpenel, J. The adventitious pin failure study under a slow power ramp. In *Proceedings of 12th International Conference on Nuclear Engineering*, Virginia, April 25–29, 2004; CD-Rom.
- Fukano, Y.; Onoda, Y.; Sato, I.; Charpenel, J. Fuel pin behaviour under slow ramp-type transient-overpower conditions in the CABRI-FAST experiments. In *13th International Topical Meeting on Nuclear Reactor Thermal-Hydraulics (NURETH-13)*, Kanazawa City, Ishikawa Prefecture, Japan, Sept 27–Oct 2, 2009.
- Papin, J.; Lemoine, F.; Sato, I.; Struwe, D.; Pfrang, W. Fuel pin behaviour under conditions of control rod withdrawal accident in CABRI-2 experiments. In *Proceedings of International Topical Meeting on Sodium Cooled Fast Reactor Safety*, Obninsk, Russia, Oct 3–7, 1994; Vol. 2, p 134.
- Carbajo, J. J.; Yoder, G. L.; Popov, S. G.; Ivanov, V. K. *J. Nucl. Mater.* **2001**, *299*, 181–198.
- Guérin, Y.; Noirot, J.; Lespiaux, D.; Chaigne, G.; Blanpain, P. Microstructure evolution and in-reactor behavior of MOX fuel. In *International Topical Meeting on Light Water Reactor Fuel Performance*, Park City, UT, Apr 16–13, 2000.
- Lemoine, F.; Cazalis, B.; Rigat, H. The role of fission gases on the high burn-up fuel in reactivity initiated accident conditions. In *10th International Symposium on Thermodynamics of Nuclear Materials*; Halifax, Canada, 2000.
- Cranga, M.; Struwe, D.; Pfrang, W.; Brear, D.; Nonaka, N. In *Proceedings of the International Fast Reactor Safety Meeting*, Snowbird, UT, Aug 12–16, 1990; American Nuclear Society: La Grange Park, IL, 1990; Vol. I, p 421.
- Fukano, Y.; Onoda, Y.; Sato, I. *Nucl. Sci. Technol.* **2010**, *47*(4), 396–410.
- Haessler, M.; Struwe, D.; Butland, A.; Nonaka, N.; Sato, I.; Papin, J. In *Proceedings of the International Fast Reactor Safety Meeting*, Snowbird, UT, Aug 12–16, 1990; American Nuclear Society: La Grange Park, IL, 1990; Vol. II, p 209.
- Sato, I.; Imke, U.; Pfrang, W.; Berne, M. Transient fuel pin behaviour and failure conditions in CABRI-2 in-pile tests. In *Proceedings of International Topical Meeting on Sodium Cooled Fast Reactor Safety*, Obninsk, Russia, Oct 3–7, 1994; Vol. 2, p 134.
- Sato, I.; Lemoine, F.; Struwe, D. *Nucl. Technol.* **2004**, *145*, 115–137.
- Struwe, D.; Pfrang, W.; Cameron, R.; Cranga, M.; Nonaka, N. Fuel pin destruction modes-experimental results and theoretical interpretation of the CABRI-1 Programme. In *Proceedings of the BNES Meeting on Fast Reactor Core and Fuel Structural Behaviour*, Inverness, UK, June 4–6, 1990; p 127.
- Berthoud, G.; Duret, B. The freezing of molten fuel: Reflexions and new results. *Nureth-4*, Karlsruhe, Germany, Oct 10–13, 1989.
- Anzieu, P.; Camaro, P. Y.; Lo Pinto, P. In *Proceedings of the International Fast Reactor Safety Meeting*, Snowbird, UT, Aug 12–16, 1990; American Nuclear Society: La Grange Park, IL, 1990; Vol. IV, p 427.
- Kayser, G.; Berthoud, G. Fuel-coolant interaction in SCARABEE. In *Proceedings of International Conference on Design and Safety of Advanced Nuclear Power Plants*, Tokyo, Japan, Oct 25–29, 1992.
- Livolant, M.; Dadillon, J.; Kayser, G.; Moxon, D. In *Proceedings of the International Fast Reactor Safety Meeting*, Snowbird, UT, Aug 12–16, 1990; American Nuclear Society: La Grange Park, IL, 1990; Vol. II, p 177.
- Papin, J.; Stansfield, R. Thermal-hydraulic behaviour of a fast breeder reactor subassembly during an undercooling

- accident: The PHYSURA-Grappe code and its validation on SCARABEE experiments. In *Proceedings of 4th International Topical Meeting on Nuclear Reactor Thermal-Hydraulics*, Karlsruhe, Germany, Oct 10–13, 1989.
32. Papin, J.; Sesny, R.; Soussan, P.; Mac Dougall, J.; Stansfield, R. The SCARABEE total blockage test series: Synthesis of the interpretation. In *Proceedings of the International Fast Reactor Safety Meeting*, Snowbird, UT, Aug 12–16, 1990; American Nuclear Society: La Grange Park, IL, 1990; Vol. II, p 367.
33. Soussan, P.; Schwarz, M.; Moxon, D.; Berthet, B. Propagation and freezing of molten material-interpretation of experimental results. In *Proceedings of the International Fast Reactor Safety Meeting*, Snowbird, UT, Aug 12–16, 1990; American Nuclear Society: La Grange Park, IL, 1990; Vol. II, p 223.

2.25 Core Concrete Interaction

C. Journeau and P. Piluso

Commissariat à l'Energie Atomique et aux Energies Alternatives, DEN, STRI/LMA, St Paul Lez Durance, France

© 2012 Elsevier Ltd. All rights reserved.

2.25.1	Introduction: Context of MCCI	636
2.25.2	Concrete	637
2.25.2.1	Effects of Heat on Concrete	637
2.25.2.2	Concrete Properties at Elevated Temperatures	638
2.25.3	Corium Material Properties	639
2.25.3.1	Corium Chemical Thermodynamics and Thermophysical Properties	639
2.25.3.1.1	Density	639
2.25.3.1.2	Viscosity	641
2.25.4	Corium–Concrete Interaction	642
2.25.4.1	Major Phenomena	642
2.25.4.1.1	Heat balance	642
2.25.4.1.2	Interface conditions	643
2.25.4.2	Experimental Programs	643
2.25.4.2.1	Early large-scale experiments	643
2.25.4.2.2	Recent large-scale experiments	645
2.25.4.2.3	Analytical experiments	647
2.25.4.3	Remaining Issues	648
2.25.4.3.1	Material effect on ablation shape	648
2.25.4.3.2	Role of metallic layer	649
2.25.5	Applications to Reactor Scales; Orders of Magnitude	650
2.25.5.1	MCCI Codes	650
2.25.5.2	Current LWRs	650
2.25.5.3	EPR™	650
2.25.5.4	VVER 1000: AES 2006	652
2.25.6	Outlook	652
References		652

Abbreviations

ACE	Advanced concrete experiments
ASTEC	Accident Source Term Evaluation Code
CCI	Corium–concrete interaction
EDX	Energy dispersive X-ray spectroscopy
EPR	European Pressurized Reactor
LOCA	Loss of coolant accident
MCCI	Molten core–concrete interaction
OECD	Organization for Economic Cooperation and Development
PWR	Pressurized water reactor
R&D	Research and Development
SARNET	Severe Accident Research NETwork of Excellence
SEM	Scanning electron microscope
TMI	Three Mile Island

VULCANO	Versatile UO ₂ Laboratory for Corium Analysis and Observation
WP	Work package

Symbols

c_p	Specific heat (under constant pressure) (J kg ⁻¹ K ⁻¹)
g	Acceleration due to gravity (m s ⁻²)
h	Heat transfer coefficient (W m ⁻² K ⁻¹)
H	Enthalpy (J kg ⁻¹)
j_G	Superficial gas velocity (m s ⁻¹)
k	Thermal conductivity (W m ⁻¹ K ⁻¹)
L	Pool height (m)
M	Molar mass (kg mol ⁻¹)

P	Pressure (Pa)
q	Power density (W m^{-3})
Q	Activation energy (J/mol)
\dot{Q}	Heat power (W)
R	Perfect gas constant ($8.31 \text{ J mol}^{-1} \text{ K}^{-1}$)
S	Area (m^2)
T	Temperature (K)
v	Ablation rate (m s^{-1})
V	Volume (m^3)
x	Mass fraction
y	Molar fraction
α	Void fraction
$\alpha_{x,y,z}$	Linear thermal expansion along x, y, or z axis (K^{-1})
β	Volumetric thermal expansion (K^{-1})
ϕ	Heat flux (W m^{-2})
η	Dynamic viscosity (Pa s)
κ	Thermal diffusivity ($\text{m}^2 \text{ s}^{-1}$)
ν	Kinematic viscosity ($=\eta/\rho$) ($\text{m}^2 \text{ s}^{-1}$)
ρ	Density (kg m^{-3})
σ	Surface tension (N m^{-1})
Fr	Froude number $Fr = j_G/gL$
Nu	Nusselt number $Nu = qL/k\Delta T$
Pr	Prandtl number $Pr = \nu/\kappa = c_p\eta/k$
Re	Reynolds number $Re = Lj_G/\nu$
St	Stanton number $St = h/\rho c_p j_G$

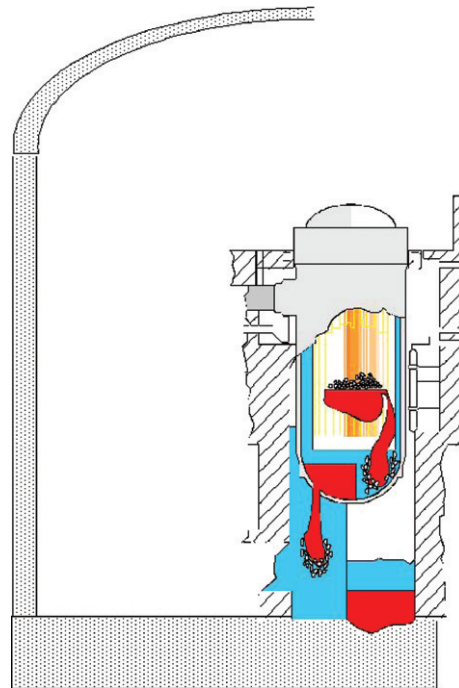


Figure 1 Scheme of a LWR severe accident progression, from core melting to vessel melt-through and molten core–concrete interaction © CEA, 1995; left side, scenario with water flooding (in blue); right side, dry scenario.

2.25.1 Introduction: Context of MCCI

In the case of a severe accident, the reactor core could melt and form a molten mixture of fuel material, partially or totally oxidized cladding, nonvolatized fission products, and various structural materials. This mixture is called *corium*. In a typical commercial pressurized water reactor (PWR), up to about 100–150 t of oxides (UO_2 , ZrO_2 , etc.) and 30–80 t of metal could melt. As corium is subject to decay heat power (30 MW initially diminishing down to 10 MW after 10 days), it may eventually melt through the reactor vessel and relocate in the reactor cavity. For a 6-m-diameter cavity, this leads to a melt height of the order of 1 m (Figure 1). The cavity concrete is part of the third and last containment barrier, and there is thus a potential for concrete erosion leading to basemat penetration. Although it could not lead to massive release rates, it would be directly responsible for fission product release to the environment. In advanced concepts such as EPRTM,¹ the molten core would interact with sacrificial concrete during the temporary retention in the reactor pit.

Molten core–concrete interaction (MCCI) is controlled by an imposed power (the decay heat mainly generated in the oxidic phase), not by an imposed temperature. If heat removal is not sufficient, the temperature of the melt will increase until melting or dissolution of adjacent structures, precluding the long-term retention by refractory materials in the absence of sufficient heat extraction.

Without additional measures, concrete melt-through may occur, after a period depending on basemat thickness. Further, the release of steam and concrete decomposition gases increases the containment pressure. MCCI is characterized by the coupling of several phenomena: high-temperature concrete behavior, bubbling corium pool thermal hydraulics, and physicochemistry of corium melts.

In the first section of this chapter, concrete high-temperature characteristics are discussed, and then the properties of corium are presented. This leads to the study of their interaction, its modeling, and a glance at the major experimental results on this issue. Finally, some results and orders of magnitudes are presented for different reactor designs.

2.25.2 Concrete

The major constituents of concrete are Portland cement, aggregates, and water. When mixed together, the cement reacts with water to form a binder that holds the aggregates together.² Lime and silica make up about 85% of the cement mass. Typical nuclear reactor basement concretes are made of aggregates mainly made of variable proportions of silica (SiO₂) and limestone (CaCO₃). **Table 1(a)** summarizes the proportion of the different constituents of concrete. **Table 1(b)** lists the overall chemical composition of some typical concretes. There is usually 6–7 wt% of steel bars in the concrete structure which is a supplementary source of metal in the long-term MCCI.

2.25.2.1 Effects of Heat on Concrete

Several authors^{9–11} have described the reactions that occur with an increase of temperature in cement paste and concrete:

- 30–105 °C: the evaporable water and part of the bound water escape. It is generally considered that the evaporable water is completely eliminated at 120 °C.
- 110–170 °C: the decomposition of gypsum with a double endothermic reaction, the decomposition of ettringite, and the loss of water from part of the carboaluminate hydrates take place.
- 180–300 °C: the loss of bound water from the first stage of decomposition of the C–S–H and carboaluminate hydrates takes place. (In concrete sciences, C stands for CaO, S for SiO₂, A for Al₂O₃, and H for H₂O.) A special type of concrete that is used in plants of Russian design to shield the radiation in the lower cavity is fabricated with serpentine aggregates. Serpentine is a mineral of the composition (MgO)₆·(SiO₂)₄·(H₂O)₄ with a substantial content of crystal water. Also this water is released during heat-up of the concrete and increases the steam rate through the melt and the potential hydrogen release.
- From 300 °C: increase in porosity and microcracking.

Table 1 Typical concrete compositions

(a) Order of magnitude of concrete constituent proportions

Constituents	Water			Air	Cement	Aggregates		
	Total	Evaporable ^a	Chemically bound ^b			Total	Sand ^c	Gravel ^d
vol%	14–22			1–6	7–14	60–78	25–45	25–45
wt%	5–9	2.5–7	1.5–4	0	9–18	65–85	30–45	30–45

(b) Chemical composition (wt%) of some typical reactor pit concretes (sum may be lower than 100% due to the presence of minor species)

	Siliceous concrete ^e	Basaltic concrete ^f	Silica-rich concrete ^g	Silico-calcareous concrete ^h	Limestone concrete ^e	EPR sacrificial concrete ⁱ
SiO ₂	69%	56%	63%	26%	7%	43%
CaO	13%	16%	16%	42%	43%	11%
Al ₂ O ₃	4%	10%	5%	2%	2%	4%
Fe ₂ O ₃	1%	3%	–	–	1%	35%
CO ₂	4%	3%	9%	25%	34%	2%
H ₂ O	4%	7%	3%	4%	6%	5%

From CIMbéton. Les bétons: Formulation, fabrication et mise en œuvre. *Technical Document of the Centre d'Information sur le ciment et ses applications*; CIMbéton: Paris-La Défense, 2006.

^aEvaporable water consists of free and physically bound (adsorbed) water. It is defined as the water released after drying in a furnace at 105 °C.³

^bChemically bound water is forming hydrates which are stable at 105 °C, mainly tobermorite gel $\sim(\text{CaO})_{1.62}\text{SiO}_2(\text{H}_2\text{O})_{1.5}$ and calcium hydroxide $\text{Ca}(\text{OH})_2$.³

^cSand (or fine aggregate) is generally defined as aggregate with a size lower than 4.75 mm corresponding to No. 4 sieve.²

^dGravel (coarse aggregate) are larger than 4.75 mm and seldom beyond 25–40 mm.²

^eRoche *et al.*⁴

^fShin *et al.*⁵ Yonggwang power plant concrete.

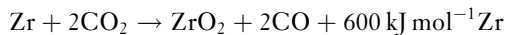
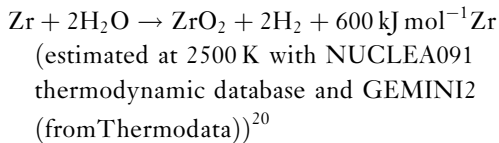
^gJourneau *et al.*^{6,7} concrete F.

^hJourneau *et al.*^{6,7} concrete G.

ⁱNie.⁸

- 374 °C: critical point of water above which no free water is possible.
- 450–550 °C: dehydroxylation of the portlandite.
- The EUROCODE¹² proposes to consider for simplified calculations that concrete above 500 °C has no mechanical strength.
- 573 °C: $\alpha \rightarrow \beta$ transformation of quartz aggregates.
- 700–900 °C: decarbonation of calcium carbonate in cement paste and carbonate aggregates.
- 720 °C: second stage of decomposition of C–S–H.
- From 1100 to 1250 °C: start of concrete melting (solidus temperature) for some phases.

Carbon dioxide and steam percolating through the corium melt will oxidize the metal fractions of the melt basically in the sequence Zr, Cr, Fe. The oxidation of Zr and Cr is a highly exothermic process that contributes to significant energy release in the melt.



The resulting gases are H₂ and CO that accumulate in the containment and may lead to flammable gas concentrations.

It is essential to note that decomposition of concrete by the thermal attack of the high-temperature corium melt is reasonably described as a melting process with simultaneous gas release.

2.25.2.2 Concrete Properties at Elevated Temperatures

Concrete density is generally around 2000–2500 kg m⁻³. During the concrete heating, its thermal properties change, mainly due to drying and decompositions.⁷ Figure 2 presents the thermal conductivity against temperature for some concretes⁵ and the EUROCODE 2¹² reference values for limestone or siliceous concretes. Concrete thermal conductivity significantly decreases with temperature.

Concretes can have a compressive strength ranging from 30 to 150 MPa depending on the nature of cement and aggregates. The EUROCODE 2¹² recommends considering a reduction of the concrete by 50% when heated at temperatures around 600 °C. Concrete loses 80% of its strength at temperatures around 800 °C; similarly at 1100 °C, it loses more than 98%.

The specific heat of concrete lies between 900 J kg⁻¹ K⁻¹ (at room temperature) and 1100 J kg⁻¹ K⁻¹ (above 400 °C). Around 100 °C, the effect of water vaporization must be considered. The EUROCODE 2 proposes to increase the specific heat of concrete between 115 and 200 °C from 900 to 1470 or 2020 J kg⁻¹ K⁻¹ for evaporable water fractions of, respectively, 1.5 and 3 wt%.

The decomposition enthalpy to bring concrete from room temperature to total melting is generally between 1.8 and 2.5 MJ kg⁻¹. Roche *et al.*⁴ have measured solidus and liquidus temperatures for several types of concretes (Table 2).

Even if concrete is a complex material without a defined melting temperature, an effective ablation

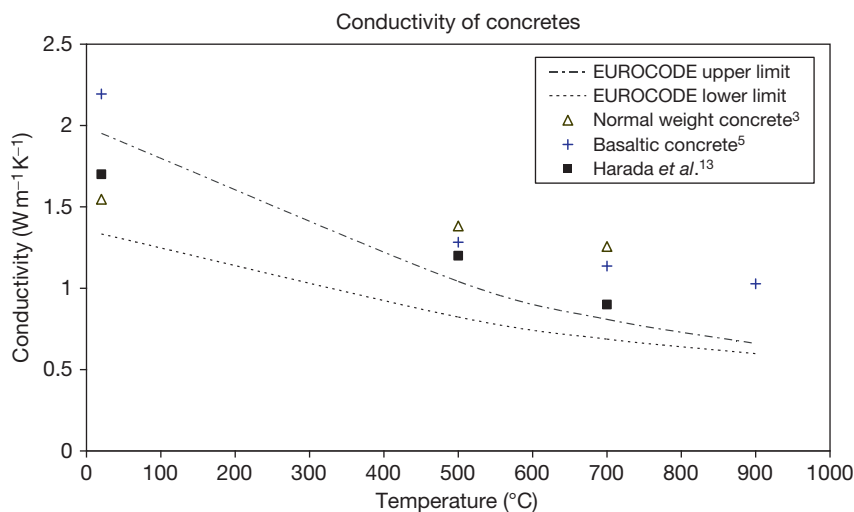


Figure 2 Concrete thermal conductivity variation as a function of temperature. EUROCODE 2¹² recommended values versus experimental data.

Table 2 Solidus and liquidus temperatures for some typical concretes

	Siliceous	Lime-siliceous	Calcareous
Solidus temperature	1130 °C	1120 °C	1220 °C
Liquidus temperature	1250 °C	1295 °C	2305 °C

Source: Roche, M. F.; Leibowitz, L.; Fink, J. K.; Baker, L., Jr. *Solidus and Liquidus Temperatures of Core-Concrete Mixtures*; U.S. Nuclear Regulatory Commission Report NUREG/CR-6032, Argonne National Laboratory Report ANL-93/9; 1993.

or degradation temperature is generally used to model the heating and ablation of concrete.

- EUROCODE¹² recommends for simplified mechanical calculations considering that concrete loses its mechanical strength at 500 °C.
- After dismounting an MCCI experiment, the position of the remaining structural concrete lies usually close to the 800 °C isotherm at the end of the test.^{6,7}
- If the formation of a liquid concrete layer is considered as the reference transition, then the effective melting temperature generally corresponds to the temperature at which 30–50 vol% is liquid. This is close to the melt escape threshold determined for the flow of magma out of a heated matrix by Vignerresse *et al.*¹⁴ at around 25 vol%. For siliceous concrete, this threshold is around 1200 °C whereas it can lie between 1400 and 1750 °C for silica–limestone concretes. To provide an order of magnitude, it requires 2 MJ kg⁻¹ to heat a typical siliceous concrete from room to melting temperature, while 2.5 MJ kg⁻¹ is needed for a limestone-rich concrete. This higher value is both due to the decarbonation latent heat and the higher effective melting temperature.

2.25.3 Corium Material Properties

Corium is a molten mixture of fuel material, partially or totally oxidized cladding, nonvolatized fission products, and various structural materials. In Three Mile Island 2 (TMI-2) accident, a corium with the following average composition was found in the vessel lower head¹⁵:

77 wt% UO₂, 17% ZrO₂, 2% Ag, 1% Fe,
1% Cr, 1% Ni, 1% In

The main constituents of in-vessel corium are UO₂, ZrO₂, Zr, and steel. The molar U/Zr ratio can vary

from 0.65 in US Boiling Water Reactor and Russian-made Vodo-Vodyanoi Energetichesky Reactor (VVER) (Water-moderated, water-cooled energetic reactor), to 1.64 in a US PWR like Zion.¹⁶ This ratio is 1.24 for EPR,⁸ 1.37 for TMI-2 PWR, and 1.52 for a French 900 MWe PWR.¹⁷ The amount of molten steel varies greatly, depending on scenarios. It can exceed 100 t (for up to 175 t of oxides) in EPR, in which there is a heavy reflector.⁸

As the concrete decomposition products are miscible with corium oxides, during its interaction with concrete, the melt will be continuously enriched in concrete decomposition products (mainly CaO and SiO₂). If several meters of basemat are eroded, silica and/or calcia can become the major constituents of the melt, as it occurred during Chernobyl accident, with a typical melt composition of the so-called ‘brown-chocolate’¹⁸ corium, in which concrete and mineral protective materials are mixed:

8 wt% UO₂, 6% ZrO₂, 57% SiO₂, 11% Al₂O₃,
6% CaO, 6% MgO, 5% Na₂O, 1% Fe₂O₃

It is thus clear that there is not a unique corium composition but a continuum of possible compositions depending on the reactor, the accident scenario, and the instant in this scenario. Therefore, it is not possible to measure the corium properties for every case and models have to be derived in order to estimate both its thermodynamic and thermophysical properties.

2.25.3.1 Corium Chemical Thermodynamics and Thermophysical Properties

Dedicated thermodynamic databases^{19–22} have been developed and are coupled with Gibbs energy minimizers in order to estimate the phases present at equilibrium for any corium composition and temperature.

UO₂ melting point is at 3120 ± 30 K.²³ This value can only be applied to nonirradiated fuel. The minimum liquidus temperature in the UO₂–ZrO₂ system is 2840 K.²⁴ When concrete is mixed with corium, the solidus temperature is lowered to about 1400 K (Figure 3). The solidification range spans over more than 1000 K for most of corium–concrete mixtures, which facilitates corium spreading.²⁵

2.25.3.1.1 Density

Three properties are linked by the following equations:

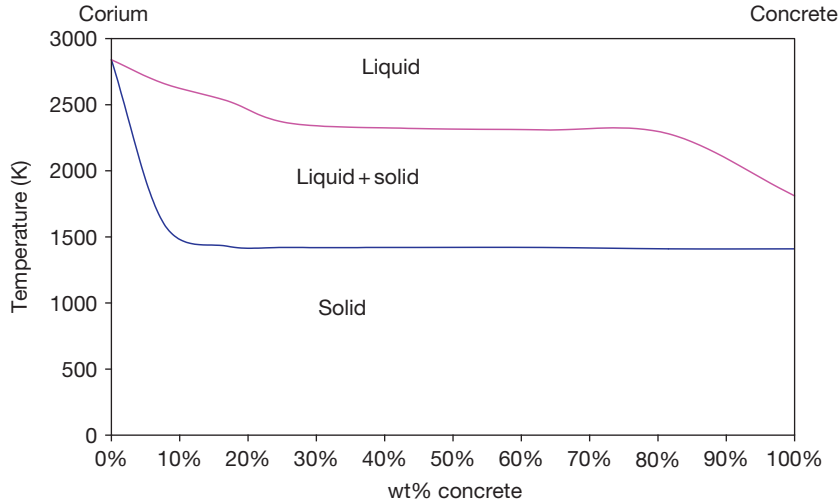


Figure 3 Typical corium–concrete pseudobinary phase diagram calculated with GEMINI2 and NUCLEA07 (for the silica-rich concrete used in Versatile UO₂ Laboratory for Corium Analysis and Observation tests). Adapted from Journeau, C.; Piluso, P.; Haquet, J. F.; *et al. Ann. Nucl. Energ.* **2009**, 36, 1597–1613; Journeau, C.; Bonnet, J. M.; Ferry, L.; Haquet, J. F.; Piluso, P. In *Proceedings of ICAPP'09 International Conference on Advances in Nuclear Power Plants*, Tokyo, Japan, May 10–14, 2009; Atomic Energy Society of Japan: Tokyo, 2009; Paper 9068.

- The molar volume V_{molar} is the volume occupied by 1 mol of the species (note that it depends on the definition of the species, for example, 1 mol of FeO_{1.5} occupies half the volume of 1 mol of Fe₂O₃).

$$V_{\text{molar}} = \frac{M}{\rho} \quad [1]$$

- The coefficient of volume expansion is defined as the ratio of the temperature derivative of the molar volume to the molar volume.

$$\alpha_V = \frac{1}{V_{\text{molar}}} \left(\frac{\partial V_{\text{molar}}}{\partial T} \right) \quad [2]$$

Volume expansion is the driving force for natural convection. Therefore, a good knowledge of this derivative is necessary.

- The linear thermal expansion α in the x , y , z directions is related to the coefficient of volume expansion by

$$\left(1 + \int \alpha_x dT \right) \left(1 + \int \alpha_y dT \right) \left(1 + \int \alpha_z dT \right) = 1 + \int \alpha_V dT \quad [3]$$

For solutions (either solid or liquid), the independence of partial molar volumes of each constituent from bulk composition and ideal mixing is assumed. Nelson and Carmichael²⁶ verified on silicate liquids

that the above assumption could lead to errors of the order of 1% or less. Harmathy³ adopted this approach for solid concrete. This has been promoted also for metallic alloys with errors of <4%,²⁷ even if some metallic alloys are nonideal²⁸ such as Na–Pb, Na–Bi, Na–In, and Fe–Si. Nevertheless, in the absence of pertinent data, the excess volumes are assumed to be negligible.

Neglecting excess volumes, the volume of 1 mol of solution is given by

$$V = \sum_i y_i V_i \quad [4]$$

where y_i is the molar fraction of species i (having a ‘partial’ molar volume V_i and a molar mass M_i) in the solution.

The density of the solution is then given by

$$\rho = \frac{\sum_i y_i M_i}{\sum_i y_i V_i} \quad [5]$$

The value of density or molar volume, which must be taken for a liquid component in mixtures that are liquids at temperatures below the melting temperature of the pure component, is an important factor. For the density calculations, we recommend that the expansion coefficient be taken as a constant below the melting point.

For a mixture of different condensed phases (liquid(s) and solid solutions), the following mixing

Table 3 Densities (at room temperature) of main corium–concrete melt constituents

Constituent	Density ($\times 1000 \text{ kg m}^{-3}$)
UO ₂	10.97
ZrO ₂	5.68
CaO	3.34
SiO ₂	2.64
Fe	7.87

Source: Lide, D. R. *CRC Handbook of Chemistry and Physics*, 2002–2003; CRC Press: Boca Raton, FL, 2002.

law is used. The volume of 1 mol of a mixture made of phases having molar fractions x_j and molar volumes V_j is given by

$$V = \sum_j x_j V_j \quad [6]$$

The major effect of gas presence (as above a heated concrete cavity), is an increase in the global molar volume. If the volume fraction of gases is α and the density of the condensed phases is $\rho_{\text{condensed}}$, then the global density, after taking the void fraction into account, is

$$\rho_{\text{global}} = (1 - \alpha)\rho_{\text{condensed}} \quad [7]$$

Table 3 indicates the densities at room temperature of several constituents of corium–concrete mixtures in order to present orders of magnitude. The temperature evolution of the density of solid or liquid UO₂ has been assessed by Fink and Petri.²³

At the beginning of the interaction, the oxidic melt is slightly heavier than steel. As it assimilates concrete decomposition products, its density decreases so that it eventually becomes lighter than steel.

2.25.3.1.2 Viscosity

2.25.3.1.2.1 Viscosity of nonsilicate liquid phases

For corium with <5% mole of silica, that is, before significant interaction with concrete,²⁹ the viscosity recommended using the Andrade³⁰ relationship is

$$\eta = K \frac{(MT_m)^{1/2}}{V^{2/3}} \exp \left[\frac{Q}{R} \left(\frac{1}{T} - \frac{1}{T_m} \right) \right] \quad [8]$$

where the coefficient K recommended for corium is the value proposed by Nazaré *et al.*,³¹ T_m is the melting temperature, M is the molar mass, and V the molar volume. The activation energies Q are 35 kJ mol⁻¹ for UO₂ and 247 kJ mol⁻¹ for ZrO₂, according to Sudreau and Cognet.²⁹ For the other materials, the following³¹ empirical relationship is recommended (although it was derived for metals):

$$Q \sim 1.8 T_m^{1.348} \quad [9]$$

Sudreau and Cognet²⁹ validated this approach against experimental data obtained from the RASPLAV project.³²

To provide orders of magnitude, the kinematic viscosity of a 62 mol% UO₂–38 mol% ZrO₂ melt at 2700 °C is around $5 \times 10^{-7} \text{ m}^2 \text{ s}^{-1}$.

2.25.3.1.2.2 Viscosity of silicate liquid phase

For silicate melts, the presence of silicate chains significantly increases the viscosity. Andrade³⁰ model is no more valid and we recommend the approach of Urbain,³³ which has been extended to corium by Ramacciotti *et al.*³⁴

The viscosity is described by the Weymann relationship:

$$\eta = 0.1AT \exp(1000B/T) \quad [10]$$

where A and B are linked by the empirical relationship

$$-\ln A = 0.29B + 11.57 \quad [11]$$

The molten silicate melt constituents are divided into three families:

- glass formers (SiO₂ and complex silicate molecules),
- modifiers (CaO, MgO, FeO, U_{1/2}O, Zr_{1/2}O) which break the glass-forming bridges reducing the melt viscosity,
- amphoteric (Al₂O₃, Fe₂O₃) which can have either behavior depending on the melt overall composition.

The parameter B in eqn [10] is obtained from the molar fractions of glass formers and modifiers. (The molar fraction of amphoteric is linked to these two molar fractions, as the sum of glass formers, modifiers, and amphoteric equals 100%.) Ramacciotti *et al.*³⁴ validated this approach against experimental data both without and with uranium dioxide.

To provide an order of magnitude, analysis by Ramacciotti³⁵ of experimental measurements of a 50% corium – 50% silica-rich concrete melt by Skoutajan *et al.*³⁶ gives a kinematic viscosity at liquidus (~ 1800 °C) of the order of $10^{-5} \text{ m}^2 \text{ s}^{-1}$.

2.25.3.1.2.3 Viscosity of bubbly flows

Another phenomenon of interest is an emulsion of gas bubbles in corium. In this case, we recommend the following³⁷ relationship established for stationary flows:

$$\eta = \eta_0(1 + 9\alpha) \quad [12]$$

where α is the void fraction and η_0 is the viscosity of the bubble-free liquid.

2.25.3.1.2.4 Viscosity of solidifying melts

In the case of a solidifying melt, we recommend the use of Ramacciotti *et al.*³⁴ correlation:

$$\eta = \eta_{\text{liquid}} e^{2.5C\phi} \quad [13]$$

where η_{liquid} is the liquid phase viscosity, ϕ the solid volume fraction, and C is an empirical parameter, usually between 4 and 8.

2.25.4 Corium–Concrete Interaction

2.25.4.1 Major Phenomena

MCCI has a highly complex phenomenology coupling concrete high-temperature behavior, molten pool thermal hydraulics, thermochemistry, mechanics, etc.

The corium contacts concrete at an initial temperature higher than 2400 °C. The first instants of MCCI are controlled by the melt overhear which heats the concrete, leading to the liberation of steam and carbon dioxide and to the initial melting of concrete. Concrete decomposition bubbles will enter the corium pool, agitate it and, when available, oxidize the metal components of corium: first zirconium, then steel. After this initial transient, lasting from 10 min to a few hours depending on reactors and scenarios, the main source of heat will be the decay heat, which is mainly (>90%) generated in the oxide phase. The decay heat can be approximated³⁸ by

$$\frac{P}{P^0} \approx \frac{0.13}{t^{0.283}} - \frac{0.266}{(t + t^0)^{0.335}} \quad [14]$$

where P^0 is the operating reactor power, t^0 is the time at power before the accident (in s), and t is the time after accident (in s).

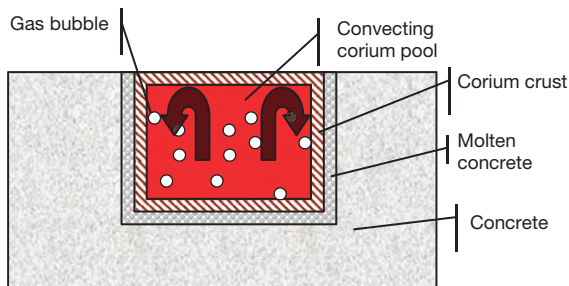


Figure 4 Schematic view of a corium pool interacting with concrete.

Figure 4 presents a simplified view of MCCI. Under the gas agitation, convection in the corium pool transfers heat to the concrete. As the interface temperature is usually above the concrete solidus and below or at the corium composition liquidus, there is simultaneous formation of a corium crust and melting of a concrete layer. This concrete crust is either porous and allows the permeation of gases or periodically destroyed (both by pressure buildup and by heating due to the insulating effect of gases) and formed.³⁹

Concrete ablation is globally controlled by thermal processes: the ablation rate is, on average, equal to the ratio of the heat flux at a given boundary to the heat needed to melt a unit volume of concrete.

$$v = \frac{\phi}{\rho(H_{\text{concrete melting}} - H_0)} \quad [15]$$

where v is the ablation rate (in m s^{-1}), ϕ the heat flux (in W m^{-2}), ρ the solid concrete density (in kg m^{-3}), $H_{\text{concrete melting}}$ the enthalpy (in J kg^{-1}) at the ‘concrete melting’ temperature, and H_0 the enthalpy at room temperature. This approximate approach is valid as conduction in concrete is so low that ablation front generally progresses at least as quickly as the conduction heat wave; thus, conductive heat losses are negligible at the first order. Spalling – breaking off of layers or pieces of concrete from a concrete surface exposed to high heat fluxes¹⁰ – plays a minor role in MCCI.⁴⁰

2.25.4.1.1 Heat balance

The heat transfer mechanisms are strongly dependent on the (varying) compositions of the melt and concrete. The heat flux ϕ_i through a given interface i is given by

$$\phi_i = b_i(T_{\text{pool}} - T_i) \quad [16]$$

where b_i is the convective heat transfer coefficient (mixed convection due to the sparging gases) and T_i is the interface temperature for the considered boundary.

The closure of this system of equations is given by the global conservation of energy:

$$\sum \phi_i S_i = \dot{Q} \quad [17]$$

Table 4 lists the most used correlations for the heat transfer to the pool walls. It must be noted that, while these correlations provide close results in water simulant experiments, their results tend to spread widely for corium conditions.

Table 4 Heat transfer correlations usually used for MCCI

Name	Correlation
BALI ⁴¹	$Nu = 19.67 \left(\frac{\rho_{\text{melt}} j_G^3}{\mu_{\text{melt}} g} \right)^{0.136} Pr_{\text{melt}}^{-0.22} \quad \text{downward}$ $Nu = 24.75 \left(\frac{\rho_{\text{melt}} j_G^3}{\mu_{\text{melt}} g} \right)^{0.073} Pr_{\text{melt}}^{-0.29} \quad \text{upward}$
Blottner	$Nu = 0.31 \left[\frac{gL^3}{\nu k} \left(\beta \Delta T + \alpha \frac{\Delta \rho}{\rho_0} \right) \right]^{1/3}$
Deckwer	$St = 0.1 (Re Fr Pr^2)^{-0.25} \text{ or } h = 0.1 k^{0.5} \rho^{0.75} c_p^{0.5} \mu^{-0.25} g^{0.25} j_G^{0.25}$
Kutateladze–Malenkov	$h = \frac{3 \times 10^{-5} k}{\sqrt{\frac{\sigma}{g \Delta \rho}} \sqrt{\frac{j_G \mu}{\sigma}}} \left(\frac{c_p P j_G}{kg} \right)^{2/3} \quad \text{when } 4 \times 10^{-4} < j_G \mu / \sigma < 10^{-2}$ $h = \frac{3 \times 10^{-4} k}{\sqrt{\frac{\sigma}{g \Delta \rho}}} \left(\frac{c_p P j_G}{kg} \right)^{2/3} \quad \text{when } j_G \mu / \sigma > 10^{-2}$

2.25.4.1.2 Interface conditions

Two main families of models have been proposed depending on the assumed interface condition at the melt periphery.

In the classical models, the boundary condition is assumed to be at the melt solidus temperature or a so-called ‘softening temperature,’⁴² or the concrete ‘melting temperature.’⁴³ The pool is then divided into a central liquid core and a ‘mushy zone’ in which the solid fraction concentration decreases with temperature. In order to take into account the fact that partial solidification near the interface increases the local equivalent viscosity,⁴⁴ it is proposed to take into account the effect of viscosity in this ‘mushy layer’ by reducing the bulk-fluid Nusselt number Nu_0 according to the following correlation:

$$Nu = Nu_0 \left[0.645 \left(\frac{\eta_{\text{interface}}}{\eta_{\text{bulk}}} \right)^n + 0.356 \right] \quad [18]$$

where n is an empirical parameter, fitted to $n = -14$ in the advanced concrete experiments (ACE) tests by Foit and Miossaedov.⁴⁵

In another modeling approach proposed by Seiler and Froment,³⁹ called the phase segregation model, the boundary temperature that has to be taken into account is the liquid pool liquidus temperature. There can be as much as 1000 K between liquidus and solidus in core–concrete mixtures. This is the case if thermodynamic quasisteady state is assumed. Under this assumption, the melted most refractory species (usually a solid solution mainly constituted of UO_2 and ZrO_2) are deposited at the concrete walls and the rest of the corium is devoid of solid particles. The melt pool composition continuously evolves during the MCCI, because of the introduction of molten concrete material and the solidification at the boundaries. This causes the evolution of the pool liquidus

temperature, that is the interface condition. As, in this approach, the whole pool is liquid (and thus has a relatively low viscosity), the heat transfer coefficient is large and the temperature difference ($T_{\text{pool}} - T_i$) is small – typically < 30 K, the pool temperature globally follows the liquidus curve. The TOLBIAC-ICB code⁴⁶ is on the basis of this phase segregation model.

Some variants of this approach have been proposed by Nie⁸ and Cranga *et al.*⁴⁷ In the Accident Source Term Evaluation Code (ASTEC)/MEDICIS code, the interface temperature can be set by user anywhere in the solidification range. Cranga *et al.*⁴⁸ have determined that interface temperatures between $(0.9 T_{\text{liquidus}} + 0.1 T_{\text{solidus}})$ and $(0.6 T_{\text{liquidus}} + 0.4 T_{\text{solidus}})$ provide the best fit with 2D MCCI experiments with prototypic materials. These temperatures correspond to solid mass fractions between 10 and 60 wt% according to thermodynamic phase equilibria calculation.^{6,7}

2.25.4.2 Experimental Programs

MCCI is characterized by intense coupling of many complex phenomena. Identification and quantification of these phenomena with respect to their importance for accident analysis require an iterative process of integral experiments, analytical experiments with simulants, and development of models and their verification. Finally, their integration into sophisticated computer codes should allow predictions for the course of a postulated severe accident in a typical light water reactor (LWR) application.

2.25.4.2.1 Early large-scale experiments

Table 5 summarizes the major experiments that were conducted in the early days of MCCI research, either with simulant oxides or prototypic UO_2 -containing melts. Most of the experiments used an electrical

Table 5 Early MCCI experiments

Program	Laboratory	Corium	Concrete	Scale (pool volume)	Geometry	Parameters
BETA ⁴⁹	FZ Karlsruhe (Germany)	Simulant (Al ₂ O ₃ + CaO + Fe)	Siliceous, limestone	~100l	2D	Decay power Melt mass 60–120 min
ACE ⁵⁰	Argonne National Laboratory (USA)	Oxide	Siliceous, limestone, limestone– common sand	40l	1D	Decay power Corium composition 30–120 min
SURC ^{51–54}	Sandia National Laboratories (USA)	Oxide (including some Zr and FPs)	Siliceous, limestone	~25l	1D	120–180 min Aerosol release
WETCOR ⁹¹	Sandia National Laboratories (USA)	Alumina based simulant	Limestone–common sand	15l	1D	Overlying water pool 120 min
MACE ⁵⁵	Argonne National Laboratory (USA)	Oxide	Siliceous, limestone– common sand	75–300l	1D	Mass, composition Up to 7 h 45 ablation Water over melt

heating technique to simulate the internal decay heat and to allow studies of long-term behavior, either induction heating when a metal melt was present, or direct resistance heating in case of pure oxidic melts. Except for the Betonschmelz Anlage (BETA) (Concrete melting facility at Karlsruhe Nuclear Research Centre, Germany) experiments with simulant melts, all of these were devoted to 1D geometries.

Alsmeyer *et al.*⁴⁹ gave an overview of these tests and their use in code development and application. The tests showed that thermal ablation was the major process governing MCCI: the ablation rate is, at the first order, the ratio of the heat flux to the enthalpy needed to heat and melt a unit volume of concrete (eqn [15]).

All experiments showed the strong release of gases bubbling through the melt and generating a well-stirred melt pool. After a first intense period of interaction upon melt release, controlled by the initial melt overheat and the chemical oxidation processes, the typical long time erosion rates are of several centimeters per hour. The 2D BETA experiments showed pronounced axial erosion through the *metal* phase, depending on the power generated in the metallic melt. This result must not be directly applied to the *oxidic* melt behavior but requires careful consideration of the fact that heat was provided in the metal and of the different transport properties of the oxide.

The gas release is higher for limestone concrete – because of the decomposition of CaCO₃ – than for

siliceous concrete and is linked to the ablation rate. A substantial fraction of carbon dioxide and steam percolating through the corium melt oxidizes the metal fractions in the melt basically in the sequence Zr, Si, Cr, Fe. Oxidation of Zr and Cr is a highly exothermic process that contributes in the initial interaction phase to significant energy release in the melt (obtained from the endothermal reduction of SiO₂ by Zr). The resulting gases are H₂ and CO, which may accumulate in the containment to flammable concentrations. Contribution of released gases during MCCI to the reactor containment pressurization is considerable: their accumulation would lead to a pressure increase of around 3 bars in the case of a siliceous concrete and of around 5 bars in the case of a limestone–sand concrete. The gas production, which in the long-term is determined mainly by the corium decay power, is not very sensitive to MCCI modeling uncertainties.

The ACE/MACE (melt attack and coolability experiments; at Argonne National Laboratory, USA) tests also provided information on the aerosol release by mainly oxidic corium (including in some tests metallic inserts) during the interaction: only a small fraction is released, especially above siliceous concretes.

In some tests, eruptions have been observed that formed debris piles like volcanoes. Ejection through orifices in the crust can be an efficient way of forming a coolable debris bed. Tourniaire *et al.*⁵⁶ have

Table 6 Recent MCCI experiments

Program	Laboratory	Corium	Concrete	Scale (pool volume)	Geometry	Parameters
CCI ⁵⁷ Figure 5	Argonne National Laboratory	Uranium thermite (oxide melt)	Siliceous, limestone– common sand	~80 l	2D (rectangular)	Concrete composition Heating duration Time of top-flooding
VULCANO ^{6,7} Figures 6 and 8	CEA Cadarache (France)	Oxide oxide + metal	Silica-rich, limestone-rich concretes	~5 l	2D (hemicylindrical)	Concrete composition Corium composition
COMET-L ^{58–60}	FZ Karlsruhe (Germany)	Alumino-thermite	Siliceous	Up to 220 l	2D cylindrical	Decay power Flooding
COTELS ⁶¹ Figure 7	NNC Kazakhstan	Oxide + metal	Siliceous	~5 l	2D cylindrical	Concrete/ mortar Flooding
ARTEMIS ^{62,63}	CEA Grenoble (France)	Simulant (salts)	Simulant (salt eutectic)	~12 l	1D–2D cylindrical	Gas bubbling Heat flux
MEK-T1A ⁵ HECLA ⁶⁴	KAERI (Korea) VTT Espoo (Finland)	Alumino-thermite Steel	Basaltic Siliceous, ferro- siliceous	10 l 7 l	1D 2D	Transient test Transient test

performed analytical experiments on this issue and proposed a dedicated model.

2.25.4.2.2 Recent large-scale experiments

Recent experiments on MCCI address mainly two subjects, namely the 2D aspects of the ablation with respect to the axial versus radial erosion and the role of crust formation and melt segregation upon onset of solidification. These subjects are especially important in the analysis of the long-term erosion and cavity formation. **Table 6** summarizes these tests. One of the major findings of these tests with pure oxidic melts on 2D erosion is the observation that dry ablation tests with silica-rich concretes tend to present an anisotropic ablation pattern (**Figures 5 and 6**) – more efficient ablation of the sidewalls compared to downward ablation – with an unsteady ablation rate, whereas the tests with limestone-rich concrete show a more isotropic and steady ablation.

In the short term of MCCI, it has been verified with the thermal concrete–melt interaction experiments (HECLA) (at the Technical research Centre of Finland) experiments⁴⁰ that the arrival of a superheated steel jet will not lead to important concrete attack, as could have occurred if there was spalling.⁶⁵

In the long-term accident situation, the corium melt is expected to form a layered configuration, in which the denser steel layer is located beneath the

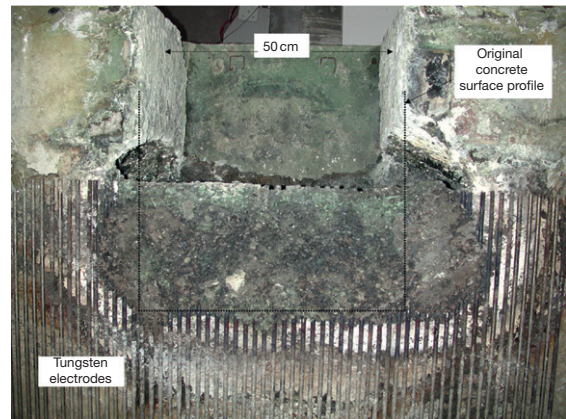


Figure 5 Posttest view of the corium–concrete interaction test 3 showing the anisotropic ablation of a silica-rich concrete. With kind permission from Mitch T Farmer, Argonne National Laboratory, USA.

oxide melt. This situation has been investigated in the COMET-L experiments,^{58–60} (performed at the Karlsruhe research centre, Germany). However, with high-temperature corium melt simulants and an imperfect simulation of the distribution of the decay power and of the density ratio between oxides and metals. It was observed that the lower steel melt forms a crust on the concrete bottom. The crust is partially removed from time to time with periods of higher and lower

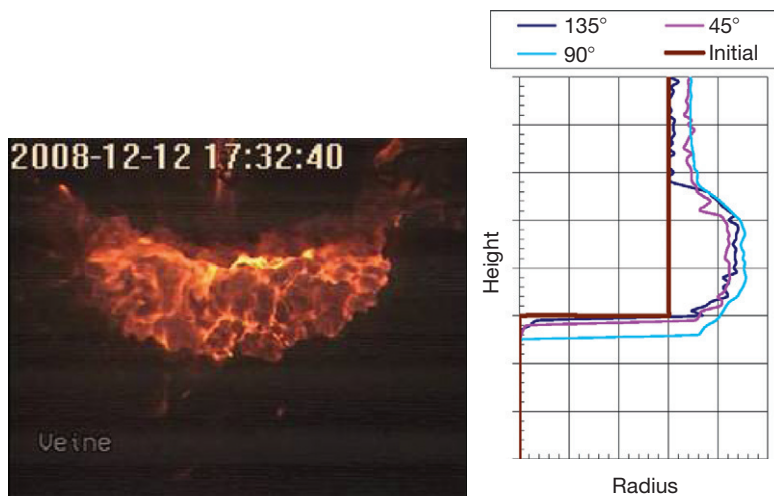


Figure 6 Versatile UO_2 Laboratory for Corium Analysis and Observation experiments with oxidic melts; left, typical view of the hemicylindric cavity filled with corium during the molten core–concrete interaction © CEA, 2008; right, measured posttest profiles for VB-U5 test with a silica-rich concrete.

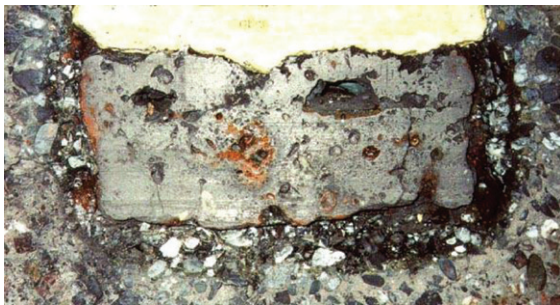


Figure 7 Cut view from a COTELS D8a corium–concrete interaction test in which the interaction was roughly isotropic. With permission from Vladimir S Zhdanov, National Nuclear Center, Kazakhstan.

gas release and varying melt agitation. Late flooding of the upper (oxidic) melt surface has also been investigated to quantify the role of flooding on concrete erosion. The COTELS tests⁶¹ (corium experimental programme in Kazakhstan under Japanese funding) also studied the interaction of concrete with oxide and metal, using prototypic compositions and induction heating. For instance in test D8a with 15% stainless steel, the ablation of the silica-rich concrete was almost isotropic (Figure 7).

Figure 8 presents an example of scanning electron microscope (SEM) micrograph taken near the vertical corium–concrete interface from the Versatile UO_2 Laboratory for Corium Analysis and Observation (VULCANO) VB-U4 test^{6,7} with a silica-rich concrete. It appears that the transport of corium

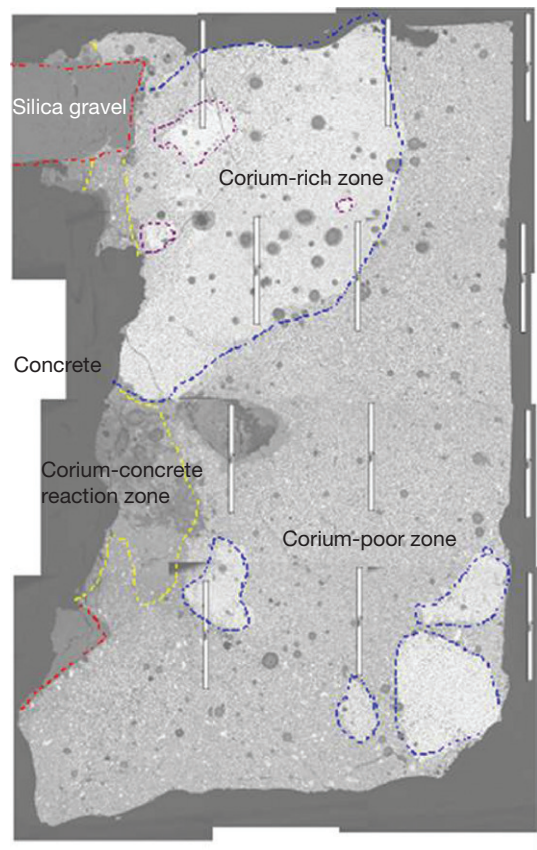


Figure 8 Composite micrograph at the vertical corium–concrete interface in Versatile UO_2 Laboratory for Corium Analysis and Observation test VB-U4 with a silica-rich concrete © CEA, 2006 White Marker Length = 5 mm.

decomposition products is made by convection rather than diffusion; there were fluid masses of two different compositions: a dark corium-poor region with an average composition of around 40 wt% (U,Zr)O₂ mixed with silicon, calcium, and iron oxides and corium-rich regions (in white) with 60–66 wt% (U,Zr)O₂. The lighter corium-poor melt seems to be flowing upward because of Archimedean forces. Unmelted silica gravels are observed (on the left side of the micrograph) and were found entrapped in the corium during dismounting.

At VULCANO facility, a series of experiments has been started to study MCCI with prototypic oxidic and metallic corium, in which the sustained heating is prototypically applied for more than 90% to the lighter oxides, in stratified configurations, thanks to electromagnetic shielding of the induction fields.⁷ Phase separation is observed between the oxidic and metallic layers (Figure 9) even though no real stratification has been observed yet.

2.25.4.2.3 Analytical experiments

Many of the correlations and models used in the computer codes were deduced from results of simulant material experiments that studied specific phenomena in analytical tests. On the basis of physical arguments, such as similarity analysis or detailed modeling, and mostly checked by large-scale experiments described above, these results are transferred to the situation and materials, which exist during the anticipated reactor accident. This section summarizes experiments performed to study heat transfer between volumetric heated pool and porous wall, heat transfer between immiscible liquids, mixing and stratification of immiscible liquids, and interface temperature.

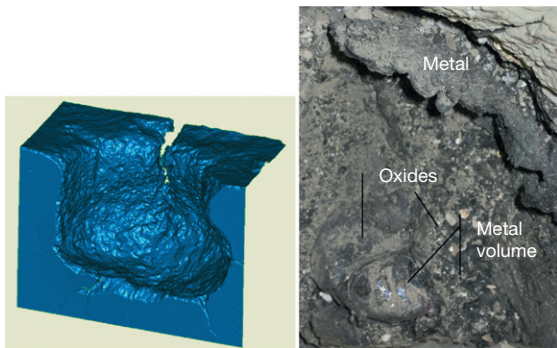


Figure 9 Versatile UO₂ Laboratory for Corium Analysis and Observation metal–oxide test (VBS-U3) © CEA, 2009; left, reconstruction of the concrete scanned surface after ablation; right, metallic volume floating within oxidic pool observed during dismounting.

2.25.4.2.3.1 Heat transfer between a heated pool and a porous wall with gas injection

Numerous separate effect tests,^{66–68} seeking to determine the heat exchange coefficient between a liquid pool and a porous wall with gas injection, have been carried out during the past 30 years. An analysis of these tests shows that the physical properties of the liquids used are often close to those of water, and that the available data mainly relate to horizontal walls.

Data relating to viscous liquids (comparable with concrete-enriched corium) and vertical walls are relatively rare.⁶⁹ It would, however, appear that the heat exchange coefficients for vertical and horizontal walls are broadly similar when water is used^{69,70} while the discrepancy is higher when considering corium melt properties.

2.25.4.2.3.2 Mixing and stratification of immiscible liquids with gas bubbling

Several studies of the mixing and stratification of immiscible liquids with gas bubbling have been carried out with the aim of predicting the configurations (mixed or stratified) of a corium pool during MCCI. Most of the experimental work on this topic has been carried out using simulants,^{71–73} and was restricted to hydrodynamic considerations only (no effects of crusting at the interface; no coupling between heat transfer and gas superficial velocity). This work aimed at determining the mixing and separation thresholds in terms of the superficial gas velocity (or void ratio) as a function of the difference in densities between the two liquids.

Epstein *et al.*⁷² consider that stratification occurs if

$$\rho_L < \frac{\rho_H(1 - \alpha)}{1 + V_L/V_H} \left(1 + \frac{\rho_L V_L}{\rho_H V_H} \right) \quad [19]$$

where V stands for the volume of the heavy (H) and light (L) layers and α is the void fraction.

According to Tourniaire and Bonnet,⁷³ the so-called BALI Stratification Experiment (BALISE) (at Atomic Energy Commission, France) stratification criterion is related to the superficial gas velocity:

$$j_g < 0.054 \frac{\rho_H - \rho_L}{\rho_L} (\text{ms}^{-1}) \quad [20]$$

A review of the data by Tourniaire and Bonnet⁷³ indicates a degree of variance, which can be marked between the results of the various tests. This is partly due to the different physical properties of the liquids

and to the fact that the proposed criteria are not in dimensionless form. Moreover, there are currently no data related to the stratification in presence of bubbling from the side walls.

2.25.4.2.3.3 Heat transfer between two immiscible liquids with gas bubbling

Results related to the heat exchange coefficient between two immiscible liquids through which a gas is passing (the same configuration as in a stratified corium melt) are even rarer.^{74,75} Analysis of the results of these tests reveals a wide scattering in the measurements (by a factor of 5–10), a lack of relevance of the systems being studied (absence of solidification at the interface layer), and no coupling between heat transfer and gas velocity. The experimental procedures are giving rise to a degree of caution. Moreover, it must be noted that no experimental data exist up to now with lateral gas bubbling, even though new work has been launched at Alternative Energies and Atomic Energy Commission (CEA), Grenoble on this issue with the A2BI facility.

2.25.4.3 Remaining Issues

2.25.4.3.1 Material effect on ablation shape

The most unexpected result of the 2D experiments performed, almost at the same time, in the Organization for Economic Cooperation and Development (OECD)–MCCI⁷⁶ and VULCANO programs^{6,7} is that ablation is not always isotropic, as previously assumed. Experiments with limestone-rich concrete (corium–concrete interaction 2, CCI-2, VULCANO VB-U6) present an isotropic ablation, while for silica-rich concretes (CCI-3, VULCANO VB-U4, VB-U5, etc.) the lateral ablation is significantly more pronounced than the downward ablation (with ratios between 3 and 7 depending on tests). In contrast to the dry configurations, in the case of water flooding, downward ablation is favored as water penetration in the degraded concrete walls limits sideward ablation, as observed in the COTELS tests with siliceous concrete.⁶¹

It is thought that the difference of ablation profiles between these two types of concretes could be either due to modification in the melt thermal hydraulics or to the stability of crusts at the different walls. A satisfactory understanding of the role of crusts, their stability, removal, and potential regeneration is however still lacking. Sevón⁷⁷ correlated the heat transfer coefficients with the superficial gas velocities

at the basemat and at the lateral walls for CCI experiments 1–3. He proved that the heat transfer coefficient and the superficial gas velocity followed the same correlation:

$$b = 2096j_g + 49 \quad [21]$$

at the basemat independently of the nature of the concrete (with a deviation of <25%) whereas for the sidewalls the correlation is dependent on the nature of the concrete:

$$b = 5736j_g + 26 \quad [22]$$

for siliceous concretes and

$$b = 3206j_g + 57 \quad [23]$$

for the limestone–common sand concrete test. This suggests that the difference between the two types of concretes comes from phenomena at the sidewalls.

There are several differences between silica and limestone concretes that could explain the different behaviors during their interaction with corium^{6,7,78}:

- Gas releases are larger for limestone-rich concretes and the larger gas superficial velocity has been considered as a possible cause explaining the isotropy with limestone. But, simulant experiments at room temperature⁷⁹ showed that a very small gas superficial velocity (<1 mm s^{−1} in water, a few mm s^{−1} in corium) is sufficient to disrupt thermal stratification and that the thermal flux profiles do not change when the gas superficial velocity is increased;
- Corium–concrete mixtures melting temperatures are usually higher for limestone-rich concretes, but this is not the case with dolomitic (carbonates of calcium and magnesium) concrete which also exhibits isotropic ablation.⁵⁷ Another difference related to melting temperature is the presence of a eutectic valley in the corium–limestone concrete pseudobinary, while it is absent from corium–siliceous concrete pseudobinary;
- Limestone loses a significant part of its condensed mass because of decarbonation; thus, concrete volume shrinks between room temperature and molten state;
- Molten concrete transport properties are quite affected by the fraction of silica which greatly increases viscosity (controlling the flow circulation in the pool) and decreases chemical diffusion coefficient (controlling the dissolution of corium crusts by molten concrete);
- Limestone gravel loses its mechanical strength around 700 °C while silica gravel remains intact

up to 1700 °C and can float inside a corium-mortar melt. The presence of colder gravel may freeze the surrounding corium and increase the crust thickness. For the tests with silica-rich concretes, if all the SEM/energy dispersive X-ray spectroscopy (EDX) window compositions are plotted on a ternary diagram (Figure 10), it appears that the measured data are well aligned. This line does not connect the original composition of the corium melt to that of the molten concrete, but with the mortar composition. Mortar corresponds to (the mixture of cement, water, and sand) corresponds to the material joining the larger gravel and is therefore depleted in silica for concretes made from silica-rich aggregates. These posttest analyses showed that siliceous gravel does not mix well with corium, while limestone gravel, in another test, proved to mix well with corium. It is understood that limestone decarbonation (around 700 °C) completely disrupts the aggregates that can then easily melt and mix with corium.

A series of separate effect tests is underway at VULCANO,⁷⁸ in which corium interacts with specially designed concretes, in order to determine which effect is determinant for the change from isotropic to anisotropic behavior. Then, the relevant modeling will have to be done.

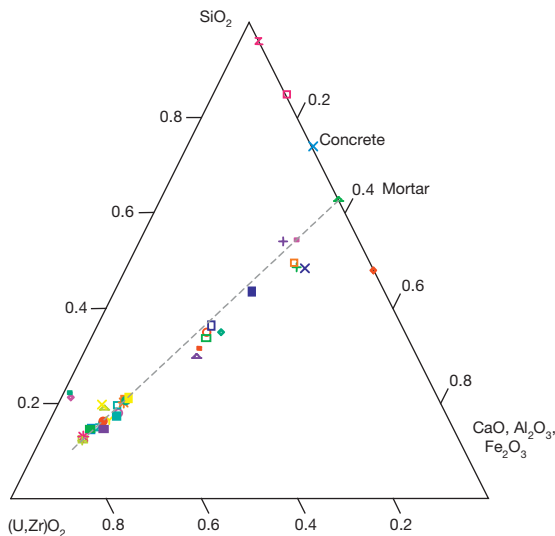


Figure 10 Ternary plot presenting the mass compositions obtained by energy dispersive spectroscopy (EDS) from all the analyzed windows in the Versatile UO₂ Laboratory for Corium Analysis and Observation VB-U4 samples (interaction between corium and a silica-rich concrete).

2.25.4.3.2 Role of metallic layer

Initially, the density ratio between the heavier oxidic phase and the lighter metallic phase is close to 1, and the superficial gas velocity is sufficiently large that it is expected that both phases will form an emulsion. As molten concrete mixes with the oxidic phase of corium, the oxidic liquid phase density decreases and becomes lower than the density of the metallic liquid phase (which keeps a quite stable composition and thus density). According to the stratification criteria,^{72,73} it is expected that the two liquid phases will eventually stratify with metal at the bottom and oxide at the top.

If Greene⁷⁴ correlation for the heat transfer from the oxidic layer to the metallic layer

$$Nu = 1.95 Re^{0.72} Pr^{0.72} \quad [24]$$

(where the Reynolds number is calculated relative to the bubble average diameter and the gas superficial velocity) is applied to a reactor case calculation,⁸⁰ it appears that there is a strong focusing of the heat toward the bottom pool interface and consequently a fast axial erosion (between 5 and 30 cm h⁻¹ of average ablation rate depending on the assumptions) compared to the radial erosion. On the contrary, using the Bain Liquide (BALI) (liquid pool, at Atomic Energy Commission, France) correlation⁴¹ (Table 4) at the oxide-metal interface, gives a much more isotropic ablation profile.⁸¹

Not only are there uncertainties about the heat transfer coefficient at the oxide-metal interface, but the interface temperatures are also an issue and two options may be chosen⁸²:

- Both liquids may be assumed to be in global thermodynamic equilibrium. Then the two layers are surrounded by one refractory crust having one boundary temperature and no crust exists at the oxide-metal interface;
- Both liquids may be bounded by a different crust (no thermodynamic equilibrium between the layers): an oxidic crust for the oxidic pool and a metallic crust for the metallic pool. In this case, the finding of an oxidic crust at the oxide-metal interface is expected. Debris from this crust may sink inside the metallic pool.

As the previous experiments used alumina (which is 3 times less dense than steel) and/or injected power in the metallic phase, the VULCANO oxide-metal test series has been recently launched.⁷ After two tests, no clearly stratified configuration has been observed. In test VBS-U1 with limestone concrete, the metal

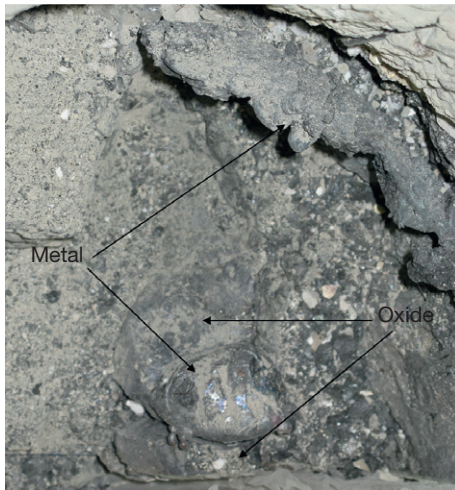


Figure 11 Metallic volumes found during the dismantling of the oxide + metal molten core–concrete interaction test Versatile UO₂ Laboratory for Corium Analysis and Observation VBS-U3 © CEA, 2009.

oxidation was more important than expected and only a very thin metallic layer has been found (in the lowest point of the cavity), while for test VBS-U3 with siliceous concrete, even if the phases were separated, a vertical stratification has not been achieved (Figure 11).

Finally, there is also some doubt on the effective stability of the stratified configuration, because of the coupling between heat transfer and gas generation: if stratification enhances heat transfer, the gas superficial velocity will increase after stratification and may well become sufficiently high for the two phases to mix again.

In summary, because of the many unknowns, a conservative approach is to suppose stratification and enhanced ablation with Greene's correlation at the oxide–metal interface, while Research and Development (R&D) is pursuing on this issue.

2.25.5 Applications to Reactor Scales; Orders of Magnitude

2.25.5.1 MCCI Codes

Codes are the means to capitalize the acquired knowledge and to transpose small-scale experimental results to reactor-scale. The first computer codes to describe the CCI are CORCON – developed by Sandia National Laboratories⁴³ from 1981 to 1993 – and WECHSL – the development of which started at Forschungszentrum Karlsruhe in 1981.⁸³ Table 7

(inspired from Cranga *et al.*⁸¹) presents the major characteristics of the various codes. Allelein and Bürger⁸⁸ have presented a detailed review of MCCI models and codes.

CORQUENCH, MELCOR, and WECHSL/WEX consider that the interface temperature is at the solidus temperature or at an immobilization temperature. On the opposite, TOLBIAC and COSACO fix it at the liquidus temperature, while the user can choose the interface temperature between solidus and liquidus with ASTEC/MEDICIS. It must also be noted that the last three codes present a deep coupling of thermalhydraulics with chemical thermodynamics.

2.25.5.2 Current LWRs

For a typical 900 MWe reactor,⁸⁰ there would be about 100 t of oxidic corium and 50 t of metal. This gives an overall thickness in a 6-m diameter pit of about 1 m (about 1/3 metal, 2/3 oxide) at the beginning. After an erosion of 3 m, the pool thickness increases to about 3 m.

For a 1-m-thick pool and an initial decay heat of 15 MW, a simple calculation with eqn [14] considering isotropic heat flux distribution of 200 kW m⁻² gives an average ablation rate of the order of 0.2 m h⁻¹. The heat flux to extract from the corium is of 500 kW m⁻² if ablation is to be prevented by cavity flooding. This is higher than the dry-out heat flux of 400 kW m⁻² estimated by Lomperski and Farmer.⁸⁹ Moreover, the dry-out heat flux decreases as concrete mixes with corium, because of the effect of concrete material on corium crust cracking behavior.⁸⁹

The time needed to ablate 3 m of a silica-rich concrete basemat ranges between 14 and 222 h (9 days), emphasizing the range of uncertainties, due to the choice of the stratification configuration, of the heat transfer between phases, and of the chosen interface temperature.⁸¹

2.25.5.3 EPR™

Nie⁸ considered that, for a large breach loss of coolant accident (LOCA) scenario in the EPR, 120 t of metallic melt and 185 t of oxidic melt would be released in the reactor pit. The decay heat decreases from 32 MW (3 h after scram) to 20 MW (30 h after scram). Eighty-five percent of the decay heat will be produced in the oxidic melt.

The EPR reactor pit concrete has a special composition including about 35% of hematite (Fe₂O₃)

Table 7 MCCI codes main characteristics

Feature/code	ASTEC/MEDICIS	CORCON	CORQUENCH	COSACO	TOLBIAC	WECHSL/WEX
References	48	44	86	8	87 47	45,88
Thermochemistry database	Interface with thermochemistry module (tabulated)	Correlations	Roche <i>et al.</i> ⁴ data	Coupling with thermochemistry Gibbs energy minimizer	Coupling with thermochemistry Gibbs energy minimizer	Correlations, input table
Pool/crust temperature	User-parameter (linear interpolation or threshold molten fraction) between T_{solidus} and T_{liquidus}	T_{solidus}	T_{solidus}	Specific model between T_{solidus} and T_{liquidus}	T_{liquidus}	$T_{\text{solidus}} < T_{\text{freez}} < T_{\text{liquidus}}$
h_{conv} at pool interfaces	Main available correlations	89	89	BALI/Kutateladze	Main available correlations	FZK models
h_{conv} at oxide/metal interface	Greene \times user's factor	Greene	Not used	BALI (oxide) + Kutateladze (metal)	BALI ⁴¹	77
Configuration evolution	Yes (simple criteria)	Yes (detailed models)	Not used	Yes (simple criteria)	Yes (simple criteria)	No
Corium quenching	Yes	No	Yes	No	Yes detailed	No

and about 40% of SiO_2 ⁴⁰ which has been chosen to promote spreading in a dedicated chamber once the cavity door is ablated.¹ A 50-cm thick concrete door can be ablated in about 2 h,⁸ corresponding to the dissolution of 100 t of concrete in the oxidic corium melt. Through this process, the oxidic melt density almost steadily declines from 8520 kg m^{-3} initially to about 5200 kg m^{-3} at the end of interaction.

2.25.5.4 VVER 1000: AES 2006

In the advanced VVER 1000 designs, corium–concrete interaction is prevented thanks to the presence of a large crucible-type core catcher below the reactor vessel.⁹⁰ About 130 t of oxidic corium and 70 t of molten steel may relocate in this core-catcher, where they would mix with 40 t of oxidic sacrificial material and 50 t of steel sacrificial material. This gives a pool depth of more than 2 m. The sacrificial material ablation phenomenology is somewhat different from that of corium–concrete interaction because of the absence of gas sparging. See **Chapter 2.02, Thermodynamic and Thermophysical Properties of the Actinide Oxides**; **Chapter 2.23, Behavior of LWR Fuel During Loss-of-Coolant Accidents**; **Chapter 2.24, Behavior of Fast Reactor Fuels During Transient and Accident Conditions**; and **Chapter 4.13, Concrete**.

2.25.6 Outlook

Molten Core Concrete Interaction (MCCI) remains a major risk of large (albeit relatively late) releases of radioactivity to the environment in a hypothetical severe accident scenario for current second generation plants. After several decades of research, the 1D ablation between an oxidic melt and concrete is well understood and modeled. Nevertheless there are still significant uncertainties mainly dealing with the 2D ablations profiles and the repartition of oxide and metal phases.⁸¹

R&D programs have been launched to tackle these remaining issues. In particular, a significant joint program of activities is devoted to MCCI within the European Severe Accident network of Activities⁷⁹ and through the OECD/NEA MCCI project. For instance, a Separate Effect Test series with prototypic corium and special concretes has been launched in the VULCANO facility to determine the properties of concrete governing the transition from isotropic to anisotropic ablation profiles.⁶⁴

Another promising approach consists in studying the ways of arresting corium melt progression by water flooding. Top flooding is not very efficient but bottom flooding, using engineered devices that could be used to backfit reactors such as for instance the COMET concept seems promising. In third and fourth generation reactors, the MCCI issue has been eliminated thanks to the use of either in-vessel retention strategies or of ex-vessel core catchers. In some cases like EPR, corium–concrete interaction is then used for temporary retention, bringing the focus to the melt properties at concrete melt through time.

Acknowledgments

The work and effort of the VULCANO experimental and analytical team (V. Saldo, E. Boccaccio, L. Ferry, J. Moneris, G. Fritz, P. Correggio, Y. Bullado, L. Brissonneau, and others) are gratefully acknowledged.

Fruitful discussions with colleagues from EDF, IRSN, FZK, and the whole SARNET2 WP6 team are also acknowledged.

References

1. Fischer, M.; Henning, A. In *Proceedings of ICAPP'09 International Conference on Advances in Nuclear Power Plants*, Tokyo, Japan, May 10–14, 2009; Atomic Energy Society of Japan: Tokyo, 2009; Paper 9061.
2. Leung, C. K. Y. In *Encyclopedia of Materials: Science and Technology*; Buschow, K. H. J., Kahn, R. W., Flemmings, M. C., et al. Eds.; Pergamon: Oxford, 2001; pp 1471–1479.
3. Harmathy, T. Z. *J. Mater.* **1970**, 5, 47–74.
4. Roche, M. F.; Leibowitz, L.; Fink, J. K.; Baker, L., Jr. *Solidus and Liquidus Temperatures of Core–Concrete Mixtures*; U.S. Nuclear Regulatory Commission Report NUREG/CR-6032, Argonne National Laboratory Report ANL-93/9; 1993.
5. Shin, K. Y.; Kim, S. B.; Kim, J. H.; Chung, M.; Jung, P. S. *Nucl. Eng. Des.* **2002**, 212, 233–241.
6. Journeau, C.; Piluso, P.; Haquet, J. F.; et al. *Ann. Nucl. Energ.* **2009**, 36, 1597–1613.
7. Journeau, C.; Bonnet, J. M.; Ferry, L.; Haquet, J. F.; Piluso, P. In *Proceedings of ICAPP'09 International Conference on Advances in Nuclear Power Plants*, Tokyo, Japan, May 10–14, 2009; Atomic Energy Society of Japan: Tokyo, 2009; Paper 9068.
8. Nie, M. Dr. Ing. Thesis, Universität Stuttgart, Germany, 2005.
9. Alarcon-Ruiz, L.; Platret, G.; Massieu, E.; Ehrlacher, A. *Cement Concr. Res.* **2005**, 35, 609–613.
10. Khoury, G. A. *Prog. Struct. Eng. Mater.* **2000**, 2, 429–447.
11. Noumowe, A. Ph.D. Thesis, Institut National des Sciences Appliquées, Lyon, France, 1995.

12. AFNOR. Eurocode 2: Design of concrete structures. Part 1-2: General rules – Structural fire design, French Standard NF EN 1992-1-2. La Plaine Saint Denis: France, 2005.
13. Harada, T.; Takeda, J.; Yamane, S.; Furumura, F. Elasticity and thermal properties of concrete subjected to elevated temperature. In *Proceedings of the International Seminar on Concrete for Nuclear Reactors*; Detroit, MI, 1972; American Concrete Institute, Farmington Hills, MI; Special Publication 34-4, pp 377–406.
14. Vigneresse, J. L.; Barbey, P.; Cuney, M. J. *Petrol.* **1996**, 37, 1579–1600.
15. Akers and McCardell (1989).
16. Farmer, M. T.; Spencer, B. W.; Aeschlimann, R. W. *Wissen. Ber. FZKA* **2000**, 6475, 380–393.
17. Baïchi, M. Ph.D. Thesis, Joseph Fourier University, Grenoble, France, 2001.
18. Pazukhin, E. M. *Radiochemistry* **1994**, 36, 97–142.
19. Bakardjieva, S.; Barrachin, M.; Bechta, S.; et al. *Prog. Nucl. Energ.* **2010**, 52, 84–96.
20. Cheynet, B. NUCLEA; 2007; <http://hal.archives-ouvertes.fr/hal-00165418/en/>.
21. Fukasawa, M.; Tamura, S.; Hasebe, M. J. *Nucl. Sci. Technol.* **2005**, 42, 706–716.
22. Guéneau, C.; Chatain, S.; Dumas, J. C.; et al. FUELBASE: A thermodynamic database for advanced nuclear fuels. In *Proceedings HTR2006: Third International Topical Meeting on High Temperature Reactor Technology*, Johannesburg, South Africa, 2006.
23. Fink, J. K.; Petri, M. C. *Thermophysical Properties of Uranium Oxide*; Argonne National Laboratory Report ANL/RE-97/2; 1997; See also www.insc.anl.gov/matpro.
24. Cohen, I.; Schaner, B. E. J. *Nucl. Mater.* **1963**, 9, 18–52.
25. Journeau, C.; Boccaccio, E.; Brayer, C.; et al. *Nucl. Eng. Des.* **2003**, 223, 75–102.
26. Nelson, S. A.; Carmichael, I. S. E. *Contrib. Mineral. Petrol.* **1979**, 71, 117–124.
27. Hull, F. C. *Met. Prog.* **1969**, 96, 139–140.
28. Crawley, A. F. *Int. Met. Rev.* **1974**, 19, 32–48.
29. Sudreau, F.; Cognet, G. *Nucl. Eng. Des.* **1997**, 178, 269–277.
30. Andrade, E. N. D. C. *Philos. Mag.* **1934**, S17, 497–511, 698–732.
31. Nazaré, S.; Ondracek, G.; Schultz, B. *Wissen. Ber. KfKA* **1976**, 2217, 381–393.
32. Abalin, S. S.; Asmolov, V. G.; Daragan, V. D.; D'yakov, E. K.; Merzlyakov, A. V.; Vishnevsky, V. Yu. *Nucl. Eng. Des.* **2000**, 200, 107–115.
33. Urbain, G. *Steel Res.* **1987**, 58, 111–116.
34. Ramacciotti, M.; Journeau, C.; Sudreau, F.; Cognet, G. *Nucl. Eng. Des.* **2001**, 204, 377–389.
35. Ramacciotti, M. Ph.D. Thesis, Université de Provence, Marseille, France, 1999.
36. Skoutajan, R.; Baukal, W.; König, R.; Wagmar, W.; Walter, G. *Durchführung von Viskositätsmessungen an oxidischen Corium-Beton Schmelzen*; Battelle Institute Report BF-R-63.556-1, Frankfurt/Rhein: Germany, 1979.
37. Llewellyn, E. W.; Mader, H. M.; Wilson, S. D. R. *Proc. R. Soc. Lond. A* **2002**, 458, 897–1016.
38. Wootton, R. O.; Avci, H. I. *MARCH (Meltdown Accident Response Characteristics) Code Description and User's Manual*; Battelle Columbia Laboratory Report BMI-2064, NUREG/CR-1711; 1990.
39. Seiler, J. M.; Froment, K. *Multiphas. Sci. Technol.* **2000**, 12, 117–257.
40. Sevón, T.; Kinnunen, T.; Virta, J.; et al. *HECLA Experiments on Melt-Concrete Interactions: Final Report*; VTT Report VTT-R-08013-09, Espoo, Finland, 2009; pp 295–303, abridged version in <http://www.vtt.fi/inf/pdf/tiedotteet/2009/T2466.pdf>.
41. Bonnet, J. M. Thermalhydraulic phenomena in corium pools for ex-vessel situations: The BALI experiment. In *Proceedings of ICONE 8*, Baltimore, MD, 2000.
42. Foit, J. J.; Reismann, M.; Adroguer, B.; Cenerino, G.; Stiefel, S. *The WECHSL-MOD3 Code: A Computer Program for the Interaction of a Core Melt with Concrete Including the Long Term Behaviour. Model Description and User's Manual*; Forschungszentrum Karlsruhe Report FZKA 5522; 1995.
43. Bradley, D. R.; Gardner, D. R.; Brockmann, J. E.; Griffiths, R. O. *CORCON-Mod3: An Integrated Computer Model for Analysis of Molten Core-Concrete Interactions*; USNRC Report NUREG/CR-5843; 1993.
44. Foit, J. J. *Nucl. Eng. Des.* **1997**, 170, 73–79.
45. Foit, J. J.; Miassaedov, A. *Wissen. Ber. FZKA* **1995**, 5507.
46. Spindler, B.; Tourniaire, B.; Seiler, J. M. *Nucl. Eng. Des.* **2006**, 236, 2264–2270.
47. Cranga, M.; Fabianelli, R.; Jacq, F.; Barrachin, M.; Duval, F. The MEDICIS code, a versatile tool for MCCI modelling. In *Proceedings of the International Congress on Advances in Nuclear Power Plants*, Seoul, Korea, 2005; Paper 5416.
48. Cranga, M.; Mun, C.; Michel, B.; Duval, F.; Barrachin, M. Interpretation of real material 2D MCCI experiments in homogeneous oxidic pool with the ASTEC/MEDICIS code. In *Proceedings of the International Congress on Advances in Nuclear Power Plants*, Anaheim, CA, 2008; Paper 8098.
49. Alsmeyer, H.; Cenerini, G.; Cordkunke, E. H. P.; et al. *Molten Corium/Concrete Interaction and Corium Coolability – A State of the Art Report*; Report EUR 16649 EN; European Commission: Luxembourg, 1995.
50. Thompson, D. H.; Farmer, M. T.; Fink, J. K.; Armstrong, D. R.; Spencer, B. W. *Compilation, Analysis and Interaction of ACE Phase C and MACE Experimental Data*; Report ACES TR-C-14; Argonne National Laboratory: Chicago, IL, 1997.
51. Copus, E. R.; Blose, R. E.; Brockmann, J. E.; Gomez, R. D.; Lucero, D. A. *Core-Concrete Interactions Using Molten Steel with Zirconium on a Basaltic Basemat: The SURC-4 Experiment*; Sandia National Laboratories Report NUREG/CR-4994, SAND87-2008; 1989.
52. Copus, E. R.; Blose, R. E.; Brockmann, J. E.; Simpson, R. B.; Lucero, D. A. *Core-Concrete Interactions Using Molten UO₂ with Zirconium on a Basaltic Basemat: The SURC-2 Experiment*; Sandia National Laboratories Report NUREG/CR-5564, SAND90-1022; 1990.
53. Copus, E. R. Sustained uranium dioxide concrete interaction tests: The SURC test series. In *2nd OECD (NEA) Specialist Meeting on Molten Core Debris – Concrete Interactions*, Karlsruhe, Germany, 1992.
54. Copus, E. R.; Blose, R. E.; Brockmann, J. E.; Simpson, R. B.; Lucero, D. A. *Core-Concrete Interactions Using Molten Urania with Zirconium on a Limestone Concrete Basemat, The SURC-1 Experiment*; Sandia National Laboratories Report NUREG/CR-5443; 1992.
55. Farmer, M. T.; Spencer, B. W.; Kilsdonk, D. J.; Aeschlimann, R. W. Status of large scale MACE core coolability experiments. In *OECD Workshop on Ex-Vessel Debris Coolability*, Karlsruhe, Germany, 1999.
56. Tourniaire, B.; Seiler, J. M.; Bonnet, J. M.; Amblard, M. *Nucl. Eng. Des.* **2006**, 236, 2281–2295.
57. Farmer, M. T.; Lomperski, S. Status and future direction of the MCCI program. In *Proceedings of the European Review Meeting on Severe Accident Research (ERMSAR07)*, Karlsruhe, Germany, 2007.
58. Alsmeyer, H.; Miassaedov, A.; Cranga, M.; Fabianelli, R.; Ivanov, I.; Doubleva, G. The COMET-L1 experiment on long-term concrete erosion and surface flooding.

- In *Proceedings of the 11th International Topical Meeting on Nuclear Reactor Thermal Hydraulics (Nureth 11)*, Avignon, France, 2005.
59. Alsmeyer, H.; Cron, T.; Fluhrer, B.; et al. *The COMET-L3 Experiment on Long-Term Melt-Concrete Interaction and Cooling by Surface Flooding*; Research Center Karlsruhe Report FZKA 7244; 2006.
 60. Sdouz, G.; Mayrhofer, R.; Alsmeyer, H.; et al. *The COMET-L2 Experiment on Long-Term MCCI with Steel Melt*; Research Centre Karlsruhe Report FZKA 7214; 2006.
 61. Maruyama, Y.; Kojima, Y.; Tahara, M.; et al. *Nucl. Eng. Des.* **2006**, 236, 2237–2244.
 62. Guillaumé, M.; Combeau, H.; Seiler, J. M. *Nucl. Eng. Des.* **2009**, 239, 1084–1094.
 63. Veteau, J. M. Experimental investigation of interface conditions between oxidic melt and ablating concrete during MCCI by means of simulating material experiments: The Artemis program. In *Proceedings of the 11 International Topical Meeting on Nuclear Reactor Thermal Hydraulics (Nureth 11)*, Avignon, France, 2005.
 64. Journeau, C.; Bonnet, J. M.; Boccaccio, E.; et al. *Nucl. Technol.* **2010**, 170(1), 189–200.
 65. Connolly, R. J. Ph.D. Thesis, Aston University, Birmingham, 1995.
 66. Blottner, F. G. *Hydrodynamics and Heat Transfer Characteristics of Liquid Pools with Bubbles Agitation*; Sandia National Laboratories Report NUREG CR-0944; 1979.
 67. Deckwer, W. D. *Chem. Eng. Sci.* **1980**, 35, 1341–1346.
 68. Duignan, M. R.; Greene, G. A.; Irvine, T. F. *Chem. Eng. Commun.* **1990**, 87, 185–194.
 69. Felde, D. K.; Kim, H. S.; Abdel-Khalik, S. I. *Nucl. Eng. Des.* **1980**, 58, 65–74.
 70. Tourniaire, B.; Varo, O. Assessment of two-phase flow heat transfer correlation for molten core–concrete interaction study. In *Proceedings of ICAPP'06*, Reno, NV, 2006.
 71. Casas, J. L.; Corradini, M. L. *Nucl. Technol.* **1992**, 99, 104–119.
 72. Epstein, M.; Petrie, D. J.; Linehan, J. H.; Lambert, G. A.; Cho, D. H. *Chem. Eng. Sci.* **1981**, 36, 84–86.
 73. Tourniaire, B.; Bonnet, J. M. Study of the mixing of immiscible liquids by sparging gas: Results of the BALISE experiments. In *Proceedings of the 10th International Topical Meeting on Nuclear Reactor Thermal Hydraulics (NURETH 10)*, Seoul, Korea, 2003.
 74. Greene, D. A. *Experimental Modeling of Heat and Mass Transfer in a Two-Fluid Bubbling Pool with an Application to Molten Core–Concrete Interaction*; Brookhaven National Laboratory Report NUREG-CR 5875, BNL-NUREG-52325; 1992.
 75. Werle, H. *Enhancement of Heat Transfer Between Two Horizontal Liquid Layers by Gas Injection at the Bottom*; Nuclear Research Centre Karlsruhe Report KfK 3223; 1981.
 76. Farmer, M. T.; Lomperski, S. Results of reactor materials experiments investigating 2D core–concrete interaction and debris coolability. In *Proceedings of ICAPP 2004*, Pittsburg, PA, 2004.
 77. Sevon, T. *Nucl. Eng. Des.* **2008**, 238, 2377–2386.
 78. Journeau, C.; Haquet, J. F.; Piluso, P.; Bonnet, J. M. Differences between silica and limestone concretes that may affect their interaction with corium. In *International Conference on Advances Nuclear Power Plants ICAPP'08*, Anaheim, CA, 2008.
 79. Journeau, C.; Haquet, J. F. *Nucl. Eng. Des.* **2009**, 239, 389–394.
 80. Spengler, C.; Allelein, H. J.; Cranga, M.; Duval, F.; Van Dorsselaere, J. P. Assessment and development of molten corium concrete interaction models for the integral code ASTEC. In *Proceedings of EUROSAFE Meeting*, Brussels, Belgium, 2005.
 81. Cranga, M.; Spindler, B.; Dufour, E.; et al. *Prog. Nucl. Energ.* **2010**, 52, 76–83.
 82. Tourniaire, B.; Spindler, B. Simulation of molten core–concrete interaction in oxide/metal stratified configuration with the TOLBIAC-ICB code. In *Proceedings of the International Conference Nuclear Energy New Europe*, Bled, Slovenia, 2005.
 83. Reimann, M.; Murfin, W. B. *The WECHSL-Code: A Computer Program for the Interaction of a Core Melt with Concrete*; Kernforschungszentrum Karlsruhe Report KfK 2890; 1981.
 84. Farmer, M. T. Modelling of ex-vessel coolability with the CORQUENCH code. In *Proceedings of ICONE 9 International Conference on Nuclear Engineering*, Nice, France, 2001.
 85. Gauntt, R. O.; Cash, J. E.; Coel, R. K.; et al. *MELCOR Computer Code Manuals*; Sandia National Laboratories Report SAND2005-5713, NUREG/CR 6119; 2005.
 86. Allelein, H. J.; Arndt, S.; Klein-Heßling, W.; Schwarz, S.; Spengler, C.; Weber, G. *Nucl. Eng. Des.* **2007**, 238, 872–889.
 87. Kutateladze, S. S.; Malenkov, I. G. Boiling and bubbling heat transfer under the conditions of free and forced convection. In *Proceedings of the 6th International Heat Transfer Conference*, Toronto, ON, 1978.
 88. Allelein, H. J.; Bürger, M. *Nucl. Eng. Des.* **2006**, 236, 2220–2236.
 89. Lomperski, S.; Farmer, M. T. *Nucl. Eng. Des.* **2007**, 237, 905–917.
 90. Khabensky, V. B.; Granovsky, V. S.; Bechta, S. V.; Gusarov, V. V. *Nucl. Eng. Technol.* **2009**, 41, 561–574.
 91. Blose, R. E.; Powers, D. A.; Copus, E. R.; Brockmann, J. E.; Simpson, R. B.; Lucero, D. A. *Core–Concrete Interactions with Overlying Water Pools – The WETCOR-1 Test*; Sandia National Laboratories Report NUREG/CR-5907, SAND92-1563; 1993.